Magn Reson Mater Phy (2023) 36:S1–S328
https://doi.org/10.1007/s10334-023-01108-9

ABSTRACTS

Book of Abstracts ESMRMB 2023 Online 39th Annual Scientific Meeting 4–7 October 2023

T1.
Time dependent diffusion and kurtosis of human brain metabolites

A. Döring[1], F. Rösler[2], K. Simsek[1,3], M. Afzali[1,4], R. Kreis[5,6], D. K. Jones[1], J. Valette[7], M. Palombo[1,3]

[1]*Cardiff University, Brain Research Imaging Centre (CUBRIC), Cardiff, United Kingdom;*
[2]*University of Bern, Department of Mathematics, Bern, Switzerland;*
[3]*Cardiff University, School of Computer Science and Informatics, Cardiff, United Kingdom;*
[4]*University of Leeds, Leeds Institute of Cardiovascular and Metabolic Medicine, Leeds, United Kingdom;*
[5]*University of Bern, MR methodology, Institute of Diagnostic and Interventional Neuroradiology, Bern, Switzerland;*
[6]*University of Bern, Translational Imaging Center, Sitem-Insel, Bern, Switzerland;*
[7]*Universite´ Paris-Saclay, CEA, CNRS, MIRCen, Laboratoire des Maladies Neurodégénératives, Fontenay-aux-Roses, France*

Introduction Metabolites are intracellular and cell-type specific and, thus, their diffusion properties can serve as a probe for cellular morphology [1]–[5]. A recent study in mice has shown that brain metabolites" apparent diffusion coefficient (ADC) and kurtosis (K) diffusion-time (TD) dependence, measured with Diffusion-Weighted MR Spectroscopy (DW-MRS), allows cellular morphology to be recovered [6]. In this study, we demonstrate that humans brain metabolites" ADC(TD) and K(TD) can be measured from short to long TDs (6 ms to 250 ms). Moreover, we show that diffusion-modelling can provide morphological information of neuronal and glial cells.

Methods Data acquisition: Measurements were conducted on a 3 T Connectom MR scanner (Siemens Healthcare) with a 32-channel headcoil. Brain metabolite diffusion was measured at: (i) short to intermediate TDs (6,21,37 ms) with semiLASER [5] (TE/TR: 76/3000 ms; b: 200, 1000, 2000, 3000 s/mm^2; Gmax: 254 mT/m, Fig. 1A) and (ii) intermediate to long TDs (50,100,250 ms) with STEAM [7] (TE/TR: 37/3000 ms; b: 200, 1000, 2000, 3000, 6000, 8000 s/mm^2; Gmax: 151 mT/m, Fig. 1B). Sequences were validated in a NIST and Braino phantom (Fig. 1 C&D) [8]. A macromolecular baseline (MMBG) was acquired for STEAM at all TDs using metabolite nulling and moderate diffusion-weighting. Metabolite cycling was used to preserve a water reference, that was used for coil-channel combination, phase-offset, frequency-drift and eddy-current correction and motion compensation [9]. Ten healthy subjects (32.8 ± 3.4 yrs, 7 female) were measured with the VOI (10.0 ± 1.5 mL) in posterior cingulate cortex (Fig. 2 inset).
Analysis, Fitting and Modeling: Metabolite basis-sets were simulated with MARSS [10]. An autoencoder network trained on synthetic data was used for denoising of the MMBG [11]. Basis-sets and MMBG were imported in FiTAID [12] for sequential linear-combination modeling. Two diffusion representation models were implemented in MatLab: (i) ADC alone at low b-values ($\leq$ 3000 s/mm^2), and (ii) ADC and K for the full b-value range. A two-compartment model of fully dispersed cylinder and spheres was implemented to infer on free diffusivity D0, sphere radius RS, cylinder radius RC, and cylinder fraction fC.

Results and Discussion Sequence validation in phantom shows no bias from different diffusion-encoding schemes or sequence types (Fig. 1). The uncertainty in ADC is higher for the strongly J-coupled metabolite myo-inositol, particularly for the spin-echo acquisition at longer TE. The fitting of in vivo spectra shows only minor residuals and allows for an accurate metabolite quantified (Fig. 2).
All metabolites have the same trend with increased ADCs at short TDs $<$ 21 ms and a plateau at long TDs $>$ 50 ms (Fig. 3). The ADCs of the neuronal markers NAA/tNAA are lower than the one for Glu/Glx particularly at short TD. The glial marker ADCs of tCho and mI are similar. All metabolites show by average a trend towards an increased K at longer TDs (Fig. 3).
Tissue modelling shows higher uncertainty (Fig. 3) for the Kurtosis. The mean estimated cellular parameters are: RS = 13.4 μm, RC = 3.0 μm, fC = 0.81 in neuronal and RS = 15.2 μm, RC = 3.5 μm, fC = 0.83 in glial cells. The soma has by average a 4.4-times larger radius than the cylindric cellular processes. The obtained free-diffusivities D0 are approximately 3-times higher than those of the long TD plateau and vary more between neuronal markers.

Conclusion The elevated metabolite ADCs at short TDs indicate a shift in compartmental sensitivity towards smaller cellular structures, while the non-zero plateau at long TD underpins the hypothesis of metabolite diffusion rather in long branched cylinders than small organelles. The increase in Kurtosis with longer TD hints at larger interactions with cellular boundaries.

The faster diffusivity observed for Glu/Glx in comparison to NAA/tNAA cannot be explained by the lower molecular weight alone and might indicate an extracellular Glu/Glx fraction that diffuses faster. Although studies in animals have shown differences in the cellular morphology between neuronal and glial cells, our results point to a uniform cell-structure [6]. This is in line with a different glial morphology in primates than in rodents [2]. The cellular features obtained by the two-compartment model agree with human histology (soma ≈ 10–15 µm, processes ≈ 1–5 µm, fraction of processes ≈ 0.65–0.85) [13].

Here, we demonstrated for the first time that metabolite ADC(TD) and K(TD) can be measured in vivo in the human brain and that reasonable microstructural information can be obtained.

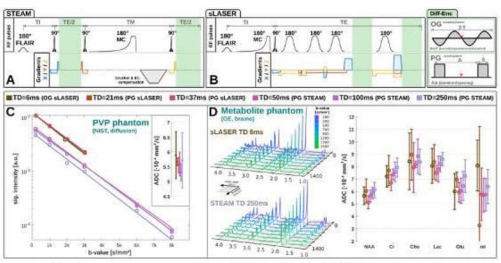

Fig. 1: A&B: Sequence diagrams of the STEAM and semiLASER sequence with pulsed and oscillating diffusion encoding (green box). C&D: Sequence validation in NIST and Braino phantom shows good agreement between sequence type (stimulated echo vs spin echo) and diffusion encoding strategy (PG vs OG).

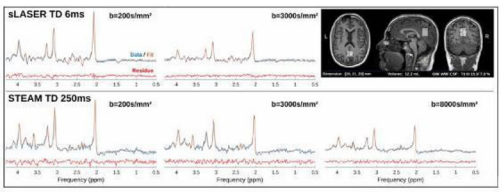

Fig. 2 Diffusion spectra acquired with semiLASER at shortest and STEAM at longest diffusion-times (blue), the fitting results (orange) and remaining residuals (red) in an exemplarily chosen subject (right inset).

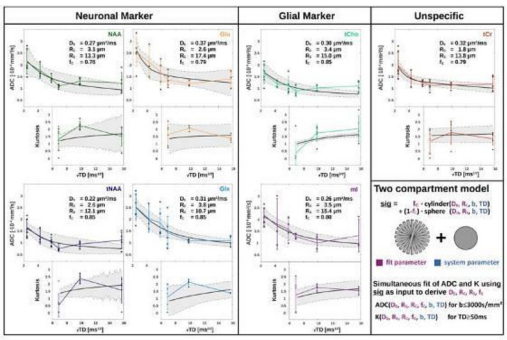

Fig. 3: Diffusion characteristics (ADC[TD] and K[TD]) of human brain metabolites for neuronal and glial markers, and tCr as non-cell-type specific metabolite. A two-compartment model of fully dispersed cylinders and spheres was used to infer on microstructural features (spherical radius RS, cylinder Radius RC, cylinder fraction fC and free diffusivity D0).

References

[1] Novikov, et al., 2014.
[2] Palombo, et al., 2016.
[3] Ligneul, et al., 2017.
[4] Valette, et al., 2018.
[5] Döring, et al., 2019.
[6] Mougel, et al., 2022.
[7] Brandejsky, et al., 2015.
[8] Palacios, et al., 2017.
[9] Döring, et al., 2018.
[10] Landheer, et al., 2019.
[11] Rösler github.com/frank-roesler.
[12] Adalid, et al., 2017.
[13] Olesen, et al., 2022.
[14] Jelescu, et al., 2022.

T2.
DW-special: A new sequence for rodent diffusion-weighted MRS at high magnetic field

J. Mosso[1,2,3], D. Simicic[2,3], B. Lanz[2,3], R. Gruetter[1], C. Cudalbu[2,3]

[1]*École Polytechnique Fédérale de Lausanne (EPFL), Laboratory of Functional and Metabolic Imaging (LIFMET), Lausanne, Switzerland;*
[2]*École Polytechnique Fédérale de Lausanne (EPFL), CIBM Center For Biomedical Imaging, Lausanne, Switzerland;*
[3]*École Polytechnique Fédérale de Lausanne (EPFL), Animal Imaging and Technology, Lausanne, Switzerland*

Introduction In vivo diffusion-weighted magnetic resonance spectroscopy (dMRS) has emerged as a powerful technique to probe tissue morphology at the micrometre scale and in a cell-specific manner via the non-invasive assessment of metabolite diffusion properties[1,2]. The STE-LASER sequence[3], consisting of a stimulated echo (STE) diffusion module followed by a LASER localization, has become the gold-standard for rodent dMRS studies at high field. In addition to preserving the advantages of diffusion-weighted STEAM, its block-design yields a sharp voxel selection with the absence of cross-terms. However, STE-LASER suffers from a long minimum echo time. In the present work, we aimed at improving the detection and subsequent estimation of the diffusion properties of strongly J-coupled metabolites in dMRS acquisitions at high field. To do so, we developed a new dMRS sequence, named DW-SPECIAL, based on the semi-adiabatic SPECIAL sequence[4] used for single-voxel spectroscopy, which benefitted from the same advantages as STE-LASER while reducing the minimum achievable echo time.

Methods DW-SPECIAL (**Fig. 1**) combines a STE diffusion block with a semi-adiabatic SPECIAL localization: the first 90° pulse of the STE was rendered slice-selective, an on/off slice-selective adiabatic inversion was inserted in the mixing time and two 180° slice-selective adiabatic pulses placed after the STE block. Diffusion gradients were inserted in the STE block in a bipolar fashion. Acquisitions with DW-SPECIAL and STE-LASER were performed at 14.1 T (diffusion time: 43 ms, 5 b-values between 0.05 and 10 ms/µm^2) in vivo on the rat brain (N = 5, voxel size: 7 × 5 × 5 mm^3), using the shorter achievable TE for each sequence. After LCModel quantification, the apparent diffusion coefficients and intra-stick diffusivities (Callaghan's model[5]) were fitted and compared between the sequences for glutamate (Glu), glutamine (Gln), myo-inositol (mIns), taurine (Tau), total N-acetylaspartate (tNAA), total choline (tCho), total creatine (tCr) and the mobile macromolecules (MM).

Results and discussion The shorter echo time achieved with DW-SPECIAL (18 ms against 33 ms with STE-LASER) limited the metabolites' signal loss caused by J-evolution (Fig. 2). In addition, DW-SPECIAL preserved the main advantages of STE-LASER: absence of cross-terms, diffusion time during the STE and limited sensitivity to B_1 inhomogeneities with the use of adiabatic pulses. Interestingly, although DW-SPECIAL did not retain the block-design of STE-LASER, the absence of cross terms in the b-value was ensured as long as the two stripped gradients on **Fig. 1** did not overlap. In vivo, compared to STE-LASER, DW-SPECIAL yielded the same spectral quality (Fig. 2) but improved the within group

homogeneity of diffusion decays for all quantified metabolites, most strikingly for Gln (**Fig. 3**). Metabolites' diffusion estimates were in good agreement between the two sequences and DW-SPECIAL reduced the standard deviation of the diffusion estimates based on individual animal fitting without loss of accuracy compared to the fit on the diffusion decay averaged across animals (**Fig. 4**). Due to its 1D ISIS scheme, DW-SPECIAL might be sensitive to motion. While this is in general not a problem in rodent experiments where the head of the animal is fixed by a stereotaxic system, special care should be taken for clinical translation.

Conclusion We conclude that due to its shorter echo time, DW-SPECIAL can serve as an alternative to STE-LASER for rodent high field dMRS when strongly J-coupled metabolites like Gln are investigated, thereby extending the range of accessible metabolites in the context of dMRS acquisitions.

Acknowledgements Supported by the European Union's Horizon 2020 research and innovation program under the Marie Sklodowska-Curie grant agreement No 813120 (INSPiRE-MED), the SNSF projects no 310030_173222, 310030_201218 and the Leenaards and Jeantet Foundations. We thank Stefanita Mitrea and Dario Sessa for the BDL surgeries, Analina Da Silva and Mario Lepore for veterinary support, Thanh Phong Lê for technical support and Vladimir Mlynarik for experimental advice.

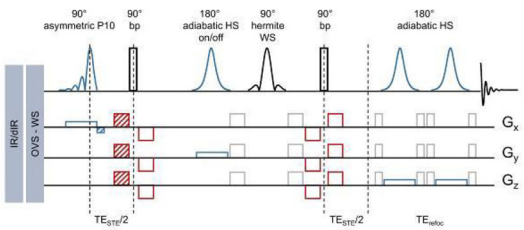

Fig. 1: DW-SPECIAL sequence design. RF pulses from the semi-adiabatic SPECIAL sequence are highlighted in blue. Gradients: blue - slice-selection, red - diffusion, grey - spoiler/crusher. Stripped gradients should not overlap to prevent cross-terms.

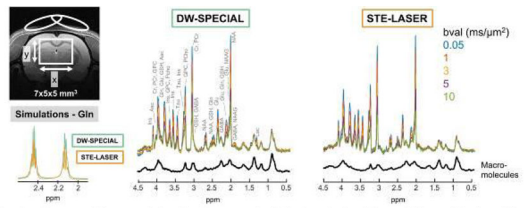

Fig. 2: Representative voxel location in one animal, basis-set simulation of Gln and in vivo diffusion sets for both sequences, after pre-processing (ECC, phase/frequency drifts correction, outlier removal, LB = 2 Hz). Macromolecules are displayed in black.

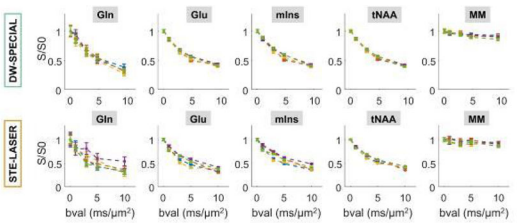

Fig. 3: dMRS signal decays of Gln, Glu, mIns, tNAA and MM as a function of the b-value for all the animals (different colors) and both sequences, normalized to their value at b = 0.05 ms/μm². Error bars: absolute Cramer Rao Lower Bounds from LCModel quantification.

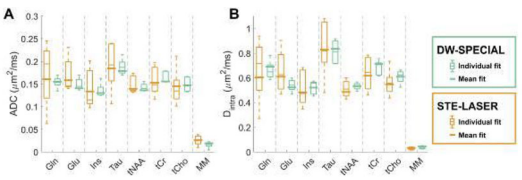

Fig. 4: ADC **(A)** and D_{intra} **(B)** fitted for all animals with both sequences. Box plots: individual fit for each animal. Wide bar: fitted ADC and D_{intra} on the averaged concentration decay over all animals ("mean fit").

References

1. Ronen I et al., *EMagRes*. American Cancer Society; 2015:733–750.
2. Palombo M et al., *NeuroImage*. 2018;182:97–116.
3. Ligneul C et al., *Magn Reson Med*. 2017;77(4):1390–1398.
4. Mlynárik V et al., *Magn Reson Med.* 2006;56(5):965–970.
5. Callaghan PT et al., *Biophys J*. 1979;28(1):133–141.

T3.
Comparison of ^{1}H localized DEPT sequence for ^{13}C MRS at 7 T: STEAM-DEPT vs ISIS-DEPT

Y. Xiao[1,2], B. Lanz[1], D. Wenz[1], L. Xin[1]

[1]*École Polytechnique Fédérale de Lausanne (EPFL), CIBM Center For Biomedical Imaging, Lausanne, Switzerland;*
[2]*École Polytechnique Fédérale de Lausanne (EPFL), Laboratory of Functional and Metabolic Imaging (LIFMET), Lausanne, Switzerland*

Introduction The combination of ^{1}H localization and distortionless enhancement by polarization transfer (DEPT)[1] can provide an enhanced ^{13}C signal as well as excellent localization for studying the cerebral metabolite. The widely used ISIS[2]-combined DEPT is susceptible to subject motion artifacts. To address this issue, PRESS-DEPT[3] has been developed. However, its in vivo application at ultra-high field (UHF) is limited by high local power depositions and large chemical shift displacement errors. In contrast to ISIS and PRESS, STEAM provides better localization performance, lower SAR and CSDEs, and shorter TE against signal loss through T_2 relaxation[4]. Though it only provides half of the proton polarization, with a lower RF power demand it enables faster repetition and potentially improves temporal SNR. As STEAM is a single-shot technique, it is less susceptible to motion artifacts relative to ISIS. In this study, we implemented STEAM-DEPT and compared it with ISIS-DEPT. Phantom experiments showed signal enhancement efficiency. Natural abundance ^{13}C of myo-inositol (mI) was measured in the human occipital lobe to explore temporal SNR (SNR/t) with ISIS-DEPT and STEAM-DEPT.

Methods Hardware MR measurements were performed on a 7 T human MR scanner (Siemens Medical Solutions, Erlangen, Germany) with a dual-tuned quadrature ^{1}H (2 circular loops, 9 cm diameter)-quadrature ^{13}C surface coil (2 circular loops, 6 cm diameter)[5].

Pulse sequences The ISIS-DEPT and STEAM-DEPT sequences were implemented as shown in Fig. 1. HS_4 and 90° asymmetric pulse durations are 3.5 ms and 1.6 ms, with excitation bandwidths of 5.0 kHz and 2.4 kHz at $\gamma B_1/2\pi$ of 1.0 kHz. TE for STEAM is set at a minimum of 4.5 ms. Hard pulses (200 μs rectangular pulses for 90° excitation) were used for ^{1}H and ^{13}C channels in the DEPT sequence. A delay of 100 μs was applied to the ^{13}C frequency pulses after ^{1}H pulses. An experimentally optimized pulse delay of 3.8 ms was used and the last ^{1}H pulse flip angle θ was set to 90° for optimal enhancement of CH groups in mI.

Phantom A phantom containing 114 mM of mI in the 1.5 L dPBS solution was prepared. Phantom spectra were acquired with ISIS-DEPT, STEAM-DEPT, and 3D-ISIS (TR = 5 s, 128 averages, bandwidth = 20 kHz, 4096 pts, ^{13}C carrier frequency offset at 71 ppm) within a 3.6 × 2 × 3.6 cm^3 voxel located near the coil surface.

Subjects In vivo measurements were performed on two healthy volunteers (females; 19 and 24 years) with the informed consent provided in accordance with the Swiss cantonal ethics committee. Each subject was scanned with both ISIS-DEPT (TR = 5 s, 272 averages) and STEAM-DEPT (TR = 2 s, 700 averages) with the same VOI (10 × 5 × 8 cm^3) in the occipital. Each protocol took around 23 min, and other scanning parameters were the same as those used in phantom experiments.

Post-processing All spectra were processed in Matlab R2021b for coil combination, frequency shift correction, phase correction, averaging, zero-filling to 8096 pts, and apodization. Signal intensity (S_{mI}) was calculated as the average height of mI resonances and the noise level (N) was determined by the standard deviation of noise in the 80–100 ppm spectral range.

Results Phantom spectra shown in Fig. 2 were acquired with three sequences (ISIS-DEPT, STEAM-DEPT, and 3D-ISIS). The absence of decoupling causes the splitting of all six carbons of mI (the center of C5 at 75.1 ppm, C1/C3 at 73.3 ppm, C2 at 73.1 ppm, and C4/C6 at 71.9 ppm), resulting in doublet separations due to J_{CH} (∼ 150 Hz). The signal enhancement of ISIS-DEPT and STEAM-DEPT, compared to 3D-ISIS, is 3.3 and 1.8 times, respectively, corresponding to the theoretical factor of γ_H/γ_C. In vivo spectra were the average of the two subjects (Fig. 3). The measured S_{mI}/N is 13 with ISIS-DEPT and 12 with STEAM-DEPT in 46 min.

Discussion The phase of the θ pulse was alternated to eliminate unwanted ^{13}C signals. This necessitated a 16-step phase cycling for ISIS-DEPT and 2-step for STEAM-DEPT, making the latter less sensitive to subject motion. TRs were established by the minimal requirement for optimal B1 at 6 cm from the surface coil, considering SAR limitations for in vivo usage with the present RF coil. While STEAM-DEPT can reach a TR of 1–2 s, ISIS-DEPT typically requires 3.5–5 s due to higher SAR deposition led by the usage of adiabatic full passage pulses. Despite half the signal intensity in STEAM, STEAM-DEPT has the advantage of lower power deposition at UHF, allowing for 2.5 to 4 times faster repetition than ISIS-DEPT, which provides a comparable temporal SNR.

Conclusion STEAM-DEPT provides adequate signal enhancement and comparable temporal SNR to ISIS-DEPT. Additionally, STEAM-DEPT is less susceptible to subject motion, making it a promising option for in vivo ^{13}C dynamic measurements which usually were conducted over a long duration at UHF.

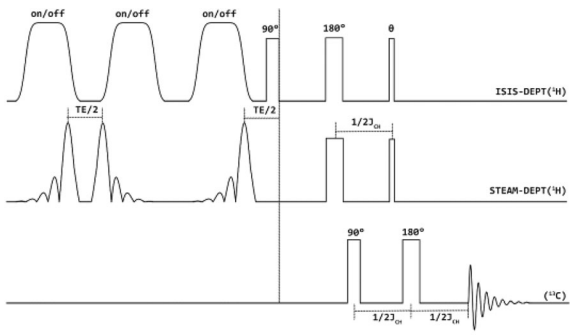

Fig. 1: ISIS-DEPT and STEAM-DEPT sequence diagram.

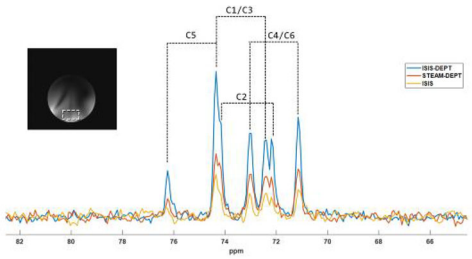

Fig. 2: Experimentally acquired ^{13}C MR spectra with ISIS-DEPT, STEAM-DEPT, and 3D-ISIS from the Myo-inositol phantom (3.6x2x3.6cm^3 voxel, TR=5s, BW=20kHz, 4096pts, 128 averages).

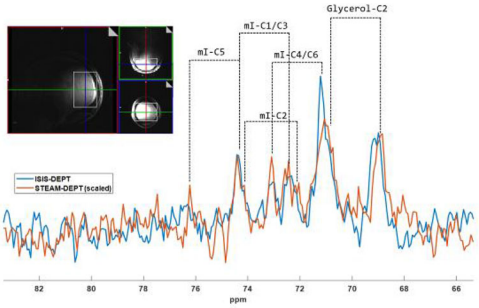

Fig. 3: Voxel localization and in vivo spectra measured in the human occipital lobe with ISIS-DEPT and STEAM-DEPT (n=2, BW=20kHz, 4096pts, in total 46 minutes acquisition for both sequences; TR=5s, 544 averages for ISIS-DEPT; TR=2s, 1400 averages for STEAM-DEPT). The spectrum acquired by STEAM-DEPT was scaled according to the peak height of mI-C1/C3 at 74.4 ppm.

References

1. Doddrell et al. (1982)
2. Ordidge et al. (1986)
3. Chen et al. (2013)
4. Öz et al. (2021)
5. Roig et al. (2015)

T4.
Analysis of multi-center ^1H-MRSI data of the prostate with multivariate curve resolution for localisation and aggressiveness prognosis of cancer lesions

A. Stamatelatou[1], C. G. Bertinetto[2], J. Jansen[2], G. Postma[2], K. Selnæs[3], T. Bathen[3], A. Heerschap[1], T. Scheenen[1]

[1]Radboud University Medical Center, Nijmegen, The Netherlands;
[2]Radboud University, Nijmegen, The Netherlands;
[3]Norwegian University of Technology and Science, Trondheim, Norway

Introduction The Multivariate Curve Resolution (MCR) approach is an easily interpretable model to reconstruct the relative intensities of spectral profiles of individual chemical components within a sample[1]. We previously showed the feasibility of the method in a small cohort of prostate ^1H MRSI data for automated localization of cancer and healthy tissue[2]. In this work, we apply the MCR method to multi-center 3D ^1H MRSI data of over 100 patients with prostate cancer and assess its potential to classify MR spectra according to prostate cancer aggressiveness.

Methods Multi-center prostate cancer 3D PRESS ^1H MRSI data from 8 centers[3,4] were included in this study, participating in the PCaMAP trail acquired on 3 T MR systems (MAGNETOM Trio and Skyra, Siemens Healthcare, Erlangen, Germany). This cohort was supplemented with 14 patients with higher-grade tumours[4]. Spectra from 63

patients (6 centers), were used as a training set, and spectra from 43 subjects (8 centers) as a test set. In previous work, expert radiologists blinded from spectra assigned voxel positions as cancerous or benign in all patients, on the basis of histopathology slides visually matched with T2-weighted images[5]. This combination of voxel location and histopathological assignment was used as the gold standard in the test set.

Magnitude spectra ($n = 49{,}776$) in the spectral range of interest (2–4 ppm) of the patients from the train set were used to perform MCR, which models the data **X** as a linear mixture of components: **X = CS**, where **C** and **S** are matrices of the pure components' relative abundances and their respective spectral profiles. These profiles are obtained by imposing mathematical constraints based on physico-chemical principles (i.e. non-negativity)[6]. The initial profiles were iteratively optimized using the MCR-Alternating Least Squares (MCR-ALS) method[1], imposing a non-negativity constraint.

Two experienced spectroscopists interpreted the model's components to patterns of *in-vivo* spectroscopic shapes[7]. The component with the highest intensity in the Choline ppm region (Fig. 1a -S5) was assigned as most suspicious for the presence of cancer. The relative intensities of each component for each voxel were normalized across all voxels from the patients in the test set, and mapped slice-by-slice for a qualitative validation of the model, using the histopathology reports as gold standard. A t-test statistical comparison was performed for the relative intensity of the tumorous component (S5) between benign and tumor voxels. An ANOVA statistical analysis was performed within the tumor-assigned voxels, separating them according to the latest Gleason Grade Group (GG) classification of prostate tumors[8] (GG1, Gleason score ≤ 6; GG2, Gleason score $3 + 4 = 7$; GG3, Gleason score $4 + 3 = 7$; GG4, Gleason scores $4 + 4 = 8$, $3 + 5 = 8$ and $5 + 3 = 8$; GG5, Gleason scores 9–10). The aim was to investigate the correlation of the relative intensity of the tumorous component with the Grade Group. Of note: no quality control of the spectra in the test set was applied: all radiologically selected voxels (blinded from spectra) were used.

Results/Discussion The optimal number of components, as assessed by SVD, was 5 for the training set (Fig. 1). We assigned the spectroscopic profiles of S1 and S2, with relatively high intensity in the Cit ppm range, to spectra for benign tissue (Fig. 1b). The spectroscopic profile of S5 (Fig. 1a), with elevated intensity in the Cho ppm range, was assigned as representative for tumor spectra (Fig. 1b).

One example of mapping the relative intensity of components S1 + S2 and S5 is presented for a slice in a patient with a GG5 tumor (Fig. 2). The quantitative assessment showed that the S5 component significantly discriminates ($p < 0.01$) between voxels from benign and tumorous tissue (Fig. 3).

For the tumor voxels that were separated into the 5 Gleason Grade Groups, the ANOVA statistical analysis showed a significant correlation between the relative intensity of the S5 component with tumor aggressiveness (Fig. 4).

Conclusion MCR-ALS can be used for the extraction of common spectroscopic components without the need of prior knowledge. The components, extracted from multi-center data, can be used to classify prostate spectra without quality control as benign and tumorous. Additionally, the method can assess tumor aggressiveness. Altogether, our approach can be considered as a step towards the development of an automated tool for the classification of prostate MRSI spectra as tumorous and benign, as well as to assess tumor aggressiveness.

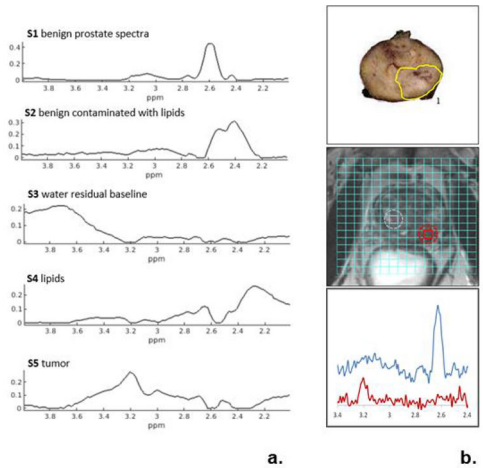

Fig. 1: **a.** Spectroscopic profiles of the MCR extracted components **b.** Examples of in vivo MR spectra from a patient with an aggressive tumor in the left peripheral zone of the prostate (yellow region on macroscopic slide picture). Red spectrum: voxel within tumor tissue, Blue spectrum: healthy transition zone tissue.

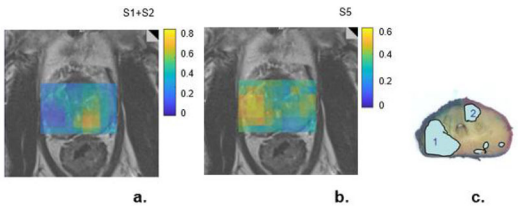

Fig. 2: Relative intensity maps of a slice including an aggressive tumor a. benign components S1+S2 and b. the tumorous component S5 c. Histopathology of the closest matching slice. Lesion 1 is a Grade Group 5 tumor and lesion 2 is a Grade Group 1 tumor.

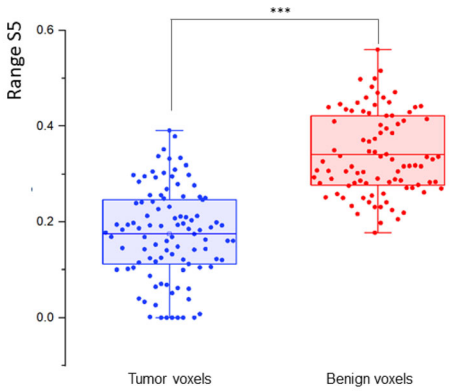

Fig. 3: Box plot of the tumorous component S5 in tumorous assigned voxels (N=91) and in benign assigned voxels (N=101) of the test set.

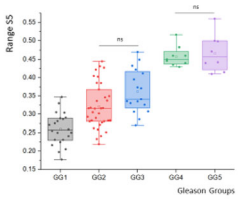

Fig. 4: Box plot of the relative intensity of the tumorous component S5 in tumorous assigned voxels separated in the 5 Gleason Grade Groups (N-GG1= 22, N-GG2 = 35, N-GG3=17, N-GG4=9, N-GG5=8). All groups differed significantly at a high level ($p < 0.001$), except for the cases indicated in the figure.

References
1. https://doi.org/10.1039/c4ay00571f
2. *Proc 31st Annual Meeting ISMRM.*; 2022.
3. *PCa-MAP; ClinicalTrials.Gov Identifier NCT01138527.*
4. https://doi.org/10.3389/fonc.2018.00516
5. https://doi.org/10.1097/RLI.0000000000000558
6. https://doi.org/10.1002/cem.3000
7. https://doi.org/10.1007/s10334-022-01011-9
8. https://doi.org/10.1016/j.eururo.2015.06.046

Acknowledgments This research was supported by EU ITN Marie-Sklodowska-Curie Grant 813120 (INSPiRE-MED).

T5.
Enhanced sensorimotor GABA level and functional connectivity in older adults through balance learning

X. Liu[1,2,3], S. Scherrer[4], S. Egger[4], S. I. Lim[2,3], B. Lauber[4], W. Taube[4], L. Xin[2,3]

[1]*École Polytechnique Fédérale de Lausanne (EPFL), Laboratory of Functional and Metabolic Imaging (LIFMET), Lausanne, Switzerland;*
[2]*École Polytechnique Fédérale de Lausanne (EPFL), Animal Imaging and Technology, Lausanne, Switzerland;*
[3]*École Polytechnique Fédérale de Lausanne (EPFL), CIBM Center For Biomedical Imaging, Lausanne, Switzerland;*
[4]*University of Fribourg, Department of Neurosciences and Movement Science, Fribourg, Switzerland*

Introduction The acquisition of motor skills has been shown to elicit widespread structural, functional, and metabolic changes throughout the human brain. Of particular interest is the role of γ-aminobutyric acid (GABA) being the primary inhibitory neurotransmitter in the brain. The modulation of GABA has been reported to be associated with resting-state sensorimotor network connectivity (SNC) as measured by functional magnetic resonance imaging (rs-fMRI) in young adults[1,2]. However, it is not clear how GABAergic modulation of intrinsic neural activity is organized in elderly population known to have reduced levels of GABA and SNC[3–5], accompanied by deterioration in motor performance. In particular, it remains elusive (1) how the interplay between GABA and resting brain activities adapts with advancing age, and (2) whether motor learning can elicit comparable modulatory effects on functional connectivity and metabolism in older individuals.

In this study, we seek to address these questions by examining longitudinal effects of balance learning on the MRS-measured GABA level and on SNC in a group of older adults in contrast to a resting control group.

Methods Thirty-one healthy volunteers (65–82 years old) gave informed consent prior to the study including 7 T MR measurements (Siemens, Erlangen, Germany) before and after balance learning. A 0.6 × 0.6 × 0.6 mm MP2RAGE sequence was used to acquire structural images. Localized 1H single-voxel spectra from the sensorimotor cortex were acquired by MEGA-sSPECIAL[6]. Furthermore, whole-brain fMRI was performed with a gradient-echo EPI sequence with voxel dimension 1.3 × 1.3 × 1.3 mm. After the first MR session, the learning group underwent three months of progressive, multifaceted balance training for 3 times per week in supervised group sessions. The control group was instructed to maintain their original lifestyle. After three months, both groups underwent the second MR session with identical protocols.

MR spectra were frequency drift, phase and tissue composition corrected and unsuppressed water signal was used for metabolite quantification. Resting-state fMRI data were corrected for head motion and distortion, normalized to MNI space, smoothed, regressed out residual signal and high-pass filtered. Processed fMRI images across all sessions are concatenated together to a 4D time series where a dual-regression approach was used to derive individual-level mean SNC[1]. Between-group difference in GABA levels and SNC before and after training were tested using mixed-design ANOVA followed by post-hoc ANCOVA and t-tests. The relationship between GABA and SNC baseline levels and changes were tested using Pearson's correlation.

Results Demographic information for the participants and spectral quality parameters are shown in Fig. 1. Figure 2 shows MRS voxel location and the identified resting-state sensorimotor network. Figure 3 shows changes in GABA levels and SNC in both groups. Mixed-design ANOVA revealed a significant interaction effect between outcome and time for both GABA levels and SNC, respectively (GABA $p = 0.02$, SNC $p = 0.002$). Post-hoc analysis found that this is driven by a significant increase in GABA and SNC in learning group (GABA $p = 0.004$, SNC $p = 0.003$). No significant correlation was found between GABA and SNC either for baseline or change ($p > 0.1$).

Discussion Our finding that long-term balance learning results in increased GABA and SNC suggests that the age-related decline in cortical GABA level and functional connectivity can be reverted (at least partly) by 3 months of learning balance tasks. However, the observed increase in GABA and SNC and their corresponding baseline levels do not correlate which is in slight contrast to prior research[1,2]. It might be speculated that the link between GABAergic modulation and functional connectivity is disrupted as a result of aging. Most importantly, the current study demonstrated that long-term balance learning can enhance sensorimotor inhibitory tone and improve connectivity within the sensorimotor network in elderly population.

	Learning Group	Control Group
Age	72.2 ± 4.2	70.8 ± 4.9
Gender	8M / 8F	6M / 9F
GABA SNR (Pre)	9.36 ± 3.3	7.46 ± 2.3
GABA SNR (Post)	10.41 ± 3.1	8.87 ± 2.6

Fig. 1: Demographics and data quality metrics for pre- and post- measurements. GABA SNR is calculated using GABA peak height divided by noise standard deviation between 9.5 to 10 ppm. There is no significant difference in SNR between two measurements.

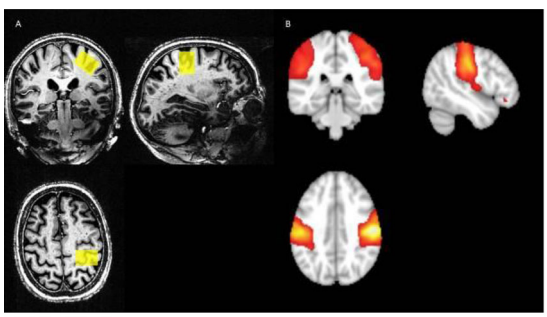

Fig. 2: (A) Exemplar voxel placement for motor cortex. (B) Group-level resting-state sensorimotor network identified in current population by performing group level independent component analysis (ICA) on concatenated data from all subjects and all scans.

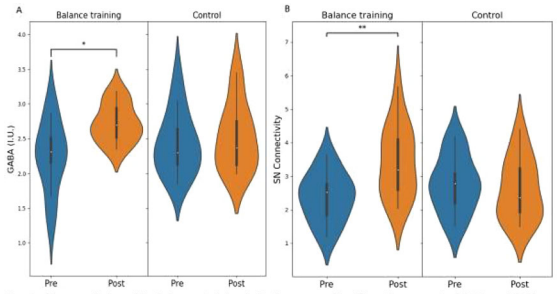

Fig. 3: Changes induced by balance training in both groups. Significant increase in GABA and SNC are observed in training group but not in control group.

References

1. Stagg, C. J. et al. Local GABA concentration is related to network-level resting functional connectivity. *Elife* **2014**, 1–9 (2014).
2. Sampaio-Baptista, C. et al. Changes in functional connectivity and GABA levels with long-term motor learning. *Neuroimage* **106**, 15–20 (2015).
3. Pauwels, L., Maes, C. & Swinnen, S. P. Aging, inhibition and GABA. *Aging (Albany. NY).* **10**, 3645–3646 (2018).
4. Hermans, L. et al. Brain GABA levels are associated with inhibitory control deficits in older adults. *J. Neurosci.* **38**, 7844–7851 (2018).
5. Cassady, K. et al. Sensorimotor network segregation declines with age and is linked to GABA and to sensorimotor performance. *Neuroimage* **186**, 234–244 (2019).
6. Lim, S. I. & Xin, L. γ-aminobutyric acid measurement in the human brain at 7 T: Short echo-time or Mescher–Garwood editing. *NMR Biomed.* 1–17 (2022) https://doi.org/10.1002/nbm.4706.

T6.
Metabolomic fingerprinting of Alzheimer's disease spectrum by brain proton MR spectroscopy

A. Dell'Orco[1,2], L. Göschel[1,3], S. Hilleke[1], L. T. Rieman[2], S. Aydin[2], B. Ittermann[2], A. Tietze[1], M. Scheel[1], A. Fillmer[2]

[1]*Charité Universitätsmedizin Berlin, Department of Neuroradiology, Berlin, Germany;*
[2]*Physikalisch-Technische Bundesanstalt (PTB), Braunschweig and Berlin, Germany;*
[3]*Charité Universitätsmedizin Berlin, NeuroScience Clinical Research Center, Berlin, Germany*

Introduction Alzheimer's disease (AD) is the primary cause of dementia and can currently only be diagnosed with invasive methods[1]. MR Spectroscopy (MRS) is a non-invasive technique, capable of giving an insight into the brain neurochemistry associated with diseases, and therefore revealing AD biomarkers.
Previous studies have investigated the levels of metabolites such as myo-Inositol (Ins), N-acetyl-aspartate (NAA), Choline (Cho), and Creatine (Cr) in the brains of AD patients[2]. However, there is not a wide consensus yet on the variation of the concentrations of the metabolites in AD[2].
Metabolites act together in metabolic networks and often the optimal biological insight can be achieved when using multivariate methods that consider the correlation between metabolites[3]. Orthogonal Projection to Latent Structures Discriminant Analysis (OPLS-DA) is one of those methods and has been successfully applied to AD classification based on the ^{1}HNMR concentrations of CSF metabolites[4] and MR volumetric data[5].
Previously, we proposed a macromolecule model that enables the quantification of both metabolites and macromolecules (MM) and applied that method to quantify a dataset comprising spectra of the PCC of the whole AD spectrum[6]. Now, our aim is 1) to discriminate the diagnosis of the AD spectrum based on the neurochemical profile in the PCC, 2) to identify the most predictive metabolites and macromolecules for classification, and 3) to compare the prediction from OPLS-DA with other approaches like logit regression.
Methods Acquisition parameters are summarized in Fig. 1. The study sample was composed of 115 volunteers: 27 AD, 26 mild cognitive impairment (MCI), 30 subjective cognitive decline (SCD), and 32 healthy controls (HC).
Spectra were processed using a MATLAB tool including the following steps: Summation of odd and even acquisitions, weighted and phase-corrected coil combination, frequency correction and averaging. A parametrized MM model with 15 MM peaks and 13 ratios of correlated MM peaks is used for quantification[6]. LCModel"s metabolite concentration estimates underwent absolute quantification following Near et al. 2021[7]. For MM, only partial volume, but no relaxation times correction was applied.
Two classifications were evaluated: HC vs AD, and HC + SCD vs MCI + AD Three methods were compared: 1. Logit regression with the most significant metabolite myo-Inositol as a predictor (MIns). 2. Logit regression with all significantly different metabolites and macromolecules as predictors (MSig). 3. OPLS-DA with all metabolites and macromolecules as features (OPLSDA).
All the models comprised a Monte Carlo cross-validation (MCCV, 200 cycles) with random train:test split 80:20. For OPLS-DA, 4 ortho components were used. All metrics were calculated by averaging across the MCCVs. ROC curves were calculated and the variables" importance in projection (VIP) was investigated. Accuracies from the individual MCCVs tested for differences with ANOVA and Tukey as post-hoc.
Results Concentrations are reported in Fig. 2. In the classification HC vs AD, OPLS-DA leads to a significantly higher AUC than MIns and MSig ($p < 0.05$ both). In the classification HC + SCD vs MCI + AD, OPLS-DA differences in ROC curves were not significant.
OPLS-DA exhibited a better accuracy compared to both MIns and MSig ($p < 0.0001$ both). MSig and MIns had similar accuracies. Accuracy data are reported in Fig. 3, VIP in Fig. 4.
Discussion To the best of our knowledge, this is the first work including the results of macro-molecule quantitation in a clinical MRS application and the first work applying OPLS-DA to AD-related MRS data. Based on MRS data alone, we could distinguish AD and HC patients with a mean accuracy of 79%. Previous MR imaging-based studies achieved accuracies between 76 and 91%[8]. Combining MR imaging with MRS might improve those classifications.
OPLS-DA performs significantly better than the other two models in terms of accuracy. ROC curves show improved performance as well. In Fig. 4, VIP shows good agreement with the significant differences in concentrations. The most predictive metabolite for both comparisons is Ins, which is associated with glial inflammation[2]. In the comparison HC vs AD, tCr which is associated with energetic metabolism and tCho associated with cell membrane degradation and demyelination[2] are predictive as well. The most discriminating MM are M4.04 and M2.05 assigned to the resonance of histidine and glutamate in brain proteins[9]. Future studies might investigate the role of proteins rich in those amino acids in the progression of AD.
Conclusion We applied explainable machine learning to classify the diagnosis of the AD spectrum, considering only brain ^{1}HMRS data. Our findings point out that considering the whole neurochemical profile with an opportune method led to a better classification of diseases and a deeper understanding of the variables that may play a significant role in the disease.

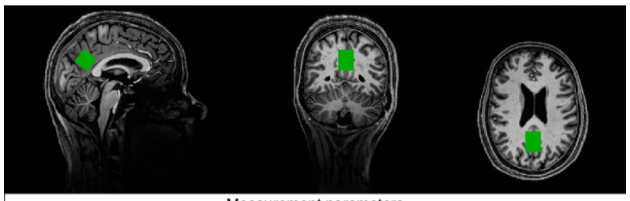

Measurement parameters	
Scanner	Siemens Magnetom 7T
Coil	NOVA Medical 1TX/32RX head coil
MRS sequence	SPECIAL
Voxel size	(20 mm)³
Repetition time	6500 ms
Echo time	9 ms
Number of acquisitions	64
Acquisition duration	512 ms
Excitation bandwidth	4000 Hz
Water suppression bandwidth	60 Hz
Sample dots	2048

Fig.1: Exemplary voxel position in the posterior cingulate cortex (PCC) and acquisition parameters

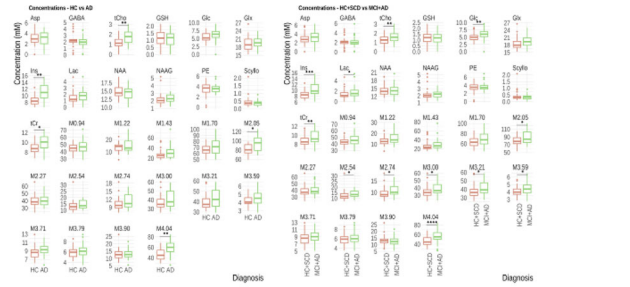

Fig.2: Concentrations of MM and metabolites for the groups in the two comparisons. Differences in concentrations were tested with the Mann–Whitney test. *: p≤0.05; **: p≤0.01; ***: p≤0.001; ****: p≤0.00001.

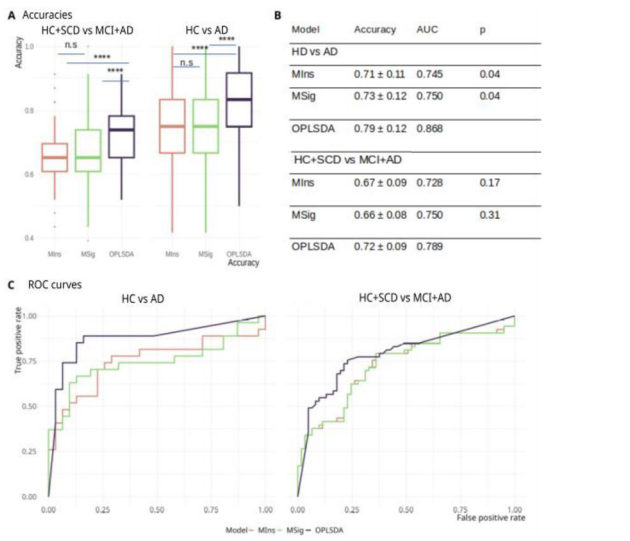

Model	Accuracy	AUC	p
HD vs AD			
MIns	0.71 ± 0.11	0.745	0.04
MSig	0.73 ± 0.12	0.750	0.04
OPLSDA	0.79 ± 0.12	0.868	
HC+SCD vs MCI+AD			
MIns	0.67 ± 0.09	0.728	0.17
MSig	0.66 ± 0.08	0.750	0.31
OPLSDA	0.72 ± 0.09	0.789	

Fig.3: A. Accuracies from the MCCV. OPLS-DA performs significantly better than the other two. C. ROC curves. Considering all metabolites and macromolecules leads to a better classification. p-values refer to one-tail Delong's test.

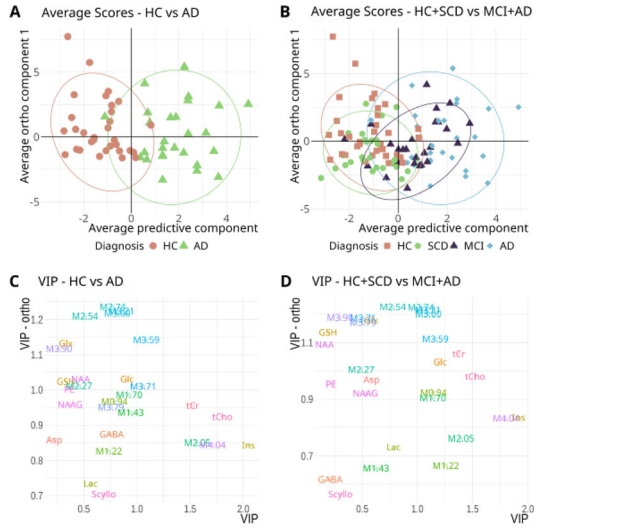

Fig. 4: A and B. Predictive and first ortho component. OPLS-DA leads to a good classification of HC vs AD (A), while the classification HC+SCD vs MCI+AD leads to a worse clustering. Interestingly, the MCI are classified into two clusters, a future study might investigate if the separation has some association with the conversion to AD. C and D. VIP for the two comparisons. A feature with a VIP value greater than one can be considered important.

T7.
Assessment of skeletal muscle energy metabolism by 31P-MRS in long-term fasting

A. Naëgel[1,2], H. Ratiney[1], T. Nguyen[1], D. Kennouche[1,3], T. Grenier[1], B. Leporq[1], F. Grundler[4], R. Mesnage[4], F. Wilhelmi de Toledo[4], M. Viallon[1]

[1]*Université de Lyon, INSA-Lyon, Université Claude Bernard Lyon 1, UJM-Saint Etienne, CNRS, Inserm, CREATIS UMR 5220, U1206, Lyon, France;*
[2]*Siemens Healthineers, Paris, France;*
[3]*LIBM—Laboratoire Interuniversitaire de Biologie de la Motricité, Saint Etienne, France;*
[4]*Buchinger Wilhelmi Clinic, Wilhelmi-Beck-Straße 27, Überlingen, Germany*

Introduction 31P-MRS and 1H-MRI are the non-invasive techniques of choice to explore lipid and energy metabolism[1,2]. The objective of this study is to provide evidence on the impact of long-term fasting (12 days, 250 kcal/day), on metabolism and muscle integrity in representative subjects. Indeed, fasting could represent a nutritional intervention of great interest for public health, whose effects on our organs must be carefully demonstrated[3,4].

Methods The GENESIS (lonG tErm FastiNg multi-systEm adaptations. In humanS) study[5] is a prospective, single-arm, interventional study of 32 subjects. All NMR acquisitions were performed on a 3 T clinical MRI (Magnetom Prisma, Siemens Healthineers) at three-time points, before, after, and 1 month after the end of fasting.

A high-resolution 3D isotropic Dixon anatomical sequence was used for segmentation[6] and muscle volume extraction[7]. A 3D gradient multi-echo chemical-shift-encoded imaging (CSE-MRI) sequence (TR = 16 ms, TE = 12 × 1.2 ms), was used to extract fat fraction map and relaxometry data[8,9]. Lipid metabolism was derived from single-voxel STEAM (TR/TE: 2 s/20 ms) 1H-MRS acquisitions on the thigh muscle.

Energy metabolism was explored by dynamics FID 31P-MRS (TR = 4 s) acquisitions on the leg of volunteers with saturation bands to minimize the signal from unstressed muscle and bone[10]. The platform was equipped with an MRI-compatible ergometer (ErgoSpect), with its calf module. Subjects were lying supine with the dual 1H/31P surface coil (Rapid GMBH) under their calf muscle (Fig. 1–2).

The physical activity of participants was measured with a MotionWatch 8© actigraphy system (CamNtech). A maximal incremental cycling cardiopulmonary exercise testing on a cycloergometer was performed following a ramped protocol to determine the VO2max, the first ventilatory threshold (VT1) and the respiratory exchange ratio (RER) values.

Comparisons between time points were performed using a repeated measures ANOVA followed by a Bonferroni multiple comparison test (Xlstat) with $\alpha = 0.05$ and $\alpha = 0.0167$, respectively and paired T-tests with $\alpha = 0.05$.

Results and Discussion Despite a 7.5% loss in total body weight and a 4% loss in leg muscle volumes, subjects showed neither significant changes in muscle integrity nor force.

Relaxometry results indicate no significant variation in T2 and body composition results indicate a significant decrease of PDFF compared to the basal state at M-1.

No significant difference was observed in PCr and Pi concentration over time. A significant difference was observed for pH after fasting, but a slight trend toward a minor decrease at all exercise steps. The PCr depletion/consumption during exercise was comparable between the fed and unfed phases, and PCr recovery characterized by τPCr showed similar values after a period of fasting to the values measured before and after one month.

The lipid metabolism and EMCL/IMCL ratio in the muscle varied during fasting, with marked lipid exchange between extra and intracellular that returned to basal level after one month re-feeding (Fig. 3).

There was no difference in maximal oxygen uptake relative to bodyweight during the ergometer test (i.e. VO2max). However, the VT1 increased significantly ($p = 0.03$) by 10% and the RER significantly decreased ($p < 0.001$) with also a 10% change during the fasting period (Fig. 4).

Actimetry data showed no changes when considering the amount of vigorous daily physical activity. Nevertheless, we observed significant changes in the amount of moderate, low and sedentary daily activity, with less moderate and low-level activities and more sedentary time during fasting period, compared to before and after.

Conclusion Muscle metabolism remains preserved and unchanged despite 12 days-long fasting, with no evidence of changes in mitochondrial respiration and/or general muscle cell function as explored by dynamic 31P-MRS.

On the other hand, we observed lipid changes including a transfer from EMCL to IMCL during fasting, which appears as an active process modifying the intracellular lipid distribution. This is likely an adaptive phenomenon for a better availability of fatty acids, which become the major energetic substrate of the mitochondrial respiratory chain. Since the diverse intracellular compartments contribute to global cell homeostasis and the intracellular trafficking of lipids and proteins are closely related, these results open new perspectives while motivating further investigations.

Acknowledgements This work was partially supported by the LABEX PRIMES (ANR-11-LABX-0063) and Siemens Healthineers.

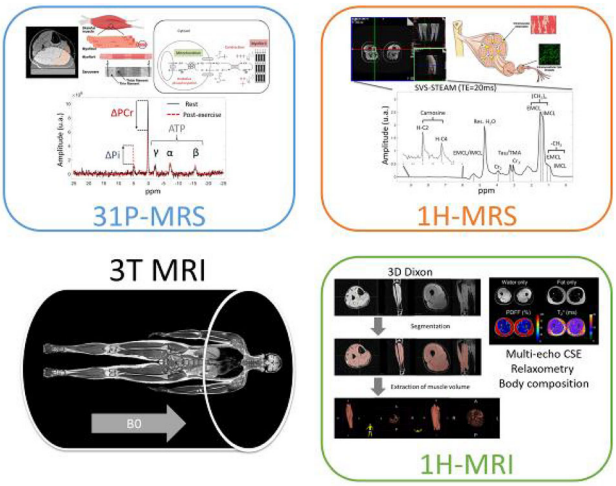

Fig. 1: All MRI/MRS acquisitions within the GENESIS protocol.

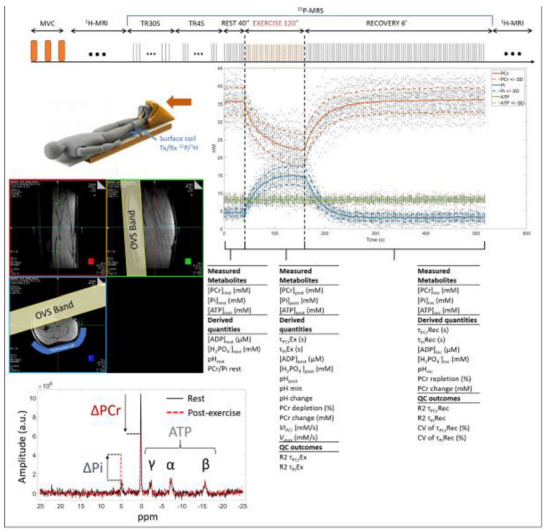

Fig. 2: The top illustration shows the position of the coil, located under the calf to acquire metabolites/signal from the gastrocnemius and soleus muscles. Metabolite concentration changes shown in the plotted data (right panel) are from a sample of healthy subjects.

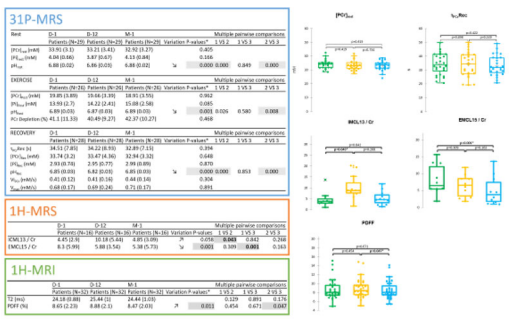

Fig. 3: Results of the statistical analysis of MRI data. Results are descriptive statistics : mean (SD) . * Statistical significance was set to p<0.05. Arrows provide the trend of the significant changes, if existing. Boxplots: Relevant parameter with significant difference.

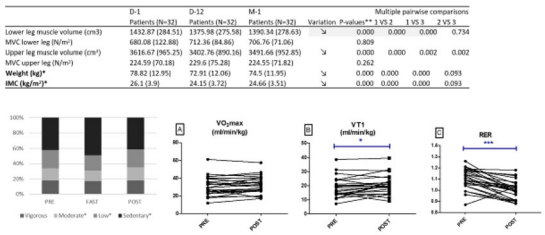

	D-1 Patients (N=32)	D-12 Patients (N=32)	M-1 Patients (N=32)	Variation	P-values**	Multiple pairwise comparisons 1 VS 2	1 VS 3	2 VS 3
Lower leg muscle volume (cm3)	1432.87 (284.51)	1375.98 (275.58)	1390.34 (278.63)	↘	0.000	0.000	0.000	0.734
MVC lower leg (N/m²)	680.08 (122.88)	712.36 (84.86)	706.76 (71.06)		0.809			
Upper leg muscle volume (cm³)	3616.67 (965.25)	3402.76 (890.16)	3491.66 (952.85)	↘	0.000	0.000	0.002	0.002
MVC upper leg (N/m²)	224.59 (70.18)	229.6 (75.28)	224.55 (71.82)		0.262			
Weight (kg)*	78.82 (12.95)	72.91 (12.06)	74.5 (11.95)	↘	0.000	0.000	0.000	0.093
IMC (kg/m²)*	26.1 (3.9)	24.15 (3.72)	24.66 (3.51)	↘	0.000	0.000	0.000	0.093

Fig. 4: Results of the statistical analysis of physiological data. Results are descriptive statistics : mean (SD) .* Statistical significance was set to p<0.05. Arrows provide the trend of the significant changes, if existing. Boxplots: Relevant parameter with significant difference.

References

1. Meyerspeer M, NMR Biomed, 2021
2. Kršśák M, NMR Biomed, 2021
3. Sparks LM, J Clin Endocrinol Metab, 2016
4. Laurens C, J Cachexia Sarcopenia Muscle, 2021
5. Grundler F, Front Nutr, 2022
6. Wang H, IEEE Trans Pattern Anal Mach Intell, 2013
7. Nguyen HT, Med Sci Sports Exerc, 2021
8. Viallon M, Front Nutr, 2019
9. Leporq B, NMR Biomed, 2014
10. Luo Y, Magn Reson Med, 2001;

T8.
Slice-selective zero echo time imaging of ultra-short T_2 tissues

J. Borreguero[1,2], F. Galve[2], J. M. Algarín[2], J. Alonso[2]

[1]*Tesoro Imaging S.L., Valencia, Spain;*
[2]*Institute for Molecular Imaging and Instrumentacion (Spanish National Research Council & Universitat Politècnica de València)., Valencia, Spain*

Introduction Here we provide an MRI sequence which allows slice selection and 2D-imaging of hard tissues with T_2* as short as 275 μs within clinically acceptable scan times even at fields as low as 260 mT. Our proposed sequence combines slice selection through spin-locking, which features a much more benign decay ($T_{1\rho} > > T_2$*), and a hard tissue imaging sequence (ZTE), providing a new and robust tool for slice selection of the shortest-lived tissue signals in the body.

Methods We present PreSLoP (Preserved Spin-Locked PETRA, Fig. 1), a 2D slice selective imaging sequence suitable for ultra-short T_2* samples. Here, slice selection is performed by means of a spin-locking (SL) RF pulse of amplitude B_1 in the presence of magnetic gradient of strength g_{SL}. In-slice signal decay during SL is delayed ($T_{1\rho} >> T_2$*), leaving a slice FWHM given by $\Delta = B_1/(2g_{SL})$. The SL time required for the slice to be selected can be roughly estimated as $t = 7\pi/(2\gamma B_1)$, even though longer spin-locking durations can be used as a tunable contrast. After SL, a -90° pulse protects the in-slice magnetization from T_2* decay while the slice-selection and imaging gradients are switched off/on respectively. Finally, a reexcitation pulse is applied and a FID is radially acquired in k-space. Missing central k-space points are then recovered in a point-wise fashion, as in PETRA. All experiments are performed in a 0.26 T scanner.

Results Fig. 2 shows a slice of a horse tooth (left, $T_2* \approx$ 260 us) acquired with 3D PETRA (middle) and the same slice encoded with PreSLoP (right). As compared to standard 3D ZTE sequences, PreSLoP achieves the same signal-to-noise ratio (SNR) in 3 times shorter scan times. This is due to the filling scheme of the finite gap at the center of k-space unavoidable with ZTE sequences.

In Fig. 3 we study the performance of PreSLoP for slice selection of an ultrashort T_2* sample in the presence of softer matter (Fig. 3a), containing two clay tooth molds ($T_2* \approx$ 550 μs) embedded in a piece of ham ($T_2* \approx$ 18 ms). In Fig. 3b we compare the middle slice of 3D-PETRA (left) and PreSLoP (right) selecting same slice with equivalent thickness. Finally, in Fig. 3c we assess the quality of the selected slice with PreSLoP (bottom row), using as reference the full phantom acquired with PETRA (top row).

Conclusions The proposed sequence is capable of slice-selective imaging of ultra-short T_2* biological tissues within clinically acceptable scan times even in our low-field MRI scanner. The nature of spin-locking enables not only imaging slices of isolated hard tissues, but also combinations of hard and soft matter These protocols may find application in clinical diagnosis of injuries in bones and oral/dental exploration, among others.

Acknowledgements This work was supported by the Ministerio de Ciencia e Innovación of Spain through research grant PID2019-111436RB-C21. Action co-financed by the European Union through the Programa Operativo del Fondo Europeo de Desarrollo Regional (FEDER) of the ComunitatValenciana (IDIFEDER/2018/022 and IDIFEDER/2021/004). JB Acknowledges support from the Innodocto program of the AgenciaValenciana de la Innovación (INNTA3/2021/17).

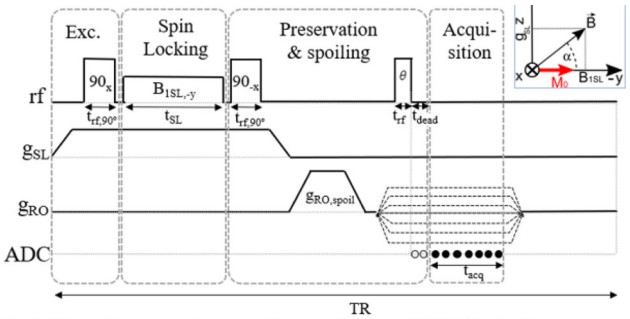

Fig. 1: Scheme of our proposed sequence: Preserved Spin-Locked PETRA (PreSLoP).

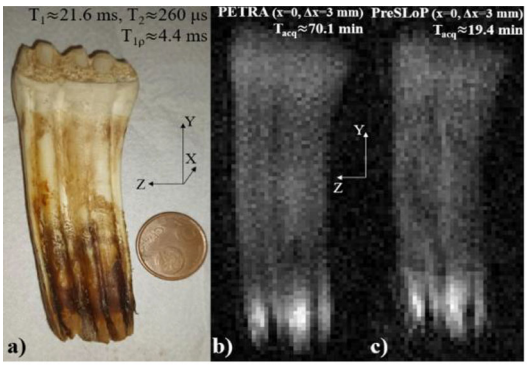

Fig. 2: Images of a horse tooth (a) acquired with 3D-PETRA (b) with slice thickness of 3 mm and same slice acquired with PreSLoP (c). Both images have been taken withsame resolution, timing and averaging parameters for reliable comparison.

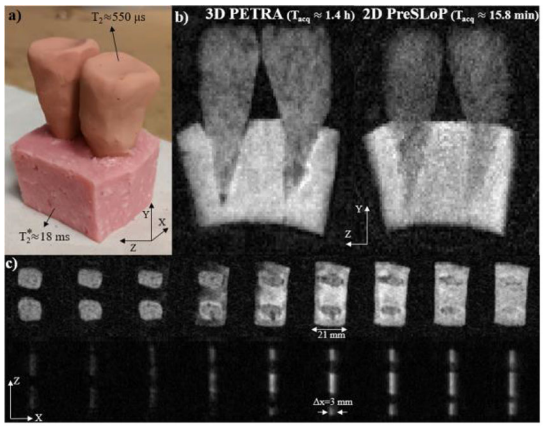

Fig. 3: Performance of PreSLoP for a combined ultrashort/long T_2* sample containing two clay tooth molds embedded in a piece of ham. a) Photograph of the sample. b)Slice of a 3D PETRA dataset (left) and same slice acquired with PreSLoP (right) with equal resolution, timing and averaging. c) Assessment of the slice quality of PreSLoP (bottom row) compared to the full phantom acquired with PETRA (upper row).

References

1. Weiger M, Pruessmann K. Short-T2 MRI: Principles and recent advances. Prog Nucl Magn Reson Spectrosc. 2019 Oct-Dec
2. Borreguero et al. Slice-selective Zero Echo Time imaging of ultrashort T2 tissues based on spin-locking. Sci Rep 13, 1662 (2023)
3. Algarín et al. Simultaneous imaging of hard and soft biological tissues in a low-field dental MRI scanner. Scientific Reports 10, 21,470 (2020)

T9.
A semi-randomized frequency selective trajectory to reduce artifacts from physiological signals in 3D steady-state MRI

A. Seginer[1], R. Schmidt[1]

[1]*Weizmann Institute of Science, Rehovot, Israel*

Introduction One of the drawbacks of 3D MRI is its vulnerability to physiological fluctuations—e.g., cardiac pulsation, breathing, and eye movements—during the scan. These *semi-periodic* fluctuations often produce artifacts in the MRI images including in some 3D steady-state GRE sequence variants used clinically. Randomizing the acquisition order can suppress such artifacts but may also increase the apparent noise[1–7], e.g., in cases of slow subject movement or slow changes in eddy currents. Here we designed a new semi-randomized trajectory having a cutoff frequency for artifacts suppression. Fluctuations above this cutoff are suppressed, whereas changes from slow movement are not affected. The new approach was examined in simulations and scanning. Two steady-state 3D GRE scan variants were scanned in vivo. One with parameters used in 3D T_2^*/SWI sequences, commonly suffering from artifacts near blood vessels, and the second with parameters of a scan used for quantitative estimation of T_2,[8] suffering from artifacts due to cardiac pulsation in the ventricles.

Methods Simulations included a point-distribution whose phase modulated with an angular frequency ω as an artifact source. The signal was analytically "sampled" on a 2D Cartesian k-space grid using different trajectories. Fig. 1 shows the trajectories examined. The simulation used 128 × 128 phase encodes (PE), TR 20 ms, and a cutoff of 1 Hz. This included five options: 1) "Ordered"—the standard sequential ordering of a 2D PE grid; 2) "Gilbert"—a generalized version of the Hilbert curve, supporting rectangular domains[9] (this option was shown useful in previous works[7]); 3) "Full-Scrambling"—full randomization; and two local scrambling alternatives: 4) "Segment-Scrambling" and 5) "Local-Scrambling" (using f_{cutoff}/1.2). In Segment-Scrambling the cutoff frequency defines a segment length within which the sampling order is scrambled. However, this design left residual sensitive frequency ranges above the cutoff frequency, see Fig. 1f. In Local-Scrambling a smoother scrambling is performed, over the same time shifts range as in Segment-Scrambling, but without splitting the acquisition into distinct segments.

In vivo scans were performed on a 7 T system (MAGNETOM Terra, Siemens Healthcare, Erlangen) using a modified GRE sequence that supports arbitrary ordering of the PE lines as well as an option to interleave two orderings—allowing a simultaneous acquisition of the two and thus a fair comparison. The scan parameters of GRE variant I were: FOV 220 × 184 × 104 mm^3, resolution 0.6 × 0.6 × 2 mm^3, BW per pixel 330 Hz, TR/TE 22/14 ms, flip angle 15°, and acceleration × 2. The actual number of acquired lines was 52 × 181 (k_z × k_y). Scan duration was 3:30 min (and 07:00 min when interleaving). The scan parameters of GRE variant II were: FOV 220 × 220 × 144 mm^3, resolution 1 × 1 × 1 mm^3, BW per pixel 400 Hz, TR/TE 10/4.38 ms, and flip angle 24°. Scan duration was 5:23 min.

Results Fig. 1 shows the orderings examined and compares the intensity of the worst "artifact" as a function of modulation frequency. Fig. 2 shows a static phantom scans with full randomization producing extra global noise at a specific bandwidth (may be eddy current related), while using local scrambling removes such noise. Fig. 3 shows human scans of GRE variant I with different ordering schemes. Fig. 4 shows both Ordered and Local-Scrambling scans of GRE variant II (using RF phase increment of 1.5°, instead of the commonly used increment for RF spoiling).

Discussion Scrambling the order of the acquisition can significantly suppress physiological artifacts. However, full randomization can also add noise (see Fig. 2), especially in cases of slow or gradual changes, from e.g. eddy currents, breathing, or slow subject movement. Local scrambling acquisition schemes reduce the artifacts from local fluctuations while giving control over the cutoff frequency (of the fluctuations) above which the artifacts are reduced. Figures 3 and 4 clearly show the benefit of using Local-Scrambling over other schemes.

Conclusions We have demonstrated a novel technique, Local-Scrambling, which can easily be implemented in the scanner to drastically reduce artifacts stemming from physiological signal fluctuations. Local-Scrambling utilized in a common 3D GRE variant used for T_2^*/SWI practically removed the artifacts near the blood vessels, with a pronounced improvement in the brainstem. Fig. 4 shows that the Local-Scrambling scheme significantly reduces artifacts—near both the eyes and the ventricles—in the scans used for quantitative T_2 mapping.

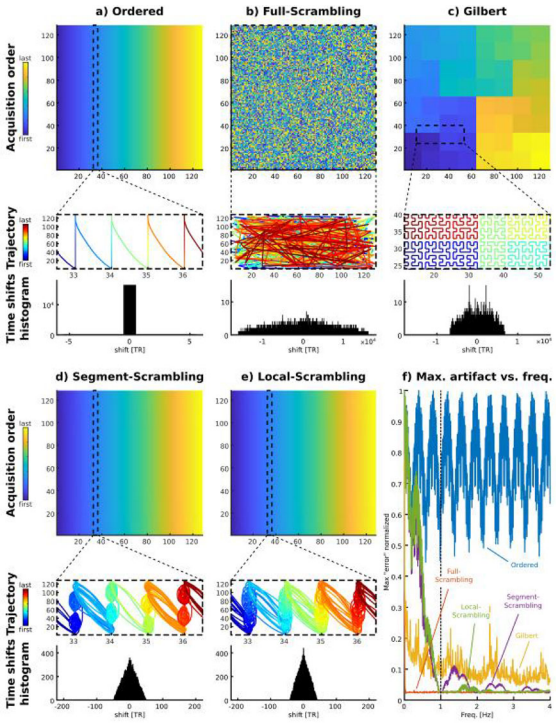

Fig. 1: Illustrative comparison of the ordering schemes. (a)–(e) The k-space PE acquisition order per scheme, including zoom-ins showing the trajectories and histograms of the sampling times shifts. (f) The normalized artifact from a point source vs. its modulation frequency for each scheme. [Trajectory in b) shows the last 500 steps only.]

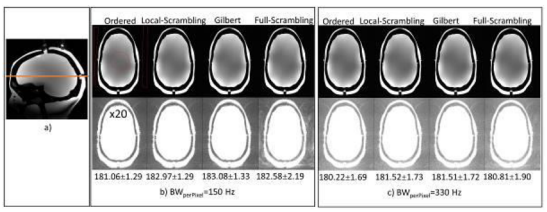

Fig. 2: A static 3D head-shaped phantom - comparison of the Ordered, Local-Scrambling, Gilbert and Full-Scrambling schemes. a) Sagittal plane with an overlay of a representative Axial slice of the 3D acquisition with BW/Pixel=150 Hz in (b) and BW/Pixel=330 Hz in (c).

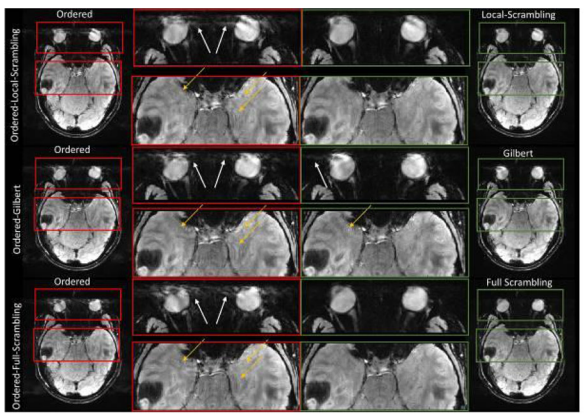

Fig. 3: Comparison of T_2'/SWI Interleaved acquisitions of Gilbert, Full-Scrambling, or Local-Scrambling with the Ordered scheme. In each case, the zoomed-in images are shown in the center.

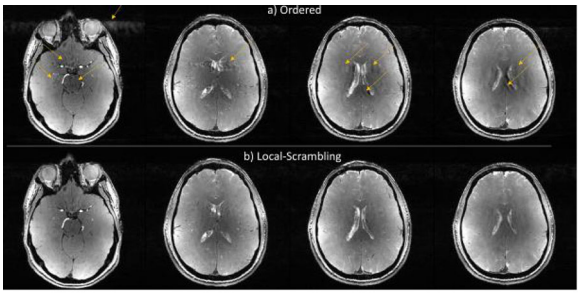

Fig. 4: Artifact reduction in a 3D steady-state scan used for quantitative T_2 mapping. (a) Ordered and (b) Local-Scrambling schemes. The artifacts are due to cardiac pulsation in the ventricles.

References

1. Bailes et al. JCAT 1985;9:835–838
2. Haacke et al. MRI 1986;4:359–376
3. Korin et al. JMRI 1992;2:687–693
4. Wilman et al. MRM 1996;36:384–392
5. Jhooti et al. JMRI 1998;8:968–980
6. Parker et al. JMRI 2003;18:121–127
7. Wermer et al. MRI 2017;37:16–20
8. Seginer et al. Sci Rep 2022;12:14088
9. Červený https://github.com/jakubcerveny/gilbert

T10.
Twisted pair transmission line coil—A new flexible and extremely robust element for 7 T MRI

J. Vliem[1], Y. Xiao[2,3], D. Wenz[2,3], L. Xin[2,3], I. Zivkovic[1]

[1]*Eindhoven University of Technology, Electrical Engineering Department, Eindhoven, The Netherlands;*
[2]*École Polytechnique Fédérale de Lausanne (EPFL), CIBM Center For Biomedical Imaging, Lausanne, Switzerland;*
[3]*École Polytechnique Fédérale de Lausanne (EPFL), Animal Imaging and Technology, Lausanne, Switzerland*

Introduction There has been ongoing research on developing highly flexible RF coil arrays that can adapt to fit a variety of body parts [1–3]. We propose a new type of coil for 7 T MRI that leverages the concept of twisted pair cables to improve flexibility and robustness [4]. A twisted pair is a type of cable that consists of two insulated wires twisted together to form a transmission line. The coil is made by shaping a twisted pair into a loop and introducing gaps in the wires. The proposed new design exhibits high flexibility and robustness towards elongation and shape deformations without the need for re-tuning. In this abstract, we present a new coil design and demonstrated its superiority in terms of transmit (B_1^+) and SAR efficiencies compared to the conventional loop coil.

Methods The twisted pair coil is made by first twisting around two 18-gauge wires (1 mm diameter) with PVC insulation, as shown in Fig. 1(a). When the twisted pair is shaped into a circular shape one of the wires is interrupted at the top, opposite of the feed point, and one at the bottom, as shown in Fig. 1(b). The gap on the signal conductor (red wire, bottom side) acts as the feed point for the coil.

For comparison, a conventional loop coil was modelled and fabricated from 1 mm diameter copper wire. Both coils were of 100 mm diameter and were tuned and matched to 297.2 MHz using fixed capacitors (AVX 800 E Series, USA) and variable capacitors (Johanson 5621, USA).

Electromagnetic simulations were performed in CST Microwave Studio 2023 (Darmstadt, Germany). The coil elements were placed at 20 mm distance from a homogeneous cubic phantom (Fig. 1(c)). To

evaluate the B_1^+ and maxSAR_{10g} the results were normalised to 1 W accepted power. For a comparison with the measurement setup, additional simulations were performed on a spherical phantom (Fig. 1(d)) with the coils placed at 5 mm distance, to match the measurement setup. When elongated the coils followed the surface of the sphere so that the coil was always at 5 mm distance from the phantom.

The phantom experiments were performed on the 7 T MR human scanner (Magnetom, Siemens Healthineers, Erlangen, Germany). The three-dimensional B1 + maps were quantitatively measured with SA2RAGE sequence (TR/TE = 2400/0.78 ms, TI1/TI2 = 45/1800 ms, $\alpha1/\alpha2 = 4/10°$, FOV = 208 × 256 mm2, slices = 64, resolution = 2.0 × 2.0 × 2.5 mm, BW = 1220 Hz/px, scan time = 115 s) [5].

Results In Fig. 2(c) the simulated and measured return loss (S_{11}) for the twisted pair and conventional coils is displayed. The twisted pair coil exhibits minimal change in resonance frequency as it is elongated, while the conventional coil's resonance frequency shifts to a higher value.

In Fig. 3(a) a comparison of simulated B_1^+ maps can be seen with three different elongations for the twisted pair and conventional coil, and (b) shows the B_1^+ profiles along the central axis (white dashed line in (a)). The conventional and twisted pair coils have similar efficiency. In Fig. 3(c) the SAR_{10g} maps can be seen together with the peak SAR values. When the twisted pair coil gets elongated the peak SAR remains the same, whereas for the conventional coil the peak SAR increases by 27% when changed from circular to the most elongated shape.

In Fig. 4 the simulated and measured field maps can be seen on a spherical phantom. A very good agreement between simulations and measurements has been achieved.

Discussion The twisted pair coil demonstrated superiority in flexibility and robustness compared to the conventional coil. The twisted pair coil has similar performance as the conventional coil in terms of B_1^+ field efficiency while being completely non-sensitive to shape deformations. Max SAR_{10g} of twisted pair coil does not change when elongated from circular to very elliptical shape while it increases in the case of the conventional coil.

Conclusion The novel twisted pair coil design, presented in this abstract, offers a promising alternative to conventional, rigid loop coils for operation at 7 T. The proposed coil is extremely robust which makes it a suitable element for densely populated arrays. Future work would include further investigation of the influence of various coil design parameters on a coil's performance. Initial experiments on a coil's decoupling properties showed that the coil is a highly decoupled element per se in any configuration and more detailed investigations will be presented in the future.

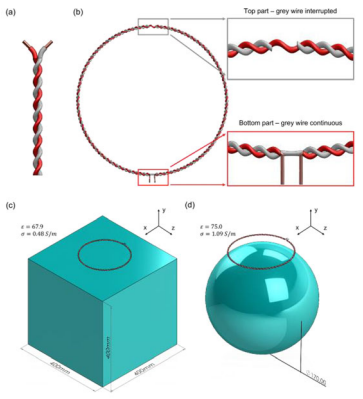

Fig. 1: (a) Illustration of the two twisted wires. (b) Forming of the twisted pair coil. (c) & (d) Illustration of the cubic and spherical phantom used in simulations and measurements.

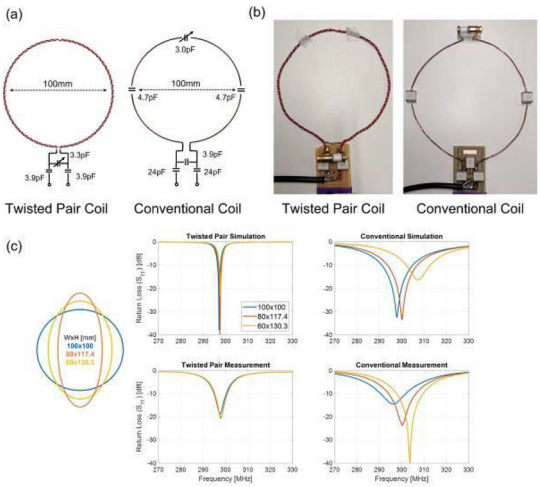

Fig. 2: (a) Schematic of the twisted pair and conventional coil (diameter of 100mm). (b) Photos of the fabricated coils. (c) The returns loss of the simulated and measured coils for three different elongations.

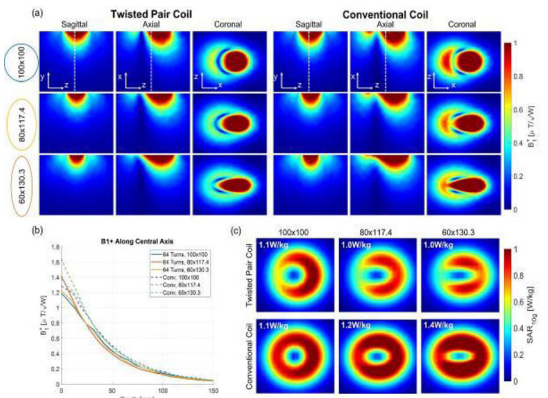

Fig. 3: (a) B_1^+ field maps comparison of the three elongations for the twisted pair and conventional coil. (b) B_1^+ plotted along the central axis of the phantom. (c) Coronal view of the SAR_{10g} maps of the three coil elongations and peak SAR value. Simulations were normalised to 1W accepted power and performed on a cubic phantom.

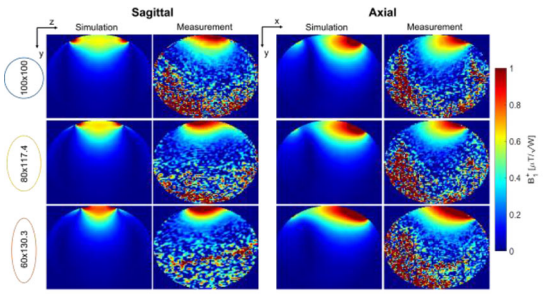

Fig. 4: Simulated and measured B_1^+ field maps for the three different elongations, on the axial and sagittal plane. The simulations and measurement were performed on the spherical phantom (Fig. 1(d)) and the simulated results were normalised to 1W accepted power.

References

1. Ruytenberg T, Webb A, Zivkovic I, Magn Reson, Med. 2020; 83(3): 1135–1146
2. Van Leeuwen CC, Steensma BR, Klomp DWJ, Van den Berg CAT, Raaijmakers AJE. Magn Reson Med. 2022 Jan; 87(1):528–540
3. Nohava L et al. IEEE Trans. Med. Imaging 2021; 40: 1267–1278

4. Maravilla JA, Gopalan K, Arias AC, Lustig, M. (2022). Proc. Intl. Soc. Mag. Reson. Med. 30
5. Eggenschwiler, Florent, et al. Magn Reson Med 2012; 67(6): 1609–1619

T11.
Physics-informed conditional autoencoder: A deep learning approach for robust B_1 correction for 7 T CEST MRI

J. R. Rajput[1], T. A. Möhle[2], M. S. Fabian[1], A. Mennecke[1], J. A. Sembill[2], J. B. Kuramatsu[2], M. A. Schmidt[2], A. Dörfler[1], A. Maier[3], M. Zaiss[1]

[1]*Friedrich-Alexander-Universität Erlangen-Nürnberg (FAU), Department of Neuroradiology, Erlangen, Germany;*
[2]*Friedrich-Alexander-Universität Erlangen-Nürnberg (FAU), Department of Neurology, Erlangen, Germany;*
[3]*Friedrich-Alexander-Universität Erlangen-Nürnberg (FAU), Pattern Recognition Lab, Erlangen, Germany*

Introduction Chemical exchange saturation transfer (CEST) is an MRI method that provides insights on the metabolic level [1]. Several metabolite effects appear in the CEST spectrum. These effects are isolated by Lorentzian curve fitting [2]. The separation of CEST effects suffers from the inhomogeneity of the saturation field B_1. This leads to inhomogeneities in the associated metabolic maps. Current B_1 correction methods require at least two sets of CEST-spectra [3]. This at least doubles the acquisition time. In this study, we investigated the use of an unsupervised physics-informed conditional autoencoder (PICAE) to efficiently correct B_1 inhomogeneity and isolate metabolic maps while using a single CEST scan.
Methods The proposed approach uses two neural networks (NNs), the Conditional Autoencoder (CAE) and the Physics-Informed Autoencoder (PIAE). CAE generates B_1-corrected CEST spectra at arbitrary B_1 levels and PIAE isolates CEST maps according to the 5-pool Lorentzian model (water, amide, amine, NOE, MT) [2] from the corrected CEST spectrum. The 5-pool model was described as follows

$$Z(\Delta\omega) = 1 - L_{DS} - L_{ssMT} - L_{Amine} - L_{rNOE} - L_{Amide}, \quad (1)$$

where L denotes the Lorentz function. Both NNs together formed the proposed PICAE method. Both NNs were trained with the mean square error with CEST measurements at 3 B_1 levels from four healthy subjects and tested with two tumor patients and one healthy subject. The acquisition time per B_1 level was 6:42 min. The proposed method was compared with the conventional method, which used interpolation to produce a B_1-corrected CEST spectrum using at least two acquisitions and Lorentzian line fitting to produce CEST maps from the corrected spectrum.
Results Fig. 1 shows Amide metabolic maps isolated from B_1-uncorrected and B_1-corrected CEST Spectra. B_1-correction and fitting was performed using conventional pipeline [2,3]. Red circles indicate the shortcomings of the conventional pipeline, as $B_1 \sim 1$, i.e., uncorrected fit $B_{1nom} = 0.72$, should have higher intensities than corrected fit $B_1 = 0.6$. Moreover, the conventional result for corrected fit $B_1 = 0.8$ completely failed, as most voxels are extrapolated for this value. In contrast, Fig. 2, which shows the result of the PICAE fit, is robust to B_1 inhomogeneities, as the intensities are lower for the 0.6-correction fit and higher for the 0.8-correction fit than for the uncorrected fit of $B_{1nom} = 0.72$.
Discussion In this work, we analyzed the use of deep learning approach to generate B_1-robust CEST contrast maps at arbitrary B_1 levels (cf. Figure 3 a, b, c), which requires multiple acquisitions in conventional methods. This is important because the B_1 dispersion contains information about the exchange rates and concentration of metabolite protons, paving the way for their quantification (cf. Figure 3d). In addition, the optimal B_1 can often only be selected at post-processing during the analysis of the clinical data, as different pools in the CEST spectrum are highlighted at different B_1 levels.
Conclusion The proposed method enables (i) a reduction in scan time of at least 50%, (ii) the generation of reliable CEST contrast maps that are robust to B_1 inhomogeneity at multiple B_1 levels, and (iii) the quantification of CEST contrast maps.

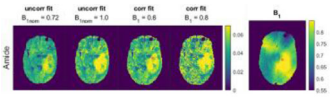

Fig. 1: Amide metabolic maps generated with conventional method and B_1 inhomogeneity map. Red circles indicate the subregion where B_1 is almost equal to the nominal setting.

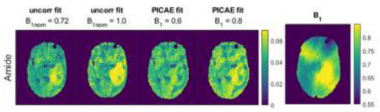

Fig. 2: Amide metabolic maps generated with the proposed PICAE method and B_1 inhomogeneity map

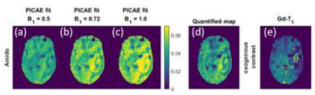

Fig. 3: Amide metabolic maps generated by the proposed PICAE method using a single scan (a, b, c) at arbitrary B_1 levels, (d) showing the quantified amide map, and (e) the exogenous Gadolinium contrast.

References
1- Van Zijl PC et al. Magn Reson Med. 2011;65(4):927–48
2- Mennecke A. NMR Biomed. 2022
3- Windschuh J et al1. NMR Biomed. 2015;28(5):529–3

T12.
On the use of autoencoder to denoise diffusion MRI

S. Soundarresan[1], Z. Tan[1], P. Liebig[2], R. Heidemann[2], F. Laun[1], F. Knoll[1]

[1]*Friedrich-Alexander-Universität Erlangen-Nürnberg (FAU), Erlangen, Germany;*
[2]*Siemens Healthineers, Erlangen, Germany*

Introduction Diffusion MRI (dMRI) is a powerful imaging modality for clinical diagnosis of stroke and tumors, as well as for the investigation of brain microstructures. However, dMRI suffers from long acquisition time, low spatial resolution, and low signal-to-noise ratio (SNR). To improve dMRI, joint k-q-space sampling and reconstruction [1–2] has been proposed to jointly reconstruction all diffusion-weighted images (DWI) by exploiting the complementary sampling pattern. Joint reconstruction, however, requires the knowledge of proper image priors. In this work, we trained a autoencoder neural network to learn the q-space prior and employed it as a denoiser.
Methods A two-shot EPI was used to collect the dMRI data at 7 T (Magnetom Terra, Siemens, Erlangen). The acquisition parameter were: 1.2 mm isotropic resolution, FOV 220 mm, and b-value of 1000 s/mm2. The dataset consisted of 32 diffusion directions with TE = 47 ms and TR 4300 ms. The total acquisition time was 5 min for 94 slices with in-plane acceleration factor of 3 and slice acceleration factor of 2.

The DAE was trained using a dictionary created using the biophysical model. The initial parameters required to create the dictionary were the b and g values that were obtained from the acquisition protocol. The free model parameters are discretized within their biophysical range as D in [0.1, 4] mm2/s. The simulated diffusion signals were modulated with white Gaussian noise at various levels. Both the real and corrupted data (with and without noise) were used for training. The training was performed using about 700,000 instances of the diffusion signals.

The network consisted of four fully connected layers with input size same as the q-space. Three DAEs were trained with data converged to 10, 15 and 5 neurons in the bottleneck layer for testing purposes. Standard DAE training procedures were utilized in Pytorch with stochastic gradient descent (SGD). The atoms were randomized during each epoch to help achieve faster convergence. 100 epochs with batch size of 210 were used with the mean-squared error (MSE) loss function. Once the DAE was trained, the diffusion signals from various recordings were transformed to image space by using SENSE or MUSE. These were then passed through the trained DAE model to generate denoised images. A schematic of this is presented in Fig. 1.

Results The latent space for the DAE is decided based on experimenting. The dataset"s b and g values were used to generate a dictionary. This dictionary was divided into training set, validation set and testing set with a distribution of 70%, 20% and 10%. The latent space of the DAE is varied from 1 to 20 and trained and validated using the training set and validation set. An analysis of the performance of the trained models was made based on MSE on testing set. The MSE vs latent space graph can be seen in Fig. 2.

After a latent of 6, there was extremely little decrease in the MSE. A latent space of 10 was hence chosen. Plus, compared to the MSE of the SVD based denoising method, the DAE method performs much better on the test data.

The k-q-space data obtained for 7 T dataset was reconstructed via parallel imaging. These DWIs were then denoised by mapping it to the learned latent space data using the trained DAE. As shown in Fig. 3, the DAE denoising on MUSE [3] reconstructed DWIs works visually better when compared to the SVD method with the same latent space of 10.

Discussion and Conclusion Autoencoder is effective in learning the q-space prior for the denoising of diffusion MRI.

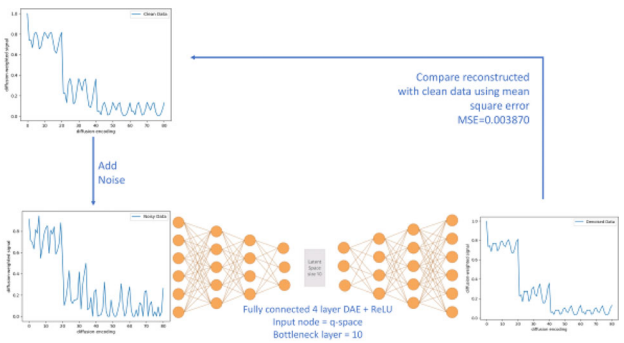

Fig. 1: Illustration of the DAE model training procedure for diffusion-weighted signal

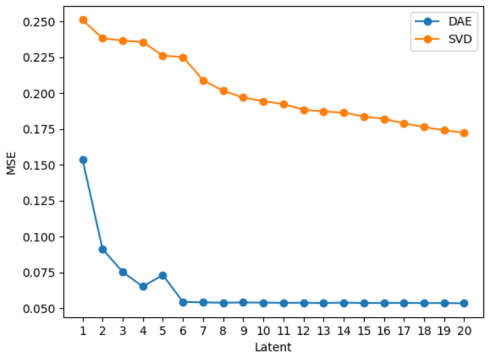

Fig. 2: Comparison on the accuracy of the DWI reconstruction between the DAE nonlinear subspace learning and the SVD linear subspace learning.

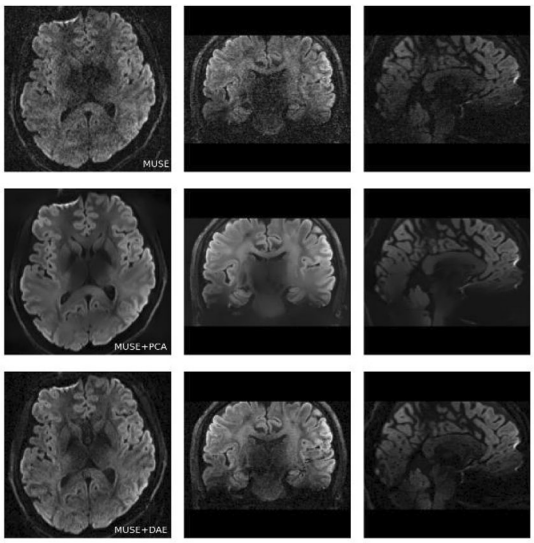

Fig. 3: Comparison of denoising with REPCOM (row 2) and DAE (row 3) anfter MUSE reconstruction (row 1) with each column representing a view from x,y and z axes

References

[1] F Lam, Y Li, X Peng. Constrained Magnetic Resonance Spectroscopic Imaging by Learning Nonlinear Low-Dimensional Models. *IEEE Trans Med Imaging* (2020).

[2] Mani M, Magnotta VA, Jacob M. qModeL: A plug-and-play model-based reconstruction for highly accelerated multi-shot diffusion MRI using learned priors. *Magn Reson Med* (2021).

[3] Chen NK, Guidon A, Chang HC, Song AW. A robust multi-shot scan strategy for high-resolution diffusion weighted MRI enabled by multiplexed sensitivity-encoding (MUSE). *NeuroImage* (2013).

T13.
Simultaneous optimization of MR sequence and reconstruction using MR-zero and variational networks

H. N. Dang[1], J. Endres[1], S. Weinmüller[1], A. Maier[1], F. Knoll[1], M. Zaiss[1,2,3]

[1]*Friedrich-Alexander-Universität Erlangen-Nürnberg (FAU), Department Artificial Intelligence in Biomedical Engineering, Erlangen, Germany;*

[2]*Friedrich-Alexander-Universität Erlangen-Nürnberg (FAU), Department of Neuroradiology, Erlangen, Germany;*
[3]*Max-Planck-Institute for Biological Cybernetics, Magnetic Resonance Center, Tübingen, Germany*

Introduction The slow acquisition speed of MRI has led to the development of a variety of acceleration methods. One approach to accelerating MRI acquisition, called Parallel Imaging, utilizes multiple receiver coils to simultaneously acquire multiple views of the object. Conventional reconstruction methods, GRAPPA[1] synthesizes missing data points directly in k-space. Another step towards the current state-of-the-art image reconstruction is by using advanced deep-learning-based reconstruction models. Variational networks[2] (VN) represent an unrolled network, which turns an iterative reconstruction algorithm into a deep neural network. Training of such networks uses large datasets of raw MRI data, such as the fastMRI[3] database. For the training fully sampled raw data is retrospectively under-sampled. However, for non-steady-state sequences, like TSE with long echo trains, this procedure is inconsistent with actual acquired under-sampled data, as it does not take the change of the signal dynamic into account. In this work, we demonstrate the benefits of simulated training data, using MRzero[4], as this can be generated with the correct signal decay, yielding correct targets for VN training. Furthermore, we extend our previous work[5] on solving T2-induced blurring in TSE sequences by including a VN as reconstruction model in the optimization pipeline to yield a fully joint reconstruction and sequence optimization.

Methods All simulations and optimizations were performed in the MRzero framework using a fully differentiable Phase Distribution Graph[6] (PDG) algorithm for signal generation. To demonstrate the differences between correct simulated and retrospective under-sampled data a single-shot PDw-TSE sequence (matrix: $128 \times 128 \times 1$, FoV = $200 \times 200 \times 8$ mm^2, FA = 180°, TE = 14.5 ms, centric reordered phase-encoding) was simulated. The sequence uses a uniform cartesian under-sampling of factor 2. As reference a two-shot TSE with full relaxation between each shot is being used to yield an ideal fully sampled target. The training data uses synthetic brain samples based on the BrainWeb[7] database consisting of 20 subject volumes with 70 slices each. The VN is implemented in PyTorch and uses T = 10 cascades. For the joint optimization, the forward simulation outputs the decaying TSE signal, which is reconstructed by the VN, and in addition the corresponding transversal magnetization as ideal sharp target. Fig. 1 visualizes the optimization process in MRzero. The gradient update propagates back through the whole chain of differentiable operators. As loss function MSE is being employed and Adam is used as optimizer. The complete FA train and VN parameters are updated at each iteration step simultaneously.

Results The difference between images generated from the correctly simulated signals and retrospective under-sampled signals reveal that the T2 decay in TSE sequences leads to considerable changes in contrast and sharpness (Fig. 2). As shown in Fig. 3 the inconsistent training data of a VN trained with retrospective under-sampled signals leads to low performance when applied on the test dataset, when compared to a VN trained with correctly simulated signals. Identical optimizations were performed for transient GRE MRI (data not shown). The simultaneous reconstruction and sequence optimization to reduce T2-induced blurring is shown in Fig. 4. The optimization discovers a suitable FA train and a matching VN resulting in a reconstructed image with strong correlation to the target transverse magnetization. Compared to the single-shot TSE sequence with constant 180° FA train, the output yields strongly improved sharpness especially in white and gray matter structures due to their low T2 relaxation time.

Discussion and Conclusion Retrospective under-sampling of data leads to inconsistencies with actually acquired data, as the signal decay is altered. We demonstrated the importance of VN training on correctly simulated under-sampled data of non-steady-state sequences. MRzero provides such simulation framework that also makes possible to train networks for novel sequences and contrasts of which no datasets are available. By using variational networks more flexibility in the reconstruction could allow a completely new degree of freedom in the sequence optimization. We showed that that the VN could be incorporated in the existing optimization pipeline of our previous work by replacing the conventional reconstruction and leading to a fully joint optimization. This is not only limited to the task of deblurring, but it also suitable to supersede any reconstruction or image processing task, as well as joint optimization of under-sampling factor and pattern, refocusing FA and the matching optimal variational network.

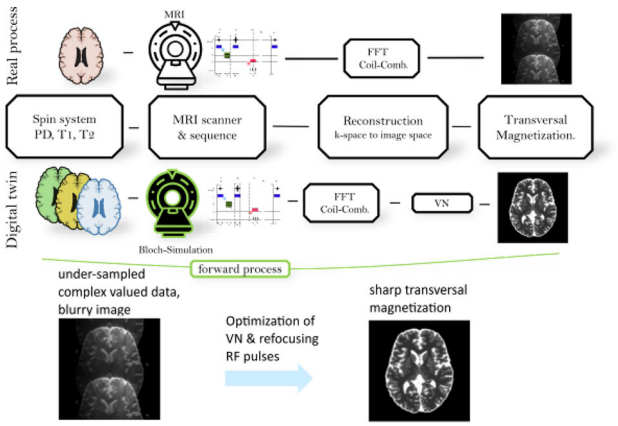

Fig. 1: Overview of the proposed optimization pipeline.

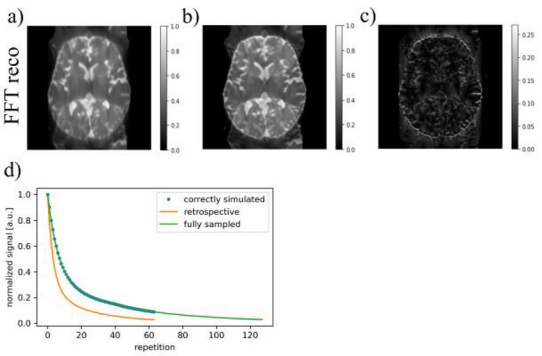

Fig. 2: FFT reconstructed images of a 180°-TSE when using correctly simulated signals (a), using retrospective under-sampled signals (b) and their difference (c). Considerable blurring is visible in (b) when compared to (a) due to the differences in T2 decay (d).

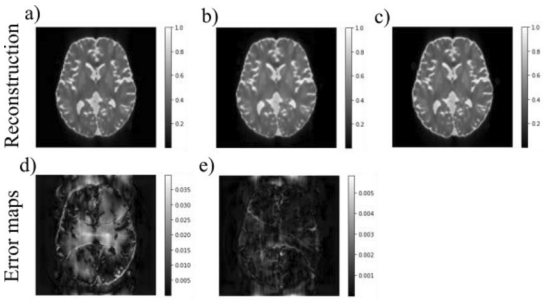

Fig. 3: Reconstructed images using a VN trained with correctly simulated signals (a), and retrospective under-sampled signals (b), compared to a fully sampled two-shot sequence (c). Corresponding absolute error maps are displayed in d) and e).

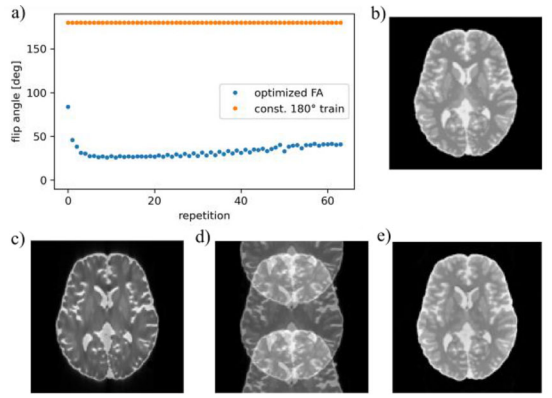

Fig. 4: Joint optimization of a deblurring task. Optimized and const. 180° FA pattern are shown in (a). The ideal sharp target is given by the theoretical transversal magnetization in (b). In (c) a 180°-TSE with GRAPPA reconstruction, (d) the TSE sequence with the optimized FA and (e) the optimized TSE sequence reconstructed by VN are being displayed. Video of the training procedure can be found at: https://streamable.com/jj17r2

References

1. Grisworld et al. MRM 2002.
2. Hammernik et al. MRM 2018
3. Zbontar et al. arXiv:1811.08839 2018
4. Loktyushin et al. MRM 2021
5. Dang et al. MRM 2023
6. Endres et al. MRM 2023 (submitted)
7. http://www.bic.mni.mcgill.ca/brainweb/

T14.
GPT4MR: Exploring GPT-4 as an MR sequence and reconstruction programming assistant

M. Zaiss[1,2,3], H. N. Dang[2], V. Golkov[4,5], J. R. Rajput[2], D. Cremers[4,5], F. Knoll[1], A. Maier[6]

[1]*Friedrich-Alexander-Universität Erlangen-Nürnberg (FAU), Department Artificial Intelligence in Biomedical Engineering, Erlangen, Germany;*
[2]*Friedrich-Alexander-Universität Erlangen-Nürnberg (FAU), Department of Neuroradiology, Erlangen, Germany;*
[3]*Max-Planck-Institute for Biological Cybernetics, Magnetic Resonance Center, Tübingen, Germany;*
[4]*Technical University of Munich, Munich, Germany;*
[5]*Munich Center for Machine Learning, Munich, Germany;*
[6]*Friedrich-Alexander-Universität Erlangen-Nürnberg (FAU), Department of Computer Science, Erlangen, Germany*

Introduction The programming of MRI sequences remains a challenging and time-consuming task for researchers, technicians and students alike. With the Pulseq standard, this process recently became simpler. In this study, we investigated the potential of GPT-4, an advanced large language model (LLM) capable of programming and producing natural language, as an MRI sequence programming assistant using the Pulseq framework, accelerating MR prototyping in development and education.

Methods We used ChatGPT [1] with the models GPT-3.5 and GPT-4. We adapted GPT for MRI sequence programming by adding a custom prompt [2] to turn it into an MRI and PyPulseq [3] coding assistant abbreviated here by GPT4MR. The prompt contained general instructions as well as PyPulseq function definitions and examples, principles known as in-context few-shot learning [4,5] and Chain-of-Thought Prompting [6]. We tested the AI model's ability to generate simple pulse sequences, composite binomial pulses, a spin echo EPI sequence with reconstruction, and a Lissajous-EPI. To facilitate user experimentation, we share an open Colab notebook [2] containing the GPT4MR prompt, comprehensive examples, guidance, and a platform to test GPT-4 as an MR coding assistant. This abstract was revised by GPT-4.

Results In our initial attempts, native GPT models often generated erroneous code, mainly using non-existing PyPulseq subfunctions. The performance is considerably improved using our tailored GPT4MR prompt, allowing it to generate MRI sequences with fewer or no errors (Fig. 1). GPT-4 outperformed GPT-3.5 in terms of number of bugs and reasoning/explaining. However, our study also revealed GPT-4's limitations in handling more complex sequence ideas or fully replicating existing sequence concepts. Prompts like "Code a spin echo EPI" lead to running code, but conceptual sequence errors (Fig. 2). Interestingly, GPT4MR was able to correct its own errors when problems were pointed out. When instructed with step-by-step instructions of the sequence implementation as plain text, GPT4MR was able to generate correct and running code in a single try for a spin echo EPI (Fig. 3), and a Lissajous EPI (Fig. 4). While timings, gradient moments etc. were not always 100% correct or optimal, running codes were produced and an easy-to-alter base sequence as well as a correct EPI FFT reconstruction (Fig. 3), as well as a non-uniform FFT reconstruction using the advanced torchkbnufft package, which yields a better outcome compared to linear re-gridding, were generated (Fig. 4).

Discussion Our findings indicate that LLMs have the potential to serve as a valuable MRI sequence programming assistant, enabling faster development of novel MRI sequences, reconstruction, or building blocks. Our last two chosen examples cannot be found on the internet (i.e. in the training set of GPT-4), demonstrating GPT4MR's capacity to accelerate the realization of new MRI sequence ideas. However, its limitations in dealing with complex ideas and sequences necessitate further research and improvement. A well designed prompt including PyPulseq documentation can improve the performance considerably. GPT4MR understood programming hints and altered the code accordingly, forming a sparring partner for fast MR prototyping.

Conclusion We propose a versatile prompt that enables GPT-4 to act as a Pulseq coding assistant for MRI sequence/recon development and prototyping, streamlining the process.

As a future outlook, integrating a PyPulseq plugin into (free, leightweight, open source) [7] LLMs could create a powerful tool for MRI sequence development and prototyping.

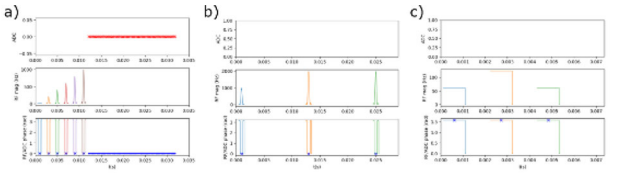

Fig. 1: Sequence plots of asked prompts (a), (b) and (c).

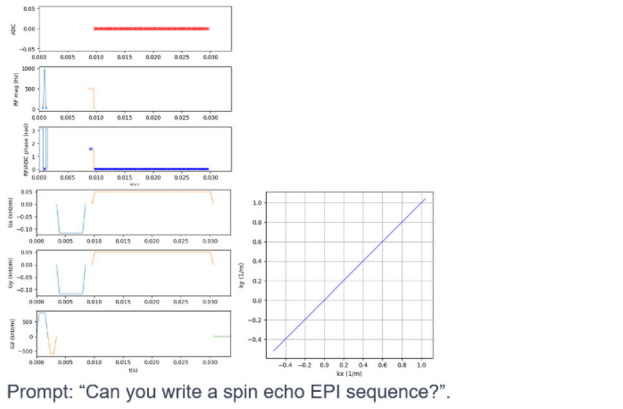

Fig. 2: Here our assistant GPT4MR fails, this resembles a gradient echo sequence, but only a single too short diagonal k-space line is acquired.

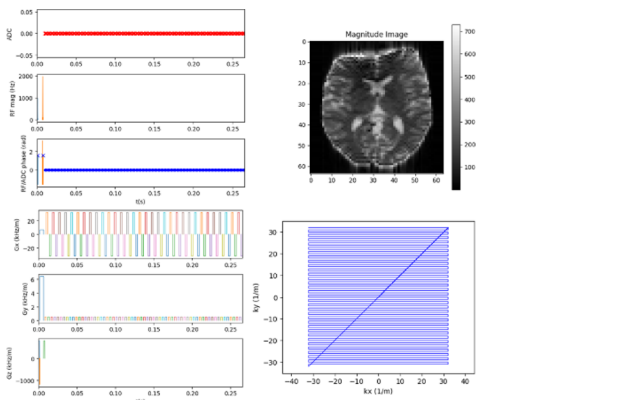

Fig. 3: Spin-Echo EPI coded by GPT4MR in the first attempt using a step-by-step prompt (Prompt 5). This is a correct implementation, just the spin echo TE does not match the time of k-space center acquisition. The reconstruction shows the typical EPI distortion artifact, but line flips and shifts were implemented correctly by GPT4MR.

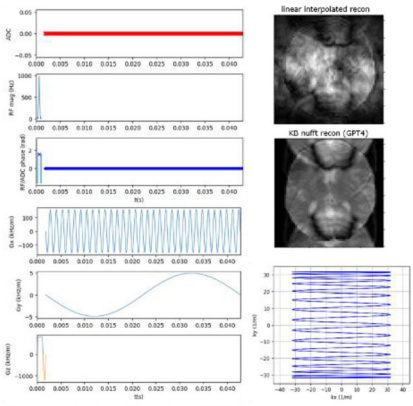

Fig. 4: Lissajous EPI coded by GPT4MR in the first attempt. This is a correct implementation, only the k-space coverage is not yet ideal.

References

[1] chat.openai.com.
[2] https://colab.research.google.com/drive/1RoubncbIAOBmX7IFy_OXeJFKI3DQK_F1
[3] https://pulseq.github.io/ & https://pypi.org/project/pypulseq/
[4] https://doi.org/10.48550/arXiv.2005.14165
[5] https://doi.org/10.48550/arXiv.2212.10559
[6] https://doi.org/10.48550/arXiv.2201.11903
[7] https://arxiv.org/abs/2302.13971

T15.
Isolating the arterial blood volume change to probe fMRI spatial specificity

N. Priovoulos[1,2], I. A. de Oliveira[1], B. A. Poser[3], D. G. Norris[4], W. van der Zwaag[1]

[1]*Amsterdam UMC, Spinoza Center for Neuroimaging, Amsterdam, The Netherlands;*
[2]*Amsterdam UMC, Department of Biomedical Engineering and Physics, Amsterdam, The Netherlands;*
[3]*Maastricht University, MR-Methods group, MBIC, Maastricht, The Netherlands;*
[4]*Radboud University, Donders Institute for Brain Cognition and Behaviour, Nijmegen, The Netherlands*

Introduction fMRI is a widely used technique to image neural activity in vivo [1]. fMRI typically uses deoxyhemoglobin as a contrast agent, which biases spatial sensitivity towards vein-rich areas [2]. Alternatively, changes in cerebral blood volume (CBV) can be measured, such as with Vascular-Space-Occupancy (VASO) which can improve fMRI localization [3], but is less sensitive. Arterial Blood Contrast (ABC) is a new technique that induces an arterial-weighted CBV signal [4], potentially with high spatial specificity. However, this has not been shown because it is challenging to isolate the arterial signal due to BOLD contamination and SAR limitations. In this study, we develop a method to isolate ABC in high spatiotemporal resolution and examine its localization and specificity.
Methods In this study, 5 participants (4 male) were scanned in a 7 T Philips Achieva with a 2Tx/32Rx whole-head coil. A T2-selective, rectangular, on-resonance phase-modulated pulse-train (B1 = 12 μT) was employed to selectively saturate the bound-pool (Fig. 1). The bound-pool was allowed to cross-relax to the free-water-pool for 60 ms before pulse train repetition, to maximize magnetization-transfer-weighting (MT; 4 pulse-trains). Following the pulse-trains, two pairwise-interleaved 3D-EPI readouts were acquired (FOV =

140 × 141 × 20 mm^3, voxel-size = 0.8 × 0.8 × 1.5 mm^3, TE/TR/TAvolume/TAtotal = 19/67/1500/3300 ms, flip-angle = 20°, SENSE$_{y/z}$ = 2.7/1). The 3D-EPIs were acquired in a center-slice-out fashion, so that the ABC k_0 occurred at the maximum gray-matter saturation, while the BOLD-only image was acquired close to the longitudinal equilibrium (Fig. 1B). The ABC signal was isolated through BOLD normalization. Coupled-compartment Bloch simulations were performed for different pulse-train-to-pulse-train times. All participants performed a hand-flexing task while the isolated-ABC sequence was recorded (ON = 30 s, OFF = 30, duration = 10 min). For 3 participants, a temporally-matched VASO scheme (TE/TR/TI1/TI2/TAtotal = 19/67/1100/2550/3300 ms) was also recorded, achieved by shifting the first 3D-EPI k_0 to the blood-nulling point by reordering the 3D-EPIs to a linear-slice-readout. The FOV was placed in the left primary motor cortex. FMRI data were motion-corrected and a GLM (finger-tapping > rest) was fitted (FSL6.0.1). Gray-matter cortical depth profiles were extracted from a manually-drawn M1 ROI (LAYNII).

Results Bloch simulations predicted maximal gray matter, white matter, and venous saturation for a pulse-train with Tsaturation-to-saturation = 60 ms (Fig. 2). Pilot data confirmed these simulations. Acquisition without this delay or without a center-slice-out scheme reduced MT-weighting. MTR images with high gray/white matter contrast were obtained from the ABC/BOLD division (MTRGM = 82%, MTRWM = 75%, Fig. 2). The saturation train reduced temporal SNR (Fig. 2E, ABC: mean(sd) = 21.8(8.4)) compared to BOLD: (mean(sd) = 25.7(9.9)). The isolated-ABC had higher temporal SNR (mean(sd) = 18.6(7.1) than VASO (mean(sd) = 5.7(3)). In all participants, the isolated-ABC response localized to M1/S1 gray matter, while BOLD responses were pial-surface-centered. Cortical-depth analysis confirmed a reduced pial-surface-bias in isolated-ABC (Fig. 3). Isolated-ABC had a similar response to VASO in terms of localization and cortical depth response (Fig. 4). ABC and VASO z-stat distributions were similar across participants, implying similar sensitivity.

Discussion Increasing the fMRI spatial specificity is an important neuroscientific target. Here we developed a new fMRI method with improved localization compared to BOLD. We created MT-weighted fMRI using a sparsely-applied optimized pulse-train with a center-slice-out readout, thus circumventing SAR-restrictions at higher-fields. BOLD-correction was achieved by interleaving an additional readout. This allowed isolating the ABC signal, which showed microvasculature dominance and much-reduced pial-surface-bias compared to BOLD. Our results replicate a similar gray-matter specific response found using magnetization-transfer fMRI in cats [5]. Similar specificity/sensitivity to VASO was found. Note that sensitivity can be increased with more extensive saturation, while the ABC signal is insensitive to inflow effects and facilitates arbitrary readouts (no blood-nulling requirement), offering a flexible CBV method applicable across the brain. The current isolated-ABC relied on hard-rectangular pulse-trains, trading off increased sensitivity to B1/B0 inhomogeneities for efficient saturation. pTX-enabled, off-resonance pulse-trains may offer a better tradeoff for high-field application across the brain.

Conclusion The proposed isolated-ABC may be a useful tool for high-resolution human fMRI at high fields with a consistent and highly-localized fMRI signal.

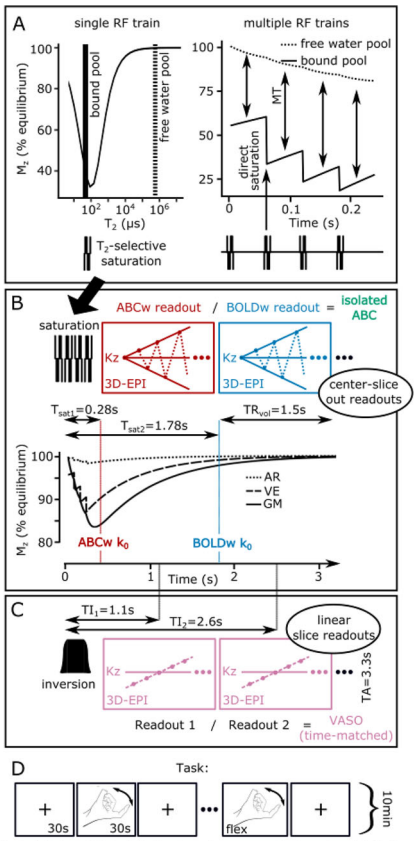

Fig.1: A, Isolated-ABC. A 12µT pulse-train saturates the bound-pool (left). Repeating the pulse-train after sufficient MT time saturates the (lipid-rich) tissue. B, A centre-out-slice ordering scheme brought the first k0 at the maximum gray-matter saturation (ABC) and the second k0 close to the longitudinal equilibrium (BOLD). C, An inversion followed by linear-readouts allowed a time-matched VASO scheme. D, Task.

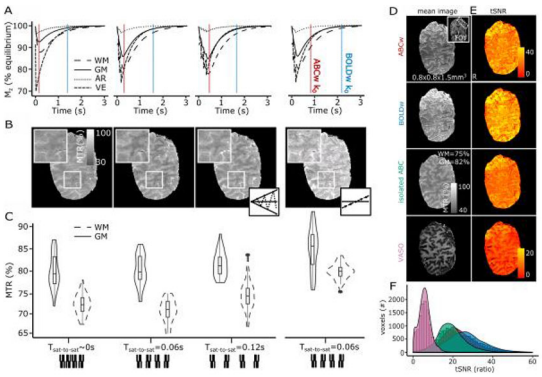

Fig. 2: A, Cross-compartment Bloch simulations. GM=gray-matter. WM=white-matter. VE=veins. AR=arteries. B Matched acquisitions, axial slices. C. GM and WM saturation. D, Mean images. E, tSNR. F, tSNR histogram.

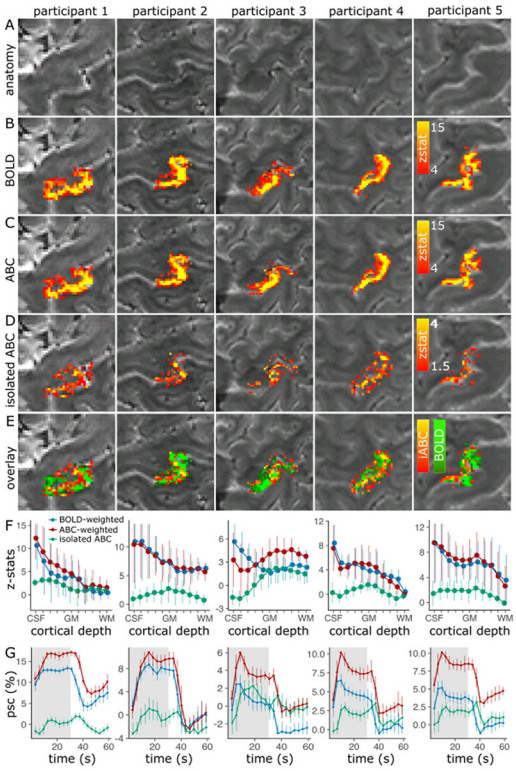

Fig. 3: A, mean image for all participants. B, BOLD (unsmoothed data). C, ABC. D, isolated-ABC. E, Overlay of isolated-ABC (red) with BOLD (green). F, Cortical depth analysis. G, Percent signal change.

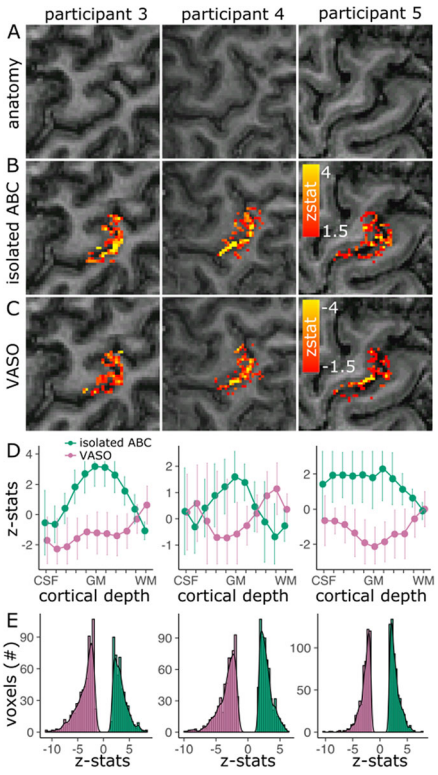

Fig. 4: A, mean image for the 3 VASO participants (columns). B, isolated-ABC. C, VASO. D, Cortical depth analysis. E, z-stat histogram.

References
1: Glover, 2011.
2: Uludag, 2009.
3: Huber, 2018.
4: Schulz, 2020.
5: Kim, 2011.

T16.

Congenital loss of aquaporin-4 leads to dysfunction of glymphatic system via brain-wide fluid stagnation—Evaluation with multi-modal MRI approach

R. S. Gomolka[1], L. M. Hablitz[2], H. Mestre[2,3], M. Giannetto[2], T. Du[2,4], N. Hauglund[1], L. Xie[2], W. Peng[1,2], P. Melero Martinez[1], M. Nedergaard[1,2], Y. Mori.[1]

[1]*University of Copenhagen, The Center for Translational Neuromedicine, Copenhagen, Denmark;*
[2]*University of Rochester Medical Center, Center for Translational Neuromedicine, Rochester, NY, United States;*
[3]*University of Pennsylvania, Department of Neurology, Philadelphia, PA, United States;*
[4]*China Medical University, School of Pharmacy, Shenyang, China*

Introduction The glymphatic system is a brain waste clearance pathway mediated by the exchange of cerebrospinal fluid (CSF) with interstitial fluid (ISF) [1]. It is comprised of a network of annular perivascular spaces formed by astrocytic endfeet ensheathing the vascular walls, and facilitated by aquaporin-4 (AQP4) channels [2]. Dysfunction of glymphatic system is associated with several neurological disorders, including Alzheimer's and Parkinson"s diseases, and stroke [3]. Still, it is not clear how AQP4 facilitates glymphatic fluid transport in part due to the lack of non-invasive whole-brain in vivo measurement of fluid dynamics. In our recent study [4], we investigated the impact of genetic loss of AQP4 on glymphatic system function using a multi-modal magnetic resonance imaging (MRI).

Methods All MRI experiments were performed in n = 34 10–16 weeks old Aqp4(−/−) (KO) and Aqp4(+/+) (WT) littermate mice, group-housed with food and water ad-libitum, temperature and humidity-controlled environment, and in 12/12 h light/dark cycle. Randomly subdivided animals underwent one of the three in vivo MRI experiments: 3D CSF space volumetry, 2D diffusion-weighted imaging (DWI), CSF dynamic contrast-enhanced (DCE) MRI via cisterna magna. MRI was performed at 9.4 T MR system (BioSpec 94/30USR, Bruker BioSpin) in animals anesthetized with Ketamin/Xylazine (K/X; *i.p.* 100/10 mg/kg). During all experiments, the animal"s body temperature was maintained at 37 ± 1 °C and monitored along with the respiratory rate. For high-resolution non-contrast CSF space volumetry, 3D constructive interference in steady-state (CISS) sequence along with a cryogenically cooled Tx/Rx quadrature-resonator (CryoProbe, Bruker BioSpin) and 240 mT/m gradient coil were used. 3D-CISS images were calculated as a MIP from two 3D-TrueFISP volumes of opposite encoding direction (TR/TE = 5.2/2.6 ms; FA = 50; 0.033 mm isometric voxel). CSF space was separated from the brain parenchyma image using an in-house automatic adaptive algorithm in Matlab [5]. To assess differences in the brain water mobility between KO and WT mice, respiratory-gated EPI DWI (TR/TE = 3600/30 ms; FA = 90; diff. enc. directions = 3; voxel dimension = 0.15 × 0.15 × 0.5 mm) was performed using a room-temperature volumetric Tx/Rx resonator (in. ø40 mm) with 1500 mT/m gradient coil, and 17 b-values measured (40–3081 s/mm^2). Voxel-wise curve-fitting took place using both monoexponential apparent diffusion coefficient (ADC), and biexponential intravoxel-incoherent

motion (IVIM) models [4]. For DCE-MRI, 3D-FISP images were acquired using CryoProbe with 1 min temporal resolution over 90 min (TR/TE = 3.26/1.63 ms; FA = 15; 0.1 mm isometric voxel; contrast agent (CA): Gadobutrol, 1 μL/min, 10 min), and evaluated with previously presented protocol [7].

Results The brain volumes were 5–10% larger (**Fig. 1A**) while the whole segmented CSF space to brain volume ratios were 23–29% smaller in KO compared to WT mice (**Fig. 1B**). The difference was mainly noted within the ventricular system (lateral, 3rd and 4th ventricles) but not the perivascular space (**Fig. 1C**). Both ADC and D-IVIM showed increased slow MR diffusion measures within the brain parenchyma, with KOs exhibiting ADC and D 5.7 ± 1.5% higher than WTs (**Fig. 2A**). The largest differences were visible in 4 brainstem, 4 cortical, and the caudate regions (**Fig. 2A-B**). No differences in perfusion-related IVIM measures between the genotypes were found within the brain parenchyma. Finally, DCE-MRI showed a significant reduction of CA clearance in KO mice, associated with accumulation of ISF in the brain parenchyma (**Fig. 3**). Furthermore, a delayed CA arrival time and time-to-peak, lower peak intensity, and duration of accumulation, as well as smaller area under the DCE curve was found in KO mice, indicating a reduced parenchymal influx and higher parenchymal resistance associated with lack of AQP4 channels [see original paper, 4].

Discussion and conclusion: Using non-invasive MRI at 9.4 Tesla, we provided important implications for understanding the mechanisms of ISF clearance from the brain. The presented findings suggest that loss of AQP4 results in brain-wide interstitial fluid stagnation, manifested by increased ADC and D due to enlarged ISF spaces, increased brain, and reduced CSF space volumes. Furthermore, with invasive DCE-MRI we have validated these results and comprehensively evaluated the impact of AQP4 loss on glymphatic system function. Concluding, our findings highlight the importance of non-invasive MRI techniques in studying the glymphatic system and, thus, in search of new therapeutic targets for neurodegenerative diseases.

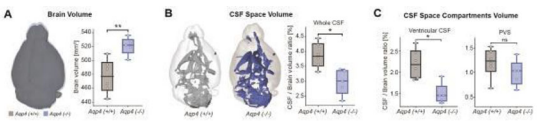

Fig. 1: Overlaid 3D surface images of the co-registered average 3D-CISS brain and CSF spaces, and whiskers-box plots comparing (A)the brain, (B)whole segmented CSF space, and (C)ventricular and perivascular compartments volumes from 6 WT and 5 AQP4 KO mice. ns-not significant, *-p<0.05, **-p<0.01; Mann-Whitney U-test.

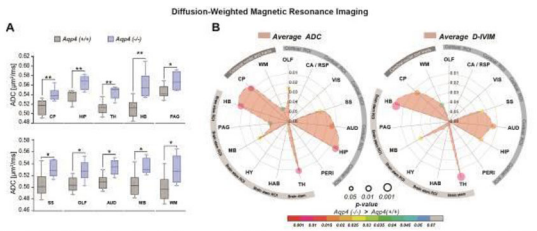

Fig. 2: (A)Whiskers-box plots for the mean ADC from 6 WT and 6 AQP4 KO mice - regions of significant differences. (B)Radar plots of p-values for the mean ADC and D (IVIM) differences between genotypes. OLF-olfactory, CA / RSP-cingulate / retrosplenial, VIS-visual, SS-somatosensory, AUD-auditory, HIP-hippocampus, PERI-perirhinal, TH-thalamus, HAB-habenula, HY-hypothalamus, MB-midbrain, PAG-periaqueductal gray, HB-hindbrain; CP-caudate, WM-white matter; *-p<0.05, **-p<0.01; Mann-Whitney U-test.

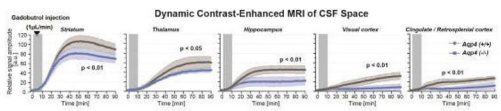

Fig. 3: (A)Mean±SD DCE curves from 6 WT and 5 AQP4 KO mice - parenchymal regions of significant differences between genotypes. *-p<0.05, **-p<0.01; nonparametric Two-way Anova.

References

1. Iliff JJ, et al. Sci Transl Med 2012;**4**:147ra111.
2. Nagelhus EA, OP Ottersen. Physiol Rev 2013;**93**:1543–62.
3. Rasmussen MK, et al. Physiol Rev 2022;**102**:1025–1151.
4. Gomolka RS, et al. Elife, 2023;**12**.
5. Gomolka R, et al. *ESMRMB 2021 38th Annual Scientific Meeting*. Online: MAGMA.
6. Stanton EH, et al. Magn Res Med 2021;**85**:3326–42.

T17.
Combining the benefits of 3D acquisitions and spiral readouts for VASO fMRI at UHF

A. Monreal-Madrigal[1], D. Kurban[1], Z. Laraib[1,2], R. Huber[1], D. Ivanov[1], N. Boulant[3], B. A. Poser[1]

[1]*Maastricht University, Cognitive Neuroscience, Maastricht, Netherlands;*
[2]*Polytechnic University of Turin, Turin, Italy;*
[3]*Universite´ Paris-Saclay, Gif-sur-Yvette, France*

Introduction VAscular Occupancy[1] can augment the widely used BOLD techniques with respect to their physiological interpretability and localization specificity; this is especially the case at UHF and at high spatial resolution[2]. Some of the main limitations of VASO are BOLD contamination, reduced detection sensitivity and temporal sampling efficiency. For BOLD contamination, a BOLD-corrected VASO image can be obtained by means of dynamic division with concomitantly acquired control images[3]. To overcome the limitations set by low temporal sampling efficiency, combining the efficiency of spiral k-space sampling with SMS acquisitions was suggested[4]. For high-resolution fMRI, however, 3D readouts can be advantageous over 2D ones[2]. This study aims to combine the benefits of 3D acquisitions and the efficiency of spiral for VASO fMRI. This is possible using a 3D stack-of-spirals readout previously proposed for BOLD fMRI[5]. Here, we demonstrate that fMRI with VASO contrast can be obtained using spirals, allowing for shorter echo times to improve tSNR, removing BOLD contamination and reducing acquisition time.

Methods A 3D stack-of-spirals (SOSP) Slab-Selective Slab-Inversion sequence was implemented using Pulseq[6]. For BOLD contamination correction, a BOLD-weighted control image was acquired right after the VASO one[2]. A 10 ms TR-FOCI inversion pulse[7] was applied 900 ms before the first excitation pulse of the spiral-out readout train; fat suppression was achieved with a 5 ms Gaussian pulse; the spiral trajectory was designed to minimize its duration within gradient constrains[8]. The sequence used in this work is shown in Fig. 1. In vivo data were acquired on a 7 T scanner (Siemens Healthineers) with 32ch headcoil (Nova Medical), visual checkerboard stimuli was presented while the subjects performed a fingertapping motor task (block-design, 33 s/33 s ON/OFF, 9 blocks). Spiral acquisition parameters were: FOV = 192 × 192 × 24 mm^3, nominal resolution = 0.8 × 0.8 × 1.0 mm^3, 24 kz partitions with linear encoding order, TRvol = 1622 ms, TE = 1.9 ms, TI1 = 1660 ms. The spiral readout was designed with variable density (α = 1.6) and a factor 3 in-plane undersampling resulting in a spiral duration of 53 ms. Cartesian 3D EPI[9] VASO with matched parameters and same task was acquired for comparison: matrix size [240 240 24], 1.02 ms echo spacing, bandwidth 1096 Hz/px, GRAPPA 3 and 6/8 partial Fourier resulting in 63 ms readout duration, linear kz encoding and selection of minimum TE/TR = 27/1754 ms. The resulting effective TR for the spiral and EPI sequences are 4140 ms and 4404 ms, respectively. EPI data were reconstructed using the vendor software on the scanner. The spiral reconstruction was performed in the open-source software

MRIReco.jl[10] using CG-SENSE and time-segmented off-resonance correction with nominal gradient trajectory; coil sensitivity and B_0 maps were taken from a separately acquired multi-echo 2D GRE scan. fMRI analysis was done in an openly available VASO pipeline consisting of motion correction, BOLD correction and conventional quality measures.

Results and Discussion Fig. 2 shows tSNR maps and mean timecourse images of the spiral and Cartesian data. In the thermal noise dominated regime of the high-resolution VASO, the spiral approach outperforms the EPI sampling by a factor of 2 in tSNR. This is expected from cumulative gains of improved signal sampling, including shorter echo times with reduced T_2* decay. Figure 3 shows the activation maps obtained from the spiral and EPI acquisitions. It can be seen that the spatial distribution of the activation pattern obtained with the current implementation is comparable to the current state-of-the-art 3D EPI sequence, confirming that the spiral acquisition effectively captures CBV and BOLD changes.

Conclusion In this work, we have shown that a fast implementation of a VASO fMRI with a 3D stack-of-spirals readout can be achieved using open source and freely available programs. The higher tSNR achieved with the spiral readout shows the potential of spiral VASO fMRI. The tSNR improvement over 3D EPI, however, is not accompanied by a z-score increase, which remains to be investigated. Further work will focus on implementing acceleration with controlled aliasing in the kz direction, reconstruction speed-up and correction for dynamic off-resonance effects. Here, we demonstrate that spiral readouts are promising and anticipate that they will become important in applications where there is a need for short TE, such as mesoscopic functional experiments at higher fields such as 9.4 T and 11.7 T where T2* is shorter.

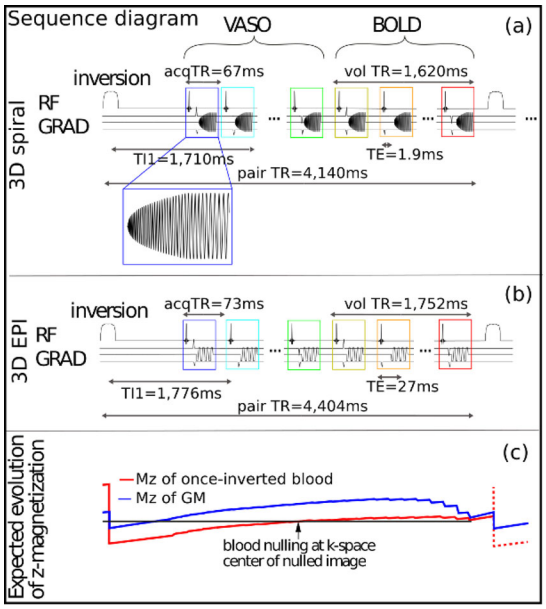

Fig. 1: (a) Sequence diagram of the SOSP acquisition. A TR-FOCI inversion pulse is applied 900ms before the first excitation of the VASO-weighted volume. A BOLD-weighted volume is acquired immediately afterwards. (b) Sequence timing diagram of the corresponding EPI acquisition; (c) Expected evolution of z-magnetization of the once-inverted blood and gray matter.

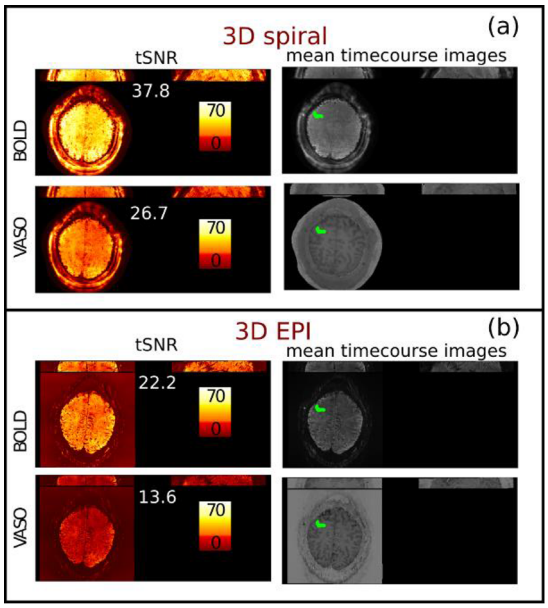

Fig. 2: tSNR maps and mean timecourse images for spiral (a) and EPI data (b). A 1.7 factor higher average tSNR for spiral BOLD and 1.9 for spiral VASO is achieved. The values in the insert refer to the ROI of GM in the primary motor cortex.

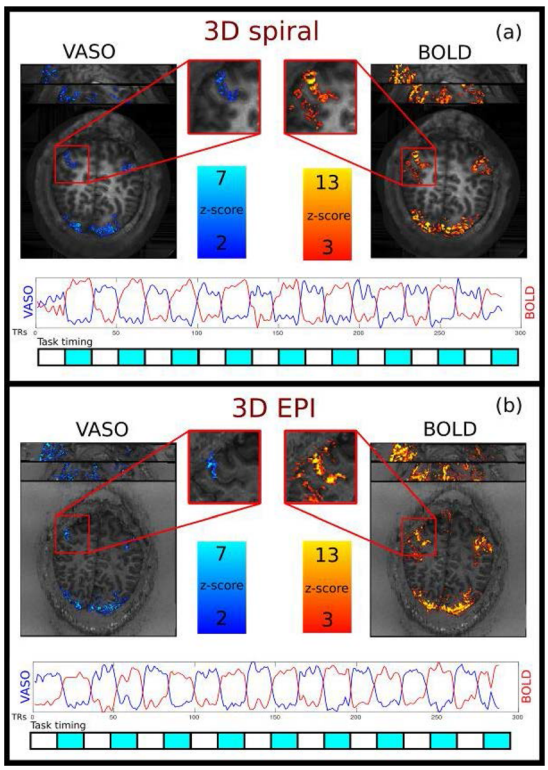

Fig. 3: VASO fMRI activation maps using 3D spiral (a) and 3D EPI (b). VASO contrast is less sensitive to large veins. Timecourse plot shows the normalized signal timecourse averages over active voxels. Note that VASO is a negative CBV contrast with an expected signal decrease during activity. The results highlight VASO's high functional detection sensitivity sampling approach.

References
1. Lu, H, et al. MRM 50(2), 263–274.
2. Huber, L, et al. NI 164, 131–143.
3. Huber, L, et al. MRM 72(1): 137–48.
4. Zahneisen, B, et al. NI 92, 8–18.
5. Hu, Y, et al. MRM 58(5), 947–951.
6. Layton, K. J, et al. MRM 77(4), 1544–1552.
7. Hurley, A. C, et al. MRM 63(1), 51–58.
8. Lustig, M, et al. IEEE T-MI 27(6), 866–873.
9. Poser, B. A, et al. NI 51(1), 261–266.
10. Knopp, T, et al. MRM 86(3), 1633–1646.

T18.
Perfusion measurements in an aging cohort using multiple inversion times pulsed ASL with simultaneous multi-slice EPI readouts at 7 T

D. Ivanov[1], S. Kashyap[2], L. Pagen[1], A. Monreal-Madrigal[1], R. van Hooren[1], H. Jacobs[1,3], B. A. Poser[1]

[1]*Maastricht University, Maastricht, Netherlands;*
[2]*Techna Institute, University Health Network, Toronto, Canada;*
[3]*Massachusetts General Hospital, Boston, MA, United States*

Introduction Arterial spin labeling (ASL) at 7 T is attractive due to the higher image signal-to-noise ratio (SNR) and the longer T_1 of blood and tissues compared to lower fields[1,2]. However, 7 T ASL has yet to be widely applied clinically, because of the technical challenges its successful implementation presents. Recently, a fast & SAR-efficient 7 T PASL approach with SMS-EPI readouts at multiple inversion times (multi-TI) has been proposed[3] to enable better characterization of the perfusion parameters. In this work we employ the proposed approach in an aging cohort to investigate its clinical applicability.

Methods Data was acquired after obtaining informed consent from 18 neurologically healthy volunteers (59 ± 14 years old, 8 female) on a 7 T MRI (Siemens Healthineers) with 1Tx/32Rx head coil (Nova Medical). A FAIR[4] Look-Locker sequence, with 2D blipped-CAIPI[5] SMS-EPI readouts was employed. Slab-selective or non-selective inversion was done using an optimized 10 ms tr-FOCI[6] pulse, and two $18 \times 18 \times 0.5$ cm^3 high permittivity dielectric pads[7] were placed on either side of the head at the level of the temporal lobes to further increase the labeling efficiency in the brain's major arteries. All ASL measurements had 2.8-mm isotropic resolution, 24 slices, 0.5 mm inter-slice gap, flip angles = 10 deg., echo time (TE)/repetition time (TR) = 11/2500 ms, echo-spacing 0.53 ms, acquisition time per slice 23.3 ms, and 80 TRs. The in-plane acceleration factor/SMS-factor/Number of TIs were 2/2/8. The first inversion time for the lowermost slice in all acquisitions was 175 ms and the duration of a 3D volume was 280 ms. Additional calibration scans were acquired to estimate the blood equilibrium magnetization (M0) with identical imaging parameters but with ASL preparation pulses amplitudes set to 0 and TR = 20 s. Voxel-wise mean perfusion-weighted signal maps were generated after motion correction with FSL. CBF and arterial arrival time (AAT) maps were computed using BASIL version 4[8]. Grey matter (GM) masks were created in the ASL voxel space and divided into 4 major sections (combinations of anterior/posterior and left/right) roughly corresponding to the main perfusion territories. Paired and unpaired t-tests were performed using GraphPad Prism.

Results and Discussion Six representative single-subject CBF maps are shown in Fig. 1. The images demonstrate the data quality and coverage achieved. High CBF values are obtained in the subcortical GM, while the inferior right temporal lobe suffers from signal loss in some subjects. Tab. 1 summarizes the GM CBF and AATs and their respective variances across the cohort along with the subjects' age and sex. The CBF values obtained are lower than from some 3 T ASL studies[9,10] and this could be a consequence from a lower labeling efficiency or a shorter labeling bolus at 7 T, despite the measures taken to minimize the effect of B_1 and B_0-field inhomogeneities[2].

Tab. 2 lists the CBF and AATs across participants and GM sections. The CBF in the posterior GM sections is significantly higher than that in the anterior sections, a finding typical for PASL approaches both at 3 & 7T[2]. The perfusion in the right posterior GM section is significantly lower than that in the left posterior section. Further, the right posterior GM section has a significantly longer arrival time than the right anterior section. In comparison, the right anterior GM section has a significantly shorter AAT than the left anterior section. These differences might have physiological origin, but may also be related to labeling asymmetries, due to B_1-inhomogeneities, typical at 7 T.

Fig. 2 plots the calculated AATs for males and females across the whole-brain GM as well as in the individual GM sections. Females exhibit significantly shorter AATs in the left and right posterior GM sections and across the whole brain. Males have more widespread and typically longer AATs. Shorter AATs in women have been previously reported multiple times[9,10]. No statistically significant differences in CBF between males and females could be found either on the section or whole-brain level. This may be due to a limited number of subjects and large variability in perfusion parameters or point to healthy neurological aging in the cohort. More homogeneous labeling enabled by parallel transmission techniques or improved transmit coil designs will help to disentangle the physiological effects from any methodological shortcomings of the approach.

In conclusion, the multi-TI PASL approach can robustly characterize the CBF and AATs in an aging cohort, but further improvements are possible and will be explored in future work.

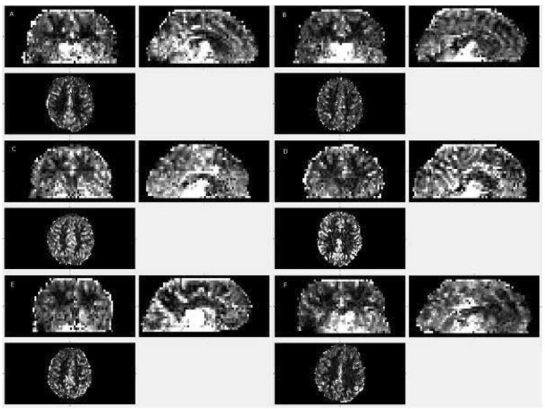

Fig. 1: CBF maps (0 - 70 ml/100g/min) from 6 representative subjects demonstrating the data quality & coverage. Subcortical grey matter (GM) exhibits high CBF values in all subjects, while in some participants (A,E,F) the perfusion in the inferior temporal lobe is very low due to B_1-inhomogeneities.

Age	Sex	Mean GM CBF (ml/100g/min)	CBF variance (ml/100g/min)	Mean GM arterial arrival time (s)	Arterial arrival time variance (s)
67	M	36.70	3.96	0.792	0.0422
71	F	31.90	3.78	0.767	0.0456
57	F	29.11	2.98	0.779	0.0429
58	F	35.40	5.31	0.770	0.0574
67	M	38.11	4.85	0.810	0.0532
69	F	38.69	4.11	0.776	0.0472
51	M	34.47	3.92	0.784	0.0478
42	F	37.50	5.43	0.771	0.0631
49	F	31.90	4.82	0.800	0.0660
46	M	32.10	4.75	0.759	0.0624
72	M	29.61	4.36	0.803	0.0472
57	M	24.97	4.05	0.795	0.0513
70	F	34.38	4.46	0.750	0.0588
47	M	33.89	5.99	0.810	0.0586
41	M	35.03	4.34	0.758	0.0579
31	F	29.68	4.25	0.782	0.0649
84	M	33.39	6.45	0.840	0.0456
80	M	30.60	5.50	0.841	0.0464

Tab. 1: Overview of the single-subject mean CBF & arterial arrival times (AAT) across the GM as well as their respective variances along with the age and sex of the participants.

Age	Sex	Mean GM CBF (ml/100g/min) LA	Mean GM CBF (ml/100g/min) LP	Mean GM CBF (ml/100g/min) RA	Mean GM CBF (ml/100g/min) RP	Mean GM arterial arrival time (s) LA	Mean GM arterial arrival time (s) LP	Mean GM arterial arrival time (s) RA	Mean GM arterial arrival time (s) RP
67	M	34.63	39.30	34.26	38.85	0.784	0.807	0.770	0.808
71	F	31.57	34.65	29.21	31.92	0.764	0.781	0.749	0.774
57	F	27.25	33.09	25.86	28.99	0.788	0.775	0.782	0.772
58	F	33.74	40.92	29.42	34.81	0.790	0.782	0.770	0.739
67	M	36.49	40.80	35.44	39.72	0.813	0.804	0.799	0.825
69	F	38.62	39.51	35.28	40.99	0.759	0.764	0.780	0.797
51	M	33.34	37.52	31.84	35.16	0.776	0.779	0.775	0.811
42	F	35.63	38.48	36.23	39.66	0.762	0.775	0.763	0.783
49	F	28.19	38.14	27.13	41.05	0.820	0.785	0.815	0.760
46	M	32.59	32.67	33.69	29.35	0.765	0.758	0.745	0.767
72	M	27.87	29.86	30.37	30.00	0.806	0.803	0.793	0.809
57	M	24.63	26.65	22.89	26.12	0.801	0.815	0.763	0.804
70	F	30.62	35.95	31.20	37.61	0.748	0.741	0.741	0.766
47	M	34.15	34.19	31.69	35.30	0.809	0.806	0.813	0.814
41	M	32.84	37.49	33.72	35.94	0.756	0.753	0.750	0.771
31	F	29.43	31.83	27.85	29.72	0.777	0.773	0.779	0.797
84	M	34.83	32.58	34.83	31.78	0.826	0.839	0.825	0.872
80	M	35.09	34.39	33.29	29.47	0.825	0.851	0.824	0.859

Tab. 2: Overview of the age, sex, single-subject mean CBF & AAT across the 4 GM sections created: Anterior Left (AL); Posterior Left (PL); Anterior Right (AR); Posterior Right (PR).

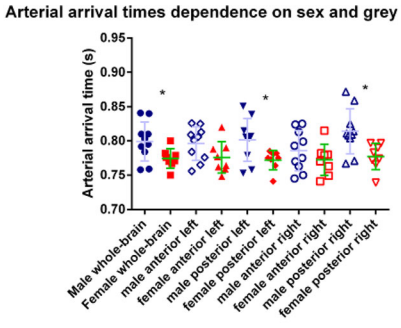

Fig. 2: Scatterplots (with the mean & st. dev. of the mean) of the AAT across the whole-brain GM and individual GM sections for males in blue / females in red. The statistically significant differences between males and females for the whole brain, posterior left and right sections are indicated with asterisk.

References

1 Gardener et al. MRM, 2009.
2 Ivanov et al. NIMG, 2017.
3 Ivanov et al. Proc. ISMRM, 2022.
4 Kim SG MRM, 1995.
5 Setsompop et al. MRM, 2012.
6 Hurley et al. MRM, 2010.
7 Teeuwisse et al. MRM, 2012.
8 Chappell et al. IEEE Trans Sig Proc, 2009.
9 Juttukonda et al. NIMG, 2021.
10 Mutsaerts et al. JCBFM, 2017.

T19.
Six-fold enhancement of pseudo-continuous arterial spin labeling perfusion mapping using a cryogenic coil at 9.4 T in an animal model of stroke

S. Pires Monteiro[1,2], R. Alves[2], L. Hirshler[3], E. L. Barbier[4], P. Figueiredo[1], N. Shemesh[2]

[1]*Universidade de Lisboa, Institute for Systems and Robotics—Lisboa and Department of Bioengineering, Instituto Superior Técnico, Lisbon, Portugal;*
[2]*Champalimaud Foundation, Lisbon, Portugal;*
[3]*C.J. Gorter Center for High Field MRI, Department of Radiology, Leiden University Medical Center, Leiden, Netherlands;*
[4]*University Grenoble Alpes, Grenoble Institut des Neurosciences, Grenoble, France*

Introduction Pseudo-continuous arterial spin labelling (pCASL) is a promising method for perfusion imaging. In preclinical MRI, pCASL perfusion measurements are particularly challenging due to brain geometry constrains, along with the higher fields that exacerbate B0 inhomogeneities at the labelling plane and off-resonance effects that affect the inversion efficiency (IE)[1]. Additionally, the reduced SNR of the acquisitions significantly limits the achievable spatial resolution. To address this issue, we explore the possibility of dramatically improving the resolution of pCASL in preclinical settings by using a cryogenic coil[2] at 9.4 T combined with a denoising method[3] and test our approach in a stroke model.

Methods All animal experiments and care were conducted according to the European Directive 2010/63 and preapproved by competent authorities.

Animal Preparation: Four Long-Evans female rats, 6–8 weeks old, weight: 200–300 g were used. Rats were sedated using 2.5% isoflurane and 35% oxygen in medical air, and their respiratory rate was kept at 40–60 bpm.

Stroke Induction: In one rat, a photothrombotic stroke model was used to induce a focal infarct in the somatosensory cortex (S1FL) with a solution of Rose Bengal dye (Sigma Aldrich, Portugal) (10 mg/ml)—delivered intravenously (13 mg/kg body weight); the rat was subsequently irradiated with a cold light source in S1FL for 15 min and scanned 1 day after stroke.

MRI experiments: Experiments were conducted on a 9.4 T Bruker Biospec Scanner equipped with an 86 mm volume coil for transmittance, a 4-element array cryogenic coil for signal reception and a gradient system able to generate up to 660 mT/m isotropically. An unbalanced pCASL sequence was used as described in Hirschler et al. (2018)[4]. For the pCASL acquisitions, the labeling plane was positioned at the rat neck ($\sim$ 1.3 cm below the isocenter), with a labelling duration (LD) of 3 s followed by a 300 ms post-labeling delay (PLD), TR/TE = 4000/40 ms, 30 repetitions, 4 averages. Inversion was achieved through a train of Hanning pulses: 400 µs duration, 800 µs pulse rate, B1 of 5µT, Gmax/Gave of 45/5 mT/m, where Gmax is the gradient applied during the RF pulse. Standard pCASL acquisitions: single-shot EPI, FOV = 22 × 22 mm^2, slice thickness = 1 mm, matrix = 94 × 94, spatial resolution of 234 × 234 m^2. Higher resolution pCASL: single-shot EPI, FOV = 19.2 × 22.0 mm^2, slice thickness = 0.75 mm, matrix = 174 × 200, spatial resolution of 110 × 110 m^2. For cerebral blood flow (CBF) quantification, a T1 map was obtained from an inversion recovery sequence[4]. A pCASL encoded FLASH was used to estimate the inversion efficiency (IE) 5 mm above the labelling plane (PLD = 0 ms, LD = 200 ms)[4].

Data Analysis: Raw data was denoised in image space with non-local PCA before CBF calculation[3]. CBF maps were calculated pixel-by-pixel as described in Alsop et al. (2015)[5]. The data analysis pipeline is presented in Fig. 1.

Results Images for each step of the pipeline are shown in Fig. 2. The tSNR highlights that higher resolution raw data have reduced SNR, but still enough to properly quantify CBF (Fig. 3). After phase optimization, the average IE was 87.0 ± 4.0%. Figure 4 shows CBF maps at standard resolution (top) and × 6 higher resolution (bottom) in 3 controls and 1 stroke case. In controls, all acquisitions show the expected CBF patterns in the healthy rat brain, with increased perfusion in grey matter (e.g. cortex and thalamus) when compared to white matter. However, in the high-resolution images, a better delineation of different brain regions becomes apparent. Perfusion in different cortical layers can be discerned, along with clearly delineated descending vessels (Fig. 4. A). Even in the hippocampus, where CBF is reduced compared with other grey matter regions, layers can be observed (Fig. 4. B). In the stroke model, the high-resolution images show a better definition of the stroke core along with the affected vessels.

Discussion In this work, we increased the state-of-the-art resolution of pCASL pre-clinical images by a factor of 6, without prolonging the experiments, which represents a significant improvement in image quality. We also managed to successfully validate this technique using a stroke model. These developments are mainly due to the use of a cryogenic coil combined with the denoising method, which provides

dramatically enhanced sensitivity. One drawback of our single-shot EPI approach is the longer TE compared to previous studies[4]; still, we observed highly consistent results across animals and high relative ASL signal, suggesting that this was not a major confounding factor. In the future, the resolution could be further increased by acquiring EPIs with multiple segments, or faster spiral trajectories. Our results bode well for future applications of quantitative CBF mapping.

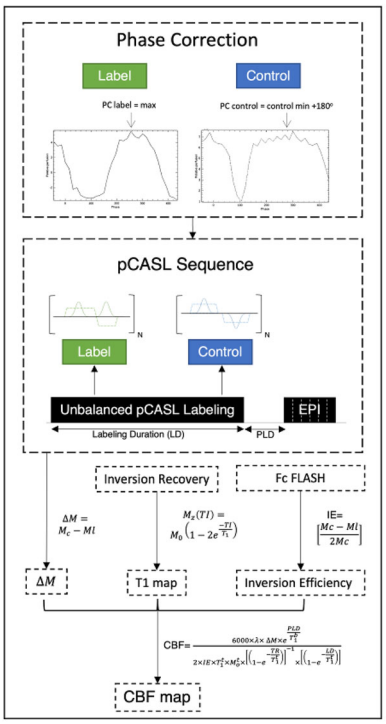

Fig. 1: Schematics of the analysis pipeline showing the phase correction implemented, the pCASL sequenced used and the different inputs for CBF quantification.

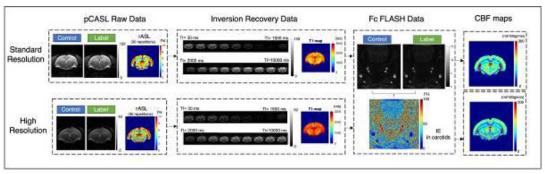

Fig. 2: Display of the pipeline for two different acquisitions - standard and high resolution – with representative images for each step.

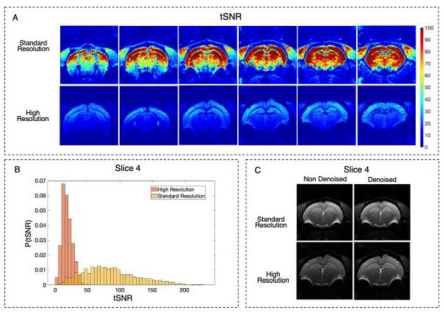

Fig. 3: Comparison of SNR between standard and high-resolution acquisitions in a representative animal in control images: A) Voxelwise maps of tSNR: average of 30 repetitions for 6 slices; B) Probability distribution of tSNR for slice 4; C) Comparison of denoised with non-denoised raw data.

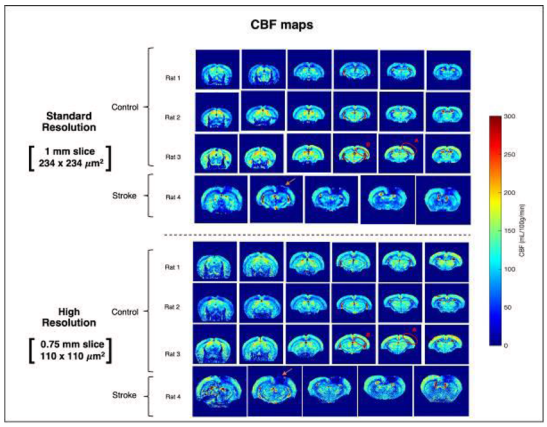

Fig. 4: Quantitative CBF maps for standard and high-resolution acquisitions across 3 healthy rats (6 slices per animal) with ROIs delimiting findings that could only be attained through high-resolution imaging: A) cortical layers and local descending vessels; B) hippocampal layers. In rat 4, a stroke was induced 24h prior to the acquisition. The orange arrow indicates the stroke core.

References

1. Larkin JR, J Cereb Blood Flow Metab, 2019
2. Ratering D, *MRM*, 2008.
3. Manjón J v., *Med Image Anal*, 2015.
4. Hirschler L, *MRM*, 2018.
5. Alsop DC, *MRM*, 2015.

T20.
Overcoming spatiotemporal resolution trade-off in DCE-MRI: Estimation of pharmacokinetic parameters directly from k-space

N. Korobova[1], S. Rauh[2], M. Troelstra[1], M. Orton[3], E. Schrauben[1], O. Maier[4], A. Nederveen[1], O. Gurney-Champion[1]

[1]*Amsterdam UMC, Radiology and Nuclear Medicine, Amsterdam, Netherlands;*
[2]*Amsterdam UMC, Department of Biomedical Engineering and Physics, Amsterdam, Netherlands;*
[3]*The Institute of Cancer Research, Radiotherapy and Imaging Division, London, United Kingdom;*
[4]*TU Graz, Institute of Biomedical Imaging, Graz, Austria*

Introduction Dynamic-contrast enhanced (DCE) MRI has shown great potential for studying perfusion in cancer patients for treatment planning and response monitoring(1). However, quantitative DCE faces numerous challenges that hinder its adoption in clinical practice. The main issue arises from the need to acquire high-resolution images for visualization of small tumor heterogeneities while simultaneously performing fast scanning to capture rapid transition of contrast agent (CA). Moreover, the estimations are influenced by outlier-voxels and Rician noise-bias present in the image domain. We suggest addressing these challenges by model-based reconstruction (MBR). Using a biophysical model, MBR reconstructs quantitative maps directly from the k-space data (Fig. 1). This approach avoids the explicit spatiotemporal trade-off as the reconstruction of intermediate image series from k-space is not required. The Gaussian noise distribution in k-space prevents a noise-dependent bias. Additionally, spatial regularization in MBR can suppress outlier-voxels. In this work, the extended Tofts-Kety (eTK)(2) model was implemented in the PyQMRI(3) MBR framework for quantitative DCE-MRI. We

validated the DCE-MBR framework in a digital phantom[4] and proved its feasibility in vivo.

Methods PyQMRI MBR framework uses an iteratively regularized Gauss–Newton algorithm with a primal–dual inner loop for non-linear fitting. A total generalized variation functional was used as a regularization[5]. The estimated pharmacokinetic (PK) parameters included fractional plasma volume *vp*, fractional volume of extracellular extravascular space (EES) *ve*, the mass reflux rate from EES back into plasma *ke*, and inflow time of CA *dt*. The eTK implementation in the forward model was taken from the OSIPI GitHub[6], in which the arterial input function was described analytically, allowing for analytical integration. An abdominal digital phantom[4] was used for the validation of MBR. The DCE signal was simulated for multiple abdominal organs. The distribution of CA was calculated based on the PK parameters either taken from the literature[7,8] or set to reasonable values. The signal model was based on the 3D spoiled GRE acquisition with golden angle radial stack-of-stars undersampling scheme (B0 = 3 T, TR = 4.5 ms, TE = 1.8 ms, flip angle = 22°, voxel size 1 × 1 × 1 mm^3, acquisition time 5 min). To assess the influence of the temporal resolution on the reconstruction of PK maps, 4 experiments with different dynamic times were preformed (1.5, 2.4, 3.9, 16.5 s/frame). The analysis was done on one coronal 2D plane. Subsequently, the feasibility of MBR was shown in vivo. One healthy volunteer was scanned with similar protocol (B0 = 3 T (Philips Ingenia, Philips, Best, The Netherlands), TR = 3.5 ms, TE = 1.4 ms, flip angle = 22°, voxel size 1.5 × 1.5 × 3.5 mm^3, acquisition time 5.2 min). The MRB approach was compared to a conventional analysis consisting of a GRASP[9] reconstruction (regulization factor of 0.01) followed by a voxel-wise non-linear LSQ fit. The mean absolute error and standard deviation of predicted PK maps were calculated in simulations for both methods. The significance of these measures was assessed by the Wilcoxon significance test with Bonferroni correction.

Results The PK parameters estimated with MBR were found to be less noisy than those obtained with LSQ fit for all temporal resolutions, which was especially visible in the *vp* map in the liver (Fig. 2A). MBR showed significantly smaller spread of values than LSQ fit while keeping the same accuracy (Fig. 2B). Figure 3. depicts the detailed distribution of predicted values in liver, pancreas, and spleen. In vivo, we found similar results: quantitative maps were more homogeneous and better depicted smaller anatomical objects when estimated with MBR (Fig. 4). However, the resolution of 2.4 s/frame showed an over-regularized *ke* map, which mean that regularization parameters may need to be tweaked further in vivo.

Discussion We implemented a DCE model in the MBR framework and assessed its performance in a digital phantom and in vivo. MBR yielded higher precision, while maintaining the accuracy of the estimated maps compared to the reference method (LSQ fit) even at high temporal resolutions Our findings indicate that MBR is robust to different temporal resolution and is capable of eliminating random errors and noise-dependent bias. This suggests that MBR can overcome the spatiotemporal trade-off in DCE.

Conclusion MBR for DCE-MRI can substantially improve PK parameter map quality at high spatial and temporal resolution.

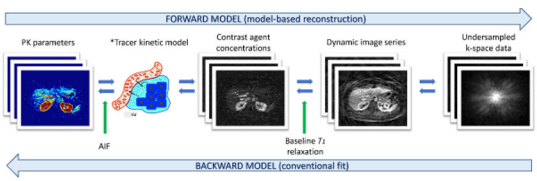

Fig. 1: Backward and forward models used to estimate PK parameters from DCE-MRI data. (*) image of TK model was adapted from DCE parameters - Questions and Answers in MRI (mriquestions.com).

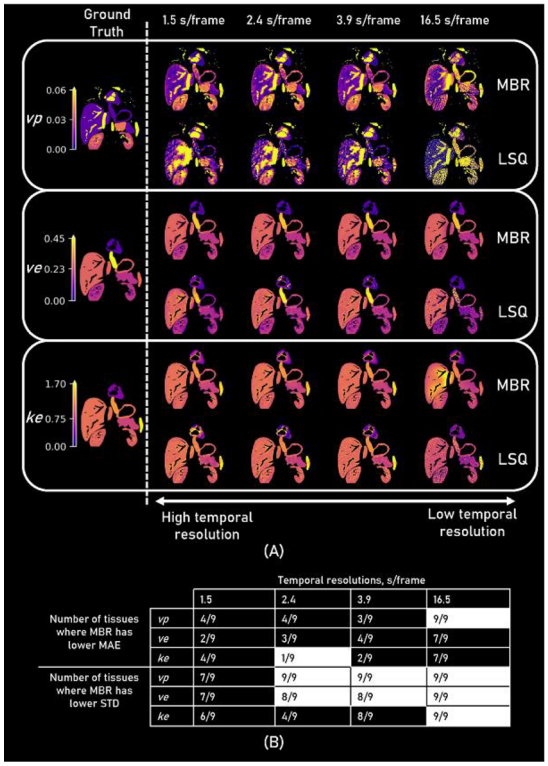

Temporal resolutions, s/frame

		1.5	2.4	3.9	16.5
Number of tissues where MBR has lower MAE	*vp*	4/9	4/9	3/9	9/9
	ve	2/9	3/9	4/9	7/9
	ke	4/9	1/9	2/9	7/9
Number of tissues where MBR has lower STD	*vp*	7/9	9/9	9/9	9/9
	ve	7/9	8/9	8/9	9/9
	ke	6/9	4/9	8/9	9/9

Fig. 2: (A) PK parameters estimated with MBR and non-linear LSQ fit in a digital phantom. The reference ground truth values are shown in the first column. (B) The number of tissues in which MBR showed lower mean absolute error (MAE) and lower standard deviation (STD). The more tissues show lower MAE and STD, the better the result. White cells show significant differences in MAE and STD calculated for MBR and LSQ.

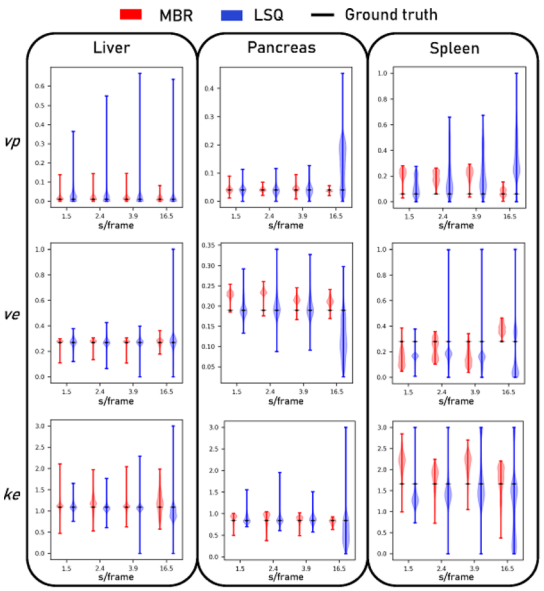

Fig. 3: Distribution of values of PK parameters in liver, pancreas, and renal medulla, estimated with MBR and non-linear LSQ fit in the digital phantom.

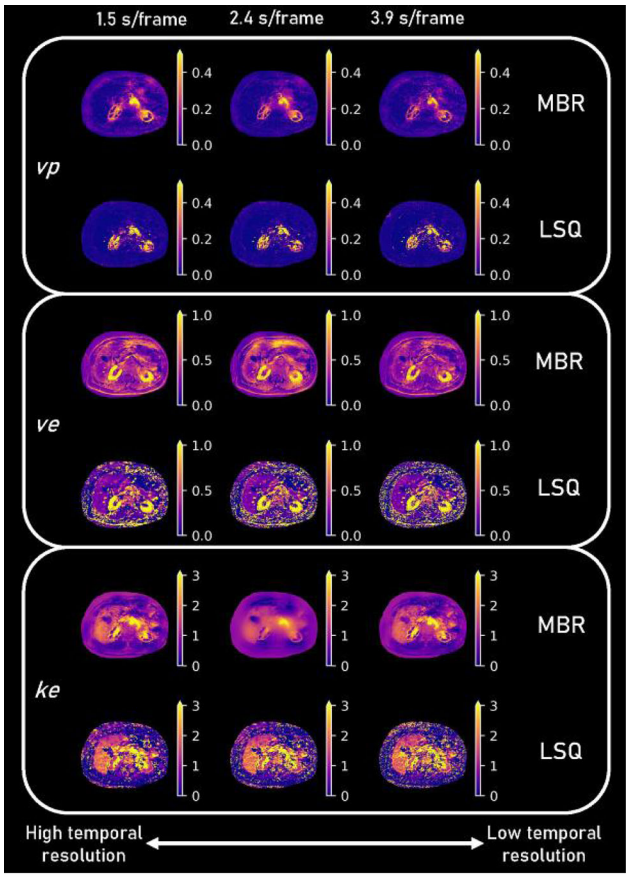

Fig. 4: PK parameters estimated with MBR and non-linear LSQ fit in vivo.

References
1. Counago F, et al. Springerplus. 2015.
2. Tofts PS. Jmri-J Magn Reson Im. 1997.
3. Maier O, et al. J Open Source Software. 2020.
4. Wissmann L, et al. J Cardiovasc Magn R. 2014.
5. Bredies K, et al. SIAM J Imaging Sciences. 2010.
6. Orton MR, et al. Phys Med Biol. 2008.
7. Holland MD, et al. Medical Physics. 2022.
8. Sun NN, et al. Diagn Interv Radiol. 2018.
9. Feng L, et al. Magn R in Medicine. 2016.

T21.
Probing glioma microvasculature: A comparison of perfusion MRI with intra-operative high frame rate µDoppler ultrasound

A. Alafandi[1], S. Soloukey[2,3], F. Arzanforoosh[1], S. R. van der Voort[1], F. Incekara[1,3], L. Verhoef[2], P. Kruizinga[2,4], M. O. Smits[1]

[1]*Erasmus Medical Center, Department of Radiology and Nuclair Medicine, Rotterdam, Netherlands;*
[2]*Erasmus Medical Center, Department of Neuroscience, Rotterdam, Netherlands;*
[3]*Erasmus Medical Center, Department of Neurosurgery, Rotterdam, Netherlands;*
[4]*Erasmus Medical Center, Department of Biomedical Engineering, Thorax Center, Rotterdam, Netherlands*

Introduction Due to the crucial role of dynamic susceptibility contrast (DSC) perfusion MRI in grading gliomas on the basis of the tumour vascularity1, relative cerebral blood volume (rCBV) has been broadly utilised in neuroradiological practice to differentiate between tumour grades and types by assessing vascular characteristics2. A relatively new modality named µDoppler ultrasound has the potential to complement and inform perfusion MRI due to its capability of visualizing the hemodynamic changes inside the brain and tumor at very high spatiotemporal resolution. In our study, we describe microvascular features of three types of adult-type diffuse glioma, comparing DSC perfusion MRI and intra-operative µDoppler ultrasound.

Materials and Methods a dataset of 10 patients with primary brain tumours who underwent surgery were included in a previously published study on µDoppler ultrasound3. Patient eligibility for this study has been reported earlier while additional inclusion criteria for our study were the availability of both the DSC perfusion MRI scans and intra-operative µDoppler ultrasound images. For µDoppler ultrasound, images were post-processed3 and segmented using 3DSlicer to obtain 3D vessel segmentation from the tumour vascular bed. The tumour mask and contralateral normal appearing white matter (NAWM) mask were created using structural MRI. For rCBV quantification, T2*w scans were used as an input for IB-Neuro software with the leakage correction feature selected, then normalised to the contralateral NAWM. Using an in-house python script, histograms were obtained from which median, mean and maximum rCBV ratios were extracted.

Results 7 patients with enhancing and non-enhancing glioma met the inclusion criteria and are presented as a case series (3 patients were excluded for missing imaging data). Overall, low grade gliomas (LGGs) showed lower perfusion compared to high grade gliomas (HGGs) as expected. Within the LGG-subgroup, oligodendroglioma showed relatively higher perfusion compared to astrocytoma, with median rCBV ratio of (1.20) and (1.14) compared to (0.46) and (0.82) for astrocytoma. In HGG, median rCBV ratio for glioblastoma was (3.12) while astrocytoma grade 4 showed low perfusion with a median rCBV of (1.19). On µDoppler ultrasound images, all tumours showed a range of rich and organised vascular networks with visually apparent abnormal vessels, even in LGG.

Discussion: Our unique case-series revealed deep in-vivo insights about the tumour vascularity using two imaging modalities, pre-operative DSC perfusion MRI and intra-operative µDoppler ultrasound images. These findings about the microvascular architecture in both high and low grade glioma challenge the current assumption behind the estimation of rCBV that the distribution of blood vessels in a voxel is random. Our µDoppler ultrasound images revealed in-vivo details of the tumour microvasculature which appear to have a dense well-structured morphology and vascular network irrespective of the MRI perfusion state.

Conclusion our µDoppler ultrasound images revealed unprecedented details about the tumour vascular bed showing rich vascularisation also in tumours with low perfusion on MRI. These findings, sowing some doubts about the assumptions regarding the vessel distribution and orientation for rCBV estimation, warrant further investigation of DSC MRI post-processing, in particular for typing and grading adult-type diffuse glioma.

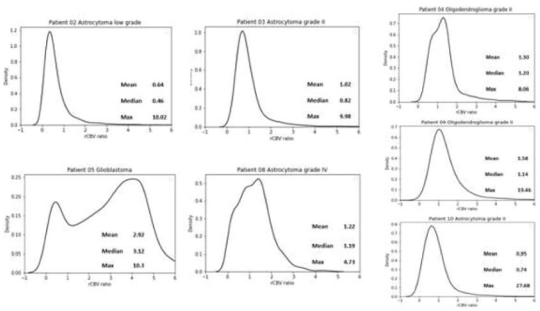

Fig.1: Tumour rCBV ratio histograms (Mean, Median,Maximum)

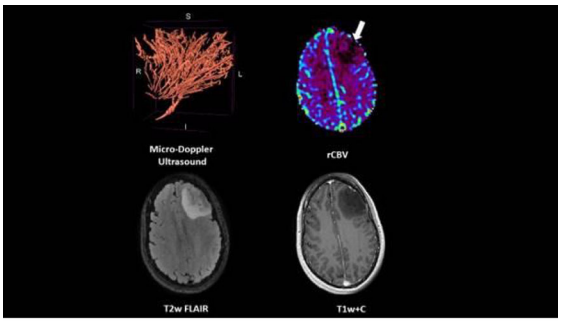

Fig. 2: Patient 02 Astrocytoma low grade *IDH-mutant*

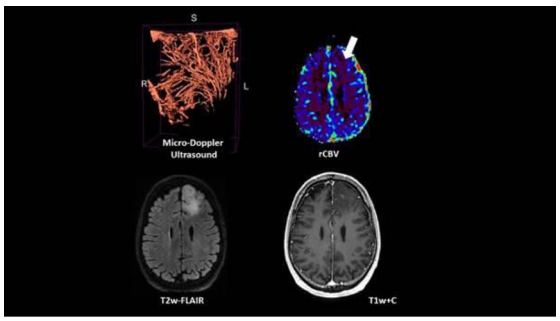

Fig. 3: Patient 09 Oligodendroglioma grade II *IDH mutant 1p/19q codeleted*

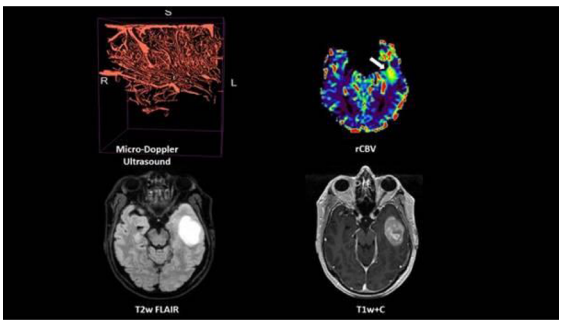

Fig. 4: Patient 05 Glioblastoma *IDH wild-type*

References

1. Covarrubias DJ, Rosen BR, Lev MH. Dynamic Magnetic Resonance Perfusion Imaging of Brain Tumors. *Oncologist*. 2004;9(5):528–537. https://doi.org/10.1634/theoncologist.9-5-528
2. Hakyemez B, Erdogan C, Ercan I, Ergin N, Uysal S, Atahan S. High-grade and low-grade gliomas: differentiation by using perfusion MR imaging. *Clin Radiol*. 2005;60(4):493–502. https://doi.org/10.1016/j.crad.2004.09.009
3. Soloukey S, Vincent AJPE, Satoer DD, et al. Functional Ultrasound (fUS) During Awake Brain Surgery: The Clinical Potential of Intra-Operative Functional and Vascular Brain Mapping. *Front Neurosci*. 2020;13. https://doi.org/10.3389/fnins.2019.01384

T22.
Breast cancer imaging at low and ultra-low magnetic fields using field cycling imaging: A clinical pilot study

V. Mallikourti[1], P. J. Ross[1], E. Husain[2], G. Davies[1], G. Lip[2], H. Lahrech[3], Y. Masannat[2], L. Broche[1]

[1]*University of Aberdeen, Aberdeen, United Kingdom;*
[2]*Breast Unit, Aberdeen Royal Infirmary, Aberdeen, United Kingdom;*
[3]*University Grenoble Alpes, Inserm U1205, BrainTech Lab, Grenoble, France*

Introduction Standard clinical MRI in breast cancer has limitations in determining the tumour subtypes, and cannot detect tumour cell infiltration generally localized in tumour margins. Field-Cycling imaging[1,2] (FCI) is a novel modality that can image over a range of low magnetic field strengths through rapid switching between magnetic field levels. This allows measuring the field-depended changes of the longitudinal T_1 relaxation time ($R_1 = 1/T_1$), known as nuclear magnetic relaxation dispersion (NMRD). NMRD profiles provide information on molecular dynamics exploiting novel biomarkers that recently have been shown in breast cancer and glioma models related to tumour invasion migration[3,4]. The goal of this clinical study is to define the specificity of FCI as medical imaging modality in breast cancer diagnosis and its precision in tumour delineation.

Methods Twenty-six females with breast cancer were recruited from January 2019 to March 2022 (ethics approved by NoSREC, number 19/NS/0064). Ten patients completed the study and were diagnosed with Invasive Ductal Carcinoma (n = 1), Ductal Carcinoma In Situ (DCIS, n = 5), borderline phyllodes (n = 1) and mixed phenotypes (n = 3). One patient presented two distinct lesions at histology and each lesion was treated separately for the analysis (n = 11 data in total). FCI was performed with four evolution fields (200, 65.8, 21.7 and 2.3 mT) using an inversion recovery spin echo sequence with five evolution times. The slice thickness was set to 10 mm and the in-plane resolution to 2 to 4 mm, depending on the FOV with matrix size of 128 × 128. The total duration of the FCI examination was 45 min. Clinical imaging including ultrasound, mammography, and in some cases MRI at 1.5 T were used for comparison. Histology analysis was considered here as gold standard imaging and was used for validation. Tumour sizes in FCI images were calculated using ImageJ. Tumour sizes were compared to histology.

Data analysis was done in MATLAB using in-house software[5]. R_1 quantification was obtained using the exponential model derived from the Bloch equations. The R_1 NMRD profiles were fitted using a power law model ($1/T_1 = aB^{-\beta}$) to derive the slope of the dispersion (β parameter). The amplitude of the quadrupolar peak at 65.8 mT was estimated by subtracting the baseline provided from interpolation following the power law model. NMRD dispersions were extracted from three ROIs: tumour and adipose and glandular breast tissue in the contralateral breast. Average R1 was calculated from the R_1 values at 200, 22 and 2.3mT and was compared between tissue types.

Results The tumour region measured by FCI exhibited hyper-intense regions at low field strengths (Fig. 1). FCI tumour sizes were found close to those obtained from histology (Fig. 2). This was not the case for the other imaging modalities for which 6 out of 8 DCIS cases were severely under-estimated.

Tumour R_1 values were markedly lower than healthy breast tissue (Fig. 3), and average R_1 values were significantly different between tumours and glandular tissue ($6.0 \pm 2.0\ s^{-1}$ vs $8.4 \pm 3.0\ s^{-1}$, $p < 0.01$) and between tumours and adipose tissue ($6.0 \pm 2.0\ s^{-1}$ vs $9.2 \pm 0.9\ s^{-1}$, $p < 0.001$). The R1 contribution from ^{14}N-^{1}H quadrupolar coupling at 65.8 mT was significantly visible in tumours ($0.9 \pm 0.6\ s^{-1}$, $p < 0.001$) and glandular tissues ($0.7 \pm 0.5\ s^{-1}$, $p < 0.01$) using a two-sided one-sample t-test (Fig. 3) but we did not observe significant differences between these tissues ($p = 0.47$).

The β parameter was significantly higher in non-invasive (0.18 ± 0.11) compared to invasive tumours (0.06 ± 0.03, $p < 0.05$) to discriminate invasion from non-invasion (Fig. 4) in line with those found in preclinic on breast cancer and glioma models[3,4]. QP amplitude ($0.5 \pm 0.5\ s^{-1}$ in invasive vs $1.1 \pm 0.6\ s^{-1}$ in non-invasive) and R_1 at 2 mT ($6.3 \pm 2.4\ s^{-1}$ in invasive vs $9.6 \pm 1.8\ s^{-1}$ in non-invasive) were markedly higher for non-invasive tumours ($p > 0.05$).

Discussion This is the first time that R_1-NMRD profiles are extracted from in vivo breast cancer patients. Despite the low spatial resolution, FCI located accurately the lesions and provided non-biased size estimates, as validated by histology. The dispersion of the NMRD profiles successfully discriminated between tumours, adipose and glandular tissues, and the slope of the dispersion discriminated between invasive and non-invasive tumours. Changes in R_1 relaxation suggest rapid transmembrane water exchange[3,4].

Conclusion FCI shows high potential for breast tumour detection without contrast agent with potentially better delineation in DCIS. We also found potential biomarkers of breast cancer invasiveness, which is of high interest for surgery planning and could improve the outcome of patient treatment if confirmed.

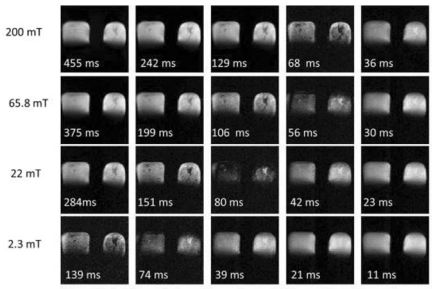

Fig. 1: Typical FCI data from a patient presenting with invasive lobular carcinoma mixed with DCIS. The evolution times are reported in ms along the columns and the evolution fields in mT along the rows.

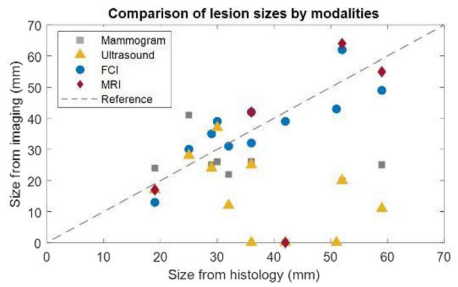

Fig. 2: Tumour size estimation by imaging modalities, compared with histology (considered as the standard).

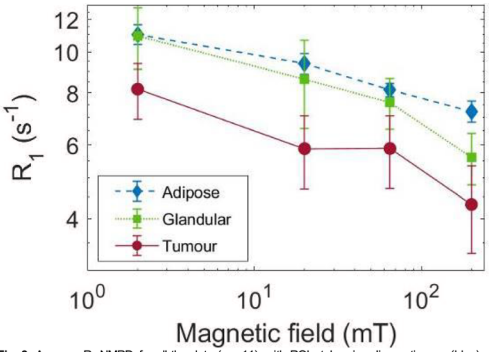

Fig. 3: Average R_1-NMRD for all the data (n = 11), with ROIs taken in adipose tissues (blue), glandular tissues (green) and tumours (red). The error bars are set to +/- sigma. The amplitude of QP peak at data point at 65.8 mT is shown by the arrow.

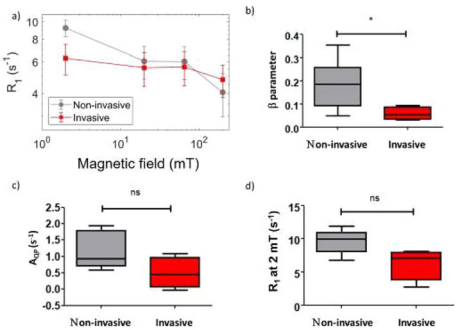

Fig. 4: FCI biomarkers of invasion tissues. Details of the tumour dispersion profiles is shown in (a), where invasive (n=4) and non-invasive tumours (n=6) are separated. The parameter b (related to water dynamics) clearly appear as a relevant FCI biomarker of invasion processes. Statistical significance is given by the p value between each group (*p<0.05). A_{QP} is the amplitude of the quadrupolar peak.

References

1. Lurie, D.J. et al. Cr Phys. 2010;11, 136–148
2. Broche LM, et al. Sci. Rep. 2019;9(1):10402
3. Petit M, et al. NMR Biomed. 2022;35(6):e4677
4. Ruggiero MR, et al. Cancers (Basel). 2022;14(17):4180
5. Broche LM, et al. Magn. Reson. Imaging. 2017;44:55–5

T23. Diffusion-weighted imaging in skin pathologies of the breast

D. Skwierawska[1], F. Laun[1], E. Wenkel[1,2], R. Janka[1], M. Uder[1], S. Ohlmeyer[1], S. Bickelhaupt[1]

[1]*Friedrich-Alexander-Universität Erlangen-Nürnberg (FAU), Institute of Radiology, Erlangen, Germany;*
[2]*Radiologie München, Munich, Germany*

Introduction Skin involvement in breast pathologies poses a diagnostic challenge, particularly in distinguishing between inflammatory breast cancers (IBC), benign skin inflammation or enhancement (BSI), Paget's disease (PD), and skin infiltration breast cancer (SIBC). Since there is currently limited literature regarding the possibility to use advanced MR imaging techniques in this clinical setting, this research aimed to investigate the effectiveness of diffusion-weighted imaging (DWI) as a tool to differentiate between these pathologies.

Methods The IRB-approved retrospective study included n = 90 female patients who underwent clinically indicated diagnostic breast

MRI, including multi-b-value DWI, with b-values ranging from 50–1500 s/mm^2 and demonstrated a skin pathology in the radiological report. The cohort consisted of n = 6 IBC, n = 12 BSI, n = 3 PD (Fig. 1), n = 11 SIBC (Fig. 2), and n = 58 women with healthy skin included as reference. All examinations were performed using 1.5 T/3.0 T scanners and regions of interest (ROIs) were defined manually on the b-value 750/800 s/mm^2 images. Pairwise comparisons using the Wilcoxon rank sum test were conducted to compare calculated apparent diffusion coefficients (ADC) between independent groups. Radiologists' reports or histology served as a standard of reference. The signal in the diffusion-weighted images was checked to ensure that it was high enough to enable proper computation of the ADC.

Results Women with SIBC demonstrated a mean ADC significantly lower compared to both BSI ($p < 0.05$) and IBC ($p < 0.05$) cases. These differences persisted for the first-order features of the ADC "mean", "median", and "minimum" ($p < 0.05$) except for the "ADC max" parameter ($p = 0.053$). PD mean ADC was not significantly different to that of SIBC ($p = 0.170$), but different to BSI ($p < 0.05$). Evaluation BSI and IBC also did not reveal significant statistical differences($p = 0.750$) between these groups for this limited sample size. Detailed values for all groups are presented in Fig. 3 and Fig. 4. ADC values in all groups with affected skin regions were statistically different from that observed in a control healthy group ($p < 0.05$), except for the "ADC min" for PD. The mean and median ADC values were almost identical and did not reveal any statistical difference. No statistical difference was also found between the ADC values derived voxel-wise and from the mean signal for any of the groups. Unlike in the other regions, the signal in the healthy skin ROIs was regularly too small to ensure a proper computation of ADC values.

Discussion Pathologies in the skin of women undergoing breast MRI can be challenging to assess, even with advanced imaging like DWI. Our study demonstrates that it is challenging to differentiate between certain pathologies, especially between IBC and BSI, possibly due to difficulties in distinguishing between findings in non-mass lesions than in mass lesions. Previous studies have shown that the ADC performs worse in differentiating non-mass lesions than in mass lesions [1, 2].

This study has some limitations that could be addressed in future research. Firstly, the sample size included in the investigation is relatively small, especially for patients with IBC or PD. Secondly, the study is retrospective; therefore, it was not possible to control certain aspects of the examination procedure that may affect the ADC calculations, such as the magnetic field strength or b-value selection. The healthy skin ADC values do not represent the correct ADC values due to limited SNR in the diffusion-weighted images. We nonetheless stated them because they should roughly reflect the values that other investigators might derive if their setup resembles ours.

Conclusion DWI can reveal differences between different skin-affecting pathologies, though without statistical significance for some of the types of pathology in our study. The ADC values allowed us to distinguish BSI from some skin infiltrating malignant lesions. However, it was not possible to accurately differentiate between benign and inflammatory breast cancer using ADC values. Larger studies are needed to assess the usefulness of quantitative DWI in supplementing the diagnostic assessment of skin pathologies in breast imaging.

Quantitative DWI is a promising contrast-free technique that can provide valuable information about the tissue structure, cellularity, physiology and water diffusion of normal and pathologic skin. However, its' clinical usefulness in discriminating between skin pathologies needs further investigation.

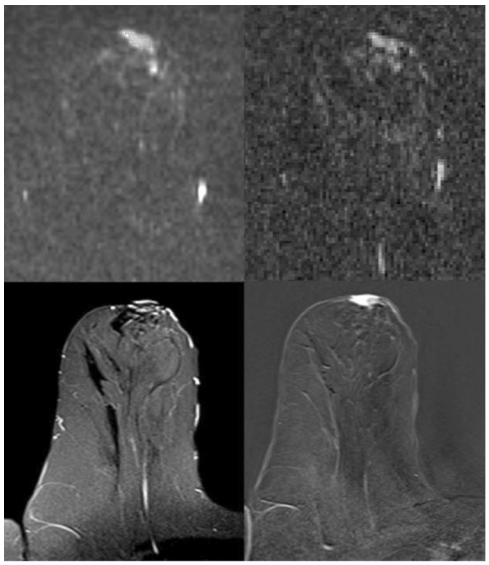

Fig.1: Breast MRI of women with the Paget's disease of the nipple. Top left: Manual ROI segmentation overlaid on the DWI image, top right: ADC map, bottom left: T2- weighted image, bottom right: T1- weighted image with fat saturation after contrast administration.

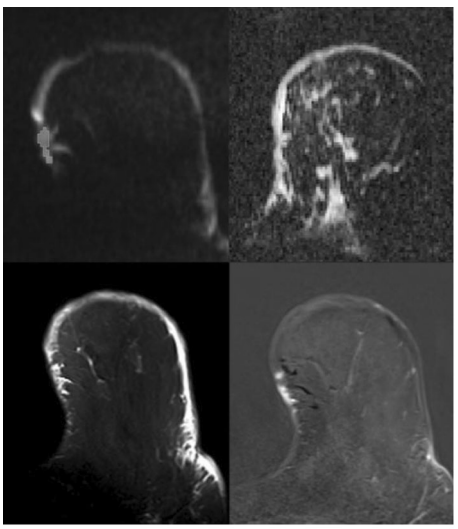

Fig. 2: Breast MRI images obtained from women with infiltrating mammary carcinoma involving the skin of the breast. Top left: Manual ROI segmentation overlaid on the DWI image, top right: ADC map, bottom left: T2-weighted image, bottom right: T1-weighted image with fat saturation after contrast administration.

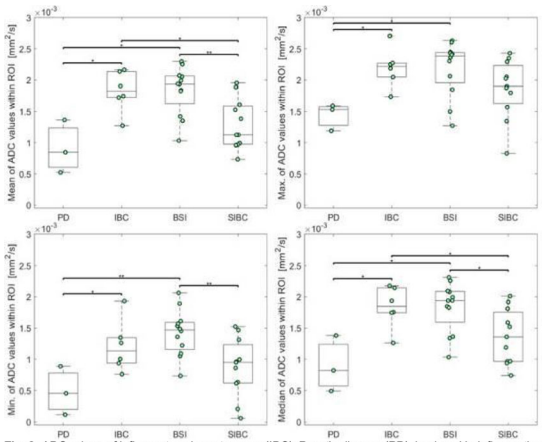

Fig. 3: ADC values of inflammatory breast cancer (IBC), Paget's disease (PD), benign skin inflammation (BSI), and skin infiltration of breast cancer (SIBC). Box and whisker plots showing the mean, maximum, minimum and median ADC values. The asterisks indicate statistical significance: "*" for p<=0.05 and "**" for p<=0.01.

Type	No.	Median ADC value ($x10^{-3}$ mm^2/s)	Max. ADC value ($x10^{-3}$ mm^2/s)	Min. ADC value ($x10^{-3}$ mm^2/s)	ADC of mean signal within ROI ($x10^{-3}$ mm^2/s)	Mean of ADC values within ROI ($x10^{-3}$ mm^2/s)
Paget's disease of the nipple	3	0.90 ± 0.26 (0.49-1.38)	1.44 ± 0.12 (1.19-1.59)	0.49 ± 0.22 (0.12-0.89)	0.94 ± 0.23 (0.59-1.37)	0.91 ± 0.24 (0.52-1.36)
Inflammatory breast cancer	6	1.84 ± 0.14 (1.26-2.18)	2.20 ± 0.13 (1.74-2.71)	1.21 ± 0.17 (0.76-1.93)	1.84 ± 0.14 (1.28-2.18)	1.82 ± 0.13 (1.27-2.16)
Benign skin inflammation or enhancement	12	1.84 ± 0.11 (1.03-2.31)	2.19 ± 0.13 (1.27-2.63)	1.42 ± 0.11 (0.73-2.06)	1.84 ± 0.11 (1.04-2.3)	1.83 ± 0.11 (1.03-2.3)
Skin infiltration breast cancer	11	1.36 ± 0.13 (0.74-2.01)	1.86 ± 0.14 (0.83-2.43)	0.87 ± 0.14 (0.06-1.52)	1.38 ± 0.13 (0.73-1.98)	1.37 ± 0.13 (0.73-1.95)
Healthy skin	58	0.48 ± 0.02 (0.22-0.84)	0.86 ± 0.03 (0.42-1.47)	0.18 ± 0.02 (0.01-0.63)	0.49 ± 0.02 (0.23-0.85)	0.48 ± 0.02 (0.23-0.84)

Fig. 4: The ranges (i.e., mean and max) of ADC values in all groups.

References

1. Partridge, S.C., et al., Apparent Diffusion Coefficient Values for Discriminating Benign and Malignant Breast MRI Lesions: Effects of Lesion Type and Size. American Journal of Roentgenology, 2010. **194**(6): p. 1664–1673.
2. Kul, S., et al., *Diagnostic efficacy of the diffusion weighted imaging in the characterization of different types of breast lesions.* J Magn Reson Imaging, 2014. **40**(5): p. 1158–64.

T24.
In-vivo and ex-vivo detection of colorectal cancer at ultra-low field using fast field-cycling methods

A. Alamri[1], N. Senn[1], G. Murray[2], L. Samuel[2], G. Ramsay[2], L. Broche[1]

[1]*University of Aberdeen, Aberdeen Biomedical Imaging Centre, Aberdeen, United Kingdom;*
[2]*Aberdeen Royal Infirmary, Aberdeen, United Kingdom*

Background Field-Cycling (FC) is a novel tool that measures changes of R_1 relaxation rate ($1/T_1$) with the magnetic field strength [1,2]. R_1 Nuclear Magnetic Relaxation Dispersion (NMRD) profiles, acquired with Fast Field Cycling (FFC) NMR relaxometry, provide promising biological biomarkers of tumours non-invasively and without using contrast media, using ultralow-field magnetic resonance [3–5]. More interestingly, Field-Cycling Imaging (FCI) provides images with T_1-dispersion contrast that can offer new insights for clinical applications in a variety of pathologies including cancer. The aim of this pilot study was to acquire R_1-dispersion profiles from colorectal cancer samples using the FFC-NMR technique and to test the feasibility of the FCI whole-body scanner to characterise rectal cancer.

Methods Twenty-eight fresh resected tumour samples and corresponding peritumoral and healthy counterparts were obtained via the NHS Grampian Biorepository (tissue request-TR000068), with informed consent obtained from all patients. The dispersion profiles were acquired using a commercial FFC-NMR relaxometry technique at a controlled temperature of 37 °C ± 0.1 °C. Field-Cycling pre-polarised and non-polarised pulse sequences were used. A two-segments power law model was applied to fit the curves of the NMRD profiles for all samples. For imaging work (study approval number 22/NS/0035), five patients diagnosed with rectal cancer were scanned by using an FCI scanner, with four evolution fields ranging from 0.2 T to 0.2 mT, TE of 21 ms, 20 kHz bandwidth, in-plane resolution of 4.3 mm and slice thickness of 10 mm. The duration of the FCI scan is approximately 45 min.

Results The difference of R_1 values measured between healthy and tumour tissue samples is increased with the decrease of the magnetic field from 3.4 to 1.01 MHz and showed a significant difference ($p < 0.0001$) between the tissue subtypes (Fig. 1). Furthermore, the numerical parameters of the power law model significantly distinguished cancerous and non-cancerous colon tissues. The mucinous samples had extreme numerical values that differed from most data points (Fig. 2). The FCI scan was done for patients with rectal tumours and correlated to the clinical MRI images to delineate the ROIs. The R_1 dispersion profiles extracted from the tumour and the healthy ROIs showed clear contrast with different dispersion shapes (Fig. 3).

Discussion This preliminary study provided the first insights into using FFC-NMR and the FCI imaging technique as it can provide a potential biomarker for the characterisation of colorectal cancer. The FFC-NMR measurements were able to discriminate tumours from peritumoral and healthy tissues in all 28 cases, below 3.4 MHz. This work is extended to in vivo imaging, and the preliminary results were reported. Although the primary source of the signals is not well defined yet, previous studies have reported that ($R_1 = 1/T_1$) is related to changes in molecular dynamics within tumour tissues, and the water exchange rate across the plasma membrane is a distinctive feature that distinguishes healthy from tumour cells [6].

Conclusion This work showed a potential new biomarker of colorectal cancer based on R_1 dispersion curves -extended to low magnetic fields -below 3.4 MHz-. Furthermore, this work is extended to in vivo imaging, and we reported the preliminary results of using our whole-body 0.2 T FCI scanner to assess if FCI can characterise rectal lesions.

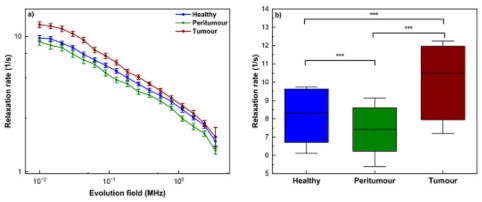

Fig. 1: a) Average R1 dispersion profile from ex-vivo analysis of colorectal cancer, peritumoral and corresponding healthy samples. A significant difference appeared in the lower field below 100 kHz. Error bars represent the standard error of the mean. b) A comparison of R1 values between the three groups of samples -below 100 kHz- shows a significant difference between the R1 values.

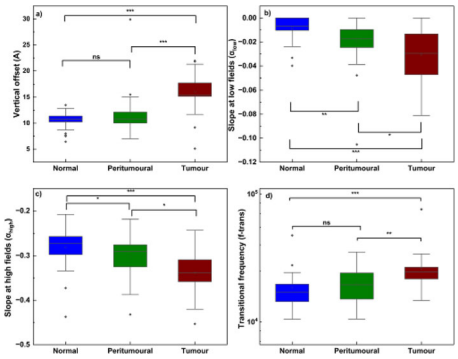

Fig. 2: Boxplots comparing the numerical parameters derived from the 2-segment power law model. (a) The vertical offset (A) of the whole dispersion curve, (b) The slope at low field (αlow), (c) The slope at high field (high), (d) The average transitional frequency between the two slope segments for healthy, peritumoral and tumour. *= p<0.05 , **= p<0.005, ***= p<0.0005, ns = not significant.

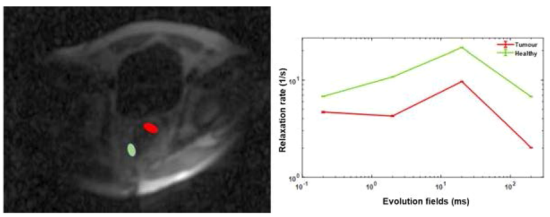

Fig. 3: FCI transverse processed image of the rectum of patient diagnosed with Rectal Cancer at 0.2 mT and the R1 dispersion profiles from tumour and healthy regions (highlighted in red and green colour, respectively).

T25.
Effect of preoperative PI-RADS assessment on pathological outcome in patients who underwent radical prostatectomy

Q. Peng[1], L. Xu[1], G. Zhang[1], J. Zhang[1], X. Zhang[1], X. Bai[1], L. Chen[1], Z. Jin[1], H. Sun[1]

[1]*Peking Union Medical College Hospital, Beijing, China*

Introduction To assess the effect of preoperative MRI with standardized Prostate Imaging-Reporting and Data System (PI-RADS) assessment on pathological outcomes in prostate cancer (PCa) patients who underwent radical prostatectomy (RP).

Methods This study included patients who underwent prostate MRI and subsequent RP for PCa between January 2017 and December 2022. Patients were divided into the PI-RADS group and non-PI-RADS group according to whether the pre-surgery MRI was with PI-RADS assessment or not. Patients" preoperative characteristics and postoperative outcomes were retrieved and analyzed using the Chi-square test, Fisher"s exact test, and Mann–Whitney U-test when appropriate. The preoperative characteristics included patient age, prostate-specific antigen level, clinical T stage (cT), Gleason score in biopsy, and surgeon"s experience. The pathological outcome analyzed in this study including pathological T stage (pT2 vs. pT3-4) and positive surgical margins (PSMs). Patients were further stratified according to statistically significant preoperative variables to assess the difference in pathological outcomes. The concordance between cT and pT in the two groups was also assessed.

Results A total of 380 patients were included in this study, with 201 patients in the PI-RADS group and 179 in the non-PI-RADS group. Patients in the PI-RADS and non-PI-RADS groups had identical preoperative characteristics, except for cT ($p < 0.001$). For pathological outcomes, PI-RADS group showed a significantly lower percentage of patients with pT3-4 (21.4% vs. 48.0%, $p < 0.001$), and a lower percentage of PSMs (31.3% vs. 40.9%, $P = 0.055$). The concordance between the cT and pT was also higher in the PI-RADS group (79.1% vs. 64.8%, $p = 0.003$). In the subgroup analysis of stratifying patients according to cT, the PI-RADS group showed a lower proportion of patients with pT3-4 (15.9% vs. 36.1%, $p < 0.001$) in the cT1-2 subgroup. Although the rates of PSMs were also not statistically significant between the two groups in subgroup analysis, the PSMs rate of cT3 patients was reduced by 39.2% in the PI-RADS group ($p = 0.089$).

Discussion The present study is the first retrospective study to evaluate the benefit of preoperative PI-RADS assessment on pathological outcomes. In the large series of patients underwent RP, preoperative PI-RADS assessment reduced the proportion of patients with pT3-4 status who are not eligible for the priority RP 1and improved the accuracy of preoperative clinical staging, the PSMs rates were not significantly lower as compared to patients who did not PI-RADS assessment. The detection rate of suspicious lesions according to PI-RADS was significantly improved, and a higher proportion of standardized reports describe information about relationships with surrounding organizations. A meta-analysis studied by Patel et al. 2 supported that a similar magnitude for reduction in PSMs rates of about 5% for patients receiving multiparametric MRI was observed. While the magnitude in reduction may fall short of what many urologists had hoped for with the implementation of MRI in CaP, the overall 9.6% reduction of PSMs in our study is a small reduction compared to the result of Patel et al. Although the rates of PSMs were not statistically significant in the context of multiple testing between the two groups in subgroup analysis, the PSMs rate of cT3 patients was reduced by 39.2% in the PI-RADS group which suggests that the value of PI-RADS assessment in benefit of surgical outcomes.

Limitations The single-center, retrospective cohort study may introduce some selection bias. Therefore, further prospective validation in a multi-center and larger patient cohort studies is needed. Furthermore, our retrospective analysis lacks the complete insight into the surgical protocol decisions of individual patient. With our data, we are not able to tell to which extent the PSMs rate attributed to standardized PI-RADS.

Conclusions: Preoperative MRI with standardized PI-RADS assessment could reduce the proportion of patients with non-organ-confined PCa undergoing PR, improve the accuracy of preoperative clinical staging and slightly reduce PSMs rate compared to non-PI-RADS assessment.

Table 1. Clinicopathological feature of patients

		PI-RADS (201)		Non-PI-RADS (179)		p
Preoperative feature	Age (year), median (IQR)	67.0 (63-70)		65.0 (61.0-70.0)		0.085
		n	%	n	%	
	t-PSA≤10	118	58.7	87	48.6	0.062
	t-PSA>10	83	41.3	92	51.4	
	Clinical T status					
	cT1	9	4.5	8	4.5	<0.001
	cT2	161	80.1	164	91.6	
	cT3-4	31	15.4	7	3.9	
	Gleason score in biopsy					
	≤6	62	31.0	54	30.2	0.187
	3 + 4	54	27.0	40	22.3	
	4 + 3	44	22.0	32	17.9	
	≥8	40	20.0	53	29.6	
	Surgical experience					
	<100	141	70.1	127	70.9	0.954
	≥100	60	29.9	52	29.1	
Postoperative feature	pathological T stage					
	pT2	158	78.6	111	62.0	<0.001
	pT3-4	43	21.4	68	48.0	
	PSMs+	63	31.3	73	40.9	0.055

IQR interquartile range;
t-PSA total prostate-specifc antigen;
PSMs positive surgical margins

Table 2. Subgroup analysis based on clinical T stage

		PI-RADS		Non-PI-RADS		p
		n	%	n	%	
cT1-2 (342)	pT2	143	84.1	110	63.9	<0.001
	pT3-4	27	15.9	62	36.1	
	PSM+	53	31.2	68	39.5	0.133
cT3 (38)	pT2	15	48.4	1	14.3	0.241
	pT3-4	16	51.6	6	85.7	
	PSM+	10	32.2	5	71.4	0.089

Table 3. Reporting of MRI with and without PI-RADS assessment

	PI-RADS (201)		Non-PI-RADS (179)		p
	n	%	n	%	
MRI performed at our institution	154	76.6	16	8.9	-
Indication of suspicious lesions	195	97.0	150	83.8	<0.001
Relationship between lesion and surrounding tissue	155	77.1	29	16.2	<0.001
Accuracy of preoperative staging	159	79.1	116	64.8	0.003

References

1. Haug, E. S.; Myklebust, T.; Juliebø-Jones, P.; Reisæter, L. A. R.; Aas, K.; Berg, A. S.; Müller, C.; Hofmann, B.; Størkersen, Ø.; Nilsen, K. L.; Johannesen, T. B.; Beisland, C., Impact of prebiopsy MRI on prostate cancer staging: Results from the Norwegian Prostate Cancer Registry. *BJUI compass* **2023,** *4* (3), 331–338.

2. Patel, H. D.; Okabe, Y.; Rac, G.; Pahouja, G.; Desai, S.; Shea, S. M.; Gorbonos, A.; Quek, M. L.; Flanigan, R. C.; Goldberg, A.; Gupta, G. N., MRI versus non-MRI diagnostic pathways before radical prostatectomy: Impact on nerve-sparing, positive surgical margins, and biochemical recurrence. *Urologic oncology* **2023,** *41* (2), 104.e19–104.e27.

T26.
Longitudinal follow-up by MRI and behavioural evaluation to assess the best neuroprotective strategy: Comparison of hypothermia and lactate in a rat model of neonatal hypoxia–ischemia

I. Omar[1], H. Roumes[1], S. Sanchez[1], M. C. Beauvieux[1,2], J. F. Chateil[1,2], L. Pellerin[3], A. K. Bouzier-Sore[1]

[1]*CRMSB Bordeaux University, CNRS, Bordeaux, France;*
[2]*CRMSB Bordeaux University, Bordeaux, France;*
[3]*IRMETIST U1313, Poitiers, France*

Introduction and purpose Neonatal hypoxia–ischemia (NHI) is a major public health challenge in terms of its occurrence (1–6‰ of births), its lethality or cognitive and motor disabilities ensuing from this event[1]. NHI results from a decrease in newborn"s brain perfusion. This disruption of cerebral blood flow, leading to a decrease in oxygen and energy substrate supplies, is responsible for brain damages. The only current treatment is moderate hypothermia but nearly 50% of newborns do not respond to this therapy[2]. Therefore, development of new treatments is a priority. In a previous study on a rat NHI model, we demonstrated that lactate injections are neuroprotective[3]. However, this novel neuroprotective strategy must be combined with hypothermia, since this procedure is the standard clinical care for NHI. Our aims were 1) to set up the best condition for hypothermia on a rat NHI model and 2) to perform lactate injections after an HI event in rat pups undergoing hypothermia, a mandatory combined study for further translation to the human neonate.

Material and methods 6 groups were considered: Sham group (without NHI, nor hypothermia or lactate injection); HI group (NHI + 2 h normothermia); HI-hypo2, HI-hypo3, and HI-hypo5 groups (NHI + 2 h, 3 h, 5 h of hypothermia, respectively) and HI-hypo + L group (NHI + 2 h of hypothermia + 3 daily consecutive lactate injections post-NHI). At P7 (7 days post-natal), except for the sham group, pups underwent NHI (left common carotid artery ligation + hypoxia (8% O2, 92% N2, 2 h)). Ligation was controlled by MR-angiography. Brain lesion volumes were measured in vivo, 3 h (P7), 48 h (P9) and 23d (P30) after NHI, using diffusion-weighted MRI (4.7 T Bruker, TE = 24 ms, TR = 2 s, 30 directions, 20 slices, 0.7 mm thick) and expressed as % of total brain volume. Motor and cognitive functions of the pups were evaluated with behavioural tests from P8 to P50 (righting reflexes, modified Neurological Severity Score -mNSS-, novel object recognition, anxiety and depression).

Results First, we compared brain lesion volumes by diffusion-weighted MRI (Fig. 1) and performed behavioural tests for the different durations of hypothermia. Brain lesions were quantified in the HI group (at P9: 37 ± 2% and P30: 17 ± 4%) and for the different groups of hypothermia (at P9: 29 ± 4%, 33 ± 5% and 32 ± 5% in HI-hypo2, HI-hypo3 and HI-hypo5 groups, respectively; at P30: 5 ± 2%, 14 ± 3% and 9 ± 3% in HI-hypo2, HI-hypo3 and HI-hypo5 groups, respectively; Fig. 2). Concerning behavioural testing, the best performances were obtained in the HI-hypo2 group (in both sensorimotor (Fig. 3) and memory (Fig. 4) tests). Therefore, 2 h-hypothermia was sufficient to have a neuroprotective effect, while minimizing animal discomfort, compared to 3 and 5 h of hypothermia. In a second step, we tested if lactate administration was still

neuroprotective in pups that underwent HI followed by 2 h of hypothermia. Brain lesion volumes were the smallest in the HI-hypo + L group (Fig. 1 and 2; lesion volume at P9: 18 ± 3% and at P30: 2 ± 1%). At the motor and cognitive levels, pups in the HI-hypo + L group presented the best behavioural performances compared to all the other groups (Fig. 3 and 4).

Conclusion While lactate is still considered as a "waste" product or a bad prognostic biomarker, our hypothesis is that lactate, administered after hypoxia–ischemia and therefore in reperfusion condition, could be used as a preferential energy substrate by neurons. Our data clearly indicated that lactate administration, in combination with hypothermia, is neuroprotective in the context of NHI. This opens up encouraging prospects for therapy in newborns who have suffered from hypoxia–ischemia at birth and for whom no pharmacological treatment can be currently proposed.

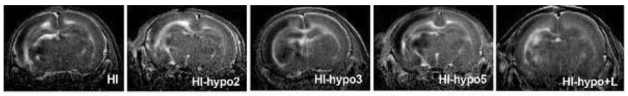

Figure 1: Diffusion-weighted imaging of P9 brains (from HI, HI-hypo2, HI-hypo3 and HI-hypo5 groups) performed at 4.7 T.

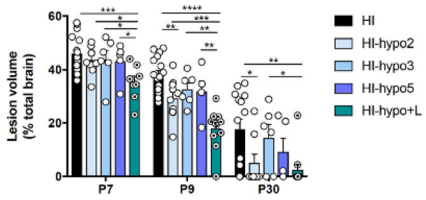

Figure 2: Quantification of lesion volume (%, relative to total brain volume) for the different groups. *P< 0.05, ** P<0.01, *** P<0.001, **** P<0.0001* by one-way ANOVA, followed by Fisher's LSD test.

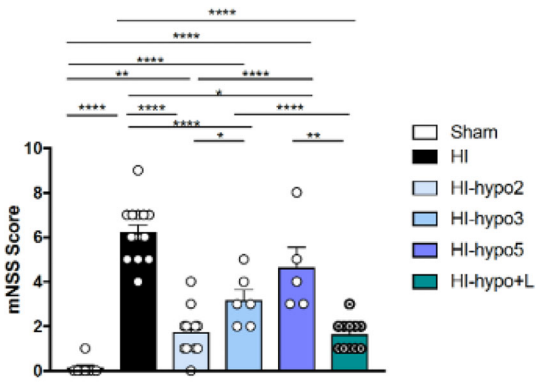

Figure 3: Modified neurological severity scores (mNSS) perfomed at P24. Results are mean values +/_ SEM. ** P< 0.05, ** P<0.01, **** P<0.0001* by one-way ANOVA, followed by Fisher's LSD test.

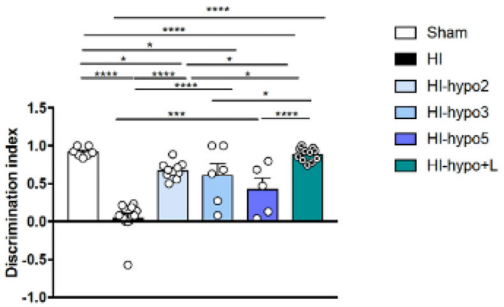

Figure 4: Novel object recognition test performed at P45. Results are mean values ± SEM. ** P< 0.05, *** P<0.001, **** P<0.0001* by one-way ANOVA, followed by Fisher's LSD test.

References

[1]Kurinczuk et al., Early Hum Dev, 2010
[2]Davidson et al., Front Neurol, 2015
[3]Roumes et al., JCBFM, 2021.

T27.
Using sqBOLD MRI in brain tumors: Exploring the relationship between Oxygen extraction fraction and HIF-1α staining

F. Arzanforoosh[1,2], M. Benger[3], M. van der Velden[1], S. R. van der Voort[1], E. M. Bos[4,2], J. W. Schouten[4,2], A. Vincent[4,2], T. C. Wood[5], T. C. Booth[3,6], J. M. Kros[7], M. O. Smits[1,2,8], E. A. H. Warnert[1,2]

[1]Erasmus Medical Center, Department of Radiology and Nuclear Medicine, Rotterdam, Netherlands;
[2]Erasmus Medical Center, Brain Tumour Centre, Rotterdam, Netherlands;
[3]King's College Hospital NHS Foundation Trust, Department of Neuroradiology, London, United Kingdom;
[4]Erasmus Medical Center, Department of Neurosurgery, Rotterdam, Netherlands;
[5]King's College London, Department of Neuroimaging, London, United Kingdom;
[6]King's College London, School of Biomedical Engineering & Imaging Sciences, London, United Kingdom;
[7]Erasmus Medical Center, Department of Pathology, Rotterdam, Netherlands;
[8]Medical Delta, Delft, Netherlands.

Introduction Sustained oxygen supply is crucial for maintaining proper brain cell function. However, aggressive brain tumors often exhibit low oxygenation levels due to the presence of rapid cell proliferation. SqBOLD enables the mapping of oxygenation-related parameters such as R_2' and OEF, which respectively reflect the concentration of deoxygenated hemoglobin and the percentage of oxygen extracted from the blood by the brain parenchyma [1]. There is limited research on using sqBOLD to measure OEF in human brain tumors [2]. Our objective is to evaluate the feasibility and reliability of sqBOLD MRI in measuring oxygen-related parameters in brain tumors.

Methods Ten patients, including five with gliomas and five with metastatic brain tumors, underwent presurgical MRI at 3 T, with an average of three targeted biopsy specimens collected per patient. Structural scans included pre- and postcontrast T1W, T2W, and T2W-FLAIR, and were used to segment four tumor VOIs: edema, non-

enhancing tumor, enhancing tumor, and necrotic core using the Glioseg algorithm [3]. SqBOLD data were acquired using a 2D asymmetric spin echo (ASE) EPI sequence with FLAIR preparation (FLAIR-ASE) [4]. In the sequence, the refocusing pulse was shifted towards the excitation pulse by different shift (τ) of 0, 16, 20, 24, 28, 32, 36, 40, 44, 48, and 52 ms and the imaging acquisition parameters of TE/TR/TI: 74/8000/2000 ms, voxel size: 2.3 × 2.3 × 3.0 mm^3, and the total number of slices: 28.

The sqBOLD model, which is illustrated in Fig. 1 and consists of two regimes, was utilized to fit each voxel signal using Bayesian fitting in Quantiphyse software (version 0.9.9) [5]. From voxels adhering to the model in Fig. 1, $R2'$ and OEF were extracted; non-adherent voxels were assigned zero.

Different tumor regions were biopsied during surgery based on R_2' and OEF values. The biopsies were fixed in formalin and paraffin-embedded. These tissue samples were stained for HIF-1α and QuPath software was used to quantify HIF-1α staining intensity and the percentage of stained cells, resulting in an "H-score" per biopsy. With the Spearman correlation test, the correlation between MRI (R_2' and OEF) and H-score was investigated.

Results Figure 2 demonstrates that the sqBOLD signal predominantly followed the expected signal drop with increasing τ in glioma. However, an unexpected rise in signal intensity was noticed in the edema areas surrounding the enhancing tumor regions in the two brain metastases.

R2' and OEF maps show low values in non-enhancing tumor regions of low-grade gliomas, high signal spots in high-grade gliomas and brain metastases within the enhancing ring and necrotic core VOIs, and low signal in the edema surrounding the enhancing ring in gliomas (Fig. 3). There was no statistically significant correlation between H-score measurements of HIF-1α staining intensity with neither R_2' (r = 0.10, P = 0.56) nor OEF (r = 0.17, P = 0.35) (Fig. 4).

Discussion The findings of our study demonstrate the applicability of sqBOLD in most regions of brain tumors. An exception was observed in the edema associated with metastases, and not with that of gliomas, despite the fact that both types of tumors cause an increase in water content and diffusion in the edematous tissue. Reasons for the observed discrepancy remain elusive, but potential variations in edema composition or distribution could be contributing to the differences in signal characteristics and may be of diagnostic value. High-grade gliomas and brain metastases exhibited increased R2' and OEF values in contrast-enhanced and necrotic areas, while low-grade gliomas demonstrated decreased values, aligning with previous studies correlating elevated OEF and R_2' with tumor aggressiveness [2], [6], [7]. The lack of a significant correlation between R_2', OEF, and HIF-1α expression was unexpected, given previous studies demonstrating that in hypoxic tissue, both MRI-derived measurements of R_2' and OEF, along with pathology-derived HIF-1α H-score, would be elevated [7], [8]. This discrepancy might stem from our broader tumor subtype range; however, subdividing by subtype results in limited sample sizes in each subtype. Future research, including the extension of the current data set with already collected data from King's College Hospital (London, UK), will be done to further elucidate our findings.

Conclusion In conclusion, our study has provided valuable insights into the applicability of sqBOLD in brain tumors, emphasizing its potential usefulness in the assessment and treatment planning of brain tumors.

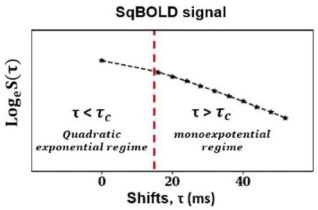

Fig. 1: The sqBOLD model diagram illustrating logarithmic MR signal decay with shifts (τ). τc (16 ms per Ref. 1) marks the transition from quadratic exponential to monoexponential regimes.

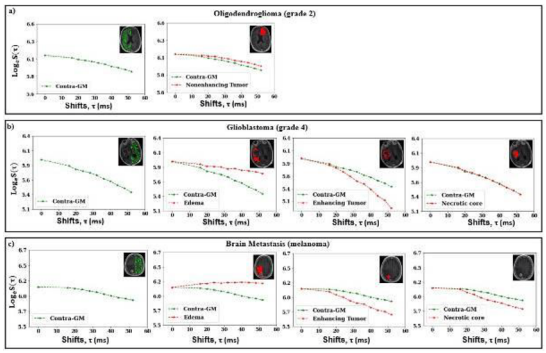

Fig. 2: Average sqBOLD signal evolution vs. ASE shift (τ) for different regions of tumors in different pathological conditions: a) Oligodendroglioma (Grade 2), b) Glioblastoma (Grade 4), and c) Metastatic melanoma.

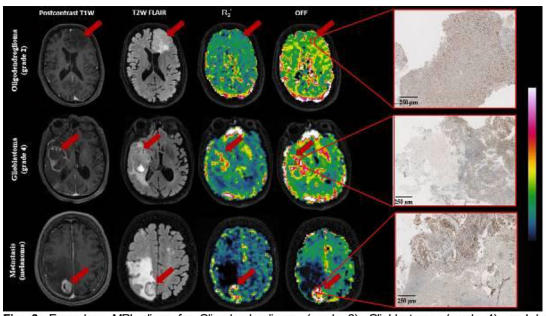

Fig. 3: Exemplary MRI slices for Oligodendroglioma (grade 2), Glioblastoma (grade 4), and brain metastasis (melanoma) from top to bottom. Images (with color bars) from left to right: postcontrast T1W, T2W FLAIR, R_2'(0-20 ms^{-1}), and OEF (0-1 %). Red arrows point to tumors. Tissue sections stained with HIF-1α (hypoxia marker) on the right, brown dots indicate HIF-1α presence.

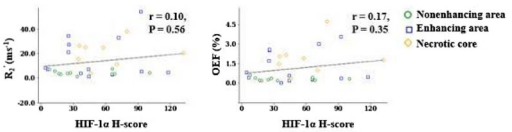

Fig. 4: correlation between HIF-1α expression and R_2' (ms^{-1}) and OEF (%), assessed via Spearman test, reporting correlation coefficient (r) and p-value.

Reference

[1] A. J. Stone et al., J. *Neuroimage*, 2017.
[2] A. Stone et al., ESMRMB *Meeting*, 2018.
[3] F. Arzanforoosh et al., J. *Cancers,* 2023.
[4] A. J. L. Berman et al., J. *Neuroimage*, 2017.
[5] M. T. Cherukara et al., J. *Neuroimage,* 2019.
[6] V. Tóth et al., *J Neurooncol,* 2013.
[7] J. Yao et al., *J. Neuro Oncol,* 2019.
[8] I. Mendichovszky et al., J. *Radiol*, 2011.

T28.
SW cardioprotective therapy: In vivo MR validation on acute ischemia–reperfusion injury in porcine model

L. Petrusca[1], P. Croisille[1,2], L. Augeul[3], M. Ovize[3,4], N. Mewton[3,4], M. Viallon[1,2]

[1]*Univ Lyon, UJM-Saint-Etienne, INSA, CNRS UMR 5520, INSERM U1206, CREATIS, F-42023, Saint-Etienne, France, Saint Etienne, France;*
[2]*Department of Radiology, Centre Hospitalier Universitaire de Saint-Etienne, Universite´ Jean-Monnet, France, Saint-Etienne, France;*
[3]*INSERM UMR 1060, CARMEN Laboratory, Universite´ Lyon 1, Faculte´ de Medecine, Rockfeller Lyon, Lyon, France;*
[4]*Heart Failure Department, Clinical Investigation Center, Inserm 1407, HCL-Lyon, Lyon, France*

Background The new frontiers in treating acute myocardial infarction (AMI) is represented by cardioprotective strategies [1] aiming the effective protection of myocardium at risk for infarction in the territory downstream of occlusion. Hence interventions to reduce final infarct size have a major clinical interest in improving the prognosis of patients referred for AMI. For now, no therapy has demonstrated its effectiveness and/or been successfully transposed to the routine therapeutic care in patients with AMI [2]. Therefore, we propose here to investigate the mechano-transduction effects induced by shock waves (SW) therapy at time of the ischemia reperfusion as a non-invasive cardioprotective innovative approach to trigger healing molecular mechanisms. Quantitative cardiac MRI at the acute phase of MI was used to evaluate therapy benefits in an experimental myocardial reperfusion-injury model.

Materials and Methods AMI was induced by a left anterior artery temporary occlusion during 50 min in 18 farm pigs at open chest, randomized in 2 equivalent groups: with SW therapy and without (control group). In the SW therapy group, treatment was initiated at the end of the ischemia period using the DUOLITH device, (Storz Medical, Switzerland) and extended during early reperfusion (600 + 1200 shots @0.09 mJ/mm2, f = 5 Hz). Multiple time-point (baseline (B), during ischemia (I), at early reperfusion (ER) (~ 15 min), late reperfusion (LR) (3 h) and after Gadolinium (Gd) administration (post Gd)) evaluation along the experiment was performed by quantitative CMR acquisitions (1.5 T magnet, Aera, Siemens healthcare). The MR protocol included at all time points Left Ventricle (LV) global function assessment, regional strain quantification and native T1 and T2 parametric mapping, Fig. 1. Then, after contrast injection of Gd, we obtained late Gd imaging and extra-cellular volume (ECV) mapping. The mean values of MR indexes were determined in the lesion, blood and remote myocardium. Before animal sacrifice, Evans blue dye was administrated after re-occlusion for area-at-risk determination. The Control group experiment respected an identical protocol but did not apply the SW treatment.

Results As expected, during ischemia, LV ejection fraction (LVEF) decreased in both groups (25 ± 4.8% in controls (p = 0.031), 31.6 ± 3.2% in SW (p = 0.02). After reperfusion, LVEF remained significantly decreased in controls (39.9 ± 4% at LR vs. 60 ± 5% at baseline (p = 0.02). In the SW group, LVEF increased quickly ER (43.7 ± 11.4% vs. 52.4 ± 8.2%), and further improved at LR (49.4 ± 10.1) (ER vs LR p = 0.05), close to baseline reference (LR vs. B p = 0.92). Strain imaging showed that regional contractile function remained severely altered in the core lesion in both groups with no significant treatment effect, while in the border and remote segments, there was only a trend to higher contractility in SW-treated animals. Furthermore, there was no significant difference of tissue changes as revealed by T1 and T2 myocardial relaxation times (i.e. edema) after reperfusion in the intervention group compared to the control group: ΔT1 (MI vs remote) was increased by 23.2 ± % for SW vs + 25.2% for the controls, while ΔT2 (MI vs remote) increased by + 24.9% for SW vs + 21.7% for the control group. A trend toward higher values was found in ECV values in the SW therapy group: + 5.7% in remote regions and + 18.6% in the border regions. While macroscopic evaluations of AAR do not indicate apparent differences between the two groups, when evaluating the 3D MR LGE data, the total IR-reperfusion lesion was calculated to be 27.3% of the LV mass in the control group versus 20.8% in the treated group. No-reflow regions, very limited in size, were observed in only 4 animals.

Discussion and conclusion We explored here the effects of non-invasive cardiac SW therapy in an AMI swine model (open-chest, 50 min LAD occlusion, 3 h of reperfusion) using full quantitative CMR evaluation of tissue biomarkers and cardiac function. The study indicates a significant and early improvement of global systolic LV function that further improved after 3 h of reperfusion in the SW treated group. While the strain imaging illustrate only a trend to higher contractility in SW-treated animals in the border and remote segments, SW therapy did not significantly modulate the amount of myocardial edema within 3 h of reperfusion. In conclusion, our protocol indicate a nearly immediate cardioprotective effect of the SW therapy in an AMI swine model, translated to a reduction in the acute ischemia–reperfusion lesion size and to a significant LV function improvement. These new and promising results related to the multi-targeted effects of SW therapy in IR injury need to be confirmed by further in-vivo studies in close chest models with longitudinal follow-up and open new questions on the role of edema.

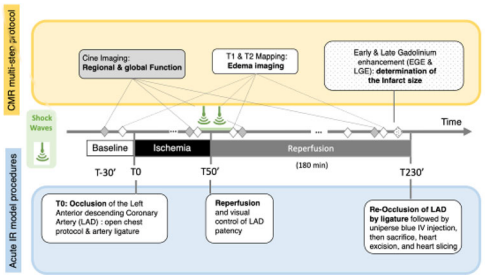

Fig. 1: MR and SW therapy multi-step protocol of acute ischemia reperfusion pig model at open chest

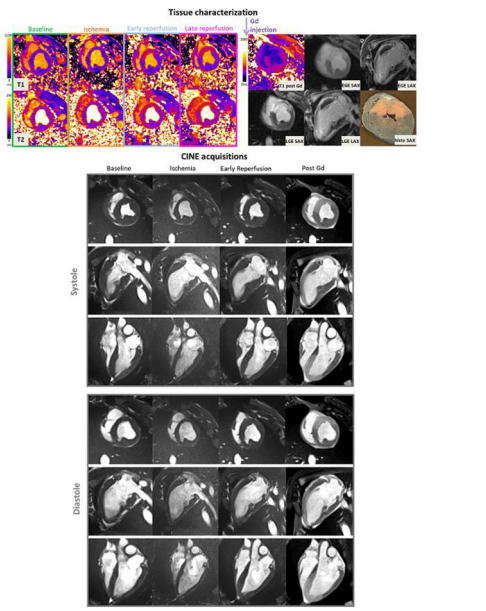

Fig. 2: Example of T1 and T2 dynamics obtained at baseline, during ischemia, early and late time-points of the reperfusion in a swine open chest model (50 min occlusion). Early and late gadolinium enhancement maps are displayed in short and long axis, together with a macroscopic picture of the lesion after Evans blue dye injection. CINE bSSFP images are also displayed (lower part) in short and long axis, in systole and diastole.

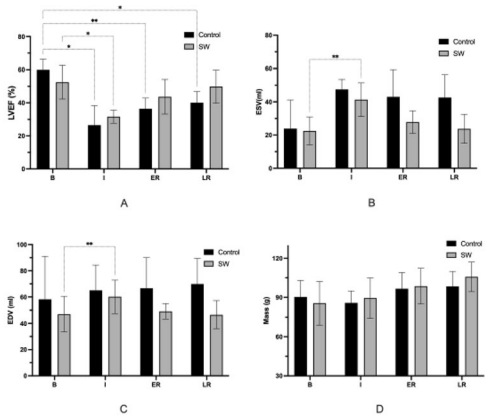

Fig. 3: Global function parameters (LVEF (A) ESV (B), EDV (C), and LV mass (D)) changes at the four stages of the experimental ischemia-reperfusion protocol: B, I, ER and LR in controls (black) and SW therapy group (grey). (*:p<0.05, **:p<0.01). LVEF: left ventricle ejection fraction, ESV: end-systolic volume, EDV: end-diastolic volume, LV: left ventricle.

References
[1] Heusch G et al., Circ Res. 2015.
[2] Hausenloy DJ et al., Cardiovascular Research. 2017.

T29.
Study of the normal cerebral development and gyrification in the *ex-vivo* ferret brain using diffusion and quantitative MRI

L. Mouton[1], A. Ruze[1], R. Valabrègue[1], J. B. Pérot[1], L. Soustelle[2], V. Sahu[3], K. Heuer[3], S. Lehéricy[1], R. Toro[3], M. Santin[1]

[1]*Institut du Cerveau (ICM)—Paris Brain Institute, Inserm U 1127, CNRS UMR 7225, Sorbonne Université, CENIR, Paris, France;*
[2]*Aix Marseille Univ, CNRS, CRMBM, Marseille, France;*
[3]*Institut Pasteur, Université de Paris, Département de neuroscience, Paris, France*

Introduction The ferret animal model is a relevant model to study brain development and gyrification as it undergoes cortical folding and white matter (WM) maturation during the first month of life[1]. Multi-contrast MRI, combining quantitative (qMRI) and diffusion-weighted MRI (DW-MRI), is a promising approach to explore maturation[2], myelination[3], microstructural changes and cortical folding[4] that occur during brain development. This study aimed at mapping normal brain development using multi-contrast MRI in ex vivo ferret brain, as immature ferret recapitulates human brain development during pregnancy[1].

Methods *Animal model:* We investigated 3 time points: day of birth (P0), 16 days (P16) and 32 days (P32) postnatally to mimic preterm human brain from the 13th week of gestation to 2 years-old children[1].
MRI acquisitions: MRI exams were performed ex vivo on 3 ferret brains (P0, P16, P32), with a 11.7 T MRI (Bruker BioSpec 117/16, Bruker, Germany). A 72-mm volume transmit coil was used in combination with a surface receiver coil. The MRI acquisitions (83 h in total) consisted in: (i) 3D-segmented echo planar diffusion-weighted pulsed-field gradient spin–echo MRI (TR/TE = 1000/24 ms, 16 segments, 8 A0, δ = 5 ms, Δ = 12 ms; b = 6000 s/mm^2, 64 directions; b = 2000s/mm^2, 29 directions; b = 600 s/mm^2, 7 directions) with spatial resolution from 100 to 200 µm isotropic depending on the brain size (ii) B1$^+$ map[5] and (iii) 3D spoiled gradient recalled echo MRI (Multi gradient echo, TR = 100 ms, Necho = 16, TE1 = 2.1 ms, ΔTE = 2.5 ms) with variable flip angles (FA = 6°,15°,30°) and magnetization transfer module to assess M0, R1 and R2* relaxation rate values as well as Macromolecular Proton Fraction (MPF)[6] with spatial resolution from 75 to 150 µm isotropic depending on the brain size.
MRI analysis: Fig. 1 describes the multi-contrast MRI workflow, from the preprocessing steps to the region-of-interest analyses performed on the quantitative maps and derived diffusion maps.

Results We observed a wider range of contrast intensity at P0 than at P16 and P32 for all the quantitative maps. Diffusion parameter maps presented a better anatomical delineation despite their lower resolution than qMRI acquisitions (Fig. 2).
The total brain volume and the gyrification index increased non linearly with age (Fig. 3).
A noticeable MPF increase between P0 and P16 was observed (Fig. 2) and quantified for 4 delineated brain regions without any striking changes between P16 and P32 stages. R1 and R2* values seemed to slightly increase with age.
Fractional anisotropy (FA) exhibited first a decrease and then an increase. This tendency seemed to be more pronounced in the cortex and subplate, and was also observed in WM for the mean (MD), axial (AD) and radial (RD) diffusivities.
Fig. 4 illustrates the fiber tracts reconstructed for the different ages. At P0, they were located in the developing WM and GM as well as the anterior commissure, whereas at P16 they were mostly located in the developing WM (corpus callosum, fornix, corticospinal tract and WM brainstem) with only few fibers in the cortex. Finally, at the later stage (P32) in addition to the previous WM tracts, cortical WM was also identified.

Discussion Cortical folding and brain volume both increase with age but the ferret brain seems to grow more first (P0 to P16) and to fold more then (P16 to P32).
MPF has already been validated as a myelin biomarker in animal models[7], therefore it can be expected that myelination has already started at P16 stage. R1 relies indirectly on the macromolecular and myelin content, and both myelin and iron load contributes to R2* increase. Their slight increases with age are consistent with myelination process but are also linked to other contributions (macromolecules, iron load) that could explain the difference between MPF, R1 and R2* variations.
High FA and AD values at P0 in the cortex could result from the tangential migration of cajal retzius cells[8]. Decreases in these values between P0 et P16 have already been observed in a rat model during cortical maturation due to cellular density change with an increased neurodendritic density and reduction in the radial glia[9].

Conclusion Fiber tracts organization exists at a very early stage (P0), but appeared to be unmyelinated as expected by the very low MPF values. Therefore, our results suggest that cortical folding, cortical maturation and myelination occurred at P16 in the ferret brain and could be investigated using multi-MRI contrast. PLI experiments are planned and additional time points will also be acquired to better estimate the onset of cortical folding and myelination.

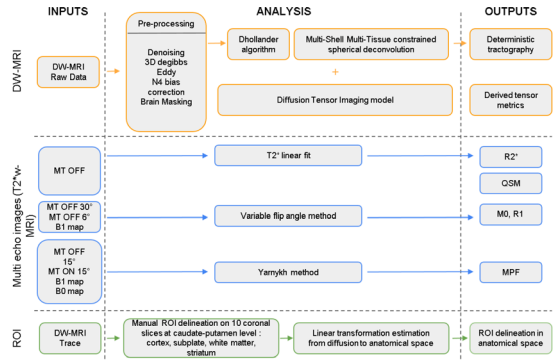

Fig. 1: Multi-contrast MRI pipeline analysis for the DW-MRI (1st row, MRTrix3 tools) and T2*w-MRI (2nd row) and ROI analysis (last row).

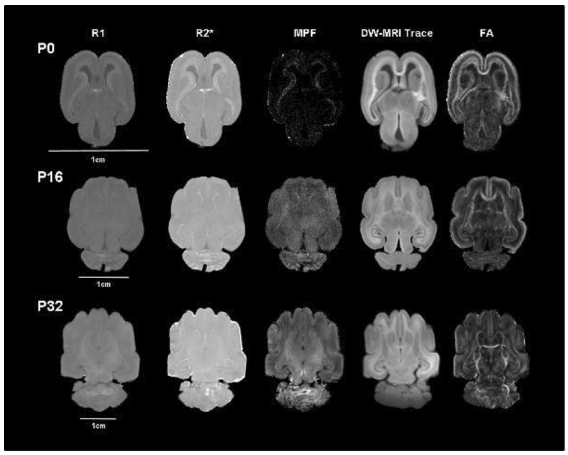

Fig. 2: Overview of the multi-contrast MRI data obtained in *ex vivo* ferret brains including R1, R2*, MPF, diffusion trace and FA maps for P0 (top row), P16 (middle row) and P32 (bottom row) brains. The same dynamic range was used for the P0, P16 and P32 brain ferret to ease the visual comparison

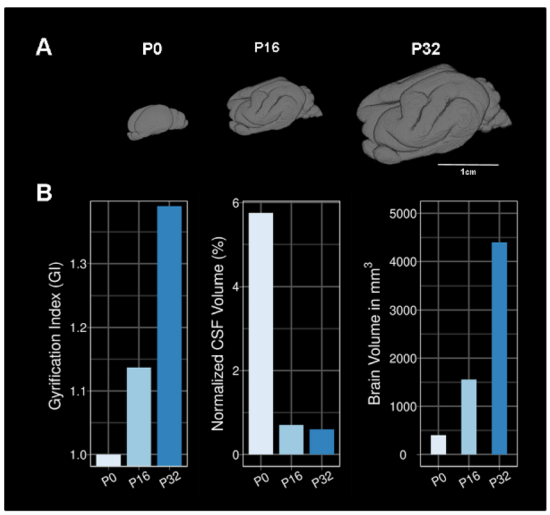

Fig. 3: 3D rendering of the brain masks from P0 to P32 (A). Measurement of the gyrification index (GI), the normalized cerebrospinal fluid (CSF) and the total brain volume for the P0, P16 and P32 brains (B).

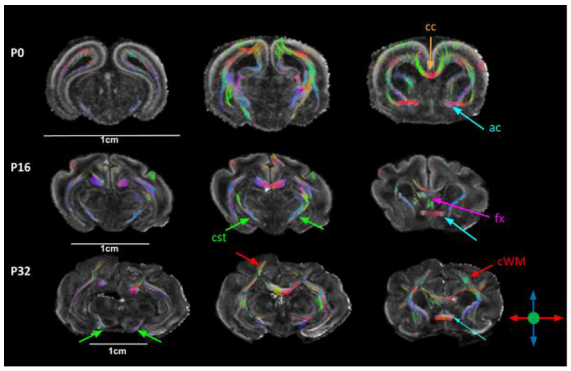

Fig. 4: Fiber tracts orientation color coded in FA maps. color code : red for left-right, blue for superior-inferior and green for anterior-posterior orientation. cc : corpus callosum, ac : anterior commissure, cst : corticospinal tract, fx : fornix, cWM: cortical white matter.

References

[1] Barnette AR et al. Pediatr. Res. 2009.
[2] Girard NJ et al. Imaging Med. 2012.
[3] Dubois J et al. Neuroscience. 2014.
[4] Neal J et al. J. Anat. 2007.
[5] Yarnykh V et al. Magn. Reson. Med. 2007.
[6] Yarnykh V et al. Magn. Reson. Med. 2012.
[7] Khodanovich MY et al. Sci. Rep. 2017.
[8] Gil V et al. Front. Neuroanat. 2014.
[9] Lodygensky GA et al. J. Anat. 2010.

T30.
Alterations in skeletal muscle water compartmentation in golden retriever muscular dystrophy dogs revealed by T2 relaxometry and IVIM MRI

E. Caldas de Almeida Araujo[1], Y. Fromes[1], I. Barthélémy[2], X. Cauchois[2], S. Blot[2], P. Y. Baudin[1], H. Reyngoudt[1], B. Marty[1]

[1]*Institute of Myology, Neuromuscular Investigation Center, NMR Laboratory, Paris, France;*
[2]*Université Paris Est Créteil, INSERM, IMRB, EnvA, Maisons-Alfort, France*

Introduction Neuromuscular diseases (NMD) are often characterized by chronic muscle damage and inflammation, leading to muscle atrophy, fatty replacement and fibrosis. Quantitative MRI (qMRI) is currently established as a crucial outcome measure in clinical studies of NMDs. While fat-fraction (FF) maps provide quantitative assessment of the disease progression, water-T2 maps reveal active muscle damage and/or ongoing microstructural tissue alterations that precede fibro-fatty replacement.[1] However, despite its sensitivity, water T2 still lacks specificity regarding the dominant underlying pathophysiological processes or tissue alterations. Exploiting the multi-exponential behavior of the water-T2 relaxation in tissue has been proposed as one approach to increase specificity.[2] The Golden Retriever Muscular Dystrophy (GRMD) dog is an animal model that has played a key role in studies of Duchenne muscular dystrophy (DMD). While the GRMD aligns very well with the progressive course of DMD, it presents much less fatty-replacement, which makes it particularly suited in the context of qMRI for investigating the alterations of the muscle water signal. In this work we investigate

alterations in tissue water compartmentation of GRMD dogs revealed by T2 relaxometry and intravoxel incoherent motion (IVIM) MRI.

Methods Experiments were performed using a 3 T clinical scanner. Dogs were examined under isoflurane anesthesia on a heating mattress. A 15-CH coil was used for RF transmission and signal detection. Water-T2 relaxation data were acquired in the tibialis cranial muscle of the right pelvic limb using a fat-suppressed single-voxel (approx. $1 \times 1 \times 4$ cm^3) ISIS-CPMG sequence[3], with 250 echoes and an inter-echo spacing of 2 ms. A bi-exponential model was fitted to the T2 relaxation curves: $S(TE) = A_1e^{-TE/T2}{}_1 + A_2e^{-TE/T2}{}_2$. Diffusion weighted images were acquired using a fat-suppressed spin-echo EPI sequence with the following relevant parameters: FOV = 180 mm, image size = 128 × 128, TE = 66 ms, TR = 4 s, bandwidth/pixel = 1185 Hz and b-values = 0, 400 and 900 s/mm2. Apparent diffusion coefficient (ADC) and IVIM-related (ADC_{IVIM} and f_{IVIM}) parameter maps were generated in 5 axial slices centered at half length of the tibia, using the following equations: $ADC = \ln(S_{b=0}/S_{b=400})/400$, $ADC_{IVIM} = \ln(S_{b=400}/S_{b=900})/500$ and $f_{IVIM} = 1 - e^{400x(ADC_{IVIM}-ADC)}$. Regions of interest were traced in the right and left tibialis cranial muscles of all five slices on the ADC_{IVIM} maps excluding any visible blood vessels, identified as hyperintense pixels. The study cohort consisted of 36 dogs (12 GRMD and 24 control) with single or multiple visits, resulting in 56 CPMG data sets (22 in GRMD and 34 in control dogs) and 41 IVIM data sets (15 in GRMD and 26 in control dogs). The mean value for each parameter was calculated for each dog exam. Groups were compared using two-sample t-tests.

Results In GRMD, the 1st component"s T2 and the relative fraction of the 2nd component were abnormally elevated and decreased with age, mainly between 60 and 180 days (Figs. 1 and 2). The 2nd T2 was abnormally lower in GRMD and did not correlate with age (Figs. 1 and 2). Although ADC was not different between groups, the IVIM-weighted ADC (ADC_{IVIM}) and the estimated IVIM fraction, f_{IVIM}, were abnormally elevated in GRMD. In controls, ADC and ADC_{IVIM} decreased with age, while no correlation was observed between the f_{IVIM} and age in both groups (Figs. 3 and 4).

Discussion Previous studies in healthy skeletal muscle suggested that the 1st and 2nd water-T2 components represent the parenchymal and vascular compartments, respectively.[3,4] From this perspective, our CPMG results in GRMD suggest that there is an increase in the vascular compartment (higher A_2) and in the transendothelial exchange rate (lower $T2_2$), both suggestive of inflammation, while the abnormally elevated $T2_1$ points towards an increase of the free-water pool in the parenchymal space, suggestive of tissue necrosis and interstitial edema. The IVIM signal attenuation is associated with flowing blood in the microvasculature and medium-sized vessels, and the results supported the CPMG findings, indicating an abnormally elevated vascular compartment in GRMD. Although the age distributions were different between groups, the observed differences for all parameters were still significant when restricting the groups to similar age ranges. Interestingly, the intensity of the disease activity decreased with age in GRMD, reflected by the decrease in T21 and A2.

Conclusion T2 compartmentation seems to allow assessing specific pathophysiological alterations in dystrophic muscles. IVIM MRI supported the parenchymal-vascular compartmentation model.

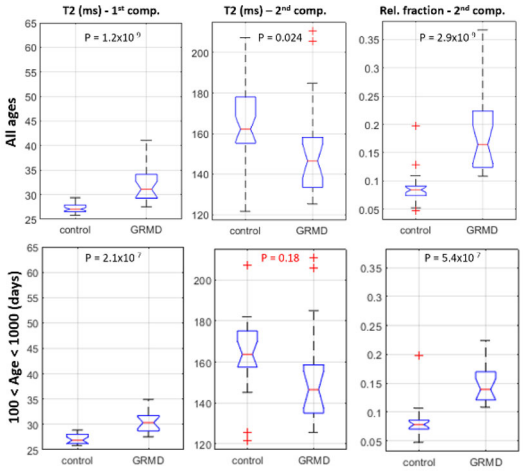

Fig. 1: Bi-exponential fitting results (in the second row the groups were restricted to the same age ranges). The p-values for the t-tests are indicated in each plot.

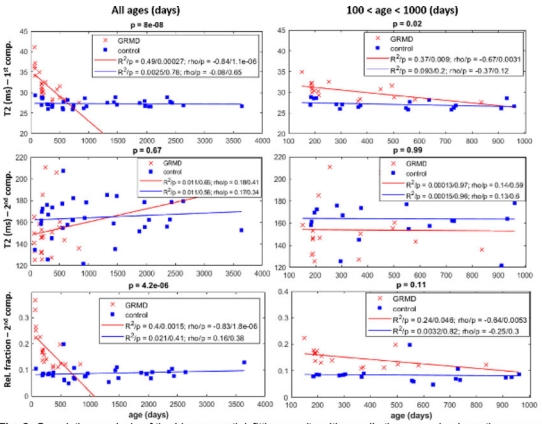

Fig. 2: Correlation analysis of the bi-exponential fitting results with age (in the second column the groups were restricted to the same age ranges). The p-values for the t-tests for differences between groups are indicated over each plot, and the Pearson (R^2/p-value) and Spearman (rho/p-value) correlation analysis results are displayed in the legends.

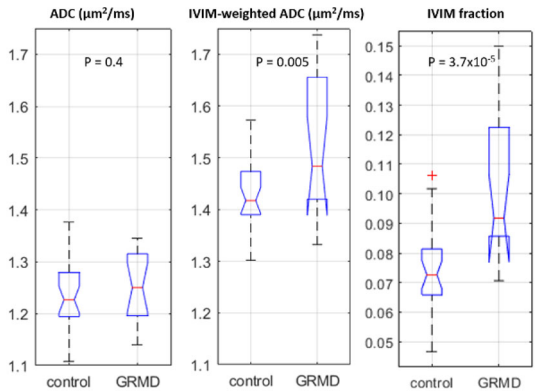

Fig. 3: Boxplots of the mean ADC, ADC_{IVM} and f_{IVM} characterizing the tibialis cranial muscle in each dog exam. The p-values for the t-tests are indicated in each plot.

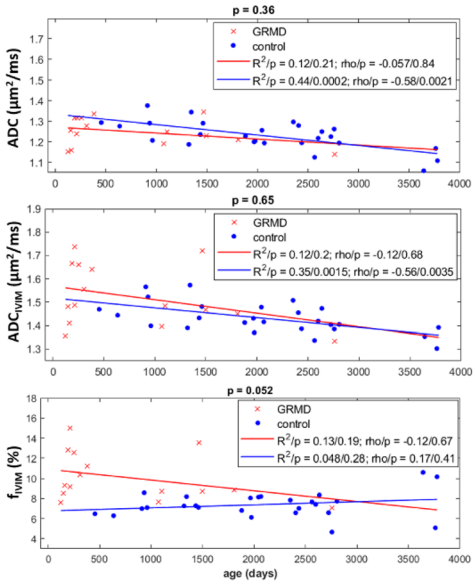

Fig. 4: Correlation analysis of the mean ADC, ADC_{IVIM} and f_{IVIM} with age. The p-values for the t-tests for differences between groups are indicated over each plot, and the Pearson (R^2/p-value) and Spearman (rho/p-value) correlation analysis results are displayed in the legends.

References

1 Marty, B. et al. *Radiology* (2023) https://doi.org/10.1148/radiol.221115

2 Araujo, E. C. A. et al. *J. Magn. Reson. Imaging* 53, 181–189 (2021).

3 Araujo, E. C. A. et al. *Biophys. J.* 106, 2267–2274 (2014).

4 Le Rumeur E. et al. *Magn. Reson. Imaging* 5, 267–272 (1987).

T31.
Giving the prostate the boost it needs: Strong gradients and spiral readout for high b-value diffusion MRI at short echo times

M. Molendowska[1,2], L. Müller[3], F. Fasano[4,5], D. K. Jones[1], C. M. Tax[1,6], M. Engel[1]

[1]*Cardiff University, Brain Research Imaging Centre (CUBRIC), Cardiff, United Kingdom;*
[2]*Lund University, Medical Radiation Physics, Lund, Sweden;*
[3]*University of Leeds, Institute of Cardiovascular and Metabolic Medicine, Leeds, United Kingdom;*
[4]*Siemens Healthcare Ltd, Camberly, United Kingdom;*
[5]*Siemens Healthcare GmbH, Erlangen, Germany;*
[6]*University Medical Center Utrecht, Image Sciences Institute, Utrecht, Netherlands*

Introduction Diffusion-weighted imaging (DWI) at high b-values is a superb MRI contrast for the characterisation of tissue microstructure, holding promise for advancing the early detection of prostate cancer (PCa)[1,2]. Unfortunately, clinical DWI currently only allows for low b-values due to limited gradient amplitudes which entail prolonged echo times (TE) and thus low signal-to-noise ratio (SNR). Developments of high-performance gradient hardware[3–8] and the use of spiral readouts allowing for short TEs[9–11] have enabled brain microstructure characterization at shorter diffusion times[12–14] and higher SNR[15]. This work demonstrates improvement of prostate DWI capitalising on strong gradients for diffusion encoding, spiral readouts for short TE, and field-camera measurements for accurate image reconstruction[16].

Methods Participants: Ethical approval for the study was obtained. A healthy control (51 y) and a patient with PCa (53 y, Gleason score 3 + 3) were scanned.

Hardware: 3 T Connectom scanner (Siemens Healthcare), field camera (Skope Magnetic Resonance Technologies)[17].

Data Acquisition: We acquired a multi-echo GRE for the B0 map and coil sensitivity estimation and a T2-weighted TSE as a structural reference.

We used a diffusion-weighted spin-echo sequence (developed in-house) that enables arbitrary readout trajectories (Fig. 1A) with diffusion encoding along 15 directions at b = [0, 0.05, 0.5, 1.5, 2, 3] ms/µm^2 (G_{max} = 247 mT/m, SR_{max} = 83.3 T/m/s, δ = 5.7 ms, Δ = 23.3 ms), TR = 3 s, 18 slices, TE = 53 and 35 ms for EPI and spiral readouts, respectively. Readouts were matched in total duration (44 ms) and k-space coverage (Fig. 1B) with G_{max} = 39 mT/m, SR_{max} = 186 T/m/s, FOV = 220 × 220 mm^2; and undersampling factor R = 2 for partial-Fourier (= 6/8) EPI, and R = 1.85 for spiral. The resolution was 1.3 × 1.3 × 5 mm^3.

Image reconstruction: We used an iterative conjugate gradient SENSE reconstruction[16,18,19] accounting for static B0-inhomogeneities and higher-order field dynamics (up to 3rd-order spherical harmonics and 2nd-order concomitant fields[20,21]).

Data processing/analysis: DWI data were corrected for gradient nonlinearity induced distortions[22–24]. Signal decay curves (median with interquartile range) from bilateral anatomical ROIs drawn on b = 1.5 ms/µm^2 data in the peripheral zone were plotted and the contrast-to-noise ratio (CNR) between cancerous and healthy tissue was computed. Mean diffusivity (MD), fractional anisotropy (FA), mean, axial, and radial kurtosis (MK, AK, RK) were estimated[25].

Results DWI data at b = 0 ms/µm^2 acquired with both readouts (Fig. 1C) preserved sharp structural features.

The direction-averaged signal (Fig. 2) showed higher signal intensities across all b-values in the spiral compared to EPI. The signal values from an ROI in the PCa lesion (Fig. 3) are well above the noise floor[30] for DWI with spiral readout. The CNR between the lesion and healthy tissue is improved by a factor 1.9, 1.7, and 2.3 for b = 1.5, 2, and 3 ms/µm^2 respectively when using spirals rather than EPI.

Quantitative maps (Fig. 4) show: I) fine anatomical details consistent with those observed in the T2-weighted image, II) more noise-biased maps obtained from DWI with EPI (e.g., elevated MD, higher FA in the transitional zone), and III) clearly distinguishable prostate zones. No change of FA in PCa lesion could be a result of the averaging effects of microscopic anisotropy at macroscopic scale[26].

Discussion & Conclusions We devised a spiral readout with advanced field sensing techniques for the prostate and achieved high DWI quality with preserved fine anatomical features at high b-values and increased CNR. Future work will comprise an in-depth SNR analysis and data comparative evaluation to the clinical protocol provided by the MR system vendor, including eddy current assessment.

The combination of strong gradients and spiral readouts unlocks short diffusion encoding times and short TEs which should enable comprehensive characterisation of the prostate gland by multidimensional MRI methods[27,28], including the short T2stroma compartment[29].

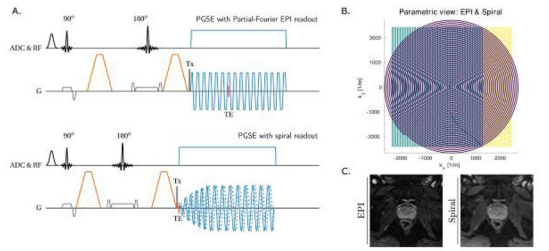

Fig. 1: A. PGSE sequences: Single-shot DWI with EPI and spiral. ADC&RF: Fat saturation, excitation and refocusing pulses, ADC. G: Slice selective, refocusing, and diffusion gradients, crushers, readout, trigger for field camera (Tx). B. Parametric view of k-space: PF EPI (dashed line - reconstructed points) and spiral. C. Example of b = 0 ms/μm² prostate images for EPI and spiral.

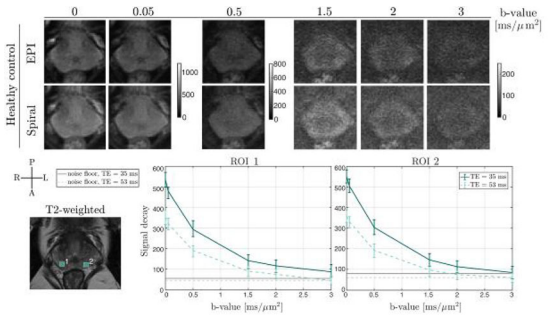

Fig. 2: Healthy control dataset: Averaged DWI data with signal decays from 2 ROIs (grey lines - estimated noise floor in each ROI[30]; TE = 35 ms – spiral, TE = 53 ms - EPI).

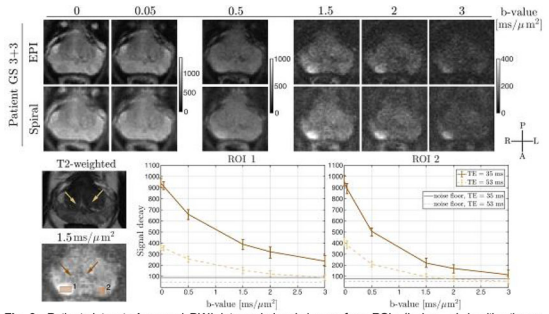

Fig. 3: Patient dataset: Averaged DWI data and signal decays from ROIs (lesion – 1, healthy tissue - 2; grey lines - estimated noise floor in each ROI[30]). The arrows highlight the anatomical feature correspondence on T2-weighted and DWI scans.

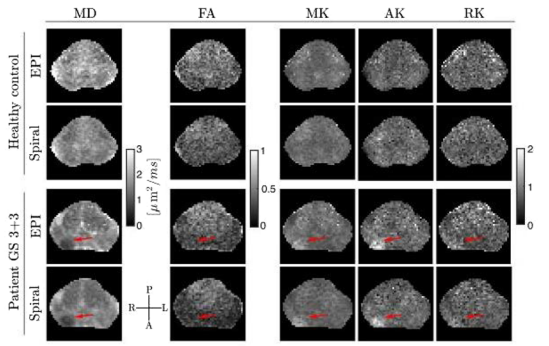

Fig. 4: Quantitative maps estimated using data from healthy control and PCa patient with delineated gland edges. The cancerous lesion (white arrows) shows lower MD, higher MK, AK, (minorly) RK.

References

1. Panagiotaki E, 2015, Invest Radiol.
2. Johnston EW, 2019, Radiology.
3. Setsompop K, 2013, NI.
4. Kimmlingen R, 2017, MAGENTOM Flash.
5. Foo TKF, 2020, MRM.
6. Weiger M, 2018, MRM.
7. Versteeg E 2021, NMR Biomed.
8. Webb AG. 2016, Society of Chemistry.
9. Mueller L, 2019, ISMRM Proc.
10. Wilm BJ, 2015, MRM.
11. Wilm BJ, 2020, MRM.
12. McNab JA, 2013, NI.
13. Jones DK, 2016, NI.
14. Fan Q, 2022, NI.
15. Lee Y, 2021, MRM.
16. Wilm BJ, 2015, MRM.
17. Dietrich BE, 2016, MRM.
18. Wilm BJ, 2011, MRM.
19. Pruessmann KP, 2001, MRM.
20. Vannesjo SJ, 2016, MRM.
21. Bernstein MA, 1998, MRM.
22. Jovicich J, 2006, NI.
23. Bammer R, 2003, MRM.
24. Rudrapatna U, 2021, MRM.
25. Veraart J, 2011, MRM.
26. Langbein BJ, 2021, Invest Radiol.
27. Chatterjee A, 2018, Radiology.
28. Lemberskiy G, 2018, Front Phys.
29. Zhang Z, 2020, Radiology.
30. Jones DK, 2004, MRM.

T32.
Fast free-breathing stack-of-stars multiparameter mapping in clinical prostate MRI—Initial clinical experience

P. García-Polo[1,2], C. Pirkl[3], S. Endt[3,4,5], M. Tosetti[6], M. Cencini[7], S. Ginés[8], L. Martí-Bonmatí[8], M. Menzel[3,4,5], R. Schulte[3]

[1]*GE Healthcare, Madrid, Spain;*
[2]*University Rey Juan Carlos, Móstoles, Spain;*
[3]*GE Healthcare, Munich, Germany;*
[4]*Technische Hochschule Ingolstadt, Ingolstadt, Germany;*
[5]*Technical University of Munich, Munich, Germany;*
[6]*IRCCS Stella Maris, Pisa, Italy;*
[7]*INFN, Sezione di Pisa, Pisa, Italy;*
[8]*Hospital Universitario y Politécnico La Fe, Valencia, Spain*

Introduction Quantitative MRI offers diagnostic information with high reliability, repeatability and scanner independency. Inclusion of quantitative biomarkers such as T1 and T2 relaxation times in clinical MRI exams (e.g. prostate MRI) has the potential for more comprehensive tissue and tumor characterization[1], bringing new opportunities for early diagnosis, treatment planning and active surveillance monitoring. Moreover, advanced MRI parameter mapping facilitates multiparametric MRI in clinically acceptable scan times. In this clinical study, we demonstrate the feasibility of 3D free-breathing quantitative transient-state imaging (QTI) technique with Stack-of-stars encoding[2] in prostate MRI.

Methods As part of an IRB-approved study, MRI data from 20 male patients, appointed for prostate MRI examination, was acquired on a 3 T HDxt system (GE Healthcare, Milwaukee, WI) after obtaining written informed consent. The MRI protocol comprised PI-RADS 2.1

standardized sequences[3] extended by the proposed QTI scan. The QTI encoding scheme comprises an initial inversion (TI = 4 ms) that is followed by an optimized RF excitation sequence (Fig. 1b) with TR/TE = 9.1 ms/3.4 ms and 1000 repetitions. The segmented QTI readout scheme (Fig. 1a) combines Cartesian phase-encoding along the logical Z direction and radial in-plane sampling where radial spokes are rotated with golden angle increments from one repetition to the next. We optimized our initial QTI sequence for prostate based on the PI-RADS v2.1 recommendations: field of view = 300 × 300 × 80 mm^3; voxel size = 1 × 1 × 4 mm^3. QTI raw image time-series were reconstructed via SVD subspace projection in the time domain[4], Cartesian re-gridding, 3D FFT, weighted apodization along the SVD domain and subsequent coil sensitivity combination[5]. Quantitative maps of T1, T2 and PD are derived by matching the reconstructed subspace images to a dictionary of reference signals as derived from the Extended Phase Graphs formalism[6]. For quantitative evaluation of T1 and T2 values we manually segmented the prostate central zone.

Results and discussion Prostate QTI T1, T2 and PD maps have clinically relevant resolution, image quality and motion robustness, thanks to the Stack-of-Stars encoding (Fig. 2). The acquisition time of 6:04 min is similar to the other clinical sequences and with the efficient online reconstruction with direct DICOM export, we make it feasible for use in routine prostate MRI workflows. Fig. 3 shows promising tissue contrast inside the central zone and peripheral zone of the prostate for different patients that could give additional insights into tissue sub-structures to improve diagnosis.

T1 and T2 mapping results (Mean ± SD: T1 = 1682 ± 327 ms, T2 = 102 ± 30 ms) are in accordance with literature[7–8].

In future work we will evaluate the T1 and T2 parameter distributions on a more granular level and in a larger patient cohort.

Conclusion In this initial study, we evaluate multiparametric quantitative transient-state imaging (QTI) for clinical prostate MRI. We present a fast Stack-of-stars variant QTI framework with a scan time, motion robustness and image quality that make it suitable for application in clinical practice. Its potential to provide quantitative diagnostic information may be a promising extension to the current PI-RADS v2.1 standard in prostate cancer patients.

Acknowledgements This project receives funding from the European Union Horizon 2020 research and innovation programme under grant agreement No. 952172.

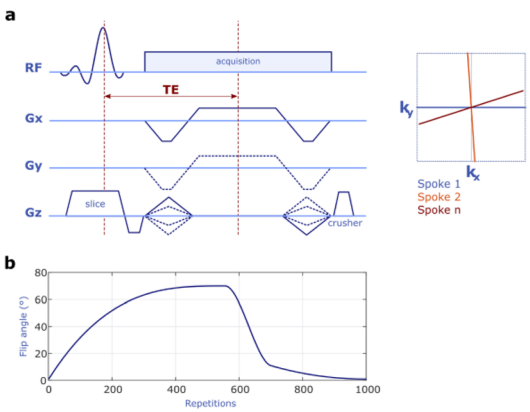

Fig. 1: Sequence diagram of the proposed QTI sequence with Stack-of-stars encoding (a) and variable flip angle RF excitations optimized based on Cramér Rao bounds (b).

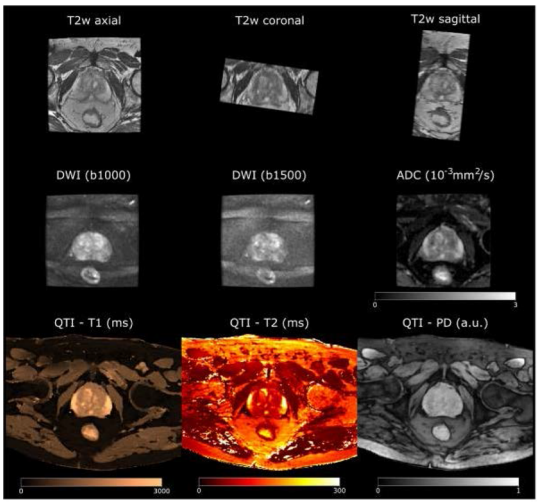

Fig. 2: Overview of the clinical prostate MRI protocol comprising T2-weighted (top row) and diffusion-weighted (b=1000,1500 s/mm2 and ADC map) (middle row) and QTI-based quantitative T1, T2 and relative PD maps.

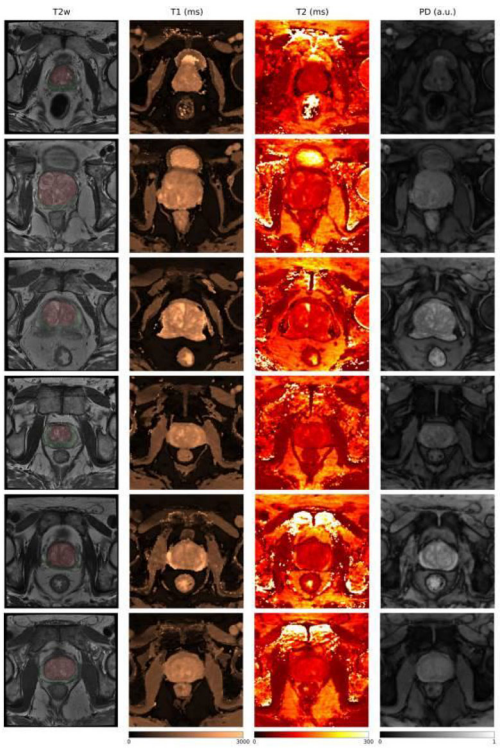

Fig. 3: Axial views of QTI-based T1, T2 and PD maps of four representative patients together with corresponding T2-weighted MRI data. All datasets are co-registered to the reference space of the axial T2-weighted sequence.

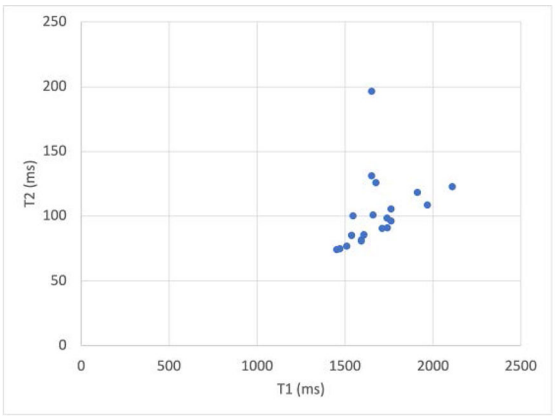

Fig. 4: Distribution of mean T1 and T2 values from the prostate central region from the 20 scanned patients.

References

1-Lo, Wei-Ching, et al. "MR fingerprinting of the prostate." *Magnetic Resonance Materials in Physics, Biology and Medicine* 35.4 (2022): 557–571.

2-Schulte, Rolf F., et al. "Quantitative Parameter Mapping of Prostate using Stack-of-Stars and QTI Encoding." ISMRM2023.

3-Turkbey, Baris, et al. "Prostate imaging reporting and data system version 2.1: 2019 update of prostate imaging reporting and data system version 2." *European urology* 76.3 (2019): 340–351.

4-McGivney, Debra F., et al. "SVD compression for magnetic resonance fingerprinting in the time domain." *IEEE transactions on medical imaging* 33.12 (2014): 2311–2322.

5-Walsh, David O., Arthur F. Gmitro, and Michael W. Marcellin. "Adaptive reconstruction of phased array MR imagery." *Magnetic Resonance in Medicine: An Official Journal of the International Society for Magnetic Resonance in Medicine* 43.5 (2000): 682–690.

6-Weigel, Matthias. "Extended phase graphs: dephasing, RF pulses, and echoes-pure and simple." *Journal of Magnetic Resonance Imaging* 41.2 (2015): 266–295.

7-Han, Dongyeob, et al. "Feasibility of novel three-dimensional magnetic resonance fingerprinting of the prostate gland: phantom and clinical studies." *Korean Journal of Radiology* 22.8 (2021): 1332.

8-Baumann, M.; Keupp, J.; Mazurkewitz, P.; Koken, P.; Nehrke, K.; Meineke, J.; Amthor, T.; Doneva, M. Towards A Clinical Prostate MR Fingerprinting Protocol. In Proceedings of the Proc. Intl. Soc. Mag. Reson. Med. 30; London, United Kingdom, 2022.

T33.
Diffusion tensor imaging in leg muscles of limb girdle muscular dystrophy R9 patients

S. Rauh[1,2,3], P. Y. Baudin[1], T. Stojkovic[4], M. Hooijmans[2,3], M. Granier[5], S. Olivier[5], G. Strijkers[2,3], H. Reyngoudt[1], B. Marty[1]

[1]*Institute of Myology, Neuromuscular Investigation Center, NMR Laboratory, Paris, France;*
[2]*Amsterdam UMC, Department of Biomedical Engineering and Physics, Amsterdam, Netherlands;*
[3]*Amsterdam UMC, Musculoskeletal Health, Amsterdam, Netherlands;*
[4]*Institute of Myology, Neuro-Myology Department, Paris, France;*
[5]*Généthon, Atamyo Therapeutics, Evry, France*

Introduction Limb-girdle muscular dystrophy (LGMD) R9 is a slowly progressing muscle disease characterized by gradual muscle wasting and fatty replacement. It originates from mutations in the FKRP-gene and still lacks an effective therapy. For monitoring disease progression and to evaluate the efficacy of novel treatment approaches, sensitive biomarkers are needed. Diffusion tensor imaging (DTI) has shown to be sensitive to microstructural changes in skeletal muscle[1,2] and might be a potential biomarker in LGMD-R9 before fatty replacement of the muscle. The aim of this study was to investigate if DTI parameters at different diffusion times can depict alterations in muscle tissue in LGMD-R9 patients.

Methods 18 patients with LGDM-R9 (17f/1 m, mean age 38.3 years, range 19–62 years) and 12 healthy controls (11f/1 m, mean age 37.4 years, range 19–67 years) with similar age-distribution (Wilcoxon rank sum test: $p = 0.85$) were included and underwent an MRI scan (3 T Siemens Prisma, Siemens Healthineers, Erlangen, Germany) of the legs at baseline, 12 and 24 months. All participants gave written informed consent. The protocol included a DTI scan of the right leg using a stimulated echo EPI sequence with four mixing times (TM). Dixon-based olefinic fat suppression (DOFS[3]) with 6 readouts was used in combination with spectral attenuated inversion recovery (SPAIR) and gradient reversal fat suppression. In the patients, a 3-point Dixon scan for fat fraction (FF) estimation was acquired in both legs. Detailed MRI parameters can be found in Fig. 1. All processing was done in Python. DTI data was denoised and fat–water separation as described by the DOFS method was performed to remove the remaining olefinic signal contamination. The b-matrix included contributions from imaging gradients and the diffusion tensor was fitted using a nonlinear least-squares method. Signal to noise ratio (SNR) was estimated from the unweighted diffusion images for quality control. The outcome measures were Dixon-derived FF (in patients), mean diffusivity (MD), diffusion tensor eigenvalues (λ_1, λ_2, λ_3) and fractional anisotropy (FA). Segmentations were drawn manually in the right leg in the soleus (SOL) and tibialis anterior (TA) muscles. Muscles with SNR < 15 were excluded from further analysis. The mean DTI parameters per TM were compared between controls and patients at baseline and between baseline and follow-up visits for patients using a Wilcoxon rank sum test. Correlation analysis between the DTI parameters and SNR, age, FF and years since diagnosis (in patients) was performed for each TM to exclude a possible bias. All statistical tests were corrected for multiple comparisons.

Results All 18 patients completed the baseline scan, whereas 16 and 14 underwent the 1-year and 2-years follow-up, respectively. The years since diagnosis ranged from 1.5 to 17.9 years (mean 9.4 years). No correlation between DTI parameters and SNR, age, FF or years since diagnosis was found ($p > 0.05$). For increasing TM, tensor eigenvalues and MD decreased while FA increased for both, patients and controls (Fig. 2). Between controls and patients, no significant differences were found for all DTI parameters and TMs. Regarding the individual patients over the years since diagnosis, it can be observed that most patients have a reasonably low FF ($< 20\%$), which remains stable over time (Fig. 3). Some patients presented with a considerably higher FF ($> 20\%$). No clear trend over time was found for the DTI parameters, but good reproducibility per patient can be observed.

Discussion In this study we have shown that DTI with several TMs and DOFS is feasible in patients with and without muscle fat replacement. We found a good reproducibility of the DTI parameters in patients between baseline and follow-up. Over the 2-year follow-up period in patients, no significant changes in DTI parameters were found, which might be related to the slow progression of LGMD-R9. In comparing the DTI parameters between controls and patients, no significant differences were found for any TM. This suggests that DTI at different TMs cannot depict alterations in muscle microstructure in LGMD-R9 patients. A possible explanation for our findings is that DTI is not sensitive enough to depict changes in the slowly-progressing, low-impacted muscles in LGMD-R9, as leg muscles are typically less affected than thigh or pelvic muscles in LGMD-R9[4].

However, this needs to be investigated in more depth in further research.

Conclusion DTI with DOFS for olefinic fat suppression proved feasible in LGMD-R9 patients with and without muscle fat replacement and showed good reproducibility over a 2-year period. Our results suggest that DTI at different TMs cannot depict microstructural changes in LGMD-R9 leg muscles compared to healthy controls.

		Stimulated echo DTI	3-point Dixon
Field of view	(mm³)	192 x 192 x 81	448 x 224 x 320
Resolution	(mm³)	2 x 2 x 6	1 x 1 x 5
Slices		9	64
Slice gap	(mm)	3	-
TE	(ms)	37	2.75, 3.95, 5.15
DOFS readout shifts	(ms)	1.1, 3.3, 5.5, 7.8, 10.0, 12.2	-
TR	(ms)	5000	10
Flip angle		90	3
Parallel imaging (GRAPPA)		2	-
Partial Fourier		6/8	-
Mixing times	(ms)	100, 200, 300, 400	-
b-values (set)	(s/mm²)	0, 400	-
Corrected b-value at b = 0 *	(s/mm²)	27 (TM = 100 ms) 50 (TM = 200 ms) 73 (TM = 300 ms) 99 (TM = 400 ms)	-
Number of diffusion directions		6	-

Fig. 1: Detailed MRI parameters. *b-values corrected for contributions from imaging gradients for all four mixing times for a chosen b-value of 0 s/mm².

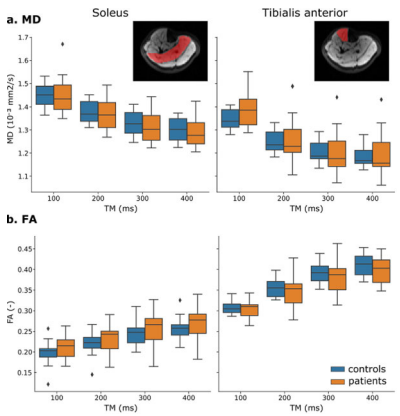

Fig. 2: Comparison of MD (a) and FA (b) between controls (blue) and patients (orange) at baseline for all TMs in the SOL and TA muscle. In two patients, the SOL was excluded and in one patient the TA at TM = 400 ms due to low SNR. No significant differences between controls and patients were found.

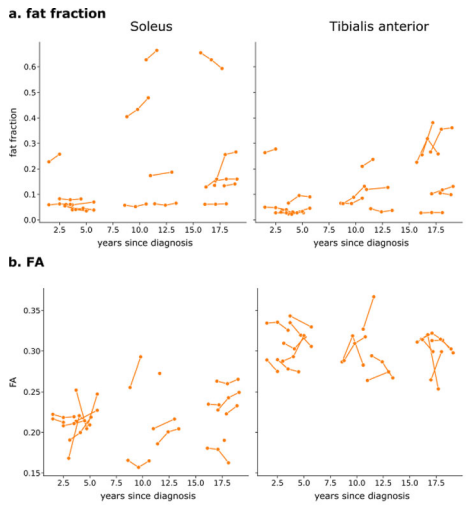

Fig. 3: Fat fraction (a) and FA at TM = 100 ms (b) versus years since diagnosis for all patients are shown for the SOL and TA muscles. Each line represents a patient and the dots represent the visits. A heterogeneous pattern in the fat infiltration can be observed, with the SOL being more severely affected than the TA. Both, in fat fraction and FA no clear trend over the years since diagnosis is visible. On a per patient basis, a good reproducibility can be observed.

References

1. Forsting et al. *Sci Rep* 2022.
2. Hooijmans et al. *NMR Biomed* 2015.
3. Burakiewicz et al. *Magn Reson Med* 2018.
4. Fischer et al. *J Neurol*. 2005.

T34.
Tissue differences in patients with peripheral artery disease identified with quantitative MRI

F. Kjellberg[1], S. Eriksson[1,2], K. Lagerstrand[1,2]

[1]*University of Gothenburg, Department of Medical Radiation Sciences, Gothenburg, Sweden;*
[2]*University of Gothenburg, Department of Medical Physics and Biomedical Engineering, Gothenburg, Sweden*

Introduction Peripheral artery disease (PAD) affects approximately 20% of the elderly western population and is caused by stenosis of the arteries supplying the lower limbs with blood. A classic symptom of PAD is leg pain after walking short distances, where the pain resolves within ten minutes of rest. [1] The group is highly heterogeneous and new diagnostic markers are warranted to classify or stage the disease. T_2 mapping and fat fraction MRI have the feasibility to offer objective markers of muscle inflammation and fat infiltration [2], reflecting increased muscle degeneration as a result of PAD. The aim of the study was to investigate whether quantitative MRI markers differ between patients with PAD and matched healthy controls.

Method The study included a group of 22 symptomatic patients with PAD (age 73.5 ± 4 years; 12 males) alongside ten healthy controls (age 67.9 ± 6.2 years; 8 males). The subjects' calf muscles were examined using a 3 T MRI system (Magnetom Skyra, Siemens Healthineers, Erlangen, Germany). In the patient group the most symptomatic leg was scanned whereas all controls had their left calves studied. The scan protocol included a six echo in phase/opposing phase DIXON sequence ($TR/TE1/\Delta TE$ = 9/1.23/1.23 ms) and an eight echo multi echo spin echo (MESE) sequence ($TR/TE1/\Delta TE$ = 1500/11.1/11.1 ms). Muscle fat fraction was calculated voxel-by-voxel using a least squares fitting model that assumes one singular broad fat peak and separate T_2^* decay rates for water and fat. The method was based on model (v) by Bydder et al. [3]. Muscle T_2 relaxation time was estimated voxel-by-voxel using log-linear regression. See Fig. 1 for an overview of the post-processing steps. For each subject, the mean fat fraction and T_2 were estimated in the calf muscles *m. gastrocnemius* (GC) and *m. soleus*, that together constitute *m. triceps surae* (TS). The group means were then compared for each muscle using two-sided Welch t-tests.

Results The mean muscle fat fractions in the patient group were 9.8 ± 3.2%, 11.7 ± 2.9% and 10.8 ± 2.7% for GC, soleus and TS respectively. Corresponding values for the controls were 6.5 ± 1.4%, 9.4 ± 2.3% and 8.0 ± 1.8%. t-tests revealed a significant difference between the groups for all three muscles ($p < 0.0003$, $p < 0.03$ and $p < 0.002$). Furthermore, the patients and the controls differed in mean muscle T_2 for all muscles (patients: 57.9 ± 6.0 ms, 57.2 ± 5.2 ms and 57.4 ± 5.1 ms; controls: 51.7 ± 3.6 ms, 51.9 ± 4.1 ms and 51.9 ± 3.3 ms; $p < 0.002$, $p < 0.006$ and $p < 0.002$). See Figs. 2 and 3 for violin plots of the data.

Discussion The elevated fat fractions and T_2 values in the patient group indicate that PAD is associated with worse muscle health through chronic inflammation and fat infiltration. Additionally, Figs. 2 and 3 display a wider range of values in patients compared with controls, suggesting that the studied markers could assist in phenotyping the disease. Due to the inclusion criteria of the study, the generalizability of these results is limited to symptomatic patients. It

should also be noted that the large overlap of the patient and control distributions in Figs. 2 and 3 limits the possibility to use these markers alone for predicting PAD severity.

Conclusion In comparison with controls, patients with symptomatic PAD displayed elevated muscle dystrophy, measured in terms of increased fat fractions and T_2 relaxation times. Further studies are warranted to evaluate how such muscle changes are associated with patient outcome and how they change over time, especially after targeted intervention.

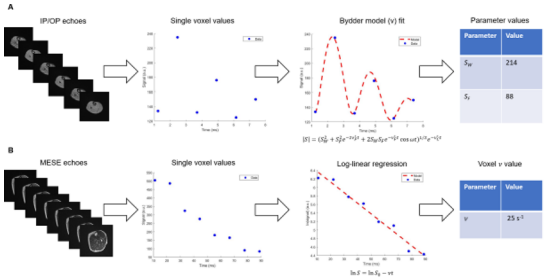

Fig. 1: (A) Estimating voxel fat fraction by separating total signal S into water and fat components S_W and S_F. The free parameters are S_W, S_F, v_C^* (common T_2^* decay rate) and v_F^* (additional fat-specific T_2^* decay rate). Water/fat dephasing rate ω is fixed. Fat fraction is then given by $S_F/(S_W+S_F)$. **(B)** Estimating voxel T_2 by performing log-linear regression on the signal decay. The regression yields the decay rate $v = T_2^{-1}$. S_0 is the signal at t=0 ms.

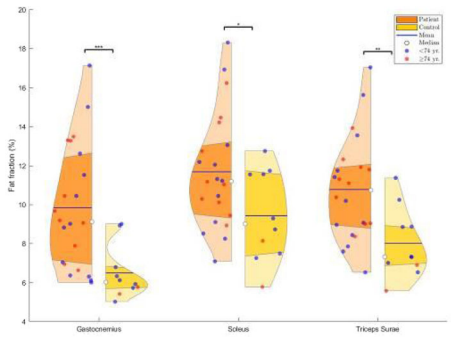

Fig. 2: Violin plot of the mean muscle fat fractions of the studied muscles. The shaded regions correspond to quartiles. A scatter plot is overlayed to display age distribution. Asterisks indicate significance level of the t-tests, where one corresponds to p<0.05, two to p<0.01 and three to p<0.001.

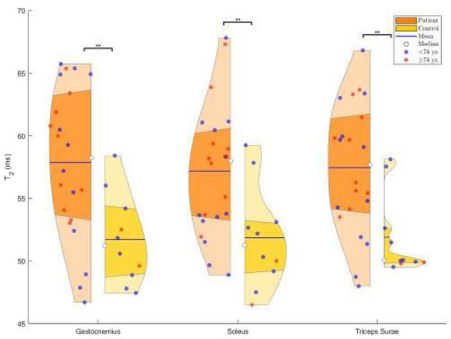

Fig. 3: Violin plot of the mean muscle T_2 of the studied muscles. The shaded regions correspond to quartiles. A scatter plot is overlayed to display age distribution. The two asterisks indicate significance level of the t-tests of p<0.01.

References

[1] Firnhaber, J. M., & Powell, C. S. (2019). Lower Extremity Peripheral Artery Disease: Diagnosis and Treatment. *American family physician*, *99*(6), 362–369.

[2] Damon, B. M., Li, K., Dortch, R. D., Welch, E. B., Park, J. H., Buck, A. K., Towse, T. F., Does, M. D., Gochberg, D. F., & Bryant, N. D. (2016). Quantitative Magnetic Resonance Imaging of Skeletal Muscle Disease. *Journal of visualized experiments: JoVE*, (118), 52352. https://doi.org/10.3791/52352

[3] Bydder, M., Yokoo, T., Hamilton, G., Middleton, M. S., Chavez, A. D., Schwimmer, J. B., Lavine, J. E., & Sirlin, C. B. (2008). Relaxation effects in the quantification of fat using gradient echo imaging. *Magnetic resonance imaging*, *26*(3), 347–359. https://doi.org/10.1016/j.mri.2007.08.012

T35.

Assessment of relationships between muscle water T1, water T2 and fat fraction in the lower limbs of healthy volunteers and subjects with myotonic dystrophy type 1

B. Marty[1], H. Reyngoudt[1], G. Bassez[2], E. Caldas de Almeida Araujo[1], P. Y. Baudin.[1]

[1]*Institute of Myology, Neuromuscular Investigation Center, NMR laboratory, Paris, France;*
[2]*Institute of Myologie, Paris, France*

Introduction Quantitative muscle MRI is increasingly proposed in clinical trials related to neuromuscular diseases (NMDs). The intramuscular fat fraction (FF) is considered as a biomarker of disease severity while water T2 and water T1 have been related to active muscle damages (1,2). These quantitative variable are often measured as mean or median values in individual muscles or muscle groups. It has recently been reported that median water T1 and T2 values measured in patients with various NMDs exhibit a moderate correlation, which depends on the extent of muscle fat replacement (2). To date, no studies have established the relationship between these variables at the pixel level in any NMD. The objective of the current study was to characterize the bi-variate (water T1, FF), (water T2, FF) and (water T1, water T2) distributions in the muscles of healthy volunteers and subjects with myotonic dystrophy type 1 (DM1), in which water relaxation parameters are known to be elevated (3, 4).

Methods Sixteen subjects (45.7 [37.6–52.7] years, 9 women) with DM1, and 9 healthy volunteers (49.1 [35.7–58.8] years, 6 women) were scanned at 3 T (Magnetom PrismaFit, Siemens) in the thighs and legs using multi-channel surface coils. FF maps were generated using 3-point Dixon (3 TEs = 2.75/3.95/7.55 ms, TR = 10 ms, T_{acq} = 3 min 12 s, pixel size = 1 × 1 × 5 mm^3). A multi- spin-echo sequence was acquired (17 echoes ranging from 9.5 ms to 161.5 ms, TR = 3 s, T_{acq} = 3 min 41 s, pixel size = 1.4 × 1.4 × 10 mm^3) from which water T2 maps were calculated using a tri-exponential fitting procedure (5). An MRF T1-FF sequence was acquired (train of 1400 spokes, varying TE, TR and FA, T_{acq} = 50 s, pixel size = 1.4 × 1.4 × 10 mm^3) to generate water T1 maps (6). For each subject, FF, water T1 and water T2 maps were interpolated. The mean values and standard deviation of FF, water T1 and water T2 were extracted in the extensor (comprising tibialis anterior and extensor digitorum muscles) and triceps (comprising gastrocnemius medialis, lateralis and soleus muscles) of the legs and in the quadriceps (comprising vastii lateralis, intermedialis and medialis and rectus femoris muscles) and hamstrings (comprising biceps femoris, semi-membranosous and semi-tendinousus muscles) of the thighs. The bi-variate (water T1,

water T2), (water T1, FF) and (water T2, FF) distributions were also estimated in these regions. Water T1 and T2 were normalized by the mean values and standard deviations measured in healthy volunteers. We characterized the normalized (water T1, water T2) distribution based on a bi-variate Gaussian hypothesis, and calculated its angle (θ) and eccentricity ($e = \sqrt{(1 - \lambda 2^2/\lambda 1^2)}$) from the eigenvectors and eigenvalues (λ1 and λ2) of the covariance matrix (Fig. 1).

Results Fig. 2 displays the mean (water T1, FF), (water T2, FF) and (water T1, water T2) distributions in various muscle groups of both healthy controls and subjects with DM1. Our results indicate that subjects with DM1 had higher water T1 and T2 values than controls in pixels across the entire FF range. Notably, we observed a slight decrease in both water T1 and water T2 in pixels with FF > 0.4.

In patients, the ranges of water T1 and T2 values were higher than in controls for all muscle groups. This was reflected by the significantly higher λ1 and λ2 values in most muscle groups (except for λ2 in the hamstrings, Fig. 3). Interestingly, θ was also different in the leg muscles of the DM1 patients compared to healthy volunteers. The eccentricity of the distribution was significantly higher in the leg extensor muscles of the subjects with DM1.

Discussion & Conclusion We characterized the bi-variate (water T1, FF), (water T2, FF) and (water T1, water T2) distributions in healthy controls and patients with DM1. We observed high water T1 and water T2 values in pixels with normal FF, which confirms that these variables can be affected by early onset tissue alterations. As reported earlier at the muscle ROIs level, we observed some pixels with decreased water T2 at high FF (7). Interestingly, we also reported here the same behavior for water T1 in a large number of voxels at high FF.

Additionally, we found that the parameters extracted from the bivariate analysis were altered in the muscles of the patients with DM1 as compared to healthy controls, which demonstrates that the relationship between water T1 and water T2 was modified by muscle alterations. Adopting this multivariate approach has the potential to enhance the specificity of water relaxation time quantification, which may aid in disentangling different type of muscle tissue alterations in NMD studies.

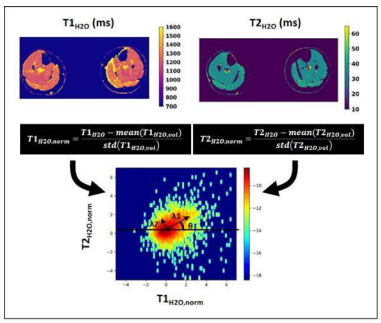

Fig. 1: Bi-variate (water T1, water T2) distribution obtained in the triceps muscle of a healthy volunteer. Water T1 and T2 values were normalized by the mean and standard deviation values of the healthy cohort (mean($T1_{H2O,vol}$), std($T1_{H2O,vol}$), mean($T2_{H2O,vol}$) and std($T1_{H2O,vol}$), respectively). The amplitude of the eigenvalues of the covariance matrix (λ1 and λ2), and the angle of the first eigenvector with the x-axis (θ) were calculated.

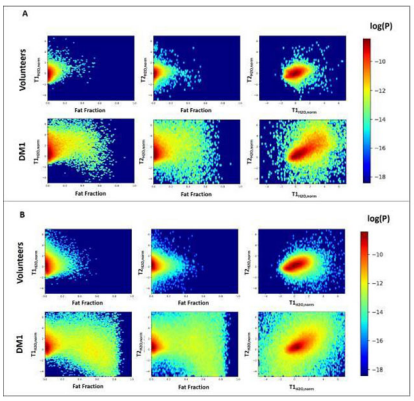

Fig. 2: Mean bi-variate (water T1, fat fraction), (water T2, fat fraction) and (water T1, water T2) distributions obtained in the extensor (A) and triceps (B) muscles of the healthy volunteers and patients with DM1.

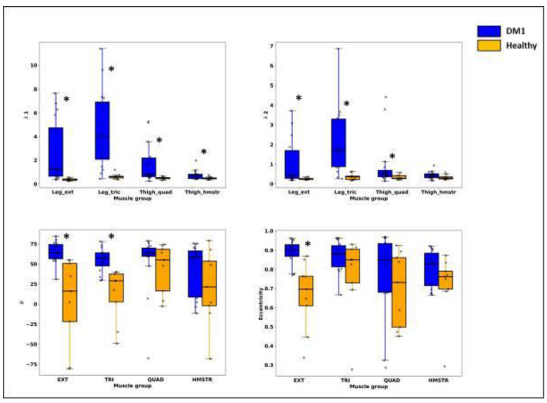

Fig. 3: Box and whisker plots of λ1, λ2 , θ and e of the (water T1, water T2) distributions in the different muscle groups of healthy volunteers (orange) and patients with DM1 (blue). EXT: extensor of the leg, TRI: triceps, QUAD: quadriceps, HMSTR: hamstrings. Mann-Whitney test, *: P<.05

References

1- Carlier et al., J Neuromuscul Dis. 2016.
2- Marty et al., Radiology. 2021.
3- Heskamp et al., Neurology 2019.
4- Marty et al., Proc. ISMRM 2023.
5- Azzabou et al., J Magn Reson Imaging. 2015.
6- Marty and Carlier, Magn Reson Med. 2020.
7- Reyngoudt et al., J Magn Reson Imaging. 2023.

T36.
Quantitative molecular imaging of cardiac fibrosis and response to treatment using a novel collagen III-specific MR imaging probe

N. Chaher[1], G. Digilio[2], S. Lacerda[3], L. Gao[1], B. L. Plaza[1,4], C. Velasco[1], G. Cruz[1,5], C. Prieto[1,6], R. Botnar[1,7,6,8], A. Phinikaridou[1,7]

[1]*Kings College London, School of Biomedical engineering and imaging science, London, United Kingdom;*
[2]*Università del Piemonte Orientale, 2 Dipartimento di Scienze e Innovazione Tecnologica, Turin, Italy;*
[3]*Universitè d'Orléans, Centre de Biophysique Moléculaire, Orléans, France;*
[4]*Autonomous University of Madrid, Department of Biochemistry*

and Molecular Biology, Madrid, Spain;
[5]University of Michigan, Department of Radiology, Ann Arbor, MI, United States;
[6]Pontificia Universidad Católica de Chile, Escuela de Ingeniería,, Santiago de Chile, Chile;
[7]BHF Centre of Research Excellence, Cardiovascular Division, London, United Kingdom;
[8]Pontificia Universidad Católica de Chile, Instituto de Ingeniería Biológica y Médica, Santiago de Chile, Chile

Heart failure (HF) has reached epidemic proportions, affecting about 64 million people globally and is the main cause of death and disability [1]. Myocardial fibrosis, characterised by changes in type I and III collagen, drives the adverse outcomes of HF [2,3]. Collagen I (COL1) provides tensile strength but when excessive it can cause myocardial stiffness. In contrast, collagen III (COL3) provides elasticity. In myocardial fibrosis, COL3 increases in the early stages and is replaced by COL1 in the later stages of remodelling. Cardiac magnetic resonance (CMR) has emerged as the preferred imaging modality to non-invasively detect myocardial fibrosis with high spatial resolution and superior soft tissue contrast. However, CMR still provides indirect or surrogate measurements, such as extracellular volume or T1 and T2 relaxation time. Alternatively, molecular imaging offers the opportunity to directly image fibrosis, but current probes are limited to COL1. Here, we combined quantitative CMR and molecular imaging using the first COL3-binding probe to directly image COL3. This would enable quantification of, previously undetectable, COL3 and can be used as a tool to monitor the treatment response.

To develop a COL3-binding probe a small peptide was conjugated to a DOTA-chelator and labelled with Europium [Eu(III)] for in vitro binding assays; Gallium (68 Ga) for in vivo PET/CT biodistribution; and Gadolinium [Gd(III)] for in vivo CMR studies. In vivo functional and molecular CMR was performed using a 3 Tesla clinical scanner at days 10 and 21 post-MI (n = 6/group). The same mice were imaged the next day with a probe carrying a scrambled peptide sequence, and again the next day with the clinically used probe Gadovist (n = 3) for comparison. The COL3-probe was used as a tool to monitor the effect of Enalapril (an ACE inhibitor commonly used to treat patients with HF) on myocardial fibrosis after MI. Mice were administered Enalapril (20 mg/kg/day) immediately after MI and imaged at days 10 and 21 (n = 6/group). 2D short-axis cine images covering the left ventricle (LV) were used to assess cardiac function parameters including end-diastolic volume (EDV, µl); ejection fraction (EF, %) and LV mass (mg). T1-weighted 3D inversion recovery (IR) images were used to acquire Late Gadolinium Enhancement (LGE) images of the LV 60 min after intravenous injection of the probe (0.2 mmol/kg). T1 mapping was performed using a 2D Look-Locker sequence with an inversion pulse applied followed by the acquisition of 30 inversion recovery images with an inversion delay ranging from 30 to 10000 ms. The T1 maps were reconstructed offline using an in-house developed MATLAB script. The MRI acquisition parameters are shown in **Fig. 2B.**

The developed imaging probe binds to COL3 with high affinity (Kd = 5.3 µM) and high specificity (no binding of the negative probe) (**Fig. 1A**). The probe has favourable pharmacokinetics with fast blood clearance (60 min) and no unspecific binding (**Fig. 1B**). Initial, molecular CMR enabled selective profiling of the natural turnover of COL3 after MI with the signal increasing at day 10 when COL3 is elevated, and decreasing at day 21 as COL3 is replaced by COL1 (**Fig. 2A**). The imaging data were validated by histology showing co-localisation of the MRI signal with COL3 (green) at day 10 and reduction at day 21. Quantitative T1 maps discriminated between infarcted and remote myocardium with lower T1 values (~ 530 ms) in the infarct and higher in the remote myocardium (~ 670 ms). Importantly, there was no enhancement using the scrambled probe or Gadovist.

In the treatment study, mice receiving Enalapril showed similar enhancement at day 10 compared to untreated mice (**Fig. 3A-B**). However, at day 21 mice treated with Enalapril showed a significantly higher LGE volume compared with untreated mice. (**Fig. 3A-B**). This data suggests that Enalapril may prolong the accumulation of COL3 that potentially delays the onset of COL1 deposition (**Fig. 3B**). However, despite changes in the fibrotic content observed with molecular imaging, cardiac function was similar between the groups (**Fig. 3C-E**) suggesting that molecular changes may precede functional changes.

We have developed the first probe suitable for molecular imaging of COL3. Combining this probe with quantitative CMR shows potential to image previously undetectable changes in COL3 remodelling after myocardial infarction and in response to treatment. Our approach may provide a new tool to investigate the functional role and regulation of COL3 in myocardial fibrosis non-invasively. This could address a considerable knowledge gap and potentially enable detection and characterisation of myocardial fibrosis earlier allowing staging of disease and monitoring of novel therapies. Future work to improve probe imaging properties and further validate in vivo imaging findings are underway.

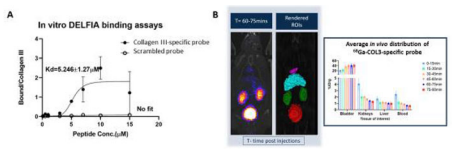

Fig. 1: Binding and biodistribution of the COL3-specific imaging probe. A. The probe has high affinity (low Kd) and specificity towards COL3. **B**. *In vivo* biodistribution showed fast blood clearance, via renal excretion and no unspecific uptake in other tissues.

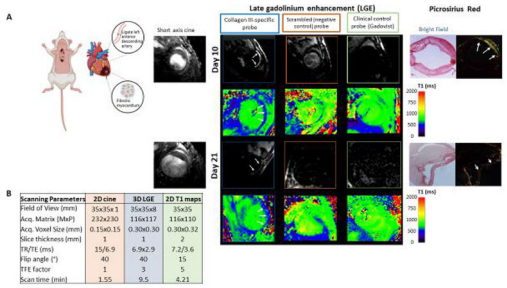

Fig. 2: First *in vivo* CMR using the COL3-specific imaging probe. A. Increased signal enhancement in the infarcted myocardium at day 10 that decreased by day 21 which co-localised with COL3 as seen by histology. Importantly no enhancement was observed with both the negative control probe and the non-targeted clinical probe. **B**. CMR scanning parameters.

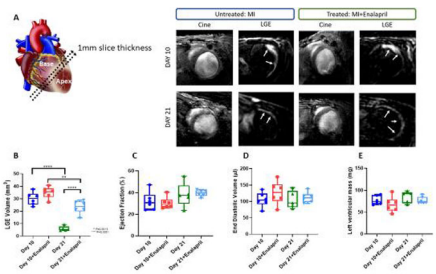

Fig. 3: Molecular CMR detects changes in COL3 in Enalapril-treated MI mice. A. Similar signal enhancement (SE) in the infarcted myocardium at day 10 following MI. However, at day 21 treated mice showed higher SE compared with untreated mice. **B**. Quantification of the LGE volume verified the observations in panel A. **C-E** Cardiac functional data were similar between both groups.

References
[1] Savarese G et al. Cardiovasc Res. 2023.
[2] Bateman, E.D. et al. Thorax 1981.
[3] Jugdutt, B.I. Circulation 2003.

T37.
A dual 9.4 T ^{1}H MRS and ^{18}F-FDG PET study probes impaired neurometabolic profiles and brain glucose uptake in a rat model of type C hepatic encephalopathy

J. Mosso[1,2,3], T. Yin[2,3], C. Poitry-Yamate[2,3], D. Simicic[2,3], M. Lepore[2,3], V. A. McLin[4], O. Braissant[5], C. Cudalbu[2,3], B. Lanz[2,3]

[1]*École Polytechnique Fédérale de Lausanne (EPFL), Laboratory of Functional and Metabolic Imaging (LIFMET), Lausanne, Switzerland;*
[2]*École Polytechnique Fédérale de Lausanne (EPFL), CIBM Center For Biomedical Imaging, Lausanne, Switzerland;*
[3]*École Polytechnique Fédérale de Lausanne (EPFL), Animal Imaging and Technology, Lausanne, Switzerland;*
[4]*University of Geneva, Swiss Pediatric Liver Center, Department of Pediatrics, Gynecology and Obstetrics, Geneva, Switzerland;*
[5]*University of Lausanne, Service of Clinical Chemistry, Lausanne, Switzerland*

Introduction Type C hepatic encephalopathy (HE) is a severe neuropsychiatric disorder occurring as a consequence of chronic liver disease. ^{1}H MRS can provide valuable information on brain metabolic pool alterations following ammonia intoxication in HE and ^{18}F-FDG PET a complementary dynamic information on glucose uptake. Energy metabolism alterations have been suggested in HE but autoradiography and PET studies have reported conflicting results[1,2]. We hypothesise that the lack of concurring results partially resides in the report of the standardized uptake value (SUV), being only a semi-quantitative approach, as a surrogate marker for glucose uptake. Here we propose a novel glucose cerebral metabolic rate (CMR_{glc}) quantification method for preclinical ^{18}F-FDG PET studies, based on an image-derived input function (IDIF) from the vena cava[3]. The obtained regional CMR_{glc} were associated with the metabolic profiles measured with ^{1}H MRS in the hippocampus and cerebellum of HE and SHAM animals and together shed new light on energy metabolism in HE.

Methods MRS experiments at 9.4 T (SPECIAL sequence[4], TE/TR = 2.8/4000 ms, 160 shots (10 blocks of 16 shots), a 5 kHz spectral width and 4096 spectral points) on male bile-duct ligated (BDL) rats, model of type C HE, were performed at week 0 (used as self-control) and 6 post-surgery on two brain regions: the hippocampus (week 0/6: N = 4/9, $2.8 \times 2 \times 2$ mm^3 voxel) and the cerebellum (week 0/6: N = 3/4, $2.5 \times 2.5 \times 2.5$ mm^3 voxel). PET experiments on BDL (N = 10) and SHAM (N = 8) rats were conducted at week 6, using a LabPET-4 preclinical scanner. After injection of a bolus of ^{18}F-FDG in the tail vein of the rat, a 45-min dynamic acquisition was performed on the region of the vena cava to extract the IDIF[3], followed by a 15-min static acquisition on the brain to derive 3D maps of CMR_{glc}[5]. The Lumped Constant (LC) was set to 0.71[6] and glycaemia values were measured for each rat after the static acquisition. Brain maps of CMRglc ($1 \times 1 \times 1.18$ mm^3 nominal resolution) were registered to an atlas for regional comparison with ^{1}H MRS metabolites' concentrations.

Results ^{1}H MRS showed a significant increase in brain glutamine in both regions (**Fig. 1**), yet stronger in the cerebellum than in the hippocampus (114% versus 73%), compensated by a decrease in the main osmolytes (Ins, Tau, tCr, tCho) (− 15%, − 13%, respectively), and a decrease in Glu (− 22%, − 13%, respectively). The FDG-PET Sokoloff method[5], using the area under the curve of the FDG IDIF (Fig. 2A), LC, the steady-state brain image and glycaemia as inputs enabled the construction of quantitative metabolic maps (Fig. 2B). PET to atlas registration enabled a quantitative comparison between PET and ^{1}H MRS data in the hippocampus and cerebellum (**Fig. 3**). A significant twofold lower CMR_{glc} in BDL rats compared to SHAM rats was measured in both brain regions. The SUV showed no significant difference between the two groups for any of the brain regions (**Fig. 4**).

Discussion Ins, tCr and Tau decrease in HE measured here with ^{1}H MRS reflects the role of these metabolites as regulators of cellular volume during induced cell swelling[7], here caused by the Gln load in the astrocytes, and where an efflux could help to restore the osmotic balance. The opposite changes in Glu and Gln with HE show that their spectral separation with ^{1}H MRS spectroscopy at 9.4 T is important for data interpretation. The absence of difference for the SUV between BDL and SHAM rats suggests that the injected dose and body weight do not provide an accurate measure of the true tracer availability for the brain when systemic effects, such as the metabolism of other organs, and particularly of the liver in this study, might affect the blood FDG available for the brain.

Conclusion This study characterized local alterations of energy metabolism in the cerebellum and in the hippocampus of the BDL rat model of type C HE, concomitant with a glutamine-associated metabolic impairment. The use of an IDIF made the quantitative PET measurement non-invasive and compatible with longitudinal studies. In contrast, we showed that the SUV, a more common metric in preclinical PET studies, but overlooking any inter-subject differences in systemic metabolism, would fail to detect such differences between the BDL and SHAM groups.

Acknowledgements Supported by the SNSF project No 310030 173222 and the EU Horizon 2020 research and innovation program under the Marie Sklodowska-Curie grant agreement No 813120 (INSPiRE-MED). We thank Dr Corina Berset and the veterinary team at CIBM for their help with PET experiments.

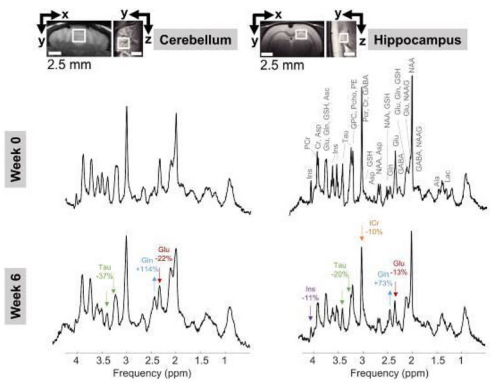

Fig. 1: ^{1}H MRS spectra acquired at 9.4T in the hippocampus and cerebellum of BDL rats at week 0 and 6 post-surgery. Arrows: significant differences between week 0 and week 6.

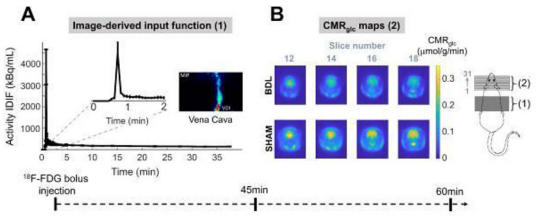

Fig. 2: **A**. Representative ^{18}F-FDG PET input function curve with corresponding VOI in the vena cava. **B**. Typical CMR_{glc} maps in a BDL and a SHAM rat for four central slices, the position of the PET scanner field of view for the two acquisitions and the slice order are display on the right.

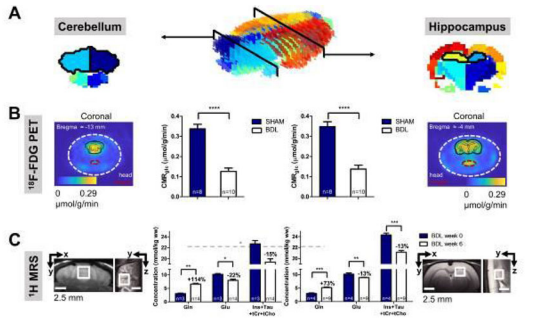

Fig. 3: **A**. Color-coded brain regions for the atlas-based co-localization of ^{1}H MRS and ^{18}F-FDG PET. **B**. ^{18}F-FDG PET CMR_{glc} values averaged over the atlas labels of the cerebellum and hippocampus. **C**. ^{1}H MRS metabolite quantifications in a voxel localized in the cerebellum and in the hippocampus.

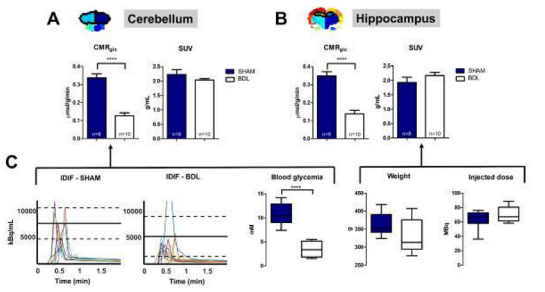

Fig. 4: Comparison between the CMR_{glc} and SUV quantification metrics in the cerebellum (**A**) and the hippocampus (**B**) with their respective normalization terms (**C**).

References

1 Cruz et al. *J Cereb Blood Flow Metab* 3, 311–320 (1983).
2 Jessy et al. *Biochem J* 277 (Pt 3), 693–696 (1991).
3 Lanz et al. *J. Nucl. Med.* 55, 1380–1388 (2014).
4 Mlynárik et al. *Magn Reson Med* 56, 965–970 (2006).
5 Sokoloff et al. *J. Neurochem.* 28, 897–916 (1977).
6 Tokugawa et al. *J. Nucl. Med.* 48, 94–99 (2007).
7 Pasantes-Morales et al. *Amino Acids* 12, 281–292 (1997).

T38.
Main rat preclinical models of glioblastoma multiforme: How to select the proper one for biomedical research based on a multiparametric MRI point of view?

C. Caro[1], N. Arias-Ramos[2], J. D. Urbano-Gámez[1], M. Á. Zúñiga-Rodríguez[1], P. Lopez-Larrubia[2], M. L. García-Martín[1,3]

[1]Instituto de Investigación Biomédica de Málaga y Plataforma en Nanomedicina (IBIMA Plataforma BIONAND), Málaga, Spain;
[2]Instituto de Investigaciones Biomédicas Alberto Sols (CSIC-UAM), Departamento de Fisiopatología Endocrina y del Sistema Nervioso, Madrid, Spain;
[3]Biomedical Research Networking Center in Bioengineering, Biomaterials & Nanomedicine (CIBER-BBN), Madrid, Spain

Introduction Glioblastoma multiforme (GBM) is the most frequent malignant brain tumor in adults[1] and also the most lethal, even after an extremely aggressive therapeutic approach[2]. Of note, great efforts have been conducted for decades to improve the treatment, with scarce success. For this reason, there is an urgent need to improve both the diagnosis and the therapeutic outcome of GBM patients. It is at this point that preclinical models, and especially orthotopic models, play an essential role. Orthotopic rat models (ORM) of GBM have been widely used in the biomedical research, being some of the most popular: Fischer rats implanted with F98 cells[3,4] and both Sprague Dawley (SD) and Wistar rats implanted with C6 cells[4,5,6]. In fact, it has been extensively described that all of them evoke genetic and physiologic human GBM features. The aim of this work was to study ORMs of GBM, generated by the orthotopic implantation of the 2 GBM cell lines in the 3 rat strains, from a multiparametric magnetic resonance imaging (MRI) point of view and, ultimately, to identify the tumor model most closely resembling human GBMs.

Methods A total of 48 male rats ($\approx$ 190 g) of 3 different strains: Wistar, Fischer, and SD, were injected orthotopically in the right caudate nucleus with 10^5 murine glioma cells, either C6 or F98, hereinafter referred to as W-C6, F-C6, SD-C6, W-F98, F-F98, SD-F98. MRI studies were carried out on a Bruker Biospec 9.4 T system equipped with 400 mT/m gradients, using an 82 mm volume resonator for excitation and a 20 mm-inner-diameter surface coil for signal detection. Tumors were followed up by T_2-weighted (T_2W) images until they showed a size of $\approx$ 1.5 cm^3, then a multiparametric (MP) MRI study was performed acquiring: T_2-maps, diffusion tensor images (DTI) and dynamic contrast enhancement (DCE) images. Gadobutrol (Gadovist®, Bayer) was used as contrast agent (CA). Parametric maps were generated by either My Map Analyzer, a homemade software built in Matlab for T_2-maps and DTI images, or DCE@ourlab[7], for DCE images. The entire analysis of parametric maps was conducted in a region of interest (ROI) placed on the tumor periphery, which was determined by active CA uptake at DCE images.

Results Around 40% of F-C6 did not develop a GBM. Regarding CA uptake, all ORMs presented a moderate homogeneity, except for W-F98 (Fig. 1). Moreover, the only group showing statistically significant differences in T_2 values (Fig. 2), DTI parameter mean diffusivity (MD) (Fig. 3) and K_{trans} parameter obtained from DCE acquisitions (Fig. 4), corresponded to W-F98. These differences were mainly observed when comparing this group with either W-C6 or SD-F98, whereas no statistically significant differences were observed with respect to the other groups. Additionally, higher K_{trans} values were observed in SD-C6 than in SD-F98 (not significant).

Discussion Based on the heterogeneity in the development of GBMs, Fischer rats injected with C6 cells and Wistar rats injected with F98 cells should be avoided as ORMs of GBM. Considering only MRI parameters, edema and vascular extravasation due to blood–brain barrier (BBB) disruption in the tumor periphery of the studied ORMs, revealed similar patterns in the 3 strains of rats injected with C6 cells, whereas heterogeneous patterns were observed among the F98-injected ones. A more prominent edema, based on T_2 and MD maps, was noticed in W-F98. In addition, this group revealed a lower BBB extravasation than F-F98 and SD-F98 rats, based on the K_{trans} maps. Finally, it is worth noting that some differences were observed comparing the same strain injected with different cells. On the one hand, W-F98 exhibited evidence of greater edema compared to W-C6. On the other hand, SD-F98 showed more BBB extravasation than SD-C6.

Conclusion As far as we know, this is the first GBM MP-MRI study, encompassing the main GBM cell lines (C6 and F98) and the 3 predominant rat strains (Fischer, SD, and Wistar). So far, our results suggested that Fischer rats injected with C6 cells and Wistar rats injected with F98 cells should be avoided as ORMs of GBM. Overall, considering only MRI parameters (mainly edema and vascularization), rats injected with C6 cells presented more homogeneity than rats injected with F98 cells. Finally, adding other variables, such as Magnetic Resonance Spectroscopy (MRS) or MP analysis of other regions, might shed some light on which model is the best option as preclinical ORM.

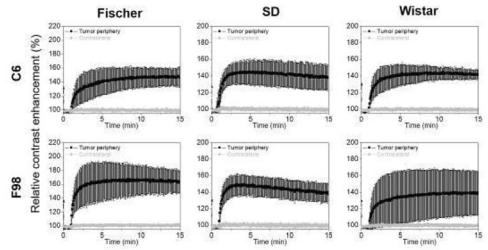

Fig. 1: Relative contrast enhancement analysis (mean ± standard deviation) of the tumor periphery and contralateral regions calculated from DCE images of the different ORMs studied.

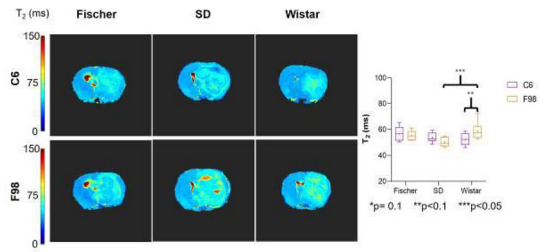

Fig. 2: T_2 maps analysis. Left: T_2 maps from a representative mouse of each ORM studied. Right: tumor periphery quantification of the different models represented by boxplots.

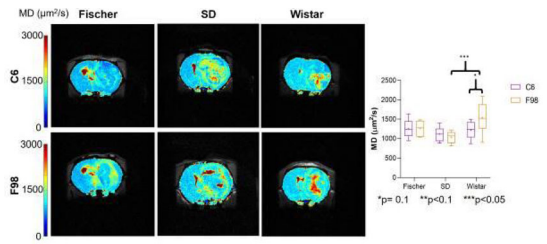

Fig. 3: MD maps analysis. Left: MD maps from a representative rat of each ORM studied obtained from DTI images. Right: tumor periphery quantification of the different models represented by boxplots.

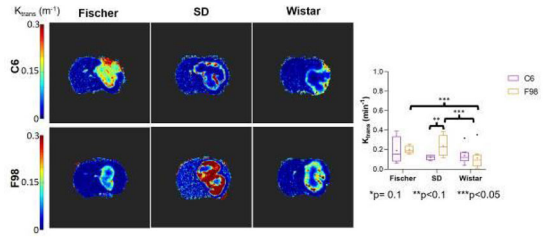

Fig. 4: K_{trans} maps analysis. Left: K_{trans} maps from a representative rat of each ORM studied obtained from DCE images. Right: tumor periphery quantification of the different models represented by boxplots.

References

1. Alifieris, et al. Pharmacol. Ther. 152, 63–82 (2015).
2. Stupp, R. et al. N. Engl. J. Med. 352, 987–96 (2005).
3. Towner RA, et al. Neuro Oncol. 2013 Mar;15(3):330–40.
4. E, Valazza A, et al. Comp Med. 2017 Mar 1;67(2):147–156.
5. Dave, N. et al. Mol. Cancer Ther. 14, 857–864 (2015).
6. Gieryng, A. et al. Sci. Rep. 7, (2017).
7. Ortuño, J. E. et al. BMC Bioinformatics 14, 316 (2013).

T39.
Low-rank reconstruction for double-half-echo ^{23}Na and undersampled ^{23}Na multi-quantum coherences MRI

C. Licht[1], J. Zapp[1], M. Bydder[2], M. Guye[2], L. Schad[1], S. Rapacchi[2]

[1]*University of Heidelberg, Computer Assisted Clinical Medicine, Mannheim, Germany;*
[2]*Aix-Marseille Université, Center for Magnetic Resonance in Biology and Medicine, Marseille, France*

Introduction Conventional sodium (^{23}Na) MRI is a promising tool to probe tissue ionic homeostasis, but often remains limited to the analysis of the sodium signal intensity. Thanks to its 3/2 spin, ^{23}Na multi-quantum coherences MRI enables disentangling the underlying multi-quantum coherences (MQC) and therefore holds potentially richer sodium tissue characterization. Especially the triple quantum (TQ) signal has shown sensitivity to the intracellular sodium compartment[1]. However, ^{23}Na MQC MRI is inherently slow since it requires 3 RF pulses that are cycled multiple times, associated with long relaxation periods. As such, ^{23}Na MQC MRI lacks conventional ^{23}Na MRI resolution.

Herein we propose two novelties: We propose a low-rank image reconstruction framework that combines 1) ^{23}Na MQC MRI with Double-Half-Echo (DHE) ^{23}Na MRI to simultaneously obtain ^{23}Na MQC MRI and a higher resolution conventional ^{23}Na image acquired during the evolution time and 2) undersampled ^{23}Na MQC MRI that can be reconstructed thanks to its multi-dimensional attribute.

Methods All measurements were performed on a 7 T MRI (Siemens Terra) with a bird-cage dual-tuned ^{23}Na/^{1}H head coil (RapidBiomedical). ^{23}Na MQC MR images were obtained by utilizing a modified CRISTINA[2] sequence (Fig. 1), with the following parameters.

Experimental phantom acquisitions FoV 225 × 225 × 210 mm^3, ^{23}Na DHE: matrix size 64 × 64 × 14, TE = 0.7 ms;
^{23}Na MQC: matrix size 40 × 40 × 14, τ = 10 ms, BW = 330 Hz/px, TE/ΔTE/NTE = 1.2/4.7 ms/10, TR = 200 ms resulting in TA = 2 × 31 min.

For brain in-vivo, two healthy volunteers, FoV 225 × 225 × 210 mm^3, ^{23}Na DHE: matrix size 68 × 68 × 14, TE = 0.7 ms;
^{23}Na MQC: matrix size 28 × 28 × 14, τ = 10 ms, BW = 330 Hz/px, TE/ΔTE/NTE = 1.1/4.2 ms/10, TR = 200 ms resulting in TA = 2 × 31 min.

Image reconstruction: ^{23}Na DHE two half k-spaces were reconstructed by utilizing a low-rank coupling constraint[3]. ^{23}Na MQC data was retrospectively undersampled by R = 3 and reconstructed utilizing the SAKE[4] framework solving the following optimization problem:

$$\min(\mathrm{u}^{f()})\|\Phi_{\mathrm{F}}(\mathrm{u}) - \mathrm{f}\|_2 \text{s.t. } \mathrm{rank}(\mathrm{A}) = k', H^*(A) = u$$

with Φ_F being the Fourier sampling operator, u being the image to reconstruct and f the actually sampled k-space data in the fidelity term. Prior rank k' is chosen to enforce low-rankness and H^* being the

inverse matrix operator to invert the Hankel-like structured matrix, A. ^{23}Na MQC's echo and phase-cycle dimensions were reshaped to enforce rank deficiency of the data matrix (Fig. 2).

Image processing Phase-cycled ^{23}Na MQC raw data were combined via Fleysher combination[5] and the MQC spectrum (SQ and TQ images) was obtained by computing the 1D Fourier transform along the phase cycle dimension.

Results Reconstruction results (Fig. 3 and Fig. 4) demonstrated reliable image quality: ^{23}Na DHE provided a high-resolution ^{23}Na image. Quantification of phantom data revealed accurate TSC (^{23}Na DHE) and TQ/SQ ratio for SAKE reconstruction. SAKE enabled to reconstruct threefold undersampled in-vivo data with SSIM = 0.95 $\pm$ 0.0, RMSE = 0.03 $\pm$ 0.002 and SSIM = 0.75 $\pm$ 0.04, RMSE = 0.09 $\pm$ 0.02 for SQ and TQ images, respectively, in the region of interest over the shown slices. However, the TQ/SQ ratio was smaller for the SAKE reconstruction.

Discussion & Conclusion Double-Half Echoes can be combined by exploiting correlations along the rows due to the low-rankness projection. Due to the signal's intrinsic redundancy, the SAKE framework is well suited to reconstruct undersampled ^{23}Na MQC data. Phase-cycling produces signal subspaces that vary in magnitude and phase, but still exhibit highly coherent patterns spanning across the multi-dimensional space. Structured low-rank matrix completion exploits the shared information efficiently and leverages them to reconstruct undersampled data. The TQ/SQ ratio was decreased in the SAKE framework due to the strong information coherence of ^{23}Na MQC MRI leading to image denoising, as observed from the background noise suppression.

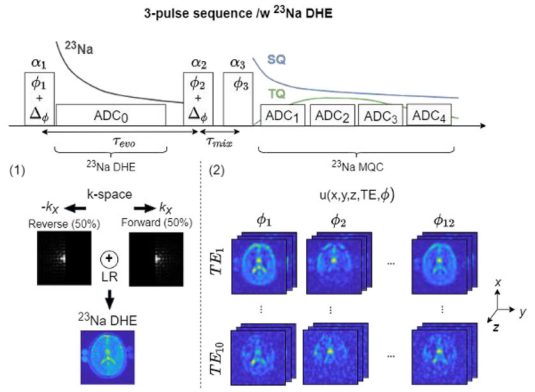

Fig. 1: The proposed algorithm to reconstruct double half echo sodium and undersampled ^{23}Na MQC images. (1) The conventional high SNR sodium image is reconstructed by combining forward and backward-sampled k-space halves with a low-rank coupling constraint. (2) undersampled ^{23}Na MQC readouts are processed by exploiting coherent information across the multi-echo and phase-cycle dimensions simultaneously by enforcing low-rankness.

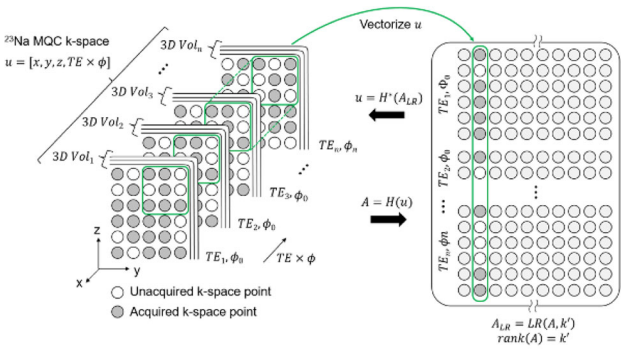

Fig. 2: Construction of data matrix to exploit coherent information and reconstruct ^{23}Na MQC data.

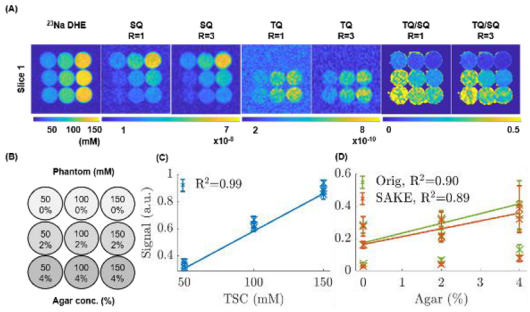

Fig. 3: (A) Reconstruction results shown for ^{23}Na DHE, original and SAKE for SQ, TQ and TQ/SQ ratio for an undersampling factor, R=3. (B) Phantom consisting of 9 vials with varying agar and sodium concentrations. (C) and (D) show the TSC (DHE) and TQ/SQ ratio (MQC) quantification results, respectively.

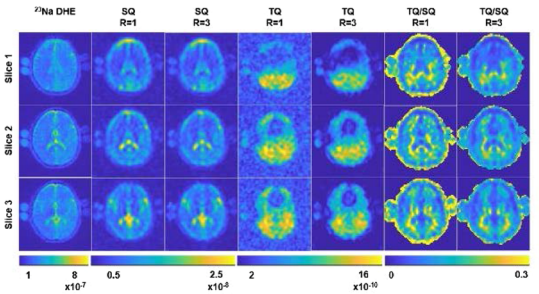

Fig. 4: In-vivo reconstruction results shown for several slices for ^{23}Na DHE, original and SAKE for SQ, TQ and TQ/SQ ratio for an undersampling factor, R=3.

References

[1]LaVerde G et al. Serial triple quantum sodium MRI during non-human primate focal brain ischemia. Magn. Reson. Med. 2007.
[2]Hoesl MAU et al. Efficient ^{23}Na triple-quantum signal imaging on clinical scanners: Cartesian imaging of single and triple-quantum ^{23}Na (CRISTINA). Magn. Reson. Med. 2020.
[3]Bydder M et al. Minimizing echo and repetition times in magnetic resonance imaging using a double half-echo k-space acquisition and low-rank reconstruction. NMR Biomed. 2021.
[4]Shin PJ et al. Calibrationless parallel imaging reconstruction based on structured low-rank matrix completion Magn. Reson. Med. 2014.
[5]Fleysher L et al. B_0 inhomogeneity-insensitive triple-quantum-filtered sodium imaging using a 12-step phase-cycling scheme NMR Biomed 2010.

Acknowledgment: This research was supported by PROCOPE mobility grant 2022 and ISMRM Research Exchange grant. Authors Lothar Schad and Stanislas Rapacchi contributed equally to this work.

T40.
Dynamic single-cell time-lapse MRI: Pushing the velocity detection limit using radial compressed sensing imaging

E. Wilken[1], A. Havlas[1], M. Masthoff[1], A. Moussavi[2], S. Boretius[2], C. Faber[1]

[1]University Münster, TRIC, Clinic of Radiology, Münster, Germany; [2]German Primate Center—Leibniz Institute for Primate Research, Functional Imaging Laboratory, Göttingen, Germany

Introduction By repetitive T2* weighted imaging, time-lapse MRI enables tracking of single iron-labeled cells non-invasively at unlimited tissue penetration. Due to temporal blurring, only slowly moving cells such as patrolling monocytes can be resolved. To study faster immune cells beyond the estimated detection limit of 1 µm/s, accelerated acquisition is needed.[1,2] We show that the detection limit can be increased using a radial MR acquisition scheme in combination with compressed sensing (CS) reconstruction. Phantom and in vivo experiments were performed.

Methods Time-lapse MRI was performed on a 9.4 T Biospec with cryogenic probe and a radial FLASH sequence with interleaved ordering scheme (TE/TR: 11/400 ms, 4 avg., 59 × 59 µm^2 in-plane res., 195 spokes, 15 slices of 300 µm, 5:12 min scan time per timeframe, 10 rep.). Images were reconstructed using all acquired spokes (fully sampled, FS) or subsets of only 39 spokes without (undersampled, US) and with CS[3], generating 5 subframes of 1 min temporal resolution. To mimic moving cells a rotating phantom system was designed and agar phantoms containing micron-sized iron particles were scanned both static and rotating with resulting particle speeds of up to 21.8 µm/s. Temporal blurring was evaluated by quantifying signal loss and void size of each particle in the rotating phantom for FS, US, and CS reconstructions, respectively. A maximum detectable speed was derived from the velocity-dependent change in signal loss. For in vivo time-lapse MRI of n = 3 mouse brains, cells were labeled in vivo by i.v. injection of Resovist 24 h before scanning. Individual cells were manually identified as hypointense spots and categorized into short-term (1–2 consecutive frames), long-term short-range (> 2 consecutive frames), and long-term long-range cells (> 2 consecutive frames with in-plane motion).

Results In phantom experiments single iron particles were resolved using radial time-lapse MRI in all three reconstruction modes (Fig. 1A). Once the phantom was rotating, temporal blurring occurred resulting in decreased signal loss and elongated shapes. Visibility of single particles was dependent on the velocity, but also on the contrast generated in the static case. In US images, motion distortion of fast-moving particles decreased compared to FS (Fig. 1), and additional fast-moving particles were recovered due to the higher temporal resolution (Fig. 1A). Although in CS reconstructed images temporal blurring was more pronounced than for US, signal voids were smaller and had higher signal loss than in FS images (Fig. 1). Moreover, for the investigated signal losses, a velocity detection limit of 2.7 to 4.8 µm/s for FS, 5.1 to 10.2 µm/s for CS and 10.4 to 17.9 µm/s for US reconstruction was derived (Fig. 2). In vivo, 42 ± 4 cells per mouse brain were detected in FS images. Out of these, 23 ± 3 were short-term, 8 ± 2 long-term short-range, and 10 ± 1 long-term long-range (Fig. 3B). The latter had a mean velocity of 0.18 ± 0.05 µm/s. In US images, streaking artifacts were too severe hindering single cell detection resulting in only 7 ± 1 detected cells. With CS, streaking artifacts were reduced allowing recovery of most low-contrast cells hidden in US (33 ± 4 counted cells). Additionally, 6 ± 1 cells were detected that were not visible in FS images (Fig. 3C).

Discussion Both, phantom and in vivo, measurements showed that single iron-labeled cells can be resolved and tracked using radial sampling in time-lapse MRI (Fig. 1A,3A). The detected hypointensities resembled those of in vitro iron-labeled monocytes and single cells in vivo assessed with Cartesian sampling[1,2]. In vivo, different motion behavior of patrolling cells was observed: Short-term cells, cells patrolling long-term within an MRI voxel (short-range), and those patrolling over several voxels in consecutive time-frames (long-range). The mean velocity of moving cells matched the velocity of patrolling monocytes as observed in previous time-lapse MRI studies[1,2] and by intravital microscopy[4]. While US reconstruction yielded the best results in phantom experiments in terms of improvement in signal loss of moving particles and velocity detection limit, the need for CS reconstruction became apparent in in vivo time-lapse MRI, where streaking artifacts were too severe in US. Owing to the higher temporal resolution of CS reconstruction, additional cells were observed that were most likely patrolling for only short time periods.

Conclusions Interleaved radial time-lapse MRI permits retrospective reconstruction of both fully sampled and accelerated images. It enables single-cell tracking at higher temporal resolution and recovery of cells hidden due to blurring at low temporal resolution. The velocity detection limit was pushed up to 18 µm/s in vitro. To capture rolling monocytes in vivo, we aim at accelerating MR acquisition further and increasing signal contrast of labeled cells.

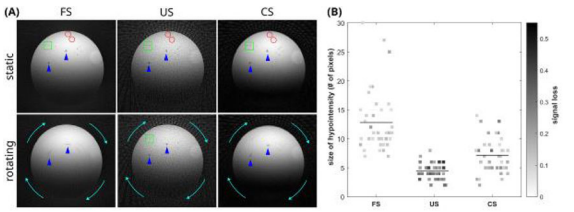

Fig. 1: A) Single particles can be resolved in phantom measurements. When rotating, particles are blurred (blue arrows) or fade (red circles). In US images, some particles are recovered (green square). B) Calculating signal loss and void size confirmed decreased temporal blurring in US and CS images.

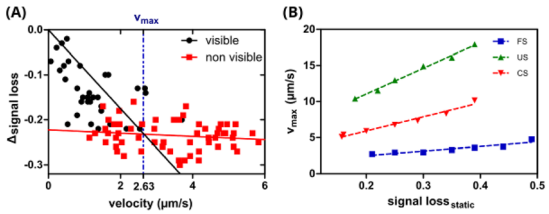

Fig. 2: A) A maximum detectable speed (blue dashed line) was derived as the intersection of linear fits of the change in signal loss between static and rotating phantom for visible and non-visible particles for a set initial signal loss (here: 20-30%, FS). B) v_{max} increases with initial signal loss.

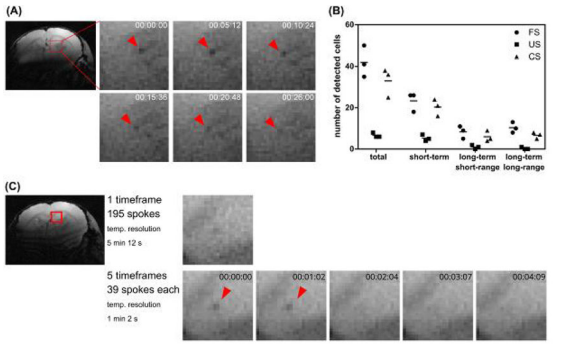

Fig. 3: *In vivo* time-lapse MRI. A) Image details (red rectangle) show a single cell (red arrows) moving across several voxels in consecutive FS time frames. B) Different patrolling behavior of detected cells was observed. C) Details (red rectangle) demonstrate a cell that is not visible in FS images (1st row), but can be seen in 2 corresponding subframes of the CS images (2nd row, red arrows).

References

[1]PMID: 29934611
[2]PMID: 34742131
[3]PMID: 24142845
[4]PMID: 17673663

T41.
Molecular MRI of MPO activity identifies ruptured human atherosclerotic plaques and predicts atherothrombosis in a preclinical model

X. Wang[1], J. Nadel[2,3,4], P. Saha[5], A. Bongers[6], S. Tumanov[2,7], N. Giannotti[8], W. Chen[2], A. Jabbour[3,4], M. Chowdhury[9], G. Lima da Cruz[10], C. Velasco[1], C. Prieto[1,11], R. Botnar[1,11,12,13], R. Stocker[2], A. Phinikaridou[1,12]

[1]*King's College London, Biomedical Engineering and Imaging Sciences, London, United Kingdom;*
[2]*Heart Research Institute, Newtown, Australia;*
[3]*St Vincent's Hospital, Sydney, Australia;*
[4]*University of New South Wales, Sydney, Australia;*
[5]*King's College London, Academic Department of Surgery, Cardiovascular Division, London, United Kingdom;*
[6]*University of New South Wales, Biological Resources Imaging Laboratory, Sydney, Australia;*
[7]*The University of Sydney, Faculty of Medicine and Health, Sydney, Australia;*
[8]*The University of Sydney, Medical Imaging Science, Sydney, Australia;*
[9]*University of Cambridge, Department of Vascular Surgery, Cambridge, United Kingdom;*
[10]*University of Michigan, Department of Radiology, Michigan, MI, United States;*
[11]*Pontificia Universidad Católica de Chile, Escuela de Ingeniería, Santiago de Chile, Chile;*
[12]*King's College London, BHF Centre of Research Excellence, London, United Kingdom;*
[13]*Pontificia Universidad Católica de Chile, Institute for Biological and Medical Engineering, Santiago de Chile, Chile*

Introduction Detecting disruption of high-risk atherosclerotic plaque with ensuing thrombosis non-invasively is crucial for reducing cardiovascular-related mortality. The intra-plaque activity of myeloperoxidase (MPO), a pro-inflammatory enzyme, is associated with unstable atherosclerosis in humans and animals [1,2], and has been detected non-invasively by molecular magnetic resonance imaging (MRI) using MPO-Gd [3]. Here, we examined the utility of MPO-Gd and molecular MRI of intraplaque MPO activity to identify ruptured human atheroma and predict atherothrombosis in a preclinical model.

Methods In the study of human samples, pre-surgical in vivo MRI was performed on a 3.0 T Siemens MAGNETOM scanner with a 2D fat suppressed quadruple inversion recovery (IR) T1 weighted (T1w) black blood (BB) sequence with Gadovist® (0.1 mmol/kg) and a 2D magnetization-prepared, rapid gradient-echo sequence for plaque characterisation. Carotid endarterectomy (CEA) specimens were subjected to ex vivo MPO-Gd enhanced MRI with a 9.4 T Bruker BioSpec system. T1 values were determined by a saturation recovery technique using a 2D Fast Spin Echo pulse sequence with multiple TRs. MPO-Gd retention was correlated to the American Heart Association (AHA) plaque grading by histology or in vivo MRI and MPO activity determined by quantifying an MPO-specific adduct, 2-chloro-ethidium (2-Cl-E +), using liquid chromatography-tandem mass spectrometry (LC–MS/MS) (Fig. 1A-B).

Molecular MRI of MPO activity was then characterized in a preclinical model of atherothrombosis. Twelve male New Zealand White rabbits were subjected to aortic endothelial denudation, cholesterol feeding, and pharmacological triggering of atherothrombosis. 8 and 12 weeks after the commencement of the cholesterol feeding, and prior to triggering atherothrombosis, plaque MPO activity was assessed with MPO-Gd (0.1 mmol/kg) MRI on a 3.0 T Philips Achieva scanner using 2D zoom T1w BB, 3D T1w IR gradient echo, and 3D Look-Locker-based IR gradient echo (T1 mapping) sequences. Contrast-free T1w BB was used to monitor developing thrombi post-trigger at 12 weeks. Based on the morphology and plaque outcome, aortic segments of each image were categorised into "lesion-free", "stable plaque" (containing plaque resistant to trigger-induced thrombosis), and "thrombosis-prone plaque" (containing plaque that developed trigger-induced thrombosis). MPO-Gd retention was compared among the three types of segments and was correlated with histology and LC–MS/MS-determined MPO activity. The capacity of MPO-Gd enhanced aortic relaxation rate (R1, s-1) to predict atherothrombosis was evaluated by receiver operating characteristic (ROC) analysis. (Fig. 1C).

Results In CEA specimens, areas of MPO-Gd retention co-localised with the expression of MPO protein as revealed by immunohistochemistry (IHC), as well as the regions of MPRAGE hyperintensity and cap disruption in ruptured plaques identified by in vivo MRI (Fig. 2A-B). MPO activity, as determined by ΔR1 values from baseline, was higher in ruptured compared with stable plaques (Fig. 2C), and higher in MRI-graded AHA type VI ruptured plaques compared with types III-V lesions (Fig. 2D). The associations were confirmed by comparing AHA grade to LC–MS/MS determined MPO activity (Fig. 2E).

In the rabbit model (representative MR images shown in Fig. 3A), IHC analysis showed that MPO was more abundant in thrombosis-prone than stable plaques, and rarely detected in the lesion-free aortic segments. Areas of high expression of MPO protein also correlated with the spatial distribution of in vivo MPO-Gd enhancement (Fig. 3B). Thrombosis-prone plaques had higher in vivo pre-trigger MRI determined by MPO-Gd retention and LC–MS/MS determined MPO activity compared with stable plaques and lesion-free aortic segments (Fig. 3C-D). MRI-derived 12-week R1 had a sensitivity of 100% and a specificity of 83.9% in predicting trigger-induced atherothrombosis (Fig. 3E).

Discussion Our results show for the first time that MPO activity is elevated in ruptured human atheroma compared with stable plaques, and higher arterial MPO activity predicts future plaque disruption in a rabbit model of triggered atherothrombosis. These results highlight the capacity of molecular imaging of MPO activity using MPO-Gd to identify culprit lesions and plaques susceptible to future atherothrombosis. As such, imaging of MPO activity using a targeted molecular probe appears to be a unique and promising strategy for translation to clinical practice for predicting adverse prognosis and guiding treatment in patients with atherosclerosis.

Conclusion MPO activity has a unique and specific role in plaque disruption. It is a potential molecular target for the detection of culprit lesions and the prediction of future atherothrombosis.

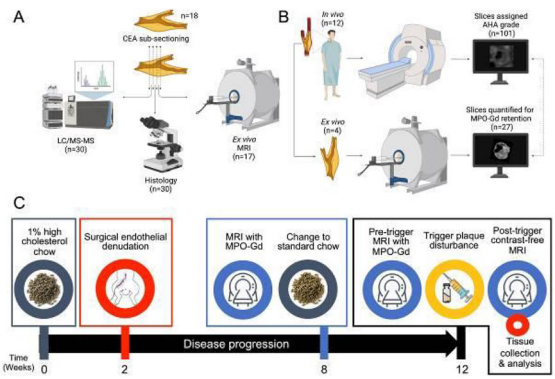

Fig. 1: Workflows for studies on **(A, B)** CEA specimens and **(C)** a rabbit model of trigger-induced atherothrombosis.

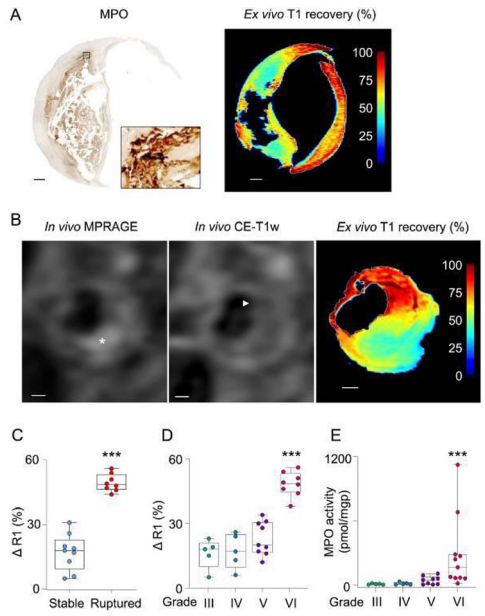

Fig. 2: Comparison between areas with low T1 recovery (%) post MPO-Gd injection and **(A)** localisation of MPO protein by IHC, **(B)** area of intraplaque haemorrhage (*) and cap rupture (arrowhead); comparison of ΔR1 (%) between plaques with different **(C)** outcomes and **(D)** AHA grading; **(E)** comparison of LC-MS/MS determined MPO activity between plaques with different AHA grading. ***p<0.001.

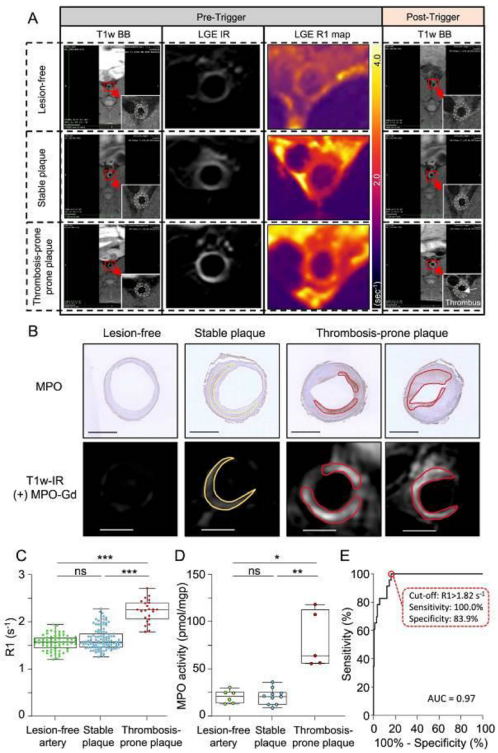

Fig. 3: Comparisons between lesion-free aortic segments, stable plaque, and thrombosis-prone plaque in rabbits. **(A)**Representative MR images, **(B)** IHC of MPO protein and co-localised *in vivo* MPO activity detected by MPO-Gd with T1w-IR sequence, **(C)** *in vivo* MPO activities determined by MPO-Gd enhanced R1, and **(D)** *ex vivo* MPO activity determined by LC-MS/MS; **(E)** ROC analysis for using R1 to predict future atherothrombosis. *p<0.05, **p<0.01, ***p<0.001.

References
1. Rashid I, et al. *Eur Heart J*. 2018;39:3301–3310.
2. Nadel J, et al. *JACC Adv*. 2023;in press.
3. Ronald JA, et al. *Circulation*. 2009;120:592–599.

T42.
A simple CEST metric robust to potential frequency sampling trajectory biases

T. Delebarre[1,2], D. Boido[1,2], L. Ciobanu[1,2]

[1]*CEA, Neurospin, Gif-sur-Yvette, France;*
[2]*Université Paris-Saclay, Gif-sur-Yvette, France*

Introduction The most common CEST quantification measures based on magnetization transfer asymmetry (MTR_{asym}) are often inaccurate due to the presence of asymmetric Magnetization Transfer (MT) and relayed Nuclear Overhauser Effects (rNOE). Other methods, such as Lorentzian multiple fits[1] or the use of a Bloch McConnell model[2] exist but require many a priori information, making them difficult to implement. Moreover, the sampling strategy of the saturation frequencies[3] can introduce additional Z-spectra asymmetries when using steady-state[4] acquisition strategies. Here, we propose a metric based on the difference between the experimental Z-spectrum and a modified Voigt Profile fit (modVP), accounting for the direct water saturation and magnetization transfer asymmetry and also correcting for asymmetries introduced by steady-state effects.

Methods One can estimate the CEST effect by fitting the direct water saturation and magnetization transfer with a Voigt function and subtracting the fit from the experimental Z-spectrum[5]. To correct Z-spectra asymmetries due to frequency sampling order, we propose to modify the Voigt profile used for the fit by introducing a parameter β, between 0 and 1, accounting for the interdependence between consecutive measurements (β = 1 corresponds to independent measurements). The relationship between the measurement at ω_n frequency, $S(\omega_n)$, and the previous one at ω_{n-1}, $S(\omega_{n-1})$, is expressed as follows:

$$S(\omega_n) = V(\omega_n)\,(\beta + (1-\beta)\cdot S(\omega_{n-1})) \quad (2)$$

where V is the Voigt function, a combination of a Lorentzian function to model water direct saturation and a Gaussian function accounting for the MT.

For the n^{th} saturation offset, Eq. [1] could be written as:

$$S(\omega_n) = \sum_{k=0}^{n-1} \beta\cdot(1-\beta)^k \prod_{i=0}^{k} V(\omega_{n-i}) \quad (3)$$

The error introduced by limiting the sum to the last *N* saturated offsets is in the order of $(1-\beta)^N$.

Using this model, we fit our Z-spectrum data, S_{exp}. The residuals, calculated as $S_{fit}(\omega_n) - S_{exp}(\omega_n)$, gives the CEST contrast corresponding to saturation offset ω_n.

Simulations: Z-spectra of a glutamate phantom at 17.2 T were simulated using a Bloch McConnell equations solver. The CEST saturation consisted of 10 Gaussian pulses (100 ms, 6μT) followed by a 1.5 s relaxation. The water peak of the resulting Z-spectrum was fitted using Eq. 2 over [− 40, − 5, − 0.75, − 0.5, − 0.25, 0, 0.25, 0.5, 0.75, 5, 40] ppm offsets. The residuals were calculated across the entire spectrum. We simulated two directions of saturation, from 40 to − 40 ppm and the opposite, labeled "+ → −" and "− → +" respectively (Fig. 1).

CEST acquisitions: CEST data were acquired at 17.2 T on a mouse using a multi-slice CEST-RARE (TR/TE = 4000/5, RARE factor = 4, 7 slices, in-plane resolution 175 × 175μm^2, slice

thickness = 500 μm). The CEST saturation module consisted of 5 Gaussian pulses (100 ms, 6μT). The sampled saturation frequencies were: − 40 − 5 − 3.5 − 3.2 − 3 − 2.8 − 2.5 − 2 − 1.5 − 1 − 0.5 0 0.5 1 1.5 2 2.5 2.8 3 3.2 3.5 5 40.

Data analysis: Experimental data were corrected using a WASSR[6] acquisition (TR/TE = 2400/5, RARE factor = 4, saturation of 3 Gaussian pulses of 100 ms/0.3 μT). CEST MTRasym maps were computed using: $MTR_{asym}(\omega) = (S(-\omega) - S(\omega))/S(-40\ ppm)$.

Results *Simulations:* Fig. 1 shows the frequency sampling directions employed and their influence on the calculated MTR_{asym}. The comparison with the ideal spectrum indicates that the sampling trajectory choice causes up to 2% error in gluCEST contrast estimation (half the true CEST effect), emphasizing the need for alternative metrics.

Fig. 2 shows the residuals obtained after fitting with a standard (2A, β = 1) and a modified Voigt function (2B). The MTR_{asym} gives the worst estimation of CEST effects, while the proposed solution produces the best results and it is the least influenced by the sampling strategy, with an error lower than 0.5% (Fig. 3).

In vivo results are shown in Fig. 4. For both MTR_{asym} and modVP, hippocampi are evident on gluCEST maps. As predicted by the simulations, the MTR_{asym} overestimates the glutamate contrast when sampling the saturation frequencies from − to + . Moreover, the MTR_{asym} maps are noisier compared to the ModVP maps (1.5 times higher standard deviation, see Fig. 4). This is most likely due to the way in which the two maps are computed.

Discussion and Conclusion The proposed modified Voigt fitting algorithm, which considers the interdependence of successive CEST measurements, allows a more accurate estimation of the CEST effect compared to the commonly used MTR_{asym} or the classical Voigt function fit. We show in silico and preliminary in vivo results for glutamate CEST. Additional in vivo experiments are necessary to validate the approach for other CEST contributions.

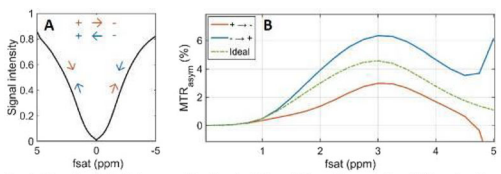

Fig. 1: Sampling trajectories, used for the simulations (A), and the resulting MTR_{asym} together with the ideal case (B).

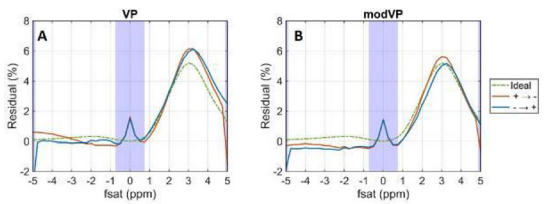

Fig. 2: Residuals obtained for the two sampling strategies presented in Fig.1 when fitting with a Voigt function (A, β=1) and a modified Voigt function (B). The areas colored in blue correspond to the points on which the water saturation was fit.

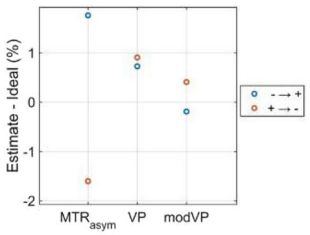

Fig. 3: Measurement errors for the glutamate CEST contribution corresponding to the different sampling strategies.

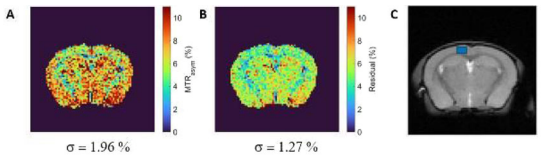

Fig. 4: Glutamate-weighted CEST maps obtained using MTR_{asym} (A) or the modVP (B). Standard deviations for the blue ROI in C are given under each map.

References

1 Schüre J-R, et al. NMR Biomed. 2021.
2 Cai K, et al. NMR Biomed. 2014.
3 Zhou J, et al. Magn. Reson. Med. 2004.
4 Sun PZ. Magn. Reson. Med. 2021.
5 Zhang L, et al. MRI. Quant. Imaging. Med. Surg. 2019.
6 Kim M, et al. Magn. Reson. Med. 2009.

LT43.
Towards a cryogen-free SQUID-MRI at ultra-low field

I. Saniour[1], E. Grimaldi[1], S. Varotto[1], Y. Belkhodja[1], R. Couvreur[1], M. Fiorito[1], D. Labat[1]

[1]*Chipiron, Paris, France*

Introduction Over the past decade, a new approach has emerged in the field of MRI, which involves the use of ultra-low field (ULF < 10 mT) scanners, diverging from the conventional trend of utilizing higher magnetic fields as the cutting-edge technology. Besides the cost-effectiveness and portability of ULF MRI, operating at these low magnetic fields has shown improvements in T1 contrast in some tissues[1,2], leading to more efficient diagnostics of various medical conditions, including cancer. The main challenge of ULF MRI lies in a detected signal typically orders of magnitude lower compared to clinical-field MRI, which impacts the signal-to-noise ratio (SNR) in the images. Several methods[3,4] are being explored to address this limitation and improve the sensitivity of ULF MRI. The inherent challenge of poor sensitivity in ULF MRI can be mitigated by choosing a superconducting quantum interference device (SQUID) for signal detection. Various groups[2,5] used SQUIDs at 4.2 K employing liquid Helium (LHe) cooled cryostats. The use of cryogenic liquid is detrimental to achieving portable and low-cost MRI systems. Here we propose our first implementation of a cryogen-free SQUID detector inductively coupled to a customized volume MRI RF coil operating at room temperature. We further present our first free induction decay (FID) signal acquired using a fully custom-made ULF MRI scanner at 1 mT, which relies on a conventional inductive reception.

Methods *SQUID sensor* A μm-sized low critical temperature Niobium-based SQUID is coupled to a larger flux transformer in a current-sensing configuration. This transformer comprises a 300 K RF pickup coil and a 4.2 K superconducting input coil positioned in

close proximity to the SQUID in a *washer design*. Fig. 1a illustrates the cryogen-free cryostat, which relies on a pulse tube cryocooler and is used to house the SQUID at a temperature of 4.2 K. The magnetic flux seen by the SQUID is directly proportional to the one passing through the second-order volume gradiometer used as RF pickup coil (Fig. 1b).

MRI hardware and sequence parameters

A Merrit coil electromagnet fed by a current source generates a polarization field (B_0) of 1 mT (Fig. 2). The RF field transmission is performed using an 80 mm-diameter saddle coil with 5 turns, while the RF reception is achieved using a solenoid-based volume gradiometer. Both RF coils are tuned to 42.5 kHz and matched to 50Ohm. The received signal is amplified using a low-noise preamplifier (FEMTO). 0.5L of tap water, contained in a bottle, is used as a phantom. A FID signal is obtained after performing a sequence with FA = 90°, TR = 2 s, TE = 52.5 ms, sampling rate = 10 kHz, with an acquisition window of 100 ms and 500 averages (Tacq = 20 min).

Results *Signal detection with a SQUID sensor coupled to a gradiometer at 300 K.*

In order to estimate the far noise filtering of our detection system, we measure the signal detected by the SQUID sensor when emitted by a dipole-like magnetic field coil as function of the distance between the RF source and the gradiometer isocenter (Fig. 3a). SNR is calculated from the experimental data (Fig. 3b), confirming a linear increase with distance, which translates to effective filtering of far-field noise.

Measurement of the FID at 1 mT

Fig. 4a exhibits the averaged demodulated spectrum of the signal received by a similar volume gradiometer RF coil (without the SQUID) in the MR experiment. The peak in the signal is observed at the expected proton Larmor frequency at 1 mT. The FID's amplitude evolves periodically with the driven flip angle, showing a maximum for 90° and a minimum for 180° (Fig. 4b).

Discussion We demonstrated hat the SQUID sensor combined with the room temperature volume gradiometer can effectively detect the signal generated by an RF source and efficiently reject far-field noise, thus significantly improving the detected SNR. In addition, we detected an FID signal using our custom-made ULF MRI, through a volume gradiometer and a low noise preamplifier. With an equivalent current noise of 500pA/$\sqrt{}$Hz, the noise introduced by the preamplifier is expected to be three orders of magnitude greater than the SQUID's equivalent current noise. Therefore, we anticipate a significantly higher detected SNR when the SQUID is connected to the MRI.

Conclusion ULF MRI is an emerging and promising technology that has yet to be fully explored. Based on our experimental results, an approximately 1000 times higher SNR is expected when replacing classical inductive detection with SQUID-based detection. The integration of the SQUID technology into our ULF scanner promises to dramatically improve signal sensitivity, hence envisioning clinical employment of MRI at such field regime.

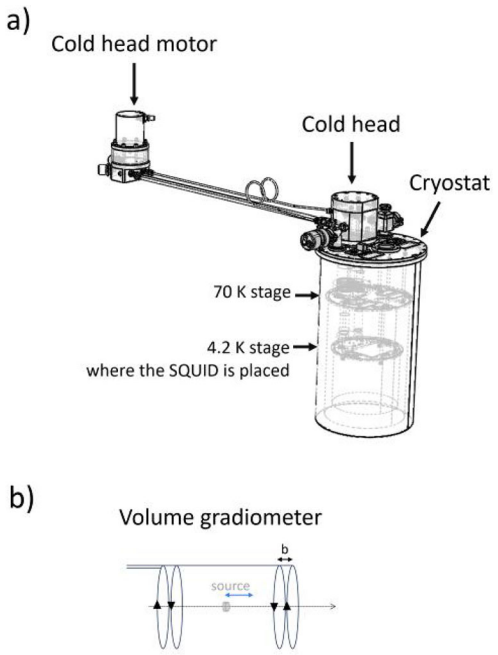

Fig. 1: Schematics of a) the cryostat structure and b) geometry of the second-order volume gradiometer.

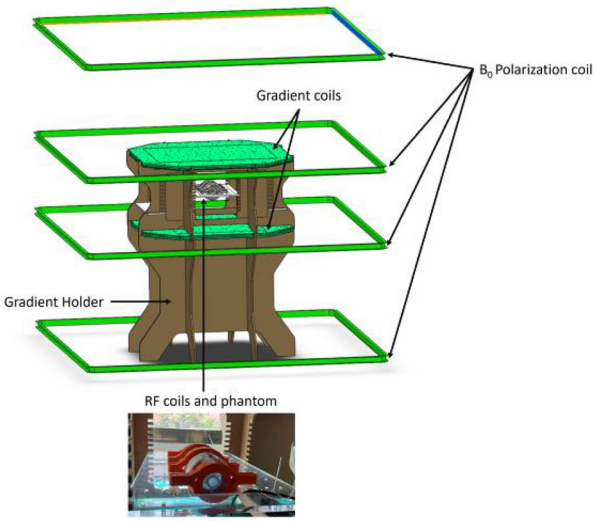

Fig. 2: Schematic of the main part of our ULF MRI machine.

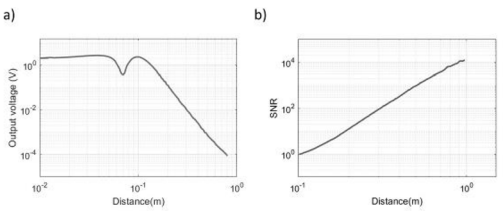

Fig. 3: Graphs of a) the signal detected by the SQUID sensor and the SNR(= $V_{SQUID}(d_{source})/V_{SQUID}(d_{noise})$) as a function of the distance between the RF source and the gradiometer isocenter.

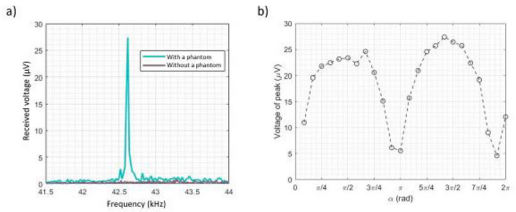

Fig. 4: a) The plot of the FID signal detected using a volume gradiometer pick up coil in a conventional inductive reception, with and without a phantom. b) The magnitude of the peak as a function of the flip angle.

References

1. Busch S. et al. MRM, 67:1138–1145, 2012
2. Clarke J. et al., Annu. Rev. Biomed. Eng., 9:389–412, 2007
3. Zotev VS et al., JMR, 207:78–88, 2010
4. Liu Y. et al., Nature Communications, 12, 7238, 2021
5. Seton, HC et al., Cryogenics, 45:348–355

LT44.
Portable MRI for major sporting events—A case study on the MotoGP world championship

T. Guallart Naval[1,2], J. M. Algarín[1], R. Bosch[1], F. Lloris[3], E. Pallás[1], J. P. Rigla[2], P. Martínez[3], J. Borreguero[2], J. M. Benlloch[1], F. Galve[1], J. Alonso[1]

[1]*MRILab, Institute for Molecular Instrumentation and Imaging (i3M), Spanish National Research Council (CSIC) and Universitat Politècnica de València, Valencia, Spain;*
[2]*Tesoro Imaging S.L., Valencia, Spain;*
[3]*PhysioMRI Tech S.L., Valencia, Spain*

Introduction Low-field MRI scanners can be designed to be low cost and small footprint, since the main evolution field *B0* can be generated by permanent or resistive, rather than superconducting, magnets [1]. Yokeless magnets furthermore allow for lightweight and portable designs [2]. The scope of applications enabled by truly portable MRI technologies is immense [3,4] and largely unexplored. We recently demonstrated the capabilities of a new low-field extremity scanner, designed to be extremely portable and which was used indoors, outdoors and for the first time at a patient's residence [4,5].

Here, we study the potential MR value of this system for use in major sporting events, specifically in the Motorcycle Grand Prix held in the Ricardo Tormo Racing Circuit in Valencia (Spain) between November 3rd and 6th, 2022 [6].

Methods The portable scanner (Fig. 1) is based on a Halbach magnet made with a discrete array of around 5,000 NdFeO magnets, generating a B0 of around 72 mT homogeneous down to 3,000 ppm over a spherical field of view of 20 cm and 75 ppm for 10 cm. The complete system weighs < 250 kg and runs from a standard wall power outlet. The system was transported in a small truck, installed in the main surgery room of the circuit medical facilities, and operational around 30 min after arrival. Overall, 15 subjects were scanned in four days; some of them previously diagnosed, some not and some healthy. We acquired T1-weighted 3D-RARE and 3D-STIR images of the subjects' wrists (1 injured, 4 healthy), knees (6 injured, 4 healthy) and ankles (3 injured, 3 healthy), for a total of 21 acquisitions. All subjects were adults and provided written informed consent for this study (CEIm-F-PE-01-16, 2022-187-1).

Results *Wrist scans.* A subject who had suffered an accident two weeks before the race reported pain in their right wrist. Following the established protocols, they were subject to an X-ray radiograph (Fig. 2c), which revealed no lesion. They were then scanned in our low-field system, where a 3D T1-weighted RARE acquisition also showed no anomaly (Fig. 2a), but the STIR scan featured a bright volume between the scaphoid, trapezium and trapezoid bones (Fig. 2b), indicating a possible traumatic arthritis as judged by the traumatologist in charge at the medical center. For comparison, we scanned the right wrists of four healthy volunteers. None of them showed a bright region between the wrist bones (Fig. 2d).

Knee scans. The circuit medical staff was able to identify a femoral shaft osteotomy in one knee (Fig. 3a), the results of an intervention on anterior cruciate ligament and the femoral insertion of the posterior (Fig. 3b) and fluid build-up due to joint effusion in two volunteers reporting pain (Fig. 3c, f). The images in Fig. 3d and e correspond to volunteers previously diagnosed with a meniscus fracture and a Baker cyst, respectively; but not visible in our low-field system with the employed protocol. The healthy knees scanned showed no anomalies (Fig. 3 g, h).

Ankle scans. The first volunteer suffered Hanglund's deformities and intra-tendineal calcification of the Achilles tendon. Both are evident in the X-ray radiograph (right), and visible in the low field MRI scan in Fig. 4a and b. The ankle in Fig. 4c suffered a bone fracture and was fixed with metallic screws and plates, which appear free of artifacts in the low-field reconstructions.

Discussion/Conclusion Our results demonstrate that LF-MRI scans can provide valuable information in the diagnosis and monitoring of injuries in sporting events. Some pathologies may still require an improved scanner performance to be detected. For example, we were able to detect traumatic arthritis in the wrist that would have otherwise gone unnoticed by the MotoGP medical staff, but we were not able to visualize meniscus tears, which need high-resolution images, or a Baker cyst, which may require T2-weighted images in the protocol.

Ultimately, we have operated in a scenario where high-field MRI is unlikely to play a role but where a low-field system can lead to improved medical attention. Arguably, this can be extrapolated to numerous other environments and diverse circumstances.

Acknowledgements This work was supported by the Ministerio de Ciencia e Innovación of Spain (PID2019-111436RBC21), the European Union (IDIFEDER/2021/004), Generalitat Valenciana (CIPROM/2021/003) and Agència Valenciana de la Innovació (INNVA1/2022/4).

Fig. 1: (a) Portable low-field extremity scanner in the circuit. (b) Scan of a professional racer in the circuit medical facilities.

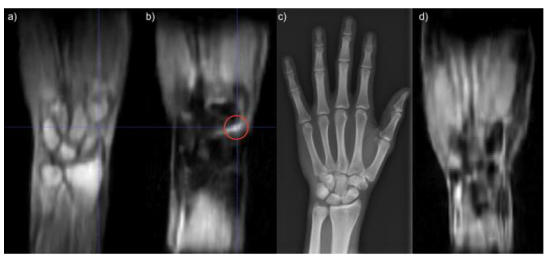

Fig. 2: (a) 3D-RARE scan of a subject's right wrist. No lesion is visible. (b) 3D-STIR scan of the same wrist. The circled bright region indicates inflammation near the scaphoid, possibly a traumatic arthritis. (c) The lesion is invisible in the X-ray image. (d) 3D-STIR scan on a healthy subject, revealing no lesion.

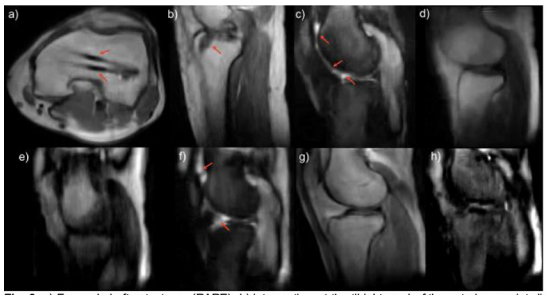

Fig. 3: a) Femoral shaft osteotomy (RARE), b) intervention at the tibial tunnel of the anterior cruciate ligament and the femoral insertion of the posterior (RARE), c) fluid build-up (STIR), d) meniscus fracture (not visible, RARE), e) Baker cyst (not visible, STIR), f) fluid build up (STIR), g) healthy (RARE), h) healthy (STIR).

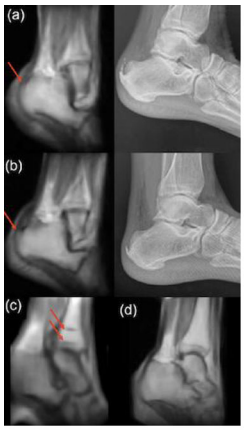

Fig. 4: Low-field MR image (left) and X-ray radiograph (right) of a right (a) and left (b) ankle with Haglund's syndrome. c) MRI scan of an operated ankle, with screws and plates. d) MRI scan of a healthy ankle.

References

[1] J.P. Marques et al. JMRI (2019). https://doi.org/10.1002/jmri.26637.

[2] T. O'Reilly et al. MRM (2020). https://doi.org/10.1002/mrm.28396.

[3] Sheth, K.N., et al. JAMA Neurol. (2020). https://doi.org/10.1001/jamaneurol.2020.3263.

[4] T. Guallart-Naval, J. M. Algarín, et al. Sci. Rep. (2022). https://doi.org/10.1038/s41598-022-17472-w.

[5] T. Guallart-Naval et al. NMR Biomed. (2022). https://doi.org/10.1002/nbm.4825.

[6] J. M. Algarín, T. Guallart-Naval, et al. (2023). arXiv:2303.09264.

LT45.
Hybrid RF coils—High permittivity resonant blocks and circular coil elements for improved transmit efficiency at 7 T MRI

D. Wenz[1,2], J. Vliem[3], Y. Xiao[1,2], L. Xin[1,2], I. Zivkovic[3]

[1]École Polytechnique Fédérale de Lausanne (EPFL), CIBM Center For Biomedical Imaging, Lausanne, Switzerland;
[2]École Polytechnique Fédérale de Lausanne (EPFL), Animal Imaging and Technology, Lausanne, Switzerland;
[3]Eindhoven University of Technology, Electrical Engineering Department, Eindhoven, The Netherlands

Introduction High-permittivity materials (HPMs) were employed in numerous studies to enhance transmit efficiency and receive sensitivity in MRI[1]. They are usually used either as active (e.g. dielectric resonator antenna DRA[2,3]) or passive (e.g. dielectric pads) components[4]. There seems to be another way to effectively use HPMs which can be considered a hybrid approach, i.e. placing HPMs in the center of a conventional active element, e.g. a loop coil. This was investigated by Ruytenberg et al. at 3T[5]—a HPM (with resonance frequency for given transverse electric mode being close to the Larmor frequency) was placed in the center of a receive-only coil and a whole-body coil was used for radio frequency (RF) transmission. We hypothesize that transmit efficiency gains might be even higher when a local RF coil is used for RF transmission instead of a large volume coil. Here we studied this approach using a HPM with higher dielectric constant (ε_r = 1070) tailored for MRI at 7 T for different types of local transmit/receive RF coils: conventional loop coil, shielded-coaxial-cable (SCC)[6] coil and a novel design called a "twisted-pair" coil.

Methods Each one of the three RF coils (Fig. 1b) were fabricated for a diameter of 110 mm and tuned and matched to 297.2 MHz using fixed capacitors (AVX 800E Series, USA) and variable capacitors (Johanson 5621, USA). The conventional loop coil was made of copper wire (diameter = 1 mm), the SCC was made with RG58 coaxial cable (RG58 LSZH, Multicomp PRO) and the twisted pair was made by twisting two 18-gauge isolated wires (diameter = 1 mm). The term "hybrid coil" refers to a combination of a given loop coil with a dielectric block placed in the center of the loop. The dimensions of the dielectric block were: 90 × 44 × 5 mm, dielectric constant (ε_r) was 1070 and electrical conductivity (σ) was 0.02 S/m.

Electromagnetic simulations were performed in CST Microwave Studio 2023 (Dassault Systèmes, Vélizy-Villacoublay, France). RF coil elements were placed 20 mm away from a homogeneous cubic phantom (Fig. 1d) and the frequency domain solver with tetrahedral meshing was used. The dielectric block was positioned in the center of each loop coil. To evaluate transmit (B_1^+) and SAR efficiencies, the results were normalized to 1W accepted power. For a comparison with the measurements, additional simulations were performed for a spherical phantom (Fig. 1d) with the coils and the block placed 5 mm away from the top of the phantom. Eigenmode simulations were performed for a dielectric block with the same dimensions as used in the experiments, and ε_r was set as a variable (100–2000).

Phantom experiments were performed on a 7 T MR human scanner (Magnetom, Siemens Healthineers, Erlangen, Germany). The three-dimensional B_1^+ map was acquired using SA2RAGE sequence (TR/TE = 2400/0.78 ms, TI1/TI2 = 45/1800 ms, $\alpha1/\alpha2$ = 4/10°, FOV = 208 × 256 mm^2, slices = 64, resolution = 2.0 × 2.0 × 2.5 mm, BW = 1220 Hz/px, scan time = 115 s).

Results When the dielectric block did not resonate close to the Larmor frequency (297.2 MHz), there was no significant effect on the B_1^+ distribution produced by a hybrid coil (with the conventional loop) up to ε_r of 800 (Fig. 2). Hybrid RF coils provided significantly higher B_1^+ efficiency up to the depth ≤ 5 cm vs. the RF coils without the dielectric block. At the depth ≥ 5 cm, the hybrid coils performed similarly as their counterparts without the dielectric blocks. In the periphery, it was found that B_1^+ efficiency was threefold higher vs. the RF coils without the dielectric block. When looking at the peak local SAR_{10g} (Fig. 3c), an average increase of 50% for the hybrid coils was observed, leading to a reduced SAR efficiency at the depth ≥ 2.5 cm. Preliminary phantom experiments showed a relatively good agreement between the simulations and the measurements (Fig. 4).

Discussion This work demonstrates that "hybrid coils" designed as combinations of different types of loop coils with a dielectric block (with its intrinsic resonance frequency close to the Larmor frequency), can provide a significant transmit efficiency increase vs. their counterparts without any dielectric block. This effect was not only present in the periphery (threefold gain), but even up to the depth ≤ 5 cm

which is substantially greater than reported earlier[5]. The data indicate that the intrinsic resonance frequency of the dielectric block should be close to the Larmor frequency to observe this effect.

Conclusion Hybrid coils designed as combinations of transmit/receive loops and dielectric resonators can provide significant transmit efficiency gains in MRI at 7 T.

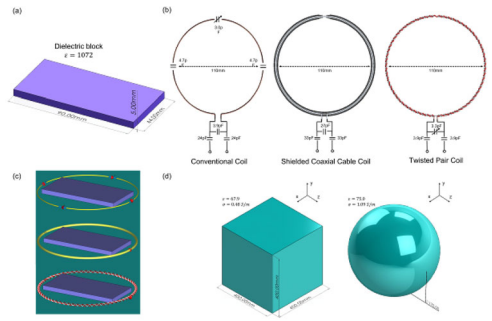

Fig.1:(a) Rectangular dielectric block (ε_r =1070). (b) Three different loop coils - conventional, shielded coaxial cable (SCC) and "twisted pair" coil. (c) "Hybrid coil", loop coil with dielectric block in the middle. (d) Phantom models (cubic & spherical).

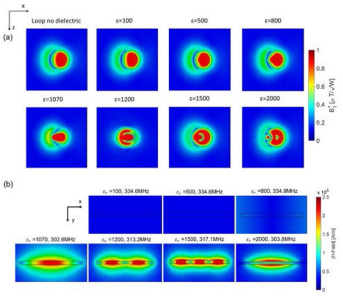

Fig.2:(a) Simulated B_1^+ maps of hybrid coil (conventional loop+dielectric block in the middle) for different ε_r. (b) Magnetic field distribution inside the block obtained from eigenmode simulations (no effect if block's resonance is too far from Lamor frequency).

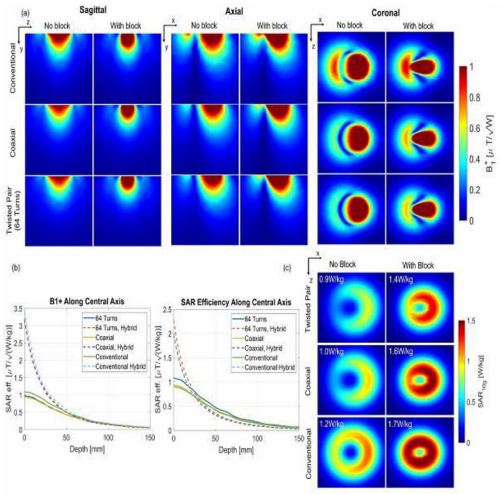

Fig.3:(a) Simulations on cubic phantom for three types of Tx/Rx elements: conventional loop, shielded coaxial cable and "twisted pair" coil; with and without the dielectric resonator placed in the middle. (b) B_1^+ and SAR efficiency along the central profile as a function of depth. (c) Local SAR_{10g} distribution for each configuration.

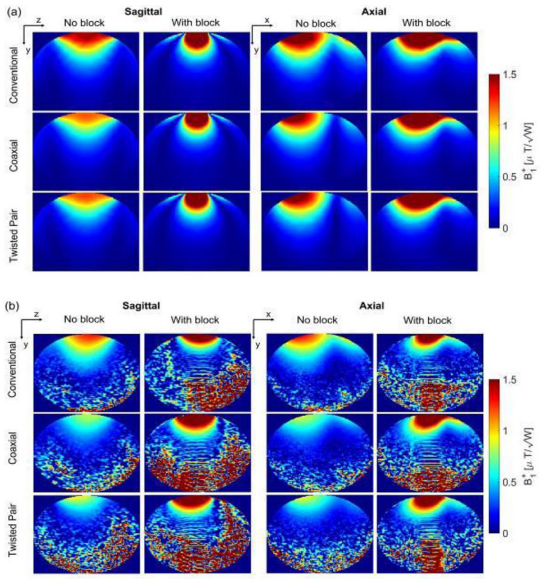

Fig.4:(a) Simulated B_1^+ distribution in a spherical phantom for the three hybrid coils, and their corresponding (b) experimental B_1^+ maps.

References

1. Webb AG, et al., MAGMA (2022) Dec;35(6):875–894.
2. O'Reilly TPA, Ruytenberg T, Webb AG. Magn Reson Med. (2018) Mar;79(3):1781–1788.
3. Wenz D and Dardano T, MAGMA (2023) Apr;36(2):227–243.
4. Teeuwisse WM, et al. Magn Reson Med, (2012) May;67(5):1285–93.
5. Ruytenberg T, O'Reilly TP, Webb AG. J Magn Reson. (2020) Feb;311:106681.
6. Ruytenberg T, Webb A, Zivkovic I. Magn Reson Med. 2020; 83(3): 1135-1146.

LT46.
Uncompromised safe imaging of patients with deep brain electrodes at 3 Tesla with multi-row parallel transmit coil arrays: Electromagnetic simulation study.

N. Karadeniz[1], J. Hajnal[1,2], Ö. Ipek[1]

[1]*King's College London, Biomedical Engineering, London, United Kingdom;*
[2]*King's College London, Centre for the Developing Brain, London, United Kingdom*

Introduction Multi-row parallel-transmit(pTx) coil arrays show better control of excessive tissue heating for patients with Deep Brain Stimulation(DBS) devices [1] and increase transmit efficiency and homogeneity at 3 T [2]. We investigate the performance of pTx coil arrays with varying row numbers on a full-body human model Duke augmented by a realistic DBS lead and electrode design. The aim is to acheive homogeneous transmit(B_1^+) fields and minimising local specific absorption rate(SAR) around DBS device, compared to the conventional head birdcage coil at 3 T.

Method Four different pTx head coil configurations at 3 T were designed: a circularly-polarised birdcage coil (low pass,16 legs) (Fig. 1.a), 16-channel single-row (1 × 16) (Fig. 1.b), 16-channel double-row (2 × 8) (Fig. 1.c), and 24-channel triple-row (3 × 8) loop coils (Fig. 1.d) each with a diameter 360 mm and height 250 mm, placed head-centred on the Duke human model [3] within the MR

bore. DBS lead trajectories were derived from intra-operative CT images of patients. The lead is formed by a conductive wire (diameter:1 mm) insulated by a 1 mm thick layer. A realistic bilateral DBS electrode model (Medtronic-3387) was created with four pad electrodes (diameter:1.5 mm, length:1.5 mm) placed 1.5 mm apart at the lead's distal end (Fig. i-l). Multiport simulations ($\sim$ 180Mcells) with harmonic excitation at 123 MHz were performed with Sim4Life 7.1 (ZMT, Switzerland) using an Axware-GPU solver on an NVIDIA RTX A5000 card, achieving steady-state conditions of $-$ 25 dB. The resulting multiport impedance data was exported to co-simulation software (Optenni Ltd, Finland). Individual B_1^+ fields and electric fields were extracted on a head and chest sensor volume (201 $\times$ 251 $\times$ 401 mm), resampled to a 1 mm isotropic image grid, and exported to Matlab (MatWorks, Inc.). Q-matrices were derived from simulated E-fields and 1-g tissue mass-average to evaluate $SAR_{1gr,avg}$ [4]. A set of Virtual Observation Points (VOP) was generated from these Q-matrices [5]. RF shimming was performed using Magnitude Least Square (MLS) optimisation [6] regularised by local SAR to achieve a uniform target field of 1 μT over the whole brain. Coil performance with and without DBS devices was assessed after RF shimming by constructing histograms of B_1^+, examining maximum intensity projections of B_1^+ and local SAR, and estimating SAR efficiency($B_1^+/\sqrt{SAR_{max,1\ g\ avg}}$).

Results For tuned coils, maximum reflection coefficients were: $-$ 10 dB (birdcage), $-$ 10 dB (single-row), $-$ 15 dB (double-row), and $-$ 16 dB (triple-row). Maximum coupling coefficients: $-$ 18 dB (birdcage) $-$ 8 to $-$ 5 dB (pTx coils) (Fig. 1e-h).

Without DBS devices, double-row and triple-row coils showed the most homogeneous B_1^+ (Fig. 2c, d) and lowest COVs (5.5%, 5.1%). With DBS devices, the trend persisted (Fig. 2.e–h).

In Fig. 3, it is illustrated that without DBS devices, double-row coil had 1W/kg $SAR_{max,1\ g\ avg}$, $\sim$ 15% lower than triple-row, 44% lower than single-row, and 33% lower than birdcage. With DBS devices, triple-row coil had 2.2W/kg $SAR_{max,1\ g\ avg}$, $\sim$ 8% lower than double-row, 15% lower than single-row, and $\sim$ 4 times lower than birdcage(8.4W/kg).

SAR efficiency was highest for double-row coil ($1\mu T/\sqrt{(W/kg)}$) (Fig. 4c) without DBS devices, 11% more efficient than triple-row, 25% more than single-row, and 37% more than birdcage. With DBS devices, triple-row coil had the highest SAR efficiency (Fig. 4 h), 5% higher than double-row, 12% higher than single-row, and $\sim$ 2 times higher than birdcage.

Discussion This study examines the performance of PTx coils with different row numbers on the Duke human model with a realistic DBS lead, targeting homogeneous B_1^+ fields and minimised local SAR at 3 T compared to conventional head birdcage coil. The investigation highlights that PTx provides a substantially enhanced capability for MRI with DBS electrodes, as multi-row coils yield only a 50% SAR increase while generating B_1^+ field nearly twice as homogeneous as compared to a birdcage coil without DBS. Moreover, by optimising multi-row coil"s B_1^+ homogeneity to match the birdcage coil without DBS, further SAR reduction can be attainable.

Conclusion PTx coils with multiple rows can achieve more homogeneous B_1^+ and lower SAR around DBS electrodes at 3 T compared to single-row and birdcage coils. These findings have implications for improving the safety and efficacy of MRI in patients with DBS devices, ultimately enhancing the diagnostic value of imaging in this growing patient population. There was little difference in performance between the 2 and 3-row coils. This favors the simpler, lower channel count design for practical implementation, although the complexity of the triple-row coil might have resulted in a less optimized design.

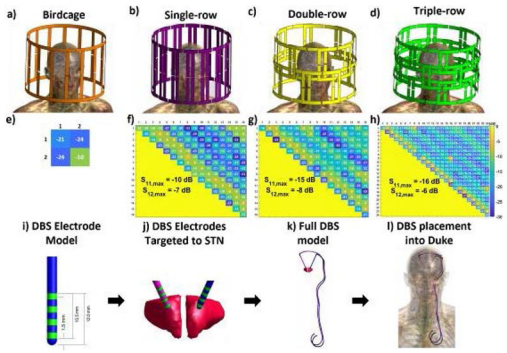

Fig.1: RF Coil Designs: a)birdcage b)single-row c)double-row d)triple-row coil arrays for human head MR, Scattering matrices c)birdcage d)single-row g)double-row e)triple-row i-l)Bilateral DBS model construction.

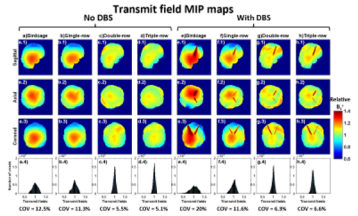

Fig 2: B_1^+ maximum intensity projection(MIP) images: No DBS for birdcage(a.1-3), single-row(b.1-3), double-row(c.1-3), triple-row(d.1-3)coils, With DBS for birdcage(e.1-3), single-row(f.1-3), double-row(g.1-3), triple-row(h.1-3)coils, Histograms of B_1^+(a-f.4),Coefficient of variation values($s(|B_1^+|)/\mu(|B_1^+|)$), normalised to $B_{1\ mean}^+$.

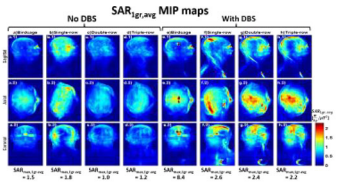

Fig. 3: $SAR_{1g,avg}$(W/kg/μT²) MIP images: No DBS for birdcage(a), single-row(b), double-row(c), triple-row(d)coils, With DBS for birdcage(e), single-row(f), double-row (g), triple-row(h)coils, normalised to $B_{1\ mean}^+$.

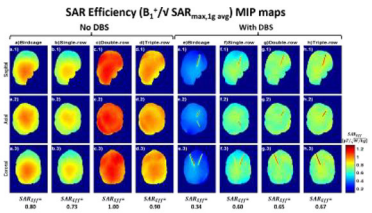

Fig. 4: SAR efficiency($B_1^+/\sqrt{SAR_{max,1g,avg}}$) MIP images: No DBS for birdcage(a), single-row(b), double-row(c), triple-row(d)coils, With DBS for birdcage(e), single-row(f), double-row(g), triple-row(h)coils, normalised to $B_{1\ mean}^+$.

Reference

[1] Guerin DA et al. https://doi.org/10.1002/MRM.27905
[2] Wu X et al. https://doi.org/10.1002/NBM.3378
[3] Gosselin MC et al. https://doi.org/10.1088/0031-9155/59/18/5287
[4] Ipek Ö et al. https://doi.org/10.1002/MRM.24794
[5] Eichfelder G et al. https://doi.org/10.1002/MRM.22927
[6] https://gitlab.com/bioengmri/ptx

LT47.
Accuracy of the RF-spoiled gradient-echo signal for common values of the RF phase-difference increment

J. Leupold[1], M. Weigel[2,3,4,5], S. Bär[1]

[1]*University of Freiburg, Department of Diagnostic and Interventional Radiology, Medical Physics, University Medical Center, Freiburg, Germany;*
[2]*University of Basel, Translational Imaging in Neurology (ThINk) Basel, Department of Biomedical Engineering, Basel, Switzerland;*
[3]*University of Basel, Neurologic Clinic and Policlinic, Departments of Neurology and Clinical Research, Basel, Switzerland;*
[4]*University of Basel, Research Center for Clinical Neuroimmunology and Neuroscience Basel (RC2NB), Basel, Switzerland;*
[5]*University of Basel, Division of Radiological Physics, Department of Radiology, Basel, Switzerland*

Introduction In RF-spoiled gradient-echo imaging, the RF phase-difference increment ψ determines RF pulse phases intending to eliminate T2-contribution from the signal and let it follow the so-called Ernst-curve [1]. Four Ψ-values that are in practical use in standard implementations of different vendors (Siemens: $\psi = 50°$, GE: $\psi = 115.4°$, Bruker: $\psi = 117°$, Philips: $\psi = 150°$) as well as $\psi = 169°$ (as proposed for GRE-based T1-quantification [2]) are compared with respect to their capability of removing T2-dependency from the signal. Influence of diffusion is considered.

Methods The presented study was performed with the following details:

- Signal simulations were performed over a multi-dimensional parameter space (including $\psi \in \{50°,115.4°,117°,150°,169°\}$, diffusion constant D, repetition time TR, relaxation times T1 and T2, flip angle α, image resolution).
- Influence of diffusion on the signal was considered by means of the EPG-formalism [3].
- Deviations ε from the Ernst-curve (i.e. signal vs. flip angle assuming perfect spoiling) were quantified as the average signal deviation per flip angle from the Ernst-curve in percent.
- Experiments were performed for both a water + CuSO4 phantom (high diffusion, $D = 1.93*10^{-3}mm^2/s$, T1 = 540 ms, T2 = 340 ms) and a silicone oil phantom (low diffusion, $D = 0.0055*10^{-3}$ mm^2/s, T1 = 1290 ms, T2 = 399 ms).
- Experiments were performed on a 7 T Bruker Biospec 70/20 small animal scanner with a mouse volume coil.

For motivation of the study, images of the silicone oil phantom and a water + Gd phantom (T1 = 1603 ms, T2 = 613 ms) with the five examined ψ-values are shown in Fig. 1. For an in-plane resolution of 300 µm, TR = 20 ms and flip angle $\alpha = 60°$. Signal variation for the silicone oil phantom is visible such that the contrast of the two phantoms is even inverted from $\Psi = 50°$ to $\Psi = 117°$.

Results Simulated (lines) and measured (dots) signal curves are shown in Figs. 2 and 3 for the water + CuSO4 and the silicone oil phantom, respectively. Imaging parameters are: 3D FLASH sequence, TR = 20 ms, TE = 4 ms, in-plane resolution 300 µm, ROI analysis performed in the central slice of 64 slices à 780 µm. Deviations from the Ernst-curve as described are: Water phantom (Fig. 2): $\Psi = 50°$: $\varepsilon = 3.6\%$; $\Psi = 115.4°$: $\varepsilon = 7.7\%$; $\Psi = 117°$: $\varepsilon = 7.6\%$; $\Psi = 150°$: $\varepsilon = 7.1\%$; $\Psi = 169°$: $\varepsilon = 0.9\%$. Silicone oil phantom (Fig. 3): $\Psi = 50°$: $\varepsilon = 18.3\%$; $\Psi = 115.4°$: $\varepsilon = 9.3\%$; $\Psi = 117°$: $\varepsilon = 13.8\%$; $\Psi = 150°$: $\varepsilon = 20.0\%$; $\Psi = 169°$: $\varepsilon = 9.6\%$. Substantial deviation from the Ernst-curve can be observed for the silicone oil phantom.

Average relative deviation per flip angle from the Ernst-curve is shown in Fig. 4, for TR = 20 ms, exemplarily for $\Psi = 50°$ and $\Psi = 117°$. For both Ψ-values, diffusion coefficients for silicone oil (left column) and brain grey matter (right column) is shown. T1 and T2 values for said substances are marked with an "o". For grey matter at 3 T, T1 = 1500 ms, T2 = 100 ms, $D = 0.8*10^{-3}mm^2/s$ were assumed [2].

Also, results for TR = 50 ms and the other Ψ-values will be shown, as well as simulations for different image resolution.

Discussion Simulations of the RF-spoiled GRE-signal for a certain Ψ-value under consideration of diffusion shows the error to the Ernst-curve is increasing with T2/TR, lower diffusion constant and lower resolution, although not in a monotonical manner (i.e., increasing resolution can increase the error before it finally approaches zero for even higher resolution). This can lead to substantial deviation from the Ernst-curve when imaging low-diffusion substances with short TR and flip angles higher than the Ernst-angle. This behaviour can have an impact when it comes to imaging of non-biological substances such as in phantoms for method development and verification of signal models. For human in-vivo imaging, the deviation from the Ernst-curve is low for any examined Ψ-value. However, in order to set up an RF-spoiled GRE sequence with a signal behaviour that can be approximated with the Ernst-equation over a wider range of parameters, we recommend to use $\Psi = 115.4°$ from the "traditional" values or even better $\Psi = 169°$ as already proposed for improving GRE-based T1 determination [2]. Then, rather uncommon scenarios as described can get handled with decent accuracy.

Conclusion In RF-spoiled GRE, the best spoiling behaviour based on a large parameter space (including low diffusion coefficients) can be obtained with $\Psi = 169°$, followed by $\Psi = 115.4°$ and $\Psi = 117°$. The increments $\Psi = 50°$ and $\Psi = 150°$ offer good signal spoiling only when influence of diffusion is high, but fail for signal spoiling in low-D substances.

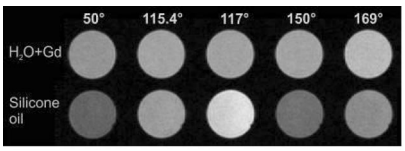

Fig. 1: Water phantom (top row) and silicone oil phantom (bottom row) for different spoil increments Ψ for a protocol with TR=20ms and α=60°.

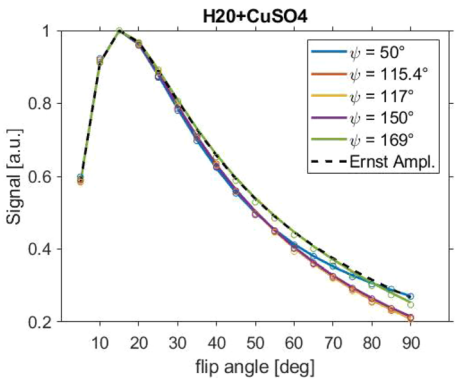

Fig. 2: Signal vs. flip angle of the RF-spoiled GRE signal for different Ψ, water phantom. Solid lines: EPG+diffusion simulation, dots: experiment data.

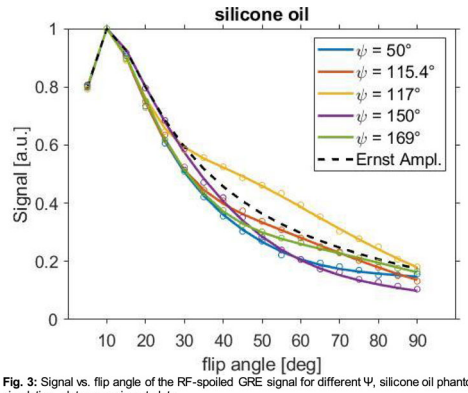

Fig. 3: Signal vs. flip angle of the RF-spoiled GRE signal for different Ψ, silicone oil phantom. Solid lines: EPG+diffusion simulation, dots: experiment data.

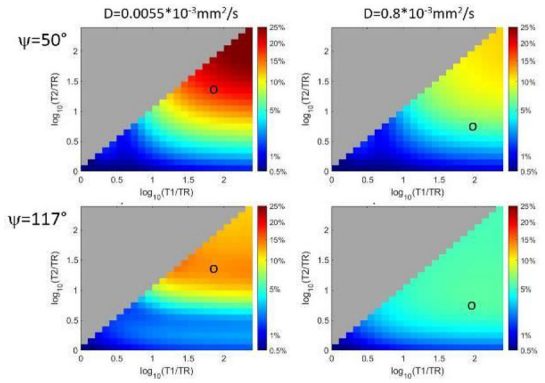

Fig. 4: Simulated average relative error ε per flip angle to the Ernst-curve for Ψ=50° (top row) and Ψ=117° (bottom row), for diffusion coefficient D corresponding to silicone oil (left column) and grey matter (right column). The concrete locations of said substances with respect to their T1 and T2 are marked.

References

[1] Zur Y, Wood ML, Neuringer LJ. Magn Reson Med 1991;21(2):251–63.

[2] Yarnykh VL. Magn Reson Med 2010;63:1610–1626.

[3] Weigel M, Schwenk S, Kiselev VG, Scheffler K, Hennig J. J Magn Reson 2010;205:276–285.

LT48.
T-Hex versus blipped-CAIPIRINHA sampling

M. Engel[1], L. Müller[1,2], A. Döring[1], D. K. Jones[1]

[1]*Cardiff University, Cardiff, United Kingdom;*
[2]*University of Leeds, Leeds Institute of Cardiovascular and Metabolic Medicine, Leeds, United Kingdom*

Introduction Sampling on tilted hexagonal (T-Hex) grids is an encoding strategy for 3D and Multiband MRI that reconciles high speed with flexible segmentation, uniform k-space density, and benign T2* effects[1]. It has been used for BOLD fMRI[2] as well as DWI[3]. The purpose of this work is to compare the SNR performance of T-Hex to the most commonly used blipped-CAIPIRINHA[5] technique.

Methods MB encoding differs from full 3D encoding solely in that it requires a lower resolution in z direction[4]. Since the required sampling density is the same, this work focuses on MB imaging.

Different sampling schemes for SE EPI were implemented on a 3 T scanner (Siemens Healthcare, Erlangen, Germany) and measured in vivo (Table 1a, Fig. 1).

T-Hex[1] with generating vector was compared to blipped-CAIPIRINHA[5] with and A) and B) (R: total undersampling factor, N: number of simultaneously excited slices, L: # distinct steps in kz direction). Since the readout was longer for T-Hex, two further comparisons were performed: Firstly, the blipped-CAIPIRINHA acquisitions were repeated with minimum TE (C & D). Secondly, they were combined with in-plane oversampling to achieve the same readout length as the T-Hex scheme in question (E & F).

The image reconstruction was based on a cg-SENSE6 algorithm including off-resonance correction [1,7] ("skope-i", Skope Magnetic Resonance Technologies, Zurich, Switzerland) and measured field dynamics up to 3rd order.

SNR maps and the respective gain of the T-Hex scheme were calculated as described in[8].

The packing density was computed for all investigated oblique lattices exhibited by the described trajectories.

The latter was repeated for (Table 1b).

Results For ((Fig. 2) and (Fig. 3), T-Hex always offers the highest packing density, which none of the other patterns reach. The average SNR for T-Hex is higher than for all other sampling strategies. The SNR yield (anti-)correlates with, TE and the packing density of the sampling grid as expected. These findings are the same for both magnitude and complex SNR which in general differ only very little. Among the blipped-CAIPIRINHA patterns, the value of that maximizes the packing density (yellow frames in Fig. 3) varies, depending on the in-plane phase-encoding (PE) spacing.

Discussion 1) T-Hex allows for a flexible choice of the in-plane PE sampling and in particular for in-plane *over*sampling and thereby decoupling of the number of simultaneously excited slices (N) from the total undersampling factor (R). This has not been done for blipped-CAIPIRINHA so far. 2) T-Hex realizes sampling on a hexagonal grid, which entails optimal conditioning of the image reconstruction problem assuming an elliptical object and spherically distributed receive coils. When the first aspect is disregarded, the SNR advantage of T-Hex over blipped-CAIPIRINHA can become small for specific imaging scenarios, i.e., combinations of FOV, and coil configuration (down to 3% for the example in Fig. 4) since, for certain choices of, sampling patterns close to a hexagonal grid can be achieved (see yellow framings in Fig. 3). However, on the one hand the SNR penalty for non-ideal sampling is expected to increase for higher. On the other hand, what to choose for optimal conditioning of the image reconstruction has so far not been studied systematically. Our findings corroborate that the T-Hex ansatz of assuming optimum image reconstruction conditioning to be reached with hexagonal sampling is a reasonable approach for typical brain scan scenarios. T-Hex provides different sampling options (generating vectors) the choice between which is subject to careful balance between readout duration (decisive for the degree of T2* filtering) and SNR just as it is the case for 2D sampling schemes such as EPI or spiral. The strict optimization of the k-space sampling in a controlled way, including the independent choice of *N* and *R* is paramount, especially for experiments with strong diffusion weighting that operate on the verge of the noise floor and are time-critical due to the need for a multitude of different diffusion weightings. Here, recovering signal by optimum k-space sampling rather than averaging is vital to minimize the g-factor penalty on the one hand and to minimize the repetition of lengthy diffusion encoding modules on the other hand.

Acknowledgements EPSRC (grant EP/M029778/1); The Wolfson Foundation; Wellcome Trust Investigator Award (096646/Z/11/Z); Wellcome Trust Strategic Award (104943/Z/14/Z); Swiss National Science Foundation Fellowship (SNSF #202962).

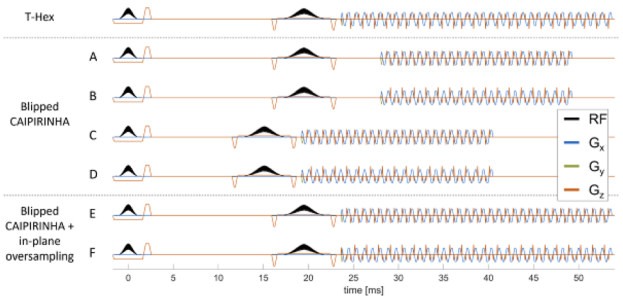

Fig. 1: Sequence diagrams. Note that the Gz blips during readouts are 5x zoomed for visibility.

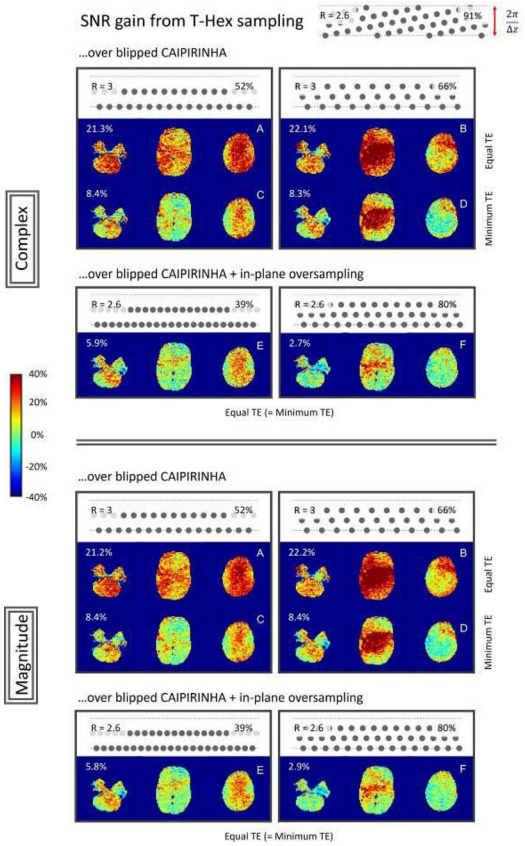

Fig. 2: Percentage SNR gain of T-Hex (upper right panel) over the respective sampling pattern. The mean gain is displayed in white numbers in the upper left corner of the maps. For each sampling pattern, the packing density of the oblique grid is displayed in the upper right corner. Dashed red lines delineate the upper and lower bound of the k-space slab to be encoded.

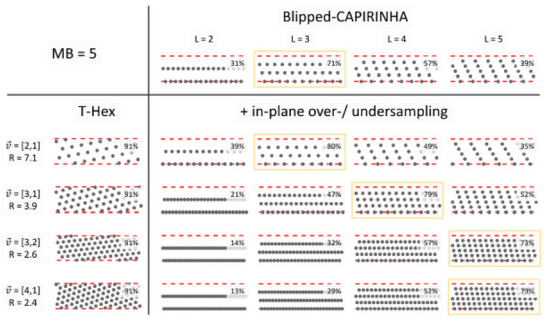

Fig. 3: Upper row: 4 different blipped-CAIPIRINHA patterns for N=5. Lower rows: 4 different T-Hex sampling patterns resulting in different undersampling factors (left). For each of these, blipped-CAIPIRINHA patterns with an adapted in-plane over- or undersampling to match the total readout time of the respective T-Hex pattern are displayed on the right side. For each undersampling factor, a yellow framing indicates the non-T-Hex pattern with the highest packing density (upper right corner).

Sampling scheme	*N*	*R*	*L*	T_{Acq} [ms]	TE [ms]	Resolution	In-plane FOV	Slice spacing Δz
a) SNR comparison								
T-Hex $\vec{p}$ = [2, 1]	3	2.6	-	30.1	39.0	4 mm	192 mm	32 mm
Blipped CAIPIRINHA (A)	3	3	2	21.4	39.0	4 mm	192 mm	32 mm
Blipped CAIPIRINHA (B)	3	3	3	21.4	39.0	4 mm	192 mm	32 mm
Blipped CAIPIRINHA (C)	3	3	2	21.4	30.2	4 mm	192 mm	32 mm
Blipped CAIPIRINHA (D)	3	3	3	21.4	30.2	4 mm	192 mm	32 mm
Blipped CAIPIRINHA + in-plane oversampling (E)	3	2.6	2	30.1	39.0	4 mm	192 mm	32 mm
Blipped CAIPIRINHA + in-plane oversampling (F)	3	2.6	3	30.1	39.0	4 mm	192 mm	32 mm
b) Sampling pattern								
T-Hex $\vec{p}$ = [2, 1]	5	7.1	-	19.0	-	4 mm	192 mm	19.2 mm
T-Hex $\vec{p}$ = [3, 1]	5	3.9	-	35.4	-	4 mm	192 mm	19.2 mm
T-Hex $\vec{p}$ = [3, 2]	5	2.6	-	50.0	-	4 mm	192 mm	19.2 mm
T-Hex $\vec{p}$ = [4, 1]	5	2.4	-	55.2	-	4 mm	192 mm	19.2 mm
Blipped CAIPIRINHA	5	5	2	22.7	-	4 mm	192 mm	19.2 mm
Blipped CAIPIRINHA	5	5	3	22.7	-	4 mm	192 mm	19.2 mm
Blipped CAIPIRINHA	5	5	4	22.7	-	4 mm	192 mm	19.2 mm
Blipped CAIPIRINHA	5	5	5	22.7	-	4 mm	192 mm	19.2 mm
Blipped CAIPIRINHA + in-plane undersampling	5	7.1	2	19.0	-	4 mm	192 mm	19.2 mm
Blipped CAIPIRINHA + in-plane undersampling	5	7.1	3	19.0	-	4 mm	192 mm	19.2 mm
Blipped CAIPIRINHA + in-plane undersampling	5	7.1	4	19.0	-	4 mm	192 mm	19.2 mm
Blipped CAIPIRINHA + in-plane undersampling	5	7.1	5	19.0	-	4 mm	192 mm	19.2 mm
Blipped CAIPIRINHA + in-plane oversampling	5	3.9	2	35.4	-	4 mm	192 mm	19.2 mm
Blipped CAIPIRINHA + in-plane oversampling	5	3.9	3	35.4	-	4 mm	192 mm	19.2 mm
Blipped CAIPIRINHA + in-plane oversampling	5	3.9	4	35.4	-	4 mm	192 mm	19.2 mm
Blipped CAIPIRINHA + in-plane oversampling	5	3.9	5	35.4	-	4 mm	192 mm	19.2 mm
Blipped CAIPIRINHA + in-plane oversampling	5	2.6	2	50.0	-	4 mm	192 mm	19.2 mm
Blipped CAIPIRINHA + in-plane oversampling	5	2.6	3	50.0	-	4 mm	192 mm	19.2 mm
Blipped CAIPIRINHA + in-plane oversampling	5	2.6	4	50.0	-	4 mm	192 mm	19.2 mm
Blipped CAIPIRINHA + in-plane oversampling	5	2.6	5	50.0	-	4 mm	192 mm	19.2 mm
Blipped CAIPIRINHA + in-plane oversampling	5	2.4	2	55.2	-	4 mm	192 mm	19.2 mm
Blipped CAIPIRINHA + in-plane oversampling	5	2.4	3	55.2	-	4 mm	192 mm	19.2 mm
Blipped CAIPIRINHA + in-plane oversampling	5	2.4	4	55.2	-	4 mm	192 mm	19.2 mm
Blipped CAIPIRINHA + in-plane oversampling	5	2.4	5	55.2	-	4 mm	192 mm	19.2 mm

Fig. 4

References

1 Engel, M. et al.*; MRM* 85, 2507–2523 (2021).
2 Engel, M. et al.*; ISMRM* 0886 (2021).
3 Engel, M. et al.; *ISMRM Diffusion Workshop* (2022).
4 Zahneisen, B. et al.*; MRM* 71, 2071–2081 (2014).
5 Setsompop, K. et al.*; MRM* 67, 1210–1224 (2012).
6 Pruessmann, K. P. et al.*; MRM* 46, 638–651 (2001).
7 Wilm, B. J. et al.*; MRM* 65, 1690–1701 (2011).
8 Lee, Y. et al.*; MRM* 85, 1924–1937 (2021).

LT49.

Abstract withdrawn at the request of the authors.

LT50.
Distortion correction at ultrahigh field: Benefit of deviation from "best" VAT

Y. H. Tung[1], O. Speck[1,2,3,4]

[1]*Otto von Guericke University, Institute for Physics, Magdeburg, Germany;*
[2]*German Center for Neurodegenerative Diseases (DZNE), Magdeburg, Germany;*
[3]*Center for Behavioral Brain Sciences (CBBS), Magdeburg, Germany;*
[4]*Leibniz Institute for Neurobiology (LIN), Magdeburg, Germany*

Introduction Susceptibility-induced field inhomogeneity and chemical shift are two primary sources of distortion in single-shot EPI (ss-EPI) at ultrahigh field ($\geq$ 7 T). These image artifacts depend on the EPI phase-encoding (PE) direction. A common strategy to tackle these artifacts is in-plane parallel imaging (e.g., GRAPPA[1], SENSE[2]), but a considerable amount remains. Another strategy, namely view angle tilting-based imaging, has been used in turbo spin-echo (VAT-TSE) sequences for correcting chemical shift[3] and metal artifacts[4,5] in musculoskeletal MR. In EPI, however, the large gradient amplitude of the tilting gradient in VAT (G_{VAT}) generates blurring and SNR reduction compared to VAT-TSE[6]. Recently, the combination of VAT and EPI with distortion correction has been proposed and showed promising results in correcting distortions from both sources[7]. In this study, we investigated if a smaller-than-ideal G_{VAT} in VAT-PSF-EPI (with spin-echo signal) is applicable.

Methods A phantom is filled with air, oil, and water to examine susceptibility-induced image distortion and chemical shift, as shown in Fig. 1. All images were scanned on a 7 T human scanner with a whole-body gradient system (70 mT/m, 200 T/m/s) and a 32-channel head coil. ss-EPI, TSE, and VAT-PSF-EPI were scanned to compare the above-mentioned image artifacts. Common parameters were 1.4 mm isotropic resolution with 160 × 160 sampling points, 31 slices, and anterior–posterior PE direction (AP). The individual parameters were: ss-EPI had 1488 Hz/pixel readout bandwidth, 0.8 ms echo spacing, GRAPPA 4, TR/TE 6300/65 ms, and TA 6.3 s. TSE has 789 Hz/pixel readout bandwidth, turbo factor 8, GRAPPA 4, TR/TE 8040/68 ms, and TA 1:04 min. The 5-shot VAT-PSF-EPI has 1838 Hz readout bandwidth, 0.8 ms echo spacing, rFoV × GRAPPA × R_{res} = 32 × 4 × 1.3[7], TR/TE 6300/65 ms, TA 31.5 s. In addition, all sequences were acquired twice; with and without the vendor spectral fat saturation. VAT-PSF-EPI was acquired with two further sets of parameters: The first set was acquired with the remaining three PE directions: posterior-anterior (PA), right-left (RL), and left–right (LR) to examine its distortion correction. The second set was acquired with the G_{VAT} deviating from its theoretically optimal value. The G_{VAT} was scaled by 0.78, 0.91, 0.95, 0.97, 1.0, or 1.18. All images were reconstructed online, and the numerical evaluation was performed in Matlab. The Boundary F1 (BF) score is used for contour match evaluation, in which 1.0 is the perfect match[8].

Results Fig. 2 shows ss-EPI, TSE, and VAT-PSF-EPI images with and without fat saturation. With fat saturation, ss-EPI has air–water susceptibility distortion in the PE direction, while VAT-PSF-EPI shows no distortion, similar to TSE. When the fat saturation was off, a strong oil–water chemical shift appears in ss-EPI. In comparison, a small shift is present in TSE and no shift in VAT-PSF-EPI. In Fig. 3, fat-saturated TSE was assumed as the geometric gold standard for numerical evaluation. VAT-PSF-EPI was evaluated in all acquired PE directions and the BF score is on average 0.99 ± 0.001. The BF for ss-EPI is 0.91 in AP. Fig. 4 shows different VAT gradient amplitudes in VAT-EPI and VAT-PSF-EPI. In VAT-EPI, the oil signal shifts promptly with the G_{VAT} change. Even with 3% G_{VAT} deviation, an oil signal shift can be recognized. In comparison, the oil signal shifts in VAT-EPI do not influence the final corrected VAT-PSF-EPI with a gradient variation of below 5%. Up to 20% deviation leads to visible fat shift but the geometry remains well corrected.

Discussion This study demonstrated the high fidelity of the geometric correction in VAT-PSF-EPI at 7 T (Fig. 3). In addition, EPI-PSF-EPI is tolerant to small (5%) deviation of the VAT gradient. VAT-PSF-EPI corrects artifacts from field inhomogeneities and chemical shift well compared to the ss-EPI and TSE. Finally, a VAT gradient amplitude change that up to 20% still allows correction of the susceptibility distortion in the five shots VAT-PSF-EPI. This indicates the G_{VAT} can be reduced by up to 20% to reduce SNR loss or increase acceleration provided fat saturation is applied.

Conclusion The fast imaging sequence VAT-PSF-EPI can correct susceptibility and chemical shift-induced artifacts well at ultrahigh field. It does not require extensive modeling, calibration, or post-processing.

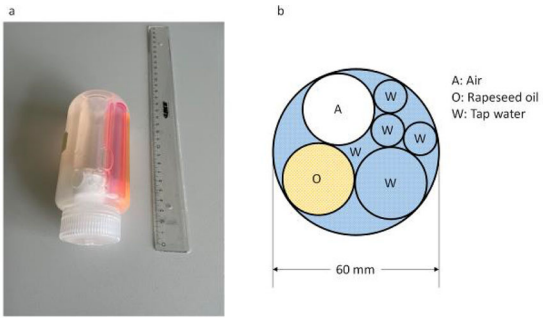

Fig. 1: The phantom is constituted of three larger tubes and three small tubes fixed steadily in a plastic cylinder. The large tubes contain air, vegetable oil (rapeseed oil), and tap water, while the smaller tubes and the outer cylinder are all filled with tap water.

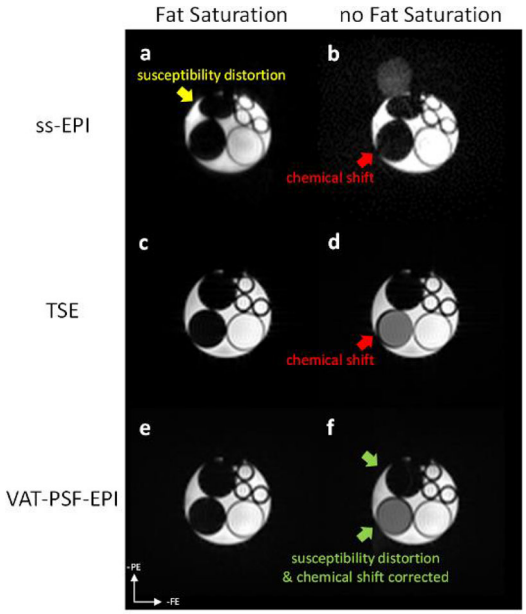

Fig. 2: The air-oil-water phantom images of ss-EPI, TSE, and VAT-PSF-EPI with (a, c, e) and without RF fat saturation (b, d, f).

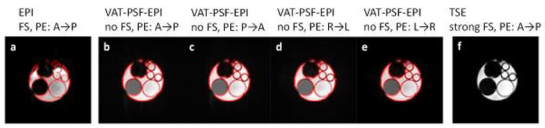

Fig. 3: Numerical evaluation of VAT-PSF-EPI for different phase-encoding directions. The image edge was extracted via the Sobel filter and the BF score is evaluated. The BF score is an average of 0.99±0.001 in VAT-PSF-EPI and 0.91 for ss-EPI, in which 1.0 is the perfect match.

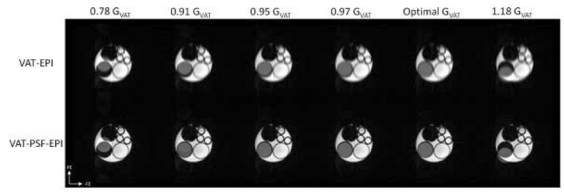

Fig. 4: Susceptibility and chemical shift distortion correction in VAT-EPI and VAT-PSF-EPI when the VAT gradient amplitude differs from the optimal value. The VAT-EPI image is generated from the VAT-PSF-EPI data.

References

1. Griswold et al., MRM 2002
2. Pruessmann et al., MRM 1999
3. Cho, Kim, and Kim, Med Phys 1988
4. Lu et al., MRM 2009
5. Koch et al., MRM 2009
6. Ahn and Hu, MRM 2012
7. Tung et al., MRM 2022
8. Csurka, Larlus, and Perronnin, BMVC 2013

LT51.
Real-time multislice-to-volume motion correction for task-based functional MRI at 7 T

S. Winata[1], D. C. Hoinkiss[2], G. A. Keith[1], S. al-Wasity[1], D. A. Porter[1]

[1]*University of Glasgow, Imaging Centre of Excellence, Glasgow, United Kingdom;*
[2]*Fraunhofer Institute for Digital Medicine MEVIS, Bremen, Germany*

Introduction 7 T MRI has higher inherent signal-to-noise ratio (SNR) than standard clinical field strengths that gives the potential for higher resolution imaging. The downside is further susceptibility to ghosting and blurring artefacts even to minimum motion. This is especially pronounced in longer acquisitions, where the effects of incidental motion are more visible [1]. Generally using long acquisitions and high resolutions, functional MRI (fMRI) protocols are prone to motion artefacts, which are typically corrected with retrospective motion correction [2]. Prospective, real-time motion correction can be performed to reduce these effects further [3]. The restricted environment in 7 T scanners (i.e. tighter head coils, narrower and longer bores) makes markerless, non-hardware techniques a compelling option. This abstract presents an implementation of the markerless Multislice Prospective Acquisition Correction (MS-PACE) technique for 7 T task-based fMRI. This includes the use of the in-plane generalised autocalibrating partially parallel acquisitions (GRAPPA) [4]. This technique reduces spatial distortion effects in higher field strength EPI [5].

MS-PACE [6] is a prospective motion correction technique adapted from Prospective Acquisition CorrEction (PACE). In-plane and through-plane motion are estimated by registering a subset of equidistant 2D-EPI slices to a reference volume, differing from the volumetric registration in PACE [7]. This allows for sub-TR motion detection and higher temporal resolution of imaging system update. This method has previously been implemented at 3 T [8].

MethodsThe study was performed in a MAGNETOM Terra 7 T scanner (Siemens Healthineers, Erlangen, Germany) with a 1Tx32Rx head coil (Nova Medical, Wilmington, MA, USA) using an in-house-developed GRE-EPI sequence on 10 healthy subjects (age 31 $\pm$ 9). The GRE-EPI fMRI protocol consisted of 3 scan groups: 2 resting; 2 left hand tapping; 2 right hand tapping. Motion correction was applied to 1 scan per group. The scan parameters were otherwise identical: voxel size 2 $\times$ 2 $\times$ 2mm3, resolution 96 $\times$ 96, GRAPPA factor 3, 60 slices, 110 volumes, echo spacing 580 ms, TR 4 s, TE 18 ms and total acquisition time 7m32s. The tapping scan block design (shown in Fig. 1) was transmitted with the aid of the PsychoPy software package [9]. Fig. 2 shows how the motion detection and correction pipeline operated. A 3-slice registration subset was used. Estimated motion parameters were subsequently fed back to the scanner and the imaging gradients were updated to account for these. The correction robustness was evaluated by retrospectively calculating rigid body motion parameters (3D translation and rotation) with the multislice-to-volume method. Online and offline processing was done within the Image Calculation Environment (Siemens Healthineers, Erlangen, Germany) using ITK open-source image registration libraries.

Results Fig. 3 compares the mean voxel displacement from each scan group across all subjects. Fig. 4 displays temporal SNR (tSNR) maps and percentage differences in tSNR (δtSNR) from the scans without and with real-time motion correction in each subject. These maps illustrate the temporal variance in noise and were calculated by comparing the mean signal of each voxel to its standard deviation over the time series.

Discussion Fig. 3 demonstrates the consistent ability of the technique to correct for motion across all subjects. The technique worked in subjects with different propensity to move, from those who moved little to those who moved much more. It also was able to correct for head motion during the tapping scans, which are more inherently motion prone to incidental motion from the hand movements. Fig. 4 also correlates with these findings. When real-time motion correction is applied, there has been a net positive temporal SNR percentage improvement in a majority of the cohort"s subjects. It is important however to note that each acquisition is separate and thus the motion patterns are variable.

It has been demonstrated that the technique can correct for longer-term motion components in 7 T task-based fMRI consistently across a cohort.

Conclusion This study has evaluated an implementation of multi-slice-to-volume prospective motion correction for 7 T task-based fMRI and shown that the technique can consistently reduce the effects of long-term motion in a motion-propensity diverse cohort of subjects.

Fig. 1: The block design for the finger tapping scans. The tapping blocks interchanged with the rest blocks. A cross was displayed at the centre of the screen during the resting blocks. Each block lasts for 10 volumes.

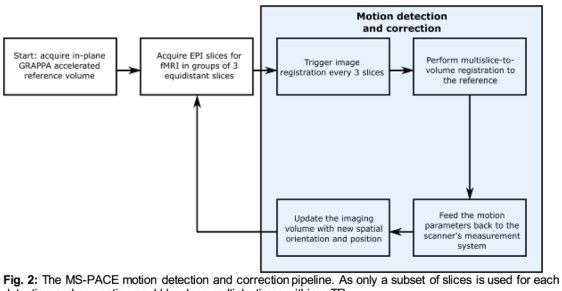

Fig. 2: The MS-PACE motion detection and correction pipeline. As only a subset of slices is used for each registration, detection and correction could be done multiple times within a TR.

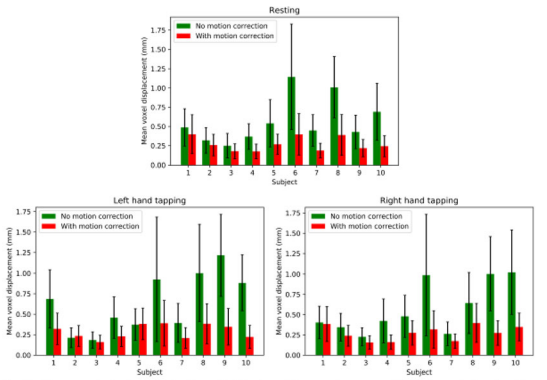

Fig. 3: Mean voxel displacement with and without real-time motion correction from each functional scan group across all subjects: resting scans (top); left-hand tapping (bottom left); right-hand tapping (bottom right). The error bars represent the standard deviation of each dataset.

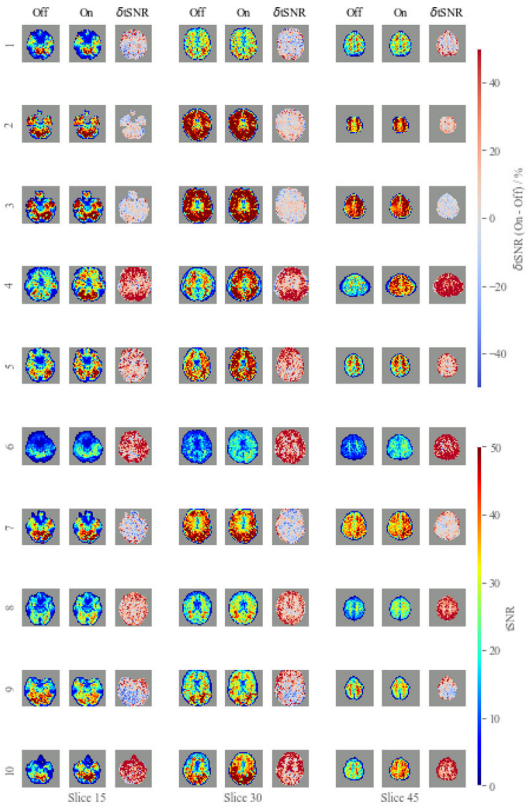

Fig. 4: Temporal SNR (tSNR) maps and differences (δtSNR) derived from the right-hand tapping scans in all ten subjects when real-time motion correction is turned off or on. The maps are plotted for slices 15, 30 (centre) and 45 in subject-native EPI space.

References

[1] Herbst M et al. MRM. 2014;71:182–90.
[2] Maknojia S et al. Front Neurosci. 2019;13:1–13.
[3] Zaitsev M et al. Neuroimage. 2017;154.
[4] Griswold MA et al. MRM. 2002;47:1202–10.
[5] Speck O et al. Magn Reson Mater Phys. 2008;21:73–86.
[6] Hoinkiss DC, Porter DA. MRM. 2017;78:2127–35.
[7] Thesen S et al. MRM. 2000;44:457–65.
[8] Hoinkiss DC et al. Neuroimage. 2019;200:159–73.
[9] Peirce, J et al. Behav Res. 2019;51:195–203.
[10] Winata S et al. 2021 BIC-ISMRM Annual Meeting.
[11] Barth M et al. MRM. 2016;75:63–81.

LT52.
Dynamic DREAM MRI: B0, B1 and Tx/Rx-phase mapping for assisting motion tracking systems

T. Baum[1], S. Weinmüller[1], A. M. Nagel[2], M. Vossiek[3], M. Zaiss[1,4,5]

[1]*Friedrich-Alexander-Universität Erlangen-Nürnberg (FAU), Department of Neuroradiology, Erlangen, Germany;*
[2]*Friedrich-Alexander-Universität Erlangen-Nürnberg (FAU), Institute of Radiology, Erlangen, Germany;*
[3]*Friedrich-Alexander-Universität Erlangen-Nürnberg (FAU), Institute of Microwaves and Photonics (LHFT), Erlangen, Germany;*
[4]*Max-Planck-Institute for Biological Cybernetics, Magnetic Resonance Center, Tübingen, Germany;*
[5]*Friedrich-Alexander-Universität Erlangen-Nürnberg (FAU),*

Department Artificial Intelligence in Biomedical Engineering, Erlangen, Germany

Introduction The "dual refocusing echo acquisition mode" (DREAM) sequence is a fast method for B0 and B1 field mapping in 2D [1], and 3D [2]. DREAM also provides a Tx/Rx-phase mapping. We implemented a dynamic DREAM sequence that provides all these information, and evaluated a dynamic scan under free breathing, and a scan where the head position in the coil was altered. With up to 1 s temporal resolution breathing induced B0 could be detected; also motion induced B0, B1 and Tx/Rx-phase changes could be detected. This information can in the future be used to assist impedance-based, optical or radar-based motion tracking systems.

Methods A centric-reordered DREAM sequence [1] (matrix: 64×64, FoV = $220 \times 220 \times 8$ mm^3, $FA_{STE1} = FA_{STE2} = 55°$, FA = 15°, TE_{FID} = 3.6 ms, TE_{STE} = 2.6 ms, TR = 5.6 ms, TA = 387 ms) was realized in Pulseq and used with a Pulseq interpreter sequence. At submission time, a first healthy volunteer was scanned under approval of our local ethics committee on a 3 T whole-body MRI system (MAGNETOM Prisma, Siemens Healthcare, Erlangen, Germany) and a 20 channel receive coil.

The DREAM provides for every image a B0 and B1 map, and a TxRx-phase map calculated by the formulas [1]:

$$\Phi_{B0} = \text{angle}(\text{FID} \cdot \text{STE}*) \quad (4)$$

$$\text{rB1} = \tan^{-1}(\sqrt{(2|\text{STE}|/|\text{FID}|)})/\text{FA}_{\text{STE1}} \quad (5)$$

$$\Phi_{tx/rx} = \text{angle}(\text{FID} \cdot \text{STE}) \quad (6)$$

In the dynamic free-breathing measurement, the DREAM was repeated 20 times with a recovery time in-between sequences of 2 s leading to a temporal resolution of 2.4 s. Here a pre-experiment showed that 1 s delay yields unaltered field maps (data not shown).

In the positioning measurement, the DREAM was scanned for four specific positions of the head in the coil. The FoV was fixed with regard to the brain using the head-scout auto-align functionality. This allows calculating exact difference maps of the different positioned images.

Results The dynamic free-breathing measurements showed that B1 and TxRx-phase seems to be stable with breathing, but B0 shows the typical breathing state induced deviations (Fig. 1). Figure 2 shows that the dynamic B0 shift and the FFT which peaks at the breathing frequency.

The positioning experiment revealed that the B0 and B1 field maps show non-linear alterations upon translation of the head (Fig. 3), while the TxRx-phase (Fig. 4) seems to translate linearly with the movement (in the head frame). I.e. the TxRx-phase seems to be almost stationary in the lab frame.

Discussion DREAM MRI can be used to dynamically map B0, B1, and the TxRx-phase with temporal resolution up to 1 frame-per-second (FPS). This makes possible to analyze the influence of physiological processes on all these maps, as well as the influence of positioning or patient movement within the scanner and the shim-coils and the Tx- and Rx-coils. 3D implementations with TA of 4.2 s [2] should be possible with around 5 s per frame, thus 0.2 FPS.

This dynamic field and phase map information is useful for assisting of motion tracking systems and corresponding dynamic field map estimation.

Conclusion Dynamic DREAM MRI mapping of B0, B1, and the TxRx-phase is possible with 1 FPS.

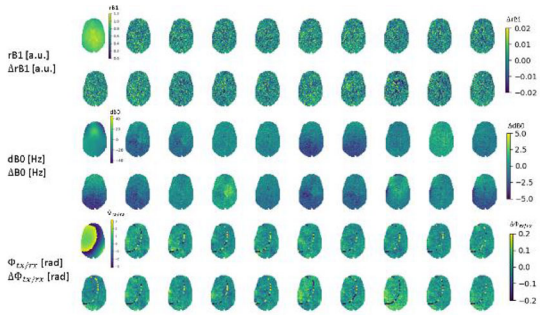

Fig. 1: Dynamic DREAM measurement. First image in each double-row is the relative B1 rB1, the B0 inhomogeneity dB0 and TxRx-phase image, followed by the 19 difference images (Δ) to make changes visible. In both, rB1 and TxRx-phase images, only images 17 show a significant change, possible due to motion. In the dB0 images, the influence of breathing is visible, as analyzed in Figure 2.

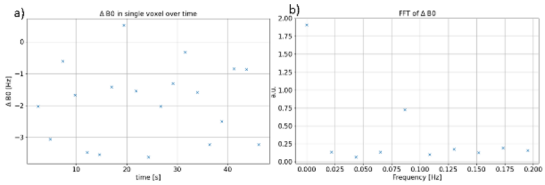

Fig. 2: (a) The dynamic change of the B0 inhomogeneity. (b) Fourier analysis reveals that the major contribution matches with the breathing frequency.

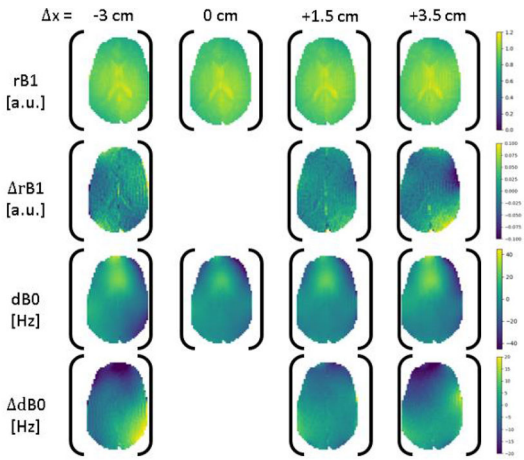

Fig. 3: Positioning affects rB1 and dB0 in a non-linear fashion. The subject moved in the unchanged B0 shim and B1 mode, leading to non-linear interactions and new field-distribution.

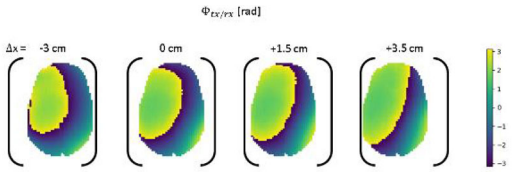

Fig. 4: Positioning seems to affect the TxRx-phase mostly linearly in the frame of reference of the moving head, meaning it is mostly stable in the stationary frame.

References

[1] Nehrke et al., DREAM—a novel approach for robust, ultrafast, multislice B1 mapping. MRM 2012.

[2] Ehses et al., Whole-brain B1 -mapping using three-dimensional DREAM. MRM 2019.

LT53.
A simple pTx Pulseq extension for pulse-specific B1 shimming

M. Freudensprung[1], S. Weinmüller[1], J. Endres[1], A. M. Nagel[2,3], M. Zaiss[1,2,4,3]

[1]*Friedrich-Alexander-Universität Erlangen-Nürnberg (FAU), Department of Neuroradiology, Erlangen, Germany;*
[2]*Friedrich-Alexander-Universität Erlangen-Nürnberg (FAU), Institute of Radiology, Erlangen, Germany;*
[3]*Friedrich-Alexander-Universität Erlangen-Nürnberg (FAU), Department Artificial Intelligence in Biomedical Engineering, Erlangen, Germany;*
[4]*Max-Planck-Institute for Biological Cybernetics, Magnetic Resonance Center, Tübingen, Germany.*

Introduction MRI scanners, especially ultra-high-field (UHF) scanners with a static magnetic field (B_0) above 7 T, create new opportunities for medical imaging, such as high SNR and spectral resolution, but also new challenges. One major challenge is the inhomogeneity of the radiofrequency field (B_1^+), leading to artifacts in the generated images. The usage of parallel transmission (pTx) can address these problems by superimposing the fields of multiple transit coils.

An essential factor for pTx development is the ability to test new ideas fast. The Pulseq (1) standard and framework recently enormously improved fast MRI sequence prototyping. However, the existing Pulseq Framework does not yet support pTx radiofrequency (RF) pulse definitions. We herein present a simple pTx-Pulseq extension.

Methods To enable the pTx functionality, a pulse-specific B_1 shimming approach was selected. This approach is well-known as global adjustment before the experiment. To apply a pTx pulse, a uniform shape is transmitted to all pTx coils. The crucial point is that every channel can modulate in magnitude and phase.

To enable pulse-specific B_1 shimming, the Pulseq standard must be extended. Each RF event needs additional B1 shimming information. The additional information of magnitude factors and phase shifts are stored in the existing shape library (Fig. 1). The specific RF events definition is extended with two new library key identifiers. Using the shape library reduced the scope of modification in the existing Pulseq environment. The other required changes are enabling the Pulseq toolboxes (e.g. MatLab or PyPulseq (2)) to write this information to the sequence file and enabling the Pulseq interpreter on the scanner to read this new information and prepare the RF Pulses appropriately.

The approach was realized with a modified version of the PyPulseq toolbox. The RF block creation is extended with a new shim parameter based on 2D NumPy arrays. Two Pulseq interpreters for Siemens scanner on VE and VA bases are enabled to read the modified Pulseq files.

Results Images are shown in Fig. 2 with B_1 shimming on the one hand adjusted globally manually, showing the same results as Pulseq sequences with the new approach. Besides the well-known circular/elliptical modes (CP/EP), single pTx channel application also leads to identical results (Fig. 2 c, d, e, h).

The first implemented application is the time interleaved acquisition of modes (TIAMO) (2) approach. Here every k-space line is measured twice directly after each other, one with CP mode and one with EP mode. The final, more homogeneous image (Fig. 3) is generated by averaging both images. These alternating modes can be realized with this new approach. However, any sequence can now be quickly recreated, analyzed and optimized, as for example B1 Mapping (3) analyzed here for different saturation flip angles and B1 modes (Fig. 4).

Discussion The extension of the existing Pulseq standard enables MRI sequence developers to prototype pTx sequences without knowledge of vendor-specific programming environments. Using high-level programming languages allows scientists and even students to use pTx for sequence development without extensive programming skills.

The approach of B_1 shimming is limited in contrast to the full pTx application. Individually-shaped pTx pulses are not possible. Also, Pulseq is not designated for the online adaption of sequences. The major advantage of significantly reduced complexity of pTx sequence programming opens the field of pTx to a wide range of new developers and reduced evolution cycles. And many interesting approaches are possible to realize, such as Multiple interleaved mode saturation (MIMOSA) (4) for CEST Imaging, PUSH for MT MRI (5), k-T Points universal pulses (6) or Direct signal Control (DSC) (7), as well as many related and new prototypes.

Conclusion The B1 shimming extension enables to use the well-known Pulseq standard to realize pTx sequences. For Pulseq users, the application of pTx pulses differs in only one additional parameter in the RF event definition. Pulseq with pulse-specific B1shimming provides pTx functionality with some limits, but with the availability to a much wider range of users.

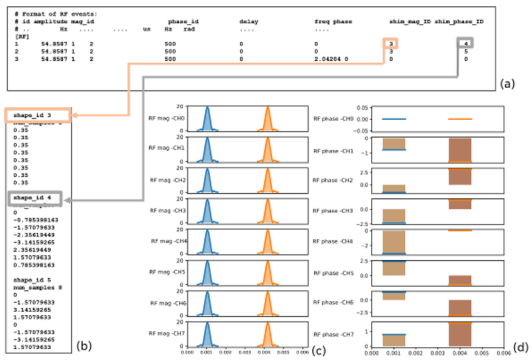

Fig. 1: (a) The first and second pulse has shim parameters stored in shape IDs 3, 4 and 5 . The other RF events have ID 0 and do not experience shim modification. (b) The shim information for magnitude (id3) , the phase for CP (id4) and EP (id5) is stored in the shape section. A new plot function (c,d) can visualize the modulated pulses.

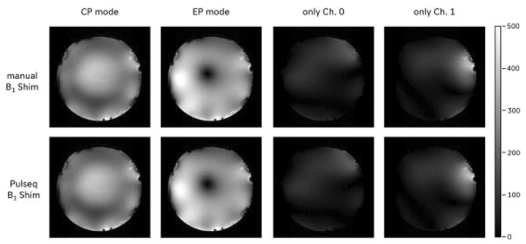

Fig. 2: (a,b,c,d) images generated with manual B1 shim. (e,f,g,h) images generated with Pulseq B1 shim. (a,e) CP mode. (b,f) EP mode, (c,g) only ch0 active. (d,h) only ch1 active.

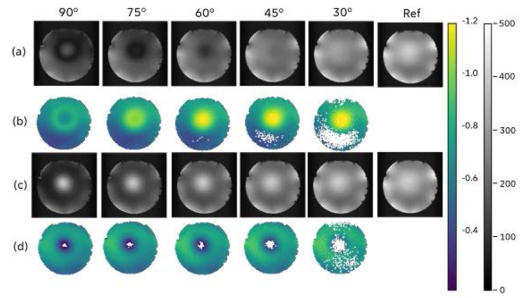

Fig. 4: The first row (a) shows the image with a preparation pulse of the corresponding flip angle. The pTx mode was CP. The 3rd row (c) shows the same with EP mode. The resulting B1-Maps are visualized in (b,d). The right column shows the reference image.

References

1. Layton KJ et al. MRM 2017, https://doi.org/10.1002/mrm.26235
2. Orzada S, et al. MRM 2010 https://doi.org/10.1002/mrm.22527
3. Chung S, et al. MRM 2010 https://doi.org/10.1002/mrm.22423
4. Liebert A, et al. MRM 2019 https://doi.org/10.1002/mrm.27762
5. Leitão, D, et al. MRM 2022 https://doi.org/10.1002/mrm.29199
6. Cloos MA, et al. MRM 2012 https://doi.org/10.1002/mrm.22978
7. Malik SJ, et al. MRM 2015 https://doi.org/10.1002/mrm.25192

LT54.
Vendor-agnostic pulse programming on gammaSTAR: A traveling head experiment to test the Philips driver

M. Nagtegaal[1,2], D. C. Hoinkiss[3], S. Konstandin[3,4], J. de Bresser[5], M. Günther[3,4,6], M. J. P. van Osch[1]

[1]*Leiden University Medical Centre, C.J. Gorter MRI Center, Leiden, Netherlands;*
[2]*Delft University of Technology, Imaging Physics, Delft, Netherlands;*
[3]*Fraunhofer Institute for Digital Medicine MEVIS, Imaging Physics, Bremen, Germany;*
[4]*mediri GmbH, Heidelberg, Germany;*
[5]*Leiden University Medical Centre, Radiology, Leiden, Netherlands;*
[6]*University of Bremen, Bremen, Germany*

Introduction One of the main things that a MR researcher does at a MR conference is admiring the novelties in newly proposed sequences and wondering how well this might work at their own institute. Often this does not come any further than wondering, since running this new sequence directly at a scanner from a different vendor or at a different software release is not trivial. Vendor-independent pulse programming environments [1–5] can overcome such problems by defining the MR pulse sequence in an open format that can be run afterwards on every MR scanner as long as a suitable driver is available for this open format. This step can be seen as essential to make MR pulse programming more accessible, reproducible and transparent, eventually making sharing sequences as easy as sharing code via github and a QR code on your poster.

Broader adaptation of vendor-agnostic pulse programming relies on the number of supported platforms, the supported functionalities and the available example sequences. GammaSTAR [5] uses a Lua based backend to support information exchange between the MR scanner and the imaging protocol, that allows for positioning and communication of hardware constraints. In this work, we focussed on the further development of a Philips driver for gammaSTAR imaging protocols and show the first traveling head results using gammaSTAR imaging protocols.

Methods The gammaSTAR backend, as implemented in Lua, is running on the Philips MR scanner and gradient shapes, RF shapes, ADC events, container objects and scaling parameters are calculated on call. Before calculating the exact pulse sequence hardware constraints, such as RF pulse waiting times and gradient slew rates, need to be taken into account. Such constraints may depend on the planning, therefore information about positioning are sent on the fly to the gammaSTAR backend. All information required for reconstruction, such as matrix size, parallel imaging factor, resolution and labels per readout are transferred to the scanner for on-scanner reconstruction. A similar implementation was already working on Siemens scanners.

Experiments In vivo brain MR scans were performed on the same volunteer on a 3 T Philips Achieva TX scanner (Philips, Best, The Netherlands) and a 3 T Siemens Magnetom Vida Fit scanner (Siemens Healthineers, Erlangen, Germany). A 3D FLASH sequence, TE = 5 ms, TR = 10 ms, flip angle = 15°,1 mm × 1 mm × 5 mm resolution, matrix size = 256 × 256 × 32, 2 ms readout duration (https://gamma-star.mevis.fraunhofer.de/3D_FLASH_sequence_readonly.html#/) and a 3D MP-RAGE, TE = 2.6 ms, TR = 2.2 s, TI = 0.9 s, flip angle = 8°, 2 mm isotropic resolution, matrix size = 128 × 128 × 32, 3 ms readout duration (https://gamma-star.mevis.fraunhofer.de/3D_MP-RAGE_sequence_readonly.html#/), were acquired on both scanners with a gammaSTAR protocol and a vendor native protocol that was set as similar as possible. Reconstruction was performed via the reconstruction framework of the vendor.

Results Fig. 1 and Fig. 2 show the obtained FLASH and MP-RAGE scans for a set of representative slices. Figure 3 and 4 show a close-up of gammaSTAR sequences on the two vendors. Images look largely similar, main differences can be seen in positioning, image homogeneity, due to different settings for coil sensitivity correction, and image blurring.

Discussion and conclusion Compared to our previous work on the development of gammaSTAR on Philips [6] we have further integrated the Philips workflow and gammaSTAR backend allowing for longer, 3D sequences with parameter transfer between vendor software and the gammaSTAR backend. All Philips safety checks are performed before the scan is executed, ensuring the safety of the subject and scanner. This could have resulted in relatively slow behaviour of the driver for higher resolutions, although this could be mitigated by introducing partial preparation stages for loop structures. A vendor-neutral reconstruction, such as BART or Gadgetron [7,8], will further increase the similarity between the acquired images as desired for future use in multi-centre, multi-vendor studies focussed on clinical trials or reproducibility. Our next step will be to explore more complex, quantitative sequences as ASL in a future traveling head study.

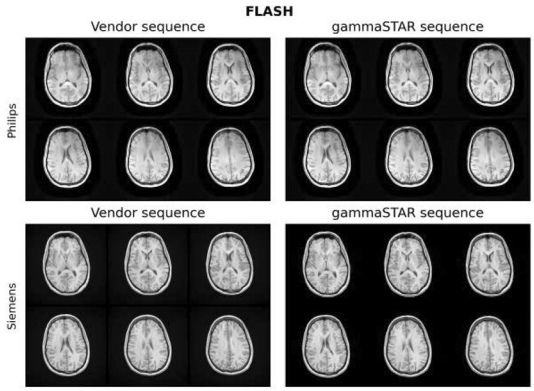

Fig. 1: In vivo FLASH scans as acquired on Philips and Siemens with gammaSTAR and vendor implementations. Grey scale was scaled from 0 to 1.5 times the mean intensity of the non-air voxels in the central slice. Central slices (6 out of 32) are shown for visibility purposes.

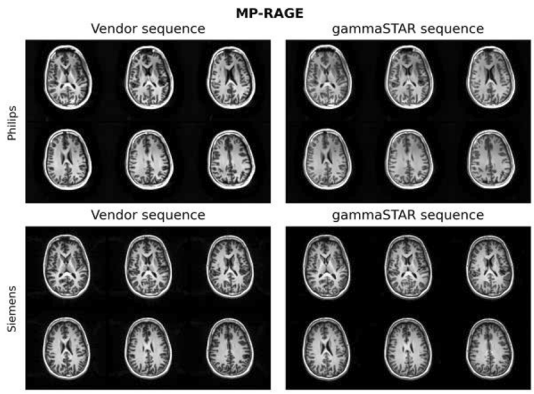

Fig. 2: In vivo MP-RAGE images as acquired on Philips and Siemens with gammaSTAR and vendor implementations. Grey scale was scaled from 0 to 2 times the mean intensity of the non-air voxels. For visibility purposes only 6 out of 32 are shown, while skipping every second slice.

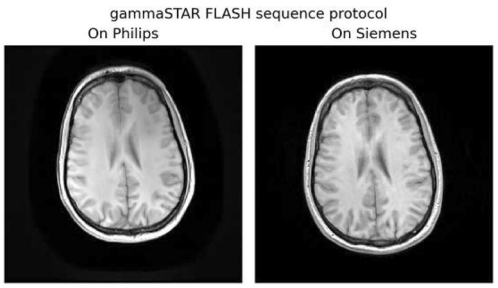

Fig. 3: FLASH scans as acquired on Philips and Siemens with gammaSTAR implementations of a centre slice for more detail. Grey scale for each image set was scaled from 0 to 1.5 times the mean intensity of the non-air voxels.

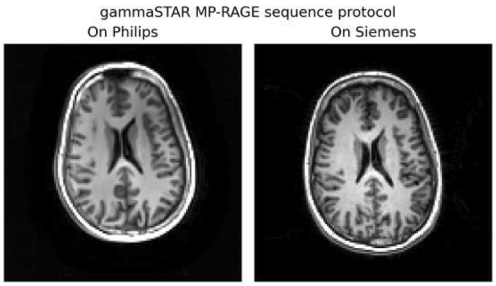

Fig. 4: MP-RAGE scans as acquired on Philips and Siemens with gammaSTAR implementations of a centre slice for more detail. Grey scale for each image set was scaled from 0 to 2 times the mean intensity of the non-air voxels.

References

[1] T. H. Jochimsen and M. von Mengershausen, *J. Magn. Reson. San Diego Calif 1997*, 2004, https://doi.org/10.1016/j.jmr.2004.05.021.
[2] J. F. Magland et al., *MRM*, 2016, https://doi.org/10.1002/mrm.25640.
[3] K. J. Layton et al., *MRM,* 2017, https://doi.org/10.1002/mrm.26235.
[4] J.-F. Nielsen and D. C. Noll, *MRM*, 2018, https://doi.org/10.1002/mrm.26990.
[5] C. Cordes et al., *MRM*, 2020, https://doi.org/10.1002/mrm.28020.
[6] M. Nagtegaal et al., in *Proc. ISMRM 31 (2023)*, Toronto, Jun. 2023.
[7] M. S. Hansen and T. S. Sørensen, *MRM*, 2013, https://doi.org/10.1002/mrm.24389.
[8] M. Blumenthal et al., "mrirecon/bart: version 0.8.00." 2022. https://doi.org/10.5281/ZENODO.592960.

LT55.
Extended validation of a deep learning-based brainstem segmentation

B. Gesierich[1], L. Sander[2,3], L. Pirpamer[1], D. Meier[1], E. Ruberte[1,3], M. Amann[1], A. Huck[4], F. E. de Leeuw[5,6], MarkVCID Consortium, PROMESA Study Group, J. Levin[7,8,9], P. Cattin[4], C. Granziera[2,3], R. Schläger[2,3], M. Duering[1]

[1]*University of Basel, Medical Image Analysis Center (MIAC), Basel, Switzerland;*
[2]*University of Basel, Neurologic Clinic and Policlinic, Departments of Neurology and Clinical Research, Basel, Switzerland;*
[3]*University of Basel, Translational Imaging in Neurology (ThINk) Basel, Department of Biomedical Engineering, Basel, Switzerland;*
[4]*University of Basel, Department of Biomedical Engineering, Center for Medical Image Analysis & Navigation (CIAN), Allschwil, Switzerland;*
[5]*Radboud University Medical Center, Donders Institute for Brain Cognition and Behaviour, Center for Neuroscience, Department of Neurology, Nijmegen, Netherlands;*
[6]*Radboud University, Donders Institute for Brain, Cognition and Behaviour, Center for Cognitive Neuroimaging, Nijmegen, Netherlands;*
[7]*Ludwig-Maximilians-University Munich, Department of Neurology, Munich, Germany;*
[8]*German Center for Neurodegenerative Diseases, Munich, Germany;*
[9]*Munich Cluster for Systems Neurology, Munich, Germany*

Introduction Previously, we developed a neural network model based on multi-dimensional gated-recurrent-units (MD-GRU) providing accurate and highly reproducible brainstem segmentations in healthy controls (HC), patients with multiple sclerosis (MS) and

Alzheimer"s disease (AD).[1] However, this model was trained on a limited set of T1-weighted (T1w) data in terms of MRI sequences and diseases.

The aim of the current study was to re-train the MD-GRU algorithm with an extended ground truth dataset, to extend clinical and technical validation, and to benchmark MD-GRU against a state-of-the-art method.

Methods The previously used ground truth (GT) dataset (161 multiple sclerosis patients from the Swiss Multiple Sclerosis Cohort[2] and 17 healthy controls; 3D T1w scans at 1.5 and 3 Tesla) was extended with data from 77 elderly subjects with cerebrovascular disease.[3] We further increased GT heterogeneity by including different T1w sequences (including MP2RAGE) and scanner manufacturers (Philips, GE, Siemens). GT masks were created as previously described,[1] and the GT dataset was split into independent training, validation and test sub-samples. Eleven models were trained with varying patch size, loss function, data augmentation or cropping around brainstem, and compared in the validation sample. The best model was further evaluated and benchmarked in the test sample (n = 39).

For clinical validation, brainstem atrophy over a one year period was assessed in a cohort of patients with multiple system atrophy (MSA) from the PROMESA trial (21 patients).[4] For technical validation, scan-rescan repeatability (46 subjects) and inter-scanner reproducibility across 3 different 3 T scanners (20 traveling subjects) was assessed in data from the MarkVCID consortium (funded by NINDS/NIA, U24NS100591).[5,6] Results were benchmarked against the FreeSurfer brainstem pipeline (version 7.2).

Results In the test sample the newly trained model showed excellent agreement with GT in all subjects (median Dice similarity coefficient (DSC) = 0.95), with higher DSCs than the previous model in most subjects (Fig. 1). As expected, the greatest improvements over the old model were observed in the newly added T1-weighted sequence variants, the new model was trained for.

In patients with MSA, MD-GRU consistently detected brainstem atrophy in all patients, while the longitudinal FreeSurfer pipeline (FS.long) showed a volume increase in two out of 21 patients. This increase is pathophysiologically implausible in a rapidly progressing neurodegenerative disease like MSA (Fig. 2).

Scan-rescan repeatability and inter-scanner reproducibility was investigated using Bland–Altman statistics, showing overall similar performance for the new MD-GRU model and longitudinal FreeSurfer (Fig. 3 and 4).

Discussion The re-trained MD-GRU model showed superior performance over the old model, with the most improvement observed in heterogeneous data. Systematic validation including benchmarking showed slightly improved (clinical validation) or similar (technical validation) performance compared with the state-of-the-art longitudinal FreeSurfer pipeline.

Conclusion Results demonstrate the importance of adapting deep learning-based models to MRI sequences and diseases of interest. The retrained model provides a robust and accurate segmentation method for research and clinical trials.

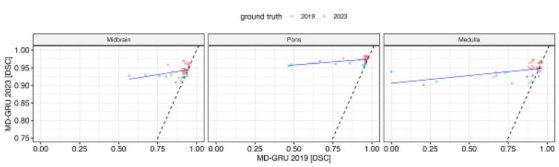

Fig. 1: DSC for new (MD-GRU 2023) versus previous (MD-GRU 2019) model in three brainstem subregions. Data points above the identity line (dashed) indicate better performance for the new model. Original test data depicted in red, newly added data in blue.

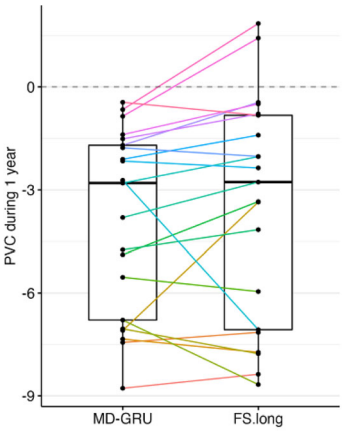

Fig. 2: Percentage volume change over one year in 21 MSA patients from PROMESA, measured with MD-GRU and FreeSurfer longitudinally. Colored lines indicate patients.

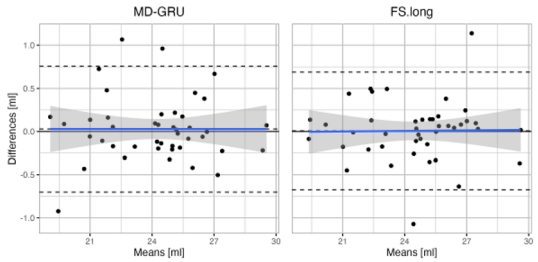

Fig. 3: Bland-Altman plot showing bias, limits of agreement (dashed lines) and proportional bias (blue line) with confidence interval (gray shade) for the comparison of inferred brainstem volumes (ml) in retest versus test scan; new MD-GRU model (left) and FreeSurfer (right).

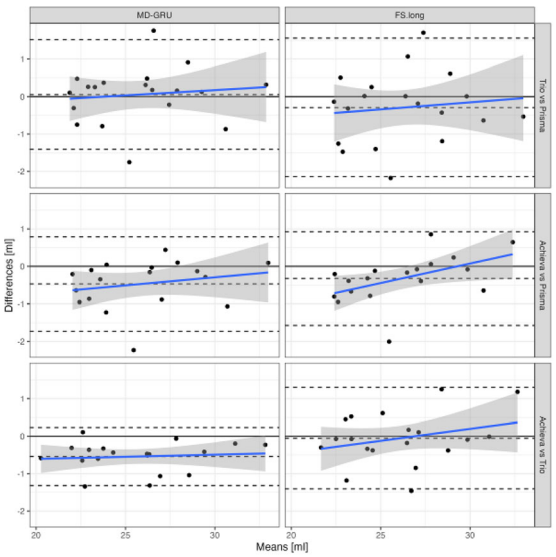

Fig. 4: Bland-Altman plot for the pairwise comparison of inferred brainstem volumes (ml) between three scanners: Siemens Prisma and Trio, and Philips Achieva; plot elements as in Fig. 3.

References

1. Sander, L. et al. Accurate, rapid and reliable, fully automated MRI brainstem segmentation for application in multiple sclerosis and neurodegenerative diseases. Hum Brain Mapp 40, 4091–4104 (2019).
2. Benkert, P. et al. Serum neurofilament light chain for individual prognostication of disease activity in people with multiple sclerosis: a

retrospective modelling and validation study. Lancet Neurol. 21, 246–257 (2022).
3. van Norden, A. G. et al. Causes and consequences of cerebral small vessel disease. The RUN DMC study: a prospective cohort study. Study rationale and protocol. BMC Neurol. 11, 29 (2011).
4. Levin, J. et al. Safety and efficacy of epigallocatechin gallate in multiple system atrophy (PROMESA): a randomised, double-blind, placebo-controlled trial. Lancet Neurol. 18, 724–735 (2019).
5. Lu, H. et al. MarkVCID cerebral small vessel consortium: II. Neuroimaging protocols. Alzheimers Dement. J. Alzheimers Assoc. 17, 716–725 (2021).
6. Maillard, P. et al. Instrumental validation of free water, peak-width of skeletonized mean diffusivity, and white matter hyperintensities: MarkVCID neuroimaging kits. Alzheimers Dement. Amst. Neth. 14, e12261 (2022).

LT56.
CNN-based automatic measurement of wrist cartilage volume from MR images

E. Brui[1], N. V. Vladimirov[1], A. Levchuk[1,2], W. Al-Haidri[1], V. Fokin[1,2], A. Efimtcev[1,2], D. Bendahan[3]

[1]*ITMO Universiry, Faculty of Physics, Saint Petersburg, Russian Federation;*
[2]*Federal Almazov North-West Medical Research Center, Department of Radiology, Saint Petersburg, Russian Federation;*
[3]*Aix-Marseille Université, Center for Magnetic Resonance in Biology and Medicine, Marseille, France*

Introduction MRI can be used to assess cartilage loss in a variety of conditions as long as cartilage regions can be properly delineated. Given that manual segmentation of small and complex joints (for example, wrists) is a tedious procedure [1], automatic methods would be of high interest. Convolutional neural networks (CNNs) are currently the most accurate automatic methods for segmenting biomedical structures. So far, very few automatic segmentation methods have been reported for wrist cartilage and the reported accuracy was very poor [2]. In the present work, we used another CNN-based approach and we hereby report the corresponding accuracy regarding volumetric wrist cartilage measurement.

Subjects/Methods The dataset contained 30 3D VIBE images of 16 volunteers (12 healthy and 4 with low grade of wrist cartilage loss) that resulted in 1297 2D slices (Dataset#1). In addition, 15 images from 15 patients with confirmed rheumatoid or osteoarthritis (826 2D slices) were acquired (Dataset#2). The images were obtained from 1.5 T and 3 T MRI. The scanning parameters were as follows: FOV varied between 75 × 75 mm^2 and 130 × 130 mm^2, TR—10 ms–18.6 ms, TE—3.38 ms–7.6 ms, voxel size—0.146 × 0.146 × 0.4 mm^3–0.508 × 0.508 × 0.5 mm^3, matrix size—256 × 256–260 × 320. The flip angle was constant (10°) in all variants of the pulse sequence. Some subjects were scanned twice with different RF coils, and some had a scan of both hands. Cartilage in MR images was manually segmented by a more than 10-year experienced radiologist. A cross-validation approach was used in order to estimate the best achievable performance, first, on Dataset#1, and then for fine-tuning of all layers of the best CNN on Dataset#2. This two-stage training was used given the significantly different morphology of healthy and diseased wrists. Using the GroupKFold from sklearn library, the datasets were divided into 5 subsets (with 20% of the total amount of 3D images in each) and used for a fivefold cross-validation analysis.

A classical U-Net architecture was supplemented by attention layers integrated into skip connections for reducing false positive results from regions out of the wrist joint area [3]. Layers of batch normalization, noise and spatial dropout were added in order to improve convergence time and decrease generalization error. The noise was added as a Tensorflow layer directly to the CNN input. Adam optimization algorithm was used for training with a fixed batch size (32) and cross-entropy was used as the loss function. Several hyperparameters were adjusted throughout the training process via a grid search i.e. learning rate (from 6*10–4 to 3*10–3), utilization of learning rate decay (from $50*10^{-4}$ to $5*10^{-4}$), noise level (from 0 to 0.5) and dropout probability (from 0 to 0.5). In addition, nn-U-Net [4] state-of-the-art framework was tested on our datasets. 3D Dice similarity coefficients and the error of cartilage volume estimation with respect to the manual labels were used as performance metrics.

Results/Discussion After training and testing on Dataset#1, U-Net_AL provided the best agreement between the predicted cartilage volumes and the manually measured ones (see the Pearson coefficients in the plots in Fig. 1). It also demonstrated the best median 3D DSC metric (0.817) and the lowest error of volume estimation (17.21%) (Fig. 2). When the U-Net_AL trained on the Dataset#1 was tested on Dataset#2 without any fine-tuning, its performance reduced dramatically (down to DSC = 0.724 and volume error = 26.10%). Fine-tuning the network allowed to achieve a higher performance i.e. DSC = 0.806, volume error = 9.52%. Examples of cartilage segmentation performance for the U-Net_AL network (with and without fine-tuning) is presented in Fig. 3 (a) and (b), correspondingly. An example of 3D cartilage image is presented in Fig. 3 (c).

To the best of our knowledge, quantification of wrist cartilage volume has not been reported so far in different stages of OA or RA. At the same time, for patients with knee osteoarthritis, the volume cartilage loss over 10 years in the medial and lateral sections has been estimated to be 19.1% and 13.8% respectively [5]. Of interest, this value is larger than the error provided by the U-Net_AL. Taking this into account, it should be further investigated whether the cartilage volume error achieved using the U-net_AL (9.52%) would be small enough to detect cartilage loss in the wrist joint in arthritis.

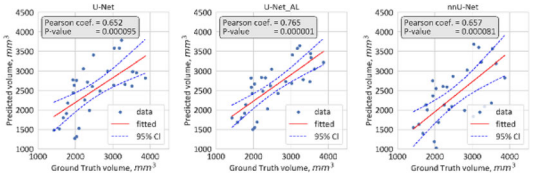

Fig. 1: Correlation plots and Pearson correlation coefficient (r) and p-value (p) between predicted (by three types of CNNs) and Ground truth cartilage volume.

Metric	U-Net	U-Net_AL	nnU-Net	U-Net_AL*	U-Net_AL**
3D DSC	0.810 [0.780, 0.822]	**0.817 [0.785, 0.838]**	0.814 [0.748, 0.849]	0.724 [0.673, 0.758]	0.806 [0.768, 0.811]
Mean Relative error of volume (%)	19.72	**17.21**	21.4	26.10	9.52

*U-Net_AL trained on Dataset#1 and tested on Dataset#2. **U-Net_AL trained on Dataset#1, fine-tuned on Dataset#2, and tested on Dataset#2. **Bold** – the best performance among three CNNs on the Dataset#1.

Fig. 2: Segmentation performance metrics

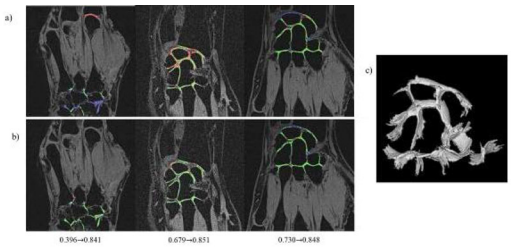

Fig. 3: Examples of segmentations of patients" data using U-net_AL a) - before fine-tuning on patients" data, b) - after fine-tuning. The corresponding 2D DSC values are shown below the images. Red – false positive, blue – false negative, green – true positive pixels. c) Example of the obtained 3D image of wrist cartilage in a healthy subject.

References

1. Zink JV, et al. World J Orthop. 2015;6(8):641
2. Brui E, et al. NMR Biomed. 2020;33(8)
3. Oktay O, et al. ArXiv. 2018;abs/1804.03999:10
4. Isensee F, et al. Nat Methods. 2021 Feb;18(2):203–211
5. McBride A, et al. BMC Musculoskelet Disord. 2016;17(1):54

LT57.
Deep learning-based lung volume segmentation of DCE-MRI data sets of 2-year-old children after congenital diaphragmatic hernia repair

M. S. Koçak[1], A. Raj[1,2], V. Sommer[3], K. Zahn[4], T. Schaible[5], M. Weis[3], F. G. Zöllner[1,2]

[1]*University of Heidelberg, Computer Assisted Clinical Medicine, Mannheim, Germany;*
[2]*Mannheim Institute for Intelligent Systems in Medicine, Medical Faculty Mannheim, Heidelberg University, Mannheim, Germany;*
[3]*Department of Radiology and Nuclear Medicine, University Medical Center Mannheim, Medical Faculty Mannheim, Heidelberg University, Mannheim, Germany;*
[4]*Department of Pediatric Surgery, University Medical Center Mannheim, Medical Faculty Mannheim, Heidelberg University, Mannheim, Germany;*
[5]*University of Heidelberg, Department of Neonatology, Mannheim, Germany*

Introduction In congenital diaphragmatic hernia (CDH) better treatment strategies shifted the focus from mortality to morbidity after repair [1]. Therefore, the follow-up and recovery of such patients with respect to lung function is important. MRI of the lungs has been proposed as a candidate to estimate perfusion and/or ventilation using non-contrast and contrast-enhanced techniques [2–4]. In this, lung segmentation can help automate not only the workup of these patients to either quantify perfusion or ventilation but also the lung volume. Lung segmentation in 2-year-old children after CDH repair has been performed so far either manually [4] or by a semi-automated approach [5]. Here, we propose an automated, deep learning-based method for lung volume segmentation of DCE-MRI images.

Methods 29 children after CDH repair were retrospectively included in this study. Briefly, DCE-MRI was performed following the protocol described in [4] using a 3D TWIST sequence with a matrix of 256 × 256, 56 slices, and isotropic resolution of 1.98 × 1.98 × 1.98 mm^3. The ground truth was obtained by two radiologists supervised by an expert radiologist in lung MRI.

For the proposed segmentation approach, preprocessing including normalization and data augmentation with constrained label sample mining approach was done [6].

Deep learning networks that we have adapted for the lung segmentation task were previously developed having a U-Net architecture with Attention Module and Sharpness Aware Minimization [7] (see Fig. 1). This structure was developed to deal with small datasets. We explored two loss functions, i) cross-entropy combined with dice similarity coefficient (DSC) and ii) cosine (COS) loss [7]. Adam optimizer is utilized during training with a learning rate of 0.001 [8]. fivefold cross-validation with a split of 14:10:5 patients in train:validation:test sets is performed. Evaluation was performed by comparing the obtained segmentation to the ground truth and calculating the DSC, the mean symmetric surface distance (MSSD), and the total lung volume (TLV).

Results The Attention U-Net parametrized with a patch size of 96 × 96 and 640 samples mined from each training data sample showed the highest performance (DSC of 0.90 ± 0.06 and MSSD of 0.57 ± 0.28). Table 1 summarizes the performance of the different tested combinations. Figure 2 depicts segmentation masks overlayed to the MRI and ground truth segmentations of two cases. Figure 3 shows the correlation between manually segmented and predicted TLVs reaching a correlation coefficient of r = 0.90.

Discussion In this work, an automated whole-lung segmentation algorithm was implemented and evaluated with the DCE-MRI data of 29 children who had undergone CDH repair. Our results show that the developed algorithm can label the right and left lungs separately using a low number of datasets. Investigating cases in the dataset with low performance, we observed that air pockets in the abdomen are falsely segmented as lungs. Connected component analysis seems to solve this issue to some extent.

To further enhance the overall performance either more annotated datasets should be included or self-supervised techniques such as few-shot learning should be explored [9]. Compared to a semi-automated approach on similar data [5] our method showed high DSC scores.

Conclusion In summary, we proposed a robust method to segment DCE-MRI images for 2-year-old children after CDH repair on a limited number of annotated data. We envision that this method further improves the workup of these patients and facilitates more easily assessment of morphological and functional parameters for the future prognosis of these children.

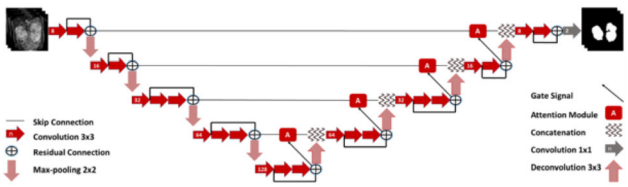

Fig. 1: Attention U-Net architecture. Adapted with permission from Ref. [7]. 2022, MDPI.

Loss Function	Training Dimension	Samples per Volume	Learning Rate	Number of Folds	DSC	MSSD (mm)	Average Predicted TLV (ml)
COS	96	80	0.001	5	0.89±0.06	0.67±0.31	388.78±85.62
Cross-entropy + DSC	96	80	0.001	5	0.89±0.06	0.71±0.34	396.26±84.39
COS	128	80	0.001	5	0.88±0.06	0.72±0.32	377.81±90.67
Cross-entropy + DSC	128	80	0.001	5	0.89±0.06	0.64±0.33	382.73±84.53
Cross-entropy + DSC	96	40	0.001	5	0.89±0.06	0.71±0.34	389.03±87.20
Cross-entropy + DSC	96	160	0.001	5	0.90±0.06	0.62±0.32	389.183±84.04
Cross-entropy + DSC	96	320	0.001	5	0.90±0.05	0.58±0.29	390.00±80.74
Cross-entropy + DSC	**96**	**640**	**0.001**	**5**	**0.90±0.06**	**0.57±0.28**	**382.54±78.90**
Cross-entropy + DSC	96	80	0.01	5	0.69±0.27	3.48±6.20	330.27±142.99
Cross-entropy + DSC	96	80	0.0001	5	0.88±0.05	0.71±0.30	384.12±88.18
Cross-entropy + DSC	96	80	0.00001	5	0.74±0.16	2.57±3.38	302.69±114.77
Cross-entropy + DSC	96	80	0.001	3	0.88±0.06	0.76±0.37	389.88±89.27
Cross-entropy + DSC	96	80	0.001	10	0.88±0.08	1.03±1.74	387.91±101.98

Table 1: DSC, MSSD, and average predicted TLV values for Attention U-Net with different loss functions and network parameters. Since Attention U-Net was the one outperforming other architectures its network settings are tested for different scenarios. DNC: Does not converge.

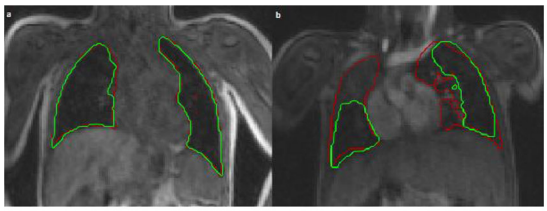

Fig. 2: Segmentation outcomes for best and worst cases. Manual segmentation is contoured with red and predicted segmentation is contoured with green. In a, segmentation with highest DSC is shown whereas in b segmentation with lowest DSC is shown.

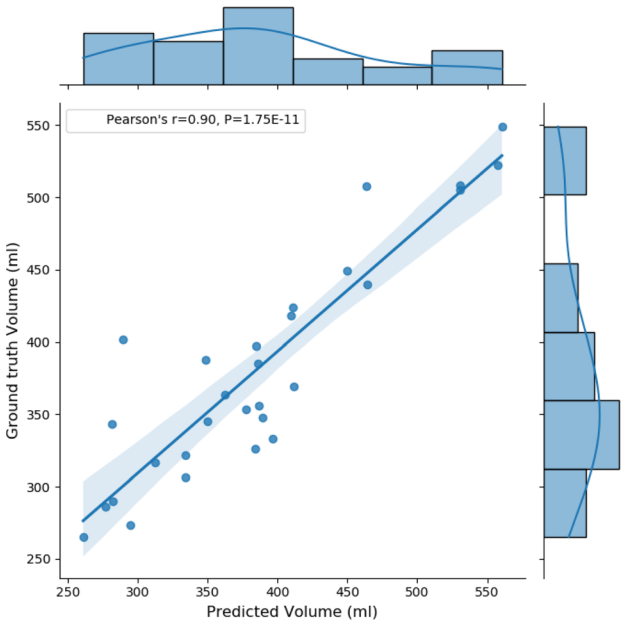

Fig. 3: The correlation scatter plot for ground truth TLV vs. predicted TLV in ml.

References

[1] K. G. Snoek, Neonatol. 110, 66–74, 2016.
[2] O. Pusterla et al., Magn Reson Med 88, 391–405, 2022.
[3] J. R. Astley et al., Brit. J. Radiol. 95, 2022.
[4] M. Weis et al., Eur. Radiol. 26, 4231–4238, 2016.
[5] Zöllner et al., Magn Reson Imaging 33, 1345–1349, 2015.
[6] A. K. Schnurr et al., Proc. 3rd Int. Conf. Funct. Renal Imag., 1–5, 2019.
[7] A. Raj et al., Diagnostics 12, 2022.
[8] D. P. Kingma & J. Ba, arXiv:1412.6980, 2014.
[9] S. Hansen et al., Med Image Anal 78, 2022.

LT58.
How to establish and maintain a multimodal animal MRI dataset using DataLad

A. Kalantari Sarcheshmeh[1], M. Aswendt[1], M. Szczepanik[2], S. Heunis[2], C. Mönch[2], M. Hanke[2], T. Wachtler[3]

[1]*University Hospital Cologne, Neurology, Cologne, Germany;*
[2]*Research Centre Juelich, Institute of Neuroscience and Medicine 11, INM-11, JARA, Jülich, Germany;*
[3]*Ludwig-Maximilians-University Munich, Faculty of Biology, Planegg-Martinsried, Germany.*

Introduction Sharing data, processing tools, and workflows require open data repositories and management tools. Despite the increasing demand from funding agencies and publishers, the number of animal studies that share raw data and processing tools is small compared to human studies. In addition, an open-sharing policy is not sufficient to achieve reproducibility if necessary metadata is missing. Here, we present a step-by-step protocol to perform version control and remote collaboration for an existing large dataset including MRI, behavioral, electrophysiological, and microscopy data.

Methods The workflow (Fig. 1) builds upon free and open-source software: Python (https://www.python.org/), the GIN server (https://gin.g-node.org), and DataLad (https://www.datalad.org). In the first step, a data management plan was implemented to ensure data safety including a decentralized automated backup scheme, a unique identi fier for each animal (Study ID), and a standardized data structure based on the "YODA principles" and the BIDS standards. The second step was to share the data in an open public repository (GIN). Finally, changes to the data, i.e., which user changed what and when were automatically tracked using DataLad [5]. The workflow can be divi ded into several steps: 1. Initialization of DataLad, 2. Version control, 3. Initialization of GIN, 4. Uploading data to GIN (Fig. 2).

Results/Discussion This work provides a step-by-step guide for non-expert users to implement a FAIR data workflow for small animal data. GIN and DataLad were used for public data availability and data management, respectively. By encapsulating all elements of a project, such as input data, codes, and outputs, along with information about their connection, we implemented a workflow that ensured data preservation, efficient collaboration, data sharing, and improved internal reproducibility (Fig. 2). Building projects with this structure resulted in a clear timeline for the project's evolution. The consequences of errors, such as the accidental deletion of data or specific outputs, and the accumulation of the same data and outputs with only different structures and names were avoided through this workflow. In summary, the establishment of this type of project structure has resulted in great time savings, not only for the project researchers but also for other external researchers.

Conclusions This use case implementation serves as a technical infrastructure blueprint with rich potential to improve data handling at other sites and extend to other research areas. In line with the 3R principle to reduce the number of animal experiments, this workflow enables the community to collect heterogeneously acquired and stored datasets not limited to a specific category of data.

Acknowledgment This work was supported by the Friebe Foundation (T0498/28960/16) and the Deutsche Forschungsgemeinschaft (DFG, German Research Foundation)—Project-ID 431549029—SFB 1451.

Disclosure I or one of my co-authors have no financial interest or relationship to disclose regarding the subject matter of this presentation.

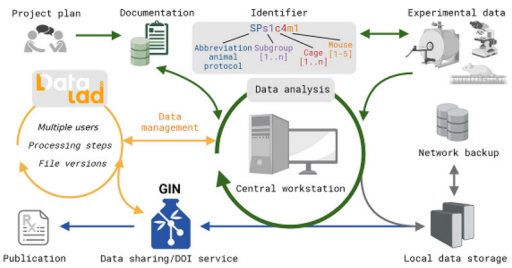

Fig. 1: Green arrows: workflow for project planning, data acquisition, processing, and storage; gray arrows: backup plan on local and network storages; orange arrows: integration of DataLad for version control; blue arrows: publication process using GIN as the online hosting service.

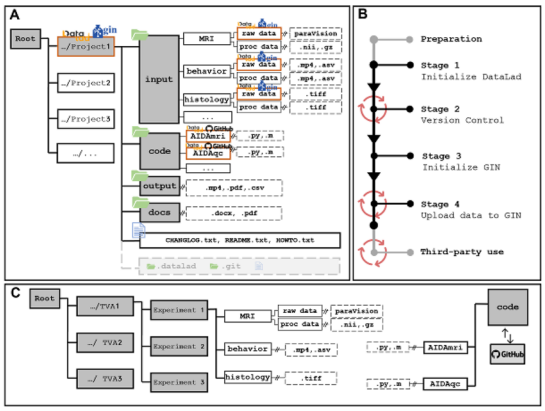

Fig. 2: (A) YODA-directory structure and integration of DataLad. During the conversion of the Project1 folder into a DataLad dataset, the corresponding DataLad files, (gray boxes), are created as additional information in the folder, without affecting the rest of the data. "raw_data" folders and all folders in "code" are independent subdatasets in the context of nesting and establishing decentralization with "code" being located in Github instead of GIN. (B) Step-by-step guide for creating the DataLad dataset (red circles highlight recurring stages). (C) Folder structure based on the permit of performing animal experiments without DataLad (TVA=Tierversuchsantrag (German: animal protocol).

LT59.
Transient hemodynamic effects in DIANA

M. Cloos[1], E. Selingue[2], S. Hodono[1], L. Ciobanu[2]

[1]*Centre for Advanced Imaging/ The University of Queensland, St Lucia QLD, Australia;*
[2]*NeuroSpin/CEA, Gif-sur-Yvette, France*

Introduction Conventional functional MRI techniques infer neuronal activity from hemodynamic changes, which limit the spatial and temporal specificity[1]. The direct imaging of neuronal activity (DIANA) method aims to overcome these limitations by measuring small MRI signal modulations expected to correlate with changes in neuronal membrane potential[2]. To observe such small neuronally specific signals, large hemodynamic signal changes must be suppressed. To first order, BOLD signal changes can be suppressed using short echo times. However, Cerebral Blood Volume (CBV) and Cerebral Blood Flow (CBF) effects are more difficult to eliminate, especially when imaging a single slice. In this work, we investigate the effect of transient hemodynamic effects on the DIANA signal using simulations and experiments performed on rats at 17.2 Tesla.

Methods *Simulations:* Simulations of the expected BOLD signal were performed in Matlab. The neuronal signal was modelled as a box-car (10 ms stimulus, 190 ms inter stimulus interval (ISI)) convolved with hemodynamic response function.

Experiments: All MRI acquisitions were performed on a 17.2 Tesla MRI system. The animals (Sprague Dawley rats, n = 2) were spontaneously breathing and anesthetized with 0.5% isoflurane and 0.1 mg/kg/h subcutaneously infused medetomidine. An optical fiber connected to a blue LED was placed in front of the left eye.

Multi-slice gradient echo echo-planar imaging (GRE-EPI) functional BOLD acquisitions were performed to determine the position of subsequent single-slice acquisitions. The visual paradigm consisted of 6 s LED-on and 12 s LED-off. Single slice Spoiled Gradient Recalled Echo (SPGRE) experiments were performed (TR/TE = 5/1.8 ms, 80 × 80 matrix, 250 × 250 × 1500 (μm)^3, FA = 6°, 240 runs) with normal k-space ordering (referred to as SPGRE, Fig. 1) and with the phase and measurement loops swapped (referred to as DIANA, Fig. 1). Each scan started with 16 s of dummy TR to stabilize the magnetization[3]. In addition, single-slice GRE-EPI data was also collected (TE/TR = 11/50 ms, 200 × 200 × 800 (μm)^3, FA = 12°, 6400 volumes). The stimulation paradigm consisted of 10 ms flashes of light with a 190 ms ISI (Fig. 2) and was turned on and off every 16 s (one run). In one rat, 6 scans were obtained with the stimulus paradigm continuously on.

Results & Discussion: *Simulations:* BOLD signal simulations show a ∼ 20 s transient before settling into a steady state (Fig. 2). Using an 80 × 80 matrix and 200 ms ISI, a single DIANA measurement takes 16 s. Therefore, simulations predict it will take more than one DIANA measurement for the hemodynamics to settle. Because of the swapped phase and measurement loops, markedly different hemodynamic signals are mixed throughout k-space. Similar to transient magnetization effects in TSE[4] and MPRAGE[5] sequences, the image contrast is dominated by the state of the transient signal in the central k-space lines, and signal variations observed between k-space lines translate to blurring. The question is: how large are these effects when using a short TE (1.8 ms)?

Experiments: Fig. 3 shows the signal detected using SPGRE and GRE-EPI acquisitions. Although the short TE in the SPGRE data reduces the BOLD signal change significantly, a clear transient (∼ 8 s) and increased steady state signal can still be observed. Given the shorter TE, it is likely that the SPGRE signal contains stronger CBV and CBF contributions. Using the same paradigm the DIANA data shows two distinct signal levels, reflecting the signal observed while collecting the central lines in k-space during rest and during stimulus driven activation (Fig. 4). Although the DIANA signal looks stable, there actually is a ∼ 1% hemodynamically driven signal mixed into the k-space data (Fig. 3C, & Figs. 4A, B), nearly one order of magnitude larger than the expected DIANA signal[2]. Arguably, a slowly evolving transient background signal would not preclude the detection of short "pulse-like" like DIANA responses. Nonetheless, DIANA acquisitions would clearly benefit from adding dummy stimuli besides dummy TR to drive both the spin-dynamics and hemodynamics into steady state before data collection. Accordingly. we acquired data with dummy stimuli (6 scans of 656 s each). However, no clear DIANA peak was detected (Fig. 4C).

Conclusion Although transient hemodynamic effects may not be apparent in the DIANA images, these signal changes are rolled into the data even when short TE and ISI are used. Using dummy stimuli to bring the hemodynamics to a steady state when collecting DIANA data should help improve data quality. In spite of implementing such an approach, no functional DIANA response could be detected in this study.

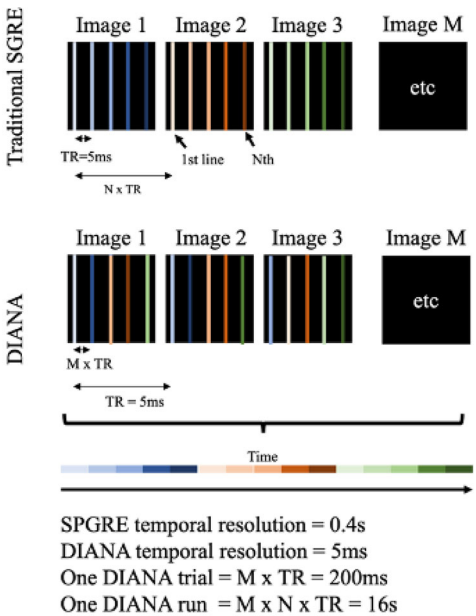

Fig. 1: *K-space sampling in SPGRE and DIANA acquisitions.*

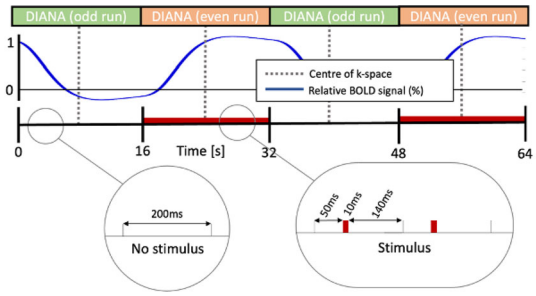

Fig. 2: *Simulated BOLD response when collecting four subsequent DIANA measurements. With 5ms TR and 80x80 matrix, one measurement takes 16s. Although a short (200ms) ISI is used, the expected BOLD response takes more than 16s to stabilize.*

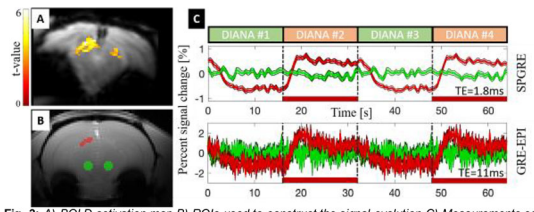

Fig. 3: *A) BOLD activation map B) ROIs used to construct the signal evolution C) Measurements collected in one rat [SPGRE (3 scans, 656s each), GRE-EPI (2 scans, 176s each)]. Data was cut into elements of 32s (one 16s block without and one 16s block with the stimulus paradigm enabled) and averaged across.*

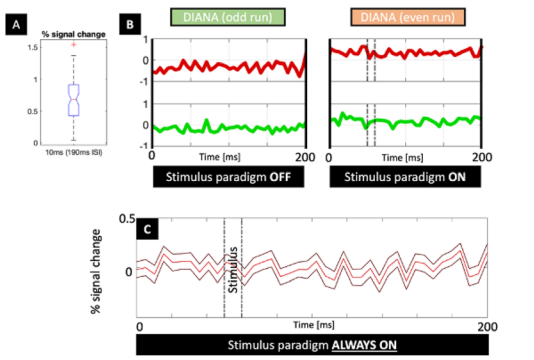

Fig. 4: *A) Percent signal change between even (stimulus paradigm on) and odd (stimulus paradigm off) DIANA measurements B) Exemplary DIANA data obtained in one rat showing the trial averaged signal in even and oddmeasurements (3 scans, 656s each) C) Exemplary DIANA data obtained in one rat showing the trial averaged signal when the hemodynamics are in a steady state (6 scans, 656s each).*

References:
1. N.K Logothetis, *Nature*. 453, 2008.
2. P.T Toi, et al. *Science*. 378, 2022.
3. S. Hodono, et al., *arXiv preprint arXiv:2303.00161*, 2023.
4. M.A. Bernstein, et al., *Handbook of MRI pulse sequences*. Elsevier, 2004.
5. J.P. Mugler 3rd, J.R. Brookeman, *Magn Reson Med,* 15, 1990.

LT60.
Pseudo-continuous arterial spin labelling but not BOLD-fMRI yields homogenous cerebrovascular reactivity of grey and white matter

F. Richter[1], J. Kufer[1], G. Hoffmann[1], L. Schmitzer[1], C. Gleissner[1], J. Göttler[1], S. Kaczmarz[1,2], C. Preibisch[1,3]

[1]*School of Medicine, Klinikum rechts der Isar, Technical University Munich, Department of Diagnostic and Interventional Neuroradiology, Munich, Germany;*
[2]*Philips GmbH Market DACH, Hamburg, Germany;*
[3]*Technical University of Munich, School of Medicine, Department of Neurology, Munich, Germany*

Introduction Cerebrovascular reactivity (CVR) reflects the brain vessels' ability to support an increase in cerebral blood flow (CBF) following a vasoactive stimulus and is a promising marker of vascular health.[1] Regional CVR can be obtained by magnetic resonance imaging (MRI) during a vasodilatory challenge, e.g., the inspiration of carbon dioxide (CO_2). Pseudo-continuous arterial spin labelling (pCASL) aims to quantify CBF-CVR directly, while blood oxygenation level dependent (BOLD) functional MRI (fMRI) is rather indirectly influenced by CBF. Still, BOLD-fMRI is most often used for CVR mapping due to its high sensitivity.[1–3] As of yet, most studies investigating the validity of BOLD-CVR by comparing it with pCASL-derived CBF-CVR have focused on grey matter (GM).[4,5] Recently, Taneja et al. examined BOLD- and CBF-CVR in GM and WM using a dual-echo sequence and found similar CBF-CVR in GM and WM, contrary to BOLD-CVR, which showed a clear GM-WM contrast.[6] As published CBF-CVR maps using different techniques are inconsistent in this regard,[1,7,8] we investigated the possible mismatch of BOLD- and CBF-CVR. To this end, we compared BOLD- and pCASL-based CVR among each other, as well as between GM and WM.

MethodsTwenty-one healthy participants (age 29.1 ± 8.6 years, 10 female) underwent MRI on a 3 Tesla Ingenia Elition X (Philips, Best, The Netherlands). We obtained T1-weighted anatomical data for GM/WM segmentation and, both, pCASL- and BOLD-fMRI within one session. As a vascular challenge, we employed a hypercapnia block paradigm (alternating medical air and 5% CO_2) with recording of end-tidal partial pressure of CO_2 (pCO_2; Fig. 1A, 1B). CVR was calculated as the percent signal (ΔS [%]) and CBF (ΔCBF [%]) change for BOLD and pCASL, respectively, divided by the change in end-tidal pCO_2 ($\Delta EtCO_2$ [mmHg]). For group-level comparisons, BOLD- and CBF-CVR were averaged across GM and WM in each subject. Subject-wise parameter averages were compared between GM and WM, as well as between BOLD and pCASL by paired t-tests and Pearson correlation (significance at $p < 0.05$).

Results Visual comparison of group-average CVR parameter maps (Fig. 1C, 1D) demonstrates a distinct GM-WM contrast for BOLD-CVR that is not apparent in CBF-CVR. BOLD-CVR shows lower absolute numbers (GM/WM: 0.25 ± 0.08/0.14 ± 0.04%/mmHg; Fig. 2A), in comparison to CBF-CVR (GM/WM: 3.6 ± 1.2/3.2 ± 1.0%/mmHg; Fig. 2B), and GM/WM differences are significant for BOLD- (Fig. 2A) but not CBF-CVR (Fig. 2B). There was a highly significant correlation between GM and WM, both for BOLD-CVR (r = 0.97; Fig. 2C) and CBF-CVR (r = 0.92; Fig. 2D). Further, correlation analysis revealed moderate agreement between BOLD- and CBF-CVR, which was comparable in GM and WM (rGM = 0.46/rWM = 0.42), approaching statistical significance (pGM = 0.06/pWM = 0.08; Fig. 3).

Discussion Our absolute GM CVR values obtained from CBF (3.6%/mmHg) and BOLD signal (0.25%/mmHg) are consistent with previous studies.[1,9,10] In accordance with Taneja et al.,[6] our values for BOLD-CVR are significantly lower in WM than GM (Fig. 2A), a contrast not seen in CBF-CVR (Fig. 2B). This also agrees with observations from PET studies.[11] Interestingly, CBF- and BOLD-CVR show a strong

WM-GM correlation across subjects (Fig. 2C, 2D). This indicates that the observed relations between GM and WM CVR (contrast for BOLD-CVR; homogeneity for CBF-CVR) are highly consistent on a single-subject level. Altogether, our findings confirm that, if optimally implemented with sufficiently long PLD (1800 ms), pCASL MRI may be used to quantify WM CBF-CVR. This is further supported by recent studies indicating the viability of CBF in GM as well as WM.[12] Regarding lower WM BOLD-CVR, lower WM cerebral blood volume has been discussed as a possible physiologic modulator.[5,13] Also, there is ongoing debate whether perfusion increases from hypercapnia are truly isometabolic,[14] which could add to discrepancies between BOLD and CBF-based CVR. In any case, these physiologic complexities affect the ratio of the BOLD- and CBF response across subjects, certainly contributing to their rather moderate correlation within GM and WM (Fig. 3).

Conclusion Our results support the notion that CBF-CVR reliably reflects comparable CVR in healthy GM and WM. Lower BOLD-CVR in WM is likely due to complexities of the BOLD signal in response to hypercapnia-induced perfusion increases in WM vs. GM, which needs to be explored in future studies.

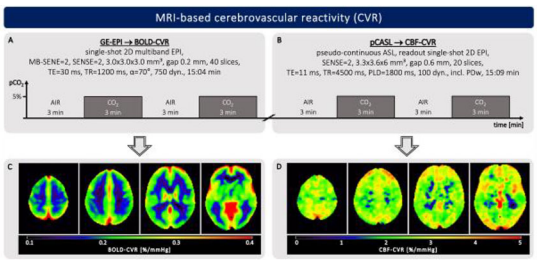

Fig. 1: A, B: MRI protocol: Sequence parameters and hypercapnia paradigm for BOLD-CVR **(A; GE-EPI)** and CBF-CVR **(B; pCASL)**. Gas mixes (AltiTrainer, SMTec, Switzerland) were applied via a sealed face mask. End-tidal partial pressure of CO_2 (pCO_2) and O_2 were recorded using a gas analyzer (AD Instruments, USA). **C, D**: Group average parameter maps of BOLD- **(C)** and CBF-CVR **(D)** with different scaling. Note the distinct mismatch of the GM-WM contrast between the two methods.

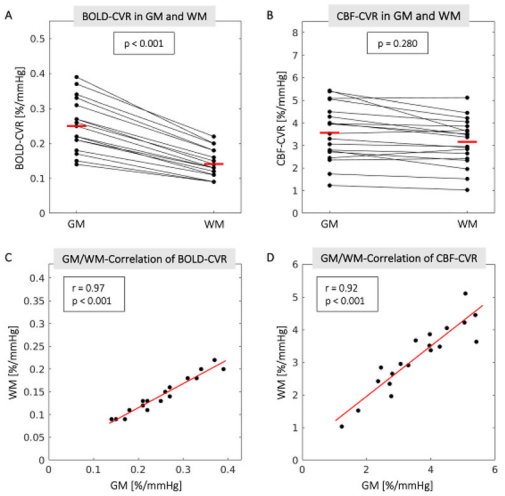

Fig. 2: A, B: Paired scatter plots of BOLD-CVR **(A)** and CBF-CVR **(B)**, comparing parameter values in GM and WM. **C, D**: Correlation of GM CVR and WM CVR for BOLD **(C)** and pCASL **(D)**. Red lines indicate mean values **(A, B)** and regression results **(C, D)**.

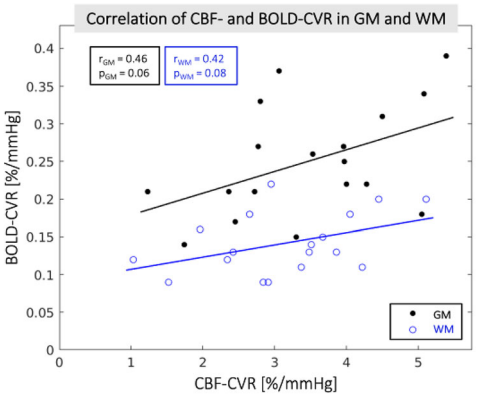

Fig. 3: Relationship of BOLD- and CBF-CVR in GM (black, filled dots) and WM (blue, open circles). Individual points indicate whole brain GM/WM averages of a single subject.

References

1: Sleight, Stringer;Front Physiol 2021.
2: Liu, De Vis;NI 2019.
3: Zhao, Woodward;JCBFM 2022.
4: Leoni, Oliviera;Braz J Med Biol Res 2017.
5: Zhou, Rodgers;MRI 2015.
6: Taneja, Liu;Front Neurol. 2020.
7: Hoffmann, Richter;ISMRM 2023.
8: Bokkers, van Osch;J Neurol Neurosurg Psych 2011.
9: Heijtel, Mutsaerts;NI 2014.
10: Bhogal, De Vis;NI 2016.
11: Zhao, Fan;NI 2021.
12: Dolui, Fan;NI Rep 2021.
13: Wang, Wang;NI 2023.
14: Driver, Front Neurosci 2017.

LT61.
BOLD cerebrovascular reactivity is correlated with baseline perfusion across the brain

C. Domingos[1], I. Esteves[1], A. R. Fouto[1], A. Ruiz-Tagle[1], C. Caballero-Gaudes[2], P. Figueiredo[1]

[1]*Universidade de Lisboa, Institute for Systems and Robotics-Lisboa and Department of Bioengineering, Instituto Superior Técnico, Lisbon, Portugal;*
[2]*Basque Center on Cognition, Brain and Language, Donostia, Gipuzkoa, Spain*

Introduction Cerebrovascular reactivity (CVR) measures the ability of vessels to change their diameter in response to vasoactive stimuli and it can be mapped across the brain using blood oxygenation level-dependent (BOLD) fMRI[1]. Two recent studies[2,3] have shown a positive coupling between BOLD-CVR and baseline cerebral blood flow (bCBF), measured using arterial spin labeling (ASL) in healthy subjects[2,3], while another study had shown a decrease of this coupling with aging[4]. However, this relationship is not well documented, with these previous studies[2,3,4] focusing on very specific resting-state networks[2] or gray matter (GM)[3,4]. Here, we investigate the relationship between BOLD-CVR and ASL-bCBF across the whole brain, including two main regions-of-interest (ROIs): GM and white matter (WM).

Methods Data AcquisitionA group of 14 healthy women (20–48 yrs) was studied on a 3 T Siemens Vida MRI System using a 64-channel head RF coil.

CVR mapping was performed using BOLD-fMRI during a breath-hold (BH) task (4 trials of 15 s BH alternated with 30 s cued normal breathing), with T2*-w GRE-EPI (TR/TE = 1260/30 ms, GRAPPA = 2, SMS = 3, 60 slices, 2.2 mm isotropic resolution). Expired carbon dioxide (CO2) was measured using a Medlab CAP10 capnograph and a nasal cannula, and the partial pressure of the end-tidal CO2 (PetCO2) signal was obtained by peak detection of the capnograph trace. The PetCO2 change was averaged across the four BH tasks for each subject to yield the mean ΔPetCO2 in mmHg.bCBF mapping was performed using pseudo-continuous ASL (pCASL) with a 3D GRASE readout (TR = 5.6 s, TE = 18.4 ms, labeling duration = 1.8 s, post-labeling delay = 1.8 s, background suppression, 4 repetitions).

Data Analysis BOLD-CVR image analysis was performed using FSL (https://fsl.fmrib.ox.ac.uk/fsl), including motion and distortion correction, spatial smoothing (FWHM = 3.5 mm) and high-pass temporal filtering (cutoff = 100 s). The bulk lag of the BOLD response to BH was obtained for each subject by computing the cross-correlation between the average GM BOLD time series and the PetCO2 signal. PetCO2 was convolved with a single gamma hemodynamic response (HRF) function and shifted between ± 9 s in increments of 1 s around the bulk lag, for each subject. For each shifted regressor, a voxelwise analysis was performed by fitting a general linear model (GLM) to the BOLD signal. The CVR map was obtained by selecting, for each voxel, the lag that explained the most variance, and dividing the parameter estimate by the mean BOLD signal and the mean ΔPetCO2 to yield values in %/mmHg.

ASL-bCBF image analysis was performed using FSL's BASIL toolbox (https://fsl.fmrib.ox.ac.uk/fsl/fslwiki/BASIL) and included motion and distortion correction. Relative perfusion maps were obtained by averaging pairwise control-label subtraction images with spatial regularization.

Both CVR and bCBF maps were registered to MNI space (FSL's FNIRT) and spatially smoothed with a FWHM = 8 mm (AFNI's 3dBlurToFWHM) to better match their spatial smoothness.

The GM and WM ROIs were defined by segmenting the subject's T1-weighted structural image (FSL's FAST), registering the partial volume (PV) estimate maps to MNI space and thresholding these at 40% for tissue classification (GM, WM and CSF). For each bCBF and CVR map, only the values between the 1st and 99th percentiles were considered within each ROI to exclude potential outliers. The bCBF values in GM and WM were then stratified into 25 and 16 bins[2], respectively. The voxels corresponding to each bin were identified and the mean bCBF and CVR values were obtained for each bin. To evaluate the relationship between the two metrics, both linear and quadratic models were fitted using Matlab.

Results Figure 1 illustrates the bCBF, CVR, and respective CVR lag maps. CVR and bCBF are strongly correlated in both GM and WM in all subjects (Fig. 2). The relationship was better fitted by a quadratic than a linear model, particularly in GM. By spatially mapping the bins corresponding to the three main components of the correlation curves (Fig. 3), we found a largely linear positive correlation across most of GM. The negative correlation observed for the lowest bCBF values (corresponding to high CVR values) was found mostly in voxels in cerebrospinal fluid (CSF) regions or in tissue boundaries likely contaminated by motion, pulsatile artifacts and PV effects.

Conclusion Our study clearly demonstrates a positive correlation between BOLD-CVR and ASL bCBF measurements across both GM and WM. Although this is mostly linear for intermediate values, a negative correlation was found in some subjects near CSF locations. Our results are consistent with the two previous reports regarding this coupling[2,3] and extend them to the whole brain.

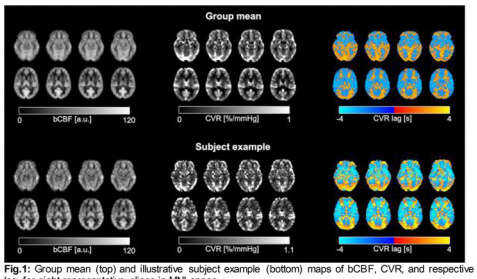

Fig.1: Group mean (top) and illustrative subject example (bottom) maps of bCBF, CVR, and respective CVR optimal lag, for eight representative slices in MNI space.

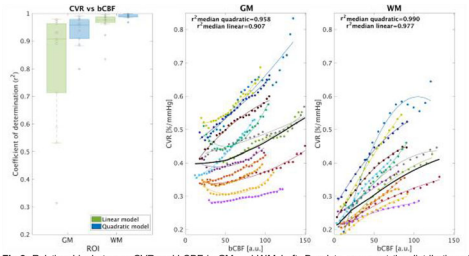

Fig.2: Relationship between CVR and bCBF in GM and WM. Left: Boxplots represent the distribution of the coefficient of determination (r^2) across the fourteen subjects, using two different models (linear and quadratic). Middle and right: The scatter plots of CVR vs. bCBF (dots) with the respective quadratic model fit (line) for each subject (colors), in GM (middle) and WM (right); the median curve across subjects is also shown (black line).

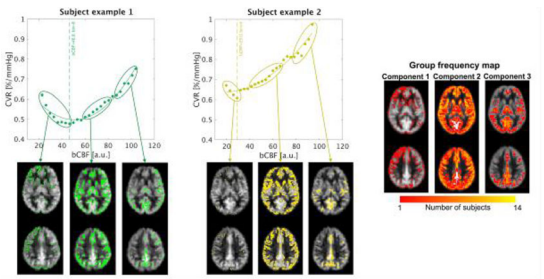

Fig.3: Spatial mapping of the correlation between CVR and bCBF in GM, for six representative slices in MNI space, across the three main components of the quadratic model curve. Left: Illustration for two example subjects, including the CVR vs. bCBF plots and respective bin maps. **Right:** Group frequency map showing the number of subjects with a bin in each voxel, for each curve component.

References

1. Pinto et al., *Front Physiol*, 11:608,475, 2021.
2. Chu et al., *Neuroimage*, 173:72–87, 2018.
3. Stickland et al., *FrontNeurosci*, 16:910,025, 2022.
4. Leoni et al., *BrazJMedBiolRes*, 50(4):e5670, 2017.

LT62.
Readout-segmented spectroscopic imaging with compressed sensing for high-resolution metabolite imaging at 7 T

A. Seginer[1], Y. Kierson[1], G. A. Keith[2], D. A. Porter[2], R. Schmidt[1]

[1]*Weizmann Institute of Science, Rehovot, Israel;*
[2]*University of Glasgow, Imaging Centre of Excellence, Glasgow, United Kingdom*

Introduction High resolution Magnetic Resonance Spectroscopic Imaging (MRSI) is of high interest for measurements in vivo as it can provide simultaneously both metabolite and spatial information. In recent work, we developed and examined RS-COKE (Readout-Segmented COnsistent K-t space Epsi)[1], a sequence for high resolution

MRSI. RS-COKE is an EPSI (Echo Planar Spectroscopic Imaging) variant[2–4] offering increased spectral width (SW) and is thus especially promising for spectral imaging of human brain metabolites at 7 T. However, mismatches between readout (RO) segments can result in pronounced artifacts, especially when lipid suppression is off. Our previous study focused on developing a procedure to measure and reduce the readout-segment mismatches, leading to robust brain MRSI in vivo at 7 T. It was previously shown that Compressed Sensing (CS)5 can be beneficially used to accelerate MRSI acquisition[6,7]. In this study, we adapted the RS-COKE pulse sequence to support CS acceleration in the spatial dimension in order to increase the achievable spatial resolution in a shorter time. A reconstruction approach was designed, incorporating both the trajectory corrections required for RS-COKE and Compressed Sensing. The method was examined on a special head-mimicking phantom and on human volunteers.

Methods Sequence/Acquisition

Figure 1 shows the RS-COKE pulse sequence, implemented on a 7 T MAGNETOM Terra (Siemens Healthcare, Erlangen, Germany). It is readout segmented and employs sine-shaped readout gradients. The COKE scheme adds alternating PE blips between the RO gradients, reversing the sign of both phase-encode (PE) blips and RO gradients every excitation, to achieve the trajectories shown, having an effective short echo-spacing. A VAPOR water-suppression module is included, as is a refocusing pulse, but no lipid suppression. The updated sequence includes an option to provide a table of the acquired PE lines for each RO segment. The sequence also includes three reference scans on water that are used to estimate the trajectory corrections as described in Ref.1.

Data Processing

The reconstruction included—i) Trajectory corrections, per segment, based on the reference scans (Ref.1); ii) phase correction of the signal acquired during negative RO gradients; iii) applying time apodization (exponential with a decay constant of 0.1 s) and Hann windowing in all k-space dimensions); iv) density compensation weights estimation and v) BART[8] reconstruction using the corrected trajectory, the weights, and sensitivity maps derived from a separate water GRE calibration scan. A schematic diagram of the reconstruction is shown in Fig. 2.

Phantom

A 3D-printed head-shaped phantom that includes an agar "brain" with brain-mimicking metabolites was used.[9]

Scan Parameters

All phantom scans had the common parameters: TR/TE 1400/14.6 ms, FOV (RO × PE) 260 × 300 mm^2, slice thickness 15 mm, SW 2778 Hz, echo spacing 0.360 ms, 256 echoes. Two variants were scanned. Scan 1) in-plane resolution 4.1 × 4.7 mm^2 (63 × 64 acquisition matrix), 3 readout segments, full acquisition duration 4:30 min, and CS acquisition 3:20 min. Scan 2) in-plane resolution 2.0 × 2.3 mm^2 (128 × 128 acquisition matrix), 7 readout segments, full acquisition duration 20:54 min, and CS acquisition 10:22 min.

For human imaging the scan parameters were: TR/TE 1400/13 ms, FOV (RO × PE) 260 × 300 mm^2, slice thickness 15 mm, in-plane resolution 4.1 × 4.7 mm^2 (63 × 64 acquisition matrix), 3 readout segments, SW 2941 Hz, echo spacing 0.340 ms, 256 echoes, and scan duration 3:20 min.

Results

Figure 3 shows phantom results; showing NAA images as well as spectra acquired without and with CS acceleration. Figure 4 shows MRSI example acquired with CS acceleration for human imaging.

Discussion and Conclusions In this work the RS-COKE pulse sequence was adapted to acquire accelerated MRSI based on Compressed Sensing. A varying PE subsampling can be acquired per RO segment, for example acquiring all PEs at the central segment and a smaller number of PEs at farther-out RO segments (see CS mask in Figs. 3, 4). This flexibility can offer an increased robustness for measurements in vivo. The current phantom results show a lower resolution of 4.1 × 4.7 mm^2 MRSI acquired within 3:20 min using CS and a higher resolution MRSI of 2 × 2.3 mm^2 acquired in 10:22 min using CS. These CS reconstructed images and spectra show similar quality to the full acquisitions. The acceleration factors used here were modest, up to × 2, however, they are extremely useful for measurements in vivo. The NAA image in human MRSI shows some residual artifacts, which require further optimization.

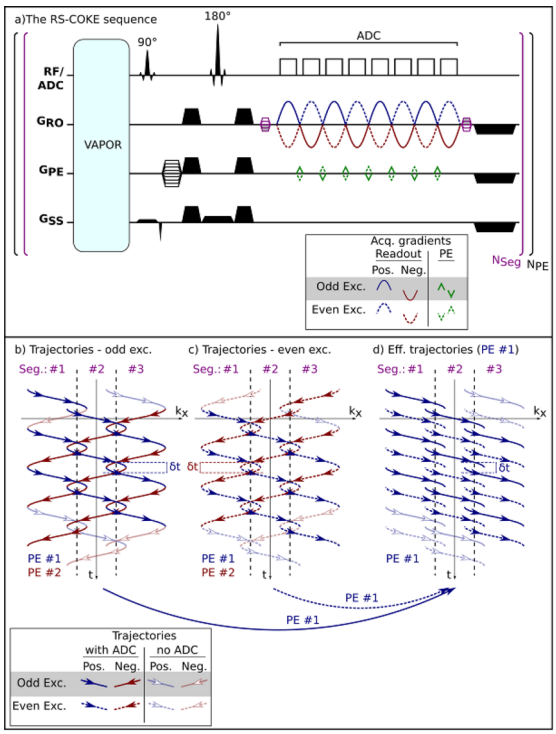

Fig. 1: (a) A schematic diagram of the RS-COKE sequence and (b–d) the resulting — trajectories. (b) and (c) are the trajectories of the odd and even excitations of a 3-segmented RS-COKE.

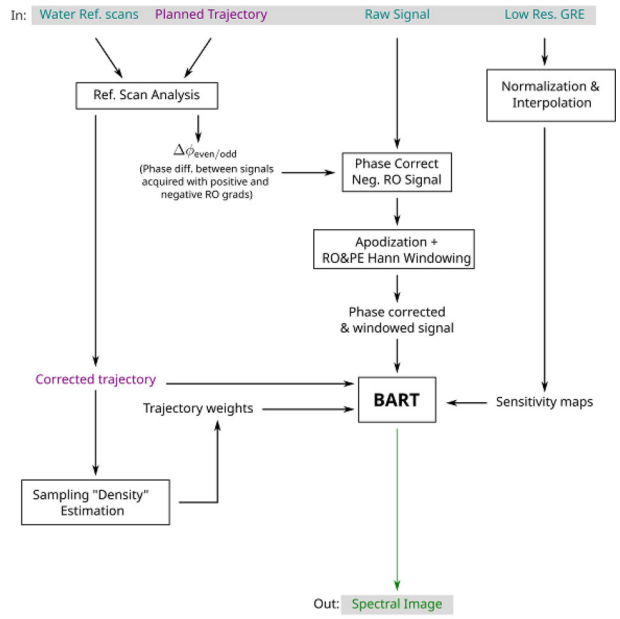

Fig. 2: A schematic flow of the reconstruction using BART.

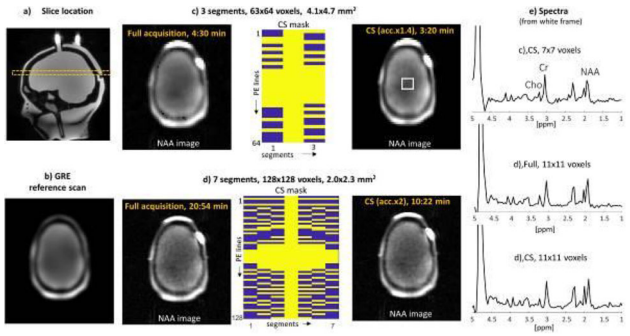

Fig. 3: Phantom results. (a) Sagittal image showing the planned slice location. (b) A GRE reference scan used to calibrate coil combination weights. (c) and (d) MRSI acquired without and with CS acceleration at 4.1x4.7 mm² and 2x2.3 mm² in-plane resolution, respectively. (c) and (d) shows the NAA images with the CS mask used for each case. e) Spectra for the cases shown in c) and d).

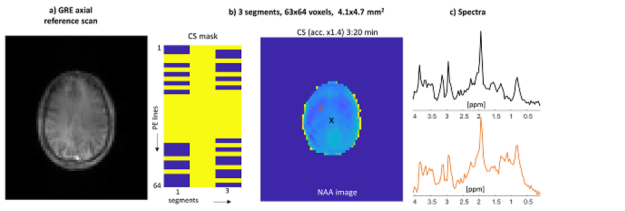

Fig. 4: In vivo results. (a) a GRE scan of the slice (with IR for T1 weighting). (b) CS MRSI (NAA map) with 4.1x4.7 mm² in-plane resolution in 3:20 minutes (c) Single-voxel spectra at the black and orange x's on the NAA image (the latter shows higher baseline which is a residual artifact coming from the outer lipids signal, still requires optimization).

References:

1. Seginer et al. MRM 2022;88:2339–2357.
2. Keith et al. ISMRM 2019.
3. Webb et al. MRM 1989;12:306–315.
4. Schmidt et al. MRM 2019;82:867–876.
5. Lustig et al. MRM 2007;58:1182–1195.
6. Hu et al. MRM 2009;63:312–321.
7. Vicari et al. ISMRM 2017.
8. https://mrirecon.github.io/bart/.
9. Jona G et al. NMR Biomed 2021;34:e4421.

LT63.
Impact of different noise reduction strategies on preclinical 1H-MRSI: *in-vivo* and Monte-Carlo simulations at 14.1 T

B. Alves[1], D. Simicic[1,2], J. Mosso[1,2], T. Lê[2], B. Strasser[3], A. Klauser[1,4], C. Cudalbu.[1]

[1]*École Polytechnique Fédérale de Lausanne (EPFL), CIBM Center For Biomedical Imaging, Lausanne, Switzerland;*
[2]*École Polytechnique Fédérale de Lausanne (EPFL), Laboratory of Functional and Metabolic Imaging (LIFMET), Lausanne, Switzerland;*
[3]*Medical University of Vienna, Department of Radiology, Vienna, Austria;*
[4]*University of Geneva, Department of Radiology and Medical Informatics, Geneva, Switzerland.*

Introduction The investigation of post-processing methods that aim at reducing the noise variance1-5 gained a lot of interest driven by the need for higher spatial resolution in 1H-MRSI. Recently the MP-PCA based denoising and the low-rank TGV reconstruction have also been implemented on preclinical in vivo 1H-FID-MRSI datasets at 14.1T1, leading to an increase in apparent SNR without any detrimental visual impact on features of the spectra such as Gaussian noise distribution1. As in vivo data lack of ground-truth, in-depth validations of the performance of these noise-reduction strategies is required. As such, we built a realistic Monte-Carlo study with known ground truth mimicking in vivo brain regional differences measured with 1H-FID-MRSI at 14.1 T to assess the impact of noise-reduction strategies on brain coverage, metabolite concentration estimation and regional difference. Finally, we further advanced the implementation of these two techniques, tested their feasibility and routine usage at 14.1 T using in vivo data.

Methods Fast 1H-FID-MRSI datasets were acquired in the rat brain on a 14.1 T MRI Bruker/Magnex system (TE = 1.3 ms, TR = 813 ms, 2 mm slice thickness centered on hippocampus, FOV = 24 × 24mm2, matrix size = 31 × 31, 1 average, 13 min). The data were triplicated and processed using an in-house MATLAB pipeline that applies HLSVD water suppression, lipid-metabolite orthogonality-based lipid suppression and one of the denoising method on each set5, resulting in a non-denoised (RAW), LR-TGV denoised and MP-PCA denoised sets. These sets were quantified with LCModel with a simulated basis set (macromolecule added)6–9 (Fig. 1A). An automatic quality control tool using SNR, FWHM, CRLB"s was applied on the metabolic maps.

Synthetic 1H-MRSI slices were created to mimic the experimental conditions of in vivo acquisitions at 14.1 T, using the metabolites of the basis set (Fig. 1A). 317 FIDs were generated and assigned to three compartments mimicing brain regions with distinct sets of concentrations using an in vivo brain mask. A B0 map acquired from in vivo data was used to apply realistic B0 inhomogeneity on the simulated slice (Fig. 1B). Gaussian noise was introduced using a range of SNR values (SNR = 5,7,10,12,15,20). The simulated slices were processed via a custom version of the pipeline used for in vivo data (without lipid and water suppression). Metabolic maps were computed and results were averaged over 10 Monte-Carlo repetitions. A set with the SNR of 300 was quantified and used as ground truth (GT).

RAW and denoised metabolite concentrations as mean and SD averaged over compartments were compared against GT data.

Results and Discussion In vivo, no significant changes on the resulting concentrations of Ins, Gln, Glu per region were observed when applying either of the denoising techniques, and their regional distribution was not affected12. Both denoising approaches reduced the standard deviation (SD) of the estimated concentrations (Fig. 2B) and increased brain coverage by at least 7%. The apparent SNR was approximately doubled for both methods. Figure 3 shows the metabolite maps as well as the concentration on each region obtained on RAW, MP-PCA and LR-TGV sets in the Monte Carlo study, with NAA, GABA and Gln as examples. For both noise reduction methods, the difference between the GT and the measured values of concentration and SD were reduced when compared to RAW. Moreover, at SNR = 5, GABA, a low concentrated metabolite, was not reliably quantified in the RAW set, while after denoising the regional difference was retrieved with concentration estimates closer to GT. Inconsistencies with LR-TGV results can be explained by the effect of the B0 map, which is specific to this technique. Figure 4 shows the concentration on each compartment and regional differences as a function of the SNR. For a SNR lower than 10, both denoising methods are closer to the GT than RAW. Moreover, whenever the RAW data was well quantified, the denoising did not change its distribution. No biases were thus introduced to the concentrations.

Conclusion We presented an initial framework for the validation of noise-reduction strategies in 1H-MRSI together with an automatic processing pipeline developed in-house. Our results highlight important steps towards the quantitative evaluation of the performance of these noise-reduction-strategies while using a known ground truth and in vivo results. We showed that both considered denoising strategies retrieved the metabolites concentrations with a decreased SD inside each compartment and increased brain coverage in vivo.

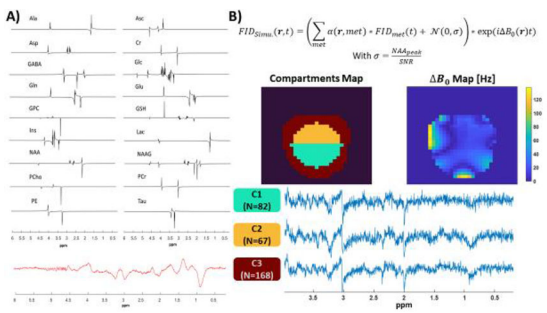

Fig. 1: A) Elements of the basis set, simulated in NMR-Scope B11. B) Sketch of the procedure for generating the Monte-Carlo sets. Maps of the distribution of the simulated spectra and of the applied ΔB0. The 3 model/compartment spectra used in the synthetic MRSI slice are displayed (with SNR=7).

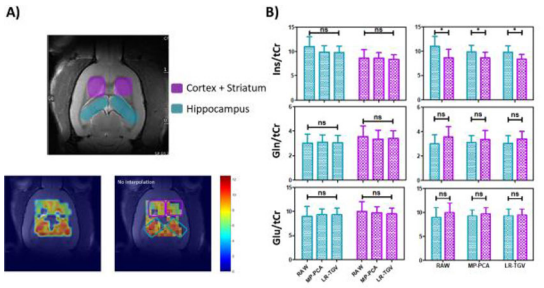

Fig. 2: A) Segmentation of the MRSI slice into two brain regions: mix of cortex and striatum (purple) / hippocampus (blue) B) Average concentration of Ins, Gln and Glu computed for each brain region and methods used. (*: 0.05 ≥ p / ns: not statistically significant)

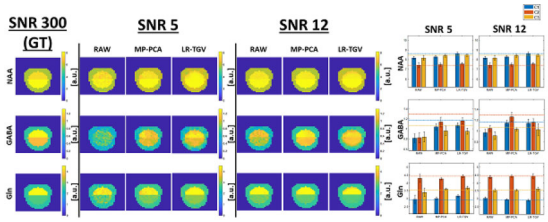

Fig. 3: Concentration maps (on the left side) and the compartment averages (on the right side) of NAA, GABA and Gln for the synthetic MRSI slices at SNR 5 and 12 (dotted lines represent the GT per compartment).

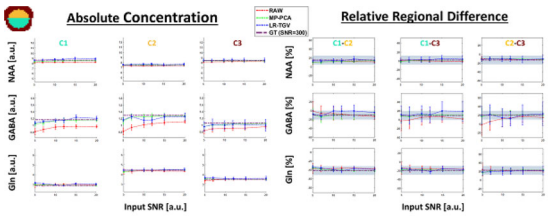

Fig. 4: Evolution of the absolute concentration in each compartment and relative regional difference with different input SNR for NAA, GABA and Gln. The blue region represents the values of difference of 10% around the GT

References

1. Alves,ISMRM,2022
2. Abdoli,Magn.Reson.Mater Physics,Biol Med.,2016
3. Nguyen,IEEE Trans.Biomed.Eng.,2013
4. Clarke,Magn.Reson.Med., 2021
5. Klauser,Magn.Reson.Med.,2019
6. Starčuk,Anal.Biochem.,2017
7. Govindaraju,NMR Biomed.,2000
8. Govind,NMR Biomed.,2015
9. Simicic,ISMRM,2022
10. Mosso,NeuroImage.,2022
11. Simicic,ISMRM,2022
12. Tkác,Magn.Reson.Med.,2003

LT64.
GABA and glutathione measurement using MEGA-sLASER at 3 Tesla

S. Alcicek[1,2,3,4], A. Manzhurtsev[1], M. Ronellenfitsch[2,3,4,5], J. Steinbach[2,3,4,5], V. Prinz[6], E. Hattingen[1,2,3,4], U. Pilatus[1,2,3,4], K. Wenger[1,2,3,4]

[1]Goethe University, Institute of Neuroradiology, Frankfurt am Main, Germany;
[2]University Cancer Center Frankfurt (UCT), Frankfurt am Main, Germany;
[3]Frankfurt Cancer Institute (FCI), Frankfurt am Main, Germany;
[4]German Cancer Research Center (DKFZ) Heidelberg, and German Cancer Consortium (DKTK), Heidelberg, Germany;
[5]Goethe University, Dr. Senckenberg Institute of Neurooncology, Frankfurt am Main, Germany;
[6]Goethe University, Department of Neurosurgery, Frankfurt am Main, Germany.

Introduction Spectral editing strategies in in vivo ^{1}H MR-Spectroscopy (MRS) are highly effective for quantification of low-concentration metabolites whose signals cannot be reliably discriminated by conventional techniques due to signal overlap. The most used strategy is J-difference-based such as MEGA editing. MEGA editing has been integrated into different spatial localization techniques, generally targeting a specific region[1]. The correct voxel placement and voxel sizing is especially crucial when examining specific brain tumor regions. However, measurements with the commonly used localization method PRESS suffer from chemical shift displacement error (CSDE), leading to a change in editing efficiency and causing uncertainty in the voxel location[12]. This problem can be overcome by employing adiabatic RF pulses, such as adopted in the sLASER pulse sequence. Here, we demonstrate simultaneous gamma amino-butyric acid (GABA) and glutathione (GSH) editing, both of which are of interest in glioma studies, using a MEGA-sLASER pulse sequence in a brain-mimicking phantom, healthy subjects and patient with diffuse glioma while keeping the voxel size $2 \times 2x2$ cm^3.

Methods Data were acquired using a 20-channel phased-array head coil on a clinical whole-body 3 T MR Scanner (MAGNETOM Prisma, Siemens Healthineers, Erlangen). The phantom contained a solution of 2 mM GABA, 3 mM GSH, 12.5 mM N-acetyl aspartate (NAA), 10 mM creatine (Cr), 3 mM choline, 7.5 mM myo-inositol (mI), 10 mM glutamate (Glu), 5 mm glutamine (Gln) and 5 mM lactate. Phantom measurements were performed to detect GABA and GSH using both MEGA-PRESS and MEGA-sLASER pulse sequences. Parameters are provided in Table 1.

Table 1 MEGA-PRESS and MEGA-sLASER parameters for phantom and in vivo measurements.

In vivo or Phantom	Repetition time	Echo time (TE)	Editing pulse BW	Voxel size	Navg	Editing pulse frequency δGABA/δGSH/δOFF
Phantom	2000 ms	80 ms	MEGA-PRESS: 64 Hz MEGA-sLASER: 90 Hz	$3 \times 3 \times 3$ cm^3	256	1.78/4.44/7.62
In vivo	2000 ms	80 ms	MEGA-sLASER: 90 Hz	$2 \times 2 \times 2$ cm^3	192	1.9/4.56/7.5

For in vivo measurements, 3D T1w MPRAGE and axial T2w images were acquired prior to MRS and used for voxel positioning. In four healthy subjects, voxels were placed in the left posterior cerebral region (see Fig. 2A). In glioma patient, voxels were located in the solid tumor area (Fig. 2D) and in the contralateral normal appearing white matter (NAWM) (Fig. 2G). Three data series of 64 acquisitions each were acquired in an interleaved manner: ON_{GABA}, ON_{GSH}, and OFF_{All}. A common OFF_{All} can be used for GABA and GSH, reducing the time required for data acquisition. Motion-corrupted dynamics were rejected, frequency and phase aligning were applied using the combination of the FID-A[3] and Gannet[4] tools. Spectral fitting and quantification were performed using the standard GannetFit function with Gaussians.

Results Phantom data (Fig. 1) indicates that the spectroscopic profiles of GABA, Glx and GSH acquired using MEGA-sLASER match those obtained by MEGA-PRESS. Even though co-editing of the (NAA) signal in the GSH spectra differs between the two methods, the GSH signal is not affected. In addition, we observed no differences in the signal-to-noise ratio (SNR) of the signals of interest. Edited GABA, Glx and GSH signals at 3.0, 3.75 and 2.95 ppm, respectively were observed clearly in all in vivo spectra acquired in this study as shown in Fig. 2. A high degree of consistency was observed between the spectra of all healthy subjects. The water suppression factor was $>$ 97% for all participants. The fitting errors in the healthy subjects did not exceed the 15% value for GABA, 10% for Glx and 20% for GSH. The spectral patterns of GABA and GSH varied between spectra obtained from tumor tissue compared to the contralateral NAWM: the intensities of Glx and GSH were higher in tumor tissue, the intensity of GABA and the co-edited NAA was lower (Fig. 2E–F).

Discussion Technical limitations restrict the TE in MEGA-sLASER to a minimum of $\sim$ 80 ms, so to date there is only one application at 3 T, which is aimed at editing lactate and β-hydroxybutyrate signals at TE = 148 ms [2]. In our phantom data we showed that GABA and GSH could be detected at TE = 80 ms with no significant difference in SNR comparing MEGA-sLASER to the "conventional" MEGA-PRESS. Considering the sufficient SNR of the in vivo spectra and the quality of fitting acquired in our study, we conclude that MEGA-sLASER with TE = 80 ms can be applied for GABA and GSH measurements, allowing to obtain results from a low-volume voxel without a chemical displacement error. This is especially important for neurooncological studies since it is crucial to avoid tumor voxel contamination with signals from surrounding normal tissue and tumor necrosis.

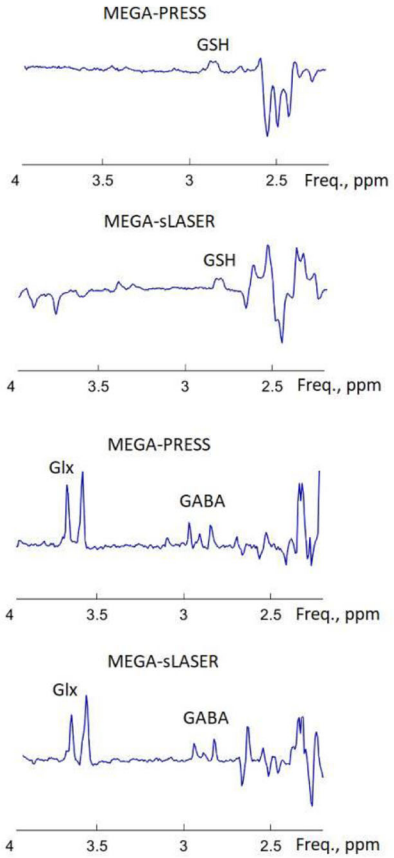

Fig. 1: The GABA and GSH spectra obtained from the phantom using MEGA-PRESS and MEGA-sLASER. In GSH spectra, the signals of the aspartyl group of the co-edited NAA are present at in the 2.3–2.8 ppm region, the shape of the co-edited resonances differs between MEGA-PRESS and MEGA-sLASER. In MEGA-sLASER GSH spectrum, the signals of Cr, Glu, Gln and ml are observed in the 3.6–4 ppm region due to the insufficient selectivity of the editing pulse. For the same reason, the signal of the NAA aspartyl group is observed in MEGA-sLASER GABA spectrum at ~2.6 ppm.

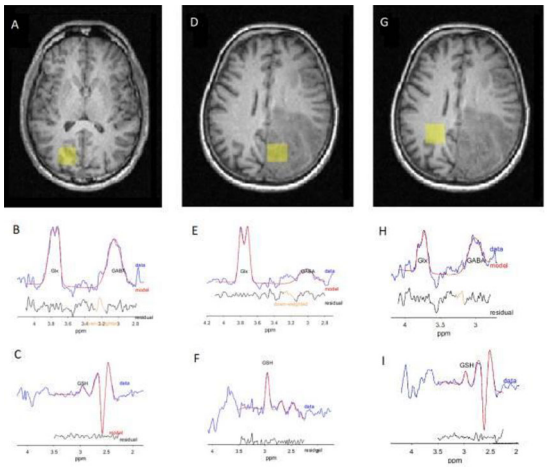

Fig. 2: Voxel location and respective GABA and GSH spectra in the parietooccipital region of a healthy subject (A–C), the tumor region of a patient with diffuse glioma (D–F), and contralateral NAWM (G–I). Fitting models generated by the Gannet program were used to quantify GABA and GSH. The differences between the experimental spectra (blue line) and fitting models (red line) are presented as residual spectra (black line).

References:
1. https://doi.org/10.1002/nbm.4411.
2. https://doi.org/10.1002/nbm.4100.
3. https://doi.org/10.1002/mrm.26091.
4. https://doi.org/10.1002/jmri.24478.

LT65.
Characterizing thalamic sodium homeostasis changes in focal epilepsy using 7 T MRI

R. Haast[1], M. M. El Mendili[1], J. Makhalova[1,2], L. Gauer[1], B. Testud[1], A. Le Troter[1], J. P. Ranjeva[1], W. Zaraoui[1], F. Bartolomei[2,3], M. Guye[1]

[1]*Aix-Marseille Université, Center for Magnetic Resonance in Biology and Medicine, Marseille, France;*
[2]*APHM, Hôpital Universitaire Timone, CEMEREM, Department of Epileptology and Clinical Neurophysiology, Marseille, France;*
[3]*Aix-Marseille Université, Institut de Neurosciences des Systèmes, Marseille, France.*

Introduction Sodium (^{23}Na) MRI provides relevant functional information on neuronal energetic status and cell viability[1]. At ultra-high field strengths (7 Tesla) and in the context of focal epilepsy, sodium accumulation has been observed in cortical regions characterized by high epileptogenicity[2] and inclusion of ^{23}Na information appeared promising to improve patient treatment[3]. The involvement of the thalamus during seizures and its structural abnormalities

observed across focal epilepsy patients[4–6], warrants investigation of thalamic sodium homeostasis changes.

Methods A total of 21 temporal lobe epilepsy (TLE, mean age ± SD: 33 ± 11 yrs, 8 males), 16 non-TLE (NTLE, 34 ± 13 yrs, 9 males) and 22 healthy controls (H, 37 ± 15 yrs, 10 males) were recruited. All patients underwent a comprehensive pre-surgical work-up including a SEEG recording for grouping in TLE and NTLE (pre-frontal, insular-opercular, central-premotor or posterior) based on epileptogenic zone network topography[7].

For each subject, ^{1}H-MRI B_1^+, T_1 (0.6 mm^3) and multi-echo ^{23}Na (3 mm^3) data were acquired using a whole-body 7 T scanner (Siemens Healthineers, Erlangen, Germany) and ^{1}H 1Tx/32Rx (Nova Medical, Wilmington, USA) and dual-tuned ^{23}Na/1H QED birdcage coils, respectively[2]. The multi-echo ^{23}Na images were fitted using a bi-exponential model and normalized relative to signals from reference tubes to characterize the apparent short (Na_{SF}) and long (Na_{LF}) fraction sodium concentration and construct whole-brain total sodium concentration (i.e., sum of Na_{SF} and Na_{LF}) and f maps (Na_{SF})[8]. In parallel, post-hoc B_1^+ corrected T_1 data were skull-stripped for automatic segmentation of the thalamus and its nuclei using the 7TAMIBrain atlas[6,9]. Gray matter density-weighted TSC and f averages were calculated in ^{23}Na image space for left and right thalami separately (Fig. 1A), and their posterior, lateral and medial segments. Average T_1 and total volume were extracted in T_1 space[6]. TSC and f estimates were corrected for age, sex, hemisphere and estimated total intracranial volume (calculated by FreeSurfer) effects (to match T_1 and volume correction) based on the controls data using the confounds Python package[10]. After z-scoring with respect to controls, group-wise, ipsi- vs.contralateral differences in thalamic (segments) and associations with clinical parameters were explored using ANOVA, (Bonferroni-corrected) pairwise comparisons and correlation analyses as implemented in the pingouin Python package.

Results Thalamic TSC ($p < 0.001$), not f, differed significantly between groups with increased TSC in both TLE ($p < 0.05$) and NTLE patients ($p < 0.01$, Fig. 1B). Increases in TSC and f appeared (i) more pronounced for the ipsilateral side (side of seizure onset) in TLE (Fig. 1C) and (ii) overlapped with decreased T_1 and volume (Fig. 1D). With respect to clinical characteristics, TSC was higher in patients with a left seizure onset zone especially ($p < 0.05$), and earlier disease onset ($r = -0.26$, $p < 0.05$).

Analyses per thalamic segment (Fig. 2, based on > 29 voxels/subject) did not reveal clear spatial differences across the thalamus with similar group patterns as at the whole thalamus scale. Nonetheless, the medial segment appeared uniquely impacted in the NTLE patients while in TLE the strongest TSC increase was observed in the lateral segment. For f, the strongest effects were observed for the lateral thalamus.

Discussion and conclusion The observed increase in thalamic TSC without f changes follows previously observed tissue degeneration (e.g., volume decrease)[5,6] and microstructural changes (i.e., shortened T_1)[6] and indicate changes in neuronal integrity rather than epileptogenicity of this structure. This effect seems strongest in patients with left hemisphere seizure and earlier disease onset. Finally, our analyses provide first estimates of differential TSC increase and f across posterior, lateral and medial segments between patient groups. Together, these findings suggest that the extent of changes in thalamic sodium homeostasis might depend on clinical and/or SEEG characteristics.

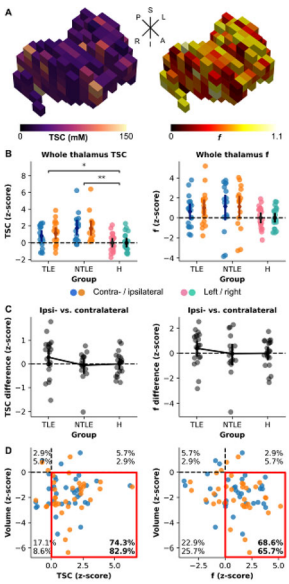

Fig. 1: Whole thalamus (A) TSC and f maps, (B) comparison between groups (color-coded for side) as well as (C) ipsi- (i.e., ipsilateral to the side of seizure onset) vs. contralateral differences. (D) Overlap with changes in volume.

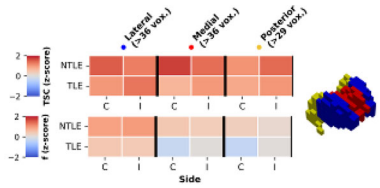

Fig. 2: TSC and f estimates per thalamic segment, patient group and side (color-coded).

References

[1] K. R. Thulborn, NeuroImage, vol. 168, pp. 250–268, Mar. 2018, [2] M. Azilinon et al., Human Brain Mapping, 2022, [3] M. Azilinon et al., medRxiv, p. 2022.12.14.22283389, Dec. 16, 2022, [4] F. Pizzo et al., Neurology, vol. 96, no. 2, pp. e280–e293, Jan. 2021, [5] S. S. Keller, J. O"Muircheartaigh, C. Traynor, K. Towgood, G. J. Barker, and M. P. Richardson, Epilepsia, vol. 55, no. 2, pp. 306–315, Feb. 2014, [6] R. A. Haast et al., bioRxiv, p. 2022.11.01.514655, Nov. 02, 2022. [7] F. Bartolomei et al., Epilepsia, vol. 58, no. 7, pp. 1131–1147, Jul. 2017, [8] S. Grimaldi et al., Frontiers in Neurology, vol. 12, p. 715,618, 2021. [9] G. Brun et al., Eur J Neurosci, vol. 55, no. 2, pp. 438–460, Jan. 2022, [10] P. R. Raamana, Zenodo, Mar. 2020.

LT66.
Creatine and phosphocreatine CEST contrast of an optimal control pulse train compared to an optimized gaussian pulse train for CEST imaging in calf muscle

C. Stilianu[1], A. Chubarov[2], S. Weinmüller[2], M. Huemer[1], M. Zaiss[2], R. Stollberger[1]

[1]TU Graz, Institute of Biomedical Imaging, Graz, Austria;
[2]Friedrich-Alexander-Universität Erlangen-Nürnberg (FAU), Department of Neuroradiology, Erlangen, Germany

Introduction In CEST-MRI measurements, saturation pulses play a crucial role in determining the quality of Z-spectra. Over time, various types of saturation pulses have been developed to maximize contrast and robustness of CEST experiments. Recent research employing optimal control (OC) optimization has facilitated the creation of pulse trains that provide contrast nearly equivalent to the theoretical optimal continuous-wave (CW) saturation in phantom measurements (1). To compare the OC saturation pulses with a state of the art protocol, a Gaussian pulse train protocol was optimized, taking into account factors such as duty cycle (DC), total saturation (Tsat), pulse duration (tp), inter-pulse delay (td), and B1 RMS across the pulse train. The optimized G and OC protocols were subjected to in vivo measurements in the calf muscle using a 3 T clinical scanner. This study forms the first in-vivo proof that OC pulses outperform conventional Gaussian trains; here for CEST preparation of creatine (Cr) and phosphocreatine (PCr) weighted CEST imaging in muscle at 3 T.

Methods A Gaussian pulse train, defined by B1rms, DC, Tsat, tp, td and the number of pulses was optimized with Pulseq-CEST (2) simulations via a conventional grid search. Guided by these insights, in vivo experiments were designed to find the experimentally optimal B1 RMS.

A healthy volunteer was measured on a clinical 3 T Siemens PRISMA scanner system (Siemens Healthineers, Erlangen, Germany) with a TxRx 15Ch knee coil after written informed consent. The readout was a 3D GRE with a FOV of 112 × 92 × 60 pixels with a voxel size of 2 × 2 × 5.

Data pre-processing involved motion correction and spline smoothing of the measured spectra (3). Furthermore, B0 field inhomogeneities were addressed by employing a WASABI measurement (4). The contrast was evaluated in ROIs in the MTR asymmetry images.

The RF-magnitude of the OC pulse train was optimized by minimizing the difference to a target CW spectrum, using a hybrid semismooth quasi-Newton algorithm (5). Comprehensive details regarding the optimization and simulation process can be found in (1, 6). The optimization was constrained to the optimal parameters of the Gaussian protocol using the same DC, Tsat, td, tp, B1 RMS and number of pulses. So the degree of saturation is entirely contingent upon the specific shape of the pulse.

Results and Discussion The Pulseq-CEST simulations revealed an optimal Gaussian saturation regime consisting of eleven pulses with a duration of 50 ms and pause of 6 ms which is a DC of 90%. The optimal B1 level was estimated by conducting measurements at levels of B1 RMS of 0.58, 0.87, 1.16, 1.45, 1.74 and 2.03 μT resulting in a maximized CEST effect at 1.74 μT B1 RMS (Fig. 1). The OC pulse train optimized with the same constraints is depicted in Fig. 2a. The corresponding simulated spectra and asymmetry for the G and OC pulse trains indicate a higher contrast for the OC pulse train.

Figure 3 shows ROIs drawn in the lateral gastrocnemius (Fig. 3a), the medial gastrocnemius (Fig. 3b), the soleus (Fig. 3c) and the fibularis longus (Fig. 3c) with the corresponding CEST-spectra and MTR asymmetry in Fig. 4. In every ROI the OC pulse expressed a 16–27% higher contrast for Cr and PCr than the Gaussian protocol. Additionally the OC saturation exhibits a narrower peak width. This characteristic contributes to a higher level of selectivity in the saturation process compared to G saturation. Remarkably, the OC pulse outperformed the original exchange weighting estimates derived from the simulations.

In previous phantom measurements, the OC framework showed exceptionally high contrast compared to state-of-the-art saturation regimes. However, the question whether the pulses could perform comparably in an in vivo environment remained unanswered. In vivo calf muscle measurements reveal superior contrast and selectivity for Cr and PCr using OC pulses as opposed to the most effective Gaussian-based saturation method.

Conclusion In this study, we investigated the efficacy of generating in vivo CEST contrast for creatine and phosphocreatine using optimal control pulse trains compared to an optimized Gaussian saturation regime. Our results demonstrated that the OC pulse trains provided higher CEST effect and selectivity for creatine and phosphocreatine in various regions of interest in the calf muscle, using a 3 T clinical scanner. Additionally, OC saturation showed a narrower peak width contributing to higher contrast and a higher level of selectivity in the saturation process compared to Gaussian saturation.

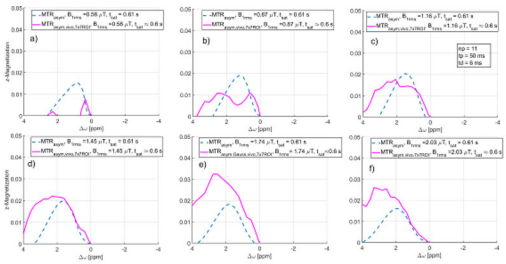

Fig. 1: MTR asymmetry for the Pulseq-CEST simulation (dashed) and measuremnt (solid) for B1 levels: B1 RMS levels of 0.58, 0.87, 1.16, 1.45, 1.74 and 2.03 μT (Fig. a-f). The optimum was estimated at a B1 RMS of 1.74. 7x7 ROI in soleus.

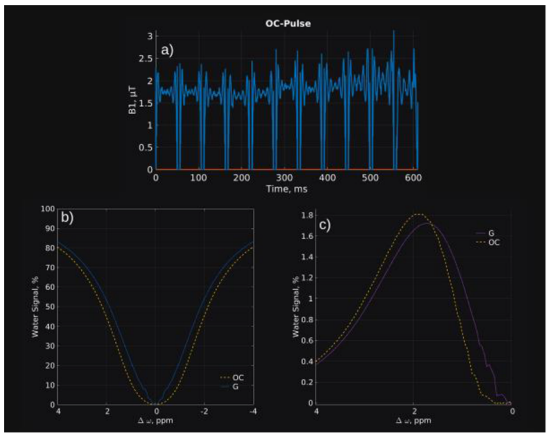

Fig. 2: a) RF pulse train optimized with an OC framework with B1 RMS of 1.74 μT, eleven pulses, DC 90 %, tp 50 ms, td 5 ms. b) Spectra simulated with a two pool Bloch McConell model (6) for the optimized G and OC saturation protocol. c) MTR asymmetry of the spectra in b).

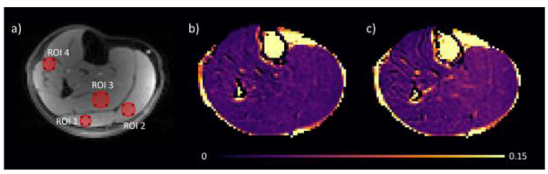

Fig. 3: a) ROIs for evaluation of spectra and MTR asymmetry in Fig. 4. MTR asymetry image at peak value (2.5 ppm) for b) G c) OC

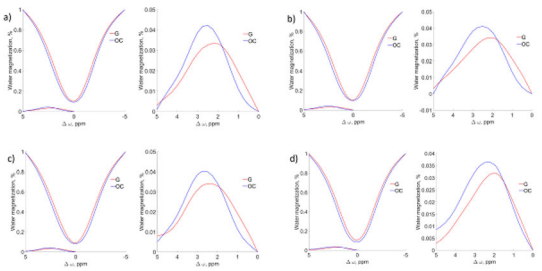

Fig. 4: CEST spectra corresponding to the ROIs in figure 3. spectrum and MTR asymmetry in a) lateral gastrocnmius, b) medial gastrocnmius, c) soleus, d) fibularis longus. In all ROIs the OC saturation (blue) expressed a higher CEST effect than the optimized G saturation (red). ROIs are mean over spectra.

LT67.
Correction of fat signal-induced artifacts in CEST-MRI: An extended normalization across the entire Z-spectrum

P. Menshchikov[1], P. S. Boyd[1], N. Kempa[1], M. E. Ladd[1,2,3], P. Bachert[1,2], A. Korzowski[1]

[1]*German Cancer Research Center (DKFZ), Medical Physics in Radiology, Heidelberg, Germany;*
[2]*University of Heidelberg, Faculty of Physics and Astronomy, Heidelberg, Germany;*
[3]*University of Heidelberg, Faculty of Medicine, Heidelberg, Germany*

Introduction The presence of adipose tissues in breast, prostate, liver etc. poses particular challenges on the correct interpretation of Z-spectra, and therefore to correct evaluation of different chemical exchange saturation transfer (CEST) signals (i.e. amide proton transfer (APT), relayed nuclear Overhauser effect (rNOE)). Recently, a normalization method was introduced by Zimmerman et al. [1] that allows to correct for fat signal-induced artifacts, but only in regions of Z-spectra where no fat resonances exist, i.e. no direct saturation (DS_{fat}) of fat signals. This normalization e.g. enables quantitative assessment of APT signals unaffected by fat without additional RF power or image acquisitions. The purpose of this study was to extent this method to correct the entire Z-spectrum for fat-signal induced artifacts by modelling multiple fat contributions and their saturation, in particular to remove strong pseudo-rNOE artifacts.

Methods
Theory

The proposed normalization method is mainly based on two assumptions: 1) Estimation of the total fat signal by the residual signal at the spectral position of the water DS ($\Delta\omega_{DS,water}$ = 0 ppm, Fig. 1 Eq. 1); 2) introducing an offset-dependent correction factor ($b(TE, \Delta\omega, \omega_1)$), Fig. 2 Eq. 5), that accounts for a realistic multipeak fat model [2] (Fig. 1 Eq. 2) and saturation of the n individual lipid resonances ($\beta_n(\Delta\omega,\omega_1,\delta\omega_n)$) for each offset ($\Delta\omega$) of the applied CEST saturation pulse. As a result, the corrected Z-spectrum is given by Eq. 3 (Fig. 1).

Correction factor modeling and CEST imaging Phantom measurements were performed on a 7 T MR scanner (MAGNETOM, Siemens) using a bilateral breast coil (1 transmit/16 receive channels, Rapid Biomedical). The phantom was filled in half with a 300 mM carnosine water solution (pH = 8), and half with sunflower oil mimicking human fat tissue.

Relative amplitudes (A_n) and chemical shifts ($\delta\omega_n$) for fat resonances were quantified from SVS 1H MR spectrum (sLASER, TE/TR = 40/10000 ms, 8 × 8 × 8 mm voxel, no water suppression) (Fig. 2A). $\beta_n(\Delta\omega,\omega_1,\delta\omega_n)$ were modeled by Lorentzians with variable width (Fig. 2, Eq. 4). A representative correction factor $b(TE, \Delta\omega, \omega1)$ for TE = 2.04 ms is visualized in Fig. 2B. For the final fat correction, the b values were smoothed for each offset $\Delta\omega$ using a 0.2 ppm window (Fig. 2B), which encompasses (i) differences in widths between all fat resonances and the applied saturation pulse and (ii) possible dispersion of the offsets $\Delta\omega$, due to the B0 inhomogeneities and possible phase errors.

CEST data was acquired with a centric-reordered 2D single-shot gradient-echo sequence (TE/TR = 2.04/3.70 ms, 2.55/4.40 ms, 1 Slice, spatial resolution—1.7 × 1.7 × 3 mm, steady-state presaturation—95 Gaussian-shaped pulses (tp = 100 ms, B1 = 0.6 µT, 0.8 µT, duty cycle = 95%) at 86 frequency offsets unequally between 150 and − 150 ppm). Fat fraction (FF) gradient across the image was created by a tilted image slice (Fig. 3). Data processing were performed using in-house MATLAB (MathWorks) software.

Results The optimal correction was observed for FWHM = 0.43 ppm, which corresponds to the FWHM of the DS water signal in the Z-spectrum (0.41 ppm). Representative results of the proposed method for different FF and TEs are presented in Fig. 4. For both "in-phase" (Fig. 4A) and "opposed-phase" (Fig. 4B) conditions, one can see a significant reduction of pseudo-rNOE artifacts between [− 2.0, − 4.0] ppm. For the regions without fat DS_{fat} the proposed method yields the same correction as in the original published normalization [1].

Discussion The proposed method was show to successfully correct fat-induced artifacts across the entire Z-spectrum, particularly correcting pseudo-rNOE artifacts, which was not possible previously. This might have diagnostic relevance, as rNOE effects are known to be changed in pathologies. The residual rNOE artifacts might be associated with an incomplete water saturation ($\alpha(\Delta\omega_{DS},\text{water} \neq 0)$). Therefore, further studies about the possible underestimation effect of the residual fat signals on the true rNOE signal calculation are still necessary for the implementation of the method into clinical practice.

Conclusion This phantom study demonstrates the potential of the proposed normalization for in vivo CEST applications in regions where fat is present. Inclusion of prior knowledge about fat resonances and their dependence on the CEST saturation pulses, allows elimination of artifacts from DS_{fat} and therefore to unlock the potential for e.g. accurate assessment of rNOE signal, which is meaningful biomarker for investigations of pathologies, such as cancer [3].

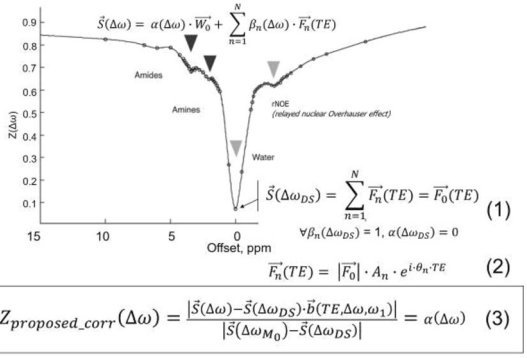

Fig.1: The residual signal at 0 ppm gives an estimate for the total fat signal (1). Using a multipeak model (2) and modeling the saturation function $\beta_n(\Delta\omega,\omega_1,\delta\omega_n)$ of n individual lipid resonances it is possible to introduce the correction factor $b(TE, \Delta\omega, \omega_1)$. $\theta_n = \gamma\cdot\delta\omega_n\cdot B_0$, $\delta\omega_n$, A_n – chemical shift and relative amplitude of n^{th}- fat resonance

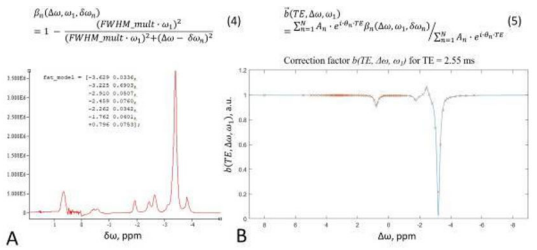

Fig.2: (A) 1H MRS spectrum of sunflower oil. (B) Visual representation of the $b(TE, \Delta\omega, \omega1)$, expressed by eq.5 with $\beta_n(\Delta\omega,\omega_1,\delta\omega_n)$ modeled as n Lorentzians (eq.4). Orange crosses represent the used correction factors smoothed for each offset $\Delta\omega$ using a 0.2 ppm window.

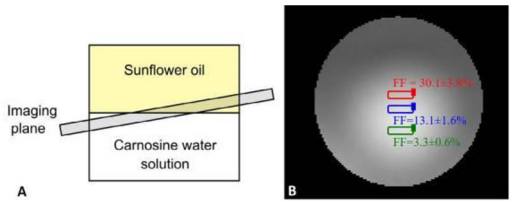

Fig. 3: (A) Schematic illustration of the phantom and the Fat Fraction (FF) gradient across the imaging slice. Image taken and adapted from [1] (B) Corresponding image slice with 3 ROIs of different Fat Fractions.

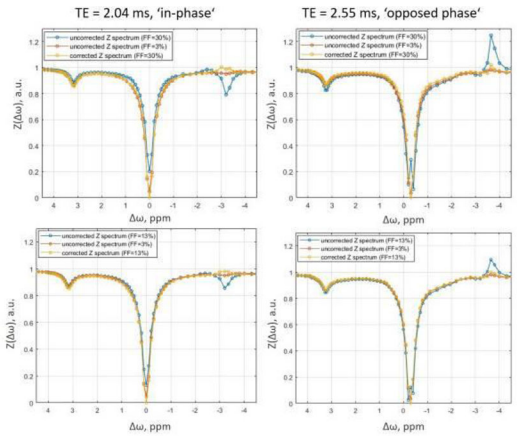

Fig 4:. Results of the proposed fat correction Z-spectra with different Fat Fractions shown for two TEs. A significant reduction of pseudo-rNOE artifact was observed.

Literature

1) Zimmermann et al. MRM 2020, https://doi.org/10.1002/mrm.27983
2) Huanzhou et al. MRM 2008, https://doi.org/10.1002/mrm.21737
3) Goerke et al. MRM 2019, https://doi.org/10.1002/mrm.27751

LT68.
A magnetization-prepared DREAM sequence for CEST imaging with an intrinsic dynamic B0 and B1 reference (CEST-MP-DREAM)

T. Baum[1], S. Weinmüller[1], J. Endres[1], P. Liebig[2], M. Zaiss[1,3,4]

[1]*Friedrich-Alexander-Universität Erlangen-Nürnberg (FAU), Department of Neuroradiology, Erlangen, Germany;*
[2]*Siemens Healthcare GmbH, Erlangen, Germany;*
[3]*Max-Planck-Institute for Biological Cybernetics, Magnetic Resonance Center, Tübingen, Germany;*
[4]*Friedrich-Alexander-Universität Erlangen-Nürnberg (FAU), Department Artificial Intelligence in Biomedical Engineering, Erlangen, Germany*

Introduction The "dual refocusing echo acquisition mode" (DREAM) sequence is an ultrafast method for B0 and B1 field mapping in 2D [1], and 3D [4]. In this work, a magnetization prepared DREAM sequence is proposed. This combination yields the advantages of magnetic preparation as well as the B1, B0 and TxRx phase maps from the DREAM sequence. As an example for MP DREAM, an APTw CEST [2] preparation is used with the standard STE first DREAM sequence as a readout. In CEST measurements, it is of great importance to correct the acquired CEST-spectra with accurate B1 and B0 maps. Until now, it was only possible to acquire B1 and B0 maps before or after the CEST measurement. With DREAM CEST, it is possible to acquire corresponding B1 and B0 reference maps for every single CEST offset.

Methods The DREAM CEST sequence was created with Pulseq, by combining the APTw_001 CEST [5] preparation block with two-dimensional, centric reordered STE first DREAM readouts (FoV: $220 \times 220 \times 8\text{mm}^3$; matrix: 64×64; $FA_{STE1} = FA_{STE2} = 55°$; $FA = 15°$; $TE_{FID} = 3.6$ ms; $TE_{STE} = 2.6$ ms; $TR = 5.6$ ms; $TA_{DREAM} = 387$ ms; CEST offsets: 34 ($-$ 300, $-$ 4:0.25:4 ppm); $TA_{total} \approx 3.5$ min). As a reference for the acquired B1 and B0 maps, a WASABI [3] sequence was applied before the DREAM CEST ($t_p = 5$ ms; nominal B1 = 3.7 T; $T_{rec,M0} = 12$ s; $T_{rec} = 3$ s; WASABI offsets: 32 ($-$ 300, $-$ 2:0.13:2 ppm); TA $\approx$ 2 min). The measurements were performed under approval of our local ethics committee at a 3 T Siemens PRISMA scanner.

The MP-DREAM provides for every CEST offset a B0 and B1 map, and a TxRx-phase map calculated by the formulas [1]:

$$\Phi_{B0} = \text{angle}(\text{FID} \cdot \text{STE}*) \quad (1)$$

$$\text{rB1} = \tan^{-1}(\sqrt{}(2|\text{STE}|/|\text{FID}|))/\text{FA}_{\text{STE1}} \quad (2)$$

$$\Phi_{tx/rx} = \text{angle}(\text{FID} \cdot \text{STE}) \quad (3)$$

In addition, the magnitude images of FID and STE can be magnetization-prepared and are evaluated using:
CEST-MP-DREAM(Δω) = 0.5·((|FID(Δω)|/|FID(− 300 ppm)|) + (|STE(Δω)|/|STE(− 300 ppm)|)) (4).

Results DREAM B1 (Fig. 1) and B0 maps (Fig. 2) show low deviations from the WASABI reference as long as CEST saturation is more than ± 1 ppm off-resonant from water. For offsets close to 0 ppm however, the B1 and B0 maps show some artifacts and thus deviate stronger from the ground truth. However, these offsets can also be omitted for MTRasym-based CEST imaging. Figure 3 shows that the DREAM magnitude images provide magnetization-prepared CEST spectra for both the STE and the FID image. Both images can be averaged (Eq. 4) to have a high SNR CEST-spectrum (Fig. 3c) with intrinsic B0 and B1 mapping as depicted in Figs. 1 and 2 for the corresponding offsets.

Discussion The presented magnetization-prepared DREAM CEST sequence allows the simultaneous mapping of B0 and B1 values during a CEST measurement. Residual tissue contrasts observed in these maps can potentially be further removed by suitable post-processing. Still the idea of a correction of the acquired CEST-spectra with individual B0 and B1 values for every CEST offset has a high potential for most accurate CEST scans. The fact that the DREAM CEST sequence works shows that the DREAM sequence can be applied after magnetization preparation as for example in the MPRAGE sequence, where B0 and B1 information can be used to further increase homogeneity.

Conclusion The known DREAM sequence can be used in a magnetization-prepared fashion. The DREAM CEST sequence as an example of MP DREAM delivers useful B1 and B0 maps for every CEST-prepared image, making dynamically corrected CEST possible.

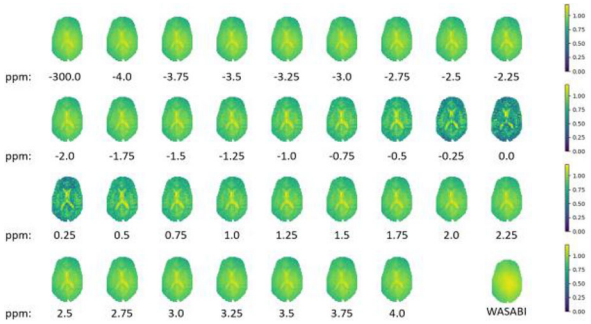

Fig. 1: *DREAM B1 maps for every CEST-prepared image (-4 to 4 ppm) with WASABI B1-map for reference.*

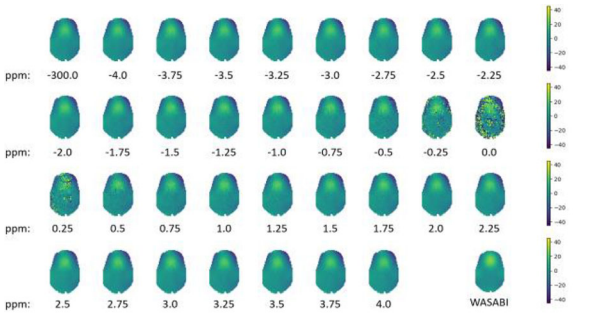

Fig. 2: *DREAM B0 maps [Hz] for every CEST-prepared image (-4 to 4 ppm) with WASABI B0-map for reference*

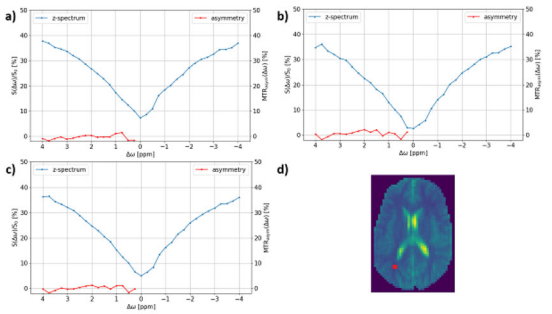

Fig. 3: *CEST-spectra and corresponding MTR_{asym} of (a) FID, (b) STE and (c) total CEST-MP-DREAM signal (eq. 4) in a (d) 4-pixel white matter ROI. This reveals that DREAM magnitude images can be magnetization-prepared.*

References

[1] Nehrke, K. and Börnert, P. (2012), DREAM—a novel approach for robust, ultrafast, multislice B1 mapping. Magn Reson Med, 68: 1517–1526.

[2] Sedykh, M, Liebig, P, Herz, K, et al. snapshot CEST++: the next snapshot CEST for fast whole-brain APTw imaging at 3 T. *NMR in Biomedicine*. 2023;e4955.

[3] Schuenke, P., Windschuh, J., Roeloffs, V., Ladd, M.E., Bachert, P. and Zaiss, M. (2017), Simultaneous mapping of water shift and B1(WASABI)—Application to field-Inhomogeneity correction of CEST MRI data. Magn. Reson. Med., 77: 571–580.

[4] Ehses, P, Brenner, D, Stirnberg, R, Pracht, ED, Stöcker, T. (2019), Whole-brain B1-mapping using three-dimensional DREAM. Magn Reson Med., 82: 924– 934.

[5] https://github.com/kherz/pulseq-cest-library/tree/master/seq-library/APTw_3T_001_2uT_36SincGauss_DC90_2s_braintumor

LT69.
Imaging the sinoatrial node without contrast agents

Y. Li[1], V. Casula[1], T. Liimatainen[1,2]

[1]*University of Oulu, Research Unit of Health Sciences and Technology, Oulu, Finland;*
[2]*University of Oulu, Department of Radiology, Oulu, Finland*

Introduction The sinoatrial node (SAN) is the main pacemaker of the cardiac conduction system (CCS), with an ellipsoidal fibrotic appearance. MRI together with Gadolinium (Gd) contrast agent has been used to image the CCS using late gadolinium enhancement (LGE)[1]. The SAN is surrounded by connective tissue, which may provide opportunities to image the CCS based on the contrast between myocardium and fibrous tissue. Previously, relaxation along fictious field (RAFF) and RAFF in nth rotating frame (RAFFn) have been applied to measure cardiac fibrosis[2,3,4]. The aim of this study was to demonstrate the contrast between sinoatrial node and myocardium without contrast agent at 7 T.

Methods Ex-vivo swine hearts (n = 6) were prepared for six tissue blocks which include SAN. All the measurements were completed at 7 T vertical preclinical MRI device (Bruker III Avance 300) using a 10 mm volume probe. The SAN sample was inserted into the NMR tube which was used for the measurement. Imaging slice was selected close to the isocenter with slice thickness of 3 mm. The matrix size was 64 × 64 and field of view (FOV) was 15 × 15 mm^2.For RAFF2, the pulse duration was set according to nominal power of 1250 Hz to 2.26 ms with number of pulses 0, 8, 16 and 32^2.For $T_{1\rho}$, the spin lock time (TSL) was set to 0 ms, 20 ms, 40 ms and 60 ms. The repetition time (TR) was 4 s and echo time (TE) was set from 11 to 44 ms to obtain T_2 images. The inversion time (TI) was from 100 to 1200 ms to obtain T_1 weighted images. For comparison, T_1, $T_{1\rho}$, and T_2 maps, as well as magnetic transfer (MT) imaging were acquired. The MT was measured with offsets (Δf) 1500 Hz, 2200 Hz, 3700 Hz, 7500 Hz and 20,000 Hz. The magnetization transfer ratio (MTR) was calculated as $100 \times (S_0 - S_{MT})/S_0$ where S_0 is the signal with 20,000 Hz offset and S_{MT} is the signal with other offsets[5]. Regions-of-interest (ROI) of SAN and myocardium were chosen based on the corresponding histology result image. After imaging, histology sections with 5 μm thickness were prepared and stained using Masson's Trichrome staining. The photographs were taken on an optical microscope equipped with a digital camera. Relaxation times (T_{RAFF2}, T_2, T_1 and $T_{1\rho}$) were averaged on the defined ROIs. Contrast to noise ratio (CNR = [T(SAN)-T(myocardium)]/σ_o(myocardium) × 100%, where σ_o is standard deviation over the ROI) of relaxation times was calculated between SAN and myocardium area. Differences of relaxation times between SAN and myocardium, and the difference between T_{RAFF2}, T_2, T_1, $T_{1\rho}$ and MT were compared. Statistical analysis was done by using Student t-test with Benjamini–Hochberg multiple comparison correction.

Results Contrast between SAN and surrounding myocardium is clear in RAFF2-weighted images (Fig. 1). Similarly, RAFF2 relaxation times in SAN are higher than in myocardium (Figs. 2, 3). The significant differences ($p < 0.001$) were found in the relaxation times between SAN and myocardium areas in RAFF2, T_2, $T_{1\rho}$ and MTR (Fig. 3). RAFF2, $T_{1\rho}$ and MT exhibited higher CNR than T_1 and T_2, which means higher contrast. The significant differences ($p < 0.01$) in CNR between RAFF2 and T_1, as well as between RAFF2 and T_2 have been found.

Discussion We considered the CNR between relaxation times and MTR to quantify the contrast between SA node and myocardium tissues. From the comparison between different imaging sequences, we have found that RAFF2, $T_{1\rho}$ maps and MT can gain higher contrast between SA node area and myocardium. Current results agree well with previous studies in mouse heart and in humans[4,6] where

higher RAFF2 and $T_{1\rho}$ relaxation times were associated with fibrous areas compared to remote areas in myocardial infarct. Longer T_{RAFF2}, $T_{1\rho}$ and T_2 in SAN compared to myocardium reflects more likely larger extra cellular space than larger proton exchange in collagen rich SAN area compared to myocardium which is supported by earlier LGE measurements[1].

Conclusion SAN was clearly visible in T_{RAFF2} and $T_{1\rho}$ maps, as well as in MTR images as higher relaxation times and MTR compared to myocardium. T_{RAFF2}, $T_{1\rho}$ maps and MT may be used to visualize SAN structure without contrast agent.

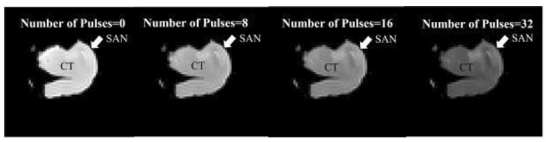

Fig.1: Example of RAFF2 weighted image series acquired with 0, 8, 16, and 32 weighting pulses. Image series demonstrate the relaxation contrast between the SAN and myocardium. The SAN region has longer relaxation time and appears bright next to the terminal crest (CT).

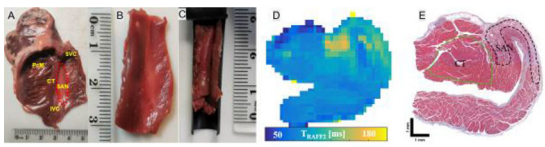

Fig.2: Photographs of the right atrium tissue block(A-C), T_{RAFF2} map (D) and corresponding histology section (Masson's Trichrome) (E) of the ex-vivo swine heart sample. The ROIs are chosen according to the histological information seen in histology image. CT- terminal crest, SVC-superior vena cava, IVC-inferior vena cava, SAN- sinus node, PcM-pectinate muscles.

	SA node	Myocardium	CNR (%)
T_{RAFF2}[ms]	114 ± 15	84 ± 8***	29 ± 6
$T_{1\rho}$[ms]	54 ± 7	42 ± 4***	25 ± 7
T_2[ms]	40 ± 6	35 ± 6***	16 ± 3 ##
T_1[ms]	1162 ± 103	1256 ± 122**	7 ± 5 ###
MTR [%]	36 ± 3	46 ± 3***	24 ± 6

Fig.3: Relaxation times (T_{RAFF2}, T_2, T_1 and $T_{1\rho}$) and MTR in the SA node and myocardium, as well as CNR were calculated between SAN and myocardium areas (mean±standard deviation). **p<0.01, ***p<0.001 relaxation time between SAN and myocardium. ## p<0.01, ###p<0.001 indicate the difference in CNR between the RAFF2 and other imaging methods.

References

1. Csepe T A, Zhao J, Sul L V, et al. European Heart Journal-Cardiovascular Imaging, 2017, 18(8): 862–869.
2. Liimatainen T, Sorce D J, O'Connell R, et al. Magnetic resonance in medicine, 2010, 64: 983–994.
3. Liimatainen T, Hakkarainen H, Mangia S, et al. Magnetic resonance in medicine, 2015, 73: 254–262.
4. Ylä-Herttuala E, Laidinen S, Laakso H, &Liimatainen T. J Cardiovasc Magn Reson. 2018; 20:34.
5. Magat J, Fouillet A, Constantin M, et al.Magnetic Resonance Materials in Physics, Biology and Medicine, 2021: 1–14.
6. Mirmojarabian A, Liukkonen E, Casula V, et al. Interventional Cardiology, 2021, 13: 381.

LT70.
3 T postmortem magnetic resonance imaging of the cerebellum at 115 µm isotropic resolution

M. Weigel[1,2,3,4], P. Dechent[5], R. Galbusera[1,2,3], E. Bahn[6], P. J. Lu[1,2,3], L. Kappos[1,2,3], W. Brück[6], C. Stadelmann[6], C. Granziera[1,2,3]

[1]*University of Basel, Translational Imaging in Neurology (ThINk) Basel, Department of Biomedical Engineering, Faculty of Medicine, Allschwil, Switzerland;*
[2]*University of Basel, Department of Neurology, Basel, Switzerland;*
[3]*University of Basel, Research Center for Clinical Neuroimmunology and Neuroscience Basel (RC2NB), Basel, Switzerland;*
[4]*University of Basel, Division of Radiological Physics, Department of Radiology, Basel, Switzerland;*
[5]*University of Göttingen, Department of Cognitive Neurology, MR-Research in Neurosciences, Göttingen, Germany;*
[6]*University of Göttingen, Institute of Neuropathology, Göttingen, Germany*

Introduction Ultra-high-resolution imaging of the human ex vivo brain has attracted significant attention recently due to its ability to reveal neuro morphology and pathology in neurological disorders like multiple sclerosis (MS)[1–5]. Usually, the focus lies on the cerebrum and lower attention is paid to the cerebellum, despite its importance for motor coordination, balance, and cognitive functions.

Recent advances in ex vivo MRI have enabled isotropic resolutions up to 100 µm (7 T) and 160 µm (3 T) using RF-spoiled gradient echo (FLASH) sequences[4–6]. Generally, FLASH sequences offer advantages like excellent contrast, low demands on the MR system, and long-term stability[5].

Balanced steady-state free precession (bSSFP), however, is the most signal-efficient approach. Apart from early work[1,2], recent work showed that 3 T bSSFP imaging is feasible up to 200 µm for the entire *ex vivo* brain[7]. However, all previous work followed the "common bSSFP rationale," which involves using high receiver bandwidths and maximal gradient amplitudes to minimize repetition time TR such that susceptibility-based artifacts are mitigated.

The purpose of this work is to show that—under ex vivo conditions—a "slow" bSSFP approach with very low receiver bandwidth, weaker gradients, and therefore "longer TR" facilitates dedicated cerebellar imaging with a 115 µm isotropic resolution on a clinical 3 T system.

Methods The brain of a patient diagnosed with MS was directly fixed in 4% formalin ~ 24 h after death (m, 63y, disease duration unknown). For MRI acquisition, the brain was immersed in fluorinated oil and positioned in a dome-shaped container[8]. Air bubbles were removed with a vacuum pump. A 3 T whole-body MR system with a standard 20-channel head coil was used.

An in-house 3D bSSFP sequence with RF phase-cycling capability was used, which circumvents typical restrictions like maximal 3D matrix size and minimal receiver bandwidth. The sequence uses all available memory on the MR system for the standard on-the-fly image reconstruction; magnitude images and phase maps were reconstructed. By taking advantage of slab selection and the readout direction, a reduced field-of-view approach dedicated to the cerebellum was realized[6]: FOV = 10.8 × 9.6 × 6.6cm^3, matrix = 832 × 936 × 576, isotropic resolution 115 µm, TR/TE = 34.0/17.0 ms, bandwidth = 50 Hz/Px, 6 phase-cyclings, avg = 2, TA_{total} = 80 h. The optimal excitation flip angle was determined to be 42 deg, based on pre-experiments.

The volume images and phase maps of the successive acquisitions were co-registered (rigid-body) with *Elastix* and then complex-averaged offline, magnitude and real-part images were exported.

Results The acquired 3D-image dataset successfully captured the detailed cerebellar architecture of tightly folded thin cortex layers and white matter interior, including deeper cerebellar nuclei such as the

dentate nucleus. Figures 1–3 display representative examples in different views, also providing deeper insight into pathological alterations associated with MS.

Discussion The presented work suggests a rather counterintuitive "slow" bSFFP approach for realizing dedicated cerebellum ex vivo imaging with an isotropic 115 µm resolution. The rationale is to increase the signal efficiency per unit time based on a low bandwidth, and thereby reducing the gradient demands for the ultra-high resolutions at the same time based on stretched gradients with lower amplitudes. Potential banding and drift artifacts were tackled well with an RF phase-cycling approach.

Generally, the low bandwidth bSSFP approach follows the concept of Weigel et al.[5], which is appealing due to its simplicity of using a clinical 3 T MR system with a standard head coil and a rather simple MRI sequence. Due to the ultra-high spatial resolution and long acquisition time of 3.3 days, co-registration of the repeated acquisitions is necessary prior to averaging up.

As a result of the developed acquisition and image reconstruction pipeline as well as the experimental setup, a 3D-image dataset of exquisite quality of the entire cerebellum ex vivo is obtained (Figs. 1–3). Additionally, microscopic pathological alterations such as caused by MS can be depicted and characterized (Figs. 1–3).

Conclusion The developed ex vivo bSSFP imaging approach realizes a comprehensive 115 µm isotropic resolution view of the entire human cerebellum with very good soft-tissue contrast, based on standard hardware and 3 T field strength. The technique provides fascinating insights into cerebellar morphology and represents an excellent approach for investigating subtle microscopic cerebellum abnormalities in MS.

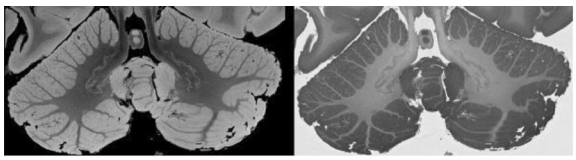

Fig. 1: (*Left*) Transverse slice of the originally acquired 115µm isotropic bSSFP acquisition. The image unveils a rather impressing image quality of the complex cerebellar fine structure. (*Right*) The real-part reconstruction represents another strong but inverted contrast.

Fig. 2: A sagittal reformation emphasizes the full isotropic 115µm resolution. Multiple focal alterations of the cerebellar cortex compatible with focal subpial demyelination can be observed, which is in agreement with previous pathological studies.

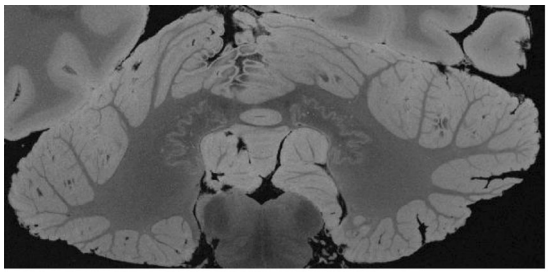

Fig. 3: Representative slice of a coronal 115µm-resolution reformation. Again, several cortical changes can be seen in the cerebellum, which may be linked to MS pathology (results prior to histopathological confirmation).

References

1. Pfefferbaum A et al. Neuroimage 2004;21:1585.
2. Miller KL et al. Neuroimage 2011;57:167.
3. Tendler BC et al. eLife 11:e73153.
4. Edlow B et al. Sci Data 2019;6:244.
5. Weigel M et al. Sci Rep 2021;11:15491.
6. Weigel M et al. Proceedings ISMRM 2022: p2022.
7. Weigel M et al. Proceedings ISMRM 2022: p1914.
8. Luciano NJ et al. J Vis Exp 2016;118.

LT71.
Molecular MRI of cardiac fibrosis monitors response to treatment after myocardial infarction

K. Amoiradaki[1], M. Tomczyk[2], G. Lima da Cruz[1,3], C. Velasco[1], F. Bortolotti[4], C. Prieto[1,5], R. Botnar[1,6,5,7], M. Giacca[2,6], A. Phinikaridou[1,6]

[1]*King's College London, Biomedical Engineering and Imaging Sciences, London, United Kingdom;*
[2]*King's College London, School of Cardiovascular and Metabolic Medicine & Sciences, London, United Kingdom;*
[3]*University of Michigan, Department of Radiology, Michigan, MI, United States;*
[4]*International Centre for Genetic Engineering and Biotechnology, Molecular Medicine Laboratory, Trieste, Italy;*
[5]*Pontificia Universidad Católica de Chile, Escuela de Ingeniería, Santiago de Chile, Chile;*
[6]*BHF Centre of Research Excellence, London, United Kingdom;*
[7]*Pontificia Universidad Católica de Chile, Institute for Biological and Medical Engineering, Santiago de Chile, Chile*

Introduction Cardiac fibrosis after myocardial infarction (MI) is a hallmark of the failing heart. Activation of myofibroblasts after MI can lead to excessive deposition of extracellular matrix (ECM) proteins and the development of a fibrotic scar rich in collagen and elastin, which can impair cardiac function. Currently, there is a clinical need to diagnose and treat cardiac fibrosis. Chordin-like 1 (Chrdl1) is a transforming growth factor-beta 1 (TGF-β1) antagonist that was recently discovered to inhibit fibrosis[1]. In this study, we used molecular MRI to non-invasively quantify cardiac fibrosis and monitor the antifibrotic effects of Chrdl1 in a mouse model of MI.

Methods MI was induced in CD1 mice by permanent occlusion of the left anterior descending artery. The adeno-associated viral vectors serotype 9 (AAV9) expressing Chrdl1 (AAV9-Chrdl1) or an empty vector (AAV9-Control) were injected intramyocardially at the border region of the infarct at the time of ligation (n = 8 per group). In vivo MRI was performed with a clinical 3 Tesla scanner at 4 weeks post-MI. 2D short axis cine images covering the left ventricle (LV) were used to assess cardiac function parameters including end-systolic (ESV, µl) and end-diastolic volume (EDV, µl); ejection fraction (EF,

%) and LV mass (mg). T1-weighted 3D inversion recovery (IR) images were used to acquire late gadolinium enhancement (LGE) images of the myocardium 60 to 90 min after intravenous administration of collagen (Gd-EP3533) and elastin (Gd-ESMA)-targeting contrast agents[2,3]. LGE size (%) was quantified as a percentage of LGE volume over myocardial volume. Subsequently, T1 mapping was performed using a 2D Look-Locker IR sequence with an inversion pulse followed by the acquisition of 30 IR images with inversion times ranging from 20 to 12,000 ms. The relaxation rate (R1, s^{-1}) was calculated as (1/T1) × 1000. The T1 maps were reconstructed offline using an in-house developed MATLAB script. The MRI acquisition parameters used in the study are listed in Fig. 1.

Results Cine MRI showed that mice treated with AAV9-Chrdl1 had significantly lower ESV, EDV and LV mass compared with the AAV9-Control group (Fig. 2A–C, E). Moreover, the AAV9-Chrdl1 group had a higher ejection fraction (39.8 ± 11.9%) compared with the AAV9-Control group (20.7 ± 3.8%; $p < 0.001$) at 4 weeks post-MI (Fig. 2A, D). Molecular MRI using the collagen and elastin agents showed selective enhancement of the infarcted myocardium (Fig. 3A). Animals treated with AAV9-Chrdl1 had significantly reduced fibrosis as seen by the lower LGE size ($LGE_{collagen}$, 7.8 ± 3.5%; $LGE_{elastin}$, 4.1 ± 1.9%) compared with the AAV9-Control group ($LGE_{collagen}$, 18.6 ± 5.6%, $p < 0.001$; $LGE_{elastin}$, 18.4 ± 6.1%) (Fig. 3B, C). Quantitative T1 mapping showed significantly higher R1 values in the infarcted compared to the remote myocardium in the AAV9-Control group but not the AAV9-Chrdl1 group (Fig. 3D, E). Importantly, the R1 of the infarct was significantly lower in mice treated with Chrdl1 ($R1_{collagen}$, 1.5 ± 0.2 s^{-1}; $R1_{elastin}$, 1.6 ± 0.3 s^{-1}) compared with the AAV9-Control group ($R1_{collagen}$, 2.3 ± 0.3 s^{-1}; $R1_{elastin}$, 2.1 ± 0.2 s^{-1}) suggesting lower contrast agent uptake. Overall, these results suggest that Chrdl1 exerts cardioprotective properties by preserving cardiac function and reducing fibrosis after MI.

Discussion Molecular MRI of myocardial fibrosis with a clinical 3 T scanner enables the selective detection and quantification of ECM remodelling in a mouse model of MI. Using this imaging technique, we show that treatment with Chrdl1 reduced cardiac dilation, preserved cardiac function, and reduced both collagen and elastin deposition at 4 weeks post-MI.

Conclusion Our findings show that molecular MRI is a powerful tool to non-invasively assess the extent of cardiac fibrosis and monitor the antifibrotic and functional effects of novel therapies.

Acknowledgements
This work was supported by the King's BHF Centre of Research Excellence RE/18/2/34213, PG/2019/34897, and RG/20/1/34802.

Disclosure
Prof. Mauro Giacca is founder, equity holder and consultant of Forcefield Therapeutics, which is developing Chrdl1 as a treatment for myocardial infarction. I and the other authors have no financial interest or relationship to disclose regarding the subject matter of this study.

Parameter	Multi-slice 2D Cine	3D inversion recovery LGE	2D Look-Locker T1 mapping
Field of view (mm)	35x35	35x35	35x35
Resolution (mm)	0.2x0.2	0.3x0.3	0.3x0.3
Number of slices	8	8	1
Slice thickness (mm)	1	1	2
Flip angle (degree)	40	25	15
Repetition time (ms)	8	7.6	7.5
Echo time (ms)	6	3.1	3.1

Fig. 1: MRI acquisition parameters.

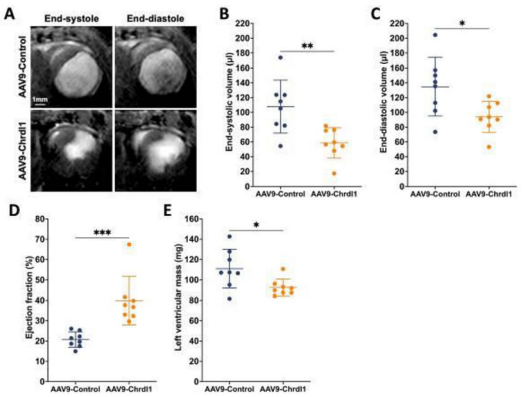

Fig. 2: Chrdl1 preserves cardiac function at 4 weeks post-MI. **(A)** Representative cine short axis images at the end-systolic and end-diastolic phases of hearts treated with AAV9-Control or AAV9-Chrdl1. Measurements **(B)** end-systolic volume, **(C)** end-diastolic volume, **(D)** ejection fraction and **(E)** LV mass in the AAV9-Control and AAV9-Chrdl1 groups. Statistical analyses: Unpaired t-test, * p<0.5, ** p<0.01, *** p<0.001.

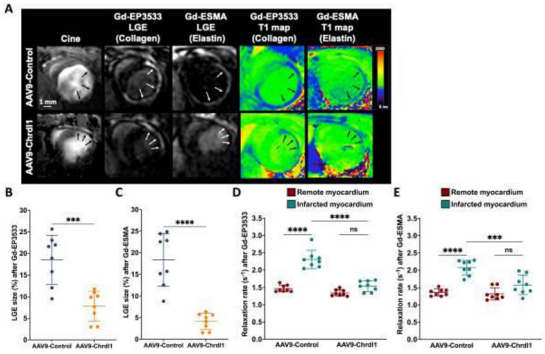

Fig. 3: AAV9-Chrdl1 has an antifibrotic effect at 4 weeks after MI. **(A)** Representative short axis images of the hearts with arrows indicating the area of myocardial wall thinning (cine) and contrast agent uptake (LGE and T1 maps). LGE size quantified after the injection of **(B)** Gd-EP3533 and **(C)** Gd-ESMA. Statistical analyses: Unpaired t-test. Relaxation rates (R1) of remote and infarcted myocardium measured after injection of **(D)** Gd-EP3533 and **(E)** Gd-ESMA. Statistical analyses: One-way ANOVA. *** p<0.001, **** p<0.0001.

References

1. Ruozi, G. et al. (2022). Cardioprotective factors against myocardial infarction selected in vivo from an AAV secretome library. *Science Translational Medicine*, *14*(660).
2. Helm, P. et al. (2008). Postinfarction myocardial scarring in mice: Molecular MR imaging with use of a collagen-targeting contrast agent. *Radiology*, *247*(3).
3. Ramos, I. et al. (2018). Simultaneous Assessment of Cardiac Inflammation and Extracellular Matrix Remodeling after Myocardial Infarction. *Circulation. Cardiovascular Imaging*, *11*(11).

LT72.
Developing a simple simulation platform for point-of-care MRI devices

M. Mach[1], A. Web[1]

[1]*Leiden University Medical Centre, Radiology, Leiden, Netherlands*

Introduction Recent papers have highlighted the lack of accessible and sustainable medical imaging infrastructure in large portions of the world[1–3]. In terms of MRI, there is not only a shortage of hardware, but also of trained personnel and training material. With low-field

portable systems such as Hyperfine and Halbach-based systems starting to be sited in both academic and clinical settings, simple simulation software based on the physics and hardware components associated with low-field MRI could play an important role in increasing the knowledge base for users of such equipment. We present details of our initial developments in this area, with open-source simulation code written in Python, which is easily run on a number of different mobile devices.

Methods The simulation code is written in Python 3.7 and uses the following freely downloadable packages: numpy, scipy, matplotlib, cv2, cmath, tkinter, and PIL. The code can be run on a standard laptop computer. Calculations are currently performed primarily in the image domain. Morphometric data was derived from the ITis Duke model at $1 \times 1 \times 1$ mm resolution. Since most POC studies are neurological, the tissue model was truncated at the level of the neck. Tissues were assigned to be white matter, gray matter, lipid, or cerebrospinal fluid with corresponding relaxation times from in vivo measurements at 50 mT. Inputs to the simulation package (Fig. 1) include a 3-dimensional B1 + map, a 3-dimensional B0 map, and a 3-axis map of the magnetic field produced by the gradient coil: each of these can be easily adapted to see the effects on the image. Image processing includes simple high-pass and low-pass spatial, as well as non-local mean filtering. Sequences are gradient-echo, spin-echo, inversion recovery (IN), double IN, FLAIR, SSFP, diffusion, and TSE with different k-space trajectories (linear, in-out, out-in). The user can also input a measured or estimated noise level, which is implemented as Gaussian noise with the appropriate mean and standard deviation. The parameters characterizing each sequence (TR, TE, etc.) can also be changed interactively in a 3D environment to view their effect (Fig. 4).

Simulations were performed using our 46 mT Halbach-array hardware system characteristics, with an inner diameter of 31 cm. The 3D B0 map was measured using an asymmetric turbo spin echo sequence; the 3D B1 + map from the Litz wire spiral elliptical solenoid was measured using a double angle method; the fields produced by the optimized gradient coils were simulated from the wire patterns using the Biot-Savart law. Each of these inputs is a simple 3D matrix of values: different maps can be loaded from the interface.

Results and Discussion Figure 2 shows the user graphical interface, with example gradient echo images in axial, sagittal and coronal planes without any post-processing. The effects of the B1+ /B1− non-uniformities from a tight-fitting spiral elliptical solenoid coil can be seen in the slightly higher SNR at the outside of the images. The effect of the gradient non-linearities (particularly along the bore of the Halbach) are shown by distortions. Figure 3 shows axial image of the different sequences with corresponding parameters. Figure 4 illustrates the impact of the changes for each parameter on a gradient echo sequence. A Gaussian filter with s = 0.7 was applied to images in Figs. 3 and 4.

Conclusion This works represents an initial implementation of a simple simulation package especially designed for low-field POC MRI systems. Compared to typical clinical scanners, effects such as B1 interactions with the body are negligible and subject-independent, whereas DB0 effects, limited and their time-dependence, as well as limited gradient strength, are much more important to consider. In future, the platform will expand to a greater range of sequences, as well as enabling k-space undersampling, iterative and model-based reconstructions, and AI-based denoising.

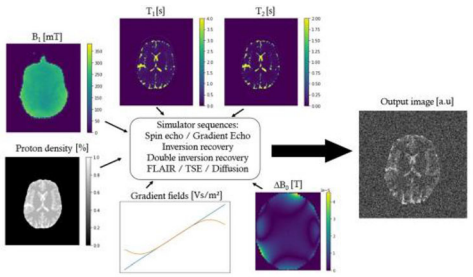

Fig. 1: Schematic of the inputs used for the low-field POC simulator. Proton density, T1, and T2 maps are derived from voxelated human models and measured relaxation times. The DB0, B1+ and gradient fields can be measured or simulated and are input as three-dimensional matrices.

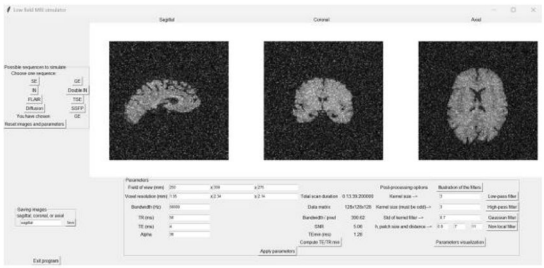

Fig. 2: Simulation graphical user interface allowing the input of different types of imaging sequences, data acquisition, and processing parameters, calculation of parameters such as relative SNR and total acquisition time, and display of the central slice in three orthogonal dimensions.

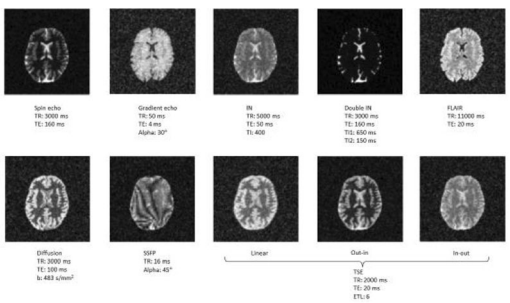

Fig. 3: Axial images of simulated spin echo, gradient echo, inversion recovery (IN), double IN, FLAIR, diffusion, SSFP, and linear, in-out, and out-in turbo spin echo (TSE) sequences.

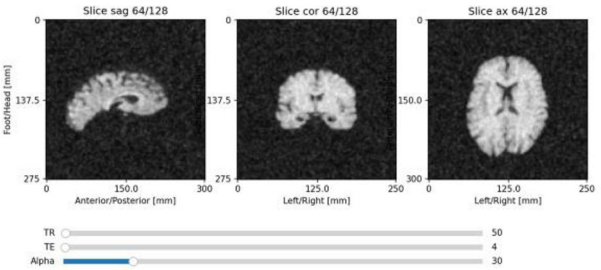

Fig. 4: Illustration of the parameters visualization in a 3D live interaction of a gradient echo sequence.

References
1. Ogbole GI, Adeyomoye AO, Badu-Peprah A, Mensah Y, Nzeh DA. Survey of magnetic resonance imaging availability in West Africa. Pan Afr Med J 2018;30:240.
2. Geethanath S, Vaughan JT, Jr. Accessible magnetic resonance imaging: A review. J Magn Reson Imaging 2019.
3. Anazodo UC, Ng JJ, Ehiogu B, Obungoloch J, Fatade A, Mutsaerts H, Secca MF, Diop M, Opadele A, Alexander DC, Dada MO, Ogbole G, Nunes R, Figueiredo P, Figini M, Aribisala B, Awojoyogbe BO, Aduluwa H, Sprenger C, Wagner R, Olakunle A, Romeo D, Sun Y, Fezeu F, Orunmuyi AT, Geethanath S, Gulani V, Nganga EC, Adeleke S, Ntobeuko N, Minja FJ, Webb AG, Asllani I, Dako F, Conesortium for Advancement of MRIE, Research in A. A Framework for Advancing Sustainable MRI Access in Africa. NMR Biomed 2022:e4846.

LT73.

Spatial dependence of hepatic glucose uptake dynamics after oral ingestion of deuterated glucose: Initial observations by Deuterium metabolic imaging (DMI) at 7 T

S. Poli[1,2], N. F. Lange[3], D. Herzig[4], L. Bally[4], R. Kreis[1,2]

[1]*University of Bern, MR methodology, Institute of Diagnostic and Interventional Neuroradiology, Bern, Switzerland;*
[2]*University of Bern, Translational Imaging Center, Sitem-Insel, Bern, Switzerland;*
[3]*University of Bern, Department of Visceral Surgery and Medicine, Bern, Switzerland;*
[4]*University of Bern, Department of Diabetes, Endocrinology, Nutritional Medicine and Metabolism UDEM, Bern, Switzerland*

Introduction Deuterium Metabolic Imaging (DMI) is a non-invasive technique to visualize and quantify metabolic activity in animals and humans1. DMI is particularly useful in the study of hepatic glucose metabolism and in a wide range of clinical disorders2. Previous publications from our group exploited the possibilities of DMI in an interleaved fashion with 13C-MRS3 to evaluate and map the metabolic fate of glucose (Glc) and its downstream products.
One of the challenges of hepatic DMI is the inability to discriminate between different biological compartments, including the discrimination of the hepatic from vascular Glc signals, given that 30% of hepatic volume consists of blood4. Defining the uptake dynamics in the portal vein and contrasting this with the dynamics in liver tissue could be a first step to address this issue. The current study builds on previously recorded data and investigates the spatial–temporal dependence of the distribution of D-Glc in the liver using DMI at 7 T.
Methods Scans were performed at 7 T (Terra, Siemens) with a triple-tuned surface coil (1H: quadrature-driven dual loop, 2H and 13C: linearly driven single loops). Ten healthy subjects ingested 60 g of [6,6“-2H2]-Glc in 200 mL of water, in a supine position.
Gradient MRIs recorded with and without breath-hold serve as spatial reference for the MRSI maps. Conventional 3D-MRSI (TR 500 ms; 4 averages with acquisition-weighting; 12 × 12 × 8 phase encodings; nominal resolution of 18.3 × 18.3 × 27.5 mm3; 1 kHz spectral width and 512 points; total acquisition time of 4:08 min) was used with a 0.50 ms rectangular excitation pulse (frequency centered on D-water, HDO) to acquire spatial kinetic D-Glc signal information. Data fitting and visualization performed in AMARES and Spectrim. Voxels selected inside the liver, minimizing partial volume effects, within the coil”s limits.
Results and Discussion Figure 1 shows time courses for hepatic D-Glc normalized by the initial HDO content for a single subject in voxels perpendicular to the coil, with a resolution of 5–10 min Voxels 1 and 2 are placed in a hepatic region where only few large blood vessels and mainly capillaries are expected. Voxel 4 is selected to overlap with large vessels, in the liver hilus region (background image obtained in breath hold while DMI is recorded in free breathing). Voxels 1 and 2 show a rise of the signal until its maximum is reached at ∼ T70 after D-Glc intake, with the signal remaining visible until the end of the scan. Voxel 4 shows a more rapid increase; it reaches its maximum at T50, before the signal drops to baseline and is not visible towards the end. This supports the assumption that the signal from voxel 4 primarily represents portal vein inflow. Voxel 3 shows an intermediate behavior.
Figure 2 shows kinetic metabolic maps of D-Glc/HDO distributions. The grid is composed of 7 × 7 voxels. Single voxel spectra show a SNR = 15–34 and linewidths = 20–25 Hz. At T0 no D-Glc signal is present. After D-Glc intake, the signal rises heterogeneously, first in the hilus region where its amplitude reaches 3–4 times the HDO signal at T40-70. In peripheral liver regions, the signal starts to rise later and at T150 the signal is evenly distributed.
Figure 3 shows metabolic maps for D-Glc/HDO for two-time points per subject. Based on the above hypothesis, an inhomogeneous distribution of the signal is expected at T20, with highest signal in the central part of the liver, while a more homogeneous signal distribution should be observed at T150. In six out of ten subjects, such a spatially dependent signal has indeed been observed. In the remaining subjects, the initial rise in the central region was not observed, probably caused by SNR limitations and partly due to larger distance to the coil (circular loop, placed laterally, while the proton field of sensitivity is larger because of a butterfly coil arrangement).
Conclusion Spatial dependence of the temporal course of the hepatic glucose signal following oral ingestion of D-Glc is detected by DMI for humans at 7 T. Our results showed a faster rise of the D-Glc signal in the region of the liver hilus, followed by a more homogeneous distribution in peripheral areas of the liver. With improved DMI resolution, increased signal-to-noise ratio, and reduced acquisition time thanks to denoising techniques, subspace reconstruction and echo-planar spectroscopic imaging5, it will be possible to acquire in breath holds to eliminate breathing-related confounds, such that localization of the glucose signal to hepatic artery, hepatic portal vein and surrounding hepatic sinusoid and tissue should become feasible and reliable. This can then be used to derive an input function for metabolic modeling of glucose metabolism and improve pathophysiological understanding.

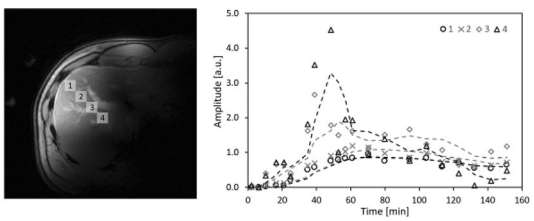

Fig. 1: Time courses of the ratio between D-Glc and water signal at T0. Signal is represented from four voxels at an incremental perpendicular distance with respect to the coil. Voxels 1 and 2 are placed on hepatic and capillary tissues. Voxel 4 is selected overlapped with the hepatic hilum. Voxel 3 is in an intermediate position. Dashed lines are a two-period moving average model.

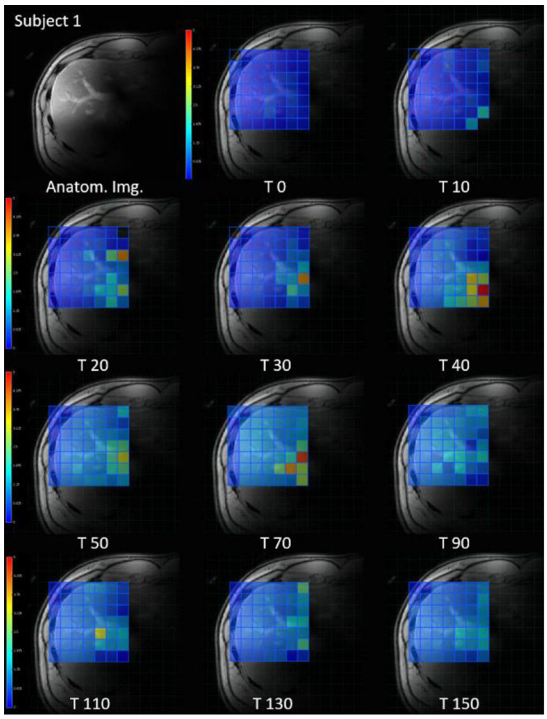

Fig. 2: Kinetic metabolic maps of D-Glc over initial water signal. The grid comprises a 7x7 grid (selected to focus on the hepatic region), overlapped with anatomical images. The metabolic maps are shown before D-Glc intake and 10, 20, 30, 40, 50, 70, 90, 110, 130, and 150 minutes after D-Glc intake.

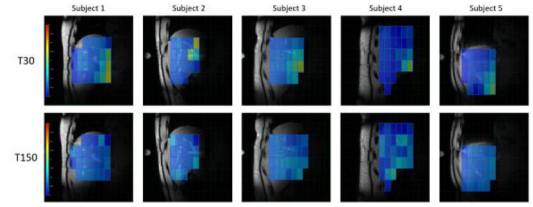

Fig. 3: Kinetic metabolic maps of D-Glc over initial water signal for five different subjects 30 minutes after D-Glc intake, showing a heterogeneous distribution of the signal with higher intensities in the hepatic blood vessel region, and 150 min after the intake, a more homogeneous signal distribution.

References

1. Chen Ming;Prog Nucl Magn Res Spec.134:39
2. Petersen;Nat Rev End.13:572
3. Poli;ISMRM2022.p.628
4. Kan;Sem Int Rad.25:77
5. Nam;ISMRM2021.p.231

LT74.
Comparison of the metabolic impact of gadodiamide (Omniscan) and gadoteridol (ProHance) by means of multi-organ and plasma metabolomics in mice

E. Gianolio[1], E. di Gregorio[1], C. Furlan[1], F. Romano[2], G. Riccardi[2], N. Cavallini[3], F. Savorani[3], A. Randazzo[2], N. Iaccarino[2]

[1]*University of Torino, Molecular Biotechnologies and Health Science, Turin, Italy;*
[2]*University of Napoli, Pharmacy, Naples, Italy;*
[3]*Polytechnic University of Turin, Applied Science and Technology, Turin, Italy*

Introduction Gadolinium-based contrast agents (GBCAs) are massively employed in radiology to increase the diagnostic power of MRI. During the past decades, warnings about potential harmful effects from the use of linear GBCAs ascribable to the release of free gadolinium cations have been raised. However, investigations aiming at detecting possible metabolic perturbations and/or potential adverse health effects due to gadolinium deposition are still lacking. Thus, the aim of the present work was to exploit a multi-organ (liver, kidney, spleen, cerebrum, and cerebellum) and plasma metabolomics approach to investigate the effects on the main metabolic pathways of multiple administrations of one linear (Omniscan, gadiodiamide) and one macrocyclic GBCA (ProHance, gadoteridol) in healthy mice.

Methods A total of 30 healthy male Balb/c mice were divided into three groups (control group, Gadodiamide-treated group, Gadoteridol-treated group) and received twenty consecutive injections of each GBCA during a 5-week period, then organs (brain, cerebellum, kidney, liver, and spleen) and plasma were retrieved 1 month after the end of the treatments. Plasma samples were analyzed through one-dimensional NOESY and CPMG 1H-NMR while aqueous extracts of mice organs were analyzed by GC–MS.

Results Principal Component Analysis (PCA) of plasma samples revealed a clear separation of the CTRL group from the Gadodiamide and Gadoteridol groups, due to a clear lipid dysregulation in the GBCAs-treated animals. PCA analysis including only Gadodiamide and Gadoteridol groups revealed that plasma of the Gadodiamide group had lower levels of alanine, pyruvate and lactate. On the other hand, the multiorgan metabolomics analysis displayed a clear separation of the Gadodiamide group from the Gadoteridol and CTRL groups, suggesting that treatment with Gadodiamide perturbs the physiological state of the mouse model. The organs most affected by the Gadodiamide treatment are the brain, cerebellum and liver, where an up-regulation of the energetic pathways, as well as a dysregulation of the amino acids and nucleotide metabolism was observed.

Discussion Multivariate analysis of plasma samples suggests the presence of a dysregulation in carbohydrate and energetic metabolism caused by the administration of the linear contrast agent (Gadodiamide). The multi-organ metabolomic study offered a global picture of the effects caused by the two GBCAs, revealing that the administration of Gadodiamide induces an up-regulation of the energetic pathways (such as glycolysis, Kreb"s cycle, fatty acids beta oxidation and gluconeogenesis), as well as a dysregulation of the amino acids and nucleotide metabolism in the brain, cerebellum and liver, while the use of Gadoteridol, seems to not cause any significant alteration of the metabolome.

Conclusion Overall, the results of this study shed light, for the first time, on the metabolic alterations related to the use of a linear GBCA vs. macrocyclic one, by identifying the organs most affected by the administration of the investigated chelates. Moreover, it suggests that the metabolomics approach can be considered as a valid additional tool for the evaluation of the toxicity of the investigated GBCAs.

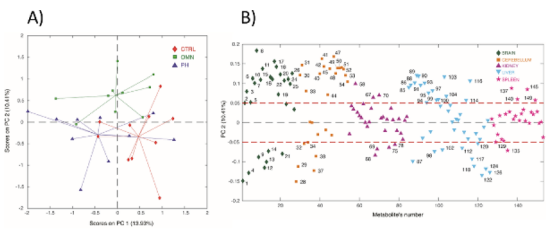

Fig. 1: PC1 vs. PC2 scores plot (A) and PC2 loadings plot (B) of the PCA model calculated using all organ extracts analyzed by GC-MS.

LT75.
3D triple-VENC flow MRI for estimation of aortic blood flow in an animal model of extracorporeal circulation: A feasibility study

J. Schrauder[1], A. K. Assmann[1], S. Reimers[1], A. Lichtenberg[1], A. Assmann[1], S. Boretius[1], A. Moussavi[1]

[1]*German Primate Center-Leibniz Institute for Primate Research, Functional Imaging Laboratory, Göttingen, Germany*

Introduction Although extracorporeal circulation (ECC) is routinely used during cardiac interventions to maintain the arrested cardiopulmonary function, the impact of different ECC scenarios on the aortic and cerebral blood flow is still under debate [1]. Recently, Assmann et al. presented the first MR-compatible in vivo small animal ECC model closely resembling ECC scenarios in humans [2]. However, due to the wide span of varying flow velocities in such ECC models (cannula: $\sim$ 180 cm/s, left subclavian artery: $\sim$ 5 cm/s), the estimated velocities using conventional single-VENC phase contrast MRI are inaccurate. To overcome this limitation, we developed and established a tailored 3D triple-VENC phase contrast MRI approach to assess the aortic blood flow more accurately.

Methods MR data was acquired with a 9.4 T MR system (BioSpec, Bruker, Germany) using a Tx/Rx quadrature birdcage coil. 3D Flow data was obtained from one healthy male rabbit during antegrade ECC intervention (cannula inserted in ascending aorta). A triple-VENC phase contrast MRI protocol using a flow compensated gradient echo with Hadamard flow encoding (TR/TE = 7.5/3.5 ms, VENC = 20, 50 and 200 cm/s, spatial resolution = 0.5 mm^3 and scan time = 12 min per VENC) was used for image acquisition.

Aortic blood flow was estimated using an in-house developed analysis pipeline (ITK-SNAP 3.8.0 and MATLAB R2021a). Firstly, the aorta was segmented and phase drifts due to eddy currents were corrected by fitting a first-order polynomial surface to static regions after excluding spatial aliasings. Secondly, phase aliasings were corrected using the unwrapping algorithm ROMEO [3]. Finally, residual phase aliasings (e.g. 4π or higher) were corrected by using the low VENC (20 cm/s) images as the initial guess and the mid and high VENC (50 and 200 cm/s) images as boundary conditions. This step was exclusively done in areas of high velocity close to the cannula.

Results Figure 1 explores the limitations of the conventional single-VENC approach. In particular, low VENCs resulted in high accuracy in regions of low velocity (e.g. aortic arch) but revealed wrong values for regions of high velocity (e.g. cannula). Vice versa, high VENCs resulted in correct values for regions of high velocity with the drawback of low precision in regions of low velocity. In contrast, the triple-VENC approach provided high accuracy and precision over the whole range of velocities, as clearly visible in the selected though-plane profile of the descending aorta. The SNR has increased by 9.4, slightly below the expected theoretical improvement of 10 (reduction of the effective VENC to one-tenth).

Qualitative (Fig. 2) and quantitative (Table 1) comparison of regions with high (e.g. cannula) and low (e.g. aortic brunches) velocity demonstrate the outstanding performance of the triple-VENC approach. Figure 2a, b shows the estimated flow vectors of the thoracic aorta using the single- and triple-VENC approach, respectively. In particular, the correct flow directionality in the left common carotid artery (LCAR) could only be observed by the triple-VENC approach (Fig. 2c, d).

Table 1 summarizes the estimated flow rates at different levels of the thoracic aorta for an antegrade ECC scenario. Using the triple-VENC approach, a much higher agreement in the estimated flow rates at a distal and proximal level of the same vessel could be achieved. In particular, the estimated range in the descending aorta is 173–217 ml/min and 139–154 ml/min for single- and triple-VENC, respectively. Noteworthy, realistic flow rates of small aortic brunches (e.g. common carotid arteries) could only be achieved using the triple-VENC approach. However, a discrepancy of 10–15% between the inflow and outflow volume was observed for both single- and triple-VENC approaches.

Discussion In this feasibility study, we have introduced a triple-VENC 3D phase contrast MRI protocol for assessing aortic blood flow in an animal model of ECC. Besides the increased SNR, high accuracy and precision could be achieved over the whole range of velocities. Although the estimated outflow (225 ml/min) of the triple-VENC approach matches the measured outflow of the heart–lung machine (220 ml/min), the estimated inflow and outflow volumes differ by 10–15%. It is assumed that this mismatch is mainly due to residual inaccuracies in the segmentation of the cannula.

Conclusion The introduced triple-VENC approach is a robust phase contrast MRI protocol, which ensures the assessment of aortic blood flow over a wide range of velocities as usually encountered in ECC interventions. In ongoing studies, this established method will be used to investigate the impact of different ECC scenarios on the aortic and cerebral blood flow and to further refine simulations using computational fluid dynamics.

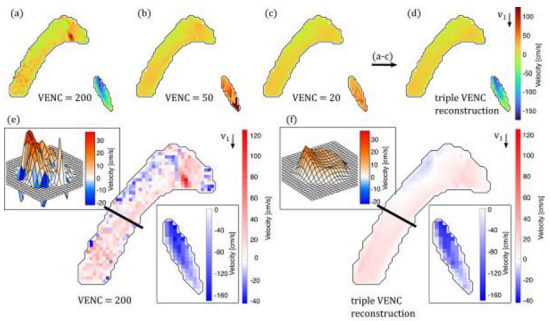

Fig. 1: Qualitative comparison of the estimated velocities of the single- and triple- VENC approach in the aortic arch and cannula of an antegrade ECC scenario. The increased accuracy and precision of the triple VENC approach yields to lower fluctuations of the estimated velocities in the aortic arch and smoothed through-plane flow profiles.

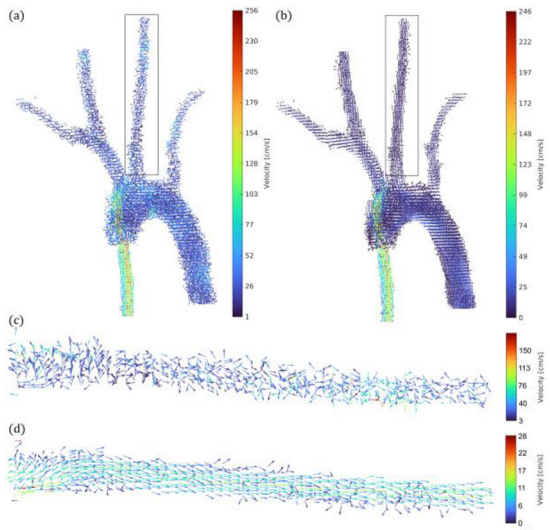

Fig. 2: Estimated flow vectors of the single (a) and triple-VENC (b) approach. The LCAR highlighted with boxes is plotted for a more detailed comparison of both (c) single- and (d) triple-VENC methods showing the clear improvement in quantification of flow directionality using the triple -VENC approach.

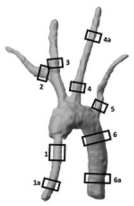

Vessel	Volume Flow [ml/min]	
	High VENC	Triple VENC
(1) Cannula	293 ± 16	261 ± 16
(1a) Cannula	271 ± 10	247 ± 16
(2) Right Subclavarian Artery	26 ± 14	25 ± 1
(3) Right Common Carotid Artery	1 ± 9	16 ± 2
(4) Left Common Carotid Artery	1 ± 6	13 ± 2
(4a) Left Common Carotid Artery	8 ± 11	10 ± 1
(5) Left Subclavarian Artery	13 ± 4	17 ± 1
(6) Descending Aorta	217 ± 7	154 ± 6
(6a) Descending Aorta	173 ± 15	139 ± 6

Table 1: Quantitative analysis of aortic blood flow. (left) Schematic visualization of the selected ROIs in antegrade perfusion. (right) Estimated flow rates of the selected ROIs for the conventional single VENC (200 cm/s) and the triple VENC experiment.

References

[1] Ouweneel DM et al. Intensive Care Med. 2016 [2] Assmann AK et al. Interact Cardiovasc Thorac Surg. 2019 [3] Dymerska B et al. MRM 2021

LT76.

Effects of arterial transit time on cerebrovascular reactivity measures from time-encoded arterial spin labelling (ASL), pseudo-continuous ASL and BOLD MRI

G. Hoffmann[1,2], M. J. P. van Osch[3,4], L. Václavů[3], J. Kufer[1], L. Schmitzer[1], C. Zimmer[1,2], S. Kaczmarz[1,2,5], C. Preibisch[1,2]

[1]*Technical University of Munich, School of Medicine, Department of Neuroradiology, Munich, Germany;*
[2]*Technical University of Munich, School of Medicine, TUM-Neuroimaging Centre, Munich, Germany;*
[3]*Leiden University Medical Centre, Department of Radiology, C.J. Gorter MRI Center, Leiden, Netherlands;*
[4]*Leiden University, Leiden Institute of Brain and Cognition, Leiden, Netherlands;*
[5]*Philips GmbH Market DACH, Hamburg, Germany*

Introduction Cerebrovascular reactivity (CVR) measurements are promising for assessing the vascular status, especially in cerebrovascular diseases.[1,2] Therefore vasoactive stimuli, such as acetazolamide (ACZ) or inhalation of hypercapnic gases (air with increased CO2-levels) are used to challenge the vascular system.[3,4] While most applications indirectly probe CVR by blood oxygenation level dependent (BOLD) MRI,[4,5] arterial spin labelling (ASL) allows direct assessment of perfusion alterations. Previous studies showed high accordance between ASL-based CBF and $H_2{}^{15}O$-positron emission tomography.[6–8] However, current single post label delay (PLD) pseudo-continuous ASL (pCASL) implementations are highly sensitive to the arterial transit time (ATT), i.e., travel time of labelled blood from the labelling region to the tissue of interest.[9] In contrast, time-encoded Hadamard pCASL[10] allows to time-efficiently collect data at multiple PLDs within clinically reasonable scan times. We hypothesize that ATT affects ASL-CVR, especially as decreased ATT has been reported during vascular challenges.[5,6,11] To explore possible effects of ATT-changes on hypercapnia-based CVR measurement, we compared Hadamard pCASL to both single-PLD pCASL and BOLD MRI.

Methods 20 healthy subjects (26.3 ± 3.0y, 13f) underwent MRI on a 3 T Elition X (Philips, NL). Medical and hypercapnic (5% CO2) air were supplied by a gas-mixer (AltiTrainer, SMTec, CH). For details of MRI parameters and gas-paradigm see Fig. 1. Single-PLD pCASL parameter settings and CBF quantification agreed with current recommendations.[12] Hadamard-encoded pCASL data were decoded prior to modelling CBF and ATT using FSL BASIL.[13] CVR was calculated as % signal (SI) change:

$$\mathrm{CVR} = (\mathrm{SI}_{\mathrm{CO2}} - \mathrm{SI}_{\mathrm{AIR}})/\mathrm{SI}_{\mathrm{AIR}}. \quad (1)$$

Hypercapnia induced ATT changes were derived from Hadamard pCASL:

$$\Delta\mathrm{ATT} = \mathrm{ATT}_{\mathrm{AIR}} - \mathrm{ATT}_{\mathrm{CO2}} \quad (2)$$

$\Delta\mathrm{ATT} = \mathrm{ATT}_{\mathrm{AIR}} - \mathrm{ATT}_{\mathrm{CO2}}$ [2].

Statistical analysis employed MATLAB (v2021b). CVR of Hadamard ASL was correlated with BOLD and pCASL CVR and Bland–Altman analysis was conducted for comparing single-PLD and Hadamard pCASL. ΔATT was correlated with all imaging methods.

Results Group-average parameter maps (Fig. 2) show generally higher CVR, when measured with Hadamard pCASL (A) compared to (single-PLD) pCASL (B), while absolute values of BOLD-CVR cannot be compared directly (C). This agrees with statistical analyses (Fig. 3) indicating almost significant (r = 0.37) and week (r = 0.15) correlations between Hadamard pCASL CVR and single-PLD- and BOLD-CVR, respectively (Fig. 3A, B). In concordance with visual impression (Fig. 2), Bland–Altmann analysis indicates systematic CVR underestimation, for single-PLD pCASL (ΔCVR = 14.0 ± 2.1% in GM, Fig. 3C). ATT globally decreased (positive ΔATT) under hypercapnia, most pronounced in GM (Fig. 2D). Interestingly, single-PLD pCASL and Hadamard ASL (Fig. 4B, C) but not BOLD CVR (Fig. 4A) correlated significantly with ΔATT.

Discussion Based on our results, single-PLD pCASL correlates well with Hadamard but seems to underestimate CVR systematically. This mainly agrees with literature, where pCASL underestimated ACZ-based CVR in a similar order of magnitude.[6] However, a study using Turbo-QUASAR ASL reported similar CVR for multi-PLD and single-PLD ASL.[11] Not surprisingly, due to the different contrast mechanism, BOLD CVR correlated rather moderately with Hadamard pCASL (rBOLD-Hadamard = 0.11), along with a low sensitivity to ATT (Fig. 4A). Compared to that, ASL-CVR was strongly correlated with ΔATT (Fig. 4B, C), yielding larger CVR for subjects with stronger ATT decreases. Interestingly, this did not only hold true for single-PLD pCASL, where ATT decreases might be misinterpreted as perfusion increases, but also for Hadamard pCASL. This appears plausible from a physiological perspective, suggesting that ΔATT itself might be a measure for adaptions of the vascular system to hypercapnia challenges. To differentiate those effects from hypercapnia induced CBF increases, the common CVR measure, Hadamard pCASL would be the method of choice. In addition, Hadamard ASL yielded larger CVR compared to pCASL, and the more commonly applied BOLD MRI appears insensitive to ATT.

In conclusion, our results indicate relevant hypercapnia-induced ATT changes, which should be considered for single-PLD pCASL-based CVR. Moreover, Hadamard pCASL based ΔATT might be an interesting additional parameter for future investigations of vascular reactivity, especially in patient studies of vascular pathologies, where large variations in ATT have been reported.[14,15]

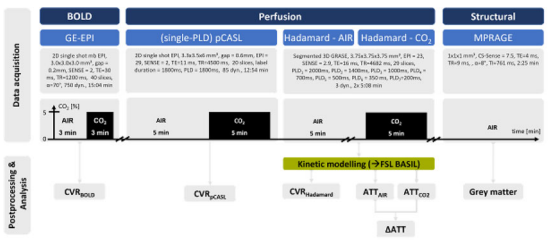

Fig. 1: MRI protocol & parameters. CVR was measured by BOLD MRI, and two ASL based perfusion MRI methods. The block designs of air and 5% CO2 application is indicated below the imaging parameters. CVR was calculated according to equation [1]. ΔATT reflects changes in ATT between hypercapnia and baseline (eq. [2]).

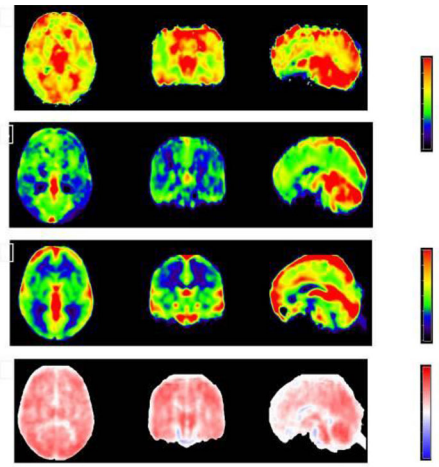

Fig. 2: Group average parameter maps. CVR derived from Hadamard-encoded pCASL (A) and single-PLD pCASL (B) are shown at identical scaling alongside with differently scaled BOLD CVR(C). Globally decreased ATT upon hypercapnia challenge corresponds to positive ΔATT (D).

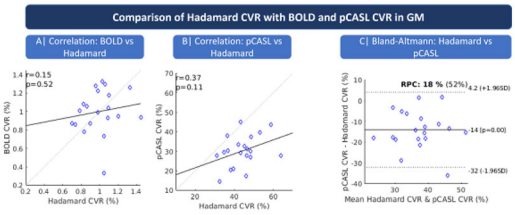

Fig. 3: Comparisons to Hadamard CVR in GM. **Hadamard CVR correlates less with BOLD CVR (A) than with pCASL** CVR (B). Bland-Altmann analysis indicates significantly lower CVR for single-PLD pCASL ($p<0.05$).

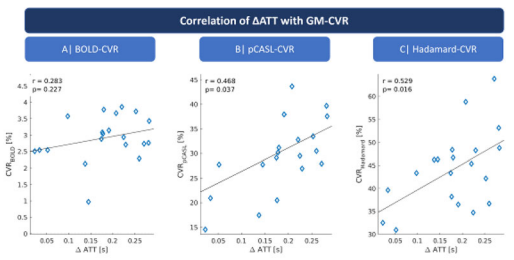

Fig. 4: Correlations with ΔATT in GM. Pearson-correlation coefficients (r) were not significant for BOLD CVR vs ΔATT (A), while CVR of single-PLD pCASL (B) Hadamard pCASL (C) correlated significantly ($p<0.05$).

References

1: Donahue,Achten,JCBFM,2018
2: Kaczmarz,Göttler,JCBFM,2021
3: Smeeing,Hendrikse,CVD,2016
4: Zhao,Woodward,JCBFM,2022
5: Donahue,Fraco,JCBFM,2014
6: Zhao,Fan,Neuroimage,2021
7: Bokkers,Bremmer,JCBFM,2010
8: Kufer,Preibisch,JCBFM,2022
9: vanOsch,Teeuwisse,JCBFM,2018
10: Günther,ProcISMRM,2007
11: Zhao,Václavů,MRM,2020
12: Alsop,Detre, MRM,2015
13: Woolrich,Jbabdi,Neuroimage,2009
14: Paling,Thade Petersen,JCBFM,2014
15: Martin,Madai,JCBFM,2015

LT77.
Age-dependent brain perfusion alteration in intrauterine growth restricted neonates at term equivalent age

S. Coraj[1,2], A. de Silvestro[3,4,5], N. Yakoub[1,2], T. D. Nguyen[2], C. Hagmann[3,6], A. Jakab[4], T. Reinelt[1,2], R. O'Gorman Tuura[3,4], G. Natalucci[1,2]

[1]*University Hospital Zurich, University of Zurich, Larsson-Rosenquist Foundation Center for Neurodevelopment, Growth and Nutrition of the Newborn, Department of Neonatology, Zurich, Switzerland;*
[2]*University Hospital Zurich, University of Zurich, Newborn Research, Department of Neonatology, Zurich, Switzerland;*
[3]*University Children's Hospital Zurich, University of Zurich, Children's Research Center, Zurich, Switzerland;*
[4]*University Children's Hospital Zurich, University of Zurich, Center for MR Research, Zurich, Switzerland;*
[5]*University Children's Hospital Zurich, Pediatric Cardiology, Pediatric Heart Center, Department of Surgery, Zurich, Switzerland;*
[6]*Children's University Hospital of Zurich, Department of Neonatology and Pediatric Intensive Care, Zurich, Switzerland*

Introduction Intrauterine growth restriction (IUGR) is a condition primarily caused by compromised placental function resulting in impaired fetal growth and neurodevelopment[1]. In IUGR pregnancies, an altered fetal cerebral blood supply due to secondary cerebral blood flow (CBF) redistribution may contribute to suboptimal brain maturation[1]. Subsequent cardiovascular abnormalities may impact cerebrovascular autoregulation and eventually lead to metabolic syndrome later in life[2–4]. However, we still lack a complete understanding of the cerebral perfusion alterations in IUGR. Besides, the role of neonatal brain perfusion in IUGR remains unclear because of the confounding concurrence of preterm birth, which by itself affects brain perfusion[5–9] and later functional outcomes[8]. Here, we compared cerebral perfusion in neonates with IUGR and intrauterine growth appropriate for gestational age (AGA) by arterial spin labeling (ASL) magnetic resonance imaging (MRI) at term equivalent age (TEA). We expected to find altered brain perfusion in IUGR.

Method Our interim analysis included 29 IUGR [15 female; postnatal age at MRI (mean ± SD) 64.2 ± 30.0 days; gestational age (GA) at birth 32.0 ± 4.1 weeks; postmenstrual age (PMA) at MRI 41.1 ± 1.3 weeks] and 33 AGA [16 female; 30.2 ± 25.2 days; 36.7 ± 4.2 weeks; 41.0 ± 1.4 weeks] infants taking part in an ongoing prospective cohort study. Group definition was based on IUGR consensus criteria[10]. Data were acquired at TEA without sedation on a 3 T GE MR750 scanner with a 3D background-suppressed pseudo-continuous arterial spin labeling (pCASL) sequence with a post-labeling delay of 2 s. CBF images were reconstructed using the default model implemented in the vendor-provided perfusion quantification software. CBF maps were normalized to an in-house neonatal perfusion template using FSL-FLIRT. To calculate the whole brain grey matter (GM) perfusion, we extracted CBF from GM regions using the Automated Anatomical Labeling (AAL) atlas mask with fslstats. Perfusion was also compared voxelwise between groups using FSL-randomise permutation testing. The significance threshold alpha was set to $p < 0.05$, threshold free cluster enhancement (TFCE) corrected. Statistical models included postnatal age at MRI, GA at birth and PMA at MRI as covariates. The covariate showing the strongest correlation with perfusion was also solitarily included and the interaction effect of this covariate by group on perfusion was investigated. From the interaction analysis, perfusion values for all

participants were extracted in the regions (defined hereafter as regions of interest, ROIs) where we found significant group difference.

Results No evidence for a significant difference in perfusion was found between the groups. A positive effect of postnatal age at MRI on both voxelwise perfusion and whole brain GM perfusion was found, showing that over both groups perfusion increases with increasing postnatal age. The voxelwise interaction analysis revealed regional group differences bilaterally in deep GM clusters extending into basal ganglia, thalamus, hippocampus, as well as in occipital and midline parietal cortices. In these ROIs the slope of postnatal age-dependent perfusion increase is larger for AGA than for IUGR (Fig. 1).

Discussion The observed association of perfusion with postnatal age within AGA infants is in line with previous literature showing that global and regional cerebral perfusion increases after birth and that at TEA it is higher in preterm than in term born infants (due to the higher postnatal age in preterms) [5–9]. In IUGR the lower perfusion increase over time might be explained by unmet metabolic demands produced by intrauterine and early postnatal insults leading to an abnormal cerebrovascular autoregulation that is still evident at TEA. In addition, some of the observed regions that showed a group difference in the rate of perfusion increase have previously been found to show a decreased CBF within preterms with brain injuries[7,8] suggesting that these areas might be particularly sensitive to deprivation during early life periods. We acknowledge the different distribution of postnatal age between groups and the cross-sectional design as two limitations for the interpretation of our results which hinder inference about perfusion trajectories related to brain maturation processes. Moreover, perfusion in infants with IUGR may depend on several aspects of IUGR pathophysiology such as the severity and onset of fetal growth restriction.

Conclusion Taken together, these findings suggest altered regional brain perfusion in IUGR compared to AGA neonates at TEA which is dependent on postnatal age.

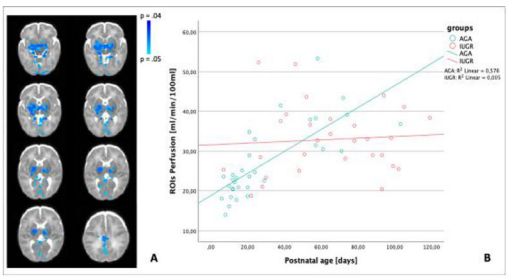

Fig. 1: A) Exemplary cross-sectional axial views of voxelwise correlation analysis between perfusion and groups accounting for the interaction term postnatal age by group. Significant clusters are overlaid in blue, depicting areas in which perfusion shows an interaction effect. Clusters are overlaid on a neonatal brain atlas [11] registered to the mean whole brain GM perfusion image of all participants. B) Scatter plot showing the association between perfusion in the identified ROIs and postnatal age in IUGR versus AGA. Perfusion was extracted in the ROIs that showed a significant group by age interaction on perfusion.

References

1) Dudink et al., 2022;
2) Rock et al., 2021;
3) Bhunu et al., 2021;
4) Bell et al., 2020;
5) Dubois et al., 2021;
6) Tortora et al., 2020;
7) Bouyssi-Kobar et al., 2018;
8) Tortora et al., 2017;
9) Ouyang et al., 2017;
10) Gordijn et al., 2016;
11) Makropoulos et al., 2016.

LT78.
Agreement between cerebral blood flow estimations derived from single- and multi-delay arterial spin labelling in Moyamoya patients

J. M. Sousa[1,2], T. Svedung-Wettervik[3], P. Enblad[3], A. Lewén[3], J. Wikström[3], M. Fahlström[2]

[1]*Uppsala University Hospital, Medical Physics, Diagnostics, Uppsala, Sweden;*
[2]*Uppsala University, Surgical Sciences, Radiology, Uppsala, Sweden;*
[3]*Uppsala University, Medical Sciences, Neurosurgery, Uppsala, Sweden*

Introduction Patients with Moyamoya disease (MMD) develop progressive bilateral steno-occlusion of the terminal section of the internal carotid arteries, leading to a decrease in cerebral blood flow (CBF) (1). Magnetic resonance-based arterial spin labelling (ASL) can be used to non-invasively acquire quantitative maps of patients" CBF. Since 2015, single post-label delay (SD) ASL has been the recommended approach. However, SD-ASL is dependent on the arterial transit time (ATT) (2). As such, accuracy of CBF maps in MMD patients, where the ATT is delayed, may be affected. Multi-delay (MD)-ASL mitigates the effects caused by delayed ATT, as multiple post-label delays (PLD) are considered. Still, MD-ASL lacks availability and may require longer scanning times (3). Recently, a variable repetition time (TR) pseudo-continuous ASL acquisition (pCASL) with dynamically optimised background suppression and 3D read-out was developed. This sequence employs a combination of labelling durations and several PLDs, allowing higher SNR and quantification in regions with a wide range of ATT at reasonable scanning times (4). The present study aimed to assess the agreement between CBF maps acquired with conventional SD-ASL and MD-ASL using a variable TR scheme in patients with MMD.

Methods Seven patients with confirmed bilateral MMD were included in this study (mean age: 45 ± 13, all female). The study was conducted in accordance with the declaration of Helsinki and approved by the Swedish Ethical Review Authority. All examinations were performed on a 3.0 Tesla Achieva dStream (Philips Healthcare, Best, The Netherlands) using a 32-channel head coil. The SD-ASL was acquired with an 3D pCASL with background-suppressed GRASE read-out with a PLD of 2500 ms and LD of 1800 ms. CBF maps were generated by the scanner software as recommended by Alsop et al. (2). MD-ASL was acquired with pCASL by changing PLD and LD for ten dynamics (PLD: 100–3000 ms, LD: 400–2000 ms). Four background-suppression pulses were applied with optimized timing for each dynamic. Read-out was performed using 3D GRASE. CBF maps were semi-automatically generated by the scanner software using the general kinetic model (5). Parametric map of ATT was also calculated, but not included in this study. Scanning time was 5 min 27 s, with 22 slices and acquired resolution of 3 × 3 × 6mm for both ASL acquisitions. Additionally, a 3D contrast enhanced T1 weighted (CE-T1w) image was acquired and used for data postprocessing. Spatial normalization to the MNI vascular regional template was used to define bilateral vascular regions (ACA, MCA and PCA) over the CE-T1w image. Left and right regions were pooled together, hence, fourteen CBF values were compared for each vascular region. Bland–Altman analysis was used to assess differences in mean CBF values from SD- (CBF_{SD}) and MD-ASL (CBF_{MD}). Data agreement was evaluated by means of orthogonal analysis and Spearman correlation, with GraphPad Prism 9 (GraphPad Software, La Jolla, CA, USA).

Results A mean difference of about 25 ml/100 mg/min was found across all vascular regions (mean ± SD, ACA: 24.93 ± 6.28, MCA: 26.49 ± 5.98, PCA: 23.00 ± 6.73) when comparing CBFMD and

CBFSD, Fig. 1a). Orthogonal analysis demonstrates a high degree of agreement between both methods ($r > 0.80$). The lowest correlation was found in the MCA ($r = 0.85$), while the highest in PCA ($r = 0.91$), Fig. 1b). A representative comparison of CBF images between SD- and MD-ASL is presented in Fig. 2.

Discussion The current study found a strong correlation between CBF_{MD} and CBF_{SD}. It was also found that CBFMD values seem to be higher than those of CBF_{SD}. Furthermore, stronger correlation between MD-ASL and ^{15}O-water PET has been reported compared to SD-ASL (6,7). CBF_{MD} values are less affected by delayed transit times, characteristically found in MMD patients, which can partly explain the systematic difference between SD- and MD-ASL found in the current study (3,6). Methodological factors pertaining to differences in acquisition protocols and CBF calculations between methods can also affect the outcome results, hence we do not consider CBF_{MD} as true CBF. Current literature, strongly suggest that MD-ASL based CBF to be closer to true CBF compared to SD-ASL in patients with MMD (7).

Conclusion MD-ASL demonstrated a strong correlation and agreement with SD-ASL. MD-ASL with variable TR scheme may be a superior method for measuring CBF in patients with MMD due to affected ATT at comparable scanning times.

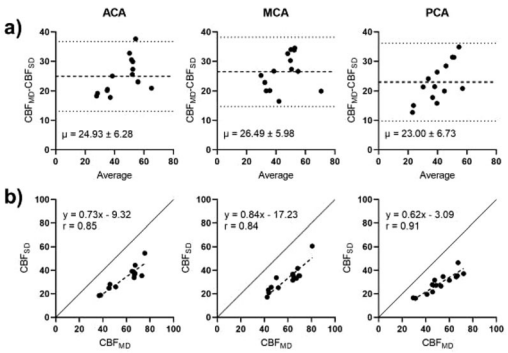

Fig. 1: Bland-Altman plots a) of CBFSD and CBFMD, bold dashed line represents the mean CBF value, while thin dashed lines represent limits of agreement. Mean and standard error of the mean are also shown. Orthogonal analysis b) as well as correlation values. The solid black line corresponds to the line of identity and the dashed lines the Deming regression.

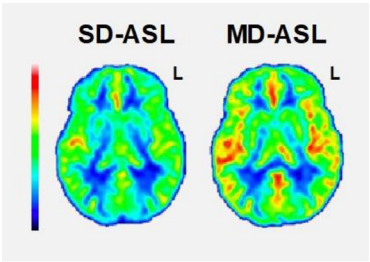

Fig. 2. Image from a representative patient illustrating the differences in CBF values across the brain for SD- (Left) and MD- (Right) ASL.

References

1-Shang S, et al. Neurosurg 2020,
2-Alsop DC, et al. Magn Reson Med. 2015,
3-Lindner T, et al. Magn Reson Med. 2023,
4-Togao O, et al. Neuroradiology 2023,
5-Buxton RB, et al. Magn Reson Med. 1998,
6-Fan AP, et al. Stroke 2017,
7-Zhao MY, et al. J Cereb Blood Flow Metab. 2022.

LT79.
Hepatic non-Gaussian apparent diffusion in NAFLD patients: A dual role for steatosis

O. Saïd[1], S. Doblas[1], D. Valla[1,2], V. Paradis[1,3], B. van Beers[1,4], P. Garteiser[1]

[1]*Inserm, Universitéʹ Paris Citéʹ, Center for Research on Inflammation Inserm U1149, Paris, France;*
[2]*Beaujon University Hospital, AP-HP, Department of Hepatology, Clichy, France;*
[3]*Beaujon University Hospital, AP-HP, Department of Pathology, Clichy, France;*
[4]*Beaujon University Hospital, AP-HP, Department of Radiologic Technology, Faculty of Associated Medical, Clichy, France*

Introduction In nonalcoholic fatty liver disease (NAFLD), hepatic fibrosis is strongly associated with patient survival(1). Diffusion imaging is proposed to monitor fibrosis due to the potential effect of the accumulated extracellular matrix components on the diffusion of water molecules(2). In NAFLD, lipid vesicles in the hepatocytes (steatosis) may also alter the diffusion of water molecules (3). Steatosis also has an effect on the measured apparent diffusion coefficient through the imperfect suppression of the fat component from the MR signal(4). Non-Gaussian diffusion imaging, where the apparent diffusion coefficient reflects diffusion kurtosis through the use of large b-values and the addition of second order terms in the signal model, is proposed as a potential marker of hepatic fibrosis(5,6), although performance is not as high in NAFLD patients despite the application of a fat correction method(7).

The main objective of this work is to evaluate the diagnostic performance of non-Gaussian diffusion imaging for liver fibrosis in NAFLD patients in absence of fat correction, with the fat correction proposed and tested by Hanniman et al (7) and with the fat correction proposed by Le Bihan et al (8).

Methods The study involved the prospective recruitment of patients with hepatic steatosis and type 2 diabetes. The study population (250 patients) was randomly selected from a total population of 300 patients. Fibrosis stage (F0–F4) and steatosis grade (S0–S3) were assessed on a liver biopsy taken on the day of imaging.

A diffusion sequence was acquired (3 T MRI) with 6 b values including a b_0 with no diffusion encoding, and the $b_1 = 200$ and $b_2 = 1500$ s/mm^2 values previously identified as important for the diagnosis of fibrosis (5).

The non-Gaussian ADC was calculated without fat correction ("sADC") as described in Fig. 1-Eq. 1 (5), and with the correction methods from Hanniman (Fig. 1-Eq. 2) and the Le Bihan (Fig. 1-Eq. 3); with S_{bi} the signal at b-value b_i, η the proton density fat fraction (measured separately on each patient using the mDixonQuant method), TE the sequence echo time (75 ms), T2w and T2f the T2 of water (23 ms) and fat (62 ms), respectively(4), and γ the residual fat percentage due to incomplete fat suppression (8.7% according to (4)).

Diagnostic performance was assessed using Kruskal–Wallis analysis and multivariate regression with NASH-CRN fibrosis stages and steatosis grades as independent variables.

Results The population studied consisted of 250 patients (67% male, median age 60 years; 54 F0, 64 F1, 41 F2, 67 F3 and 24 F4; 9 S0, 73 S1, 129 S2 and 39 S3). Significant steatosis (S2 or S3) was present in 42% of F0 patients, 78% of F1 patients, 83% of F2 patients, 75% of F3 patients and 46% of F4 patients.sADC and $sADC_{Hanniman}^{corr}$ were not significantly different between fibrosis stages, and $sADC_{Le\ Bihan}^{corr}$ was significantly different between fibrosis stages (Kruskall–Wallis $p = 0.034$).

When considering steatosis, a significant variation of sADC was obtained without fat correction (Fig. 2) (Kruskall–Wallis

$p < 0.000001$). $sADC_{Hanniman}^{corr}$ and $sADC_{Le\ Bihan}^{corr}$ both did not display any significant differences between steatosis grades.

At multivariate regression analysis, sADC and sADCHannimancorr were significantly determined by steatosis (rpartial/p of $-0.39/< 0.0001$ and $-0.13/0.03$, respectively), while sADCLe Bihancorr was not found to be determined by fibrosis or steatosis.

Discussion Based on our results, it appears that suppressing the residual fat from the signal removes the effect of steatosis on the non-Gaussian ADC. This points towards a diminished importance of lipid vesicles as diffusion barriers and an increased importance of the confounding effect of fat on the MR signal, as determinants of the apparent ADC in the presence of both fibrosis and steatosis.

In accordance with previous results on a comparable but different population(7), this NAFLD patient study confirms that $sADC_{Hanniman}^{corr}$ does not appear to depend on fibrosis stages. The correction applied for $sADC_{Le\ Bihan}^{corr}$ removes the influence of steatosis on the diffusion, enabling an effect of fibrosis on the diffusivity of water molecules to appear.

Conclusion The dual effects of hepatic steatosis on diffusion coefficients, through an indirect effect on the MR signal, and through a direct effect on the diffusivity of water molecules, must be carefully unraveled before diffusion-based markers such as the non-Gaussian apparent diffusion coefficient can be considered as potentially useful for fibrosis diagnosis in NAFLD patients.

$$sADC = \frac{\ln(S_{b_1}/S_{b_2})}{b_2 - b_1} \tag{1}$$

$$sADC_{Hanniman}^{corr} = \frac{1}{b_2} \cdot ln\left(\frac{(1-\eta)\cdot exp(-TE/T2_w)}{\frac{S_{b_2}}{S_{b_1}}\cdot\left((1-\eta)\cdot exp(-TE/T2_w)\cdot exp(-b_1\cdot ADC_m^{b_1-b_2})+\gamma\cdot\eta\cdot exp(-TE/T2f)\right)-\gamma\cdot\eta\cdot exp(-TE/T2_f)}\right) \tag{2}$$

$$sADC_{LeBihan}^{corr} = \frac{b_2\cdot ADC_w^{b_1-b_2} - b_1\cdot ADC_w^{b_1-b_2}}{b_2 - b_1} \tag{3}$$

$$ADC_w^{b_1-b_2} = \frac{1}{b}\cdot ln\left(\frac{(1-\eta)\cdot exp(-TE/T2_w)}{\frac{S_b}{S_0}\cdot\left((1-\eta)\cdot exp(-TE/T2_w)\cdot exp(-b_1\cdot ADC_m^{b_1-b_2})+\gamma\cdot\eta\cdot exp(-TE/T2f)\right)}\right) \tag{3a}$$

Fig. 1: equations used for sADC evaluations, depicting the different fat correction methods.

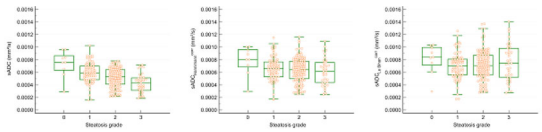

Fig. 2: Box plots of sADC vs. steatosis grades (left: no fat correction, middle: Hanniman correction, right: Le Bihan correction). The application of fat correction methods suppresses the effect of steatosis on the apparent diffusion coefficients.

References

(1) Sanyal AJ, et al. N Engl J Med 2021.
(2) Taouli B, et al. J Magn Reson Imaging 2008.
(3) Leitao HS, et al. Radiology 2017.
(4) Hansmann J, et al. Magn Reson Med 2013.
(5) Le Bihan D, et al. Radiology 2017.
(6) Kromrey ML, et al. Radiology 2020.
(7) Hanniman E, et al. J Magn Reson Imaging 2022.
(8) Le Bihan D, et al. J Magn Reson Imaging 2023.

LT80.
Short-term consumption of high-fat high-sugar diet causes cerebral changes on diffusion MRI

Y. Martín-Sánchez[1], R. González-Alday[1], N. Arias-Ramos[1], P. Lopez-Larrubia[1], B. Lizarbe[1,2]

[1]*Instituto de Investigaciones Biomédicas Alberto Sols (CSIC-UAM), Fisiopatología Endocrina y del Sistema Nervioso, Madrid, Spain;* [2]*Autonomous University of Madrid, Department of Biochemistry and Molecular Biology, Madrid, Spain*

Introduction Obesity is a chronic disease associated to several comorbidities such as type 2 diabetes or hypertension[1]. The accumulation of fat stores induces inflammation in many organs, like the brain or the liver, due to augmented cytokine production and the activation of inflammatory pathways[2]. Some studies have reported obesity induced cerebral changes detectable by magnetic resonance imaging (MRI)[3]. Here, we investigated the effects of high-fat high-sugar (HFHS) diet consumption on the mouse brain areas associated with appetite and energy homeostasis using diffusion tensor imaging (DTI) and magnetization transfer imaging (MTI).

Materials and Methods Animals fed with a chow diet (CD) (n = 16, 8 males) or with a 40% fat and 35% carbohydrate (HFHS) (n = 16, 8 males) (Research Diets, D12450Hi and D08112601i) were investigated before (T = 0), 7 and 28 days after diet diversification on a 7 T magnet (Bruker Biospect). Body weight (BW) was controlled on a weekly basis. The hypothalamus (Hyp), hippocampus (Hipp), nucleus accumbens (ACB) and infralimbic area (ILA) were localized in a T2-image using an anatomical atlas, and MT (pulse on/off, TE/TR = 9.8/2500 ms) and DTI (2 "b" $400 < b < 1800$ s mm^{-2},15 directions, 5 slices, 1.25 mm thickness, 0.16×0.16 mm^2) were acquired. DTI images were pre-processed using the non-local means algorithm and processed using the Dipy package[4]. Mean regional values of axial diffusivity (AD), radial diffusivity (RD), mean diffusivity (MD), anisotropic fraction (FA) and magnetization transfer ratios (MTR), were calculated for each region, animal and time point. To assess the relevance of the type of diet, sex and time under diet on the MR coefficients and on BW, data was fitted to linear mixed-effects (LME) models[5] using the R[6], and the "*lme*" function[7]. We followed a multilevel selection strategy[3] that consisted in: 1) fitting several LME models, 2) choosing the best model according to the Akaike"s information criterion8, using the "stepAIC" function[9], and 3) on the best fitting model, performing type III anova tests to assess the significance of each effect on the MRI variables[8]. Particularly, the response variables (MD, AD, RD, FA and MT) were fitted independently to a variety of LME regression models, including linear combinations of either type of diet (CD or HFHS), sex (male or female), time under diet (0, 7 or 28 days), brain region (Hyp, Hipp, ACB or ILA), and the double interactions, as fixed effects, and the animal and brain region as random terms.

Results BW increased significantly on males under HFHS and CD, but the increase was faster under the high calorie diet ($p < 0.001$). On females, BW only increased under HFHS (Fig. 1). Following the multilevel model selection strategy, we found that some fixed effects

affected significantly all the MRI parameters, like *area*, while others, like *time:diet*, which expresses how time affects the MRI variable depending on the diet, only changed relevantly MD and RD (Tab. 1). Interactions between *sex* and *area*, or *sex* and *time*, altered all diffusion parameters, but not MTR, where the only significant effect was *area*. LME fitting showed that HFHS diet caused augmented increases of MD and RD with time that were not sex-dependent (Figs. 2, 3). FA values increased more significantly on males, under both diets (Fig. 4).

	MD	AD	RD	FA	MTR
Area	$p < 0.001$	$p < 0.001$	$p < 0.001$	$p < 0.001$	$p < 0.001$
Sex	n.s	n.s	n.s	$p < 0.05$	n.s
Time	n.s	n.s	n.s	$p < 0.001$	n.s
Time:Diet	$p < 0.01$	n.s	$p < 0.05$	n.s	n.s
Sex:Time	n.s	$p < 0.05$	n.s	$p < 0.05$	n.s
Sex:Area	$p < 0.001$	$p < 0.001$	$p < 0.001$	n.s	n.s
Area:Time	$p < 0.05$	n.s	$p < 0.01$	n.s	n.s

Table 1 Summary of the p-values from the anova tests of the fixed effects on Mean Diffusivity (MD), Axial Diffusivity (AD), Radial Diffusivity (RD), Fractional Anisotropy (FA) and Magnetization Transfer Ratios (MTR) (n.s. not significant).

Discussion Our work shows that the HFHS administration for 4 weeks altered significantly the BW of male and female animals, as compared to CD mice. The LME approach yielded robust fittings that showed significant increases of MD and RD diffusion parameters under HFHS that are compatible with vascular inflammation, and with previous results with animals under HF diets[10]. Sex affected significantly many diffusion MRI parameters, highlighting the importance of sexual dimorphism on obesity studies, and on the underlying cerebral changes of obesity development.

Conclusions HFHS short-term consumption induces body weight changes, with brain alterations that can be identified using MRI that reveal increased diffusion parameters and sexual dimorphism.

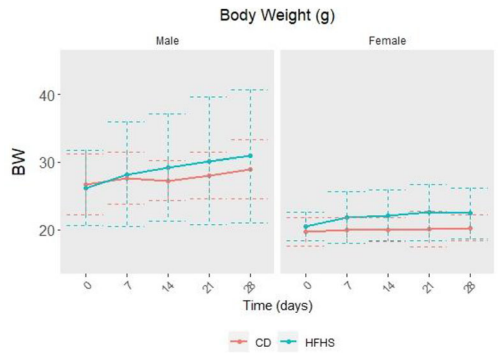

Fig. 1: Mean±SD BW values of males (left) and females (right) animals under HFHS (blue) and CD (red) diets, measured 0, 7 and 28 days after diet.

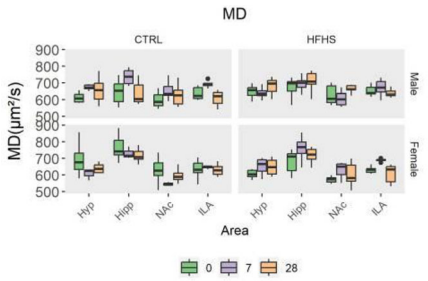

Fig. 2: MD values per region, time point (0, 7 and 28 days after diet, in green, purple and orange, respectively). HFHS diet mice (right) show slightly augmented increases with time of MD ($p<0.01$), as compared to the time increase of MD on CTRL animals (left). No sex:diet effects are reported on MD, but some sex:area differences exist.

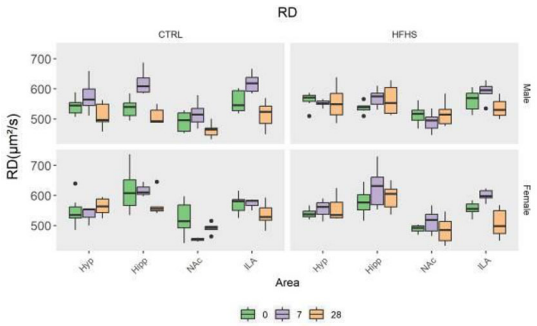

Fig. 3: RD values per region, time point (0, 7 days and 28 after diet, in green, purple and orange, respectively). Like on MD, HFHS diet mice (right) show faster RD increases with time ($p<0.05$), than CTRL animals (left). No sex:diet effects are reported on MD, but some sex:area differences exist.

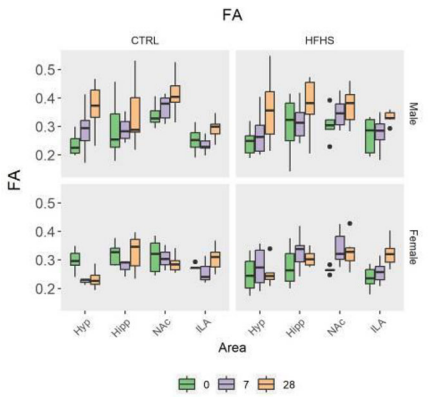

Fig. 4: FA values per region, time point (0, 7 days and 28 after diet, in green, purple and orange). Sexual differences are reported, with augmented increases of FA with time on male mice ($p<0.05$).

References

[1]Frisardi et al., 2010, Ageing research reviews.[2]Cazettes F. et al. 2011 Brain Research. [3]Campillo et al., 2022. Frontiers in Neuroscience.[4]Bates et al., 2015. J. Stat. Soft.,[5]Garyfallidis et al.Front Neuroinf. (2014)[6]R Core Team (2020). [7]Pinheiro et al., 2022.[8]Fox et al., 2019. SAGE Publications, Inc. [9]Venables and Ripley, 2002.[10]Guadilla et al., Int. J. Obes. (2021).

LT81.
Isotropic high-resolution DTI of the cervical spinal cord

S. Tounekti[1], D. Middleton[1], S. Shahrampour[1], Z. Zariri[2], K. Talekar[1], M. Alizadeh[3], B. Hiba[2], L. Krisa[4], F. Mohamed[1]

[1]*Thomas Jefferson University, Radiology, Philadelphia, PA, United States;*
[2]*Institut des Sciences Cognitives, Lyon, France;*
[3]*Thomas Jefferson University, Neurosurgery, Philadelphia, PA, United States;*
[4]*Thomas Jefferson University, Occupational Therapy, Philadelphia, PA, United States*

Introduction Low-spatial resolution and poor signal-to-noise ratio (SNR) are major limiting factors in diffusion-weighted MRI (dMRI) of the spinal cord (SC). In this work, a 3D echo-planar-imaging (EPI)-based MRI pulse sequence employing a 2D radiofrequency (2DRF) pulse for reduced field of view (rFOV) selection was implemented and optimized to perform DWI on SC with an isotropic spatial resolution of 1.2 mm3 on a clinical 3 T MR scanner.

Methods Five healthy adult subjects (1 Female, 4 males) were scanned using a 3 T Siemens Prisma MR scanner (Erlangen, Germany). Neck-elements of the vendor 64-channel coil are used for signal reception. A peripheral pulse oximeter was used to trigger the DWI scans to the subject"s cardiac cycle.

Sagittal dMRI images were collected with the 3D-EPI-rFOV pulse sequence using the following parameters: TE = 48 ms, FOV = 89 × 36 mm2, Matrix Size = 74 × 30 pixels, Slices = 26, Bandwidth = 1608 Hz/Px, Echo-spacing = 0.77 ms, Spatial Resolution = 1.2 mm3, Partial Fourier in Y-axis (PFy) = 6/8. A b-value of 800 s/mm^2 was applied along 12 non-collinear diffusion encoding directions. One B0 was collected prior the DWI images. The scan was prescribed in sagittal orientation to cover C1-C5. The total scan time was approximately 11 min.

Initially, DW images were corrected for motion and eddy current artifacts. Next tensor fitting was applied to computed quantitative indices including fractional anisotropy (FA) and mean diffusivity (MD). These indices were calculated at each cord level where segmented from mean DW images using propseg feature of SCT toolbox.

Additional datasets were collected on one healthy volunteer using the 3D- and 2D-rFOV pulse sequences in order to quantify the SNR efficiency improvement. Pixel-wise derived SNR map was computed as the ratio of mean signal to standard deviation of noise over time. Ten axial b0-volumes were collected using the 3D sequence using the same scan parameters listed above in 4 min. Whereas sixty four b0-images were collected using the 2D-rFOV-EPI pulse sequence with the following parameters: TR = 3900 ms, TE = 91 ms, EPI-factor = 30, FOV = 89 × 36 mm^2, matrix size = 74 × 30 pixels, number of slices = 26, slice thickness = 1.2 mm, Bandwidth = 1876 Hz/Px, Echo-spacing = 1.28 ms, PFy = 6/8, the scan time was 4 min.

Results The colored Fractional Anisotropy (FA), FA, and Mean Diffusivity (MD) maps obtained on one volunteer are displayed on Fig. 1. the obtained maps show a gray/white matter contrast with clear visualization of central gray matter throughout the cord.

3D/2D SNR over time measurements showed an average increase of ~ 5 × in the 3D versus 2D sequence with equivalent acquisition times (Fig. 2).

Figure 3 displays the averaged 2D-FA as well as 3D-FA values of White matter (WM) for all subjects for vertebral level C1 to C5.

Figure 4 illustrates the ability of the high-resolution 3D data to better visualize the SC structure (yellow arrows, better delineation of cord CSF interface) as well as the central canal path (red arrow).

Conclusion This work demonstrates the feasibility of performing isotropic high-spatial resolution of 1.2 mm3 dMRI of the SC using a clinical scanner.

Improvements in SNR using 3D approach could enhance the accuracy of atlas-based analysis, the visualization of fine-scale anatomic details, and the reduction of partial volume effects.

Further implementations are required to improve the time efficiency and motion insensitivity of the pulse sequence. Our results show 3D dMRI has potential to be used in clinical applications such as Cervical Spondylotic Myelopathy (CSM).

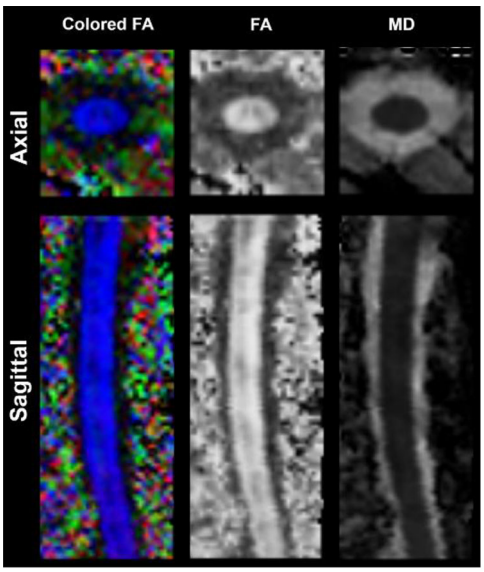

Fig. 1: The computed colored FA, FA and MD maps collected on one subject with an isotropic spatial resolution of 1.2 mm^3 using the 3D-rFOV-EPI pulse sequence

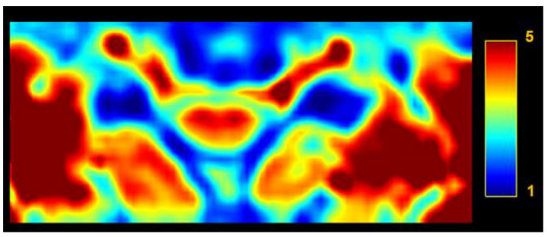

Fig. 2: The pixel-wise 3D/2D SNR gain map computed as the ratio between the 3D-SNR and 2D-SNR maps. The 3D sequence provides near 4-fold higher SNR efficiency compared to the standard 2D method at a b-value of 0 s/mm^2.

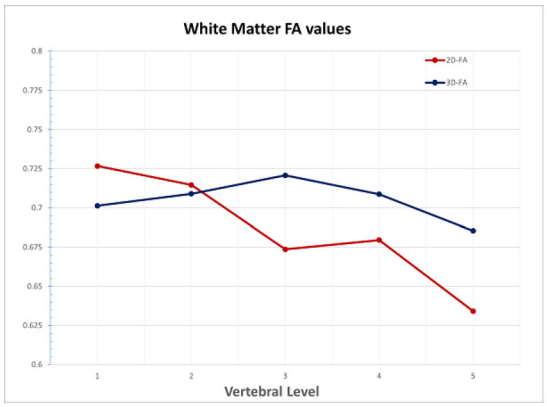

Fig. 3: The averaged FA, from all the five subjects extracted form 3D-dMRI (blue line) and 2D-dMRI data (red line) at White Matter ROIs.

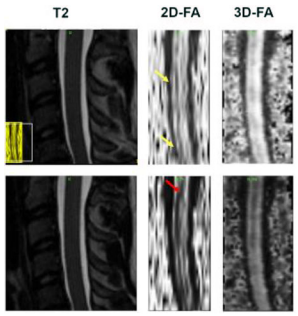

Fig. 4: The SC structure (yellow arrows; delineation between cord/CSF) and canal path (red arrow) are better shown at high-resolution 3D compared to the classic 2D-FA map.

LT82.
Characterizing the effect of dendritic spines on brain metabolites diffusion in cerebellar and cerebral cortex non-invasively with diffusion-weighted MRS

K. Simsek[1,2], C. Gallea[3,4], G. Genovese[4,5], S. Lehéricy[3,4], F. Branzoli[4,5], M. Palombo[1,2]

[1]*Cardiff University, Brain Research Imaging Centre (CUBRIC), Cardiff, United Kingdom;*
[2]*Cardiff University, School of Computer Science and Informatics, Cardiff, United Kingdom;*
[3]*Brain and Spine Institute, ICM, Movement Investigations and Therapeutics Team, Paris, France;*
[4]*Sorbonne University, INSERM U 1127, CNRS UMR 7225, Paris, France;*
[5]*Brain and Spine Institute, ICM, Centre for NeuroImaging Research, Paris, France*

Introduction The brain cortex is highly complex and heterogeneous. The cerebellar cortex comprises Purkinje cells with high spine density (ρ_{spine}), whereas Pyramidal cells characterizing the cerebral cortex have lower ρ_{spine}[1,2,3]. Recent works focusing on quantifying this microstructural feature have used invasive post-mortem microscopy methods and shown ρ_{spine} plays an important role in synapse development and plasticity in healthy brain and diseases[2,4,5].
Diffusion-weighted MR spectroscopy (DW-MRS) is a non-invasive technique able to quantify the complexity of cell morphologies with higher specificity than diffusion-weighted MRI[6–11]. This work uses DW-MRS to characterize non-invasively the impact of ρ_{spine} on brain metabolite diffusion in the cerebellar and cerebral cortex.
Methods *DW-MRS acquisition/processing.* DW-MRS data were acquired in 20 healthy subjects using a DW-semi-LASER[12] (Fig. 1C) (TE/TR = 125 ms/3 cardiac-cycles) at 3 T (Siemens/PRISMA). Volumes of interest (VOI) were placed in the cerebellum ($15 \times 16x22$ mm^3) and in the posterior cingulate cortex (PCC, $20 \times 20 \times 20$ mm^3) (Fig. 1A, B). Diffusion weighting was applied in 4 tetrahedral directions with diffusion-time = 62.5 ms, gradient duration 26.4 ms, and b-values up to 24 ms/μm^2 (24 averages). Unsuppressed-water data were acquired for eddy-current corrections. At each b-value, frequency/phase corrections were performed on single spectra, then averaged (Fig. 1D) before quantification using LCModel[13]. Signal amplitudes at each b were direction-averaged and analyzed.
Data analysis. To characterize metabolite diffusion, we used a randomly oriented sticks model with effective intra-stick diffusivity along the stick direction $D_{eff}(D_{app}, K_{app}, b) = D_{app}(1 - K_{app}D_{app}b\cos^2\theta)$[7,14–16], where D_{app} is the metabolite intra-stick apparent diffusivity, K_{app} is the metabolite intra-stick apparent kurtosis introduced to account for non-Gaussian diffusion due to the presence of spines[14,15], and θ is the angle between the stick direction and the applied diffusion gradient direction. The resulting direction-averaged signal was computed by solving the relation numerically: $S/S_0 = \int_0^1 \exp[-bD_{eff}\cos^2\theta]d(\cos\theta)$. To estimate D_{app} and K_{app} associated with glial and neuronal compartments, we fitted the signal model to the measured tCho and tNAA DW-MRS signals as functions of the b-value. As a reference, we also report results from tCr, which is supposed to be compartmentalized in both glia and neurons.
Results Figure 1D shows DW-MRS spectra acquired from each VOI in one subject. Figure 2 depicts the non-Gaussianity in the metabolite diffusion for all subjects. Highlighted signals represent the diffusion signal of the cohort average. Figure 3 shows the results of our biophysical model fitting. D_{app} is higher in PCC than in the cerebellar cortex, while K_{app} is higher in the cerebellar cortex for all metabolites. Focussing on the neuronal marker, tNAA, Fig. 4 shows the age dependence in our cohort of D_{app} and K_{app} for tNAA in both cortexes. K_{app} shows an increasing trend with age in both brain regions. In contrast, D_{app} increases with age in PCC and decreases in the cerebellar cortex.
Discussion and Conclusion Our findings suggest that the non-gaussian diffusion of tNAA may be a marker of neuronal ρ_{spine}. Indeed, estimated D_{app} and K_{app} values for the tNAA data are compatible with the larger ρ_{spine} in the cerebellar compared to the cerebral cortex. Noticeably, we also measured larger K_{app} values for tCho in the cerebellar compared to the cerebral cortex, possibly due to the presence of highly-arborized Bergmann glia[17], specifically the cerebellar. Estimated metabolite K_{app} values agree with other recent estimates of non-gaussianity in the cerebral cortex[18].

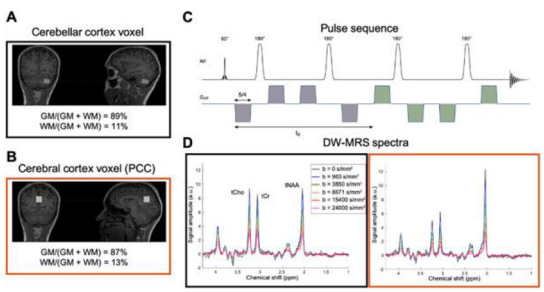

Fig.1: Location of the DW-MRS voxel in cerebellar (A) and PCC (B), together with estimated intra-voxel grey matter (GM) and white matter (WM). C) Schematic representation of the sequence. D) Example of DW-MRS spectra at each b value for one subject, with tNAA, tCho, and total creatine (tCr) peaks labeled for cerebellar (left) and cerebral (right) cortex.

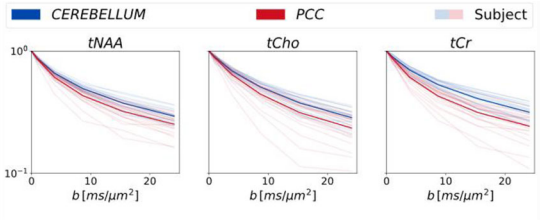

Fig. 2: Non-Gaussian diffusion decays obtained from all subjects are illustrated for the cerebellum (blue) and PCC (red). Highlighted lines represent the diffusion decay of the cohort.

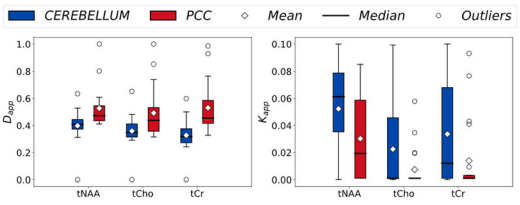

Fig. 3: Estimated model parameters D_{app} and K_{app} obtained from 20 subjects are illustrated in the box-and-whiskers plot for the cerebellum (blue) and PCC (red) results.

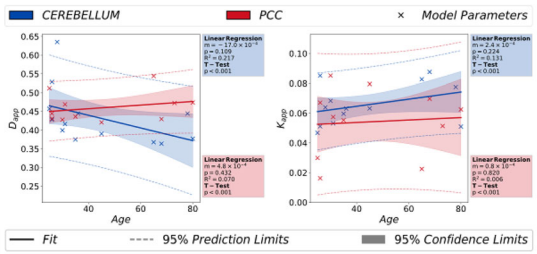

Fig. 4: Age dependence of the estimated parameters obtained from tNAA signals is depicted in the figure. For each cortex, a linear regression and a T-test are applied to analyze the statistical significance of the estimated parameter change.

References

1. Hoxha E, et al. (2017) *Front Cell Neurosci* 11:343.
2. Louis ED, et al. (2014) *Brain* 137(Pt 12):3142–3148.
3. Holtmaat AJ, et al. (2005) *Neuron* 45(2):279–291.
4. Hutsler JJ & Zhang H (2010) *Brain Res* 1309:83–94.
5. Perez-Cruz C, et al. (2011) *Journal of Neuroscience* 31(10):3926–3934.
6. Palombo M, et al. (2016) *Proc Natl Acad Sci U S A* 113(24):6671–6676.
7. Palombo M, Ligneul C, & Valette J (2017) *Magnet Reson Med* 77(1):343–350.
8. Vincent M, Palombo M, & Valette J (2020) *Neuroimage 207:116,399*.
9. Palombo M, Shemesh N, Ronen I, & Valette J (2018) *Neuroimage 182:97–116*.
10. Cao P & Wu EX (2017) *Nmr Biomed* 30(3).
11. Ronen I & Valette J (2015) *eMagRes* 4:733–750.
12. Genovese G & al. e (2018) *Proceedings of the 26th Annual Meeting of ISMRM, 4447*.
13. Provencher SW (1993) *Magn Reson Med* 30(6):672–679.
14. Sukstanskii AL & Yablonskiy DA (2008) *J Magn Reson* 190(2):200–210.
15. Yablonskiy DA & Sukstanskii AL (2010) *Nmr Biomed* 23(7):661–681.
16. Palombo M, Ligneul C, Hernandez-Garzon E, & Valette J (2018) *Neuroimage 182:283–293*.
17. Sild M & Ruthazer ES (2011) *Neuroscientist* 17(3):288–302.
18. Ingo C, Brink W, Ercan E, Webb AG, & Ronen I (2018) *Brain Structure & Function* 223(8):3841–3854.

LT83.
μGUIDE: A framework for microstructure imaging via generalized uncertainty-driven inference using deep learning

M. Jallais[1], M. Palombo[1]

[1]*Cardiff University, Brain Research Imaging Centre (CUBRIC), Cardiff, United Kingdom*

Introduction Diffusion-weighted MRI is a promising technique for characterizing brain microstructure in-vivo[1,2]. Traditional approaches quantify histologically meaningful features of brain microstructure by fitting a biophysical model voxel-wise to the set of signals obtained from images acquired with different sensitivities, yielding model parameter maps[1]. However, traditional maps only represent the best solution and do not provide confidence measures that could guide the interpretation.

Posterior distributions are powerful tools to characterize all possible parameter estimations that could explain an observed measurement, the uncertainty in those estimations and existing model degeneracies. Conventional Bayesian inference approaches (e.g. Markov-Chain-Monte-Carlo) are computationally expensive and time consuming. Recent machine learning methods developed to accelerate posterior distribution estimation rely on the definition of summary statistics to handle the high-dimensionality of data[3,4]. However, the summary statistics are model-specific, not easy to define and rely on specific acquisition requirements.

Harnessing a new deep learning architecture for automatic signal feature selection and efficient sampling of the posterior distributions, we propose μGUIDE: a general Bayesian framework to estimate posterior distributions of tissue microstructure parameters from any given biophysical model/signal representation without acquisition constraints.

Methods The μGUIDE framework relies on a simulation-based inference formulation[3,4], which takes as input a multi-shell diffusion-weighted signal x and outputs the posterior distributions p(θ|x) of the model parameters θ in each voxel. We define four measures to characterize the obtained posterior distributions: best estimate of model parameters, uncertainty, degeneracy and ambiguity (Fig. 1).

We compare the posterior distributions obtained using μGUIDE and previous methods based on manually defined summary statistics[4,5]. We show applications to two biophysical models from the literature:

- The Standard Model[5] (SM): a two-compartment model with neurite signal fraction f, intra-neurite diffusivity D_a, orientation dispersion index ODI, and parallel/perpendicular diffusivity within the extra-neurite space $D_e^{\parallel}/D_e^{\perp}$. We use the LEMONADE[5] framework to define six summary statistics.
- An extended-SANDI model[4]: a three-compartment model with neurite signal fraction f_n, intra-neurite diffusivity D_n, orientation dispersion index ODI, soma signal fraction f_s, a proxy of soma radius

and diffusivity[4] C_s, and extra-cellular isotropic diffusivity D_e. We use the six summary statistics defined in[4].

The training was performed on 10^6 numerical simulations for each model using random combinations of the model parameters, each uniformly sampled from physically plausible ranges.

We applied the method first on simulated test-sets generated similarly to the training-set, and then on real data acquired using a PGSE acquisition with b-values = [200,500,1200,2400,4000,6000]s/mm2, [20,20,30,61,61,61] uniformly distributed directions, δ/Δ = 7/24 ms, TE/TR = 76/3200 ms. Only the b $\leq$ 2500 s/mm2 data were used for the SM.

Results Figure 2A showcases µGUIDE ability to highlight degeneracies in the model parameter estimation, considering a noise-free acquisition. Figure 2B presents the posterior distributions obtained on simulations by using either µGUIDE or summary statistics for Signal-to-Noise-Ratio = 50. Sharper and less biased posterior estimations are obtained with µGUIDE.

Figure 3 presents the parametric maps of an exemplar set of model parameters, alongside their uncertainty, degeneracy and ambiguity, obtained on real data using µGUIDE with both models.

Figure 4 demonstrates µGUIDE application to an epileptic patient. Noteworthy, *f* estimates from SM within the epileptic lesion show low uncertainty/ambiguity hence high confidence, while *ODI* estimates show high uncertainty/ambiguity suggesting low confidence.

Discussion The reduced bias and variance in the posterior distributions estimated with µGUIDE promise to improve parameters estimation over current methods. µGUIDE can be easily applied to multiple models/representations and obtain faster posterior distributions estimations. Constraints imposed by the definition of the manually-defined summary statistics are removed, but µGUIDE is still a model-dependant method (training is model-based).

Conclusion µGUIDE allows to highlight degeneracy and obtain information about the uncertainty/ambiguity of an estimation, guiding results interpretation. As demonstrated by our pathologic example, changes of those measures can help clinicians decide which parameters are the most reliable and better interpret microstructure changes within diseased tissue.

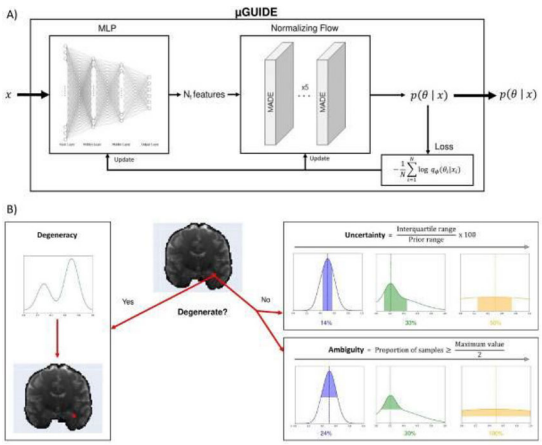

Fig.1: A)µGUIDE architecture. Input: an observed signal. Output: posterior distributions of the parameters. Based on a SBI[3,4] framework, it combines a multi-layer perceptron, used for dimensionality reduction, and a normalizing flow[6]. B)Presentation of the four measures introduced to quantify a posterior distribution

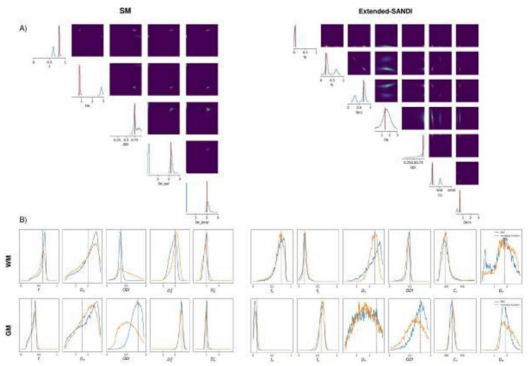

Fig. 2:Simulation results. A)Posterior distributions (diagonal) and joint posterior distributions (upper diagonal) of microstructure parameters for the SM and extended-SANDI model using µGUIDE (SNR=∞) B)p(θ|x) for both models using µGUIDE (blue) or manually-defined summary statistics[4,5](orange)(SNR=50)

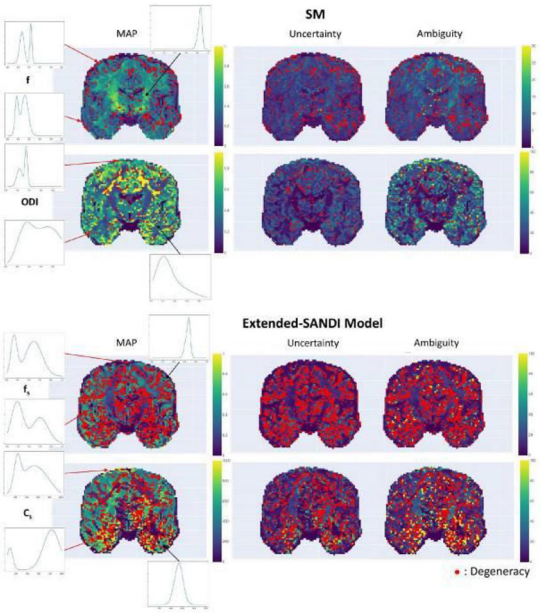

Fig. 3: Parametric maps for both models, obtained using µGUIDE: Maximum A Posteriori estimation, uncertainty and ambiguity, overlayed with voxels considered degenerate.

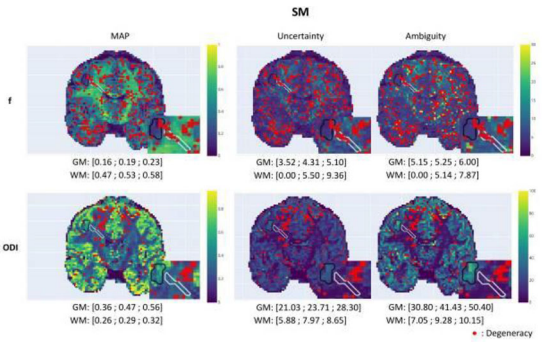

Fig. 4: Parametric maps of an epileptic patient for the SM obtained using µGUIDE, superimposed with the GM (black) and WM (white) lesion segmentations. First quartile, mean value and third quartile are reported.

References
[1]Alexander et al., NMR in Biomed 2019 [2]Jelescu et al., J Neurosci Methods 2020 [3]Cranmer et al., PNAS 2020 [4]Jallais et al., MELBA 2022 [5]Novikov et al., NMR in Biomed 2019 [6]Papamakarios et al., JMLR 2021.

LT84.
Characterising fibrosis in deep vein thrombosis using non-invasive and quantitative magnetic resonance imaging (MRI)

L. Gao[1], N. Chaher[1], J. C. Serralha[2], C. Velasco[1], G. Cruz[1,3], C. Prieto[1,4], R. Botnar[5,1,6,4], A. Smith[5,2], P. Saha[5,2], A. Phinikaridou[5,1]

[1]*King's College London, School of Biomedical Engineering & Imaging Sciences, London, United Kingdom;*
[2]*King's College London, School of Cardiovascular and Metabolic Medicine & Science, London, United Kingdom;*
[3]*University of Michigan, Department of Radiology, Michigan, MI, United States;*
[4]*Pontificia Universidad Católica de Chile, Escuela de Ingeniería, Santiago de Chile, Chile;*
[5]*King's College London, BHF Centre of Research Excellence, London, United Kingdom;*
[6]*Pontificia Universidad Católica de Chile, Instituto de Ingeniería Biológica y Médica, Santiago de Chile, Chile*

Introduction Deep Vein Thrombosis (DVT) is a significant cause of morbidity and mortality worldwide[1]. DVT resolves naturally through a fibrotic process that involves the replacement of fibrin with collagen[2]. The extent of fibrosis in DVT can determine the effectiveness of treatments[3], but current non-invasive diagnostic methods are not informative of the collagen content of the thrombus and the vein wall. Here, we investigate whether molecular MRI using a collagen I targeting probe can quantify and stage fibrosis in a murine model of DVT.

Methods Thrombosis was induced in the inferior vena cava (IVC) of mice using a combination of stenosis and endothelial injury[4]. Mice were scanned using a clinical 3 Tesla MRI scanner before and after injection of a gadolinium agent targeting collagen I (EP-3533; i.v; 10 μmol/kg) at days 7, 14 and 21 post-surgery (n = 3/group). 2D MR venography (MRV) was used to calculate thrombus size and 2D MR aortography used for anatomical reference. 3D T1w inversion recovery (IR) gradient echo was acquired pre and post injection of the probe and was used to visualise the Late Gadolinium Enhancement (LGE) and to analyse the Contrast-to-Noise Ratio (CNR) = $(SI_{tissue} - SI_{muscle})/SD_{outside\ body}$ (SI = signal intensity; SD = standard deviation) and $\Delta CNR = CNR_{post\text{-}contrast} - CNR_{pre\text{-}contrast}$. T1 mapping was carried out using a 3D Look-Locker sequence with an inversion pulse followed by the acquisition of 20 inversion recovery images with the inversion delay ranging from 20 to 5000 ms. T1 maps were then reconstructed offline using an in-house developed MATLAB script. T1 maps pre and post injection were used to analyse relaxivity R1 $(s-1) = 1/T1$ and $\Delta R1 = R1_{post\text{-}contrast} - R1_{pre\text{-}contrast}$. MRI acquisition parameters are listed in Table 1. The collagen content of the thrombus and surrounding vein wall was quantified using Masson's Trichrome and Picrosirius red stain.

Results Fused MR venography and aortography images localise the thrombus and showed reduction of thrombus size concurrent with thrombus resolution from day 7 to 21 post-surgery (Fig. 1A). Pre-contrast IR images showed a bright signal in the thrombus originating from paramagnetic methaemoglobin (Fig. 1B) at days 7 and 14. Post-contrast LGE images showed selective enhancement within thrombus and venous wall at days 7, 14 and 21 that became more evident at day 21 (Fig. 1B). Pre-contrast T1 mapping showed lower T1 values at days 7 and 14 driven by the presence of methaemoglobin. Administration of the probe further reduced the T1 values with the reduction becoming more evident at day 21 (Fig. 1V). Quantification of ΔCNR and ΔR1 was higher at day 21 compared with days 7 and 14 indicating higher uptake of the probe and thus increased fibrosis (Fig. 1D). Ex vivo histology verified the presence of collagen in the periphery of the thrombus and within the venous wall where signal enhancement was observed in vivo (Fig. 2A). Further histological analysis validated the imaging data and showed reduction of thrombus size from days 7 to 21 and increased collagen fibrosis as the disease progresses (Fig. 2B).

Discussion Collagen I can be detected in vivo with a specific molecular MRI probe and a clinical 3 T scanner, enabling selective detection and quantification of extracellular matrix remodelling in the environs of a venous thrombus. Using quantitative molecular MRI we show that fibrosis increases over time in a murine model of DVT.

Conclusion We have shown the feasibility to detect and quantify DVT-associated fibrosis with molecular MRI using a collagen I targeting probe. Further work is needed to establish the sensitivity of imaging fibrosis to stage disease and monitor the response to treatments. Such an approach may help stratify patients with DVT for specific interventions.

Acknowledgement This work is supported by a King's-CSC studentship and the King's BHF Centre of Research Excellence (RE/18/2/34213 & RE19140) & BHF PG/2019/34897. Many thanks to my supervisors Dr Alkystis Phinikaridou and Mr Prakash Saha and the support from co-authors and all collaborators.

Fig. 1

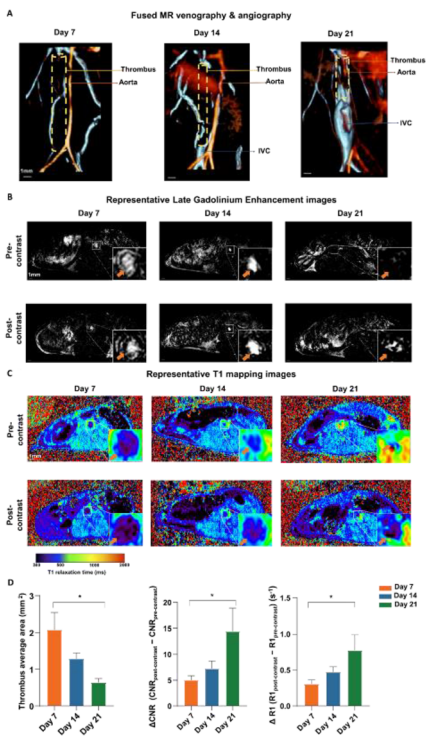

Fig. 1: Molecular imaging using collagen I target agent allows detection of fibrosis associated with DVT. **A**. Fusion of MRV & MR angiography at days 7, 14 and 21. (Scale bar =1mm) **B**. Representative pre- and post-contrast LGE images of the thrombus area at days 7, 14 and 21. (Scale bar =1mm) **C**. Representative pre- and post-contrast T1 mapping images of the thrombus area at days 7, 14 and 21. (Scale bar =1mm) **D**. Quantification of thrombus average size based on MRV, ΔCNR and ΔR1 analysis in the thrombus area at days 7, 14 and 21. (n=3/per timepoint). *: $P < 0.05$ (Kruskal-Wallis test)

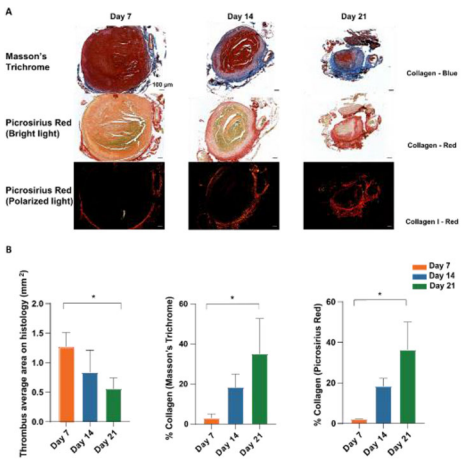

Fig. 2: Spatiotemporal profiling of changes in collagen I associated with DVT. **A**. Masson's Trichrome and Picrosirius Red stain of days 7, 14 and 21 in the thrombus area. (Scale bar =100μm) **B**. Quantification of thrombus average area, the percentage of collagen expression in the thrombus area at day 7, 14 and day 21 based on histology. (n=3/per timepoint). *: ***P***< 0.05

	2D Time of flight-venography	2D Time of flight-angiography	2D Look-Locker (60 bpm)	3D Inversion Recovery (60 bpm)	3D T1 mapping
Repetition Time (TR) / Echo time (TE) (ms)	50/6.1	40/6.2	19/8.6	27/8.2	8.9/4.6
Flip angle	60°	60°	10°	30°	10°
Field of view (FOV) (mm)	35x35x17	35x35x17	30x30	40x40x15	36x22x12
In-plane Resolution (mm)	0.3x0.3	0.3x0.3	0.38x0.38	0.1x0.1	0.2x0.2
Slice thickness (mm)	0.3	0.3	2	0.5	0.5
Duration	9min 20s	7min 28s	53s	13min 15s	20min 48s

Table 1: MRI acquisition parameters

References

[1] White RH. The epidemiology of venous thromboembolism. Circulation. 2003;107(23 Suppl 1): I4-8.
[2] Mukhopadhyay S, Johnson TA, Duru N, Buzza MS, Pawar NR, Sarkar R, Antalis TM. Fibrinolysis and Inflammation in Venous Thrombus Resolution. Front Immunol. 2019;10:1348.
[3] Comerota AJ, Oostra C, Fayad Z, Gunning W, Henke P, Luke C, Lynn A, Lurie F. A histological and functional description of the tissue causing chronic postthrombotic venous obstruction. Thromb Res. 2015;135(5):882–7.
[4] ***Saha P***, Andia ME, Modarai B, Blume U, Humphries J, Patel AS, ***Phinikaridou A***, Evans CE, Mattock K, Grover SP, Ahmad A, Lyons OT, Attia RQ, Renné T, Premaratne S, Wiethoff AJ, ***Botnar RM***, Schaeffter T, Waltham M, ***Smith A***. Magnetic resonance T1 relaxation time of venous thrombus is determined by iron processing and predicts susceptibility to lysis. Circulation. 2013;128(7):729–736.

LT85.
Quantification of the perineural satellitosis of pretreatment glioblastoma by the use of individual structural MRI data and diffusion tensor imaging

R. van den Elshout[1], B. Ariens[1], J. Blaauboer[1], A. Meijer[1], A. van der Kolk[1], M. Esmaeili[2], T. Scheenen[1], D. Henssen[1]

[1]*RadboudUMC, radiology, Nijmegen, Netherlands;*
[2]*Akershus university hospital, Diagnostic Imaging, Lørenskog, Norway*

Introduction Glioblastoma is the most common malignant brain tumor with an abysmal prognosis with a median survival of 15 months and frequently occurring tumor recurrence (1). Understanding the growth patterns of glioblastoma using advanced imaging modalities could potentially be used as a prognostic and/or diagnostic marker. The aim of this study was to investigate whether tumor growth direction in pre- and posttreatment glioblastoma patients can be quantified and correlated to white matter microstructure using improved image registration and deformation strategies.
Methods In 78 glioblastoma patients, two pretreatment scans (diagnostic and neuronavigation T1 post-contrast) were segmented and co-registered to a template Diffusion Tensor Imaging (DTI) atlas. In 96 posttreatment glioblastoma patients, two follow-up scans (T1 post-contrast) were segmented and co-registered to patient-specific DTI data, using an in-house written image registration and deformation pipeline. Growth vectors were derived and divided into vector populations parallel- ($\theta = 0°–20°$) and perpendicular ($\theta = 70°–90°$) to white matter.
Results The pretreatment glioblastoma lesions showed a predominant preference of perineural satellitosis ($p < 0.001$), with a mean percentile growth of 30.8% (95 CI 29.6–32.0%) parallel ($0° < |\theta| < 20°$) to white matter. Perpendicular tumor growth with respect to white matter microstructure ($70° < |\theta| < 90°$) showed to be 22.7% (95 CI 21.3–24.1%) of total tumor growth direction. MGMT status did not influence growth direction or growth rate. The posttreatment glioblastoma lesions with patient specific DTI data show promising results with regard to early detection of tumor recurrence.
Discussion Our findings indicate that the contrast-enhancing bulk of GBM lesions tend to grow predominantly along the course of white matter tracts, as opposed to perpendicular to their orientation. Visualizing this growth pattern on MRI data is an important and relative novel observation as it sheds light on the complex interplay between tumor growth and white matter structure. The results corroborate the growth patterns and perineural satellitosis of glioblastoma as described in histopathological studies (2), as well as other DTI studies (3). This study provides insight by quantifying visible tumor growth directions in vivo, possibly providing a stepping stone in determining invasion beyond the perilesional contrast-enhancing rim or aiding in the differentiation between treatment related abnormalities (e.g. pseudoprogression) and tumor progression in future studies. Hopefully, clinical implementation of this technique to optimize glioblastoma treatment becomes more feasible in the future.
Conclusion The here described image registration and deformation strategy provides further evidence that tumor growth direction in pretreatment glioblastoma patients was correlated to white matter architecture. Patient-specific DTI data can be a potential clinical metric for non-invasive diagnosis of tumor recurrence.

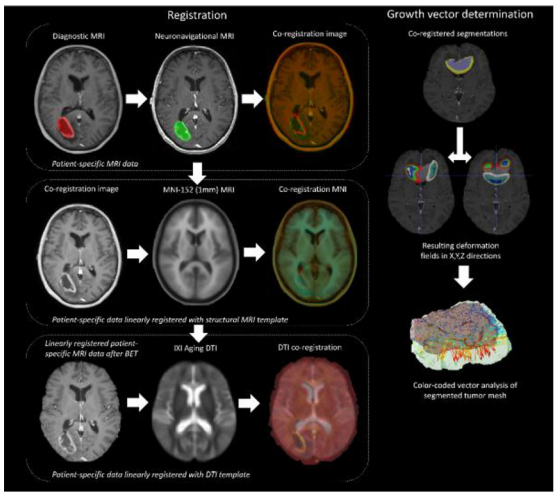

Fig. 1: Simplified overview of the image registration and tumor growth vector deformation field resulting in the vector populations parallel or perpendicular to white matter according to the DTI atlas

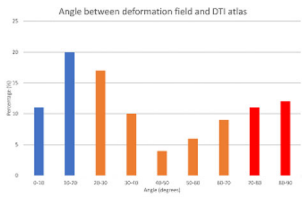

Fig. 2: Angle distribution between vector population of the DTI template and obtained deformation field. Vector populations parallel to white matter (blue) occur more often than vector populations perpendicular to white matter (red)

References

1. Brown NF, Ottaviani D, Tazare J, Gregson J, Kitchen N, Brandner S, et al. Survival Outcomes and Prognostic Factors in Glioblastoma. Cancers. 2022;14(13).
2. Scherer HJ. Structural Development in Gliomas. American Journal of Cancer. 1938;34:333–51.
3. Esmaeili M, Stensjøen AL, Berntsen EM, Solheim O, Reinertsen I. The Direction of Tumour Growth in Glioblastoma Patients. Scientific reports. 2018;8(1):1199.

LT86.

T2* mapping covering the full cardiac cycle detect myocardial changes in hypertrophic cardiomyopathy

O. Laghzali[1,2], S. Lehmann[1,3], J. Dos Santos Periquito[1], A. Pohlmann[1], L. Carrier[4,5], S. Waiczies[1], T. Niendorf[1,2,6], M. C. Ku[1,2]

[1]*Max Delbrueck Center for Molecular Medicine in the Helmholtz Association, Berlin Ultrahigh Field Facility (B.U.F.F.), Berlin, Germany;*
[2]*DZHK (German Centre for Cardiovascular Research), partner site Berlin, Berlin, Germany;*
[3]*Technical University of Berlin, Berlin, Germany;*
[4]*University Medical Center Hamburg-Eppendorf, Department of Experimental Pharmacology and Toxicology, Hamburg, Germany;*
[5]*DZHK (German Centre for Cardiovascular Research), partner site Hamburg/Kiel/Lübeck, Hamburg, Germany;*
[6]*Max Delbrueck Center for Molecular Medicine in the Helmholtz Association, Berlin, Germany*

Introduction The myocardium undergoes dynamic changes throughout the cardiac cycle. Under disease conditions such as Hypertrophic Cardiomyopathy (HCM), covering the whole cardiac cycle is crucial for detecting subtle changes in myocardial tissue. Myocardium can be non-invasively characterized via T_2^* quantification. T_2^* is prolonged in HCM patients and when assessed over the full cardiac cycle, transient T_2^* differences between diastole and systole are diminished in HCM patients [1]. The mechanisms underlying these preclinical observations are unexplored so far. We hypothesize that myocardial T_2^* mapping in a humanized mouse model of HCM will provide a framework for deciphering the underlying T_2^* changes in HCM. To test our hypothesis, we implemented a data acquisition scheme that enables retrospective data sorting and full cardiac cycle coverage for T_2^* mapping in healthy mice and in HCM mice at 9.4 T and further assessed the signs of cardiac remodelling with immunohistochemistry methods.

Method For evaluating the retrospectively sorted T_2^* mapping scheme, two Ferumoxytol (Fe) phantoms were prepared in 2% agarose in a volume of 1.5 mL Eppendorf tube (C1 = 50 µg/mL, C2 = 25 µg/mL). T_2^* mapping was conducted using a 9.4 T animal scanner (Biospec 94/20, Bruker, Germany) using the following parameters: TR = 14 ms, TE = 1.5–11.1 ms, echo spacing = 1.6 ms (7 TEs),300 repetitions (acquired continuously to fill 300 k-space lines). Conventional multi gradient echo (MGE) imaging (TR = 35 ms, TE = 1.5–31.9 ms, echo spacing = 1.6 ms, 20 TEs) was used as a reference. In vivo experiments were performed on Mybpc3-KI mice that harbour a point mutation in the *Mybpc3* gene [2]. All animal experiments were carried out in accordance with local animal welfare guidelines (LAGeSo). Four Mybpc3-KI and four wildtype controls (all C57BL/6J background and 6 weeks old) were examined. B0 shimming was performed. Continuous acquisition of T_2^* weighted multi-echo GRE data was accompanied by simultaneous tracking of cardiac activity using pulse oximetry (SA instruments). For image reconstruction, the time points of the MR k-space lines were matched to the corresponding cardiac phases. Short axis views were used to acquire whole cardiac cycle coverage CINE images (adapted FLASH, cardiac frames = 10, TE/TR = 2.1/10 ms, FA = 20°, FOV = 20 × 20 mm^2, matrix = 192 × 192, thickness = 0.8 mm) and T_2^*-maps (MGE, cardiac frames = 7, TE/TR = 2.1/20 ms, FA = 10°, FOV = 35 × 35 mm^2, matrix = 128 × 128, thickness = 0.8 mm). After detecting signs of cardiac remodelling, we used confocal microscopic imaging (Leica Stellaris 8). Briefly, the mouse hearts were removed, and perfused with Lycopersicon esculentum (Tomato) Lectin-LEA (DyLight™ 488, Thermo Fisher Scientific).

Results In Fe phantoms, we observed an agreement in T_2^* results between the retrospective sorting-based approach and the conventional MGE (Fig. 1). The in vivo study provided mean myocardial T_2^* values (averaged over the entire cardiac cycle) of $T_2^*_{Ctrl} = 9.52 \pm 0.63$ ($T_2^*_{systole} = 9.08 \pm 0.46$ ms, $T_2^*_{diastole} = 9.82 \pm 0.57$ ms) and $T_2^*_{HCM} = 10.0 \pm 0.23$ ms ($T_2^*_{systole} = 9.82 \pm 0.22$ ms, $T_2^*_{diastole} = 10.12 \pm 0.16$ ms). Our findings show a T_2^* prolongation in HCM mice compared to healthy control (Fig. 2). A close examination of T_2^* throughout the cardiac cycle revealed a transient change in myocardial T_2^*. Overall T_2^* was decreased during systole and increased during diastole (Fig. 3). The difference between $T_2^*_{diastole}$ and $T_2^*_{systole}$ (ΔT_2^*) was decreased in HCM mice ($\Delta T_2^* = 1.03 \pm 0.03$) compared to healthy controls ($\Delta T_2^* = 1.08 \pm 0.08$) ($p < 0.05$). Microvasculature and fibrosis staining showed a significant difference in capillary density and the amount of collagen deposition in the myocardium between HCM and WT mice (figure in preparation).

Conclusion and discussion This work demonstrates the feasibility of retrospective gating based T_2^* mapping in mice with whole cardiac cycle coverage. Our findings demonstrate an increase of myocardial T_2^* in HCM, which accords with previous preclinical human studies [1]. Alterations in the dynamic T_2^* change between systole and

diastole could reflect early signs of microvascular dysfunction consistent with early progression of HCM. To conclude, our study provides an important foundation for gaining a better understanding of the pathophysiological underpinnings of myocardial changes in the HCM.

Acknowledgment This work was supported by the German Research Foundation, KU 3722/4-1 (Gefördert durch die Deutsche Forschungsgemeinschaft [DFG], KU 3722/4-1).

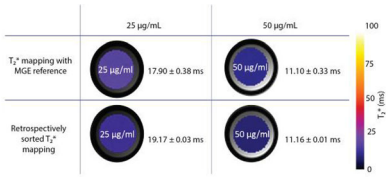

Fig. 2: Short axis view T_2^* maps of the left ventricular myocardium using the retrospective gating approach. Top: T_2^* maps obtained for HCM mice, Bottom: T_2^* maps derived from control mice. T_2^* maps are shown for end-systolic and end-diastolic cardiac phases.

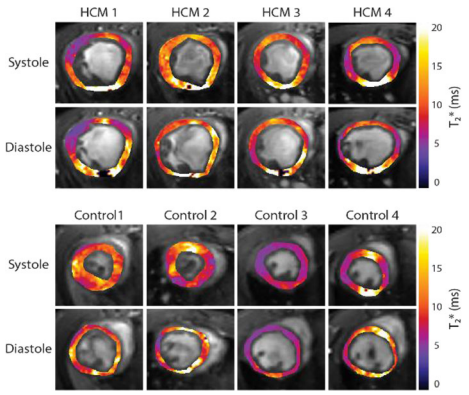

Fig. 1: Validation of the retrospectively sorting T_2^* mapping technique against the MGE reference. For evaluation, Ferumoxytol phantoms with two concentrations of iron were used. The corresponding T_2^* maps show agreement between our retrospectively sorted approach and the MGE reference.

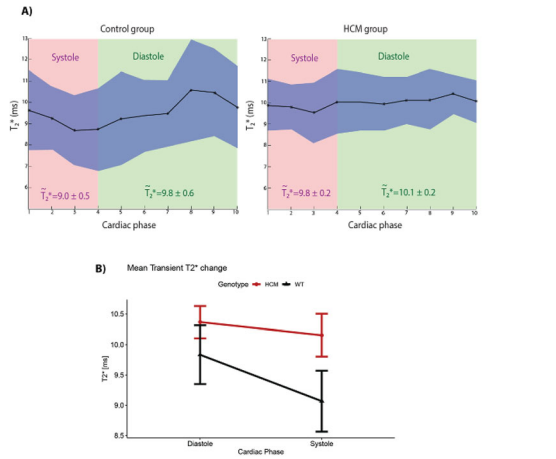

Fig. 3: Transient T_2^* changes throughout the cardiac cycle. (A) Average T_2^* obtained for systole and diastole are indicated, while the curve shows the changes of T_2^* over the entire cardiac cycle. The blue zone represents the standard deviation. (B) Average T_2^* change between Systole and Diastole in Healthy (black) and HCM (red) group. The healthy control group shows larger changes in T_2^* throughout the cardiac cycle compared to the HCM group.

References

1. Huelnhagen, T., et al., *Myocardial Effective Transverse Relaxation Time T 2(*) is Elevated in Hypertrophic Cardiomyopathy: A 7.0 T Magnetic Resonance Imaging Study.* Sci Rep, 2018. **8**(1): p. 3974.

2. Vignier, N., et al., *Nonsense-mediated mRNA decay and ubiquitin–proteasome system regulate cardiac myosin-binding protein C mutant levels in cardiomyopathic mice.* Circ Res, 2009. **105**(3): p. 239–48.

LT87.
Towards carotid artery quantitative susceptibility mapping: An isotropic acquisition to investigate susceptibility anisotropy in *ex-vivo* arteries

B. Tornifoglio[1,2], S. McElroy[3], F. Digeronimo[1,2], A. J. Stone[4], K. Shmueli[5], C. Lally[6]

[1]*Trinity College Dublin, Department of Mechanical, Manufacturing and Biomedical Engineering, Dublin, Ireland;*
[2]*Trinity College Dublin, Trinity Centre for Biomedical Engineering, Dublin, Ireland;*
[3]*Siemens Healthineers, MR Research Collaborations, Frimley, United Kingdom;*
[4]*St. Vincent's University Hospital, Department of Medical Physics and Clinical Engineering, Dublin, Ireland;*
[5]*University College London, 5Department of Medical Physics and Biomedical Engineering, London, United Kingdom;*
[6]*Royal College of Surgeons in Ireland and Trinity College Dublin, Advanced Materials and BioEngineering Research Centre (AMBER), Dublin, Ireland*

Introduction Quantitative susceptibility mapping (QSM) can map the magnetic susceptibility (c) of biological tissues1 and has shown sensitivity to key microstructural components in vascular tissue2. In vivo carotid QSM focuses on atherosclerotic morphologies3–5; however, has yet to look at the alignment of individual components which can be linked to the mechanical integrity of the tissue6. These studies also use anisotropic acquisition, when it has been shown that isotropic resolution is preferrable for accurate QSM7. Using ex vivo porcine aortae, this study investigated the sensitivity of c to collagen at different orientations with an isotropic QSM sequence on two clinical scanners with a view to clinical translation of carotid QSM.

Methods Fixed porcine aortae were prepared using previously established protocols for arterial tissue2. Three falcon tubes were each filled with phosphate buffered saline and contained three aortic segments positioned at 90° to each other (Fig. 1a). The tubes were secured around a vendor-supplied phantom (Fig. 1b) and imaged with an isotropic 3D multi-echo gradient echo (ME-GRE) QSM sequence acquired on both 3 T Siemens MAGNETOM Prisma (Siemens Healthcare, Erlangen, DE) and Philips Achieva (Philips Healthcare, Best, NL) systems: see Table 1 for sequence parameters. A previously published anisotropic carotid QSM acquisition5 was also acquired on the 3 T Siemens for comparison. Magnitude and phase images were exported from both scanners and processed using the following pipeline2,8: echo combination with a nonlinear fit and with Laplacian-based phase unwrapping. Magnitude images (TE1) were used to threshold a mask, which included only the phantom and falcon tubes, which was used for background field removal via projection onto the dipole fields, then four different c calculation algorithms were compared: direct and iterative Tikhonov, morphology enabled dipole inversion (MEDI)9 and truncated k-space division (TKD). Manually drawn ROIs on magnitude images (TE1) were used to compare mean c values of each sample.

Results Figure 2 shows a comparison of c maps from the anisotropic5 and the proposed isotropic acquisition. Isotropic data showed fewer artifacts/residual background fields compared to the anisotropic data (Fig. 2a, b). Within axial aortic samples there was only a significant difference between the acquisitions when using MEDI to calculate c (Fig. 2c). Using the isotropic carotid QSM sequence, the c anisotropy

was investigated in the arterial samples on two scanners. Figure 3 shows the significant difference between arterial samples when oriented 90° to each other for all processing tools except MEDI. Figure 3 also shows no significant difference between the scanners, with the c for both orientations agreeing well.

Discussion In this work, for the first time, an isotropic carotid QSM sequence was acquired and compared across two scanners. Previous carotid QSM acquisitions used anisotropic resolution, however we found that isotropic acquisition resulted in fewer residual background fields and artifacts, agreeing well with previous work in head and neck regions7. We saw good agreement in a direct comparison between a Siemens and Philips scanner, where no significant differences were observed in c measured between scanners. We did find a significant difference between cdepending on the orientation of the arterial samples for three out of four c calculation algorithms. It is interesting to note that despite being significantly affected by the anisotropic acquisition, the MEDI algorithm was the only method which did not detect c anisotropy. Previous observations of the effect of collagen content on the c of arterial tissue2suggests that the orientation dependence observed here is likely due to its perpendicular alignment between the arterial samples, highlighting their c anisotropy—similar to that in cartilaginous tissue9. **Conclusion:** An isotropic carotid QSM sequence was acquired and found to be reproducible across two clinical scanners. The orientation dependence of mean c in arterial samples highlighted c anisotropy that is probably due to the alignment of collagen. This technique offers significant promise for QSM of the carotid arteries and to assess the underlying microstructure of atherosclerotic plaques. Future work will compare carotid QSM in healthy volunteers and patients with carotid plaques to further assess this technique"s clinical potential.

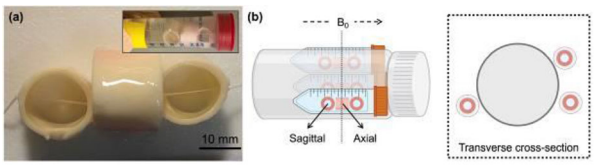

Fig. 1: *Ex vivo* (a) aortic segments were secured in tubes which were (b) positioned around a large phantom.

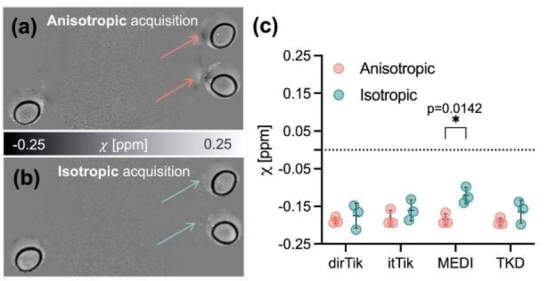

Fig. 2: Anisotropic and isotropic acquisition on the 3T Siemens Prisma. (a, b) c maps show fewer artifacts using an isotropic resolution. (c) A two-way ANOVA with multiple comparisons on the c of axial samples showed a significant difference only when using the MEDI algorithm. c values are displayed as mean per tissue volume ± SD across the group; n=3.

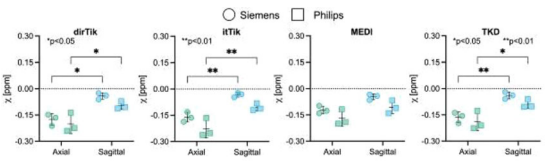

Fig. 3: Arterial phantoms imaged with an isotropic carotid QSM sequence on two clinical scanners in two orientations. Axial (n=3) and sagittal (n=3 as 3 were outside FOV) samples presented for both scanners. Data analysed via two-way ANOVA; *p<0.05, **p<0.01. c values are displayed as mean per tissue volume ± SD across the group.

	3T Siemens Prisma	3T Philips Achieva
Sequence	VIBE	THRIVE
Coil	2 x 4-channel special purpose coils	8-channel carotid coil
FOV [mm]	224 x 224 x 28	210 x 210 x 25
Matrix size	224 x 224 x 28	212 x 210 x 25
Imaging resolution [mm]	1.0 x 1.0 x 1.0	1.0 x 1.0 x 1.0
Recon. Resolution [mm]	0.5 x 0.5 x 0.5	0.525 x 0.525 x 0.50
Echoes	6	6
TEs [ms]	4.6, 9.2, 13.8, 18.4, 23, 26	4.6, 9.2, 13.8, 18.4, 23, 26
TR [ms]	31	31
Flip angle [°]	10	10
Flyback/Monopolar gradients	on	on
Bandwidth [Hz/Px]	470	543
Orientation	Transverse	Transverse
Averages	2	2
Acquisition time [min:sec]	5:33	6:44

Table 1. Acquisition parameters for the 3D ME-GRE sequence on both scanners. In-phase TEs and isotropic resolution were used based on a sequence optimised for head and neck QSM8.

References

1. Wang, et al. J Magn Reson Imaging, 46:951–971 (2017)
2. Stone, et al. Magn Reson Med, 00:1–6 (2021)
3. Ikebe, et al. Magn Reson Med Sci, 1–6 (2019)
4. Wang, et al. J Magn Reson Imaging, 1–8 (2020)
5. Nguyen, et al. Magn Reson Med, 1–9 (2020)
6. Johnston, et al. Acta Biomater, 124:291–300 (2021)
7. Karsa, et al. Magn Reson Med, 81:1833–1848 (2019)
8. Karsa, et al. Magn Reson Med, 84:3206–3222 (2020.
9. Liu, et al. Neuroimage, 59(3):2560–2568 (2012)
10. Nykänen, et al. Magn Reson Med, 2702–2716 (2018)

LT88.
Quantitative MRI in fluorescence-guided brain tumor needle biopsies

E. Klint[1], A. Tisell[2,3], J. Richter[1,4], J. Hillman[4,5], K. Wårdell[1]

[1]*Linköping University, Department of Biomedical Engineering, Linköping, Sweden;*
[2]*Linköping University, Department of Radiation Physics, Linköping, Sweden;*
[3]*Linköping University, Department of Health, Medicine and Caring Sciences, Linköping, Sweden;*
[4]*Linköping University, Department of Neurosurgery, Linköping, Sweden;*
[5]*Linköping University, Department of Biomedical and Clinical Sciences, Linköping, Sweden*

Introduction Quantitative MRI (qMRI) relaxometry difference maps can detect contrast-enhancement (CE) outside the CE observed on conventional MRI [1, 2]. However, this approach has not yet been validated intraoperatively. Our group has developed a method to connect MRI, intraoperative optical information, and neuropathology, for frameless brain tumor needle biopsies [3]. Thus, MR parameters, tissue fluorescence, and neuropathology could be compared on a millimeter scale. The aim of this work was to develop a pipeline for multimodal analysis as a first step toward validating qMRI with intraoperative data.

Methods The study included three patients with suspected high-grade brain tumors identified on MRI (informed written consent, EPM 2020-01404). MR data (3 T Siemens Prisma or Skyra, 20-channel head coil, Siemens Healthineers, Germany) were acquired preoperatively (T1-weighted (T1w) 3D MPRAGE with and without gadolinium (Gd)). Additionally, qMRI multidimensional multi-echo imaging (voxel size = 0.7 × 0.7 × 4 mm^3; slice gap 1 mm; FOV = 230 × 187 mm^2; scan time = 6 min) [4] was added before and after Gd-administration. Synthetic T1w, T2w (synTxw), and relaxation maps were calculated in the SyMRI software (v0.45.38, SyntheticMR AB, Sweden) (Fig. 1). During surgery, a 3.2 mm burr-hole was made in the skull, the dura was opened, and the trajectory was locked. The optical probe was secured in the outer cannula of the biopsy needle, fastened, and inserted along the trajectory in millimeter steps. In each position, fluorescence measurements and corresponding preoperative MRI coordinates were collected. When the region of the largest fluorescence peak at 635 nm was identified, the inner cannula replaced the probe, and tissue samples were taken. Postoperative imaging, either CT (SOMATOM Definition Edge, Siemens) or 3D T1w MRI, was acquired within 12 h of surgery.

A postprocessing pipeline was constructed in Python using a wrapper for FMRIB's Software Library (FSL) [5] and Advanced Normalization Tools (ANTs) [6] illustrated in Fig. 1. All modalities were registered to T1wGd image space used for navigation; synT1wGd, postoperative images, and final measurement coordinates. Moreover, the synT2w was registered to the synT2wGd. The resulting transformations were applied to the relaxation maps. The final measurement positions and biopsy ROI (150, 38, and 120 mm^3) were defined in the postoperative image (Fig. 2), where the mean and standard deviation R1 difference values were calculated.

Results For the three patients, the R1 difference values in the biopsy region were 0.43 (± 0.43), 0.94 (± 0.34), and 0.74 (± 0.18), respectively (Fig. 3). Along the trajectory, the values were − 0.042 (± 0.10), − 0.0032 (± 0.036), and − 0.11 (± 0.11). A pathologist confirmed the samples to be tumors with final diagnoses of high-grade astrocytoma, IDH-wildtype; glioblastoma IDH-wildtype, grade 4; and primary diffuse large B-cell lymphoma of the CNS.

Discussion A pipeline for combined analysis of qMRI, tissue fluorescence, and neuropathology could indicate altered R1 difference values in tissue identified as tumors compared to R1 difference values along the trajectory. Additional MRI protocols and optical techniques for a larger patient cohort are currently being investigated.

Conclusion We have shown that we can combine qMRI, optical, and neuropathology data. This will add new insights regarding the extent of tumor, even beyond the CE zone on conventional MRI.

Acknowledgments This project is financially supported by the Swedish Foundation for Strategic Research (grant number RMX18-0056). The authors are grateful to the clinical staff at the Departments of Neurosurgery and Clinical Pathology at Linköping University Hospital.

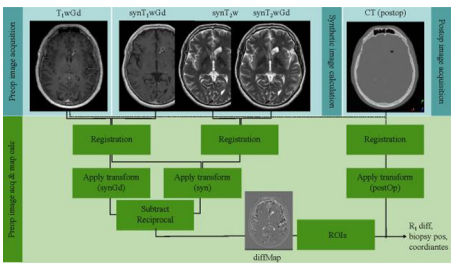

Fig. 1: Workflow from image acquisition to calculation of relaxation values.

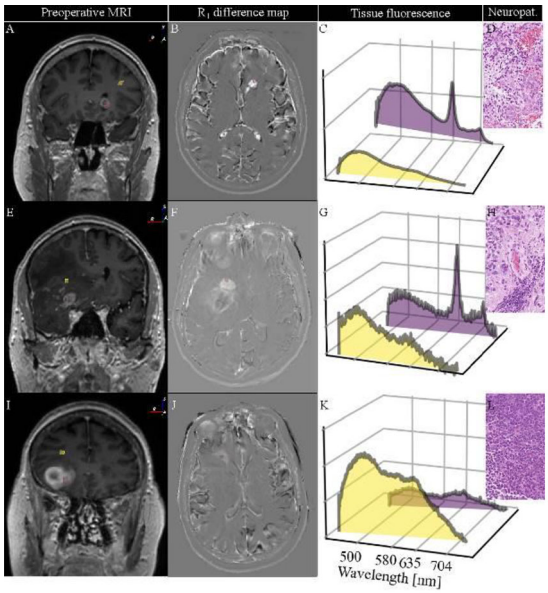

Fig. 2: Multimodal data examples for three patients; preoperative MRI with final measurement points (A, E, I), T1-difference map (B, F, J), optical fluorescence spectra (C, G, K), and neuropathology image (D, H, L). The superior ROI and first spectrum (yellow) are marked along the trajectory, while the inferior ROI and second spectrum (purple) correspond to the biopsy position.

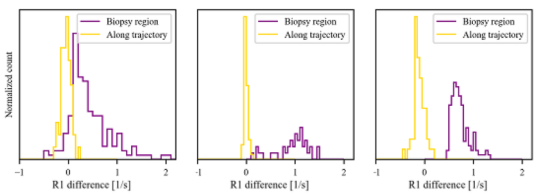

Fig. 3: Histogram of R1 difference values in the biopsy region and along the trajectory for the three patients.

References

1. Blystad, I., J. B. M. Warntjes, Ö Smedby, P. Lundberg, E. M. Larsson, and A. Tisell. "Quantitative Mri Using Relaxometry in Malignant Gliomas Detects Contrast Enhancement in Peritumoral Oedema." Sci Rep 10, no. 1 (2020): 17986.

2. Müller, A., A. Jurcoane, S. Kebir, P. Ditter, F. Schrader, U. Herrlinger, T. Tzaridis, B. Mädler, H. H. Schild, M. Glas, and E. Hattingen. "Quantitative T1-Mapping Detects Cloudy-Enhancing Tumor Compartments Predicting Outcome of Patients with Glioblastoma." Cancer Med 6, no. 1 (2017): 89–99.

3. Klint, E., J. Richter, and K. Wårdell. "Combined use of frameless neuronavigation and in situ optical guidance in brain tumor needle biopsies". *Submitted* (2023).

4. Warntjes, J. B., O. D. Leinhard, J. West, and P. Lundberg. "Rapid Magnetic Resonance Quantification on the Brain: Optimization for Clinical Usage." Magn Reson Med 60, no. 2 (2008): 320–9.

5. Jenkinson, M., C. F. Beckmann, T. E. Behrens, M. W. Woolrich, and S. M. Smith. "Fsl." NeuroImage 62, no. 2 (2012): 782–90.

6. Avants, B. B., N. J. Tustison, G. Song, P. A. Cook, A. Klein, and J. C. Gee. "A Reproducible Evaluation of Ants Similarity Metric Performance in Brain Image Registration." NeuroImage 54, no. 3 (2011): 2033–44.

LT89.
Human respiratory adaptation to position through lung strain tensor dynamics by 3D MR spirometry in free-breathing

A. Duwat[1], N. Barrau[1], K. Sambourg[1], A. Nemeth[1], A. Beurnier[2], T. Boucneau[3], C. Pellot-Baraka[1], V. Lebon[1], X. Maître[1]

[1]*BioMaps (CEA, CNRS, Inserm, Universite´ Paris-Saclay), Orsay, France;*
[2]*Hôpital Bicêtre, APHP, Le Kremlin-Bicêtre, France;*
[3]*GE Healthcare, Buc, France*

Introduction Three-dimensional MR spirometry produces local flow-volume loops across an average respiratory cycle integrated over a 12 min dynamic lung MRI acquisition [1]. Lung function can then be regionally characterized along the lines of standard spirometry, which is routinely performed but only limited to a global measurement at the subject"s mouth in forced respiration and fails to assess the extent of respiratory diseases in the organ. Additional markers can further be extracted from 3D MR spirometry to track the dynamic biomechanical behaviour of the lung. The Green–Lagrange strain tensor was evaluated at each of the 32 processed respiratory phases in 25 healthy volunteers in supine and prone positions. It diagonally contains the directional dilatations, which, beyond the gravity lung dependence, can be conditioned by the subject"s position and organ configuration.
Methods MR acquisitions were carried on a cohort of 25 subjects freely-breathing in supine and prone positions in a GE Signa PET/MR at 3 T using a 3D UTE sequence with AZTEK [2] and a 30-channel thoracic coil array. The centre of the acquired k-space was used as a surrogate respiratory signal to retrospectively rephase MR data to reconstruct 32 3D lung dynamic images over the acquisition-integrated respiratory cycle. The dynamic Green–Lagrange strain tensor was inferred at each respiratory phase from the deformation fields resulting from elastic registration with respect to a reference phase at the beginning of inspiration. The maps of the compressive strain tensor diagonal elements (or normal strains) along the three anatomical directions (superior–inferior, SI, anterior–posterior, AP, and left–right, LR) were then morphology- and histogram-based normalized before computing mean maps over the volunteers across the 32 respiratory phases for analysis. Eighteen cubic ROIs of 25 voxels were selected throughout the lung to probe the evolution of the normal strains and the overall volume change, over the respiratory cycle. Results.
The maximal normal strain maps at the end of inspiration show greater lung extensions along SI in prone, than in supine, (Fig. 1a,d) whereas, along AP, they show lower lung extensions in prone than in supine, 50% less (Fig. 1b, c, e, f). For both positions, the SI normal strain is largely enhanced in the basal regions and the AP and LR normal strains, in the apical regions. The three normal strains are found highly dependent with the position with larger extensions in the anterior regions in prone and in the posterior regions in supine. The evolution of the normal strains shows the balance between the three normal strain components and the volume change redistribution among the three directions with the position (Fig. 2).
Discussion In lying healthy volunteers, the main respiratory driving force is produced by the diaphragm as it is assessed here with a dominant SI normal strain in basal pulmonary regions. Reduced SI normal strain in supine position is expected as a result of the abdominal compression over the diaphragm [3]. It is compensated by augmented AP and LR normal strains. The different strain components take place at different moments of the respiratory cycle. The evolution of the normal strains highly depends on the position. It is governed by the gravity and the inferred biological conditions onto the pulmonary parenchyma and the respiratory muscles. It reveals the strategy the lung follows with respect to the the physical constraints to which the body is subjected. It also reveals the hysteresis behaviour of the respiration.
Conclusion Numerous parametric maps can be extracted from 3D MR spirometry. The normal strains provide rich spatial and temporal information on the biomechanical function of the lung. They are comprehensive and sensitive parameters which characterize the respiratory function and its adaptation to condtions. They might also explicit the lung dysfunction when muscles are impaired or more generally in most respiratory pathology when the lung function is altered and the volume changes are modified at the regional level.

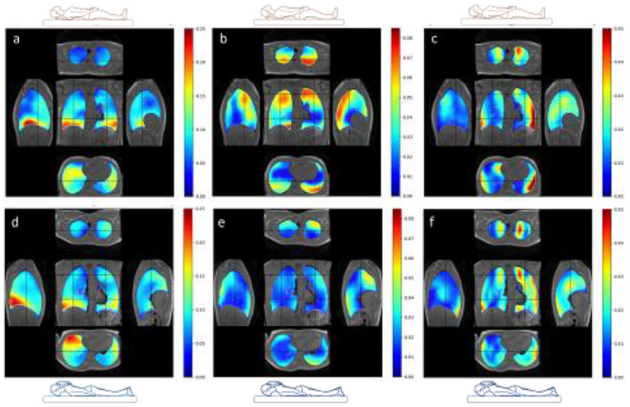

Fig. 1: Normal strain maps along SI, AP and LR in supine and prone position

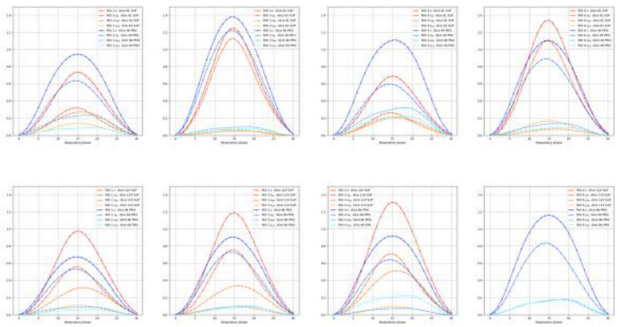

Fig.2: Evolution of biomarkers during one breath for several ROIs

References
[1] Boucneau T, Fernandez B, Larson P, Darrasse L, Maître X. 3D Magnetic Resonance Spirometry. *Scientific Reports*. 2020;10(1):9649. https://doi.org/10.1038/s41598-020-66202-7
[2] Boucneau T, Fernandez B, Besson FL, Menini A, Wiesinger F, Durand E, Caramella C, Darrasse L, Maître X. AZTEK: Adaptive zero TE k-space trajectories. *Magnetic Resonance in Medicine*. 2021;85(2):926–935. https://doi.org/10.1002/mrm.28483
[3] Yang X, Sun H, Deng M, Chen Y, Li C, Yu P, Zhang R, Liu M, Dai H, Wang C. Characteristics of Diaphragmatic and Chest Wall Motion in People with Normal Pulmonary Function: A Study with Free-Breathing Dynamic MRI. *Journal of Clinical Medicine*. 2022;11(24):7276. https://doi.org/10.3390/jcm11247276

LT90.
On the variations of liver B0 inhomogeneities within the respiratory cycle at 3 T

T. Straßer[1], J. Stelter[2], V. Spieker[3], K. Weiss[4], R. Braren[1], J. Schnabel[3,2], D. Karampinos[1]

[1]*Technical University of Munich, Munich, Germany;*
[2]*Technical University of Munich, School of Computation, Information and Technology, Munich, Germany;*
[3]*Helmholtz Center Munich, Munich, Germany;*
[4]*Philips GmbH Market DACH, Hamburg, Germany*

Introduction Quantitative imaging in the abdomen is challenging due to several types of motion that can lead to artifacts. Respiratory motion is particularly challenging for liver imaging due to its pseudo periodic nature and non-rigid deformations. Self gated acquisitions like Radial stack-of-stars (SoS) acquisitions have been extensively used to reduced motion sensitivity and to enable motion-resolved reconstructions[1,2]. However, besides the gross motion, it has been shown in various anatomies that parameter quantification can also be affected by temporal B0 effects [3,4,5]

The analysis of temporal B0 effects in the liver is in itself challenging due to deformations within the respiratory cycle but has considerable implications on free-breathing acquisitions used for parameter mapping. In this work, we analyze B0 inhomogeneities in the liver at 3 T on realistic numerical simulations and in vivo using a free-breathing SoS acquisition.

Methods *Simulation study.*

Male and female body models[9] were used to simulate B0 inhomogeneities for predefined organ-specific magnetic susceptibility values[7] based on a forward dipole convolution. We defined 10 equidistant motion frames within the breathing cycle.

Volunteer study

Measurements were performed at 3 T (Ingenia Elition, Philips Healthcare) on 8 volunteers using a 2-echo SoS acquisition (Scan parameters here). As a reference, a 4-echo SoS acquisition with similar parameters (Scan parameters here) was acquired in one volunteer.

Motion states were defined based on the principal component analysis (PCA) on the central k-space region[1] which was corrected for eddy currents[6] for retrospective self-navigation. The in-plane resolution was reduced to 3 mm by masking the spokes. Spokes were sorted into motion states and an iterative reconstruction with L1-Wavelet regularization yielded the complex image data (Fig. 1). Water and fat images and the field-map were computed based on a multi-resolution graph cut algorithm[7]. For the 2-echo scan, the algorithm was adapted for the dual echo separation problem[11].

B0 temporal analysis

To analyze the spatial–temporal variation of the field-map at each position in the liver, a region of interest (ROI) of $\sim$ 5 mm $\times$ 10 mm a coronal slice with the highest position of the liver in feet-head (FH) direction. The mean value of each row in FH direction was computed per motion state (in vivo) or motion frame (simulation). The data was shifted to visualize the field-map values at the same spatial location relative to the diaphragm. For the evaluation in all volunteers, the minimum, maximum, and standard deviation along the motion states were plotted.

Results Figure 2 depicts the field-map variations at the upper part of the liver in the anatomical body model and Fig. 3 in a volunteer for scans with 2 and 4 echoes. These figures illustrate that the differences in field-map values between motion states were most prominent near the diaphragm and decreased with increasing distance. For the simulation and the in vivo analysis, there is no visual correlation between the liver displacement in FH-direction notable. In Fig. 4, we can observe the temporal variations of B0 inhomogeneities across different subjects. It is noteworthy that the overall field-map values in the upper part of the liver range between 0 and 300 Hz. The variations were subject-dependent with standard deviations between motion states varying between 10 and 50 Hz.

Discussion and Conclusion Our study provides insight into the variations of B0 inhomogeneities in the liver at 3 T within the respiratory cycle by realistic simulation of respiratory motion in anatomical body models and by analyzing the field-map differences across motion states in free-breathing SoS acquisitions. We observed the largest differences in the field-map between motion states near the lung-liver interface which decreased with increasing distance from the interface. This finding was consistent between simulation and in vivo results, for 2 and 4 echoes and across the subjects. The B0 inhomogeneities were not visually correlated to the liver displacement in FH direction and their variations showed to be subject-dependent.

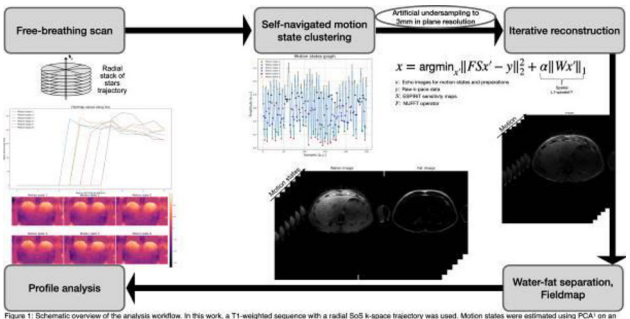

Figure 1: Schematic overview of the analysis workflow. In this work, a T1-weighted sequence with a radial SoS k-space trajectory was used. Motion states were estimated using PCA[1] on an eddy current-corrected[6] autocalibration region. Iterative reconstruction using coil sensitivity maps[8] yielded complex images for each motion state, which were then decomposed into water and fat images and the field-map using a dual echo multi-resolution graph cut algorithm. The resulting fieldmaps values along a line across the lung-liver interface were then analyzed. Note that respiratory motion causes a shift in the fieldmap values in the FH direction. During inhalation, the liver moves downwards, shifting the values towards the foot direction, and during exhalation, the liver moves upwards, shifting the values towards the head direction.

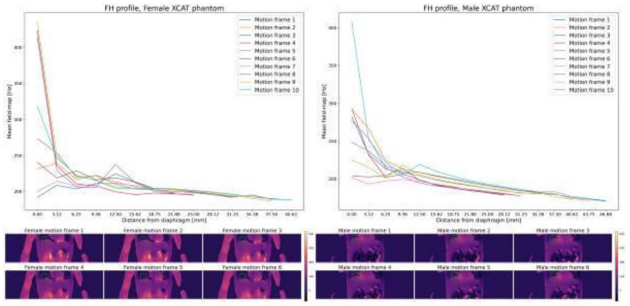

Figure 2: Mean row values of liver field-map in the FH direction for the XCAT phantom[9] in the ROI for 10 different motion frames. The field-map values near the diaphragm show the greatest variation across individual motion states, while the values decrease at a comparable rate across all motion states with increasing distance. Consequently, the differences between motion states become smaller with distance from the diaphragm.

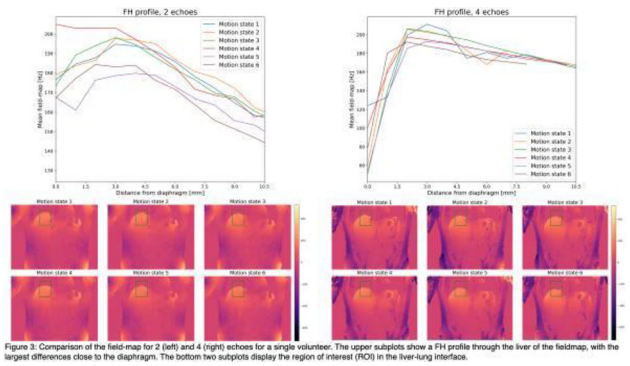

Figure 3: Comparison of the field-map for 2 (left) and 4 (right) echoes for a single volunteer. The upper subplots show a FH profile through the liver of the fieldmap, with the largest differences close to the diaphragm. The bottom two subplots display the region of interest (ROI) in the liver-lung interface.

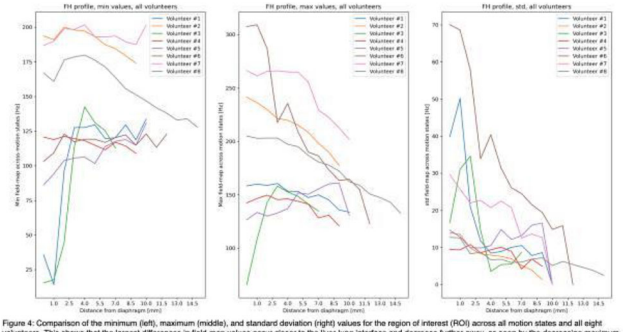

Figure 4: Comparison of the minimum (left), maximum (middle), and standard deviation (right) values for the region of interest (ROI) across all motion states and all eight volunteers. This shows that the largest differences in field-map values occur closer to the liver-lung interface and decrease further away, as seen by the decreasing maximum values and slightly increasing minimum values.

References
1: Feng,MRM,2015
2: WangMRM,2022
3: Baboli,MRM,2021
4: Vannesjo,NI,2018
5: Wu,ISMRM,2021
6: Rosenzweig,IEEETMI,2020
7: Stelter,IEEETMI,2022
8: Ücker,MRM,2013
9: Segars,MedPhys,2010
10: Collins,JMRI,2002
11: Eggers,MRM,2010

P91.
A non-uniform distribution of dielectric and conducting strips in a metamaterial-based structure at 7 T MRI

S. Maurya[1], R. Schmidt[1]

[1]*Weizmann Institute of Science, Brain Sciences, Rehovot, Israel*

Introduction In a recent study the RF field coverage of a dipole-antenna at 10.5 T was increased using a non-uniform dielectric design1. We pick up on this work to examine the benefits of the non-uniform distributions and implement it in metamaterial-based structures for 7 T MRI. Here we examined a metamaterial-based structure that is based on a dielectric layer and set of copper strips2–4. Such structure was shown to provide useful for MRI resonant modes such as the electromagnetic (EM) TE01 mode which offers a local increase in the B1 field. In this work we examined two new options—a non-uniform distribution of the dielectric layer and a non-uniform distribution of the conducting strips. The study included EM simulations with setups including phantom and human model and phantom experiments at a 7 T MRI.

Methods EM simulations (including eigen-mode solver and full setup simulations) were performed to compare the uniform and non-uniform distribution. The characterization of the resonant modes was performed with an eigen-mode solver in which the frequency of the deepest transverse electric mode was adjusted to 298 MHz. In full simulations, all B1 maps were normalized to an accepted power of 1 Watt. The full simulation setup included a 16-rung high-pass quadrature birdcage coil (inner diameter 30 cm; rung length 18 cm). The simulated phantom electrical properties were εr = 53 and conductivity (σ) = 0.3 S/m.

Three structures consisting of a dielectric layer and copper strips having three distributions were examined. The total dimensions for all three were kept the same—16 × 11 × 0.7 cm3 (length, width and thickness, respectively). The configurations of the three designs are:

1. i) A *Uniform* dielectric with *uniformly* spaced copper lines (”UD-UL“), using a dielectric layer with relative permittivity (εr) = 72 and six copper strips equidistantly spaced, 20 mm apart.
2. ii) A *Non-uniform* dielectric with *uniformly* spaced copper lines (”NUD-UL“) made up of three dielectric sections, a central one 10 mm wide with εr = 60 and two, 20 mm wide with εr = 252, at each edge. The six copper strips were equidistantly spaced 20 mm apart.

- iii) A *Non-uniform* dielectric with *non-uniformly* spaced copper lines (”NUD-NUL“) made up of three dielectric sections, a central one 10 mm wide with εr = 52 and two, 20 mm wide with εr = 252, at each edge. The six copper strips were spaced 10, 20, 40, 20 and 10 mm apart (see Fig. 1).

The εr = 252 dielectric layer was prepared with a BaTiO3–water suspension and the εr = 52 layer consisted of a sucrose-water suspension. In the simulations with human model the metamaterial-based structure was curved to best fit the shape of the head.

Phantom scanning: The metamaterial-based structures were added on top of the phantom and scanned in a 7 T MRI (Terra, Siemens, Erlangen). Scans with the vendor B1 map sequence were collected with FOV of 20 × 20 cm2 and spatial resolution of 2.5 × 2.5 × 3.5 mm3.

Results Figure 1 shows the |H| and |E| fields of the resonant mode (simulated by the eigen-mode solver) at 20 mm and 5 mm from the structures, respectively. Figure 2 shows the EM simulations with the phantom and the three metamaterial-based structures. FWHM distance (width measured at two points at half maximum), calculated at 10 mm inside the phantom (in parallel to the structure) is ∼ 80 mm for ”UD-UL“ and 110 mm for ”NUD-NUL“. The ”NUD-NUL“ has a similar FWHM to ”NUD-UL“ but has an overall more homogeneous distribution. Figure 3 demonstrates measured B maps in the phantom, demonstrating a larger coverage with the ”NUD-NUL“ structure in the Z and Y directions (in parallel to the structure and deeper into the phantom, respectively). Figure 4 shows the simulations of a full setup including human brain with the metamaterial-based structures. The B1 maps show that ”NUD-NUL“ provides increased B1 field coverage in both axial and sagittal planes. The maximal SAR value for the non-uniform dielectric setups is higher compared to the uniform one, but the non-uniform copper strips help to reduce the SAR.

Conclusions. This study has demonstrated a novel design of a metamaterial-based structure with non-uniform distribution of both the dielectric and the conducting strips. The non-uniform dielectric increased the effective electric dipoles, thus prolonging the RF field coverage in the direction of the dipoles. The non-uniform copper strips arrangement was useful to tailor the RF field distribution, which resulted in more homogeneous B1 distribution and lower SAR. The new design also provides a more compact and flexible setup which can easily be placed in a patient setup.

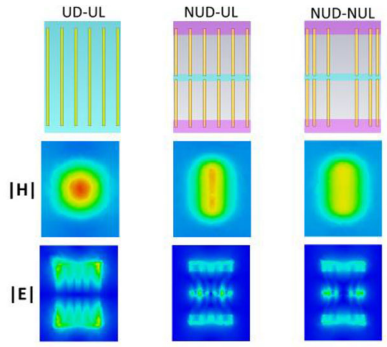

Fig. 1: H- and E-fields distribution of the designed resonant mode. Top - Schematic setup with uniform distribution – "UD-UL", non-uniform dielectric only – "NUD-UL" and non-uniform distribution of both the dielectric and the conducting lines "NUD-NUL". Maps of |H|-field are at 20 mm from the structure and |E|-field are at 5 mm from it.

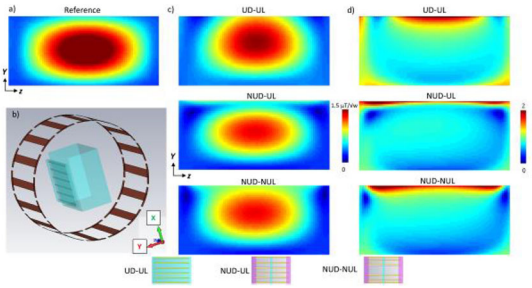

Fig. 2: EM simulations with phantom. a) Reference B1 map. b) Schematic setup, c) and d) B1 and B1with-structure/B1reference maps for all 3 structures .

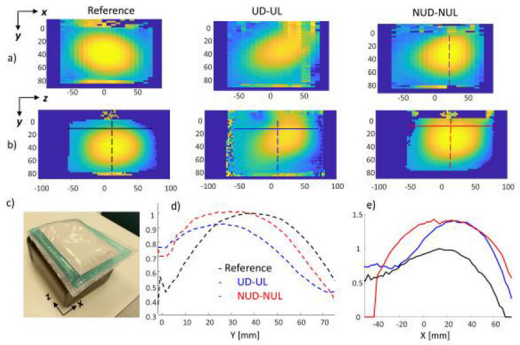

Fig. 3: Measured B1 maps in a phantom setup. a) and b) B1 maps in YX and YZ planes for three setups. c) photo of the setup. d) and e) compares B1 1D plots in perpendicular (dashed) and in parallel (solid) to the structure. The maps are with the same color-bar. The plots are normalized to the maximum of the reference B1.

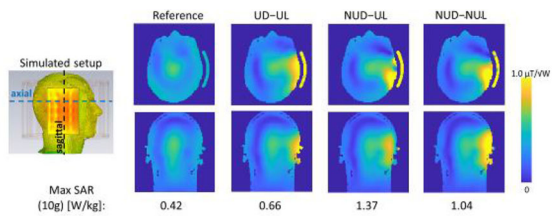

Fig. 4: Simulated B1 field with human model. The maximal SAR value for each case is added at the bottom.

References

[1] Alireza S.T. et al. Magn.Reson.Med. 2021; 87: 2074–2088.
[2] Slobozhanyuk, A. P., et al. Adv. Mater. 2016; https://doi.org/10.1002/adma.201504270,
[3] Schmidt R. et.al. Sci. Rep., 2017, 7,
[4] Schmidt R., & Webb A. ACS Appl. Mater. Interfaces, 2017, 9(40), 34618–34624.

P92.
Demonstration of the metasurface-based pad impact on fetal MRI

V. Koloskov[1], V. Puchnin[1], E. Koreshin[1], A. Kalugina[1], I. Mashchenko[2], W. Brink[3], A. Shchelokova[1]

[1]*ITMO University, School of Physics and Engineering, Saint Petersburg, Russian Federation;*
[2]*Federal Almazov North-West Medical Research Center, Department of Radiology, Saint Petersburg, Russian Federation;*
[3]*University of Twente, Magnetic Detection & Imaging Group, TechMed Centre, Enschede, The Netherlands*

Introduction Ultra-high field (i.e., 3 T) MRI offers higher spatial resolution and a more precise depiction of the fetus with less scan time than 1.5 T scanners[1]. However, the higher magnetic field strength can cause the radiofrequency (RF) wavelength to become comparable to the size of the body. This can lead to constructive and destructive interference of standing waves, resulting in bright or dark areas. This issue is particularly prevalent in women with high body mass index or in the last months of pregnancy. The concept of passive shimming with dielectric pads made of mixed ceramic powders and heavy water was introduced to increase the RF magnetic field in regions with low signal intensity[2–4]. However, these pads are bulky and can weigh up to 4–5 kg, significantly reducing patient comfort. Recently, the concept of using ultralight and compact metasurface (MS) was proposed to improve abdominal[5] and fetal[6] imaging at 3 T. In this study, we investigate the effectiveness of the MS-based pads for realistic pregnant models at different stages of gestation, both numerically and experimentally, with volunteers.

Methods All numerical simulations were performed in CST Studio Suite 2021. Two voxel models (Sim4Life family), representing gestation periods of 7 and 9 months (Fig. 1), were utilized. The RF magnetic field (B_1^+) distribution was carried out using a whole-body high-pass birdcage coil (BC) tuned to 123 MHz. The cases without (reference case) and with the MS were compared for both voxel models. The proposed MS comprised 15 × 15-unit cells of the metal crosses printed on a 25 μm-thick dielectric substrate connected via capacitors of 30 pF with total dimensions of 30 × 30 cm^2. The MS was centered on the fetus for all cases. To quantify the impact of the proposed structure, we calculated the root mean squared (RMS) value of the $|B_1^+|$ amplitude and its coefficient of variation (C_v) as the ratio of its standard deviation mean value and multiplied by 100% in the region-of-interest (ROI). The B_1^+ and $SAR_{av.10\ g}$ distributions were normalized to 1 W of the total accepted power. The experimental studies were performed on a clinical Siemens Magnetom Trio A Tim 3.0 T scanner using the whole-body BC in transmit mode and Siemens 6-channel body flex coil in receive mode. MR images were acquired for two healthy volunteers (29–30 and 38–39 weeks of gestation period) with approval from the local ethic committee of Federal Almazov North-West Medical Research Center (Saint Petersburg, Russia). T_2-weighted images were acquired using spin echo sequence: TR/TE = 1500/97 ms, FA = 150°, matrix = 256 × 256, field-of-view = 380 × 380 mm^2, slice thickness = 5 mm.

Results Figure 2 shows simulated B1+ maps for the voxel model at the 7th and 9th month of gestation for two cases: (1) reference one and (2) with the MS placed on the top of the abdomen close to the fetus. Adding the MS improves the $|B_1^+|_{RMS}$-field amplitude in the ROI by 1.3-fold for a 7-month-old fetus, while for the 9-month-old model, this value was improved only by 2%. Also, a decrease in C_v by 2.4% for a 7-month-old fetus was found compared with the reference case. However, no improvement in C_v for a 9-month-old fetus was present because the MS in simulations was difficult to shape anatomically near the fetus, keeping the correct structure meshing. At the same time, adding the MS does not significantly increase local SAR in ROI (Fig. 3). Maximum SAR was located in the right arm and was less than 0.28 W/kg for all three cases.

Experimentally obtained T_2-weighted images of two volunteers in the axial and sagittal planes are shown in Fig. 4. For the reference cases, one can observe dark regions (shown by white dashed lines), which can be effectively eliminated by adding the MS (located tight to the ROI), improving the diagnostic capabilities of MR images.

Discussion and conclusion The proposed MS-based pad has been optimized to improve the quality of fetal MRI at 3 T. Numerical simulation results have shown that MS can improve the B_1^+-field distribution homogeneity and RF safety in pregnant women at the 7th and 9th months of gestation. Experimental studies showed improved quality of the fetus and extra-fetal structures imaging for standard clinical protocol, with higher contrast in areas where dielectric artifacts were present. Thus, it is possible to replace conventional dielectric (ceramic) pads with ultralight and flexible MSs, improving patient comfort and MR diagnostic capabilities of the fetus at different stages of pregnancy.

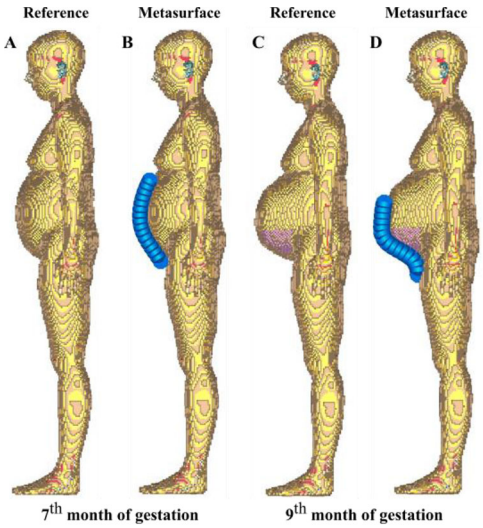

Fig. 1: Schematic representation of numerical setups for voxel models without (A,C) and with metasurface (B,D) at 7th and 9th months of gestation, respectively.

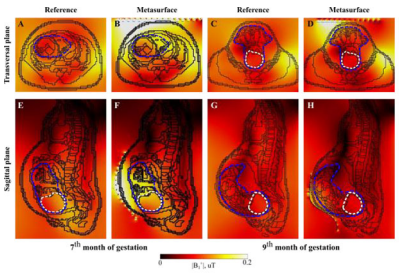

Fig. 2: Numerically calculated B_1^+ maps for 1 W of total accepted power for voxel models of pregnant women at 7th and 9th months of gestation without (A,C) and with (B,D) MS, respectively, for the transversal plane, and (E,G) and with (F,H) MS, respectively, for the sagittal plane. White dashed line – fetus brain, blue dashed line – fetus.

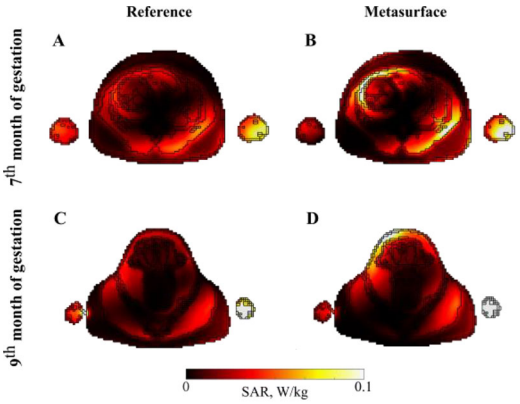

Fig. 3: Numerically calculated $SAR_{av.10g}$ maps for 1 W of total accepted power for voxel models of pregnant women at 7th and 9th months of gestation without (A,C) and with (B,D) MS, respectively.

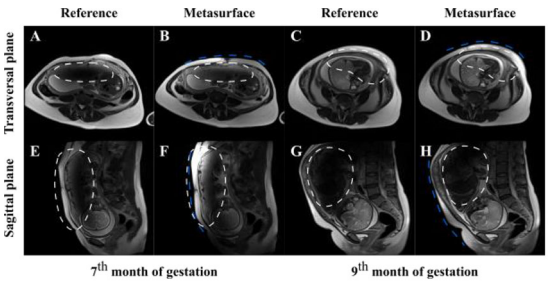

Fig. 4: T_2-weighted MR images of pregnant women at 7th and 9th months of gestation without (A,C) and with (B,D) MS, respectively, for the transversal plane, and (E,G) and with (F,H) MS, respectively, for the sagittal plane. Blue dashed line – MS.

References

1. Weisstanner C et al. The British Journal of Rad. 2016; 90:1069.
2. Collins CM et al. JMRI 2005; 21: 192–6.
3. De Heer et al. MRM 2012; 68(4): 1317–1324.
4. van Gemert et al. MRM 2019; 82(5): 1822–1831.
5. Vorobyev V et al. MRM 2022; 87(1): 496–508.
6. Puchnin V et al. Proc. ISMRM 2022.

Acknowledgment.

This work was supported by the Ministry of Science and Higher Education of the Russian Federation (Project No. 075-15-2021-592).

P93.
Metasurface of capacitively loaded rings for SNR improvement of MRI coils

M. Freire[1], R. Marques[1], J. Tornero[2]

[1]*Universidad de Sevilla, Electronics and Electromagnetism, Seville, Spain;*
[2]*Center for Clinical Neuroscience. Hospital Los Madroños, Madrid, Spain.*

Introduction Metamaterials consist of periodic arrays of subwavelength-sized resonant elements that exhibit exotic electromagnetic properties. The main drawback of metamaterials to find applications is their inherent narrowband response but this does not pose a problem in MRI. Metamaterial slabs with negative permeability consisting of three-dimensional arrays of capacitively loaded rings (CLR) have been investigated to locally increase the SNR and improve the g factor of surface coils in parallel imaging [1]-[3]. A metasurface (MS) that behaves as a surface impedance and consists of a two-dimensional (2D) array of CLR is more flexible and easy to fabricate than bulk metamaterials, and has also been investigated to improve the SNR of surface coils [4]. The CLR of the MS are detuned to behave capacitively at the operating frequency, so that the field produced by the CLR adds to the field produced by the coil [4]. However, the CLR of the MS also introduces additional noise in the coil [4]. The CLR of the array are inductively coupled between them and therefore the array supports the waves due to voltages induced by time-varying magnetic fields or magnetoinductive (MI) waves [5]. Standing MI waves introduce resonances in the frequency dependence of the coil input resistance and the MS can improve the SNR at the frequency corresponding to a local minimum existing between these resonances [4].

Methods In the present work, an MS consisting of an array of 4 × 4 CLR has been designed to enhance the SNR of a squared coil 12 cm in length and 1 cm in strip width at the typical operation frequency of 63.6 MHz corresponding to a 1.5 T system. The noise resistance introduced in the coil by the MS can be minimized by increasing the mutual inductive coupling between the CLR [4]. In this work, this is achieved by using squared CLR and by minimizing the distance between neighboring CLR. The analysis was carried out with Simulia CST. Figure 1 shows different screenshots (perspective top and side views) of the two configurations under analysis: a squared coil 12 cm in length placed at 6 mm from a cubic phantom (Fig. 1 top row) and the same coil loaded with a MS placed at 6 mm from the coil and the cubic phantom placed at 6 mm from the MS (Fig. 1 bottom row). The 12-cm squared coil is split and 154 pF are inserted in three gaps to homogenize the current. The conductivity of the cubic phantom is 0.7 S/m. The squared CLR have 24 mm of external length, strip width 2 mm, and periodicity 25 mm. Each CLR is loaded with a capacitor of 170 pF and an ESR of 0.03 Ohms. In the simulations the coil was matched to 50 Ohms both in the presence and in the absence of the MS through suitable matching networks, with return loss − 30 dB and − 20 dB, respectively.

Results Figure 1 shows 2D maps for the B1- receive field pattern in an axial plane with a proper scale to enhance the differences between the presence and the absence of the MS. Figure 2 shows the input resistance vs. frequency obtained in the coil loaded with the MS and the cubic phantom. At an operating frequency of 63.6 MHz the input resistance is minimum. The curve in Fig. 2 shows peaks or resonances corresponding to the excitation of standing MI waves. These peaks are far from each other due to the strong mutual coupling between the CLR and this significantly reduces the resistance at the central frequency between the peaks [4].

Discussion The comparison of the 2D maps shown in Fig. 1 shows that the MS can provide an enhancement of the SNR. The data from these maps are used to obtain the plots shown in Fig. 3 for the normalized SNR along the coil axis inside the cubic phantom in the presence and in the absence of the MS. The results in Fig. 3 make clear that the MS enhances the SNR up to 5 cm inside the phantom.

Conclusion It has been shown that MS of strongly coupled CLR can locally enhance the SNR of surface coils.

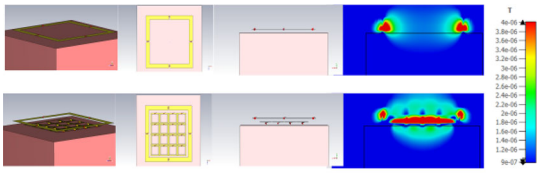

Fig. 1: screenshots (perspective top and side views) of the two configurations under analysis: a squared coil 12 cm in length placed at 6 mm from a cubic phantom (Fig. 1 top row) and the same coil loaded with a MS placed at 6 mm from the coil and the cubic phantom placed at 6 mm from the MS (Fig. 1 bottom row).

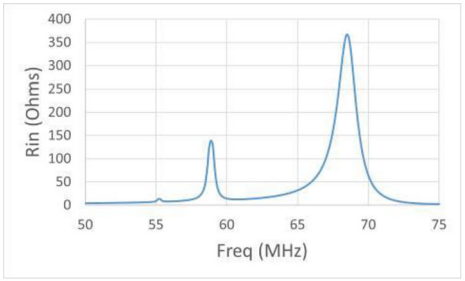

Fig. 2: Input resistance vs. frequency obtained with CST for the coil loaded with the MS and the cubic phantom

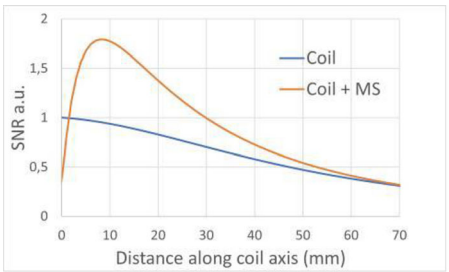

Fig. 3: Normalized SNR along the coil axis inside the cubic phantom in the presence and in the absence of the MS.

References

[1] M. Freire, L. Jelinek, R. Marques, M. Lapine, On the applications of ? = − 1 metamaterial lenses for magnetic resonance imaging, Journal of Magnetic Resonance 203 (2010). https://doi.org/10.1016/j.jmr.2009.12.005

[2] J. Algarín, M. Freire, F. Breuer, V. Behr, Metamaterial magnetoinductive lens performance as a function of field strength, Journal of Magnetic Resonance 247 (2014). https://doi.org/10.1016/j.jmr.2014.08.006

[3] J. Algarin, F. Breuer, V. Behr, M. Freire, Analysis of the noise correlation in MRI coil arrays loaded with metamaterial magnetoinductive lenses, IEEE Transactions on Medical Imaging 34 (2015). https://doi.org/10.1109/TMI.2014.2377792

[4] M. J. Freire, Metasurfaces of capacitively loaded metallic rings for magnetic resonance imaging surface coils, Scientific Reports, vol. 13, 2998 (2023), https://doi.org/10.1038/s41598-023-30185-y

[5] Shamonina, E., Kalinin, V. A., Ringhofer, K. H. & Solymar, L. Magnetoinductive waves in one, two, three dimensions. J. Appl. Phys. 92, 6252–6261. https://doi.org/10.1063/1.1510945 (2002)

P94.
Effect of flip angle in traveling-wave MRI experiments using metamaterials at 7 T

S. Solis-Najera[1], J. Lazovic[2], F. Vazquez[1], A. O. Rodriguez[3]

[1]*Universidad Nacional Autonoma de Mexico, Departamento de Fisica, FC, Mexico City, Mexico;*
[2]*Max Planck Institute for Intelligent Systems, Department of Physical Intelligence, Stuttgart, Germany;*
[3]*Universidad Autonoma Metropolitana Iztapalapa, Department of Electrical Engineering, Mexico City, Mexico*

Introduction The travelling-wave MRI (twMRI) approach offers the advantage of acquiring images with larger field-of-view at ultra high magnetic field MRI. The use of a parallel-plate waveguide (PPWG) together with a surface coil in the twMRI approach can generate a uniform traveling wave that propagates through the sample being imaged, providing more uniform excitation but lower signal-to-noise ratio (SNR) values [1–2]. The use of a metasurface can potentially improve image quality and enable larger field-of-view imaging [3]. We investigated the effect in the image acquired with the twMRI approach using a PPWG together with a metasurface and a bio-inspired surface coil for transmission and reception of the RF signals.

Method The RF signal was both transmitted and received using a bio-inspired surface coil, as seen in Fig. 1a. This coil was made by laminating copper sheets onto a nonconductive board and then soldering tuning and matching capacitors directly onto the surface. Two parallel ceramic capacitors were placed as shown in Fig. 1a, and the coil was tuned and matched to 50 Ω and 300 MHz, respectively. A flexible metasurface was then constructed using hydrocarbon ceramic laminates (RO4003C3: $?$ = 3.55 and tan($?$) = 0.0027, thickness = 0.508 mm, 65 mm long and 55 mm wide), with a 4 × 4 C-shape unit metasurface formed on top, as shown in Fig. 1b. The C-shapes had a diameter of 23 mm and a gap of 2 mm, and the resonant frequency of the cell was calculated according to [4]. To evaluate the performance of the metasurface, phantom images were acquired using a cylindrical phantom filled with saline solution and with the metasurface inserted into it, as shown in Fig. 1c. The bio-inspired surface coil was located outside the waveguide and parallel to the plates. Figure 2 shows the experimental setup. Phantom images were acquired using a standard gradient echo sequence with acquisition parameters of TE/TR = 4.39 ms/200 ms, FOV = 40 mm × 40 mm, matrix size = 256 × 256, Flip angle = 45^0 and 90^0, slice thickness = 2 mm, and NEX = 1. Images were acquired with and without the metasurface, as well as with a quadrature birdcage coil (4 cm diameter, 64 cm long, and 4 rungs) for comparison purposes. All MRI experiments were conducted on a 7 T/30 cm Bruker imager (Bruker, BioSpin MRI, GmbH, Germany).

Results and Discussion The experimental gap capacitance was 6.45 pH, and the resonant frequency of the cell was theoretically calculated to be 302.29 MHz, while the resonant frequency of the C-shaped unit was experimentally computed to be 297 MHz using the method reported in [4]. The phantom images obtained using the metasurface and twMRI with flip angles of 45° and 90° were shown in Fig. 3c). The SNR values and uniformity profiles were computed and presented in Fig. 3a). The SNR values for the metasurface were $SNR_{metasurface}(45°)$ = 22.60 and $SNR_{metasurface}(90°)$ = 25.22, while the SNR value for the birdcage coil was SNR_{BC} = 32.42. Although the profile obtained with the birdcage coil had greater intensity values, the profile obtained with the twMRI and metasurface showed reasonably uniformity with lower values. The slight difference in values between the profiles obtained with the two flip angles for twMRI suggested that slice-selection gradients, off-resonance excitations, and B_0 field inhomogeneities did not significantly affect the image quality. These results confirmed previous findings obtained at 4.7 T [2] and 15.2 T [1] and demonstrated the feasibility of this approach for obtaining high-quality phantom images at HF MRI without the need for electronic components to tune the metasurface at the resonant frequency of the MR imager.

Conclusions. The experimental results demonstrate that the use of a travelling-wave approach with a flexible metasurface can produce high-quality images with good SNR for different flip angles. However, further studies are required to explore other approaches that may potentially improve the overall performance of the system.

Acknowledgments. The authors would like to thank the UAM Division of Basic Science and Engineering for funding this project under the Special Program for Education and Research (DCBI-190-2022).

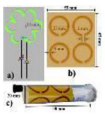

Fig. 1: a) Schematic of the bio-inspired surface coil showing some dimensions. b) C-shaped-unit metasurface showing configuration and dimensions. d) Phantom with metasurface inserted in the cylindrical phantom.

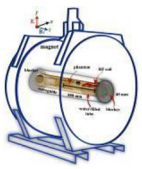

Fig. 2: This is the experimental setup used for the acquisition of MR images, including the dimensions of the cylindrical phantom with the metasurface inside and the bio-inspired surface coil.

Fig. 3: a) Phantom images acquired using a transceiver bio-inspired surface coil, both with and without the metasurface. c) Comparison of uniformity profiles taken along the green line in (b).

References

1. Vazquez, F., Solis-Najera, S. E., Lazovic, J., Zopf, L. M., Martin, R., Medina, L., Marrufo, O., Rodriguez, A. O. (2021). Remote RF excitation for small-bore MR imager at 15.2 T. *J. Magn. Reson. 323*, 106896

2. Vazquez, F., Marrufo, O., Martin, R., Solis, S., & Rodriguez, A. O. (2016). Travelling-wave transmitted with a simple waveguide for rodents Magnetic Resonance Imaging at 9.4 T. *33rd Ann. Meet. ESMRMB*, *32*, S31-S32

3. Wiltshire, M. C. K. (2007). Radio frequency (RF) metamaterials. *Phys. Stat. Sol. (b)*, *244*(4), 1227–1236. https://doi.org/10.1002/pssb.200674511

4. Solis-Najera, S. E., Lazovic, J., Vazquez, F., Rodriguez, A. O. Remote detection MRI using a flexible non-selective metamaterial at 7 T. Abstract # 4798, ISMRM, 2023

P95.
Metamaterial position determination for B1 improvement of a birdcage coil at 7 T

S. Solis-Najera[1], J. Lazovic[2], R. Ruiz[1], F. Vazquez[1], A. O. Rodriguez[3]

[1]*Universidad Nacional Autonoma de Mexico, Departamento de Fisica, FC, Mexico City, Mexico;*
[2]*Max Planck Institute for Intelligent Systems, Department of Physical Intelligence, Stuttgart, Germany;*
[3]*Universidad Autonoma Metropolitana Iztapalapa, Department of Electrical Engineering, Mexico City, Mexico*

Introduction The introduction of metamaterials has shown great potential in improving B_1 for different types of RF coils in MRI [1]. Previously, we have studied the theoretical performance of a metasurface [2] and the signal-to-noise (SNR) improvement using a dielectric material [3]. Kretov et al. have experimentally demonstrated the use of metamaterials to increase the SNR as a function of their position [4]. These results have motivated us to experimentally investigate the role of a flexible metasurface's position in the birdcage coil B_1 at 7 Tesla using a preclinical MR imager.

Method To obtain a low specific absorption rate (SAR) and avoid field homogeneity problems, a high-pass birdcage coil with a diameter/length ratio of 4 cm/6.4 cm (0.625) was constructed, quadrature driven, operated in transceiver mode, and tuned to 300 MHz [5]. Figure 1a displays a photograph of the coil prototype. The metasurface was created using flexible hydrocarbon ceramic laminates (RO4003C3: ? = 3.55 and tan(?) = 0.0027, thickness = 0.508 mm) and was formed by an array of 4 × 6 C-shape units (Fig. 1b), based on the cylinder of split-ring resonators reported by Vakili et al. [6]. For the imaging experiments, phantom images were acquired using a cylindrical phantom (30 mm diameter and 110 mm length) filled with saline solution and wrapped with the flexible metasurface as shown in Fig. 1c). The phantom and the metasurface were then inserted into the birdcage coil as shown in Fig. 1a), with the phantom placed in two different positions, see Fig. 1c). A standard gradient echo sequence was used to acquire the phantom images, with TE/TR = 4.39/200 ms, FOV = 40mmx40mm, matrix size = 256 × 256, flip angle = 45°, slice thickness = 2 mm, and NEX = 1. Phantom images without the metasurface were also acquired for comparison purposes. All MRI experiments were conducted on a 7 T/30 cm Bruker imager (Bruker, BioSpin MRI, GmbH, Germany).

Results and Discussion The resonant frequency of the C-shaped unit cell was experimentally determined to be 307.5 MHz based on the S_{11}-parameter measurement. The axial plane of a cylindrical phantom filled with saline solution and wrapped with the flexible metasurface was imaged using the high-pass birdcage coil prototype, with the phantom in two different positions as shown in Fig. 1c). The acquired phantom images (Fig. 2a-c)) exhibited good B1 uniformity in the axial plane, as evidenced by the corresponding uniformity profiles (Fig. 2d). The image SNR values were 85.5, 98.4, and 102.2 for the no metasurface and two metasurface positions, respectively. The gray profile showed an improvement in both B1 and SNR compared to the other two profiles. While the blue and green profiles showed nearly identical B_1 values, their SNR values were different. Notably, no passive components or dielectric materials were used for tuning or matching, and the position of the metasurface was found to be crucial in improving the birdcage coil performance, consistent with findings reported in [6]. These results demonstrate the potential of flexible metasurfaces to enhance B_1 and SNR in birdcage coils without additional tuning or matching components.

Conclusions. Our research project has yielded important findings regarding the use of metasurfaces to enhance the performance of birdcage coils in MRI applications. Our experimental results indicate that the positioning of the flexible metasurface is a crucial factor in improving the B_1 field of the birdcage coil. By strategically placing the metasurface in the right position, we were able to achieve significant improvements in the B_1 field and SNR. These results suggest that our approach provides a simple and easy-to-implement alternative for improving the B_1 field in preclinical HF MRI applications. We believe that our findings have the potential to pave the way for further research and development in the field of metamaterials and their applications in MRI.

Acknowledgments. This project was funded by the UAM Division of Basic Science and Engineering under the Special Program for Education and Research (DCBI-190–2022).

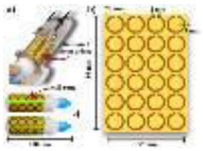

Fig. 1: a) The experimental setup consisted of the birdcage coil, the metasurface, and the phantom for the imaging experiments. b) The metasurface prototype was composed of an array of C-shaped unit cells and had specific dimensions and unit cell distribution. c) The cylindrical phantom was covered with the metasurface and was positioned in two different locations to investigate the behavior of the B_1 field.

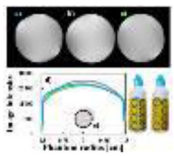

Fig. 2: Phantom images were taken with and without the metasurface in two different positions, as well as without the metasurface. The resulting images are shown in (a)-(c), with a comparison uniformity plot displayed in (d) and profiles taken along the red line in (e).

References

1. M. C. K, Wiltshire. Phys. Stat. Sol. (b), 244, 2007. https://doi.org/10.1002/pssb.200674511.
2. F. Vazquez, et al. 34th ESMRMB. Abs. No. 291, pp. S276, 2017.
3. F. Vazquez, et al. 28th ESMRMB. Abs. No. 591, p. 145, 2011.
4. E. I. Kretov, et al. App. Phys. Let. 112, 033501, 2018. https://doi.org/10.1063/1.5013319.
5. R. Martin, et al. Measurement, 82, 482, 2016. https://doi.org/10.1016/j.measurement.2016.01.013.
6. I. Vakili, et al. IEEE Trans. Micro. Theo. Tech. 62, 2574, 2016. https://doi.org/10.1109/TMTT.2014.2354592.

P96.
Two metamaterial configurations for preclinical MRI at 7 T

S. Solis-Najera[1], J. Lazovic[2], A. O. Rodriguez[3], R. Ruiz[1], F. Vazquez[1]

[1]*Universidad Nacional Autonoma de Mexico, Departamento de Fisica, FC, Mexico City, Mexico;*
[2]*Max Planck Institute for Intelligent Systems, Department of Physical Intelligence, Stuttgart, Germany;*
[3]*Universidad Autonoma Metropolitana Iztapalapa, Department of Electrical Engineering, Mexico City, Mexico*

Introduction. Metamaterials have shown promising potential for significantly improving B_1 in different types of RF coils for MRI [1]. These specialized structures typically take the form of an array of resonant elements that can be placed near the imaged region to

enhance B_1 and improve image quality. Previous studies have explored the theoretical performance of metasurfaces [2] and the signal-to-noise (SNR) improvement achieved using a dielectric material [3]. Kretov et al. have experimentally demonstrated the efficacy of metamaterials in increasing SNR as a function of their position [4]. We aimed to experimentally investigate the use of a flexible metasurface with two different configurations, one placed inside and the other outside a solution-filled phantom. Our goal was to evaluate the potential of the metasurface to enhance image quality and SNR.

Method. To address field homogeneity issues and reduce specific absorption rate (SAR), we constructed a quadrature high-pass birdcage coil (4 rungs and diameter/length = 4/6.4 cm). Operating in transceiver mode and tuned to 300 MHz, the coil was designed to be low-SAR and high-performance [5]. We then fabricated two metasurfaces using flexible hydrocarbon ceramic laminates (RO4003C3: $?$ = 3.55 and tan($?$) = 0.0027, thickness = 0.508 mm). The first metasurface comprised an array of 6 × 4 C-shaped cells, while the second one had an array of 2 × 2 C-shaped cells (Fig. 1b, c) [6]. We conducted phantom imaging experiments using a cylindrical phantom (30 mm diameter and 110 mm length) and a syringe (20 mm diameter and 90 mm length), both filled with a saline solution. The first flexible metasurface was wrapped around the phantom (Fig. 1e), while the second one was inserted inside the phantom (Fig. 1d). To acquire the phantom images, we used a standard gradient echo sequence with the following parameters: TE/TR = 4.39 ms/200 ms, FOV = 40 × 40mm^2, matrix size = 256 × 256, flip angle = 45°, slice thickness = 2 mm, NEX = 1. To compare the results, we also acquired phantom images without the metasurfaces. All MRI experiments were conducted on a 7 T/30 cm Bruker imager (Bruker, BioSpin MRI, GmbH, Germany).

Results and Discussion We experimentally determined the resonant frequency of the C-shaped unit cell to be 307.5 MHz (6 × 4 array) and 325 MHz (2 × 2 array) based on the S_{11}-parameter measurement. We used our birdcage prototype with a cylindrical saline-filled phantom and the two different metasurface configurations to acquire axial images, as shown in Fig. 2b)-d). Uniformity profiles were calculated, revealing good B1 uniformity in the axial plane (Fig. 2a). The 6 × 4 array configuration demonstrated a significant improvement in intensity compared to the 2 × 2 array and the profile without the metasurface. The image SNR values were as follows: birdcage coil = 85.5, 6 × 4 array = 98.4, and 2 × 2 array = 26.43. These results indicate that the number of units in an array is a crucial factor in improving coil sensitivity, with greater numbers yielding better improvements. Additionally, the location of the metasurface in the phantom was found to be optimal when covering the phantom from the outside. Encouragingly, no passive components or dielectric materials were used for tuning and matching the cells in the arrays. Our results are in agreement with the findings reported in [6], highlighting the importance of metasurface positioning for improving birdcage coil performance.

Conclusions The use of metamaterials offers a promising solution for improving the B_1 field in preclinical MRI applications. The experimental results presented in this study demonstrate the potential of using flexible metasurfaces with C-shaped unit cells to improve image quality. The results show that the number of units in the array plays a crucial role in improving coil sensitivity, with the 6 × 4 array offering the best improvement in B_1 field and SNR. Moreover, the location of the metasurface also affects its performance, with the best results obtained when the metasurface is covering the phantom from the outside. Importantly, this study shows that no passive components or dielectric materials were used for tuning and matching the cells in the arrays. This easy-to-implement approach offers an alternative to improve B_1 field homogeneity and SNR in preclinical applications at high field.

Acknowledgments This project was funded by UAM Division of Basic Science and Engineering under the Special Program for Education and Research (DCBI-190-2022).

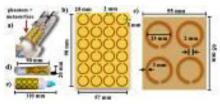

Fig.1: a) The experimental setup included a birdcage coil, a metasurface, and a phantom. The metasurface prototypes were shown in photographs (b) and (c), which showed the distribution of the unit cells and their dimensions. The metasurface was inserted into the cylindrical phantom (d) and also externally covered the phantom (e).

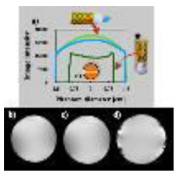

Fig. 2: The image in (a) compares the uniformity of the three different phantom images, shown in (b), (c), and (d). The profiles were taken along the white line in (e). The image in (b) was obtained using only the birdcage coil, while the images in (c) and (d) were obtained using the external 6x4 metasurface and the 2x2 metasurface inserted in the phantom, respectively.

References

1. Wiltshire, Phys. Stat. Sol. (b), 244, 2007. https://doi.org/10.1002/pssb.200674511
2. Vazquez, et al. 34th ESMRMB. Abs. No. 291, pp. S276-S277. 2017
3. Vazquez, et al. 34th ESMRMB. Abs. No. 291, pp. S276, 2017
4. Kretov, et al. App. Phys. Let. 112, 033501, 2018. https://doi.org/10.1063/1.5013319
5. Martin, et al. Measurement, 82, 482, 2016. http://dx.doi.org/10.1016/j.measurement.2016.01.013
6. Vakili, et al. IEEE Trans. Micro. Theo. Tech. 62, 2574, 2016. https://doi.org/10.1109/TMTT.2014.2354592

P97.
A 16-channel Sodium/Proton transmit/receive array design for 7 T MRI head imaging

M. Wu[1,2], R. Tomi-Tricot[1,2,3], Ö. Ipek[1,2]

[1]*King's College London, Biomedical Engineering and Imaging Sciences, London, United Kingdom;*
[2]*London Collaborative Ultra high field System (LoCUS), London, United Kingdom;*
[3]*Siemens Healthineers, MR Research Collaborations, Frimley, United Kingdom*

Introduction Combining proton(^{1}H) and sodium(^{23}Na) imaging offers valuable insights into neurological activities beyond anatomical data. However, the intrinsically low sensitivity of ^{23}Na leads to low SNR.[1] To exploit ultra-high field benefits, we proposed a 16-channel dipole/loop array targeting simultaneous ^{1}H/^{23}Na acquisition at 7 T. The aim of this study is to examine the coil array performance with experimental measurements and EM simulations. The coil was compared to market-leading commercial coils in terms of B_1^+ field efficiency and the safety parameters are evaluated by SAR_{10g} levels.

Methods A 16-channel dipole/loop array was designed and constructed for ^{1}H/^{23}Na 7 T MRI. The array comprised 8 Tx/Rx centre-shortened ^{1}H dipole antennas(230 mm × 15 mm) with each dipole

etched from 35 µm copper on a FR-4 substrate[2] and 8 Tx/Rx ^{23}Na surface loops(25 cm × 15 cm) distributed symmetrically around a cylinder(d = 30 cm). In-house tuned baluns were integrated along the feeding coaxial cable to reduce coupling. Additionally, optimised overlapping and LC traps were implemented on ^{23}Na loops to decouple between ^{1}H/^{23}Na (Fig. 1a) We achieved satisfying return loss($S_{ii} \leq -15$ dB, $S_{ij} \leq -7$ dB) with fixed-value capacitors and hand-wounded copper-wire inductors, verified with S-matrices from VNA (Fig. 1b).

MR data were acquired on parallel-transmit system for ^{1}H and single-transmit for ^{23}Na on a 7 T MR scanner (*MAGNETOM Terra,Siemens,Germany*) with a spherical phantom(d = 15 cm,125 mmol NaCl) (Fig. 1c) The B_1^+ maps for ^{1}H array were assessed with 3D actual-flip-angle AFI sequence (TR = 200 ms, 4.4 × 4.4 × 4 mm^3, FA = 60 deg,1 average)[3]. For ^{23}Na elements, B_1^+ maps were calculated with the double-angle method[4] on middle axial slices acquired by 2D GRE sequences (TR/TE = 150/1.92 ms,FA = 45/90 deg, 6.6 × 6.6 × 25.0 mm^3, 32 averages, BW = 600 Hz/pixel). We performed the same acquisitions and calculated the average B_1^+ for ^{1}H/^{23}Na Rapid coil and 1Tx Nova coil to compare efficiencies.

Electromagnetic field simulations were performed using a finite-difference time-domain(FDTD) simulation software(*Sim4life 7.0, ZMT, Switzerland; Optenni Lab 5.2, Optenni Ltd, Finland*). The centre-shortened dipoles were modelled with the FR-4 substrate($\varepsilon_r = 4$) and dipole legs as lossy metal($\sigma = 5.8e^7$ S/m). The magnet bore and ^{23}Na loop array were added to the simulation model and defined as perfect electric conductor (PEC). Two simulation setups were conducted: a central spherical phantom and a brain-focused Duke adult human model (Fig. 1d) Q matrices[5] were computed for 10 g tissue mass-average and SAR_{10g} was calculated for adult head. Virtual observation points(VOPs) were derived from Q matrices calculations, and maximal SAR_{10g} values were computed for 150 k random RF shim sets.

Results For our in-house built 16ch dipole/loop array, experimental measurements and EM simulations exhibit similar field patterns and comparable B_1^+ magnitudes(Fig. 2). An overall 50% and 20% B_1^+ gain was reported comparing our 8ch ^{1}H dipole array to the ^{1}H elements of ^{1}H/^{23}Na Rapid coil and 1Tx Nova coil, respectively. VNA measurements indicated a high Q-factor ratio of 330/35(unloaded/loaded) for ^{23}Na loop array and a 38% overall B_1^+ gain was reported from MR measurements comparing to the ^{1}H/^{23}Na Rapid coil in CP mode (Fig. 3). Similar B_1^+ to the phantom results was reported in EM simulations with Duke head model with peak SAR_{10g} at 0.5W/kg for ^{1}H and 0.55W/kg for ^{23}Na (Fig. 4a, b) The distribution over 150 K RF shims indicated 95% of the computed $SAR_{10g,max}$ values are below 0.55W/kg for ^{1}H and below 0.8W/kg for ^{23}Na (Fig. 4c).

Discussion The 16ch dipole/loop array showed consistent B_1^+ maps from measurements and simulations. The coil array exhibited robust performance in subsequent ^{1}H and ^{23}Na imaging with considerable B_1^+ gain compared to market-leading commercial coils. Maximum SAR_{10g} for both 8ch arrays are comparable to those of the commercial coils, and the worst case SAR_{10g} computed with 150 K random RF shims remains compliant with the relevant safety limits(i.e. head SAR limit as 3.2 W/Kg). SNR quantification and in-vivo data will be acquired for further assessment.

Conclusion In this work, we have presented the initial phantom imaging results to characterise a custom-built 16ch dipole/loop array for 7 T MRI. The coil demonstrated great potential for high-signal ^{23}Na imaging with improved performance in ^{1}H elements than ^{1}H-only arrays, making one unified examination sufficient. EM simulation results aligned with experimental measurements and established safe RF power limits for in vivo studies. Future development would enable simultaneous ^{1}H/^{23}Na imaging to benefit patient diagnosis.

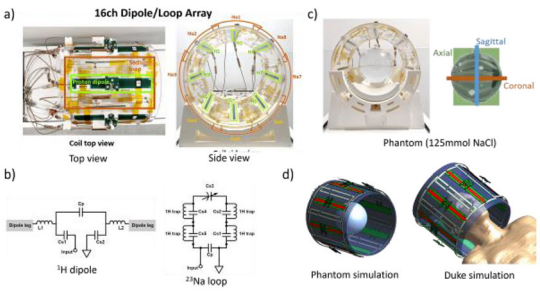

Fig 1: a)Photos of 16ch dipole/loop array from top and side;b)Circuit for ^{1}H dipole and ^{23}Na loop;c)Spherical phantom in coil centre on custom-designed 3D-printed holders;d)Simulation setup with phantom and Duke

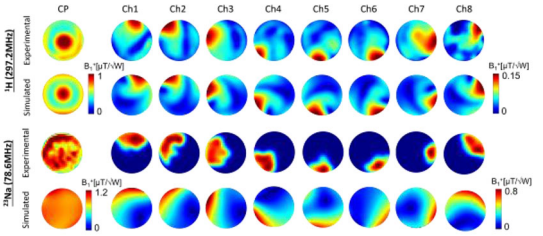

Fig 2: Measured and simulated B_1^+ maps normalised to 1W input power for CP mode and individual Tx elements for ^{1}H (top) and ^{23}Na (bottom)

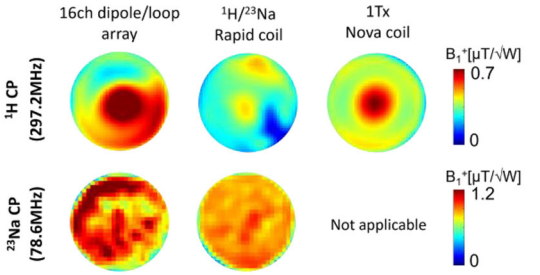

Fig 3: Comparison of measured ^{1}H/^{23}Na CP B_1^+ maps, in µT/sqrt(W), of 16ch dipole/loop array(left) and market-leac commercial coils: ^{1}H/^{23}Na Rapid coil(middle) and 1Tx ^{1}H Nova coil(right)

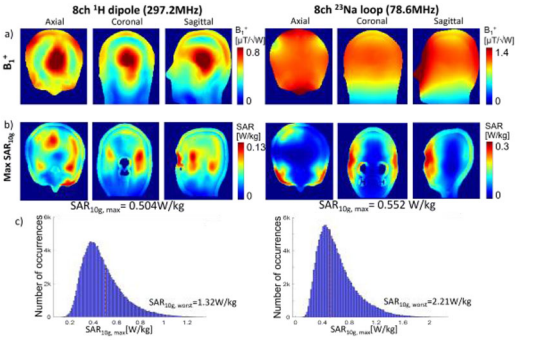

Fig 4: EM simulation results on adult head model(Duke) for 16ch dipole/loop array showing B_1^+ maps in CP mode(a) and maximum SAR_{10g} maps(b) in three anatomical planes for ^{1}H and ^{23}Na. RF phases were optimised over an ROI in a slice for $SAR_{10g,max}$ reduction. (c)Local Q-matrix SAR_{10g} distribution for 150K random RF phase sets for ^{1}H(left) and ^{23}Na(right). The orange dashed line indicates SAR_{10g} of the shim set for B_1^+. All results were normalised to 1W input power

References

1. Lachner S,Z Med Phys.2020 May;30(2):104–15;
2. Clément J, Magma.2022;35(5):765–78;

3. Yarnykh VL,MRM.2007 Jan;57(1):192–200;
4. Bottomley PA,JMRB. 1994 Jun 1;104(2):159–67;5.Ipek Ö,MRM 2014;71(4):1559–67.
Acknowledgment This work was supported by core funding from Wellcome/EPSRC Centre for Medical Engineering[WT203148/Z/16/Z].

P98.
Relation between the transmission coefficient and mutual impedance at the port: Proof of concept for loop coils and shielded coaxial cable (SCC) coils

G. Costa[1], M. M. Paulides[1], I. Zivkovic[1]

[1]*Eindhoven University of Technology, Department of Electrical engineering, Eindhoven, The Netherlands*

Introduction Recently, the SCC captivated the interest of the MRI community as a flexible surface element, providing similar transmit efficiency and SAR of a loop coil, with intrinsic decoupling characteristics—i.e. lower S_{21} than a loop in most of the 2-element array configurations relevant to MRI [1][2]. In a previous work, we expressed the mutual impedance as a function of electric and magnetic coupling, and we demonstrated that SCC show less magnitude of electric and magnetic coupling than a loop, thus resulting in lower value of the open circuit voltage per Ampere of current [3]. Aim of this work is to provide a general relationship between the mutual impedance of the unmatched coils and the S_{21} parameter of matched coils, and approximate it to analyze coupling mechanisms of loops and SCC.

Methods For a tuned and matched 2-port network, $S_{21} = a*V_2$, where V_2 is the induced voltage on a matched load at port 2, and $a = 1/V_1$ = const only depends on excitation and reference impedance and can be neglected. If network is tuned and matched at frequency f_0 then $|V_2(f_0)| \propto k = \text{sqrt}(\text{Re}\{Z_{tune}(f_0)\}/(\text{Re}\{Z_{in}(f_0)\}*|Z_{tune}(f_0) + Z_{22}(f_0)|^2)) *|Z_{21}(f_0)|$ (Eq. 1).

Where Z_{tune} is the equivalent impedance of the tuning and matching network as seen from port 2, Z_{ij} (i,j = 1,2) are Z parameters at the input of the coil, $Z_{in} = Z_{11} - (Z_{12}.*Z_{21})/(Z_{tune} + Z_{22})$. If LC networks are used for tuning and matching then $Z_{tune} = Z_{out}*$, where $Z_{out} = Z_{22} - (Z_{12}*Z_{21})/(Z_{tune} + Z_{11})$ (same circuits were used at both ports). When coupling is weak $Z_{out} \sim Z_{22}, Z_{in} \sim Z_{11}$ leading to a coupling coefficient $k_{weak} = |Z_{21}|/\text{sqrt}(\text{Re}\{Z_{11}\}*\text{Re}\{Z_{22}\})$ (Eq. 2).

A simulation software (CST Studio Suite 2023) was used to compute the Z-matrix of three 2-coil arrays—one of SCC, two of loops (Fig. 1)—in different geometrical configurations, (50%, 30%,10% overlap, 1 mm, 5 mm, 10 mm distance with adjacent coplanar elements), at 1.2 cm distance from a square phantom e = 78 s = 0.6 S/m. Coils were tuned and matched at 300 MHz using an internal tool, the resulting tuning and matching circuits were identical on both ports. The value of S21 computed by the software was compared with k. The value of Z22 was compared with Zout to distinguish strong coupling and weak coupling regions. Ratios between |Z21|, Re{Z11}, and Re{Z22} of different coils were used to explain different values of S21.

Results Figure 2 shows the normalized difference between Zout and Z22. Differece between Zout and Z22 was high when coils were 50% overlapped (strong coupling). Zout $\sim$ Z22 in other configurations (weak coupling).

Figure 3 shows k, S21, and correlation between S21 and k. S21 was lower for SCC, but comparable with loops in all the geometrical configurations. 1 mm loops provided lower S21 than 2.5 mm loops when overlapped, while 2.5 mm loops showed an advantage in adjacent configuration.

Figure 4 shows ratios between |Z21|, Re{Z11}, and Re{Z22} of different coils. All the parameters |Z21|, Re{Z11} and Re{Z22} were significantly lower for SCC, and the ratios between self impedances of loops was almost constant ($\sim$ 10% higher self impedance for 2.5 mm loops). The ratio between of loops instead crossed 1 when coils switched from overlap to adjacent.

Discussion When coupling was strong, the contribution of backscattering to the input impedance could not be neglected, and Eq. 2 was not proportional to S21. In other cases, approximated expression (2) was sufficient. Linear correlation between S21 and k confirm that S21 = b*k with constant b. While |Z21| was orders of magnitudes lower for SCC, this was associated with proportionally less Re{Z11} and Re{Z22}, thus the order of magnitude of S21 was comparable for loops and SCC. The switching behavior of S21 between loops was instead associated with a change in the mutual impedance with constant Re{Z11} and Re{Z22} ratios.

Conclusion In general, lower S21 is achieved by decreasing |Z21| with constant or higher values of input impedances at the port. Equations (1) or (2) can be used to rescale the mutual impedance depending on weak or strong coupling. While |Z21| was order of magnitudes lower for SCC, this was associated with proportionally less value of Re{Z11} and Re{Z22}, thus resulting in comparable S21 for the proposed designs of loops and SCC. In a future study, we will analyze how this result translates in terms of electric coupling, magnetic coupling, SAR and B1+. Changing wire diameter caused opposite effects when coils were overlapped or adjacent: this suggests that coupling behavior of a SCC cannot be imitated using straight wires. The theoretical expressions reported in this study confirm results on decoupling reported in literature, with the additional value of providing a connection between S21 and individual contributions of electric and magnetic coupling, thus paving the way to the design of optimized arrays for parallel imaging.

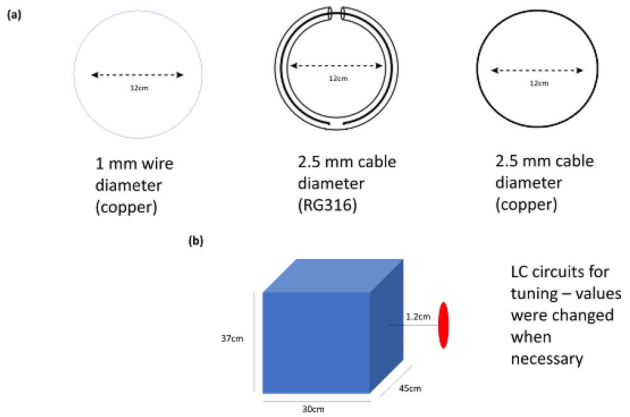

Fig.1: Design of simulations (a) Geometry of simulated coils (b) Geometry of simulations

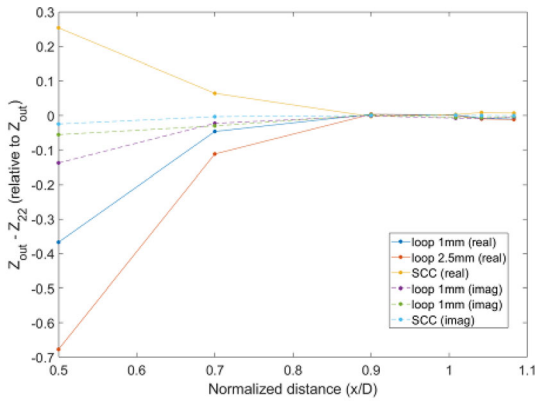

Fig. 2: Plot of difference Zout-Z22. Difference was normalized to the value of Zout.

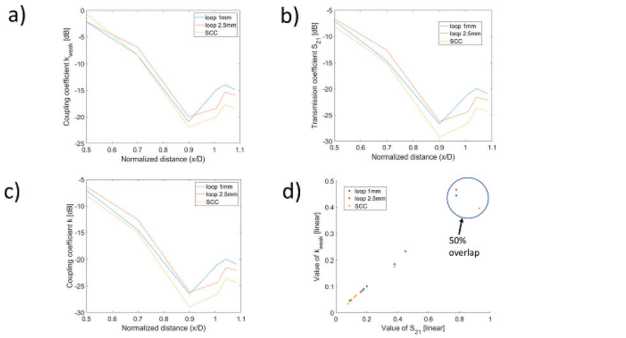

Fig. 3: Coupling coefficient and transmission coefficient a) coupling coefficient kweak (equation (2)) b) transmission coefficient S21 for loops, coils and SCCs c) coupling coefficient k (equation (1)). The correlation between k (equation(1)) and S21 was linear for each value of overlap and distance d) Scatter plot between S21 and kweak. In the plot, we point out 50% overlap data (strong coupling)

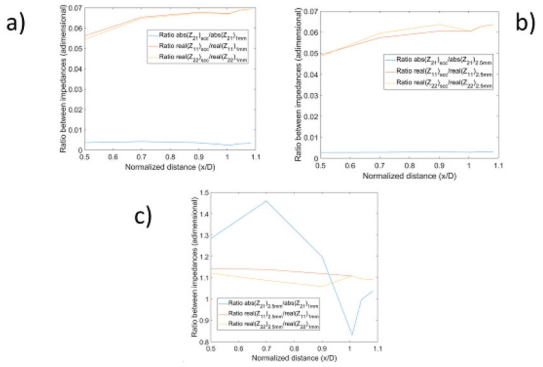

Fig. 4: Ratios between |Z21|, Re{Z11} and Re{Z22} a) ratio scc/1mm b) ratio scc/2.5mm c) ratio 2.5mm/1mm

References

[1] T. Ruytenberg et al. MRM 2020
[2] T.Ruytenber, et al. MRM 2019
[3] G.Costa et al. ISMRM 2023

P99.
Investigation on the improvement of the sensitivity of multi-loop-coils using the overlap principle

C. Thibault[1,2], V. Cap[3], C. Dubuc[1], L. Jourdain[1], G. Willoquet[1], M. Poirier-Quinot[1], R. Frass-Kriegl[3], A. Vignaud[2], J. C. Ginefri[1]

[1]*Universitéˊ Paris-Saclay, CEA, CNRS, Inserm, BioMaps, Orsay, France;*
[2]*Universitéˊ Paris-Saclay, BAOBAB, NeuroSpin, Gif-sur-Yvette, France;*
[3]*Medical University of Vienna, Division MR Physics, Center for Medical Physics and Biomedical Engineering, Vienna, France*

Synopsis A multi-loop coil (MLC) is composed of small loops in series and can improve the SNR as compared to a single loop coil (SLC), but at the cost of an inhomogeneous magnetic field and noise correlation between loops. To overcome this, we have investigated 4-loop MLCs with different overlap level between loops, experimentally and by simulation to evaluate Q-factors and B_1^- homogeneity.

Introduction The development of high-density coil arrays in MRI, to achieve both a high SNR and a large FOV[1], gives rise to increased complexity with respect to mutual decoupling as well as electronic circuitry required for array interfacing. To overcome this, a novel coil concept referred to as the multi-loop coil (MLC) was recently introduced[2], where the coil is composed of small loops, similarly to arrays but operated in series. MLCs were shown to improve the SNR at moderate distance inside the sample and could advantageously replace SLCs or coil-elements of arrays. However, in a preliminary study, it has been highlighted that the magnetic field is inhomogeneous near the MLC conductors and that noise correlation effect may occur between loops. This work investigates novel MLCs design for 7 T MRI using variable overlap between the loops of the MLC to reduce the RF field, B_1^-, inhomogeneity and noise correlation effect.

Materials and methods ***MLC design*** MLCs composed of 4 loops (outer diameter of 31 mm, conductor width of 1 mm) were investigated. The distance between diagonal-loop centers, *d*, was varied from 7 to 40 mm (3 mm step) and from 40 to 60 mm (5 mm step) resulting in a total of 16 MLCs. Figure 1 illustrates the 3 overlap configurations: loops non-overlapped (Fig. 1a), nearest loops overlapped (Fig. 1b) and all loops overlapped (Fig. 1c).

3D EM simulations Fullwave electromagnetic simulations were performed (Remcom XFdtd 7.8) in combination with circuit co-simulation[3,4]. A box-shaped phantom was used as load (200 × 200x120 mm^3, σ = 0.7 S/m, ε_r = 75). Coils were tuned and matched at the Larmor frequency, and loaded Q-factors were extracted from S-parameters. B_1^- was evaluated and used to calculate a homogeneity factor, *H-factor* = *(1 − StdDev/Mean)*, quantified over a circular ROI having the same diameter than the equivalent SLCs used for comparison.

Experimental measurements Measurements were conducted using MLCs made from standard printed circuit board (PCB). For all MLCs, 4 fix distributed capacitors and a variable one were used to tune the MLCs. Loaded Q-factors were measured when MLCs were placed on a rectangular phantom (280 × 190 × 135 mm^3) filled with a saline solution (σ = 0.7 S/m, ε_r = 75). Measurements were done using a network analyzer and the single-loop probe method[5].

Results The loaded Q-factors, are displayed in Fig. 2. While a factor 1.6 between simulated and measured values can be observed, the tendency of the two curves is similar: When none of the loops overlap, the Q-factor decreases when *d* decreases. For adjacent loops overlap, the Q-factor is almost constant. When all loops overlap each other, the Q-factor increases when *d* decreases.

The *H-factor* values, presented in Fig. 3, show similar tendencies for distances inside the sample of 2 mm, 4 mm and 8 mm. Among the

simulated configuration, the MLC with $d = 7$ mm and with $d = 31$ mm were selected because they achieved the highest *H-factor* and did not exhibit signal loss areas as compared to the other overlap configurations.

The MLCs with $d = 7$ mm and $d = 31$ mm were compared to their equivalent SLCs covering approximately the same sensitivity area, SLC_{MLC7} and SLC_{MLC31} respectively. The B_1^- maps, displayed in Fig. 2, indicate that the two MLCs achieve higher B_1^- amplitude than their corresponding SLCs. The loaded Q-factor of the MLC with $d = 31$ mm, equal to 15, is higher than the one of its equivalent SLC_{MLC31} equal to 9.7. The MLC with $d = 7$ mm and its equivalent SLC_{MLC7} have comparable loaded Q values, equal to 22 and 23 respectively. The *H-factor* of the SLCs, displayed in Fig. 3, were found to upper than their corresponding MLCs.

Discussion The present study shows that overlapping the loops of an MLC can achieve a more intense B_1^- than an equivalent SLC, together with higher loaded Q-factors. However, these improvements are counterbalanced by a reduced homogeneity achieved by the MLCs. Compared to the non-overlapped case, overlapping the loops improves the homogeneity with a moderate impact on the B_1^- amplitude and the loaded Q-factor. MLC with overlapped loops offers additional degree of freedom for coil design. Adding more loops and/or using other placement strategies, are work in progress to improve the image homogeneity and increase the benefit of the MC principle.

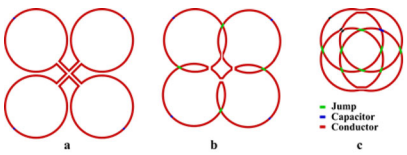

Fig. 1: *MLC configurations as a function of the distance, d, between diagonal loops: loops being non-overlapped (a), d ∈ [45 mm - 60 mm], nearest loops being overlapped (b), d ∈ [31 mm - 40 mm], and all loops being overlapped (c), d ∈ [7 mm - 28 mm].*

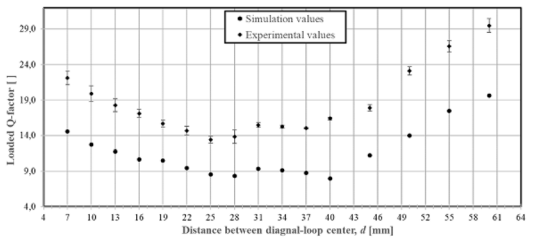

Fig. 2: *Loaded Q-factor values for the 16 MLCs. Measured (black diamond) and simulated (black circle). The bars for experimental values represent the standard deviation resulting from 15 measurement series.*

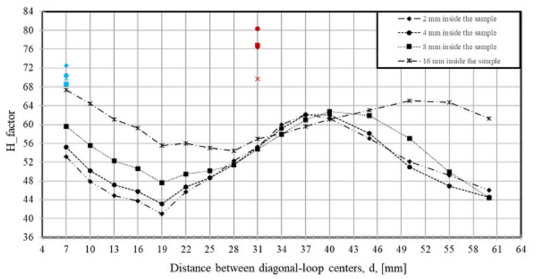

Fig. 3: *H-factor for the 16 MLCs (black), the SLC_{MLC7} (blue) and SLC_{MLC31} (red) at various depth, 2 mm (black diamond), 4 mm (black round), 8 mm (black square) and 16 mm (black cross) in the sample.*

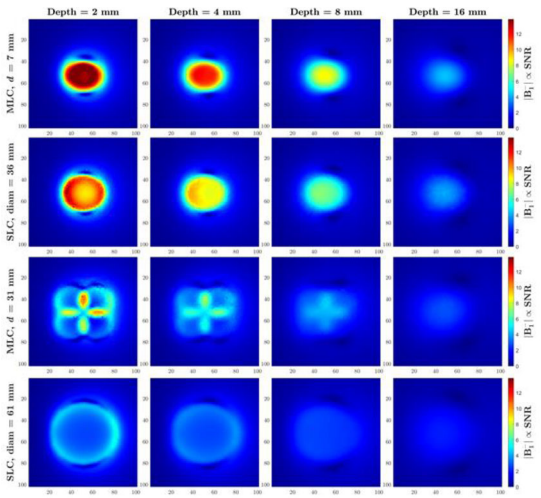

Fig. 4: Simulated SNR (B_1^- per input power) at different depths inside the phantom, produced by the MLC with $d = 7$ mm (first line), its equivalent SLC having a diameter of 36 mm (second line), the MLC with d = 37 mm (third line), its equivalent SLC having a diameter of 68 mm (fourth line).

References

1. Roemer et al. *Magn Reson Med.* 1990.
2. Frass-Kriegl et al. *Front. Phys.* 2020.
3. Kozlov et al. *J. Magn. Reson.* 2022.
4. Lemdiasov et al. *Concepts Magn Reson.* 2011.
5. Ginefri JC et al. *Rev. Sci. Instrum.* 1999.

P100.
Progress towards cardiac T1 dispersion imaging using field-cycling imaging

P. J. Ross[1], G. Davies[1], R. Stormont[1,2], D. Lurie[1], D. Dawson[1]

[1]*University of Aberdeen, Aberdeen Biomedical Imaging Centre, Aberdeen, United Kingdom;*
[2]*GE Healthcare, Waukesha, WI, United States*

Background/Introduction Field-Cycling Imaging (FCI) is a novel low-field magnetic resonance technique where the external magnetic field, B0, is deliberately and stepwise decreased during the imaging sequence. Varying B0 allows the spectrum of the spin–lattice relaxation time T_1 to be probed as a function of magnetic field, known as T_1 dispersion. Our research team have previously shown that T_1 dispersion has new diagnostic potential in ischaemic stroke and breast cancer without the need for exogeneous contrast agents using a home-built FCI scanner with a maximum field strength of 0.2 T. Our previous work made use of transceiver coils, however these are impractical for thoracic applications which typical employ larger receive-only arrays. Although common at high field, array technology has had little development in the low field regime below 20 MHz. In this work we describe the construction of a six-channel anterior–posterior torso array and present the first in-vivo FCI cardiac images and T_1 dispersion from healthy volunteers.

Methods Both the anterior and posterior coils of the array were constructed with three elements [each element made of a 2-turn 160 mm loops wound from high-frequency 1699 × 0.020 litz wire (Elektrisola Co., Reichshof-Eckenhagen, Germany)] and arranged in a "Venn Diagram" configuration with a 40 mm overlap (Fig. 1) to provide a degree of passive geometric decoupling. Additional decoupling and transmit protection was achieved by impedance matching through a lattice-balun to custom built low impedance preamplifiers (WMA08HA-WanTcom Inc., Chanhassen, MN, USA).

The lateral inter-element and axial inter-element coupling figures and Q factors were measured using a vector network analyser (Rhode and Schwarz Co. Munich, Germany).

As a proof of concept, we then used the torso array to collect full left ventricular coverage, short-axis cardiac images (Fig. 2) from n = 20 healthy volunteers with scan parameters: slice thickness = 15 mm, slice gap = 2 mm, in-plane resolution = 5.75 mm, FOV = 460 mm, bandwidth = 33 kHz, TE = 22 ms with spin-echo readout. Images were collected ats four predefined field strengths (200 mT, 20 mT, 2 mT, 200 μT from which T_1 dispersion information was derived for healthy left ventricular myocardium. Data is shown as mean ± SD.

Results After localisation, the left ventricle was readily visible in all volunteer FCI images. The derived mean T_1 dispersion values were 0.2 T: 215 ms ± 88, 0.02 T: 149 ms ± 42, 0.002 T: 36 ms ± 19.1, 0.0002 T: 32 ms ± 14. Repeat T_1 dispersion measurements show good reproducibility (Fig. 3). Our results are in keeping with T_1 dispersion measurements observed in skeletal muscle.

Conclusions We built a six-channel torso array coil for imaging at 0.2 T and below, and demonstrated the first in-man field-cycling cardiac imaging with T_1 dispersion values of healthy human myocardium. This paves the way for exploring new applications of field-cycling imaging in cardiovascular disease.

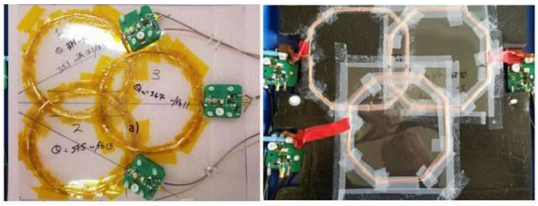

Fig. 1: Complete anterior (left) and posterior right) coils of the array with the projective jacket removed. The feedboards (green) contain the coil decoupling and preamplifiers.

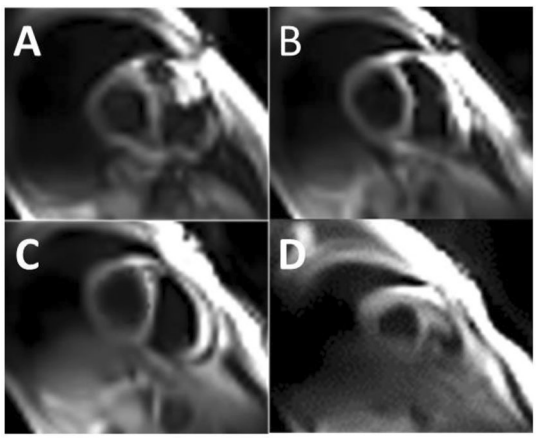

Fig. 2: Four short-axis views (A: base, B-C: mid venticle, D: apex) from a volunteer acquired at 0.2T using the array coil demonstrating good image quality and excellent left ventricle delineation.

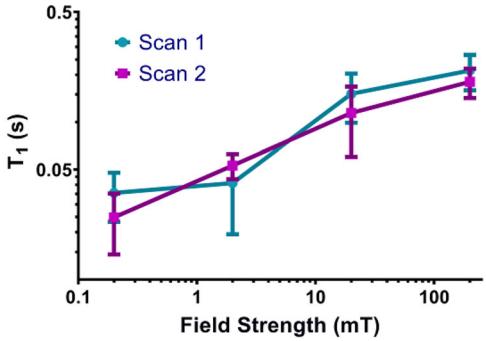

Fig. 3: T_1 dispersion results derived from the left venticle of healthy volunteers. Volunteers underwent two scans in order to assess repeatibility of T1 dispersion measurements.

P101.
Portable MRI indoors, outdoors and at home

T. Guallart Naval[1,2], J. M. Algarín[1], R. Bosch[1], F. Lloris[3], E. Pallás[1], J. P. Rigla[2], P. Martínez[3], J. Borreguero[2], J. M. Benlloch[1], F. Galve[1], J. Alonso[1]

[1]*MRILab, Institute for Molecular Instrumentation and Imaging (i3M), Spanish National Research Council (CSIC) and Universitat Politècnica de València, Valencia, Spain;*
[2]*Tesoro Imaging S.L., Valencia, Spain;*
[3]*PhysioMRI Tech S.L., Valencia, Spain*

Introduction Magnetic resonance imaging (MRI) is an essential tool for the diagnosis and treatment of numerous health conditions. However, its use is limited to a small fraction of potential patients due to its high cost and lack of portability. Low-field (< 0.3 T) cheap and light MRI systems are starting to become a valuable complement to standard MRI [1,2]. The main penalty to pay for operating in this regime is a significant loss in signal to noise ratio (SNR) and spatial resolution. Nevertheless, the diagnostic value of the resulting reconstructions is not necessarily compromised; for example, contrast-to-noise ratio (CNR) is less strongly dependent on field strength, and it is a more relevant metric for diagnosis than SNR [3].

Here we present a light, small footprint, low-field extremity MRI scanner with which we have taken in vivo images outside the controlled environment provided by medical facilities, so as to demonstrate the true portability of the system and benchmark its performance in various relevant scenarios, including a patient's home [1]. Altogether, this work paves the way towards highly accessible MRI under circumstances previously unrealistic.

Methods The system is an extremity MRI scanner based on a yokeless Halbach magnet, inspired on a previous system by LUMC [4]. The Halbach cylinder magnet (Fig. 1a) includes almost 4600 N48 NdFeB cubes of side 12 mm to generate B0 ≈ 72 mT at the field of view, and another ≈ 1100 N42 smaller cubes (64 mm3) to shim the

inhomogeneity from ≈ 15,700 down to ≈ 3100 ppm over a spherical volume of 20 cm in diameter. The gradient coil geometry (Fig. 1b) is optimized with conventional target-field methods and is capable of at least 24 mT/m along any direction. For the RF system, we used a Tx/Rx solenoid coil (Fig. 1c) tuned and impedance-matched to the proton Larmor frequency (≈ 3 MHz). The control electronics is based on MaRCoS, an open-source, high-performance Magnetic Resonance Control System [5]. Finally, we have mounted the complete system on a wheeled structure of width 70 cm (Fig. 1d), with an overall weight ≈ 250 kg and component cost < 50 k€. The scanner runs from a standard wall power outlet. These characteristics are key to portability.

To demonstrate the true portability of the system and benchmark its performance in various relevant scenarios, we have acquired images of a volunteer's knee in: (a) an MRI physics laboratory; (b) an office room; (c) outside a campus building, connected to a nearby power outlet; (d) in open air, powered from a small fuel-based generator; and (e) at the volunteer's home (Fig. 2). These images were all acquired on the right knee of the same volunteer with the same parameters: T1-weighted 3D-RARE sequence, with FoV = 180 × 200 × 200 mm3, a resolution of 1.2 × 2 × 10 mm3, ETL = 5, TE = 20 ms, TR = 200 ms, BW = 37.5 kHz, and 9 averages for a total scan time of 12 min. To compare image quality, we estimate the SNR of each image (Fig. 2 right) calculating the signal strength as the average voxel brightness in a region of the femur (red boxes), and the noise as the average voxel brightness in the background (white boxes).

Results Despite small differences in SNR, the main anatomical features and different tissues remain clearly identifiable across all acquisitions (Fig. 2 right), demonstrating the true system portability with the world-first MRI images of patients outdoors and even inside their house.

Furthermore, the volunteer carries a fixation metallic implant screwed to the femur, which leads to strong artifacts in standard clinical systems but appears sharp in our low-field acquisitions (Fig. 3).

Discussion/Conclusion We have characterized the performance of a truly portable, low-cost and easy to maintain and install MRI scanner. These devices pave the way to expanding MRI applications to home and hospice care, small clinics, rural areas, NGO camps, etc., making MRI available to a large fraction of the world's population with no or insufficient access.

Acknowledgements This work was supported by the Ministerio de Ciencia e Innovación of Spain through research grant PID2019-111436RB-C21. Action co-financed by the European Union through the Programa Operativo del Fondo Europeo de Desarrollo Regional (FEDER) of the Comunitat Valenciana (IDIFEDER/2018/022 and IDIFEDER/2021/004). JB acknowledges support from the Innodocto program of the Agencia Valenciana de la Innovación (INNTA3/2021/17).

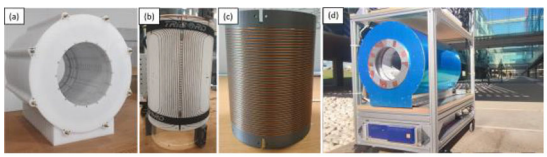

Fig. 1: Photographs of the low-field extremity scanner: (a) 72 mT Halbach magnet; (b) gradient assembly; (c) RF Tx/Rx coil; and (d) full system mounted on a transportable structure and in open air.

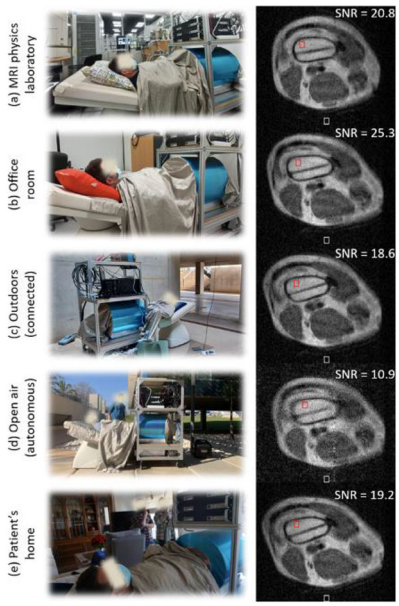

Fig. 2: Photographs during acquisitions (left) and axial slice from 3D-RARE reconstructions (right, no post-processing) at five different locations: (a) in an MRI physics laboratory; (b) in an office room; (c) outside a campus building, connected to a nearby power outlet; (d) in open air, powered from a small fuel-based generator; and (e) at the volunteer's home.

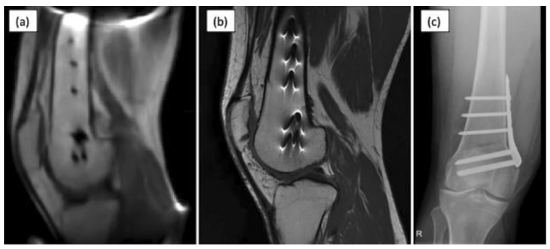

Fig. 3: Images of volunteer's fixation metallic implant attached to the femur: (a) sagittal view acquired with our scanner; (b) sagittal view acquired with a 3T system; and (c) lateral X-ray computed radiography.

References

[1] T. Guallart-Naval, J. M. Algarín, et al. Sci. Rep. (2022). https://doi.org/10.1038/s41598-022-17472-w

[2] Sheth, K.N., et al. JAMA Neurol. (2020). https://doi.org/10.1001/jamaneurol.2020.3263

[3] S. Ghazinoor et al. JMRI (2007). https://doi.org/10.1002/jmri.20854.

[4] T. O'Reilly et al. MRM (2020). https://doi.org/10.1002/mrm.28396.

[5] T. Guallart-Naval et al. NMR Biomed. (2022). https://doi.org/10.1002/nbm.4825.

P102.
New graphical user interface and gradient control electronics for the MaRCoS open-source console

J. M. Algarín[1,2], N. Allek[3], Y. Vives-Gilabert[4], T. Guallart Naval[5], J. Borreguero[5], B. Menküc[3], V. Negnevitsky[6], A. Webb[7], J. Alonso[1,2]

[1]*Universitat Politècnica de València, i3M, Valencia, Spain;*
[2]*CSIC, i3M, Valencia, Spain;*
[3]*University of Applied Sciences and Arts, Dortmund, Germany;*
[4]*Universitat de València, Valencia, Spain;*
[5]*Tesoro Imaging S.L., Valencia, Spain;*
[6]*Oxford Ionics Ltd, Oxford, Germany;*
[7]*Leiden University Medical Centre, Leiden, Netherlands*

Introduction MaRCoS (MAgnetic Resonance COntrol System) [1], [2] is an open-source electronic control system for low field MRI that provides high performance at a reduced cost (< 2 k€). The core of MaRCoS is the Red Pitaya SDRLab 122–16, which has two RF analog inputs and outputs, multiple digital outputs, and can control either a GPA-FHDO [3] or an OCRA1 [4] for gradient pulse generation. Pulse sequences can be designed and executed directly with MaRCoS via user-defined scripts with numpy arrays [5].
In this work, we present a new plugin module for the GPA-FHDO to control external analog gradient amplifiers and we introduce a new graphical user interface (GUI) [6] designed to facilitate the interaction between users and MaRCoS.
Methods Figure 1 shows pictures of a MaRCoS setup. It contains the SDRLab board, the adapter to connect the SDRLab to the GPA-FHDO, the GPA-FHDO itself, and the newly-developed Bipolar module. The latter is an add-on outputting four low voltage (+ -12 V) waveforms that can be fed into external analog gradient amplifiers. This module can be plugged directly on top of the GPA-FHDO.
The GUI is written in Python with PyQt5. The resulting data and images are visualized with the pyqtgraph library modified to provide specific functionalities, like selecting the size or angle of the field of view for the acquisitions. Figure 2 illustrates the basic workflow of the GUI. Once it is connected to the MaRCoS server, a *sniffer* module continuously checks for pending tasks in a waiting list. These tasks can be pulse sequences for calibration or imaging. If a pulse sequence is in the waiting list, it is executed, and the results are saved. Two methods are called by the *sniffer*: *sequenceRun* and *sequenceAnalysis*. The *sequenceRun* method defines the experiment according to the selected sequence and input parameters, including the specific waveforms for gradients, radiofrequency, and acquisition windows, which are then saved into the MaRCoS server. Next, the experiment is run, and the code waits until data is acquired. Finally, the *sequenceAnalysis* method operates on the acquired data to fill k-space, reconstruct the image, and save the results.
Results Figure 3 shows a waveform generated with MaRCoS measured with an oscilloscope at the output of the Bipolar module. The waveform generated corresponds to a Pointwise Encoding Time Reduction with Radial Acquisition (PETRA) sequence, typically used for hard tissue imaging.
Figure 4 shows a screenshot of the "session" interface (left) and main window (right). In the session interface, users can input information about the scanned patient or sample. This metadata is later saved in the DICOM file generated once the images are acquired. In the main window, users interact with the sequences and results. It includes a menu bar and toolbars for interacting with the MaRCoS server, running calibrations, visualizing or executing pulse sequences, saving or loading input parameters, and creating or deleting protocols. Additionally, there is a space to show previously executed or pending sequences and the parameters used in those sequences.
Discussion MaRCoS is used in a variety of low-field settings in different laboratories. With the new Bipolar module, high current waveforms can be produced with an external amplifier, no longer bound by the approximately 10 A limit of the original GPA-FHDO design. For instance, in several low-field systems ranging between 70 and 260 mT in Valencia, we switch between OCRA1 and the GPA-FHDO. This is convenient because the latter is fully open-sourced.
The GUI contains sequences for imaging like RARE, GRE or PETRA, as well as sequences for calibration like Rabi flops, shimming, Larmor frequency and others. From the GUI we can also run autocalibration sequences. To this end, we set the field of view directly from a scout image, we select the region of interest, we show the mean value and standard deviations to get a quick estimation of the signal-to-noise ratio, and we develop protocols to generate standardized sets of images from different sequences to make the GUI accessible to non-expert users. Additional sequences such as balanced steady state free precession, or echo planar imaging, as well as new sampling trajectories beyond Cartesian trajectories, will eventually enrich the possibilities offered by the GUI.
Conclusion In this work we show the latest updates of the MaRCoS project, including the new Bipolar plugin module to control external analog gradient amplifiers, and a GUI to easily interact with MaRCoS, run pulse sequences and visualize the results.

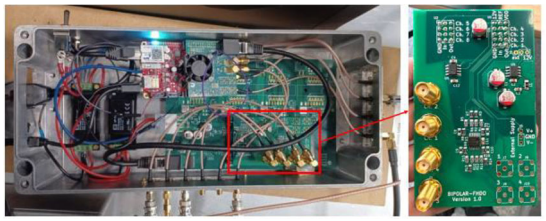

Fig. 1: Picture of the MaRCoS electronic setup with an FHDO (left). A bipolar pcb (right) is connected to the FHDO to control analog gradient amplifiers.

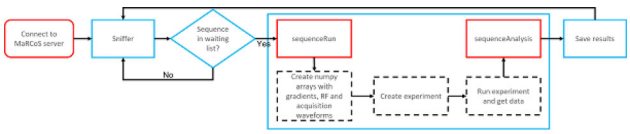

Fig. 2: Basic workflow of the GUI to execute sequences.

Fig. 3: Waveform generated with the Bipolar module corresponding to a PETRA sequence.

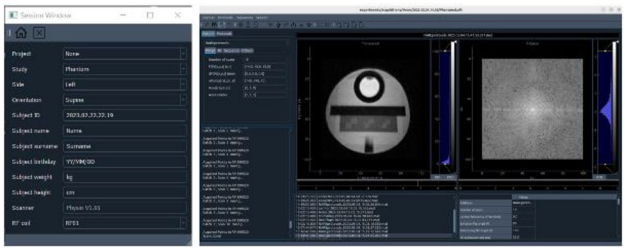

Fig. 4: Session window (a) and main window (b) of the GUI.

References

[1] T.Guallart-Naval et al., NMR Biomed, 2023; 36(1):e4825
[2] V. Negnevitsky et al., JMR 350, (2023), 107424
[3] https://github.com/menkueclab/GPA-FHDO
[4] https://zeugmatographix.org/ocra/2020/11/27/ocra1-spi-controlled-4-channel-18bitdac-and-rf-attenutator
[5] https://github.com/vnegnev/marcos_extras/wiki
[6] https://github.com/yvives/PhysioMRI_GUI

P103.
Markerless monocular head tracking for pediatric MRI

L. Bartsch[1,2], S. Röll[1], O. Speck[2]

[1]*Neoscan Solutions GmbH, Magdeburg, Germany;*
[2]*Otto von Guericke University, Magdeburg, Germany*

Introduction Patient motion during MR examinations leads to motion artifacts, which is why several motion detection and correction strategies have been developed. Camera-based tracking with markers shows promising results but is hardly, as markers pose a burden in clinical routine [1][3]. Especially pediatric scans are challenging because the patients cannot be considered cooperative [2]. This abstract presents an external head tracking method based on a monocular camera setup neither with markers nor structured light. The missing depth information is supplemented via a head model. The algorithm is tested with a child-size doll head.

Methods Facial landmarks are identified in the camera images with FacemarkLBF trained for a doll head with ten landmarks [4]. No landmarks within the eyes are used because pediatric patients often sleep. The landmark position change is tracked by combining sparse optical flow and re-calculating the landmark positions for each camera frame.

Since no depth information is available, geometric constraints are required to estimate the head position. The head model consists of 3D coordinates of the previously determined 2D landmarks. To reduce the head model-dependent error, the model is adjusted to the doll head used. The head position is determined as a translation vector and Euler angles by minimizing the re-projection error of the transformation between the 2D camera image and the 3D coordinates. The change between two consecutive frames is calculated. The coordinate system used is shown in Fig. 1.

A doll head was placed below a calibrated MR-compatible camera to test the algorithm. To estimate the tracking noise, the still doll head is tracked for $\sim$ 6 min. To analyze whether the tracking is suitable for MR applications, the excerpt of the noise shown in Fig. 4 (a) and (b) is fed into the MR motion artifact simulation toolchain "retro-MoCoBox" from Gallichan [5]. Furthermore, the tracking error is analyzed by manually moving the doll"s head along different axes.

Results Figure 2 shows the landmark detection result and a visualization of the Euler angles.

Figure 3 shows histograms of the noise data for each axis. The mean and standard deviation are noted in the caption. The histogram of the x-axis shows two side peaks. This can be explained by the more concise structures in the x direction in a face. The deviation of the in-plane rotation θ_z is much smaller than the similar out-off-plane rotational axes.

Figure 4 (d) shows the resulting motion corruption caused by the noise of the tracking system. When the figure is compared to Fig. 4 (c) qualitatively, blurred edges are visible.

The doll head was shifted ten times along each axis and angle. The results (expected, mean, standard deviation) are:e_x = 10 mm, m_x = 9.56 mm, σ_x = 1.3 mm,e_y = 10 mm, m_y = 9.81 mm, σ_y = 1.21 mm,e_z = 5 mm, m_z = 5.55 mm, σ_z = 0.67 mm,$e_{\theta y}$ = 5°, $m_{\theta y}$ = 5.12°, $\sigma_{\theta y}$ = 1.2°,$e_{\theta z}$ = 10°, $m_{\theta z}$ = 9.37°, and $\sigma_{\theta z}$ = 1.44°.

Discussion The standard deviation is comparable to other markerless tracking in the literature [7]. The comparison is difficult due to various differences: human vs. doll, the head model used and the distance to the camera. The large uncertainty in the tracking probably results from an uncertain ground truth due to manual movement. A big competitor is marker-based tracking which achieves accuracies of $\sim$ 0.01 mm, respectively $\sim$ 0.01°[3]. Since the tracking system"s accuracy should be at least fives time higher than the MR image resolution, the shown markerless tracking does not seem suitable for high-fidelity or high resolution motion correction[3].

Conclusion The abstract shows that tracking a head with a monocular camera setup works but is limited in accuracy compared to marker-based tracking. It may be used for motion detection.

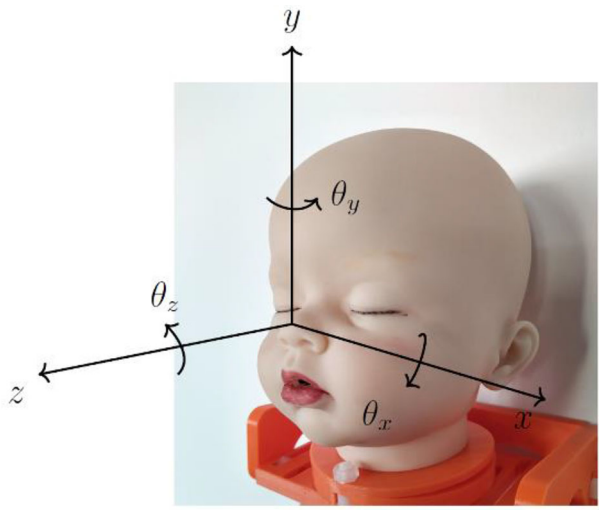

Fig. 1: Coordinate system definition.

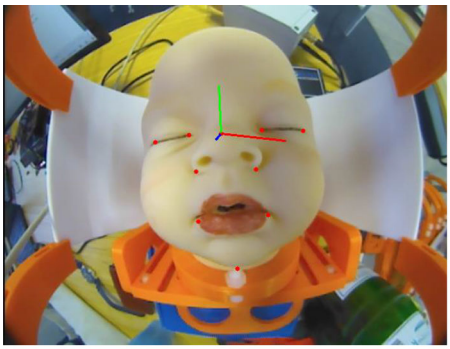

Fig. 2: Qualitative landmark detection results and head orientation coordinate system attached to the nose tip as origin.

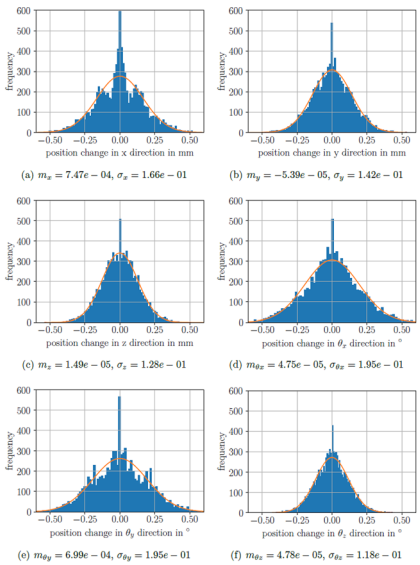

Fig. 3: Histograms of the noise of the algorithm with 100 bins (blue) for each degree of freedom of the motion tracking and fit of the Gaussian bell curve (orange).The histograms show only approximately a normal distribution. 9203 frames and thus tracking results of a still-lying doll head were used. In the image captions is the axis, the corresponding mean value and standard deviation noted.

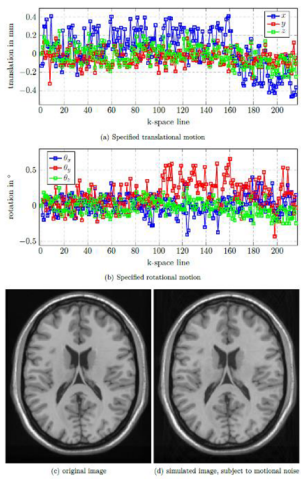

Fig. 4: Simulation of the corruption caused by the noise of the head tracking. The translational and rotational motion fed to the motion artifact simulation toolchain is shown in (a) and (b). The artifacts caused by the specified motion is shown in (d). For comparison, the original image is shown in (c). The motion artifacts were simulated with "retroMoCoBox" [5] and the head image is from [6].

References

[1] Dijk et al.: The influence of head motion on intrinsic functional connectivity MRI. In: NeuroImage 59 (2012), jan, Nr. 1, S. 431–438. https://doi.org/10.1016/j.neuroimage.2011.07.044

[2] Harrington et al.: Strategies to perform magnetic resonance imaging in infants and young children without sedation. In: Pediatric Radiology 52 (2021), apr, Nr. 2, S. 374–381. https://doi.org/10.1007/s00247–021–05062–3

[3] Godenschweger et al.: Motion correction in MRI of the brain. In: Physics in medicine & biology 61 (2016), Nr. 5, R32. https://www.ncbi.nlm.nih.gov/pmc/articles/PMC4930872/pdf/nihms796209.pdf

[4] Kurnianggoro, Laksono: Facemark API for OpenCV. Version: Juni 2015. https://github.com/kurnianggoro/GSOC2017

[5] Gallichan, Daniel: retroMoCoBox. Version: November 2022. https://github.com/dgallichan/retroMoCoBox

[6] Holmes et al.: Colin 27 Average Brain, Stereotaxic Registration Model, original 1998 version, 2015, aug. http://www.bic.mni.mcgill.ca/ServicesAtlases/Colin27—last access: 17.04.2023

[7] Hammadi et al.: Evaluation of Various State of the Art Head Pose Estimation Algorithms for Clinical Scenarios. In: Sensors 22 (2022), sep, Nr. 18, S. 6850. https://doi.org/10.3390/s22186850

P104.
Motion detection in propeller MRI of the brain using rigid body transformation network with self-information loss

U. Yarach[1], A. Suwannasak[1], P. Ratiphunpong[1], T. Ruadrew[1]

[1]*Chiang Mai University, Department of Radiologic Technology, Faculty of Associated Medical, Chiang Mai, Thailand*

Introduction Traditional reconstruction pipeline of PROPELLER performs several steps such as motion detection, motion correction, phase correction, intensity compensation, and blade combination. Although several step can be performed simultaneously through model-based framework [2] and advance constrained reconstruction [3–5], an efficient motion detection is still sought. In this work, we proposed a rapid technique to detect motions among blade images by implementing rigid-body transformation network (Motion-Net) with no need ground truth data.

Methods *Discrete single-blade signal model:* A single-blade signal measured during readout m ∈ [1 M] of phase encoding line n ∈ [1 N] can be modeled as: (see Eq. 1 in Fig. 1).where p ∈ [1 P] and q ∈ [1 Q] are pixel indices. u is the complex-valued target image, $k_{x,\alpha}$ and $k_{y,\alpha}$ are the k-space coordinates in the readout and phase-encoding dimensions associated with blade angle α ∈ [1 N_α]. s_c is the sensitivity profile for coil c ∈ [1 C], and ε is white Gaussian noise. Defining $S = [\text{diag}\{S_1\},\ldots,\text{diag}\{S_c\}]^T$, Eq. (1) abstracts to: (see Eq. 2 in Fig. 1)

Where $F_\alpha \in C^{MNxPQ}$ is either fully or under-sampled discrete Fourier transform (or NUFFT-II) [6] and ⊗ is Kronecker"s product.

Motion signal model: to describe rigid-body motion specific to acquired blade data, Eq. 2 can be modified as: (see Eq. 3 in Fig. 1). Operator Ω_Φ rotates u with angle Φ. Parameters t_x and t_y are translations along x and y, respectively.

Network design: In Fig. 2, the Localization Net [7] takes the input single blade (coil combined) image H × W × C with width W = 256, height H = 256 and channel C = 1. The outputs K × C is parameters of the transformation. In this work, K is 4 which was arranged into rigid-body transformation matrix as: (see Eq. 4 in Fig. 1).

Note that first blade image is untouched by Localization Net and kept as a reference. Other blade images were transformed to new coordinates (i.e., $[x_{new}\ y_{new}]^T = T_\theta[x\ y]^T$).

Self-Information Loss: First blade image was referred to as "y_{true}". The rest were average and referred to as "$y_{predict}$". Normalized Root Mean Squares Error (NRMSE) loss was performed as: (see Eq. 5 in Fig. 1).

Deep Learning Implementation: The model was implemented in Tensorflow [8] and trained by minimizing the NRMSE loss between the predicted and ground truth using the Adam optimizer [9] with a learning rate of 1×10^{-4} and batch size of 8, running on NVIDIA Tesla P100 with 16 GB GPU.

Data acquisition and preparation: In-vivo experiments were performed on 1.5 T clinical MRI (Ingenia; Philips, Best, the Netherlands) equipped with a 12-channel receiver head coil). 22 healthy volunteers were scanned after informed consent according to institutional review board-approved (IRB) protocol. Cartesian fully sampled T2W and T2-FLAIR (matrix: 256 × 256, 25 slices) were acquired. Equation 3 was applied to create motion corrupted data. 2X-oversampled type-II NUFFT with a width J = 5 Kaiser-Bessel kernel was used. The assigned blade number and ETL were 10 and 48, respectively. The ranges of translations in *x*,y and rotation Φ were [− 5 5] pixels, [− 5 5] pixels, and [− 10 – 10] degrees, respectively. 3200, 800 slices of simulated motion data (from 20 volunteers) were used for training, validating, respectively. 50 slices from 2 volunteers were use for testing.

Results The model can detect motion parameters about 0.03 s/blade. In Fig. 3A, mean of residual translation in x-direction and rotation parameters are less than 1 mm. and 1 degree for all blades of T2W. There are only two blades that residual translations in y-direction are slightly higher than 1 mm. In Fig. 1B, it is similar trend in (3A). Mean of residual motion parameters of seven blades are less than 1 mm. and 1 degree. The rest are only slightly higher than 1 mm. and 1 degree. In Fig. 4A, B, the motion corrupted images appear very blurry, while the motion corrected images appear much improved from visual inspection. Their NRMSE values are lower than those of non-corrected images (4C and 4D). Note that the motion correction was performed by updating k-space trajectory using predicted rotation parameters. The translation was performed through Fourier shift theorem.

Discussion The proposed Motion-Net nicely performed in detecting rigid-body motion parameters from simulated 2D propeller T2W and FLAIR data. However, some residual motion parameters (1–2 mm and degree) slightly degraded the reconstructed images (about 17% of NRMSE). In this work, we investigated only fully sampled data with 48 ETL/blade. The under-sampled data with different ETL should be investigated further. Main reconstruction pipeline may be unrolled [10–11] with including Motion-Net to speed up the propeller reconstruction. Finally, large number of training data would enhance the performance of the network even further.
(see Fig. 1).

$$g_{c,\alpha}[m,n] = \sum_{p=1}^{P}\sum_{q=1}^{Q} s_c[p,q]u[p\cdot q]e^{-i(k_{x,\alpha}[m]p+k_{y,\alpha}[n]q)} + \varepsilon_{c,\alpha}[m\cdot n] \quad \text{(Eq. 1)}$$

$$G_\alpha = \left(1 \bigotimes F_u\right) Su + \mathcal{E}_\alpha = A_\alpha u + \mathcal{E}_\alpha \quad \text{(Eq. 2)}$$

$$G_{\alpha,t_x,t_y,\phi} = e^{-2\pi i\left(k_{x,\alpha}t_x + k_y t_y\right)} A_{\alpha,\phi}\Omega_\phi(u) + \mathcal{E}_\alpha \quad \text{(Eq. 3)}$$

$$T_\theta = \begin{bmatrix} \theta(1) & -\theta(2) & \theta(3) \\ \theta(2) & \theta(1) & \theta(4) \\ 0 & 0 & 1 \end{bmatrix} \quad \text{(Eq. 4)}$$

$$\text{NRMSE} = \sqrt{\frac{1}{N}\sum_{1}^{N}\left(y^i_{predict} - y^i_{true}\right)^2} \Big/ \sqrt{\frac{1}{N}\sum_{1}^{N}\left(y^i_{true}\right)^2} \quad \text{(Eq. 5)}$$

References

1. Pipe JG et al. Multishot diffusion-weighted FSE using PROPELLER MRI. MRM 2002; 47(1): 42-52.
2. Yaraeb U, In MH, Chatnuntawech I, et al. Model-based iterative reconstruction for single-shot EPI at 7T. MRM 2017;7 8(6): 2250-2264.
3. Haldar P., Low-rank modeling of local k-space neighborhoods (LORAKS) for constrained MRI, IEEE transactions on medical imaging 2014; 33(3): 668-681
4. Mani M et al. "Multi-shot sensitivity-encoded diffusion data recovery using structured low-rank matrix completion (MUSSELS)," MRM 2017; 78(2): 494-507
5. Hu Y et al. Motion-robust reconstruction of multishot diffusion-weighted images without phase estimation through locally low-rank regularization. MRM 2019; 81(2): 1181-1190.
6. Feuiler JA and Sutton BP, Nonuniform fast Fourier transforms using min-max interpolation. in *IEEE Transactions on Signal Processing*, 2003; 51(2), pp. 560-574.
7. Jaderberg, M et al. Spatial Transformer Networks 2015. *NIPS*.
8. Abadi M et al. TensorFlow: a system for large-scale machine learning; Proceedings of the 12th USENIX Symposium on Operating Systems Design and Implementation; 2016 November 2-4; Savannah, GA, USA. Berkeley: USENIX Association; pp. 265–283.
9. Kingma DP, Ba J. Adam: a method for stochastic optimization. arXiv 2014:1412.6980.
10. Aggarwal HK et al, "Multi-Shot Sensitivity-Encoded Diffusion MRI Using Model-Based Deep Learning (Modl-Mussels)," Proc IEEE Int Symp Biomed Imaging 2019; 1541-1544.
11. Hu Y. et al., "RUN-UP: Accelerated multishot diffusion-weighted MRI reconstruction using an unrolled network with U-Net as priors," Magn. Reson. Med. 2021; 85(2): 709-720.

Fig. 1: Equations and References

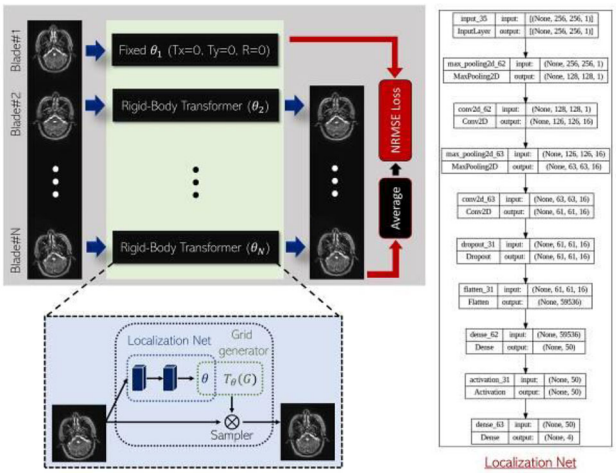

Fig. 2: Motion Detection Network. There are 29M total trainable parameters.

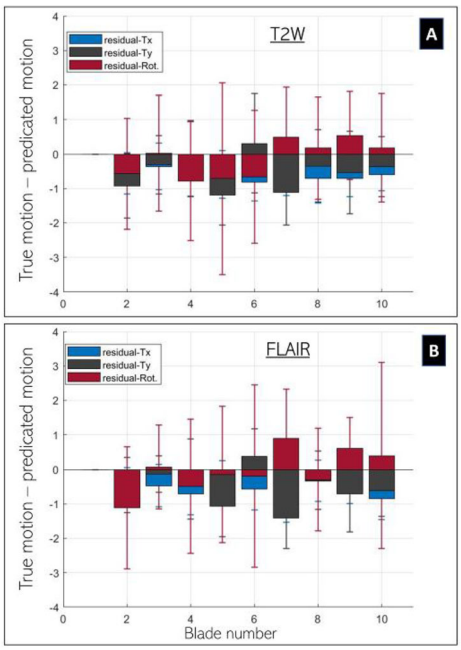

Fig. 3: The mean and standard deviation of differences between true motion and model predicted motion parameters in T2W (A) and FLAIR (B) among 10 blades.

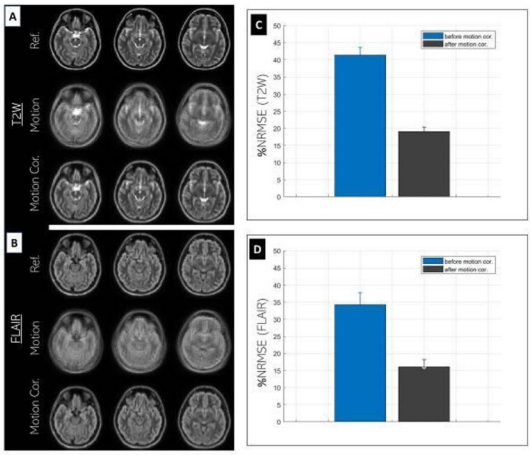

Fig. 4: (**A** and **B**) T2W and FLAIR at three different slices displayed to show reference, motion, and motion correction. (**C** and **D**) Mean and standard deviation of normalized root mean square errors (NRMSEs) obtained from 50 testing slices (25 slices of T2W and 25 slices of FLAIR).

References

P105.
Fast procedure for routine quality assurance of prospective motion correction during in vivo scanning: A pilot study

K. Pine[1], K. Podranski[1], L. Edwards[1], N. Weiskopf[1,2]

[1]*Max Planck Institute for Human Cognitive and Brain Sciences, Department of Neurophysics, Leipzig, Germany;*
[2]*Leipzig University, Felix Bloch Institute for Solid State Physics, Leipzig, Germany*

Introduction Prospective motion correction (PMC) has been shown to reduce artifacts at their source with the potential to impact clinical routine[1]. Typically, movement of the imaged object is tracked and passed to the MR pulse sequence to update the imaging FOV. For external systems such as optical PMC motion is tracked by means of a marker attached to the object; the model relating the scanner FOV and the image object position and orientation relies on accurate knowledge of the transforms (cross-calibration) between the multiple frames of reference, and on the rigid-body assumption.

Practically, degraded cross-calibrations or poor marker attachment results in PMC corrupting recorded data beyond repair[2]. We offer a procedure for human brain imaging which identifies a subset of PMC errors before starting the main imaging scans, can be integrated into routine scanning, and can be used for PMC QA.

Methods Twenty participants undergoing lengthy ($\sim$ 17 min) whole-brain 3D GRE imaging requiring PMC (Kineticor, USA) on a 3 T Connectom scanner (Siemens, Germany) were instructed at the conclusion of the session to comfortably turn their head to the left and hold for a brief low-resolution 3D dual-echo GRE scan (2 mm isotropic, 30 s), then to the right for an identical second 3D GRE. The PMC system was configured to apply corrections during the second scan with reference to the initial position of the first (perfect PMC performance would result in both images being in complete alignment). Other parameters: TR 8.6 s, TE1/TE2 2.36/4.66 ms, FA 12°, matrix size 128 × 112x88, GRAPPA 2 × 2. Participants wore a bespoke mouthpiece moulded to the front teeth with an attached tracking marker[3].

In post-processing, the first echoes of both 2 mm volumes were skull-stripped with FSL's BET[4] before affine 3D 6-DOF registration with FLIRT[5]. A scalar quality metric (QM) was defined as the geometric mean of the transformation matrix"s six translations (in mm) and rotations (in degrees), normalized by the geometric mean of the measured rotation and multiplied by 100. Note that weighting rotations/translations identically is the same as assuming a rotational radius of 5.7 cm for areas in the periphery of the brain—reasonable considering typical head sizes[6].

For external validation we calculated previously-validated motion metrics, specifically average edge strength (AES)[2] and the standard deviation of R_2^* [7], for a 1 mm resolution T1-weighted multiecho 3D GRE volume PMC-corrected in the same session (TR 25 ms, 8 equispaced echoes TE 2.36.0.18.46 ms, FA 21°, TA 16:30 min).

Results Initial testing after the PMC system sat unused in 2020 revealed corrupted images (Fig. 1), high registration errors ($\sim$ 20 mm) and high QM (first two participants QM = 634, 609). Subsequent investigation determined dust on the reference marker led to a false scanner-camera transform (cross-calibration). After marker cleaning and recalibration, registration errors were typically < 1 mm and QM < 6. Figure 2 shows scatter plots of QM against AES and R_2^* SD, which demonstrate that QM could well differentiate between normal and erroneous calibrations, predicting the pronounced drops in image quality.

Discussion The proposed QA procedure successfully detected major failures in cross-calibration. Sharp drops in image quality were predicted by QM due to the PMC failure but not smaller differences observed with a well-performing PMC system, since they are driven by noise sources not correctable by PMC. The procedure requires ca. 1 min of scanning and results can be analysed in < 1 min. Thus, the procedure could also be used each session for rapid performance assessment and correction of potential issues.

It provides an alternative to more-complex phantom-based routine QA. The cross-calibration error could also be determined retrospectively and corrected for using autofocusing[2]. Improper marker attachment causes a violation of the rigid-body assumption, but the degree to which this impacts the QM is unknown. There are several other limitations. During the normalization process, errors in the rotational aspect of the cross-calibration transform are expected to lead to smaller errors in measured voluntary rotation[8]. Geometric distortion could be addressed by limiting the analysis to the central voxels.

Conclusion A rapid and relatively simple QA procedure determines the performance of the PMC setup. It promises pre-scan quality control to address potential issues. After further study, it could become a reliable indicator to track system calibration accuracy over time.

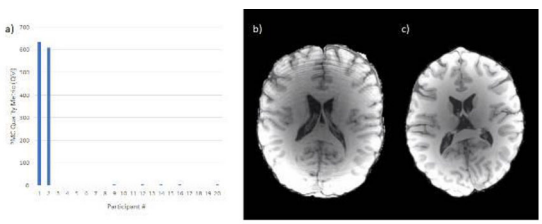

Fig. 1: Quality metrics for all twenty participants and exemplary fully-sampled 1mm T1w whole-brain (first echo). (a) Quality metric per participant. Axial slice at similar position from two different participants (b) #2 measured before and (c) #12 measured after correcting an error in the cross-calibration transform of the PMC system. Corresponding quality metrics for the acquisitions were (b) QM=609, (c) QM=5.9.

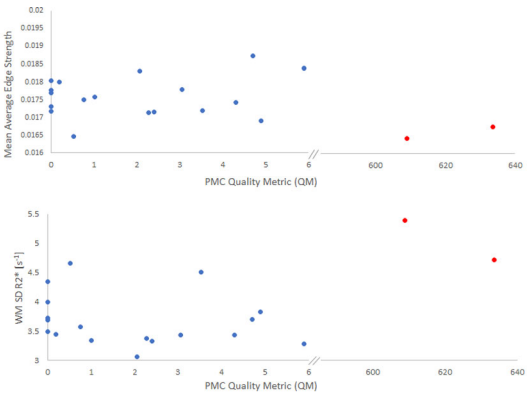

Fig. 2: Scatter plots of quality metric (QM) against image degradation metrics (top) average edge strength (lower=worse; brain masked, central 40 axial slices, first echo) and (bottom) R_2' standard deviation (higher=worse; measure in white matter mask) for fully-sampled 1mm whole-brain T1w images. Outliers when the PMC system transform was known to be erroneous are shown in red on split axes. The PMC QM metric is a good predictor of PMC failure and the consequent changes in both image quality metrics.

References

1. Maclaren et al., Magn Reson Med. 69, 621–636 (2013)
2. Aksoy et al., Magn Reson Med. 67, 1237–1251 (2012)
3. Vaculčiaková et al., Magn Reson Med. 88, 787–801 (2022)
4. Smith, Hum Brain Mapp. 17, 143–155 (2002)
5. Jenkinson M et al., Med Image Anal. 5, 143–156 (2001)
6. Todd et al., Neuroimage. 113, 1–12 (2015)
7. Castella et al., Magn Reson Med. 80, 2415–2426 (2018)
8. Smith et al., Proc ISMRM 25, 1296 (2017)

P106.
Predicting image quality from k-space aware motion detection

L. Bartsch[1,2], S. Röll[1], O. Speck[2]

[1]*Neoscan Solutions GmbH, Magdeburg, Germany;*
[2]*Otto von Guericke University, Magdeburg, Germany*

Introduction Patient motion in MR is ubiquitous, and many MR examinations contain significant motion artifacts [1]. However, correction and detection strategies are hardly available in daily clinical routines [3]. The lack of availability is particularly problematic for pediatric MR, where the patients cannot be considered cooperative [2]. This abstract proposes a live image quality prediction considering the k-space position and head motion tracking. Such a motion detection is an intermediate step between the advanced motion correction techniques used in research and the absence of motion detection in clinics.

Methods The MR image quality is influenced by the k-space position at which motion takes place. To simplify the description, a 2D Cartesian k-space sampling is presumed. Since the read direction is acquired fast compared to the camera's sampling rate, the k-space trajectory can be specified as a list of relative line indexes. The MRI scanner provides the current position l_{rel} to the detection software. As shown in Fig. 1, the trajectory is stored.

A camera-based head tracking provides the position change m(t") in 6° of freedom between consecutive camera frames. m(t")at the time t' is stored in the motion memory, as shown in Fig. 1. When using external tracking, the time series $l_{rel}(t)$ and m(t') are on different grids but can be correlated via Unix timestamps.

All m(t') are weighted and accumulated. The weights are derived from motion artifact simulations with Gallichan's "retroMoCoBox" [5]. A rapid translational motion of 1 mm in the x-direction in a brain image from [6] between two specific k-space lines is simulated. For quantification, the difference background energy (DBE) algorithm from Maclaren [4] is used. The algorithm uses the increase of background energy of the image with and without artifacts. The simulation is repeated for motions at different k-space lines, and so the resulting weight function shows the dependence of DBE to the motion line. Each m(t') is multiplied with a corresponding weight and then accumulated. The result is compared against a threshold.

The algorithm is tested by feeding the same motion pattern into the motion detection algorithm and simulation toolchain. A constant rotation across multiple k-space lines at different positions is simulated. The motion patterns are shown in Fig. 3a.

Results Figure 2 shows the weight function. The same motion leads to much more significant artifacts the closer it is to the k-space center. In Fig. 3, the same motion with different distances to the k-space center is simulated and shown as the blue and red case. The motion of the blue case is farther away from the center, the artifacts are less significant, and the motion detection algorithm returns no motion alarm. The motion of the red case is closer to the center, the artifacts are more significant, and motion is detected. The motion position is the same but with different amplitudes in the cyan and green examples. The smaller motion leads to more minor artifacts and no motion alarm (green), and the cyan case triggers a motion alarm.

Discussion The weight function shows that considering the k-space position of motion for motion detection is suitable because the result will be more meaningful concerning the image quality.

The weight function and hence the motion detection concept can be generalized to 3D k-space and arbitrary trajectories. For this purpose, the distance of each k-space point to the center can be considered. A remaining challenge is redundant k-space sampling. A solution would be to adapt the threshold or even the weight function depending on the sequence.

Conclusion With real time k-space aware motion detection, a practically relevant alarm can be triggered before the sequence is completed. Hence the acquisition may be repeated earlier or partially to reduce motion artifacts in clinical routine.

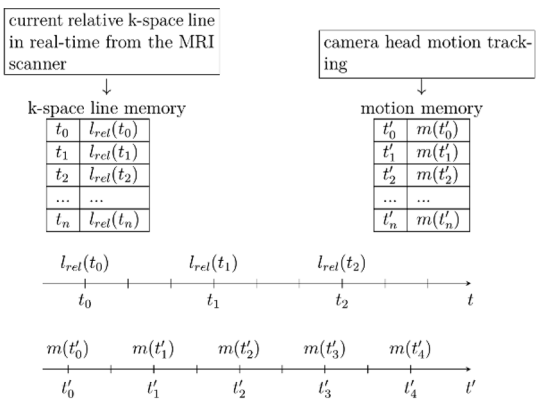

Fig. 1: Motion detection algorithm overview: the k-space line memory contains the so-far k-space trajectory received from the MRI scanner as a tuple of timestamps and relative k-space lines. The motion memory contains incremental displacements and corresponding timestamps. Based on the timestamps, each incremental displacement is a corresponding k-space line assigned.

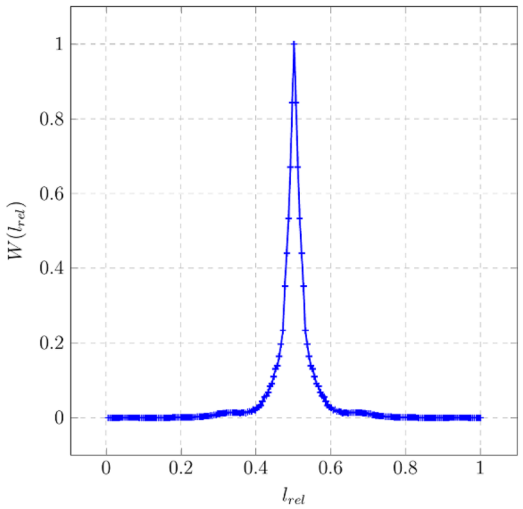

Fig. 2: The weight function shows a normalized quantification of motion artifacts depending on different relative k-space lines l_{rel}. The influence of a rapid translational 1mm motion in the k-space center, denoted with 0.5, on the resulting image quality is much bigger than in the outer regions.

References

[1] Andre et al.: Toward Quantifying the Prevalence, Severity, and Cost Associated With Patient Motion During Clinical MR Examinations. In: Journal of the American College of Radiology 12 (2015), Nr. 7, 689–695

[2] Harrington et al.: Strategies to perform magnetic resonance imaging in infants and young children without sedation. In: Pediatric Radiology 52 (2021), apr, Nr. 2, S. 374–381

[3] Godenschweger et al.: Motion correction in MRI of the brain. In: Physics in medicine & biology 61 (2016), Nr. 5, R32. https://www.ncbi.nlm.nih.gov/pmc/articles/PMC4930872/pdf/nihms796209.pdf

[4] Maclaren, Julian R.: Motion detection and correction in magnetic resonance imaging, Diss., 2007. https://ir.canterbury.ac.nz/bitstream/handle/10092/1220/thesis_fulltext.pdf

[5] Gallichan, Daniel: retroMoCoBox. Version: November 2022. https://github.com/dgallichan/retroMoCoBox

[6] Holmes et al.: Colin 27 Average Brain, Stereotaxic Registration Model, original 1998 version, 2015, aug. http://www.bic.mni.mcgill.ca/ServicesAtlases/Colin27—last access: 17.04.2023

P107.
Impact of coil polarization on the rf-induced heating worst-case selection of hip implants

M. Schwarz[1], Z. Ihsan[2], V. Hammersen[1], G. Schaefers[1,2]

[1]*MRi-STaR, Gelsenkirchen, Germany;*
[2]*MR:comp GmbH, Gelsenkirchen, Germany*

Introduction The electromagnetic (EM) radiation that is being utilized by magnetic resonance (MR)-scanners is not considered harmful by itself. However, a patient who uses passive metallic implants may experience adverse effects, such as radiofrequency (RF)-induced heating. This abstract will focus on the hazard caused by the RF-induced heating produced by an implant. The electromagnetic field is generated by an RF body coil. The RF body coil may have a linear polarized (LP) or circular polarized (CP) mode, which might have an influence on the assessment of the worst-case for multi-configuration passive medical devices. For this reason, the polarization mode should be specified in the MR safety label [1]. Currently, 1.5 T MR systems use the circular polarization [2]. However, the linear polarization mode is often used for laboratory RF-coils. In this contribution, the effect of linear and circular polarization on the worst-case selection for a hip implant in a 1.5 T MR system is investigated, in order to determine, if the difference between the laboratory and the clinical setup may lead to different worst-case scenarios.

Methods The EM-simulations are carried out at the frequency of 64 MHz, which is equivalent to the RF-exposure used in a Magnetic Resonance Imaging (MRI)-Scanners with a field strength of 1.5 T. The simulation platform Sim4Life FDTD (Finite Difference Time Domain) solver[3] was used to calculate the specific absorption rate (SAR) peak value in tissue. The simulation setup was taken from the design of the ASTM-standard F2182–19e2[4]. However, due to the size of the implant, the phantom gel height had to be increased to 120 mm. The investigated implant was a generic hip implant. The assembly of the implant consisted of a stem, a head, a cup liner, and a cup. The implant was placed 2 cm from the sidewall of the phantom and was oriented to the same orientation of the phantom. The product matrix of the generic hip implant is shown in TAB. 1.

In order to determine the overall worst-case, the strategy described in [5] was utilized. For this purpose, a total number of 7 simulations per polarization mode were performed. Once all simulations had been performed, the configuration producing the greatest peak local SAR would then be considered as the global worst-case. This procedure was then be repeated for the linear polarization mode.

Results The difference of the polarization mode is illustrated by the electric field (E-field) distribution in the phantom as shown in Fig. 1. The 14 planned simulations were performed, and the resulting peak local SAR values were plotted over the configuration number as shown in Fig. 2. From the simulation results, the same tendency of the SAR peak values are shown for both polarizations. Configuration was considered as the worst-case for both polarization modes.

Discussion During the various stages of the investigation, similar results were produced, despite the difference in polarization. As identical conclusions were obtained at all steps of the investigation, the selected worst-case was identical for both polarizations. While the different polarizations lead to different E-field distributions at the test area in the phantom, there are differences in the exposition, particular in the area close to the top and bottom of the phantom. As the selected type of implant has large dimensions, they reach the areas that experience a difference in the E-field exposure. However, these differences do not appear to be large enough to impact the selection of the worst-case implant.

Conclusion This study indicates that the difference of linear and circular polarization generated by the RF coils would not cause a different selection of worst-case for the hip implant system.

This work was solely focused on 1.5 T MR systems and was tested for a small product matrix of a hip system. We suggest that a similar investigation is performed for 3 T MR systems, since both MR systems are widely used. However they have a different operating frequency, which would generate a significant difference in the RF induced heating. In addition, different implant systems such as femoral nails and spinal systems, may be investigated as well.

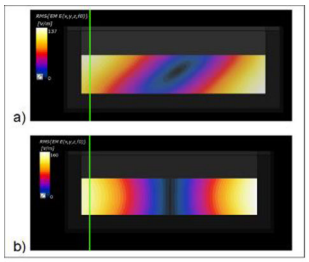

Fig. 1: E-field distribution within the phantom through the isocenter on the transversal slice. The green line marks the distance of the implants from the phantom wall; a) CP, b) LP

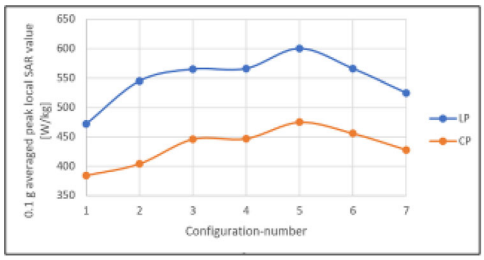

Fig. 2: Peak local SAR values for CP and LP of identical configurations

Implant component	Variable parameters	Number of options
Stem	Design	3
	Length	11
Head	Size	5
	Material	2
	Diameter	2
Cup liner	Size	5
	Diameter	2
Cup	Size	15
	Material	2

Tab. 1: Variable parameters of the generic hip system

References

[1] U.S. Department of Health and Human Services, FDA, Testing and Labeling Medical Devices for Safety in the Magnetic Resonance (MR) Environment, 2021

[2] "ISO/TS 10974:2018 Assessment of the safety of magnetic resonance imaging for patients with active implantable medical device," 2018.

[3] Zurich MedTech, Sim4Life V7.0, Zurich, Switzerland, 2022

[4] ASTM F2182-19e2: Standard Test Method for Measurement of Radio Frequency Induced Heating on or Near Passive Implants During Magnetic Resonance Imaging, West-Conshohocken, PA: ASTM International, 2019

[5] U.S. Department of Health and Human services, FDA, Assessment of Radiofrequency-Induced Heating in Magnetic Resonance (MR) Environment for Multi-Configuration Passive Medical Devices, 2016

P108.
Worst-case assessment of tissue damage due to magnetically induced force for multi configuration passive medical devices

Z. Ihsan[1], M. Schwarz[2], G. Schaefers[1,2]

[1]*MR:comp GmbH, Gelsenkirchen, Germany;*
[2]*MRi-STaR, Gelsenkirchen, Germany*

Introduction A magnetically induced displacement force on an implant can cause hazard to a patient inside an MRI scanner. In accordance with the current standard, the test procedure is performed through evaluation of the experimentally measured ratio of the magnetically induced (MI) force to the gravitational force acting on the tested device [1]. A rational approach is generally used to select the worst-case scenario for multi-configuration passive medical devices by considering the largest mass and the highest permeability. However, the geometry effects are often omitted in the analysis. Moreover, various possible superpositions of the gravitational force and the MI force are often neglected. This work is a subsequent study of the tissue damage investigation due to the MI force [2]. The MI force may cause pain to the patient due to stress in the tissue surrounding the implant, which might become comparable to the hazard due to the RF-induced heating. The stress in the biological tissue can be concentrated at a small location which is equivalent to the temperature hot spot. The calculated stress in the tissue could be used for selecting the worst-case, as a numerical approach has been implemented to evaluate the worst-case in the RF-heating. In this contribution, a numerical framework to select the worst-case configuration due to the MI force is presented.

Methods The computations were performed by employing both static and mechanic solvers of the simulation platform 3DS CST Studio Suite 2019 (Darmstadt, Germany). The static magnetic field was generated by a cylindrical magnet modelled by using the static solver. The force density calculated from the interaction of the induced magnetic field was imported as the field source of the mechanic solver. Secondly, the implantable clip surrounded by tissue was generated in the mechanic solver as described in Fig. 1, where a displacement boundary was defined at the bottom of the tissue.

The scenario for this investigation is a product matrix consisting of eight clip-configurations as given in Tab. 1. These clips are available in two different geometries, as shown in Fig. 2, where the sharp clip sharp has a sharper tip than the standard clip provided in two predefined relatives permeabilities μ_r. They can be oriented into two orientations: in parallel to the magnetic field vector B_0 (horizontal) and perpendicular to B_0 (vertical). Four configurations under test (C_{test}) were selected to find the worst-case by changing the parameter in the product matrix stepwise. First, the standard and the sharp geometry were compared to evaluate the worst-case geometry while by keeping the same orientation and μ_r. Then, the worst-case geometry was selected for the following configuration to find the worst-case orientation. Finally, the effect of μ_r was tested by using the worst-case geometry and orientation.

Result The simulation results of the C_{test} are summarized in Tab. 2. The peak value of the first principal stress in the tissue was calculated in three steps to determine the worst-case for each parameter. First,

the sharp clip was found as the worst-case geometry by comparing configuration 2 and 6. Secondly, the horizontal clip was obtained as the worst-case orientation by comparing configuration 5 and 6. Finally, $\mu_r = 500$ is evaluated as the worst-case μ_r by comparing configuration 6 and 8. The worst-case configuration, indicated by the highest stress peak value, is denoted by configuration 6. Furthermore, the stress distribution in the tissue for the worst-case configuration is illustrated in Fig. 3, where the "stress hot-spot" was found at the surrounding tips of the clip.

Discussion A stepwise simulation strategy has been performed to find the worst-case configuration and this strategy can decrease the simulation effort (number) by a factor of 50% instead of simulating all configurations. The sharp clip with the higher magnetic permeability and parallel the magnetic field vector was found to generate the highest stress in the tissue. This worst-case configuration agrees with the rational approach. By comparing the stress to the tensile stress, C_{test} 1 to 3 were assessed to generate a displacement and may deform the tissue.

Conclusion A framework for assessing the worst-case tissue damage has been demonstrated by evaluating the stress in the tissue. The worst-case scenario analyzed in the simulations confirmed the rational approach. The next investigation will address validation of the MI-force resulting from the simulation with the MI force measured in the standard laboratory test.

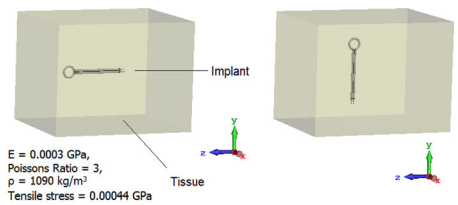

Fig. 1: Model of clip surrounded by the tissue, horizontal (left) and vertical (right); E = modulus elasticity, ρ = mass density

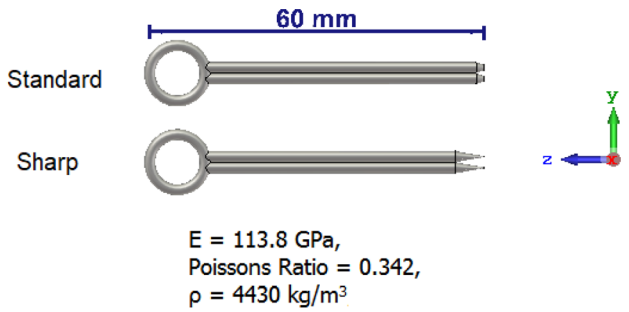

Fig. 2: Geometries of the clip

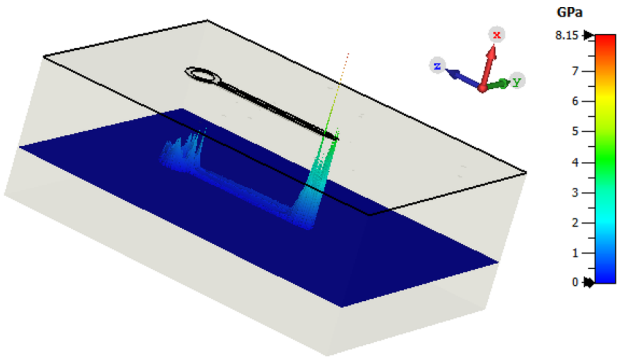

Fig. 3: The carpet plot for the stress distribution in the tissue of configuration 6 on the coronal slice

Configuration	Parameter		
	Geometry	Orientation	μ_r
1	Standard	Vertical	500
2	Standard	Horizontal	500
3	Standard	Vertical	1.004
4	Standard	Horizontal	1.004
5	Sharp	Vertical	500
6	Sharp	Horizontal	500
7	Sharp	Vertical	1.004
8	Sharp	Horizontal	1.004

Tab. 1: The product matrix of generic clips

Step	C_{test}	Configuration	Parameter			Stress (GPa)
			Geometry	Orientation	μ_r	
1	1	2	*Standard*	Horizontal	500	2.7
	2	6	*Sharp*	Horizontal	500	**8.15**
2	3	5	Sharp	*Vertical*	500	0.27
3	4	8	Sharp	Horizontal	*1.0004*	0.00012

Tab. 2: Stress peak values of C_{test}

References

[1] American Society for Testing and Materials. Standard Test Method for Measurement of Magnetically Induced Displacement Force on Medical Devices in the Magnetic Resonance Environment, 2015

[2] Numerical Simulation of Tissue Damage Due to Magnetically Induced Force for Multi Configuration Passive Medical Devices, ISMRM Conference, 2022

P109.
Influence of three substances used for the preservation of food and MRI phantoms on water relaxation

I. Dieterle[1,2], V. Fritz[2], A. Fischer[2], P. Martirosian[2], F. Schick[2]

[1]*University Tübingen, Tübingen, Germany;*
[2]*University Hospital Tübingen, Section on Experimental Radiology, Tübingen, Germany*

Introduction MRI is a non-invasive method and one of the most used imaging methods for medical diagnosis. For optimizing the MRI sequences and measurement protocols, there is a need of phantoms with well-defined characteristics mimicking those of human tissues. In order to ensure that the phantoms do not change over time due to mould or bacterial decomposition of organic substances it is necessary to add preservatives to the phantoms. A thorough examination of the MRI-properties of these preservatives seems necessary. This contribution reports on examinations of three preservatives of different material classes regarding their influence on relaxation times of the solvent water.

Methods The following chemical substances were examined: citric acid, sodium sulfite and sodium benzoate. The aqueous solutions used for the experiments were manufactured with demineralised water and the preservatives.

The concentration of each preservative was varied between 0 and 3% and for citric acid additionally between 5 and 20%. Each concentration was prepared in a sample tube (50 ml) and a series of concentrations between 0 and 3% (with steps of 0.5%) was prepared for every preservative. Afterwards the steps were adjusted for each preservative in order to obtain more data points in the non-linear part of the curve.

The measurements were performed using a 3.0 T MRI. For the relaxation time T1 an inversion-recovery FSE sequence and for assessment of T2 a Call-Purcell-Meiboom-Gill-sequence were used. Each sample of a measurement series had the same temperature, but this temperature differed slightly between different runs between 17.7 and 20.6 °C.

Results The measurements of the relaxation rates R2 (for 0–3%) of the preservatives (Fig. 1) show a linear increase for R2 for rising concentrations for each preservative in the concentration range of 0.5–3%. The highest T2 effect for the mentioned concentration range was found for sodium benzoate with 0.016 1/s%, the smallest for citric acid with 0.004 1/s%. Remarkably, for low concentrations of 0.0 to 0.5% a steep decay of 16.1% respectively 23.8% was found for T2 relaxivity in citric acid and sodium sulfite. Sodium benzoate has its maximum at 0.02% and its minimum at 0.5%.

We also examined the linear dependency for higher concentrations of citric acid (Fig. 2). The slight offset in the data probably derives from a difference of roughly 0.5 °C in temperature between the two measurement runs. Because of the curve progression for small concentrations, a solution with a concentration of roughly 14–16% citric acid has the same R2 as demineralised water.

The relaxation rates R1 of citric acid and sodium benzoate are depicted in Fig. 3. Both substances show a linear dependency with a gradient of 0.005 1/s%. In contrast, R1 of sodium sulfite has a drop of 11.5% at 0–0.05% whereas for higher concentrations (0.05–3%) a linear dependency of R1 on the concentration is shown with a gradient of 0.007 1/s%.

Conclusion In contrast to other substances used in phantoms (like agarose, nickel or Gd-DTPA), the preservatives show a relatively small influence on the relaxation times. The preservatives seem to have a linear influence on the relaxation times for concentration between 0.5 and 3% (and higher concentrations). It is very interesting that for very low concentrations ranging from 0.0 to 0.5% the dependency is not linear and the relaxation rate was found even smaller than that of pure water. As a result of the measurement data in Fig. 2, preservative concentrations can be chosen in a way that relaxation time T2 remain unchanged compared with pure water.

With the measurements a proper use of substances for preservation of phantoms is intended. The tested preservatives are probably enabling us to produce more stable and therefore more cost-efficient phantoms. These phantoms can be built easily and can be customized to fit the desired characteristics.

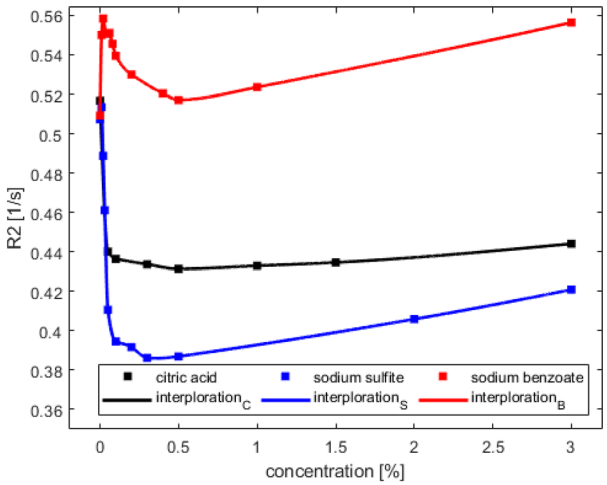

Fig. 1: Relaxation rate R2 for different concentrations of tree preservatives

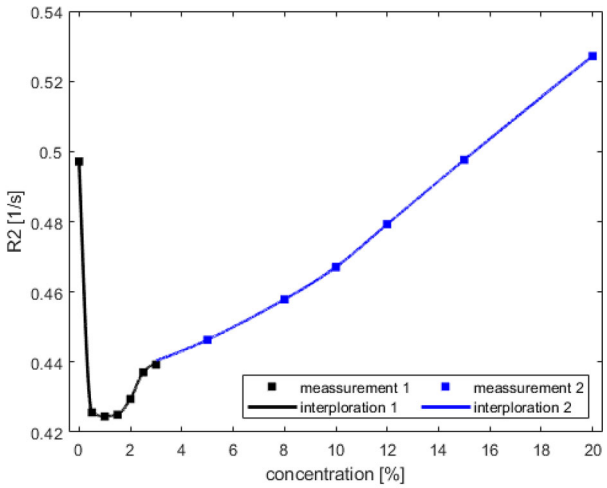

Fig. 2: Relaxation rate R2 for citric acid for concentrations ranging from 0 to 20%

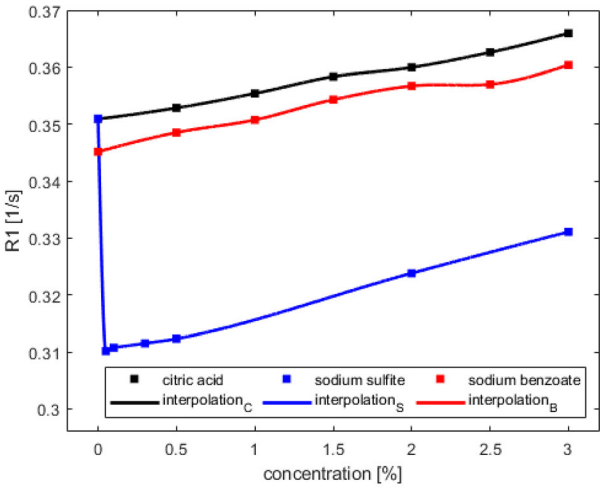

Fig. 3: Relaxation rate R1 for different concentration of tree preservatives

References

Hattori K. et al., Development of MRI phantom equivalent u human tissues for 3.0-T MRI, 2013

Woletz M. et al., Technical Note: Human tissue-equivalent MRI phantom preparation for 3 and 7 Tesla, 2021

Tofts P.S. et al., Ni-DTPA doped agarose gel- a phantom material for Gd-DTPA enhancement measurements, 1992

Lavdas I. et al., A Phantom for Diffusion-Weighted MRI, 2013

P110.
Multiple Labeling PCASL Imaging of the Lung: Preliminary results of an ongoing study

P. Martirosian[1], L. Ostreicher[2], M. Munz[2], R. Pohmann[3], M. Schwartz[1], T. Küstner[2], C. Liang[2], F. Schick[1], F. Seith[2]

1University Hospital of Tübingen, Section on Experimental Radiology, Tübingen, Germany;
[2]University Hospital of Tübingen, Department of Diagnostic and Interventional Radiology, Tübingen, Germany;
[3]Max Planck Institute for Biological Cybernetics, High-Field MR Center, Tübingen, Germany

Introduction Assessment of regional blood flow in the lungs is important for clinical diagnosis of pulmonary diseases. Arterial spin labeling (ASL) techniques have been used for non-invasive quantitaive evaluation of perfusion in the lung.[1,2] We recently demonstrated that ECG triggered pseudo-continuous arterial spin labeling (PCASL) with bSSFP readout provides high quality perfusion images of the lungs in patients under free breathing condition.[3] Nonetheless, although perfusion deficits caused by acute pulmonary embolism can be detected reliably, the perfusion signal of the parenchyma is dependent on the individual cardiac cycle and a further increase of the perfusion signal is helpful for the use in clinical routine. Here, we present the first results of a new PCASL approach using multiple ECG-triggered labeling in several preceding cardiac cycles to measure the temporal and spatial characteristics of pulmonary blood flow.

Methods Four healthy volunteers (two male) were examined on a 1.5 T MR scanner using a PCASL sequence with ECG-triggered multiple labeling pulses and a bSSFP readout. Twenty measurements with varying number of labeling pulses (NLs = 1, 2, 3, 4) and post labeling delays (PLDs = 200, 400, 600, 800, 1000 ms) were performed. The labeling plane was placed nearly perpendicular to the pulmonary trunk (Fig. 1A) and applied during the systolic period by ECG-triggering. A bSSFP readout was played once after series of labeling pulses (Fig. 1B). Each measurement was performed with 8 label/control image pairs with a repetition delay of $\geq$ 2 s under free breathing condition. A proton-density weighted bSSFP image was acquired at the start of each measurement. Depending on NL, PLD and cardiac cycle, the measurement time was about 1–2 min. The measurement parameters are listed in Table 1. The PCASL images were registered non-rigidly using an optical flow-based image registration approach.[4] For evaluation of the perfusion signal in the lung parenchyma, the regions of interest (ROIs) were placed in left and right lungs, carefully avoiding large vessels (Fig. 3A).

Results PCASL measurements of the lungs with multiple labeling were successfully performed in all four subjects. First, the perfusion signal of the lung parenchyma increases with increasing number of labeling pulses for all measured PLDs: the perfusion signal at NL = 3 is approx. twice as high as the standard PCASL measurements with NL = 1 and PLD = 1000 ms. Second, at short PLDs of 200 and 400 ms, both pulmonary arteries and lung parenchyma show high signal. Finally, with increasing number of labelling pulses, the parenchymal perfusion signal seems to be less sensitive to changes in PLD. The perfusion-weighted images of one subject are shown in Fig. 2 and corresponding signal evaluations in the parenchymal ROIs (mean) are depicted in Fig. 3B.

Discussion Based on the preliminary results of our study, application of multiple labeling pulse trains in several preceding cardiac cycles significantly increase the perfusion signal in lung parenchyma and pulmonary arteries compared with the conventional PCASL sequence with only one labeling pulse in the previous heartbeat. The proposed strategy could reduce the sensitivity to PLD changes and cardiac cycle variations and further increase the robustness of the method for future application in clinical practice.

Conclusion The ECG-triggered multiple labeling PCASL bSSFP sequence was able to provide a significantly higher perfusion signal of the lung parenchyma and pulmonary arteries than the commonly used measurements with only one labeling pulse.

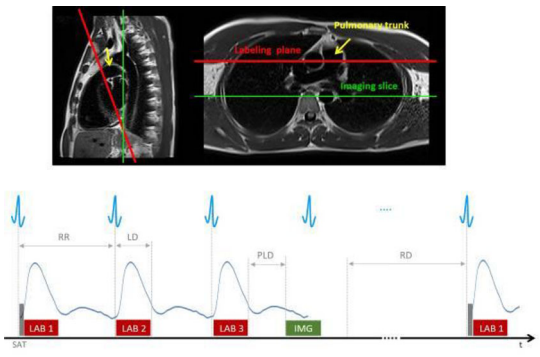

Fig. 1: (A) Labeling plane was positioned perpendicular to pulmonary trunk (red) and a coronal image (green) was acquired. **(B)** Schema of PCASL sequence with series of three ECG-triggered labeling pulse trains (LAB 1-3) and bSSFP readout (IMG). SAT: saturation pulse; RR: cardiac cycle; LD: labeling duration; PLD: post-labeling delay; RD: repetition delay.

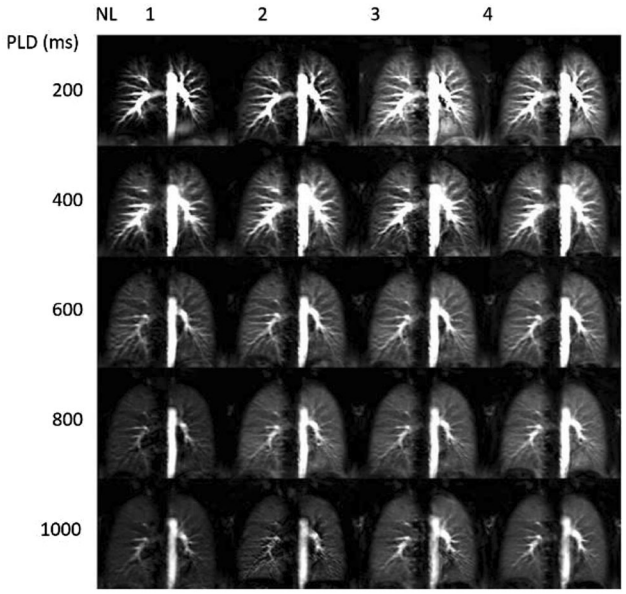

Fig. 2: PCASL perfusion-weighted images of the lungs of a healthy subject: the number of labeling (NL) pulses were varied from 1 to 4 (left to right) and the post-labeling delay (PLD) was changed from 200 to 1000 ms (top to bottom).

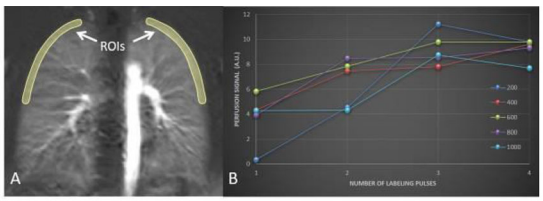

Fig. 3: (A) Perfusion-weighted image of the lung acquired at NL=3 and PLD=800 ms. Regions of interest (ROIs) were placed in the parenchyma of the left and right lung. **(B)** The perfusion signal of the lung parenchyma (mean of ROIs) increases up to NL of 3. With increasing NL, the perfusion signal is less sensitive to changes in PLD.

Table 1: Measurement parameters of multiple labelling PCASL sequence

Imaging		Labeling	
TR/TE	2.1/0.9 ms	Post labeling delay	200-1000 ms
Flip angle	70°	Num. labeling pulses	1-4
Bandwidth	1260 Hz/Pixel	Tag duration	400 ms
FoV	480x480 mm^2	Labeling flip angle	25°
Matrix size	144x192	Gradient strength	7 mT/m
In-plane resolution	3.3x2.5 mm^2	Label/Control scans	8/8
Slice thickness	20 mm	Repetition delay	2000 ms

References

1. Bolar DS, Levin DL, Hopkins SR, et al. Quantification of Regional Pulmonary Blood Flow Using ASL-FAIRER. Magn Reson Med 2006;55:1308–17
2. Martirosian P, Boss A, Fenchel M, et al. Quantitative lung perfusion mapping at 0.2 T using FAIR True-FISP MRI. Magn Reson Med 2006;55:1065–1074.
3. Seith F, Pohmann R, Schwartz M, et al. Imaging Pulmonary Blood Flow Using Pseudocontinuous Arterial Spin Labeling (PCASL) With Balanced Steady-State Free-Precession (bSSFP) Readout at 1.5 T. J Magn Reson Imaging. 2020;52:1767–82.
4. Gilliam C, Küstner T, Blu T. 3D motion flow estimation using local all-pass filters. 2016 IEEE 13th International Symposium on Biomedical Imaging (ISBI), 2016; 282–285.

P111.
Comparison of the spatial performance of phase-based and image-based methods in MREPT

P. Soullié[1,2], F. Odille[1,2], J. Felblinger[1,2]

[1]*IADI-INSERM U1254, Nancy, France;*
[2]*University of Lorraine, Nancy, France*

Introduction: Many methods of reconstruction of electrical properties (MREPT) at the Larmor frequency in MRI have been proposed in the last decade [1]. However, reconstruction methods based on partial differential equations have primarily started to be studied systematically because they are easier to set up and use with common clinical data. These last methods focus essentially on the reconstruction of conductivity (S/m) from phase images, from which the RF component is extracted. Another class of methods now referred to as "image-based" methods proposes the direct use of complex MRI images to reconstruct conductivity. Difficulties in obtaining reliable images and accurate quantitative measurements include, in the case of phase or image-based methods, strong assumptions about the curvature of the data that depend on the geometry and position of the imaged object. The purpose of this study is to evaluate the superiority of either class of methods by using a homogeneous phantom placed at different locations in the MRI bore.

Methods: Phantom: Our phantom was prepared from water, with the addition of NaCl (10 g/L) and agarose (1.5%). The reference conductivity (1.43 S/m–22 °C) was measured with a dielectric assessment kit (DAK 12, SPEAG, Zurich, Switzerland). The phantom was placed orthogonally to the main magnetic field and coronal/axial views were used in reconstructions. MRI: Imaging studies were performed on a 3 T MAGNETOM Prisma (Siemens Healthcare, Erlangen, Germany). Standard QBC was used for transmission and a 18-channel phased array torso coil was used for reception. 3D magnitude and phase images for six different spatial positions (Fig. 1) were acquired using a UTE Spiral VIBE sequence prototype (TE = 50 µs, TR = 5 ms, FA = 1°, Size = 1.5 mm). The phantom was scanned while maintaining the same position in all spatial configurations. We used the complex combination obtained using the vendor"s reference-based adaptive coil combine approach. MREPT: We compared two reconstruction methods in MREPT. One based on phase maps from UTE images [3], and the other based on the total complex signal from the same images [4]. For each volume, we reconstructed the conductivity for the median coronal slice as well as for the median axial slice. A Savitzky-Golay type pre-filtering preceded each reconstruction pipeline ([5 5 5]) and a Gaussian post-filtering (SD: 1.5) was used on generated maps. The regularization parameters used for each method are respectively equal to 0.02 and 0.02i.

Results: From a qualitative point of view, the conductivity maps obtained from the phase-based method (Fig. 2) show some homogeneity despite visible value errors on the edges of the ROI. The same homogeneity is found for the reconstruction from the image-based method (Fig. 3) but the conductivity has a more consistent general visual aspect depending on the position, and there are less reconstruction artifacts on the edges. In all cases, the axial views seem to show more variation. The numerical comparison table (Fig. 2) between the two methods shows the average conductivity measured

the phantom. Overall, we observe that the reconstruction method based on complex UTE images seems to perform slightly better in positions far from the center of the scanner (bold values) because values are closer to the ground truth. The results in terms of Sharpness Index, at the bottom of the same table, also show stronger discontinuities in the conductivity maps reconstructed from the phase.

Discussion: Overall, we do not observe a huge difference between the two types of reconstruction even if the balance tilts slightly towards image-based reconstruction. This was not self-evident despite everything because simulation studies had shown that the assumptions made in the phase-based methods are "stronger" in terms of requirements on the shape of the data, in particular when one is away from the center of the MRI tunnel [5]. One of the reasons why these conclusions are moderate could be that the reconstruction of the data by the vendor uses a correction of distortion, which naturally homogenizes the contrast and makes sure to optimize the combination of antennas to have an optimal signal in any what spatial position. We nevertheless insist on the fact that the image-based methods are more versatile in that they also allow the reconstruction of the permittivity, which we have not discussed here.

Conclusion: We tested the capacities of two classes of reconstruction methods in MREPT. These studies are important because they make it possible to advance arguments on the reliability of the quantitative estimation of the dielectric parameters in a clinical environment, where the imaged subjects have variable and asymmetrical body geometries.

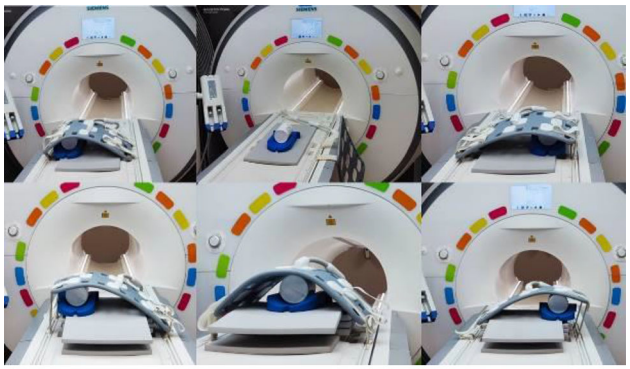

Fig.1 : The 6 spatial positions for the homogeneous cylindrical phantom

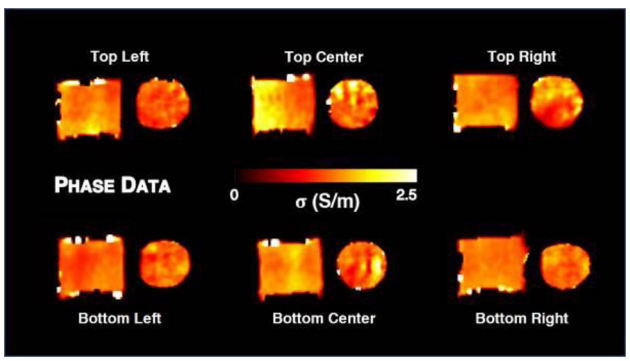

Fig. 2 : The reconstruction results for the phase-based method (finite-difference scheme, λ = 0.02)

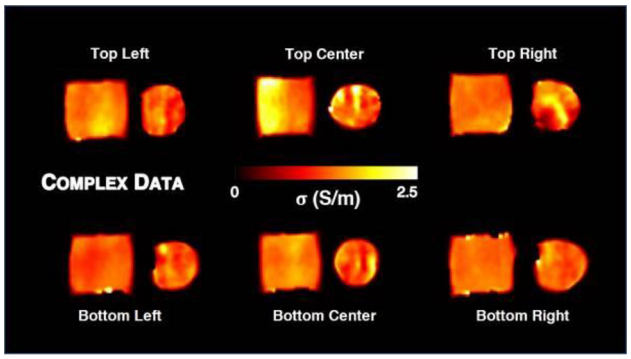

Fig. 3 : The reconstruction results for the phase-based method (finite-difference scheme, λ = 0.02i)

		Bottom Left	Bottom Center	Bottom Right	Top Left	Top Center	Top Right
GB	σ (S/m)	1.27 ± 0.14	1.50 ± 0.14	**1.36 ± 0.18**	1.43 ± 0.13	**1.59 ± 0.24**	1.50 ± 0.10
GIB		**1.28 ± 0.17**	**1.44 ± 0.10**	1.31 ± 0.09	**1.45 ± 0.14**	1.62 ± 0.26	**1.38 ± 0.08**
GB	SI	342	1621	1148	2003	1248	478
GIB		**201**	**105**	**442**	**147**	**413**	**217**

Fig. 4 : Quantitative comparison table of reconstructed conductivity for each position and for each method. The Sharpness Index is used to assess the inhomogeneity of conductivity maps.

References: [1] Leijsen et al. *Diagnostics*, 2021 [2] Lee et al., *IEEE Trans. Med. Imaging*, 2015 [3] Gurler et al., *Magn. Reson.*, 2017 [4] Soullié et al., *Magn. Reson.* 2021 [5] Katscher et al., *Comput. Math. Methods Med.*, 2013.

P112.
Comparison of non-invasive MR and ultrasound techniques for the detection of steatosis in non-alcoholic fatty liver disease patients

M. Hajek[1], H. Gottfriedova[2], F. Dolecek[3], E. Sticova[4], O. Snizkova[5], M. Dezortová[1], D. Pajuelo[1], M. Burian[1], P. Sedivy[1]

[1]*Institute for Clinical and Experimental Medicine, MR-Unit, Dept. Diagnostic and Interventional Radiology, Prague, Czech Republic;*
[2]*Institute for Clinical and Experimental Medicine, Dept. Hepatogastroenterology, Prague, Czech Republic;*
[3]*Horovice Hospital, Department of Surgery, Horovice, Czech Republic;*
[4]*Institute for Clinical and Experimental Medicine, Clinical and Transplant Pathology Centre, Prague, Czech Republic;*
[5]*UNILABS, Department of Pathology, Prague, Czech Republic*

Introduction Detecting non-alcoholic fatty liver disease (NAFLD) requires determining steatosis. Biopsy is invasive and impractical for screening, so non-invasive methods like ultrasonography, MR imaging (MRI), and MR spectroscopy (MRS) are used [1]. This study compared histology with MR spectroscopy, MR imaging, and new quantitative ultrasound (QUS) methods based on shear wave measurement of sound speed and attenuation coefficient in 60 subjects with biopsy-proven steatosis.

Methods

Subjects Sixty patients with indicated liver biopsy underwent clinical examination, including ultrasound and MR examinations. The experimental protocol was approved by the local ethics committees. All subjects provided their written informed consent prior to participation in the study.

Ultrasound We used an ultrasound machine SuperSonic® MACH™ 30 ultrasound system (Hologic, USA) with new QUS techniques [2] for the measurement of sound speed (SSp.PLUS; [m/s]) and attenuation coefficient (Att.PLUS; [dB/cm/MHz]). We followed WFUMB and EFSUMB guidelines [3] while scanning the right liver lobe in the supine position. All US examinations were performed by experienced physician.

MR imaging and spectroscopy MR examination was performed in the supine position using a VIDA 3 T MR system (Siemens, Erlangen, Germany) equipped with an eight-channel surface body array coil. The standard Siemens LiverLab protocol [4] was used to evaluate liver fat content in all subjects. The protocol included a HASTE sequence as a standard localizer sequence; proton density fat fraction (PDFF) was measured by Dixon sequences from a small region of interest (roi) and from whole liver (VIBE roi and VIBE all), and fat fraction (FF) was obtained by a HISTO MR spectroscopic sequence with a volume of interest of 40 × 30 × 25 mm.

Histology Liver biopsies obtained from the right lobe were used to determine hepatic steatosis. Hematoxylin–eosin staining was used to calculate the percentage of hepatocytes containing macrovesicular fat droplets. Samples were classified according to the histological scoring system based on the percentage of fat droplets as S0 (none; $< 5\%$ fat droplets), S1 (mild; 5–33% fat droplets), S2 (moderate; 33–66% fat droplets), and S3 (severe; $> 66\%$ fat droplets) according to the NAFLD histological scoring system. Two histopathologists trained in liver pathology performed histological analysis of samples that were collected no more than 7 days before the MR or ultrasound examination.

Results Histology results were used to group patients by steatosis level (S0-S3) and compared with QUS and MR steatosis results. ROC curves and AUC values were calculated to find the best cut points for two classes of subjects: a) no steatosis (S0) vs steatosis (S1 + S2 + S3), and b) mild steatosis (S0 + S1) vs severe steatosis (S2 + S3). The results are shown in Table 1. The MR parameters had excellent AUC values and higher sensitivity and specificity for both classes. The QUS parameters had good or fair AUC values, but lower specificity and sensitivity.

The comparison of MR and US methods with histology was performed using correlation analysis. Figure 1 shows a very good correlation between the histology and MR methods (Spearman $r > 0.89$), while the correlation between QUS parameters and histology is slightly lower (Spearman $r < 0.68$).

Discussion The literature [5] suggests that MR-based determination of steatosis is more effective than controlled attenuated parameter (CAP) from transient elastography in detecting and classifying hepatic steatosis in patients with NAFLD. Our comparison of QUS and MR data using ROC and correlation analyses also indicates that the performance of the MR method is superior to the speed of sound and attenuation coefficient obtained by the 2D shear wave technique for the characterization of steatosis. The results suggest that the sound speed parameter may be a more useful tool for identifying steatosis in NAFLD patients than the attenuation coefficient.

Conclusion The use of QUS is more suitable for the screening assessment of steatosis, while quantitative MRS and MRI should be preferred for clinical studies where accurate non-invasive determination of steatosis is needed.

Acknowledgement *The study was supported by the Ministry of Health of the Czech Republic-DRO ("Institute for Clinical and Experimental Medicine-IKEM, IN 00023001"), and by the project National Institute for Research of Metabolic and Cardiovascular Diseases (Programme EXCELES, ID Project No. LX22NPO5104)—Funded by the European Union-Next Generation EU.*

STEATOSIS grade	parameter	ATT	Sound Speed		HISTO	VIBE roi	VIBE all
S(x)		[dB/cm/MHz]	[m/s]		%	%	%
(S0+S1) vs (S2+S3)	AUC	0.9241	0.8802		0.9986	0.9864	0.9933
	Std. Error	0.0351	0.04695		0.002296	0.01135	0.006794
	P value	<0.0001	<0.0001		<0.0001	<0.0001	<0.0001
	Youden index %	78.1	68.6		97.1	94.3	90.0
	CUT point	>0.46	<1518		>11.77	>9.2	>9.75
	sensitivity %	100	90.5		100	100	100
	specificity %	78.1	78.1		97.1	94.3	90.0
(S0)+(S1+S2+S3)	AUC	0.7743	0.8048		0.979	0.9581	0.9438
	Std. Error	0.06651	0.06971		0.01769	0.02538	0.03046
	P value	<0.0023	<0.0007		<0.0001	<0.0001	<0.0001
	Youden index %	47.6	59.0		90.5	77.1	79.0
	CUT point	>0.515	<1531		>2.86	>4.2	>5.15
	sensitivity %	54.3	85.7		97.1	77.1	85.7
	specificity %	93.3	73.3		93.3	100	93.3

The area under the ROC curve (AUC) results were categorized as excellent for AUC values between 0.9-1, good for AUC values between 0.8-0.9, fair for AUC values between 0.7-0.8, poor for AUC values between 0.6-0.7, and failed for AUC values between 0.5-0.6.

Fig. 1. Spearman correlation table of experimental parameters

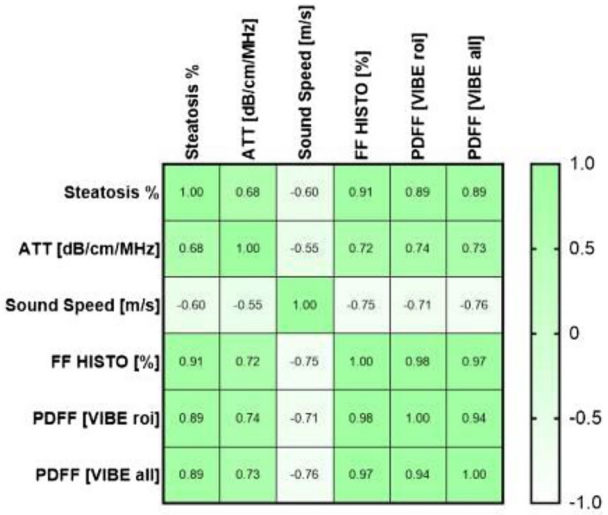

Table 1:****

References

[1] Park CC, et al. (2017) Gastroenterology **152**(3): 598–607.e592
[2] Popa A, et al. (2021) Diagnostics (Basel) **11**(5)
[3] Ferraioli G, et al. (2021) Ultrasound Med Biol **47**(10): 2803–2820
[4] Sellers R. (2016) "MR LIver lab." MAGNETOM Flash **66**(3): 39–43
[5] Runge JH, et al. (2018) Radiology **286**(2): 547–556

P113.
3D dual flip-angle T1 mapping for liver imaging: Comparison with look-locker T1 mapping

C. Kremser[1], M. Plaikner[1], B. Henninger[1]

[1]*Medical University of Innsbruck, Dept. of Radiology, Innsbruck, Austria*

Introduction Currently there is an increased interest in the quantification of hepatic T1 values, which were suggested as biomarker for liver fibrosis or inflammation (1). Available methods for hepatic T1 estimation are frequently based on a 2D Look-Locker method (2, 3) which is widely used for cardiac imaging, or alternatively on a 3D variable flip-angle approach (4). It was the purpose of this work to compare hepatic T1 values obtained by a 2D Look-Locker sequence and a commercially available 3D dual flip-angle sequence, which allows full liver coverage with one single breath-hold.

Methods In 62 patients, who underwent 1.5 T MRI (MAGNETOM AvantoFit, Siemens, Germany) due to a clinical suspicion of diffuse liver disease, two different T1 mapping sequences were performed in addition to the routine protocol, which included a multi-echo gradient-echo DIXON sequence for iron and fat quantification. The first T1 mapping sequence (2D Look-Locker like) is based on an inversion recovery snapshot FLASH sequence (IRSFL) using a low flip-angle approach (5), which allows accurate T1 quantification over a wide range of T1 values and is insensitive to B1 inhomogeneities. Details of sequence implementation and T1 calculation have been published elsewhere (6). The second T1 quantification method was a commercial 3D dual flip-angle VIBE sequence (T1Map_vibe), which was preceded by a 3D B1 mapping sequence for B1-correction. T1 calculation and B1 correction were performed automatically during image calculation. Both sequences were acquired in breath hold, whereby the IRSFL sequence only allows the acquisition of up to four slices during one breath-hold, while the T1Map_vibe sequence allows the acquisition of a full 3D volume covering the whole liver. Hepatic T1 values were obtained for both sequences at corresponding slice positions using manually co-registered ROIs. Agreement between both sequences was determined by Bland–Altman (BA) analysis and the calculation of Lin"s concordance correlation coefficient (CCC).

Results For all patients the BA plot (Fig. 1) shows a highly significant ($p < 0.001$) bias of 142.3 ms with limits of agreement (LoA) of − 73.0 ms and 357.6 ms, respectively. The CCC of 0.38 (95% CI 0.26–0.49) showed rather poor agreement. In addition, the BA plot also indicates a systematic effect for the difference between T1Map_vibe and IRSFL for increasing T1 values. By comparing only patients without hepatic iron overload and without fatty liver (n = 21, Fig. 2), the bias and LoA between both sequences were decreased (bias: 73.5 ms; LoA: − 46.4 ms and 193.3 ms) but the bias was still highly significant ($p < 0.001$). Without hepatic iron overload and without fatty liver the CCC of 0.66 indicated increased agreement.

Discussion The T1Map_vibe sequence showed significantly higher hepatic T1 values compared to the reference IRSFL sequence resulting in poor to moderate agreement. The results indicate that iron and fat have to be considered as confounding factors, amongst others.

Conclusion The application of the 3D T1Map_vibe sequence for hepatic imaging still necessitates further study of these confounding factors.

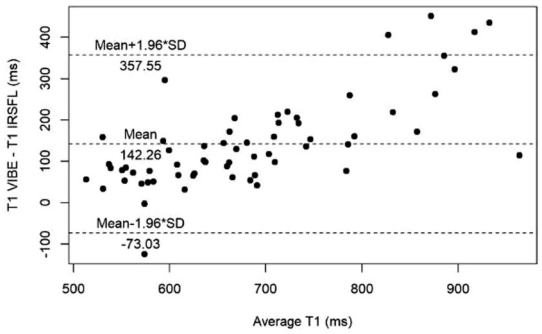

Fig. 1: The Bland-Altman plot for all patients shows a significant (p<0.001) bias of 142.3ms with a rather large standard deviation of 109.8ms between T1Map_vibe and IRSFL and also indicates a systematic effect for increasing T1 values.

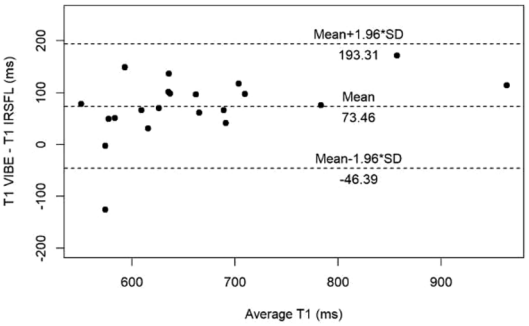

Fig. 2: For patients without iron overload and without fatty liver (n=21) the Bland-Altman plot still shows a significant (p<0.001) bias of 73.5ms with a standard deviation of 61.1ms. Interestingly the systematic effect for increasing T1 values is not seen for these patients.

References

[1] von Ulmenstein S, et al. Abdominal Radiol 2022; 47: 3746–3757
[2] Look DC, et al. Rev. Sci. Instrum. 1970; 41: 250–251
[3] Hoffman DH, et al. Abdominal Radiol 2020; 45: 692–700
[4] Brooks JA, et al. JMRI 1999; 9: 163–171
[5] Deichmann R, et al. JMR 1992: 96:608–612
[6] Kremser C, et al. JMRI 2007: 26:662–671

P114.
A novel MRI-based measure of liver function to predict post-hepatectomy liver failure: Comparison to ICG and bilirubin

A. Al-Mutairi[1], S. Patel[2,3], C. Konstantinou[2,3], D. Shelley[4], M. Saysell[4], L. Cash[4], M. Elsharif[3], A. Ghoneima[3], M. Attia[3], R. Prasad[3], M. Gilthorpe[5], A. Guthrie[3], I. Rowe[6], D. Vijayanand[3], R. Feltbower[2], D. Treanor[6], D. Wilson[7], L. Roberts[2], L. White[3], C. Moriarty[3], P. Armitage[8], L. Lichtenstein[2], S. Sourbron[8]

[1]*Universit of Leeds, International PhD Academy in Cardiovascular and Metabolic Disease, Leeds, United Kingdom;*
[2]*Leeds university, Leeds Institute of Cardiovascular and Metabolic Medicine, Leeds, United Kingdom;*
[3]*Saint James university hospital, Hepatobiliary and transplant surgery, Leeds, United Kingdom;*
[4]*Leeds teaching hospitals NHS trust-Leeds general infirmary, Clinical Imaging Facilities, Advanced imaging centre, Leeds, United Kingdom;*
[5]*School of medicine, University of Leeds, Department of Leeds institute for data analytics, Leeds, United Kingdom;*

[6]*University of Leeds, Department of medical research, Leeds, United Kingdom;*
[7]*Leeds teaching hospital NHS trust, Department of MR physics, Leeds, United Kingdom;*
[8]*Medical school-University of Sheffield, Department of infection, immunity and cardiovascular disease, Sheffield, United Kingdom*

Introduction Post-hepatectomy liver failure (PHLF) is a serious postoperative complication, but the risk is difficult to predict in patients with underlying liver disease. We hypothesise that the liver clearance of Gadoxetate (Gadoxetate Clearance or GC, in mL/min per kg body weight), a routine liver-specific contrast agent for MRI, will improve risk assessment by predicting the function of the future liver remnant. Here we present preliminary data on the correlation of the novel marker GC with preoperative bilirubin and the preoperative plasma disappearance rate of Indocyanine Green (ICG-PDR).

Method HEPARIM study (Hepatectomy risk assessment with functional MRI) recruited patients with colorectal liver metastases selected for hepatectomy of 2 segments or more. PMI software was used to measure Gadoxetate Clearance (mL/min/kg) (Fig. 1). Whole liver GC, ICG-PDR and Bilirubin were measured before surgery. Associations of preoperative ICG-PDR and preoperative Bilirubin with GC were assessed separately using Pearson correlation coefficient (r) and linear regression (significance at $p < 0.05$).

Results First 40 patients of the HEPARIM study were selected for this intermediate analysis (Fig. 2). Bilirubin ranged from 5 to 28 (µmol/L) (10.29 ± 4.8), ICG-PDR from 10 to 37.6 (%/min) (20.6 ± 5.12), and GC from 52.36 to 190.69 (mL/min/1.73 m^2) (110.42 ± 32.42). All but one of the bilirubin values were in the normal range (< 20.5 µmol/L), 27.3% of the ICG-PDR values were lower than normal (< 18%/min), and 15.9% were above normal (> 25%/min). Whole liver-GC was weakly and positively correlated with ICG-PDR, whereas, bilirubin and whole liver-GC were not correlated, as presented in Table 1, although scatter plot representation suggests a tendency (Fig. 2).

Discussion HEPARIM revealed no correlation between GC and bilirubin, possibly because GC is a biomarker that measures hepatocyte functionality, and most participants fall within the normal bilirubin range. Furthermore, hepatocytes uptake a significant amount of gadoxetate acid via organic anion-transporting polypeptides OATP1B1 and OATP1B3, where OATP1B3 has sixfold higher affinity to gadoxetate acid (Leonhardt et al., 2010). In contrast, unconjugated bilirubin is entering the hepatocyte via different transporter, mostly OATP2, suggesting bilirubin would not compete with gadoxetate transport (Haimerl et al., 2017).

The results showed a weak positive correlation between GC and ICG-PDR. This could be because ICG-PDR is considered more a biomarker of liver perfusion than a direct measure of hepatic functionality (Derpapas et al., 2013), in comparison to GC, which is a biomarker of hepatocellular function. Finally, ICG-PDR is highly influenced by many factors, such as hepatic and cardiac blood flow (Levesque et al., 2016), making ICG-PDR results to be interpreted cautiously.

Conclusion In our study with relatively preserved liver function, ICG is a measure of perfusion, whereas GC reflects hepatocellular function, explaining the weak positive correlation we observed. In contradiction to ICG, bilirubin is almost in the normal range, which confirms its limitations as a direct measure of function and is consistent with the absence of correlation with GC. The results indicate that GC can act as an independent marker of liver function and may potentially improve risk prediction for hepatectomy.

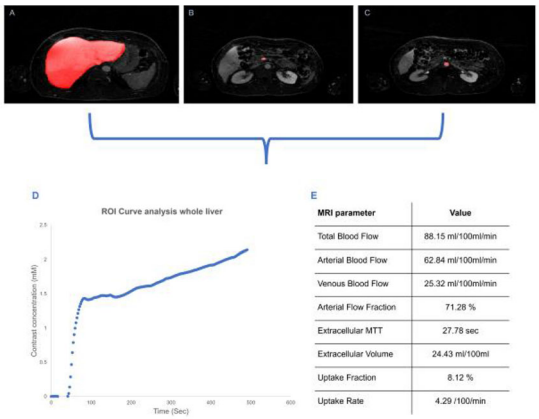

MRI parameter	Value
Total Blood Flow	88.15 ml/100ml/min
Arterial Blood Flow	62.84 ml/100ml/min
Venous Blood Flow	25.32 ml/100ml/min
Arterial Flow Fraction	71.28 %
Extracellular MTT	27.78 sec
Extracellular Volume	24.43 ml/100ml
Uptake Fraction	8.12 %
Uptake Rate	4.29 /100/min

Fig. 1: MRI image analysis using PMI **PMI analysis of one patient; A. Liver mask, B. Venous input function (VIF), C.** Arterial input function (AIF), D. ROI curve analysis showing fit lines according to the actual MRI data, E. PMI -derived functional and perfusion liver MRI readings, MTT= mean transit time (sec).

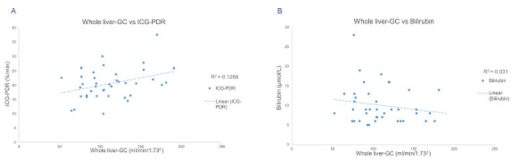

Fig. 2: Scatter plot of GC vs Bilirubin and ICG-PDR A: **Preop ICG-PDR (%/min) versus GC Scatter plot. Preop ICG-**PDR accounts for 12.68 % (R^2= 0.1268 0.1268*100) of the GC variation. **B**: Scatter plot between the independent variable preop bilirubin (µmol/L) against GC and R^2 = 0.03, meaning (3.1 %) of the variance in GC is explained by preop bilirubin.

Statistics	Gadoxetate Clearance (GC) (mL/min/1.73m²) Vs	
	Bilirubin (µmol/L)	ICG-PDR (%/min)
r, p	r = - 0.175, p = 0.133	r = 0.356, p = 0.012
R^2, p	R^2 = 0.031, p = 0.267	R^2 = 0.1268, p = 0.024
β, 95% (CI)	β = -0.175, 95% (CI) = - 3.303, 0.938	β = 0.356, 95% (CI) = 0.325, 4.371

Table 1: Statistical analysis of GC against bilirubin and ICG-PDR **Statistical analysis of GC (mL/min/1.73m²) vs** preoperative bilirubin (µmol/L) and preoperative ICG-PDR (%/min), Pearson correlation (r), Coefficient of determination (R^2) and (Pvalue), Regression coefficient (β) and 95% confidence interval (CI).

References

- Derpapas, M. K., Contis, J., Fragulidis, G. P., Lykoudis, P. M., Polymeneas, G., Ntourakis, S. & Voros, D. 2013. Correlation of the ICG test with risk factors and postoperative outcomes following hepatic resection. *J buon,* 18**,** 703–7.
- Haimerl, M., Verloh, N., Zeman, F., Fellner, C., Nickela, D., Lang, S. A., Teugel, A., Stroszczynski, C. & Wiggermann, P. 2017. Gd-EOB-DTPA-enhanced MRI for evaluation of liver function: Comparison between signal-intensity-based indices and T1 relaxometry. *Sci Rep,* 7**,** 43347.
- Leonhardt, M., Keiser, M., Oswald, S., Kühn, J.-P., Jia, J., Grube, M., Kroemer, H. K., Siegmund, W. & Weitschies, W. 2010. Hepatic Uptake of the Magnetic Resonance Imaging Contrast Agent Gd-EOB-DTPA: Role of Human Organic Anion Transporters. *Drug Metabolism and Disposition,* 38**,** 1024–1028.
- Levesque, E., Martin, E., Dudau, D., Lim, C., Dhonneur, G. & Azoulay, D. 2016. Current use and perspective of indocyanine green clearance in liver diseases. *Anaesthesia Critical Care & Pain Medicine,* 35**,** 49–57.

P115.
The accuracy of commonly available segmentation software for liver segmentation from MR images

P. Kordač[1], B. Setinova[1], M. Hajek[1], M. Dezortová[1], J. Kovář[1], M. Burian[1], D. Pajuelo[1], P. Sedivy[1]

[1]*Institute for Clinical and Experimental Medicine, Department of Imaging Methods, Prague, Czech Republic*

Introduction It is essential to repeatedly monitor the size of the liver using a reliable and accurate method in clinical studies focused on monitoring liver morphology and metabolism. MR imaging is the only non-invasive method that allows repeated examinations with sufficient accuracy, but the accuracy of liver volume determination can vary depending on the software used. To address this issue, we aimed to compare the accuracy of liver volume determination using several of the most commonly used freeware segmentation software and automatic segmentation of the Siemens MR system. Additionally, we aimed to determine the accuracy in liver volume change induced by two-day fasting (liver reduction) and two-day refeeding (liver enlargement).

Methods Subjects and MR examination.

Seven healthy women underwent three MR sessions (before fasting—basal; after 48 h of fasting—fasting; and after 48 h of high-carbohydrate refeeding [1]—refeeding) on 3 T MR system VIDA (Siemens, Erlangen, Germany) equipped with 30-channel surface body matrix and 32-channel spine coil. VIBE (Volumetric interpolated breath-hold examination) sequence (TR/TE = 3.97/1.29 ms, resolution 1.2 × 1.2 × 3 mm, flip angle = 9°, 80 slices; acceleration factor 2 × 2 caipirinha) in transversal plane was used for volumetry of the liver.

All subjects provided written informed consent with the participation in the study. The study was conducted in compliance with the principles of the Declaration of Helsinki and with the approval of local ethics committee.

Data evaluation and statistics

The reference liver volumes (V_{manual}) were obtained by time-consuming manual slice to slice segmentation by an experienced MR specialist using the ITK-SNAP software. Then, they were compared to four different (semi)automatic algorithms in software programs:a) "Grow from seeds" in 3D Slicer [2]b) "Total Segmentation Module" in 3D Slicer [3]c) "Thresholding", ITK-SNAP [4]d) "Automatic Segmentation Routine" in the LiverLab module from Siemens [5]

Coefficients of variation (CV), intraclass correlation coefficients (ICC) and Bland–Altman graphs were used to compare different methods for the liver volume calculation.

Results Comparison of the accuracy (CA) of the liver volume acquired by different (semi)automatic segmentation methods are shown in Tab. 1 and Fig. 1. Tab. 2 and Fig. 2 show accuracy of liver volumes change calculated by (semi)automatic methods during fasting and refeeding.

Discussion In our study, we compared several basic, easily available semi-automatic methods and one fully automatic segmentation procedure of the Siemens MR system for liver volume measuring.

All methods showed good accuracy in determining the absolute size of liver volume, with CV < 10%, ICC > 0.97, and ΔV < 100 ml.

The Total segmentation method from 3D Slicer yielded the best results, especially when assessing the accuracy of volume change during dietary interventions (CV = 4% and 11%, Fig. 2). The Siemens automatic segmentation was also very accurate, with a CV < 3% and an ICC > 0.99 (Tab. 1 and Fig. 1). However, it is important to note that the segmentation mask cannot be manually edited, and it is a paid extension of the MR system. The worst semiautomatic method was Thresholding in ITK-SNAP, see its Bland–Altman plot in Fig. 1 (the widest 95% limits of agreement and the error interval of difference does not interfere with zero).

Conclusion Our findings suggest that the semi-automatic and fully automatic segmentation methods evaluated in this study are reliable and accurate alternatives to manual segmentation for measuring liver volume.

Supported by Ministry of Health of the Czech Republic, GN: NU20J-01–00005 and DRO ("Institute for Clinical and Experimental Medicine – IKEM, IN 00023001").

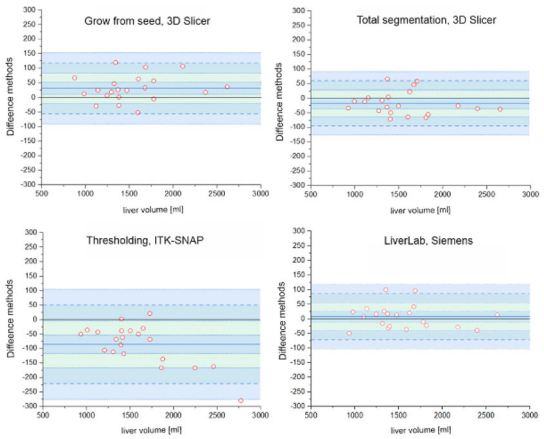

Fig. 1. Comparison of the accuracy (CA) of liver volumes determined by different methods by Bland-Altman graphs (*x*-axis: mean of testing and reference method, *y*-axis: difference of testing and reference manual segmentation) for Grow from seeds (3D Slicers), Total segmentation (3D Slicers), Thresholding (ITK-SNAP) and LiverLab (Siemens).

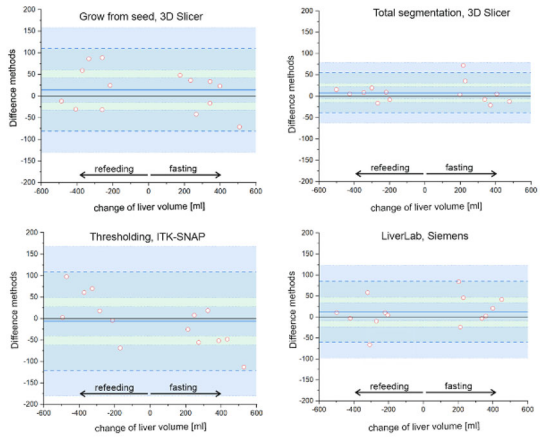

Fig. 2 CA of liver volume changes during fasting and refeeding determined by different methods by Bland-Altman graphs (*x*-axis: mean of testing and reference method, *y*-axis: difference of testing and reference method) for Grow from seeds (3D Slicer), Total segmentation (3D Slicer), Thresholding (ITK-SNAP) and LiverLab (Siemens).

Table 1. CA of liver volume acquired by different (semi)automatic segmentation methods (n=21; V_{manual}=1615±489 ml; ΔV = mean absolute difference between manual and (semi)automatic segmentation; CV – coefficient of variation, ICC – intraclass correlation coefficient consistency and agreement).

Method	Grow from seeds (3D Slicer)	Total segmentation (3D Slicer)	Thresholding (ITK-SNAP)	LiverLab (Siemens)
mean ΔV [ml]	42±34	36±22	88±66	32±25
CV [%]	2.8	2.4	5.4	2.2
ICC consistency	0.995	0.996	0.989	0.996
ICC agreement	0.992	0.995	0.972	0.996

Table 2. CA of the liver volume change acquired by different (semi)automatic segmentation methods during fasting and refeeding (n=7; fasting/refeeding change V = mean change in the liver volume during fasting/refeeding; fasting/refeeding CV-coefficient variation of change liver volume during fasting/refeeding between reference and selected (semi)automatic segmentation methods). Reference change liver volume during fasting and refeeding (V_{manual} basal - V_{manual} fasting; V_{manual} fasting - V_{manual} refeeding) was 324 ml and -321 ml.

Method	Grow from seeds (3D Slicer)	Total segmentation (3D Slicer)	Thresholding (ITK-SNAP)	LiverLab (Siemens)
Fasting change				
V [ml]	322	313	362	300
fasting CV [%]	19	11	23	16
Refeeding change				
V [ml]	-347	-326	-346	-321
refeeding CV [%]	17	4	15	8

References

1. Sedivy P, et al. Liver response to fasting and isocaloric high-carbohydrate refeeding in lean and obese women. ISMRM-ESMRMB 2022. Abstract #2766
2. Egger J, et al. Pituitary adenoma volumetry with 3D Slicer. 2012; 7(12):e51788
3. Wasserthal J, et al. TotalSegmentator: robust segmentation of 104 anatomical structures in CT images. https://doi.org/10.48550/arXiv.2208.05868
4. Sellers R. MR LiverLab. MAGNETOM Flash. 2016; 66(3):39–43
5. Yushkevich P, et al. User-guided segmentation of multi-modality medical imaging datasets with ITK-SNAP. Neuroinformatics. 2019; 17(1):83–102

P116.
Numerical optimization of DWI acquisition and ADC computation in biological tissues

S. Kuczera[1], S. Maier[1,2]

[1]*University of Gothenburg, Department of Radiology, Gothenburg, Sweden;*
[2]*Brigham Women's Hospital, Harvard Medical School, Department of Radiology, Boston, MA, United States*

Introduction Numerical simulations and calculations are a commonly employed strategy for sequence optimizations in diffusion weighted imaging (1). In our previous work (2) we presented a novel framework for ADC and image generation for prostate imaging, where a large number of b-values is acquired without repetitions, instead of a small number with multiple repetitions. In order to account for the lower SNR of the individual b-value images, model fitting is applied. From these fits synthetic images can be reconstructed that are of similar quality as the ones obtained from repeated acquisition with averaging. In the current work, we investigate with simulations how the SNR of these synthetic images depends on the underlying parameters of commonly applied diffusion signal models. Calculations are based on the work by Richter (3). In particular we show how underlying model parameters influence the SNR of the synthetic images, which effect repeated measurements have on reproducible ADC calculation described in (2) and how the acquisition scheme can be modified to achieve constant SNR for synthetic images over a certain b-value range.

Methods Two tissue type models, representing normal and cancerous prostate tissue, based on a biexponential function were used for analytical calculations. Both have a fast diffusion component D_1 of 2.2 μm^2/ms, while the slow diffusion parameter D_2 and the fast signal fraction f differ, i.e., D_2 = 0.4 μm^2/ms and f = 0.8 in the normal case and D_2 = 0.2 μm^2/ms and f = 0.6 for the cancerous case. Measured points were 21 b-values, evenly spaced over the range of 0 to 2000s/mm^2. Considered model functions were biexponential and kurtosis. True kurtosis model parameters were generated by fitting the biexponential model without noise. This resulted in ADC_K = 1.866 μm^2/ms and K = 0.627 for normal tissue, and ADC_K = 1.296 μm^2/ms and K = 1.231 for cancerous tissue.

With the true model parameters as basis, model parameters and amount of signal averaging were varied one at a time and the averaging effect (AE) was calculated as $AE(b) = (1/\sigma_y(b))^2$, where $\sigma_y(b)$ represents the data standard deviation given by Richter (2,3). Furthermore, the ADC standard deviation for the two-step ADC calculation as described in (2) was determined for signal averaging applied individually at all 21 measured b-values for repetitions of 2, 10, 20 and 30. The two-step ADC was calculated at b-values of 100 and 1000 s/mm^2. Finally, the distribution of measured b-values was optimized in order to achieve a constant SNR over the range b = 0–2000s/mm^2 for synthetic images. Optimization started with an even distribution for 100 b-values evenly spaced over the b-value range. In each optimization step the frequency of each b-value is divided by the corresponding SNR calculated with equations given by Richter (3) resulting in an updated b-value distribution.

Results AE for certain model functions and different number of repetitionsis shown in Figs. 1 and2, respectively. In Fig. 3, the relative improvement in standard deviation with regards to no averaging for the two-step ADC is shown. Optimized b-value schemes are shown in Fig. 4.

Discussion By means of analytical expressions the AE for a synthetic DWI image generated by model fitting can be determined as a function of the underlying model parameters. AE is higher for the kurtosis model, which has 3 free parameters in comparison to 4 in the case of the biexponential model. Dependence of the AE with regards to the model parameters and number of averages is complicated. With regards to the two-step ADC, averaging at b = 900 or 1000 s/mm^2 has the strongest effect on increasing the ADC precision depending on underlying model function. Finally we have shown that acquisition schemes can be constructed in a way that an almost constant SNR over a b-range from 0 to 2000s/mm^2 can be achieved. Interestingly the number of peaks in the resulting b-value distribution corresponds to the number of model parameter. As expected, the number of repetitions increases with the amount diffusion weighting.

Conclusion With the help of analytical models, we have shown that a set of mathematical expressions can be used for the prediction of synthetic image SNR generated by means of model fitting and for sequence optimization in various aspects. We believe this work is of interest to develop novel acquisition schemes.

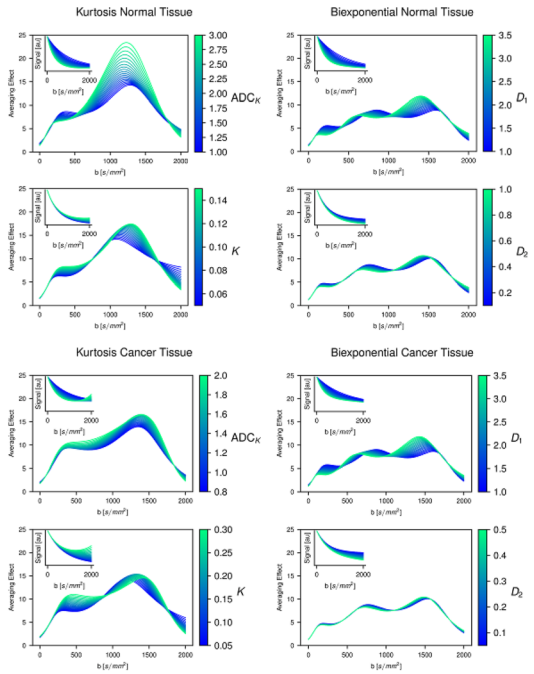

Fig. 1: *Average effect as function of b-value and model parameters for normal and cancerous tissue. Model parameters were varied one at a time. Parameter names and ranges are indicated in the colorbar. Insets show the corresponding signal decays.*

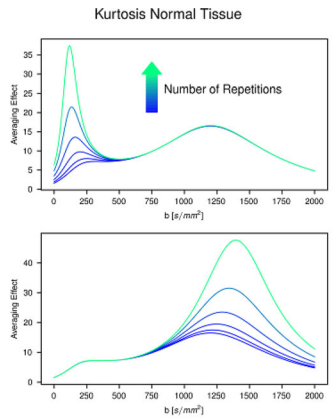

Fig. 2: *. Average effect for normal tissue and kurotosis function at repetitions of 1, 2, 4, 8, 16 and 32 at b-values of 100 (top) and 1500 s/mm²(bottom)*

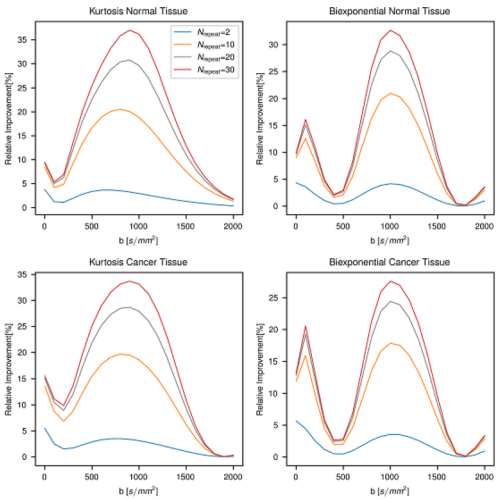

Fig. 3: *Relative improvement in standard deviation for two-step ADC described in (2) for averaged repetitions of 2, 10, 20 and 30 in comparison to no averaging. Averaging was applied individually at each of the 21 measured b-values, i.e. only the corresponding b-value was averaged for each data point in the plots*

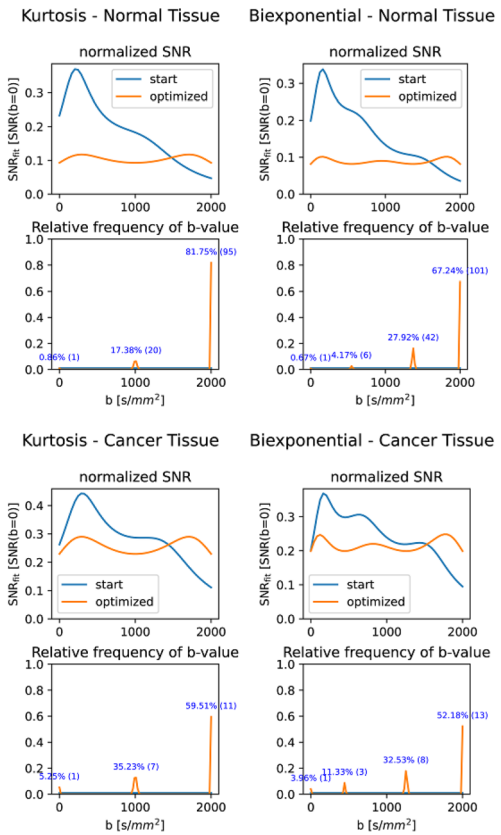

Fig. 4. *Optimized b-value schemes for both tissue types and kurtosis and biexponential function. For each distribution peak the relative proportions are given, as well as the number of repeated measurements (in parenthesis), assuming a single measurement at b=0.*

References

1. Jones DK. The effect of gradient sampling schemes on measures derived from diffusion tensor MRI: A Monte Carlo study. Magn Reson Med. 2004;51(4):807–15
2. Kuczera S, Langkilde F, Maier SE. Truly reproducible uniform estimation of the ADC with multi-b diffusion data—Application in prostate diffusion imaging. Magn Reson Med. 2023;89(4):1586–600
3. Richter PH. Estimating errors in least-squares fitting. Telecommun Data Acquis Rep 1995

P117.
Measurement of renal perfusion by arterial spin labeling (ASL) MRI in dogs: Quantification and reproducibility

A. Hillaert[1], L. C. Sanmiguel Serpa[2,3,4], K. Vanderperren[1], S. Bogaert[2,3], P. Pullens[2,3,5]

[1]*Ghent University, Department of Morphology, Imaging, Orthopedics, Rehabilitation and Nutrition, Merelbeke, Belgium;*
[2]*Ghent University, Department of Radiology and Nuclear Medicine, Ghent, Belgium;*
[3]*Ghent University, Ghent Institute of Functional and Metabolic Imaging (GIFMI), Ghent, Belgium;*
[4]*Ghent University, Department of Diagnostic Sciences, Ghent, Belgium;*
[5]*Ghent University, Institute of Biomedical Engineering and Technology (IBiTech), Ghent, Belgium*

ASL MRI is a method for non-invasive quantification of renal perfusion that magnetically labels blood water and uses it as an endogenous tracer[1]. Many kidney disorders are associated with vascular or hemodynamic changes, which appear early in the progression of kidney disease and may occur well before other indications of renal dysfunction[2,3]. As a result, ASL-MRI might enable earlier diagnosis and quicker therapeutic intervention. As in human medicine, substantial research is done in veterinary medicine on renal disorders and their causes[4,5]. Given the similarities between the canine and human kidneys in both morphology and pathophysiology of kidney disease, the dog could serve as a human model[6]. To date, only preliminary studies on renal ASL-MRI have been done in dogs by our research team[7]. The aim of this study was to evaluate the feasibility and variation of renal perfusion in healthy dogs using ASL MRI.

Eight healthy purpose-bred beagles were used. Figure 1.1 summarizes the details of the studied group. The beagles were scanned in dorsal recumbancy on a Siemens PrismaFit 3 T. An overview of the anesthesia protocol is illustrated in Fig. 1.2. Two consecutive ASL scans were performed, see Fig. 1.3 for sequence parameters. Motion corrected data was analyzed offline in Python, with dog specific parameters for RBF quantification[8]. Manual masks were created with 3D Slicer, segmentation was done in Spyder and statistics were done with R. The TLCO (Twelve-Layer Concentric Objects) method was used to calculate mean RBF of each of the 12 concentric layers[9]. In addition, a new analysis method called the Ten Equiangular Object (TEO) method was used to evaluate RBF from the cranial to the caudal poles[10]. This method calculated the mean RBF of 10 equiangular segments. The Bland–Altman and violin plot were used to assess the reproducibility of ASL within the same session.

The division of the kidney using the TLCO method in twelve concentric layers and the mean RBF in each layer is depicted in Fig. 2.1. A higher RBF is found in the cortical layers (layers 1–3) than in the medullary layers[11] (layers 8–10), 343.5 ± 63.5 and 160.8 ± 38.7 ml/100 g/min respectively. The mean RBF of the whole kidneys is 233.8 ± 35.8 ml/100 g/min. The division of the kidney in ten equiangular segments using the TEO method and the mean RBF in each segment is depicted in Fig. 2.2. Certain segments near the kidney poles seem to have a lower RBF than other segments. The Bland–Altman and violin plot are presented in Figs. 3 and 4. Both plots generally showed good agreement between 2 consecutive measurements in the same session, with the cortex showing a greater bias than the medulla.

This study demonstrates the feasibility of non-invasive renal RBF quantification with ASL in dogs. ASL-MRI derived RBF agree with renal perfusion studies in healthy dogs using invasive reference methods[12] and are comparable to those in humans[13]. Based on the values obtained with the TEO method, renal perfusion appears to differ regionally from one pole to the other, with cranial and caudal segments showing lower perfusion. Possibly, these less perfused sections at the renal poles are more prone to renal disorders. A recent study found that dogs suffer renal infarctions primarily in the caudal pole[14]. The reproducibility between runs seems acceptable, although the measured values of the runs are not identical, possibly due to patient and scanner-related factors. Using the mean values from both runs may minimize variation.

Using FAIR ASL MRI, renal perfusion measurements in dogs are feasible and reproducible. This is the first study to describe normal RBF values in a group of healthy dogs using ASL MRI. Further research is needed to determine whether less perfused regions at the renal poles are more prone to kidney disease.

1

Number of subjects	Number of males	Number of females	Mean (± SD) age	Mean (± SD) body weight
8	4	4	5.4 ± 1.6 years	12.5 ± 1.9 kg

2

Preparation	Sedation	Induction	Maintenance
Food deprivation 12h before scan	butorphanol (0.2 mg/kg IV)	propofol (4-6 mg/kg IV) + midazolam (0.2 mg/kg IV)	isoflurane (1.2-1.4%)

3

Sequence	Flow-sensitive Alternating Inversion Recovery (FAIR) Q2TIPS ASL (Siemens WIP ASP 1023H)
TI_1	2000ms
Bolus length	1000ms
TR/TE	4500/23.58ms
Matrix	64x64
FOV	272x136mm
Voxel size	2.1x2.1x8.0mm
Slices	8 oblique coronal 8mm slices
Flip angle	180°

Fig. 1: (1) Details of studied group. (2) Details of anesthesia protocol. (3) Details of the ASL sequence.

1. Nery, F. et al. Diagnostics. 2018;8:1–15.
2. Selby, N.M. et al. Curr Opin Nephrol Hypertens. 2021;30:138–43.
3. Dong, Y. et al. PLoS One. 2013;8:1–7.
4. Lund, E.M. et al. J Am Vet Med Assoc. 1999;214:1336–41.
5. Miyagawa, Y. et al. J Vet Med Sci. 2010;72:1129–36..
6. Hall, J.E. et al. Circ Res. 2015;116:991–1006.
7. Hillaert, A., Vanderperren, K., Pullens, P. (2022, May 07–12) [Conference presentation abstract] Joint Annual Meeting ISMRM-ESMRMB & ISMRT 31st Annual Meeting, London, UK.
8. Sanmiguel, L., Hillaert, A. and Pullens, P. (2023, June 3–8) [Conference presentation abstract] 2023 ISMRM & ISMRT Annual Meeting & Exhibition, Toronto, Canada.
9. Piskunowicz, M. et al. Magnetic Resonance Imaging 2015; 33:253–261.
10. Sanmiguel, L., De Visschere, P., Speeckaert, M. and Pullens, P. (2023, June 3–8) [Conference presentation abstract] 2023 ISMRM & ISMRT Annual Meeting & Exhibition, Toronto, Canada.
10. Pruijm, M. et al. Kidney Int. 2018;93:932–40.
12. Aumann, S. et al. Magn Reson Med. 2003;49:276–87.
13. Gillis, K.A. et al. BMC Nephrol; 2014;15:1–10.
14. Sutthigran, S. et al. J Vet Intern Med. 2022;36:164–70.

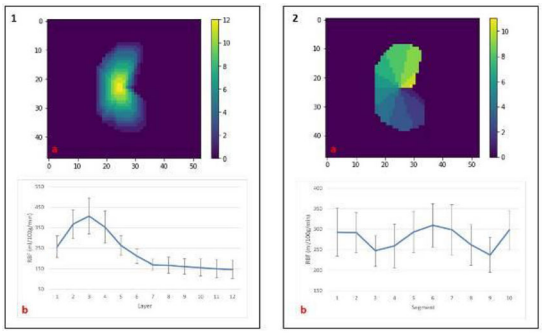

Fig. 2: Division of the kidney in 12 layers of equal thickness according to the TLCO method (1.a) and in 10 equiangular segments according the TEO method (2.a). Mean (± SD) renal blood flow of 7 subjects in each layer using the TLCO method (1.b) and in each segment using the TEO method (2.b). Within the TLCO method 1 represents the outer layer, 12 the inner layer. Within the TEO method, 1 represents the segment at the caudal pole and 10 represents the segment at the cranial pole.

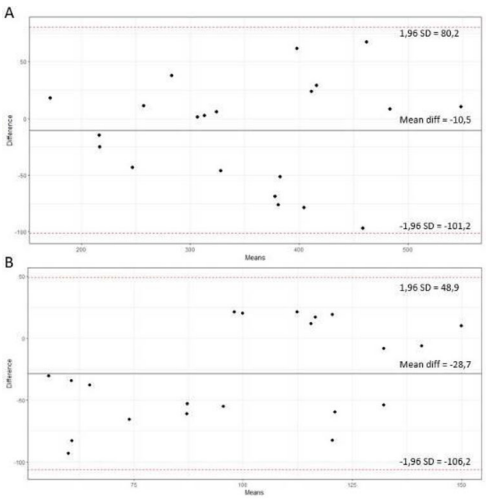

Fig. 3: Bland Altman plot of cortical (A) and medullary (B) perfusion measurements from 2 consecutive ASL runs for 7 subjects. Cortical and medullary perfusion was based on layers 1-3 and 8-10, respectively. In one subject, a second run was not conducted.

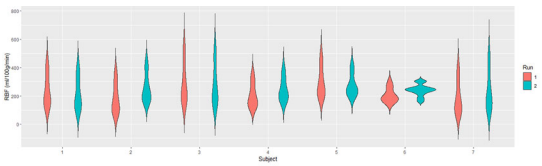

Fig. 4: Violin plot representing RBF data from 2 consecutive ASL runs of 7 subjects. In one subject, a second run was not conducted.

P118.
A new method to analyse renal perfusion: A proof of concept

L. C. Sanmiguel Serpa[1,2,3], P. de Visschere[1,2], M. Speeckaert[4,5], P. Pullens[2,3,6]

[1]*Ghent University, Department Of Diagnostic Sciences, Ghent, Belgium;*
[2]*Ghent University, Department of Radiology and Nuclear Medicine, Ghent, Belgium;*
[3]*Ghent University, Ghent Institute of Functional and Metabolic Imaging (GIFMI), Ghent, Belgium;*
[4]*Ghent University, Department of Nephrology, Ghent, Belgium;*
[5]*Ghent University, Department of Internal Medicine and Pediatrics, Ghent, Belgium;*
[6]*Ghent University, Institute of Biomedical Engineering and Technology (IBiTech), Ghent, Belgium*

Renal Arterial Spin Labeling(ASL) literature suggests the region of interest (ROI) analysis[1,2,3]. This method is observer-depenent[4]. In healthy kidneys it's usually easier to differentiate cortical and medullar regions. Unfortunately, in non-healthy kidneys this process is more complex due to anatomical degradation[4]. Previously Piskunowicz et al. used the **Concentric-Objects** (CO) in blood oxygenation level-dependent images. In this paper, we tested CO method in renal ASL images and, following the same principle of this algorithm, we implemented a new analysis method called **Equiangular Object** (EO) method, which allows for analysis along the renal cortex. To date, renal ASL has been only analyzed by the classical ROI[5] and the histogram[1,6] method, therefore the goal is to test if these algorithms are comparable with these methods and if additional information might be retrieved.

13 subjects were scanned (7 healthy, 6 patients) in supine position on a Siemens PrismaFit 3 T. The patient variety is resumed in Fig. 1, 1. ASL images were obtained using a work-in-progress Siemens sequence, see Fig. 1, 2. Perfusion was calculated inline using the classical compartment model. Both kidneys were segmented with FSLeyes. For each mask the center of mass C(x,y) is calculated. Twelve-layer **CO** (TLCO) method classifies each point P(x,y) inside the mask according to its distance (in 12 equal sections) to C. TLCO was implemented in Python and used to calculate mean perfusion values at different distances to the center. Consequently, a label image with 12 concentric layers was obtained. Ten regions are defined for the **EO** method, thus, a label image with 10 equiangular object is obtained. TEO was used to calculate mean perfusion values across different sections of the kidney. See Fig. 1, 3.

The mean RBF value of each layer/section is plotted to analyze the variation of RBF across the kidney. Healthy volunteers (HV) are pooled to estimate a healthy profile for each kidney and compare it against patients. In TLCO, layer 0 is the outermost section of the kidney. In TEO method 0 represents the lower pole of the kidney. Figures 2, 3 and 4 show the result of both methods in HV and Patients.

In literature not all studies examine different regions of the kidney. The RBF values in cortex range between 255[1] and 290[5] mL/100 g/min for HV and 71[6]–83[1] for patients. One study[5] reported for HV for outer medulla 91 ± 14 and inner medulla 42 ± 16. For HV, the obtained values with the TLCO method show higher RBF in the outer layers and a decrease in the inner region of the kidney. This seems to be comparable with the results found in literature. For the whole kidney RBF values in literature the value for HV is 185.2[8]–228[7] and 94.6[8] for patients. The obtained values with the TEO method show that the RBF values in HV change from the lower pole to the upper pole of the kidney, and that higher perfusion values are seen in the central section.

Human kidney has a challenging geometry that requires robust algorithms to perform deeper analysis. Using only the mean of a region may underestimate different regional conditions of the kidney. The TEO and TLCO method results show that RBF values across the kidney change in different directions. By combining TE and TLCO, or changing the number of layers or sections, an optimal configuration may be found depending on the application. Future applications include the use of EO to pinpoint under perfused areas in the kidney for more accurate steering of kidney biopsies.

Age	(1) Status	GFR (ml/min)	KDIGO classification
37	2 transplant kidneys	≥90	1
82	Aorta aneurysm, 2 x 2 kidney arteries	49	3a
59	CKD since 2016 because of calineurine inhibitor medication after heart1x	51	3a
88	CKD, diabetes, hypertension nefrectomy l, cysts R, RCC R, CNI	18.8	4
83	renal transplant	53	3a
54	healthy	≥90	1
27	healthy	≥90	1
32	healthy	≥90	1
24	healthy	≥90	1
22	healthy	≥90	1
42	healthy	≥90	1
25	healthy	≥90	1
35	healthy (L accessory kidney artery)	≥90	1

(2) Sequence	Turbo Gradient Spin-Echo, pseudo-Continuous Arterial Spin Labeling (p-CASL)
voxel size	3.8×3.8×5.0mm
TR/TE	5000/27.14ms
T_1 Blood	1650.0ms
Start T_1	3000ms
PCASL duration	1500ms
PCASL flip angle	28.0 deg

(3)

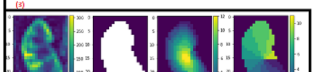

Fig. 1: (1) Details of Patient group. (2) Details of the used ASL sequence. (3) (a) The RBF map from human kidney, (b) The mask image of the same kidney, (c) TLCO method applied to the mask image, (d) TEO method applied to the mask image.

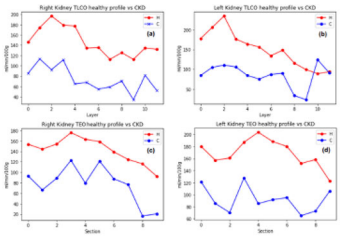

Fig. 2: Healthy volunteers profile vs CKD patients in (a) The TLCO right kidney, (b) The TLCO left kidney, (c) The TEO method in right kidney RBF, (d) The TEO method in left kidney RBF. (c) and (d) show that perfusion is not constant along the cortex but is lower in both poles than in the central sections of the kidney.

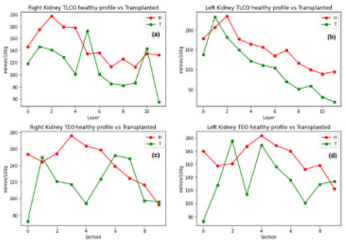

Fig. 3: Healthy volunteers profile vs Transplanted kidney patient in (a) The TLCO right kidney, (b) The TLCO left kidney, (c) The TEO method in right kidney RBF, (d) The TEO method in left kidney RBF.

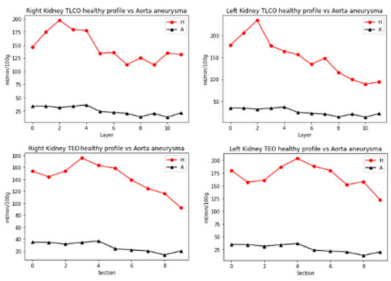

Fig. 4: Healthy volunteers profile vs Aorta aneurysm patient in (a) The TLCO right kidney, (b) The TLCO left kidney, (c) The TEO method in right kidney RBF, (d) The TEO method in left kidney RBF.

References

1 Cox EF, et al. Multiparametric Renal Magnetic Resonance Imaging: Validation, Interventions, and Alterations in Chronic Kidney Disease. Frontiers in physiology 2017;8:696

2 Selby NM, et al. Magnetic resonance imaging biomarkers for chronic kidney disease: a position paper from the European Cooperation in Science and Technology Action PARENCHIMA. European Renal Association 2018 Sep;33:ii4–ii14

3 Nery F, et al. Consensus-based technical recommendations for clinical translation of renal ASL MRI. MAGMA. 2020 Feb;33(1):141

4 Piskunowicz M, et al. A new technique with high reproducibility to estimate renal oxygenation using BOLD-MRI in chronic kidney disease. Magnetic resonance imaging 2015 Apr;33:253–61

5 Eckerbom P, et al. Multiparametric assessment of renal physiology in healthy volunteers using noninvasive magnetic resonance imaging. Am J Physiol Renal Physiol. 2019 Apr 1;316(4):F693

6 Buchanan CE, et al. Quantitative assessment of renal structural and functional changes in chronic kidney disease using multi-parametric magnetic resonance imaging. Nephrol Dial Transplant. 2020 Jun 1;35(6):955

7 Gillis K.A. et al. Inter-study reproducibility of arterial spin labelling magnetic resonance imaging for measurement of renal perfusion in healthy volunteers at 3 Tesla. BMC Nephrol 15, 23 (2014.

8 Cai YZ. et al. Diagnostic value of renal perfusion in patients with chronic kidney disease using 3D arterial spin labeling. J Magn Reson Imaging. 2017 Aug;46(2):589

P119.

Quantitative measurement of renal artery spin labeling imaging: A noninvasive indicator of perfusion improvement after interventional therapy for renal artery stenosis

X. Zhang[1], G. Zhang[1], H. Sun[1], Z. Jin[1], L. Xu[1], J. Zhang[1], X. Bai[1], L. Chen[1]

[1]*Peking Union Medical College Hospital, Radiology, Beijing, China*

Introduction Renal artery stenosis (RAS) is the most common cause of secondary hypertension, with atherosclerosis currently the primary cause[1]. Severe narrowing of both renal arteries can lead to serious consequences, such as end-stage renal kinetic failure, left heart dysfunction, and even left heart failure[2]. MRI, as a non-invasive imaging method, has shown advantages in diagnosing RAS because of its absence of ionizing radiation, its ability to image in any direction, and its high soft-tissue resolution. And with the development of MRI technology, quantitative measurement of arterial spin labeling (ASL) images shows potential in renal function and perfusion studies[3]. Hence, the aim of this study is to assess the feasibility of ASL imaging as a non-invasive indicator to evaluate the perfusion improvement of interventional therapy in patients with RAS.

Methods Eleven patients who were determined with RAS by Digital Subtraction Angiography and underwent preoperative ASL exam were enrolled in the prospective study. All patients received interventional therapy, and seven patients underwent postoperative ASL examination. The renal blood flood (RBF) of the renal cortex and local abnormal perfusion region were measured in both preoperative and postoperative ASL imaging. The local abnormal perfusion region was subjectively assessed by the radiologist. The correlation between RBF and kidney glomerular filtration rate (GFR) was evaluated. The differences between preoperative and postoperative RBF in patients with RAS were compared.

Results The Systolic and diastolic blood pressure decreased in all RAS patients after interventional therapy. There was a significant correlation between preoperative cortical RBF and preoperative single kidney GFR ($r = 0.504$, $p = 0.024$), but no significant correlation between preoperative cortical RBF and preoperative estimated GFR ($r = 0.159$, $p = 0.530$). Of the seven patients who underwent postoperative ASL imaging, the renal cortical RBF was higher than preoperative RBF (203.19 ± 51.42 vs.164.00 ± 68.10, $p = 0.005$). The postoperative RBF in the region of abnormal perfusion was also

higher than the preoperative RBF (159.92 ± 46.10 vs. 108.55 ± 39.57, p = 0.001).

Discussion: In this study, we found that renal cortical RBF based on renal ASL images was a good noninvasive indicator of renal perfusion in RAS patients. Cortical RBF is significantly correlated with unilateral renal function, and its increase after interventional therapy can also be used to evaluate the improvement of renal perfusion. At present, the most commonly used index to characterize renal function is GFR which can be estimated by blood creatinine clearance but can"t reflect unilateral renal function. In RAS patients, the inconsistent degree of bilateral RAS can result in the inconsistent degree of bilateral renal perfusion injury [4]. Initially, unilateral renal perfusion may have been reduced, yet GFR remains in the normal range. By the time there is a detectable decrease in GFR, irreversible damage may have occurred to the renal structure[5]. However, our study shows that ASL-based cortical RBF could be used to diagnose unilateral renal function decline and facilitate early intervention in patients. Another finding of our study was that the RBF of the cortex increased after interventional therapy in patients with RAS, as well as a significant increase in the RBF of areas with reduced abnormal perfusion. The finding suggested that the intervention of the renal artery can help restore normal renal perfusion and also suggested that RBF parameters based on ASL images can be used as a noninvasive indicator to evaluate the efficacy of treatment for RAS.

Conclusion Renal RBF obtained by ASL images was significantly correlated with single renal function and could be used to evaluate the perfusion improvement in RAS patients after interventional therapy.

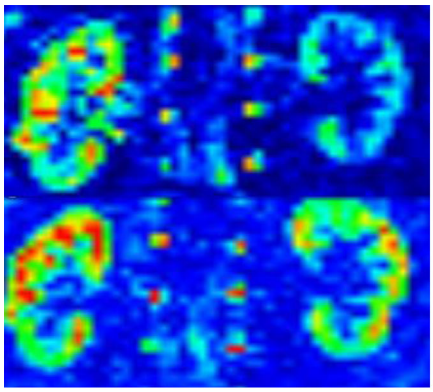

Fig.1: Preoperative and postoperative ASL images of a 53-year-old male patient. Preoperative ASL images showed significant impaired perfusion of the left kidney. The patient underwent left renal artery stenting and ASL examination again 2 months later, and imaging showed significant improvement in left renal perfusion. ASL: arterial spin labeling.

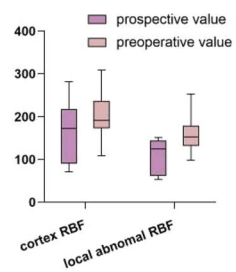

Fig. 2.: The preoperative and postoperative RBF of renal cortex and local abnormal perfusion region. The renal cortical RBF was higher than preoperative RBF. The postoperative RBF in the region of abnormal perfusion was also higher than the preoperative RBF. RBF: renal blood flood.

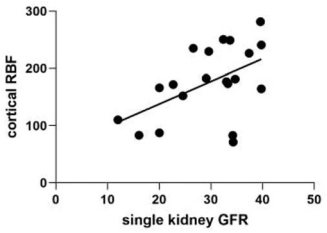

Fig. 3: The correlation between RBF and kidney glomerular filtration rate. There was a significant correlation between preoperative cortical RBF and preoperative single kidney GFR. GFR: glomerular filtration rate.

References

[1] R.D. Safian, Renal artery stenosis, Prog Cardiovasc Dis 65 (2021) 60–70

[2] V. Aboyans, I. Desormais, J. Magne, G. Morange, D. Mohty, P. Lacroix, Renal Artery Stenosis in Patients with Peripheral Artery Disease: Prevalence, Risk Factors and Long-term Prognosis, European journal of vascular and endovascular surgery: the official journal of the European Society for Vascular Surgery 53(3) (2017) 380–385

[3] J.L. Zhang, V.S. Lee, Renal perfusion imaging by MRI, J Magn Reson Imaging 52(2) (2020) 369–379

[4] C. Cuspidi, R. Dell'Oro, C. Sala, M. Tadic, E. Gherbesi, G. Grassi, G. Mancia, Renal artery stenosis and left ventricular hypertrophy: an updated review and meta-analysis of echocardiographic studies, Journal of hypertension 35(12) (2017) 2339–2345

[5] S. Manohar, A. Hamadah, S.M. Herrmann, S.C. Textor, Total Renal Artery Occlusion: Recovery of Function After Revascularization, Am J Kidney Dis 71(5) (2018) 748–753

P120.
Diffusion-weighted MR spectroscopy provides evidence for an association between citrate and spermine in lumen of the prostate

A. Heerschap[1], A. Stamatelatou[1], R. Rizzo[2], K. Simsek[3], J. van Asten[1], T. Scheenen[1], R. Kreis[2]

[1]*Radboud University Medical Centre, Medical Imaging, Nijmegen, Netherlands;*
[2]*University of Bern, MR methodology, Institute of Diagnostic and Interventional Neuroradiology, Bern, Switzerland;*
[3]*Cardiff University, Brain Research Imaging Centre (CUBRIC), Cardiff, United Kingdom*

Introduction Prostate tissue is composed of epithelial and stromal cells and large extracellular (luminal) spaces (LS) filled with prostatic fluid (PF). Major metabolites in PF are citrate (Cit), spermine (Spe) and myo-inositol (mI) of which the levels decrease in male fertility disorders and cancer development[1−3]. Cit and Spe concentrations are strongly correlated and, together with Zn, a Cit-Spe complex has been suggested[2−4]. Recently, we obtained evidence from metabolite T2 relaxometry for the existence of such a complex in a solution mimicking PF[5]. Diffusion-weighted MR Spectroscopy (DW-MRS) is ideally suited to explore microstructures in vivo with metabolites selectively present in different subspace[6,7]. The diffusivity of metabolites, expressed in apparent diffusion coefficients (ADC), may be restricted by complex formation and diffusion boundaries. **Aim:** To find evidence from DW-MRS measured ADC values for the luminal origin of Cit and Spe and their association in the prostate.

Methods Experiments were performed on phantoms with solutions containing PF compounds[5] and on the prostate of 9 healthy males. *DW-MRS* was done at 3 T with an external reception coil, employing a single voxel, non–water-suppressed STEAM (TE/TM/TR 33/35/

2500 ms) with metabolite-cycling to measure metabolite and water signals simultaneously[6] using 6 b-values up to 2516 s/mm^2. The same DW-MRS was applied to the phantoms and in vivo (Fig. 1).

Post-processing included motion corrections using the water signal as reference. To obtain metabolite ADCs the spectroscopic and diffusion decaying signals were fitted simultaneously to deal with limited SNR[7], assuming mono-exponential decay.

Results and discussion *Solutions with PF compounds:* The ADC values derived from the signals of 90 mM Cit and 18 mM Spe decreased upon mixing these compounds (Fig. 2, columns 2,3) demonstrating (transient) Cit-Spe complexation, in agreement with T2 relaxometry studies[5]. The effect on the ADC of Spe was larger than on Cit, but reversing the concentrations of these compounds showed a larger effect on the ADC of Cit (Fig. 2, column 4), indicating that the ADCs are a weighted average of bound and free compounds. After adding the index protein BSA to create a PF mimic solution (Fig. 2, column 5) the ADCs of Cit and Spe decreased further, and also the ADC of mI decreased demonstrating protein interaction of all these PF metabolites.

In vivo *prostate:* MR spectra of prostates recorded at increasing b-values were of good quality (Fig. 1). Excellent fits of metabolite signals were achieved as demonstrated by the small residuals. These experiments revealed that tCho and tCr have the lowest ADC values (Fig. 2), in agreement with their intracellular origin, while the higher values for Cit, Spe and to a lesser extent for mI concur that these compounds dominantly reside in the LS[3,4] with less diffusion restrictions. However, the ADC of Cit is substantially higher than that of Spe ($p < 0.05$). As the luminal Cit concentration is much higher than that of Spe, and assuming a 1:1 complex, it follows that the fraction of free Cit is much larger than that of Spe, which explains the higher ADC for Cit compared to Spe, as also observed in the PF mimic. The ratio of the Cit and Spe ADCs are comparable to that in the PF mimic suggesting also their complexation in vivo. At an average luminal diameter of ~ 150–200 μM[8] nearly unrestricted diffusion is expected for Cit, Spe and mI with much higher ADCs for such small molecules than what we report here (~ 6 to 9 rather than 2–3 10^{-4} mm^2/s). Apart from Cit-Spe complexation this may be due to irregular shapes of acini and further macromolecular (protein) binding in the LS as suggested by the ADC decreasing effect of BSA in the PF mimic.

Conclusions This is the first exploration of DW-MRS of the human prostate, successfully correcting motion with a simultaneously recorded water signal. The observed diffusivity of prostate metabolites is in agreement with their proposed cellular and luminal origin, although ADCs of luminal metabolites are lower than anticipated from their ADCs in a PF mimic. The relative diffusivities of Cit and Spe indicate their association in PF of the lumen, which may play a role in their (trans-membrane) transportation and the coordination of their metabolic activity.

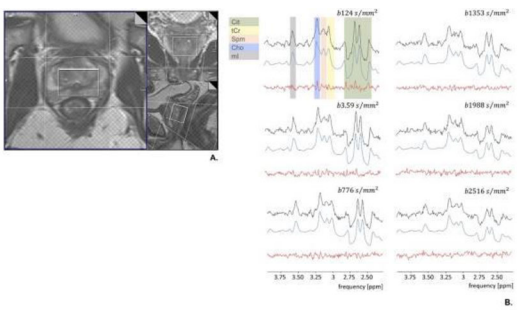

Fig. 1 In vivo single-voxel DW-MRS – ***A.*** *T2wMRI showing voxel position (volume= 13.2 cm3)* ***B.*** *MR spectra acquired for 6 b-values. Black: spectra after corrections; Blue: fitting of metabolite signals; Red: fit residual.*

	A. In vitro solutions (37 °C). ADC(± CRLB)				B. Prostate in vivo (n=9)	
	Individual metabolites	Cit 90 mM + Spe 18 mM	Cit 18 mM + Spe 88 mM	Prostatic fluid mimic	ADCs from average spectrum (± CRLB)	Average ADCs (± SD)
tCho	-	-	-	-	1.64 ± 0.13	1.47 ± 0.45
tCr	-	-	-	-	1.34 ± 0.09	1.63 ± 1.02
Cit	7.269 ± 0.003	6.651± 0.003	5.670± 0.003	5.964± 0.002	2.48 ± 0.07	2.86 ± 0.51
Spe	7.183 ± 0.006	5.513± 0.005	6.435± 0.001	4.998± 0.004	1.80± 0.06	1.91 ± 0.87
mI	10.659 ± 0.074			8.282± 0.053	1.41 ± 0.06	1.93 ± 0.81
H_2O				29	Cell: 5.51 Extra cell: 30	Cell: 4.8 ± 1.3 Extra cell: 22.1± 5.3

Fig. 2: Table of prostate metabolite ADCs x 10^{-4} mm^2/s. ***A. ADCs of individual metabolites (2nd column) are for*** *solutions of Cit (90mM), Spe (18mM) and mI (6 mM). The 3d and 4th column represent ADC values for mixtures of Cit and Spe. The 5th column represents ADC values for the PF mimic containing 90 mM Cit, 18 mM Spe, 6 mM mI and 15 g/l BSA at pH7.1. All solutions contained Na+, K+, Ca++, Mg++ and Zn++ at pH 7.1 as representative for ions in PF[5]. The ADC of H_2O in the PF mimic is also presented. B. ADC values of prostate compounds obtained in vivo. Left column: ADC obtained after averaging spectra of 9 subjects. Right column: averages of ADC per subject. A bi-exponential fit of the H_2O signal decay provided ADCs of cellular and extra-cellular H_2O content*

References

1. Verze ea. *Nat Rev Urol*. 2016;13(7). https://doi.org/10.1038/nrurol.2016.89 Costello & Franklin. *Arch Biochem Biophys* 2016 1;611. https://doi.org/10.1016/j.abb.2016.04.014.
2. Serkova ea. *Prostate*. 2008;68(6). https://doi.org/10.1002/pros.
3. Lynch ea. *Prostate*. 1997;30(4). https://doi.org/10.1002/(SICI)1097-0045(19970301)30:43.0.CO;2-H.
4. Jupin ea. NMR. *Magma.*. 2022. https://doi.org/10.1007/s10334-021-00983-4
5. Döring ea. *Magn Reson Med*. 2018;80(6). https://doi.org/10.1002/mrm.27222
6. Chong ea. *Magma*. 2011;24. https://doi.org/10.1007/s10334-011-0246-y
7. Lemberskiy ea. *Front Phys*. 2018;6. https://doi.org/10.3389/fphy.2018.00091

Acknowledgements: Research supported by EU ITN Marie-Sklodowska-Curie Grant 813120 (INSPiRE-MED).

P121.
Improving PRFS-based MR thermometry in prediction of ablation zones during MR-guided prostate ultrasound ablation using a probabilistic thermal dose model

S. Schröer[1], M. Gutberlet[1], J. Glandorf[1], I. Peters[2], S. Hellms[1], F. Wacker[1], B. Hensen[1]

[1]*Hannover Medical School, Department of Diagnostic and Interventional Radiology, Hannover, Germany;*
[2]*Krankenhaus Nordwest, Clinic for Urology, Frankfurt am Main, Germany*

Introduction MR-guided transurethral ultrasound ablation using the TULSA Pro setup has been shown to be a safe and feasible treatment of prostate tumors [1]. Using the proton resonance frequency shift (PRFS) MR-thermometry can be obtained to monitor the procedure [2]. Ablation zones are estimated using thermal dose models such as the CEM43 model [3]. However, the CEM43 model tends to produce many false positives due to motion artifacts, noise and susceptibility changes arising from air in the rectum. To prevent this, Schmitt et al. proposed a spatiotemporal filter [4]. However, the spatiotemporal filter needs to be adjusted to the treatment device requiring additional information and it may reduce, but not eliminate the false positve rate in prediction of the ablation zone. We therefore propose a

probabilistic thermal dose model (pCEM43) that reduces the number of false positives caused by artifacts and measurement noise without the need of any manual adjustment to the treatment setup.

Methods We evaluated the pCEM43 model using 18 out of 22 data sets of MR-guided high intensity focused ultrasound prostate ablation procedures. 4 data sets were excluded due to technical issues. The ablations were monitored using a 1.5 Tesla MRI machine (Siemens Aera, Siemens Healthineers, Erlangen, Germany). MR-Thermometry was acquired intraoperatively with an EPI sequence (echo time (TE): 16 ms, repetition time (TR): 45 ms, bandwidth: 1300 Hz / pixel, flip angle (FA): 60°, field of view (FOV): 256 mm × 256 mm, matrix size: 128 × 128, slice thickness: 4 mm, slice distance: 5 mm) using the PRFS. The ablation zones derived by manual segmentation of post-ablative contrast-enhanced T1-weighted MR-imaging by an experienced interventionalist were used as ground truth to evaluate MR-thermometry.

The post-ablative images were registered to MR-thermometry using ANTs [5]. To prevent errors due to mismatching registration, only the central four slices of the treatment zone were evaluated. Two erosion and two dilation passes were added to the necrosis maps of the pCEM43 model to reduce noise.

The metrics used for evaluation were the Dice-Sorensen-Score (DSC), the Sensitivity, and the relative false positive rate (rFPR). The rFPR is computed by the sum of the false positives divided by the sum of the true positives and false negatives. The results of the unfiltered and filtered CEM43 and the pCEM43 model were compared using the Wilcoxon signed-rank test.

Results The mean DSCs are 39.42% ± 10.44%, 65.31% ± 10.63%, and 71.57% ± 8.00%, the mean rFPRs are 2.50 ± 1.12, 0.65 ± 0.44, and 0.30 ± 0.28, and the mean Sensitivities are 79.34% ± 7.4%, 76.87% ± 8.29%, and 71.44% ± 9.30% for the unfiltered CEM43, the filtered CEM43, and the pCEM43 model, respectively. The unfiltered CEM43 model has the lowest DSC for any of the data sets. The pCEM43 model has the highest DSC.

The DSC was significantly different between the unfiltered and the filtered CEM43 model (+ 25.89%, p = 0.000196), between unfiltered CEM43 and pCEM43 model (+ 32.15%, p = 0.000196) and between filtered CEM43 and pCEM43 model (+ 6.26%, p = 0.003286). The family-wise error rate (FWER) is 0.37%.

Exemplary, the ablation zones for data set 3 estimated by the different models can be seen in Fig. 1.

Discussion The filtered CEM43 model predicts the ablation zone better than the unfiltered CEM43 model. However, out of the three methods, the pCEM43 model best estimates the ablation zone. In comparison to filtered CEM43, pCEM43 shows an increased underestimation of the necrosis zone indicated by the lower mean sensitivity, but also a reduced overestimation provided by the lower rFPR. This may prevent premature termination of the ablation procedure and consequently may increase the success rate.

Conclusion pCEM43 may help to improve monitoring MR-guided transurethral ultrasound ablation and thereby may increase the success rate of this treatment. In future, the proposed model will be evaluated in other applications of thermal ablation. Furthermore, a connected component analysis may be added to further reduce false positives.

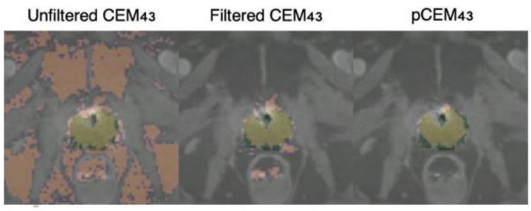

Fig. 1: Data set 3 with estimated ablation zones (orange) of unfiltered CEM43 (left), filtered CEM43 (center), and pCEM43 (right) and ground truth (green).

References:

1. Joseph L. Chin et al. "Magnetic Resonance Imaging-Guided Transurethral Ultrasound Ablation of Prostate Tissue in Patients with Localized Prostate Cancer: A Prospective Phase 1 Clinical Trial." European urology 70 3 (2016): 447–55.
2. Viola Rieke and Kim Butts Pauly. "MR thermometry." Journal of Magnetic Resonance Imaging. 27 2 (2008): 376–90.
3. W C. Dewey "Arrhenius relationships from the molecule and cell to the clinic." International journal of hyperthermia: the official journal of European Society for Hyperthermic Oncology, North American Hyperthermia Group 25 1 (2009): 3–20.
4. Alain Schmitt, Charles Mougenot and Rajiv Chopra. "Spatiotemporal filtering of MR-temperature artifacts arising from bowel motion during transurethral MR-HIFU." Medical physics vol. 41,11 (2014): 113302.
5. Advanced Normalization Tools (ANTs): http://stnava.github.io/ANTs/

P122.
Role of IVIM MRI in response assessment in rectal carcinoma

C. Das[1], A. Soni[1], H. Bhattacharjee[2]

[1]*AIIMS New Delhi, Radiodiagnosis, New Delhi, India;*
[2]*AIIMS New Delhi, Surgery, New Delhi, India*

Introduction IVIM-DKI possesses the ability to delineate the changes in the diffusion and capillary perfusion microenvironment of the tumor. In this study, we want to assess the usefulness and performance of Diffusion-weighted imaging with intravoxel incoherent motion and diffusion kurtosis imaging (DKI) for assessing the chemotherapy (CT)/Chemo and Radiotherapy (CTRT) response in colorectal carcinoma and compare with PET/CT parameters.

Methods A total of 40 patients of rectosigmoid cancer underwent baseline staging multiparametric MRI and 18-FDG PET/CT and follow-up with both scans post-chemo radiotherapy. Quantitative diffusion, IVIM and DKI parameters, viz. ADC, D, f, and K were measured from the solid non-necrotic areas and semi-quantitative PET parameters including SUV max, SUV ratio, Metabolic tumor volume (MTV), and total lesion glycolysis (TLG) were derived from the PET/CT images, and correlated with the patient"s response keeping RECIST 1.1 criteria as the gold standard.

Results No significant difference in the baseline IVIM parameters was found among the patients with different stages of the disease { T2 (n = 3), T3 (n = 28), and T4 (n = 9)}. No significant difference in the baseline IVIM parameters was found among the patients with metastatic and non-metastatic rectosigmoid cancer. Statistically significant increase in diffusion coefficient D & apparent diffusion coefficient ADC was noted after therapy in all patients. A statistically significant decline in kurtosis K was noted after therapy in all patients. No significant difference was seen in the baseline and post-therapy perfusion coefficient f in all patients. No significant difference was seen among the percentage change in the parameters observed post-therapy among the responders and non-responders. Δ ADC % showed the highest AUC on an RO curve among all parameters, of 0.714, whereas Δf% showed the least strong correlation with a positive response with an AUC of 0.345. Both the responders, as well as non-responders, depicted a statistically significant increase in D and ADC, and a significant decline in K values post-therapy.

Among the 17 patients that underwent follow-up PET/CT imaging, a significant decline in SUVmax, SUVratio, MTV, and TLG of the primary lesion was seen post-therapy. Responders (n = 12) showed a significant decline in the SUVmax, SUVratio, MTV, and TLG values

from baseline after therapy, whereas non-responders did not show any statistically significant change from baseline values in all parameters. Post-therapy MTV, followed by TLG was found to have the strongest correlation with a positive response with the AUCs of 0.933 and 0.900 on the receiver operator curves.

Discussion Differentiation of non-responders to therapy from responders would protect patients from unnecessarily prolonged treatment and the related adverse effects, and reduce treatment costs. The patients may be referred for treatment with alternative modalities or a different regimen.

Conclusion IVIM-DKI possesses the ability to delineate the changes in the diffusion and capillary perfusion microenvironment of the tumor. 18-FDG PET/CT is the more accurate single modality for assessing both the response as well as tumor burden post-therapy, while ADC and D derived from DWI and IVIM respectively are useful adjuncts for the assessment of response.

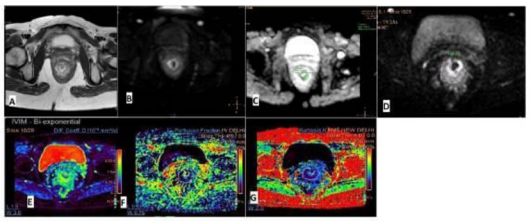

Fig. 1: (Pre-therapy): A – Axial T2. image showing an intermediate signal intensity circumferential wall thickening involving the upper and middle thirds of the rectum. Corresponding Diffusion (B), ADC map(C), IVIM (b=1000) (D), Diffusion Coefficient D map (E), Perfusion. Coefficient f (F)and Kurtosis K (G)maps.

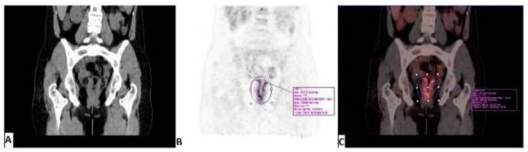

Fig. 2: (Pre-therapy): Baseline pre-therapy 18-FDG PET/CT scan images of the patient. CT (A), PET (B), and fused PET/CT images (C) show an FDG avid wall thickening of the upper and middle rectum.

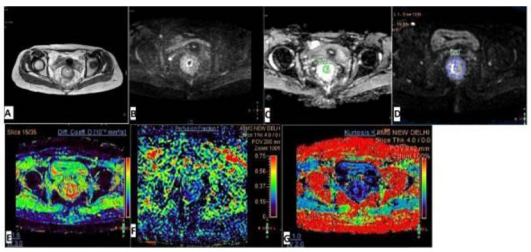

Fig. 3: (post-therapy): Residual tumor as seen on the T2W images (A) with corresponding diffusion and ADC maps (B,C). IVIM images (D) to derive true diffusion, perfusion and kurtosis maps (E, F,G) which showed an increase in the D & f values and a decrease in the kurtosis values.

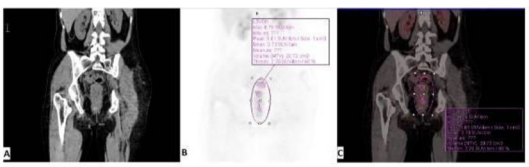

Fig. 4:(post-therapy PET-CT): Post-therapy PET/CT images of the patient (B & C) shows a decrease in the FDG uptake and a resultant reduction in the SUVmax of the rectal wall thickening.

P123.
Evaluation of the MIX and TopoPro fitting algorithms on the IVIM parameter landscape

I. A. Rashid[1], C. Jamtheim Gustafsson[2,3], A. Gunnlaugsson[2], L. E. Olsson[2,3], P. Brynolfsson[2]

[1]*Lund University, Department of Clinical Sciences, Medical Radiation Physics, Lund, Sweden;*
[2]*Skåne University Hospital, Department of Hematology, Oncology and Radiation Physics, Lund, Sweden;*
[3]*Lund University, Department of Translational Medicine, Medical Radiation Physics, Malmö, Sweden*

Introduction Intravoxel incoherent motion (IVIM) is an imaging technique that provides information on tissue perfusion and diffusion, where the signal is described by the following bi-exponential model [1]:

$S = S_0[fe^{-bD*} + (1-f)e^{-bD}]$, (1).where f is the fraction of the signal derived from perfusion effects, $D*$ the pseudo-diffusion coefficient of blood, D the diffusion coefficient of water. S, S_0, b are the signal, signal without diffusion encoding, and the diffusion encoding strength respectively.

Acquiring meaningful information by fitting this model to data is challenging since the problem is ill-conditioned and sensitive to noise (Fig. 1a,b). Two fitting algorithms have recently been proposed; MIX [2] and TopoPro [3], which claim to be more accurate and less sensitive to noise [3] compared to the conventional Segmented method. Currently, no independent evaluation of these methods has been performed.

The aim of this work is to evaluate the bias and noise sensitivity of the proposed and conventional algorithms to find the best performing method. This was done by simulating signals for a wide range of tissue properties.

Methods The Segmented algorithm used is a 2-step process where D is estimated from b-values $\geq$ 150 s/mm^2 using a mono-exponential S_0e^{-bD} least-squares fit, followed by a least-squares estimation of f and $D*$ to Eq. (1) keeping D fixed [4]. MIX and TopoPro are based on variable projection and are described in [2] and [3] respectively.

To account for various tissue properties, a total of 1000 parameter combinations ordered in a 10 $\times$ 10 $\times$ 10 array were defined; with each dimension corresponding to increasing f, $D*$, and D, such that each element consisted of a unique parameter combination (Fig. 1c). Linear ranges were used, where $f \in [0.02, 0.5]$, $D* \in [5, 30]$ μm^2/ms, and $D \in [0, 3]$ μm^2/ms. Signals were simulated using Eq. (1) for b-values 0, 20, 40, 60, 80, 100, 150, 200, 300, 400, 500, 600, 700, and 800 s/mm^2.

To investigate noise sensitivity, Rician noise was simulated 100 times for each parameter combination such that a specific SNR was obtained for S(800 s/mm^2), giving a total of 100 000 signal curves. SNR for lower b-values were exponentially propagated with the signal assuming constant noise. Evaluation was performed for SNR 3 and 10. Parameter estimates were produced using the Segmented, MIX, and TopoPro algorithms for all 100 000 signal simulations, for each of the two SNR-levels. Bias (estimate − ground truth) and root-mean-square error (RMSE = $\sqrt{[\text{bias}^2 + \text{standard deviation}^2]}$) of each parameter estimate were used to compare the total error of the three algorithms.

Results The Segmented method was least sensitive to noise (Fig. 2), but had the largest bias in f and D as $D*$ approached D. MIX and TopoPro were more sensitive to noise, while their biases for $D*$ was restricted to low values of f. At SNR 3, errors in f can be expected to be 15–20%, errors in D 0.4–0.6 μm^2/ms, and $D*$ 30–60 μm^2/ms for the tested ranges. Results are only shown for ground truth D = 1.0 μm^2/ms as the general patterns were similar for all simulated D.

Discussion The Segmented method is less sensitive to signal noise in the estimation of f and D. However, MIX is not far behind, and

performs the best in the estimation of D^*. TopoPro shows greater noise sensitivity.

The biases of MIX and TopoPro are low to non-existent, except in a parameter range where the problem becomes degenerate at low values of f. MIX and TopoPro handle the $D^* \sim D$ degeneracy better than the Segmented method. Despite their bias, it can still be noted in the RMSE maps of MIX and TopoPro that difficulties arise in the ranges where the Segmented method shows a large bias. These errors are however lower than the bias of the Segmented method.

The computation time for MIX and TopoPro were approximately 15 times greater compared to the Segmented method, which could influence the choice of fitting algorithm if computation time is an important factor.

Conclusion The Segmented method was least sensitive to signal noise at the cost of a larger bias when D^* approached D. MIX has the lowest overall RMSE with little to no bias and low noise sensitivity, at the cost of greater computation time.

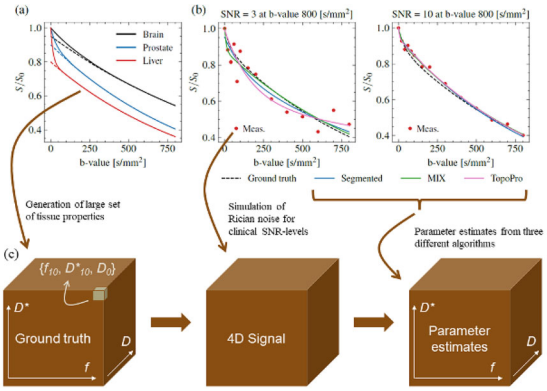

Fig. 1: (a) IVIM signals vary between tissues. (b) Fitting algorithms may yield different parameter estimates based on their bias and noise sensitivity. (c) The simulation sequence. Noised signals were simulated for 1000 parameter combinations to evaluate RMSE for parameter estimates using different algorithms.

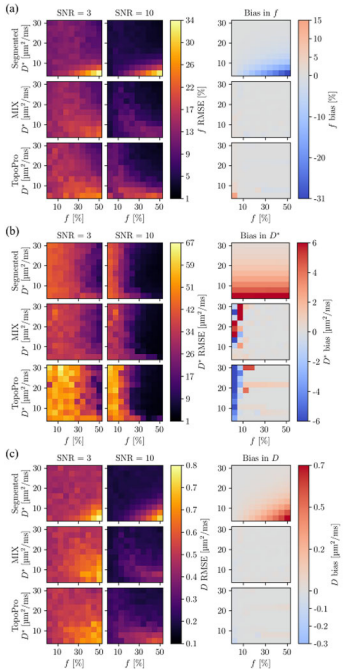

Fig. 2: RMSE and bias maps of f (a), D^* (b), and D (c), for ground truth D-value 1.0 μm²/ms. (a): The Segmented method was least sensitive to noise but showed a bias. Both MIX and TopoPro showed little to no bias. (b): MIX was the best estimator of D^*. Biases can be observed for all three algorithms. The bias was an order of magnitude lower than the RMSE. (c): The Segmented method is slightly better at low SNR. All methods show difficulties estimating D when D^* is low and f high, where only the Segmented is biased.

References

1. Le Bihan D. What can we see with IVIM MRI? NeuroImage. 2019 Feb 15;187:56–67.
2. Farooq H, Xu J, Nam JW, Keefe DF, Yacoub E, Georgiou T, et al. Microstructure Imaging of Crossing (MIX) White Matter Fibers from diffusion MRI. Sci Rep. 2016 Dec 16;6(1):38,927.
3. Fadnavis S, Endres S, Wen Q, Wu YC, Cheng H, Koudoro S, et al. Bifurcated Topological Optimization for IVIM. Front Neurosci. 2021;15:779,025.
4. Merisaari H, Movahedi P, Perez IM, Toivonen J, Pesola M, Taimen P, et al. Fitting methods for intravoxel incoherent motion imaging of prostate cancer on region of interest level: Repeatability and gleason score prediction. Magn Reson Med. 2017;77(3):1249–64.

P124.
Microcalcification detection and classification in breast cancer using ultrashort echo time (UTE) MRI

Y. Ayoub[1], S. M. Cheung[1], B. Maglan[1], E. Husain[2], Y. Masannat[3], J. He.[4]

[1]*University of Aberdeen, Institute of Medical Sciences, School of Medicine, Medical Sciences and Nutrition, Aberdeen, United Kingdom;*
[2]*Aberdeen Royal Infirmary, Pathology Department, Aberdeen, United Kingdom;*
[3]*Aberdeen Royal Infirmary, Breast Unit, Aberdeen, United Kingdom;*
[4]*Newcastle University, Newcastle Magnetic Resonance Centre, Translational and Clinical Research Institute, Faculty of Medicine, Newcastle, United Kingdom.*

Introduction Breast cancer is the most prevalent cancer affecting women, while the presence of calcium in solid form, known as calcification, is a central feature[1]. The detection and classification of calcification in breast cancer holds significant prognostic value in treatment planning[2]. Mammography, as the only current clinical radiological approach sensitive to the presence of calcification, cannot reveal the precise classification of calcification[3]. Ultrashort Echo Time (UTE) imaging, a novel radiological method, addresses the limitation of conventional MRI to primarily soft tissue application by capturing rapid signal decay in solid state matters such as calcification. We therefore set out to examine the feasibility of UTE imaging in identifying histological characteristics of microcalcifications in freshly excised breast tumours.

Methods *Image Acquisition:* 20 freshly excised invasive ductal carcinoma specimens were scanned on a 3 T whole-body MRI scanner (Achieva TX, Philips Healthcare, Best, Netherlands) using a 32-channel receiver coil for high sensitivity detection and a body coil for uniform transmission. For tumour localisation, anatomical images were acquired using standard T1-weighted and T2-weighted sequences with conventional diffusion weighted images (2 *b*-values of 0 and 800 s/mm^2). The UTE images were acquired with a 3D-radial dual echo UTE sequence, with echo times (TE) of 0.17 ms and 4.60 ms, repetition time (TR) of 8.5 ms, FOV of 141 × 141 mm^2, voxel size of 2.2 × 2.2 × 2.2 mm^3.

Image Analysis: The whole tumour was manually delineated across the tumour volume in MATLAB (Mathworks Inc., Natick, USA) and the signal intensity of the two echoes were derived as the mean of the image intensity within the whole tumour for each echo (Fig. 1). The degree of calcification was computed as the signal difference between the two echoes normalised by the long echo. The tumour size was quantified as the maximum diameter and the average area (spatial extent) of the whole tumour.

Pathology: Standard pathological analysis was conducted to determine the tumour grade, calcification status, Nottingham Prognostic Index (NPI) and proliferative activity marker Ki-67 to assess differences between clinical features.

Results There was a significant difference (P = 0.012) in the degree of calcification between specimens with malignant calcification (1.054 ± 0.132) and specimens with no calcification (0.842 ± 0.091) (Fig. 2). There was no significant difference (P = 0.355) in the degree of calcification between specimens with malignant calcification (1.054 ± 0.132) and benign calcification (0.951 ± 0.158). There was no significant correlation between the degree of calcification against NPI and Ki-67 scores (Fig. 3). A summary of the results and statistical analysis are shown in Table 1.

Discussion UTE enhances the detection of short T2* species and may have potential in the detection of solid state signal from calcifications in breast tumours. We examined the degree of calcification in tumour specimens through the separation of quantitative solid state signal in the short first echo from the soft tissue signal in the second long second echo, using dual echo UTE approach. Although UTE showed potential in sensitivity to calcified tumours, further work is required for non-invasive differentiation of calcification classes. Malignant calcifications have a crystalline structure as a result of the formation of hydroxyapatite crystals, while benign calcifications, generally composed of calcium oxalate crystals, may form amalgamate with hydroxyapatite crystals, introducing challenges in the differentiation of solid state signals[4]. No correlation between histologic calcification classes and tumour grade and size was found, although both are reported to have an association with calcified tumours[5].

Conclusion

Tumours with malignant calcification may be differentiated from tumours without calcification using UTE imaging, while benign calcification did not show a significant difference.

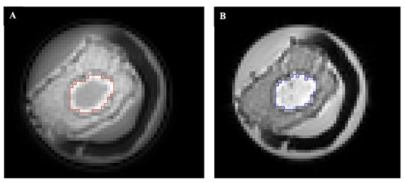

Fig. 1: *Delineation of whole tumour region on dual echo UTE image: (A) Time of Echo 1 (TE_1) at 0.17ms and (B) Time of Echo 2 (TE_2) at 4.6ms*

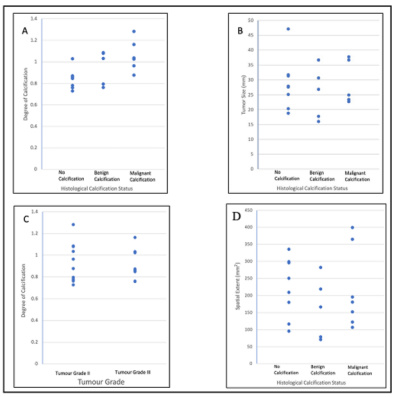

Fig. 2: *Graphical representation of UTE image analysis in relation with histology data. (A) Degree of calcification based on the three calcification groups, (B) Tumour size based on the three calcification groups, (C) Degree of calcification based on the tumour Grade II or III, (D) Spatial extent based on the three calcification groups*

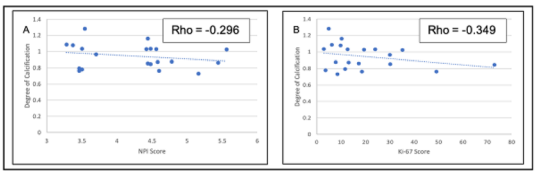

Fig. 3: *Association between degree of calcification against NPI and Ki-67 scores. (A) Correlation plot between the degree of calcification and the NPI score, (B) Correlation plot between the degree of calcification and the Ki-67 score*

	n	Mean ± SD	Median (IQR)	t	F	r	P-value
Calcification load							
Tumour grade[1]							
Grade II	10	0.939 ± 0.180		0.118			0.908
Grade III	10	0.947 ± 0.124					
Histological calcification status[2]							
No calcification	8	0.842 ± 0.091			5.405		0.012*
Benign calcification	5	0.951 ± 0.158					
Malignant calcification	7	1.054 ± 0.132					
Histological tumour prognosis[3]							
Ki-67 score	20		12.85 (8.13-27.1)			-0.349	0.132
NPI score	20		4.44 (3.50-4.59)			-0.296	0.205
Tumour size (mm)							
Histological calcification status[2]							
No calcification	8	28.7 ± 8.8			0.231		0.796
Benign calcification	5	25.6 ± 8.7					
Malignant calcification	7	27.3 ± 6.7					
Spatial extent of calcification (mm^2)							
Histological calcification status[2]							
No calcification	8	223.0 ± 87.8			0.609		0.555
Benign calcification	5	163.9 ± 90.8					
Malignant calcification	7	217.6 ± 116.9					

** Indicates significance at 5%.*

[1] Independent t-test, [2] One-way ANOVA test, [3] Spearman's rho correlation.

Table 1: *A summary of the results and statistical tests*

References

DeSantis CE, Ma J, Gaudet MM, Newman LA, Miller KD, Goding Sauer A, Jemal A, Siegel RL. Breast cancer statistics, 2019. CA Cancer J Clin. 2019 Nov;69(6):438–451.

Baker, R. et al. *New relationships between breast microcalcifications and cancer. British Journal of Cancer, (2010);103(7),1034–1039.*

Bennani-Baiti, B. & Baltzer, P. A. MR Imaging for Diagnosis of Malignancy in Mammographic Microcalcifications: A Systematic Review and Meta-Analysis. Radiology. (2017);283(3),692–701.

Morgan M, Cooke M, Mc Carthy G, Microcalcifications Associated with Breast Cancer: An Epiphenomenon or Biologically Significant Feature of Selected Tumors? Journal of Mammary Gland Biology and Neoplasia, Vol.10, No.2, (2005);181:187.

Mun HS, Shin HJ, Kim HH, Cha JH, Kim H. Screening-detected calcified and non-calcified ductal carcinoma in situ*: differences in the imaging and histopathological features. Clin Radiol. 2013 Jan;68(1):27–35.*

P125.
Feasibility of chest spiral 3D ultrashort echo time magnetic resonance imaging in intrathoracic metastasis workup of breast cancer

K. J. Nam[1], K. Lee[1], J. W. Lee[2], T. Kang[3], K. I. Kim[1], Y. J. Jeong[1]

[1]*Pusan National University Yangsan Hospital, Radiology, Yangsan-si, South Korea;*
[2]*Pusan National University Hospital, Radiology, Busan-si, South Korea;*
[3]*Pusan National University Hospital, Surgery, Busan-si, South Korea*

Introduction Chest computed tomography (CT) is routinely performed to evaluate intrathoracic metastasis in patients with breast cancer. However, radiation exposure and its potential carcinogenic risks are major drawbacks [1]. Pulmonary imaging with magnetic resonance imaging (MRI) has been limited by the low proton density, rapid signal decay, and sensitivity to respiratory and cardiac motion present in lung tissue [1]. Recently, a respiratory gating spiral three-dimensional (3D) ultrashort echo time (UTE) sequence has been developed, enabling lung MRI to be used in clinical practice with high spatial-resolution images and reasonable scan times [2, 3]. Our objective was to investigate the feasibility of chest spiral 3D UTE MRI in breast cancer patients to detect intrathoracic metastasis.

Methods Institutional review board approved this retrospective study of a prospectively collected database and all participants provided informed consent for MRI scans. Between February and July 2019, 93 female patients with breast cancer were retrospectively enrolled and all underwent preoperative breast MRI including chest spiral 3D UTE VIBE (volume interpolated breath-hold examination) sequence. Two chest radiologists evaluated the image quality in terms of visibility of intrapulmonary vessels and bronchial wall, artifact/ noise, and overall image quality using a five-point scoring system, presence of pulmonary nodules, other lung abnormalities, and significant lymph nodes on the spiral 3D UTE MRI and compared them using chest CT as a reference standard.

Results Intrapulmonary vessels and bronchial wall were visible up to the sub-subsegmental and sub-subsegmental levels, respectively, on spiral 3D UTE MRI. 95.7% and 98.9% of patients had above fair quality in regarding to artifact/ noise and overall image quality (Fig. 1). The detection rate of overall pulmonary nodules was 62.8% (59/94). Among 81 solid nodules detected on CT, 59 were detected on the spiral 3D UTE MRI (72.8%). Among 33 solid nodules $\geq$ 5 mm in diameter, 31 nodules were identified on spiral 3D UTE MRI (93.9%) (Figs. 2, 3). Significant LNs in the axillary area were similarly detected on spiral 3D UTE MRI and chest CT.

Discussion Our study shows that spiral 3D UTE VIBE sequence can provide good-quality images of the lungs in semiquantitative analysis. In our study, solid nodules $\geq$ 5 mm showed a detection rate of 93.9%. For solid nodules, previous studies demonstrated detection rates of 60 to 90% for lesions with a diameter of 5—8 mm, which were consistent with our results [4, 5]. The UTE VIBE, which presents high signal-to-noise (SNR) ratio and high resolution images, is useful for lung morphological evaluation [6]. Significant LNs in axillary area were similarly detected on chest CT and spiral 3D UTE MRI, but were identified in one case more on spiral 3D UTE VIBE sequence. The LNs found in the spiral 3D UTE VIBE sequence but not in the chest CT were an axillary level II LNs which could not be distinguished due to the same density as the surrounding pectoralis muscles on the chest CT (Fig. 4). In addition, diagnostic accuracy of spiral 3D UTE VIBE images for predicting axillary lymph node metastasis were similar to that of chest CT.

Conclusions Preoperative breast MRI including chest spiral 3D UTE VIBE sequence could evaluate not only breast cancer and axillary LNs, but also intrathoracic metastasis at once without additional radiation exposure, which could be a potential alternative to chest CT for the breast cancer patient.

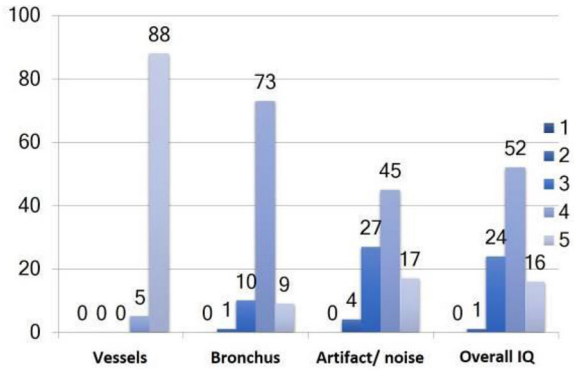

Fig. 1: Semiquantitative analysis of the image quality of UTE sequence in 93 patients with breast cancer.

Parameters	Spiral 3D UTE	CT (reference)	Detection rate (%)
No. of overall nodules detected	59	94	62.8
No. of GGNs	0	13	0.0
Mean diameter (mm)	0.0 (0.0-0.0)	4.5 (1.2-7.3)	
No. of solid nodules	59	81	72.8
Mean diameter (mm)	5.0 (1.8-14.2)	4.9 (1.6-13.7)	
Nodule composition			
Calcified	9	14	64.3
Non-calcified	50	67	74.6
Nodule size			
< 5 mm	28	48	58.3
5 mm ≤ < 10 mm	26	28	92.9
≥ 10 mm	5	5	100.0
Nodule location			
Right upper lobe	12 (5, calcified)	19 (7, calcified)	63.2
Right middle lobe	8 (0, calcified)	11 (1, calcified)	72.7
Right lower lobe	14 (3, calcified)	20 (4, calcified)	70.0
Left upper lobe	13 (1, calcified)	15 (1, calcified)	86.7
Left lower lobe	12 (0, calcified)	16 (1, calcified)	75.0

Fig. 2: Characteristics and detection rate of pulmonary nodules.

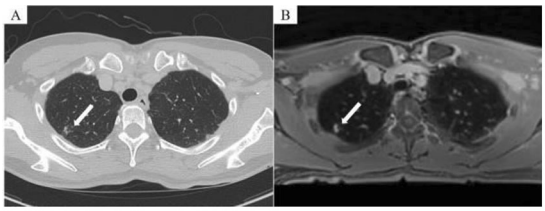

Fig. 3: A 61-year-old woman with invasive ductal carcinoma of right breast. (A) Lung window image of axial non-enhanced CT scan at the level of upper trachea shows two clustered small nodules in right upper lobe. (B) Contrast-enhanced axial T1-weighted 3D spiral UTE VIBE with fat saturation image at the same level shows two clustered small nodules in right upper lobe.

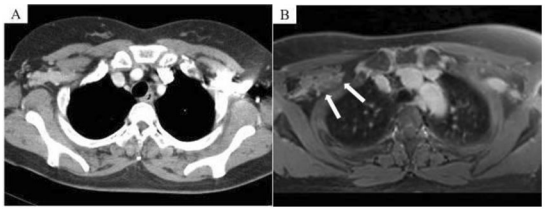

Fig. 4: A-54-year-old woman with invasive ductal carcinoma of right breast. (A) Contrast-enhanced axial CT image shows no enlarged lymph node at right axilla level II. (B) Contrast-enhanced axial T1-weighted 3D spiral UTE VIBE with fat saturation image shows multiple enlarged lymph nodes with eccentric cortical thickening at right axilla level II, which were confirmed metastatic lymph nodes at pathologic examination.

References

1. Cha MJ, Park HJ, Paek MY, et al. Free-breathing ultrashort echo time lung magnetic resonance imaging using stack-of-spirals acquisition: A feasibility study in oncology patients. Magn Reson Imaging 2018;51:137–43.
2. Dournes G, Yazbek J, Benhassen W, et al. 3D ultrashort echo time MRI of the lung using stack-of-spirals and spherical k-Space coverages: Evaluation in healthy volunteers and parenchymal diseases. J Magn Reson Imaging 2018;48:1489–97.
3. Cha MJ, Ahn HS, Choi H, et al. Accelerated Stack-of-Spirals Free-Breathing Three-Dimensional Ultrashort Echo Time Lung Magnetic Resonance Imaging: A Feasibility Study in Patients With Breast Cancer. Front Oncol 2021;11:746059.
4. Cieszanowski A, Lisowska A, Dabrowska M, et al. MR imaging of pulmonary nodules: detection rate and accuracy of size estimation in comparison to computed tomography. PLoS One 2016;11:e0156272.
5. Meier-Schroers M, Kukuk G, Homsi R, et al. MRI of the lung using the PROPELLER technique: Artifact reduction, better image quality and improved nodule detection. Eur J Radiol 2016;85:707–13.
6. Ohno Y, Koyama H, Yoshikawa T, et al. Pulmonary high-resolution ultrashort TE MR imaging: Comparison with thin-section standard- and low-dose computed tomography for the assessment of pulmonary parenchyma diseases. J Magn Reson Imaging 2016;43:512–32.

P126.
T2 mapping of patellar cartilage after single and first-time traumatic lateral patellar dislocation episode

E. Voronkova[1,2], P. Menshchikov[2,3], I. Melnikov[1], O. Bozhko[1], A. Manzhurtsev[1], M. Ublinskiy[1,2], D. Vorobyev[1], A. Kobzeva[1], T. Akhadov[1]

[1]*Clinical and Research Institute of Emergency Pediatric Surgery and Trauma, Moscow, Russian Federation;*
[2]*Institute of Biochemical Physics, Russian Academy of Sciences, Moscow, Russian Federation;*
[3]*LLC Philips, Moscow, Russian Federation*

Introduction Chondromalacia is a pathology of the patella cartilage that is often initiated by patellar dislocation and has the highest prevalence in adolescent population. Patellar dislocations tend to occur in a lateral direction (lateral patellar dislocation, LPD). The usual clinical MRI protocol may not be sufficient for an accurate diagnostic of cartilage condition. So new quantitative MRI (qMRI) methods could be effective alternatives. T2 mapping is a proven technique for quantifying the water content and collagen component of the cartilage extracellular matrix[1]. The purpose of the present study is to examine short-term consequences of the first-time LPD on patellar cartilage quality in teenagers using T2 mapping.

Methods The study includes 77 patients (15.1 ± 1.8 years) with different stages of chondromalacia caused by first time LPD and 48 healthy volunteers (14.7 ± 2.2 years). All research participants underwent knee joint MRI with 3 T scanner and 16-chanel transmit-receive knee coil. Chondromalacia grades were determined by two radiologists according to a modified Outerbridge scale using PDw SPAIR images. The condition of patients with chondromalacia grades 1 and 2 was classified as mild, and those with grades 3 and 4 as severe. The scientific protocol included T2 mapping (TSE, 6 TE from 13 to 78 ms, TR: 2000 ms, voxel size: $0.4 \times 0.4 \times 3$ mm). T2 values were calculated in manually segmented cartilage area via averaging over three middle level slices in 6 cartilage regions: deep, intermediate, superficial layers and medial, lateral parts (Fig. 1). To identify the difference between control, mild, and severe groups, a one-way repeated measure janalysis of variance (ANOVA) was used. Tukey''s multiple comparison test was performed when statistical significance was determined through the ANOVA. The threshold of significance was set at $p < 0.05$. A multiclass classification models was created using One-vs-Rest (OVR) logistic regression using the scikit-learn library (0.24.2) in python.

Results In the lateral part of the cartilage, an increase in T2 values was found for both the mild and severe chondromalacia group in the deep and intermediate layers compared to the control group. No differences were revealed for the comparison of T2 values between groups in the lateral superficial layer. In the medial part, an increase in T2 values compared to the control group is observed only for the severe group in the deep layer, while T2 in the mild chondromalacia group either doesn“t change (deep and intermediate layers) or decreases (superficial layer) (Fig. 2). The best classification model is shown to be the one that uses T2 from all six regions as input features compared to models that included less input features (Fig. 3).

Discussion In the current study, chondromalacia patella was investigated after a single and first-time traumatic LPD episode. Our new findings showed a principal difference in T2 changes between medial and lateral cartilage facet. While T2 values rise with increasing damage in the deep and intermediate layers of lateral part for mild and severe groups, they tend to decrease in the medial part for mild chondromalacia.

The increase in T2 is likely associated with matrix damage. The loss of collagen integrity leads to heightened matrix permeability, an increase in the content and motion of water, and, therefore, to prolonged T2 times. Mechanics of the LPD is characterized by contusion of the medial patella at the lateral femoral condyle, thus the medial part usually suffers first after LPD whereas lateral compartment lesions appear at later stages. So elevated T2 values are most likely an indirect consequence of the injury through the metabolic problems and additional loading due to medial patellofemoral ligament injury. Unchanged or reduced T2 may indicate the presence of processes that compensate for the increase in relaxation time. The possible processes are altered biomechanics, dehydration and loss of capacity to retain water. In addition, reparative processes can lead to T2 decrease[2]. Thus, the absence of T2 changes for the mild group in medial facet may indicate completed reparative processes, while the decreased T2 indicates that the reparation is still ongoing.

Conclusion Principal difference in T2 changes between medial and lateral patellar cartilage areas revealed in our study is a result of the LPD traumatic mechanism—primary medial patella contusion with the signs of recovery processes and secondary damage of lateral facet.

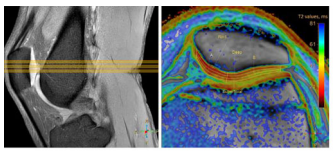

Fig. 1: Position of the three axial slices in the middle level of the patellar cartilage (left); An example of a T2 map of the patella cartilage (right).

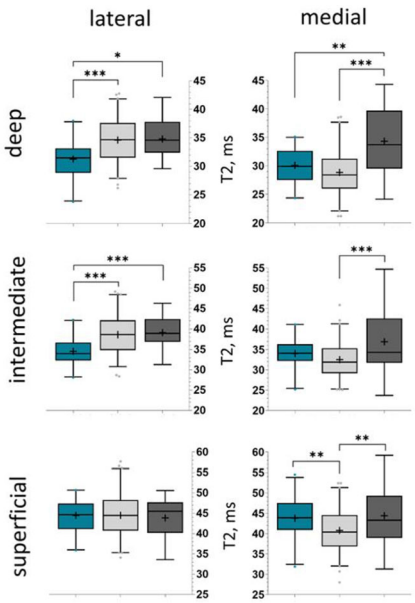

Fig. 2: Box plot of the T2 relaxation times in the control group and mild and severe chondromalacia groups, quantified separately in the lateral and medial facets of patellar cartilage, considering segmentation of the patellar cartilage into deep, intermediate and superficial layers *p ≤ 0.05, **p ≤ 0.01, ***p ≤ 0.001.

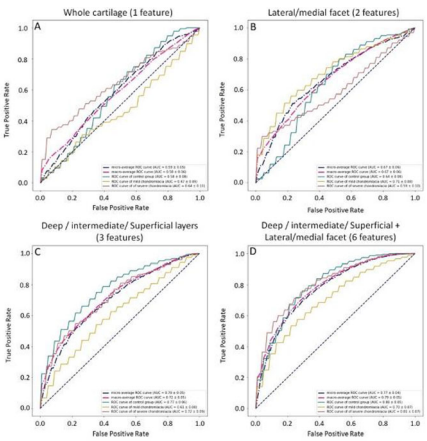

Fig. 3: ROC curves and appropriate ROC AUC scores for classification models, depending on the number of the features: from the whole ROI that delineated the cartilage (A); from the deep, intermediate, and superficial layers of the cartilage, which were automatically segmented through the uniform division of the ROI (B); from lateral and medial cartilage areas (C); from medial and lateral cartilage areas which were further divided into a three layers resulting in six regions of interest (D).

References

1. van Eck CF, Kingston RS, Crues J V, Kharrazi FD. Magnetic Resonance Imaging for Patellofemoral Chondromalacia: Is There a Role for T2 Mapping? Orthop. J. Sport. Med. 2017;5(11):325967117740554.
2. Welsch GH, Mamisch TC, Weber M et al. High-resolution morphological and biochemical imaging of articular cartilage of the ankle joint at 3.0 T using a new dedicated phased array coil: in vivo reproducibility study. Skeletal Radiol. 2008;37:519–526.

P127.
Dynamic contrast-enhanced MRI of the synovium in knee osteoarthritis: Semi-automatic segmentation of synovial subregions and test–retest repeatability

J. Mostert[1], T. van Zadelhoff[1], D. Poot[1], D. van der Kaaij[1], L. Strong[1], K. Zijlstra[1], E. Oei[1], R. van der Heijden[1,2]

[1]*Erasmus Medical Center, Radiology & Nuclear Medicine, Rotterdam, Netherlands;*
[2]*University of Wisconsin-Madison, Radiology, Madison, WI, United States*

Introduction Knee osteoarthritis (OA) is a common joint disorder and a leading cause of morbidity, with pain as the most prevalent symptom. Inflammation of the joint lining (synovitis) is often seen in OA, and is strongly associated with both knee pain severity and disease progression(1). Dynamic contrast-enhanced magnetic resonance imaging (DCE-MRI) can be used to visualize the uptake and washout of gadolinium-based contrast, and enables quantification of blood perfusion as a surrogate measure of inflammation. DCE-MRI could therefore be used to characterize the extent of synovitis and serve as a biomarker for response to treatment in clinical trials. However, (semi)-automatic segmentation methods and thorough technical and clinical validation are needed to fully adopt DCE-MRI in this setting. We aim to evaluate semi-automatic segmentation of synovial subregions and test–retest repeatability of DCE-MRI to measure synovial perfusion in patients with knee OA.

Methods Patients with mild-to-moderate knee OA (Kellgren-Lawrence grade 1–3) who were allocated to the control group in a prospective randomized controlled trial of genicular artery embolization were included(2). Patients underwent MRI at 3 T (GE Healthcare) at baseline and after 1 month. Image acquisition consisted of native T1 mapping with variable flip angle, followed by a dual-echo SPGR sequence (DISCO; DIfferential Sub-sampling with Cartesian Ordering), in which the spatial resolution was optimized to allow for visualization of small vessels. After the initial phase, 0.1 ml/kg gadovist was injected and 34 dynamic phases were acquired, with a temporal resolution of 10.2 s.

Segmentation of the synovium comprised an initial rough manual segmentation followed by selection of enhancing voxels using a shuffle transform method(3). Synovial subregions were created by semi-automatic vessel mapping using MeVisLab and mathematically assigning synovial voxels to the corresponding closest genicular artery. Motion compensation was performed using Elastix (Elastix, version 5.0.1), and native T1 mapping and pharmacokinetic modelling was done using open source software for DCE analysis (MADYM, version 4.21.1)(4). The commonly used combination of the Parker literature arterial input function, and the Extended Toft"s model pharmacokinetic model was implemented. Voxelwise perfusion parameters were calculated, after which median Ktrans values were extracted for the whole synovium and separately for each synovial subregion. Agreement was visualized with a Bland–Altman plot, and test–retest repeatability was evaluated using intraclass correlation

coefficients (ICC; single rating random sample) and within-subject coefficients of variation (CV).

Results 30 patients were included, of which two patients were lost to follow-up and one patient was excluded due to errors during image acquisition. For the remaining 27 participants, median Ktrans values ranged from 0.017 to 0.121. ICC of Ktrans for the whole synovium was 0.51, and CV was 0.14. Sensitivity analysis by exclusion of two statistical outliers yielded an ICC of 0.66 and a CV of 0.11. For the individual synovial regions, ICCs ranged between 0.27 and 0.58 while CVs ranged between 0.13 and 0.25.

Discussion Our results indicate only moderate test–retest repeatability of Ktrans in the synovium of patients with knee OA compared to a prior study with an ICC up to 0.90 (5). This difference might be attributable to a potentially bigger fluctuation in OA related inflammation in the time between measurements in our population or differences in acquisition or segmentation.

Conclusion Semi-automatic segmentation of the synovium and synovial subregions through vessel mapping on DCE-MRI in knee OA is feasible. Perfusion parameters determined through pharmacokinetic modeling have moderate repeatability and should be interpreted with caution.

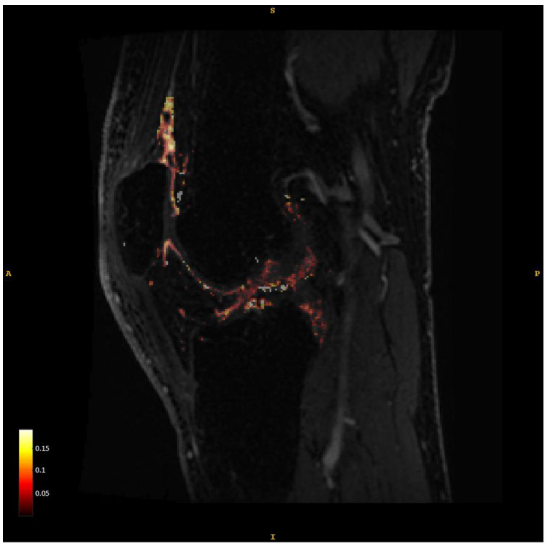

Fig. 2: Example of a DCE-MRI image of a patient with knee osteoarthritis, with the Ktrans map [min-1] of the synovium displayed as overlay.

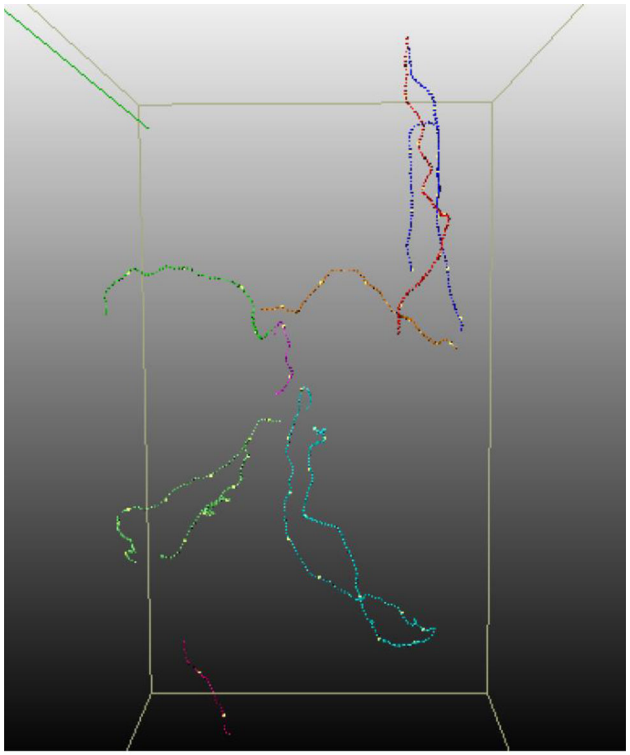

Fig. 1: Example of a semi-automatically segmented vessel structure of the knee using MeVis Lab.

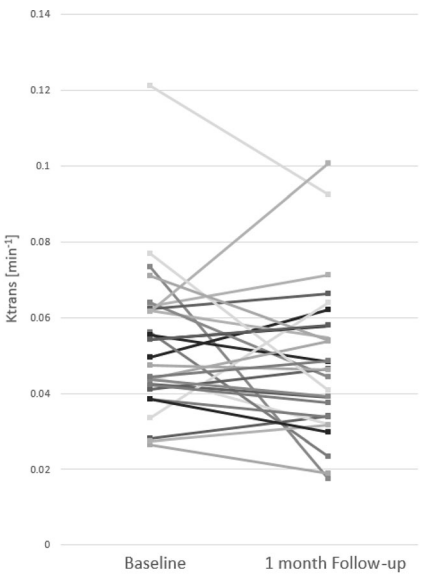

Fig. 3: Change in median Ktrans values for the whole synovium in patients with knee osteoarthritis, measured at baseline and 1 month follow-up.

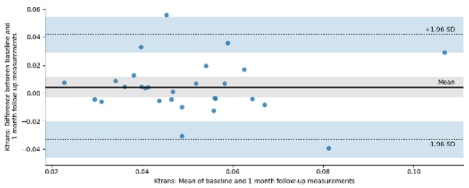

Fig. 4: Bland-Altman plot of Ktrans values [min-1] (baseline and 1 month follow-up) for the whole synovium in patients with knee osteoarthritis.

References
1. Baker K, Grainger A, Niu J, Clancy M, Guermazi A, Crema M, et al. Relation of synovitis to knee pain using contrast-enhanced MRIs. Ann Rheum Dis. 2010 Oct 1;69(10):1779–83.
2. van Zadelhoff TA, Moelker A, Bierma-Zeinstra SMA, Bos PK, Krestin GP, Oei EHG. Genicular artery embolization as a novel treatment for mild to moderate knee osteoarthritis: protocol design of a randomized sham-controlled clinical trial. Trials. 2022 Dec;23(1):24.
3. Xanthopoulos E, Hutchinson CE, Adams JE, Bruce IN, Nash AFP, Holmes AP, et al. Improved wrist pannus volume measurement from contrast-enhanced MRI in rheumatoid arthritis using shuffle transform. Magn Reson Imaging. 2007 Jan;25(1):110–6.
4. Berks M, Parker G, Little R, Cheung S. Madym: A C + + toolkit for quantitative DCE-MRI analysis. J Open Source Softw. 2021 Oct 7;6(66):3523.
5. MacKay JW, Nezhad FS, Rifai T, Kaggie JD, Naish JH, Roberts C, et al. Dynamic contrast-enhanced MRI of synovitis in knee osteoarthritis: repeatability, discrimination and sensitivity to change in a prospective experimental study. Eur Radiol. 2021 Aug;31(8):5746–58.

P128.
Spondyloarthopaty assessment using 6-point DIXON T2*-mapping as a differential edema biomarker at the sacroiliac joints

R. N. Alcalá Marañón[1,2], M. P. del Pópolo[1,2], M. Melchor M.[1,2], A. Verge S.[1,2], F. Gonzalez N.[1,3], R. Isoardi[1,3], D. Fino Villamil[1,3]

[1]*Fundación Escuela de Medicina Nuclear, Magnetic Resonance, Mendoza, Argentina;*
[2]*Fundación Argentina para el Desarrollo en Salud, Mendoza, Argentina;*
[3]*Comisión Nacional de Energia Atómica, Mendoza, Argentina*

Introduction Parameterizing quantitative biomarkers in the study of spondyloarthropathy (SpA) aimed to the analysis of bone marrow edemas (BMEs) through the measurement of T2 and T2* relaxation time (T2m–T2*m) and fat-fraction (FF), can improve the diagnosis and follow-up of this type of diseases at the musculoskeletal protocols. The aim of this work is to study the T2*m and FF values obtained from a single DIXON proton density fat fraction (dPDFF) 6-point/echoes sequence, T2m from a Spin-Echo sequence and to evaluate their performance in the SpA characterisation of BMEs.
Methods This study was approved by the institutional Ethics Review Board. The acquisition was performed in 21 patients (53 +—7 y/o) and consisted in both a STIR and T1w anatomical sequences (axial and coronal) of the sacroiliac bones followed by a T2-Mapping Spin-Echo (T2mSE) and a dPDFF GRE with the same geometry, the sequence parameters can be observed in Fig. 1. Two expert radiologists delimited VOIs corresponding to BMEs and healthy tissue; for each region 3D Slicer (v5.1.0) segmentation toolkit was implemented in order to obtain quantifications and the STIR images were used as the anatomical reference for BMEs identification, these were merged with the corresponding T2mSE, T2*m and FF slices for visualization purposes (Fig. 2). Using a Python (v3.10.5) script, t-tests were performed on the collected data, a ROC curve for T2mSE (Fig. 3), T2*m and FF (Fig. 4) were generated and cut-off values were determined.
Results The obtained p values (significance level of 0.05) were the following: p = 1.083e−7 (T2mSE), p = 3.69e−6 (T2*m) and p = 0.025 (FF). A T2 relaxation time of 63.5 ms and fat-fraction 63.50% were the corresponding cut-off values for the dPDFF and a T2 time of 104 ms for the T2mSE sequence.
Discussion Although the obtained results are promising, a bigger patient cohort is needed and due to the effects of bone aging in the population, future studies will have to separate the patients into different age groups. Furthermore the extra acquisition time should be taken into account when deciding to add these extra sequences for obtaining these biomarkers.
Conclusion The t-tests showed a statistical significant difference when comparing BMEs and normal tissue in the sequences and the cut-off value were found to be excellent biomarkers differentiators for BMEs, particularly for T2*m and T2m. These quantifications can be an useful tool for radiologists and clinicians alike in the follow-up and control of patients that present some type of SpA.

Sequence Acquisiton		
Name	**T2mSE**	**dPDFF**
Type	**SE**	**GRE**
TR (ms)	**2000**	**8.20**
TE (ms)	**n*13**	**1.47**
Flip Angle (°)	**90**	**90**
Acqusition Voxel (mm)	**1.00 / 1.12**	**1.96 / 2.01**
Reconstruction Voxel (mm)	**0.49 / 0.49**	**1.53 / 1.53**
Slice Thickness (mm)	**3.00**	**2.00**
Acqusition Mode	**Cartesian**	**Cartesian**

Fig. 1: Sequence acquisition parameter for T2mSE and dPDFF

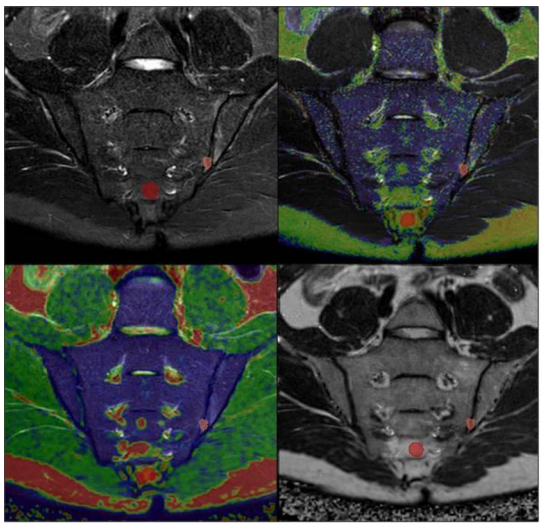

Fig. 2: Acquired images in a representative patient (same slice), from top to bottom, from left to right, Coronal STIR with segmented lesions. T2mSE-STIR fusion with color LUT and segmented lesions. T2*m-STIR fusion with segmented lesions. FF-STIR fusion with segmented lesions.

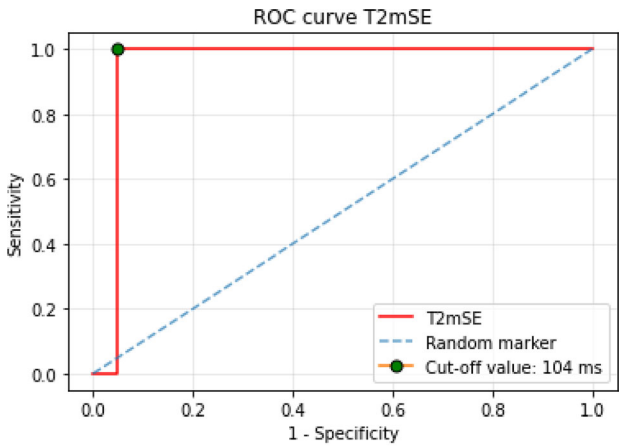

Fig. 3: T2mSE ROC curve with cut-off value.

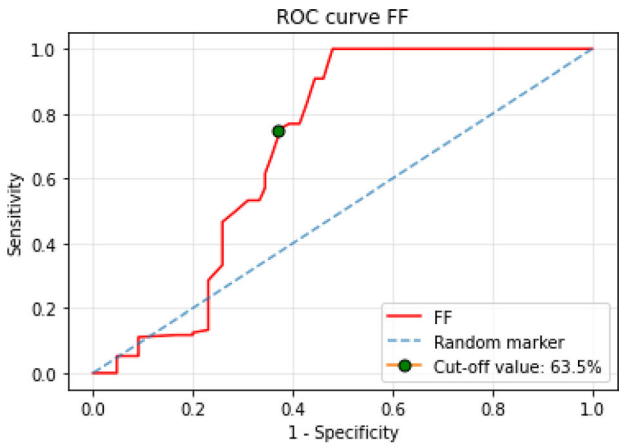

Fig. 4: FF ROC curve with cut-off value.

References

Kasar, S., Ozturk, M. & Polat, A.V. Quantitative T2 mapping of the sacroiliac joint cartilage at 3 T in patients with axial spondyloarthropathies. Eur Radiol 32, 1395–1403 (2022). https://doi.org/10.1007/s00330-021-08357-z

Huang, H., Zhang, Y., Zhang, H., Chen, J., Zheng, Q., Cao, D., & Zhang, Z. (2020). Qualitative and quantitative assessment of sacroiliitis in axial spondyloarthropathy: can a single T2-weighted dixon sequence replace the standard protocol?. Clinical radiology, 75(4), 321.e13–321.e20. https://doi.org/10.1016/j.crad.2019.12.011

Albano, D., Chianca, V., Cuocolo, R. et al. T2-mapping of the sacroiliac joints at 1.5 Tesla: a feasibility and reproducibility study. Skeletal Radiol 47, 1691–1696 (2018). https://doi.org/10.1007/s00256-018-2951-3

P129.
Comparing strategies for addressing fatty tissue in quantitative susceptibility mapping of the knee

C. Säll[1], E. Lind[1], P. Peterson[2,3], M. Englund[4], E. Einarsson[2,3]

[1]*Lund University, Department of Medical Radiation Physics, Lund, Sweden;*
[2]*Lund University, Department of Translational Medicine, Malmö, Sweden;*
[3]*Skåne University Hospital, Imaging and Physiology, Lund, Sweden;*
[4]*Lund University, Department of Clinical Sciences, Clinical Epidemiology Unit, Ortopedics, Lund, Sweden*

Introduction Osteoarthritis is strongly associated with degeneration of articular cartilage. Recently, studies have been performed indicating that quantitative susceptibility mapping (QSM) may be used to study the degeneration of this tissue [1–2].

However, QSM in the knee is complicated due to the many frequency components of the fatty tissue surrounding the articular cartilage, such as bone marrow and the infrapatellar fat pad. One approach for avoiding this complication has been to exclude areas containing fatty tissue from the reconstruction process by masking [2–3]. While straightforward, this approach may introduce errors as the susceptibility of the excluded tissue might not be fully accounted for, and as background field removal may be challenging in regions close to the edges of the mask.

To what extent masking of fatty tissue affects the resulting susceptibility values in the articular cartilage has not been investigated. The purpose of this work was to use simulations to assess how this approach affects QSM of the articular cartilage in the knee.

Method Numerical phantoms were created based on in vivo images of two female study participants (aged 42 and 53 years), included in the study with permission from the ethics review authority and after written informed consent. For each knee, compartments corresponding to subcutaneous fat, bone marrow, lean tissue, and air were given literature susceptibility values [2]. The resulting susceptibility map was used to generate simulated phase and magnitude images (see Fig. 1).

The effect of masking fatty tissue was evaluated by comparing the local fields and susceptibility maps obtained using the masking alternatives: 1) Excluding no tissue, 2) excluding bone marrow only and 3) excluding all fatty tissues before background field removal with projection onto dipole fields (PDF) [4] and the Laplacian boundary value method (LBV) [5] was performed. In all cases, the morphology enabled dipole inversion (MEDI) software was used [6].

The performance of each masking alternative was evaluated as the homogeneity of values over the cartilage area (expected to be homogenous as no internal structures were simulated in this area). For this, profiles between the femur and tibia, given by the mean value of each row of the box shown in Fig. 1d, were extracted. For easier comparison, these were shifted, so that the middle point of each profile had zero susceptibility.

Results Comparison of the local fields obtained with the different masking alternatives indicated that the susceptibility distribution of fatty tissue may be partially accounted for when excluded from the

mask, see Fig. 2. This could be seen for both background field removal techniques.

The profiles extracted from the cartilage region in the susceptibility maps seen in Fig. 3 are shown in Fig. 4. When no tissue was excluded, the expected flat profile between the femur and tibia was seen for both background field removal techniques and knees. Biases were seen for the masking alternatives where bone marrow or all fatty tissue was excluded. Generally, PDF introduced a larger bias than LBV.

Discussion The results indicate that the susceptibility of fatty tissue is at least partially accounted for in the background field removal step when excluded, likely because it is then treated as a source of the background field. However, including fatty tissue in the reconstruction produced results which were closer to the ground truth and more robust between geometries and reconstruction techniques. To make the inclusion of fatty tissue possible, the chemical shift must be accounted for, e. g. through chemical-shift encoded imaging [7]. Since the expected range of susceptibility values of healthy articular cartilage may be as small as 0.2 ppm [1–2], the bias observed using masking of fatty tissue was non-negligible.

Conclusion Inclusion of fatty tissue in QSM reconstruction gave accurate and robust results. In contrast, masking of fatty tissue may cause biases, the size of which depend on the choice of background field removal technique and masking alternative.

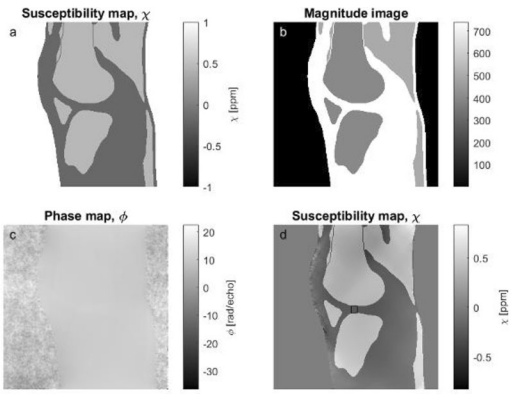

Fig. 1: The susceptibility distribution (a), magnitude image (b) and phase image (c) used for the simulations. A reconstructed susceptibility map is seen in (d), along with the region where the profiles were extracted marked by the black box. The susceptibility of air was set to 9 ppm in (a).

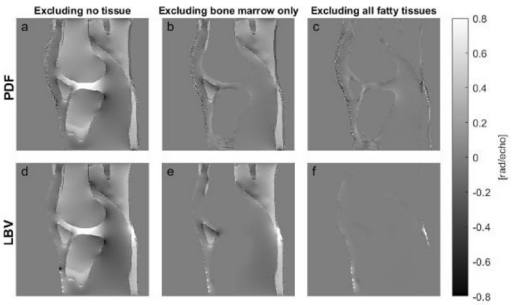

Fig. 2: The local magnetic field obtained using PDF (a-c) and LBV (d-f) with no tissue excluded (a,d), only bone marrow excluded (b,e) and all fatty tissues excluded (c, f).

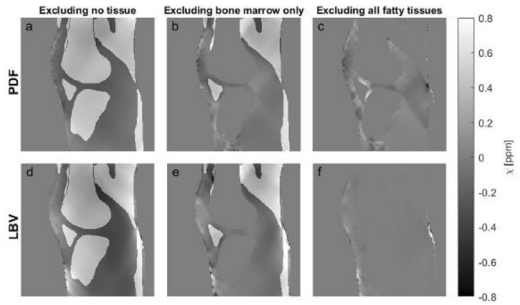

Fig. 3: Susceptibility maps obtained using PDF (a-c) and LBV (d-f) with no tissue excluded (a,d), bone only marrow excluded (b,e), and all fatty tissues excluded (c,f).

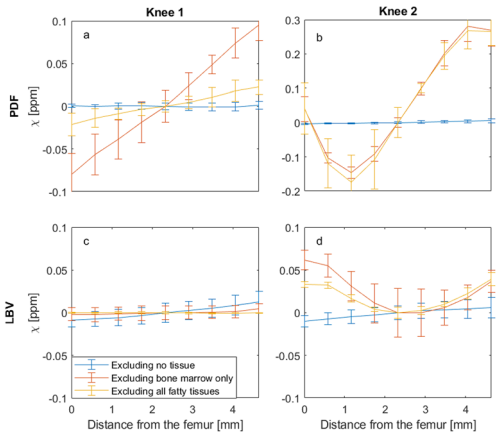

Fig. 4: Profiles extracted over the area corresponding to the articular cartilage of the two simulated knees comparing masking and background field removal techniques. Generally, the most accurate results (equal to zero) were obtained when fatty tissue was not excluded. Observe, that the scale of the y-axis in (b) differs from the others.

References

1. Wei H, Lin H, Qin L, Cao S, Zhang Y, He N, et al. J. Magn. Reson. Imaging. 2019 Jun;49(6):1665–75.
2. Wei H, Dibb R, Decker K, Wang N, Zhang Y, Zong X, et al. Magn Reson Med. 2017 Nov;78(5):1933–43.
3. Zhang M, Li Y, Feng R, Wang Z, Wang W, Zheng N, et al. J Magn. Reson. Imaging. 2021 Nov;54(5):1585–93.
4. Liu T, Khalidov I, de Rochefort L, Spincemaille P, Liu J, Tsioris AJ, et al. NMR Biomed. 2011 Nov;24(9):1129–36.
5. Zouh D, Liu T, Spincemaille P, Wang Y. NMR Biomed. 2014 Mar;27(3):312–9.
6. Liu J, Liu T, de Rochefort L, Ledoux J, Khalidov I, Chen W, et al. Neuroimage. 2012 Feb;59(3):2560–8.
7. Dimov AV, Liu T, Spincemaille P, Ecanow JS, Tan H, Edelman RR, et al. Magn Reson Med. 2015 Jun;73(6):2100–10.

P130.
Quantitative spatial, temporal analysis of spontaneous muscular activities visualized by diffusion-weighted imaging

M. Schwartz[1,2], P. Martirosian[1], G. Steidle[1], T. Feiweier[3], B. Yang[2], L. Schöls[4,5], F. Schick[1]

[1]*University Hospital of Tuebingen, Section on Experimental Radiology, Tübingen, Germany;*
[2]*University of Stuttgart, Institute of Signal Processing and System Theory, Stuttgart, Germany;*
[3]*Siemens Healthcare GmbH, Erlangen, Germany;*
[4]*Hertie Institute for Clinical Brain Research, Department Neurodegenerative Diseases, Tübingen, Germany;*
[5]*German Center for Neurodegenerative Diseases (DZNE), Tübingen, Germany*

Introduction: Spontaneous muscular activity (SMAM) can be detected and visualized in several different muscle groups of the human musculature system using time-series diffusion-weighted imaging (DWI).[1] In healthy individuals as well as patients suffering from amyotrophic lateral sclerosis (ALS), the spatial and temporal distribution of these spontaneous activities could provide important findings[2–4]. However, pattern analysis might be challenging due to the high variation of the individual muscle groups and the visual appearance of these spontaneous muscular activities.
In this work, an approach is presented which allows both spatial and temporal analysis of spontaneous muscular activities visible in DWI.
Subjects and methods: MR imaging: DW images were acquired from six healthy subjects (age: 30 ± 11) and six patients suffering from ALS (age: 58 ± 13) on a 3 T MR system (MAGNETOM Prisma^{fit}, Siemens Healthcare GmbH, Erlangen, Germany) using a diffusion-weighted stimulated-echo EPI research sequence. Protocol parameters are given in Fig. 1. Spatio-temporal analysis: The complete image processing steps are given in Fig. 2. In the first step, all DWI recordings were preprocessed and muscular activities were detected and annotated using a deep learning-based method according to our former work[4–5]. Then, individual spontaneous muscular activities are grouped based on their local position in the muscle groups. Therefore, a position filter is applied by means of Dice coefficient between each detected muscular activity. Afterwards, textural features for each individual spontaneous muscular activity were calculated using PyRadiomics[6]. These textural features were further processed by a classical clustering method (DBSCAN) using scikit-learn (v1.2.2). In order to evaluate the temporal distribution of muscular activities in local muscle regions, e.g., uniform or non-uniform distribution of activities over time, each subset of activities in the same muscular region is tested for uniform distribution using a Kolmogorov–Smirnov test based on the empirical cumulative distribution function.
Results: It can be seen that the median relative cross-sectional area of SMAMs is increased for the shoulder and tongue musculature in patients (Fig. 3A). In the calf muscle, relative SMAM size in patients is mostly comparable to the healthy subjects in TP and GL with differences in GM, PL, SOL and EDL (Fig. 3B). The activity distribution in patients is clearly different from healthy subjects, since the absolute mean number of SMAMs in TA and PL is increased (Fig. 3C). Fig. 4A shows an example of three different patterns of spontaneous muscle activity in one patient after textural clustering. The differences in the shape of the recruitment pattern can be clearly seen. In Fig. 4B, areas with repetitive activity, i.e., events equally distributed in time, are highlighted. Most spontaneous activities were single events; however, some muscle regions show repetitive patterns. Spontaneous muscular activity with a repetitive pattern was detected in 83% of patients suffering from ALS, while only 16.6% of healthy subjects have also revealed this kind of temporal behavior.
Discussion/conclusion: Analysis of spontaneous muscular activities recorded by DWI with respect to spatial and temporal patterns revealed distinct individual differences. Furthermore, it can be shown that few individual patterns are repetitive in the respective muscular area. Clustering spontaneous muscular activities within a subject has been shown to be feasible.
Since categorization between subjects may be more difficult due to different anatomical structures, more sophisticated clustering approaches may be required.

body region	matrix	FoV [mm²]	slice thickness [mm]	b-value [s/mm²]	TE [ms]	TR [ms]	repetitions	Δ [ms]	orientation
shoulder	166x90	498x270	8	100	31	500	500	145/28	transverse
calf	80x80	170x170	6	100	28	500	500	145	transverse
tongue	80x80	200x200	8	100	31	500	500	145/28	sagittal

Fig. 1: Protocol parameters of the DWI sequence (Δ is the diffusion-sensitive time) optimized for the three different body regions: shoulder, calf, and tongue musculature.

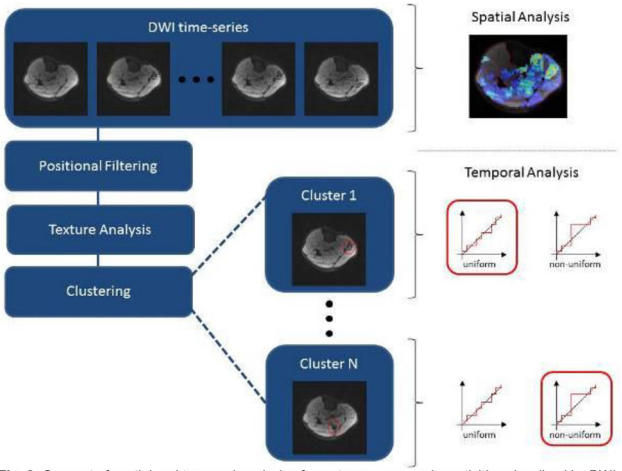

Fig. 2: Concept of spatial and temporal analysis of spontaneous muscular activities visualized by DWI.

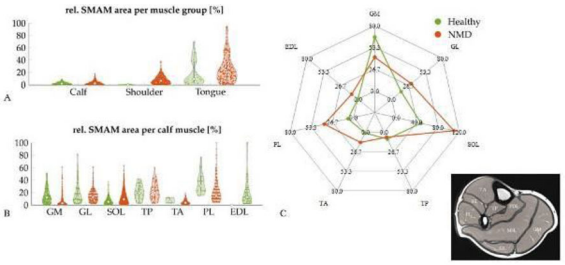

Fig. 3: A: Relative SMAM area per muscle group in % for patients (red) and healthy (green) subjects. **B:** Relative SMAM area per calf muscle in %. **C:** Absolute mean number of SMAMs per calf muscle.

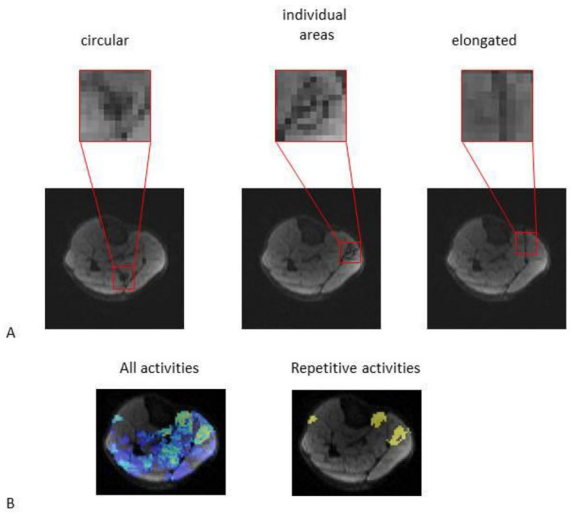

Fig. 4: A: Three different kind of muscular activities after intra-subject textural clustering. **B:** One subject with all spontaneous muscular activities (left) and only the locations of repetitive activities (right).

References:
[1]Steidle, NMR, 2015.
[2]Schwartz, ISMRM, 2020.
[3]Whittaker, Ann Neuro, 2019.
[4]Schwartz, ISBN 978-3-8439-5252-1, 2023.
[5]Schwartz, ESMRMB, 2019.
[6]van Griethuysen, *Cancer Research, 2017.*

P131.
A multimodal approach to understand skeletal muscle water dynamics using magnetization transfer and blood oxygen level dependent (BOLD) signal

A. Amador-Tejada[1,2], M. D. Noseworthy[1,2,3,4]

[1]*McMaster University, School of Biomedical Engineering, Hamilton, Canada;*
[2]*St. Joseph's Healthcare, Imaging Research Centre, Hamilton, Canada;*
[3]*McMaster University, Electrical and Computer Engineering, Hamilton, Canada;*
[4]*McMaster University, Department of Radiology, Hamilton, Canada*

Introduction: As musculoskeletal disorders increase globally (1), the ability to differentiate healthy from diseased muscle has become a priority. Magnetization transfer (MT) has become a recognized quantitative and non-invasive technique to study the interaction between free and bound tissue proton pools. Prior studies $\sim$ 30 years ago focusing on exercise (2–4) suggested clinical value in studying skeletal muscle with MT. Nevertheless, these studies faced significant challenges, such as low magnetic fields, lack of exercise reproducibility and standardization. Here we aimed to revisit this with higher field and better imaging technology. Our goal was to assess muscle MT ratio in healthy volunteers performing a plantar flexion exercise and correlate the MT with the muscle BOLD response. This multimodal approach could benefit from the addition of the BOLD response giving more comprehensive information on muscle activation.

Methods: In a study approved by our local ethics committee, healthy subjects (11 males, age = 25.72.2 year, height = 1758.9 cm, weight = 73.511.1 kg) were recruited. Experiments were performed using a Discovery MR750 3 T MRI (GE Healthcare, Milwaukee, WI) and 16-channel T/R extremity coil. An MT (SPGR, 2 slices, 128 $\times$ 128 matrix, 10 mm thick, TE/TR/flip = 4.4/100 ms/70, MSAT = 1.5 kHz) followed by a BOLD (EPI, 2 slices, 64 $\times$ 64 matrix, 10 mm thickness, TE/TR/flip = 35/110/70) and a post-exercise MT were acquired from the lower leg (Fig. 1). Subjects performed 8.8 min of plantar flexion exercise at 40% MVC using an in-house built MRI-compatible ergometer during a block design (30 s/30 s activation/rest) BOLD acquisition. The MT ratio (MTR)(5) and BOLD correlation(signal vs. haemodynamic response function, HRF, Fig. 2) analysis were computed. The MTR and BOLD correlation were analyzed using ANOVA tests across muscle groups and subjects, and for pre vs post-exercise (for the MTR).

Results: Muscles either showed positive or negative BOLD time courses compared to the exercise paradigm. Negative correlated muscles were EDL, GL, SOL and GM, while positively correlated were TA and TP. The MTR post–pre exercise map (Fig. 3) showed a negative trend for all muscles, i.e. MTR(post) $<$ MTR(pre). A repeated measures 3-way ANOVA was performed on the MTR, yielding statistical significance in the mean MTR across conditions (pre vs post-exercise), muscle groups, and subjects ($p < 0.001$). In addition, a 2-way ANOVA was performed on the BOLD correlation, indicating a significant difference in the mean correlation across muscles and subjects ($p < 0.001$). Finally, to investigate if there is any relationship between these two MRI techniques (MT and BOLD), a linear regression model was employed (using means and standard deviations), yielding an R2 value of 0.62 (Fig. 4).

Discussion: The interaction between free and bound water pools is complex, as there are changes in water concentration, pool exchange rates, and metabolism (5). Studies have shown that post-exercised skeletal muscle exhibits an increase in T2 compared to inactive muscle, suggesting a local increase in the water content (2, 6, 7). Therefore, the decrease in MTR post-exercise could be attributed to a change in the bound water pool concentration or the exchange rate between the free and bound water pools. For BOLD, a positive correlation value means the ideal function and the BOLD response are aligned, i.e. the muscle is metabolically active during exercise compared to baseline. On the other hand, a negative correlation suggests that muscle is "deactivating", i.e. there is a decrease in blood flow and muscle oxygenation. Integrating both metrics, it is seen that TA had the highest positive BOLD correlation (indicating the muscle was metabolically active during exercise) and the greatest change in the MTR (suggesting changes in the exchange rates or concentrations of the free and bounded water pools). Similarly, muscles such as GL and GM showed the lowest change in MTR and the highest negative BOLD correlation.

Conclusion: We showed a correlation between the MT and BOLD techniques in healthy skeletal muscle during an exercise protocol. One of the principal advantages of this study is the use of a relatively short MT sequence ($\sim$ 1 min), which decreased the chances of introducing motion artifacts during scanning. Even more, the short duration of this sequence also reduced the averaging over time effects, decreasing the chances of skeletal muscle returning to its baseline state after exercise. Further research is required to understand the exchange rate dynamics i.e. between the free and bounded pools in both directions for MT during exercise in healthy skeletal muscle.

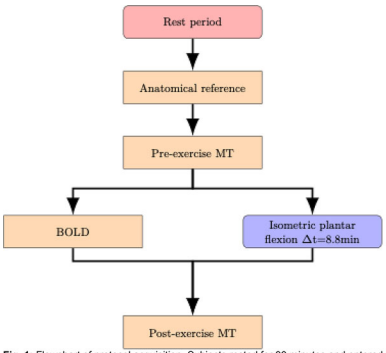

Fig. 1: Flowchart of protocol acquisition. Subjects rested for 30 minutes and entered the MRI. An anatomical and a pre-exercise MT were acquired. Then a BOLD was acquired while subjects performed exercise. Finally, a post-exercise MT was acquired.

References

1. Z. Jin *et al., Ann. Rheum. Dis.* **79**, 1014–1022 (2020).
2. J. L. Fleckenstein *et al., Am. J. Roentgenol.* **151**, 231–237 (1988).
3. X. P. Zhu *et al., Br. J. Radiol.* **65**, 39–43 (1992).
4. H. Yoshioka *et al., Magn. Reson. Imaging.* **12**, 991–997 (1994).
5. R. M. Henkelman *et al., NMR Biomed.* **14**, 57–64 (2001).
6. A. T. Nygren *et al., J. Appl. Physiol.* **93**, 1716–1722 (2002).
7. L. L. Ploutz-Snyder *et al., Magn. Reson. Med.* **37**, 676–682 (1997).

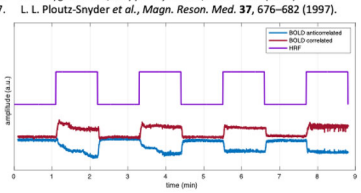

Fig. 2: Plot showing (purple) the ideal response function used for the BOLD correlation analysis and (blue, red) an example of the BOLD time course for a voxel positively and negatively correlated.

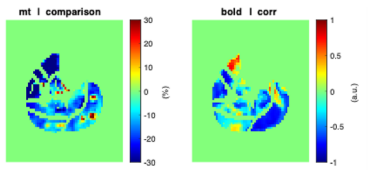

Fig. 3: Example of (left) the MTR comparison post-pre exercise and (right) the BOLD correlation analysis. The two slices were averaged.

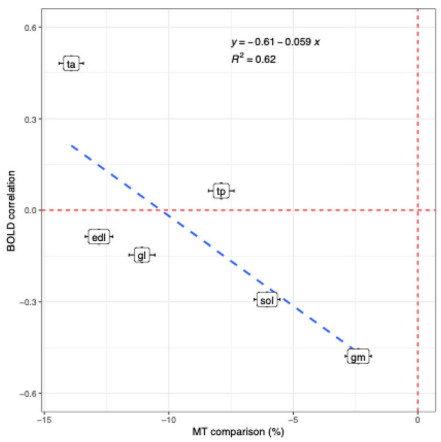

Fig. 4: Plot showing the mean and standard deviation of the MTR post-pre exercise (x-axis) and BOLD correlation (y-axis). A linear regression was used to investigate if there is any relationship between these two MRI techniques. The yielded regression showed a negative correlation between the BOLD and MT, with an R-squared of 0.62.

P132.
Sodium quantification in skeletal muscle tissue: A comparison study between GRE and UTE ^{23}Na MRI techniques

T. Gerhalter[1], F. Schilling[1], N. Zeitouni[1], L. Ruck[1], P. Linz[1], D. Kannenkeril[1], C. Kopp[1], M. Uder[1], A. M. Nagel[1], L. Gast[1]

[1]*Friedrich-Alexander-Universität Erlangen-Nürnberg (FAU), Erlangen, Germany*

Introduction: Dedicated pulse sequences are needed to capture the fast-decaying ^{23}Na signal. However, several clinical studies still use Cartesian gradient-echo (cGRE) sequences with echo times (TE) of $\approx$2 ms to monitor changes in the apparent total sodium concentration (aTSC) (among others[1,2]). Here, we compared the ability of using a cGRE sequence versus an ultra-short echo 3D radial-readout sequence[3] (radUTE) to measure sodium levels in skeletal muscle tissue.

Methods: 200 data sets of 107 volunteers (age: 68.3 ± 11.8 year, with or without kidney diseases) were retrospectively evaluated. The data have been acquired at 3 T (Skyra and Vida, Siemens) with a singled-tuned ^{23}Na volume knee coil (Stark Contrast). Acquisition parameters are listed in Table1,A. Parts of the cGRE data have been published before[4].

ROIs were outlined on 7 muscles using ^{1}H DIXON images with DAFNE[5]. The ^{23}Na signal calibration was performed with the standard deviation (SD) of the background signal and the mean value of the Reference tubes containing 1) 20 and 40 mM NaCl with 5% agarose and 2) 20 and 40 mM NaCl without agarose.

Due to the non-normal distribution of the data, a paired Wilcoxon signed rank test (WSRT) was used to test differences in aTSC between imaging acquisition methods and calibration approaches.

In addition, ^{23}Na relaxometry was performed at 3 T (Vida, Siemens) with the same knee coil in 14 healthy volunteers (age: 36.9 ± 8.1y). Acquisition parameters are listed in Table1,B. The T_1 signal recovery was fitted to $S(TR) = M_0(1\text{-}e(\text{-}TR/T_1))$. The bi-exponential T_2* signal decay was fitted to $S(TE) = sqrt(A^2(0.6e(\text{-}TE/T_2\text{*}s) + 0.4e(\text{-}TE/T_2\text{*}l))^2 + n^2)$ including the Rician noise-related parameter n. ROIs were drawn manually on the soleus muscle in the middle slice and the Reference phantoms. Reference tubes without agarose were fitted to $S(TE) = sqrt(A^2(e(\text{-}TE/T_2\text{*}l))^2 + n^2)$.

Besides, we simulated the signal behavior with the FLASH equation using our fitted relaxation times as well as the used TE and TR from the cGRE and radUTE sequences for aTSC quantification: $S = M_0\ sin\alpha\ \ (1\text{-}e(\text{-}TR/T_1))/(1\text{-}e(\text{-}TR/T_1)cos\alpha)\ \ (0.6e(\text{-}TE/T_2\text{*}s) + 0.4e(\text{-}TE/T_2\text{*}l))$.

Results: Figure 1 shows ^{23}Na maps of the lower leg of one volunteer with the corresponding calibration curves. The mean aTSC values were measured for the UTE and GRE data sets (Fig. 2). While aTSC for radUTE images was significantly lower when agarose References were used for calibration compared to NaCl References (median: 22.8 mM vs. 19.5 mM, WRST, $p < 0.001$), the opposite was observed for cGRE imaging (median: 16.8 mM vs. 19.5 mM, WRST, $p < 0.001$). Quantification based on NaCl tubes underestimated the aTSC for cGRE in comparison to radUTE. As the slope is steeper for the agarose tubes, the aTSC is lower for cGRE at normal aTSC values, but achieves higher aTSC values in muscles with sodium accumulation in comparison to the radUTE.

Exemplary fits of T_1 recovery and T_2* decay are presented in Fig. 3. The average T_1 in muscle was 27.1 ± 2.2 ms. The average short T_2* was 3.5 ± 0.5 ms and the average long T_2* was 31.6 ± 4.1 ms. The agarose Reference phantoms showed similar relaxation times with the exception of the long T_2*, which was half of the time of the muscle tissue. For the Reference phantoms without agarose T_1 and T_2* were longer than for muscle.

Based on the signal simulations with the calculated relaxation times, we observed different signal behaviors between short and long TE acquisitions (flip angle 90°, TR 100 ms). For TE = 2.07 ms, NaCl had the highest intensity at 0.74a.u., followed by muscle at 0.69a.u. and 5% agarose at 0.63a.u. For TE = 0.3 ms, muscle and 5% agarose had higher signal intensities at 0.92a.u. and 0.91a.u., respectively, compared to NaCl at 0.8a.u. These variations in signal intensities can be also clearly seen in the intensities of the Reference tubes in Fig. 1 and the observed variations in the boxplots in Fig. 2.

Discussion: Quantification of the $_{23}$Na signal varies with the acquisition scheme as well as with used Reference tubes. As the relaxation times in skeletal muscle tissue of ^{23}Na are very short, they do have an impact on sodium quantification. Given the TR = 100 ms, the ^{23}Na images are T_1 weighted, which particularly influences the quantification based on NaCl References ($T_1 \approx 60$ ms) leading to an over- or underestimation of the aTSC depending on the used TE. Non-UTE sequences furthermore experience an important T_2* weighting, which was also confirmed by simulations. The short T_2* component in muscle of roughly 3.5 ms requires fast data acquisition. At TE = 2.07 ms, 15% less signal intensity is recorded than with TE = 0.3 ms.

Conclusion: The study examined how different ^{23}Na MRI acquisition and calibration approaches affect signal quantification. We recommend using agarose phantoms for calibration to simulate muscle tissue's signal behavior and UTE sequences to capture the fast-decaying ^{23}Na signal. Furthermore, relaxation correction should be applied to minimize the effect of sequence parameters on the quantification.

Parameters	A) aTSC quantification		A) ^{23}Na relaxometry	
Sequence	2D Cartesian GRE sequence	3D radial UTE sequence	T_2* mapping with UTE sequences	T_1 mapping with UTE sequences
Specification	Vendor-provided sequence	3D density-adapted radial-readout[1]	4 stack-of-stars sequences with different TEs	8 stack-of-stars sequences with different TRs
TE [ms]	2.07	0.3	59 TEs: 0.3 – 70	0.3
TR [ms]	100	100	82	11, 20, 30, 40, 60, 80, 120, 300
FA [°]	90	90	88	90
Nominal resolution [mm]	3x3x30	3x3x20	4x4x20	4x4x20
Readout duration [ms]	2.3	10	2	2
Projections	-	6152	1910	1910
Averages	128	1	1	1
Number of slices	1	-	10	10
Acquisition time [min:sec]	13:41	10:15	4 x 2:37 Total: 10:28	0:21,0:38,0:57,1:16, 1:55,2:33,3:49,6:22 Total: 17: 51

References

1) Dahlmann et al. *Kidney Int Rep* (2021)
2) Ruggeri Barbaro et al. *Cardiovasc Res* (2021)
3) Nagel et al. *MRM* (2009)
4) Kolwelter et al. *Clin Research Cardiol* (2023)
5) Santini et al. *arXiv* (2023)

Table 1: Acquisition parameters for A) aTSC quantification and B) ^{23}Na relaxometry, and Reference list.

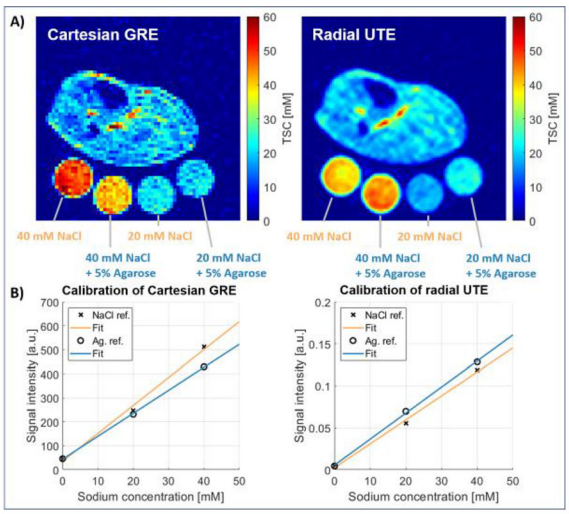

Fig. 1: A) Exemplary ^{23}Na maps and B) calibration curves using either the Reference phantoms without or with agarose. Note the differences in the signal intensities between the Reference tubes with and without agarose and between cGRE and radUTE due to T_1 and T_2 weighting (see simulation for discussion).

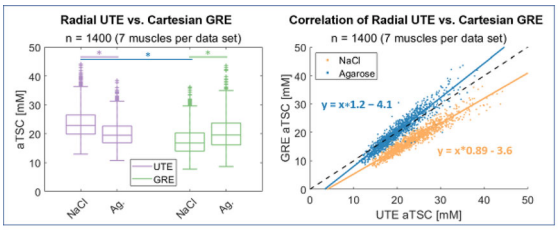

Fig. 2: Boxplot and correlation plot of the different approaches to measure aTSC. Significant differences are marked with * (WSRT, p<.001). Quantification based on NaCl tubes underestimates the aTSC for cGRE in comparison to radUTE for all values. As the slope is steeper for the agarose tubes, the aTSC is lower for cGRE at normal aTSC values, but achieves higher aTSC values in muscles with sodium accumulation in comparison to the radUTE.

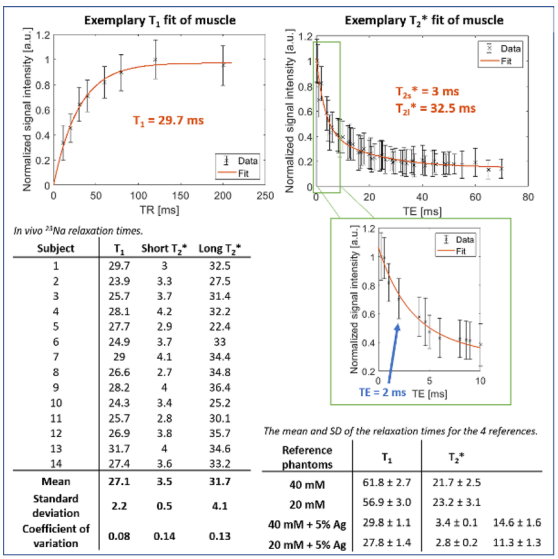

In vivo ^{23}Na relaxation times.

Subject	T_1	Short T_2*	Long T_2*
1	29.7	3	32.5
2	23.9	3.3	27.5
3	25.7	3.7	31.4
4	28.1	4.2	32.2
5	27.7	2.9	22.4
6	24.9	3.7	33
7	29	4.1	34.4
8	26.6	2.7	34.8
9	28.2	4	36.4
10	24.3	3.4	25.2
11	25.7	2.8	30.1
12	26.9	3.8	35.7
13	31.7	4	34.6
14	27.4	3.6	33.2
Mean	**27.1**	**3.5**	**31.7**
Standard deviation	**2.2**	**0.5**	**4.1**
Coefficient of variation	**0.08**	**0.14**	**0.13**

The mean and SD of the relaxation times for the 4 references.

Reference phantoms	T_1	T_2*	
40 mM	61.8 ± 2.7	21.7 ± 2.5	
20 mM	56.9 ± 3.0	23.2 ± 3.1	
40 mM + 5% Ag	29.8 ± 1.1	3.4 ± 0.1	14.6 ± 1.6
20 mM + 5% Ag	27.8 ± 1.4	2.8 ± 0.2	11.3 ± 1.3

Fig. 3: Measured relaxation times. The fast T_2* decay is highlighted in the green box; at TE=2ms, roughly 25% of the signal is decayed.

P133.
Validity tests of 5 MRI based methods for measuring perfusion in the foot

M. Bisgaard[1,2,3], K. Houlind[2,4], A. D. Blankhold[5], S. Ringgaard[6], H. Precht[1,2,3]

[1]*Hospital Lillebaelt, Radiology, Kolding, Denmark;*
[2]*University of Southern Denmark, Department of Regional Health, Odense, Denmark;*
[3]*UCL University College, Health Sciences Research Centre, Odense, Denmark;*
[4]*Hospital Lillebaelt, Department of Vascular Surgery, Kolding, Denmark;*
[5]*Aarhus University, Department of Radiology, Aarhus, Denmark;*
[6]*Aarhus University, Department of Clinical Medicine, Aarhus, Denmark*

Introduction: Peripheral artery disease (PAD) affected around 202 million people globally in 2015, and the number growths as life expectancy increases (1, 2). The main pathophysiological issue with PAD is the reduction of perfusion in the tissue of the foot and lower leg, which leads to different symptoms. In the most severe state of PAD, the patient may develop critical limb ischemia (CLI). When the

patient suffers from CLI the risk of amputations and mortality increases (3).

Different non-IV-contrast MRI sequences can measure parameters related to tissue perfusion. The validity of these sequences performed in the foot has, to our knowledge, not been compared previously. This study aims to test the validity of five different non-contrast MRI sequences to measure perfusion in the muscles of the foot.

Method: Sixteen healthy young volunteers were MRI scanned in a 3 T scanner (Siemens Healthcare, Erlangen, Germany). Volunteers relaxed supine for 30 min, and ankel-brachial index (ABI) was measured. In the MRI scanner, the volunteers underwent a cuff-induced ischemia test. A baseline scan for 30 s was followed by an ischemic period of 2 min. To measure the hyper-reactive response, the volunteers were scanned continuously over three min after the cuff was deflated. The cuff was placed below the knee and was inflated for 2 min with a pressure of 50 mmHg above the systolic blood pressure.

The following MRI sequences were included: 2D and 3D pseudo-continuous arterial spin labeling (pCASL), a Flow-sensitive Alternating Inversion recovery pulsed arterial spin labeling (FAIR PASL), a multi-gradient echo sequence to quantitatively assess T2*, and a dynamic Blood oxygenation level-dependent (BOLD), T2*-weighted sequence. The images were analysed drawing a volume of interest (VOI) in the foot muscles using DIXON water images. The VOI"s were copied to the same position for each of the five different perfusion sequences. Perfusion data were extracted from VOI"s, using the software Siswin. The validity was measured by comparing the minimum perfusion or oxygenation level at the end of the occlusion period vs. the hyperactive response. The results were analysed with paired t-tests.

Results: All 16 volunteers accomplished all five MRI perfusion sequences. Perfusion measurement were extracted from the VOI (Fig. 1).

The 0-hypotheses were rejected for the BOLD, FAIR, and multi gradient echo sequences, meaning that the validity was high for those three sequences (Table 1).

Discussion: A large difference is found between the included MRI sequences regarding perfusion. To our knowledge, no former studies have compared the performance of five different non-contrast MRI sequences in the foot. Former research projects have examined perfusion in the calf demonstrating valid results using a pCASL sequence (4). Other studies have used exercises to generate a hyperactive response also in the calf (5).

The signal curves for all five perfusion sequences are affected by shallow movements at in- and de-flation of the cuff. By clamping the foot in a foot coil, and optimizing the positioning of the volunteers, it is possible to minimize the movement of the foot. However, because the BOLD and perfusion signal changes are very small, the signal variation caused by the slight motion can easily shadow the ischemic signal variations.

All sequences can be implemented in different ways and the provided conclusions might only be valid for the specific implementations used.

Conclusion: The highest validity was found using BOLD, Multi gradient echo, and FAIR sequences. Before clinical implementation, it is relevant to test BOLD, Multi Gradient Echo, and FAIR in patients with claudication and critical ischemic.

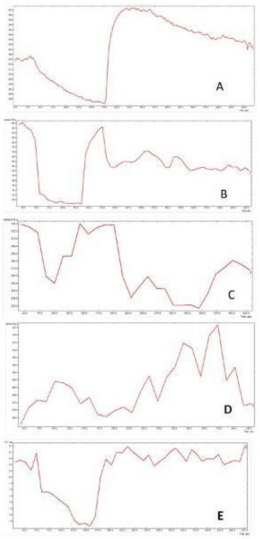

Fig. 1: A shows a signal intensity curve for the BOLD sequence. B shows a perfusion curve for a FAIR measurement. C is the perfusion curve for the 2D pCASL. D is the perfusion curve for the 3D pCASL sequence. And E is a T2* curve for the multi-echo gradient sequences.

MRI Sequence	p-value
BOLD	0.03*
FAIR	<0.01*
pCASL 2D	0.18
pCASL 3D	0.45
Multi gradient echo	<0.01*

Table 1: **The p values for the validity of five different perfusion sequences were as shown below. Values marked with * indicate a significant difference between minimum perfusion under occlusion and maximum under the hyperactive response.**

References:

1. Song P, Rudan D, Zhu Y, Fowkes FJI, Rahimi K, Fowkes FGR, et al. Global, regional, and national prevalence and risk factors for peripheral artery disease in 2015: an updated systematic review and analysis. Lancet Glob Health. 2019

2. Horváth L, Németh N, Fehér G, Kívés Z, Endrei D, Boncz I. Epidemiology of Peripheral Artery Disease: Narrative Review. Life (Basel). 2022

3. Misra S, Shishehbor MH, Takahashi EA, Aronow HD, Brewster LP, Bunte MC, et al. Perfusion Assessment in Critical Limb Ischemia: Principles for Understanding and the Development of Evidence and Evaluation of Devices: A Scientific Statement From the American Heart Association. Circulation. 2019

4. Suo S, Zhang L, Tang H, Ni Q, Li S, Mao H, et al. Evaluation of skeletal muscle microvascular perfusion of lower extremities by cardiovascular magnetic resonance arterial spin labeling, blood oxygenation level-dependent, and intravoxel incoherent motion techniques. J Cardiovasc Magn Reson. 2018

5. Ohno N, Miyati T, Fujihara S, Gabata T, Kobayashi S. Biexponential analysis of intravoxel incoherent motion in calf muscle before and after exercise: Comparisons with arterial spin labeling perfusion and T(2). Magn Reson Imaging. 2020

P134.
Low-field MRI gastrocnemius segmentation and correlation with physical performance on sportspeople

J. M. Algarín[1,2], T. Guallart Naval[3], A. Ferri-Caruana[4], R. Bosch[1,2], F. Juan[5], E. Pallás[1,2], J. P. Rigla[3], P. Martínez[5], J. Borreguero[1,2], J. M. Benlloch[1,2], F. Galve[1,2], J. Alonso[1,2]

[1]*Universitat Politècnica de València, i3M, Valencia, Spain;*
[2]*CSIC, i3M, Valencia, Spain;*
[3]*Tesoro Imaging S.L., Valencia, Spain;*
[4]*Universitat de València, Valencia, Spain;*
[5]*Physio MRI S.L., Valencia, Spain.*

Introduction: Low-field scanners can be designed to be light, low-cost and with small footprint [1, 2], opening a new window of opportunities that enable studies rarely carried out at high-field systems due to their low accessibility.

We present the first systematic study carried out with our low-field 72 mT "Physio MRI" scanner [3, 4], including preliminary results of image segmentations to show the relation between muscle volume and sport performance tests on 35 volunteers.

Methods The study involved a total of 35 participants (mean (SD) age of 24.8 (4.3) years; weight of 69.2 (11.2) kg and height of 1.74 (0.10) m). Performance measurements of common explosive exercises such as counter movement and horizontal jumps were performed uni and bi-laterally. After the tests, we acquired axial images of their lower legs.

We employed the "Physio MRI" scanner (Fig. 1, [3]). This operates with a Halbach array of NdFeB magnets, providing $\sim$ 72 mT over a spherical region of 200 mm in diameter with homogeneity of 3,000 ppm. The system is equipped with a gradient stack capable of reaching strengths > 24 mT/m along any spatial direction. Field homogeneity can be actively shimmed with the gradients to reduce the homogeneity down to 75 ppm in a spherical volume of 100 mm in diameter. We control the scanner with MaRCoS [4], [5], a Red Pitaya based system (Fig. 1(g)) controlling a custom gradient driver board.

To acquire the images, we used RARE sequences. We acquired proton density weighted axial images with TR = 750 ms, echo spacing 20 ms, echo train length 5, effective echo time 20 ms, matrix size 140 $\times$ 120x24, acquisition bandwidth 35 kHz, and averaged acquisitions for a total scan time of 15 min.

We filtered the acquired images with a block match 4D (BM4D) filter and saved then in NiFTI format. ITK-SNAP [6] was used for image segmentation, and matlab to obtain the cross-section areas and volumes of the muscles.

Results: Figure 2a shows a representative example corresponding to one of the volunteers. The image includes the segmentation of the lateral (red) and the medial (green) gastrocnemius muscle for one of the transversal slices of the 3D image. Making use of this segmentation for all the slices we could obtain the slice cross-sectional area as well as the muscle volume. Figure 2b shows the volume (left) and area (right) as a function of the slice for this representative volunteer. Figure 3 shows the cross-sectional area (a) and the volume (b) of the medial gastrocnemius obtained from different images as a function of the weight of the volunteer. This is obtained for the slice with the larger area of the medial gastrocnemius. To calculate the volume, we take as a Reference the slice with the larger cross-sectional area of the medial gastrocnemius, then we measure the volume from this slice to 7.5 cm distal.

Discussion: We observe that there is a statistically significant correlation between the volunteer weight and the area (volume), with a Pearson correlation coefficient of 0.626 (0.657). Also, a preliminary analysis of the results indicates a negative correlation between the volume of the medial gastrocnemius of the left leg with the unilateral right and left counter movement jump height ($r = -0.502$ and $r = -0.409$, respectively). The statistical significance was set at $p < 0.05$.

Conclusion: In this work, we studied systematically calf images acquired with our portable, low-cost and low-field "Physio MRI" scanner. A first analysis of the results indicates significant correlation between the weight and volume of the medial gastrocnemius, as well as with the cross-sectional area of the muscle. Furthermore, a preliminary analysis shows correlation between unilateral right and left counter movement jump height and the volume of the medial gastrocnemius.

Fig. 1: Picture of the volunteer while getting an image of the calf in the "Physio MRI" scanner.

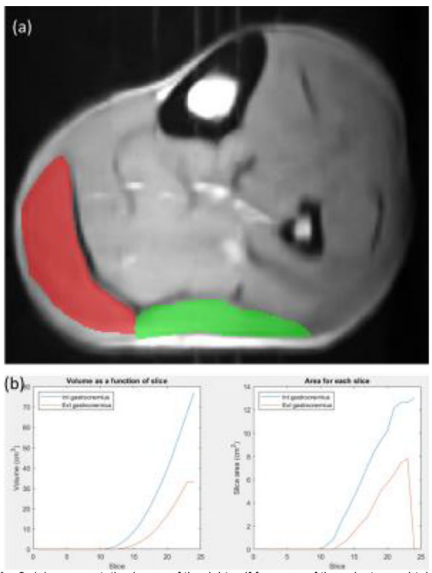

Fig. 2: (a) representative image of the right calf from one of the volunteers obtained with proton density 3D-RARE. The picture includes the segmentation of the medial (red) and lateral (green) gastrocnemius. (b) Volume (left) and slice area (right) of the medial (blue) and lateral (red) gastrocnemius.

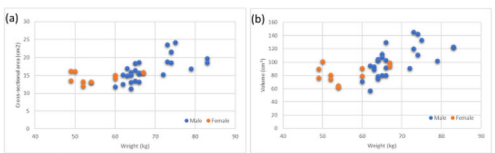

Fig. 3: (a) Cross-sectional area and (b) volume of the medial gastrocnemius as a function of weight. Blue (orange) dots represents male (female) volunteers. The Pearson coefficient for cross-sectional area (volume) is 0.626 (0.657).

References:
[1] J. P. Marques, F. F. J. Simonis, and A. G. Webb, "Low-field MRI: An MR physics perspective," *J. Magn. Reson. Imaging*, vol. 49, no. 6, pp. 1528–1542, Jun. 2019, https://doi.org/10.1002/jmri.26637.
[2] M. Sarracanie and N. Salameh, "Low-Field MRI: How Low Can We Go? A Fresh View on an Old Debate," *Front. Phys.*, vol. 8, no. June, pp. 1–14, 2020, https://doi.org/10.3389/fphy.2020.00172.
[3] T. Guallart-Naval et al., "Portable magnetic resonance imaging of patients indoors, outdoors and at home," *Sci. Rep.*, vol. 12, 2022, https://doi.org/10.1038/s41598-022-17472-w.
[4] T. Guallart-Naval et al., "Benchmarking the performance of a low-cost magnetic resonance control system at multiple sites in the open MaRCoS community," *NMR Biomed.*, no. March, pp. 1–13, 2022, https://doi.org/10.1002/nbm.4825.
[5] V. Negnevitsky et al., "MaRCoS, an open-source electronic control system for low-field MRI," *J. Magn. Reson.*, p. 107424, 2023, https://doi.org/10.1016/j.jmr.2023.107424.
[6] P. A. Yushkevich et al., "User-guided 3D active contour segmentation of anatomical structures: Significantly improved efficiency and reliability," *Neuroimage*, vol. 31, no. 3, pp. 1116–1128, 2006, https://doi.org/10.1016/j.neuroimage.2006.01.015.

P135.
Assessment of myocardial first-pass perfusion and T1-mapping using radial sampling and k-space weighted image contrast in the common marmoset

M. Ramedani[1,2], T. R. Memhave[1,2], J. Koenig[1], S. Boretius[1,2,3], A. Moussavi[1,2]

[1]*German Primate Center—Leibniz Institute for Primate Research, Functional Imaging Laboratory, Göttingen, Germany;*
[2]*DZHK, partner site, Göttingen, Germany;*
[3]*University of Göttingen, Johann-Friedrich-Blumenbach Institute for Zoology and Anthropology, Göttingen, Germany*

Introduction: The common marmoset, a small non-human primate, has become increasingly popular in preclinical research. Recently, it was shown that aging led to abnormalities in ventricular function and signs of myocardial remodelling. 1. To better understand the underlying pathomechanisms, quantitative techniques investigating the myocardium's microstructure (e.g. collagen volume) and perfusivity (e.g. vessel volume) are required. 2. The aim of this translational study was to develop an MRI protocol for precise estimation of extracellular volume and first-pass perfusion of the myocardium, which we could apply to study age-related myocardial differences between young and senescent marmosets.
Methods: Experiments were conducted on 20 healthy adult marmosets divided into two groups young adult (n = 10, age = 2.5 ± 0.5 years) and senescent (n = 10, age = 13.6 ± 2.1 years). Cardiovascular MRI was obtained on a 9.4 T MR system (Biospec 94/30, Bruker BioSpin, Germany) using a single-loop receive coil (Rapid Biomedical, Germany). First-pass perfusion and T1-mapping of a mid-ventricular short-axis slice were measured with a non-ECG gated, golden angle, radial FLASH (TR = 4–6 ms, TE = 1.5–2 ms, spatial resolution = 0.5 × 0.5 × 2 mm^3) sequence with additional saturation and inversion recovery modules, respectively. A schematic of the protocol is shown in Fig. 1. The first-pass perfusion images were acquired during the injection of contrast agent (0.125 mmol/kg Gadovist). The T1-mapping was acquired before (pre-contrast T1) and ~ 12 min after (post-contrast T1) contrast agent injection. Raw radial data was gridded to Cartesian coordinates using a Kaiser-Bessel kernel. We analyzed the data using two different undersampling schemes: conventional undersampling using only a subset of spokes and k-space weighted image contrast (KWIC)3 undersampling.. Both conventional and KWIC undersampling were reconstructed with different undersampling factors (Fig. 2) (ns = 13, 21, 34, 55, …) based on the golden angle ordering scheme.
Myocardial perfusion ratio (MPR) was assessed semi-quantitatively using the first-pass perfusion data. MPR is defined as the ratio of the slope in myocardium and blood of the signal-time curve during the first pass of the contrast agent: MPR = upslopemyo/upslopeblood 4. T1 maps were estimated by fitting a three-parameter equation. An automatic tissue segmentation was used to separate blood from myocardium for calculating the MPR and the extracellular volume fraction (ECV). The ECV was calculated from pre-contrast and post-contrast T1 maps: ECV = (1 − hct) × (ΔR1myo/ΔR1blood) 5.
Results: Due the intrinsic image averaging property of the radial sampling scheme, images are free of breathing artifacts and a static image of the beating heart is reconstructed. Fully sampled (ns = 137) radial reconstruction will lead to superior image quality, however, the relative long saturation time of 420 ms leads to signal saturation of the peak concentration in the signal-time curves. Conventional radial undersampling can overcome this limitation by reducing the effective saturation time to 42 ms (ns = 13), 66 ms (ns = 21) or 102 ms (ns = 34) with a drawback of significantly reduced SNR. In contrast, radial undersampling in combination with KWIC undersampling has the advantage of reducing the effective saturation time while retaining the SNR. Similar optimization was performed for the reconstruction of T1 maps. By considering both the SNR and effective saturation and inversion time, the optimal number of spokes were selected as 21 for first-pass perfusion and 55 for T1-mapping. Figure 3 shows a representative pre-contrast and post-contrast map of the T1 time using the suggested radial reconstruction with KWIC undersampling.
Preliminary results of the marmosets aging study reveals a significant decrease of the MPR as well as an increase in the pre-contrast T1-time and ECV in senescent monkeys, which is in agreement with findings in humans (data not shown).
Discussion: KWIC undersampling in combination with radial encoding allows for reconstruction of images with saturation times shorter than 100 ms for first-pass perfusion, which prevents signal saturation of the peak concentration. Similarly, T1 maps can be measured with a single-shot inversion pulse and a look-locker radial encoding. The achieved image quality allows for reliable automatic myocardial segmentation and assessment of quantitative parameters of the myocardial microstructure.
Conclusion: The introduced MR protocol allows for robust quantification and detection of microstructural changes of the myocardium during aging in marmosets and other small animal models.

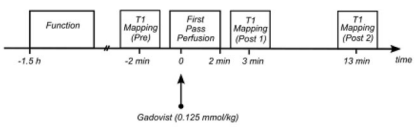

Fig. 1: Cardiac magnetic resonance examination paradigm. Scan protocol was shown from function (left) to T1-mapping (right) in time sequence.

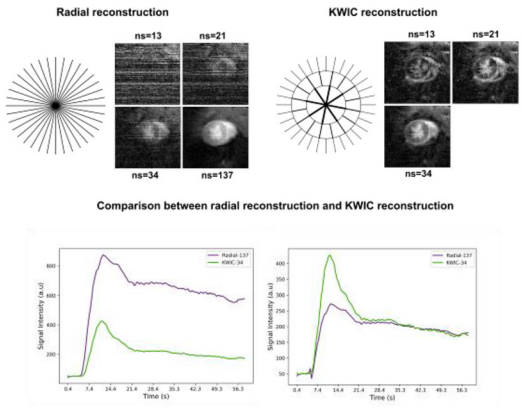

Fig. 2: Schematic of two different radial reconstruction undersampling schemes (conventional and KWIC) used to analyze the first-pass perfusion images. The number of spokes (ns) used for the reconstruction is shown in each Figure. Time-signal intensity curves of the left ventricle cavity for each reconstruction is shown in the bottom row.

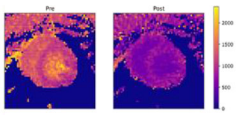

Fig. 3: Shows the pre-contrast and post-contrast T1 map for reconstructed with 55 spokes per frame in a subject at the mid-ventricular short-axis level.

References:
1. Moussavi A, et al. Scientific reports, 2020; 10(1).
2. Knott D, et al. J Magn Reson Imaging, 2019; 50(3).
3. Song H, et al. Magn Reson Med, 2000; 44(6).
4. Hsu L, et al. J. Magn Reson Imaging, 2006; 23(3).
5. Haaf P, et al. JCMR, 2016; 18(1).

P136.
Evaluation of T1 mapping in the aging heart

V. Tambè[1], A. Esseridou[1], S. de Simoni[1], R. Moltrasi[1], S. Bentivegna[1], E. Schwarz[1], M. Zanardo[2], F. Secchi.[2]

[1]*C.D.C Igea-Health Centre-Milan, Milan, Italy;*
[2]*IRCCS- San Donato Policlinico, Milan, Italy*

Introduction: The world"s population is aging: every country is experiencing growth in both the size and the proportion of older people. Aging is without a doubt the dominant risk factor for developing cardiovascular diseases. We investigated native and post-contrast T1 mapping as a quantitative method to appraise its clinical potential in the evaluation of the aging heart. T1 mapping consists in quantifying the intrinsic T1 relaxation time of a tissue and it may be considered as a marker for the extent of myocardial disease. This article aimed to provide Reference values of T1 mapping in order to quantify the expansion of the extracellular matrix in older people.
Methods: We retrospectively selected subjects ranged in age from 82 to 100 years old that underwent contrast cardiac magnetic resonance (CMR). All subjects were imaged on a 1.5 T system. T1 measurements were performed with a Modified Look Lockers Inversion (MOLLI) recovery sequence. MOLLI images generally use bSSFP readouts to improve blood-tissue contrast. Regions of interest (ROI) were drawn in the left ventricle for blood T1 measurement and in the interventricular septum. We used T1 data obtained before and after contrast injection. ECV (extracellular volume) was calculated. We also measured the volume and function of both ventricles. Spearman's Rho was used for correlations.

Results: We analysed 62 patients (mean age 82.26 ± 2.95 years old). Mean value of T1 in the blood pool (T1bp) was 1625.72 ± 95.06 before contrast and 361.21 ± 62.32 after contrast. Mean value of T1 in the septum (T1s) was 1010.64 ± 37.60 before contrast and 496.46 ± 57.85 after contrast. Mean value of ECV in the septum was 0.28 ± 0.06%. Left ventricle (LV) EDVI was 49.66 ± 15.99 ml/m^2 and ESVI was 17.34 ± 8.85 ml/m^2, LV ejection fraction (EF) and stroke volume (SV) were 65.99 ± 10.15% and 56.24 ± 19.72 ml respectively. Right ventricle (RV) EDVI was 49.33 ± 13 ml/m^2 and ESVI was 18.73 ± 6.17 ml/m^2, RV ejection fraction (EF) and stroke volume (SV) were 61.83 ± 9.09% and 53.33 ± 19.85 ml respectively. A significant negative correlation was found between ECV and LVEF ($r = -0.348$ and $p = 0.03$) and RVEF ($r = -0.250$ and $p = 0.026$). No significant correlations were found between ECV and age.
Discussion: The preliminary findings of this research suggest a potential correlation between fibrosis and age. Cardiac aging is linked with morphological and functional changes. These changes can be used to guide clinical decision-making and treatment. To ensure that our health system is ready to face this demographic shift toward an aging population, this study aimed to establish Reference values of T1 mapping in the elderly.
Conclusions: This study shows a correlation between ECV and biventricular systolic function in an aged population.

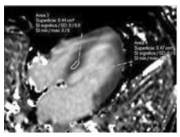

Fig. 1: Sampling regions of interest in the left ventricle for T1 blood measurement and interventricular septum

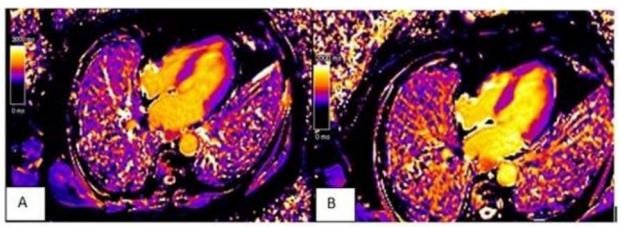

Fig. 2: MRI T1 mapping before (A) and after (B) contrast injection.

References:
1. World Health Organization. Ageing and Heath. World Health Organization, 2022.
2. Paola Maria Cannaò et al. "Novel cardiac magnetic resonance biomarkers: native T1 and extracellular volume myocardial mapping" EURHEARTJ 18:E64-E71(2016).
3. Henrik Engblom et al. "Importance of standardizing timing of hematocrit measurement when using cardiovascular magnetic resonance to calculate myocardial extracellular volume (ECV) based on pre- and post-contrast T1 mapping" JCMR (2018).
4. Matthew Gottbrecht et al. "Native T1 and Extracellular Volume Measurements by Cardiac MRI in Healthy Adults: A Meta-Analysis" Radiology 00:1–10(2018).
5. Scott A. Hamlin et al. "Mapping the Future of Cardiac MR Imaging: Case-based Review of T1 and T2 Mapping Techniques" RadioGraphics 34:1594–1611(2014).
6. Jeremy R. Burt et al. "Myocardial T1 Mapping: Techniques and Potential Applications" RadioGraphics 34:377–395(2014).
7. Daniel R. Messroghl et al. "Clinical recommendations for cardiovascular magnetic resonance mapping of T1, T2, T2* and

extracellular volume: A consensus statement by the Society for Cardiovascular Magnetic Resonance (SCMR) endorsed by the European Association for Cardiovascular Imaging (EACVI)"JCMR 19:75 (2017).

P137.
Fontan circulation under moderate hypoxia insights from real-time cardiac MRI

D. Gerlach[1], C. Hart[2], A. Bach[1], P. Rosauer[1,3], N. Müller[2], J. Härtel[2], A. Hoff[1], D. Voit[4], J. Frahm[4], J. Breuer[2], J. Jordan[1], J. Tank[1]

[1]*German Aerospace Center, Institute of Aerospace Medicine, Cologne, Germany;*
[2]*University Hospital Bonn, Children's Heart Center, Bonn, Germany;*
[3]*German Aerospace Center, Institute for Software Technology, Cologne, Germany;*
[4]*Max Planck Institute for Multidisciplinary Sciences, Biomedical NMR, Göttingen, Germany*

Background: In patients with Fontan circulation, the lungs are passively supplied with venous blood and the univentricular heart performs the function if the left ventricle. In other words, the Fontan circulation connects the large veins from the lower and upper body with the lung arteries bypassing the heart. Therefore, such patients are excellent models to study hypoxia influences on the cardiovascular system, which is relevant for aeronautics and space medicine alike. Hypoxia leads to vasoconstriction in pulmonary vessels and to systemic vasodilation which has an impact on cardiac output especially under physical load. Thus, the clinical recurrent question arises whether children and adults with Fontan circulation should expose themselves to prolonged hypoxia ($\geq$ 12 h) such as during airplane travel or travel to higher altitude. Our aim was to study how patients with Fontan circulation respond to moderate hypoxia of 15.1% O_2 over 24 h, which is equivalent to about 2400 m. Assessing the Fontan circulation is challenging with conventional imaging methods. Breath-hold capacity is very limited in these patients, especially under hypoxic conditions. Cardiac real-time MRI offers rapid image acquisitions during spontaneous breathing, which allow new insights in the hemodynamics and the specific cardiac anatomy in these unique patients. Patients with univentricular hearts show large interindividual variability and conventional imaging techniques often fail to provide reliable data. Real-time MRI during free breathing can solve those problems but respiratory variability of hemodynamic parameters is an additional challenge. Thus, we aim to train an artificial intelligence network with pre-segmented images and to synchronize the obtained results with respiration.
Material and method: We recruited 18 patients with Fontan circulation (9 women, 9 men; 24.8 $\pm$ 6.3 years; 23.0 $\pm$ 3.6 kg/m^2) and performed real-time cardiac MRI in normoxia and in normobaric hypoxia (24 h of 15.1% O_2). We acquired conventional cine MRI (25 phases) during normoxia and real-time cardiac MRI (temporal resolution of 33 ms over 10 s) in the short axis during both, normoxia and hypoxia. We quantified blood flow in the ascending and descending aorta, the vena cava superior and inferior, in the Fontan tunnel and in the left and right pulmonal arteries with the same temporal resolution over 30 s each. We also recorded brachial blood pressure, beat-to-beat finger arterial blood pressure, ECG, and respiration. We analyzed real-time images with Cafur (Mevis Fraunhofer) and obtained mean values over the acquired time periods. We analyzed cine images using Circle CVI42 software. We used expert annotations of cardiac short axis images of the univentricular hearts to teach the U-net [1] based AI for segmentation. In addition, we compared the automatic detection of systole, diastole, inspiration and expiration with corresponding time points in the physiological recordings.
Results: Hypoxia increased heart rate from 65 $\pm$ 13 bpm to 74 13 bpm ($p < 0.001$) while systolic blood pressure remained unchanged (normoxia: 110 $\pm$ 10 mmHg, hypoxia: 111 $\pm$ 11 mmHg), however, diastolic blood pressure increased from 59 $\pm$ 8 mmHg to: 63 $\pm$ 9 mmHg ($p = 0.011$). Stroke volume decreased from 58 $\pm$ 17 ml to 54 $\pm$ 15 ml measured in the ascending Aorta ($p = 0.005$). Cardiac output remained unchanged due to increased heart rate. Left pulmonary artery flow increased from 1.55 $\pm$ 0.36 l/min to 1.80 $\pm$ 0.49 l/ min ($p = 0.015$). Flow in the right pulmonary artery was 1.23 $\pm$ 0.51 l/min during normoxia and 1.13 $\pm$ 0.52 l/min ($p = 0.305$) in hypoxia. The difference between pulmonary blood flow (RPA plus LPA) and systemic blood flow (cardiac output) did not change during hypoxia compared to normoxia. Blood flow per heart beat decreased in the descending aorta (34.4 $\pm$ 13.4 ml vs. 30.5 $\pm$ 11.3 ml, $p = 0.027$), right pulmonary artery (19.7 $\pm$ 8.6 ml vs. 15.9 $\pm$ 7.9 ml, $p = 0.021$) and in the Fontan tunnel (35.5 $\pm$ 12.6 ml vs. 32.7 $\pm$ 12.5 ml, $p = 0.038$).
Conclusion: Patients with Fontan circulation exposed to moderate hypoxia over 24 h did not show clinically relevant changes in pulmonary or systemic flow. Moreover, shunt volume remained unchanged during moderate hypoxia. These findings suggest that patients with Fontan circulation should not be generally excluded from airplane travel. However, further analysis of possible subgroups may be needed. Given the utility of responses, we will use the methodology in future studies to assess diastolic filling during deep breathing maneuvers and under different cardiac loading conditions to differentiate functional capabilities of individual Fontan circulations.
Reference:
[1] Isensee F, Jaeger PF, Kohl SAA et al. (2021) nnU-Net: a self-conFiguring method for deep learning-based biomedical image segmentation, Nat Methods 18, 203–211

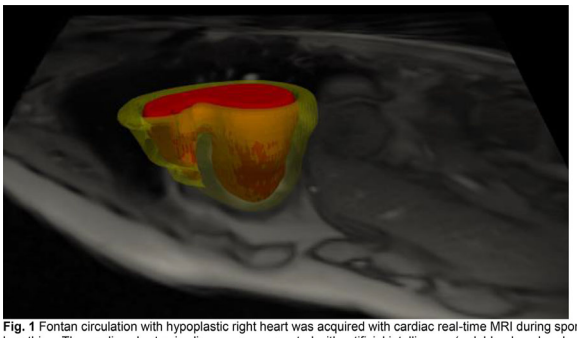

Fig. 1 Fontan circulation with hypoplastic right heart was acquired with cardiac real-time MRI during spontaneous breathing. The cardiac short axis slices were segmented with artificial intelligence (red: blood pool and yellow: myocardial volume) sorted automatically for their cardiac and respiratory phase to create and 3D stack representing end-diastolic and end-expiratory phase. The result shows the blood pool and heart muscle. The 3D model shows the end-diastole and end expiration.

P138.
RAKI algorithm for cardiac CINE images: The more layers the merrier?

L. Quillien[1], J. Oster[1,2], P. A. Vuissoz[1]

[1]*IADI, INSERM U1254, Université de Lorraine, Nancy, France;*
[2]*CIC-IT, INSERM 1433, Université de Lorraine and CHRU Nancy, Nancy, France*

Introduction: Accelerated MRI reconstruction techniques are necessary to fasten long cardiac exams and avoid the use of breath holds. Parallel imaging (PI) techniques are widely used in clinical practice to reduce the number of k-space lines acquired, by taking advantage of multiple receiver coil information. GRAPPA[3] is a PI reconstruction

algorithm aiming at interpolating the missing k-space lines using convolution kernels determined during a calibration based on fully sampled central k-space lines. RAKI[2] algorithm recently proposed to incorporate non-linearity by applying CNN with multiple layers. The advantage of this approach lies in the single shot training, which is uncommon for Deep Learning techniques usually requiring large training dataset.

The objective of this study is to assess the need of multiple CNN layers and non-linear activation for a RAKI reconstruction. As such, we propose the use of a single layer RAKI network, that comes close to a parallelised GRAPPA algorithm[4,5] to further accelerate the reconstruction, while guaranteeing imaging quality.

Methods: RAKI was implemented on Pytorch based on code available online[6] (Fig. 1A). Training was performed by optimising the Mean-Absolute Error (MAE) over 600 epochs with an ADAM optimiser (lr = 0.001 with exponential decay). The architecture was then modified to contain a single layer of CNN (5X5 kernel) (Fig. 1B).

We evaluated the proposed method on the OCMR database[7,8], comprising 64 fully sampled single slice CINE acquisitions. These images were acquired on different Siemens scanners (28 acquired at 1.5 T and 36 at 3 T), 21 in short-axis view and 43 in long-axis view. Imaging parameters were as follows (min/max): FOV = 80 × 180 mm^2/800 × 343mm^2, matrix size = 320 × 121/512 × 208, slice thickness = 6.5 mm/8 mm, TR = 2.71 ms/3.21 ms, TE = 1.36 ms/1.61 ms, flip angle = 33°/ 70°, cardiac phases = 15/31.

The images were retrospectively subsampled in a uniform pattern with an acceleration rate of R = 4.

Techniques were assessed using the following image quality metrics: Peak Signal to Noise Ratio (PSNR), Structural Similarity Index (SSIM) and Normalised Mean Squared Error (NMSE), measured thanks to the availability of a ground-truth image reconstructed with fully sampled data. The reconstruction time was also evaluated, and included the time required for data loading, training and evaluation/reconstruction.

We compared our proposed single-layer network with the standard RAKI and two GRAPPA implementations[9,10].

Results: The standard RAKI seems to show a better calibration with a loss function converging to a lower value than the single-layer network (Fig. 2).

Boxplots (Fig. 3) show that the single-layer network has similar or better quantitative results as standard RAKI, and the average of both GRAPPA implementations. The reconstruction time of the proposed model outperforms the other methods, making it almost 2 times faster than standard RAKI and as fast as the fastest GRAPPA implementation.

Both RAKI methods appear to be less noisy than GRAPPA (Fig. 4) and with a lower error compared to the ground-truth, though some artefacts remain (striped lines).

Discussion: The RAKI k-spaces (Fig. 4) seem to show an overfitting of the model, with better results for central lines of the k-space. This "overfitting" looks less present with the single-layer network. The GRAPPA reconstruction also seems to create this effect, yet in a less obvious manner, without a clear distinction between the centre and the rest of the k-space. The k-space interpolation appears to cause an underestimation of the intensity in the outer lines. This intensity difference between the real acquired and interpolated lines repeats throughout the k-space in a patterned manner that may create the stripping artefacts.

The difference between both loss functions indicates that the complexity of the network allows for a better interpolation but further overfitting. This overfitting seems to be confirmed by better quantitative results with the "less complex" network. The proposed loss function (MAE) might also not be optimal for k-space data, supporting the need for k-space specific loss functions[11].

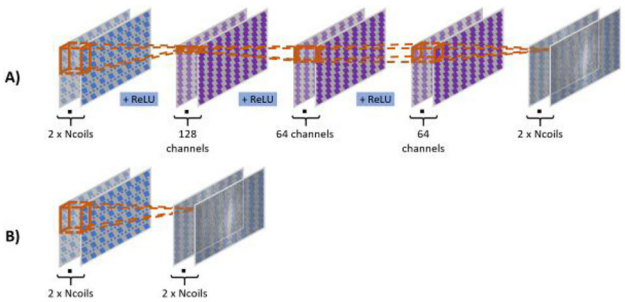

Fig. 1: Network architectures for A) Standard RAKI and B) Optimised RAKI.

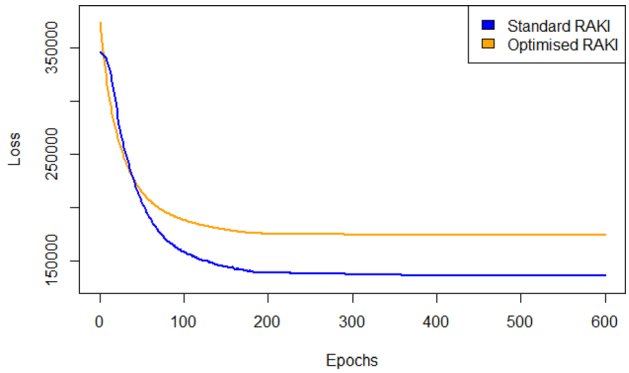

Fig. 2: Loss function for Standard RAKI and Optimised RAKI over 600 epochs.

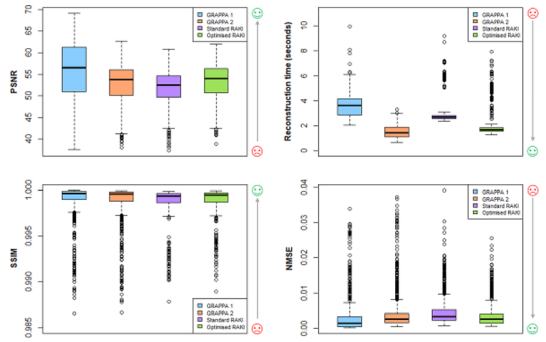

Fig. 3: Boxplots of the PSNR, NMSE, SSIM and reconstruction time for GRAPPA 1[9] and GRAPPA 2[10], Standard RAKI and Optimised RAKI.

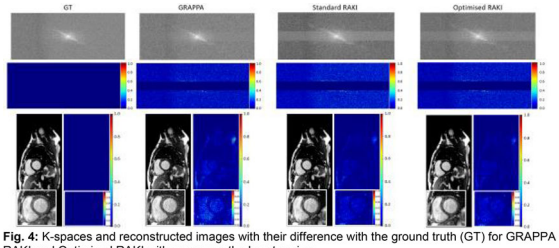

Fig. 4: K-spaces and reconstructed images with their difference with the ground truth (GT) for GRAPPA 1[9], Standard RAKI and Optimised RAKI with zooms on the heart region.

Conclusion: This study has shown that the depth of the neural network does not ensure better reconstruction performance. The proposed method shows comparable results to standard methods while being significantly faster and therefore more easily transferred in clinical practice.

References:
[1]Wang et al., BSPC, 2021, https://doi.org/10.1016/j.bspc.2021.102579
[2]Akçakaya et al., MRM, 2019, https://doi.org/10.1002/mrm.27420
[3]Griswold et al., MRM, 2002, https://doi.org/10.1002/mrm.10171
[4]Saybasili et al., MICCAI, 2008, https://doi.org/10.1007/978-3-540-85990-1_20
[5]Saybasili et al., MRM, 2014, https://doi.org/10.1016/j.mri.2014.02.022
[6]https://github.com/geopi1/DeepMRI
[7]www.ocmr.info
[8]Chen et al., arXiv,2020, https://doi.org/10.48550/ARXIV.2008.03410
[9]https://github.com/mckib2/pygrappa
[10]https://github.com/pdawood/iterativeRaki
[11]Huang et al., arXiv, 2022, https://doi.org/10.48550/ARXIV.2212.08479

P139.
Accelerated RAKI for multi-slice cardiac CINE data

L. Quillien[1], J. Oster[1,2], P. A. Vuissoz[1]

[1]IADI, INSERM U1254, Université de Lorraine, Nancy, France; [2]CIC-IT, INSERM 1433, Université de Lorraine and CHRU Nancy, Nancy, France

Introduction: Parallel Imaging techniques are widely used in clinical practice to accelerate MRI acquisition, especially for cardiac MRI. By exploiting sensitivity differences of multiple receiver coils, PI methods have been shown to accurately reconstruct images up to a reasonable acceleration rate. GRAPPA[1] aims at interpolating the missing k-space lines by using convolution kernels. Recently, Deep Learning (DL) have been explored to accelerate both the acquisition and reconstruction procedure while maintaining good imaging quality[2]. DL methods usually require large databases, which are pretty scarce in medical imaging. RAKI[3] is a scan-specific DL reconstruction technique derived from GRAPPA, that incorporates non-linearity with multiple CNN layers and non-linear activation units. Training of the model weights only need a patient-specific calibration signal (k-space central lines) which alleviates the need of a big database but requires longer reconstruction time due to the need of specific training for each scan. To overcome this limitation several works have recently been proposed to extend RAKI to simultaneous multi-slice[4,5].

Our proposed work aims at accelerating RAKI for cardiac CINE images by accelerating the training of the CNN weights and using the redundancy of information between the cardiac phases and adjacent slices.

Methods: The proposed method trains the RAKI network weights on one randomly selected cardiac phase of a given slice, and then reconstruct images (based on these weights) on all cardiac phases from this specific slice as well as all data from the adjacent slice. Therefore, one single training is used for 3XN images (all cardiac phases from 3 slices).

The proposed RAKI architecture consists of a single linear layer (5X5 kernel) (Fig. 1A). Training of the model has been performed by optimising the Mean-Absolute Error (MAE) loss function over 600 epochs with an ADAM optimiser (lr = 0.001 with exponential decay).

We evaluated the proposed method on the OCMR database[6,7], using only the multi-slice CINE data, which consisted of 10 stacks of CINE images (with 10 to 14 slices). These images were acquired on different Siemens scanners (8 acquired at 1.5 T and 2 at 3 T) in short-axis view. Imaging parameters were as follows (min/max): FOV = 600 × 233mm^2/760 × 308mm^2, matrix size = 288 × 112/384 × 156, slice thickness = 6 mm/8 mm, TR = 2.81 ms/3.05 ms, TE = 1.41 ms/1.53 ms, flip angle = 33°/70°, cardiac phases = 18/30. For comparison purposes, only 9 central adjacent slices were randomly selected for the reconstruction.

The images were retrospectively subsampled in a uniform pattern with acceleration rates of R = 4.

The proposed technique (Fig. 1E) was compared to the following methods: "standard" RAKI trained for each cardiac phase and slice independently (Fig. 1B), RAKI trained on a single phase while the slices were learned independently (Fig. 1C) and RAKI trained on each phase independently but on the middle slice (Fig. 1D).

Techniques were assessed using the Peak Signal to Noise Ratio (PSNR) measured with the available fully sampled data. The reconstruction time was also evaluated and included the time required for data loading, training and evaluation/reconstruction.

Results: The PSNR (Fig. 2) of the proposed method is almost as good as Standard and Multiphase RAKI and much better than Multislice RAKI, while the reconstruction time is reduced.

Figure 3 shows PSNR boxplots representing the impact of the learning slice position. The reconstruction on three adjacent slices showed the best compromise between image quality and reconstruction acceleration (Fig. 3E).

Standard RAKI and our method seem to show comparable visual results (Fig. 4).

Discussion: The proposed method greatly reduces the reconstruction time of RAKI for CINE images, with an acceleration factor of 21, making it more applicable in clinical practice.

Artefacts remain for several examples (Fig. 4). These artefacts seem to be present on standard RAKI and intrinsic of the approach. Future works will pinpoint these artefacts in the hope of reducing or eliminating them. One assumes that these artefacts seem to be due to overtraining on the calibration data, and structures of the subsampling. One will investigate the use of more raw-data specific loss functions, and/or the use of non-cartesian subsampling.

Conclusion: The proposed strategy significantly reduced the reconstruction time of cardiac CINE data while preserving reconstruction quality, by restricting the training of the RAKI network on a single cardiac phase and specific limited number of slices.

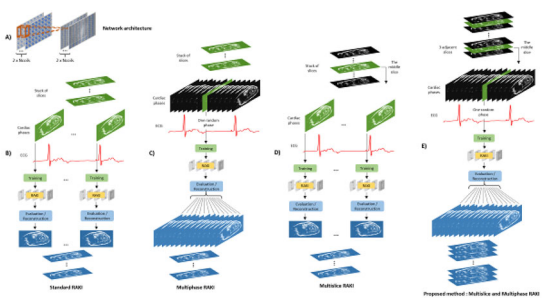

Fig. 1: Network architecture (A), with the different methods implemented: B) Standard RAKI, C) Multiphase RAKI, D) Multislice RAKI, E) Multislice/Multiphase RAKI. Training is done on the green data, while the reconstruction is on the blue data.

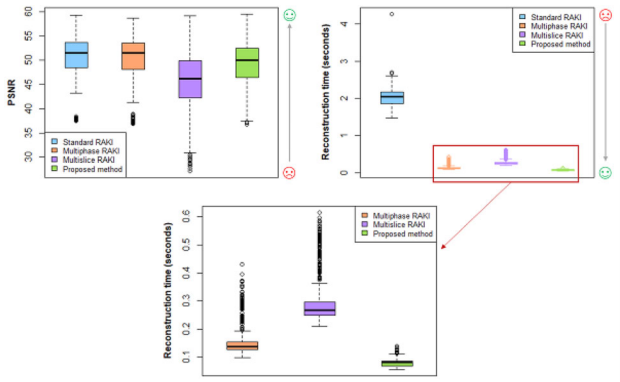

Fig. 2: Boxplots of the PSNR and reconstruction time for all methods.

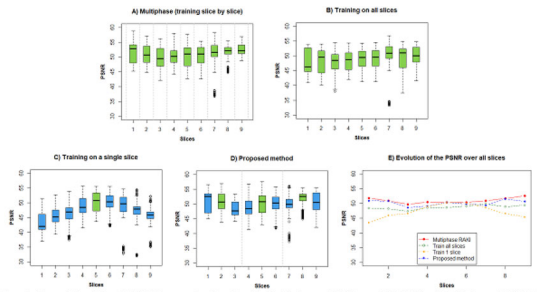

Fig. 3: Boxplots of the PSNR for each slice for A) Multiphase RAKI, and Multislice/Multiphase RAKI for different training schemes: B) training on all slices, C) training on only one slice (the middle one) and D) training 3 slices by 3 slices (the proposed method). Green boxplots represent trained slices while blue boxplots are only reconstructed slices. The dashed lines in A) and D) show the training pattern (slice by slice, or 3 slices by 3 slices). PSNR evolution over all slices for the four evaluated methods are presented in E).

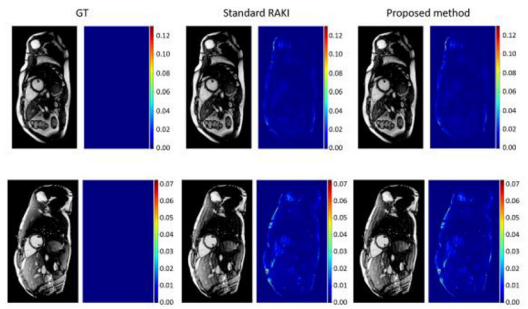

Fig. 4: Examples of reconstructed images with their difference with the ground truth (GT) for Standard RAKI and the proposed method.

References:

[1]Griswold et al., MRM, 2002, https://doi.org/10.1002/mrm.10171
[2]Wang et al., BSPC, 2021, https://doi.org/10.1016/j.bspc.2021.102579
[3]Akçakaya et al., MRM, 2019, https://doi.org/10.1002/mrm.27420
[4]Nencka et al., MRM, 2021, https://doi.org/10.1002/mrm.28634
[5]Zhang et al., ACSSC, 2018, https://doi.org/10.1109/ACSSC.2018.8645313
[6]www.ocmr.info
[7]Chen et al., arXiv, 2020, https://doi.org/10.48550/ARXIV.2008.03410

P140.
Comparison of mitral valve regurgitation quantification using 4D flow and standard cardiac magnetic resonance methods

Y. Safarkhanlo[1], M. Boscolo[1], G. Spano[1], J. Schütze[1], A. W. Stark[1], J. A. M. Bastiaansen[2], C. Gräni.[1]

[1]*University of Bern, Cardiology, Bern, Switzerland;*
[2]*University of Bern, Diagnostic, Interventional and Pediatric Radiology (DIPR), Bern, Switzerland*

Introduction: The accurate quantification of mitral valve regurgitation (MVR) is critical in the diagnosis and management of cardiovascular disease. Cardiac magnetic resonance imaging (CMR) has emerged as a valuable tool for detecting and measuring MVR. However, the development of new techniques such as intraventricular four-dimensional (4D) flow has opened up new avenues for more precise and detailed quantification of blood flow within the heart (1, 2).

In this study, we aimed to compare 4D flow against established CMR MVR quantification methods in patients with severe MVR. Our goal was to evaluate the performance of 4D flow in this clinical setting and to determine whether it could offer any advantages over existing methods. Specifically, we sought to assess the accuracy, reproducibility, and feasibility of 4D flow in the quantification of MVR.

Methods: We analyzed consecutive transcatheter edge-to-edge repair (TEER) candidates with severe MVR according to echocardiography, who underwent CMR including 4D flow, and who were included in the PRE-MITRA study. Patients underwent a CMR scan at a 1.5 T Siemens scanner (Magnetom Trio, Siemens Healthineers). MVR was quantified using four different methods (Fig. 1): Regurgitant volume (RVol) was derived using 1) 4D-flow intraventricular annular inflow (4D-flow$_{AIM}$) method, (2) 2-dimensional phase-contrast standard method (2D-PC$_{standard}$), (3) 2D-PC mitral valve method (2D-PC$_{MV}$), and (4) the volumetric method (Fig. 1). Quantification was compared among the different methods, using R software version 4.2.2 (R Foundation for Statistical Computing).

Results: A total of 7 patients (72 ± 16, 100% male) with severe MVR who underwent CMR scanning were included in this study. The mean left ventricular (LV) end-diastolic volume was 243 ml (range 52–424 ml) with a mean left ventricular ejection fraction (EF) of 30% (range 15–51%). There was a strong to excellent correlation between flow quantification methods ($r = 0.82–0.99$, $p < 0.05$) except 2D-PCMV. Average regurgitant volumes were 34 ± 12 ml for 4D-flow$_{AIM}$, 26 ± 21 ml for 2D-PC$_{standard}$, 26 ± 15 ml for 2D-PC$_{MV}$, and 34 ± 25 ml for the volumetric method (Fig. 2).

Discussion: The accurate quantification of MVR is critical in diagnosing and managing cardiovascular disease. CMR has emerged as a valuable tool for detecting and measuring MVR. However, the development of new techniques such as 4D flow has opened up new avenues for more precise and detailed quantification of blood flow within the heart. Our study aimed to compare 4D flow against established CMR MVR quantification methods in patients with severe MVR. We found that there was a strong to excellent correlation between the different methods of quantification, except for the 2D-PC$_{MV}$ method. In addition, the 4D-flow$_{AIM}$ method provided comparable regurgitant volume measurements to the standard CMR methods.

Conclusion: In conclusion, our study suggests that 4D-flow$_{AIM}$ is a viable adjunctive method for quantifying MVR in a clinical setting, with a strong correlation to standard CMR MVR methods. This technique may offer improved accuracy and reproducibility in the

quantification of MVR and could be a valuable tool for clinicians in diagnosing and managing cardiovascular disease.

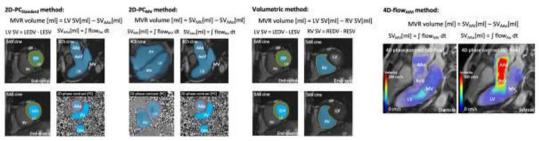

Fig. 1: Illustration of MVR quantification methods. 2D-$PC_{standard}$, CMR flow gold standard (Left Ventricle Stroke Volume [LV SV] – Stroke Volume derived from Aortic Forward Flow [SV_{AAo}]); 2D-PC_{MV}, directly quantifying flow through Mitral Valve (Stroke Volume derived from Mitral Valve Flow [SV_{MV}] – Stroke Volume derived from Aortic Forward Flow [SV_{AAo}]); Volumetric (Left Ventricle Stroke Volume [LV SV] – Right Ventricle Stroke Volume [RV SV]); 4D-$flow_{AIM}$ (Stroke Volume derived from Mitral Valve Flow [SV_{MV}] – Stroke Volume derived from Aortic Forward Flow [SV_{AAo}]); AoPC, Aortic Forward Flow; EDV, Left Ventricle End Diastolic Volume; ESV, Left Ventricle End Systolic.

Patient Number	LVSV (ml)	RVSV (ml)	LV EF (%)	SV_{AAo} (ml)	SV_{MV} (ml)	2D-$PC_{standard}$ (ml)	2D-PC_{MV} (ml)	Volumetric (ml)	4D-$flow_{AIM}$ (ml)
1	41.72	74.87	15.48	33.15	122.41	8.57	7.97	33.15	34.01
2	99.62	18.76	33.34	29.59	133.99	70.03	30.13	80.86	45.40
3	58.84	81.68	33.66	41.61	38.67	17.23	25.79	22.84	12.58
4	90.48	41.57	29.39	58.74	136.38	31.74	17.56	48.91	49.04
5	73.11	53.08	30.90	45.60	140.19	27.51	15.38	20.03	25.30
6	87.66	61.24	20.66	77.19	35.87	10.47	53.30	26.42	32.26
7	78.16	81.99	51.34	61.72	97.60	16.44	35.76	3.83	39.51

	2D-$PC_{STANDARD}$ (ML)	2D-PC_{MV} (ML)	VOLUMETRIC (ML)	4D-$FLOW_{AIM}$ (ML)
2D-$PC_{STANDARD}$ (ML)	1.00	−0.35	0.99***	0.82*
2D-PC_{MV} (ML)	−0.35	1.00	−0.39	−0.30
VOLUMETRIC (ML)	0.99***	−0.39	1.00	0.83*
4D-$FLOW_{AIM}$ (ML)	0.82*	−0.30	0.83*	1.00

Fig. 2: Measured parameters for the patients and the Pearson correlation coefficient table. The level of significance is presented as follows: * = (p<0.05), ** = (p<0.01), *** = (p<0.001).

References:

1. Fidock B, Archer G, Barker N et al. Standard and emerging CMR methods for mitral regurgitation quantification. International Journal of Cardiology 2021;331:316–321.

2. Spampinato RA, Jahnke C, Crelier G et al. Quantification of regurgitation in mitral valve prolapse with four-dimensional flow cardiovascular magnetic resonance. Journal of Cardiovascular Magnetic Resonance 2021;23.

P141.
Impact of BMI and electrode positions relative to the field of view on the electrocardiogram signal quality

C. Bringtown[1,2], P. M. Lefebvre[1], A. Guillou[2], J. Felblinger[1,3], J. Oster[1,3]

[1]*INSERM and Université de Lorraine, IADI U1254, Nancy, France;*
[2]*Schiller Medical, Wissembourg, France;*
[3]*INSERM,CHRU de Nancy and Université de Lorraine, CIC-IT 1433, Nancy, France*

Introduction: Electrocardiogram (ECG) is required during MRI for two main purposes: first for the monitoring of the patient during the exam; second for the synchronization of acquisitions with the heart activity in order to avoid motion artifacts during cardiac MRI[1].
However, the MRI environment distorts the ECG signals, making the ECG analysis highly complex. Several specific processing of ECG signals in MRI have been suggested[1,2,3]. Moreover, the electrode positions can affect the signal quality and artifact amplitude, and there is currently no consensus on the optimal electrode placement. In this work, we studied the impact of the Body Mass Index (BMI) and the position of the sensor relative to the field of view (FOV) on ECG signal quality and the amplitude of MRI-induced artifacts.

Methods: Data was collected during a clinical trial performed at the Nancy University hospital (EDEN, NCT0521846). The database consists in the collection large bandwidth [0–3.5 kHz] ECG signals sampled at 16 kHz with a MR-conditional ECG sensor (*Schiller medical, Wissembourg, France*). The sensor was positioned as recommended by the manufacturer. 6 female subjects with a mean BMI of 27.3 (BMI max 39.1; BMI min 17.9) were included in this study. MRI protocol was divided into two parts: (i) with pulse sequences used during brain examination and (ii) with pulse sequences used during cardiac examinations. Neurological exam included FLAIR, DIFFUSION and SWI pulse sequences with the FOV located on the head and smaller than 25 cm, therefore ECG sensor being outside the FOV, while cardiac exam included CINE, bSSFP, black blood images with inversion pulses and T1 maps, with the ECG sensor being located inside the FOV. One 60-s ECG recording was also performed outside the MRI bore. An in-house device (SAEC)[4] was used to record ECG signals and the three gradients coils currents simultaneously.
The amplitude of the R wave was estimated on the recording outside the MRI bore, by averaging the R peak amplitude after applying a commercial QRS detector. The maximum absolute value of each recording during pulse sequence was calculated to assess the gradient artefact amplitude for each pulse sequence.
The mean artifact peak value per subject was calculated and reported for each different BMI. Moreover, the average gradient artifact amplitude for head and heart centered pulse sequences were computed and compared.
Results: The evolutions of R-peak amplitudes, gradient artifact amplitudes and SNR, with BMI, are depicted in Fig. 1 a), b) and c) respectively. As BMI increases, the R-peak amplitude and SNR seems to decrease (with a R2 coefficient of 0.73 for R-peak amplitude and 0.71 for SNR); while gradient artifacts seem to be correlated to BMI (R2 = 0.87).
A boxplot comparing gradient artifact amplitude in the head protocol with heart protocol is depicted in Fig. 2, and indicate larger amplitudes for out of FOV acquisitions (head).
Discussion: It was long assumed that gradient artifacts were stronger when ECG electrodes were positioned outside of the FOV, which seems to be confirmed by Fig. 2. This can be explained by the presence of concomitant gradient fields (in each direction of the space).
Figure. 1 seems to indicate a strong correlation between BMI and the amplitude of gradient artifacts (and SNR). Possible explanations could be that distance between electrodes and heart is larger for higher BMI, meaning the heart amplitude is lower. Moreover gradient-induced currents are higher due to the presence of larger layers of tissue. Another explanation could also come from the fact that electrodes for subjects with higher BMI are closer to the outer region of the bore, which may be corrupted by concomitant gradients.
The use of a large bandwidth ECG sensor allows for the recording of well-preserved induced currents, but their magnitude can reach several hundred of mV (many orders of magnitude higher than the QRS complex and ECG signal or interest ($\sim$ 1 mV)). This will require to develop robust and accurate denoising strategy, such as adaptive filtering2. Early experiments have shown that these techniques might not work well in the current setting and might need further optimization (see Fig. 3).
Further works will include analyzing the impact of the position of the electrodes regarding MRI related distortions (both the MagnetoHydroDynamic effect and gradient artifacts).
Conclusion: In this study, we presented a new database of ECG signals acquired during MRI using a large bandwidth sensor. This database will allow for further analysis of optimal electrode

positioning for a woman population, and also serve as a tool for the development of effective gradient artifact suppression strategies.

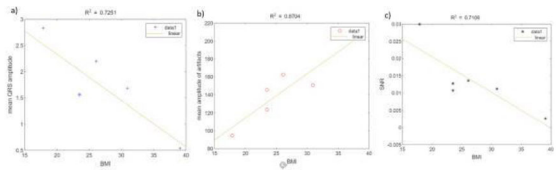

Fig. 1: a) Mean R-peak amplitude as a function of BMI, b) Mean artifact amplitude as a function of BMI, c) Ratio of mean R-peak amplitude to mean artifact amplitude as a function of BMI.

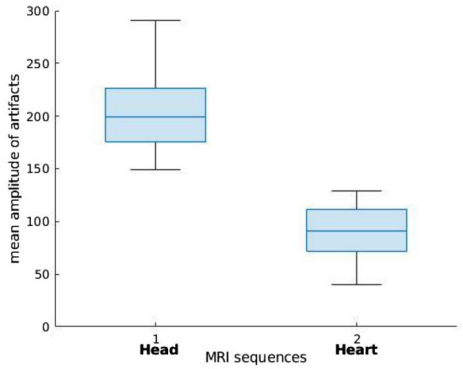

Fig. 2 : Amplitude of the gradient artifacts depending in the electrode position relative to the field of view (head and heart) protocol.

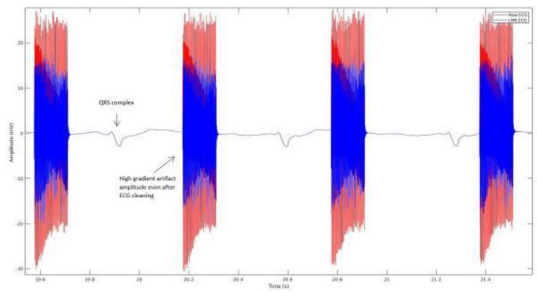

Fig. 3: Example of LMS denoising of a large-bandwidth ECG acquired during a T1 MAPPING sequence at 3T, with red signal representing raw ECG signals while the blue signal depicts the cleaned ECG. It can be seen that the amplitude of the QRS complex (indicating by an arrow) is ten times lower than the amplitude of the artifacts even after denoising.

References:

[1] OSTER et al., Physiol Meas. 2017, https://doi.org/10.1088/1361-6579/aa6e8c
[2] GUILLOU et al., MAGMA. 2017, https://doi.org/10.1007/s10334-017-0638-8
[3] Wu et al., JMRI. 2011, https://doi.org/10.1002/jmri.22530
[4] ISAIEVA et al., MRM. 2022, https://doi.org/10.1002/mrm.29280

P142.
An MRI Safety study of ECG devices by electromagnetic simulation, with comparison to experimental heating measurements

G. Paillart[1], G. Romero[2], N. Weber[1], W. Bouzid[1,2], C. Bringtown[1,3], P. Ferry[2], J. Felblinger[1,4], F. Odille[1,4]

[1]*INSERM and Université de Lorraine, IADI U1254, Nancy, France;*
[2]*Healtis MRI Safety, Nancy, France;*
[3]*Schiller MEDICAL, Wissembourg, France;*
[4]*INSERM, CHRU de Nancy and Université de Lorraine, CIC-IT 1433, Nancy, France*

Introduction: ElectroCardioGraphy (ECG) devices are essential for cardiac MRI exams, in order to synchronize image acquisition to the heartbeat and monitor the patient. To ensure MRI safety, most commercial MR-ECG devices use short cables from the chest electrodes to the analog-to-digital conversion unit, and ECG signals are transferred by optical fibers or wireless transmission[1]. There is currently no MRI safety standard specifically for devices placed on the body surface, so standards for implanted devices (ISO/TS 10974) are generally applied and adapted. Electromagnetic (EM) simulation is increasingly used to design radiofrequency (RF) heating experiments for such devices, as it can help identify worst-case scenarios and critical parameters. Furthermore, it might help design new use cases of the device, e.g. with multiple sensors[2], or at ultra-high field (7 T). The aim of this work was to model a commercial MR-ECG device, and qualitatively compare EM simulation results to experimental temperature measurements.

Methods: *Experimental setup* The experimental setup was designed to test a set of 5 ECG sensors (modified version of the W-ECG, Maglife RT-1 system from Schiller Médical, Wissembourg, France). Experiments were performed on a PRISMA 3 T MRI machine (Fig. 1). The sequence was a 2D Turbo-Spin-Echo to maximize RF power transmission (flip angle 90/166 deg, echo train length = 32, TR/TE = 4660/113 ms, 40 slices). The heating sequence was applied for 15 min for each test and followed by 2 min of rest. The phantom was composed of tapped water in an torso-shaped tray. The ECG sensors were placed on polystyrene blocks in order not to be immersed in water, and the electrodes were sticked onto agar gel blocks (Fig. 2) which had electrical properties similar to salty water (ε_R = 78 and σ = 0.5 S/m).

Temperature measurements were obtained with four optical probes (Reflex Signal Conditioner, NEOPTIX, Québec, Canada), which were placed at each electrode-gel interface. One experiment allowed monitoring one ECG sensor (4 electrodes), it was repeated to monitor each of the 5 sensors.

Simulations Simulations were executed on CST Studio Suite 2022 (Dassault Systems, Vélizy-Villacoublay, France). Models of the ECG sensors were created to reproduce the ECG sensor geometry faithfully, and material properties (cables, electrodes, gels etc.), which were not available in this preliminary work, were estimated with typical values. The radiofrequency transmission coil was a validated birdcage model of either a 1.5 T SIEMENS AVANTO FIT or a 3 T SIEMENS PRISMA MRI machines, both used at our institution. The torso phantom had the same properties as water and the same dimensions as that used in the experiment. Furthermore, a Siemens ECG sensor (PERU 098 ECG/Respiratory Unit) has been modeled on the CST Studio Suite 2022 software to compare qualitatively the heating distribution of both ECG sensors (Fig. 3).

Results: From the experiment, the C electrode, whatever the location of the sensor, showed the highest temperature elevation (4.8 °C), and the maximum heating appeared when the ECG sensor was closest to the center of the MRI system.
So far, simulations on the in the simulation, the highest SAR was observed in the C electrode in all tested locations of the ECG sensor model, when using the 1.5 T birdcage model (Fig. 4).
Discussion and Conclusion: The phantom experiment and the preliminary simulation results showed the same trend: the electrode which is the farthest from the ECG sensor in the birdcage axis showed highest SAR/temperature elevation. Quantitative comparison of simulations and experiments was not performed at this stage. In future work, material properties will be refined, and the device transfer function will be measured and integrated to the simulation. The simulation framework might help in the development of ECG sensors for 7 T MRI.

Acknowledgements
Funding
French ANR project ELECTRA (ANR-21-CE19-0040).

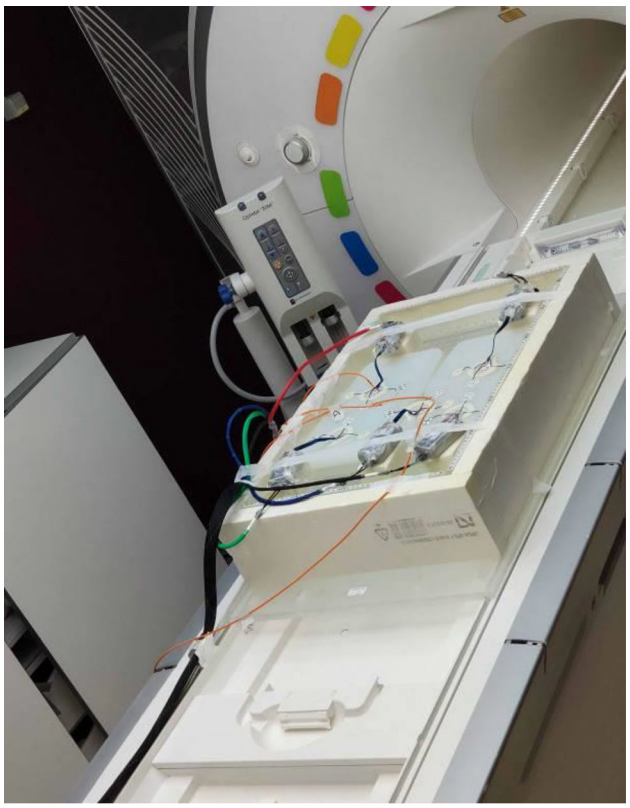

Fig. 1: Picture of the five Schiller ECG sensors on a phantom in front of the 3T Prisma MRI machine.

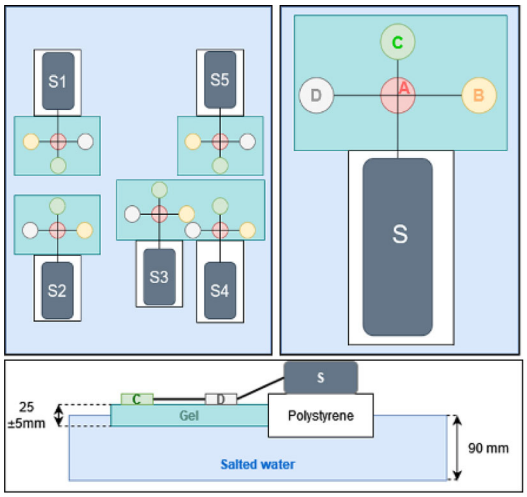

Fig. 2: Placement of Schiller ECG sensors and electrodes for the clinical MRI experiment.

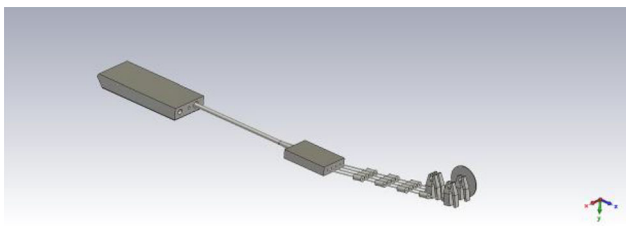

Fig. 3: Siemens ECG sensor modeled in the CST Studio Suite 2022 software.

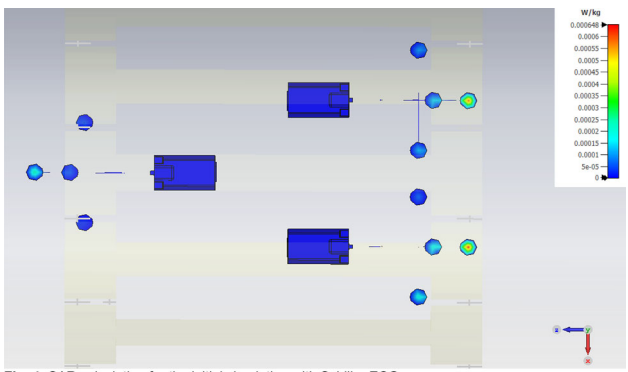

Fig. 4: SAR calculation for the initial simulation with Schiller ECG sensors.

References:
1. Felblinger J, Lehmann C, Boesch C. Electrocardiogram acquisition during MR examinations for patient monitoring and sequence triggering. *Magn Reson Med*. 1994;32(4):523–529. https://doi.org/10.1002/mrm.1910320416
2. Dos Reis JE, Soullié P, Oster J, et al. Reconstruction of the 12-lead ECG using a novel MR-compatible ECG sensor network. *Magn Reson Med*. 2019;82(5):1929–1945. https://doi.org/10.1002/mrm.27854

P143.
Dynamic glucose enhanced (DGE) MRI at 7 T: The influence of head motion on the B_1^+ field

P. Lehmann[1], R. Wirestam[1], P. Sundgren[2,3,4], P. van Zijl[5,6], L. Knutsson[1,5,6], K. Markenroth Bloch[2]

[1]*Lund University, Department of Medical Radiation Physics, Lund, Sweden;*
[2]*Lund University, Lund University Bioimaging Centre, Lund, Sweden;*
[3]*Lund University, Department of Radiology, Lund, Sweden;*
[4]*Lund University, Department of Medical Imaging and Physiology, Lund, Sweden;*
[5]*Johns Hopkins University, Russell H. Morgan Department of Radiology and Radiological Sciences, Baltimore, MD, United States;*
[6]*Kennedy Krieger Institute, F.M. Kirby Research Center for Functional Brain Imaging, Baltimore, MD, United States*

Introduction: Ultra-high field magnetic resonance imaging (MRI) systems can provide both high spatial and high temporal resolution. However, spatial inhomogeneities of the transmit magnetic field B_1^+ can lead to modified signal and contrast in the acquired image. Furthermore, alterations in head position due to motion relative to the transmit coil may cause B_1^+ changes at the voxel level. One way of measuring these inhomogeneities is by using the Dual Refocusing Echo Acquisition Mode (DREAM) method.[1] DGE MRI is sensitive to changes in B_1^+ affecting the saturation efficiency for targeted glucose. In this study, we investigated the changes in the B_1^+ field distribution caused by motion during dynamic glucose-enhanced (DGE) MRI in order to assess the order of magnitude of these effects.
Methods: The study was approved by the local ethics committee and written informed consent was obtained from all participants. Three healthy male volunteers aged 24–27 years were scanned at 7 T (Achieva, Philips Healthcare, Eindhoven, Netherlands) using an 8-channel-transmit/32-channel-receive head coil (NovaMedical). An experienced neuroradiologist examined the morphologic images (MP2RAGE) of each healthy volunteer to exclude any pathology. DGE MRI was performed to monitor the uptake of D-glucose infusion using a 23-min dynamic chemical exchange saturation transfer (CEST) MRI sequence. DREAM flip angle mapping was performed before and after the DGE MRI, using 3 different flip angles (25, 40, and 60 degrees) to reduce bias.[2] The DREAM flip angle mapping involved an ultra-fast multi B_1^+-mapping single-shot STEAM sequence with the following parameters: TE(free induction decay, FID) = 0.99 ms, TE(stimulated echo, STE) = 1.39 ms Ts(STEAM preparation pulse interval) = 2.4 ms, TR = 2.4 ms, FA = 24°, 40° and 60° and an isotropic voxel size of 3.75 × 3.75 × 3.75 mm^3. The sequence generated a B_1^+-map together with maps of STE and FID. The different flip angle maps were combined according to Olsson et al.[2] using Matlab R2020a (MathWorks, Natick, MA, USA) to generate one flip angle map before and one after the DGE MRI. The STEs before and after the DGE MRI were used to generate motion estimates using Elastix as a retrospective motion correction algorithm.[3,4] The generated motion estimates were applied to the combined flip angle maps assuring proper realignment. The required Elastix parameter file was optimized by choosing the cost function as a normalized mutual information metric and the transform being restricted purely to rigid motion. Difference images of the B_1^+-maps before and after the DGE protocol were calculated. Skull stripping was performed. Line profiles were drawn in the coronal slice from inferior to superior, in the sagittal slice from anterior to posterior, and in the transversal slices from left to right.
Results and Discussion: Different B_1^+-profiles are shown in transversal slice direction (Figs. 1A-C), with a hyperintensity in the center of the brain, being the lowest for the volunteer in Fig. 1A. The changes in B_1^+ due to motion seem to be of the same order of magnitude throughout all volunteers estimating a nominal flip angle in the range of ± 10% (Figs. 2–4). However, the patterns of inhomogeneity strongly differ between volunteers mainly due to variations in head position within the transmit array after the DGE MRI protocol but also due to differences in head size. Motion during a long scan protocol, such as DGE MRI, often involves a large value in pitch due to involuntary relaxation of the neck muscles, which, even with padding, is challenging to prevent.[5] B_1^+-changes in DGE MRI may lead to different saturation efficiencies, hence it is important to know the nominal flip angle.
Conclusion: The true nominal flip angle can be corrupted by rigid head motion leading to moderate changes in the B_1^+ field. This small study gives a rough estimate of the order of magnitude of changes in B_1^+ due to motion when performing DGE MRI at 7 T. The severity of these changes depends also on how long the applied DGE MRI is, but for proper registration of uptake and minimization of side effects during injection, a scan time of a minimum of 15 min is needed.[6] To reduce the effects of B_1^+ inhomogeneity, advanced methods such as B_1^+ shimming can be applied.

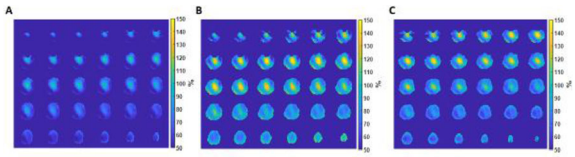

Fig. 1: B_1^+-maps of all three volunteers (A-C) before the DGE MRI throughout all slices depicting the nominal flip angle in percent.

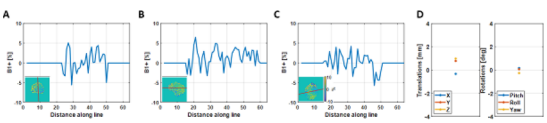

Fig. 2: Slice profiles of changes in B_1^+ caused by motion for volunteer 1 in coronal (A), sagittal (B), and transversal (C) slice direction in percent together with a corresponding map of the slice of interest. Motion estimates (D) after the DGE MRI for translations and rotations.

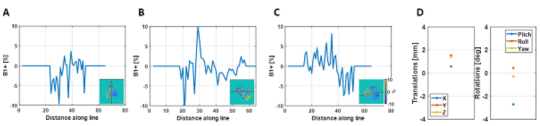

Fig. 3: Slice profiles of changes in B_1^+ caused by motion for volunteer 2 in coronal (A), sagittal (B), and transversal (C) slice direction in percent together with a corresponding map of the slice of interest. Motion estimates (D) after the DGE MRI for translations and rotations.

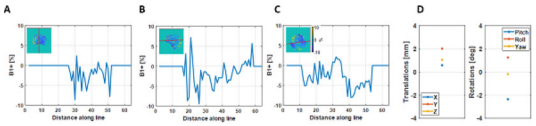

Fig. 4: Slice profiles of changes in B_1^+ caused by motion for volunteer 3 of coronal (A), sagittal (B), and transversal (C) slice direction in percent together with a corresponding map of the slice of interest. Motion estimates (D) after the DGE MRI for translations and rotations.

References:

1. Nehrke K, et al., *Magn Reson Med* 68, 1517–1526 (2012). https://doi.org/10.1002/mrm.24158

Olsson, H, et al., *Magn Reson Imag* 72, 71–77 (2020). https://doi.org/10.1016/j.mri.2020.07.002

Shamonin DP, et al., *Frontiers in Neuroinformatics* 7, 1–15 (2014). https://doi.org/10.3389/fninf.2013.00050

Klein S, et al., *IEEE Transactions on Medical Imaging* 29, 196–205 (2010). https://doi.org/10.1109/TMI.2009.2035616

Zaitsev M, et al., *JMRI* 42, 887–901 (2015). https://doi.org/10.1002/jmri.24850

Knutsson L, et al., *NMR Biomed*, 1–25 (2022). https://doi.org/10.1002/nbm.4784

P144.

In-vivo MRI-CEST imaging of extracellular tumor pH heterogeneity reveals a different invasive phenotype in two glioblastoma murine models

A. Carella[1], E. Botto[1], A. Corrado[1], E. Pirotta[1], F. Gammaraccio[2], D. Villano[2], E. Micotti[3], D. Longo[1]

[1]*Consiglio Nazionale delle Ricerche, Istituto di Biostrutture e Bioimmagini, Turin, Italy;*
[2]*Università di Torino, Dipartimento di Biotecnologie Molecolari e Scienze per la Salute, Turin, Italy;*
[3]*Istituto Ricerche Farmacologiche "Mario Negri"—IRCCS, Milan, Italy*

Introduction: Glioblastoma is the most aggressive brain tumor with a poor prognosis, despite recent advances in treatment options [1]. Despite MRI gadolinium contrast-enhanced imaging being widely utilized examination in the diagnosis, treatment selection and post-treatment management of patients with glioblastoma, more accurate imaging approaches are needed for identifying alterations of the tumor microenvironment. A salient feature of solid tumor is tumor acidosis (caused by dysregulated metabolism and reduced perfusion), that is associated to cancer aggressiveness and resistance to therapy [2]. However, few studies have investigated how tumor acidosis in glioblastoma models is associated to cancer invasiveness. In this study, we evaluated whether MRI-CEST tumor pH imaging, coupled to metabolite quantification and WB/IHC studies, can elucidate the invasiveness and metabolic alterations of two glioblastoma murine models.

Methods: We investigated two glioblastoma models (n = 10 per each model) with different invasive phenotype upon stereotaxic injection: U87 (1×10^6 U87 cells into athymic nude mice), and GL261 (2×10^5 GL261 cells into C57BL/6 mice) [3, 4]. Images were obtained with a 7 T MRI Bruker Avance NEO scanner equipped with a 1H quadrature mouse head coil with the following scans: MRI-CEST tumor pH imaging of the whole tumors was obtained following Iopamidol injection (Bracco Imaging, Milan, Italy, dose 4 g iodine / kg b.w.) with a multi-slice single-shot RARE sequence (TR/TE 11 s/ 3.7 ms 8 slices × 1.5 mm slice thickness, FOV 20 mm, MTX 128 × 128, in plane spatial resolution 0.156 mm^2 [5]); metabolites were assessed by single voxel spectroscopy (MRS) with a PRESS sequence with short (16 ms) and long TE (135 ms, for lactate quantification), VAPOR suppression, in a voxel size of 2 × 2x2mm^3. In addition, we acquired T_{1w} contrast-enhanced images (GRE sequence, TR/TE/FA: 86 ms/2.7 ms/60°, FOX: 20 mm, MTX: 128 × 128, in plane spatial resolution 0.16 mm^2) following Gd-based contrast agent injection (Prohance, Bracco Imaging, Milan, Italy dose 0.2 mmmol Gd/kg b.w.) to delineate tumor borders. Western blot and IHC analysis for LDHA, LDHB, PDK1, LAMP2 and CAIX both in cellulo and in tumor sections were performed to assess metabolism and acidosis.

Results: Both the two glioblastoma models exhibited metabolic alterations, with the U87 model showing higher lactate levels (**Fig. 1c, d**) and significant increased PDK1 expression (**Fig. 1e**), indicating a higher glycolytic-dependent phenotype compared to the less glycolytic phenotype of GL261. Moreover, the GL261 showed higher contrast enhancement suggesting increased vascularization in comparison to the U87 model (**Fig. 1f, g**). The U87 glioblastoma model showed a stronger extracellular acidification, correlated to the higher lactate levels, than the Gl261 (**Fig. 1a, b**). Of note, the GL261 tumors showed increased tumor acidosis during tumor progression and higher spatial tumor pH heterogeneity, related to a more invasive phenotype.

Conclusion: In conclusion, our study confirms that the U87 glioblastoma model has a higher glycolytic-dependent phenotype than the GL261 model, associated to a more acidic microenvironment, but the increased spatial tumor pH heterogeneity can distinguish the two different invasive phenotypes.

Acknowledgements This work was supported by grants from the Associazione Italiana Ricerca Cancro (AIRC MFAG 2017—ID 20153 project—to Dario Livio Longo).

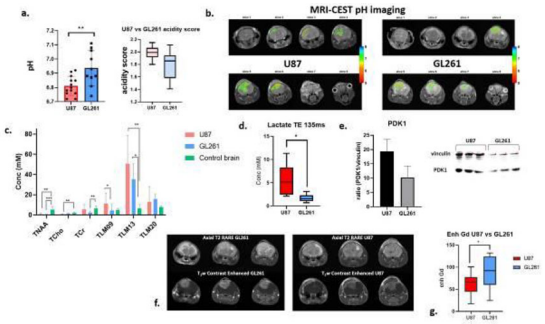

Fig. 1: a) Analysis of the extracellular pH in U87 and GL261 orthotopic glioblastoma models. **b)** Comparison of extracellular tumor pH maps on multiple slices in U87 and GL261 that allows to monitor tumor acidosis in the whole tumor. **c)** Quantification of the metabolites through single voxel spectroscopy (MRS) with 16ms TE. **d)** Evaluation of Lactate signal in U87 and GL261 orthotopic glioblastoma models, analyzed from 135ms TE. **e)** Western Blot analysis of PDK1 expression in U87 and GL261 cell lines. **f)** Comparison of axial T_2 RARE and T_{1w} CE images following Gd injection and **(g)** enhancement quantification.

References:
1. Davis ME, Glioblastoma: Overview of Disease and Treatment. Clin J Oncol Nurs. 2016 Oct 1;20(5 Suppl):S2-8.
2. Estrella V, et al. Acidity generated by the tumor microenvironment drives local invasion. Cancer Res. 2013 Mar 1;73(5):1524–35.
3. Kramp TR, Camphausen K. Combination radiotherapy in an orthotopic mouse brain tumor model. J Vis Exp. 2012 Mar 6;(61):e3397.
4. Lo Dico, A et al. 2015 "Identification of imaging biomarkers for the assessment of tumour response to different treatments in a pre-clinical glioma model" Eur J Nucl Med Mol Imaging, June;42(7):1093–1105
5. Longo DL, et al. Tumor pH Imaging Using Chemical Exchange Saturation Transfer (CEST)-MRI. Methods Mol Biol. 2023;2614:287–311.

P145.
CEST sidebands: How to generate, recognize, use or avoid them

J. R. Schüre[1], M. Sedykh[1], S. Weinmüller[1], M. S. Fabian[1], M. Zaiss[1,2,3]

[1]*Friedrich-Alexander-Universität Erlangen-Nürnberg (FAU), Department of Neuroradiology, Erlangen, Germany;*
[2]*Magnetic Resonance Center, Max-Planck-Institute for Biological Cybernetics, Tübingen, Germany;*
[3]*Friedrich-Alexander-Universität Erlangen-Nürnberg (FAU), Department Artificial Intelligence in Biomedical Engineering, Erlangen, Germany*

Introduction: CEST imaging is a molecular imaging method that allows the detection of molecules in the millimolar range. This is achieved by using selective radiofrequency (rf) irradiation[1,2,3] to obtain a saturation spectrum, the so-called Z-spectrum[4,5,6]. At clinical scanners, pulsed CEST sequences are needed to stay within amplifier and SAR limits. During off-resonant rf-pulses, as well as during the inter-pulse delay the magnetization vector and the rotating system can accumulate specific relative phases. Until now, this phase information accumulated within the pulse train was not investigated and its influence neglected. In this draft we show that these phases are important to consider and can lead to unexpected artifacts and sidebands in the Z-spectra.

Method: We investigated sidebands using an CEST 3D snapshot GRE sequence with a saturation module consisting of 36 Gaussian pulses (tp = 50 ms, td = 5 ms, duty cycle = 91%) at B1 = 2 μT over a spectral range from -4 to + 4 ppm. In this study, the influence of sampling, rf cycling, pulse shape, and gradient spoiling was analyzed. Initially, Bloch-McConnell simulations were carried out with Pulseq-CEST[7] to observe the sideband pattern with different sampling rates and B0 inhomogeneities. In addition, measurements were performed in vivo (after written informed consent) and in vitro on a 3 T PRISMA system, and compared with adapted simulations regarding B0 and B1 inhomogeneities.

Results: Sidebands can be hidden in Z-spectra and their structure becomes clearly visible only at sufficiently high sampling (Fig. 1), this means that at low sampling and B0 inhomogeneities an unpredictable influence can occur at the actual measured sampling points. The sidebands are influenced by the rf phase cycling within the pulse train (Fig. 2a-c). None of the tested phase cycles could eliminate sidebands. For the first time, we could show that with an exact implementation using Pulseq-CEST, these sidebands can be also detected in a real MRI scan in vitro (Fig. 2d-f) including the rf cycling behavior. In vivo, the sidebands are mostly visible in the liquid compartments such as CSF, but also slightly reduced in WM/GM (Fig. 3). Analysis of the B0 inhomogeneity influence revealed that Z-spectra without gradient spoiling show a complicated sideband pattern originating from the combination of off-resonance phase shifts and B0 inhomogeneity (Fig. 4a–e). This is resolved by gradient spoiling, leading to translation invariant Z-spectra again (Fig. 4f–j), as all phase information is destroyed and the pulse train response is similar to the single pulse response.

Discussion: Our results showed that in pulsed CEST imaging, sidebands are hidden in the Z-spectrum and can have unpredictable effects depending on the selected sampling and B0 inhomogeneities. However, changing the phase modulation did not suppress the sidebands, but only changed their appearance in the Z-spectrum. With a precise implementation using Pulseq-CEST, we were able to demonstrate for the first time that these sidebands could be detected in a real MRI scan as well.

We further showed that the sideband distribution is strongly dependent by B0 inhomogeneities, leading to unpredictable appearance patterns. This can affect post-processing steps such as the B0 correction or the evaluation of CEST effects, e.g. hydroxyl or amine groups.

By using spoiler gradients during the delay time between the rf pulses, the asymmetric sideband pattern could almost be eliminated and the Z-spectra are then translationally invariantly with regard to the B0 shifts. Thus, the use of spoiling in pulsed CEST experiments seems to be an important aspect to avoid possible misinterpretations of the data in liquid compartments. However, the use of spoiler gradients is only possible for pulsed CEST sequences with less than 100% duty-cycle, which is contrary to the first consensus recommendation[4].One way to further mitigate the sideband artifacts are tailored optimal control pulses[8].

A way to actually make use of sidebands could be to use them as a B0 Reference, as the sharp sideband peaks could be designed to appear in the actual offset range of interest giving insight on the B0 shift.

Conclusion: We give first detailed insights into sidebands occurring in pulsed CEST experiments, and show that similar as in imaging sequences gradient and RF spoiling play an important role. Gradient spoiled pulses trains seem to be generally indicated, to avoid misinterpretations of sidebands as CEST effects especially in liquid environments or for CEST resonance close to water.

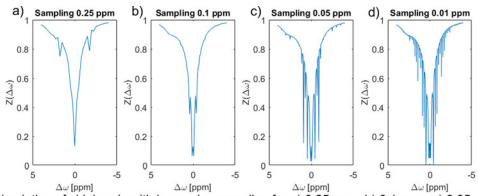

Fig. 1: Simulation of sidebands with increasing sampling for a) 0.25 ppm, b) 0.1 ppm, c) 0.05 ppm, d) 0.01 ppm. Relaxation times for the simulation are given by T1,W=1500ms, T2,W=1000ms, T1,S=1000ms, T2,S=100ms

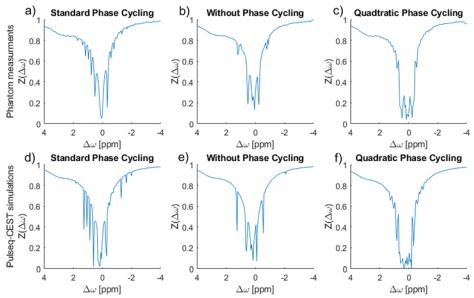

Fig. 2: Comparison of the CEST sequence with a sampling rate of 0.05 ppm in vitro for different phase cycle methods (a,b,c) and the adapted simulations with Pulseq-CEST (d,e,f)

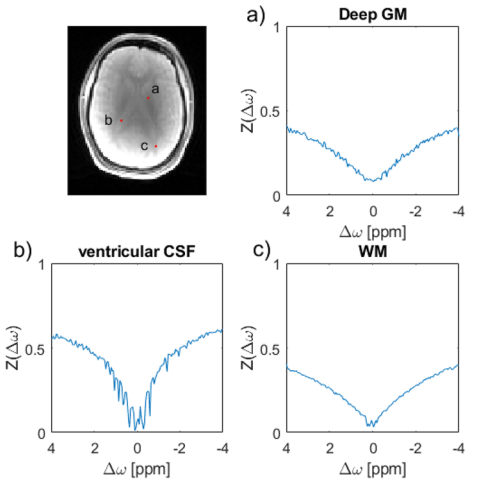

Fig. 3: Single voxel Z-spectra show the appearance of sidebands in vivo, particularly in the CSF, but also in the deep gray matter (GM) and white matter (WM), although in a markedly reduced form

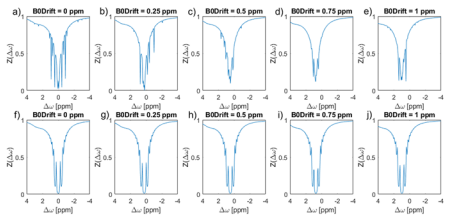

Fig. 4: Simulation of the described CEST sequence with a sampling rate of 0.05 ppm and an increasing B0 shift from 0.25 ppm to 1 ppm without (a-e) and with gradient spoiling between the RF pulses (f-j). Z-spectra without gradient spoiling show an asymmetric contamination due to the occurring sideband patterns, while the use of gradient spoilers leads to a translation invariant shift of the Z spectrum

References:

1 Ward KM, et al.,*J Magn Reson*. 2000;143(1):79–87.
2 Zaiss M, et al.,*NMR Biomed*. 2022;35(11):e4789.
3 Zaiss M, Bachert P.,*Phys Med Biol*. 2013;58(22):R221-269.
4 Zhou J, et al., *Magn Reson Med*. 2022;88(2):546–574.
5 Shah SM, et al., *Neuroimage*. 2018;167:31–40.
6 Goerke S, et al., *NMR Biomed*. 2018;31(6):e3920.
7 Herz K, et al., *Magn Reson Med*. 2021;86(4):1845–1858.
8 Stilianu C, et al.,ISMRM 2023.

P146.
Histological validation of tumour microenvironment acidosis imaging using Iopamidol-based MRI-CEST on three mouse models of human tumors

R. Maniyani[1], T. Mangeat[2], B. Robert[2], D. Longo[3], H. Lahrech[1]

[1]*University Grenoble Alpes, Grenoble, France;*
[2]*IRCM INSERM U1194, Montpellier, France;*
[3]*Institute of Biostructures and Bioimaging (IBB), Turin, Italy*

Introduction: In tumour microenvironment, acidosis is linked to the Warburg effect[1] and recognized as one of main pathological driver that influences cancer cells by increasing their resistance to apoptosis, genomic instability and their local invasive growth. To date, no acidosis imaging has been rigorously validated in clinic. MRI-CEST (Chemical Exchange Saturation Transfer magnetic resonance imaging) upon Iopamidol injection is a promising imaging technique for mapping the extracellular pH (pHe) in cancer tissues[2] that has been applied to investigate tumor acidosis as a promising biomarker to characterize tumor microenvironment and response to therapies[3].
Despite its success as an imaging tool for tumor pH mapping at very high fields (7 T), its translation at lower fields remain under-investigated. In this study, we explored tumor pH mapping in three different mouse models of human cancers at 4.7 T and validated this method by using immunohistochemistry (IHC).
Methods Mouse models: Three human cancer cell lines were used: CFPAC-1 from pancreas (n = 4); H1299 from lymph node metastatic site of lung (n = 4) and MDA-MB-231 from metastatic site of breast/mammary gland (n = 6). Tumour cells were implemented subcutaneously in one or in both mouse legs.
MRI was performed at 4.7 T (Bruker magnet with 20 cm diameter, maximum gradient intensity: 660 mT/m). The radiofrequency (RF) system was composed with a quadrature coil for emission and a surface coil for reception. A multiparametric MRI protocol including T2w, T2w*, T1w sequences was applied before and after Iopamidol injection (dose: 4 g I/kg b.w.), followed 30 min later by Gd-DOTA injection (Fig. 1).
T2W MRI (TR/TE = 36/2200 ms, matrix size: 256 × 256, FOV: 35 × 35 mm^2, 19 slices of 1 mm thickness) was used to select the tumour slice position for CEST MRI. T2w* was exploited to define Iopamidol biodistribution which was compared to that obtained from T1w Gd-DOTA contrast enhanced images.
For CEST sequence, a RF pulse of 1.5 μT and 5 s (saturation pulse) was applied at several frequencies (fsat) followed by a single-shot centric-encoding T2w sequence (TE = 36 ms, TR = 2200 ms, size matrix: 64 × 64). Values of fsat were varying between -15 and 15 ppm, where 0 ppm corresponds to the bulk water resonance. In vitro Iopamidol Z-spectra on PBS solutions titrated at several pH values were acquired. Ratiometric values (from 4.2 and 5.5 ppm) versus pH were used to convert in vivo ratiometric values to pH unit. Both are illustrated in (Fig. 2).
Data analysis: Images were analysed using a made home MATLAB software. CEST pH maps were obtained by analysing Z-spectra pixelwise after B0 inhomogeneity correction. Z-spectra were fitted by a Lorentzian model with five pools. Ratiometric (RST) values were calculated according to References[2–4]
Chemical agent biodistribution were evaluated by calculating R2* signal variation.

Immunohistochemistry (IHC): At the end of MRI, tumours were removed and immediately frozen for IHC analysis, by Ki-67 and NHE-1. Ki-67 is a marker of cell tumour proliferation and NHE-1 is a sodium-hydrogen exchanger marker related to the pHe. For each IHC marker, area of staining was quantified in at least three tumour slides.
Results and discussion: For all tumours, Iopamidol R2w* signal variation was found correlated to that from R1-Gd-Dota confirming that biodistribution of the both agents are similar.
For the three cancer models, two groups G1 and G2 were defined on the basis of pHe versus Ki-67 expression (Fig. 3a). According to our previous work[4], pHe should be more acidic (low values) when Ki-67 expression increases. G1 includes all tumours that satisfy this criteria (Pearson correlation = − 0.88) and G2 those does not satisfy it (outlined by red circle) that are characterized by high pHe heterogeneity (high standard deviation) as seen in Fig. 3b.
In G1, and as expected, a tumor pHe decrease was found correlated to IHC NHE-1 expression increase (Fig. 4a). pHe heterogeneity of G2 was assessed by analysing small ROIs defined in T2W: high pHe values were found linked to edema (pH around 7) and low values to viable tumour cells (pHe around 6.3) (Fig. 4d) and were found in line with IHC data.
Conclusion: MRI-CEST tumor pHe was found correlated to IHC data and being one main validation endpoints. This preclinical study confirms the high potential of Iopamidol MRI-CEST for tumor pHe mapping that could be used in clinical investigations.

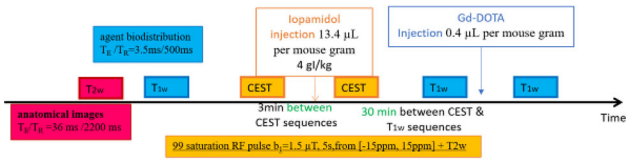

Fig. 1: Scheme of MRI protocol.

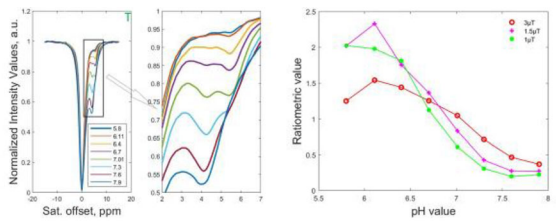

Fig. 2: in vitro Z-spectra of Iopamidol in PBS solutions titrated at several pH and the corresponding calculated ratiometric curves. For our study b1 was selected equal to 1.5 µT.

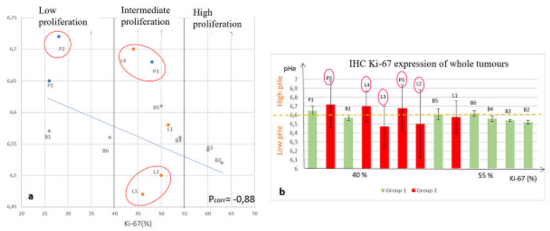

Fig. 3: a: pHe of the whole tumour versus Ki-67 of breast (B), lung (L) and Pancreas (P) cancers. Data of G2 are outlined by red circle: two from pancreas: P2, P3 and three from lung: L2, L3, L4. **b:** pHe histogram of the two groups showing high pHe heterogeneity in G2 as quantified by standard deviation.

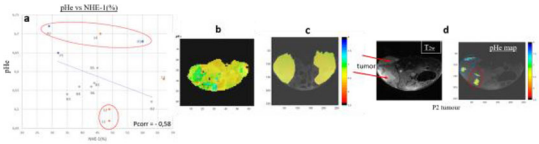

Fig. 4: a: pHe versus NHE-1. Data of G2 are outlined in red and correspond to those in Figure3. **b**: typical example of heterogeneous pHe map (pancreas tumour P2). **c:** typical homogeneous pHe map (two breast cancers B1 and B2). **d**: pHe maps of small ROIs in edema and in viable tumours showing a pHe around 7 and 6.3, respectively.

References:

1. Warburg O Science. **68**, 437-843 (1928)
2. Longo DL, Sun PZ, Consolino L, Michelotti FC, Uggeri F, Aime S. J Am Chem Soc.;136(41):14333-6 (2014)
3. Longo DL, Bartoli A, Consolino L, Bardini P, Arena F, Schwaiger M, Aime S. Cancer Res;76(22):6463-6470. (2016)
4. Ferrauto G, Di Gregorio E, Auboiroux V, Petit M, Berger F, Aime S, Lahrech H. NMR Biomed. 31(11):e4005. (2018)

P147.
Lorentzian model based reconstruction for CEST-MRI

M. Huemer[1], C. Stilianu[1], R. Stollberger[1,2]

[1]*TU Graz, Institute of Biomedical Imaging, Graz, Austria;*
[2]*BioTechMed, Graz, Austria*

Introduction: CEST MRI is a powerful image modality that allows for the detection of small metabolite concentration, which would be difficult to detect using traditional methods. The limitations of CEST imaging lay mainly in the trade-off between acquisition time and SNR, as CEST images typically suffer from poor SNR and a number of images have to be measured for a complete CEST Spectrum. Here we present a model based reconstruction technique that directly fits the commonly used Lorentzian lineshapes to undersampled k-space data [1]. The reconstruction is regularized by joint spatial total generalized variation (TGVj) [2]. In this way, a comparable result to the fully sampled results can be achieved using reduced data and therefore opening the possibility to shorten the measurement time.
Methods: In this work two different data-set were investigated: First, a numerical brain phantom with an artificial tumor and five separate

tissues each with five components. The spectra for the phantom were simulated in an in-house Bloch-McConnell simulation.

The second dataset was acquired by constructing a MnCL2 doped water phantom containing falcon tubes with changing concentrations of Nicotinamide and Creatine and scanning this phantom on a 3 T Scanner (Siemens Healthcare GmbH, Erlangen, Germany).

Three different methods were compared. The Reference fit, which consisted of a pixel wise (PW) fit using MATLABs lsqcurvefit function in image space without undersampling.

For the other two methods both datasets were retroactively undersampled using an incoherent pattern shifting the undersampling mask for each image. The center four k-space line was kept for all images and every forth line in the shifting pattern. Then a Reference reconstruction using BART pics and l1-wavelet regularization was performed, followed by the pixel wise fit in MATLAB.

Finally, the model-based fit with multiple Lorentzian lineshapes, using joint spatial total generalized variation, was implemented in PyQMRI [4]. The non-linear problem was solved by employing the iteratively regularized Gauss-Newton (IRGN) method combined with a primal-dual splitting algorithm [2].

Results: Fig. 1. shows the results for the numerical brain phantom. In particular the amplitude maps of the Amide, Amine, rNOE and ssMT pools are displayed. The first column shows the pixel wise fit results, which shows visible noise in the Amide and especially the Amine amplitudes. In the second column the results for the pixel wise fit after reconstruction are shown. For this method the Amine and Amide maps show strong noise. In the Amine amplitude the different tissues are not distinguishable. The last column shows the model based reconstruction, which shows similar results to the PW fit with some bias especially in the Amine map.

In Fig. 2. the results for the phantom measurements are displayed. Again, the pixel wise fit shows a high amount off noise especially in the water only background of the phantom.

The second method results high noise levels especially for the Amine amplitude map. The proposed method reconstructs the parameter maps with minimal added artifacts and comparable SNR. For the Amide maps the edges of the tubes show some inconsistencies.

Fig. 3. shows the undersampled k-space of the measured phantom dataset. The incoherent nature of the undersampling can be observed. In each image different k-space lines are retained.

Discussion: For both the numerical and measured phantom data, the reconstruction followed by the fit fails to produce usable images, with substantial biases and noise introduced in some parameter maps, due to the reduced SNR from undersampling. The proposed reconstruction achieves acceptable result for all maps, due to the strong prior information available through the Lorentzian lineshape approximation of the Z-Spectrum. The proposed method even exceeds the fully sampled pixel wise fit in parameter maps SNR for some parameters such as the Amine map in Fig. 2.

Conclusion: In this work we proposed a model based reconstruction for multipool Lorentzian fitting. The added prior information of the model based reconstruction combined with the spatial TGV regularization makes this method produce reasonable results for data-sets with noise and cartesian undersampling, where the standard approach of reconstructing the images and applying a pixel wise fit fails. This opens up a range of possibilities for speeding up the acquisition of CEST datasets.

Acknowledgements

This work was funded by the FWF-I4870.

The authors thank Moritz Blumenthal, Daniel Mackner, Philip Schaten and Nick Scholand for their help with the Reference reconstruction in BART.

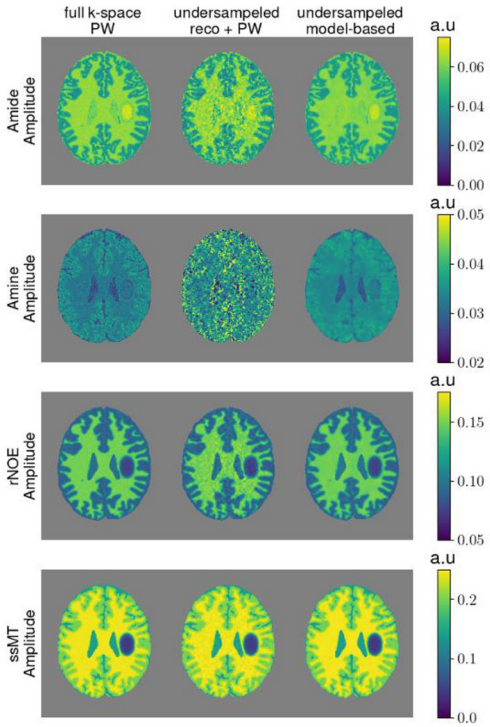

Fig. 1: Selected parameter maps of the amplitudes of the four pools for the numerical phantom. First column shows the fully sampled pixel wise fit. In the second column the standard reconstruction followed by the pixel wise fit and finally the results for the model based reconstruction.

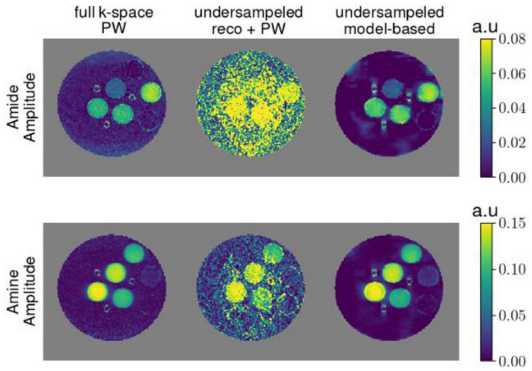

Fig. 2: Selected parameter maps of the amplitudes of the two pools for the measured phantom for all three methods. For the Amine map the model based reconstruction even exceed the fully sampled pixel wise fit.

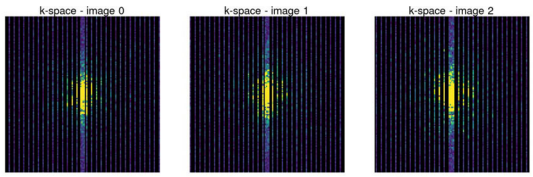

Fig. 3: Representation of the k-pace data of the first three images showing the shifting undersampling pattern.

References:

1. Zaiss, M. et al. *Magn. Reson. Med.* 211(2) (2011)
2. Maier, O. Proceedings 30. Annual Meeting ISMRM 2079 (2022)
3. BART, https://doi.org/10.5281/zenodo.592960
4. Maier, O. et al. *J. Open Source Softw.* 5, 2727 (2020).

P148.

A novel method for multipool Lorentzian line-shape fitting of CEST MRI spectra to improve accuracy in quantification of lactate and glucose contributions

C. Lippe[1], D. Schache[1], V. Hoerr[1,2]

[1]*University of Münster, Clinic of Radiology, Münster, Germany;*
[2]*University Hospital Bonn, Heart Center Bonn, Department of Internal Medicine II, Bonn, Germany*

Introduction: Chemical exchange saturation transfer (CEST) MRI enables the measurement of low concentrated metabolites that contain exchangeable protons. This is achieved with enhanced sensitivity through indirect water saturation.

To distinguish the contributions from individual metabolites in the acquired Z-spectrum, multipool Lorentzian fitting is commonly employed as individual peaks obtain an approximate Lorentzian line-shape [1]. However, this technique becomes high-dimensional and multimodal for large pool sizes, which can lead to instability of optimization algorithms. Therefore, appropriate boundary conditions and initial values have to be set to restrict model parameters [2], requiring prior knowledge or additional measurements. Furthermore, another problem arises from peak interference, which leads to insufficient separation of Z-spectrum contributions using multipool fitting.

Here, we propose a novel fitting approach based on particle swarm optimization (PSO) that naturally incorporates boundary conditions. This approach is combined with derivative spectroscopy, which has been shown to improve the separation of strongly interfering spectral peaks [3]. We demonstrate the effectiveness of our technique in separating individual metabolites in Z-spectra using mixed glucose/lactate phantoms as the differentiation and quantification of these two metabolites are crucial for the diagnosis of various pathologies [4].

Methods: Glucose and lactate were dissolved in sterile water at three different concentrations each (5 mM, 15 mM, 30 mM) resulting in nine concentration pairs. Measurements were performed on a 9.4 T small animal Bruker Biospec MR system equipped with a 72 mm quadrature coil using a CEST EPI sequence (4 s saturation, B1 = 1.6 μT). The pH was maintained between 6.5-7.0 and the temperature was kept at 20 °C. Z-spectra were B0-corrected using spline interpolation and fitted with a 6-pool Lorentzian model of peaks L(x) using a PSO implementation to minimize the sum of squared residuals:

$$L(x) = \sum_i a_i/(1 + 4 * ((x - b_i)/c_i)^2$$

Boundaries of peak positions b_i were chosen with a minimal margin (± 0.05 ppm) around literature values [5,6], while peak amplitudes a_i were only loosely restricted to the range of (− 0.6, 0) and widths c_i to a range of (0.3 ppm, 0.6 ppm). All computations were performed using Python.

Additionally, the PSO regression function was modified to minimize the sum of squared residuals of both the original Z-spectra and their respective first derivative, which was numerically obtained using central difference. For quantification, the area under curve (AUC) was calculated for each Lorentzian function.

Results: Figure 1 illustrates the 6-pool PSO fit results for the 30 mM glucose/30 mM lactate phantoms using (A) the standard sum of squared residuals regression function and (B) an additional regression term to fit the first derivative. The global fit quality slightly decreased when the derivative fitting was included, as the sum of squared residuals increased from 0.00035(8) to 0.032(4) on average. However, the linear correlation between glucose concentration and AUC quantification improved significantly, as the R^2 increased from 0.902 to 0.986 (Fig. 2). Figure 3 depicts similar improvements in lactate quantification, although the R^2 values were generally lower (0.687 for standard fitting vs 0.876 for simultaneous derivative fitting).

Discussion: The proposed fitting approach using PSO in combination with derivative spectroscopy demonstrated improved accuracy in quantifying lactate and glucose contributions in Z-spectra. Inclusion of the first derivative term in the regression function resulted in better separation of strongly overlapping peaks, as evidenced by the improved linearity between metabolic concentration and AUC (Figs. 2, 3).

The decrease in global fit quality (Fig. 1) could be explained by noise amplification caused by numerical differentiation. However, the benefits of enhanced peak separation and reduced peak interference clearly outweighed this drawback.

The generally lower R^2 values in lactate quantification might result from spillover effects caused by direct water saturation [1], as the lactate resonance frequency is very close to water. This issue will be addressed in future studies to further improve metabolite quantification.

Conclusion: In conclusion, we presented a novel multipool Lorentzian line-shape fitting method for Z-spectra based on PSO and derivative spectroscopy which successfully improves the accuracy of lactate and glucose quantification in mixed phantoms. This method shows great promise for enhancing CEST MRI data analysis and the characterization of metabolic processes in vivo.

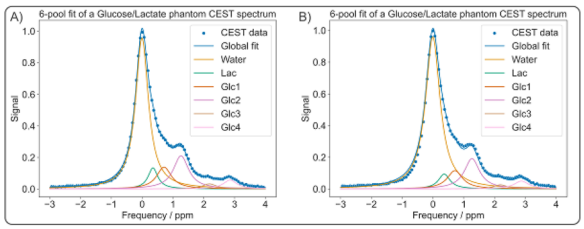

Fig. 1: Results of the 6-pool fit for 30 mM glucose / 30 mM lactate phantoms using A) standard sum of squared residuals regression function and B) additional regression term to fit the first derivative. Global fit quality slightly decreased when derivative fitting was included.

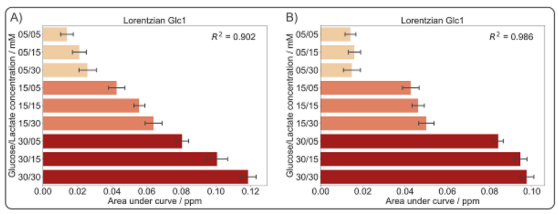

Fig. 2: AUC of the first glucose peak (at 0.66 ppm [5]) for different concentration combinations A) without derivative fitting and B) including derivative fitting, along with corresponding R^2 values. Identical hues of red represent identical glucose concentrations. R^2 improved from 0.902 to 0.986 when the derivative was utilized.

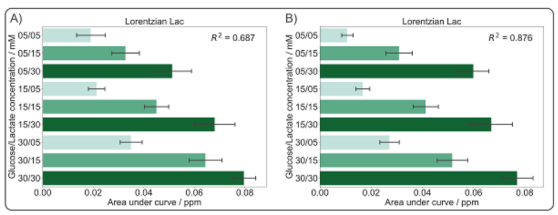

Fig. 3: AUC of the lactate peak (at 0.4 ppm [6]) for different concentration combinations A) without derivative fitting and B) including derivative fitting along with corresponding R^2 values. Identical hues of green represent identical lactate concentrations. R^2 improved from 0.687 to 0.876 when the derivative was utilized.

References:
[1] Zaiss M et al. (2013), PMID: 24201125
[2] Wittsack H et al. (2023), PMID: 36961580
[3] Karpińska J (2004), PMID: 18969675
[4] Li X et al. (2022), PMID: 36050306
[5] Zaiss M et al. (2019), PMID: 31313865
[6] DeBrosse et al. (2016), PMID: 26794265

P149.
31P MR spectroscopy as a predictor of liver transplantation survival

M. Dezortová[1], P. Sedivy[1], D. Pajuelo[1], M. Burian[1], D. Kyselova[2], P. Trunecka[2], M. Hajek[1]

[1]*Institute for Clinical and Experimental Medicine, MR-Unit, Dept. Diagnostic and Interventional Radiology, Prague, Czech Republic;* [2]*Institute for Clinical and Experimental Medicine, Dept. Hepatogastroenterology, Prague, Czech Republic*

Introduction: Skeletal muscle changes, especially the presence of sarcopenia and myosteatosis, have a significant impact on the mortality, morbidity, and quality of life of patients with liver cirrhosis. However, there is inconsistency and even contradiction in the literature regarding their effect on the prognosis of patients following liver transplantation (LT). The objective of this study was to describe the metabolic state of the calf muscles using 31P MR spectroscopy before and after LT and to evaluate the degree of its influence on the course of transplantation. Additionally, the study aimed to analyze the long-term survival of patients following LT.

Methods: A total of 134 liver transplant (LT) candidates were examined of which 105 (60f/45 m) underwent cadaver LT (mean age 57.6 ± 10.0 years at the time of LT). Data on MR spectroscopy results along with clinical and laboratory tests were obtained before, 6, 12 and 24 months after the LT. Long-term patient survival was assessed with a median follow-up of 6 years. All subjects provided written informed consent with the participation in the study, the experimental protocol was approved by the local ethics committee.

MR examinations were performed using a 3 T MR system TRIO (Siemens, Germany) with a dual-channel 1H/31P surface coil (Rapid Biomedical, Germany) in a supine position with the coil fixed underneath the calf. The positioning of the coil was verified using a standard localizer sequence. 31P MR spectra were acquired by the non-localized FID sequence (most of the 31P MR signal from m. gastrocnemius and soleus) at rest with the following parameters: echo time (TE*) = 0.4 ms, repetition time 15 s, 16 acquisitions, matrix size 1024, total acquisition time 4 min. Magnetic field homogeneity was optimized manually by the localized shimming of the water signal.

31P MR spectra were analyzed by AMARES in the jMRUI 5.0 software package (http://www.jmrui.eu/). Lorentzian line shapes were applied for fitting the following singlets: phosphocreatine (PCr), inorganic phosphate (Pi), and phosphodiesters signals. The adenosine triphosphate (ATP) peaks were fitted as two doublets and a triplet. The relative chemical shift of Pi and PCr was used to calculate the intramyocellular pH according to the equation: $pH = 6.75 + \log[(\delta - 3.27)/(5.63 - \delta)]$.

We used two parameters for discriminating impaired muscle metabolism: $\beta ATP/P_{tot}$ (where P_{tot} is a sum of all 31P signals in the spectrum) and intramyocellular pH at rest.a) The cut-off value for $\beta ATP/P_{tot}$ was < 0.074, and it was used as a representative of the energy state of the muscle cell.b) The cut-off value for intramyocellular pH was > 7.045, and it was used as an indicator of overall muscle cell homeostasis.

The specific cut-off values for ATP decrease and pH were chosen based on previously published results on elderly healthy controls (mean age 65 ± 9 years) [1] who underwent the same examination protocol. The cut-off values were calculated using the mean and standard deviation of ATP/P_{tot} and pH.

Results: The patients who showed pathological changes in their 31P MR spectra and pH had significantly worse long-term survival ($p = 0.0021$, hazard ratio 3.4, 95% confidence interval 1.5-7.6), as depicted in Fig. 1. Additionally, they experienced greater blood loss during LT ($p = 0.038$), longer hospitalization periods in both the intensive care unit ($p = 0.041$) and overall ($p = 0.007$), and required a higher number of red blood cell transfusions during LT ($p = 0.006$). Figure 2 illustrates the development of calf muscle metabolism, demonstrating a gradual improvement in energy turnover indicated by MRS parameters after LT.

Discussion: Although there are several factors that can impact the quality and length of survival of transplant patients, the ATP and pH values obtained from rest 31P MR spectra in the calf muscle seem to be adequate biomarkers for predicting survival.

The cut-off values used in our study were defined from elderly controls [1], although it is worth noting that their energy metabolism may already indicate mild sarcopenia. Nonetheless, using elderly controls better matches the age of our patients and involves the age-related changes in muscle metabolism.

Conclusion: The patient's physical condition prior to LT is a critical factor in their posttransplant recovery and should be closely monitored and improved. Our study found that abnormal values of calf muscle metabolism, as determined by resting 31P MR spectroscopy, were highly predictive of both peritransplantation complications and long-term survival after the transplant. Therefore, careful monitoring of calf muscle metabolism using 31P MR spectroscopy could be a useful tool in assessing a patient's suitability for LT and predicting their prognosis post-transplant.

Supported by the Ministry of Health of the Czech Republic – DRO ("Institute for Clinical and Experimental Medicine – IKEM, IN 00023001").

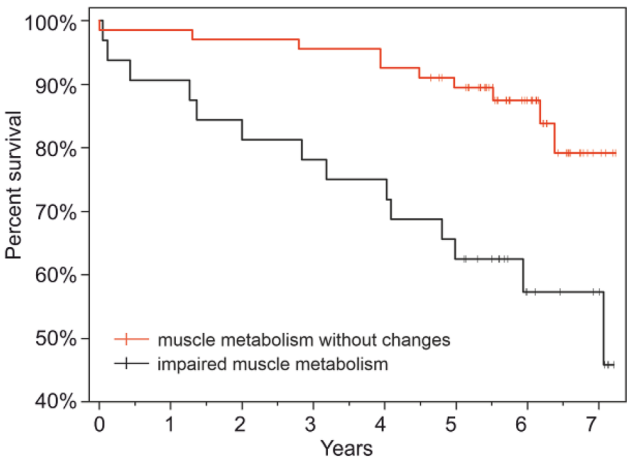

Fig. 1: Kaplan-Meier survival curves of patients with healthy and impaired muscle metabolism.

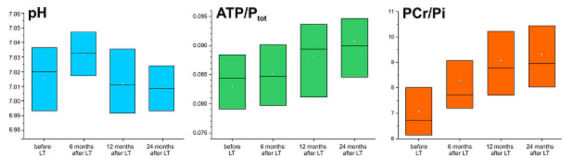

Fig. 2: Development of the muscle metabolism before and after the liver transplantation (6m, 12m, 24m). Boxplots show medians with Q1 and Q3, white squares indicate mean values in the groups.

Reference:
[1] Sedivy P, et al. Int Angiol 2018;37(4):293-9.

P150.
Progress towards high sensitivity localized ^{13}C MRS of human brain glycogen at 7 T: The role of T_1 and T_2 relaxation times

E. Serés Roig[1]

[1]*École Polytechnique Fédérale de Lausanne (EPFL), Laboratory of Functional and Metabolic Imaging (LIFMET), Lausanne, Switzerland*

Introduction: Localized carbon-13 magnetic resonance spectroscopy (^{13}C MRS) allows the non-invasive detection of human brain glycogen in vivo, which, due to the low concentration of glycogen in the brain, is typically done via ^{13}C-glucose intravenous infusion labelled at the C_1-carbon to enhance the ^{13}C sensitivity while giving rise to three C_1-resonances: glycogen, glucose-β, and glucose-α [1, 2]. To further improve both ^{13}C sensitivity and spectral resolution, we have recently explored the potential of ^{13}C MRS at 7 T in conjunction with broadband ^{1}H decoupling, resulting in an improved separation of the glycogen, glucose-β, and glucose-α C_1-resonances [3], compared to 4 T [1, 2]. In addition, we have found disparities between ^{13}C sensitivities of the glycogen and glucose C_1-resonances upon applying broadband ^{1}H-decoupling during ^{13}C acquisition [3]. The aim of this study was thus to evaluate the relation between these ^{13}C sensitivity disparities and the MR properties of the glycogen and glucose C_1-resonances at 7 T.

Methods: In vitro ^{1}H-decoupled ^{13}C MRS measurements of glycogen and glucose C_1-resonances were performed on a 7 T human scanner (Siemens Erlangen/Germany) using a home-built ^{13}C-linear/^{1}H-quadrature RF surface coil [4]. A pulse-acquire sequence for localized ^{13}C MRS using broadband ^{1}H-decoupling during ^{13}C signal acquisition was developed using the WALTZ-16 scheme [5] (Fig. 1). All in vitro measurements were performed using a two-compartment phantom containing (1) 800 mM natural abundance of glycogen and (2) 8 mM of glucose-C_1 labelled, while all spectra were acquired using uniform adiabatic ^{13}C-excitation (2 ms) [6] by placing the carrier frequency at the glucose-β resonance (96.6 ppm). The performance of the ^{1}H-decoupling scheme was investigated by increasing successively the number of WALTZ cycles from 1 to 8 (i.e., 4 WALTZ cycles corresponds to the WALTZ-16 scheme), while adjusting in each case the decoupling duration accordingly to the FID ($\sim$ 96 ms). Of particular interest to the present study, the spin-lattice (^{13}C-T_1) and spin-spin (^{13}C-T_2) relaxations times of glycogen and glucose C_1-resonances were measured in vitro at 7 T using optimized adiabatic inversion recovery and Hahn spin-echo [7] sequences, over a range of inversion times (TI) and echo times (TE), respectively. T_1 and T_2 were determined using three and two parameter fitting, respectively.

Results and discussion: By successively increasing the number of WALTZ cycles, the ^{13}C signal intensities of glucose-β and glucose-α increased or decreased depending on whether an odd (^{1}H spin down) or an even (^{1}H spin up) number of WALTZ cycles was applied, respectively, while this effect was not observed for glycogen in which the ^{13}C signal intensity remained fairly constant (Fig. 2A, B). The slight decrease of the glucose-β slope (Fig. 2B) could be attributed either to the presence of sidebands (Fig. 2A bottom/ ocher-arrows) and/or to the proximity of glucose-β ^{1}H-resonance to that of water (Fig. 2 C). Besides, the ^{13}C-T_1 and ^{13}C-T_2 of glycogen C_1 in vitro (Fig. 3B, C) were found in close agreement with what is expected at 7 T compared to 8.5 T [8], while the small difference of T_2 compared with [8] may be due to a difference in temperature. The ^{13}C-T_1 of glucose-α and glucose-β in vitro were found to be rather similar to each other (Fig. 3B), while their ^{13}C-T_2 were slightly disparate (Fig. 3C). The long ^{13}C-T_1 of glucose-α and glucose-β compared to that of glycogen C_1 may explain the ^{13}C sensitivity disparities of the glycogen and glucose C_1-resonances upon applying broadband ^{1}H-decoupling during ^{13}C acquisition. A residual saturation of the ^{1}H spin of glucose upon its rotations during ^{13}C acquisition may cause the ^{13}C sensitivity enhancement or NOE of glucose. Because of the faster molecular motion of glucose compared to glycogen, dipolar interaction between the ^{1}H spin and the ^{13}C spin becomes the main source of ^{13}C-T_1 relaxation, inducing cross-relaxation between energy states, and thereby enhancing the ^{13}C sensitivity of glucose, when its ^{1}H spin is saturated. The ^{13}C-T_2 of glucose being longer than that of glycogen determines the overall ^{1}H-decoupling duration, while the use of 3 versus 4 WALTZ cycles may be advantageous in terms of optimal ^{13}C sensitivity and low ^{1}H-power towards measuring human brain glycogen in vivo at 7 T.

Conclusion: An increased ^{13}C sensitivity or NOE of glucose occurs upon applying broadband ^{1}H decoupling, when the ^{1}H spin ends up "down", while this effect was not observed for glycogen. The long ^{13}C-T_1 of glucose compared to that of glycogen may explain such disparities.

Fig. 1: Pulse-acquire sequence for ^{1}H-decoupled localized ^{13}C MRS at 7T using the WALTZ-16 scheme. Each WALTZ cycle (Q) performs an inversion of the ^{1}H-spin, the latter resulting oriented down or up depending on whether an odd or an even number of WALTZ cycles is applied, respectively.

Fig. 2: (A) ^{13}C MR spectra of glycogen and glucose C_1 *in vitro* at 7T. From left to right, ^{1}H decoupling was applied by increasing successively the number of WALTZ cycles while adjusting the decoupling duration accordingly to the FID. (B) Normalized ^{13}C signal intensities of spectra from (A)). (C) Diagram illustrating the ^{1}H chemical shift of glycogen and glucose H_1 resonances, and water.

Fig. 3: (A) ^{1}H-decoupled ^{13}C MR spectrum of glycogen and glucose C_1 *in vitro* at 7T. Inversion recovery (B) and Hahn spin echo (C) fitting curves of ^{13}C signal intensities of glycogen and glucose C_1-resonances from spectra acquired *in vitro* at 7T over a range of inversion times (TI) and echo times (TE), respectively.

References:
1. Gruetter R. JNR. 2003;74(2):179-83
2. Oz G. NInt. 2003;43:323-9
3. Serés Roig E. ESMRMB 2020
4. Serés Roig E. MRM. 2015;73:894–900
5. Shaka AJ. JMR. 1983;52:335-338
6. Serés Roig E. NMR Biomed. 2019;32(12): e4171
7. Hahn EL. Phys. Rev. 1950;80,580
8. Sillerud LO. Bioch. 1983;22,1087-1094

P151.
Tracking of immune cells using ^{19}F MR imaging in a murine model of pancreatic cancer under immune therapy

W. Reichardt[1], T. Gewalt[1], P. Haffner[2], S. Keller[2], H. Jumaa[2], C. Xun[2], A. Alrawashdeh[2], D. von Elverfeldt[1], Y. Li[1], D. A. Ruess[2]

[1]*University of Freiburg, Department of Diagnostic and Interventional Radiology, Medical Physics, University Medical Center, Freiburg, Germany;*
[2]*University of Freiburg, Klinik für Allgmein- und Viszeralchirurgie, Freiburg, Germany*

Introduction: Targeting the major oncogenic driver mutant *KRAS* and its related pathways has shown promise as a treatment option for pancreatic cancer, and in addition might sensitize recalcitrant pancreatic cancer to immunotherapies. In this context, in vivo monitoring of therapeutic response and migratory pattern of immune cells remains a challenge. ^{19}F magnetic resonance imaging (19F MRI) has emerged as a powerful tool for noninvasive longitudinal imaging of immune cells in vivo [1] in oncologic mouse models [2]. In this study, we investigated the potential of ^{19}F MRI to monitor immunomodulatory effects of dual SHP2/MEK inhibition in a genetic mouse model of pancreatic cancer.

Methods: We used the LSL-KrasG12D/ + ;Trp53fl/fl; Ptf1a-Cre (KPC) model. In this model, Cre-mediated recombination results in expression of mutant Kras and homozygous deletion of the tumor suppressor Trp53 specifically in the pancreas, which leads to the development of PDAC already at early age (5 to 8 weeks) and involves a strong and characteristic inflammatory tumor microenvironment. Mice were screened with MRI and randomly assigned to different treatment groups (n = 4 × 5), when a tumor was detectable. Mice were treated with a combination of SHP2 and MEK, a single therapy with SHP2 or MEK and a control group, treated with vehicle only. To label the immune cells internally with perfluorocarbon (PFC) emulsion, we injected the formerly commercially available perfluorocarbon (PFC) emulsion V-Sense DM-Green (Celsense) according to the manufacturer's recommendations 24 h before initiation of treatment. MRI experiments were performed on a Bruker 9.4 T Biospec system imaging (Bruker, Ettlingen, Germany) using two separate mouse volume quadrature-resonators (Bruker, Ettlingen, Germany) with identical geometry. One coil was optimized for ^{1}H, the other for ^{19}F imaging. MRI was performed at serial time points (24 h after injection of the nanoemulsion, 1 week and 2 weeks later). A Reference tube (100 µl V-sense CA + 400-µl saline) was included in each scan. The.^{1}H imaging protocol consisted of a localizer and a T2-RARE sequence (TR/TE = 2500/23 ms, FOV 28 mm × 28 mm × 1 mm, mtx: 280 × 280, 30 slices). We recorded the exact geometry of the 1H imaging, exchanged the coils and transferred the geometry to the 19F imaging protocol which consisted of a localizer and a T2 Rare sequence (TR/TE = 3200/76 ms, FOV: 28 mm × 28 mm × 3 mm, mtx: 56 × 56, 10 slices, bandwidth 20 kHz, acquisition time 19 min 24 s). Both sequences were chosen to provide morphological information about the tumor model and the migration of phagocytic cells such as Macrophages and Dendritic Cells (DCs) (Fig. 1)

Results: Tumor volumetry showed a decreased volume in all of the treated groups, most prominently in the group treated with the combination of SHP2 and MEK (Fig. 2A). 19F MRI detected an increased accumulation of labeled immune cells in the tumor in the treated groups, again most pronounced in the group treated with the combination of SHP2 and MEK (Fig. 2B). We further investigated the spatial distribution of labeled immune cells within the tumors using high-resolution 19F MRI, however we could not observe a consistent distribution pattern of the labeled immune cells. Finally, we validated the ^{19}F MRI results using flow cytometry and immunohistochemistry and observed a significant increase in the number of phagocytic immune cells in the tumors of mice in the treated groups.

Discussion: In addition to tumor volumetry, we could show that it is possible to track immune cells in the KPC genetic mouse model for pancreatic cancer using 19F MR imaging. We were able to detect and quantify the migratory patterns and the dynamics of the trafficking of immune cells to the tumor microenvironment. ^{19}F MRI provides high spatial resolution and does not require ionizing radiation or contrast agents that could potentially harm the subject. However, the signal intensity of PFC-labeled immune cells may decrease over time due to cell division or clearance by the immune system.

Conclusion: Our results demonstrate the potential of 19F MRI as a noninvasive imaging modality to monitor immunotherapy response in pancreatic cancer. 19F MRI can provide valuable information on the spatial distribution of immune cells within the tumor microenvironment and can serve as a biomarker for predicting response to immunotherapy.

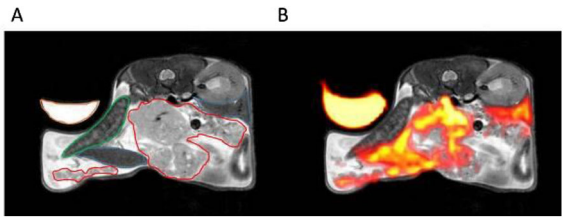

Fig.1: A) ^{1}H image of the Tumor (red), the spleen (green), the liver (blue) and the Reference (orange). ^{19}F overlay image on 1H Image.

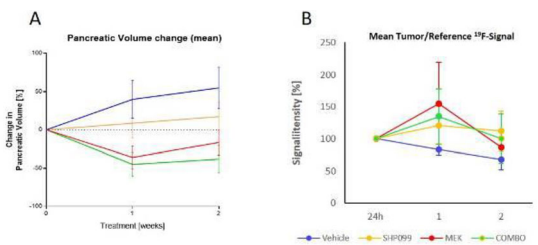

Fig. 2: A) Pancreatic volume over the time of the treatment, starting from day 0, over 1 week and 2 weeks. B) Mean ^{19}F signal relative to the Reference signal, over the time of the treatment. ^{19}F Imaging startet 24h after the injection of the PFC-emulsion.

References:
[1] Chapelin F, Capitini CM, Ahrens ET. Fluorine-19 MRI for detection and quantification of immune cell therapy for cancer. J Immunother Cancer. 2018 Oct 11;6(1):105. https://doi.org/10.1186/s40425-018-0416-9. PMID: 30305175; PMCID: PMC6180584.
[2] Croci D, Santalla Méndez R, Temme S, Soukup K, Fournier N, Zomer A, Colotti R, Wischnewski V, Flögel U, van Heeswijk RB, Joyce JA. Multispectral fluorine-19 MRI enables longitudinal and noninvasive monitoring of tumor-associated macrophages. Sci Transl Med. 2022 Oct 19;14(667)

P152.
Suppletion of magnesium or phosphate to patients with symptomatic renal hypomagnesemia or hypophosphatemia: Assessing the muscle with 31P MRSI

J. van Asten[1], M. F. Verploegen[2], T. Nijenhuis[2], T. Scheenen[1]

[1]*Radboud University Medical Center Nijmegen, Medical Imaging, Nijmegen, Netherlands;*
[2]*Radboud University Medical Center Nijmegen, Nephrology, Nijmegen, Netherlands*

Introduction: The intracellular electrolytes magnesium (Mg2+) and inorganic phosphate (Pi) are involved in intracellular cell signalling and energy metabolism. The kidney regulates the magnesium and phosphate levels into homeostasis. Disturbances in this regulatory mechanism lead to renal wasting of Mg2+ or Pi, causing hypomagnesemia or hypophosphatemia. Patients with Mg2+ and Pi deficiency suffer from fatigue, muscle weakness, paraesthesia and tremors. Severe magnesium depletion can lead to cardiac arrhythmias, seizures and tetany [1–3]. Treatment of this rather unknown and rare disease consists of lifelong magnesium or inorganic phosphate supplementation, of which dosage is limited due to side effects. Despite near normalization of serum magnesium and phosphate, often patients remain symptomatic, which raises the question if serum levels are the best parameters to monitor the effect of suppletion. We hypothesize that intracellular levels of Mg2+ and Pi in muscle are better parameters, as symptoms might be more related to low intracellular levels of Mg2+ and Pi than to low serum levels. Therefore, the aim of this work is to evaluate the intracellular levels of magnesium and phosphate in patients with hypomagnesemia or hypophosphatemia and the effect of magnesium and phosphate supplementation on these levels determined with phosphorous MR spectroscopic imaging (31P MRSI) in muscle [4, 5].
Methods: An ongoing pilot observational diagnostic study of symptomatic renal hypomagnesemia and of renal hypophosphatemia has started. Intracellular levels of magnesium and phosphate are assessed in erythrocytes, peripheral blood mononuclear cells and in skeletal muscle before and after a 5-day intravenous supplementation of magnesium and phosphate at continuous normal physiological blood levels. In the calf muscle of the patient's right leg, anatomical T1 weighted MRI and MRSI-scans (TR = 1250 ms, FA = 25O, 16 × 16 × 16 reconstructed voxels of 11.4 × 11.4 × 22.8 mm) at a SIEMENS 3 T scanner, are performed, pre and post Mg2+ or Pi infusion therapy. The MRSI data is acquired with a 31P birdcage coil (Rapid), operating at 49.89 MHz. MRSI voxels were selected using SpectrIm (Fig. 1) and analysed by jMRUI's AMARES [6]. Absolute quantification was established assuming a concentration of 8.2 mM for total ATP [7]. The estimated concentrations were corrected for T1 saturation effects [5].
Results: Two patients have been examined, one with hypophosphatemia (P01) and one with hypomagnesemia (P02). Serum levels of Pi and Mg were supplemented (P01: serum Pi increased from 0.68 to 1.19 mmol/l; P02: serum Mg increased from 0.48 to 0.93 mmol/l). Assessing the Mg2+ and Pi concentrations in the muscle using 31P MRSI seems feasible. In patient P01, 102 voxels were selected before, and 153 voxels after infusion. After the Pi infusion, the Pi concentration in muscle significantly increased in patient P01 (Fig. 2). In patient P02, 27 voxels were selected before, and 81 voxels after infusion. Although Mg2+ was supplemented, the [Mg2+] concentration significantly decreased after Mg2+ infusion, and Pi levels increased (Fig. 3). In both patients basic Mg2+ and Pi levels as well as pH before supplementation were low as compared to healthy volunteers.
Discussion: Intravenous supplementation of Mg2+ and Pi, as a therapy in patients with renal magnesium or phosphate wasting, might be monitored by assessing the intracellular levels of these electrolytes using 31P MRSI. The infusion of Mg2+ and Pi can restore normal serum levels, but does not necessarily restore intracellular levels. The patient with Mg2+ deficiency also showed an increased concentration of inorganic phosphate after Mg2+ infusion, which might partly explain the decrease of [Mg2+] in the muscle of that patient, due to binding interactions [8]. These findings might better explain why some patients remain symptomatic to this rare disease, after supplementation therapy.
Conclusion: Intracellular Mg2+ and Pi concentrations in patients with renal hypomagnesemia or hypophosphatemia can be noninvasively monitored by 31P MRSI. In two patients intracellular Pi levels in muscle increased with Pi or Mg2+ supplementation.

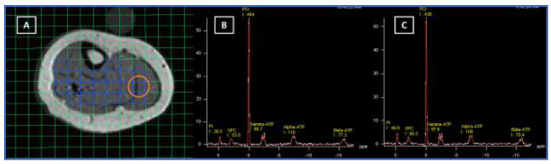

Fig. 1: Multiple MRSI voxel selection in calf muscle of a patient, using SpectrIm (A). 31P spectra of orange voxel prior (B) and after suppletion therapy (C).

P01 (Pi infusion)	*PRE*	*Phosphor components in mM*			
102	PI	PCR	ATP	pH	[Mg2+]
MEDIAN:	3,40	37,23	8,24	6,93	0,38
AVERAGE:	3,40	37,99	8,26	6,93	0,41
SD:	0,66	3,49	0,44	0,02	0,15
	POST	*Phosphor components in mM*			
153	PI	PCR	ATP	pH	[Mg2+]
MEDIAN:	4,66	39,85	8,29	6,92	0,29
AVERAGE:	4,58	40,18	8,30	6,92	0,31
SD:	0,66	3,69	0,53	0,03	0,08
P(<0,01)	0,000				0,009

Fig. 2: Averaged phosphorous concentrations of patient with Pi deficiency. Student T-test, P<0.01.

P02 (Mg infusion)	*PRE*	*Phosphor components in mM*			
27	PI	PCR	ATP	pH	[Mg2+]
MEDIAN:	3,89	46,48	8,40	6,92	0,40
AVERAGE:	4,23	54,20	8,82	6,92	0,44
SD:	1,10	21,60	1,47	0,06	0,17
	POST	*Phosphor components in mM*			
81	PI	PCR	ATP	pH	[Mg2+]
MEDIAN:	5,75	42,78	8,29	6,90	0,36
AVERAGE:	5,83	43,62	8,32	6,90	0,37
SD:	0,97	9,41	0,66	0,05	0,09
P(<0,01)	0,000				0,002

Fig. 3: Averaged phosphorous concentrations of patient with Mg deficiency. Student T-test, P<0.01.

References:
[1] Basso LE, et al. Clin Chim Acta. 2000;291(1):1-8.
[2] Bech AP, et al. Am J Kidney Dis. 2019;73(2):288-90.
[3] de Baaij JH, et al. Clin Kidney J. 2012;5(sup1):i15-i24.
[4] Elin RJ, et al. Magn Res. 2010;23(4):S194-8.
[5] Meyerspeer M, et al. NMR Biomed. 2021;34:e4246.
[6] Stefan D, et al. Meas Sci&Techn. 2009;20:104035-44.
[7] Kemp GJ, et al. NMR Biomed. 2007;20:555-565.
[8] Iotti S, et al. MRI 2000;18:607-614.

P153.
Assessment of reconstruction accuracy for under-sampled 31P-MRS data using a low-rank Hankel Matrix completion approach

A. Santos-Díaz[1], M. D. Noseworthy[2]

[1]*Tecnologico de Monterrey, School of Engineering and Sciences, Mexico City, Mexico;*
[2]*McMaster University, Electrical and Computer Engineering, Hamilton, Canada*

Introduction: Compressed sensing (CS) has grown in popularity as an acceleration method for acquisition of MR signals. To succeed, one of the main criteria states that the aliasing generated due to the sub-sampling scheme has to be incoherent[1]. This is usually achieved through a pseudo-random pattern. The purpose of this study was to analyze the influence of the sampling schedule in the reconstruction accuracy of under-sampled ^{31}P-MRS data, using a Low-Rank approach[2].

Methods: Simulated brain spectra was created using a modified version of the FID-A toolbox[3] tailored for simulation of ^{31}P MRS. Experiments were performed using a 60 cm bore 3 T GE MR750 (GE Healthcare, Milwaukee, WI) scanner. Data was collected using a 12.7 cm diameter surface coil (51.705 MHz) matched for brain and a pulse-acquire sequence (hard pulse excitation, 0.5 ms duration, 60° flip angle, 2000 Hz spectral bandwidth, 512 points, TR = 3 s, 16 averages). A single spectrum was collected using a custom-built spherical phantom (volume = 1L, pH = 6.7) containing 25 mM and 10 mM concentrations of sodium phosphate and phosphocreatine disodium salt, respectively. In addition, a spectrum was collected from the parietal lobe of a healthy volunteer, using the same parameters but 128 averages. The collected FIDs were retrospectively under-sampled (uniformly distributed pseudo-randomly selected samples) using 256, 170, 128 and 103 data points to simulate the undersampling factors (USF) of × 2, × 3, × 4 and × 5, respectively. Then, the under-sampled FIDs were reconstructed using a Low-Rank Hankel matrix completion algorithm[2], in a Monte Carlo like simulation where 1000 different sub-sampling schemes per USF were tested. To measure accuracy of the reconstruction, we calculated the root mean squared error (RMSE) of the original and reconstructed FID signals. Additionally, we computed the peak to side lobe ratio (PSLR) for the transformed point spread function (TPSF) of the sampling schemes in order to assess their incoherence[1].

Results: Figure 1 shows the RMSE of the reconstructed spectra for all data types and acceleration factors. Mean values for RMSE and PSLR of the under-sampling patterns are included in Table 1. Of note, the minimum error for the × 5 USF is lower than the maximum error of the × 2 USF. Figures 2 and 3 depict examples of the original, best and worst reconstructed spectra along with their difference for × 2, × 3 and × 4, × 5, USFs, respectively.

Discussion: In this work we tested the performance of multiple (1000) under-sampling patterns for acceleration factors ranging from × 2 to × 5 in the reconstruction of one-dimensional ^{31}P-MRS using a Low-Rank Hankel Matrix completion approach. We discovered that the performance of the reconstruction is entirely dependent on the chosen samples, even when applying a pseudo-random selection. Furthermore, we observed that the error using the best sampling scheme for the maximum acceleration factor is lower than the worst scheme for the × 2 factor. Traditional compressed sensing strategies suggest using sampling distributions weighted at the center of k-space[1,4], however for ^{31}P-MRS/MRSI approaches shown elsewhere[5,6], the uniform pseudo-random distribution is required. Additionally, our PSLR showed that the under-sampling schemes with the lowest values did not correspond to the lowest error reconstructions. These findings suggest that for ^{31}P MRS data, the lowest PSLR for the TPSF do not guarantee an accurate reconstruction.

Conclusion: In conclusion, an assessment of the reconstruction performance of pseudo-randomly under-sampled ^{31}P-MRS data using a Low Rank approach showed that the accuracy in the reconstruction is highly dependent on the chosen samples. Thus, methods for optimizing the sampling scheme should be further investigated. Finally, more recent approaches for the Low Rank Hankel Matrix completion[7] reconstruction may yield better results.

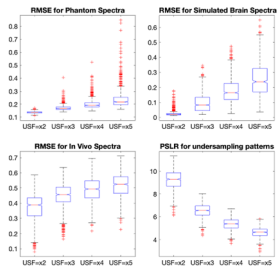

Fig. 1: RMSE for phantom, simulated brain and in vivo brain data. USF: Under-sampling factor for two, three, four and five fold acceleration.

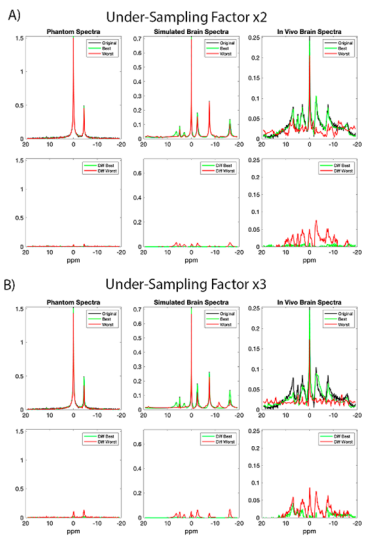

Fig. 2: Examples of the original (fully sampled), best and worst reconstructions for the A) x2 and B) x3 USFs along with their difference (Original - best and original - worst reconstructions).

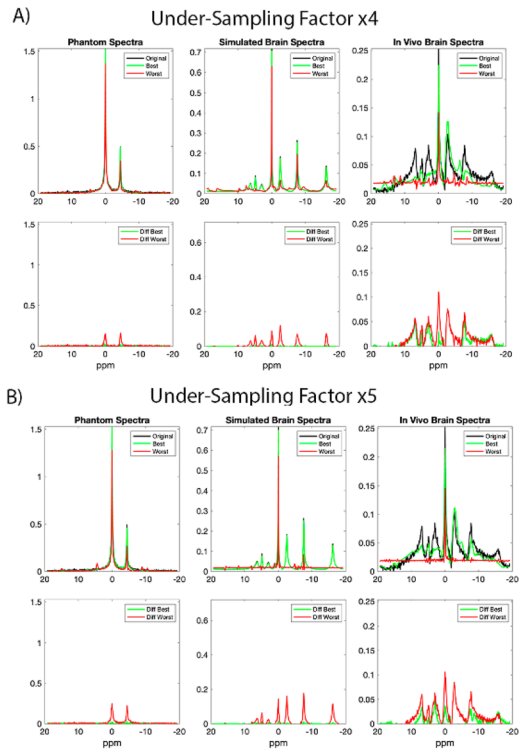

Fig. 3: Examples of the original (fully sampled), best and worst reconstructions for the A) x4 and B) x5 USFs along with their difference (Original - best and original - worst reconstructions).

Metric	USF = x2			USF = x3			USF = x4			USF = x5		
	mean±SD	Min	Max	mean±SD	Min	Max	mean±SD	Min	Max	mean±SD	Min	Max
PSLR	9.251±0.873	6.123	11.337	6.533±0.597	4.373	8.028	5.366±0.495	3.672	6.701	4.637±0.427	2.943	5.804
RMSE Phantom	0.137±0.008	0.113	0.172	0.172±0.02	0.141	0.405	0.202±0.037	0.148	0.523	0.239±0.072	0.161	0.850
RMSE sBrain	0.026±0.020	0.012	0.176	0.096± 0.062	0.018	0.345	0.177±0.083	0.025	0.473	0.254±0.106	0.035	0.650
RMSE vBrain	0.365±0.097	0.081	0.586	0.450±0.080	0.165	0.637	0.490±0.077	0.217	0.697	0.517±0.079	0.228	0.711

Table 1: Statistical values for PSLR and RMSE for all under-sampling factors.

References

1. Lustig M, Donoho D, Pauly JM. *Magn Reson Med*. 2007;58(6):1182–1195.
2. Qu X, Mayzel M, Cai JF, Chen Z, Orekhov V. *Angew Chemie—Int Ed*. 2015;54(3):852–854.
3. Simpson R, Devenyi GA, Jezzard P, Hennessy TJ, Near J. *Magn Reson Med*. 2015;33(November 2015):23–33.
4. Hu S, Lustig M, Balakrishnan A, et al. *Magn Reson Med*. 2010;63(2):312–321.
5. Santos-Díaz A, Harasym D, Noseworthy MD. *Magn Reson Med*. 2019;81(6):3453–3461.
6. Santos-Díaz A, Noseworthy MD. *Magn Reson Imaging*. 2019;59:88–96.
7. Qiu T, Wang Z, Liu H, Guo D, Qu X. *Magn Reson Chem*. 2021;59(3).

P154.
Bayesian optimization for batch tuning in deep learning-based 129xe lung MRI reconstruction

M. Tavakkoli[1,2], S. Svenningsen[3,4], N. Konyer[2], P. Nair[3,4], M. D. Noseworthy[1,2,5]

[1]*McMaster University, Electrical and Computer Engineering, Hamilton, Canada;*
[2]*St. Joseph's Healthcare, Imaging Research Centre, Hamilton, Canada;*
[3]*McMaster University, Medicine, Hamilton, Canada;*
[4]*St. Joseph's Healthcare, Firestone Institute for Respiratory Health, Hamilton, Canada;*
[5]*McMaster University, Department of Radiology, Hamilton, Canada*

Introduction: Deep Learning (DL) techniques have shown potential in improving quality of MR image reconstruction. However, numerous factors, including hyperparameters that need fine-tuning for each dataset, influence the performance of these models. Conventional methods such as Grid Search and Random Search often exhibit slow performance and/or unreliability in this context [1]. In this study, the improvement of hyperpolarized (HP) 129Xe lung MRI reconstruction was examined through the application of Bayesian Optimization for hyperparameter tuning in DL techniques, including Variational Networks (VarNet) and Model-based DL (MoDL) [2–4]. We particularly investigated the influence of batch size (i.e., the number of samples processed before the model is updated) on critical performance metrics, such as the structural similarity index (SSIM) [5] and Mean Squared Error (MSE), using the Scikit-optimize Python package [6].
Methods: In a study approved by our local research ethics board, 155 subjects were scanned using a GE MR750 3 T MRI, acquiring fully sampled 3D multi-slice HP 129Xe ventilation MR images (128×80x16, polarization: $10 \pm 0.46\%$) [7]. The k-space for all datasets was corrected into 128×128 matrices using a partial Fourier transform (PFT), then a variable density Cartesian pseudo-random mask was generated by sampling 25% of the data while the central parts of k-space remained fully sampled [8,9]. Each slice in the entire dataset was retrospectively subsampled, maintaining a consistent sampling ratio of 25%. However, unique sampling masks were used for each individual slice. This was done to minimize the impact of acquisition settings, such as undersampling patterns [4]. Furthermore, the sampling masks applied during training were different from those utilized in the evaluation phase.
Gaussian process-based Bayesian Optimization was employed to determine the optimal hyperparameters, namely batch size for the VarNet and MoDL models [2–4]. The batch size was varied between 2 and 64. The optimization process aimed to maximize SSIM [5] and minimize MSE, using the sum of negative SSIM and positive MSE as the objective function (Min f(x) = Min MSE-SSIM). The VarNet and MoDL models were trained on the same dataset, which consisted of 140 of the 155 patients. To ensure high SNR, the first and last slices, which are predominantly noisy, were removed from each dataset ($140 \times 14 = 1960$ slices in total), and these were not included in the evaluation set. For the evaluation phase, a total of 210 central slices were selected from 15 subjects. The Berkeley Advanced Reconstruction Toolbox (BART) [10] was utilized on the Google Colab platform to perform all image reconstruction
Results: Optimized batch sizes were found to be 42 for VarNet and 19 for MoDL. The optimization convergence trace, illustrating the optimal point and various iterations for VarNet and MoDL, is shown in Fig. 1. The function value reaches its minimum and ceases to improve after 11 iterations for VarNet and 12 iterations for MoDL, indicating convergence. The comparison of reconstructed images using VarNet and MoDL techniques emphasizes enhancements from hyperparameter optimization (batch sizes of 42 for VarNet and 19 for

MoDL) versus non-optimized results and zero-filling images (Fig. 2). Lastly, the mean ± standard deviation (std) of SSIM and MSE values for 210 slices during the evaluation phase (Table 1) provide a quantitative understanding of the enhanced image quality resulting from hyperparameter optimization. Comparing the default setting (batch size of 10) to optimized VarNet and MoDL methods, improvements in both the SSIM and MSE metrics were noted. The optimized VarNet method showed an increase in SSIM and a reduction in MSE (Table 1). Similarly, the optimized MoDL method showed considerable improvement with SSIM and a decrease in MSE (Table 1). These quantitative results further emphasize the importance of hyperparameter optimization in obtaining superior image quality for both VarNet and MoDL methods.

Discussion: Bayesian Optimization improved image quality compared to baseline models, as evidenced by higher SSIM and lower MSE values. However, there are limitations, such as reliance on the quality of the initial search space. The optimization process can be challenging in situations where quick results are needed, or computational resources are limited. Future research could explore advanced optimization techniques and the applicability of this approach to other medical imaging modalities.

Conclusion: This study demonstrates that optimizing hyperparameters significantly improves image quality for VarNet and MoDL MRI reconstruction methods, as evidenced by higher SSIM and lower MSE metrics. Visual comparisons through a series of images and convergence plots further emphasize the effectiveness of the optimization approach in addressing the time-consuming challenges associated with hyperparameter tuning in DL 129Xe lung MRI reconstruction.

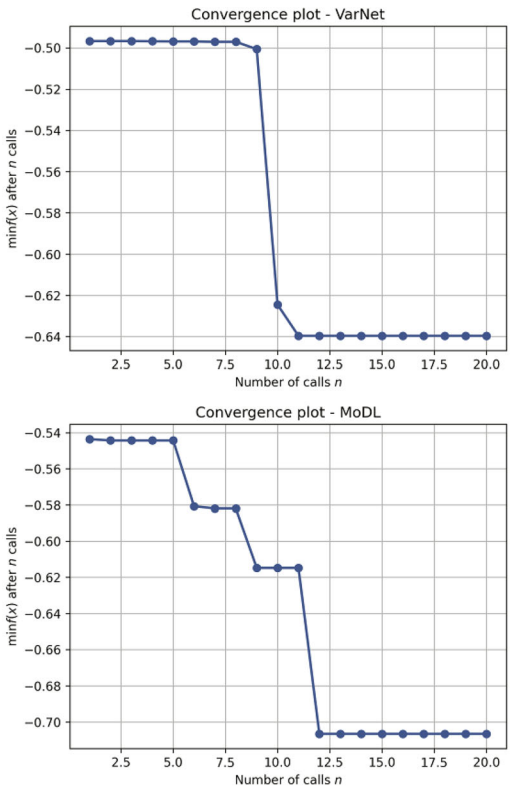

Fig. 1: Convergence plots of the Bayesian optimization process for VarNet and MoDL methods. The plots show the progression of the objective function values across different iterations. The optimization process converges for both methods (at iteration 11 for VarNet and 12 for MoDL), indicating that an optimal set of hyperparameters has been found.

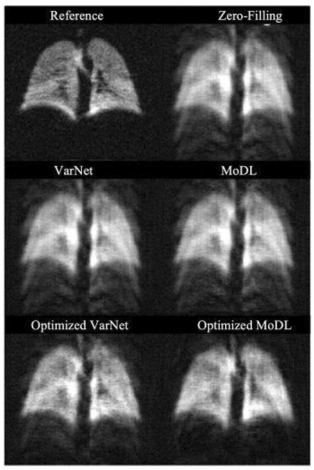

Fig. 2: A comparison of reconstructed images using VartNet and MoDL methods, both with and without hyperparameter optimization. The top row presents ground truth and zero-filled images. The results on the middle row are from VartNet and MoDL obtained with default setting (batch size=10). The bottom row showcases enhanced image quality achieved through hyperparameter optimization (batch size= 42 and 19 for VarNet and MoDL respectively).

	Zero-filling	VarNet-Default	Optimized VarNet	MoDL-Default	Optimized MoDL
SSIM	0.5877± 0.0432	0.6178± 0.0523	0.6965± 0.0356	0.6335± 0.0481	0.7496± 0.0295
MSE	0.1511± 0.0198	0.1208± 0.0183	0.0545± 0.0097	0.0911± 0.0169	0.0432± 0.0124

References

[1] Li L, et al. (2017) *J. Machine Learning Res.* 18(1):6765-6816. **[2]** Shahriari B, (2015) *Proc IEEE* 104(1):148-175. **[3]** Hammernik K, et al. (2018) *Magn. Reson. Med.* 79(6):3055-3071. **[4]** Aggarwal H, et al. (2018) *IEEE Trans. Med. Imag.* 38(2):394-405. **[5]** Wang Z, et al. (2004) *Imag. Proc.* 13(4):600-612. **[6]** Head T, et al (2020) scikit-optimize/scikit-optimize, September 2020. **[7]** Svenningsen S et al. (2021) *Acad. Radiol.* 28(6):817-826. **[8]** Kojima S, et al. (2018) *Radiol. Phys. Technol.* 11:303-319. **[9]** Margosian PM, et al. (2007) *eMagRes.* **[10]** Blumenthal M, et al. (2023) *Magn. Reson. Med.* 89(2):678-693.

Table 1: A comparison of mean± std of SSIM and MSE values. The table highlights improvements in image quality (higher SSIM and lower MSE) using optimized hyperparameters for both VarNet and MoDL methods.

P155.
Noninvasive *in-situ* pH determination of postmortem brain tissue by 1H-MRS measurements

S. Frese[1], D. Gascho[1], M. Thali[1], S. Kozerke[2], N. Zoelch[1,3]

[1]*Institute of Forensic Medicine / University of Zurich, Department of Forensic Medicine and Imaging, Zurich, Switzerland;*
[2]*Institute for Biomedical Engineering / ETH, Department of Information Technology and Electrical Engineering, Zurich, Switzerland;*
[3]*University Hospital for Psychiatry / University of Zurich, MR Center, Zurich, Switzerland*

Introduction: The study of postmortem tissue changes after a person's death is an essential task of forensic medical research to find indicators for estimating the time since death and to discover correlations with the mechanism and/or cause of death. One of these indicators could be the postmortem pH value of the brain. Usually, anaerobic glycolysis ceases at a pH of approximately 6.3 after a postmortem interval of about 10 h. However, depending on the cause of death and the duration of the agonal phase, the postmortem brain tissue pH value may be correspondingly lower. To study cerebral pH levels postmortem in situ, a noninvasive method is sought. Magnetic resonance spectroscopy (^{1}H-MRS) may provide such a method for noninvasive study. The aim of this study is to evaluate the feasibility of pH measurements based on chemical shift changes in the transition

from acetate to acetic acid and lactate to lactic acid, which are metabolites that occur postmortem in measurable concentrations and may respond to pH changes in a range that is meaningful for postmortem studies.

Methods: As part of the Virtopsy® concept, postmortem ^{1}H-MRS measurements were performed on deceased persons (study population: n = 50) before autopsy. Using a 3 T MRI scanner (*Achieva, Philips Healthcare, Best, the Netherlands*) and an 8-channel phased-array receive-only head coil (*Philips Healthcare, Best, the Netherlands*), single-voxel measurements with a voxel volume of 6 ml and 256 signal averages were conducted in white matter tissue of the right hemisphere (PRESS localization, TE/TR: 26/2288 ms, VAPOR water suppression, second order shimming, volume-based RF power optimization). Myo-inositol was selected as a pH-stable Reference metabolite based on its acid dissociation constant and chemical structure. An adapted Henderson-Hasselbalch equation was used to calculate pH values [1]:

$$\mathrm{pHMRS} = \mathrm{pK_a} + \log_{10}((\delta_{\mathrm{obs}} - \delta_{\mathrm{acid}}) / (\delta_{\mathrm{base}} - \delta_{\mathrm{obs}}))$$

where pK_a refers to the pK_a value of the indicator species lactate (pK_a = 3.680) or acetate (pK_a = 4.578), δ_{obs} is the observed difference between the lactate doublet and myo-inositol respectively between acetate and myo-inositol, and δ_{acid} and δ_{base} are acidic and basic limits for these chemical shift differences (lactate doublet and myo-inositol: δ_{acid} = 2.126 ppm, δ_{base} = 2.225 ppm; acetate and myo-inositol: δ_{acid} = 1.456 ppm, δ_{base} = 1.635 ppm)[1,2].

For comparison measurements, a brain tissue sample was taken from the measured position of each subject during the autopsy. The sample was homogenized with a mortar, and its pH value was measured with a conventional pH-meter (*761 Calimatic, Knick, Berlin, Germany*). Finally, the observed chemical shifts were plotted against the measured pH values and compared to a simulated titration curve based on an adapted Henderson-Hasselbalch equation.

Results: Preliminary results based on 23 of the 50 subjects and the use of peak picking in MATLAB are presented in the following. The median full-width-at-half-maximum of the water peak was 7.6 (min: 4.4, max: 9.3). Median SNR of lactate doublet was 144.6 (min.: 70.0, max.: 166.3). Exemplary spectra are shown in Fig. 1. The pH values measured in the samples ranged from 5.29 to 6.79, with 15 of 23 samples having pH values below 6.3. While the observed chemical shift difference between acetate and myo-inositol matched well with the simulated titration curve, this was not the case for the observed chemical shift difference between lactate doublet and myo-inositol. Thus only acetate-based calculations were performed. From a pH value of less than 6.3, the values matched the pH-meter-based values.

Discussion: Our preliminary results demonstrate that postmortem brain tissue can indeed reach pH values of less than 6.3. Furthermore, the non-invasive method presented here for pH determination of brain tissue based on the chemical shift difference between acetate and myo-inositol can be applied postmortem and provides accurate results at low pH values below 6.3. Since a pH value of less than 6.3 has already been determined in 15 of the 23 subjects so far, and since postmortem brain pH may depend on the mechanism and/or cause of death, noninvasive determination of pH may provide a suitable basis for further studies in deceased subjects.

Conclusion: ^{1}H-MRS allows the determination of low pH values in the brain tissue of deceased persons and thus offersrelevant information before/without autopsy on the one hand, and on the other hand further application opportunities in scientific studies.

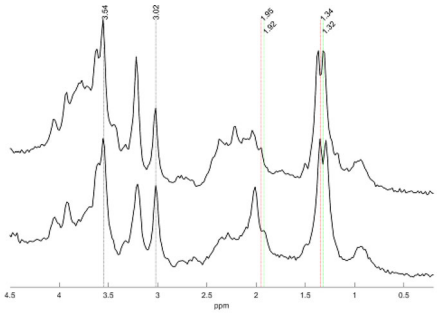

Fig. 1: Exemplary postmortem MR spectra from the deceased with a pronounced difference in measured pH. The lactate doublet and acetate peaks are shifted downfield in the upper spectrum compared to the lower spectrum. In contrast, the peaks from myo-inositol or creatine are unchanged with respect to their position. The corresponding pH values are 5.31 for the upper spectrum and 6.44 for the lower. The elevated glucose (~3.4 ppm), acetone (~2.2 ppm) and beta-hydroxybutyrate (~1.19 ppm) signals in the upper spectrum indicate diabetic ketoacidosis in this case.

References:

1. Ackerman JJ, Soto GE, Spees WM, Zhu Z, Evelhoch JL. The NMR chemical shift pH measurement revisited: analysis of error and modeling of a pH dependent Reference. Magnetic resonance in medicine. 1996;36(5):674–83.

2. Tredwell GD, Bundy JG, De Iorio M, Ebbels TM. Modelling the acid/base (1)H NMR chemical shift limits of metabolites in human urine. Metabolomics: Offcial journal of the Metabolomic Society. 2016;12(10):152.

P156.
Magnetic resonance spectroscopy detects the progression of the MAFLD in eNOS KO mice, and it has a gender difference

L. Manjarrés[1,2], A. Xavier[1,3], L. González[1,2], C. Garrido[1,2], K. Rivera[1,2], F. Zaconni[4], C. Sing-Long[1,2], M. Andia[1,2]

[1]*Millennium Institute Intelligent Healthcare Engineering, iHEALTH, Santiago de Chile, Chile;*
[2]*Pontificia Universidad Católica de Chile, Biomedical Imaging Center, School of Medicine, Santiago de Chile, Chile;*
[3]*Universidad de Santiago de Chile, Biomedical Engineering, Faculty of Engineering, Santiago de Chile, Chile;*
[4]*Pontificia Universidad Católica de Chile, Faculty of Chemistry and of Pharmacy, Santiago de Chile, Chile*

Introduction: The critical pathophysiological hallmark of Metabolic dysfunction-associated fatty liver (MAFLD) is the hepatocyte's accumulation of intracellular fats 1. A biopsy is the current gold standard for MAFLD diagnosis and staging. However, it is expensive and a risk for the patient 2.

Changes, not only in the total amount of liver fat but also in the fatty acid composition during the progression of the MAFLD, have been reported as promising biomarkers 3. Most of those studies have been made in male murine models but have not compared the development of the disease between males and females.

This study aims to investigate the gender differences in the fatty liver profile during the progression of MAFLD in an eNOS KO mice

model. The eNOS KO model recapitulates disease evolution in 12-14 weeks when fed a high-calorie, high-fat diet.

Subjects/methods: We fed six groups of 12 weeks age eNOS KO mice (3 groups of females and 3 groups of males) with a Western diet (AIN-76A, TestDiet) for 4 weeks (n = 8), 8 weeks (n = 8), and 12 weeks (n = 8), and we had two control groups fed with chow diet (1 group of females and 1 group of males n = 8 for each one).

At each time point, an in vivo 3 T MRS was acquired (Philips Ingenia, 3 T), then a portion of the liver was used for histology, and the remaining liver was analyzed with a 9.4 T MRS (Bruker Avance) after a fatty acid extraction.

The peaks corresponding to fatty acids obtained with 9.4 T MRS were used as an input to perform PCA, and then it was clustered using the hierarchical clustering method.

Results/discussion: The mice's weight and the amount of fat accumulated increased during the Western-diet intervention, especially in males. The correlation between the fat percentage in the liver obtained in the in vivo 3 T MRS and the percentage of fatty acids weight is linear and significant (Fig. 1).

The fat percentage of the liver obtained 3 T MRS was calculated considering only the peak of fat (1.28 ppm) and the peak of water (4.7 ppm). On the other hand, the percentage of fatty acids was calculated making a relationship between the weight of the extracted fatty acid and the weight of the liver.

We have identified seven metabolite peaks in the 9.4 T MRS spectra (Methyl terminal protons, bulk methylene protons, b-methylene protons, allylic protons, a-methylene protons, diallyc protons, and olefinic internal protons). Males showed a significant change in allylic protons and diallyc protons. However, females showed variations in different metabolite peaks, such as in bulk methylene, allylic protons, diallyc protons, and a-methylene protons (Fig. 2).

The principal component analysis (PCA) was able to differentiate the progression of the MAFLD in both genders, with better differentiation in females (Fig. 3).

Conclusion: MRS allows differentiating the progression of MAFLD. Disease progression trajectories appear to be different in young males and females, suggesting that this disease should be studied with sex-adjusted References. Future studies incorporating age and fertility will be necessary to evaluate if it has implications for the diagnosis and prognosis of MAFLD.

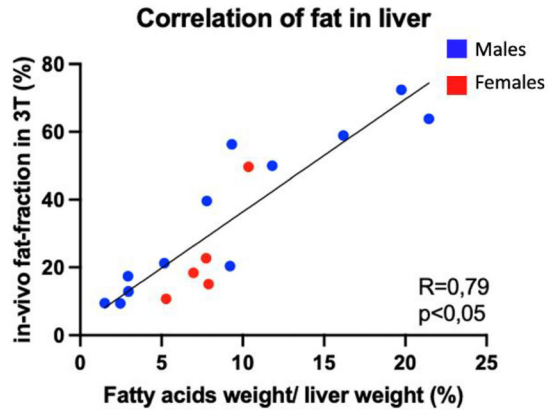

Fig. 1: Correlation between liver fat fraction estimated from in vivo 3T MRS and extracted liver fatty acids in male and female eNOS KO mice.

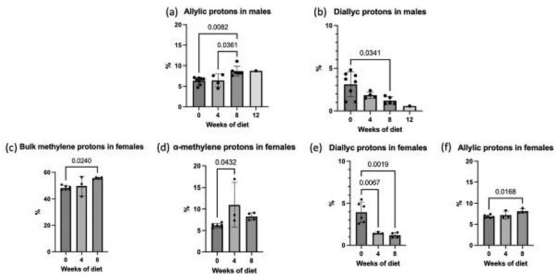

Fig. 2: Peaks that showed changes in both genders were evaluated with an ANOVA analysis and Turkey's multiple comparisons tests (mean±SD). (a) Peak of allylic proton (~2ppm) in males (b) Peak of diallyc protons (~2,8ppm) in males. (c) Peak of bulk methylene protons (~1,3ppm) in females. (d) Peak of α- methylene protons (~2,2ppm) in females (e) Peak of diallyc protons (~2,8ppm) in females (e) Peak of the allylic proton (~2ppm) in females.

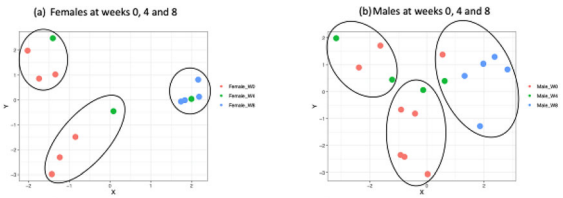

Fig. 3: PCA based on the eight metabolite peaks obtained from the 9.4T MRS spectra evaluated at 3 times points, baseline (W0), 4 weeks (W4), and 8 weeks (W8).

P157.
Metabolic abnormalities in the pregenual anterior cingulate cortex in obsessive-compulsive disorder measured using 1H MR spectroscopy

D. Pajuelo[1,2], E. Kosová[2,3], D. Greguš[2], M. Brunovský[2,3], P. Stopková[2,3], I. Fajnerová[2,3], J. Horáček[2,3]

[1]*Institute for Clinical and Experimental Medicine, MR Unit, Department of Diagnostic and Interventional Radiology, Prague, Czech Republic;*
[2]*National Institute of Mental Health, Klecany, Czech Republic;*
[3]*Third Faculty of Medicine, Charles University, Prague, Czech Republic*

Introduction: The anterior cingulate cortex (ACC) plays a role in error detection and monitoring and processing of conflicting information which are core clinical signs of obsessive-compulsive disorder (OCD) [1]. The pathophysiology of OCD is supposed to be linked to metabolic abnormalities in this area; however, published 1H MRS studies yield conflicting results [2].

This study compares metabolic concentrations in the ACC between OCD patients and healthy controls (HC) as well as between subgroups of patients with and without medication. It should lead to a better understanding of metabolic changes associated with OCD and the treatment.

Methods: *Subjects* 54 patients with OCD according to International Statistical Classification of Diseases (ICD-10) criteria and Diagnostic and Statistical Manual of Mental Disorders (DSM-IV) criteria, and 54 age- and sex-matched HC were included in the study. The patients were without medication at least 5 days before MR examination or on a stable dosage of selective serotonin reuptake inhibitor (SSRI) antidepressants for at least 4 weeks. The severity of the symptoms of the patients was assessed using the Yale-Brown Obsessive-

Compulsive Scale (YBOCS). No history of mental disorder or psychotropic medication use was allowed for HC. The study was conducted in compliance with the principles of the Declaration of Helsinki and was approved by the local ethics committees. All subjects provided their written informed consent prior to participation in the study.

MR examination and metabolite evaluation The subjects underwent MRI and 1H MRS (PRESS: TE/TR/NA = 30 ms/5000 ms/64, VOI = 3.8 ml, with and without WS) on a 3 T Magnetom Prisma scanner (Siemens, Germany) equipped with a 64-channel volume head coil. MR spectra measured in pregenual ACC (pgACC) were evaluated using LCModel. Metabolic values were calibrated using a water signal and corrected for water content in each VOI [3] based on MPRAGE image segmentation.

Statistics After exclusion of subjects with abnormal MRI findings (not connected with OCD) and/or low spectra quality, 28 OCD and 28 HC were included in the statistical analysis. Intergroup differences were assessed by the Mann–Whitney U test. Spearman's rank correlation was used for determination of any relationship between demographic, clinical and metabolic data.

Results: OCD patients revealed significantly decreased total creatine (tCr) ($p = 0.022$), myo-inositol (mI) ($p = 0.001$) and the sum of glutamine and glutamate (Glx) ($p < 0.001$) in the pgACC than HC group (Fig. 1). A significant negative correlation between tCr and YBOCS compulsions subscale ($r_s = -0.380$, $p = 0.046$) was found in OCD group. No significant differences were found for total *N*-acetylasparate (tNAA), gamma-aminobutyric acid (GABA) and choline-containing compounds (tCho); however, tCho revealed a trend towards lower concentrations in OCD than HC ($p = 0.067$). No significant correlation was found between metabolic values and age and duration of illness. Subgroups with or without medication did not differ.

Discussion: Our metabolic results, as well as most other MR studies, do not support the hypothesis of hypermetabolism in the cortico-striatal-thalamo-cortical circuit, mostly based on PET/SPECT results [4], as a pathophysiological mechanism of OCD. In contrast, our data show reduced bioenergetic and glutamatergic metabolism in the pgACC. It seems that the hypometabolism affects especially glial cells, manifested by decreased mI. Neuronal cell function appears to be intact (unchanged tNAA), either by the disease itself or thanks to ongoing therapy and medication.

A significant negative correlation between tCr levels and the YBOCS compulsions subscale, also found by O'Neill [5], implicates an important relationship between tCr concentrations and OCD symptomatology.

Our data also shows that the use of metabolic values corrected on CSF content in the examined VOI is crucial for the detection of small metabolic changes expected in OCD.

Conclusions: This study confirmed abnormal bioenergetic and glutamatergic metabolism in the pgACC in OCD patients. tCr may be considered as a biomarker of severity of compulsions in OCD patients. OCD reveals changes in glial cell metabolism in the pgACC rather than neuronal damage or dysfunction.

Acknowledgment Supported by the MH CZ NU20-04-00147, by the Charles University Cooperatio: Neuroscience program, by MH CZ—DRO ("IKEM, IN 00023001").

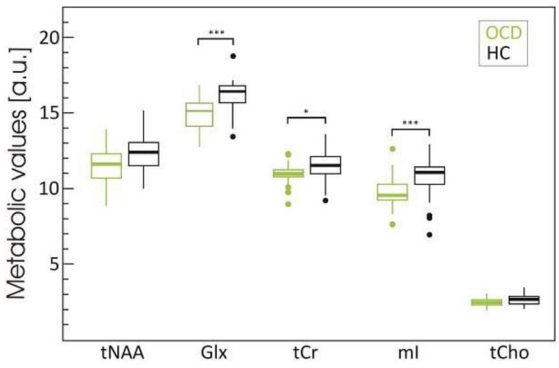

Fig. 1: Metabolic levels in pgACC in OCD patients and healthy controls. OCD: obsessive-compulsive disorder; pgACC: pregenual anterior cingulate cortex; HC: healthy controls; tNAA: N-acetylaspartate + N-acetylaspartylglutamate; Glx: glutamate + glutamine; tCr: creatine + phosphocreatine; tCho: choline-containing compounds (tCho), mI: myo-inositol; a.u.: arbitrary units, *** $p < 0.001$, * $p < 0.05$

References:

1. https://doi.org/10.1016/s0031-9384(02)00930-7
2. https://doi.org/10.1007/7854_2020_201. Biria M et al. 2021
3. https://doi.org/10.1002/mrm.20901
4. https://doi.org/10.1016/j.pscychresns.2004.07.001
5. https://doi.org/10.1016/j.pscychresns.2016.05.005

P158.
Comparing the efficacy of MR spectroscopic and MR imaging methods for assessing hepatic fat changes in obese patients undergoing dietary intervention and GLP-1 agonist treatment

P. Kordač[1], D. Pajuelo[1], M. Hajek[1], M. Burian[1], P. Sedivy[1], M. Dezortová[1], J. Kovář[1]

[1]*Institute for clinical and experimental medicine, ZRIR, Prague, Czech Republic*

Introduction: Non-alcoholic fatty liver disease (NAFLD) is the most common cause of chronic liver disease in adults, with a prevalence of 17-46%. It is commonly associated with obesity and type 2 diabetes [1]. One of the early signs of NAFLD is hepatic steatosis, which is characterized by increased hepatic fat content (HFC) that can be diagnosed using biopsy or imaging methods [2]. In this study, we compared four different MR methods for assessing HFC in obese subjects undergoing dietary intervention with or without the agonist of incretin hormone glucagon like peptide-1 (GLP-1).

Methods: Sixteen obese non-diabetic men (age: 47.0 ± 12.4 years, BMI: 36.2 ± 3.8 kg/m^2) with HFC > 4% underwent a 16-week dietary intervention (nutritional counselling) and 16-week treatment with GLP-1 agonist (semaglutide 0.25–1 mg/week; Ozempic®). The order of both interventions was randomized. All participants underwent seven MR examinations—three before the study (each at least 2 weeks apart) and two at week 14 and 16 of each intervention period. The study was conducted in compliance with the principles of the Declaration of Helsinki and with the approval of the local ethics

committee. All subjects provided written informed consent with the participation in the study.

MR examinations were performed using 3 T MR system VIDA (Siemens, Germany) equipped with 30-channel surface matrix and 32-channel spine coil. The examination protocol included standard Siemens LiverLab protocol [3] containing proton density fat fraction measurement using VIBE e- and q-Dixon sequences and automatic spectroscopy sequence HISTO (STEAM sequence; TR = 3000; TEs = 12, 24, 36, 48, 72 ms). Moreover, our laboratory liver spectroscopic protocol was applied (STEAM sequence; TR = 4500 ms; TEs = 20, 20, 20, 30, 50, 68, 80, 100, 135, 150, 180, 270 ms). STEAM and HISTO volume of interest (40 × 30 × 25 mm) and VIBE roi were placed in the liver segment V/VIII in the area without visible big vessels. The entire sequences were measured during exhalation.

Mean steatosis from whole liver volume (VIBE all liver) was measured by q-Dixon images using liver mask segmented from e-Dixon images. Spectra from laboratory protocol were evaluated by LCModel and obtained signal intensities were corrected to individual T2 relaxations. The results of fat fraction measurements from all four methods were recalculated to HFC using Longo correction [4].

Intergroup differences were assessed using paired t test. A p value of less than 0.05 was considered statistically significant. All values are shown as average ± SD.

Results: Dietary intervention did not affect neither body weight nor HFC quantified by all four methods whereas semaglutide treatment led to significant decrease in both body weight and HFC (Fig. 2). However, the differences in change of HFC between dietary intervention and semaglutide treatment were not statistically significant. All MR methods correlated very well with each other (Table 2).

Discussion: Both spectroscopy protocols revealed an excellent correlation in HFC (Fig. 2). Although HISTO is based on automatic T2 relaxation time measurement only from TEs = 12–72 ms, compared to manual STEAM measurement with TEs = 20–270 ms, HISTO is faster and more user-friendly than the STEAM method. This is because spectra from STEAM have to be manually evaluated using LCModel software or other suitable software.

On the other hand, slightly higher HFC assessed by HISTO protocol compared to our STEAM protocol can be attributed to shorter T2 relaxation times obtained by HISTO. HFC calculated from the whole liver volume revealed the weakest correlation with the other methods especially because of occasional bad liver segmentation and counting bile ducts. All methods showed statistically similar HFC in both examined groups.

Conclusion: All of the listed MR methods are suitable for monitoring of HFC changes during therapeutic and life style interventions.

Acknowledgement Supported by Ministry of Health of the Czech Republic, grant nr. NU20-01-00121 and MH CZ—DRO (”IKEM, IN 00023001“).

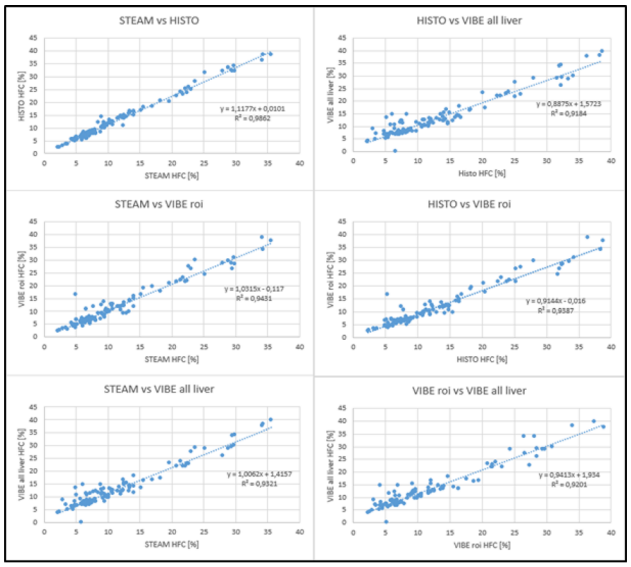

Fig. 1: Correlation between different MR methods used for HFC measurement

		STEAM [%]	HISTO [%]	VIBE roi [%]	VIBE all l. [%]	Weight [kg]
Dietary int.	Start	12.2 ± 8.5	13.6 ± 9.4	12.4 ± 9.1	14.1 ± 8.9	116.8 ± 13.0
	End	10.8 ± 7.6	12.2 ± 9.1	11.3 ± 8.1	12.9 ± 8.1	114.3 ± 11.9
	Diff.	-1.4 ± 4.8	-1.4 ± 4.9	-1.2 ± 5.9	-1.1 ± 5.5	-2.5 ± 5.8
Semaglutide	Start	10.8 ± 7.6	13.7 ± 8.3	12.3 ± 7.1	13.6 ± 7.5	118.8 ± 12.1
	End	8.3 ± 4.9***	9.3 ± 5.7***	8.6 ± 5.4**	10.8 ± 4.8*	112.1 ± 12.4***
	Diff.	-3.7 ± 3.2	-4.5 ± 4.4	-3.7 ± 3.8	-2.9 ± 4.5	-6.7 ± 2.6‡

Fig. 2: Changes in HFC and weight in the group only on diet and in the group on diet with semaglutide (GLP-1 agonist). * = p < 0.05; ** = p < 0.01; *** = p < 0.001… difference between start and end of intervention ‡ = p < 0.05… difference between dietary intervention and semaglutide treatment

	STEAM [R2]	HISTO [R2]	VIBE roi [R2]	VIBE all l. [R2]
STEAM [R2]		0.99	0.94	0.93
HISTO [R2]	0.99		0.94	0.92
VIBE roi [R2]	0.94	0.94		0.92
VIBE all l. [R2]	0.93	0.92	0.92	

Fig. 3: Pearson correlation coefficient (R2) between different MR methods used for HFC measurement

References:

1. Younossi, Z.M., et al., Global epidemiology of nonalcoholic fatty liver disease-Meta-analytic assessment of prevalence, incidence, and outcomes. Hepatology, 2016. 64(1): p. 73–84.
2. Šedivý P, et al. Comparison of Accuracy of Magnetic Resonance Spectroscopic and Imaging Techniques for the Liver Steatosis Assessment. Chemické listy. 2021; 115(1): 46–53.
3. Sellers R. MR LIver lab. MAGNETOM Flash. 2016; 66(3): 39–43
4. Longo R, et al. Proton MR spectroscopy in quantitative in vivo determination of fat content in human liver steatosis. Journal of Magnetic Resonance Imaging. 1995; 5(3):281–5.

P159.
Characterization of the sequelae of experimental cerebral malaria with MRI and MRS

A. Comino Garcia-Muñoz[1], I. Varlet[1], A. Lokossou[1], E. Royer[1], Y. Le Fur[1], M. Bernard[1], T. A. Perles-Barcacaru[1], A. Viola[1]

[1]*Aix-Marseille Université, CRMBM, UMR CNRS, Marseille, France*

Introduction: Cerebral malaria (CM), the most lethal complication of *P. falciparum* infection, is an encephalopathy that results in coma and leads to death in 15-20% of cases. Although 10-20% of survivors develop neurological disorders, these are poorly studied [1]. The aim of this project is to characterize the brain sequelae in a murine CM model at the anatomical, metabolic, vascular and functional levels on the long term using in vivo MRI and MRS.

Methods: Male and female C57Bl/6 J mice were infected with *Plasmodium Berghei* ANKA and treated with chloroquine at the peak of the disease (dose: 25 mg/kg, 1 ip injection /day during 10 days). Mice were explored before and after induction of CM, then 1x/month for 6 months. Metabolic and perfusion study: Bruker AVANCE 500 WB @11.75 T, with isoflurane anesthesia (1–2%/air). Anatomical MRI: RARE, TE = 9.21 ms, TR = 5000 ms, RARE factor 8, 4 av, FOV 15 × 15 mm^2, 194 × 194 matrix, 31 contiguous slices of 0.5 mm thickness. Localized 1H-MRS in brainstem (voxel 3 × 3 × 1.5 m^3), hypothalamus (1.5 m^3), hippocampus (3 × 3 × 1.5 m^3) and cerebellum (3 × 2 × 1.5 m^3): PRESS, TE 20 ms, TR 1700 ms, 256 averages, with and without VAPOR. Perfusion MRI: EPI-pCASL, TE = 9.08 ms, TR = 6414 ms, 5 slices of 0.75 mm, FOV of 25 × 25 mm^2, matrix 128 × 128). Connectome study: Pharmascan 70/16 US @7 T with a cryoprobe. Animals were explored under light anesthesia (medetomidine 0.13 mg/kg/isofluorane 0.5%). T2*w images (fast GE, TE = 14 of ms, TR = 1700 ms, FOV of 16 × 16 mm^2, 200 × 200 matrix, 62 contiguous slices of 0.25 mm thickness), 2D-DTI (EPI, TE = 19 ms, TR = 3000 ms, 40 contiguous 0.4 mm slices, 96 × 96 matrix, FOV 16 × 16 mm^2) and rs-fMRI (FID-EPI, TE 16.3 ms, TR 1750 ms, 40 contiguous 0.4 mm slices, 96 × 96 matrix, FOV 16 mm). Behavioral tests: elevated cross maze and novel object recognition test. Statistics: data were analyzed using non-parametric statistics and the two-way ANOVA with multiple comparisons test, significance set to $p < 0.05$

Results: 62 mice (36 F and 26 M) were analyzed for 6 months. Males were more vulnerable to CM, as they showed less response to treatment, with a 20% lower survival rate. Their recovery was slower than that of the females at the same parasitemia levels, as they maintain a hypothermic state for an average of 2 days more. In all mice with untreated CM, we observed cerebral edema, white matter hyperintensities and hemorrhages in the cortex and olfactory bulbs. The lesions at the level of the olfactory bulbs (atrophy, microhemorrhages) persist for up to six months after recovery and clearance of the parasite.

As seen with 1H-MRS, the surviving mice presented significantly lower levels of metabolites including glucose, GABA, choline-containing compounds, and macromolecules, among others, in the brainstem and the hippocampus. Cerebral blood flow of the thalamus was still reduced in the first months after recovery.

At the end of the follow-up, the CM survivor mice showed lower scores than the control mice of open arm exploration in the elevated plus maze and a lower discrimination index in the object recognition test.

Discussion: CM causes a cerebral syndrome that leaves neurological sequelae months after the clearance of the parasite. These include lesions in the anterior part of the brain visible at anatomical MRI whereas perfusion MRI revealed anomalies in CBF in the thalamus. The metabolic study showed a reduction in some neurotransmitters, in choline-containing compounds and in compounds linked to energy metabolism. Some of these abnormalities could be related to the phenotype of higher anxiety-like behavior and reduced non-spatial memory shown by CM survivor mice six months after recovery. This phenotype is similar to what has already been described in human CM [1]. The DTI and fMRI data are being analyzed to verify a possible relation between the metabolic and perfusion changes and alterations in the structural or functional connectome.

Conclusion: Cerebral malaria affects male and female subjects differently. Some characteristic lesions [2] persist several months after recovery. 1H-MRS and perfusion MRI data show a persisting perfusion and metabolic abnormalities. This is the first study with MRI and MRS showing the possible causes of the neurological sequelae of CM and the influence of sex in the disease development and recovery.

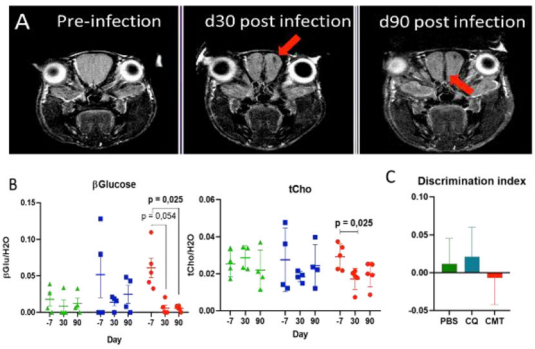

Fig. 1: CM survivor mice show cerebral sequelae that include, among others, (A) lesions at the anterior part of the brain (red arrows) visible with anatomical MRI 30 and 90 days after the infection, (B) reduction in β-glucose and choline-containing compounds from 1 to 3 months after the infection (green: PBS control, blue: chloroquine control, red: CM survivors) and (C) reduced non-spatial memory as shown by lower discrimination indexes in the object recognition test (PBS control, CQ chloroquine control, CMT cerebral malaria treated mice).

References:

[1] J.T. Langfitt, M.P. McDermott, R. Brim, S. Mboma, M.J. Potchen, S.D. Kampondeni, K.B. Seydel, M. Semrud-Clikeman, T.E. Taylor, Neurodevelopmental Impairments 1 Year After Cerebral Malaria, Pediatrics. 143 (2019).

[2] Penet MF, Viola A, Confort-Gouny S, Le Fur Y, Duhamel G, Kober F, Ibarrola D, Izquierdo M, Coltel N, Gharib B, Grau GE, Cozzone PJ. J Imaging experimental cerebral malaria in vivo: significant role of ischemic brain edema. J Neurosci. 2005;25(32):7352-8

P160.
Validation of apparent intra- and extra-myocellular lipid content indicator using spiral spectroscopic imaging at 3 T

A. Naëgel[1,2], M. Viallon[1], J. Karkouri[1,2,3], T. Troalen[2], P. Croisille[1], H. Ratiney[1]

[1]*Université de Lyon, INSA-Lyon, Université Claude Bernard Lyon 1, UJM-Saint Etienne, CNRS, Inserm, CREATIS UMR 5220, U1206, Lyon, France;*
[2]*Siemens Healthineers, Paris, France;*
[3]*University of Cambridge, Wolfson Brain Imaging Center, Cambridge, United Kingdom*

Introduction: This work presents a fast and simple method based on spiral MRSI for mapping the IMCL and EMCL[1,2] apparent content, which is a challenging task[3,4] and it compares this indicator to classical quantification results in muscles of interest.

Methods: A spiral MRSI sequence was developed on a 3 T clinical MRI (MAGNETOM PRISMA, Siemens Healthineers, Erlangen, Germany). Main parameters were TR/TE = 2 s/2 ms, FOV = 200 ×

200 × 25 mm, spatial resolution = 64 × 64, voxel size = 3.1 × 3.1 × 25mm, temporal resolution = 500 ms, temporal points = 1024, spatial interleaving = 22 and temporal interleaving = 5, TAcq = 3 min 48 s. Spiral MRSI was performed using a dual resonance 1H/31P transmit/receive coil (Rapid GMBH, Würzburg, Germany) positioned under the right calf of 16 volunteers. A Fast (SE-EPI-based) diffusion-weighted and a T1 vibe Dixon sequence was subsequently acquired to derive the fibres" orientation, high-resolution water, fat and Fat Fraction (FF) images. MRSI data were analyzed using homemade processing tools (Matlab). After standard MRSI reconstruction, the analysis of the spectra was centered on the characteristic peaks of IMCL and EMCL (1.3–1.5 ppm). To realize an automatic phasing and frequency registration of the spectra (unsuppressed water), a Fourier transform on the absolute value of the time domain signal was performed[5]. Then, the evolution of the cumulative sum of the amplitudes (CSA) of a fixed area, defined between 1.1 and 1.7 ppm, was used to analyze the apparent content of IMCL and EMCL for each voxel. Mapping the value of this curve index at 1.40 ppm enables displaying the apparent content of IMCL over EMCL in the fat component (Fig. 1). The new proposed apparent IMCL/EMCL content indicator was compared to the classical IMCL/(EMCL + IMCL) ratio quantified using LCModel fitting method (basis set "muscle-5") on region of Interested (ROI) selected in soleus medial (SM), and gastrocnemius medial (GM) muscles (Fig. 2). FF was calculated with the Dixon acquisition and compared to FF obtained by 2 methods derived from the MRSI data: one based on the CSA of the lipid and water signal, and another based on the quantification of the signal with LCModel.

Results: The average FF obtained by the 3 methods on the muscles of interest were resumed in Fig. 3 and coherent with previously obtained values in volunteers[6]. The apparent content indicator and its quantitative equivalent were both significantly different between the GM and SM muscles. There is a significant positive correlation between the apparent content indicator and its quantitative equivalent (Fig. 4). In addition, the GM muscle fibers displayed an overall alignment along the direction of the B0 field. In contrast, the SM's ones had an orientation between the Y and Z-axis.

Discussion: The MRS measure of IMCL is influenced by the quantity in the tissue and the orientation of the fibers. Our results are in agreement with literature[7]: The SM muscle had a high IMCL content due to its high percentage of type I fibers, with a pronounced angular fiber orientation to B0; the GM muscle had smaller IMCL content and a less pronounced angular fiber orientation. Despite a less advantageous fiber orientation, the observation of IMCL was feasible in the SM due to its high level in this muscle. The quantification of IMCL and EMCL on MRSI data is fastidious due to phase and frequency shifts from voxel to voxel and results in time-consuming data processing. The rapid analysis provided by the apparent indicator can be used to rapidly generate maps of the IMCL/EMCL distribution. Also, this map enables analyzing lipid MR spectra as a function of fiber orientation, which is known to influence.

Conclusion: The proposed exploration technique is a promising, fast, and straightforward approach to map the apparent content of IMCL compared to EMCL lipids. It is correlated with results from standard quantification procedure and appear to be robust to signal-to-signal fluctuations related to B0 variations. Further work should evaluate the reproducibility prior to transfer to clinic for longitudinal studies. This preliminary work highlights the potential of this high-resolution spiral spectroscopic imaging technique to provide more insights on the coupling between structure, function, metabolism, energy consumption and the underlying pathophysiology in muscles, especially in the context of refining our understanding of impaired exercise performance, intolerance to sustained exercise and premature fatigability.

Acknowledgements This work was partly supported by the LABEX PRIMES (ANR-11-LABX-0063), Siemens Healthineers and Jabrane Karkouri was supported by the European Union's Horizon 2020 research and innovation program under grant agreement No-801075.

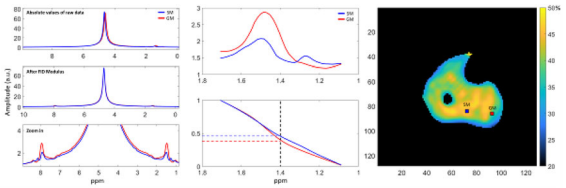

Fig. 1: Apparent Content Indicator procedure. Left: FID modulus: automatic phasing and frequency registration. Middle: Magnitude spectrum centered on EMCL and IMCL and the evolution of the CSA. Right: apparent content indicator mapping and ROI highlighted for SM, GM muscles.

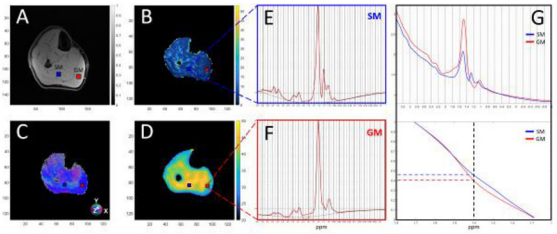

Fig. 2: (A) T1-vibe Dixon water (B) Dixon FF map (C) fiber orientation as EigVector (X,Y,Z=R,G,B) (D) apparent content indicator map. Spectrum obtained in SM muscle (E) and GM muscle (F), processed with LCModel and (G) with the apparent content indicator procedure.

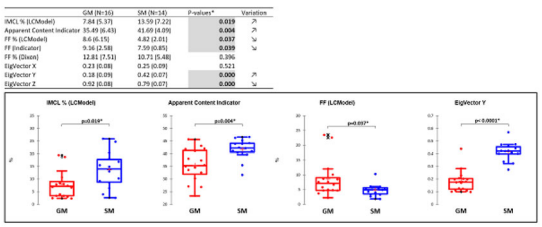

	GM (N=16)	SM (N=14)	P-values*	Variation
IMCL % (LCModel)	7.84 (5.37)	13.59 (7.22)	**0.019**	↗
Apparent Content Indicator	35.49 (6.43)	41.69 (4.09)	**0.004**	↗
FF % (LCModel)	8.6 (6.15)	4.82 (2.01)	**0.037**	↘
FF (Indicator)	9.36 (2.58)	7.39 (0.85)	**0.039**	↘
FF % (Dixon)	12.81 (7.51)	10.71 (5.48)	0.396	
EigVector X	0.23 (0.08)	0.25 (0.09)	0.521	
EigVector Y	0.18 (0.09)	0.42 (0.07)	**0.000**	↗
EigVector Z	0.92 (0.08)	0.79 (0.07)	**0.000**	↘

Fig. 3: Table: Results of the statistical analysis of GM and SM muscles: mean (SD). *T-test with statistical significance set to p<0.05. Arrows provide the trend of the significant changes. Boxplots: Relevant parameter with significant difference between GM and SM muscles.

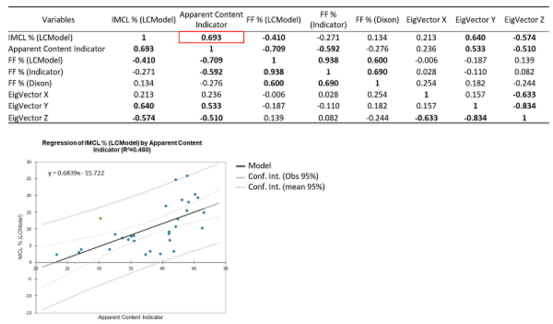

Variables	IMCL % (LCModel)	Apparent Content Indicator	FF % (LCModel)	FF % (Indicator)	FF % (Dixon)	EigVector X	EigVector Y	EigVector Z
IMCL % (LCModel)	1	**0.693**	**-0.410**	-0.271	0.134	0.213	**0.640**	**-0.574**
Apparent Content Indicator	**0.693**	1	**-0.709**	**-0.592**	-0.276	0.236	**0.533**	**-0.510**
FF % (LCModel)	**-0.410**	**-0.709**	1	**0.938**	**0.600**	-0.006	-0.187	0.139
FF % (Indicator)	-0.271	**-0.592**	**0.938**	1	**0.690**	0.028	-0.110	0.082
FF % (Dixon)	0.134	-0.276	**0.600**	**0.690**	1	0.254	0.182	-0.244
EigVector X	0.213	0.236	-0.006	0.028	0.254	1	0.157	**-0.633**
EigVector Y	**0.640**	**0.533**	-0.187	-0.110	0.182	0.157	1	**-0.834**
EigVector Z	**-0.574**	**-0.510**	0.139	0.082	-0.244	**-0.633**	**-0.834**	1

Fig. 4: Table: Spearman correlation matrix, correlation coefficients in bold have a p<0.05. Graph: Linear regression between the IMCL % and the apparent content indicator.

References:
1. Kršňák M, NMR Biomed, 2021
2. Boesch C, Magn Reson Med, 1997
3. Weis J, PLoS ONE, 2014
4. Hwang JH, J Appl Physiol, 2001
5. Le Fur Y, Magn Reson Mater Phys, 2014
6. Alhulail AA, Magn Reson Med, 2020
7. Vermathen P, Magn Reson Med, 2004

P161.
MR imaging characteristics of breast cancer and adjacent parenchyma: Correlation with mRNA expression of hormone receptor, HER2 and TP53

T. H. Kim[1], Y. N. Kim[1], J. Moon[1]

[1]*Ajou University Medical Center, Radiology, Suwon, South Korea*

Introduction: Breast cancer is a heterogeneous disease and the treatment plan and prognosis are different according to the status of estrogen receptor (ER), progesterone receptor (PR) and human epidermal growth factor receptor 2 (HER2). Recently, the prognostic role of androgen receptor (AR) in breast cancer has been reported in many studies. The TP53 is a gene making a tumor suppressor protein p53. Therefore, any change of p53 in normal breast parenchyma has the potential to cause breast cancer. The purpose of our study is to characterize the imaging phenotype of breast cancer and normal breast parenchyma according to the mRNA expression of ER, PR, AR, HER2 and TP53.
Methods: From June 2020 to January 2023, 79 women who were newly diagnosed with breast cancer and underwentpreoperative magnetic resonance imaging (MRI) at our hospital were included. Two radiologists with 11 and 3 years of experience in breast imaging interpreted the images and they were blinded to the clinical-pathologic data. According to the BIRADS lexicon, radiologists evaluated the background parenchymal enhancement, tumor shape, margin and internal enhancement pattern. We also evaluated T2 bright signal intensity within the tumor and peritumoral edema on T2-weighted image. Expression levels of mRNAs were determined using a reverse transcriptase-polymerase chain reaction (qRT-PCR) kit, SYBR Green Master Mix and RT-PCR machine.
Results: According to the mass shape, 69 (87%) of 79 breast cancers were irregular shape and 10 (13%) were round or oval shape. ER-α mRNA expression was significantly higher in breast cancer showing irregular shape rather than round or oval shape (p = 0.005). Other mRNA expression were not significantly different according to the mass shape. 65 (82%) of 79 breast cancers showed heterogeneous enhancement and 14 (18%) showed rim enhancement. Expressions of ER-α, PR, AR and HER2 mRNA were significantly higher in breast cancer with heterogeneous internal enhancement compared to rim enhancement.
In terms of bright signal intensity within the mass on T2-weighted image, 64 (81%) of 79 cancers did not show internal bright signal intensity and 15 (19%) had internal bright signal intensity. Expressions of ER-α, ER-β, PR, AR and TP53 mRNA were significantly lower in breast cancer with bright signal intensity on T2WI compared to cancer without T2 bright signal intensity. Regarding peritumoral edema on T2-weighted image, 62 (78%) of 79 cancers showed peritumoral edema and 17 (22%) didn"t show. Expressions of ER-α, PR and AR mRNA were significantly lower in breast cancer with peritumoral edema on T2WI.
Of 57 patients whose parenchymal mRNA data were available, 16 (28%) patients showed minimal BPE and 41 (72%) patients showed mild, moderate or marked BPE. Parenchymal ER-α, PR, HER2 and TP53 mRNA expressions were significantly higher in patients with mild, moderate or marked BPE than patients with minimal BPE (p = 0.016, p = 0.0001, p = 0.038, p = 0.035, respectively).
Conclusion: MR imaging phenotype of breast cancer was correlated with mRNA expressions of hormone receptor, HER2 and TP53. Parenchymal mRNA is also correlated with background parenchymal enhancement on contrast-enhanced MRI.

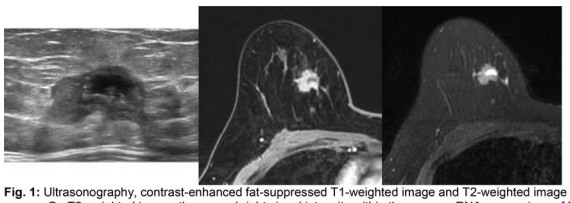

Fig. 1: Ultrasonography, contrast-enhanced fat-suppressed T1-weighted image and T2-weighted image of breast cancer. On T2-weighted image, there was bright signal intensity within the mass. mRNA expressions of ER-α (1.9), PR (0.011), and TP53 (0.382) were significantly lower than breast cancer without bright signal intensity on T2WI.

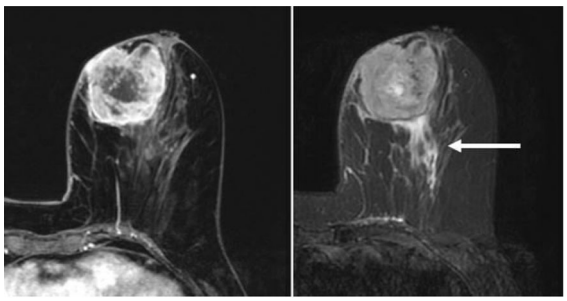

Fig. 2: Contrast-enhanced fat-suppressed T1-weighted image and T2-weighted image of breast cancer. On T2-weighted image, there was peritumoral edema around the mass (arrow). mRNA expressions of ER-α (0.107), PR (0.084), and AR (0.171) were significantly lower than breast cancer without peritumoral edema on T2WI.

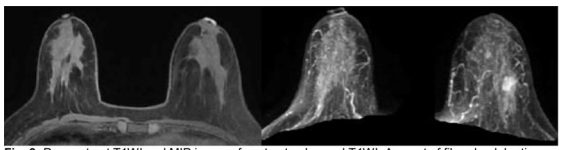

Fig. 3: Pre-contrast T1WI and MIP image of contrast enhanced T1WI. Amount of fibroglandular tissue on T1WI was heterogeneous fibroglandular tissue. Background parenchymal enhancement of MIP image was moderate. Parenchymal ER-α (0.448), PR (0.366) and TP53 (2.786) mRNA expressions were significantly higher compared to minimal BPE.

References:
1. Wiechmann L, Sampson M, Stempel M, Jacks LM, Patil SM, King T, Morrow M. Presenting features of breast cancer differ by molecular subtype. Ann Surg Oncol 2009;16(10):2705–2710. https://doi.org/10.1245/s10434-009-0606-2
2. Nguyen PL, Taghian AG, Katz MS, Niemierko A, Abi Raad RF, Boon WL, Bellon JR, Wong JS, Smith BL, Harris JR. Breast cancer subtype approximated by estrogen receptor, progesterone receptor, and HER-2 is associated with local and distant recurrence after breast-conserving therapy. J Clin Oncol 2008;26(14):2373–2378. https://doi.org/10.1200/JCO.2007.14.4287
3. Bagaria SP, Ray PS, Sim MS, Ye X, Shamonki JM, Cui X, Giuliano AE. Personalizing breast cancer staging by the inclusion of ER, PR, and HER2. JAMA Surg 2014;149(2):125–129. https://doi.org/10.1001/jamasurg.2013.3181
4. Arteaga CL, Sliwkowski MX, Osborne CK, Perez EA, Puglisi F, Gianni L. Treatment of HER2-positive breast cancer: current status and future perspectives. Nat Rev Clin Oncol 2011;9(1):16–32. https://doi.org/10.1038/nrclinonc.2011.177

P162.
In situ 1H-MRS of muscle tissue to detect metabolic changes during the postmortem interval and to study temperature-induced changes in T2 relaxation times

D. Gascho[1], M. Thali[1], N. Zoelch[1,2]

[1]*Institute of Forensic Medicine/University of Zurich, Department of Forensic Medicine and Imaging, Zurich, Switzerland;*
[2]*University Hospital for Psychiatry/University of Zurich, MR Center, Zurich, Switzerland*

Introduction: The change of tissue in the course of the postmortem interval (PMI) is of particular interest in forensic medicine. Hitherto, mainly postmortem studies of tissue samples have provided insights into the decomposition process at the molecular level. However, a certain limitation of such ex-situ studies is given by the collection and preparation of the sample. In contrast, postmortem magnetic resonance spectroscopy (^{1}H-MRS) provides the ability to study postmortem tissue changes at the molecular level in situ in deceased individuals.
In the present studies, we aim to investigate the postmortem changes of muscle tissue by ^{1}H-MRS. In addition, we determine the T_2 relaxation times of water in the investigated volume and correlate the T_2 values with the temperature in the tissue. The temperature is thereby measured with MRS thermometry.
Methods: As part of the Virtopsy® concept, ^{1}H-MRS examinations were performed in the musculus vastus intermedius and/or musculus adductor magnus of deceased persons (study population: n = 43). Using a 3 T MRI scanner (*Achieva, Philips Healthcare, Best, the Netherlands*) and an 8-channel phased-array receive-only head coil (*Philips Healthcare, Best, the Netherlands*), single-voxel measurements were conducted. Differences in the ratio between the trimethylammonium-containing compounds (TMA) and the methyl group of creatine (Cr) were evaluated in relation to the PMI, muscle orientation relative to the magnetic field, and the age of the deceased. Water T_2 relaxation times in the measured voxel were estimated based on a series of measurements with 8 different echo times (ranging from 35 to 350 ms) and analyzed with respect to the dependence on PMI and tissue temperature. The local temperature of the muscle tissue was calculated using the temperature-dependent resonance frequency of water with creatine as a temperature-independent Reference peak[1]. The 1H-MRS-based temperature estimates were compared with rectal temperature measurements.
Results: Multiple regression analysis shows that PMI, age, and the orientation of the muscle all have an effect on the measured TMA/Cr. 68% (Adjusted R-squared: 0.6869) of the dispersion in TMA/Cr is explained by the four variables. TMA/Cr increased with increasing PMI. Contrary to expectation, the T_2 relaxation times of muscle tissue increased as the tissue temperature decreases. The MRS thermometry measurement agreed well with the rectal temperature measured in relative proximity to the measured voxel. The median difference was 0.9 °C with 70% of the measurements within ± 2 °C.
Discussion: This study revealed that PMI-dependent changes in TMA/Cr can be observed with ^{1}H-MRS, which may serve as an additional indicator for time since death estimations. This result is consistent with observations made on severed sheep legs where ^{1}H MRS measurements were performed every 24 h for three or four days [2]. The increase in T_2 values of muscle tissue as the tissue temperature decreased is surprising. It is usually assumed that the reduced movement of the molecules at reduced temperature leads to lower T_2 values. The fact that this is not the case postmortem in situ might be of particular relevance for postmortem imaging using T_2-weighted MRI. The results indicate that MRS thermometry-based estimates of the temperature are valid also for postmortem muscle tissue. This noninvasive method offers the possibility to correct temperature effects in order to emphasize other postmortem effects in postmortem MRI research.
Conclusion: ^{1}H-MRS provides scientifically valuable opportunities for postmortem examination of tissue changes.
References:
[1]Zoelch N, Heimer J, Richter H, et al. Finding the optimal temperature calibration for postmortem MRS thermometry in forensic medicine—Abstract ISMRM 2022. https://archive.ismrm.org/2022/2172.html
[2]Gascho D, Richter H, Karampinos DC, et al. (2020) Noninvasive in situ proton MRS in muscle tissue and bone marrow as a novel approach to identify previous freezing in a completely thawed cadaver. NMR in Biomedicine 33:e4220. https://doi.org/10.1002/nbm.4220

P163.
Liver disfunction: An increasing risk of Alzheimer's disease?

K. Pierzchala[1], J. Mosso[1], D. Simicic[1], D. Sessa[1], O. Braissant[1], V. A. McLin[1], C. Cudalbu[1]

[1]*École Polytechnique Fédérale de Lausanne (EPFL), CIBM Center For Biomedical Imaging, Lausanne, Switzerland*

Introduction: Despite the recent progress in the research on the mechanisms behind type C hepatic encephalopathy(HE), a complication of chronic liver disease(CLD) that arises in 80% of the patients, this disease remains incompletely understood, and it is still unclear how HE progression influences cognition[1,2].
It is known that brain neurodegenerative diseases can lead to changes in the brain metabolism and cellular alterations. The cognitive dysfunction in patients with type C HE is marked by attention and memory deficiency. However, whether CLD is associated with dementia risk is unclear. In addition, there is grooving evidence of an important role of liver-gut-brain axis in neuropathology, suggesting that liver disfunction is the origin of Amyloid-β (Aβ) deposits[3,4]. Therefore, the aim of this study was to investigate if there are neurometabolic and cellular (morphological) signatures of AD in type CHE.
Methods: Animal experiments were approved by the Service for Veterinary Affairs of the canton of Vaud(VD3022). Male Wistar rats (n = 38, ∼ 200 g), 35 rats underwent BDL surgery(model of type C HE[5]). In-vivo 1H-MRS: 9.4 T (Varian/Magnex,SPECIAL sequence(TE = 2.8 ms)). Two regions of were measured: hippocampus (Hipp) (2 × 2.8 × 2 mm^3) and cerebellum (Cer) (2.5 × 2.5 × 2.5 mm^3). Metabolites quantification: LCModel. The scans were performed before (week 0) and after BDL at weeks 2, 4, 6, and 8(each animal was its own control).
Histology: At week4 and 8 post-BDL and Sham-surgery rats were perfused and brains fixed (4% formaldehyde), embedded in paraffin and cut into 5 µm thick slices (3 brains/group).
Aβ pathology—Congo Red staining.
Tau protein pathology—Gallyas Silver Stain.
Results: In-vivo ^{1}H-MRS: Longitudinal and brain region related differences in metabolite concentrations were observed over the disease progression in two studied brain regions.
At week4 post-BDL in all brain regions a statistically significant increase in Gln was observed (Fig. 1). In addition, the Lac concentration was significantly increased in cerebellum at week 8 (Fig. 1C). Decrease of tCho, Cr, Glu, and GABA was observed in all brain regions being significant for tCho(Hipp:week8**), Cr(Cer:week6*) (Fig. 1). The antioxidant system was also altered. The Asc showed a

tendency of decrease in Cer at week6 post-BDL(***). GSH displayed no significant tendency to decrease in hippocampus, while in cerebellum an increase was found already at week2 (Fig. 1).
Congo red staining revealed intracellular Amyloid-β(Aβ) accumulation in Fr, FrPaM, Hipp and Cer(Fig. 2A).
Gallyas staining revealed tau-bodies in the accumulation in Fr, FrPaM and Cer(Fig. 2B).

Discussion: The underlying pathophysiology of several dementias significantly overlaps[6], therefore biomarkers of neurodegeneration are important for early diagnosis and treatment.
Increased Gln, the hallmark of HE, was measured with a stronger increase in Cer. Gln increase can potentially lead to a Glu decrease. As Glu metabolism is related to neurons and plays an important role in cognition[7], its reduction may imply dysfunction and loss of glutamatergic neurons[7]. Glu decreased level was found in patients with AD and correlated with increased Aβ load[7,8]. The GPC and PCho present in myelin and cell membrane are the primary sources of the Cho signal in MRS. Decreased tCho in HE is due to an osmotic answer to Gln increase but towards the end of the disease might indicate alterations in membrane turnover and WM integrity[7]. Decrease of Cr was detected in all studied brain regions, and dysfunction in brain Cr is also associated with AD[9].
OS, a key mechanism causing neurodegeneration[10]. The low antioxidants level are linked with cognitive impairment[12]. A significant decrease in Asc was observed herein. Studies have shown Asc decrease in blood of CLD and AD patients[12,13].
A region and time-dependent Aβ and Tau bodies deposits (Fig. 2) were observed. Aβ and Tau bodies build up over time is a sign of degeneration of the synapses that govern cognition[14].

Conclusion: Patients with type C HE develop cognitive dysfunctions, significantly lowering their quality of life. Our findings emphasize the possibility that liver disease may significantly affect cognitive decline and increase the risk of AD. Tau bodies and Aβ aggregates are the two neuropathological indicators of neurodegeneration. In order to propose neuroprotective treatments that will open up a new therapy option for HE patients and enhance their long-term cognitive outcome, a more physiological approach is necessary to bring better knowledge of HE mechanisms.

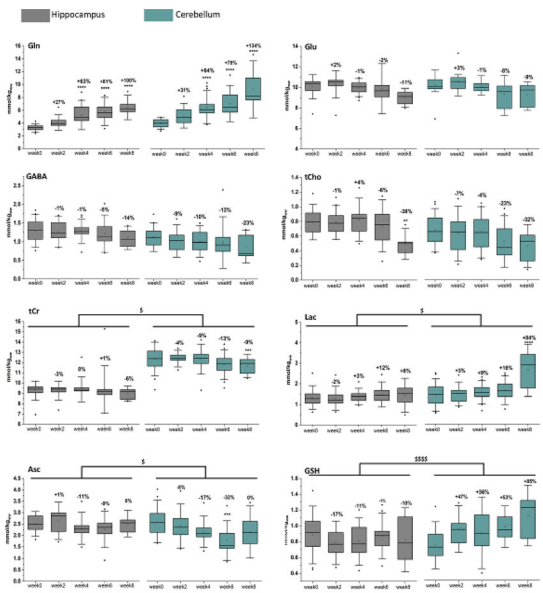

Fig. 1: 1H-MRS: longitudinal evolution of disease progression related changes in CNS metabolites (osmolytes, neurotransmitters and antioxidants). MeanSD; *p<0.05, **p<0.01, ***p<0.001, ****p

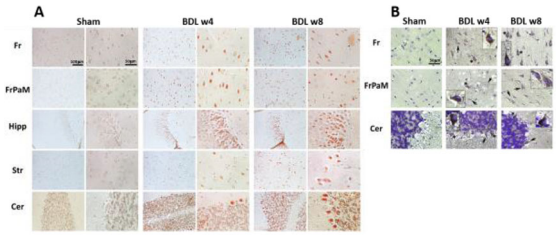

Fig. 2: **(A)** Aβ accumulation in the brain visualized with Congo red histochemical stain. Representative microphotographs of the BDL p21 rats" brain (columns 3 and 4) and age-matched Sham controls (columns 1 and 2). **(B)** Representative micrographs of Gallyas silver stain of the BDL rat brain and age-matched Sham controls. Fr – frontal cortex, FrPaM - frontoparietal cortex, motor area, Hipp – hippocampus, Cer – cerebellum, NFTs – asterisk, pretangle neurons – arrow.

References:

1. Pierzchala,FBBM 2022
2. Simicic,Anal.Biochem2022
3. Bassendine,JAlzheimersDis2020
4. Estrada,FrontAgingNeurosci2019
5. DeMorrow,LiverInt2021
6. Schneider,Epub2007
7. von Kienlin,NeurobiolDis2005
8. Fayed et al.,AmJAlzheimersDisOtherDemen2011
9. Mlynárik,JAlzheimersDis2012
10. Pierzchala,AmJGastroenterol2019
11. Rupsingh,Epub2009
12. Monacelli,Nutrients2017
13. Colpo,NutrHosp2015
14. Bloom,JAMANeurol2014

P164.
Preliminary in-vivo characterization of healthy gray and white matter of patients treated for brain neoplams using chemical biopsy and ^{1}H-MRS

S. Gazdzinski[1], J. Bogusiewicz[2], K. Burlikowska[2], K. Łuczykowski[2], R. Rola[1], Ł. Dziuda[1], B. Kossowski[3], M. Birski[4], J. Furtak[4], M. Harat[4], J. Pawliszyn[5], B. Bojko[2]

[1]*Military Institute of Aviation Medicine, Warsaw, Poland;*
[2]*Nicolaus Copernicus University in Torun, Pharmacodynamics and Molecular Pharmacology, Bydgoszcz, Poland;*
[3]*Nencki Institute for Experimental Biology, Warsaw, Poland;*
[4]*10th Military Research Hospital and Polyclinic, Neurosurgery, Bydgoszcz, Poland;*
[5]*University of Waterlo, Chemistry, Waterloo, Canada*

Introduction: Interpretation of MRI and MRS results is ambiguous, as their lipidomic correlates in health and disease are largely not known. MRS-based lipid profiles might be useful for discriminating tumorous and healthy breast tissue [1]. Here, we evaluated the relationships between MRS spectra and lipidome of healthy brain gray matter (GM) and white matter (WM) in patients with brain neoplasms undergoing biopsy, accompanied by micro-extractions (SPME), known as a chemical biopsy; it is used to characterize human brain in vivo in terms of the metabolic profiling and accounts for unstable and short-lived species.

Methods: We studied 26 patients treated for various brain neoplastic changes. Sampling was conducted during conventional patient brain biopsy procedures. In vivo SPME sampling was performed simultaneously on WM and GM that were not affected by neoplastic changes. The procedure involved inserting a thin fiber coated with a biocompatible sorbent into the tissue along the trajectory of the biopsy needle. SPME probe was left in the studied tissue for 4 min. During this time analytes from brain were bound to the sorbent. Lipidomic

analysis of the extract was performed using Liquid Chromatography coupled with High-Resolution Mass Spectroscopy (LC-HRMS). Two chromatography modes were applied: hydrophilic interactions—HILIC (n = 19) and revered phase chromatography—RPLC (n = 7). RPLC enabled analysis of glycerides, ceramides and phospholipids, while HILIC majorly phospholipids and sphingolipids [2, 3].

^{1}H SVS was measured in GM and WM with semi-LASER (TR/TE = 2000/35 ms, 128 acquisitions, standard VOI = 2 × 2 × 2 cm), as close as possible to the SPME extraction sites. When the VOI had to be smaller, the number of acquisitions was increased to assure satisfactory spectral quality. In some case the WM VOI had to be placed ipsilaterally, symmetrically to the GM VOI. The spectra were processed with LC Model and metabolite concentrations corrected for tissue contributions. The results were correlated with concentrations of lipid classes with Spearman method.

Results: When the sample analyzed with RPLC–HRMS (n = 19), MRS-derived concentrations were interpolated to concentrations of pure WM and GM. Here, lipids resonating at 1.3 ppm in GM inversely correlated with all lipid classes but monoglycerides ($r = -0.71$, $p < 0.05$). In WM, though, lipids resonating at 1.3 ppm were positively correlated with monoglycerides ($r = 0.87$, $p < 0.05$), whereas lipids resonating at 2 ppm correlated with all lipid classes but monoglycerides ($r = 0.71$, $p < 0.05$).

For data obtained with the use of HILIC-HRMS in positive ion mode (n = 7), MRS-derived concentrations of glycerol-phosphadylo choline and phospadylocholine were negatively related to concentrations of hexoylceramides, diacylglicerides, phosphatidylcholines, phosphatidyloethanolamine, and phosphatidyloserines in GM ($r < -0.79$, $p < 0.05$), but not in WM. Interestingly, higher combined concentration of *N*-acetyl-aspartate and NAAG in GM, but not in WM, was related to (a) higher concentrations of phospatydyloglicerides, (b) lower concentrations of hexosylceramides, diglicerides, phosphatidyloethanolamines, phosphatidyloserines, and sphingomyelins ($r < -0.86$, $p < 0.05$), but (c) not phosphatidylcholines. Concentrations of lipids were not related to concentrations of any of the lipid classes obtained with chemical biopsy.

Correlation results for data obtained with the use of HILIC-HRMS in positive ion mode demonstrated that concentration of WM lipids resonating at 1.3 ppm correlated positively with concentration of phosphatidyloethanolamines ($r = 0.78$, $p < 0.05$), and negatively with concentration of sphingomyelins and hexosylceramides ($r = -0.78$, $p < 0.05$). Except for negative correlation of Cr with lysophosphatidylcholines in GM ($r = -0.82$, $p < 0.05$) and negative correlation of PCr with lysophosphatidylcholines in WM ($r = -0.86$, $p < 0.05$), no other correlations reached significance.

Discussion: We found associations between ^{1}H-MRS derived metabolite concentrations and concentrations obtained with two methods of lipidomic analyses. The pattern of correlations was different between the analyses, as the two chromatography types detect different groups of lipids. RPLC enabled analysis of glycerides, ceramides and phospholipids, while HILIC majorly phospholipids and sphingolipids. Furthermore, it should be remembered that ^{1}H-MRS is limited to mobile fractions of lipids.

Conclusion: Chemical biopsy may improve the delineation of tumor resection in a minimally invasive manner, which would increase the patient's safety during an operation and decrease the radicalness of the surgery. The improved interpretation of ^{1}H-MRS results may help better understand the spectroscopic results.

The work was supported by Ministry of National Defence of Poland (508/2017/DA).

References:

1. Bitencourt, A., et al., Diagnostics, 2021. **11**(3).
2. Bogusiewicz, J., et al., Scientific Reports, 2021. **11**(1).
3. Bogusiewicz, J., et al., Molecules, 2022. 27(7).

P165.
Apparent diffusion coefficient and blood oxygenation level dependent imaging during neural activity in white and grey matter

J. Nguyen-Duc[1], I. de Riedmatten[1], W. Olszowy[2], I. Jelescu[1]

[1]*CHUV, Radiology, Lausanne, Switzerland;*
[2]*École Polytechnique Fédérale de Lausanne (EPFL), CIBM Center For Biomedical Imaging, Lausanne, Switzerland*

Introduction: Diffusion functional Magnetic Resonance Imaging (dFMRI) is a promising technique for studying brain activity with a contrast more closely related to neuronal activity than the hemodynamic response [1]. It tracks the variation of Apparent Diffusion Coefficient (ADC) induced by neuromorphological coupling, contrarily to Blood Oxygenation Level Dependent (BOLD) imaging that relies on neurovascular coupling. The ADC fluctuations can reveal morphological changes in brain cells during the transition from rest to activity, making dFMRI highly sensitive to microstructure. One of the advantages of dFMRI could be the ability to study white matter (WM) activity, which has fewer blood vessels than grey matter (GM) and where the BOLD response is weak. Mapping WM activity is currently a blind spot for all neuroimaging techniques, whether BOLD fMRI, EEG or MEG. In this study, we compare the ADC timecourses to BOLD timecourses in the human white matter (WM) and grey matter (GM) during visual and motor tasks in the human brain.

Methods: The data used in this study is obtained from a prior investigation [2]. Briefly, 9 subjects were scanned on a 3 T Prisma MRI scanner (Siemens Healthineers). Two imaging modalities were utilized for fMRI: (i) DW-TRSE-EPI with interleaving b-values of 200 and 1000 s/mm^2, leading to ADC timecourses with a temporal resolution of 2 s (300 volumes, TE = 35 ms), and (ii) SE-EPI that yielded T2-BOLD contrast with a temporal resolution of 1 s (600 volumes, TE = 35 ms). The dfMRI sequence (i) was designed to reduce BOLD-like contributions resulting from blood susceptibility changes, which was accomplished by calculating ADC instead of considering plain diffusion- and T2-weighted signals, limiting blood pool contributions with $b > 200$ s/mm^2, and minimizing cross-terms between diffusion and background gradients through the TRSE scheme. During the scanning, participants were instructed to gaze at a cross on the screen for 18 s and tap their fingers with both hands for 12 s while viewing a flashing checkerboard (8 Hz), in 20 repeated blocks. Data processing was conducted according to the procedures described in [2].

Results: The ADC timecourse shows a decrease starting directly from the onset of the task with an amplitude of 0.7% in GM and 0.3% in WM (Fig. 1) while the BOLD response shows a delayed increase of 2%. The BOLD response temporal features appeared to adapt to the temporal features of the ADC response: the latter decreased immediately upon onset (t = 6 s), and gradually up to t = 14 s, before reversing the trend and increasing back to baseline until t = 22 s. In parallel, BOLD started increasing sharply at t = 8 s until t = 14 s, when it gradually leveled off to plateau until t = 22 s, beyond which it sharply decreased to baseline. As for the locations of activation areas (Figs. 2 and 3), those obtained with diffusion fMRI are more sparse and have smaller z-score amplitudes than those with BOLD. BOLD shows clear activation clusters in the visual and motor cortex, with spillover in subcortical WM, whereas ADC also shows activity in the deep WM.

Discussion: The BOLD response amplitude was surprisingly similar for both tissues even though there are more blood vessels in the GM. Inspection of activation maps revealed that the "WM" voxels were adjacent to GM clusters and likely benefited from spill-over, which may explain the similarity. The WM tracts uncovered by ADC-

derived activation maps on the other hand may display connections that are crucial during the visually induced motor task. The difference in amplitude in the ADC decrease between the WM and GM could be due to the difference in the microstructural fluctuations between tissues, with possible contributions from both neurons and astrocytes in GM, and preferentially astrocytes in the WM assuming myelinated axons are more rigid. The single arbitrary direction of diffusion-weighting used in the acquisition may also introduce spatially variable sensitivity in WM depending on the orientation of WM fibers. Using higher b values may have increased the amplitude of the ADC decrease, as observed in cats in [3].

Conclusion: The features of ADC and BOLD responses during neuronal activity were studied, with a focus on deep white matter activity, which is not visible with BOLD alone. BOLD imaging reveals activity in the visual and motor cortex, while ADC also shows some white matter activity. In further works, we will focus on maximizing dfMRI sensitivity throughout all of WM irrespective of fiber orientation, and on investigating whether the WM activation clusters are positioned along tracts that link GM regions involved in the task. This may increase our understanding on the connecting pathways that become active during visual and motor tasks.

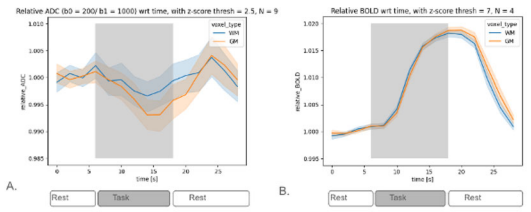

Fig. 1: The ADC and BOLD signals in white and grey matter averaged per subject during the experiment, relative to the baseline (mean of the 6 first seconds of the trial). The confidence interval at 95% is represented by the shaded area. For each volunteer, the average time-course of significant voxels within the white and grey matter is averaged across trials. Then, subject-level estimates are normalized to a baseline level and averaged across the cohort[2]. Each epoch is 30 seconds long and repeated 20 times per subject (10 minutes in total).

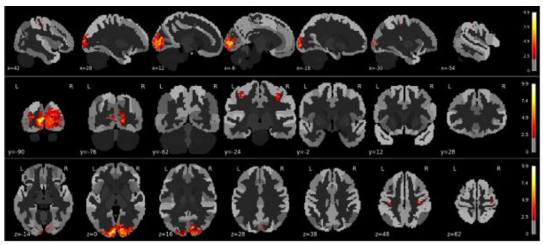

Fig. 2: Averaged z-scores across 4 subjects with the BOLD signal, placed over the standard MNI template. Enhanced activity can be observed in the visual and motor cortex as the motor task is initiated with a strong visual stimulus.

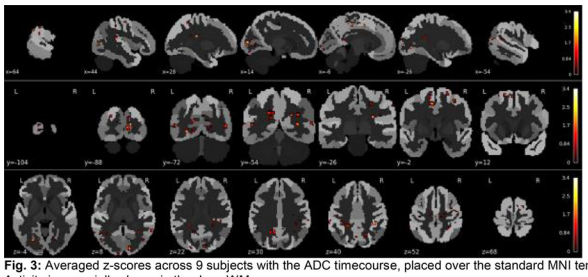

Fig. 3: Averaged z-scores across 9 subjects with the ADC timecourse, placed over the standard MNI template. Activity is especially shown in the deep WM.

References:

[1] Denis Le Bihan et al., Proceedings of the National Academy of Sciences, 2006.
[2] Wiktor Olszowy et al., bioRxiv, 2021.
[3] Essa Yacoub et al., Magnetic Resonance Imaging, 2008

P166.
Data-driven signal analysis of sensory cortical processing using high-resolution fMRI

B. Pradier[1], L. Plagwitz[2], J. Varghese[2], C. Faber[1]

[1]*Translational Research Imaging Center, Clinic of Radiology, University Hospital Muenster, Münster, Germany;*
[2]*Institute of Medical Informatics, University of Muenster, Münster, Germany*

Introduction: Analysis of functional magnetic resonance imaging (fMRI) data is challenging due to the large amount of measured signals and the low signal-to-noise ratio (SNR). Data-driven approaches are becoming more prevalent since they quickly provide insights despite complexity of the datasets. Furthermore, these approaches have the potential to reveal novel patterns, including temporal kinetics, in blood-oxygen-level-dependent (BOLD) time series. We used line scanning fMRI measurements with high temporal (50 ms) and spatial (78 µm) resolution obtained from a previous study (1) and investigated the added value of different unbiased time series clustering techniques for the analysis of somatosensory processing during electrical paw stimulation and optogenetic stimulation of the cortex.

Methods: 9 female Fisher rats (157–202 g) were used in this study. MRI measurements were conducted on a 9.4 T Bruker Biospec 94/20 small animal scanner using a 10-mm surface coil (Fig. 1A). Functional MR acquisitions were recorded with a GE-EPI sequence without phase encoding (TR/TE: 50/18 ms, FA: 13°, 1.2 mm slice thick., FOV: 10 × 2.1 mm, resolution: 78 µm) as described earlier (2). Line scanning experiments were conducted under medetomidine sedation (0.04 mg/kg bolus, 0.05 mg/kg*h continuous) with two stimulation modalities: electrical fore paw stimulation (9 Hz/1.5 mA) and optogenetic stimulation of the cortex (9 Hz/70–100 mW/mm^2) using a block design (10–5–15 s) with 64 repetitions. For the latter, animals were injected with a viral construct (AAV2/CamKIIa-C1V1) into the primary somatosensory fore limb cortex (S1FL) to allow expression of the excitatory channelrhodopsin variant C1V1. For data analysis, time series were filtered and averaged over the stimulus repetitions (Fig. 1B). First, we calculated the similarity distance in unscaled time series using Euclidean and correlation distance metrics in an interval twice the stimulus period (Fig. 1C, left). Next, to focus on temporal characteristics of BOLD responses, the series were scaled and analyzed with Euclidean distance and dynamic time warping at different time intervals (DTW, Fig. 1C, right). Based on the computed distances, voxels were partitioned using hierarchical agglomerative clustering for the cluster formation ((3), Fig. 1D). For visualization, data were aligned to the corpus callosum (CC) and cluster probability profiles (CPP) were calculated that map the cluster group (1, 2 or 3) for each voxel and scan onto a standardized line spanning S1FL, CC and striatum.

Results: Using the correlation metric, we identified time series with positive (red) and negative (blue) signs (Fig. 2A, left). These clusters were spatially segregated into voxels that were dorsal (d, red) or ventral (v, blue) to the CC as shown in the CPP plot, thereby providing the possibility to discriminate cortical from sub-cortical clusters (Fig. 2A, right). Using the Euclidean distance, we detected four cortical clusters: three were characterized by increasing positive amplitudes that contrasted with a neutral cluster (white, Fig. 2b, left). We observed a gradient along the d-v axis in the S1FL and found time series with larger amplitudes in the dorsal cortex (Fig. 2b, right). To

gain information on temporal kinetics of the BOLD responses we performed Euclidian-based clustering of the interval 1–3 s following the stimulation on scaled positive time series (Fig. 3a, left). Red clusters collected fast responses, orange clusters represented medium and blue delayed ones. Like before, we detected a gradient in the d-v axis of the cortex with the fastest clusters (red) in the dorsal-most area of the cortex (Fig. 3a, right). Next, we studied the decay characteristic of BOLD signals using the DTW distance. These clusters segregated during the second half of the considered time interval (gray shaded area) according to their decay characteristics (Fig. 3b).

Discussion: Depending on the similarity formulation, our results show that multiple patterns in BOLD time series can be revealed and that this workflow produces consistent results across modalities. Further, we introduce a statistical analysis that is entirely based on cluster distribution; each cluster represents a set of BOLD response parameters instead of single parameters, which makes this procedure more robust and generalizable. Importantly, we find that this analysis validates previous study results using a completely data-driven approach (1).

Conclusion: All in all, our data-driven approach proves high sensitivity, robustness, and reproducibility; it further quickly provides highly detailed insight into characteristics of BOLD time series and—in theory—also allows statistical comparison across different study protocols. Therefore, it holds great potential for further applications in fMRI including whole-brain task and resting-state fMRI to support fMRI routines.

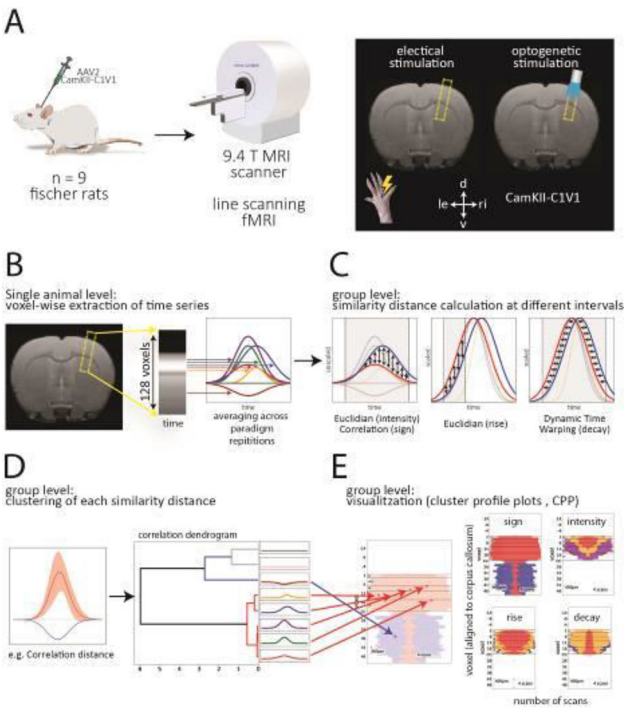

Fig. 1: (A): Study design. (B-E) workflow for data analysis.

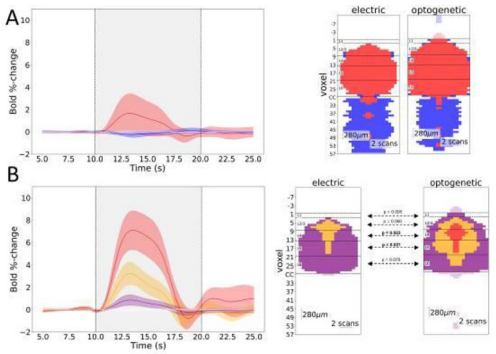

Fig. 2: General aspects of BOLD time series. (A) Correlation metric reliably separates positive and negative responses. (B) The Euclidean metric separated time series according to BOLD amplitude characteristics. A layer-wise statistical comparison of cluster distribution between both stimulations revealed significantly higher signal intensities following optogenetic stimulation in cortical L4 and 5 (Mann-Whitney U (M-WU), $p < 0.05$).

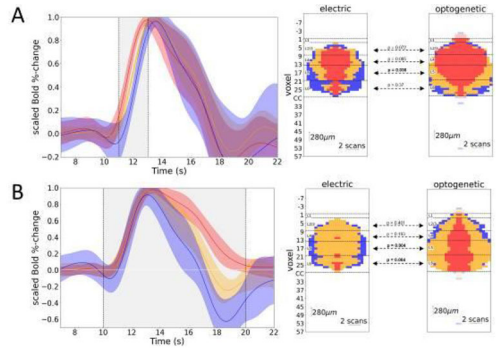

Fig. 3: Rise and decay characteristics of BOLD time series. (A) Using the Euclidean metric during the rising phase, we found an overall higher incidence of clusters with faster rise levels following optogenetic stimulation, which was statistically significant in layer V (M-WU, $p < 0.05$, Fig. 3a). (B) The DTW metric identified clusters with the slowest decay characteristic (red) almost exclusively following optogenetic stimulation. This effect was significant in the LV and VI (M-WU, $p < 0.05$).

References:

1. Albers et al. 2018
2. Yu et al. 2014
3. Ward et al. 1963

P167.

Functional CBV measurements based on T2 relaxation enhancement after administration of H217O

L. Wachsmuth[1], H. F. Chen[1], B. Pradier[1], H. Lambers[1], C. Faber[1]

[1]*University of Münster, Clinic of Radiology, Münster, Germany*

Introduction: Brain activation upon sensory stimulation in both rodents and men is most commonly measured using Blood oxygenation dependent (BOLD) functional MRI. However, in particular in mice, sensitivity is limited. Techniques to measure cerebral blood volume (CBV) in rodents offer higher sensitivity compared to BOLD, but require intravenous (i.v.) application of iron particles. Here, we introduce $H_2{}^{17}O$ as an alternative reporter for CBV changes. $H_2{}^{17}O$ can be detected indirectly in ^1H MRI, because ^{17}O–^1H scalar coupling and proton chemical exchange effectively reduce proton T_2 [1]. Previous studies applied 17O proton MRI for measuring cerebral blood

flow [2]. Here, we explore this approach for functional CBV measurements.

Methods: ^{1}H MRI was conducted at 9.4 T (Biospec, Cryoprobe) with 14 C57/BL6 mice of both sexes under Medetomidine-Isoflurane anesthesia. We applied pinprick stimulation (stim) (10 cycles, 10 s stim, 20 or 30 s rest) of one hindpaw with a custom-made stimulator. BOLD fMRI (TR/TE/FA 1000/18 ms /60°, 18 slices, 200 μm^2, 0.5 mm slice thickness (sth)) was acquired for Reference. Dynamic cortex signal after i.v. application of $H_2{}^{17}O$ (diluted to 80% with saline to physiological osmolarity) was monitored by T2w RARE (20-60 min, TR/TE 3000/62 ms, 48 s/cycle, resolution (res) 125 × 125 μm^2, sth 0.42 mm). Functional imaging was performed using T2w single shot SE-EPI (TR/TE 1000/50 ms, res 296 × 296 μm^2, sth 1 mm). T2*w GE-EPI (TR/TE 1000/10.5 ms, FA 60°) from four animals (dynamic and upon pinprick stim) was obtained after i.v. injection of iron particles (SPIO, MoldayIon, 20 mg Fe/kg). Preprocessing was performed using SPM, functional analysis using MatLab.

Results: Cortical signal loss was detected in ^{1}H MRI after i.v. $H_2{}^{17}O$ injection, but was less pronounced than after injection of SPIO (Fig. 1). A stable signal level of 95% pre-contrast level was reached within 10 min and persisted for at least 60 min, enabling functional measurements. CBV with $H_2{}^{17}O$ and with SPIO had higher success rates and higher signal amplitudes compared to BOLD. In 8/14 SE-EPI experiments signal time courses upon sensory stim showed a hemodynamic response. On average 19 voxels (7-30 voxels in 8 experiments) in the S1HL region showed significant signal drop compared to baseline (U-test, $\alpha = 0.05$). Negative signal amplitude of averaged time course of 1.5% (Fig. 2) was close to the Reference value of 1.9% obtained after SPIO injection.

Discussion: In contrast to previous assertions that $H_2{}^{17}O$ quickly distributes throughout tissue, our results suggest that most $H_2{}^{17}O$ remains intravascular, enabling functional CBV measurements. This observation is in line with the lack of a concentration gradient that would drive diffusion into brain tissue. Stimulus-induced CBV-changes, therefore, lead to enhanced T2 relaxation, which is detectable as reduced signal in T2w ^{1}H MRI.

Conclusion: We provide proof of concept that $H_2{}^{17}O$ can be used as sensitive reporter for functional CBV measurements. The new approach based on measuring T2 effects in ^{1}H MRI after i.v. application of $H_2{}^{17}O$ water has no impact on animal physiology. Further, T2w SE-EPI is less prone to geometric distortions than GE-based methods. Contrary to iron-based CBV measurement, $H_2{}^{17}O$ can be safely applied in humans. Its use, however, is currently limited by costs of $H_2{}^{17}O$.

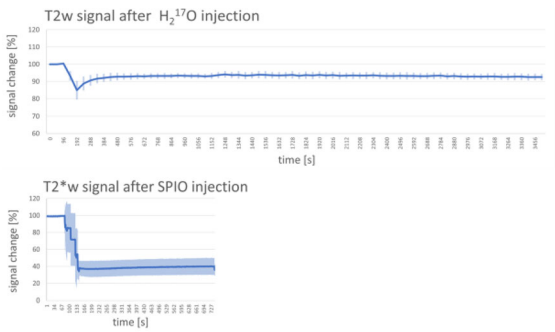

Fig. 1: Average percent cortex signal change from baseline after i.v. injection of 150 μL of **(A)** 80% $H_2{}^{17}O$ (n=14, mean ± SD, SE-EPI) or **(B)** 20 mg/kg Fe (n=4, GE-EPI) over time. Although the negative signal amplitudes differed considerably, with both agents a stable signal level was reached within 10 minutes and persisted for at least 1 hour.

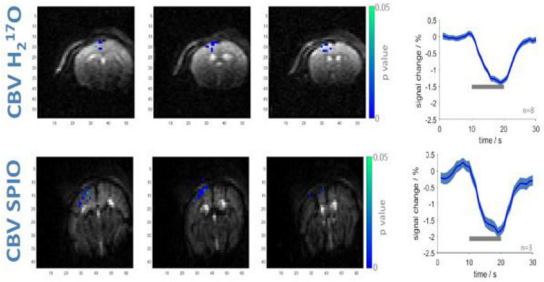

Fig. 2: (Left) Respresentative activation maps upon 10 s pinprick stimulation after i.v. $H_2{}^{17}O$ (SE-EPI) or SPIO (GE-EPI) injection. **(Right)** Average time courses of measurements upon pinprick stimulation (stimulation period indicated by grey bar) after $H_2{}^{17}O$ or SPIO i.v. bolus injection (mean ± SEM).

References:

1. Meiboom S. NMR study of the proton transfer in water. J. Chem. Phys. 1961; 34: 375–388.
2. Zhu XH, Zhang N, Zhang Y, Zhang X, Ugurbil K, Chen W. In vivo ^{17}O NMR approaches for brain study at high field. NMR Biomed. 2005; 18(2):83–103.

P168.
MR-based objective assessment of COVID-19 olfactory rehabilitation based on VBM, fMRI, DTI and ASL

P. García-Polo[1,2], J. Díaz Pereira[2], A. Matamoros Alonso[2], A. Toledano[3], C. Gómez[3], M. Jiménez[4], V. Martínez de Vega[4], S. Borromeo López[2], A. Torrado-Carvajal[2]

[1]*GE Healthcare, Madrid, Spain;*
[2]*University Rey Juan Carlos, Móstoles, Spain;*
[3]*Hospital Universitario Fundación de Alcorcón, Alcorcón, Spain;*
[4]*Hospital Universitario Quirsonsalud, Madrid, Spain*

Introduction: Studies have found that over 50% of COVID-19 patients experience sudden loss of smell (anosmia), higher than other respiratory diseases. Olfactory rehabilitation is a promising approach to treatment and the Connecticut Chemosensorial Clinical Research Centre test is currently used to assess olfactory function. This work explores the use of fully synchronized olfactory fMRI and studies anatomical, connectivity and perfusion changes as an objective tool to assess the physiological activation of the olfactory system and related areas after rehabilitation therapy.

Methods: As part of an IRB approved study, MRI data from 4 female patients ranged 45-54y, that presented persistent olfactory loss after COVID-19 infection, was acquired on a 3 T Signa Premier (GE Healthcare, Waukesha, USA) at Hospital Quironsalud (Madrid, Spain), after obtaining written informed consent.

Participants underwent a targeted olfactory rehabilitation therapy of 10 sessions over 2.5 months; MRI data were obtained prior to the start of the therapy and after the end of the therapy.

The MRI protocol included an anatomical 3D-T1-MPRAGE (1 mm iso-voxel), a CUBE T2-FLAIR, a 10 min fMRI study (TR = 1 s, TE = 20.6 ms, FOV = 22 cm, voxel size 2.3 mm iso, flip angle = 62°, HyperBand factor = 3, ASSET factor = 2) fully synchronized with the scanner trigger and respiratory belt delivered two different odors (mint and vanilla) randomized in an event-related fashion within the duration of the study, a diffusion HARDI scheme (150 directions, b-value = 1500 s/mm2), and a pcASL scheme (PLD = 1.45 s, labeling time = 1.5 s) sequences.

SPM12 was used to segment the structural MPRAGE T1 images and to realign, coregister and run a first and second analysis (paired t-test) on the fMRI images.

DSI Studio was used to segment diffusion-weighted images, reconstruct and normalize diffusion tensor scalar maps. Longitudinal changes in fractional anisotropy (FA) and mean diffusivity (MD) were evaluated for each patient with differential tractography. Next, group analysis using correlational tractography was performed.

Acquired ASL volumes (proton-weighted, M0, and perfusion-weighted) were used to obtain the Cerebral Blood Flow (CBF) maps. These were analyzed using SPM12 performing a paired t test to obtain changes in perfusion after rehabilitation. ANCOVA technique was used to neglect basal perfusion in subjects.

Results: VBM analyses show increased volumes in the cerebellum, temporal lobe, parahippocampal region and cuneus at therapy onset, which may be related to inflammation due to virus infection (Fig. 1). Brain regions involved in olfactory rehabilitation such as the fusiform gyrus, caudate and orbital gyrus also changed in volume. Olfactory rehabilitation therapy has an impact on the activation of several brain areas after odorant delivery, including parahippocampal gyrus, frontal gyrus, amygdala, caudate, putamen and insula [1] (Fig. 2).

The correlational tractography analysis (T-score = 2.5) showed increased FA (red) in Corpus Callosum Forceps Minor and Arcuate Fasciculus and decreased MD (blue) in Corpus Callosum Forceps Major, Middle Cerebellar Peduncle, and Fornix (Fig. 3).

Perfusion analyses shows perfusion increment in the right hemisphere of the pons, the cerebellum and the dorsolateral right prefrontal cortex (p value = 0.05). Without ANCOVA, equal results with bigger clusters of significant voxels appear. It shows a significant cluster on the right occipital lobe and posterior region of the parietal lobe (p value = 0.02) (Fig. 4).

Discussion: Changes seen in volumetry could be caused by inflammatory processes that decline during the time of rehabilitation with the counterpart of increased volumes in the areas targeted in the olfactory rehabilitation. Functional changes are correlated with patient qualitative scores on rough odor discrimination and threshold activation. Diffusion measures indicate improved white matter connectivity in pathways related to brain regions affected by COVID-19 in anosmic patients, consistent with previous studies [2]. Perfusion increases in the cerebellum, dorsolateral prefrontal cortex [3], and occipital lobe might indicate the efficacy of olfactory therapy.

Conclusion: Olfactory therapy proves to be useful in olfactory rehabilitation for COVID-19 patients suffering anosmia and fMRI, VBM, DTI and ASL assessment provide the necessary tools to perform a comprehensive and complete analysis of the effects of the therapy.

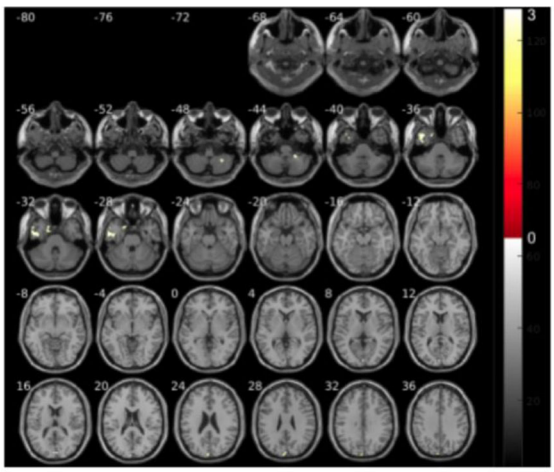

Fig. 1: Areas with a decrease in volume after rehabilitacion therapy (2.5months). These regions may be affected by neuroinflammatory process (p_{unc}<0.05)

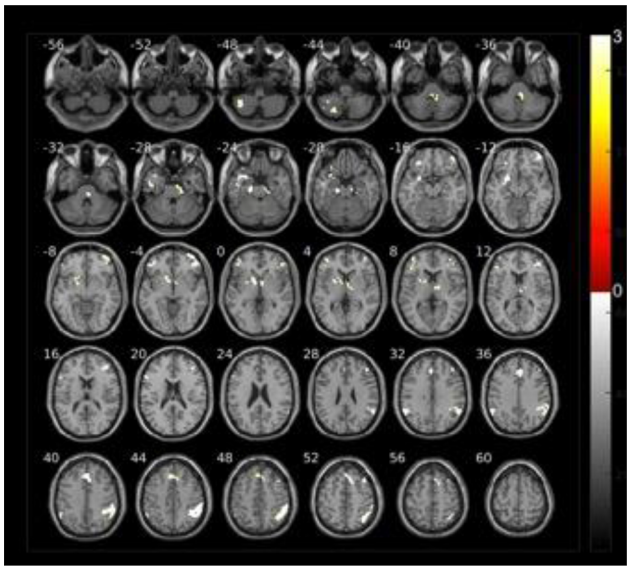

Fig. 2: Olfactory fMRI changes after rehabilitation therapy (p_{unc}<0.05)

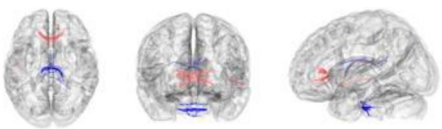

Fig. 3: The correlational tractography analysis (T-score = 2.5) showed increased FA (red) in Corpus Callosum Forceps Minor and Arcuate Fasciculus and decreased MD (blue) in Corpus Callosum Forceps Major, Middle Cerebellar Peduncle, and Fornix.

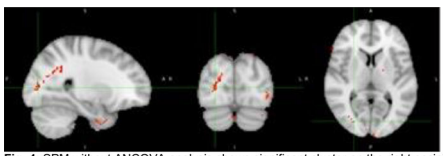

Fig. 4: SPM without ANCOVA analysis shows significant cluster on the right occipital lobe and posterior parietal lobe (p-value = 0.02)

References:

1. Savic, Ivanka, et al. "Olfactory functions are mediated by parallel and hierarchical processing." Neuron 26.3 (2000): 735-745.

2. Kremer, Stéphane, et al. "Brain MRI findings in severe COVID-19: a retrospective observational study." Radiology 297.2 (2020): E242-E251.

3. Dogahe, Mohammad Haghani, et al. "Magnetic Resonance Spectroscopy Findings of Brain Olfactory Areas in Patients with COVID-19 Related Anosmia: a Preliminary Comparative Study." Authorea Preprints (2022).

P169.
Assessing susceptibility artifacts of adhesives for simultaneous optic fiber-based recordings and fMRI

A. Z. Szinyei[1], B. Maus[1], H. F. Chen[1], L. Wachsmuth[1], B. Pradier[1], C. Faber[1]

[1]*University of Münster, Clinic of Radiology. Translational Imaging Center, Münster, Germany*

Introduction: The combination of optic fiber photometry with functional MRI (ofMRI) allows for studying local cell-specific neural activity in the context of whole-brain processing. The glue for fiber fixation should provide low magnetic susceptibility, combined with fast curing and strong adhesive properties. While ofMRI is well established in rats, such experiments are more challenging to perform in mice: The impact of susceptibility effects caused by the glue may be tolerated in larger rat brains but may compromise ofMRI of smaller mouse brains.[1] This effect is particularly prominent at higher field strengths.[2] Since fMRI employs T2*-weighted sequences, like gradient echo (GE) EPI, to detect the BOLD response, the application of such adhesives may preclude a combined ofMRI approach. We therefore examined the susceptibility effects of adhesives on phantoms with a T2*w GE-EPI sequence to evaluate the best candidates for combined ofMRI experiments.

Methods: MRI phantoms were made from 20 mL polypropylene syringes (Ø = 2 cm) filled with 1% agarose. 31 adhesives from different areas of use were applied on the syringe surface in three different amounts per adhesive (Fig. 1). The amounts simulated realistic needs to fix an optical fiber to the mouse skull. MRI was performed on a 9.4 T Bruker BioSpec 94/20 small animal scanner using a multi-slice single-shot T2*w GE-EPI and standard scan parameters for mouse fMRI (TE = 18 ms, TR = 1000 ms, FA = 60°, 18 slices, 0.5 mm thickness, 300 mm isotropic resolution, BW = 200 kHz). The magnitude of the susceptibility artifact was determined by volumetric analysis of the signal void underneath the adhesive: The position of half-maximum was determined in an intensity profile over the syringe cross section. This distance was related to the diameter of the signal void at the syringe surface and used to define an adhesive"s susceptibility effect as extent of signal void (Fig. 1). One light-curing dental acrylic was applied to investigate the effect of shape on the in vivo susceptibility artifact (Fig. 2).

Results: Susceptibility effects were lowest for silicone-based glues ($magnitude_{min}$ = 0.06 mm/mm^2), followed by cement-based medical glues ($magnitude_{min}$ = 0.10 mm/mm^2), industrial acrylics ($magnitude_{min}$ = 0.21 mm/mm^2) and nail acrylics ($magnitude_{min}$ = 0.23 mm/mm^2; Fig. 3). While all classes of glues displayed a range of susceptibility effects, the widest range and largest overall susceptibility effects were found for dental adhesives containing radiopaque and inorganic compounds to adjust adhesive properties (filled glues, magnitude = 0.29–1.37 mm/mm^2). Even though some industrial acrylics had decent susceptibility properties, they proved difficult to apply on a mouse skull, had long drying times and lacked biocompatibility. Silicone-based glues detached from the mouse skull easily, while cement-based medical adhesives (bone cement and dental cement), nail acrylics and all other dental adhesives withstood normal mouse handling procedures. Cement-based medical adhesives required a curing time of 5 min after two-component-mixing. Most dental adhesives and nail acrylics were light-cured (curing time = 40 s). Dental wax could only be applied at ~ 80 °C. The shape of the applied glue had a considerable impact on the magnitude of the susceptibility artifact. Smaller, concave glue spots of an unfilled dental acrylic lead to negligible signal voids in vivo, while spherical spots of that glue incurred signal voids reaching 1 mm into the cortex (Fig. 2).

Discussion: While silicone glues caused the smallest susceptibility artifacts compared to other glues, their low adhesion to the mouse skull makes them impractical for in vivo MRI, where handling time and space in the scanner are limited. Cement-based medical adhesives combine low susceptibility with high adhesion but are usually two-component glues with 5-10 min drying time and are difficult to apply in desired shapes. Dental adhesives provide good application properties, adhesion and curing times, with minimal susceptibility effects found in the subgroup of dental acrylics without inorganic filling or radiopaque supplements (group 5.1; Fig. 3). The signal voids of these glues can be further reduced by concave application of the glue, which is paramount for the smaller skulls of mice compared to rats. Industrial glues containing methacrylate are usually precluded from animal experiments due to their lack of biocompatibility.

Conclusion: Dental acrylics without radiopaque or inorganic compounds and applied in shapes with a concave surface combine low susceptibility, fast curing and strong adhesion, making them best suitable for mouse ofMRI.

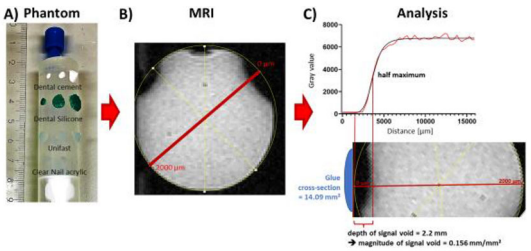

Fig. 1: A) Different amounts of adhesives applied on a polypropylene syringe filled with 1% agarose. B) T2*-weighted MRI of axial slice placed at the center of one type of glue. The syringe outline (2 cm) was fit to the MR image. Numbers = different glue spots. C) Signal-void-limits of glue spots were defined as 50% signal loss from the radial signal (red trajectory).

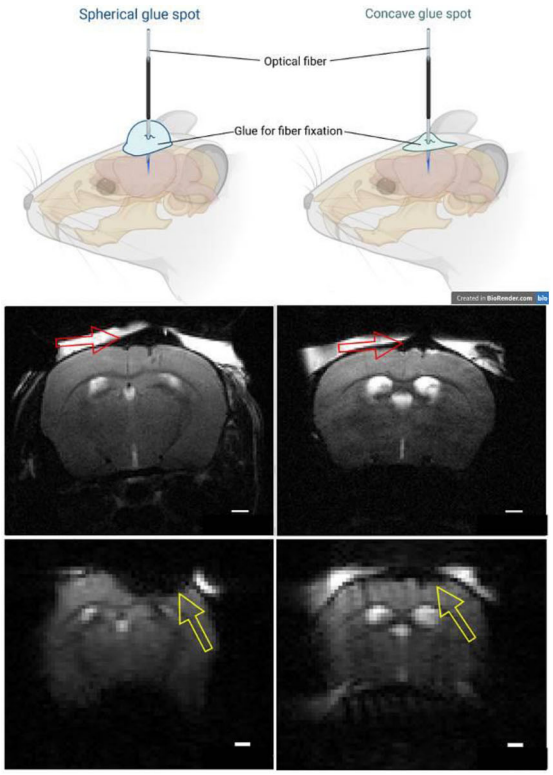

Fig. 2: Fibers were fixed to mouse skulls with either large, spherical (left) or small, concave (right) amounts of adhesive 5.1.1 (top). T2w anatomy (middle) and T2*-EPI scans (bottom) of the fiber implantation site (S1HL cortex). Glue shape is visible as hypointense area above the skull (red arrows), embedded in 1% agarose to further suppress susceptibility effects in functional EPI images (yellow arrows). Created with BioRender.com.

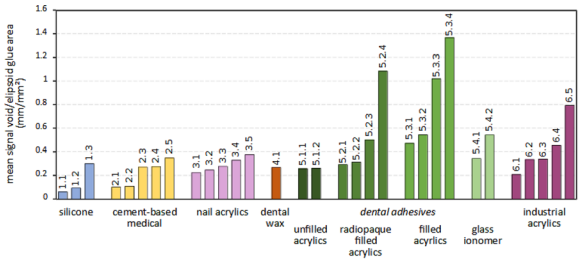

Fig. 3: Comparison of susceptibility artifact magnitudes (for definition see Fig. 1). 31 different adhesives were assessed, including 4 different classes of dental adhesives (green bars).

References:
[1]Ioanas et al. (2022) Hybrid fiber optic-fMRI for multimodal cell-specific recording and manipulation of neural activity in rodents. Neurophotonics. 9(3):032206
[2]Schlegel et al. (2018) Fiber-optic fluorescence-based calcium recordings and BOLD fMRI in mice. Nat Proto. 13:840-855

P170.
The effect of NORDIC denoising on high-resolution fMRI data at 7 T

V. Pfaffenrot[1], D. G. Norris[2,1]

[1]*University of Duisburg-Essen, Erwin L. Hahn Institute for Magnetic Resonance Imaging, Essen, Germany;*
[2]*Radboud University, Donders Institute, Nijmegen, Netherlands*

Introduction: High-resolution fMRI even at 7 T suffers from thermal rather than physiological noise. The NORDIC PCA filter 1, 2 removes signal components indistinguishable from zero-mean Gaussian noise. Recently, the feasibility of NORDIC for laminar fMRI at 3 T was demonstrated.3 Here we aim to evaluate the performance of NORDIC for laminar fMRI at 7 T and examine whether the spatial fidelity of laminar profiles is preserved when applying NORDIC.

Methods: Laminar fMRI data from one male subject (32 years old) were acquired using a 3D GRE-EPI sequence4 at a 7 T (MAGNETOM Terra, Siemens Healthcare, Erlangen, Germany) scanner. A 256 × 256 × 72 matrix was scanned at 0.75 mm isotropic resolution at a TE = 22.5 ms and a volume TR of 2.1 s. The echo spacing was 1.05 ms (1086 Hz/Px bandwidth). An acceleration factor of R = 4 × 2, with a CAIPI shift of 1 and a partial Fourier (PF) factor of 6/8 were used. We performed a flickering checkerboard fMRI experiment split into 3 runs, each 14:28 min long, resulting in 400 volumes per run.

Magnitude and phase images were reconstructed using adaptive coil combination and eigenvalue decomposition with coil sensitivity phase correction from a separate adjustment. PF reconstruction used the POCS algorithm.

Different NORDIC settings (https://github.com/SteenMoeller/NORDIC_Raw downloaded 06122021) were compared:

G-factor noise map was estimated from a Marchenko-Pastur PCA (MPPCA) implemented in the NORDIC algorithm ("implicit g-map") G-factor noise map was taken from the vendor-provided IcePAT reconstruction pipeline (referred to as "NORDIC"). Noise threshold was estimated taking complex differences between time-points and testing for normality. We additionally investigated two cases where 6/8 and 4/8 of the noise level was taken. We tested the effect of a finer patch size of 73 against the standard of 113.

Structural data were acquired with an MP2RAGE sequence and processed with FreeSurfer to estimate WM and pial surface boundaries. Functional data were processed using ANTs. Coregistration was performed with ITK-SNAP. The processed functional data were equidistantly sampled between WM and pial boundary to create laminar profiles with SPM12.

Results: Figure 1 shows differences between beta-maps obtained from smoothed data (2.25 mm isotropic kernel). A T2* map shown in 1C highlights large venous vessels. The differences indicate a mild loss of signal variations of interest. The amount scales with the assumed noise level, i.e. the higher the assumed noise level, the worse the effect (1F,G). A smaller patch size increases the amount of removed signal variation of interest (1H). Interestingly, the bulk of variation removal is collocated with large venous vessels.

In Fig. 2A, signal change laminar profiles taken from all volumes are shown for Reference (dark blue line, best seen in zoomed inlay) and for the NORDIC variations. With the exception of the analysis with 1/2 of the noise threshold, all variations of NORDIC affect the profiles. This effect scales with the noise threshold and the patch size. NORDIC using the implicitly estimated g-factor affects the profiles more than using the vendor provided one. The profiles" shape and the effect NORDIC has on them is to a large extent independent of the number of volumes used in the GLM (2B-F) until the GLM fitting becomes unreliable (2F). Here, NORDIC can recover some signal change (profiles with NORDIC more accurate than Reference).

Discussion: All investigated variations of NORDIC preserve the spatial resolution, but NORDIC removes some signal variations of interest, as previously found at 3 T. 3 Careful estimation of the g-factor as well as the noise threshold can reduce the amount of signal removed. As voxels are pooled from a larger area in laminar fMRI, the final layer profiles and the effect NORDIC has on them are largely unaffected by reducing the number of volumes, also due to the strong effect size of the visual experiment.

Acknowledgements
This work was funded by Mercur grant Ko-2021-0010 and DFG grant 432657511.

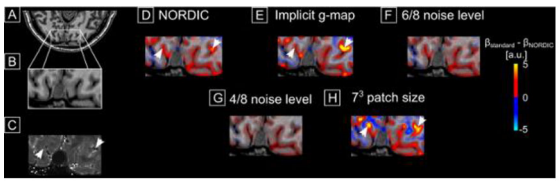

Fig. 1: (A-B) Anatomical Reference, (C), T2*-map showing large veins (white arrows). (D-H) Differences between β-maps (standard-NORDIC) obtained from smoothed data showing a small removal of wanted signal variation with NORDIC scaling with estimated noise level, patch size and g-map accuracy. The bulk of signal variation removal seems to be collocated with larger veins.

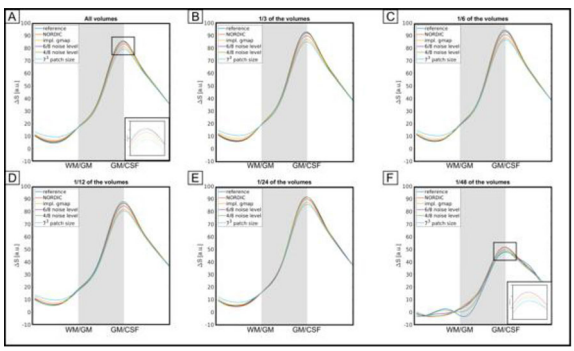

Fig. 2: (A) Cortical depth-dependent signal change for the Reference (dark blue line) and the NORDIC variations using all volumes in a GLM. NORDIC does affect the shape of the profiles, the most to be seen at the pial surface. (B-F) Profiles for varying fractions of volumes used in the GLM. The profiles and the effect NORDIC has on them are to a large extent independent of the number of volumes until the GLM fitting becomes too unreliable (F). Here, NORDIC can recover some signal change.

References:
1. Moeller, S. et al. NOise reduction with DIstribution Corrected (NORDIC) PCA in dMRI with complex-valued parameter-free locally low-rank processing. *Neuroimage* **226**, (2021).
2. Vizioli, L. et al. Lowering the thermal noise barrier in functional brain mapping with magnetic resonance imaging. *Nat. Commun.* **12**, (2021).
3. Knudsen, L. et al. Feasibility of 3 T layer-dependent fMRI with GE-BOLD using NORDIC and phase regression. *bioRxiv* 1–26 (2022).
4. Stirnberg, R. & Stöcker, T. Segmented K-space blipped-controlled aliasing in parallel imaging for high spatiotemporal resolution EPI. *Magn. Reson. Med.* **85**, 1540–1551 (2021).

P171.
Off-resonance magnetization transfer (MT) fMRI at 7 T using 3D stack-of-spiral acquisitions: initial attempts and results

D. Kurban[1], A. Monreal-Madrigal[1], V. Pfaffenrot[2], D. Ivanov[1], B. A. Poser[1]

[1]*Maastricht University, Maastricht, Netherlands;*
[2]*University of Duisburg-Essen, Erwin L. Hahn Institute for Magnetic Resonance Imaging, Essen, Germany*

Introduction: Laminar fMRI is conventionally performed with GE-BOLD acquisitions due to their high sensitivity. However, spatial specificity of the BOLD signal is limited due to the signal bias towards the ascending and pial veins. In order to reduce the effect of these spatially non-specific contributions, cerebral blood volume (CBV) weighted acquisition strategies have been proposed. CBV-weighted signal is expected to originate from the microvasculature, colocalized with neural activity. The popular vascular space occupancy (VASO) method achieves CBV weighting by nulling the blood signal [1, 2], whereas magnetization transfer (MT) based methods saturate the gray matter signal directly, leaving the blood signal largely unaffected [3, 4]. Pfaffenrot et al. [4] showed with an off-resonance MT-prepared 3D ME-FLASH readout that extravascular (EV) contributions can be reduced and a signal more specific to the microvasculature can be sampled at short echo times (TE). The method should therefore benefit from spiral-out acquisitions which we explore in this work with an off-resonance MT-prepared 3D stack-of-spirals readout in order to investigate the possibility of an MT-weighted, fast, laminar fMRI sequence with higher specificity than BOLD contrast.

Methods: The spiral MT sequence was developed in-house using the open-source sequence development environment Pulseq [5]. The MT preparation consists of a 4 ms, − 650 Hz off-resonance Gaussian RF pulse. The MT pulse was played out every 200 ms. 3D stack-of-spirals readout is employed with a variable density spiral-out trajectory and center-out kz sampling. Functional data were acquired on one volunteer at 7 T (Siemens Healthineers). The acquisition parameters were as follows: FOV = $(192\ \text{mm})^2$, $0.8 \times 0.8 \times 1.0\text{mm}^3$, TR_{vol} = 1.5 s, 24 slices, TE_{min} = 2.5 ms. One run was acquired with MT-on and MT-off (BOLD), respectively. The participant was shown a flickering-checkerboard stimulus during which they performed finger tapping. Images were reconstructed using the MRIReco.jl package, including static B0 correction. The functional data is aligned to a T1-weighted image acquired in the same session using the same spiral readout for matching geometrical distortions. GLM analysis was performed using FSL-FEAT. Layer profiles are obtained using LAYNII software within a hand-drawn ROI in the visual cortex. No smoothing was performed.

Results and discussion: In MT-on run signal attenuation was observed in white and to a lesser extent, gray matter. Even though both MT-on and MT-off acquisitions resulted in images with sufficient SNR, blurring, strong geometric distortions near air-tissue boundaries and fat artifacts cause strong degradation in image quality, especially in inferior slices (Fig. 1). Overall the MT-on acquisition resulted in less activation in veins compared to MT-off (Fig. 2). However, the laminar activation profiles obtained from various ROIs in the visual cortex did not yield to any significant differences between MT-on versus MT-off acquisitions. This might be due to the long readout, where most of the higher spatial frequencies are sampled under stronger T2* effects (> 4 ms) [4]. Moving forward, segmented spirals and higher undersampling factors can be employed to reduce readout duration. Fat artifacts can be tackled with water-selective excitation pulses without running into further SAR issues.

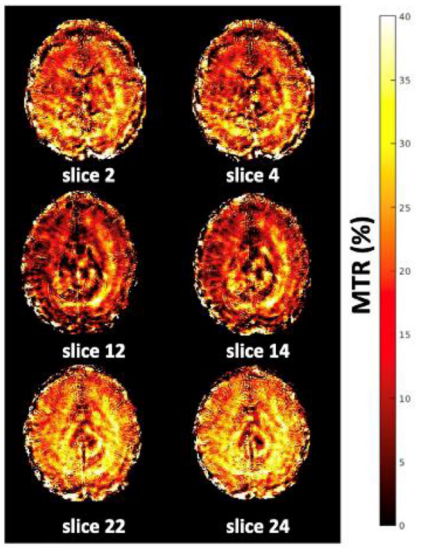

Fig. 1: MTR calculated as [1 - MTon / MToff] shown on inferior, middle and superior slices.

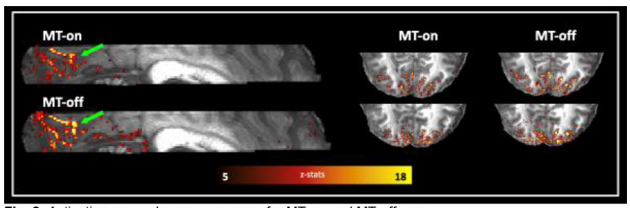

Fig. 2: Activation maps shown as z-scores for MT-on and MT-off runs.

P172.
Proprioceptive engagement in the human cerebellum using 7 T-fMRI

E. Brouwer[1,2], J. Hashimoto[1,3], N. Priovoulos[1,2], W. van der Zwaag[1,2]

[1]*Amsterdam UMC, Spinoza Centre for Neuroimaging, Amsterdam, Netherlands;*
[2]*Netherlands Institute for Neuroscience, Computational Cognitive Neuroscience and Neuroimaging, Amsterdam, Netherlands;*
[3]*Amsterdam UMC, Amsterdam, Netherlands*

Introduction: The human cerebellum forms an important part of sensory and motor networks[1,2]. Multiple diseases affect the cerebellum, often leading to motor impairment[3,4,5]. An important part of motor control is proprioception: the perception of limb position[6]. Prior rodent studies postulate that proprioceptive mechanisms are located deeper into the cerebellar fissures compared to exteroceptive mechanisms[7]. Naturally, the human cerebellum is conjectured to be involved in proprioception. The cerebellum receives proprioceptive information through spinocerebellar pathways which project on to the anterior lobe and lobule VIII[8]. Also, cerebellar damage has shown to result in difficulty to do proprioceptive tasks[6,9,10]. Thus, studying functional cerebellar organisation using a proprioceptive paradigm can be of great neuroscientific and, possibly, clinical interest. We compare two motor tasks: same hand finger tap(SHFT) compared to a less proprioceptive reliant task: opposite hand finger tap(OHFT). Functional mapping of BOLD responses in the cerebellum requires high-resolution images due to the thin and highly-foliated cerebellar cortex. High-resolution images are more easily achieved at 7 T. Yet, at higher field strengths, images suffer from severely destructive B1-interference, hence a specific hardware set up is needed. We investigated the cerebellar BOLD response with a proprioceptive paradigm and B1-shimmed, 7 T fMRI.

Method: 8 volunteers, were scanned with a 7 T-Phillips MRI-scanner (8Tx/32Rx whole-head coil). A 0.64 mm-isotropic MP2RAGE sequence[12] (TR/TE = 2.3 ms/6.2 ms, FOV = 230 × 230 × 185) was acquired to generate cerebellar surfaces (Fig. 1A). A 3D-EPI slab covering the cerebellum (1 × 1 × 1 mm^3, TR/TE = 3288 ms/21 ms, FOV = 192 × 60 × 192 mm^3) was recorded during a proprioceptive paradigm. A DREAM B1 + map[11] and phase modulations were calculated to optimise B1 + over the cerebellum using MRCodeTool. A session consisted of 4 × 5 min runs alternating SHFT and OHFT tasks (20 s-ON,10 s-OFF, Fig-1B).FMRI data were motion/distortion-corrected, a higher level GLM over the four first level runs (OHFT > rest SHFT > rest z > 3.1) was fitted[13]. A cerebellar lobule mask was projected into the anatomical space of each participant[14] dividing the cerebellum into 4 quadrants: right/left upper quadrant and the right/left lower quadrant. Maximum z-stats and a paired t test ($p < 0.05$) were reported. The 4000 voxels with the highest z-stats were extracted and a weighted centre of gravity (wCOG) was calculated[15] for each task. Differences between task wCOGs were reported to assess the task cluster location on the cerebellar surface. White-matter segmentations were extracted[16], and unfolded[17]. FMRI activation was projected onto the surface.

Results: Both tasks resulted in bilateral activation for all participants in the cerebellum. OHFT resulted in higher ($p < 0.05$) maximum Z-stats than SHFT (Fig. 2). Figure 3 presents the differences between the wCOGs of OHFT and SHFT. On the RL axis differences between task wCOGs were positive in the right quadrants and negative in the left quadrants for all participants (Fig. 3A). Hence, OHFT-clusters were found more medial compared to SHFT-clusters. Along the IS axis, the difference between wCOGs was positive for all participants in the upper quadrants, indicating that the SHFT cluster wCOGs were found inferior to OHFT. Along the PA axis no consistent organisation was found (Fig. 3B). We reconstructed the cerebellar surface and projected fMRI results for both tasks. FMRI projection similarly showed the difference between the OHFT and SHFT clusters in all quadrants on a single subject level (Fig. 4).

Discussion: Both tasks reliably engaged the cerebellar hand areas[2], implying that our particular acquisition and analysis setup adequately sampled all cerebellar lobes. Higher z-stats in the OHFT task may indicate that the cerebellum activates more strongly to tasks requiring more proprioceptive information. More medially located OHFT clusters compared to SHFT clusters, show a different area of the cerebellum is engaged with the control of proprioceptive actions. This agrees with earlier rodent studies where proprioceptive movements are found deeper into cerebellar fissures compared to exteroceptive mechanisms[7].

Conclusion: We successfully compared BOLD responses in the human cerebellum using a proprioceptive task paradigm. Movements with higher proprioceptive engagement result in stronger activations an activation pattern found more medially on the cerebellar surface compared to movements less reliant on proprioception.

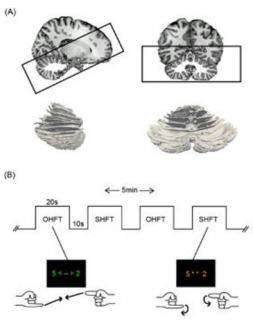

Fig. 1: (A)The 0.64mm isotropic MP2RAGE acquisition, overlayed with the white matter(WM) segmentation and the EPI FOV presented by the black box. 3D rendering of the WM surface. (B)The task design:4x5min runs with each a different finger combination series.

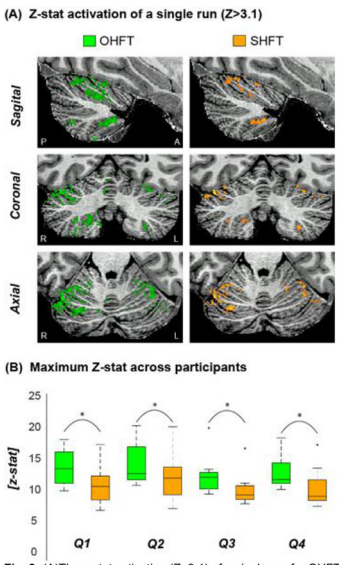

Fig. 2: (A)The z-stat activation (Z>3.1) of a single run for OHFT and SHFT presented in three orientations (B) The maximum z-score for each task across participants. Note: The OHFT task resulted in significantly($p<0.05$) higher max z-stats compared to the SHFT task in all quadrants. Q1=upper right quadrant Q2=Upper left quadrant Q3=Bottom right quadrant Q4=Bottom left quadrant

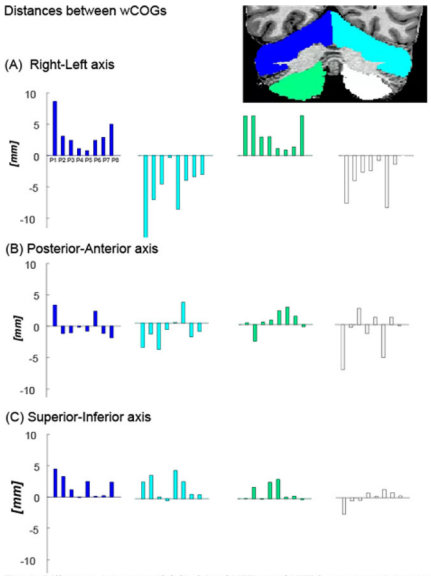

Fig. 3: Difference between wCOG of the OHFT and SHFT for each participant in each quadrant. (A)RL axis, Note: an opposite shift between the left and right quadrant, indicating a mediolateral shift.(B)PA axis.(C)SI axis.

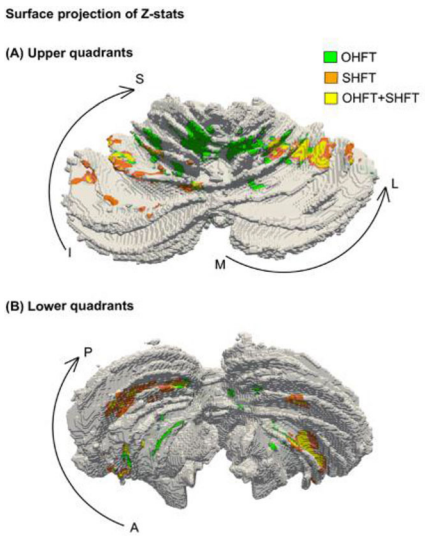

Fig. 4: Surface rendering of a participant. Note: The OHFT is found more medial compared to the SHFT in both (A):Q1/2 and (B):Q3/4

References:

1. Mottolese, Neurol. (2013)
2. Boillat, Neuroimage, (2020)
3. DMello, Neurosci. (2015)
4. Weissert, Neurol (2017)
5. Schmahmann, Neurosci (2004)
6. Bhanpuri, Neurosci (2013)
7. Voogd, Neurosci (2014)
8. Oscarsson, Physiol. Rev (1965)
9. Manto, Cerebellum (2012)
10. Weeks, Cerebellum (2017)
11. Nehrke, MRM (2012)
12. Marques, Neuroimage (2010)
13. M, Neuroimage (2012).
14. Diedrichsen, Neuroimage (2006)
15. Lehmann, Insight J. (2022)
16. Schlerf, Neuroscience (2012)
17. Huntenburg, (2018)

P173.
Denoising of the gradient artifact present in simultaneous studies of muscle blood oxygen level dependent (BOLD) signal and electromyography (EMG)

A. Amador-Tejada[1,2], J. E. McGillivray[1,2], H. de Bruin[1,3], M. D. Noseworthy[1,2,3,4]

[1]*McMaster University, School of Biomedical Engineering, Hamilton, Canada;*
[2]*St. Joseph's Healthcare, Imaging Research Centre, Hamilton, Canada;*
[3]*McMaster University, Electrical and Computer Engineering, Hamilton, Canada;*
[4]*McMaster University, Department of Radiology, Hamilton, Canada*

Introduction: There is an increased need to record, characterize, and correlate a motor task with skeletal muscle BOLD signals to better understand regional muscle activation and its modulation (1–3). Simultaneous BOLD/EMG acquisitions could provide this insight, as complementary non-invasive approaches provide functional and electrophysiological information with high spatial (fMRI) and temporal (EMG) resolution (4). Nevertheless, the coupling of these two techniques is complex. Also, the MRI gradient artifact (GA) interferes with characterizing EMG signals (5–7). To account for this, some studies recorded EMG prior/post-scanning outside the MRI environment, leading to 2 different activation events (2). EMG researchers also use MRI-compatible EEG systems, but these electrodes and system bandwidth are not optimized for EMG (8). Therefore, we aimed to improve the coupling of simultaneous acquisition of muscle BOLD/EMG by investigating denoising procedures that require different setup times, hardware, and post-processing to remove the GA.
Methods: In a study approved by our local ethics committee, simultaneous BOLD signals and EMG recordings were acquired from the anterior tibialis muscle in a volunteer (age: 23 years, height: 178 cm, weight: 65 kg). Experiments were performed using a Discovery MR750 3 T MRI (GE Healthcare, Milwaukee, WI) and a 16-channel T/R extremity coil. A BOLD sequence (EPI, 2 slices, 64 × 64 matrix, 10 mm thick, TE/TR/flip = 35/250/70) was used during simultaneous EMG recording with an in-house developed EMG acquisition system (Fs: 5 kHz, Bandwidth: 20–500 Hz). The subject performed 5 repetitions of plantar flexion using a home-built MRI-compatible ergometer, with a 30 s rest/activation period per recording. Furthermore, in order to establish a reliable baseline, EMG was collected outside of the magnetic room (Fig. 1). Three GA denoising methods were tested based on the average artifact subtraction (AAS) algorithm (9, 10). The three methods to estimate slice-timing information for artifact template creation were as follows: (1) Slice timing information was provided from the MRI scanner's internal clock output. Like an fMRI/EEG acquisition, this requires additional hardware (*BrainProducts GmbH*). (2) Slice timing was estimated as TR/(# of slices), assuming the GA is periodic. (3) Slice timing was determined by finding the local maxima of the gradient artifact in EMG recordings. This is robust if the GA has significant time variations. Once the artifact template was created, the AAS algorithm was applied to denoise the GA from the signal, followed by a post-processing procedure. Finally, SNR analysis followed by a 3-way ANOVA was performed to assess the efficacy of the denoising methods, compare any differences between repetitions, and compare EMG inside and outside the MR magnet room.

Results: Six EMG recordings were collected. Method M1 was successfully applied using the slice-timing information collected from the EEG (*BrainProducts GmbH)* hardware. Additionally, it showed a well-behaved periodicity that enabled the utilization of the method M2 denoising method. Manually building the artifact template yielded a similar periodicity of the artifact, which was used for method M3 (Fig. 2). There were no apparent differences in denoised signals, comparing raw and denoised EMG recordings (Fig. 3). A 3-way ANOVA showed no statistical differences in SNR between denoising methods ($p = 0.361$), exercise repetitions ($p = 0.626$), or conditions ($p = 0.057$) (Fig. 4).

Discussion: There were no significant differences in mean SNR between exercise repetitions, suggesting the in-magnet exercise did not cause significant muscle fatigue. The GA characterization was confirmed as periodic, consequently allowing the use of methods M2 and M3. The statistical test performed within denoising methods showed no significant differences in mean SNR across methods, meaning that any of the three methods can be chosen. Method M1 required the highest amount of hardware, including an EEG workstation, the SyncBox, amplifiers, setup time (15 min) and post-processing. On the contrary, given that the GA is periodic, methods M2 and M3 do not require additional time or specialized hardware, making them more suitable for ease of use. Finally, the results show no post-denoising differences in mean SNR between the three conditions under which EMG recordings were obtained. This suggests that previously reported electrical noise sources inside the MR environment (11) are not affecting the underlying EMG signal.

Conclusion: Our work shows that EMG signals from concurrent BOLD/EMG recordings can be easily denoised usingthe AAS algorithm. Method M2 was the most optimal, requiring no extra hardware, no additional setup time and minimal post-processing. These advantages could increase the use of EMG during muscle BOLD studies. The choice of optimal method exclusively relies on available hardware, time availability and processing capabilities of each MR centre.

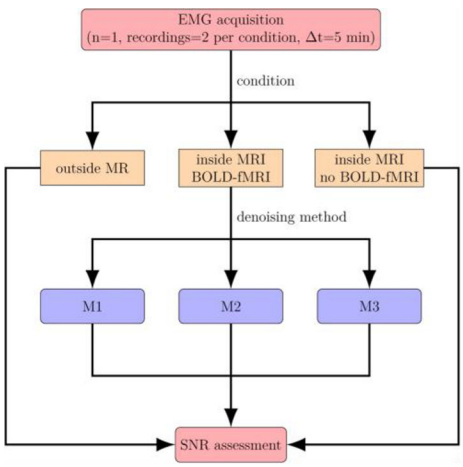

Fig. 1: Flowchart of EMG acquisition during 3 different conditions (inside MRI no muscle BOLD, inside MRI muscle BOLD, and outside MR) with 3 different denoising methods (M1,M2,M3), requiring different levels of hardware and processing

References

1. J. E. McGillivray *et al., Crit. Rev. Biomed. Eng.* **49** (2021).
2. H. H. Ehrsson *et al., J. Neurophysiol.* **85**, 2613–2623 (2001).
3. J. Z. Liu *et al., J. Neurophysiol.* **90**, 300–312 (2003).
4. K. J. Mullinger *et al., J. Magn. Reson. Imaging*. **27**, 607–616 (2008).
5. A. Delorme *et al., J. Neurosci. Methods*. **134**, 9–21 (2004).
6. I. Neuner *et al., Hum. Brain Mapp.* **31**, 1675–1685 (2010).
7. P. Ritter *et al.*, in *EEG-fMRI: physiological basis, technique, and applications*, C. Mulert et al., Eds. (Springer Science & Business Media, 2009).
8. H. van Duinen *et al., NeuroImage*. **27**, 240–246 (2005).
9. P. J. Allen *et al., NeuroImage*. **8**, 229–239 (1998).
10. P. J. Allen *et al., NeuroImage*. **12**, 230–239 (2000).
11. T. Nierhaus *et al., NeuroImage*. **74**, 70–76 (2013).

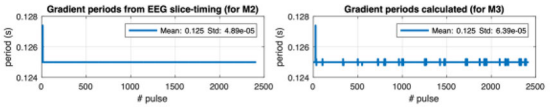

Fig. 2: (L) Plot showing the consistent timing between TTL pulses (slice timing information) as a function of the pulse/slice selection gradient number. (R) The manually slice-timing template built from the EMG signal (method M3) showed slight variations in the periodicity

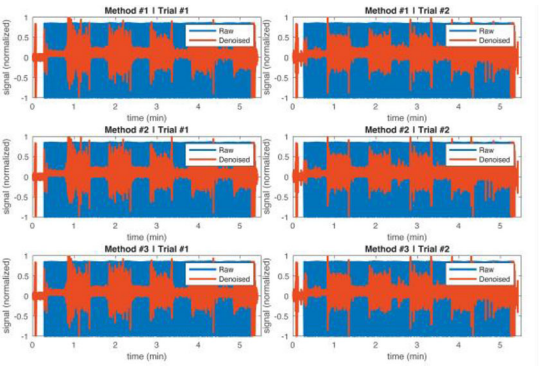

Fig. 3: (Blue) Raw EMG recordings with the gradient artifact. (Orange) Denoised EMG recordings for the 3 methods (M1,M2,M3) and the two recordings were taken. The raw data plot shows that the GA masks the actual EMG signal, making it useless unless denoised

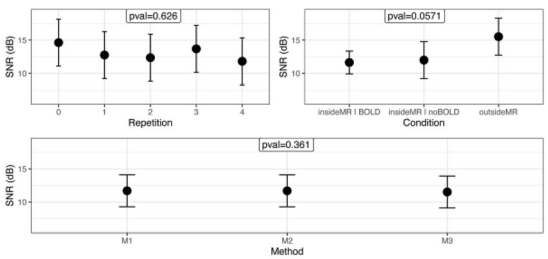

Fig. 4: Repeated measures ANOVA testing differences in the SNR between rest-activation repetitions (T,L), conditions (T,R) and denoising methods (Bottom). Denoised EMG was compared to the EMG recorded outside of the MR magnet room

P174.
The lack of b0 maps in RS-FMRI databases: A big problem or no big deal?

C. Nowikow[1,2], B. Sharma[2,3], M. D. Noseworthy[1,2,3,4]

[1]*McMaster University, School of Biomedical Engineering, Hamilton, Canada;*
[2]*St. Joseph's Healthcare, Imaging Research Centre, Hamilton, Canada;*
[3]*McMaster University, Electrical and Computer Engineering, Hamilton, Canada;*
[4]*McMaster University, Department of Radiology, Hamilton, Canada*

Introduction: Large publicly available resting-state functional magnetic resonance imaging (rs-fMRI) datasets are now commonplace. These datasets are invaluable for a "big data" approach to neuroimaging, which is critical for a new wave of research that can leverage these datasets to answer questions that were previously unanswerable owing to limited statistical power. One specific application is in clinical research, where open-source neuroimaging data can serve as a large control group for prospectively recruited clinical subjects (thereby making analyses more robust and reducing the need and resources required to recruit controls). However, the majority of rsfMRI repositories lack B_0 maps, and/or it is unclear if opensource data has been passed through field homogeneity corrections. This queries whether these data sets can adequately serve as control data to prospectively collected clinical fMRI data. It also questions if it is necessary for B_0 corrections to be applied to the subject data if the open-source control data do not contain B_0 corrections.
The goal of this work was to determine the impact B_0 correction on resting state fMRI at both single subject and group level analysis. Due to the extensive preprocessing that fMRI data undergoes, we hypothesized that the impact would be minimal.
Methods: In a study approved by our local ethics board 18 pediatric subjects were scanned on a GE MR750 3 T system (Waukesha, WI) with a 3D T1-weighed fSPGR (TR/TE = 11.36/4.25 ms, $\theta = 12°$, 512 × 512, 22 cm FOV, 1 mm thick) and a gradient echo EPI fMRI sequence (TR/TE = 2000/35 ms, $\theta = 90°$, 64 × 64, 180 time points, 22 cm FOV, 3 mm thick). For each of these subjects, fieldmaps were created using the *epiunwarp* package[1], which uses two GRE images of different TEs (5/8 ms) to create the B_0 fieldmap. Data was processed using the default pre-processing pipeline in CONN 21c[2], which involved: functional realignment to the first acquired image; functional data outlier detection per SPM"s Artifact Detection Tool, set with "conservative" settings; normalization/registration to MNI space passed on posterior tissue probability maps; and spatial smoothing of functional data with a 6 mm Gaussian kernel. The average B_0 map (Fig. 1) was used in conjunction with the least homogeneous subject B_0 maps to determine the ROIs to include in the analysis (Fig. 2). ΔB_0 was calculated using a pk–pk method.[4]
The time correlation coefficient was calculated using Matlab[4] between the BOLD signal with and without B_0 correction for each subject across 24 ROIs/Network seeds chosen to highlight regions of low and high inhomogeneity as determined from Figs. 1 & 2 (ROIs chosen shown in Fig. 3). The standard deviation of the residual of the BOLD signal with and without correction was also calculated as another metric of signal similarity. Using CONN, group analysis was performed on a ROI-by-ROI basis to compare the BOLD signal with and without correction.
Results: On a per-subject basis 90.1% of ROIs had a correlation coefficient > 0.9. 4.6% of ROIs had values between 0.8 and 0.9 and 5.3% had correlation coefficients 0.7 and lower (Fig. 3). The majority of the low correlations occurred in regions of low B_0 homogeneity (temporal lobe), however the frontal lobe regions did not experience this. The average correlation over all subjects and ROIs was 0.9563. Figure 4B illustrates that even the ROI with the highest ΔB_0 and lowest time correlation still had temporal BOLD signals that followed the same pattern, albeit with temporal dependant scaling. When comparing the BOLD signals with and without B_0 correction (which included data from the worst performing ROIs; see Fig. 4B), no differences survived groupwise analysis. This suggests that the B_0 corrected and uncorrected BOLD signal do not differ between groups, suggesting that the fieldmap correction may not be critical.
Conclusions and discussion: Based on these results we suggest that opensource neuroimaging data can be used in the absence of a B_0 fieldmap. The statistical power that these data offer, when serving as control data for various studies, their inherent time and resource efficiency should be leveraged in neuroimaging studies. While fieldmap data can be used to further improve the quality of neuroimaging analyses, our data show that their absence may not be a detriment. Future studies with a larger clinical group should be performed to corroborate and build on our findings.

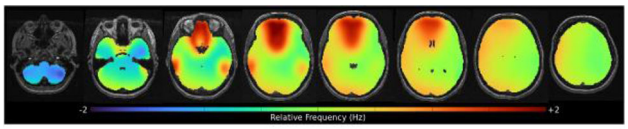

Fig. 1: The average B0 map in Hz relative to the expected Larmor frequency, overlayed on MNI space.

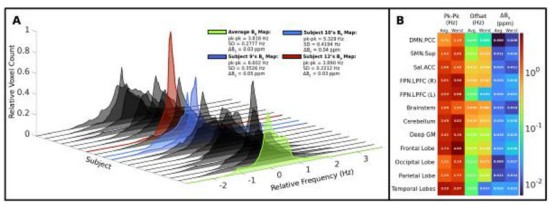

Fig. 2: (A) Histogram of the frequency distribution of the B0 maps for each subject, and (B) B0 metrics across various ROIs for both the average B0 map and the least homogeneous B0 map.

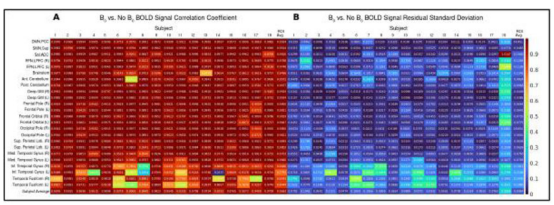

Fig. 3: (A) time correlation coefficient between the BOLD signal with and without B0 correction; and (B) the standard deviation of the residual BOLD response signal with and without B0 correction on an ROI basis for each subject. The p-values for all correlation coefficients are under e-48, except for the left inferior temporal gyrus for subjects 8 and 14 which are 3.17e-4 and 0.653 respectively.

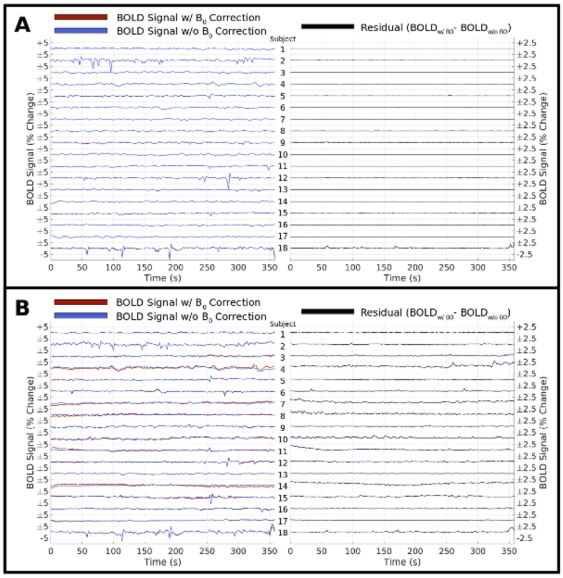

Fig. 4: BOLD signal time courses with and without B0 correction. Figure 4A shows the signal of the most homogenous ROI (left deep grey matter) while Figure 4B shows the least homogeneous ROI (left inferior temporal gyrus).

References:

1. Davis AD, Noseworthy MD. (2016) Motion and distortion correction of skeletal muscle echo planar images. *Magn. Reson. Imaging* 34:832–838.
2. Whitfield-Gabrieli S, Nieto-Castanon A. (2012) Conn: A functional connectivity toolbox for correlated and anticorrelated brain networks. *Brain Connect*. 2:125–141.
3. Gach HM, Curcuru AN, Mutic S, Kim T. (2020) B_0 field homogeneity recommendations, specifications, and measurement units for MRI in radiation therapy. *Med. Phys.* 47:4101–4114.
4. MATLAB version R2022b, Mathworks, Natick, MA.

P175.
Enabling in vivo assessment of motor cortex vessel dominance patterns using 7 T MRI and vessel distance mapping

G. Mietzner[1], F. Schreiber[2,1], L. Lümkemann[1], J. Brüggemann[3], A. Sciarra[3,4], C. Knoll[2,5], E. Kuehn[5,6], O. Speck[3,2,7,8], S. Schreiber[2,7,1], H. Mattern[3,2,7]

[1]*Otto von Guericke University, Department of Neurology, Magdeburg, Germany;*
[2]*German Center for Neurodegenerative Diseases (DZNE), Magdeburg, Germany;*
[3]*Otto von Guericke University, Department of Biomedical Magnetic Resonance, Magdeburg, Germany;*
[4]*Otto von Guericke University, Medicine and Digitalization—MedDigit, Magdeburg, Germany;*
[5]*Otto von Guericke University, Institute of Cognitive Neurology and Dementia Research (IKND), Magdeburg, Germany;*
[6]*Hertie Institute for Clinical Brain Research (HIH), Tübingen, Germany;*
[7]*Center for Behavioral Brain Sciences (CBBS), Magdeburg, Germany;*
[8]*Leibniz Institute for Neurobiology, Magdeburg, Germany*

Introduction: The motor cortex can be parcellated into the paracentral and precentral gyrus. Branches of the Anterior Cerebral Artery(ACA), i.e. the pericallosal artery(A.Peri) and callosomarginal artery(A.Callo), supply predominately the paracentral gyrus, while Middle Cerebral Artery(MCA) branches, i.e. precentral, central, and postcentral group, supply predominately the precentral gyrus[1]. The relevance of each ACA and MCA branch to the supply is subject-specific. Hence, vessel dominance (VDom) patterns exist, currently only studied post mortem[1]. Leveraging the high-resolution capabilities of 7 T MRI[3], improved vessel contrast of MPRAGE at 7T[2], and the recently proposed vessel distance mapping(VDM) framework[4] we aim to identify VDom patterns in vivo. Further, potential group differences between VDom patterns w.r.t. cortical thickness, vessel distance, and number of branches are tested.

Methods: 19 healthy volunteers(7 females, 31.18 ± 6.48 years old) were scanned at 7 T after given written consent witha prospectively motion corrected MPRAGE at 0.45 mm isotropic resolution(TI/TR = 1050/2820 ms)[5]. Per hemisphere, the motor cortex was segmented as the union of the precentral and paracentral gyrus parcellated with FreeSurfer[6]. All ACA and MCA branches were labeled individually per hemisphere by an expert rater. Using VDM[4], the Euclidian distance of each voxel to all arteries was computed. By assigning the label of the closest artery to each motor cortex voxel, VDM-based vessel territory maps were generated (Fig. 1). Volume ratios were used to determine the VDom for ACA and MCA branches, respectively. For the ACA, the volume supplied by the A. Peri was set into relation to the volumes supplied by A. Peri and A. Callo, i.e. all ACA branches, with the extremes 0 and 1 meaning no supply/supply entirely by the A.Peri. Similar, for the MCA the ratio of central group volume to central and precentral volume was computed and VDom evaluated. Note that the postcentral group was not included as it was found in only 11 out of 38 hemispheres and never contributed considerably. To differentiate between equal or dominant contribution, a lower and upper threshold were used (equal contribution defined by a volume ratio in between both thresholds). To evaluate the effect of thresholds on frequency of VDom patterns, the upper and lower thresholds were varied jointly (Fig. 2). Group differences between equal contribution ($0.33 <$ volume ratio < 0.66) and single vessel dominance patterns (volume ratio < 0.33 or > 0.66) were assessed for the ACA branches in the paracentral gyrus and MCA groups in the precentral gyrus, respectively. Mann-Whitney-U-test were used to test if the mean cortical thickness (provided by FreeSurfer), mean vessel distance(provided by VDM), and number of branches going to the motor cortex(manual count by expert) from both groups had the same underlying distribution.

Results: Volume ratios, hence VDom patterns, varied considerably across subjects (Fig. 2). While the choice of upper and lower threshold to determine equal contribution had an expected influence on the pattern frequency, subsequent analysis used equally spaced intervals, i.e. thresholds of 0.33 and 0.66, which coexisted with a plateau in ACA pattern frequencies (Fig. 2). Comparing the VDom patterns from ex vivo[1] to our in vivo data yields good agreement for the ACA (33%/40%/27% vs. 34%/34%/32% for A.Peri, A.Callo, and equal contribution, respectively). For the MCA, the precentral group contribution was higher in our study, leading to overall more equal cases (72%/10%/18% vs. 34%/16%/50% central, precentral group, and equal contribution). Figure 3 shows 3D renderings for two representative hemispheres with different VDom patterns. Significant group differences between single vessel dominance and equal

contribution were only observed for the mean cortical thickness in the paracentral gyrus for the ACA branches (Fig. 4).

Discussion: We presented a method to determine VDom patterns, previously only established ex vivo[1], in vivo and non-invasively using the high-resolution capabilities of 7 T MRI and the recently introduced VDM framework. Interestingly, even in healthy volunteers, significant differences in mean paracentral cortical thickness between single and equal vessel dominance were found. The VDM-based volume ratios are based on structural scans, hence, perfusion-based territory mapping would be ideal as ground truth. However, planning the labeling for the intertwined branches is non-trivial and requires future methodological efforts.

Conclusion: 7 T MRI and VDM enable in vivo VDom pattern identification, paving the way to assess vascular resistance and resilience mechanisms in i.e. ALS patients[7].

Acknowledgement

This work was funded by the DFG (501214112, 446268581, 425899996, 362321501) and by the DAG e.V. (MD-DARS).

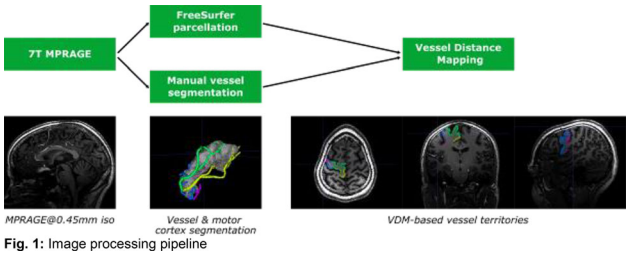

Fig. 1: Image processing pipeline

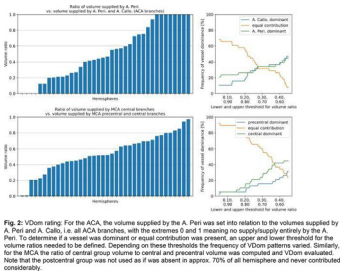

Fig. 2: VDom rating: For the ACA, the volume supplied by the A. Peri was set into relation to the volumes supplied by A. Peri and A. Callo, i.e. all ACA branches, with the extremes 0 and 1 meaning no supply/supply entirely by the A. Peri. To determine if a vessel was dominant or equal contribution was present, an upper and lower threshold for the volume ratios needed to be defined. Depending on these thresholds the frequency of VDom patterns varied. Similarly, for the MCA the ratio of central group volume to central and precentral volume was computed and VDom evaluated. Note that the postcentral group was not used as if was absent in approx. 70% of all hemispheres and never contributed considerably.

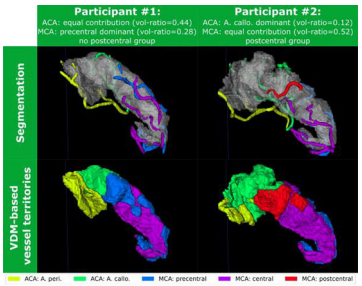

Fig. 3: Color-coded 3D renderings

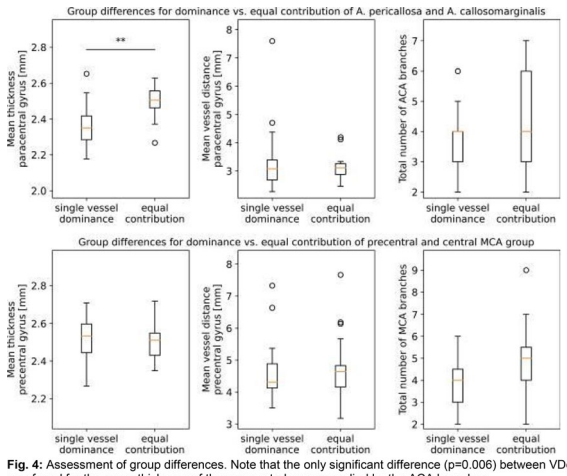

Fig. 4: Assessment of group differences. Note that the only significant difference (p=0.006) between VDom patterns was found for the mean thickness of the paracentral gyrus supplied by the ACA branches.

References:

[1]Ugur et al.2005
[2]Maderwald et al.2008
[3]Ladd et al.2018
[4]Garcia-Garcia et al.2023
[5]Sciarra et al.2022
[6]Fischl 2012
[7]Schreiber et al.2023

P176.
Parallel transmit imaging with real-time multislice-to-volume motion correction for task-based functional MRI at 7 T

S. Winata[1], D. C. Hoinkiss[2], G. A. Keith[1], S. N. Williams[1], B. Y. Ding[3], S. al-Wasity[1], G. Shajan[1,4], D. A. Porter[1]

[1]*University of Glasgow, Imaging Centre of Excellence, Glasgow, United Kingdom;*
[2]*Fraunhofer Institute for Digital Medicine MEVIS, Bremen, Germany;*
[3]*Siemens Healthineers, Frimley, United Kingdom;*
[4]*MR CoilTech Ltd, Glasgow, United Kingdom*

Introduction: The radiofrequency (RF) wavelength decreases with increasing magnetic field strength. This poses an issue for routine human imaging at ultra-high field strengths, such as 7 T, due to greater RF field (B1 +) inhomogeneity. Parallel transmission (pTx) uses a dedicated RF coil with independent transmit channels that generate individual RF fields. These fields can be tailored for a homogenous, combined excitation that is simultaneously subject to SAR constraints.

While the improved SNR in 7 T increases the capacity for higher resolution imaging, it is also more prone to motion-induced artefacts. Prospective, real-time motion correction techniques, can help to reduce these effects. MS-PACE [1] is a technique adapted from Prospective Acquisition CorrEction (PACE). In-plane and through-plane motion are estimated by registering a subset of equidistant EPI slices to a Reference volume, differing from the volumetric registration in PACE [2]. This allows for sub-TR motion detection and higher temporal resolution of imaging system updates.

This abstract presents an integration of pTx with real-time MS-PACE motion correction for a functional MRI (fMRI) protocol, harnessing both techniques to deliver more homogenous and motion-insensitive

imaging. This study integrated a subject-specific pTx workflow [3] with slice-by-slice B1 + field shimming [4].

Methods: The study was performed on a MAGNETOM Terra 7 T scanner (Siemens Healthineers, Erlangen, Germany) with an 8Tx64Rx head coil (MR CoilTech Ltd, Glasgow, Scotland, UK) [5, 6] using an in-house-developed GRE-EPIsequence on 5 healthy subjects (age 49 ± 15). Following localisation and B0 shimming, B1 + and B0 field mapping was performed at the slice positions used by the EPI protocol, and the results were used in MATLAB (MathWorks, Natick, MA, USA) offline to generate pTx slice-specific B1 + shim weights. T1-weighted data were also acquired using a 3D FLASH sequence. After the structural scan was completed, 4 EPI scans were acquired: 2 in circularly-polarised (CP) mode (equivalent to conventional single transmission) and 2 in pTx shim mode. In each case, one scan was acquired with motion correction and one without. The scan parameters were otherwise identical: voxel size $2 \times 2 \times 2$ mm^3, resolution 96×96, GRAPPA factor 3, 51 slices, 110 volumes, echo spacing 580 ms, TR 4 s, TE 18 ms and total acquisition time 7 m 32 s.

A simple paradigm with resting and finger-tapping segments alternating every 10 volumes was instructed to the subject with the aid of PsychoPy [7].

A 3-slice registration subset was used for real-time motion correction. Estimated motion parameters were fed back to the scanner and the imaging gradients were updated accordingly. The correction robustness was evaluated by calculating residual rigid-body motion parameters with the multislice-to-volume method. Online and offline processing was done within the Image Calculation Environment (Siemens Healthineers, Erlangen, Germany) using ITK open-source libraries.

Results: Figure 1 compares the mean voxel displacement in the pTx scans in all subjects. Figure 2 compares temporal SNR (tSNR) maps and percentage differences in tSNR (δtSNR) from the motion corrected scans in both CP and pTx modes across all subjects Fig. 3 shows the mean δtSNR of pTx compared to CP in all subjects, normalised into Montreal Neurological Institute (MNI) space.

Discussion: Figure 1 shows that the motion correction capability was preserved when pTx was used. For the acquisitions with real-time motion correction, Fig. 2 demonstrates tSNR improvements when pTx is used, although this observation was not universal in all slices acquired from all subjects. In particular, there was a marked tSNR pTx improvement for slices in which the tSNR of the corresponding CP acquisition was low, as in Subject 3. The averaged difference across all subjects, when normalised into MNI space (Fig. 3), also shows tSNR improvements in pTx versus CP across the central slices, although there was a decrease in tSNR in the temporal lobe on some slices. This preliminary analysis of the data has focused on assessing the performance of pTx when they are integrated into a real-time motion correction procedure. The results confirm that the overall benefit of pTx and motion correction is preserved.

Conclusion: This study has evaluated an integrated method of EPI acquisition that combines real-time motion correction with subject-specific pTx using slice-by-slice B1 + shimming. An overall improvement in tSNR was demonstrated with the motion-corrected data acquired with pTx compared to acquisitions using standard CP pulses.

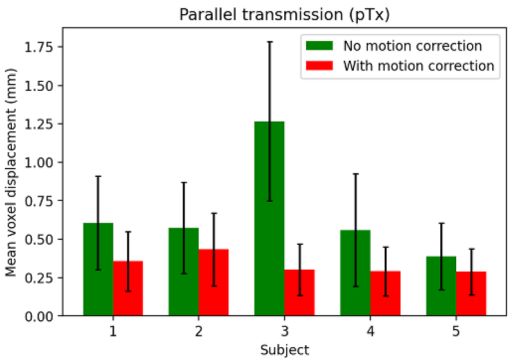

Fig. 1: Mean voxel displacement without and with real-time motion correction from the scans using parallel transmission (pTx). The error bars represent the standard deviation of each dataset.

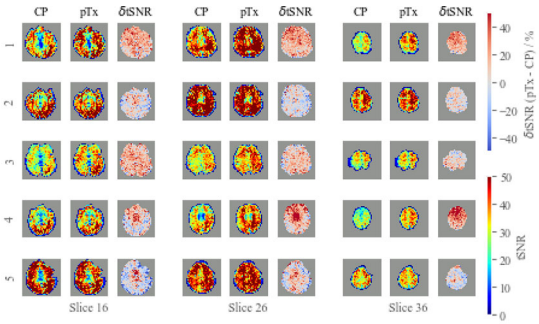

Fig. 2: Temporal SNR (tSNR) maps and differences (δtSNR) derived from the motion corrected scans in all subjects on both circularly-polarised (CP) and parallel transmit (pTx) modes. The maps are plotted for slices 16, 26 (centre) and 36 in subject-native EPI space.

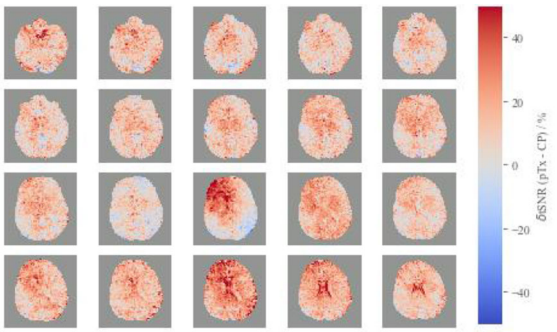

Fig. 3: Average δtSNR (pTx-CP) of the motion corrected scans in all subjects. The maps demonstrate an overall improvement in tSNR when motion-corrected data are acquired with pTx pulses compared to a standard CP acquisition.

References:

[1] Hoinkiss DC et al. Neuroimage. 2019;200:159-73.
[2] Thesen S et al. MRM. 2000;44:457-65.
[3] Ding B et al. JMRI. 2022;93:163-74.
[4] Curtis AT et al. MRM. 2012;68:1109-16.
[5] Williams SN et al. Front Phys. 2021;9:701330.
[6] Shajan G et al. 2022 ISMRM Annual Meeting.
[7] Peirce J et al. Behav Res. 2019;51:195–203.

P177.
An overview of 3 T functional magnetic resonance imaging protocols of the amygdala and subregions

S. Foster[1,2], I. Breukelaar[3], K. Ekanayake[4], S. Lewis[2,5], M. Korgaonkar[3,5]

[1]*Westmead Hospital, Radiology, Westmead, Australia;*
[2]*The University of Sydney, Faculty of Medicine & Health, Sydney, Australia;*
[3]*Westmead Institute for Medical Research, Brain Dynamics Centre, Westmead, Australia;*
[4]*The University of Sydney, University Library, Sydney, Australia;*
[5]*Co-Senior author, Sydney, Australia*

Introduction: Functional Magnetic Resonance Imaging (fMRI) is widely used in neuropsychiatric disorders, in particular the amygdala which is associated with the brain's emotional circuitry. 3 T MR systems are commonly utilised for BOLD imaging but optimal functional imaging of the amygdala remains difficult as it is relatively small structure with average volumes of 1240 mm^3 [1]. Its location deep in the temporal lobe also presents technical challenges and a further complication is its subregional structure. The amygdala is composed of nine functionally different nuclei forming three distinct subregions, the laterobasal (LB), centromedial (CM) and superficial (SF), each of which has differing functional connections to remote brain areas [2]. To resolve subregional activation, high spatial resolution images with adequate SNR and sufficiently small voxel volumes (VV) are required.

The simple step of optimising VV for the study endpoint can positively impact data quality, accuracy of results and validity of conclusions. Our objective was to produce an overview of current 3 T fMRI protocols used for the amygdala for the purpose of generating discussion on data quality, heterogeneity and the potential advantages of protocol harmonisation.

Methods: A database search identified 386 publications for screening following which data was extracted from 192 covering six categories:

1. sequence type
2. spatial resolution (VV in mm^3)
3. imaging plane
4. brain coverage
5. acquisition time (TA)
6. radiofrequency (RF) coil type

The Preferred Reporting Items for Systematic reviews and Meta-Analyses extension for Scoping Reviews (PRISMA-ScR) methodology was followed.

Results: Figure 1: Data summary of all studies (n = 192)

Discussion: This review provides a snapshot of 3 T fMRI protocols from a range of institutions worldwide. Although the same sequence type and imaging plane were used in over 90% of studies, TA and spatial resolution values were quite varied (Fig. 1). Overall, only 16% of studies acquired high resolution data (VV = 1–20 mm^3). Subregional findings were reported in 21 studies, with only four using high resolution data, four with low resolution data (50–100 mm^3) and 13 with mixed data. Although larger voxels possess inherently higher SNR theoretically, localised main magnetic field inhomogeneity causes signal loss at bone/air/tissue interfaces around the amygdala; intravoxel dephasing has a similar effect but is mitigated by reducing VV. Contrast-to-noise (CNR) is also maximised by matching VV to the size of the expected activation [3]. Use of axial/oblique acquisition planes is preferred as 30% fewer slices are required compared to the coronal plane. This has temporal implications for data acquisition; the repetition time (TR) for each whole brain volume is lower and a slice gap technique can be avoided, an important consideration when imaging a very small structure such as the amygdala.

There was considerable variation in sequence TA with the largest group using 6–8 min. Six minutes is reportedly adequate for demonstrating functional connectivity patterns [4]. Because of the relationship between TA and temporal SNR, optimal TA for each fMRI sequence can be calculated by pre-determination of the required effect size to a given p value.

Multi-channel array RF coils allow the use of parallel imaging (PI) and Simultaneous Multi Slice (SMS). The primary benefit of PI in fMRI is increased data quality resulting from echo time (TE) optimisation; this outweighs the concomitant undersampling SNR penalty. Multi-channel coils were used in the majority of studies.

Conclusion: Spatial resolution of fMRI data investigating amygdala and subregional connectivity shows broad inconsistency; the vast majority of studies relied on standard or low resolution data to report findings. Wide variation in protocols and use of suboptimal data is potentially responsible for contradictory findings across studies and an obstacle to success in study replication. Careful deliberation regarding parameter choices in the context of study objectives can result in improvements in data quality. A broad discussion focusing on these findings may lead to an increasingly collaborative approach involving protocol harmonisation to address the challenges of data heterogeneity in big data collaborations**.**

Sequence Type		Spatial Resolution		Imaging plane		Full brain coverage		Acquisition time (TA)		RF Coil Type	
		VV range = 7.3mm^3 to 100mm^3; Slice thickness (ST) range = 2mm to 5mm						TA range = 2m 44s to 24 m			
GE-EPI	175	High Res 1-20 mm^3	30	Axial/axial oblique	186	Yes	185	< 6 min	23	8 Channel	35
Spiral version	8	Std Res > 20-50 mm^3	126	Coronal/coronal oblique	2	No	7	6 to 8 min	52	12 Channel	21
GE-EPI & Spiral	3	Low Res > 50mm^3	29	Sagittal	4			> 8 to 10 min	21	16 Channel	1
SE-EPI	2	Mixed Resolution	7					> 10 min	13	20 Channel	1
DE-EPI	1							Mixed TA	4	24 Channel	1
Gradient SE	1	ST <=3.5mm	127					Not Stated	79	32 Channel	42
ASL	1	ST >3.5mm	65							64 Channel	3
GE-EPI & ASL	1	No Slice Gap	143							Mixed	3
		Slice Gap	45							Other	17
		Mixed gap/no gap	4							Not Stated	68

Fig. 1: Data summary of all studies (n=192)

References:

1. Brabec, J., et al., *Volumetry of the human amygdala — An anatomical study.* Psychiatry Research: Neuroimaging, 2010. **182**(1): p. 67–72.
2. Bzdok, D., et al., *An investigation of the structural, connectional, and functional subspecialization in the human amygdala.* Human Brain Mapping, 2013. **34**(12): p. 3247–3266.
3. Yoo, S.-S., C.R.G. Guttmann, and L.P. Panych, *Multiresolution Data Acquisition and Detection in Functional MRI.* NeuroImage, 2001. **14**(6): p. 1476–1485.
4. Van Dijk, K.R., et al., *Intrinsic functional connectivity as a tool for human connectomics: theory, properties, and optimization.* J Neurophysiol, 2010. **103**(1): p. 297–321.

P178.
Comparative analysis between tools used in the evaluation of studies by functional magnetic resonance imaging

R. Ruiz[1], L. Flores[1], A. O. Rodriguez[2], F. Vazquez[1], S. Solis-Najera.[1]

[1]*Universidad Nacional Autonoma de Mexico, Departamento de Fisica, FC, Mexico City, Mexico;*
[2]*Universidad Autonoma Metropolitana Iztapalapa, Department of Electrical Engineering, Mexico City, Mexico*

Introduction: Currently there are various tools used in digital processing of images for the evaluation of studies of Functional Magnetic Resonance. Through this work, we want to evaluate two of the most common tools used in the analysis of Functional Magnetic Resonance, to determine if it is possible that there are significant variations between both, since the result obtained with these tools has clinical consequences significant (for example, a correct diagnosis, or even a surgical intervention).
Methods: fMRI studies were obtained from different open free datasets (OpenNeuro and Stanford Libraries), two different studies were chosen randomly. All data were processed using SPM12 and FSL using same parameters during image processing for each study. After image processing, we used some qualitative (presence, size, and localization of clusters; and using Neurosynth brain location) and quantitative (Sorensen-Dice metric, overflow percentage, and Bland-Altman analysis) tools to evaluate how this commonly used softwares agree or disagree with each other.
Results: Within the study that contains motor function as an objective, we chose one from the database that contains finger movement, lip movement, and foot movement. The results obtained in both SPM and FSL are shown in Fig. 1. On the other hand, we chose a cognitive study from the same databases, where the patient is visually asked to think if what he sees is consistent with what he sees. what the screen says Similarly, the results obtained are shown in Fig. 2. The activation clusters presented by each of the studies were analyzed for each case using the online NeuroSynth tool. The results shown in Table 1, are the areas in which both tools have a concordance when the resulting clusters were analyzed with the help of the NeurSynth tool. The Sorensen-Dice metric was also performed, obtaining the overflow percentage as shown in Fig. 3. And finally, Bland-Altman graphs were obtained for the two studies, shown in Fig. 4.

	SPM		FSL	
	Associated term	Corr	Associated term	Corr
Finger	Finger	0.190	Parietal	0.310
	Parietal	0.190	Inferior Parietal	0.229
	Finger movements	0.176	Finger	0.229
	Hand	0.169	Hand	0.223
	Inferior parietal	0.166	Action	0.222
	Action	0.155	Finger movements	0.218
	Dorsal premotor	0.150	Dorsal premotor	0.218
Foot	Foot	0.296	Foot	0.255
	Limb	0.186	Superior parietal	0.185
	Superior parietal	0.109	Limb	0.159

Table c continued

	SPM		FSL	
	Associated term	Corr	Associated term	Corr
Lips	Medial	0.274	Speech production	0.309
	Speech	0.234	Production	0.266
	Speech production	0.309	Speech	0.209
	Production	0.216	Medial	0.183
Incongruent	NONE	NONE	NONE	NONE
Congruent	Visual	0.331	Visual	0.227

Conclusions: From image processing we can visually appreciate important differences between both image processing tools. Even though when we analyze the obtained activation clusters and compare with the NeuroSynth tool, we can see that main areas are involved in the different tasks for both studies, except for the Incongruent task in cognitive study. Correlation factors are different, but they still are present. We can see from Fig. 3, that a significant overflow percentage from both software is present mainly when we compare FSL versus SPM, but we still can appreciate that the main areas are present for the different tasks. The Bland-Altman method can help us visualize how this methods are correlated between them, we expect that graphs show a more narrow Figure, and from Fig. 4 we can see that the graphs look more spread for this particular studies analyzed, but we have to consider that for this Bland-Altman method used, we had to transform the statistics maps conformed by Z-statistics in FSL, into T-statistics.

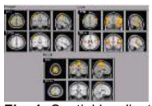

Fig. 1: Spatial localization obtained with FSL and SPM, for the study containing motor responses.

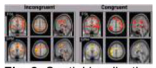

Fig. 2: Spatial localization obtained with FSL and SPM, for the study containing cognitive responses between congruent and incongruent tasks.

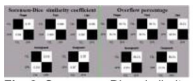

Fig. 3: Sonrensen-Dice similarity coefficient for both studies (left), and the Overflow percentage obtained for the studies analyzed (right).

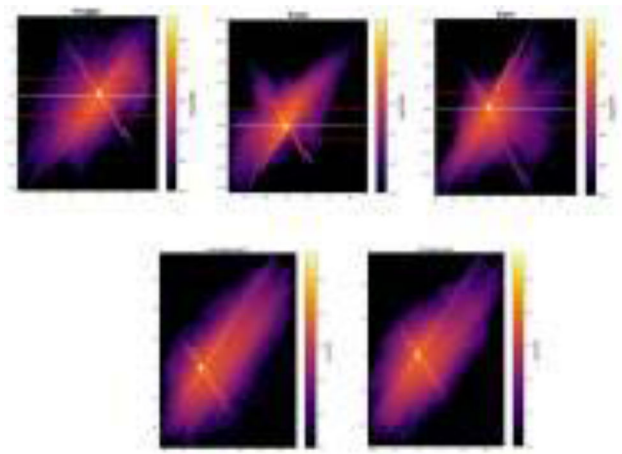

Fig. 4

References:
1 Flandin G., Novak M.J.U. fMRI Data Analysis Using SPM. In: Ulmer S., Jansen O. (eds) fMRI. Springer, Cham. https://doi.org/10.1007/978-3-030-41874-8_8. (2020)
2 Penny WD., Friston KJ., Ashburner JT., Kiebel SJ., Nichols TE. Statistical Parametric Mapping: The Analysis of Functional Brain Images. Academic Press. (2006)
3 Poldrack RA., Mumford JA., Nichols TE. Handbook of Functional MRI Data Analysis. Cambridge University Press. (2011)
4 Bijsterbosch J., Smith S., Beckmann C. Introduction to Resting State fMRI Functional Connectivity. Oxford University Press. (2017)
5 Jenkinson M., Chappell M. Introduction to Neuroimaging Analysis. Oxford University Press. (2018)

P179.
Multiple delay ASL can characterize impaired cerebrovascular reserve and transit time in pediatric moyamoya patients

M. Zhao[1], E. Tong[2], K. Yeom[2], M. Moseley[2], G. Zaharchuk[2], G. Steinberg[1]

[1]*Stanford University, Department of Neurosurgery, Stanford, United States;*
[2]*Stanford University, Department of Radiology, Stanford, United States*

Introduction: Cerebrovascular reserve (CVR) reflects the change in CBF in response to vasodilation. Studies have demonstrated that impaired CVR is associated with a higher risk for stroke. Arterial spin labeling is a quantitative MRI technique that enables non-invasive CBF and CVR measurement. The effectiveness of multiple delay ASL has been demonstrated in detecting impaired CVR and arterial transit time (ATT) in adult Moyamoya patients. In this work, we compare the CBF and CVR of pediatric Moyamoya patients measured by ASL with single and multiple delays.
Methods: Imaging data were acquired from 6 Moyamoya patients (between 3 and 16 years old, 4 females) using a 3 T MRI using single-delay and multi-delay ASL. ASL images were acquired at baseline and 10-15 min after the injection of the vasodilator acetazolamide. CBF was computed using the general kinetic model. CVR was computed as the percentage of CBF change compared with baseline CBF.
Results: Figure 1 shows the CBF, CVR, and ATT of a patient with bilateral ACA and MCA occlusion, whereby vascularsteal (negative CVR) can be seen in left MCA territories (CVR = − 13% and − 24% by single and multi-PLD ASL respectively). The vasculopathy caused delayed ATT in bilateral MCA regions. CBF and CVR obtained by multi-delay ASL were higher than the ones measured by single-delay ASL.
Discussion: Multi-delay ASL was effective in identifying CVR and ATT impairment in pediatric Moyamoya patients. It can potentially replace the Gd-based PWI MRI technique to characterize vascular hemodynamics in patients with cerebrovascular diseases.

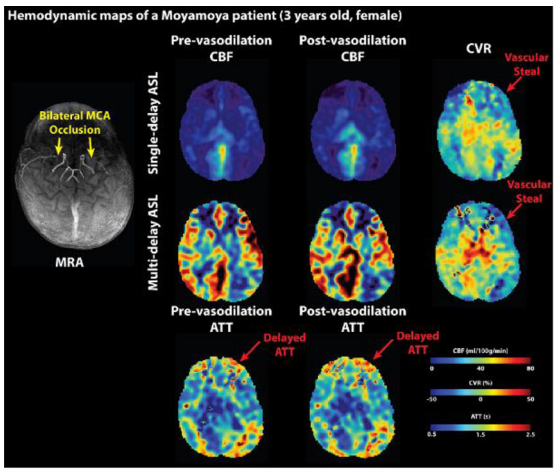

Fig. 1: Hemodynamic maps of a Moyamoya patient with bilateral ACA and MCA occlusion (3 years old, female). Overall, both ASL techniques reveal impaired CVR (CBF augmentation) after vasodilation. The vasculopathy caused vascular steal (negative CVR, red arrows) in left MCA regions. Delayed ATT (red arrows) can be observed in regions affected the occluded vessels. Comparing between the two ASL methods, CBF and CVR measured by multi-delay ASL were higher than the results obtained by single-delay ASL.

References:
1. Yonas, H., Smith, H. A., Durham, S. R., Pentheny, S. L. & Johnson, D. W. Increased stroke risk predicted by compromised cerebral blood flow reactivity. J. Neurosurg. 79, 483–489 (1993).
2. Zhao, M. Y. et al. Cerebrovascular reactivity measurements using simultaneous 15O-water PET and ASL MRI: Impacts of arterial transit time, labeling efficiency, and hematocrit. NeuroImage 233, 117955 (2021).
3. Zhao, M. Y. et al. Using arterial spin labeling to measure cerebrovascular reactivity in Moyamoya disease: Insights from simultaneous PET/MRI. J. Cereb. Blood Flow Metab. 0271678X221083471 (2022) https://doi.org/10.1177/0271678X221083471.
4. Buxton, R. B. et al. A general kinetic model for quantitative perfusion imaging with arterial spin labeling. Magn. Reson. Med. Off. J. Soc. Magn. Reson. Med. Soc. Magn. Reson. Med. 40, 383–396 (1998).
5. Smith, S. M. et al. Advances in functional and structural MR image analysis and implementation as FSL. in NeuroImage (2004). https://doi.org/10.1016/j.neuroimage.2004.07.051.

P180.
Robust implementation of a 3D velocity-selective ASL sequence for breast imaging

M. A. Buck[1,2], J. Huber[1], M. Günther[1,2,3]

[1]*Fraunhofer Institute for Digital Medicine MEVIS, Bremen, Germany;*
[2]*University of Bremen, MR-Imaging and Spectroscopy, Faculty 01 (Physics, Electrical Engineering), Bremen, Germany;*
[3]*mediri GmbH, Heidelberg, Germany*

Introduction: Breast cancer is the most common form of cancer among women. Studies have shown that MRI is the best technique for detecting tumors[1]. Generally, a dynamic contrast-enhanced MRI with the injection of contrast-agent (CA) is used. Arterial Spin Labeling (ASL) is a non-invasive method for measuring perfusion without the need of CA by typically labeling inflowing blood magnetically upstream of the organ of interest[2]. Velocity selective ASL (VSASL)[3] is a specialized technique of ASL which labels blood above a certain velocity (cutoff velocity v_{cut}) directly inside the imaging region. It has the advantage that no extra time is needed for the blood to arrive in the imaging region. This technique is getting increasingly more interest especially in organs with slow blood flow velocities or without clear and straight feeding arteries as in breast tissue. For the use of VSASL in breast imaging, challenges like breathing motion, off-resonances, unknown arteries localization and a not negligible amount of fat around the breast tissue have to be considered. In this work, initial proof-of-principle measurements were performed to find the best parameters for measuring breast perfusion with minimal acquisition artifacts.

Methods: *Theory:* For the development of a robust acquisition protocol different parameters were tested to minimize especially the influence of fat signal. For this, different velocity encoding directions ($venc_{dir}$) were tested to maximize the ASL signal. Single-shot (ss) as well as multi-shot acquisitions (ms) with two-fold k-space segmentation were compared using a 3D GRASE[4] readout. In addition to the fat suppression module using the CHESS technique[5], background suppression pulses were played out to specifically suppress fat signal. B1-field inhomogeneities and resulting off-resonances are common in abdominal MRI which can result in poor performance of spectral fat suppression. Therefore, a subject-specific preparation scan was developed (submitted to ESMRMB, as well)[6] to calculate the optimal frequency and flip angle FA for the fat suppression pulse.

Acquisition: A VSASL inversion sequence[7] was used with following parameters: v_{cut} = 2 cm/s, TR = 6500 ms, TI = 1050 ms, $venc_{dir}$ = x/y/z, velocity-compensated control module, no arterial crusher, partitions = 8/16 and TF = 8 (ss/ms), fat suppression with FA = 110° and a frequency shift of − 427.88 Hz, 4 × 4 × 4 mm^3 resolution. 3 healthy female volunteers (27–34 years) were measured under time-controlled breathing on a 3 T scanner (vidaFit, Siemens Healthineers, Erlangen, Germany) using the vendor independent sequence development framework gammaSTAR[8].

Results and discussion: In this study, all images were visually inspected regarding the influence of occurring artifacts. Fig. 1b shows the measurements of the 3 different $venc_{dir}$. It can be seen that the gradient in the x-direction has the highest perfusion signal compared to the y- and z-directions, especially in the right breast. This could be related to the anatomical structure of the breast, as more arteries may run in the back-to-front direction (x) than left-to-right (y) or top-to-bottom (z). Figure 2 shows the difference between the ss- and ms-acquisition. The images clearly show that although the measurements were performed with time-controlled breathing, residual motion entails minor phase errors resulting in increased ghosting artifacts. In addition, the best previously determined parameters ($venc_{dir}$ = x, ss) were adapted individually based on the fat preparation scan. The preparation scan analysis showed that a slightly different fat frequency shift of − 400 Hz and FA = 90° would be better in this case. Figure 3 shows the adjusted measurement compared to the standard settings. It can be seen that the fat artifacts are very low in both settings and visually almost the same, but in the adapted sequence the signal in the right breast seems to be slightly more homogeneous to the edge of the FoV.

Conclusion: These initial proof-of-principle measurements show that both the selection of $venc_{dir}$ and the ss- or ms-acquisition have a major impact on the perfusion signal and the general image quality. The individual adjusted sequencedoes not influence the signal that much, only the signal of the right breast seems to be a bit more homogeneous. Nevertheless, the measurements show that the perfusion signal in the breast can be measured with those parameter settings relatively robustly. In future work, it is important to analyze why the perfusion signal is lower in the left breast than in the right and to test the sequence for its applicability for tumor detection in initial studies in clinics.

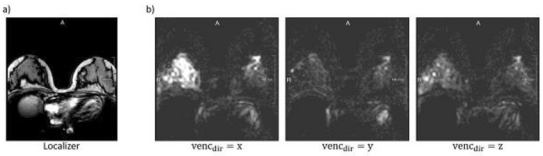

Fig. 1: a) Localizer scan for a structural overview of the breast is displayed b) Shown are the 3 different ASL images in the breast for the different $venc_{dir}$. It can be seen that for $venc_{dir}$=x the perfusion signal is highest, especially in the right breast. In the z-direction, signal is also still measurable and clearly seen, especially in the right breast, but also in the left. In the y-direction, the perfusion signal is the lowest.

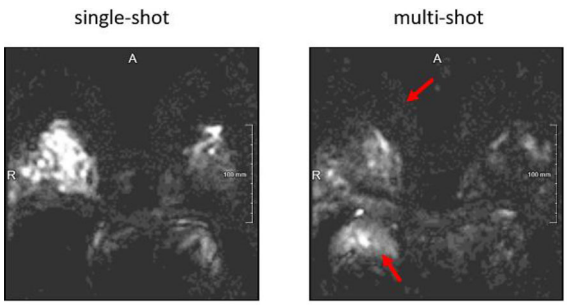

Fig. 2: Displayed are the different perfusion signals for the ss- as well as the ms-acquisition. It can be clearly seen that the fat suppression does not work as well in the ms-measurement as in the ss and fat artifacts occur along the phase encoding direction (red arrows).

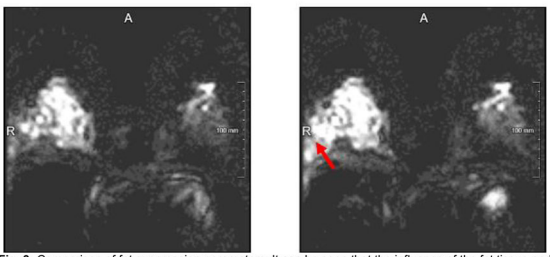

Fig. 3: Comparison of fat suppression parameters: It can be seen that the influence of the fat tissue and the artifacts which appear are almost the same. In the adapted sequence, the signal appears to be slightly more homogeneous in the right breast at the edge of the FoV (red arrow).

References:
[1]Mann et al. JMRI 2019
[2]Wong. JMRI 2014
[3]Wong et al. MRM 2006

[4]Günther et al. MRM 2005
[5]Del Grande et al. RadioGraphics 2014
[6]Huber et al. ESMRMB Abstract ID 87, 2023
[7]Qin et al. MRM 2016
[8]Cordes et al. MRM 2020 and https://gamma-star.mevis.fraunhofer.de/

P181.
Vessel-encoded ASL in non-healthy subjects and comparison to pilot normative CBF data acquired with pcASL

J. Keller[1,2], M. Chappell[3], T. Okell[4]

[1]Na Homolce hospital, Radiodiagnostics, Prague, Czech Republic;
[2]3rd Faculty of Medicine, Charles University, Prague, Czech Republic;
[3]Sir Peter Mansfield Imaging CentreSchool of Medicine, University of Nottingham, Nottingham, United Kingdom;
[4]Wellcome Centre for Integrative Neuroimaging (FMRIB), Nuffield Department of Clinical Neurosciences, University of Oxford, Oxford, United Kingdom

Introduction: Cerebral blood flow (CBF) can be studied using arterial spin labeling (ASL), with several acquisition possibilities. To set up a robust acquisition and analysis solution for the clinical use of ASL, we analyzed CBF data from a cohort of healthy volunteers (HV) and checked the known dependence of CBF on age. We also tested the feasibility of including Vessel-encoded ASL (VE-ASL) for separating the signals from the vertebral (VA) and internal carotid (ICA) and/or external carotid (ECA) arteries in scans on HVs and two patients (PT) described below.

Methods: ASL data of 11 HV (48-73Y,mean 61,SD 5.9) was acquired on 3 T Siemens Skyra (PCASL [1], 3 × 3 × 36 mm, 21 slices, distance factor 10%, TR = 4500 ms, TE = 14.3 ms, 80 measurements, labeling duration = 1800 ms, PLD = 2000 ms, TA = 6:05), T1 MPRAGE (1 × 1 × 1 mm, no fat sat., TR = 2.3 s, TE = 2.24 ms, PAT = 2, TA = 4:44 min) and T2 SPC FLAIR (1 × 1 × 1 mm, TA = 5:56 min). The data were processed using FSL tools [2], the statistical analysis was performed using R.

Due to corregistration issues, FLAIR had to be used to calculate partial volume effect (PVE) estimates for gray matter (GM) and white matter (WM). Masks excluding susceptibility artifacts were used. VE-ASL was performed using a custom sequence [3] and processed with custom scripts built around respective FSL tools [2].

53-year old male A had several older ischemic lesions in the left hemisphere and one in the right cerebellar hemisphere related to the full occlusion of the right VA and the left ICA (blood flow only from the ECAs, right ICA and right VA).

51-year old male B had a history of bleeding in the right cerebellar hemisphere, operated 28 years ago. 7 years ago he was scanned using 2D and 3D Siemens ASL sequences. Currently, these sequences were repeated and mbPCASL and VE-ASL were added.

Results: The susceptibility and non-linear registration artifacts severely disrupt CBF analysis with FSL tools. In older subjects, both HV and PT, a fatty bone marrow degeneration is often present, which, along with modern short TE 3 T acquisitions, create yet another "surface" for skull removal tools. Furthermore, these subjects often have metal dental implants of various types. Even though they are MRI conditional, eddy currents are induced and may modify signal in relatively large scale. With strict masking and FLAIR-based registration a clear relation of CBF decline with age was detected in the artifact-free area between the level of basal ganglia and the highest common brain tissue levels with masks excluding frontal artifacts (mean CBF 41.7 ± 6, p = 0.025). After PVE correction, the average CBF was analyzed for GM (mean CBF = 76.11 ± 12, p = 0.071) and WM (mean CBF = 22.0 ± 4, p = 0.001). The same pipeline was used for PT.

In A, it was impossible to find a level with both hemispheres without any lesion. In the level used for the normative evaluation, only healthy right hemisphere was masked. As expected with respect to the vessel occlusion, CBF values were decreased compared to the healthy subject of the same age (calculated from our normative data, calculated norm, CN), in the "healthy" hemisphere average CBF 33.0 (CN 47.0), GM 37.5 (CN 85.7). VE-ASL in the same area gave CBF values for left ICA 14.51 ± 8.1, left VA 5.05 ± 6.1, left ECA 0.98 ± 1.3 and right ECA 0.93 ± 0.5 mL/100 g/min, confirming major inflow from the left ICA.

In B, the CBF measurements were higher in average CBF: 52.5 (CN 48.6), but lower in GM: 61.3 (CN 88.1). VE-ASL in the same area gave CBF values for right ICA 10.88 ± 12.9, left ICA 22.10 ± 16.7, right VA 0.88 ± 1.0 and left VA 3.04 ± 5.4 mL/100 g/min, suggesting no diaschisis is present.

Discussion: On the limited dataset the known CBF decline with age was best detected in WM (typical WM geometry has lower PVE, resulting in more voxels with pure WM volume than GM). GM relation was statistically insignificant, contrary to PVE-uncorrected CBF. In PT, PVE correction may fail due to several reasons (eg. lesional brains are more problematic to segment, CBF itself may be lower etc.).

VE-ASL can be used not only for the qualitative maps or on the voxel-based way, but as well for measuring in larger volume. In actual patients, VE-ASL may help to track the changes in the vessel territories—worsening caused by the disease or improvement due to medical intervention.

Conclusion: ASL and VE-ASL can be used in clinical settings, however the processing pipeline has to be carefully monitored and HV data may help to interpret the data.

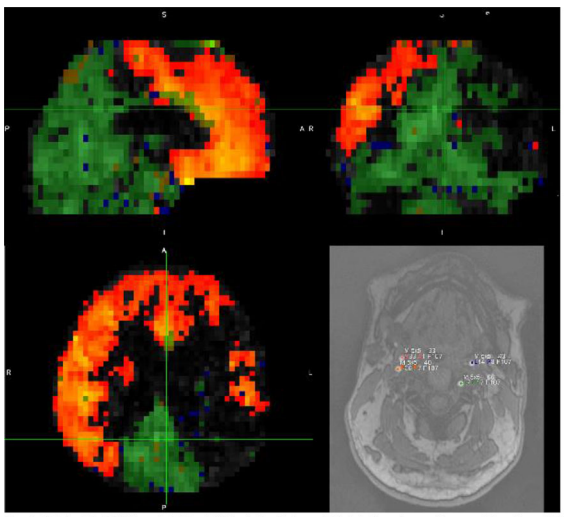

Fig. 1: Subject A, CBF threshold 5 mL/100 g/min. Bottom right: labeling plane with vessel locations. CBF maps: left ICA (LICA) red-yellow,left VA (LVA) green,left ECA blue, right ECA pink. LICA is a major cortical supply, smaller is LVA, minimum is from ECAs.

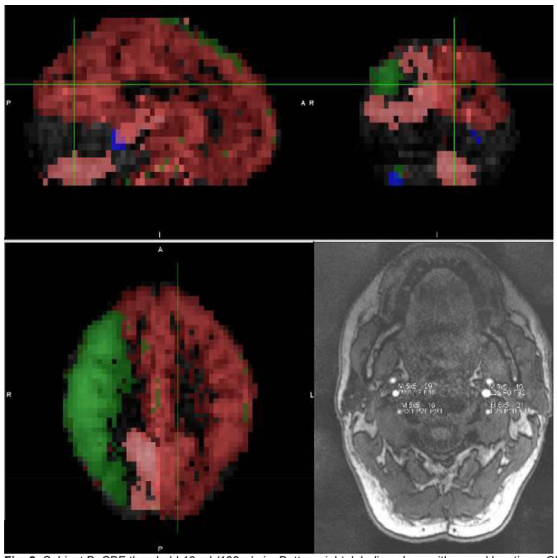

Fig. 2: Subject B, CBF threshold 10 mL/100 g/min. Bottom right: labeling plane with vessel locations. CBF maps: left ICA red,right ICA green,left VA blue,right VA pink. Left VA atypically supplies part of the right cerebral hemisphere and also right cerebellar hemisphere (CH), as the left CH is destroyed by bleeding. The left vertebral artery contribution is small. Supratentorially, left carotid artery supplies also a part of the right hemisphere.

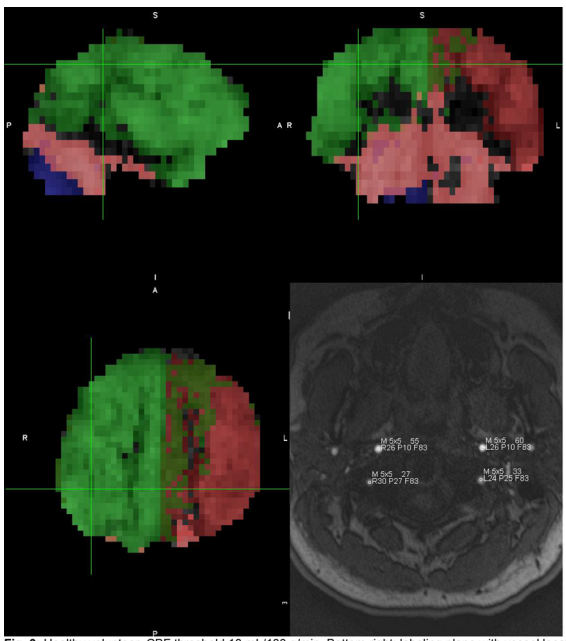

Fig. 3: Healthy volunteer, CBF threshold 10 mL/100 g/min. Bottom right: labeling plane with vessel locations. CBF maps: left ICA red,right ICA green,left VA blue,right VA (rVA) pink. rVA partially supplies very small part of occipital lobes.

References:

1. Auerbach EJ et al. Multiband accelerated spin-echo echo planar imaging with reduced peak RF power using time-shifted RF pulses. Magn Reson Med. 2013;69:1261–1267.
2. Chappell MA et al. Variational Bayesian Inference for a Nonlinear Forward Model. IEEE Trans. Signal Process. 2009;57:223–236.
3. Okell TW et al. Cerebral blood flow quantification using vessel-encoded arterial spin labeling. J Cereb Blood Flow Metab. 2013;33:1716–1724.

Supported by Ministry of Health, Czech Republic (NHH, 00023884) and NV 18-04-00346.

P182.
Investigation of technical variability in ASL data using MR phantoms

G. van Couwenberghe[1], S. Beun[1], A. Oliver-Taylor[2], X. Golay[2,3], E. Achten[1], P. Clement[1,4]

[1]*Ghent University, Department of Diagnostic Sciences, Ghent, Belgium;*
[2]*Gold Standard Phantoms, London, United Kingdom;*
[3]*UCL Queen Square Institute of Neurology, University College London, London, United Kingdom;*
[4]*Ghent University, Department of Medical Imaging, Ghent, Belgium*

Introduction: Arterial Spin Labeling (ASL) is a non-invasive MR imaging technique used to quantify perfusion, showing high promise for the diagnosis of many neurological and psychiatric disorders1. However, the clinical application of ASL is limited due to the possible influence of technical factors such as scanner and coil variability. To address this limitation, MR phantoms, such as the Quantitative Arterial Spin Labeling Perfusion Reference (QASPER), are being developed to investigate the technical variability in ASL measurements. QASPER is a flow phantom that mimics the process of arterial blood delivery to the brain. Although QASPER promises to be a controllable and reproducible tool to evaluate ASL measurements, it is a newly developed phantom that requires validation before it can be used in research and clinical settings2. This project aims to optimize the QASPER data acquisition protocol by defining the optimal post-label delay (PLD) for multiple flow rates and is a first effort to evaluate the short- and long-term stability of the QASPER phantom.
Methods: Structural and perfusion data of the QASPER phantom were acquired on a Siemens 3 T Prisma Fit MRI (Siemens, Erlangen, Germany), using the 64-channel head coil (Siemens, Erlangen, Germany). PCASL data, with a label duration of 1.8 s. PLDs ranging from 100 to 2900 ms were used for QASPER flow rates of 450, 350, 250, and 150 ml/min, to optimize the scanning protocol. To assess the longitudinal stability of the phantom, ASL data was acquired with a label duration of 1.8 s, a PLD of 650 ms, and a phantom flow rate of 350 ml/min for four consecutive days, after which the phantom was scanned weekly for another two months. Mean perfusion values were calculated using ITK-SNAP3, and plotted over time. Additionally, the Functional Stability Reference (FUNSTAR) phantom was analysed using the Neurospin QA package4 to evaluate the technical variability of the scanner.
Results: The optimal PLD values for the flow rates are illustrated in Fig. 1: 500, 650, 900, and 2450 ms for flow rates 450, 350, 250, and 150, respectively. Additionally, the QASPER phantom appears to show instability around a PLD of 2000 ms, as illustrated in Fig. 2. Furthermore, the short- and long-term stability of QASPER is illustrated in Fig. 3. Measured perfusion on most time points remained around an average value of 0.014 ($\pm$ 0.00439). However, on two time points, the measured perfusion significantly deviated to lower values of 0.006 and 0.005 (timepoint 2 and 3), which was not recorded for the tSNR measured using the FUNSTAR phantom.
Discussion: The optimal PLD for flow rates of 450, 350, 250, and 150 ml/min were defined for the QASPER phantom. Additionally, a measurement instability at a PLD of 2000 has been detected. It is currently unsure if this instability is scanner, sequence, or phantom related, but should be further examined as this PLD falls within the optimal PLD range for human perfusion imaging1. Additionally, perfusion measurements on QAPSER appear to be relatively stable, however, deviating perfusion on two time points have been detected. These might be explained by an instability of the phantom (i.e. bubble formation in the perfusion chamber or variations in the perfusate temperature) or a user-induced variability during scanning. More research is needed to further evaluate the short- and long-term

stability of the QASPER phantom to assess its usability for quality assessment of perfusion measurements.

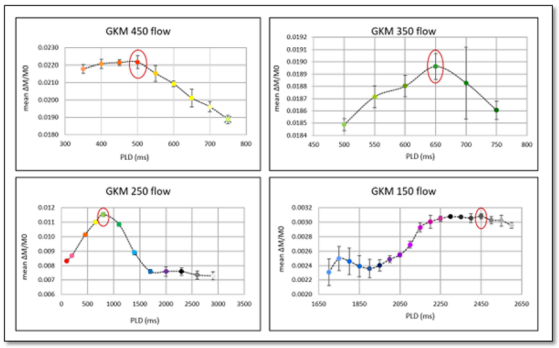

Fig. 1: General Kinetic Models of the investigated flow rates. The red oval indicates the optimal PLD of a flow rate.

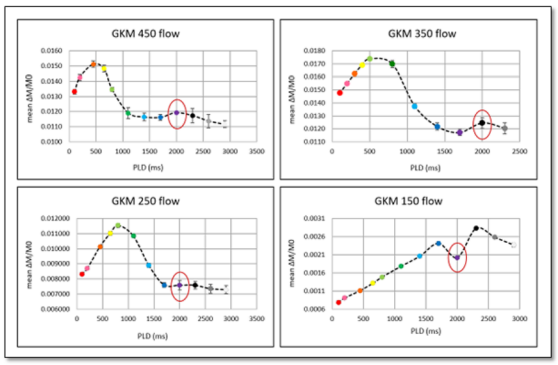

Fig. 2: General Kinetic Models of the investigated flow rates. The red oval indicates the instability around a PLD of 2000 milliseconds.

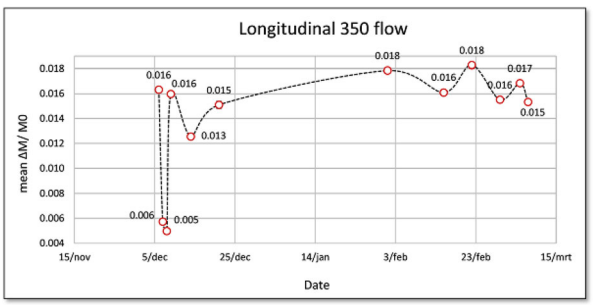

Fig. 3: Longitudinal scan results plotted over time using a flow rate of 350 ml/min and its optimal PLD of 650 milliseconds.

References:

1 Alsop, D. C. et al. Recommended Implementation of Arterial Spin-Labeled Perfusion MRI for Clinical Applications: A Consensus of the ISMRM Perfusion Study Group and the European Consortium for ASL in Dementia. *Magnetic Resonance in Medicine* **73**, 102-116 (2015). https://doi.org/10.1002/mrm.25197

2 Oliver-Taylor, A. & Golay, X. Avortical phantom forASL perfusion MRI.

3 Yushkevich, P. A. et al. User-guided 3D active contour segmentation of anatomical structures: Significantly improved efficiency and reliability. *Neuroimage* **31**, 1116-1128 (2006). https://doi.org/10.1016/j.neuroimage.2006.01.015

4 Mauconduit, F. Documentation QUALITY ASSURANCE PACKAGE. *NeuroSpin*, 14 (2021).

P183.
Repeated ASL measurements as a method for detection of altered cerebral blood flow in patients in the neurointensive care unit

S. Tapper[1], S. Wyss[1], A. Tisell[1], K. Wårdell[1]

[1]*Linköping University, Linköping, Sweden*

Introduction: Patients in the Neurointensive Care Unit (NICU) who have suffered from brain damage such as subarachnoid hemorrhage or traumatic brain injury, need to be monitored carefully to prevent secondary brain insults [1]. Altered cerebral blood flow (CBF) can be a first sign, and therefore, early detection is crucial for the patient to start appropriate preventative treatment in time [2]. At the Department of Neurosurgery in Linköping University Hospital, a unique setup is available with an MRI scanner located in the NICU. This setup facilitates daily repeated MR measurements without the extra risk of moving the patient to another department. However, most MR-based perfusion techniques require a contrast agent, which is not recommended for daily repeated measurements due to patient risks from repeated exposure [3]. Arterial Spin Labeling (ASL) is a subtraction-based MRI technique not requiring any contrast agent and instead relies on magnetically labeling arterial blood water [4]. Therefore, the current aim of this project is to implement an ASL-based workflow using repeated MRI measurements for the detection of altered CBF in the NICU patient.

Methods: MR data was acquired from a healthy participant using a 3 T MR system (Skyra, Siemens Healthineers) equipped with a 20-channel head coil. Informed written consent was obtained from the participant and this study was approved by the local ethics committee (Dnr 2012/434-31, 2018-143/32). The imaging protocol consisted of structural high-resolution 3D MPRAGE T1-weighted (T1w) imaging, pulsed ASL with perfusion mode FAIR QII [5, 6] (FOV = 205 × 205 mm^2; voxel size = 1.6 × 1.6 × 3.0 mm^3; scan time = 5 min; collecting four control-pairs of 40 slices with 3 mm thickness), and proton density weighted (PDw) turbo spin echo imaging using the same geometry as for the ASL acquisition. MRI measurements were performed on six different occasions (Day 1, 3, 5, 8, 9, 12) during a 12-day period mimicking a potential monitoring scenario for a patient in the NICU. Processing steps were mainly built upon the FMRIB Software Library (FSL) [7] and the workflow is summarized in Fig. 1. Both PDw images and ASL data were motion corrected and brain masked using the T1w images, which were processed using *fsl_anat*. Furthermore, the T1w images were also used for computation of partial volume estimates (PVEs), which were used for calculation of voxelwise values of the brain/blood partition coefficient, λ, and for T_1 and T_2^*-correction. The relative CBF map was calculated by subtraction and averaging of control/label pairs and by performing kinetic model inversion to account for the T_1-relaxation of blood. The calibration was performed with a voxelwise approach using scaling constants, λ_{PVE}, and the signal intensity of the processed PDw images, to generate a map in absolute units of ml/100 g/min. The resulting absolute CBF maps were registered to the structural T1w images acquired at baseline (day 1) to enable day-to-day comparison. Finally, the mean CBF in GM was calculated using the FSL function *fslstats* for all processed and calibrated CBF maps.

Results: Figure 2 illustrates the processed, calibrated, and registered CBF maps computed for all six repeated MRI measurements. The mean CBF_{GM} was 54.6, 56.2, 52.9, 60.1, 58.2, 59.7 ml/100 g/min for day 1, 3, 5, 8, 9, 12, respectively. For this experiment, the total

variation was 57.0 ± 2.9 ml/min/100 g over the six measurements. Difference maps illustrating the change in CBF between two subsequential measurement days were computed to detect an altered CBF (Fig. 3). The largest changes in CBF were observed around the edges of the brain and a small increase in mean CBF was observed during the second measurement week. The mean change in CBF was calculated for each slice of the CBF map to show the change in CBF on a global level.

Discussion: We have implemented a workflow for absolute quantification of repeated ASL measurements, which showed a low variation between the measurement days when evaluated on a healthy participant. This work is continuous and patient measurements are currently being performed and evaluated. At a later stage, we are also aiming to combine this workflow with MR flow measurements of the larger arteries entering the brain and with local microcirculation recording with laser Doppler flowmetry. Thus, to investigate the CBF from a macro- to a micro perspective.

Conclusion: Developing a workflow for daily MR measurements of patients in the NICU for non-invasive observation of changes in CBF could be beneficial to prevent secondary brain insults. Future work includes incorporating MR measurements within the clinical neurointensive care monitoring protocol.

Acknowledgement

This work was supported by The Swedish Foundation for Strategic Research (RMX18-0056) and The Swedish Research Council (2020-03131).

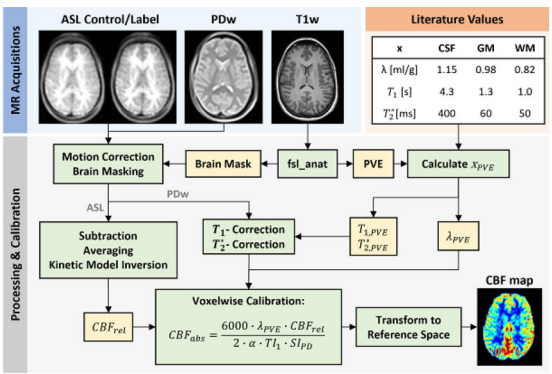

Fig. 1: Analysis workflow illustrating the processing and calibration steps. ASL data was calibrated using a voxelwise approach to obtain the CBF map in absolute units of ml/100g/min. Partial volume estimates and literature values of λ, T_1, and T_2^* were used for calculation of voxelwise values. λ = brain/blood partition coefficient, α = labeling efficiency, TI_1 = bolus duration, SI_{PD}= signal intensity of PDw images [4].

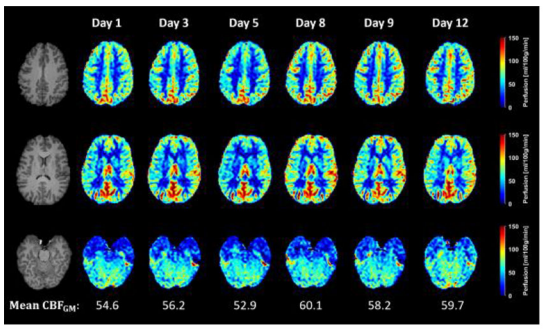

Fig. 2: Illustration of three example slices from the processed, calibrated, and registered CBF maps. The maps are in absolute units and the calculated mean CBFs in GM are shown at the bottom of the Figure.

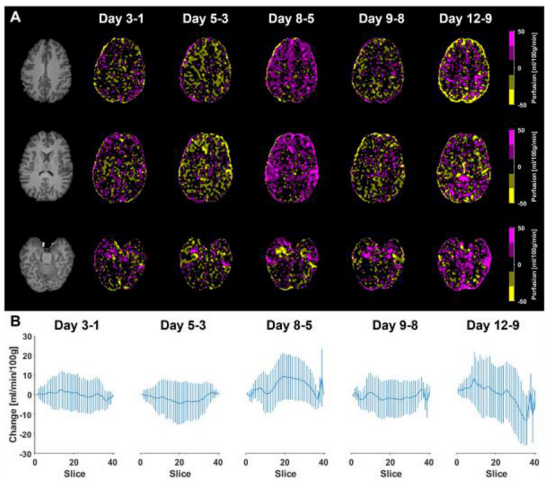

Fig. 3: Illustration of three example slices from the computed difference maps. The segmented colorbar indicates an increased perfusion in magenta, a decreased perfusion in yellow, and a small/no change in black, between two sequential measurement days (A). The corresponding mean change ± SD calculated for each slice of the map (B)

References

1. Neifert, 2021
2. Geraghty, 2017
3. Do, 2020
4. Alsop, 2015
5. Kim, 1995
6. Wong, 1998
7. Jenkinson, 2012

P184.
Evaluation of blood–brain barrier leakage in an ALS mouse model using $H_2{}^{17}O$-MRI

Y. Komaki[1], H. Kameda[2], F. Seki[1], K. Kudo[2]

[1]*Central Institute for Experimental Animals, Live Animal Imaging Center, Kawasaki, Japan;*
[2]*Hokkaido University, Hokkaido, Japan*

Introduction: Amyotrophic lateral sclerosis (ALS) is a neurodegenerative disease characterized by the progressive degeneration of motor neurons, resulting in muscle weakness and atrophy. The blood-brain-spinal cord barrier (BBSB) in ALS is known to be damaged, and swellings of astrocyte endfeet around blood vessels are also observed (Nicaise et al., 2009). However, conventional gadolinium (Gd)-enhanced MRI cannot clearly assess this BBSB leak (Evans et al., 2014). Therefore, we investigated the use of oxygen-17 (^{17}O) MRI (Kudo et al., 2018) to evaluate the BBSB leak in an ALS mouse model.

Methods: Behavioral and multimodal MRI evaluations were performed on SOD1-G93A transgenic mice (B6SJL-Tg(SOD1*G93A)1Gur/J, The Jaxon laboratory, USA) as a model of ALS like. This study was approved by the local Animal Experiment Committee and was conducted in accordance with the Guidelines for Conducting Animal Experiments of the Japanese Central Institute for Experimental Animals (approval number: 21086). The animals were imaged using a 7.0 T MRI system equipped with actively shielded gradients (Biospec 70/16, Bruker BioSpin, Ettlingen, Germany), and $H_2{}^{17}O$-MRI was performed. In addition, behavior analysis, diffusion tensor imaging (DTI), and dynamic contrast-enhanced MRI (DCE-MRI) were performed. The $H_2{}^{17}O$-MRI was conducted via Intracisternal injection (i.c.), and via intravenous injection (i.v.).

Anatomical T2WI: RARE sequence, TE 40 ms, TR 3000 ms, average 3, RARE factor 8, Resolution 75 × 75 × 500 µm, scan time 3 m 54 s
DTI: DWI-EPI sequence, TE 18.3 ms, TR 4000 ms, average 1, segments 8, diffusion direction 6 (1 B0), b value 1000 smm^2, Resolution 125 × 125 × 600 µm, scan time 3 m 44 s
DCE-MRI: FLASH sequence, TE 1.4 ms, TR 39 ms, Flip angle 11 deg., average 1, 204 repetitions, Resolution 150 × 150 × 1000, scan time 17 m
Dynamic T2WI: RARE sequence, TE 100 ms, TR 3000 ms, average 1, 130 repetitions, RARE factor 16, Resolution 100 × 100 × 1000 µm, scan time 65 min
$H_2{}^{17}O$: 90% 17O-enriched water, NUKEM Isotopes, Germany

Results: Behavior analysis revealed a decline in general condition and hind foot reflex after the onset of ALS-like symptoms. T2-weighted imaging (T2WI) showed a high signal in the hypoglossal nerve after the onset of symptoms. DTI revealed a decrease in fractional anisotropy (FA) in the cerebellum and corticospinal tract (CST) after the onset of symptoms (Fig. 1). DCE-MRI showed an increase in MR signal in the cerebellum during the late phase after the onset of symptoms (Fig. 2). The $H_2{}^{17}O$-MRI (i.v.) revealed a significant increase in ^{17}O concentration in the CST before the onset of symptoms (Fig. 3). The $H_2{}^{17}O$-MRI (i.c.) showed an increase in ^{17}O concentration in the cerebellum during the early phase before and after the onset of symptoms (Fig. 4).

Discussion: Our results demonstrate the feasibility of using ^{17}O-MRI to evaluate BBSB leak in an ALS mouse model. In addition, our findings suggest that BBSB leak in the cerebellum and CST may be associated with the development of ALS-like symptoms. The increase in ^{17}O concentration in the CST before the onset of symptoms suggests that this technique may have potential as an early diagnostic tool for ALS.

Conclusion: In conclusion, our study demonstrates the potential of ^{17}O-MRI to evaluate BBSB leak in an ALS mouse model. Further studies are needed to confirm the utility of this technique in the diagnosis and monitoring of ALS in humans.

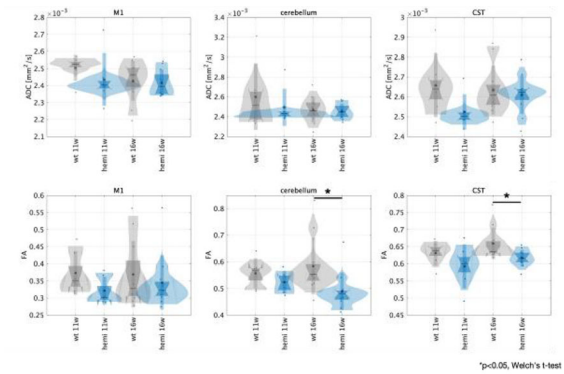

Fig. 1: Comparison of FA and ADC in ALS models and wild-type mice by DTI measurements. DTI revealed a decrease in fractional anisotropy (FA) in the cerebellum and corticospinal tract (CST) after the onset of symptoms (16w).

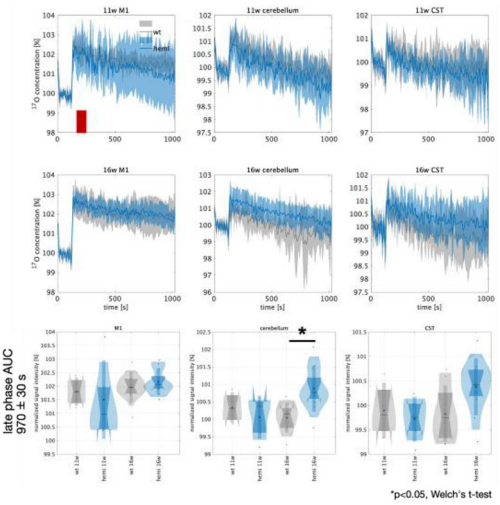

Fig. 2: Comparison of ALS models and wild-type mice by DCE-MRI. DCE-MRI showed an increase in MR signal in the cerebellum during the late phase after the onset of symptoms (16w).

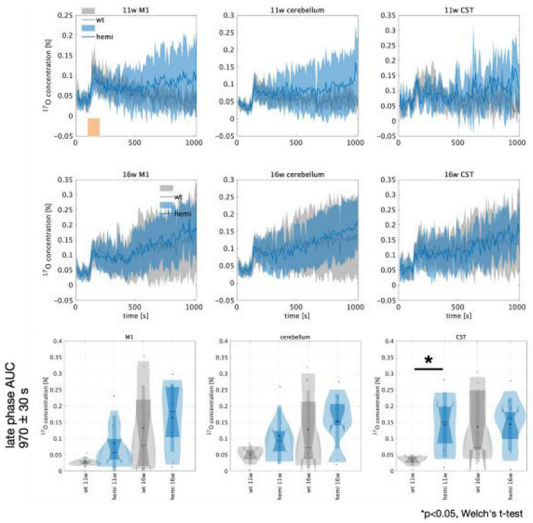

Fig. 3: Dynamic MRI in a mouse model of ALS with intravenous $H_2{}^{17}O$. The $H_2{}^{17}O$-MRI (i.v.) revealed a significant increase in ^{17}O concentration in the CST before the onset of symptoms (11w).

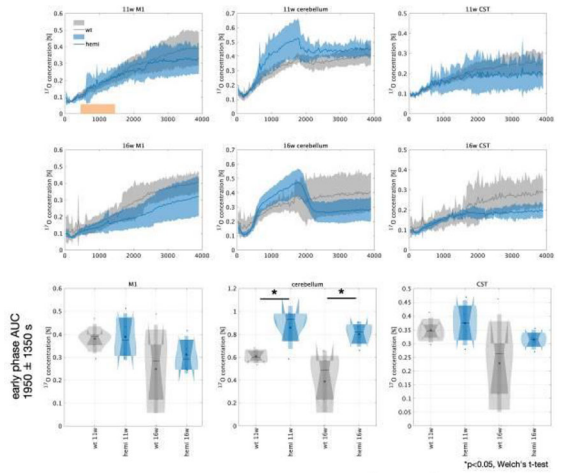

Fig. 4: Dynamic MRI in a mouse model of ALS with intracisternal $H_2{}^{17}O$. The $H_2{}^{17}O$-MRI (i.c.) showed an increase in ^{17}O concentration in the cerebellum during the early phase before and after the onset of symptoms (11, 16w).

References:

1. Evans, M. C., Serres, S., Khrapitchev, A. A., Stolp, H. B., Anthony, D. C., Talbot, K., Turner, M. R., & Sibson, N. R. (2014). T2-weighted MRI detects presymptomatic pathology in the SOD1 mouse model of ALS. *Journal of Cerebral Blood Flow and Metabolism*, *34*(5), 785–793. https://doi.org/10.1038/jcbfm.2014.19

2. Kudo, K., Harada, T., Kameda, H., Uwano, I., Yamashita, F., Higuchi, S., Yoshioka, K., & Sasaki, M. (2018). Indirect proton MR imaging and kinetic analysis of 17O-labeled water tracer in the brain. *Magnetic Resonance in Medical Sciences*, *17*(3), 223–230. https://doi.org/10.2463/mrms.mp.2017-0094

3. Nicaise, C., Mitrecic, D., Demetter, P., De Decker, R., Authelet, M., Boom, A., & Pochet, R. (2009). Impaired blood-brain and blood-spinal cord barriers in mutant SOD1-linked ALS rat. *Brain Research*, *1301*, 152–162. https://doi.org/10.1016/j.brainres.2009.09.018

P185.
Possibilities of the dynamic MRI perfusion assessment of the intact white matter

V. Popov[1], Y. Stankevich[2], L. Vasilkiv[2], A. Tulupov[2]

[1]*Novosibirsk State University, Novosibirsk, Russian Federation;* [2]*International Tomography Center Siberian Branch of Russian Academy of Sciences, Novosibirsk, Russian Federation*

Introduction: Multiple sclerosis (MS) is a chronic inflammatory demyelinating disease of the central nervous system, which gives rise to multifocal focal lesions and to diffuse neurodegeneration entire brain clinically characterized by physical disability and cognitive impairment affect quality of life. Recent studies show that hemodynamic disorders and disruption of white matter integrity are important components in the pathophysiology of neurodegenerative diseases [1]. A comprehensive assessment of the patient's neurovascular system should include not only the diagnosis of lesions area, but also visually intact areas of the brain in different periods of time. It is supposed the neurovascular dysfunction unit contribute to the multiple sclerosis. The aim of this study was investigate possibilities the dynamic MRI perfusion assessment of the intact white matter on the example of vascular pathologies. The ischemic stroke is the most studied vascular pathologies, so it was chosen for investigation of the possibilities of non-contrast MRI perfusion dynamic evaluation of the intact white matter assessment.

Methods: The prospective cohort analytical observation of 42 patients with acute ischemic stroke was performed. Patients were examined on the 3 T MR-scanner by routine protocol (T1-WI, T2-WI, 3DFLAIR, DWI). The perfusion was evaluated by pseudo-continuous arterial spin labeling (pCASL) in the ischemic focus and contralateral region, in visually intact white matter in the same and contralateral hemispheres. Dynamic assessment was carried out for 1–3, 7–10 days and 3 months.

Results: At the ischemic stroke focus the cerebral blood flow (CBF, ml/100 g/min) was significantly ($p < 0.05$) increased from 19.86 ± 5.69 to 27.57 ± 4.86 (mean ± Std) by first to the second examination respectively and significantly decreased to 14.48 ± 3.66 by the 3rd study. The CBF was significantly increasing in the intact area of the contralateral hemisphere opposite to the stroke focus from 38.00 ± 6.19 on the first study, reaching by the second (39.64 ± 5.15) and by the third study (40.02 ± 4.52) normoperfusion. In other regions of interest, the CBF of visually intact white matter was significantly increased from the first to the third examination ($p < 0.05$), starting with hypoperfusion and reaching normoperfusion by the third study (Fig. 1).

Discussion: The authors (by Xi Xu, Zefeng Tan et al. in 2021 [2]) note the high efficiency and the presence of a correlation between perfusion parameters from pCASL and CT perfusion imaging in patients with ischemic stroke. The obtained results show significantly reduced CBF on 1st study (1–3 days) and the increase to the 3rd study (3 months) from hypo- to normoperfusion in visually intact areas of the brain after stroke manifestation. This demonstrates the possibility of successfully using non-contrast MRI perfusion (pseudo-continuous arterial spin labeling) in the dynamic assessment of visually intact white matter. Furthermore, it was shown that not only ischemic focus but brain as a complex structure is involved to the pathology. Dynamic assessment of cerebral perfusion and diffusion has been established its usefulness also in evaluating normal-appearing white matter (NAWM) that are difficult to evaluate with routine clinical MRI in demyelinating and vascular diseases [3]. This highlights the need for dynamic observation not only of the focal lesion area, but also of other intact areas of the brain—normal-appearing white matter in MS case.

Conclusion: The pCASL may be applied for the effective non-invasive dynamic evaluation visually intact areas indifferent neurodegenerative or neurovascular diseases and allowed consider the brain as an organ as a whole. Complex dynamic assessment of the lesion focus and visual intact white brain matter contributes to successful disease pathogenesis investigation, so therapy and prevention.

Yu. Stankevich, L. Vasilkiv and A. Tulupov received support from the Russian Science Foundation (project № 23-15-00377) in a part of the analysis of perfusion in multiple sclerosis.

Index	1st study	2nd study	3rd study	Significant (p)
	ml/100g/min			
CBF in the intact region of the stroked hemisphere	38,37±4,99	39,75±5,19	41,47±5,01	1-2, 1-3, 2-3 examinations – P<0,05.
CBF in the intact region of the normal hemisphere	43,97±4,69	45,09±3,33	44,67±3,37	1-2, 1-3 examinations – P<0,05; 2-3 examination – P>0,05.

Fig. 1: CBF values (mean +/- Std) of intact white matter of the same and contralateral hemispheres on day 1-3 (1 study), after 7 days (2 study) and 3 months (3 study).

References:

1. Li L, Chopp M et al. Perfusion and Diffusion Abnormalities of Multiple Sclerosis Lesions and Relevance of Classified Lesions to Disease Status. J Neurol Neurophysiol. 2014 Apr;2014(Suppl 12):12. https://doi.org/10.4172/2155-9562.S12-012. PMID: 25642354; PMCID: PMC4309012.

2. Xu X, Tan Z et al. Comparative Study of Multi-Delay Pseudo-Continuous Arterial Spin Labeling Perfusion MRI and CT Perfusion

in Ischemic Stroke Disease. Front Neuroinform. 2021 Aug 11;15:719719. https://doi.org/10.3389/fninf.2021.719719. PMID: 34456703; PMCID: PMC8386683.
3. Hori M et al. Advanced Diffusion MR Imaging for Multiple Sclerosis in the Brain and Spinal Cord. Magn Reson Med Sci. 2022 Mar 1;21(1):58–70. https://doi.org/10.2463/mrms.rev.2021-0091. Epub 2022 Feb 15. PMID: 35173096; PMCID: PMC9199983.

P186.
A novel calibration scan for subject-specific tissue suppression in arterial spin labeling

J. Huber[1], M. Günther[1,2], D. C. Hoinkiss[1]

[1]*Fraunhofer Institute for Digital Medicine MEVIS, Bremen, Germany;*
[2]*University of Bremen, MR-Imaging and Spectroscopy, Faculty 01 (Physics, Electrical Engineering), Bremen, Germany*

Introduction: Accurate suppression of static tissue signal and nulling of unwanted fat components are crucial steps towards robust application of Arterial Spin Labeling (ASL). However, the suppression of static tissue signal might be supoptimal due to subject-specific variations in T1 values. In addition, the spectral fat saturation pulse might be ineffective due to off-resonance effects and B1 variations. This work demonstrates a quick preparation scan which can be executed prior to ASL experiments, allowing subject-specific adaption of ASL background suppression.

Methods: The preparation scan is based on ideas from MR fingerprinting which itself might be challenging in abdominal organs and therefore not well suited. Here, multiple EPI readouts without fat saturation and with an excitation flip angle of 45° are acquired first to fit multiple T1 components into the resulting signal curve. Subsequently, additional preparation scans with 90° excitation follow for signal preparation. The fat saturation pulse is fixed to theoretically optimal values here. Next, the frequency and flip angle of the fat saturation pulse are varied to estimate the subject-specific optimal configuration for spectral fat suppression using a proper analysis algorithm (cf. Fig. 1). Therefore, the acquired timeseries is split into two separate datasets: The first dataset consists of the timeseries without fat saturation and is used to fit the T1 components of the tissue in the region of interest. The second dataset is used to estimate the optimal fat saturation configuration.
In this work, the calibration scan was applied to breast, brain, and a custom phantom. Written informed consent was acquired from all volunteers. The phantom consisted of two bottles, holding water and peanut oil. Sequence settings were: 15 EPI shots with 45° excitation flip followed by five preparation shots with 90° flip and 48 shots, varying the fat saturation off resonance from − 500 to − 400 Hz with an increment of 50 Hz, each applied with nominal fat saturation flip angles ranging from 10° to 170° with an increment of 10°. Other constant parameters of the EPI readouts were TE/TR = 25 ms/400 ms, Echo-train-length = 64, Matrix = 64 × 64, FoV = (256 × 256) mm^2, total acquistion time = 27 s. Using the bottle phantom, additional scans were performed using a single EPI readout with (1) No fat saturation, (2) Fat saturation with standard settings at 3 T, (3) Fat saturation with optimal adaptive settings, (4) Same as 3 but with additional inversion recovery preparation using the fitted fat T1 value. During T1 fitting, two major components were assumed for brain scans, while a single component was assumed in breast and phantom scans. In all cases, a single fat T1 component was assumed. All scans were carried out using implemented sequences in the gammaSTAR framework [1] on a 3 T Siemens Vidafit (Siemens Healthineers, Erlangen, Germany).

Results: Figure 2 shows calculated fat and tissue masks (a) and the residual summed fat signal (b). Fig. 3 shows the tissue signal evolution as well as estimated tissue parameters. Fig. 4 shows resulting adaptive fat suppression.

Discussion: The proposed calibration scan allowed identification of optimal settings for spectral fat saturation as demonstrated in Fig. 2a and b. Calculated configurations significantly differ from the standard setup, indicating the importance of adaptive calibration. Smeared minima in breast calibration scans indicate that stronger local off resonance exists in abdominal organs (cf. Fig. 2b). The proposed calibration scan helps to find the best global compromise. The fact that flip angles smaller than 110° appear to be optimal potentially indicates effects of B1 inhomogeneities which are also object-specific and therefore unknown prior to the scan. The calibration scan yielded realistic T1 estimates (cf. Fig. 3), which can be used for calculation of optimal timings of inversion pulses in subsequent ASL experiments. Using the adaptive settings, a reduction of ∼ 95% of the original fat signal was achieved which is significantly higher than using the standard settings (∼ 85%) (cf. Fig. 4). The suppression was further improved when combined with an inversion recovery module using estimated T1 values of fat. In future work, estimated parameters from the calibration scan should be directly used in ASL experiments. Therefore, the algorithms performance should be investigated with increased EPI slice thickness for combination with 3D ASL readouts and in cases where fat and tissue signal are not well spatially seperated.

Conclusion: We demonstrated a novel preparation scan which can be used to calibrate the background suppression as well as fat saturation pulses of an ASL sequence. This might be especially helpful in breast or liver ASL imaging.

Acknowledgements This work was funded by the Deutsche Forschungsgemeinschaft (DFG, German Research Foundation)—508707144

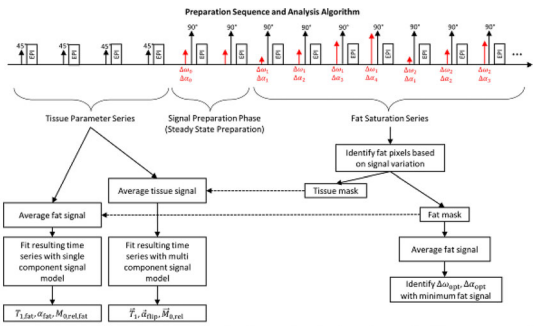

Fig. 1: Calibration sequence and analysis algorithm. ω_0,α_0 refer to the standard fat saturation conFiguration at 3T.

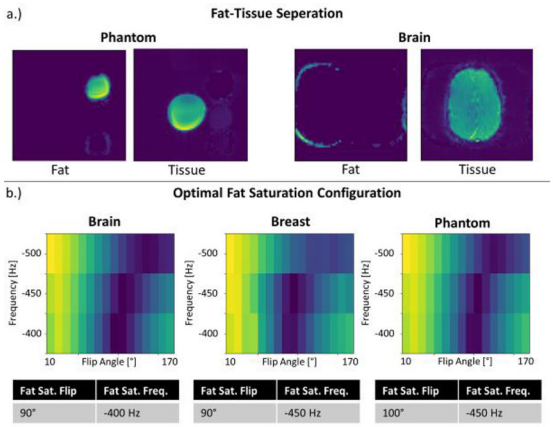

Fig. 2: a.) Examples for separation of fat and tissue pixel for the phantom and brain measurements; and b.) Evolution of fat signal for different fat saturation flip angles and frequencies.

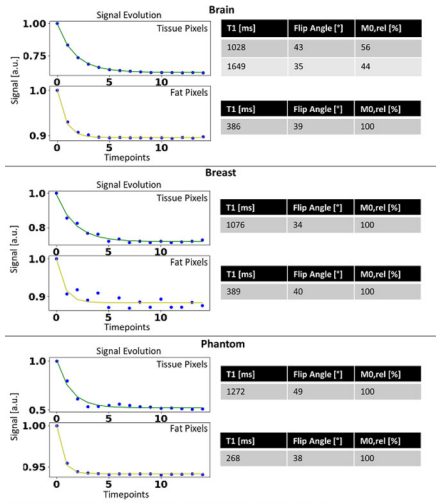

Fig. 3: Fitted tissue parameters for brain, breast, and phantom measurements.

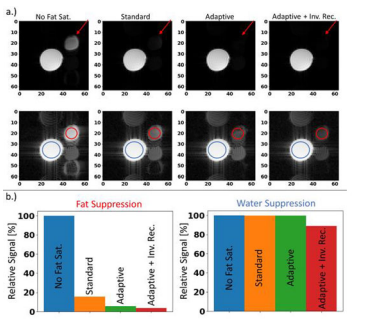

Fig. 4: a.) Examples images using different fat suppression techniques; and b.) Averaged signal in the indicated region of a.).

Reference:

[1] Cordes et al. MRM 83, 1277–1290

P187.
Surface-based analysis for partial volume corrected perfusion in The Irish Longitudinal Study on Ageing (TILDA)

J. Hu[1,2], M. Chappell[1,2], S. P. Knight[3,4], C. D. Looze[3,4], J. F. Meaney[4,5], R. A. Kenny[3,4,6]

[1]*University of Nottingham, Mental Health & Clinical Neurosciences, School of Medicine, Nottingham, United Kingdom;*
[2]*University of Nottingham, Sir Peter Mansfield Imaging Centre, School of Medicine, Nottingham, United Kingdom;*
[3]*Trinity College Dublin, The Irish Longitudinal Study on Ageing (TILDA), Dublin, Ireland;*
[4]*Trinity College Dublin, School of Medicine, Dublin, Ireland;*
[5]*St. James's Hospital, The National Centre for Advanced Medical Imaging (CAMI), Dublin, Ireland;*
[6]*St. James's Hospital, Mercer's Institute for Successful Ageing (MISA), Dublin, Ireland*

Introduction: Arterial spin labeling (ASL) MRI provides non-invasive measurements of cerebral blood flow (CBF) using blood water as an endogenous tracer. Aging is an important risk factor for cerebrovascular disease and neurodegenerative diseases. In order to properly interpret CBF changes in these disease conditions, it is important to understand normal age-related changes in CBF [1]. However, CBF estimates are significantly affected by partial volume (PV) effects, due to the relatively low resolution of ASL, which is often neglected. Additionally, regional analyses are conventionally performed using volumetric (i.e., voxel-wise) methods, which do not take advantage of the cortical information, e.g., the cortical surface representation of grey matter. In this study, a dual volumetric and surface-based analysis pipeline was proposed for The Irish Longitudinal Study on Ageing (TILDA) [2] data with the correction of partial volume effects (PVEc). Normal age-related changes in CBF were reported for non-PVEc and PVEc ASL data in the brain as well as surface-based and volumetric regions of interest (ROIs).

Methods: TILDA [2] is a prospective, cohort study, which collects health, economic and social data from nationallyrepresentative, community-dwelling Irish adults and investigates how various factors interact. This study included 468 participants (242 females) aged from 54 to 84 years old for whom T1-weighted and ASL data were available.

T1-weighted and pseudo-continuous ASL (pCASL) sequences were acquired on a 3 T system, using a 32-channel head coil. pCASL acquisition parameters were as follows: 30 interleaved pairs of images acquired alternating with and without arterial spin labelling, FOV = 240 × 240 mm^2, matrix = 80 × 80, TR = 4000 ms, TE = 9 ms, FA = 90°, SENSE = 2.5[SK1], and scan duration = 4 min 16 s. 13 slices (8 mm thick, 1 mm gap) were acquired sequentially in a caudocranial direction. A labelling duration of 1800 ms and a post-label delay (PLD) of 1800 ms were used. Calibration scans measuring the equilibrium magnetisation (M0) were also acquired using the same geometry as the pCASL sequence, with TR = 10,000 ms, TE = 9 ms, and scan duration = 20 s. B0 field maps were measured using a two-echo 2D gradient echo sequence with the same in-plane resolution as the pCASL scans and the following acquisition parameters: TR = 455 ms, TE1 /TE2 = 1.69/7.0 ms, FA = 90°, and scan duration = 39 s.

The Human Connectome Project (HCP) pipeline [3] was used for structural image processing. After the cortical surfaces were obtained from HCP pipeline, PVEs were derived using Toblerone [4] in surface-based approaches. OXASL [5], a toolbox for performing Bayesian analysis of ASL MRI data, was used for ASL data analysis including pre-processing, voxel-wise calibration, quantification,

partial volume correction and region analysis. The resulting non-PVEc and PVEc ASL data were projected onto individual"s structural cortical surface using Toblerone [6] and then registered to fsaverage5 from Freesurfer using Multimodal Surface Matching (MSM) by HCP work bench. Referring to the previous study [7] on TILDA data, linear regression models were built to measure CBF GM variation with age and sex as covariates for non-PVEc and PVEc ASL data in the whole brain as well as Destrieux atlas[8] for cortical ROIs and Harvard-Oxford atlas for volumetric ROIs. PV GM at 0.8 was used for thresholding pure GM in above atlases and PVEc. Fig. 1 presents the workflow of the pipeline.

Results: Figure 2 presents the projected non-PVEc and PVEc ASL images on the cortex of a subject in the structural space.

Fig. 3 shows the normative values for non-PVEc and PVEc GM CBF variation with age over all subjects.

Table 1 shows the regional CBF variation with age stratified by sex for non-PVEc and PVEc ASL on the cortical surface over all subjects.

Discussion: This work presented a dual surface-based and volumetric analysis method for TILDA ASL data. The partial volume effects were corrected to complement the former study which only examined whole brain GM [6]. Increased CBF GM was found for PVEc ASL on the cortex (table 1) compared to non-corrected results, consistent with previous comparisons with and without PVEc. Values of GM CBF were higher than the typically expected value ($\sim$ 60 ml/100gmin) in some regions, but this may be related to macrovascular contamination that cannot be corrected for in single-PLD ASL data. Age-related CBF changes were investigated and presented in the cortical ROIs which provide Reference CBF values for similar aged individuals. The results could also help subsequent research on CBF changes in disease.

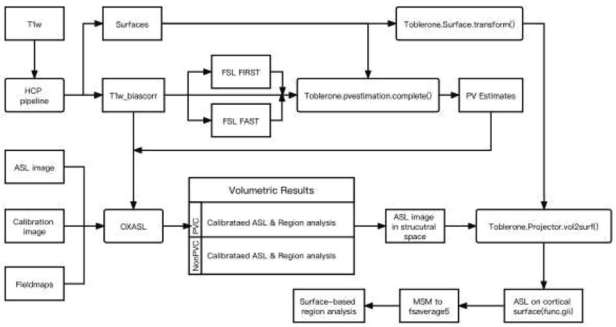

Fig. 1: The workflow of the pipeline used in this study.

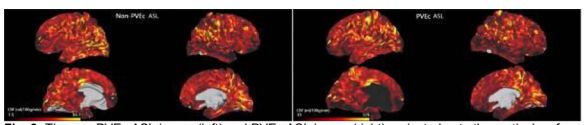

Fig. 2: The non-PVEc ASL image (left) and PVEc ASL image (right) projected onto the cortical surface from an example subject.

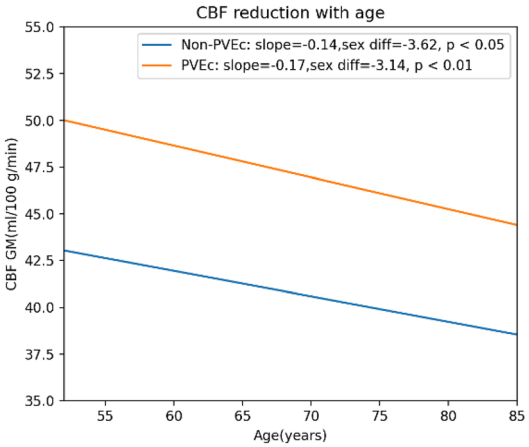

Fig. 3: Age-related CBF variation in non-PVEc and PVEc ASL data. Mean CBF GM of male is lower than female's

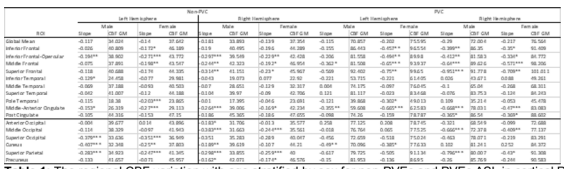

Table 1: The regional CBF variation with age stratified by sex for non-PVEc and PVEc ASL in cortical ROIs over all subjects. Slope Unit: ml/100g/min per year, CBF GM Unit: ml/100g/min, ***p<0.01, **p<0.05, *p<0.1.

References

[1] https://doi.org/10.3389/fnagi.2018.00214
[2] https://doi.org/10.1093/ije/dyy163
[3] https://doi.org/10.1016/j.neuroimage.2018.10.009
[4] https://doi.org/10.1109/TMI.2019.2951080
[5] https://github.com/physimals/oxasl
[6] https://doi.org/10.1101/2022.01.28.477071
[7] https://doi.org/10.1016/j.neuroimage.2021.117741
[8] https://doi.org/10.1016/j.neuroimage.2010.06.010

P188.
Neurovascular functional protocol's optimization by use of PC MRA fast acquisition and CFD simulation

M. P. del Pópolo[1,2], R. N. Alcalá Marañón[1,2,3], E. Petra[2], L. Ancari[1,4], S. Moguilner[1,5], R. Isoardi[1,3,4,6], F. Gonzalez N.[1,3,4,6], D. Fino Villamil[1,2,3,4]

[1]*Fundación Escuela de Medicina Nuclear, Magnetic Resonance, Mendoza, Argentina;*
[2]*Fundación Argentina para el Desarrollo en Salud, Mendoza, Argentina;*
[3]*Universidad Nacional de Cuyo, Mendoza, Argentina;*
[4]*Instituto Balseiro, Medical Physics, San Carlos de Bariloche, Argentina;*
[5]*Harvard University, Cambridge, MA, United States;*
[6]*Comision Nacional de Energia Atomica, Buenos Aires, Argentina*

Introduction: 3D PC MRA has become a widely used functional characterization of vascular pathologies, providing novel biomarkers to the standard geometrical assessment [1, 2]. Nevertheless, due to the acquisition's high temporal demands and the temporal and spatial resolution trade-off, its application at the clinical level is limited. The implementation of CFD allows the acquisition of a mere slice in order to simulate the entire response.

The aim of this work is to standardize a 3D PC MRA fast protocol to simulate the hemodynamic response and compare the obtained velocity fields with the previous information acquired for the entire vascular branch.

Methods: This study was approved by the institutional Ethics Review Board. The acquisition was performed in 4 patients in a 1.5 T Ingenia Philips scanner using a Head-Neck dStream 16 channels coil. The protocol includes: wT1 volumetric anatomical sequence, 3D ToF, 4D Flow and 1D-PC MRA. The parameters of both PC sequences are shown in Figs. 1 and 2 and their acquisition times were 11 and 1.20 min respectively.

To compare 3D ToF and 4D Flow sequences were compared performing an F-test (SPSS) in which the number of counts and SNR were evaluated.

Regarding the functional information and postprocessing procedures, VMTK V1.4.0 toolkit was used for mesh generation, OpenFOAM V9 for simulation, Python V3.8.10 for velocity field registration and ParaView V5.6.0 for visualization. Meshes with a number of tetrahedral cells ranging from 300 to 700 thousand units (including boundary layers) were generated. Due to the low Re number ($50 < Re < 600$) a laminar model was implemented, and blood was assumed as a Newtonian fluid. A transient model was implemented using the PISO algorithm. No slip conditions were set for the contact zones of the fluid with the walls and the pressure at the inlet was set as a non-zero gradient. The visualization was made by means of ParaView and subsequently converted to raw format.

The validation of the numerical result was done making a comparison of the velocity profile obtained by 4DFlow acquisition and the numerical result through the assessment of 4 cross-sectional planes, for this, a mapping of the corresponding pixels with the nodal information was performed by use of Python.

Results: A SNR comparison was performed between 3D ToF and 4DFlow sequences, where the arterial information (ARI) of the 3D ToF was 75.2 and ARI 4DFlow: 78.4; Brain Parenchyma Information of the 3D ToF: 25.86 and 4DFlow 30.5. The difference was seen in the number of counts, where the 3D ToF/4DFlow ratio was 3.5/1.

Fig. 3 shows the 3 analyzed velocity profiles with 4DF and CFD simulations. The numerically estimated behavior was verified by the raw data acquired with the sequence with a mean relative error range between 5 and 9% for the three velocities (Fig. 4).

Discussion: Due to the fact that the maximized speed readout in the case of 1D PC MRA depends on a correct cross-sectional programming of the sequence, it would be interesting to implement a 3D PC MRA acquisition with a mere slice for an optimal lecture of the velocity field.

Reduction of the acquisition time is feasible, and the simulation predicts the local properties of the studied flow correctly. However, when making a post intervention assessment it is not possible to work only with input data, unless we work with fluoroscopy data, in which case we could obtain accurate information. In such cases 4D flow should still be used in the whole region of interest as it would be the only MRA sequence capable of correctly characterizing the pathology.

Conclusion: Better characterization of the arteries is achieved through the use of 3D ToF. By use of CFD simulations, 3D ToF and 1D PC MRA sequences, time can be reduced 13.85 times. Time resolution can be increased in the future and consequently the simulation can be improved.

Sequence name	1D PC MRA	
Sequence parameters	Values	Comments
Spatial resolution [mm3]	1.2x1.2x3	Spatial resolution maximization
GAP [mm]	0	Optimal volumetric reconstruction
Matrix	288x288	-
Velocity encoding [cm/s]	100	Codification maximization
Flip angle [º]	10	In concordance with the encoding
AP-Sense	1.5	Acceleration of the acquisition
Respiratory motion compensation	None	Not required
Fold-over suppression	None	In order to diminish the acquisition time
VCG synchronism	On	In concordance with the trigger time requirement
Reconstructed phases	20	Diminish acquisition time

Fig. 1: Sequence parameters of the 1D PC MRA

Sequence name	3D PC MRA	
Sequence parameters	Values	Comments
Spatial resolution [mm3]	1.5x1.5x1.5	Spatial resolution maximization
GAP [mm]	-	Single slice
Matrix	288x288	-
Velocity encoding [cm/s]	100	Codification maximization
Flip angle [º]	10	In concordance with the encoding
AP-Sense	1.5	Acceleration of the acquisition
Respiratory motion compensation	None	Not required
Fold-over suppression	None	In order to diminish the acquisition time
VCG synchronism	On	In concordance with the trigger time requirement
Reconstructed phases	20	Diminish acquisition time

Fig. 2: 3D PC MRA Sequence Parameters

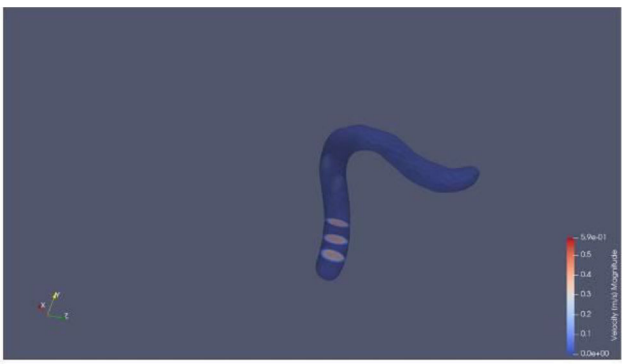

Fig. 3: Assessed cross sections of the carotid artery.

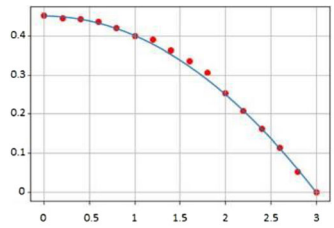

Fig. 4: Velocity profile [m/s] vs vessel cross-section [mm] for image information (red) and CFD simulation (Blue)

References:
[1] TURSKI, Patrick, et al. Neurovascular 4DFlow MRI (Phase Contrast MRA): emerging clinical applications. *Neurovascular Imaging*, 2016, vol. 2, no 1, p. 1-11.
[2] YOUN, Sung Won; LEE, Jongmin. From 2 to 4d phase-contrast mri in the neurovascular system: Will it be a quantum jump or a fancy decoration?. *Journal of Magnetic Resonance Imaging*, 2022, vol. 55, no 2, p. 347-372.
[3] SOUZA, Maria Sabrina, et al. Fluid flow and structural numerical analysis of a cerebral aneurysm model. *Fluids*, 2022, vol. 7, no 3, p. 100.

P189.
Contrast-enhanced MRA with GRASP outperforms the conventional TWIST in aortic diseases patients cohort

C. Calastra[1], F. Haupt[1], E. Kleban[1], A. Huber[1], H. von-Tengg Kobligk[1], B. Jung[1]

[1]*University of Bern, Department of Interventional and Pediatric Radiology, Bern, Switzerland*

Introduction: gadolinium-based contrast-enhanced time-resolved magnetic resonance angiography (CE-MRA) techniques depict the anatomy and dynamics of complex vascular structures [1]. This is desirable to reduce the number of invasive procedures for patients who otherwise may undergo repetitive X-ray angiograms during follow-up. Time-resolved angiography With Interleaved Stochastic Trajectories (TWIST) sequence is conventionally used to perform a time-resolved 3D CE-MRA; it is based on Cartesian acquisition and sharing of k-space data between adjacent time frames [2]. This trajectory is prone to respiratory-motion-induced image artefacts, such as spatial blurring of vascular boundaries. Radial-sampling-based techniques, such as GRASP (Golden-angle radial sparse parallel) sequence, are less sensitive to motion than cartesian sampling, and consequently improve the overall image quality [3]. GRASP is used in clinical routine to acquire CE liver dynamics. Here we aim to compare the performance of TWIST and GRASP for time-resolved CE-MRA on patients with aortic diseases.
Method: 30 patients (60.87 $\pm$ 16.11.y.o., seven females) with aortic diseases underwent a clinical examination including a TWIST and a GRASP sequences (acquisition parameters are summarised in Table 1). Prior each CE-MRA acquisitions the same amount of Gadovist-contrast-agent (Bayer, Switzerland AG Zurich) was administered (0.075 ml/kg, flow 4 ml/s). Data was acquired on a 1.5 T Magnetom SolaFit scanner equipped with a 32 channel body coil (Siemens, Erlangen).
A radiologist assessed overall image quality, contrast, vessel sharpness and image artefacts. To perform quantitative image analysis, circular regions-of-interest (ROIs) were placed at three aorta levels: ascending aorta (AA), descending aorta at the level of the pulmonary trunk (DA_pulm), and descending aorta at the level of the infrarenal arteries (DA_renal). Maximum slope of the contrast agent uptake, the full width at half maximum (FWHM) were calculated from normalized signal intensity time courses; vessel sharpness and signal to noise ratio (SNR) was calculated from the intensity profiles at the same levels in the aorta respectively as in [4, 5]. Temporal signal-to-noise ratio (tSNR) was calculated from the second half of the time course.
Result: GRASP was superior in tSNR, SNR, soft tissue contrast, vessel sharpness, and the overall image quality, TWIST was superior in FWHM and lower artifacts level. Maximum upslope is similar (Table 2)
Figure 1 shows the signal intensities over time for AA (red), DA at the levels of pulmonary trunk (blue) and infrarenal arteries (green) for GRASP and TWIST: with the current acquisition and reconstruction parameters, the absolute signal of GRASP is clearly higher than TWIST and corresponding time-courses are smoother. Representative images of TWIST and GRASP are in Fig. 2: one can see a superior soft tissue contrast and a better impression regarding image sharpness.
Discussion: GRASP sequence provided a superior overall image quality index, resulting from the qualitative scores of vascular contrast, soft tissue contrast and vessel sharpness—despite an increased artifact level compared to TWIST. The level of streaking artifacts can increase with the level of undersampling, i.e. when the number of acquired spokes is reduced. However, most streaking artifacts appeared in the periphery of the field-of-view (FOV) and the images remained of diagnostic value in the aortic regions. The improved vessel sharpness, both qualitative and quantitative, for all ROIs in GRASP compared to TWIST is assumed to result from the higher in-plane resolution and from reduced sensitivity of the radial trajectory to respiratory motion. The higher levels of tSNR in GRASP data compared to TWIST data (also visible in smoother signal-time-courses in Fig. 1 in all locations of the aorta) are likely linked to the smaller temporal footprint (temporal resolution). In TWIST, k-space lines are taken from a wider time range to reconstruct a single time frame resulting in a temporal footprint three times higher than temporal resolution [2]. Contrary, FWHM was lower for TWIST in all locations indicating the weighting of the k-space center for the image contrast in TWIST. It is possible to improve FWHM of GRASP by taking fewer radial projections to reconstruct a single time frame at the cost of increased radial undersampling artifacts. Higher SNR for GRASP sequence despite its higher spatial resolution and streaking artefacts shows that a significant spatial blurring in GRASP has not been found as further corroborated by both qualitative and quantitative analysis.
Conclusion: CE-MRA with GRASP allowed us to acquire better data compared to TWIST. Further research will becentred around the optimisation of the CS parameters.

	GRASP	TWIST
Temporal resolution [s]	1.8	1.98
Temporal footprint [s]	1.8	5.94
Spatial resolution [mm²]	1.56×1.56	2.89×1.56
Slice thickness [mm]	2.5-3.5	2.5-3.5
FOV [mm²]	400×400-500x500	400×400-500x500
Number of slices	52-56	52-56
Undersampling factor	19.1	-
PAT	-	2
Flip angle	17 °	17 °

Table 1: Acquisition parameters. Slice thickness and number of slices FOV vary depending of patient" characteristics and are equal for the same patient for the two sequences.

fwhm [s]	GRASP	TWIST
AA (pulm)	10.41±8.41	7.11±2.71
DA (pulm)	10.68±7.33	7.01±3.29
DA (renal)	11.31±8.23	6.51±2.90
Maximum slope [1/s]		
AA (pulm)	0.17±0.04	0.17±0.03
DA (pulm)	0.18±0.04	0.16±0.03
DA (renal)	0.18±0.04	0.15±0.02
tSNR after peak		
AA (pulm)	11.14±2.49	8.27±1.46
DA (pulm)	13.17±4.29	8.17±1.08
DA (renal)	9.13±1.98	7.75±1.31
Vessel sharpness [1/mm]		
AA (pulm)	0.16±0.09	0.10±0.05
DA (pulm)	0.23±0.13	0.11±0.06
DA (renal)	0.13±0.04	0.06±0.04
Contrast	1.33±0.52	1.83±0.41
Vascular sharpness	1.17±0.41	2.17±0.41
Image artefacts	3±0	2.17±0.41
Overall image quality	1.17±0.41	2±0.63

Table 2: Quantitative and qualitative assessment. Mean±standard deviation.

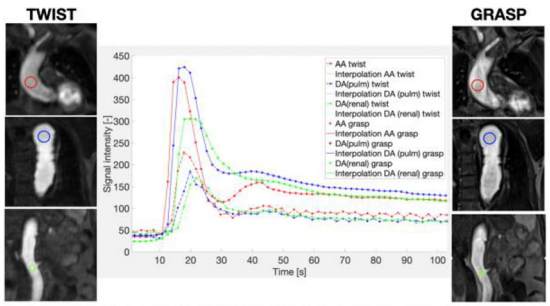

Fig. 1: Signal intensity over time for AA (red), DA at the level of pulmonary arteries (blu) and DA at the level of renal arteries (green) for GRASP and TWIST. On left and right it is respectively shown an example of where the ROIs were drawn at three aorta levels for TWIST and GRASP.

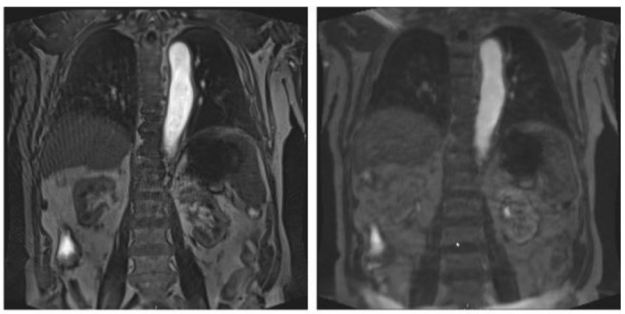

Fig. 2: Overall image quality comparison between GRASP (left) and TWIST (right). FOV=400X400.

References:
[1] Grist TM et al., 2012
[2] Laub G. Et al., 2006
[3] Feng L et al., 2014
[4] Goerner FL et al., 2011
[5] Larson AC et al., 2005

P190.
Magnetic resonance angiography of the aorta in the North Estonia medical centre

J. Šalina[1]

[1]*North Estonia Medical Centre, Radiology, Tallinn, Estonia*

Introduction: The aorta is the largest artery in the body. Early diagnosis of the aortic diseases can prevent life-threatening conditions. One of the diagnostic imaging modalities is magnetic resonance angiography (MRA). It is a form of magnetic resonance imaging that provides anatomical, functional and pathological information about the cardiovascular system and can be divided into two main types: contrast and non-contrast. The purpose of this paper is to share the experience of a radiologic technologist in performing MRA examinations of the aorta and to give an overview about different examination options of the aorta in magnetic resonance imaging (MRI) on the example of the North Estonia Medical Centre.

Methods: This paper describes three most commonly used contrast-enhanced techniques in the North Estonia Medical Centre, which are Continuously moving table MRA (CT-MRA), Time-resolved angiography With Interleaved Stochastic Trajectories (TWIST) and Electrocardiogram (ECG)-gated MRI + MRA. Also there are other types of MRA, such as single-station MRA, multi-station MRA and MRA for stented aorta. Since CT-MRA and TWIST have more advantages, single-station and multi-station MRA are currently not used. The all information is based on diagnostic protocols of the

North Estonia Medical Centre including personal experience of radiologic technologists and radiologists.
Results: The paper gives an overview about three main MRA techniques as well as other MRA methods used in the North Estonia Medical Centre, including advantages and disadvantages of MRA, indications for examination, patient preparation and positioning, radiologic technologist's responsibilities along with planning and performing MRA.
Conclusions: Nowadays there are several contrast and non-contrast techniques of MRA, allowing to evaluate aortic diseases. Type of MRA examination should be considered in each case individually depending on the examination purpose, patient medical history and condition. Information provided in this paper could be applied in practice in medical institutions and be useful for radiologic technologists and radiologists.

P191.
Multimodal perfusion PET/MR imaging with [18F]-Labeled FDG, FBB and PI-2620 within the AT(N) framework

A. Fettahoglu[1], M. Zhao[1], M. Khalighi[1], E. Mormino[1], M. Zeineh[1], M. Moseley[1], G. Zaharchuk[1]

[1]*Stanford University, Radiology, Stanford, United States*

Introduction: The National Institute on Aging-Alzheimer's Association (NIA-AA) proposed the AT(N) framework, a descriptive scheme for biomarkers used in Alzheimer's Disease (AD) [1]. Within this framework, [^{18}F]-FDG can infer the extend of neurodegeneration (N), [^{18}F]-FBB can relay the amyloid burden (A) and [^{18}F]-PI-2620 can image tauopathies (T) using positron emission tomography (PET). Taken together, these three PET probes can complete the AT(N) framework and lead to the biomarker classification of neurodegenerative diseases. In tandem, recent studies have identified Cerebral Blood Flow (CBF) to be a critical biomarker for various neurological disorders, including its involvement in early detectable pathological changes in Alzheimer's disease (AD) and its close relation to cognitive status of memory patients [2]. The overlapping pathophysiological changes that can be identified with CBF and metabolic maps emphasizes the importance of multimodal diagnostic evaluation in the clinical setting, where a dual-marker imaging paradigm would enable clinicians to have a more complete picture of disease pathogenesis and progression. Early-phase PET (ePET) imaging has shown promising results in identifying perfusion related changes [3–5]. The aim of this study was to validate early-phase static PET imaging of these three ligands as a viable perfusion test, using a new scaling approach to arterial spin labeling (ASL) MR measurements of the whole-brain cerebral blood flow (WB-CB) to generate semi-quantitative maps, and report the optimal time frame for ePET perfusion.
Methods: Subject characteristics of this retrospective study are given in Fig. 1. ePET static images at 30 s, 60 s, 120 s and 300 s post-injection were reconstructed using a time of flight (TOF)-enabled PET/MRI scanner (Signa, GE Healthcare, Waukesha, WI) with TOF-ordered subset expectation maximization (TOF-OSEM) algorithm with 3 iterations, 28 subsets, and with a 256 × 256 matrix size. 4 mm Gaussian filter was applied post-reconstruction. Images were registered to the MNI152 template space with FSL-FLIRT (Analysis Group, FMRIB, Oxford, UK) using a 12 degrees of freedom non-linear affine registration model. Whole Brain (WB) Cerebral Blood Flow (CBF) WB-CBF coefficient was calculated from pseudo-continuous multi-delay ASL-MRI CBF after applying a brain mask which was derived from the T1-structural images using FSL-BET. ePET static images were normalized using the WB PET signal intensity and scaled to match the WB-CBF coefficient. ASL-MRI CBF maps were also registered to the template space using the aforementioned method and voxel-wise cross correlation coefficient was calculated between ePET and ASL-CBF images to determine the optimal perfusion window for each respective tracer.
Results: Whole brain voxel-wise correlation coefficient between ASL-MRI CBF maps versus ePET reconstruction time post injection is given in Fig. 2. The highest mean voxel-wise correlation coefficients were reported at 120 s for [^{18}F]-PI-2620 (r = 0.93), [^{18}F]-FBB (r = 0.95) and at 300 s for [^{18}F]-FDG (r = 0.77).
Discussion: ePET perfusion window is determined for each tracer as 120 s post injection for [^{18}F]-PI-2620 and [^{18}F]-FBB and 300 s for [^{18}F]-FDG. Representative images for each probe and the Reference standard ASL-CBF is given in Fig. 3. Using a semi-quantitative static ePET method with ASL-MRI, we validated the optimal early-time frame for a complete set of probes within the AT(N) system and demonstrated that ePET alone can be used to estimate a relative perfusion map in the clinical workflow.
Conclusion: We conclude that a 5-min early-frame static PET acquisition added to the routine clinical protocol can provide additional information on perfusion related changes to complement the late-phase PET images with respective AT(N) probes. Taken as a whole, ePET perfusion images may relay the extent of neurodegeneration and reduce the number of scans needed, although this requires additional studies for further validation.

	[18F]-FDG		[18F]-FBB		[18F]-PI2620	
	Healthy	Memory Concerns	Healthy	Memory Concerns	Healthy	Memory Concerns
Population (n)	17	15	15	11	34	20
Gender (M)	15	14	3	9	18	9
Age (Average)	68	69	70	73	71	69

Fig. 1: Subject demographics.

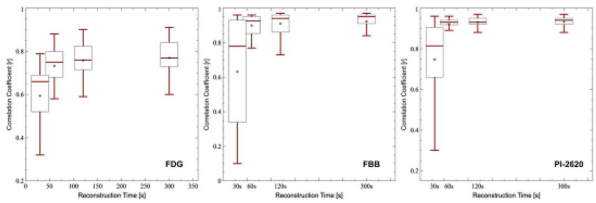

Fig. 2: Voxel-wise cross-correlation plots.

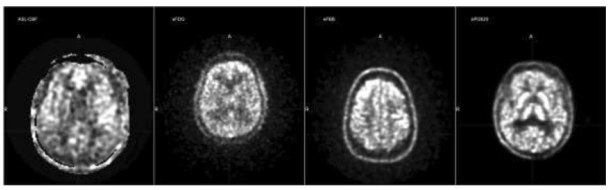

Fig. 3: Representative images.

References:

[1] CR Jack Jr, et al. "NIA-AA research framework: toward a biological definition of Alzheimer's disease," *Alzheimers Dement.,* vol. 14, pp. 535–562, 2018
[2] N Korte, et al. "CBF decrease as an early pathological mechanism in Alzheimers's disease," Acta Neuropathologica, vol. 140, no. 6, pp. 793–810, 2020

[3] S. J. Kwon, et al. "Comparison of early F-18 Florbetaben PET/CT to Tc-99 m ECD SPECT using voxel, regional, and network analysis," Scientific Reports, vol. 11, 2021
[4] J. Ottoy, et al. "(18)F-FDG PET, the early phases and the delivery rate of (18)F-AV45 PET as proxies of cerebral blood flow in Alzheimer's disease: Validation against (15)O–H(2)O PET," Alzheimers Dement., vol. 15, no. 9, pp. 1172–1182, 2019
[5] AP Seiffert, et al. "High correlation of static first-minue-frame (fmf) PET Imaging after 18F-Labeled amyloid tracer injection with [18F]FDG PET imaging," Sensors, vol. 5182, pp. 1–14, 21

P192.
Mitigating undersampling artifacts in magnetic resonance fingerprinting for proton resonance frequency shift based temperature monitoring of microwave ablation

M. Gutt[1], J. J. Löning Caballero[1], D. Horstmann[1], F. Wacker[1], B. Hensen[1], M. Gutberlet[1]

[1]*Hannover Medical School, Hannover, Germany*

Introduction: In clinical practice, MR guided temperature monitoring during minimally invasive tumor ablation is an important topic. A high accuracy in estimating the temperature as well as the resulting necrosis zone is needed to provide a real impact on the clinical routine.It was shown in a previous proof-of-concept study[1] that magnetic resonance fingerprinting (MRF) can be used in proton resonance frequency shift (PRFS) based temperature monitoring by providing a high temporal resolution and temperature sensitivity. 80 images at different echo times were aquired with an undersampling factor of 40. However, this high undersampling has led to a rather large error in temperature estimation of 1.9 °C ± 1.0 °C. Here, we demonstrate an approach to mitigate those undersampling errors.
Methods: The data used in this study was the same as in the previous proof-of-concept experiment[1]. It was aquired with a 2D multi-echo radial FLASH sequence. The echo times were varied with every TR. Thus, the total range of TEs was between 2.57 ms and 29.114 ms with a step size of 0.336 ms. The field of view was 320 × 320 mm^2 with a resolution of 256 × 256 and a slice thickness of 5 mm.A microwave ablation (modified ECO-100E, Eco Microwave System Co., Ltd., Nanjing, China, 2.45 GHz, 150 W) on a static bioprotein phantom[2] was performed on a 1.5 T scanner (Siemens Avanto) and monitored by the fingerprinting sequence. Three Minutes of baseline data were acquired before starting the ablation. A fiber optical temperature sensor with an approximate distance of 1 cm to the ablation needle was used for gaining Reference temperatures. Manual segmentation of the denaturation zone in post-ablative T2-weighted Turbo-Spin-Echo imaging was used as ground truth for comparison with the denaturation map calculated from the MRF thermometry using the CEM43[3] model.The dictionary used for MRF reconstruction consisted of off-resonance values between − 200 and 200 Hz with a step size of 0.1 Hz. The temperature change was calculated by utilizing the linear dependency of the temperature and the proton resonance frequency of water between temperatures of − 15 °C and 100 °C[4]. For every echo time, 10 spokes were acquired such that the k-space was undersampled by a factor of 40. The temporal resolution was 3.2 s.The toolbox BART[5] was used for reconstructing the data from each TE with parallel imaging and compressed sensing (PICS) and regularization regarding the total variation and the l2 norm. After reconstruction, the dictionary matching process was performed by taking the highest inner product between the reconstructed signals and the dictionary entries.Since the image reconstruction can be seen as a non-convex optimization problem, its performance is highly dependent on the initialization of the algorithm, especially in the presence of heavy undersampling. Following this thought, the first time point was reconstructed using 400 Spokes and therefore without undersampling and all following images were reconstructed using the previous time point as an initial guess. The performance of this approach was compared to the case where no initialization was provided to the reonstruction algorithm.
Results: The proposed method was able to improve the dice score between the calculated denaturation zone and the ground truth from 89.48 to 95.87% and the temperature accuracy from 1.9 ± 1.0 °C to 0.46 ± − 0.35 °C.
Discussion: Starting the reconstruction algorithm with an initial guess has led to better results regarding the temperature accuracy and the calculated denaturation zone. In future studies, an MRF sequence which is additionally sensitive to T1 relaxation could be utilized to monitor the temperature of adipose tissue as well.
A problem with MRF is its high reconstruction time. The image reconstruction of 80 images of different TEs led to an overall reconstruction time of about 15 s for each time point. This could potentially be reduced by using singular value decomposition[6] or neural networks[7]. Providing an initialization to the algorithm did not affect the reconstruction time.
Conclusion: This proof-of-principle approach has shown that MRF is a promising tool for temperature monitoring. By mitigating the undersampling errors it has achieved a high temperature accuracy of 0.46 ± − 0.35 °C. Further research will be done to discover the full potential of MRF in temperature monitoring.

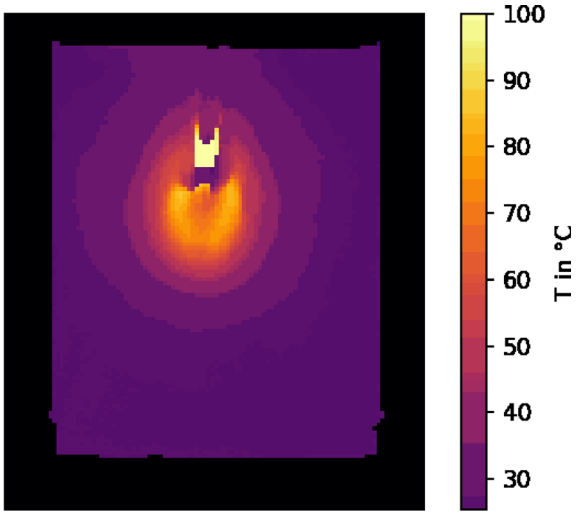

Fig. 1: A temperature map generated with the MRF reconstruction

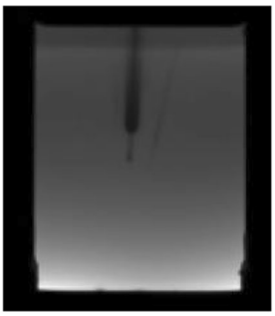

Fig. 2: Magnitude image of the phantom with the ablation needle and the optical temperature sensor

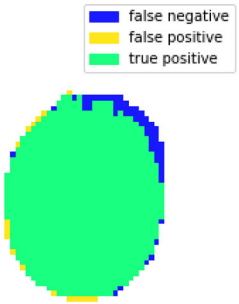

Fig. 3: Denaturation zone calculated from the MRF temperature maps compared to the ground truth

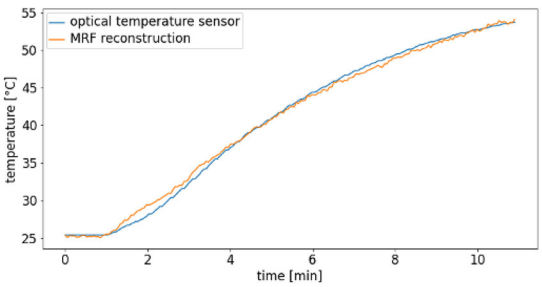

Fig. 4: Calculated temperature compared to ground truth values from the optical temperature sensor

References:

[1] GUTT, M et al.; *13.th Interventional MRI Symposium* 2022
[2] BU-LIN, Z et al.; *International Journal of Hyperthermia 2008* 24(7) 568–576
[3] PEARCE, JA et al.; *International Journal of Hyperthermia* 29 (2013), Nr. 4, S. 262–280
[4] RIEKE, V et al.; *JMRI 2008* 27(2) 376–390
[5] UECKER, M et al.; *Proc. Intl. Soc. Mag. Reson. Med. 23* (2015), S. 2486
[6] MCGIVNEY, DF et al.; I*EEE Trans Med Imaging.* 2014 Dec;33(12):2311-22.
[7] LIU, Y et al.; *MICCAI* 2021. vol 12906, Springer

P193.
A steady-state MRF sequence optimization framework for 3D simultaneous water T1 and fat fraction mapping

C. Slioussarenko[1], B. Marty[1]

[1]*NMR Laboratory, Institute of Myology, Neuromuscular Investigation Centre, Paris, France*

Introduction: In the field of neuromuscular disorders (NMD), the intramuscular fat fraction (FF) is an established biomarker of disease severity and muscle water T1 ($T1_{H2O}$) has been shown to be a potential biomarker of disease activity [1]. The use of MR Fingerprinting (MRF) enables the simultaneous quantification of various parameters, such as FF and $T1_{H2O}$ [2]. However FLASH T1 MRF sequences (such as MRF T1-FF proposed in [3]) generally require long recovery times between repetitions for allowing the longitudinal magnetization to grow back to equilibrium. Shortening the sequence would highly benefit 3D imaging, where multiple acquisitions of the MRF scheme are required to encode along the partition encoding direction. A shorter sequence is likely to degrade the parameter estimation quality. Hence we need to optimize the acquisition parameters of fast MRF sequences for maintaining the quality of FF and $T1_{H2O}$ quantification. The precision of MRF parameter estimation is heavily influenced by the undersampling artefacts in the image series which cannot be modelled as Gaussian noise [4]. In this work, we introduced an optimization framework that takes into account the longitudinal steady-state equilibrium of the MRF sequence with fat/water separation and simulates undersampling noise on a realistic numerical leg phantom. Through this framework, we obtained a novel MRF sequence with optimized echo times (TE), flip angles (FA) and recovery time and compared its mapping accuracy and precision to the original MRF T1-FF implementation.

Methods: The optimization framework consisted of 5 blocks: (i) a dictionary simulation block for steady-state MRF FLASH sequences with intial inversion pulse and variable TE,TR and FA, (ii) a block simulating the time series of undersampled images based on a realistic leg numerical phantom (iii) an MRF pattern matching algorithm, (iv) a cost function and (v) an optimizer (Fig. 1). Regarding the MRF FLASH simulation block, the initial magnetization reaches a steady-state after only a few repetitions, which can be calculated through a closed-form formula.

We simulated undersampling noise using a realistic numerical leg phantom sampled with a radial golden-angle trajectory. For the pattern matching, we used exhaustive search into a bicomponent dictionary of fingerprints [5]. The cost function was the weighted difference between the ground truth parameter maps and the estimated maps for $T1_{H2O}$, FF, RF pulse attenuation (B1), and B0 inhomogeneities (df). The algorithm used for minimizing the cost function was differential evolution, which is an efficient global optimization method when the gradient of the cost function is not easily accessible. The maximum functions evaluations was set at 150,000 but the algorithm stopped earlier. We fixed the number of spokes for the new sequences at 760, which represents the minimum value at which the estimation accuracy did not significantly decrease. We compared the original sequence (MRF T1-FF 1400), a shorter version of the original sequence with 760 spokes (MRF T1-FF 760) and the sequence obtained using the optimization framework described above (Fast MRF T1-FF). The performances were evaluated on a fat-infiltrated 3D numerical leg phantom (16 slices, 256 × 256) and on in vivo acquisitions obtained at 3 T (Prisma^{Fit}, Siemens Healthineers) on the thighs of one healthy control (20 partitions, resolution 1 × 1 × 5 mm^3, FOV 10 × 40 × 40cm^3).

Results: Each repetition of Fast MRF T1-FF lasted 7.6 s against 10.8 s for MRF T1-FF. On the numerical leg phantom, $T1_{H2O}$ and FF estimation accuracy was better than the Reference sequence as shown

by structural similarity (SSIM) and root mean squared error (RMSE) against the ground truth maps (Fig. 3). On in vivo data, the artefacts visible in the maps reconstructed by the original sequence and amplified with the MRF T1-FF 760 sequence were visually reduced on the Fast MRF T1-FF data (Fig. 4).

Discussion and conclusion: We proposed a new version of the MRF T1-FF sequence that was optimized using a dedicated framework to account for steady-state magnetization and undersampling artifacts. This enabled fast and accurate quantification of $T1_{H2O}$ and FF with a reduced acquisition time, while maintaining comparable performance to the Reference sequence. By explicitly calculating the steady-state value, we were able to reduce computation time for sequence optimization and eliminate the need for simulating multiple repetitions of the MRF patterns. We plan to further validate the performance of the optimized sequence by conducting additional out-of-sample testing and incorporating a diverse range of numerical phantoms in the optimization framework to reduce the risk of overfitting.

Acknowledgment This study was funded by ANR-20-CE19-0004.

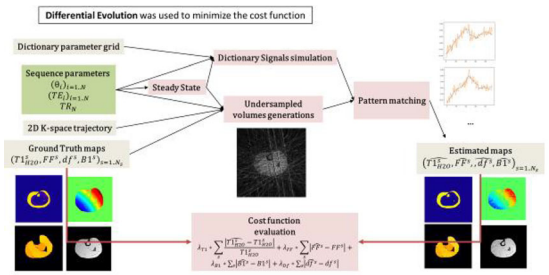

Fig. 1: Workflow diagram describing the sequence optimization framework: dictionary and undersampled image series simulation, pattern matching, cost function and differential evolution

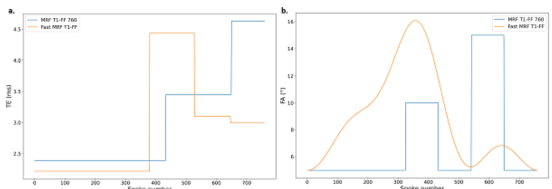

Fig. 2: 1. Flip angle (FA) evolution for MRF T1-FF 760 and Fast MRF T1-FF; 2.Echo time (TE) evolution for MRF T1-FF 760 and Fast MRF T1-FF

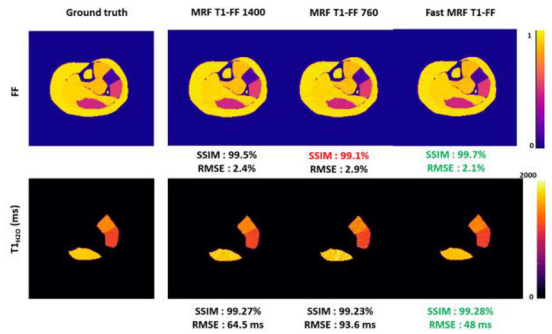

Fig. 3: Comparison of the sequences on the middle slice of a 3D fat-infiltrated numerical leg phantom. Accuracy of the methods were assessed by calculating root mean squared error (RMSE) and structural similarity (SSIM) against the ground truth. Green (resp.red) values highlight the best (resp. worst) metrics among the sequences.

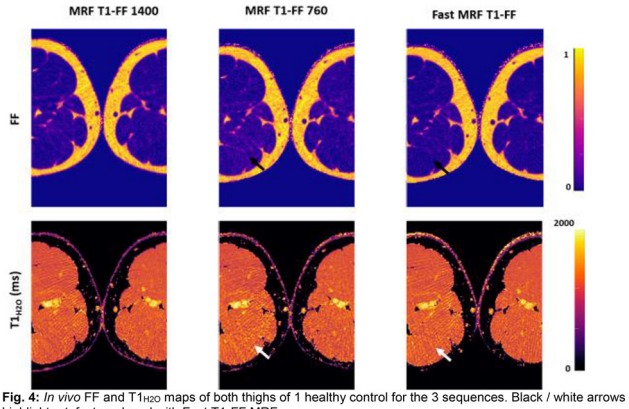

Fig. 4: *In vivo* FF and $T1_{H2O}$ maps of both thighs of 1 healthy control for the 3 sequences. Black / white arrows highlight artefacts reduced with Fast T1-FF MRF.

References:

[1] Marty et al. Radiology 2021
[2] Ma et al. Nature 2013
[3] Marty et al. Magn Reson Med. 2021
[4] Heesterbeek et al. Magn Reson Med.2022
[5] Slioussarenko et al. Proc. ISMRM 2022

P194.
NIIM: A nested iteration interpolation method enabling high dimensional parameter estimation in MT-31P-MRF

M. Widmaier[1,2,3], S. I. Lim[2,3], D. Wenz[2,3], L. Xin[2,3]

[1]*École Polytechnique Fédérale de Lausanne (EPFL), Laboratory of Functional and Metabolic Imaging (LIFMET), Lausanne, Switzerland;*
[2]*École Polytechnique Fédérale de Lausanne (EPFL), CIBM Center For Biomedical Imaging, Lausanne, Switzerland;*
[3]*École Polytechnique Fédérale de Lausanne (EPFL), Animal Imaging and Technology, Lausanne, Switzerland*

Introduction: A new magnetization transfer (MT) phosphorus Magnetic Resonance Fingerprinting (^{31}P-MRF) [1] was introduced to measure the creatine kinase (CK) chemical exchange rate kCK in vivo human brain. Exploiting the MRF framework [2, 3] can largely reduce the scanning time compared to the conventional MT-^{31}P spectroscopy methods. The inherent obstacles of MRF, the exponential growth in the size of dictionaries with the number of free parameters, is overcome by introducing the nested iteration interpolation method (NIIM) [1]. Biased estimations of multiple nested iteration paths are used to perform a linear interpolation and resulting corrected estimations. NIIM shows great efficiency in both computational and data resources, estimating a total of 6 free parameters in just 1 min 30 s with 55 MB data per subject. This abstract aims to evaluates the performance of NIIM in simulations and compares it with the efficient ^{31}P band inversion transfer approach (EBIT) [4] using in vivo ^{31}P-MRF data.

Methods: The MRF pattern matching process is split into several nested iterations instead of matching all the parameters simultaneously. A schematic framework is shown in Fig. 1. The nested iteration is looped N = 5 times, each time with a different initial condition k_{CK}^{0} = [0.35,0.2,0.5,0.3,0.4]s^{-1}. All other parameters in an iterative step are either free (objects of the estimation) or fixed. Parameters are fixed to literature values or estimated values in previous steps. Successively all parameters are estimated as indicated in Fig. 1. In the last iterative step, all parameters are fixed to estimated values and

k_{CK}^{n} is the objective of the estimation. The other 5 parameters are the longitudinal relaxation rates $T_1^{ATP,n}$ and $T_1^{PCr,n}$, the off resonance f_{off}^{n}, the B_1 factor $C_{B1}{}^{n}$ and the concentration ratio $C_r^{n} = M_0^{PCr}/M_0^{ATP}$. The 6 estimates in the nth loop are biased, dependent on the difference between the starting value $k_{CK}^{0,n}$ and the underlying k_{CK}. In a value range expected in vivo, this bias can be assumed to be linear (Fig. 2c). The final estimate of k_{CK} is found by the zero crossing (ZC) of the linear regression (LR) in least square sense of k_{CK}^{0} over Δk_{CK}, where

$$\Delta k_{CK}^{n} = k_{CK}^{0,n} - k_{CK}^{n} \quad (8)$$

Further, the LR for all free parameters from the N estimates over $k_{CK}^{0,n}$ are computed. The bias-corrected estimate of each parameter is then found by determine the linear regression function value at $k_{CK}^{0} = k_{CK}$.

In vivo data acquisition is described in Widmaier et al. [1].

The NIIM performance is evaluated using Monte Carlo (MC) simulations. Therefore, 1000 signal evolutions with random assigned ground truth values are generated and Gaussian noise is added. The estimation error quantified with the mean absolute percentage error (MAPE) and its standard deviation (STD. The *in-vivo* test-retest reproducibility was analysed with the coefficient of variance (CV).

Results: Fig. 2 shows the NIIM estimation procedure on 3 exemplary simulated signal evolutions (Signal A, B & C) with random assigned ground truth parameters (Fig. 2a). Fig. 2b shows the simulated ground truth signal evolution (grey) and corresponding matched signal evolutions for 3 of the 5 loops (n = 1, 3, 5) of the 4 iteration steps (IT1-IT4) proceeded in the iteration part. The final k_{CK} estimation in the interpolation part by the ZC of the Δk_{CK}-LR (Fig. 2c) is then used to correct T_1^{PCr} and T_1^{ATP} (Fig. 2d, e).

The MAPE of k_{CK}, T_1^{PCr} and T_1^{ATP} for different SNR levels is shown in Fig. 3a. Fig. 3b, c are showing the correlation and BA plot of the NIIM k_{CK} estimations versus the ground truth for SNR = 12 dB (measured in vivo full-length acquisition SNR).

Fig. 4a–c shows the estimated mean values of k_{CK}, T_1^{PCr} and T_1^{ATP} for different acquisition lengths compared to the state-of-the-art EBIT estimation. For full-length acquisition mean estimation are in good range to each other. The mean test-retest reproducibility is validated in Fig. 4d–f using the coefficient of variation (CV). For a scan time of 4:15 min, the CV of k_{CK} is still in range of the CV of EBIT with 18.5 min scan time.

Discussion and conclusion: We demonstrate with simulation data, that NIIM delivers accurate and robust estimations. In vivo human brain data at 7 T showed that the estimated values are consistent with those reported in the literature [5] and comparable to those obtained with the NIIM and EBIT [4]. Overall, the NIIM possesses superior reproducibility on subjects over the EBIT through a test–retest experiment. We conclude that applying NIIM in the MT-^{31}P-MRF pattern matching process shows a great potential in a fast and quantitative measurement of metabolic reactions.

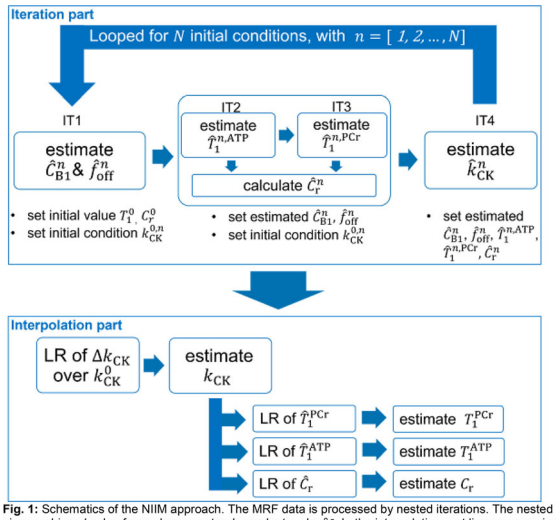

Fig. 1: Schematics of the NIIM approach. The MRF data is processed by nested iterations. The nested iteration path gives an biased value for each parameter dependent on $k_{CK}^{0,n}$. In the interpolation part linear regressions (LR) are used to find corrected estimates.

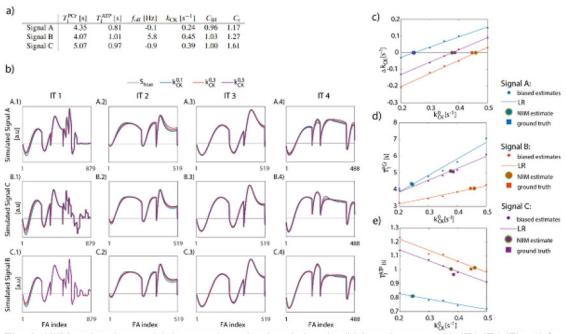

Fig. 2: NIIM estimation on (a) 3 exemplary simulated signals. (b) Iteration part with IT1-IT4 (Fig. 1) for each signal evolution. (c) Zero crossing of the Δk_{CK}-LR gives final k_{CK}. (d,e) k_{CK} is used to find the final estimates of T_1^{PCr} and T_1^{ATP}.

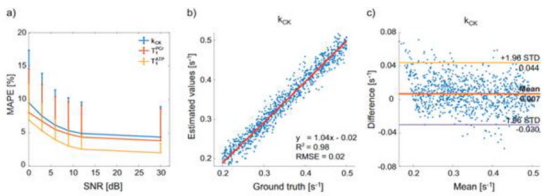

Fig. 3: (a) NIIM performance evaluation: MAPE of k_{CK}, T_1^{PCr} and T_1^{ATP} of the MC simulations are displayed over different SNRs [dB]. (b) NIIM-estimates of k_{CK} over their ground truth value and (c) the BA analyses at SNR= 12 dB.

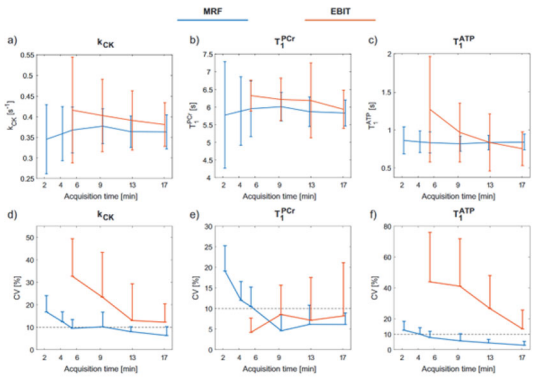

Fig. 4: (a, b, c) Estimated parameters for MT-^{31}P-MRF and the EBIT method over the acquisition time. (d, e, f) CV [%] of MT-^{31}P-MRF and the EBIT method over the acquisition time. All values are shown as the mean and STD over all subjects and grouped averages.

References:
[1] Widmaier M. et al., *Research Square* 2022
[2] Ma D. et al., *Nature* 2013
[3] Wang CY. et al., *NMR in Biomedicine* 2017
[4] Ren J. et al., *Magnetic Resonance in Medicine* 2017
[5] Lei H. et al., *Magnetic Resonance in Medicine* 2003

P195.
Simultaneous brain and cervical spinal cord MP2RAGE for T1 measurement: Robustness and sensitivity for tissue modification assessment in multiple sclerosis in a multicenter context

M. Gaubert[1,2], B. Combès[2], J. C. Ferré[1,2], A. Dufey[2], R. Chouteau[3], A. Kerbrat[3,2], E. Bannier[1,2], V. Callot[4,5]

[1]*CHU Pontchaillou Rennes, Department of Neuroradiology, Rennes, France;*
[2]*University Rennes, Inria, CNRS, Inserm, IRISA UMR 6074, Empenn U1228, Rennes, France;*
[3]*CHU Pontchaillou Rennes, Department of Neurology, Rennes, France;*
[4]*Aix-Marseille Université, Marseille, France;*
[5]*APHM, Hôpital Universitaire Timone, CEMEREM, Marseille, France*

Introduction: Recent optimisations of T1 quantification through magnetization-prepared two rapid acquisition gradient echoes (MP2RAGE; Marques et al. 2010) allow to perform both brain and cervical spinal cord acquisitions simultaneously with good trade-off between acquisition time, robustness and accuracy (Rasoanandrianina et al. 2019; Forodighasemabadi et al. 2021). This sequence is of particular interest to investigate tissue microstructural modifications in pathologies such as multiple sclerosis (MS; Demortière et al. 2020; Mchinda et al., 2021). In order to spread out the use of the MP2RAGE sequence, we evaluated the reproducibility and variability in two different centres.

Methods: The data included in this work were collected in the context of the multicentric MSTRACTS (NCT04220814), OSV-IRM (NCT05107232) and T1-M3C-SEP (FLI-RE2) studies. Six healthy controls (HC; F/M: 4/2, mean age 38.9 years) were scanned 3 times each (separated sessions), in two different centres both equipped with 3 T Siemens scanners (Prisma with 20 channels in centre 1, Vida with 64 channels in centre 2). Additionally 26 HC (centre 1/2: 20/6) were scanned one time (F/M: 19/7, mean age 39.2 years). The same acquisition protocol was performed in both centres and included MP2RAGE and B1 map acquisitions covering both brain and cervical spinal cord (cSC). The acquisition parameters were previously described in Rasoanandrianina et al. (2019; 4000 ms TR, 243 × 300 mm^2 FOV, 176 slabs, 6/8 partial Fourier (PF) factor 0.9 × 0.9 × 1mm^3 voxel size, TI1/TI2 = 650/2000 ms, $\alpha1/\alpha2$ = 4/5°, GRAPPA 2). After B1 correction (Massire et al. 2016), mean T1 values were extracted in different regions including brain white matter (bWM), deep grey matter (dGM) and cortical grey matter (cGM; all computed using CAT12 [(Ashburner and Friston 2000)]) and all cSC segments (computed using the SCT toolbox [De Leener et al. 2017]). We evaluated the variability between centres and subjects using linear mixed-effects models with subject as random effect and centre as fixed effect. The coefficients of variation (CV) and the intraclass correlations (ICC) of between-session and between-participant variabilities were computed according to Combès et al. (2019). In order to interpret these results with respect to potential application in MS pathology, we also reported exploratory analyses based on the extraction of T1 values in the same regions for 5 MS patients (centre 1/2: 3/2, same acquisition protocol and image processing) without cSC lesions.

Results: For the whole dataset collected in HC, the mean (and standard deviation) T1 values in the brain were 1281.5 (28.8), 1176.5 (20) and 823.9 (21.1) ms for cGM, dGM, and bWM, respectively and were ranging from 921 (22.6) to 954 (30.5) ms over the 7 cSC segments (see Fig. 1)

For the brain, we observed evidence of centre differences for the three regions (all $p < 0.01$). Nevertheless, the estimated differences between centres were low, ranging from 4.71 (bWM) to 25.31 (dGM) ms (ie. 0.57–1.98% of the mean). Between-participant CV were 2.1, 1.7 and 1.8%, and between-session CV were 0.2, 2.2 and 0.5% for bWM cGM and dGM, respectively. Between-session ICC were 0.01, 0.61 and 0.06 for the same regions.

For the SC, we observed evidence of centre differences for all vertebrae (all $p < 0.05$), except C4, C5 and C7 ($p = 0.149$, 0.163, 0.062, resp.). The estimated mean differences were also low, ranging from 9.6 (C5) to 20.2 (C1) ms (ie. 1.03–2.15%). To simplify the results, T1 values from C3 to C5 levels were averaged. In this region, between-participant and between-session CV were 1.5 and 1.6%, while between-session ICC was 0.53.

MS patients showed a mean T1 value increase ranging from 19.5 (cGM) to 44.2 (dGM) ms for the brain, and from 14 (C7) to 122.7 (C3) ms for the cSC compared to the mean in all HC. Fig. 2 shows that, for each region, the majority of patients (coloured triangles) have higher T1 values than the third quartile of HC.

Discussion: Our results showed that, even if differences exist between the two centres, the variability is low, especially for bWM (0.57%) and central cSC segments (1.03%). Moreover, the T1 variability is primarily explained by between-participant variability for the brain and by both session- and participant-variabilities for cSC. The differences between scanners were found to be less important than the differences observed between HC and MS patients with no cSC lesions. Overall, our results highlight the multicenter robustness of simultaneous brain and cervical spinal cord acquisition and its potential for further applications in multicenter MS studies to assess regional tissue impairment.

Acknowledgements This work was partly funded by the France Life Imaging (FLI RE2) (ANR-11-INBS-0006 grant from the French "Investissements d"Avenir" program). The authors would like to thank L.Pini, C. Costes, V. Gimenez, MP. Ranjeva and C. Guillemot, L. Patier, G. Morrisse, V. Even, C. Picot for study logistics.

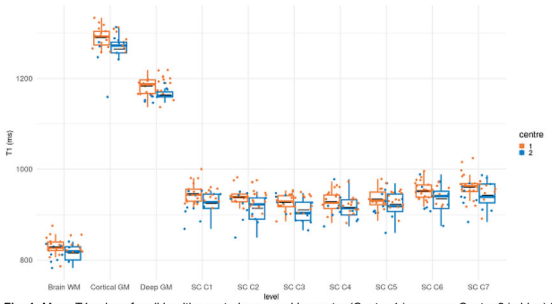

Fig. 1: Mean T1 values for all healthy controls grouped by centre (Centre 1 in orange, Centre 2 in blue) for the regions of interest located in the brain and the cervical spinal cord. Boxplots display the median, the first and third quartiles. Black bars display the mean of all healthy controls for each centre and each region. Legend: WM=white matter; GM=grey matter; SC=spinal cord; ms=millisecond.

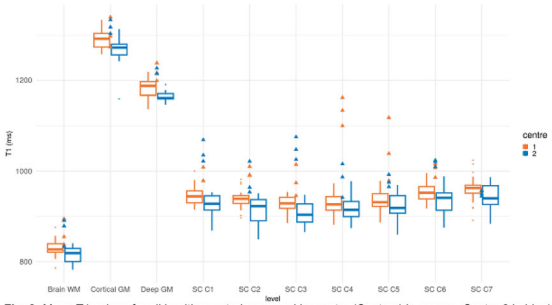

Fig. 2: Mean T1 values for all healthy controls grouped by centre (Centre 1 in orange, Centre 2 in blue) and the 5 MS patients for the regions of interest located in the brain and the cervical spinal cord. Boxplots display the median, the first and third quartiles in the HC group.Triangles represent the mean signal for each MS patient. Dots represent outliers for healthy controls. Legend: WM=white matter; GM=grey matter; SC=spinal cord; ms=millisecond.

P196.
MRI sequence analysis with phase distribution graphs

J. Endres[1], H. N. Dang[1], S. Weinmüller[1], M. Zaiss[1,2,3]

[1]*Friedrich-Alexander-Universität Erlangen-Nürnberg (FAU), Department of Neuroradiology, Erlangen, Germany;*
[2]*Friedrich-Alexander-Universität Erlangen-Nürnberg (FAU), Department Artificial Intelligence in Biomedical Engineering, Erlangen, Germany;*
[3]*Max-Planck-Institue for Biological Cybernetics, Magnetic Resonance Center, Tübingen, Germany*

Introduction: Extended Phase Graphs[1] (EPGs) are often cited as a valuable tool for sequence analysis, as they can explain the different magnetization pathways leading to various kinds of echoes. Previously, we modified the phase graph formalism in the form of Phase Distribution Graphs[2] (PDGs), enabling the exact analytical calculation of measured ADC signal at any point during the sequence. With this novel tool, new techniques for sequence analysis are possible, allowing to easily answer questions along the lines of "Is TrueFISP a gradient-echo or a spin-echo sequence?[3]" and to visualize the echo path origins of measured signals or artifacts. In the following, we demonstrate these two applications as an example of the multitude of capabilities of PDG simulation.

Methods: With PDGs, each pulse splits the magnetization into multiple parts, called states. Each state has a gradient- and time-based dephasing, stored as (k, τ) vector. This data in the context of the PDG is visualized in Fig. 1. This is important for calculating the measured ADC signal, including k-space encoding and T2' dephasing. The measured signal can be split into the contributions of all states, allowing to tell which parts of the magnetization produce a spin echo, gradient echo or any other categorization.As PDGs can handle sequences with arbitrary timing, the number of states can potentially explode. One employed technique to combat this problem is the use of two metrics, emitted and latent signal, which help to narrow down the simulated states to those actually contributing to the signal. While the emitted signal approximates how much signal a state will emit itself, latent signal estimates to how much emitted signal a state will produce at max. This means that even states that don"t emit signal themselves can have high latent signal, if they are refocused later on.In the following, the main contributors to the signal of a TrueFISP[4] sequence are determined by splitting the sequence into the contributions of the most important states, answering the question posed by Scheffler and Hennig[3] Additionally, the general distribution of magnetization and signal to all states is evaluated.

Results: TrueFISP sequences could be categorized as spin-echo sequences when only judging by the presence of a signal peak in the center of the readout, or by its B0 insensitivity, both of which are shown in full simulation in Fig. 2. When separating the signal into singals of individual states, two dominating magnetization pathways can be seen, one of which experiences a signal at the beginning of the readout, the other one at the end. These two parts of the signal could be labelled as FID and spin-echo and both show the same B0 dependence with opposite sign. This means that TrueFISP has a B0 dependence, it just happens to cancel out in the phase image, with the famous banding artifacts occuring when the FID-to-spin-echo phase is 180°. Therefore, TrueFISP is best described as being an equal mix of gradient- and spin-echo.

More general properties of bSSFP sequences can be seen when visualizing the whole PDG (Fig. 3) using the aforementioned latent and emitted signal metrics. Most of the magnetization remains in only weakly dephased states at the center of the graph. Even with low flip angles, most of the magnetization is refocused over time and multiple pulses, resulting in wave patterns in the visualization. The emitted signal has an additional drop off to the edges as T2" dephasing increases. Even though most signal comes from FID and spin-echoes, stronger dephased states are important to the high SNR of bSSFP. The latent signal of these states can be large, as parts of their magnetization is refocused by RF pulses and subsequently measured. Unbalanced SSFP sequence spoil this magnetization, which means that all the latent signal shown here is lost.

Discussion: When using PDG for sequence simulation, all the necessary information for deep analysis of magnetization and signal is available automatically. Because the simulation does not need to be modified for specific sequence types, it is possible to translate all approaches of analysis to different measurements. As a side effect of PDG extending EPG to support full signal calculation, more data is available for visualization. Using this data allows to answer sequence-specific questions quickly that would require developing targeted experiments otherwise.

Conclusion: PDG offers a new way of MR simulation as well as new ways to analyze MRI sequences. Two approaches were applied here, but more analysis tools can be developed in the future, based on the multitude of information provided by PDG. These new visualization techniques can simplify and improve the understanding of existing and future sequences.

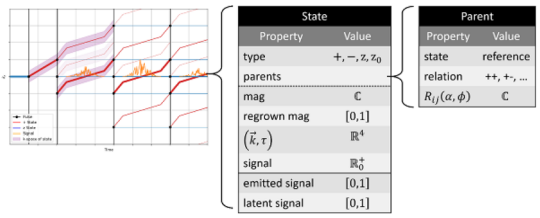

Fig. 1: Schematic of a Phase Distribution Graph. Magnetization is divided into multiple transversal + and longitudinal z states. All transversal states can contribute to the measured signal. Their dephasing depends on all gradients, including those for k-space readout, and time. The relation of states is stored for calculation of the latent signal.

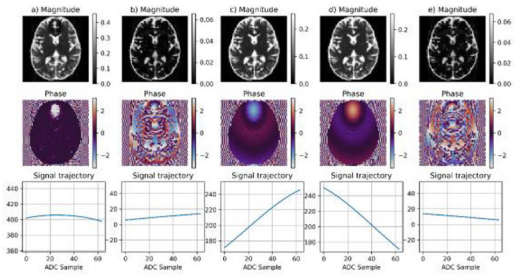

Fig. 2: Simulated signal and its reconstruction of a TrueFISP sequence. a) shows the magnitude and phase image of the full bSSFP signal, a banding artifact is visible. b) to e) show isolated PDG states with varying τ dephasing. Most signal is generated by the two states that describe magnetization with first order rephasing (c) and dephasing (d) magnetization.

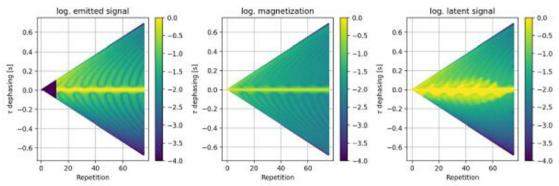

Fig. 3: τ – dephasing view of an bSSFP PDG, showing the magnetization and emitted and latent signal metrics. No signal is measured in the first 10 repetitions. Even though most signal is emitted by few weakly dephased central states, more states contribute to it in the long term.

References:
1. Weigel JMRI 2015, https://doi.org/10.1002/jmri.24619
2. Endres et al. ISMRM 2022, prog. no. 0750
3. Scheffler and Hennig MRM 2003, https://doi.org/10.1002/mrm.10351
4. Bieri et al. JMRI 2013, https://doi.org/10.1002/jmri.24163

P197.
Non linear inversion applied to preclinical multifrequency magnetic resonance elastography data

P. Sango-Solanas[1], E. E. W. van Houten[2], O. Beuf[1], K. Tse Ve Koon[1]

[1]*Univ Lyon, INSA-Lyon, Inserm, UCBL1, CNRS, CREATIS, UMR 5220, U1294, Villeurbanne, France;*
[2]*Department of Mechanical Engineering, Université de Sherbrooke, Sherbrooke, Canada*

Introduction: Magnetic resonance elastography (MRE) enables non-invasive quantitative assessment of the mechanical properties of tissues and has been successfully applied on clinical MR scanners for of liver fibrosis staging [1]. Its usage is not limited to detecting global changes in mechanical properties as done in fibrosis and applications can also include detection of tumour nodules [2]. Its application on preclinical MR scanners is also of interest with the availability of different animal models. However, MRE parameters have to be adapted with the standout feature being the smaller imaging volume. To deal with this, higher mechanical frequencies are required to be able to characterize smaller regions of interest and detect nodules.
For tissue characterization, multifrequency MRE [3] has been proposed as a valuable tool enabling detection of tissue alterations occurring below the MR image resolutions through the measurement of the dispersion relationship of the shear storage modulus [4]. However, tackling multifrequency data reconstruction is still an open question; the simplest approach being to apply mono-frequency reconstruction and analyzing the subsequent summation of the individual results. On the other hand, more evolved algorithms try to consider simultaneously all the individual harmonic data such as the K-MDEV [5] or the Non Linear Inversion (NLI) [6]
In this work, we seek to process multifrequency MRE data acquired on a preclinical MR scanner using the NLI approach and demonstrate its advantages compared to Helmholtz-based inversion methods.
MRE acquisitions were carried out on 5 different agarose phantoms with cylindrical inclusions of diameters ranging between 4.5 and 21 mm. Inclusions and surrounding medium consisted of 3% and 2% concentration agarose respectively thus mimicking a stiffer inclusion. The phantoms were made simultaneously from the same agarose solutions and stored in distilled water to limit dehydration and changes in mechanical properties.
Methods: All the phantoms underwent multifrequency MRE acquisitions during the following week on a @Bruker Biospec 7 T MR scanner using a Turbo Spin Echo MRE sequence (turbo factor = 4) developed inhouse [7]. Single frequency acquisitions ranging between 200 and 700 Hz were run and for each frequency, 4 equally distributed phase-steps were acquired. For each frequency, 2 acquisitions with opposite motion encoding gradient (MEG) polarity were completed, 3 orthogonal MEGs were applied and 5 contiguous slices (1 mm) were acquired to obtain 3D wave field images. Complex MR images were extracted and processed to obtain magnitude and unwrapped phase images.
The multi-frequency phase images were then collectively processed using NLI inversion method yielding shear storage (G“) and loss (G”) modulus maps for each of the acquired frequencies. Power-law NLI reconstruction minimizes a multi-frequency objective function combining the uniformly weighted displacement error at each measurement frequency using gradient descent algorithms based on the adjoint. NLI reconstruction parameters included a subzone size of 5 mm, total variation regularization and spatial filtering with a Gaussian kernel width of 0.15 mm. For the phantom with the smallest inclusion (4.5 mm diameter), to be able to compare NLI-reconstructed elastograms with other frequently used reconstruction method, a Helmholtz-based inversion reconstruction [8] was also performed using motion encoded in the slice direction only.
Results: Figures 1–3 display the reconstructed elastograms for three out of the five phantoms which were tested with the biggest inclusion (21 mm diameter) (Fig. 1) and the smallest inclusion (4.5 mm) (Fig. 3). The inclusions are highlighted in red in the magnitude images. Reconstructed shear storage and loss moduli at the different acquired frequencies are displayed on the top, respectively bottom rows. Finally, Fig. 4 illustrates the results of running Helmholtz-based inversion.
Conclusion: This work presents the first application of NLI inversion algorithms on preclinical multifrequency MRE data. NLI inversion is able to precisely detect the stiffer inclusion for all the inclusion sizes and all the acquired frequencies, demonstrating the advantage of operating a conjunct reconstruction over individual frequency analysis. Helmholtz inversion on the other hand is not able to do so for all the frequencies and inclusion sizes. For instance, for the 4.5 mm inclusion, only G“ elastograms at 600 Hz faintly contrasts the inclusion from the surrounding medium. The NLI reconstruced G” elastograms display very good homogeneity and shows a small variation of G“ with frequency which is expected for an agarose phantom. G” values are low as expected from an agarose-based phantom but it can be noted that G“ elastograms are noisier than those for G”. Reconstructed G“ and G” are also within the range of values described in the literature. In future works other materials displaying higher dissipative and dispersive nature will be tested.
Acknowledgments LABEX PRIMES (ANR-11-LBX-0063), CNRS (IEA00289-2020). The experimental data is based upon work carried out on the ISO 9001:2015 PILoT facility

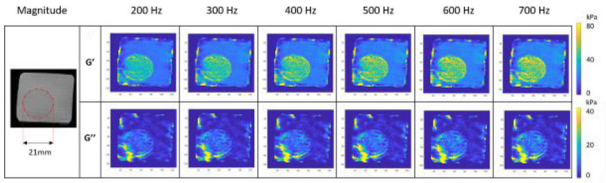

Fig. 1: Magnitude image (left column) and reconstructed elastograms through NLI at the different acquired frequencies for the phantom with a cylindrical inclusion of diameter 21 mm.

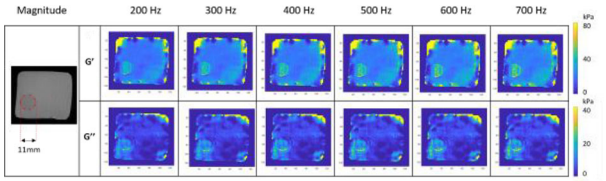

Fig. 2: Magnitude image (left column) and reconstructed elastograms through NLI at the different acquired frequencies for the phantom with a cylindrical inclusion of diameter 11 mm.

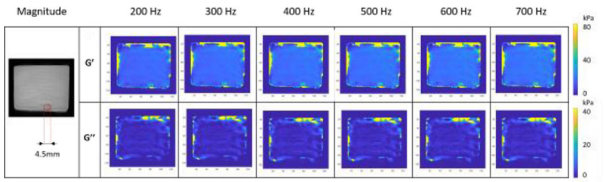

Fig. 3: Magnitude image (left column) and reconstructed elastograms through NLI at the different acquired frequencies for the phantom with a cylindrical inclusion of diameter 4.5 mm.

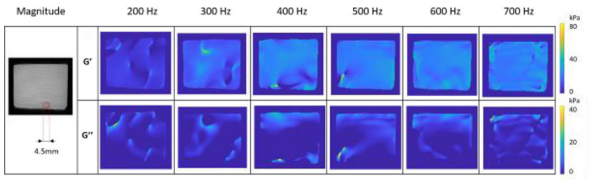

Fig. 4: Magnitude image (left column) and reconstructed elastograms through direct inversion at the different acquired frequencies for the phantom with a cylindrical inclusion of diameter 4.5 mm.

References:

[1] Hoodeshenas et al. 2018 Top MRI
[2] Bunevicius et al. 2020 Neuroimage Clin
[3] Asbach et al. 2008 MRM
[4] Jugé et al. 2015 NMR Biomed
[5] Tzschätzsch et al. 2016 Med Imag Anal
[6] Brazy et al. 2020 J Med Phys
[7] Sango-Solanas et al. 2021 NMR Biomed
[8] Oliphant et al. 2001 MRM.

P198.
DREAM-zero: optimized variable flip angles for decreased image blurring in magnetization-prepared DREAM sequences

S. Weinmüller[1], T. Baum[1], H. N. Dang[1], J. Endres[1], M. Zaiss[1,2,3]

[1]*Friedrich-Alexander-Universität Erlangen-Nürnberg (FAU), Department of Neuroradiology, Erlangen, Germany;*
[2]*Max-Planck-Institute for Biological Cybernetics, Magnetic Resonance Center, Tübingen, Germany;*
[3]*Friedrich-Alexander-Universität Erlangen-Nürnberg (FAU), Department Artificial Intelligence in Biomedical Engineering, Erlangen, Germany*

Introduction: The "dual refocusing echo acquisition mode" (DREAM) sequence is one of the fastest methods for B1 mapping in 2D, and 3D [1]. The DREAM sequence acquires two signals jointly, the stimulated echo (STE), and a free induction decay (FID) signal. The STE decays to zero, while the FID signal approaches a steady state via a T1 Look-Locker-decay, leading to a strong signal blurring affecting intensity and contrast of both, the STE and FID image. The DREAM sequence can be used to acquire a prepared magnetization [2], thus also an anatomical magnetization prepared (MP) image can be generated, which also suffers from blurring artifacts. To improve the MP-DREAM image quality, we optimized the readout flip angle (FA) train using the end-to-end approach MR-zero [3].

Methods: As one important example of a prepared magnetization a T1-weighted image (inversion FA of 180°, TI = 3 s) is used. It is normalized by a measurement without preparation (acquired after 10 s relaxation), which removes bias-fields and makes the MP-DREAM quantitative. The MP-DREAM image is calculated by

$$\text{MP-DREAM} = |\text{FID}| + |\text{STE}|. \quad (1)$$

The readout sequence is a centric-reordered DREAM sequence [1] (matrix: 96 × 96, FoV = 220 × 220x8mm^3, $FA_{STE1} = FA_{STE2} = 55°$, FA = 15°, $TE_{FID} = 4.0$ ms, $TE_{STE} = 2.4$ ms, TR = 6.7 ms, Pulseq-file attached [4]). FAs of the readout are optimized using as target the fully relaxed and segmented MP-DREAM sequence, where each k-space line is prepared individually with a long TR of 100 s. The first FA of the train is fixed at 15° since same signal intensity is wanted. All other FAs are optimized to improve the signal decay and the correlation with the prepared magnetization. Signal simulations and optimization are performed using the Phase Distribution Graph (PDG) algorithm [5] implemented in the MR-zero framework [2], using brain data acquired from the BrainWeb [6] database. MSE of the magnitude images is used as loss function.

For in vivo measurement an 8 shot MP-DREAM sequence is used as ideal Reference. It requires 175 s while the single shot MP-DREAM sequences with normalization need 14.3 s.

Most interesting in the context of quantitative MRI, the MP-DREAM provides for every image a B0 and B1 map calculated by the MP invariant formulas [1]:

$$\Phi = \arg(\text{FID}\cdot\text{STE}^*) \quad (2)r$$

$$B1 = \arctan(\sqrt{(2\cdot|\text{STE}|/|\text{FID}|)})/FA_{STE1}. \quad (3)$$

B0 und B1 maps were compared to a WASABI Reference measurement [7].

At submission time, a first healthy volunteer was scanned under approval of our local ethics committee on a 3 T whole-body MRI system (MAGNETOM Prisma, Siemens Healthcare, Erlangen) and a 20 channel receive coil.

Results: The different FA patterns and the MP-DREAM images are shown in Fig. 1. The calculated MSE and SSIM (with regard to the 96 shot MP-DREAM) are improved for the optimized MP-DREAM. Especially blurring and respective signal change in regions with long T1 values is improved in silico (Fig. 1) as well as in vivo (Fig. 2) indicated by the calculated MSE and SSIMs. The acquired Reference B0 and B1 map are shown in Fig. 3. The MP-DREAM sequences show similar performance in generating these field maps. Due to a B0 shift during the measurements, the B0 maps are shifted by their mean value. Small variations in DREAM B1 maps might be caused by the different signal decay of the FID and STE signal.

Discussion: As has been shown previously, variable FAs can reduce the signal alterations due to the readout. Here, we demonstrated an optimized readout by a FA optimization for a novel magnetization prepared 2D DREAM sequence. This has three major applications:

This approach can be extended to 3D-DREAM where blurring of the STE image is a problem already for B1 mapping [8].
This approach improves the MP-DREAM sequences that provide simultaneous B0 and B1 field maps, as well as anatomical contrast that requires low blurring. With a normalized anatomical and simultaneous field mapping, this is a candidate for full quantitative MRI.
Finally, also MT- or CEST-MP-DREAM sequences are possible [2], that require field maps for intrinsic B0 and B1 contrast correction.
Conclusion: Thus, DREAM-zero provides an optimal MP-DREAM, which is a versatile sequence for quantitative MRI when both prepared-contrast and simultaneous field maps are required.

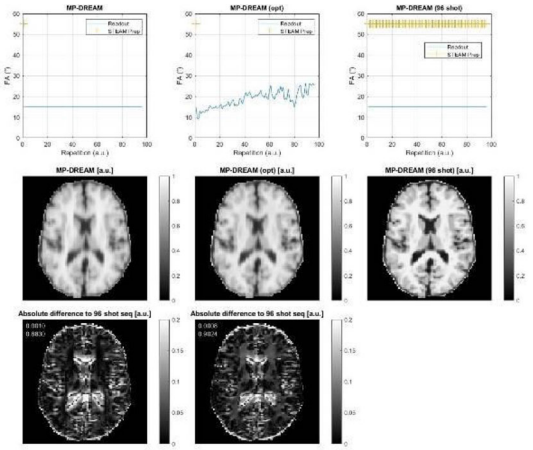

Fig. 1: The flip angle trains and simulation of MP-DREAM (first column), optimized MP-DREAM (second column) and 96 shot MP-DREAM (third column) sequence and the absolute differences between (optimized) MP-DREAM and 96 shot sequence are shown. Additionally, MSE (upper value) and SSIM (lower value) are given for the difference maps.

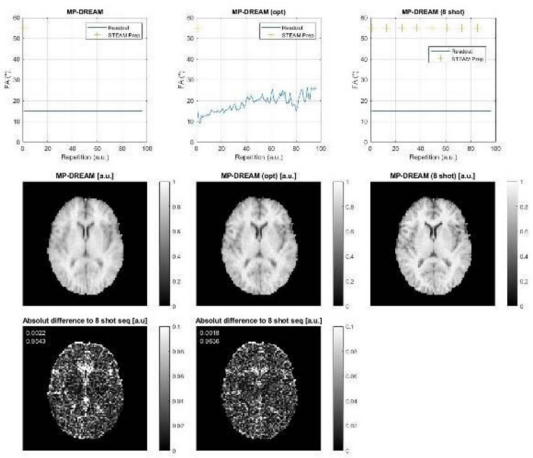

Fig. 2: The flip angle trains and in vivo measurement of MP-DREAM (first column), optimized MP-DREAM (second column) and 8 shot MP-DREAM (third column) sequnce and the absolute differences between (optimized) MP-DREAM and 8 shot sequence are shown. Additionally, MSE (upper value) and SSIM (lower value) are given for the difference maps.

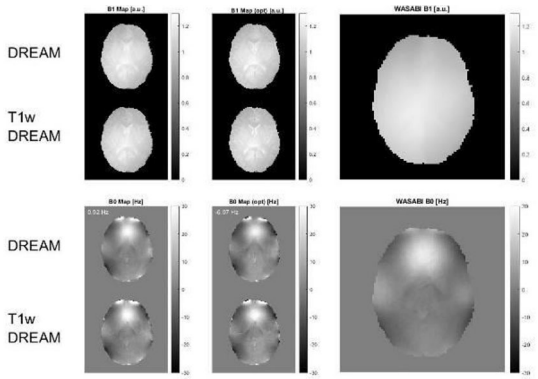

Fig. 3: B1 and B0 maps are shown for the (optimized) DREAM and the (optimized) T1w DREAM image. B0 field maps are shifted due to a B0 shift during the measurement. As Reference the field maps from a WASABI measurement are used.

References:

[1] Nehrke et al., DREAM—a novel approach for robust, ultrafast, multislice B1 mapping. MRM 2012.
[2] Baum et al., Submitted to ESMRMB 2023.
[3] Loktyushin et al., MRzero—Automated discovery of MRI sequences using supervised learning. MRM 2021.
[4] https://colab.research.google.com/drive/1zY9B51nJeVjNDxhQHrkimxaeXsx8zEGr?usp=sharing
[5] Endres et al., Phase distribution graphs for differentiable and efficient simulations of arbitrary MRI sequences. ISMRM 2022.
[6] http://www.bic.mni.mcgill.ca/brainweb/
[7] Schuenke et al., Simultaneous mapping of water shift and B1 (WASABI)-Application to field-Inhomogeneity correction of CEST MRI data. MRM 2017.
[8] Ehses et al., Whole-brain B1-mapping using three-dimensional DREAM. MRM 2019.

P199.

Analysis of visceral adipose tissue distribution in healthy subjects along the body axis: Gender, age and BMI effects

T. Haueise[1,2,3], F. Schick[1,2,3], N. Stefan[2,3,4], F. Bamberg[5], J. Machann[1,2,3]

[1]*University Hospital Tübingen, Section on Experimental Radiology, Tübingen, Germany;*
[2]*Helmholtz Center Munich, Institute for Diabetes Research and Metabolic Diseases, Tübingen, Germany;*
[3]*German Center for Diabetes Research (DZD), Tübingen, Germany;*
[4]*University Hospital Tübingen, Division of Diabetology, Endocrinology and Nephrolog, Tübingen, Germany;*
[5]*University of Freiburg, Department of Diagnostic and Interventional Radiology, Medical Physics, University Medical Center, Freiburg, Germany*

Introduction: Abdominal obesity, as manifested by increased visceral adipose tissue (VAT), shows a strong correlation to insulin sensitivity which is associated with the risk of developing type 2 diabetes [1]. Observations of volume and topography of VAT in the German National Cohort (GNC) suggest that the VAT distribution along the craniocaudal axis is sex-, age- and BMI-dependent (see Fig. 1 [2]). In CT as well as MRI studies, single slice measurements of VAT are performed [3–5] and optimal anatomical Reference sites for estimation of total VAT volume are still subject of discussion [6, 7].

The aim of this analysis is to perform a sex-, age- and BMI-dependent description of spatial VAT distribution in a large sample size of 3D MRI datasets from the GNC in order to define the position which best reflects VAT volume.

Methods: High resolution 3D 2-pt VIBE Dixon data-sets of the body trunk from 11141 participants of the GNC [8] (all acquired on 3 T whole-body imagers, Magnetom Skyra, Siemens Healthineers, Germany) were analyzed. Automatic segmentations of VAT and the spine were used to compute the ratio of VAT per slice and total VAT volume at defined locations (i.e. center of vertebral bodies, intervertebral disks, see Fig. 2). Interpolation with a fixed number of data points in head-feet direction served as a scale between femoral heads and L5. Correlation between VAT area at distinct anatomical locations and total VAT volume was performed in 4 BMI groups (I: 18.5–24.9 kg/m^2, II: 25–29.9 kg/m^2, III: 30–34.9 kg/m^2, IV: 35–39.9 kg/m^2) with age ranging in decades from 20 to 70 years.

Results: Fig. 3 lists maximum correlation coefficients and corresponding anatomical position for all BMI- and age-groups in male subjects. Fig. 4 presents corresponding numbers in females. Coefficients indicate that strength of correlation is not strongly influenced by sex, age or BMI whereas the anatomical landmarks differ for all three variables. Intersections of age-dependent VAT profiles reveal locations that are independent of age for a given BMI group for both sexes. In males, this point of intersection shifts in caudal direction with increasing BMI.

Discussion: VAT distribution in head-feet direction depends on sex, age and BMI. In studies using single slice MRI for estimating the total volume of VAT, this indicates an additional potential source of error.

Conclusion: Taking advantage of a large study cohort, body fat distribution and its influence on single slice estimation is studied in greater detail and reveals, besides sex, additional age- and BMI-dependent factors to be considered.

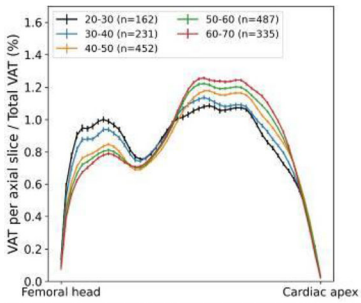

Fig. 1: Example of VAT profile along the craniocaudal axis (male participants with BMI 18.5–24.9kg/m²)

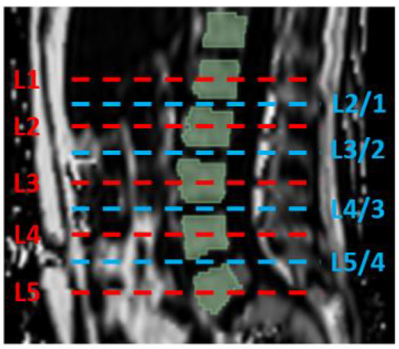

Fig. 2: Anatomical landmarks of VAT evaluation based on automatic segmentation of the spine.

	BMI / Alter	20-29	30-39	40-49	50-59	60-69	>70
$R^2\ A_{VAT}(cm^2) \sim V_{VAT}(l)$ (Position)	18.5 – 24.9 kg/m²	0.94 (L3)	0.95 (L3)	0.96 (L3/2)	0.96 (L3/2)	0.96 (L3/2)	0.98 (L4/3)
	25 – 29.9 kg/m²	0.97 (L2)	0.96 (L3/2)	0.94 (L2)	0.94 (L2)	0.94 (L3/2)	0.95 (L2)
	30 – 34.9 kg/m²	0.96 (L2/1)	0.94 (L3/2)	0.91 (L2)	0.91 (L3/2)	0.92 (L2)	0.83 (L3)
	35 – 39.9 kg/m²	0.98 (L2)	0.95 (L5-5.5cm)	0.94 (L3/2)	0.90 (L2)	0.92 (L3)	0.99 (L2)

Fig. 3: Maximum correlation coefficients and corresponding anatomical location dependent on BMI and age in men.

	BMI / Alter	20-29	30-39	40-49	50-59	60-69	>70
$R^2\ A_{VAT}(cm^2) \sim V_{VAT}(l)$ (Position)	18.5 – 24.9 kg/m²	0.92 (L3)	0.92 (L4/3)	0.94 (L4/3)	0.95 (L4/3)	0.96 (L3)	0.94 (L3/2)
	25 – 29.9 kg/m²	0.93 (L2)	0.94 (L2)	0.94 (L3)	0.94 (L3)	0.94 (L3)	0.93 (L4/3)
	30 – 34.9 kg/m²	0.95 (L2)	0.91 (L3/2)	0.94 (L3)	0.93 (L3)	0.92 (L3)	0.91 (L4/3)
	35 – 39.9 kg/m²	0.99 (L4/3)	0.97 (L2/1)	0.93 (L3)	0.90 (L3)	0.89 (L3)	0.97 (L4)

Fig. 4: Maximum correlation coefficients and corresponding anatomical location dependent on BMI and age in women.

References:

1. Neeland IJ et al. (2019) Visceral and ectopic fat, atherosclerosis, and cardiometabolic disease: a position statement. Lancet Diabetes Endocrinol 7:715–725.
2. Haueise T et al. (2023) Analysis of volume and topography of adipose tissue in the trunk: results of MRI of 11,141 participants in the German National Cohort. Sci Adv, in press
3. Yamazaki H et al. (2022) Fat Distribution Patterns and Future Type 2 Diabetes. Diabetes 71:1937–1945.
4. Taylor JL et al. (2021) Accuracy of dual-energy x-ray absorptiometry for assessing longitudinal change in visceral adipose tissue in patients with coronary artery disease. Int J Obes 2005 45:1740–1750.
5. Storz C et al. (2018) The role of visceral and subcutaneous adipose tissue measurements and their ratio by magnetic resonance imaging in subjects with prediabetes, diabetes and healthy controls from a general population without cardiovascular disease. Br J Radiol 91:20170808.
6. Chen S et al. (2022) The Optimal Axial Anatomical Site for a Single-Slice Area to Quantify the Total Volume of Visceral Adipose Tissue in Quantitative CT. Front Endocrinol 13:870552.
7. Linder N et al. (2020) Estimation of abdominal subcutaneous fat volume of obese adults from single-slice MRI data—Regression coefficients and agreement. Eur J Radiol 130:109184.
8. Bamberg F et al. (2015) Whole-Body MR Imaging in the German National Cohort: Rationale, Design, and Technical Background. Radiology 277:206–220.

P200.
Super-resolved dynamic 3D vocal tract imaging during natural speech

K. Isaieva[1], F. Odille[1,2], Y. Laprie[3], J. Leclère[1,4], J. Felblinger[1,2], P. A. Vuissoz.[1]

[1]*Université de Lorraine, IADI—INSERM U1254, Nancy, France;*
[2]*CIC-IT 1433, INSERM, CHRU de Nancy, Nancy, France;*
[3]*Université de Lorraine, LORIA—CNRS, INRIA, Nancy, France;*
[4]*University Hospital of Reims, Oral Medicine Department, Reims, France*

Introduction: MRI is a gold standard modality for speech imaging. However, it remains relatively slow, which complicates imaging of fast movements. For this reason, an MRI of the vocal tract is often performed in 2D. 3D MRI [1] provides more precise information, but the quality of such images is often insufficient. The goal of this study

was to test the applicability of super-resolution algorithms for dynamic vocal tract MRI.

Methods: *Volunteers and the speech task* 1 male and 1 female native French speaker were asked to read the text [2]. Two different strategies were tested. The male volunteer was reading the integrality of the text repeatedly 25 times, while the female volunteer was reading 25 repetitions of each small text fragment, and then passed to the next one. The female volunteer had also a teleprompting visual support forcing her to keep a similar speech rate during each repetition.

Data acquisition The images were acquired on a 3 T Siemens Prisma with a radial undersampled 2D FLASH sequence [3] (TE/TR = 1.47/2.22 ms, 9 radial spokes, slice thickness 8 mm, in-plane resolution 1.6 × 1.6 mm). 5 parallel volumes of 5 slices each were acquired with a shift of 1.6 mm, allowing an isotropic 1.6 × 1.6x1.6 mm super-resolution reconstruction. The sound was recorded simultaneously with the images, with a FOMRI III opto-acoustic microphone.

Slice alignment Slice alignment of the vocal tract during natural speech is a challenging task due to the poor reproducibility of the delay from the sequence start and speech rate between the repetitions. In our work, we based the alignment on sound recordings. The proposed approach is schematically illustrated in Fig. 1. Step 3 was applied to the male volunteer only.

Super-resolution The super-resolved images were obtained solving the following inverse problem:$x = \mathrm{argmin}_x \sum_{i=1}^{5} \|D_i B_i M_i - \rho_i\|^2 + \lambda\|x\|^2$

Where x—is the super-resolved volume, ρ—acquired anisotropic images, D—downsampling operator, B—blurring operator (calculating mean within a rectangular volume), M—geometrical transform (shift), λ = 10-6—regularization constant.

Validation The sharpness of the central slice of the resulting super-resolved volumes was evaluated using the sharpness index [7] and compared to that of the central anisotropic images. Additionally, the synchronization, quality of the rigid registration, and sharpness (potential to be automatically segmented) were evaluated visually using 3D dynamic videos in different projections.

Results: An example of the resulting volume at different reconstruction stages is presented in Fig. 2. It can be seen that some residual inconsistencies were present after the registration and were smoothed out after the super-resolution application. The 3D volumes corresponded to the pronounced phonemes and did not demonstrate ambiguous air-tissue boundaries which potentially enables an automatic segmentation (examples in Fig. 3).

The sharpness of the super-resolved images was inferior to that of the anisotropic images. This difference was more pronounced for the male volunteer (see Fig. 4).

Discussion: The strategy used for the female volunteer, i.e. repeating rather small fragments, and imposing a fixed speech rate, improves the sharpness of the super-resolved images explained by better reproducibility. However, some inconsistencies were still observed. An image-based alignment algorithm could improve these results.

Nevertheless, despite its low sharpness, the air-tissue boundary for both volunteers was unambiguous and potentially allowed its automatic segmentation. Despite a longer acquisition time, the images demonstrate considerably fewer motion artifacts than the 3D dynamic imaging [1]. The quality of the resulting volume is comparable to that presented in [8] in terms of motion artifacts, however, offers a greater spatial resolution and represents a significantly more complex speech task.

Conclusion: The proposed algorithm allows a dynamic 3D super-resolved vocal tract reconstruction during natural speech. A correct handling of the speech task improves the reproducibility and, consequently, the image quality. While time-consuming, the proposed approach offers 3D volumes with a sharpness sufficient for a potential automatic segmentation.

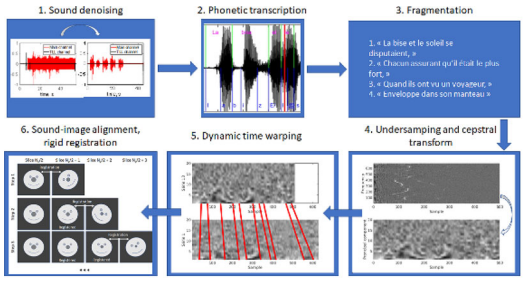

Fig. 1: Schematic illustration of the slice alignment. (1) The sound was denoised using a source separation approach [4]. (2) A phoneme-wise sound segmentation was applied using a forced alignment with the known text [5]. (3) This allowed text fragmentation. (4) A cepstral transform was applied with 64 times undersampling. Then a principal component analysis was used to keep only 20 features per time element. (5) Sound recordings corresponding to different slices were aligned to that corresponding to the central slice using the dynamic time warping algorithm. (6) Finally, the warping was applied to the image series. The nose region was manually selected, and a rigid registration was performed.

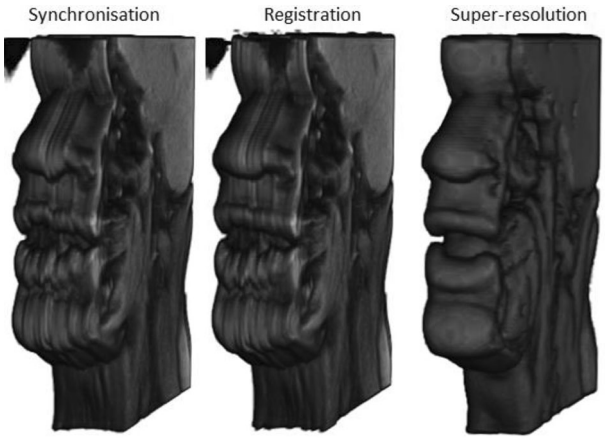

Fig. 2: Example of the 3D volume from the male speaker after different stages of the reconstruction.

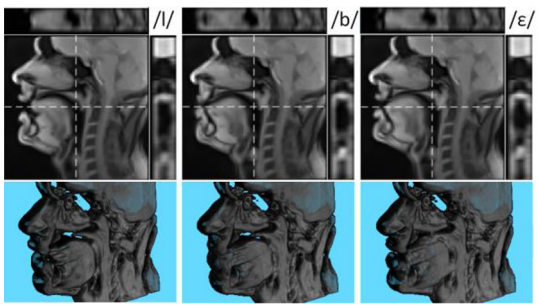

Fig. 3: Super-resolved 3D volume from the male speaker in different projections during pronunciation of phonemes /l/, /b/ and /ɛ/.

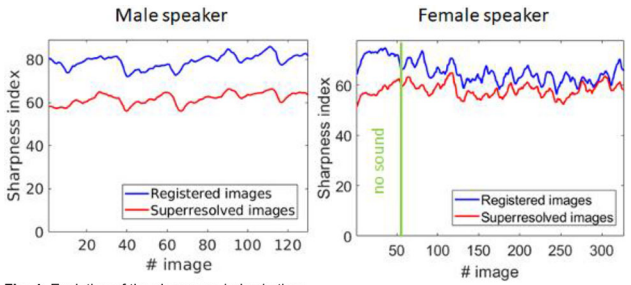

Fig. 4: Evolution of the sharpness index in time.

References:
[1] Jin, R., et al. (2022) Enhancing linguistic research… MRM.
[2] I. P. Association et al. (1999), Handbook of the International Phonetic Association. Cambridge University Press.
[3] Uecker, M., et al. (2010). NMR in Biomedicine, 23(8), 986-994.,
[4] Ozerov, A., et. al. A general flexible framework… IEEE Trans. Audio. Speech. Lang. Processing 20, 1118–1133 (2012).
[5] http://ortolang108.inist.fr/astali/
[6] Delbany, M. et al. (2019). MRM, 81(4), 2588-2599.,
[7] Leclaire A. et al. J. Math. Imaging Vis. 2015;52:145–172.
[8] Rusho, R. Z. et.al. Accelerated Pseudo 3D Dynamic Speech MRI… In *MICCAI 2022: 25th International Conference,* Springer Nature Switzerland.

P201.
Super-resolution with hybrid regularization for in-vivo free-breathing human placental MRI

M. A. Ngremmadji[1], F. Odille[2,1], R. Draveny[1], C. Bertholdt[3], O. Morel[3], M. Beaumont[2,1], B. Chen[2]

[1]*INSERM U 1254, IADI, Universitéde Lorraine, Vandoeuvre-lès-Nancy, France;*
[2]*INSERM CIC-IT 1433, Vandoeuvre-lès-Nancy, France;*
[3]*Service d'obstétrique et de médecine fœtale, Nancy, France*

Introduction: MRI has become the routinely secondary imaging method to ultrasound for pregnant women [1]. Due to the time limitation and the number of exams needed to be done during a single examination according to the current clinical recommendation, anisotropic low-spatial-resolution images without breath holding are acquired within a short time. However, isotropic high-resolution and high SNR data are always needed. Motion-compensated super-resolution techniques are therefore of great interest in this field.
Many methods combining slice-to-volume registration and super-resolution (SR) have been proposed in the literature. The quality of these methods mainly focuses on the sharpness of the image, however, the robustness of the texture and coherence of structures when registration is imperfect due to the limitation of the acquisition were less considered**.** Herein, we propose a hybrid super-resolution framework, combining an edge-preserving regularizer (Beltrami) with an anisotropic diffusion regularizer (Perona–Malik [4]), designed to improve the reconstruction of homogeneous regions. The framework is evaluated in free-breathing human placental MRI data to address the above problems.
Method: a) In-vivo Data acquisition: 4 patients were recruited under DIANE protocol (NCT04328532). The gestational age is between 30 and 38 weeks, 35 ± 6.4 years old. A 3 T clinical scanner (MAGNETOM Prisma, Siemens Healthcare, Erlangen, Germany) was used for imaging. For each patient, 2D multislice T2-weighted (Half Fourier Single-Shot Turbo Spin Echo) sequences were acquired in three quasi-orthogonal orientations, axial, coronal, and sagittal, in order to cover the whole volume of placenta. The in-plane image resolution is 0.893 × 0.893 mm^2, the slice thickness is 5 mm with a 1 mm ap, the acquisition matrix is 448 × 448, the repetition time (TR) is 2000 ms, and the echo time (TE) is 90 ms. The total acquisition time was 2.5 min. b) Image Processing: The acquisition model for the 3D image y_k (k = 1,2,3) is defined by the following equation:
$y_k = D_k B_k T_k x + n_k$ (1)
Where T_k is the interpolation operator on a given orientation, B_k is the blurring operator, D_k is the downsampling operator, and n_k is a zero-mean Gaussian noise. Initially, a rigid slice-to-volume image registration was performed in order to correct motion. We used the intersection-based motion correction [3] with cross-correlation as a similarity metric. The super-resolution reconstruction is an optimization problem:
$\min_u$ ½|| Hu-y||.^{2} + λR(u) (2)
H is the operator considering the blur, the interpolation, and the downsampling, y is the motion-corrected image, R is the Beltrami regularization term [2], and λ is the regularization weight. We proposed to use the following Partial Differential Equation (PDE) model:
∂u(t,x,y,zγ∂t − ηdiv(g_ρ(||∇u||) ∇u) + H′*(Hu-y) + λ ∂R(uγ∂u (3)
The first two terms in (3) are related to the anisotropic Perona-Malik (PM) diffusion model [4], g_ρ is the edge function defined by Eq. (6) in [5], where ρ and η are positive parameters. A Dirichlet-boundary condition is used. This PDE is numerically solved using an explicit finite difference scheme with a fixed step-time dt.c) Validation: The proposed method was compared with the super-resolution with Beltrami regularizer [2] which emphasizes the sharpness. A visual assessment was performed to show the advantages of this method.
Results: The values of the parameters used are: $\eta = 10^{-5}$, ρ = 2, dt = 0.001, and $\lambda = 10^{-2}$. A qualitative comparison was performed between natives and the super-resolved images. Fig. 1 illustrates the comparison among the native, the Beltrami-regularization results (SR-Beltrami) [2], and our results (SR-Hybrid).
Discussion: A novel super-resolution with hybrid regularization was proposed for free-breathing human placenta MR in a clinical scenario. Although in the fetal head area, Beltrami regularizer is still slightly superior to the proposed method, for the placenta where more homogeneous tissues are present, the proposed methods showed its advantageous by preserving the texture and appearance.
Conclusion: Together with motion compensation, the proposed hybrid super-resolution technique may improve the characterization of placenta morphology. Future work includes validation on more patients with quantitative metrics, and application to other type of sequences.

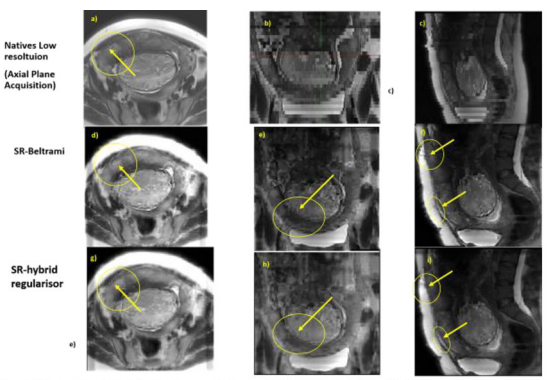

Fig. 1: The comparison between low resolution multislice 2D acquisition obtained at axial plane from one subject. Although the in-plane image quality is good (a), due to the big slice thickness, slice gap and motion during acquisition, information was incomplete and signal loss occurs at certain slice, making it impossible to obtain precise 3D information of the placenta at the other two planes (coronal (b) and sagittal (c)). Both super-resolution technique with Beltrami and hybrid regularization managed to improve this issue and quality are equally good in the placenta area. However, Beltrami regularization tends to prompt the sharpness of the image therefore leads to certain false positive as shown in the Figure (circled in yellow) while the hybrid regularization method managed to preserve the true structure. From (d) to (e):slices of SR-Beltrami reconstruction from axial, coronal and sagittal plane respectively, from (g) to (i) corresponding slices of SR-hybrid)

References:
1. ISUOG Practice Guidelines Ultrasound in Obstetric Gynecol 2023
2. F. Odille et al. MICCAI. 2015
3. Le Bars, A.-L. et al. *Diagnostics* 2022
4. P. Perona et al. IEEE Trans on Pattern Analysis and Machine Intelligence.1990
5. V. Kamalaveni et al. Procedia Computer Science. 2015
6. El Mourabit et al. Evolution Equations and Control Theory.2023.

P202.
Amplified MRI (aMRI) at ultra-high (7 T) field strength: first insights and feasibility

T. Zenger[1], A. L. Mayer[1], M. A. Schmidt[1], M. Zaiss[1,2,3], A. Dörfler[1], A. Mennecke[1]

[1]*Friedrich-Alexander-Universität Erlangen-Nürnberg (FAU), Neuroradiologisches Institut, Erlangen, Germany;*
[2]*Max-Planck-Institute for Biological Cybernetics, Magnetic Resonance Center, Tübingen, Germany;*
[3]*Friedrich-Alexander-Universität Erlangen-Nürnberg (FAU), Department Artificial Intelligence in Biomedical Engineering, Erlangen, Germany*

Introduction: Amplified MRI (aMRI) is a novel signal processing technique that uses motion amplification algorithms to reveal (sub)-voxel movement of the imaged tissue. Data from time-resolved bSSFP cine imaging sequences in combination with cardiac gating is used as raw data for the algorithm to amplify. Banding artefacts are a known issue in bSSFP sequences resulting from B0 inhomogeneity, aggravating at higher field strengths. In recent studies, initially imperceptible motions of the brain have been visualised with great success using aMRI at 3 T systems[1,2,3]. The higher spatial resolution available at 7 T systems would provide an interesting opportunity to visualise brain movement using aMRI in even greater detail. To the authors' best knowledge, no instance of aMRI performed at 7 T systems has been reported yet. In this study, we aim to utilise 7 T-aMRI, compare the results to 3 T-aMRI, and determine whether the increased banding artefacts pose too much of a hindrance to prefer 7 T over 3 T.

Methods: Images were obtained using a bSSFP TrueFISP (BEAT) sequence at the Siemens Magnetom™ Terra 7 T and Siemens Magnetom™ Vida 3 T systems (Siemens Healthineers, Erlangen, Germany). Phantom measurements were performed at equal resolution (FOV 230 mm^2, 0.63 × 0.63 × 3 mm^3, number of segments (N_{Seg}) = 6, bandwidth (BW) = 618 Hz/px, GRAPPA = 2) at 3 T (TR/TE/FA = 30 ms/2.5 ms/25°, 1Tx/64Rx head coil) and 7 T (TR/TE/FA = 27.12 ms/2.26 ms/25°, 8Tx/32Rx head coil in CP-mode) with a simulated 60 bpm heartbeat.
Additionally, three transversal slices (FOV = 230 mm^2, 0.96 × 0.96 × 3 mm^3, N_{Seg} = 6) of a healthy volunteer were measured at 7 T (TR/TE/FA = 21.6 ms/1.8 ms/24°, BW = 1042 Hz/px) using different shimming options and at 3 T (TR/TE/FA = 23.28 ms/1.94 ms/25°, BW = 947 Hz/px).
Motion amplification was performed using a phase-based amplification algorithm for video processing[4]. The algorithm was adjusted to facilitate a smoother workflow using arrays of DICOM data as input. Phantom amplification parameters were: amplification factor = 10, amplified frequency bands [0.1, 0.89] Hz, [0.9, 1.6] Hz, and [1.61, 10] Hz, smoothing parameter = 5, half octave steerable pyramid. In vivo, measurements were amplified at [f_{Heart}—0.1, f_{Heart} + 0.1] Hz with the same remaining parameters. Frequencies outside the examined frequency bands were set to zero in all cases.

Results: Subtle brain motion was successfully amplified in three transversal slices at 7 T (see e.g. https://gitlab.com/TZenger/Figures/-/blob/main/SL1_Looped.mp4).
Banding artefacts were present in both phantom measurements (Fig. 1a & b). After amplification, the artefacts were prominent in coefficient of variation (CV) maps (Fig. 1c). The three frequency bands each showed different motions both at 3 T and 7 T. Advanced shimming in transversal 7 T in vivo measurements mitigated banding artefacts (Figs. 2 & 3). 7 T-aMRI results are comparable to 3 T-aMRI (Fig. 3 & animated versions at https://gitlab.com/TZenger/Figures).

Discussion: Despite the aggravation of banding artefacts at 7 T, similar quality of motion amplification results could be produced as at 3 T. No advanced shim was used in 3 T measurements, which was assumed as a quality baseline for 7 T. The used phantom had no intrinsic mechanism that would suggest movement; however, motion could be seen both visually in the amplified movies and in the calculated CV maps (Fig. 1c). One possible explanation could be a small variation of the B_0 field during the examination.
Movement of banding artefacts could also be seen in vivo (Fig. 3), implying the need for caution when interpreting aMRI results in their presence. Especially since these artificial movements can be of an equal or higher order than actual amplified brain motion (Fig. 3 bottom row). Further, in two out of three slices of the 7 T in vivo measurement, banding artefacts could be removed with great success (Fig. 2), giving hope for artefact-free, high-quality, and high-resolution aMRI at 7 T. Although advanced shimming entails a longer acquisition time, the benefits clearly outweigh.

Conclusion: We showed first aMRI results at 7 T, using bSSFP cine MRI. bSSFP banding artefacts not only obscure the underlying anatomy but also show movement visible in e.g. CV maps after amplification. Using advanced shimming, similar quality (3 T vs. 7 T) measurements could be obtained, and banding artefacts removed from the region of interest in two out of three transversal slices in vivo at 7 T. Given successful shimming, results were comparable to 3 T-aMRI and 7 T-aMRI thus shows potential as an alternative, especially if higher spatial resolution is desired.

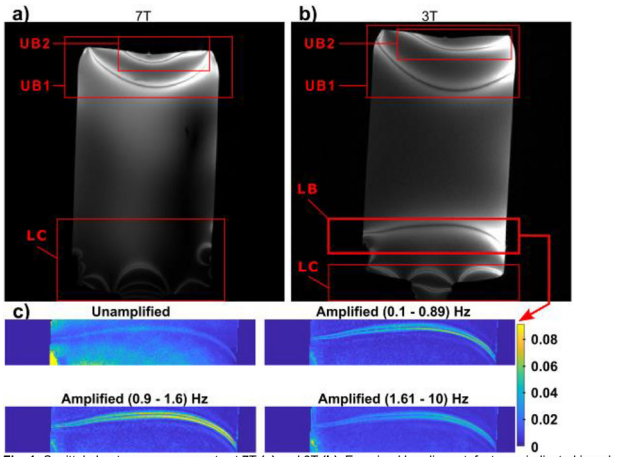

Fig. 1: Sagittal phantom measurements at 7T **(a)** and 3T **(b)**. Examined banding artefacts are indicated in red rectangles. **1c.** Coefficient of variation (CV) maps of 3T-LB (cf. b) unamplified (top left) and amplified in the three examined frequency bands. The visible motion in the amplified videos was strongest in this case.

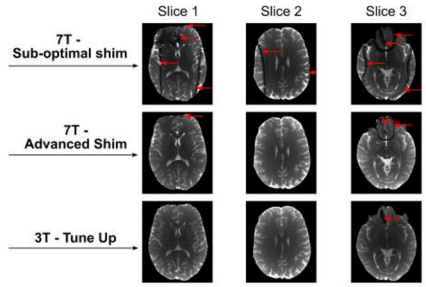

Fig. 2: Three transversal slices with two different shimming options at 7T and three similar slices at 3T. Banding artefacts can be seen in the measurement with sub-optimal shimming **(top)**, indicated by red arrows. In the advanced shimming measurement only three artefacts remain.

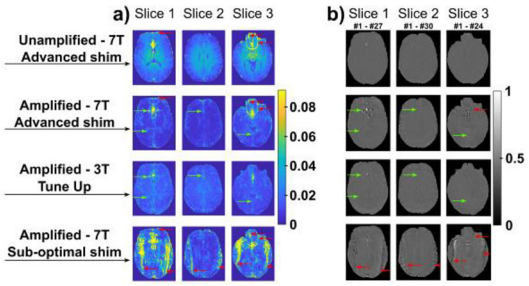

Fig. 3: CV **(a)** and normalised difference maps **(b)** before (advanced shim 7T) and after (sub-optimal shim 7T, advanced shim 7T, & 3T) amplification. Banding artefacts show motion when present (red arrows). With advanced shimming, subtle brain movements are more clearly visible. 7T and 3T results are comparable (exemplarily marked by green arrows). The color bar in a is identical to **Fig. 1c**.

References:

1. Holdsworth et al. (2016), MRM, https://doi.org/10.1002/mrm.26142
2. Terem et al. (2018), MRM, https://doi.org/10.1002/mrm.27236
3. Terem et al. (2021), MRM, https://doi.org/10.1002/mrm.28797
4. Wadhwa et al. (2013), ACM Transactions on Graphics, https://doi.org/10.1145/2461912.2461966

P203.
Fraction estimation for two compartment systems with phase-cycled BSSFP

B. C. Acikgoz[1,2], J. A. M. Bastiaansen[1,2]

[1]*University of Bern, DIPR, Bern, Switzerland;*
[2]*University of Bern, GCB, Bern, Switzerland*

Introduction: Tissue fraction estimation is essential for various clinical applications such as detection of fatty infiltration in myocardium [1], diagnosis and prognosis of liver steatosis [2]. Magnetic resonance imaging (MRI) is can be used to noninvasively estimating tissue fractions [3]. However, current MRI methods rely on a priori knowledge on frequencies of resonance peaks of present tissues in a region of interest (ROI) [3]. In this study, a novel method for proton density fraction estimation is proposed, experimental studies are conducted on an acetone/water phantom and results are presented. The aim of the study was to leverage phase cycled balanced steady state free precession (PC-bSSFP) profile asymmetries induced by the presence of multiple compartments [4]. The proposed method does not require knowledge of the multiplet in ROI and magnetic field inhomogeneity.

Methods: A dictionary composed of simulated single-compartment elliptic PC-bSSFP profiles was fitted to the measured PC-bSSFP profiles. For the fitting, a non-negative orthogonal matching pursuit (NNOMP) [5] algorithm was applied to each voxel separately. This algorithm was selected for its speed and its ability to predetermine a level of sparsity. After the dictionary fitting step, the value of the largest weight is divided by the sum of all nonzero weights to calculate the tissue fraction. Current fraction calculation algorithm confuses fraction values that sum up to 100% (e.g., 40% and 60%). An acetone–water phantom with vials of varying acetone–water fractions submerged into agar gel was used for experimental studies. Acetone was selected for its solubility in water to create a neat two-compartment system. Experiments were conducted on a 3 T Siemens Prisma scanner with the acquisition parameters presented in Table 1. For the dictionary creation, a T_1/T_2 array of [1:1:16] and off-resonance array of [-1/TR, 1/TR] Hz and T_2 of 80 ms are simulated. The estimated fraction value Ψ for the vial with 60% acetone is replaced by 1-Ψ due to the aforementioned method of fraction calculation. To evaluate the efficacy of the proposed algorithm, root mean squared error (RMSE) in each vial with the reference values were calculated. Also, mean value and standard deviation of estimated fractions in each vial were calculated. From the estimated fractions a linear regression analysis was performed. For the analyses and for visualization, binary masks were created manually. 0% and 100% regions are also masked since dictionary fitting was performed for a two-compartment system and does not yield correct results for single-compartment regions.

Results: In each vial, the estimated fraction values demonstrate good visual homogeneity and are discernible (Fig. 1). The largest mean error of acetone fraction estimations were 2.1% and the largest standard deviation of 0.6% (Fig. 2). Largest RMSE obtained was 2.2% (Fig. 2). Linear regression analysis of reference and estimated fraction values produced an R^2 value of 0.99.

Discussion: The proposed method using dictionary fitting to the PC-bSSFP asymmetries provided good estimates of acetone-to-water fractions by means of mean error, standard deviation in vials and RMSE. Linear regression analysis linear regression analysis demonstrates the strong correlation between the reference and estimated fraction values. The results indicate that the method could potentially be used in other two-compartment systems such as myelin water where there is a slight variation in resonance peaks observed for certain directions of fiber orientation [11]. Further extensions of this work may include multiplet systems with more than two spectral peaks.

Conclusion: The proposed method provides an accurate technique for estimating tissue fractions in two-compartment systems without prior knowledge of the spectral peaks of the system.

References

[1] P. Kellman, D. Hernando, and A. E. Arai, "Myocardial Fat Imaging", *Curr. Cardiovasc. Imaging Rep.*, vol. 3, no. 2, pp. 83–91, Apr. 2010.
[2] S. B. Reeder and C. B. Sirlin, "Quantification of Liver Fat with Magnetic Resonance Imaging", *Magn. Reson. Imaging Clin. N. Am.*, vol. 18, no. 3, pp. 337–357, Aug. 2010.
[3] H. H. Hu et al., "ISMRM workshop on fat–water separation: Insights, applications and progress in MRI", *Magn. Reson. Med.*, vol. 68, no. 2, pp. 378–388, Aug. 2012.
[4] K. L. Miller, "Asymmetries of the balanced SSFP profile. Part I: Theory and observation: Balanced SSFP Asymmetry: Theory", *Magn. Reson. Med.*, vol. 63, no. 2, pp. 385–395, Feb. 2010.
[5] M. Yaghoobi, D. Wu, and M. E. Davies, "Fast Non-Negative Orthogonal Matching Pursuit", *IEEE Signal Process. Lett.*, vol. 22, no. 9, pp. 1229–1233, Sep. 2015.
[6] D. A. Yablonskiy and A. L. Sukstanskii, "Biophysical mechanisms of myelin-induced water frequency shifts: Biophysical Mechanisms of Myelin-Induced Water Frequency Shifts", *Magn. Reson. Med.*, vol. 71, no. 6, pp. 1956–1958, Jun. 2014.

Parameter	Value
Resolution ($mm \times mm \times mm$)	$0.9 \times 0.9 \times 1.5$
Repetition Time (ms)	5
Echo Time (ms)	2.5
# Phase Cycles	36
Flip Angle (deg)	35
Bandwidth (Hz/Px)	488

Table 1: Acquisition parameters for MRI experiments.

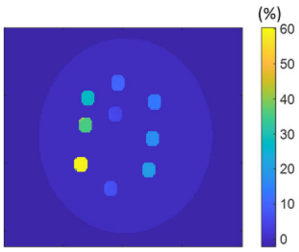

Fig. 1: Acetone-water fraction map of the imaging phantom. Acetone-water mixture vials are masked by hand.

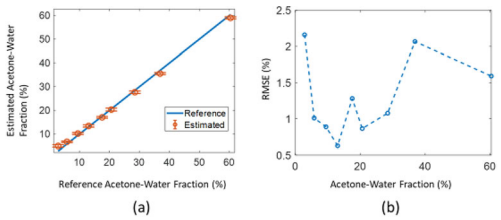

Fig. 2: (a) Error bars for the estimated vs. reference acetone-water fractions. Mean values in each vials are [4.97,6.70,10.17,13.31,16.99,20.31,27.66,35.61,58.93] and standard deviations are [0.51,0.30,0.41,0.49,0.31,0.60,0.55,0.46,0.55]. (b) RMSE vs acetone-water fraction in different vials.

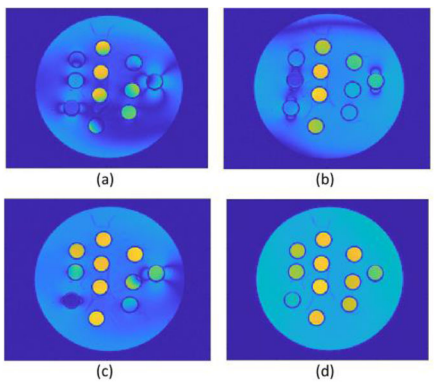

Fig. 3: Phase-cycled images (a-c) of phase-cycle angles (a) 0°, (b) 120°, (c) 240° and (d) banding-free complex-sum image of the acetone-water phantom.

P204.
MR-ARFI using single-shot HASTE imaging to detect displacement due to transcranial ultrasound

D. van den Heuvel[1], A. Arbabi[1], S. Meijer[1], B. Kop[1], A. Chetverikov[1], L. Verhagen[1], D. G. Norris.[1]

[1]*Radboud University, Donders Institute, Nijmegen, Netherlands*

Introduction: Transcranial Ultrasound (TUS) is a promising technique for non-invasive brain stimulation. This is because it can in theory stimulate a small, well-defined volume of tissue at any depth in the brain. Furthermore, it is readily compatible with MRI. To localise the focal point of the TUS beam to the target of interest within the brain attenuation, refraction and dispersion caused by the skull must be accounted for. The properties of the skull vary enormously between individuals, so it is challenging to compute the correct intensity and modulation pattern for the TUS transducer elements a priori. The focal point of the TUS can be measured using MR-ARFI (1), and in an ideal setup an undistorted ARFI image would be rapidly obtainable at low TUS intensity and used as input to an (iterative) procedure to adjust the position and intensity of the beam focus. The presence of (multiple) bulky ultrasound transducers can limit the number of receiver coils available, and hence a sequence should be selected that does not rely heavily on acceleration using partial parallel imaging. In this abstract we propose the use of a single-shot modified diffusion-weighted HASTE sequence and demonstrate its efficacy in a phantom experiment.

Methods: Ultrasound pulses were generated in a TPO (Transducer Power Output device, Sonic Concepts, NeuroFUS TPO version 5.04), which drives an MR-compatible 2D active annular phased array ultrasound transducer (Sonic Concepts, NeuroFUS Cortical Focused Transducer—CTX-500-4CH). The transducer array has 3 concentric elements around a circular element in the centre and a total active diameter of 64 mm2. It was operated at its central frequency of 500 kHz in continuous wave mode. The focal depth of the transducer was adjusted to 6 and 8.12 cm at 30/10 W/cm2 SPPA (spatial-peak pulse average, i.e. intensity at the focal spot). The US was initiated through a trigger that was encoded in the MRI pulse sequence.

The tofu phantoms were store-bought soft silken tofu to create a phantom that was large enough to contain the focal spot of the transducer (Fig. 1). It was determined that soft tofu was a suitable material for MR-ARFI measurements in terms of T2 relaxation time and elastic properties.

A Diffusion-Weighted Half-Fourier Acquisition Single-shot Turbo spin Echo (DW-HASTE) pulse sequence was adapted for the different MR-ARFI experiments. The sequence contained two 180 degree refocusing pulses. Each one occurred at the centre of a bipolar displacement-encoding gradient. There was a delay between the two gradients of 4 ms (Fig. 2). Imaging was performed on a 3 T MRI scanner (Siemens MAGNETOM Skyra). Images were acquired at a resolution of 64 × 64 voxels (2.3 mm isotropic). The TE/TR were 69/1000 ms. Twenty interleaved images were acquired alternating between US on and off. All data analysis was done in MATLAB (2021) using standard methods to generate phase images.

Results: Figure 3 shows the phase difference map generated for the tofu phantom at 30 W/cm2 SPPA and a focal depth of 8.12 cm. Figure 4 shows a comparison for 30 and 10 W/cm2 SPPA. The focal spot at lower intensity was barely visible outside two slices. A P-value < 0.05 was then used to create the focal spot profile. For 30 W a maximum displacement of 1.071 μm was found and for 10 W a displacement of 0.442 μm. Mean displacements were calculated based on a 3 by 3 area around the maximum value. For 10 W the mean displacement was 0.273 ± 0.085 μm. For 30 W this was 0.998 ± 0.061 μm. These values conform to the expected linear relationship between ultrasound intensity and measured displacement.

Discussion: We have demonstrated the feasibility of using DW-HASTE for MR-ARFI in a realistic tissue-phantom. Sensitivity could be further increased by reversing the polarity of the diffusion-weighting gradients between measurement and further optimisation of the acquisition sequence. When further technical and ethical hurdles are overcome, we intend to start testing in humans. This approach offers high-fidelity images without distortion in an acquisition time that is compatible with iteratively adjusting the beam"s focus.

Reference

McDannold N, Maier SE (2008) Magnetic resonance acoustic radiation force imaging. Med Phys 35:3748–3758.

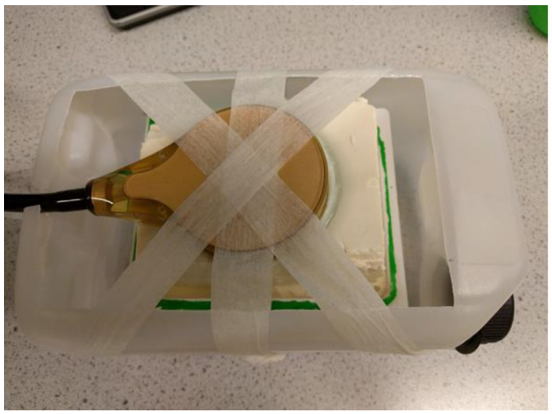

Fig. 1: Top down view of the setup with a tofu phantom. The circular transducer is placed on top of the blocks of tofu. The bottom piece of tofu remained in its hard plastic packaging for stability.

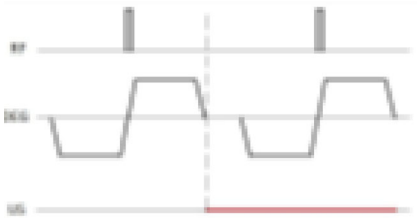

Fig. 2: Displacement-encoding gradients (DEG) of the ARFI sequence as used in the displacement experiments with tofu. Top: the 180° refocusing pulses. Middle: DEG. The vertical line signifies the trigger. Bottom: the ultrasound stimulation.

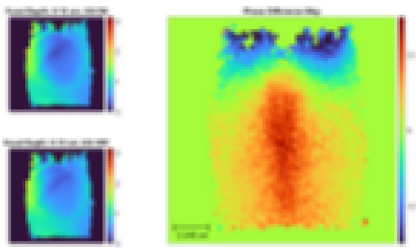

Fig. 3: Phase image slices collected with the MR-ARFI sequence on the soft tofu phantom. The focal depth was set to 8.12 cm. Top left: a phase image with US on. Bottom left: a phase image with US off. Right: the phase difference between the left two images. The values are in radians.

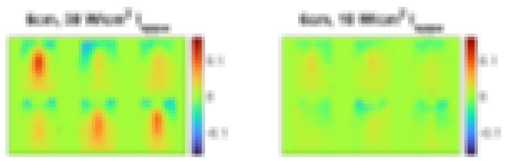

Fig. 4: Focal spots at different intensities at 6 cm focal depth. Left: 30W/cm^2, Right: 10 W/cm^2

P205.
Deep learning pipeline for under-sampled MR images reconstruction

G. Kanli[1], D. Perlo[1], S. Boudissa[1], O. Keunen[1]

[1]*Luxembourg Institute of Health (LIH), Department of Oncology, Luxembourg, Luxembourg*

Introduction: MRI (magnetic resonance imaging) is a medical imaging technique that uses strong magnetic fields and radio waves to produce images of the human body. Raw MR data is collected in the spatial frequencies domain (known as k-space) before images are reconstructed using an Inverse Fourier Transform (IFT). The scan time is proportional to the amount of k-space data collected [1]. Shortening the MR scan time is desirable to lower the medical care costs, reduce motion artifacts, and increase patient comfort. However, this implies reducing the acquired measurements, which in turn reduces the image quality [2]. We explored the possibility to speed up MRI acquisitions by skipping some phase-encoding lines in k-space, under-sampling strategy (US), and using deep learning methods to recover missing information and restore images quality [3, 4].

Methods: T2w images of in vivo mouse brains were obtained using a 3 T preclinical system (MRSolutions, UK) with Cartesian sampling trajectories. In our experiments, US was simulated by retrospectively dropping phase-encoding lines using one of three distinct strategies: uniform, random, and gradient. The central area of k-space, which corresponds to the low frequencies, was preserved to reduce the aliasing artifacts.

Pre-processing of k-space data consisted in filling the skipped lines using one of the following strategies: (1) no pre-filling, (2) mean pre-filling, that is filling missing k-space data with average values from neighbors, (3) conjugate symmetry pre-filling, using the read-conjugate symmetry property of the k-space, (4) combination of mean and conjugate symmetry pre-filling.

In this project, we used U-Net models in both the k-space domain (K-net), and in the image domain (I-net), Fig. 1; the proposed model builds upon of the combination of the papers [3] and [4]. The first K-net model is used to recover the skipped lines of k-space. The output of U-net model is a restored k-space in which we replace the predicted k-space data with the original k-space US data available, to produce the K-net output. The input to the image domain U-net model, called I-net, is the K-net output image to which an IFT has been applied. This model is used to improve reconstructed images consistency and the output of the I-net is the final output of our proposed model. SSIM, FSIM, PSNR, and MSE are the quality metrics of this work.

Results: Fig. 2A shows the performance achieved with different US strategies. The first column shows images reconstructed from the ground-truth while the second, third, and fourth columns represent images reconstructed from k-space US using the uniform, random, and gradient strategy, respectively. The first line represents the IFT of the US k-space and the second one the images restored by our proposed method.

Figure 2B illustrates the impact of k-space pre-processing. The first, second, third, and fourth columns represent the ground-truth, the US image, the output of the K-net model, and the output of the I-net

model, respectively. The first, second, third, and fourth lines show the reconstructed images obtained with the various pre-processing strategies: no, mean, conjugate symmetry, and combination pre-filling, respectively.
Figure 2C shows the performance of the proposed method for different US levels, 60%, 70%, 80%, and 90% faster than the ground-truth.
Discussion: The goal of this work is to speed up MRI acquisitions by k-space US, while salvaging images quality using deep learning models. We trained models in both the k-space and image domains with various US levels and k-space data pre-filling strategies. The proposed method provides surprisingly sharp and natural-looking images with limited artifacts and noise, with the K-net and I-net models providing complementary benefits in images details and contrast restoration and image consistency enforcement. The best results were achieved with the gradient US strategy and pre-processing steps to pre-fill missing k-space values were found to have little influence on the quality of the reconstructed images.
Conclusion: K-space US and images restoration by deep learning is possible and allow the reconstruction of sound quality images even under strong US situations. Models trained in the k-space and image domains provide complementary benefits in the process. Future work will address US of non-Cartesian data acquisitions and the use of alternative models architectures.
References
[1] Zhang, et al. (2019) Reducing uncertainty in undersampled MRI reconstruction with active acquisition https://doi.org/10.1109/CVPR.2019.00215
[2] Huang, et al. (2022) *Data and Physics Driven Learning Models for Fast MRI.*
[3] Eo, et al. (2018) KIKI-net: cross-domain convolutional neural networks for reconstructing undersampled magnetic resonance images https://doi.org/10.1002/mrm.27201
[4] Hyun, et al. (2018) Deep learning for undersampled MRI reconstruction. https://doi.org/10.1088/1361-6560/aac71a

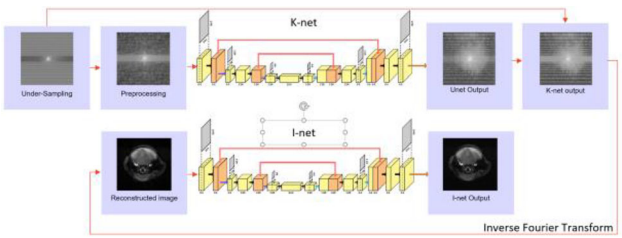

Fig. 1: Our proposed models: K-net and I-net

P206.
Optimal control pulses simulations applied to magnetic resonance elastography for clinical examination with liver iron overload

T. Bakir Ageron[1], K. Tse Ve Koon[1], P. Sango-Solanas[1], E. van Reeth[2], O. Beuf[3]

[1]*CREATIS / UCBL, Medical Imaging Research, Villeurbanne, France;*
[2]*CREATIS / CPE, Medical Imaging Research, Villeurbanne, France;*
[3]*CREATIS / CNRS, Medical Imaging Research, Villeurbanne, France*

Introduction: Magnetic resonance elastography (MRE) is a non-invasive imaging technique enabling quantitative assessment of the mechanical properties of tissues as demonstrated for liver fibrosis [1]. However, technical error rates remain important preventing the development of MRE in clinical use [2].
One of the causes of failure is liver iron overload which induces a decrease in T2 enhancing the need to reduce Echo Times (TE), so as to preserve the NMR signal from the liver.
However, conventional MRE sequences include motion encoding gradient (MEG) which encodes the propagation of shear waves generated by an external actuator in the phase images. Placed between the RF excitation pulse and signal readout, MEG leads to increased TE.
Recent work based on RF pulses designed by using optimal control (OC) theory have shown on preclinical MRI [3, 4] that OC-pulses can simultaneously perform slice excitation and motions encoding when applied concomitantly with a constant gradient G, therefore enabling tremendous TE reduction. However, application to a clinical context has yet to be done. In clinical MRE, the mechanical excitation frequency, maximum amplitudes of gradient and RF pulses ($B1_{max}$) are lower but the amplitudes of mechanical excitations are higher.
In this work, we investigate the possibility to extend the previously proposed OC framework to design motion encoding excitation pulses that are applicable in a clinical context. In particular, the impact of $B1_{max}$ and the pulse length (T_f) is analysed.
Methods: The GRAPE (Gradient Ascent Pulse Engineering) algorithm based on gradient descent numerically solves optimal control problems applied to NMR pulse design [5]. It allows computing RF pulses and magnetization trajectories by fulfilling optimality conditions. Based on an initial estimate, the control field is iteratively updated according to the constraints imposed in order to minimise a defined cost function [6] (Fig. 1**, Eq. 1**).
With $M^{(i,j)}$ the macroscopic magnetization, $T^{(i,j)}$ the expected target state, ρ the magnetization amplitude (between 0 and 1) and $\theta^i = (2\pi x^i)/\lambda$ the magnetization phase which depends on the isochromats' displacement (x^i) along the wavelength. Two isochromats separated by a quarter of a wavelength ($\theta^1 = 0$, $\theta^2 = \pi/2$) are considered to obtain a pulse that encodes the wave propagation in the phase images [6].
The slice selection is achieved by applying an RF excitation pulse and G simultaneously, in presence of the shear wave with frequency f_e and motion amplitude A. The resonance offset undergone by the isochromats in the position (x^i,z^j), along the propagation direction of the wave (z^j) and the slice selection direction (Fig. 1, Eq. 2).
Several OC pulses were optimized with clinical MRE parameters. Then, these pulses were propagated through Bloch Equations by simulation. The final obtained transverse magnetization were plotted for each pulse.
F_e was set to 60Hz and A = 1mm. The constant gradient G amplitude was set to 40mT/m in accordance with typical clinical MRI gradient characteristics. Relaxation times were set to T1= 500ms and T2=20ms (Fig. 2).
The pulse duration was changed from 5 to 25ms by step of 5ms and $B1_{max}$ from 10μT to 40μT by step of 10μT (Fig. 3). Then, for a T_f 25ms, a gradual decrease of $B1_{max}$ from 80 to 10μT was carried out (10μT steps) (Fig. 4).
Results: The variation of the pulse length T_f allowed to see the real impact of this parameter, on the desired target states. Combinations of T_f and $B1_{max}$ show that satisfactory optimizations (framed in green) can be reached for $B1_{max}$ of 20μT and above and that for lower $B1_{max}$, higher T_f are required (Fig. 3).
For 10μT $B1_{max}$ value (Fig. 4), the final states of the isochromat populations are quite far off from the desired target states, the different groups (identified by the three colors) being dispersed on the transverse plane.
Conclusion: The various simulations showed the influence of $B1_{max}$ and T_f on the final states and that $B1_{max}$ above 20μT allows

satisfactory convergence. Optimizations with $T_f > 25$ ms were unsuccesful (not shown here) due to convergence issues. Such results give the framework for the successful application of OC-MRE in a clinical context.

Future work will consist in decreasing the amplitude of the constant gradient, to move away from the maximum limits of the clinical systems and to evaluate its influence on the isochromat final trajectories.

Acknowledgments: This work was performed within the scope of LABEX PRIMES (ANR-11-LBX-0063) and PIONEER (ANR-22-CE19-0023-01).

Eq. 1: Cost function equation

$$C(B_1) = \sum_{j=1}^{J} \sum_{i=1}^{N} \left\| \vec{M}^{(i,j)}(T_f) - \vec{T}^{(i,j)} \right\|^2$$

With $\vec{M}^{(i,j)}$ the final magnetization, $\vec{T}^{(i,j)}$ the expected target states:

$$\vec{T}^{(i,j)} = \begin{matrix} \rho\left[\cos(\theta^i), \sin(\theta^i), 0\right] if\ j \in \Delta z_{in} (\text{slice thickness}) \\ [0,0,1]\ if\ j \notin \Delta z_{in} \end{matrix}$$

Eq. 2: Resonance offset equation

$$\Delta B_0^{(i,j)}(t) = G\left[A sin\left(-2\pi f_e t + \frac{2\pi x^i}{\lambda}\right) + z^j\right]$$

Fig. 1: Cost Function (Eq. 1) and Resonance Offset (Eq. 2) equations.

Figure Reference		f_e (Hz)	A (mm)	G (T/m)	Bandwidth (Hz)	$B1_{max}$ Amplitude	T_f (ms)	T1 (ms)	T2 (ms)
Fig.1	1st line	60	1	0,04	1800	70µT	5,10, 15, 20, 25, 30	500	20
	2nd line	60	1	0,04	1800	80µT	5,10, 15, 20, 25, 30	500	20
Fig.2		60	1	0,02	1800	10µT	25	500	20
		60	1	0,04	1800	20µT	25	500	20
		60	1	0,02	1800	30µT	25	500	20
		60	1	0,04	1800	40µT	25	500	20
		60	1	0,02	1800	50µT	25	500	20
		60	1	0,04	1800	60µT	25	500	20
		60	1	0,02	1800	70µT	25	500	20
		60	1	0,04	1800	80µT	25	500	20

Fig. 2: ***Table*** : Optimization parameters of the different simulations.

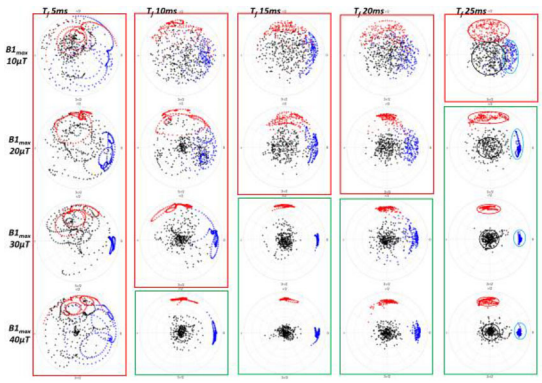

Fig. 3: Final transverse magnetization states in the transverse plane. Visualization of the different variations of T_f pulse durations (between 5 to 25ms), for $B1_{max}$ 10, 20, 30 and 40µT. The green boxes highlight satisfactory final states while the red boxes indicate the unachieved target states.

Interpretation: Final states of the red and blue isochromats should be close to the plane edges and along the π/2 and 0 axes respectively. The black isochromat cluster is expected to be in the center.

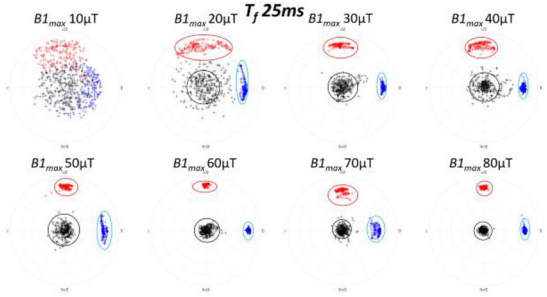

Fig. 4: Final transverse magnetization states for different $B1_{max}$ and for T_f set to 25ms. The ellipses highlight the different isochromat groups.

References

[1] S. Hoodeshenas et al., **2018**, https://doi.org/10.1097/RMR.0000000000000177

[2] H. M. Ghoz et al., **2019**, https://doi.org/10.21037/qims.2019.05.13

[3] P. M. Lefebvre et al., **2017**, https://doi.org/10.1016/j.jmr.2017.05.008

[4] P. Sango-Solanas et al., **2022**, https://doi.org/10.1038/s41598-022–05262-3

[5] E. Van Reeth et al., **2018**, https://doi.org/10.1016/j.jmr.2018.07.013

[6] N. Khaneja et al., 2005, https://doi.org/10.1016/j.jmr.2004.11.004

P207.
Nonlinear shear modulus quantification using the theory of acoustoelasticity in MR-elastography

G. Pagé[1], J. L. Gennisson[1], P. Garteiser[2], B. van Beers[2,3]

[1]*BIOMAPS UMR 9011 CNRS, INSERM, CEA, Orsay, France;*
[2]*INSERM UMR 1149, Paris, France;*
[3]*Beaujon University Hospital, AP-HP, Department of Radiologic Technology, Faculty of Associated Medical, Clichy, France*

Introduction: In ultrasound elastography (US-elastography) and MR-elastography, the study of mechanical parameters such as stiffness or storage and loss moduli has shown to be effective for diagnosing various diseases[1, 2]. However, assessing shear modulus may be insufficient for tumor characterization, as observed in breast tumors[3]. In US-elastography, the acoustoelasticity theory-based approach enables the determination of the nonlinear coefficient of the shear modulus (A)[4]. The purpose of this study is to develop a method for assessing the nonlinear storage modulus with MR-elastography.

Methods: According to the acoustoelasticity theory, the experiment involves measuring the speed of a shear wave propagating in a specific direction within a medium subjected to uniaxial stress. Under these conditions, Gennisson et al.[4] developed the equations to estimate the nonlinear coefficient in three configurations of shear wave displacement (Fig. 1).

$$G'_{12} = G'_0 - \sigma_2(1+(A/12G'_0)) \quad (1)$$
$$G'_{21} = G'_0 - \sigma_2(A/12G'_0) \quad (2)$$
$$G'_{13} = G'_0 + \sigma_2(1+(A/6G'_0)) \quad (3)$$

Where G" is the storage modulus, the first subscript is the direction of polarization, the second subscript is the direction of propagation and σ_2 is the uniaxial stress.

We developed a specific compression setup to uniaxially compress a phantom inside the MRI tunnel (Fig. 1). We prepared two homogeneous phantoms with respective agar concentrations 1% and 1.5% (AGAR_1 and AGAR_2). In addition, we prepared a heterogeneous phantom consisting of a sample of bovine liver embedded in a gel containing concentrations of 1.5% agar and 2% gelatin.

MRI acquisitions were performed on a 7 T MRI scanner (Pharmascan, Bruker, Erlingen, Germany). T2-weighted MR images of the phantoms were acquired with a RARE spin-echo sequence (15 ms TE, 1300 ms TR). The resolution was 0.4 mm, the acquisition matrix 87 × 87, number of slices 9, and acquisition time 2 min. MR-elastography was performed with 300 Hz mechanical vibrations synchronized with a modified spin-echo sequence. Nine slices were obtained with a volumetric resolution of 0.4 mm3, TE 23 ms, TR 1023 ms, four dynamic scans over a vibration period and acquisition time of 6 min for each of the three acquired spatial directions. The morphological T2-weighted images and the functional MR-elastography images were acquired without compression and were repeated after compression steps of 0.5 mm.

To obtain storage modulus maps according to Eq. (1), a spatio-temporal filter was applied along direction 2. Phantom deformation (ε) maps were calculated by performing 3D affine registration on the T2 images. Stress (σ) was calculated with the Hooke law, as $\sigma_2 = 3\varepsilon G'$ The slope between the shear modulus for each propagation axis and the applied stress was estimated and the nonlinear shear modulus A was computed using (1). The same reconstruction process was used for 21 and 13 subscripts.

Results: Storage moduli according to uniaxial stress in agar phantoms are shown in Fig. 2. For AGAR_1 (G' = 1.8 ± 0.1) and AGAR_2 (G' = 2.5 ± 0.3), similar nonlinear coefficients were estimated, independently of the chosen configuration (AGAR_1, (12): A = – 34.0 kPa, (21): A = – 34.8 kPa, (13): A = – 31.3 kPa; AGAR_2 (12): A = – 13.7 kPa, (21): A = – 23.7 kPa, (13): A = – 17.1 kPa).

T2-weighted image and storage modulus map of the bovine liver phantom are shown in Fig. 3. At zero stress, the storage modulus in the gel was 1.5 times higher than in the liver (1.5 ± 0.9 kPa versus 1.0 ± 0.4 kPa). The nonlinear shear modulus maps computed for each pair of subscripts are shown in Fig. 4. The nonlinear storage modulus coefficient averaged over the 3 configurations was 4 times higher in the gel than in the bovine liver (A_{Gel} = – 6.6 kPa versus A_{Liver} = – 25.7 kPa), showing high contrast between liver and gel.

Discussion At zero stress, the phantoms are isotropic. In contrast, when a stress is applied, the storage modulus evolves differently according to the propagation direction and the phantoms become anisotropic. Moreover, the changes of storage modulus under compression differ in the liver and the background gel, showing high gel-liver contrast on the nonlinear elasticity maps. These results are consistent with those previously observed with compression US-elastography[5].

Conclusion The results of our study show the feasibility of measuring nonlinear storage modulus with MR-elastography.

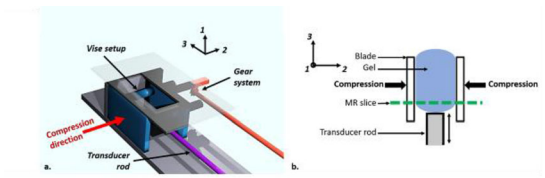

Fig. 1: a. Compression setup of MR-elastography. Main component of the cradle is a vise setup which is controlled by a gear system to exert controlled compression on soft solids. A transducer rod transmits the mechanical vibrations generated by an electronical shaker. b. Coronal view of the setup.

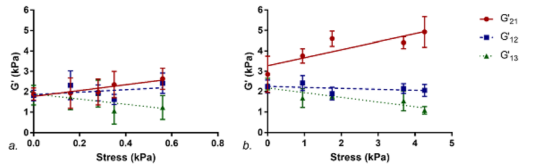

Fig. 2: Storage modulus (G') according to applied uniaxial stress for each propagation in AGAR phantom AGAR_1 (a.) and AGAR_2(b.). Slope is obtained by least mean square fit.

References

[1] Deffieux et al. J Hepatol. 2015
[2] Pagé et al. Front. Phys. 2022
[3] Kim et al. Acta Radiol. 2015
[4] Gennisson et al. J. Acoust. Am. 2007
[5] Bernal et al. IEEE Trans Untrason Ferroelectr. 2016

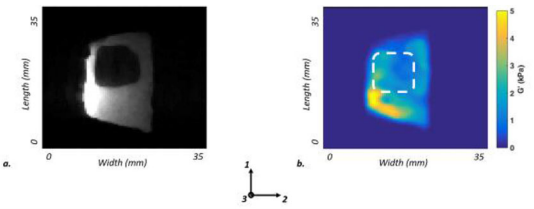

Fig. 3: T2-weighted image of the liver phantom embedded in gel at zero stress (**b.**) map of phantom at zero stress.

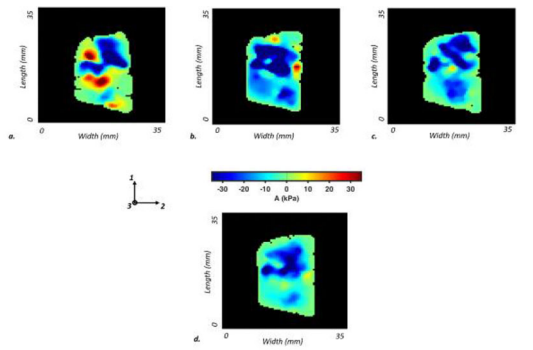

Fig. 4: Nonlinear shear modulus maps of bovine liver embedded in gel reconstructed for the three configurations 21 (**a.**), 12 (**b.**) and 13 (**c.**). In **d.** nonlinear shear modulus map averaged for the subscript pairs 21, 12 and 13 is shown.

P208.
Microstructural changes of the main frontal fiber tracts in COVID-19 infection

J. R. Schüre, E. Hattingen[1], C. Arendt[1]

[1]*Friedrich-Alexander-Universität Erlangen-Nürnberg (FAU), Department of Neuroradiology, Erlangen, Germany*

Introduction: SARS-CoV-2 infection is associated with a broad spectrum of structural cerebral changes in which the central nervous system (CNS) may be indirectly affected[1,2,3,4] that may be related to brain disease through the olfactory fiber pathways to the limbic system. In our initial studies at 3 T, we demonstrated that those structural changes can indeed be detected via quantitatively measured T1/T2 relaxation times[5]. The aim of this study was to detect microstructural changes using tract-based spatial statistics (TBSS) analysis of whole-brain diffuse tensor imaging (DTI) metrics in recovered COVID-19 patients compared to age-matched healthy controls serving the disease course.

Methods and Materials: Patients with previous SARS-CoV-2 infection were examined on a 3 T Prisma scanner (Prisma) and compared with age- and sex-matched control subjects who did not have COVID-19 (detected by a negative serological antibody test). For the detection of microstructural changes, subjects were further subdivided with a cutoff of 40 years to exclude age-related changes. Using FSL (FMRIB v.5.0) diffusion toolbox, fractional anisotropy (FA), and mean (MD), radial (RD) and axial diffusivity (AD) maps were generated from preprocessed DTI datasets. FA maps were nonlinearly registered onto the FMRIB58_FA template and then normalized to MNI space to create a mean FA skeleton map. After data thresholding, TBSS was carried out voxel-wise to detect FA skeleton voxels with significant differences ($p < 0.05$) between patients and controls. Areas adjacent to the altered fiber tracks were further investigated using T1 relaxation time maps which were measured by the variable flip angle method[6]. Besides TBSS for FA, factorial analysis of variance tests was used for the other microstructural properties.

Results: 145 subjects (mean age, 46 years; 50% female) were included between Sept 2020 and Dec 2021: 69 patients (43 home-recovered, 26 hospitalized) and 76 controls without significant differences in the TBSS analysis. Yet, changes of FA were detectable when comparing previously hospitalized patients ≥ 40 years old (n = 23/69) and their matched controls (n = 47/76) along some fiber tracts in the frontal lobe. Predominantly on the right side, FA values were significantly decreased in the frontobasal lateral, fronto-opercular medial and frontal cingulate white matter (Fig. 1). Simultaneously, an significant increase of RD and decrease of T1 values were observed along this pathway, whilst MD and AD remained stable (Fig. 2).

Discussion: Our results showed changes of microstructural properties in specific frontal white matter areas in recovered, ≥ 40 years old patients with previous hospitalization due to COVID-19. These findings might be due to an active process of Wallerian degeneration of myelin sheets that could represent a propagation path from the olfactory fibers through the frontobasal brain to cingulum as part of the limbic system. Longitudinal analyses with larger time intervals between the infection and microstructural imaging are needed to depict reversibility or irreversibility, or even a further spread of degeneration.

Conclusion: This study demonstrated structural changes in the major fiber tracts of recovered patients which had a severe COVID-19 infection. Our findings supports the thesis that a SARS-CoV-2 infection can involve the brain directly via the olfactory fiber tracts to the limbic system, depending on the age and severity of the disease and lead there to strucutreally detectable changes.

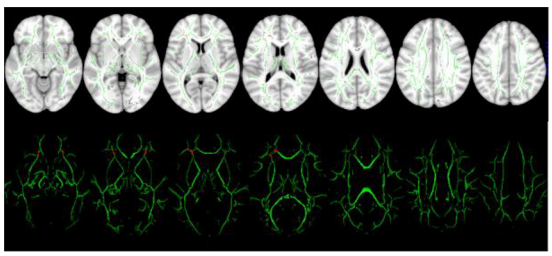

Fig. 1: TBSS analysis of the age-matched healthy control population against the Covid ambulatory courses based on FA maps. Mean fibe tracts are presented in green while significant changes towards a Covid infection is highlighted in red with reduced FA values.

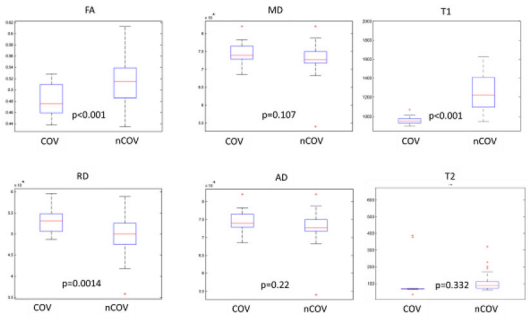

Fig. 2: ROI-based analysis of diffusion (FA, MD, RD, AD) and quantitative T1/T2 parameters based on the disturbed fiber path sections from figure 1.

References

1. Pensato U. et al., *Ann Clin Transl Neurol* 2021
2. Gwenaëlle D. et al., Nature,2022
3. Toniolo S. et al., J Alzheimers Dis,2021
4. Singh, B. et al., Journal of Neurology,2021
5. Fahim et al., DGNR,2022
6. Preibisch and Deichmann, Magnetic Resonance in Medicine,2009

P209.
Evaluation of corpus callosum microstructural changes in post-COVID patients

I. Ibrahim[1], M. Dezortová[1], A. Škoch[1], D. Pajuelo[1], M. Nagy[1], E. Rolencová[1], V. Flusserová[1], J. Rydlo[1], J. Tintěra[1]

[1]*Institute for Clinical and Experimental Medicine, Department of Diagnostic and Interventional Radiology, Prague, Czech Republic*

Introduction: COVID-19 is an infectious disease that primarily affects the respiratory system, but can also damage other organs such as the brain (1).

Advanced magnetic resonance imaging (MRI) techniques such as MR tractography (MRT) and arterial spin labeling (ASL) can be used to assess pathophysiological changes in brain perfusion and diffusion in acute and chronic phase of the disease. The aim of our study was to evaluate perfusion of the entire brain and the diffusion changes in the largest structure of white matter in the brain, the corpus callosum (CC).

Methods: Twelve healthy volunteers [(mean age 32.42 ± 12.22 years, range 18–58 years)] and 12 post-COVID patients with neurological symptoms (mean age 38.36 ± 11.26, ranges 18–56 years) were enrolled in this study.

All subjects underwent MRI examinations on a 3 T MR scanner (VIDA 3 T, Erlangen, Germany) using a 64-channel head/neck coil with the following measurement protocol for:

(1) Diffusion-weighted images using the bipolar diffusion scheme and q-space mode with a total of 122 diffusion directions and 12 different b-values ranging from b = 0 to b-value = 4000 s/mm^2. TR = 4900 ms, TE = 134 ms, and 72 axial slices.

(2) MR perfusion imaging of the brain using the ASL with pseudo-continuous mode to measure cerebral blood flow (CBF) in individual subjects with the parameters: labeling duration of 1800 ms, post-labelling delay of 1800 ms, and TR = 4300 ms.

Diffusion data were evaluated in DSI studio (https://dsi-studio.labsolver.org) and diffusion DTI/GQI-based indices were calculated in the corpus callosum (forceps minor (CC.F.min.), body (CC.B), tapetum (CC.T) and forceps major (CC.F.maj)), Fig. 1, and statistically analysed with the linear mixed-effects model (R Development Core

Team (2008). MR perfusion maps were visually-qualitatively evaluated.

The above-mentioned techniques have been complemented by other MR images such as susceptibility-weighted imaging (SWI), 3D T2-weighted fluid-attenuated inversion recovery (FLAIR), 3D T1-weighted magnetization-prepared rapid acquisition gradient echo (MPRAGE) and MR angiography (MRA), Fig. 2.

Results: Patients with post-COVID conditions may continue to have neurological symptoms. In our group, 83.3% (8/12) of our patients demonstrated multifocal white matter hyperintense lesions on FLAIR images mainly in the frontal areas (Fig. 2), difficulty thinking or concentrating was present in 75%, headache in 58,3%, insomnia in 41,7%, change in smell or taste in 41,7%, fatigue syndrome in 66,7% and one half of patients suffered from depression or anxiety.

The results of the linear mixed-effects model (Fig. 3.) show that the fractional anisotropy (FA) values significantly decrease in the patient's CC compared to controls in the CC-forceps minor (p = 0.02), CC-body (p = 0.01), CC-tapetum (p = 0.00) and CC-forceps major (p = 0.00). Similarly, QA shows a decrease in the CC – forceps minor (p = 0.02). The results of FA and QA are depicted in the graphical form in Fig. 4. Mean diffusivity (MD) values in patients are significantly higher than controls in CC-f.min (p = 0.00), and CC-F.maj (p = 0.00), and lower in the CC-body (p = 0.00). In addition, a significant increase in axial diffusivity (AD) values was found in the cc-body of the patients (p = 0.00). For other diffusion indices, there were no significant differences between the two groups. There was no significant difference in age between both groups (p = 0.13).

Discussion: The CC is a well-organized fibre structure having high anisotropy in the normal condition, so COVID-related changes can modify the integrity of CC bundles, detectable by diffusion indices. The presence of hyperintense lesions in the white matter on FLAIR images may be the cause of significant changes in diffusion indices mainly in forceps minor of the corpus callosum (Fig. 3–4). Except for diffuse changes in CC, no hypoperfusion or other abnormal changes were observed (Fig. 2).

Conclusion: COVID-19 infection changes the integrity of white matter in the CC. The combination of different MRI methods can be used to refine the diagnosis of COVID and to confirm or exclude other causes of problems that patients suffer from.

Supported by Ministry of Health of the Czech Republic, grants No. NU22-A-124, and MH CZ – DRO ("IKEM, IN 00023001").

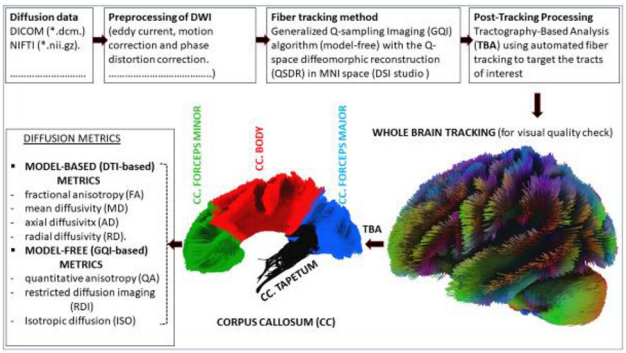

Fig. 1: Flowchart describing the preprocessing and postprocessing of DWI data

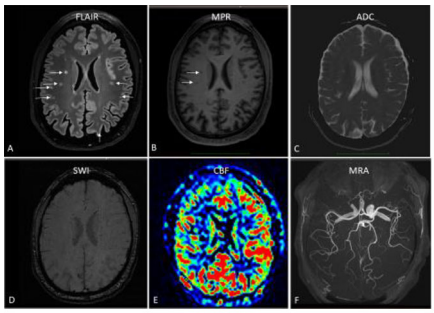

Fig. 2: MRI images show an example of different types of examination of the patient's brain after COVID-19. FLAIR MR image (a) shows hyperintense signal abnormality (arrows) with the corresponding findings on MPR (b). Other images (ADC (C), SWI (D) and CBF (E) and MRA (F)) are normal.

DTI	FA (mean ± SD)				MD (mean ± SD)				AD (mean ± SD)				RD (mean ± SD)			
Regions	CC.F.min	CC.B	CC.T	CC.F.maj	F.min	CC.B	CC.T	CC.F.maj	CC.F.min	CC.B	CC.T	CC.F.maj	CC.F.min	CC.B	CC.T	CC.F.maj
controls	0.48±0.02	0.49±0.03	0.55±0.02	0.53±0.02	0.86±0.04	0.83±0.05	1.05±0.11	0.84±0.05	1.30±0.06	1.20±0.04	1.61±0.06	1.54±0.06	0.61±0.06	0.56±0.06	0.68±0.06	0.64±0.05
Patients	0.46±0.02	0.48±0.03	0.53±0.02	0.53±0.02	0.94±0.05	0.77±0.05	0.99±0.06	0.94±0.05	1.29±0.05	1.27±0.05	1.68±0.13	1.51±0.08	0.64±0.04	0.62±0.06	0.74±0.10	0.64±0.06
p.value	**0.02**	**0.01**	**0.00**	**0.00**	**0.00**	**0.00**	0.72	**0.002**	0.96	**0.00**	0.38	0.64	0.16	0.11	0.85	0.18

GQI	QA (mean ± SD)				RDI (mean ± SD)				ISO (mean ± SD)			
Regions	CC.F.min	CC.B	CC.T	CC.F.maj	CC.F.min	CC.B	CC.T	CC.F.maj	CC.F.min	CC.B	CC.T	CC.F.maj
controls	0.17±0.02	0.24±0.03	0.30±0.04	0.30±0.03	0.32±0.02	0.39±0.03	0.45±0.04	0.45±0.03	0.43±0.04	0.49±0.03	0.59±0.05	0.59±0.04
patients	0.14±0.04	0.23±0.05	0.29±0.05	0.30±0.04	0.29±0.07	0.38±0.07	0.44±0.07	0.44±0.06	0.40±0.10	0.49±0.10	0.59±0.09	0.59±0.09
P-value	**0.02**	0.51	0.61	0.59	0.20	0.79	0.68	0.91	0.32	0.89	0.92	0.87

Fig. 3 : Mean DTI/GQI-based indices values and standard deviations calculated in both groups. FA: fractional anisotropy, MD: mean diffusivity (x10-3 mm2/s), AD: axial diffusivity (x10-3 mm2/s), RD: radial diffusivity (x10-3 mm2/s), QA: quantitative anisotropy, RDI: restricted diffusion imaging, ISO: isotropic diffusion

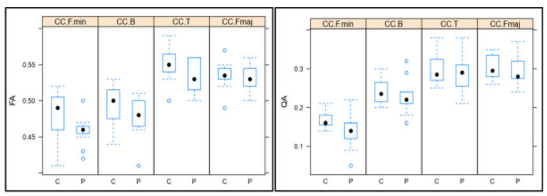

Fig. 4: An example of a graphical representation of fractional anisotropy (FA) and quantitative anisotropy (QA) in contro subjects (C) and post-COVID patients (P).

References

1) Kremer S, et al. Brain MRI Findings in Severe COVID-19: A Retrospective Observational Study. Radiology 2020;297(2):E242-E251.

P210.
Thalamic connectivity topography in newborns with spina bifida: Association with neurological functional level but not developmental outcome at 2 year

H. Ji[1], K. Payette[1], L. Mazzone[2], M. Meuli[2], U. Moehrlen[2], B. Latal[3], A. Hackenberg[4], D. Alexander Wille[5], B. Padden[6], A. Jakab.[1]

[1]*University Children's Hospital Zurich, MR-Research Center, Zurich, Switzerland;*
[2]*University Children's Hospital Zurich, Department of Pediatric Surgery, Zurich, Switzerland;*
[3]*University Children's Hospital Zurich, Child Development Center, Zurich, Switzerland;*
[4]*University Children's Hospital Zurich, Department of Pediatric Neurology, Zurich, Switzerland;*
[5]*Cantonal Hospital of Baden, Baden, Switzerland, Department of Pediatric Neurology, Baden, Switzerland;*
[6]*University Children's Hospital Zurich, Division of Pediatric Rehabilitation, Zurich, Switzerland*

Introduction: Spina bifida is a congenital disorder that leads to structural abnormalities in the brain and spinal cord due to the derangement of neural tube development during early embryogenesis. Children with spina bifida display varying degrees of motor and cognitive delay, as well as vegetative dysfunctions1,2. Our study aimed to examine the link between connectivity organization of the thalamus and neurological and developmental outcomes in newborns with open spina bifida.

Methods: This retrospective study included 44 newborns (gestational age (GA) at MRI: 37.97 (± 1.13) weeks) with spina bifida who underwent prenatal repair and neurological and developmental outcomes. At two years of age, eurological status was evaluated as the functional level of the spinal lesion, while developmental outcome was assessed with the Bayley III Scales of Infant and Toddler Development. Neonatal MRI was acquired on a 3.0 T scanner using structural and diffusion tensor imaging sequences (DTI). T2-weighted MRI was performed with a fast recovery fast spin echo sequence (image resolution of 0.7 × 0.7 × 1.5 mm3). DTI was acquired with 35 gradient encoding directions with b = 700 s/mm2. We employed a super-resolution reconstruction algorithm3 to create a 3D brain volume with T2 images (isotropic image resolution of 0.5 × 0.5 × 0.5 mm3), then segmented the 3D-T2w images into tissue classes using an in-house network4, and created a custom spina bifida template and region-of-interest system using a non-linear template reconstruction script in ANTs5. All diffusion data corrected for eddy current and head motion-induced geometric distortions, and bias field inhomogeneity. The study used BedpostX6 in FSL to estimate fiber orientations and their uncertainties, and performed connectivity-based thalamus parcellation using probabilistic tractography and cortical target-based clustering in FSL7,8, where thalamus was segmented into four clusters based on seed-to-target connectivity pattern obtained from probabilistic tractography.

Results: We used multivariate linear regression models and cluster-wise statistical analysis to investigate the associations between thalamocortical(TC) connectivity and developmental outcomes, using two approaches of clusters volumetric analysis and voxel-wise analysis, with correction for multiplicity using threshold-Free Cluster Enhancement9, and included gestational age at MRI, lesion subtype (myeloschisis or myelomeningocele), and ventricular volume as covariates.No significant associations were found between thalamocortical connectivity and developmental outcomes. We found smaller thalamic parietal projection (cluster) volume in newborns with higher functional level (Lumbar 3), while a reverse trend was observed for thalamic clusters interconnected with the temporal lobe (Fig. 1). Voxel level analysis demonstrated a similar correlation between left hemispheric thalamic parietal lobe connections and functional level (Fig. 2), with a weaker thalamic parietal connectivity strength being associated with higher functional level. This effect was the strongest in voxels corresponding to the ventrolateral and ventral anterior nuclei within the left thalamus.

Conclusion: Higher functional level in infants with spina bifida is a predictor of more severe lower extremity motor dysfunction and a reduced likelihood of achieving independent ambulation. Our study suggests that altered thalamocortical circuitry development in newborns with spina bifida is a contributing factor to the impaired lower extremity function. An altered topology of thalamocortical circuits interconnected with parietal lobe might be implicated in the functional level, but not developmental outcomes at two years of age.

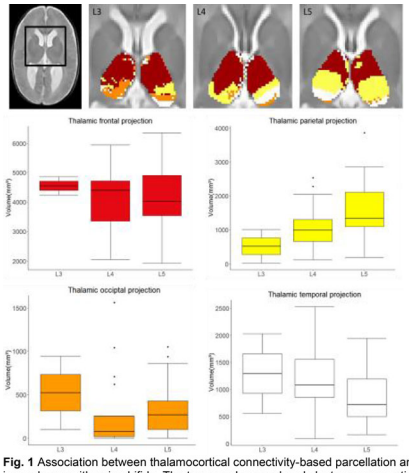

Fig. 1 Association between thalamocortical connectivity-based parcellation and the 2-year functional neurological level in newborns with spina bifida. The top row shows colored clusters representing the thalamocortical connectivity-based clusters in three selected cases with functional level at L3, L4, and L5. The middle and bottom rows display boxplots of each cluster volume in the three functional levels

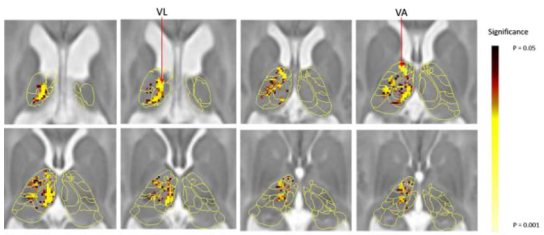

Fig. 2 Voxel-wise analysis of the association between thalamocortical (TC) connections at newborn age and functional level at 2 years of age. Localization of thalamocortical (TC connectivity correlated with newborns functional level. (a) Thalamic voxels where left thalamo-temporal connectivity was significantly ($p<0.05$, TFCE-corrected) associated with functional level are shown as red and yellow overlay on a neonatal thalamus atlas and a T2-weighted SB template. VL, thalamic ventral lateral nuclei; VA, ventral anterior nuclei

References

1. Kelly NC, Ammerman RT, Rausch JR, et al. *Child Neuropsychol*. 2012;18(5):417–431.
2. Kelly LM, Zebracki K, Holmbeck GN, Gershenson L. *J Pediatr Rehabil Med*. 2008;1(4):291–302.
3. Kuklisova-Murgasova M, Quaghebeur G, Rutherford MA, Hajnal J V., Schnabel JA. *Med Image Anal*. 2012;16(8):1550.
4. Ronneberger O, Fischer P, Brox T.. *Lect Notes Comput Sci*. 2015;9351:234–241.
5. Avants BB, Epstein CL, Grossman M, Gee JC. *Med Image Anal*. 2008;12(1):26–41.
6. Behrens TEJ, Woolrich MW, Jenkinson M, et al. *Magn Reson Med*. 2003;50(5):1077–1088.

7. Behrens TEJ, Berg HJ, Jbabdi S, Rushworth MFS, Woolrich MW. *Neuroimage*. 2007;34(1):144–155.
8. Behrens TEJ, Johansen-Berg H, Woolrich MW, et al. *Nat Neurosci 2003 67*. 2003;6(7):750–757.
9. Smith SM, Nichols TE. T. *Neuroimage*. 2009;44(1):83–98.

P211.
Transgenerational neuroprotection of vegetal extract in neonatal hypoxia–ischemia

P. Goudeneche[1], C. Guichard[1], S. Sanchez[1], M. C. Beauvieux[1], J. F. Chateil[1], L. Pellerin[2], C. Romain[3], J. Cases[3], A. K. Bouzier-Sore[1], H. Roumes[1]

[1]*CRMSB Bordeaux University, Biologie, Bordeaux, France;*
[2]*IRMETIST, Poitiers, Germany;*
[3]*Fytexia, Vendres, France*

Introduction and purpose: Therapeutic strategy in neonatal hypoxia–ischemia (NHI), a major cause of perinatal death and chronic disability, is limited to hypothermia. As many newborns do not respond to it, new treatments are needed. In rats, intraperitoneal injection (i.p.) of resveratrol (RSV, polyphenol present in grapes) has shown neuroprotective properties in NHI-pups but the doses used were high (20–100 mg/kg), the i.p. has a proinflammatory character and RSV has a low bioavailability (< 1%). In order to overcome these limitations, we evaluated the effects of maternal supplementation with VE (vegetal extract rich in polyphenol), in the context of NHI.
Material and methods: NHI (left common carotid artery ligation + hypoxia (8% O2, 92% N2, 2 h) was induced in Wistar P7 rats (7 days post-natal). Maternal drinking water was supplemented with EV (0.15 mg/kg eq RSV), during the two weeks preceding the NHI event (EV group, n = 16) or not supplemented (sham group, n = 11 and Ct group, n = 16). Brain lesion volumes (BLV) were measured in pups in vivo, 3 h (P7), 48 h (P9) and 23d (P30) after NHI, using diffusion-weighted MRI (4.7 T Bruker, TE = 24 ms, TR = 2 s, 30 directions, 20 sections, 1 mm thick) and expressed as % of total brain volume. The severity of edema was assessed by measuring the apparent diffusion coefficient (ADC). Finally, motor and cognitive abilities were evaluated by behavioral tests.
Results: NHI induced brain lesions in 100% of the Ct group (BLV, at P7: 46 ± 1%), and 56% of the EV group (BLV, at P7: 17 ± 5%). Cytotoxic edema was significantly lower in the EV group (higher ADC values compared to the Ct group, $p < 0.001$). At P30, 79% of the Ct group still had cerebral lesions compared to only 13% in the EV (BLV at P30: 22 ± 3% vs 2 ± 2%, for the groups HIC and EV, respectively). For behavioral tests, EV group recovered motor and cognitive abilities comparable to sham group.
Conclusion: This study shows for the first time a neuroprotective role of EV maternal supplementation in the context of NHI. A nutritionally realistic daily amount was sufficient to avoid brain damage in some pups and to recover cognitive and motor functions.

1. Arteaga O. et al. PLoS One. 2015;10(11):e0142424.
2. Karalis F. et al., Brain Res. 2011;1425:98–110.

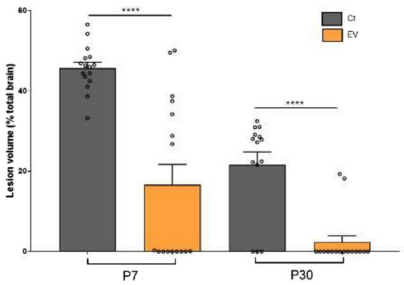

Neuroprotection offered by maternal supplementation of EV. Groups: Ct (pups without maternal supplementation but with HI); EV (maternal supplementation with EV, during two weeks before HI). Brain lesion volumes (% total brain volume) at P7 (3 h after the common carotid artery ligation) and P30 (23 days after hypoxia ischemia). *Significant difference between 2 groups: **** $p < 0.0001$.

Neuroprotection offered by maternal supplementation of EV. Groups: Ct (pups without maternal supplementation but with HI); EV (maternal supplementation with EV, during two weeks before HI). Brain lesion volumes (% total brain volume) at P7 (3 h after the common carotid artery ligation) and P30 (23 days after hypoxia ischemia). *Significant difference between 2 groups: **** $p < 0.0001$.

P212.
Contextual cell growth (ConCeG) to generate numerical phantoms for grey matter modelling

C. Aird-Rossiter[1]

[1]*Cardiff University, Brain Research Imaging Centre (CUBRIC), Cardiff, United Kingdom*

Introduction: Numerical phantoms provide an essential tool in the validation and development of MRI techniques and are particularly useful when developing diffusion-weighted MRI (dMRI) techniques for the characterization of tissue microstructure. Simulated dMRI signals from numerical phantoms with microstructural properties known by design can be used as a reference to validate dMRI techniques in place of real measurements1, for which ground truth values of microstructural features are unknown. However, this approach requires establishing a means of generating tuneable, accurate phantoms. A successful method for creating white matter phantoms was developed by Callaghan et al.2, titled "contextual fibre growth" (ConFiG). Here, we aim to expand upon the ConFiG algorithm to create grey matter phantoms and propose a new method called "contextual cell growth" (ConCeG) to grow contextually neural cells.

	Real		Grown	
Characteristic	mean	Std	mean	Std
Path Length	27.78	14.14	35.40	22.19
Branch Length	11.49	8.59	12.96	8.94
Branch Order	2.50	1.52	2.33	1.37
Branch Angle	1.35	0.61	1.30	0.70

Table 1. Mean and standard deviations for the key characteristics of 845 real and fifty-three contextually grown artificial cells

Method: Similarly to ConFiG, ConCeG relies on a network of triangulated points through which cellular projections radiating from the cell body grow. Edges within the graph represents possible paths the projections could take, and projections are grown iteratively from node to node following simple, biologically motivated cost functions. Once a node had been accessed by a projection, all edges to the node are removed to ensure that no other projection can access that node, resulting in distinct non-overlapping and non-intersecting projections.

To replicate real cells, key features as proposed in3,4 were learnt from real data sets obtained from neuromorpho.org (here, as an example 845 astrocyte cells from the mouse hippocampus). These features are: projection length, branch length, branch order and number of primary projections radiating from the cell body. Another feature obtained from the real data was the termination points of the cell projections, which define the global morphology of the cells (e.g., the orientation dispersion of the cellular fibres). In ConCeG, cells are assigned a soma within the network, then initial characteristics are drawn from distributions taken from real cell data (Fig. 2, black), starting with the number of projections and initial branch length. Projections are grown one by one towards "attractor points" which are randomly selected from the list of termination points. Once the projection has satisfied the branch length the probability of the projection branching into two is assessed depending on the branch order. If the branching condition was satisfied the projection continues along two new segments, if not then the projection terminates. This process is continued until all projections are terminated.

Results: As seen in table 1 and Fig. 2 the means and standard deviations of the grown cells, as well as the cellular features distributions, closely resemble the statistics of the original cells.

Continuations and future work We aim to develop a library of cell characteristics by cell type and origin, with the intention of being able to flexibly create any number of grey matter phantoms. As well as use the meshed skeletons to preform dMRI simulations.

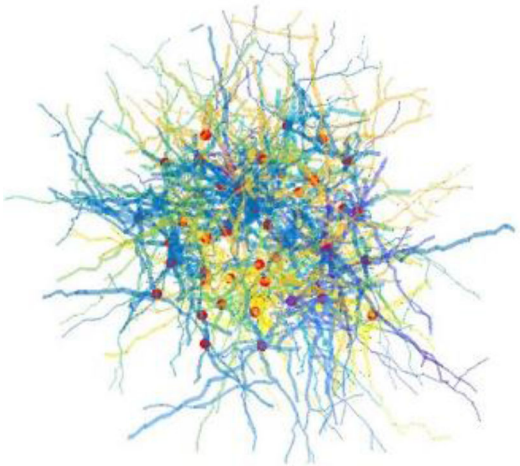

Figure 1. 53 contextually grown cells, with somas highlighted in

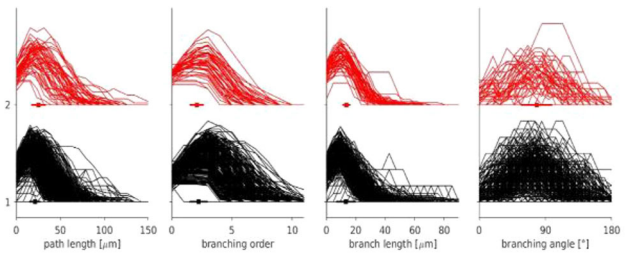

Figure 2. Distributions of real (black) and artificially grown (red) cells

References

1) Alexander et al. NMR Biomed 2017.
2) Callaghan et al. Neuroimage 2020.
3) Palombo et al. PNAS 2016.
4) Palombo et al. Neuroimage 2019.

P213.
Assessment of fixel based analysis derived metrics variability in the evaluation of white matter tissue integrity

E. Elizondo-Pereo[1], A. Santos-Díaz[1]

[1]*Tecnológico de Monterrey, School of Engineering and Sciences, Monterrey, Mexico*

Introduction: Fixel Based Analysis (FBA)[1] is a relatively new method for analyzing Diffusion Weighted Images (DWI) that has gained popularity during the past few years[2]. FBA proposes a new set of metrics for evaluation of white matter (WM) tissue integrity superior to traditional ones such as fractional anisotropy and mean diffusivity, derived from diffusion tensor imaging (DTI). However, FBA metrics are yet to be analyzed in terms of their variability across session, scanner and subject, in contrast to those derived from DTI[3]. The purpose of this study was to evaluate the variability of the FBA derived metric fiber density and cross-section (FDC) across the brain in different sessions, scanners and subjects.

Methods: The analysis was performed using the MASiVar[3] dataset preprocessed using the PreQual[4] pipeline. FBA was performed on the dataset using MRTrix3[5] and the pipeline suggested by Raffelt et al.[1] to obtain the fiber cross-section (FC), fiber density (FD) and FDC metrics. Next, subjects were subdivided into the following labels: intrasession, intersession, interscanner and intersubject with 24, 22, 9 and 14 groups, respectively.

For each subgroup the fixel-wise Coefficient of Variation (CoV) and the fixel-wise median for each metric were obtained. Then, the JHU white matter atlas[6–8] was used to segment 48 different regions of interest (i.e. white matter fiber bundles).

For the CoV, we report the regional median across the groups for each label. For the FBA metrics, we report the regional median FDC for each label.

Results: Fig. 1 shows the CoV values for each label where intrasession has the lowest variation whereas intersubject shows the highest for all metrics. On the other hand, Figs. 2 and 3 show the variability of FDC for each fiber bundle across all labels. Of note, the variability of the metric changes considerably depending on the white matter fiber bundle. These images depict Limits of Agreement with the Median (LOAM) graphs.

Discussion: Fig. 1 shows that the variability of the three FBA analysis metrics increases depending on their group where the intrasession groups are the ones with the least variability and the intersubject groups are the ones with the most variability. This is to be expected since images taken from different subjects tend to be more different than images taken from the same subject.

In general Figs. 2 and 3 show a high concentration around the mean of the different data points and while the Limit of Agreement with the mean is larger for the intrasession and intersession groups, this might be an artifact of there being more data points for these two groups of data. Interestingly for all labels, both the variability and the mean values are highly dependent on the region of interest, suggesting that region based analysis provides more information than global brain metrics, as it is usually reported.

In conclusion, the results obtained from FBA seem to follow similar patterns to those obtained for DTI reported by Cai et al.[3]

References

1. Raffelt D. A., Tournier J.D., et al. Investigating white matter fibre density and morphology using fixel-based analysis. NeuroImage. 2017;144:58–73.
2. Dhollander T., Clemente A., et al. Fixel-based Analysis of Diffusion MRI: Methods, Applications, Challenges and Opportunities. NeuroImage. 2021;241:118,417.
3. Cai L. Y., Yang Q, et al. MASiVar: Multisite, multiscanner, and multisubject acquisitions for studying variability in diffusion weighted MRI. Magnetic Resonance in Medicine. 2021;86(6):3304–3320.
4. Cai L. Y., Yang Q., et al. PreQual: An automated pipeline for integrated preprocessing and quality assurance of diffusion weighted MRI images. Magnetic Resonance in Medicine. 2021:86(1):456–470.
5. Tournier J. D., Smith R., et al. MRtrix3: A fast, flexible and open software framework for medical image processing and visualisation. NeuroImage. 2019;202:116,137.
6. Mori S, Wakana S, Van Zijl PCM, Nagae-Poetscher LM. MRI Atlas of Human White Matter. Amsterdam, Netherlands: Elsevier; 2005.
7. Wakana S, Caprihan A, Panzenboeck MM, et al. Reproducibility of quantitative tractography methods applied to cerebral white matter. Neuroimage. 2007;36:630–644.
8. Hua K, Zhang J, Wakana S, et al. Tract probability maps in stereotaxic spaces: analyses of white matter anatomy and tract-specific quantification. Neuroimage. 2008;39:336–347.

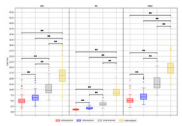

Fig. 1: Visualization of variation across intrasession, intersession, interscanner, and intersubject groups illustrates increased variability with session, scanner, and subject effects. Statistical significance was determined with the Wilcoxon rank-sum test with and without Bonferroni correction (corrected: ** p < 0.008, uncorrected: * p< 0.05).

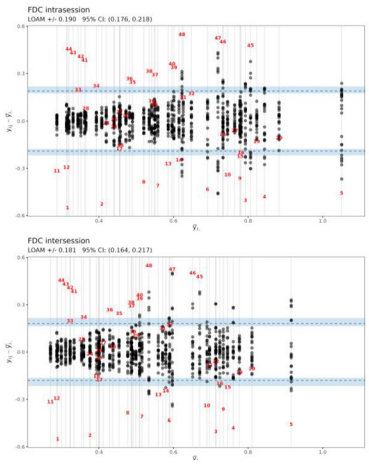

Fig. 2: LOAM plots for FDC intrasession and intersession. The plots suggest a relative uniform distribution of the regions of interests around the mean with greater dispersion in the regions with a greater mean value. The red numbers indicate the regions of interest the JHU atlas[6-8]

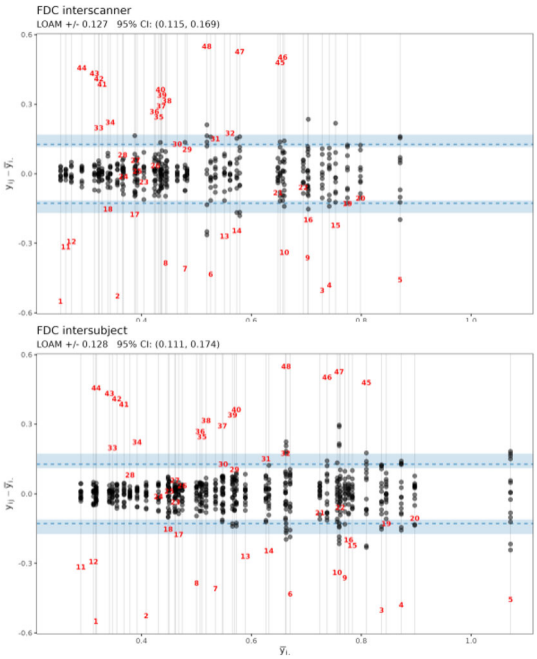

Fig. 3: LOAM plots for FDC interscanner and intersession. The plots suggest a similar behavior as the observed in Figure 2.

P214.
Riemann-Finsler framework in HARDI

A. Bansal[1], S. Kaushik[2,3], P. While[2,3], T. Bihnogen[1], J. Slovak.[1]

[1]*Masaryk University, Brno, Czech Republic;*
[2]*St. Olav's University Hospital, Trondheim, Norway, Department of Radiology and Nuclear Medicine, Trondheim, Norway;*
[3]*NTNU—Norwegian University of Science and Technology, Department of Circulation and Medical Imaging, Trondheim, Norway*

Introduction: The 2nd-order tensors from diffusion tensor imaging (DTI) provide anisotropy scalars that are helpful in the diagnosis of white matter diseases, but cannot distinguish multi-fiber crossings from isotropic regions. In contrast, higher-order tensors derived from HARDI [2, 3] can describe these complicated tissue structures. We introduce two descriptors for HARDI data: FFA based on Finsler geometry, and FA4 based on the Riemann framework. We demonstrate that they can classify voxels according to the number of independent fiber-crossing directions.

Methods: The HARDI acquisition protocol [2] can provide 4th-order tensors [3], represented in Voigt-Mandel notation, provide basic (S) and principal (J) invariants, describing complex fiber structures. The diffusion of water molecules in tissue can be modeled using the generalized Stejskal-Tanner equation: $\mathbf{S(v) = S0\ exp\ (-\ b\ D(v)))}$, with, $\mathbf{D(v) = \sum \sum \ldots \sum \sum D_{ij\ldots kl}\ v_i\ v_j \ldots\ v_k\ v_l}$, **where** $\mathbf{D_{ij\ldots kl}}$ are diffusion coefficients, $\mathbf{v_i}$ is the i^{th} component gradient vector.

A Finsler norm $\mathbf{F(x,\ y)}$ corresponding to the 4th order tensor is defined:

$\mathbf{F(x,\ y) = (D_{ijkl}\ y_i\ y_j\ y_k\ y_l))1/4}$where **x** is the position **y** ? is the direction, and the fully symmetric tensor. The Finsler metric, $\mathbf{g_{ij}}$ for each choice of **y** is defined as $\mathbf{g_{ij}(x,y) = 1/2\ x\ (\partial^2\ F^2\ (x,\ y))/(\partial y^i\ \partial y^j)}$ These Finsler diffusion tensors are approximations of higher-order tensors representing complex can reconstruct [4] complex fiber crossing regions.

We define the Finsler fractional anisotropy (FFA) as follows:

FFA(x) = FA(($\sum^{p}_{s=1}$ g_{ij} (x, v_s)/p)where, are the unit gradient vectors, and is the number of gradient directions over the hemisphere. The sum of positive definite quadratic forms ensures positive definiteness, such that FFA lies in [0, 1].

As an alternative to Finsler geometry, we may consider a Riemann metric as a more direct extension to DTI, the eigenvalues obtained from the Voigt-Mandel representation of 4th-order tensors signify the diffusivity profile, relating to the probability distribution in the corresponding gradient direction. In the 6D hyper-ellipsoid case, we define the fractional anisotropy from 4th-order tensors (FA4) as follows:

FA4(x) = $\sqrt{(6/5)}$ $\sqrt{(\sum_i[(\lambda_i - \lambda_a))/(\sqrt{(\sum_i \lambda_i^2)})}$where λ_a is the average diffusion at a voxel, λ_i are eigenvalues of Voigt-Mandel notation and

Results We used an adaptive kernel method [5] to simulate images at b = 1500 s/mm2 for 81 gradient directions. We generated four groups of tensors for isotropic, one-fiber, two-fiber, and three–fiber regions. 50 instances of each group were generated by imposing random rotations while maintaining the same crossing angle (90°).

Table 1 shows the mean and standard deviation of each descriptor under rotations without noise. The low standard deviations reflect their invariance to rotations.

Figure 1 shows that the descriptors can delineate the four regions at low levels of noise. At higher levels (0.09), the descriptors possibly confound regions of three fibers with isotropic diffusion (especially FFA).

For comparison, we may consider the basic (S) and principal (J) Kelvin invariants derived also from the Voigt-Mandal notation [3]. Figure 2 shows results for a selection of S and J scalars (out of 12) that display distinct characteristics. Some of these fail to characterize fibers even at lower noise. J42 and S43 performed similarly to FFA and FA4, but either provided inverted contrast, which is non-intuitive or were unbounded, limiting their practical use.

Figure 3 shows simulated maps, demonstrating that the proposed descriptors can discriminate the different regions, whereas most of the Kelvin invariants provide poor contrast between regions, except for S42, S43, and J42.

Figure 4 shows results for in-vivo data, where some of the Kelvin invariants fail to retain any structural information, and others provide limited contrast. FFA and FA4, on the other hand, provide clear and detailed contrast throughout the brain, clearly delineating, for example, the white and grey matter.

Discussion: The Finsler approach can potentially provide multiple metrics per voxel for HARDI data, and hence multiple contrast maps to characterize tissues. The FFA descriptor can be obtained from an ODF corresponding to any HARDI model (i.e. tensor of any order), whereas FA4 is restricted to 4th-order tensors. Moreover, FFA uses a wider range of values than FA4 for characterizing multi-fiber regions.

Conclusion: Descriptors based on Finsler geometry provide potential biomarkers from HARDI data. FFA and FA4 exhibit more relevant contrast than most of the Kelvin invariants. Further work should assess their efficacy in a clinical setting.

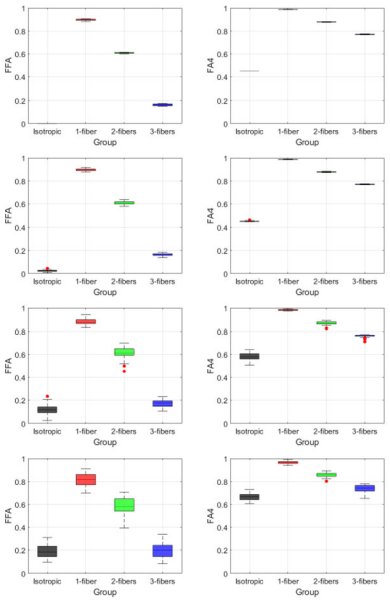

Fig. 1: The boxplots of FFA (left) and FA4 (right) for the four groups of synthetic data (in colors). Each row shows results for different levels of Rician noise (top-bottom): without noise, 0.01, 0.05, and 0.09.

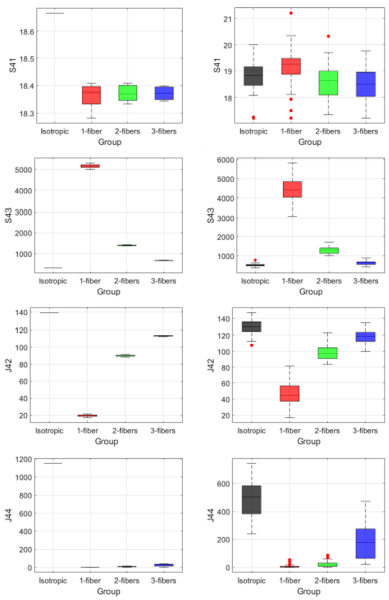

Fig. 2: The boxplots of a selection of Kelvin invariants (top-bottom: S41, S43, J42, J44) for the four groups of synthetic data (colors). Each column shows results for different levels of Rician noise: (left) without noise; (right) 0.09.

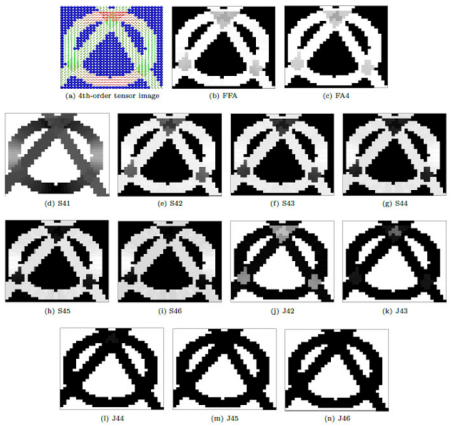

Fig. 3: (a) Synthetic tensor field image (two linear fibers and a curved fiber, forming four distinct groups: isotropic diffusion, one fiber, two fibers, and three fibers), maps of (b) FFA, and (c) FA4. The remaining rows show maps of the Kelvin invariants.

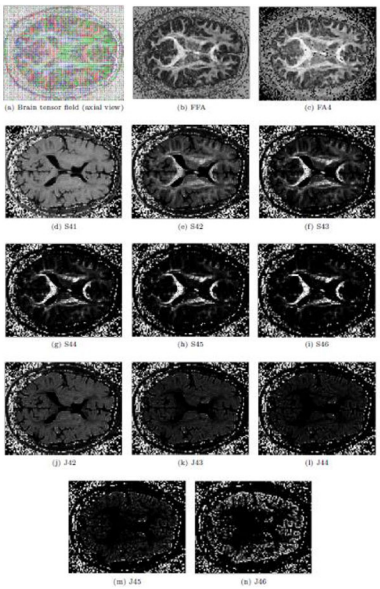

Fig. 4: (a) 4th-order tensor field image (brain, axial slice), and corresponding maps of (b) FFA, and (c) FA4. The remaining rows are maps of the Kelvin invariants. The intensity values of Kelvin maps are kept between the 10th and 90th percentiles.

P215.
Whole-brain connectomics in the newborn: The choice of algorithm for constrained spherical deconvolution impacts tract density estimates in a clinical dataset

A. Speckert[1,2], M. Feldmann[3], K. Payette[1], W. Knirsch[3], M. von Rhein[3,2], B. Latal[3,2], A. Jakab[1,2]

[1]*University of Zurich, Center for MR Research, Zurich, Switzerland;*
[2]*University of Zurich, URPP Adaptive Brain Circuits in Development and Learning, Zurich, Switzerland;*
[3]*University Children's Hospital Zurich, Child Development Center, Zurich, Switzerland*

Diffusion magnetic resonance imaging (dMRI) offers a noninvasive way to study the white matter pathways of the brain, tract density and the macro-scale structural connectome. However, we still lack optimized methods for applying structural connectomic analysis to early brain development. The goal of this study was to examine if the choice of algorithm for the estimation of fiber orientation distribution leads to differences in tract density mapping in a newborn cohort when comparing healthy controls with individuals suffering from congenital heart disease (CHD).

We included 43 healthy control and 51 CHD newborns in our analysis. dMRI with 35 diffusion encoding directions (b = 700 s/mm2, spatial resolution: 0.7 mm * 0.7 mm * 3 mm) on a 3.0 T clinical scanner was acquired. Next, anatomical T2-weighted images were super-resolution reconstructed and segmented into seven tissue types using an in-house developed convolutional neuronal network. The anatomical segmentations and the dMRI data were used for anatomically constrained tractography. We compared two different algorithms for constrained spherical deconvolution (CSD) as implemented in the MRtrix software. First, data was processed with the "Tournier" algorithm for single-shell single tissue (SSST) CSD and then with the "Dhollander" algorithm for single-shell multi tissue (SSMT) CSD. After performing whole-brain tractography, we calculated tract density images (TDI). The effect of the CSD algorithm was tested using a variance analysis with permutation tests, corrected for multiplicity using the TFCE method in the FSL software.

Comparing the TDI between the SSST and SSMT based CSD methods in healthy controls, significant differences ($p < 0.001$) especially in the deep grey matter were found. When comparing the CHDs to controls using the SSST algorithm, no significant differences were detected. However, when using the SSMT algorithm, controls showed significantly denser tracts than the CHDs ($p < 0.01$). This effect can be observed especially in the deep white matter tracts in the temporal and frontal lobes, in the external capsule and association pathways (see Fig. 1).

These results suggest on one hand that neonates suffering from CHD might show altered white matter microstructure which is in line with the current literature (Ehrler et al., 2019). On the other hand, the TDI values and the CHD vs. control differences depended on the chosen algorithm. It is unclear which algorithm shows the biologically correct result (SSMT: false positive group effects or SSST false negative group effects). Hence, further analyses are needed to reproduce these results.

Overall, structural connectomic analysis of dMRI requires complex postprocessing that relies on analytical models. Our findings imply that the choice of algorithm and models can affect patient-control group level effects. This necessitates a careful evaluation of the postprocessing pipeline, particularly when studying early brain development.

References

Bastiani, M., Andersson, J. L., Cordero-Grande, L., Murgasova, M., Hutter, J., Price, A. N., … & Sotiropoulos, S. N. (2019). Automated processing pipeline for neonatal diffusion MRI in the developing Human Connectome Project. *Neuroimage*, *185*, 750–763.

MRtrix3Tissue (https://3Tissue.github.io).

Pannek, K., Guzzetta, A., Colditz, P. B., & Rose, S. E. (2012). Diffusion MRI of the neonate brain: acquisition, processing and analysis techniques. *Pediatric radiology*, *42*(10), 1169–1182.

Payette, K., Li, H., de Dumast, P., Licandro, R., Ji, H., Siddiquee, M. M. R., … & Jakab, A. (2022). Fetal Brain Tissue Annotation and Segmentation Challenge Results. *arXiv preprint arXiv:2204.09573*.

Smith, R. E., Tournier, J. D., Calamante, F., & Connelly, A. (2012). Anatomically-constrained tractography: improved diffusion MRI streamlines tractography through effective use of anatomical information. *Neuroimage*, *62*(3), 1924–1938.

Smith, R. E., Tournier, J. D., Calamante, F., & Connelly, A. (2013). SIFT: Spherical-deconvolution informed filtering of tractograms. *Neuroimage*, *67*, 298–312.

Tournier, J. D., Smith, R., Raffelt, D., Tabbara, R., Dhollander, T., Pietsch, M., … & Connelly, A. (2019). MRtrix3: A fast, flexible and

open software framework for medical image processing and visualisation. *Neuroimage*, *202*, 116,137.
Tournier, J. D., Yeh, C. H., Calamante, F., Cho, K. H., Connelly, A., & Lin, C. P. (2008). Resolving crossing fibres using constrained spherical deconvolution: validation using diffusion-weighted imaging phantom data. *Neuroimage*, *42*(2), 617–625.von Rhein, M., Buchmann, A., Hagmann, C., Dave, H., Bernet, V., Scheer, I., … & Sennhauser, F. H. (2015). Severe congenital heart defects are associated with global reduction of neonatal brain volumes. *The Journal of pediatrics*, *167*(6), 1259–1263.

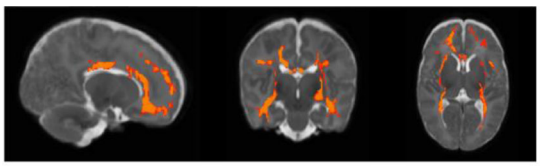

Fig. 1: Comparison of healthy controls with CHD using the SSMT algorithm, orange showing the significant denser regions in healthy controls.

P216.
3D printed low diffusivity phantom for eddy current characterization in diffusion MRI

T. Ruadrew[1], U. Yarach[1], P. Ratiphunpong[1,2], A. Suwannasak[1], S. Udomsom[3], W. Powcharoen[4]

[1]Chiang Mai University, Department of Radiologic Technology, Faculty of Associated Medical, Chiang Mai, Thailand;
[2]HRH Princess Chulabhorn College of Medical Science, Chulabhorn Royal Academy, Radiological Technology School, Faculty of Health Science Technology, Bangkok, Thailand;
[3]Chiang Mai University, Biomedical Engineering, Chiang Mai, Thailand;
[4]Chiang Mai University, Dentistry, Chiang Mai, Thailand

Introduction: Diffusion-weighted magnetic resonance imaging (dMRI) [1] with echo-planar imaging (EPI) [2] is commonly utilized due to its speed. However, accurate determination of water diffusion parameters, particularly at higher diffusion-encoding gradients, is hindered by eddy current-induced distortions [3]. Various approaches have been proposed to alleviate these effects, including twice refocused spin echo sequences and phantom-based strategies [4]. In this study, we examine the impact of eddy currents on dMRI using a structure phantom filled with low diffusivity material to characterize the eddy current. Our aim is to provide insights into the performance of phantom-based strategies in addressing the challenges presented by eddy currents in dMRI.

Material and Methods: *Software tools for phantom design* The phantom was designed in-house using a computer-aided design (CAD) program (Fusion 360, Autodesk Incorporation, San Francisco, CA, USA) and printed using an LCD-based 3D printer (Anycubic Photon Mono x, Hong Kong Anycubic Technology, Hong Kong, China) based on Stereolithography (SLA) technology. Acrylic resin-based 3D printing enabled precise manufacturing, suitable for the high-precision phantom platform [5]. The cylindrical phantom had specific dimensions of outer = 200 mm, inner = 184 mm, height = 200 mm, and contained 69 rods with a diameter of 10 mm. The phantom was filled with Polyvinylpyrrolidone (PVP) water solutions (80% w/v) prepared using pure water to ensure setup consistency and accuracy [6].

Data Acquisition The MRI data were acquired at 1.5 T (Ingenia; Philips, Best, the Netherlands) with a 16-channel head-coil. A 2D diffusion-weighted spin echo-echo planar imaging (DWI-SE-EPI) sequence was utilized with a voxel size of 2.0 × 2.0 × 2.5 mm^3, a matrix size of 112 × 110, and 80 slices. The TR/TE = 3016/107 ms, and a SENSE factor = 2 was used for image acquisition. B-value 2000s/mm^2 was acquired with 48 diffusion gradient directions and Anterior–Posterior (AP) gradient polarity. 3D-TFE-T1W structural images were also acquired to facilitate the testing of Coherent Point Drift (CPD) registration algorithms [7].

Eddy Current Distortion Correction The overall pipeline, as depicted in Fig. 1, aims to mitigate distortions induced by eddy currents in DWI through following steps. Firstly, a B0 Shift map is estimated by CPD registration between a distorted b = 0 s/mm^2 image and a T1 anatomical image. Secondly, the B0 shift maps are applied to the diffusion-weighted images to remove object-related B0 distortion. Thirdly, the segmentation process on the B0-corrected diffusion images was performed. Lastly, the binary diffusion images and binary T1 images are registered to estimate eddy-current maps. The data processing was performed using MATLAB 2022b.

Results Fig. 2 demonstrates the eddy-current maps for 48 diffusion directions of b-value 2000s/mm^2 at -76.25 mm (2A) and 1.25 mm (2B) farther from the isocenter along Z direction. The absolute maximum of the eddy current displacement at location -76.25 is are up to 5 mm, while such displacement at location 1.25 mm is less than 3 mm. Figure 3 depicts examples at a distance of Z = – 76.25 mm (1st row) and Z = 1.25 mm (2nd row) from the isocenter. The images exhibit a considerable reduction in distortion after correction (B and E) when compared to the images before correction (A and D), with greater distortion observed at Z = – 76.25 mm. The normalized root mean square errors (NRMSEs) values were reduced by 17.05% (Z = – 76.25) and 3.86% (Z = 1.25 mm) after correction. Therefore, our phantom method can effectively characterize eddy current effect in dMRI.

Discussion In this study, we presented a method that primarily focuses on characterizing eddy-current-induced distortions using a low diffusivity phantom. Our study used an 80% w/v PVP solution phantom, which may be good SNR even at higher than b-value 2000s/mm^2 [8]. Unlike FSL-TOPUP, our propose method requires only single diffusion gradient polarity. Our approach is considered as a fundamental step towards correcting complex distortions, involving other factors such as SNR reduction in brain tissue at high b-values and the influence of patient motion.

Reference
(see Fig. 4).

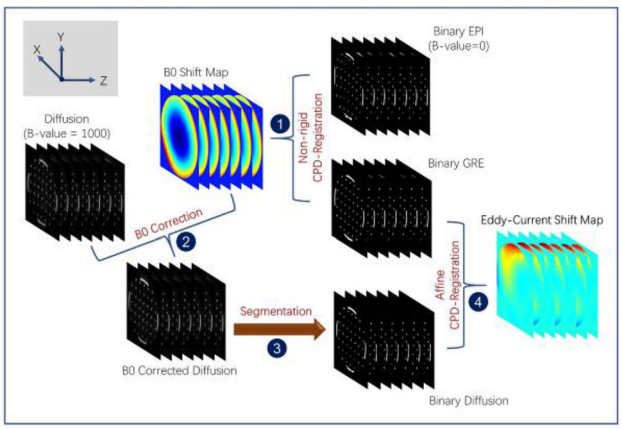

Fig. 1: Diagram of the Eddy-Current Shift Map estimation.

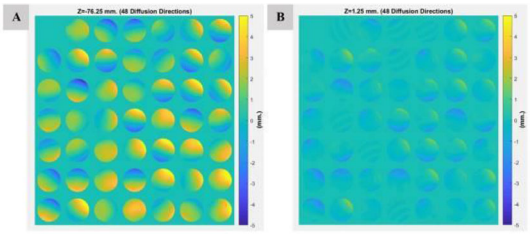

Fig. 2: Eddy-Current Shift Map of 48 diffusion directions at Z=-76.25 mm (A) and Z=1.25 mm (B) further away from the socenter.

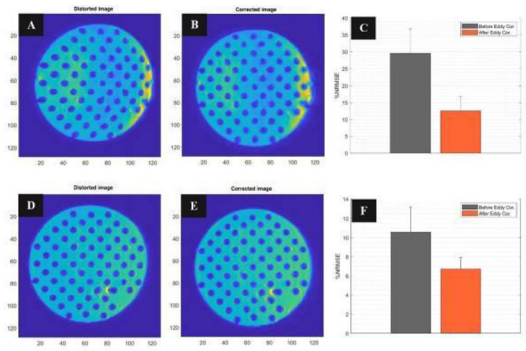

Fig. 3: Example images before (A and D) and after (B and E) eddy current correction at Z=-76.25 mm (first row) and Z=1.25 mm (second row) further away from the isocenter. Mean and standard deviation values of normalized root mean square errors (NRMSEs) across 48 directions at Z=-76.25 mm (C) and Z=1.25 mm (F).

1. Bammer R. Basic principles of diffusion-weighted imaging. European journal of radiology. 2003;45(3):169-84.
2. Schmitt F, Stehling MK, Turner R. Echo-planar imaging: theory, technique and application: Springer Science & Business Media; 2012.
3. Reese TG, Heid O, Weisskoff R, Wedeen V. Reduction of eddy-current-induced distortion in diffusion MRI using a twice-refocused spin echo. Magnetic Resonance in Medicine: An Official Journal of the International Society for Magnetic Resonance in Medicine. 2003;49(1):177-82.
4. Robison RK, Li Z, Wang D, Ooi MB, Pipe JG. Correction of B0 eddy current effects in spiral MRI. Magnetic resonance in medicine. 2019;81(4):2501-13.
5. Scotti CK, Velo MMdAC, Rizzante FAP, de Lima Nascimento TR, Mondelli RFL, Bombonatti JFS. Physical and surface properties of a 3D-printed composite resin for a digital workflow. The Journal of Prosthetic Dentistry. 2020;124(5):614. e1-. e5.
6. Pierpaoli C, Sarlls J, Nevo U, Basser PJ, Horkay F, editors. Polyvinylpyrrolidone (PVP) water solutions as isotropic phantoms for diffusion MRI studies. Proc Intl Soc Magn Reson Med; 2009.
7. Myronenko A, Song X. Point set registration: Coherent point drift. IEEE transactions on pattern analysis and machine intelligence. 2010;32(12):2262-75.
8. Palacios EM, Martin AJ, Boss MA, Ezekiel F, Chang YS, Yuh EL, et al. Toward precision and reproducibility of diffusion tensor imaging: a multicenter diffusion phantom and traveling volunteer study. American Journal of Neuroradiology. 2017;38(3):537-45.

Fig. 4: References

P217.
Synthetic contrast weighted images for T2-based water suppression diffusion MRI (T2wsup-dMRI)

T. Kimura[1]

[1]*Shizuoka College of Medical care Science, Dept. of Radiological Technology, Hamamatsu, Japan*

Introduction: A synthetic MRI technique (SynMRI) [1] can provide quantitative maps of PD, T2, T1 and those-based synthetic contrast weighted images of PDW, T2W, T1W, FLAIR etc., but CSF partial volume effects (CSF-PVE) was problematic especially in the synthetic FLAIR [2, 3]. To solve those, we have proposed a T2-based water suppression technique while keeping those tissue SNRs (T2wsup-SynMRI) [4, 5]. In addition, a diffusion MRI applying this technique (T2wsup-dMRI) provided tissue specific quantitative diffusion images of ADC and FA and fiver tractography was also improved in CSF-PVE regions compared with the standard dMRI technique [6, 7].

The purpose of this study was to improve the synthetic contrast weighted images by using our T2wsup-dMRI then to provide almost the same quality images as actually acquired in synthetic (computed) DWI [8–9] including the other synthetic images of inversion recovery (IR) images (FLAIR and DIR) in CSF-PVE regions.

Methods: In in-vivo MRI study, head volunteer 5 contrast images with the parameters shown in Fig. 1 were acquired on Galan 3 T[ZGO] (Canon medical systems, Otawara, Japan) after obtaining written informed consent. A single-shot EPI sequence was used, and the acquisition parameters were the following: parallel imaging (SPEEDER) of speed-up factor 3 acquisition matrix of 192 × 256; FOV = 23 cm; slice thickness = 5 mm; number of slices = 16 was commonly selected; number of average, 1; DWIs of 6 axes MPG directions.

Water suppression for originally acquired images were performed first (Fig. 2) then followed by quantitative maps and synthetic contrast weighted images were calculated similarly as the standard SynMRI technique with parameters in Fig. 1. SynMRI images with the given parameters were assessed with and without our T2wsup technique, and partially compared with actually acquired images.

In those, isotropic DWI images with b = 2000 [s/mm^2] were compared among the standard, actually acquired, and the synthetic DWI image with the ADC with (b_0, b_1) = (0, 1000) [s/mm^2]. ROI study was also performed on the portions of CSF-PVE portions.

Results: The synthetic quantitative maps and synthetic contrast weighted images with the T2wsup provided almost the similar contrast as the pure tissues compared with the standard even at CSF-PVE portions especially in the T2W-FLAIR and DIR. (Fig. 3).

The synthetic DWI image with T2wsup provided almost the similar contrast as the actually acquired even at the CSF-PVE portions, where the standard was underestimated due to the CSF component. (Fig. 4).

Discussion Through this study and former studies, [4–7] our T2wsup technique enabled to provide quantitative maps of T2, PD, T1, MD, and FA, and several synthetic contrast weighted images with arbitral combination of parameters of T2W, PDW, T1W, and high b-value DWI, in which CSF-PVEs were almost perfectly suppressed. Current results were obtained from the minimum 5 kinds of different parameter images by a simple closed form (CF) algorithm. When multiple images with different parameters are used to improve the quantitativity, several least square fitting (LSQ) algorithms and random sampling in 2D (*TE*, *b*) space can be applied [7].

	Imaging Sequence	Parameter	Standard		T2wsup	
			Acq. Time [s/slice]	CSF-PVE	Acq. Time [s/slice]	CSF-PVE
Acquired Images	SE_PDW(TR,TE)	(10000, 30) [ms]	10		10	
	SE_T2W(TR,TE)	(10000, 80) [ms]	10		10	
	SE_T2W(TR,TE)	(10000, 500) [ms]	-		10	
	IR_T1W(TR,TI,TE)	(10000, 1000, 30) [ms]	10		10	
	DWI[(TR,TE),b]	[(10000, 80)[ms], 1000 [s/mm^2]]	60		60	
	Acquisition Total Time		90		100	
Synthetic Images	SE_T2W(TR,TE)	(10000,80) [ms]				
	T2_FLAIR(TR,TI,TE)	(10000, 1520, 80) [ms]	10	Y	10	N
	DIR_WAIR(TR,TI_1,TI_2,TE)	(10000, 2126,2623, 80) [ms]	10	Y	10	N
	DIR_GAIR(TR,TI_1,TI_2,TE)	(10000, 2424,3085, 80) [ms]	10	Y	10	N
	DWI[(TR,TE),b]	[(10000, 80)[ms], 2000 [s/mm^2]]	60	Y	60	N
	Total Time if Acquired the Synthetic images		90		90	
	Total Time if Acquired All		180		190	
	Synthetic/AcquiredAll Time Ratio		0.50		0.53	

DIR_WAIR, Double IR for CSF and White Matter Suppression
DIR_GAIR, Double IR for CSF and Gray Matter Suppression
Parameters for synthetic IR sequences were obtained by assuming T1(CSF)=2200 ms, T1(GM)=1200 ms, and T1(WM)=800 ms.

Fig. 1: Imaging conditions for acquired and synthetic images in Standard- and T2wsup- dMRI. The T2wsup method, compared with the Standard method, requires heavy T2W image additionally but can suppress CSF-PVE effects. By using Synthetic dMRI technique, the total imaging time is almost half of the case of acquiring all.

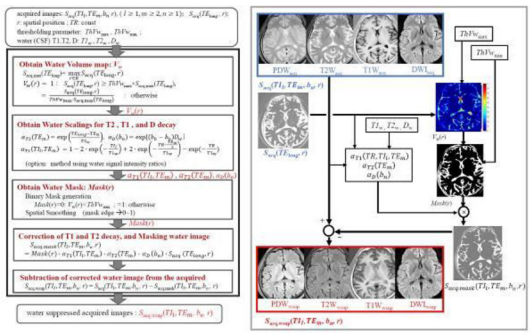

Fig. 2: Schematic of suppressing water (CSF) signals in acquired contrast weighted images in T2wsup-dMRI method. Those wsup acquired images were followed by calculating quantitative maps and synthetic images.

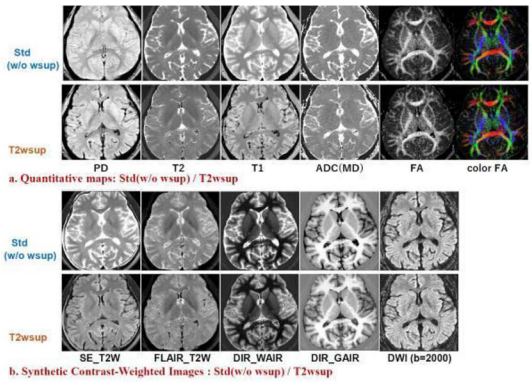

Fig. 3: Quantitative maps (**a**) and contrast weighted images (**b**) each with standard- (Std) (w/o wsup) and T2wsup- dMRI methods.

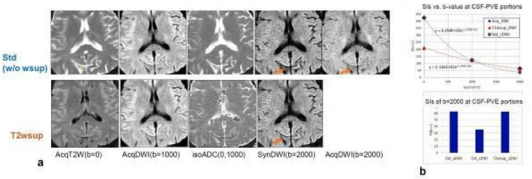

Fig. 4: Images (**a**) and ROI results (**b**) for Synthetic dMRI with Standard (Std: w/o wsup) and T2wsup method. Note that signal intensities (SIs) at CSF-PVE portions (arrows) for synthetic DWI (SynDWI) of b=2000 s/mm^2 for Std was underestimated due to CSF-PVE but the T2wsupSynDWI was almost the same as the actually acquired image (AcqDWI).

References

1. Tanenbaum LN, Tsiouris AJ, Johnson AN, et al. Synthetic MRI for clinical neuroimaging: results of the Magnetic Resonance Image Compilation (MAGiC) prospective, multicenter, multireader trial. AJNR Am J Neuroradiol 2017;38:1103–1110.
2. Hagiwara A, Hori M, Yokoyama K, et al. Synthetic MRI in the detection of multiple sclerosis plaques. AJNR Am J Neuroradiol 2017; 38:257–263.
3. Granberg T, Uppman M, Hashim F, et al. Clinical feasibility of synthetic MRI in multiple sclerosis: a diagnostic and volumetric validation study. AJNR Am J Neuroradiol 2016; 37:1023–1029.
4. Kimura T, Yamashita K, Fukatsu K. Synthetic MRI with T2-based Water Suppression to Reduce Hyperintense Artifacts due to CSF. Magn Reson Med Sci 2021; 20:325–337.
5. Kimura T, Yamagishi N, Masuda Y. et al. Water Suppression of T1 map and Synthetic Inversion Recovery images in T2-based Water Suppression Synthetic MRI (T2wsup-synMRI). In: Proc of ISMRM,2023 (Accepted)
6. Kimura T, Yamashita K, Fukatsu K. Diffuson MR Imaging with T2-based Water Suppression (T2wsup-dMRI). Magn Reson Med Sci 2022; 21; 499–515.
7. Kimura T. Enhancing Analysis Algorithm for T2-based water suppressed diffusion MRI (T2wsup-dMRI) by adding least-square fitting. In: Proc of ISMRM, 2022, #3823.
8. Blackledge MD, Leach MO, Collins DJ, Koh DM. Computed diffusion-weighted MR imaging may improve tumor detection. Radiology 2011;261(2):573–581.
9. Higaki T, Makamura Y, Tatsugami F et al. Introduction to the Technical Aspects of Computed Diffusion-weighted Imaging for Radiologists. RadioGraphics 2018; 38:1131–1144.

Acknowledgment: This study was supported by Policy-based medical services foundation in Japan, and MRI data acquisition was supported by Canon medical systems corp., Oatawara, Japan.

P218.
Improved geometric accuracy of high b-value diffusion brain MRI using 3D printed low diffusivity phantom

P. Ratiphunpong[1,2], A. Suwannasak[1], T. Ruadrew[1], U. Yarach[1], S. Udomsom[3]

[1]*Chiang Mai University, Department of Radiologic Technology, Faculty of Associated Medical, Chiang Mai, Thailand;*
[2]*HRH Princess Chulabhorn College of Medical Science, Chulabhorn Royal Academy, Radiological Technology School, Faculty of Health Science Technology, Bangkok, Thailand;*
[3]*Chiang Mai University, Biomedical Engineering, Chiang Mai, Thailand.*

Introduction: Diffusion Magnetic Resonance Imaging (dMRI) is commonly acquired using Echo-planar imaging (EPI). One well-known challenge of EPI-dMRI is susceptibility from B0 field inhomogeneities and eddy currents induced by switching of strong diffusion-weighted gradients, which can cause geometric distortion and impact the derived quantities obtained from diffusion tensor (DT) analysis. The twice refocused spin echo sequence can effectively minimize these distortions at the cost of increased echo time [1]. Reverse polarity approaches are suitable for images with sufficient signal-to-noise ratio [2, 3], but may provide suboptimal results at high b-values dMRI. Phantom-based strategies have shown different performance levels based on the materials and designs used. In this work, we utilized in-house 3D printed phantom filled with low diffusivity material to characterize and correct the eddy current effect on high b-value dMRI of the brain.

Material and Methods: *Phantom construction:* A phantom was designed in-house using a computer-aided design program (Fusion 360) and printed using an LCD-based 3D printer (Anycubic Photon Mono x) based on Stereolithography technology. The cylindrical phantom has an outer diameter of 200 mm, an inner diameter of 184 mm, and a height of 200 mm. It contains 69 rods arranged equidistantly in nine rows, each with a diameter of 10 mm. The phantom was filled with an aqueous solution of polyvinylpyrrolidone (PVP, 80%w/v of distilled water).

Data acquisition: The experiments were performed on 1.5 T clinical MRI (Ingenia; Philips, Best, the Netherlands) with a 12-channel receiver head coil. A healthy volunteer was scanned after informed consent according to institutional review board-approved protocol. Diffusion data were acquired using a 2D spin echo EPI-dMRI sequence with following parameters: voxel size = 1.5 × 1.5x5.0 mm, FOV = 240 × 240 mm, and 40 slices, TR/TE = 3306/120 ms, SENSE = 2, b-value = 0 and 3000 s/mm^2 with 64 diffusion

directions. In addition to the above protocol, the phantom was scanned using 3D-SPGR T1W sequence.

Eddy current estimation: Prior to eddy current estimation, B0 field inhomogeneity-related distortion was eliminated by registering non-distorted SPGR T1W and non-diffusion (b-value = 0) EPI images, as shown in Fig. 2. The displacements from the registration were then applied to all diffusion direction images. Eddy displacement was estimated by registering SPGR T1W images with each diffusion direction images (after B0 induced distortion correction). Note that Edge detection [4] was performed before Coherent Point Drift registration [5].

Performance assessment: The performance of the in-house phantom was accessed through fractional anisotropy (FA) map matric. Three different datasets were prepared prior to FA map calculation, including 1) original diffusion data, 2) pre-processed data using FSL-Eddy [6], 3) pre-processed data using in-house Eddy phantom. FSL-DTIFIT [7] was used for FA map calculation for all data sets.

Results: The eddy displacements associated with 64 diffusion directions at slice location 47.5 mm away from isocenter of the scanner (along head-feet direction) are shown in Fig. 3. The displacements obtained from FSL-eddy (3A) do not appear to represent real field, as almost all directions look similar with absolute values less than 0.05 mm. At the same slice location, the displacements obtained from our phantom (3B) appear realistic and vary according to diffusion directions. Their absolute values are up to 5 mm.

Examples of overlaid images between 1st and 2nd diffusion direction images are shown in Fig. 3C. Geometric mismatches are clearly seen on images before eddy current correction, as highlighted by arrows, whereas the images are well-aligned after correction. The geometric improvement is shown in Fig. 3D, where the mean of normalized root mean square errors (NRMSEs) (between 1st direction and others) decreased from 20.11% to 10.87%.

Figure 4A and B show directional FA and colored maps of three different data sets at a slice location 47.5 mm away from the isocenter of the scanner. The results reveal that the pre-processed data using the phantom can improve the FA maps, as they appear visually sharper than those obtained from the other two data sets, as highlighted by yellow circles.

Discussion: In this work, the phantom-based eddy current correction method showed better performance compared to FSL-Eddy and the original diffusion data. The discrepancy can be attributed to the fact that FSL-Eddy relies on model-based estimation of eddy current-induced fields and requires diffusion data [6]. The high noise level compromised FSL-Eddy at high b-values, while the low diffusivity phantom exhibited robust signal even at b-value of 3000 s/mm^2, suggesting potential for higher b-values, which will be further investigated.

Reference

(see in Fig. 1).

[1] TG Reese et al., Magnetic Resonance in Medicine: An Official Journal of the International Society for Magnetic Resonance in Medicine **49** (1), 177 (2003).
[2] JL Andersson et al., Neuroimage **20** (2), 870 (2003).
[3] MS Graham et al., PloS one **12** (10), e0185647 (2017).
[4] J Canny, IEEE Transactions on pattern analysis and machine intelligence (6), 679 (1986).
[5] A Myronenko and X Song, IEEE transactions on pattern analysis and machine intelligence **32** (12), 2262 (2010).
[6] JL Andersson and SN Sotiropoulos, Neuroimage **125**, 1063 (2016).
[7] TE Behrens et al., Magnetic Resonance in Medicine: An Official Journal of the International Society for Magnetic Resonance in Medicine **50** (5), 1077 (2003).

Fig. 1: Reference

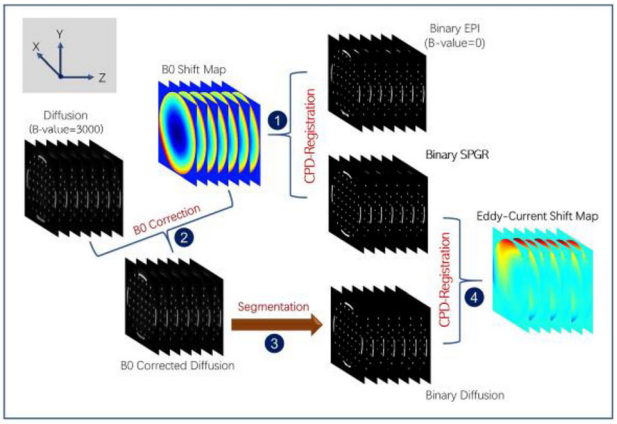

Fig. 2: Diagram of eddy current estimation

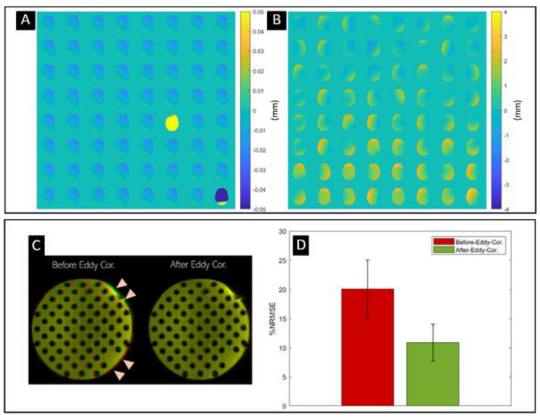

Fig. 3:
(A) Eddy displacement field obtained from FSL-Eddy.
(B) Eddy displacement field obtained from the proposed phantom. The 1st to 64th diffusion directions are from top left to bottom right.
(C) Overlaid between two different diffusion directions.
(D) Mean and standard deviation values of normalized root mean square errors (NRMSE) at slice location 47.5 mm away from iso-center entire 64 diffusion directions, in which b-value 0 was a reference.

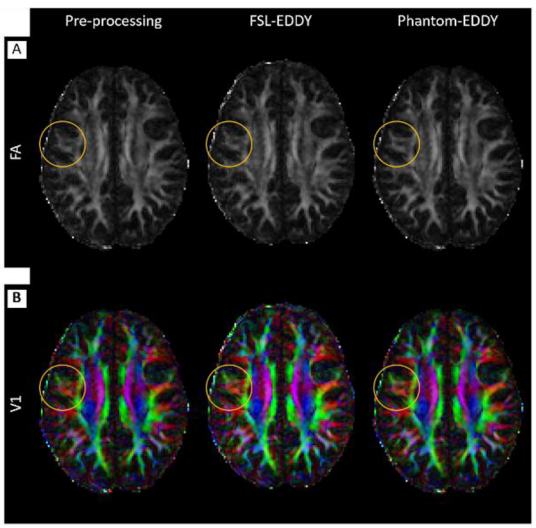

Fig. 4 (A) FA map and (B) color-coded vector map of the primary eigenvector (V1) derived from the FSL-DTIFIT toolbox using diffusion data with 64 diffusion directions according to The original diffusion data (**1st column**), the pre-processed data using FSL-Eddy (**2nd column**), and the pre-processed data using the in-house Eddy phantom (**3rd column**). The yellow circles highlighted the improvement when using low diffusivity phantom based technique.

P219.
Optimization of b-value threshold for the segmented fit to intravoxel incoherent motion measurements for different SNR

I. A. Rashid[1], C. Jamtheim Gustafsson[2,3], A. Gunnlaugsson[2], L. E. Olsson[2,3], P. Brynolfsson.[2]

[1]*Lund University, Department of Clinical Sciences, Medical Radiation Physics, Lund, Sweden;*
[2]*Skåne University Hospital, Department of Hematology, Oncology and Radiation Physics, Lund, Sweden;*
[3]*Lund University, Department of Translational Medicine, Medical Radiation Physics, Malmö, Sweden*

Introduction: Intravoxel incoherent motion (IVIM) is an imaging technique that provides information on tissue perfusion and diffusion. The signal is described by the following bi-exponential model [1]: $S = S_0[fe^{-bD^*} + (1-f)e^{-bD}]$, (1)where f is the fraction of the signal derived from perfusion effects, D^* the pseudo-diffusion coefficient of blood, D the diffusion coefficient of water. S, S_0, b are the signal, signal without diffusion encoding, and the diffusion encoding strength respectively.

Acquiring meaningful information by fitting this model to data is challenging since the problem is ill-conditioned and sensitive to noise (Fig. 1a,b). One popular strategy is to use a b-value threshold (b_{thresh}) over which the effects of D^* are assumed to be negligible [1]. D is estimated using b-values $> b_{\text{thresh}}$, followed by estimating D^* and f keeping D fixed. It is known that a lower threshold inflicts a positive bias on D, which is propagated to biases in f and D^* [1], while higher b_{thresh} may increase the influence of noise. Conventionally a b_{thresh} of 200 s/mm^2 or higher is recommended to avoid bias [1, 2]. It has been shown that lower b_{thresh} may perform better than the conventional ones [3], which warrants further investigation into the optimal b_{thresh}. The aims of this work is to 1) investigate the error contributions of estimation bias and signal noise for different b_{thresh} and SNR. 2) Present general recommendations for b_{thresh} for a range of SNR.

Method: The Segmented algorithm used is a 2-step process where D is estimated from b-values $> b_{\text{thresh}}$ using a mono-exponential S_0e^{-bD} least-squares fit, followed by a least-squares estimation of f and D^* to Eq. (1) keeping D fixed.

To account for various tissue properties, a total of 1000 parameter combinations ordered in a 10 × 10 × 10 array were defined; where each dimension corresponds to increasing f, D^*, and D, such that each element consisted of a unique parameter combination (Fig. 1c). Linear ranges were used, where f ε [0.02, 0.5], D^* ε [5, 30] μm^2/ms, and D ε [0, 3] μm^2/ms. Signals were simulated using Eq. (1) for b-values 0, 20, 40, 60, 80, 100, 150, 200, 250, 300, 350, 400, 500, 600, 700, and 800 s/mm^2.

To investigate noise sensitivity, Rician noise was simulated 100 times for each parameter combination such that a specific SNR was obtained for S(800 s/mm^2), giving a total of 100 000 signal curves. Evaluation was performed for SNR ε [3, 21] with step size 3. Parameter estimates were produced using b_{thresh} ε [100, 400] s/mm^2 with step size 50 s/mm^2 for all 100 000 signal simulations of each SNR. Estimation bias (estimate – ground truth) and standard deviation were used to determine the root-mean-square error (RMSE = $\sqrt{[\text{bias}^2 + \text{standard deviation}^2]}$) of all estimates for each parameter. For every combination of SNR and b_{thresh}, the RMSE was summed for each parameter, summarizing the results in metrics of total error.

Results: Bias and standard deviation of f and D estimates have similar contribution to the error, giving optimal b_{thresh} for different SNR (Fig. 2). For D^*, noise was the most dominant contributor to the total error, making low b_{thresh} favorable. For low SNR, the b_{thresh} that minimized the total RMSE was 150 s/mm^2, and increased with SNR to 200–250 s/mm^2.

Discussion: Since SNR decreases with increasing b-value, a higher b_{thresh} results in greater estimation uncertainties in D. As D is fixed in the estimation of f and D^*, uncertainties in D are propagated to all parameters. If b_{thresh} is too low, a positive bias may be inflicted in the estimation of D, as effects of perfusion are included in the estimation. We have shown that an SNR-dependent optimal b_{thresh} exists where the RMSE is minimized. For low SNR, this optimal b_{thresh} is lower than the conventionally recommended b_{thresh}, therefore a larger bias may need to be tolerated.

Our results agree with a previous study which found an optimal b_{thresh} of 150 s/mm^2 [3]. To optimize b_{thresh} for a specific organ, one may need to evaluate for IVIM parameter sets relevant to the organ of interest; due to varying bias caused by different tissue properties.

Conclusion: For low SNR, a general b-value threshold of 150 s/mm^2 is recommended and may be increased to 200 s/mm^2 for higher SNR.

References

1. Le Bihan D. What can we see with IVIM MRI? NeuroImage. 2019 Feb 15;187:56–67.
2. Englund EK, Reiter DA, Shahidi B, Sigmund EE. Intravoxel Incoherent Motion MRI in skeletal muscle: Review and future directions. J Magn Reson Imaging JMRI. 2022 Apr;55(4):988–1012.
3. Wurnig MC, Donati OF, Ulbrich E, Filli L, Kenkel D, Thoeny HC, et al. Systematic analysis of the intravoxel incoherent motion threshold separating perfusion and diffusion effects: Proposal of a standardized algorithm. Magn Reson Med. 2015;74(5):1414–22.

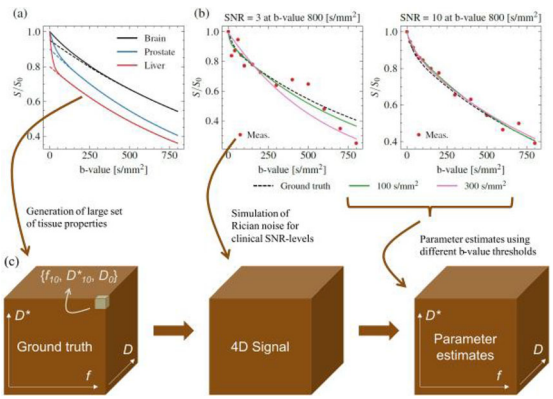

Fig. 1: (a) IVIM signals vary between tissues. (b) The effect of b-value thresholds on parameter estimates at low and high SNR, illustrated by SNR 3 and 10. (c) The simulation sequence. Noised signals were simulated for 1000 parameter combinations to evaluate RMSE for parameter estimates using a range of b-value thresholds.

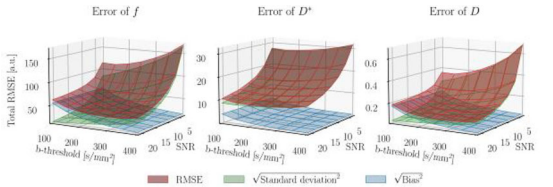

Fig. 2: The total RMSE for all estimates of each parameter as a function of SNR and b-threshold of the 2-step Segmented fit. For low SNR-levels, lower b-thresholds minimize the total RMSE as the general SNR is increased by the lower b-value diffusion-weighted images. As SNR is increased, so is the optimal b-threshold. The errors due to noise are reduced, making bias a more important factor, thus pushing the optimal threshold toward larger values.

P220.
Enabling high resolution diffusion brain at clinical 1.5 T MRI through model-based reconstruction

A. Suwannasak[1], U. Yarach[1], I. Chatnuntawech[2], K. Wantanajittikul[1], P. Ratiphunpong[1], T. Ruadrew.[1]

[1]*Chiang Mai University, Department of Radiologic Technology, Faculty of Associated Medical, Chiang Mai, Thailand;*
[2]*Nanotechnology Center (NANOTEC), Pathum Thani, Thailand*

Introduction: Diffusion-weighted imaging (DWI) scan is a powerful MRI technique that provides information about tissue microstructure in vivo[1], but the use of Echo Planar Imaging (EPI) can lead to geometric distortion and T2* blurring due to lengthy Echo spacing (ESP) in the presence of B0 field homogeneity. This makes difficulty to achieve high resolution DWI at clinical scanner.Short-Axis Propeller (SAP)-EPI[2,3] allows shortening ESP and may allow high resolution DWI with small distortion. However, geometric inconsistency among the rotated blades needs to be addressed prior to blade combination. In this work, we implemented model-based iterative reconstruction (MBIR)[4] which enables managing off-resonance effect. Moreover, locally low-rank (LLR)[5] regularization was incorporated to handle phase variations without calibration scan.

Methods 1. Discrete single-shot SAP-DWI signal model: Due to high readout bandwidth (i.e., dwell time (Δt) $<<$ echo spacing (T)) and off-resonance along phase encoded, it is reasonable to approximate Δt as 0. Upon discretizing and time-segmenting, the signal at readout m $\in$ [0 M] of phase-encoding line n $\in$ [0 N] can be modeled as: (see in Eq. 1 in Fig. 1).p $\in$ [0 P] and q $\in$ [0 Q] are pixel indices, s_c is the coil sensitivity profile of coil c, u is the target image, $\Delta\omega_0$ is the off-resonance, $k_{x,\sigma,a}$ and $k_{y,\sigma,a}$ is k-space coordinates in readout and phase-encoding dimensions of each shot σ and number of average a, and ε is the Gaussian noise. Equation 1 can be modified to algebraic form as: (see in Eq. 2 in Fig. 1)

Where F is the Fourier transform implemented as NUFFT type-II, $W_l = \text{diag}\{e^{(-j(\Delta\omega_0[p,q][l-(N-1)/2]T)}\}$, and $S = [\text{diag}\{S_0\}\cdots\text{diag}\{S_{(c-1)}\}]^T$.

2.Joint reconstruction of virtual-coil locally low-rank (LLR) The virtual-coil LLR[6,7] was implemented for solving the partial Fourier (pF) effect and entailed the target image (u) by minimizing the following optimization problem: (see in Eq. 3 in Fig. 1).

The term $\|A_{(\sigma,a)}\, u_{(\sigma,a)}\text{-}G_{(\sigma,a)}\|_2{}^2$ represents the data consistency through sensitivity encoding. λ denotes a regularization parameter, the operator R_b selects the b^{th} out of $2N_\sigma$ blocks and transforms into a Casorati matrix. It should be note that actual acquired blades and virtual blades denoting u^- as complex conjugation result in $2N_\sigma$ blocks. The local low-rankness is enforced by penalizing the nuclear norm ($\|\bullet\|_*$). δ denotes a Kronecker delta. To solve the optimization problem in Eq. 3, an advanced version of the Fast Iterative Shrinkage Algorithm (FISTA) known as fast composite splitting algorithm (FCSA)[8] can be employed to manage penalties independently with blockwise singular value thresholding (SVT).

3. Data acquisition and preparation: A healthy volunteer with informed consent approved by the institutional review board-approved (IRB) underwent scanning on 1.5 T MRI scanner with 12-channel head coil. To obtain SAP-DWI, the FOV was tilted eight times with varying angles (22.5 degree each) for single-shot EPI and the acquisition with 64 readout samples, 256 phase-encoding steps, SENSE-factor of 4, and 6/8 partial Fourier. MBIR was implemented on MATLAB using 30 iterations of FISTA with 2X-oversampled NUFFT type-II, a width J = 4 Kaiser-Bessel kernel, block-size 9 $\times$ 9, λ = 0.0005, and L = time segments of phase-encoding. Each blade was used to estimate B0 field map using TOP-UP[9] and T1w-FFE was acquired for coil sensitivity maps using ESPIRiT technique[10]. Additionally, Nyquist ghost phase correction and ramp sampling are included in MBIR.

Results: Fig. 2 shows k-space data (2A) and DWI images (2B) of each blade reconstructed using standard SENSE, where cannot recover the missing pF data. We also highlighted the geometric distortion appearances of different blades with red circles. Compared to MBIR with virtual-coil LLR in Fig. 3, which efficiently recovers such missing k-space data (3A) and reduces blurry and residual aliasing of each blade images (3B). Figure 4 depicts the eight blades combination which obtained from sum-of-squares after SENSE, the missing k-space data (4A) and image (4C) with blurring and geometric distortion, particularly in B0 field inhomogeneity (4E) can be observed whereas MBIR provides recovered k-space data (4B) and notably improves overall image resolution as shown with image (4D).

Discussions: In this study, model-based framework with virtual-coil LLR that manages magnetic susceptibility and pF effects without phase calibrations was achieved with high-resolution SAP-DWI images. Despite these findings, some issues should be further explored. These include reducing the reconstruction time which is proportional to blade numbers, coil numbers, and time-segments using coil compression and parallel computing, discussing the other methods[11,12] for estimating B0 field maps with high accuracy, and optimizing the number of blades with LLR for a more efficient model.

Equations

$$g_{c,\sigma,a}[m,n] = \sum_{l=0}^{L}\left\{\sum_{p=0}^{P-1}\sum_{q=0}^{Q-1} s_c[p,q]u[p,q]e^{-j(\Delta\omega_0[p,q][l-\frac{N-1}{2}]T}e^{-j(k_{x,\sigma,a}[m]p+k_{y,\sigma,a}[n]q)}\right\} + \varepsilon_{c,\sigma,a}[m,n] \quad \text{Eq.1}$$

$$g_{\sigma,a} = \left(I \otimes \sum_{l=0}^{L} F_{\sigma,a}W_l\right)Su_{\sigma,a} + \varepsilon_{\sigma,a} = A_{\sigma,a}u_{\sigma,a} + \varepsilon_{\sigma,a} \quad \text{Eq.2}$$

$$\min_{\{u_{1,1},\cdots,u_{N_\sigma,N_a}\}}\left\{\sum_{\sigma=1}^{N_a}\left\|A_{\sigma,a}u_{\sigma,a} - G_{\sigma,a}\right\|_2^2 + \lambda\sum_{b\in 2N_b}\left\|R_b\left(\sum_{\sigma=1}^{N_\sigma}\left(u_{\sigma,a}\delta_{\sigma,a}^T + \overline{u_{\sigma,a}}\delta_{\sigma,a}^T\right)\right)\right\|_*\right\} \quad \text{Eq.3}$$

References

1. Baliyan, V., Das, C.J., Sharma, R. & Gupta, A.K. Diffusion weighted imaging: technique and applications. *World journal of radiology* **8**, 785 (2016).
2. Holdsworth, S.J., O'Halloran, R. & Setsompop, K. The quest for high spatial resolution diffusion-weighted imaging of the human brain in vivo. *NMR in Biomedicine* **32**, e4056 (2019).
3. Skare, S., Newbould, R.D., Clayton, D.B. & Bammer, R. Propeller EPI in the other direction. *Magnetic Resonance in Medicine: An Official Journal of the International Society for Magnetic Resonance in Medicine* **55**, 1298-1307 (2006).
4. Yarach, U., *et al.* Model-based iterative reconstruction for single-shot EPI at 7 T. *Magnetic resonance in medicine* **78**, 2250-2264 (2017).
5. Liao, C., *et al.* High-fidelity submillimeter-isotropic-resolution diffusion MRI through gSlider-BUDA and circular EPI with S-LORAKS reconstruction. *ISMRM, London* (2022).
6. Yi, Z., *et al.* Joint calibrationless reconstruction of highly undersampled multicontrast MR datasets using a low-rank Hankel tensor completion framework. *Magnetic Resonance in Medicine* **85**, 3256-3271 (2021).
7. Lyu, M., *et al.* Robust SENSE reconstruction of simultaneous multislice EPI with low-rank enhanced coil sensitivity calibration and slice-dependent 2D Nyquist ghost correction. *Magnetic Resonance in Medicine* **80**, 1376-1390 (2018).
8. Huang, J., Zhang, S., Li, H. & Metaxas, D. Composite splitting algorithms for convex optimization. *Computer Vision and Image Understanding* **115**, 1610-1622 (2011).
9. Chang, H. & Fitzpatrick, J.M. A technique for accurate magnetic resonance imaging in the presence of field inhomogeneities. *IEEE Transactions on medical imaging* **11**, 319-329 (1992).
10. Uecker, M., Virtue, P., Vasanawala, S.S. & Lustig, M. ESPIRiT reconstruction using soft SENSE. in *Proceedings of the 21st Annual Meeting ISMRM*, Vol. 21 127 (2013).
11. Matakos, A., Balter, J.M. & Cao, Y. A robust method for estimating b0 inhomogeneity field in the liver by mitigating fat signals and phase-wrapping. *Tomography* **3**, 79-88 (2017).
12. In, M.-H. & Speck, O. Highly accelerated PSF-mapping for EPI distortion correction with improved fidelity. *Magnetic Resonance Materials in Physics, Biology and Medicine* **25**, 183-192 (2012).

Fig. 1: Equations and References

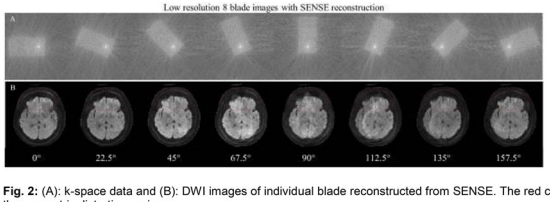

Fig. 2: (A): k-space data and (B): DWI images of individual blade reconstructed from SENSE. The red circles highlight the geometric distortion regions.

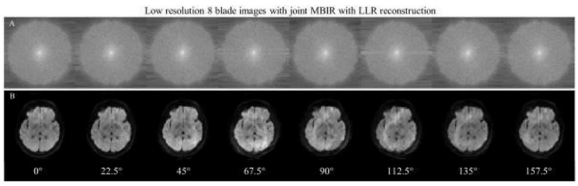

Fig. 3: (A): k-space data and (B): DWI images of individual blade reconstructed from MBIR with virtual-coil LLR.

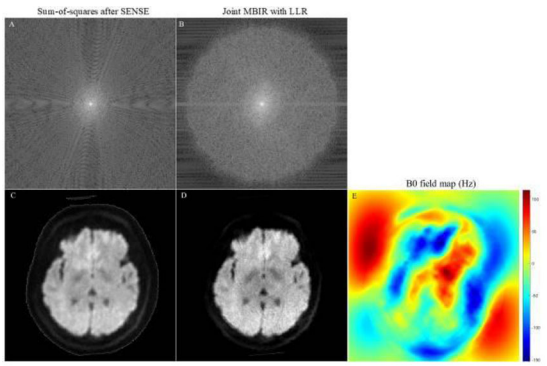

Fig. 4: The combination of eight blades, (A-B): reconstructed k-space data and (C-D): DWI images corresponding to k-space data obtained from sum-of-squares after SENSE and MBIR with virtual-coil LLR, respectively. (E): B0 field map obtained from TOP-UP.

References
(see in Fig. 1).

P221.
Preliminary comparison of *ex-vivo* quantitative susceptibility mapping and mechanical properties of human carotid atherosclerotic plaque to characterise rupture risk

F. Digeronimo[1,2], B. Tornifoglio[1,2], A. J. Stone[3], K. Shmueli[4], C. Lally[1,2,5]

[1]*Trinity College Dublin, Trinity Centre for Biomedical Engineering, Dublin, Ireland;*
[2]*Trinity College Dublin, Department of Mechanical, Manufacturing and Biomedical Engineering, Dublin, Ireland;*
[3]*St. Vincent's University Hospital, Department of Medical Physics and Clinical Engineering, Dublin, Ireland;*
[4]*University College London, Department of Medical Physics and Biomedical Engineering, London, United Kingdom;*
[5]*Royal College of Surgeons in Ireland and Trinity College Dublin, Advanced Materials and Bioengineering Research Centre (AMBER), Dublin, Ireland*

Introduction: Carotid artery disease (CAD) is a high-risk factor for acute ischaemic stroke, with plaque rupture estimated to account for 15–20% of ischaemic stroke cases [1]. Current CAD clinical assessment relies on the quantification of stenosis percentage alone, despite other biomarkers having been identified for the characterisation of "vulnerable plaques" [2]. Quantitative susceptibility mapping (QSM) has previously been explored ex vivo in porcine arterial tissue where the tissue susceptibility value was found to be sensitive to collagen content [3]. Collagen is a critical load-bearing component in arterial tissue and may play a key role in plaque stability [4]. This study aims to further investigate the sensitivity of QSM to collagen in excised human atherosclerotic plaques and gauge the potential of this modality to inform on plaque rupture risk.
Methods: Fresh atherosclerotic plaques (n = 5) were obtained from five patients undergoing carotid endarterectomy surgery at St. James's Hospital, Dublin and cryopreserved. After thawing, specimens were imaged individually using a 7 T system. System specifications and acquisition parameters are summarised in Fig. 1. A novel two-pass masking QSM pipeline [5] was used to produce susceptibility maps. MRI data analysis, including tissue mask extraction, is summarised in Fig. 2. The samples presented in this study are part of a larger dataset, for which diffusion tensor imaging and mechanical characterisation were previously published [6]. After whole-plaque MRI, plaques were sectioned into 2 mm wide circumferential strips using a 3D-printed microtome blade holder. Strips were then uniaxially extended to failure and histologically analysed (results not shown). Tissue masks for each strip were obtained using previous registration data and manually refined to remove tissue placed within the tester grips. Strip susceptibility distributions obtained from this study, were compared to the previously obtained mechanical properties, i.e. final elastic modulus, known to be dominated by tissue collagen fibres [7].
Results: Processing of the phase data using a conventional masking approach proved unsuccessful. This was attributed to large low-signal regions, i.e. calcifications, which caused significant streaking artefacts and residual background fields in the susceptibility maps. Therefore, a two-pass masking pipeline was implemented (summarised in Fig. 2). This analysis approach provided interpretable tissue susceptibility maps and distributions for all specimens (Fig. 3). Susceptibility distributions for the individually tested strips are shown in Fig. 4(b). Correlation analysis between mean strip susceptibility and previously obtained collagen dominant final elastic modulus for the strips did not indicate any correlation ($r = -0.2613$) (Fig. 4(c)).
Discussion: The susceptibility values observed within plaque tissue and specific regions, such as calcifications and intra-plaque haemorrhages, are comparable to available data in the literature, with calcifications showing diamagnetic ($\chi < 0$) values [8]. Preliminary analysis does not indicate any correlation between the average tissue susceptibility and the final elastic modulus of plaque strips. However, as plaques are extremely heterogenous, a more spatially refined approach when investigating the link between susceptibility and mechanical metrics is likely needed. From the previous study, locations of fibrous cap rupture were associated with axial collagen fibre alignment in some strips [6], and collagen may have a susceptibility anisotropy in arterial tissue [3,9]. Future work will explore image processing approaches to unveil any potential susceptibility map features which can provide key mechanical indicators for plaque vulnerability.
Conclusion: Preliminary analysis on five specimens showed no correlation between mean plaque strip susceptibility and final elastic modulus. These initial correlation investigations between tissue susceptibility and mechanical properties suggest the need to look at local changes in susceptibility within each strip. Future work aims to further optimise this technique and investigate its potential to yield mechanically sensitive indicators for atherosclerotic tissue.

IMAGING SET-UP	Container	15 mL Falcon Tube
	Surrounding Environment	Immersed in Fresh Phosphate Buffered Saline
	Temperature [°C]	20
SYSTEM SPECIFICATIONS	Manufacturer	Bruker (Ettingen, Germany)
	Model	BioSpec 70/30 USR
	System Field Strength [T]	7
	Bore Type	Horizontal
	Bore Diameter [cm]	30
	Number of Coil Channels	8
ACQUISITION PARAMETERS	Sequence Type	T2*-weighted 3D Multi-Echo Gradient Echo
	Averages	4
	Echoes	4
	Repetition Time [ms]	150
	1st Echo Time [ms]	4.8
	Echo Spacing [ms]	7.68
	Flip Angle [°]	30
	Field of View (FoV) [mm]	16 x 16 x 16
	Matrix Size [voxels]	128 x 128 x 128
	Resolution [µm]	125 x 125 x 125
	Acquisition Time	2 h: 44 min

Fig. 1: MRI data acquisition specifications.

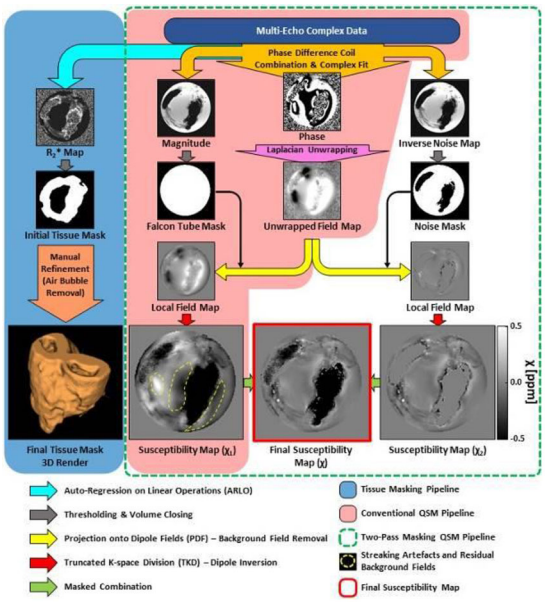

Fig. 2: MRI data processing overview: tissue masking and comparison between conventional [10] vs two-pass masking QSM pipeline. Central axial slice of plaque (#1) is shown for each of the processing steps.

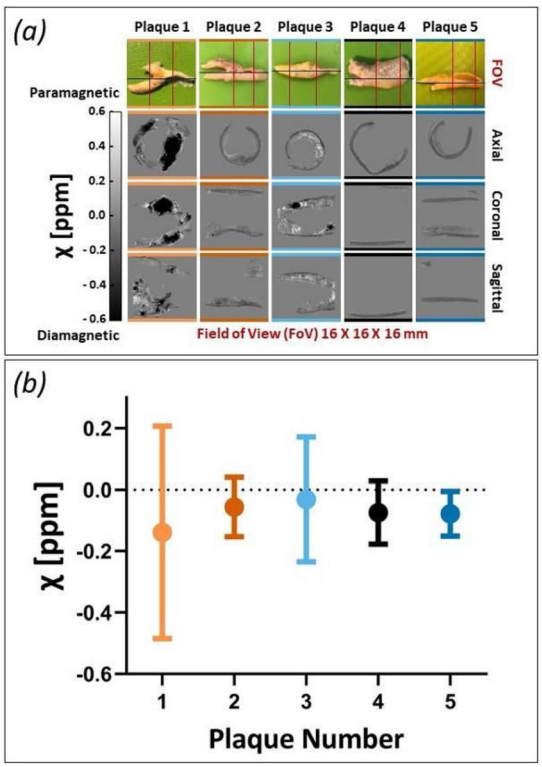

Fig. 3: Overview of susceptibility maps for whole plaques. (a) Photographs of plaques (MRI FoV: red lines; iso-centre axis: black line) and corresponding MRI susceptibility maps in axial, coronal and sagittal views. (b) Susceptibility distribution within tissue (mean ± standard deviation). Matched colour coding for (a) and (b).

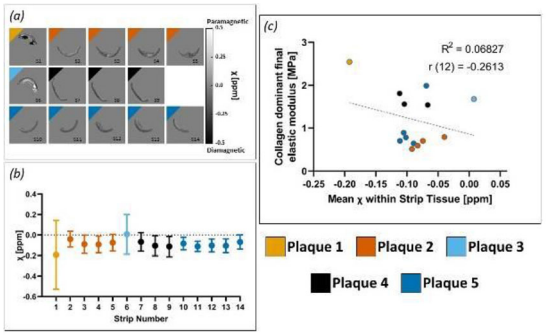

Fig. 4: Overview of susceptibility maps for plaque strips (S1 to S14). (a) Axial view of susceptibility maps. (b) Susceptibility distribution within tissue (mean ± standard deviation). (c) Correlation between mean plaque strip susceptibility and the collagen dominant final elastic modulus; Pearson's correlation coefficient (r = -0.2613, p = 0.3669). Matched colour coding for (a), (b) and (c).

References

1. Dossabhoy S, et al. Seminar Vasc Surg. 2021;34(1):3–9
2. Saba L, et al. JVS Vascular Science, 2021;2:149–158
3. Stone A J, et al. Magn Reson Med. 2021;86(5):2512–2527
4. Johnston R D, et al. Acta Biomater. 2021;124:291–300
5. Karsa A and Shmueli K. ISMRM Annual Meeting, London. 2022; Abstract Number: 2462
6. Tornifoglio B, et al. Biomech Model Mechanobiol. 2023
7. Loree H M, et al. J. Biomech. 1994;27:195–204
8. Azuma M, et al. AJNR Am J Neuroradiol. 2020;41(2):310–317
9. Nykänen, O. et al. Magn Reson Med. 2021;80(6):2702–2716
10. Shmueli K. "Quantitative Susceptibility Mapping", in Seiberlich N, et al. (ed.) Advances in Magnetic Resonance Technology and Applications. Cambridge, MA, US: Academic Press. 2020;V1:819–838

P222.
Improved visualization of breast micro calcifications in high spatial resolution quantitative susceptibility mapping using deep learning-based denoising

S. Ravichandran[1], C. Boehm[1], K. Weiss[2], A. Ziller[1], G. A. Kaissis[1], D. Rueckert[3], T. Borde[1], J. Meineke[2], M. R. Makowski[1], E. M. Fallenberg[1], D. Karampinos[1]

[1]*Technical University of Munich, School of Medicine, Department of Diagnostic and Interventional Radiology, Munich, Germany;*
[2]*Philips GmbH Market DACH, Hamburg, Germany;*
[3]*Technical University of Munich, School of Medicine, Artificial Intelligence in Healthcare and Medicine, Munich, Germany*

Introduction: Cluster of microcalcifications (MCs) in the breast are considered a frequent precursor of malignant breast lesions[1]. In clinical routine, MCs are only detected by X-ray mammography. However, for young patients a radiation-free method would be strongly desirable. Quantitative susceptibility mapping (QSM) has been proposed for the MR-based visualization of calcifications based on complex multi-echo gradient-echo (mGRE) images. However, for the visualization of MCs, high spatial resolution is needed which substantially reduces the SNR. Deep learning-based denoising could be an approach to improve the apparent SNR for range of applications, including phase-sensitive ones like QSM[2,3]. Complex multi-echo images are well-known to contain Gaussian noise. The present work proposes the use of a bias-free denoising convolutional neural network (BFCNN) to denoise the complex mGRE images trained with artificial Gaussian noise[4]. Based on a simulation, the improved visualization of MCs when using denoising is demonstrated along with a proof of principle in an in vivo scan.

Methods: In vivo measurements A high resolution effective multi-peak in-phase gradient echo sequence was performed on a 3 T scanner (Ingenia, Philips Healthcare)[5]. The imaging parameters were TE = [3.07,7.48]ms, FA = 12, readout-direction = anterior–posterior, FOV = 384 × 384 × 192mm^3, TR = 10.85 ms, compressed sense acceleration R = 6, and an isotropic voxel-size of 0.6mm^3. The images were reconstructed online using the vendor"s compressed SENSE.

Pipeline: BFCNN, trained on Gaussian noise in grayscale images can robustly denoise across various Gaussian noise levels[4]. BFCNN was applied to the real and imaginary part of complex-MR data separately for denoising. A hierarchical multi-resolution graph-cut was used to obtain an unwrapped field map[6]. A nonlinear preconditioned total field inversion algorithm was used to invert the field map to susceptibility (χ) map7. Figure 1 shows the pipeline of denoising and QSM processing.

Simulation: Cluster of MCs with negative χ(< -1 ppm) of one voxel size each(0.6mm^3) are simulated in a reference scan based on the in vivo scan. Gaussian noise was added to the reference scan (real & imaginary) and QSM was performed on noisy and denoised data.

Results: Fig. 2 shows the magnitude data and estimated parameters for simulated the reference, noisy, denoised. The noisy χ-map(green) shows MCs like artefacts (dark voxels) while the denoised χ-map(red) only shows the simulated MCs. Figure 3 shows the magnitude data and estimated parameters of original and denoised data. The effective noise removed can be seen in the difference maps especially further from the receiver coils.

Discussion: The BFCNN can substantially reduce the noise in real and imaginary part of the complex MR data. In the simulation, the noisy χ-map shows artefacts that could be misinterpreted as MCs. The denoised χ-map shows only true MCs that appear as single voxel of strong negative χ. Denoising improves visualization of MCs. Although no MCs are present in the in vivo scan, a substantial improvement in apparent SNR was observed, demonstrating the proof of concept for this approach.

Conclusion: For high resolution QSM, low SNR limits the visualization of MCs. BFCNN substantially reduces noise in the complex MR data and s improves the apparent SNR in high resolution QSM to further enable the better visualization of MCs.

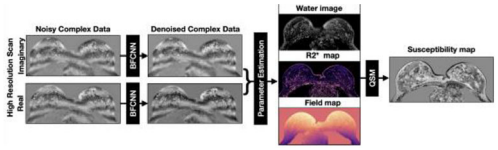

Fig. 1: Pipeline of QSM processing combined with denoising network. The HR scan is first denoised in the real and imaginary part using BFCNN and then denoised data is used to estimate field map using a hierarchical multi resolution graph cut method[6]. The field map from the denoised data is then inverted to χ-map using non-linear total field inversion[7].

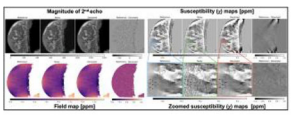

Fig. 2: Magnitude data and estimated parameters of simulated reference, noisy and denoised data are shown. It can be seen that in the noisy χ-map (reference-blue, noisy-green, denoised-red), MC-like artefacts appear. The denoised χ-map only shows the simulated MCs.

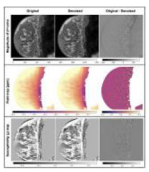

Fig. 3: The first column shows magnitude, field map and χ-map of the in vivo scan of a volunteer. The second column shows its denoised versions. In the difference map (last column) the noise removed from the original data can be seen.

References

1. Logullo, Breast microcalcifications: Past, present and future,MolClinOncol,2022.
2. Bazin ,Denoising High Field Multi-Dimensional MRI With Local Complex PCA,Frontiers in Neuroscience, 2019.
3. Allen, Effect of a Low-Rank Denoising Algorithm on Quantitative Magnetic Resonance Imaging-Based Measures of Liver Fat and Iron, Computer Assisted Tomography, 2017.
4. Mohan, Robust and interpretable blind image denoising via bias-free convolutional neural networks, arXiv, 2019.
5. Boehm, High spatial resolution quantitative susceptibility mapping using in-phase echoes enables the depiction of breast microcalcifications, Proceedings ISMRM, 2023.
6. Boehm, Improved body quantitative susceptibility mapping by using a variable-layer single-min-cut graph-cut for field-mapping, MRM, 2021.
7. Boehm,P reconditioned water-fat total field inversion: application to spine quantitative susceptibility mapping, MRM, 2022.

P223.
An external reference to facilitate absolute QSM estimates of magnetic susceptibility: Theoretical considerations, simulations and phantom-based evaluation

A. Lundberg[1], R. Wirestam[1], L. Knutsson[1,2], E. Lind[1]

[1]*Lund University, Department of Medical Radiation Physics, Lund, Sweden;*
[2]*Johns Hopkins University, Russell H. Morgan Department of Radiology and Radiological Sciences, Baltimore, MD, United States*

Introduction: Quantitative susceptibility mapping (QSM)[1–3] is inherently unable to provide absolute magnetic susceptibility values. Furthermore, spatially separated objects within the image are numerically disconnected in the QSM reconstruction, which prevents direct calibration using an external reference. In this study, an approach based on phase measurement in external references and a simulated relationship between phase and susceptibility[4] is proposed to enable absolute QSM estimates. By comparing the QSM reconstructed susceptibility with a predefined susceptibility source, the concept is validated in simulations of a numerical brain and in MRI phantom measurements.

Methods: MRI phase has a non-local property. For two cylinders parallel to the B_0 field, placed outside the skull, the total phase in each cylinder, Φ_{tot_cyl}, is described as a sum of the internal, Φ_{int_cyl}, and the external,Φ_{ext_cyl}, phase contributions, related to the susceptibility in the cylinder and in the brain, respectively, and a rest term A to address phase uncertainties:

$\Phi_{tot\_cyl1} = \Phi_{int\_cyl1} + \Phi_{ext\_cyl1} + A$ Eq. 1

$\Phi_{tot\_cyl2} = \Phi_{int\_cyl2} + \Phi_{ext\_cyl2} + A$ Eq. 2

MRI phase is proportional to the convolution of the susceptibility distribution with the unit dipole kernel. For a specific position and geometry, the relation between phase and susceptibility can be expressed using a proportionality factor F[4]. Thus, Φ_{ext_cyl} is given by:

$\Phi_{ext\_cyl} = F_{brain\_cyl} \cdot \Delta X_{brain}$ Eq. 3where ΔX_{brain} is the susceptibility difference between air and the absolute mean susceptibility in the brain, X_{mean_brain}. Hence, if the total phase in each cylinder is extracted from measured images, and internal phase contributions and F-factors are predicted by phase map simulations, Eqs. 1–3 provide:

$X_{mean\_brain} = X_{air} - ((\Phi_{tot\_cyl1} - \Phi_{tot\_cyl2}) - (\Phi_{int\_cyl1} - \Phi_{int\_cyl2}))/(F_{brain\_cyl1} - F_{brain\_cyl2})$ Eq. 4

A numerical brain phantom[5] with external references parallel to the B_0 field was used to mimic an MRI measurement. Phase and magnitude images were created for morphology enabled dipole inversion (MEDI)[3,6–8] QSM reconstruction (matrix $256 \times 256 \times 98$, $B_0 = 1.5$ T, voxel size = $1 \times 1 \times 1$ mm^3, $\Delta TE = 5$ ms). Region-growing unwrapping and removal of the background field[9] were performed before dipole inversion (Fig. 1). Absolute X_{mean_brain} was assessed as follows: *(i)* Φ_{tot_cyl} was measured in each cylinder in the unwrapped phase map, *(ii)* Φ_{int_cyl} and F-factors were predicted by simulated phase maps of the defined geometry (Fig. 2). Presuming susceptibility-independent F-factors, brain susceptibility was temporarily defined as 0.40 ppm. Finally, the QSM map was shifted to absolute X_{mean_brain} and compared with predefined susceptibility, for gradually increased source values.

A Gd-doped phantom and two external cylinders were scanned at 3 T (Aera, Siemens Healthcare, Erlangen, Germany), using a 3D multi-echo GRE: voxel size = $1 \times 1 \times 1$ mm^3, TE1/ΔTE/TR = 3.65/5.8/37 ms, #TEs = 6, FA = 15°, matrix $224 \times 222 \times 208$. QSM calculation and absolute X_{mean_brain} assessment were performed as above, and shifted QSM was compared with the theoretical susceptibility, $X_{true} = 0.25$ ppm.

Results: The disconnection of numerical QSM values, occurring for spatially separated objects, is visualized in Fig. 3. The simulation-based numerical brain validation showed excellent agreement between shifted QSM and ground truth susceptibility maps (Fig. 4). For the scanned phantom, a mean of 44 ROIs (11 slices/4 ROI sizes) yielded $X_{mean\_brain} = 2.5 \pm 1.4$ ppm. A ROI in a central slice of the phantom yielded $X_{mean\_brain} = 0.40$ ppm (vs. $X_{true} = 0.25$ ppm).

Discussion: Absolute susceptibility values are of considerable interest, but internal QSM references show limited robustness. The proposed approach using external references yielded excellent susceptibility agreement for simulated data. For the MRI phantom, X_{mean_brain} displayed considerable variability depending upon ROI selection in the external references. However, reasonable agreement could be seen for central ROI evaluation. The theoretical framework depends on highly accurate phase estimates and elimination of phase uncertainties A (Eqs. 1–2); minor phase errors substantially influence the estimated susceptibility. Extended TE range, increased field strength, and re-positioned external cylinders could potentially improve results. Future experimental investigations will include optimized design and positioning of the external references.

Conclusion External references and a simulated phase-susceptibility relationship facilitate absolute QSM estimates in simulated data. Application to experimental data is not fully optimized.

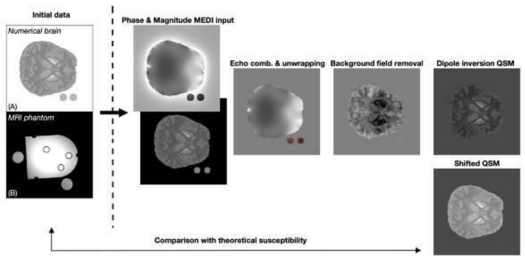

Fig. 1: Flow chart with initial (A) numerical brain or (B) MRI phantom data, for input to MEDI. Φ_{tot_cyl} is measured in ROIs marked in red. Obtained QSM map is shifted to estimated absolute X_{mean_brain} before comparison with theoretical susceptibility. Note: The process shows initial data for case A.

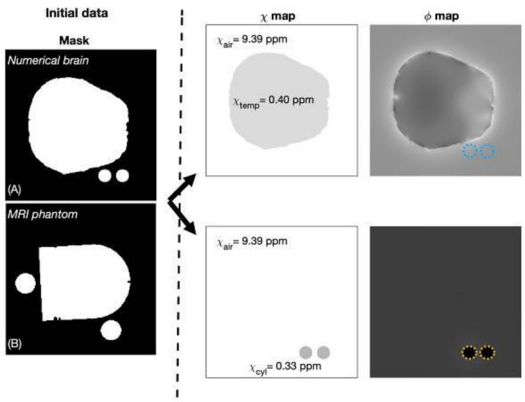

Fig. 2: Flow chart with an initial mask of the specific geometry. Phase maps are simulated from defined susceptibility maps. Phase values in ROIs marked in blue and orange are used to predict F-factors and Φ_{int_cyl}, respectively. Note: The process shows initial data for case A.

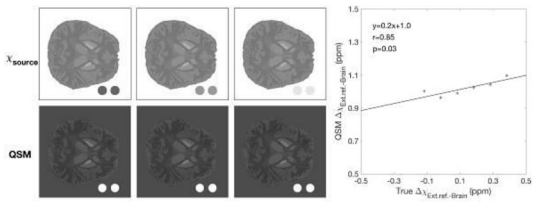

Fig. 3: Gradually increasing true susceptibility (range 0.1-0.6 ppm) in the external cylinders (top row). The susceptibility difference is not preserved after QSM reconstruction (bottom row).

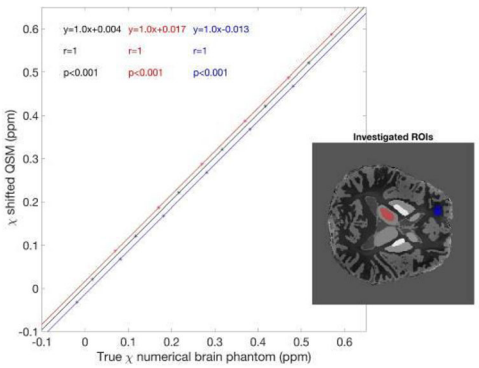

Fig. 4: Shifted QSM estimates versus true susceptibility of the numerical brain phantom, comparing the mean susceptibility of one slice (black) and tissue ROIs (red and blue). All data are shifted according to X_{water}=0 ppm.

References

1. Marques & Bowtell, Concepts Magn Reson B, 2005:**25B,**65–78
2. Salomir et al., Concepts Magn Reson B, 2003:**19B,**26–34
3. de Rochefort et al., MRM, 2010:**63,**194–206
4. Conturo et al., MRM, 1992:**27,**375–90
5. Langkammer et al., Neuroimage, 2015:**111**,622–30
6. Liu et al., Neuroimage, 2012:**59,**2560–8
7. Liu et al., MRM, 2011:**66,**777–83
8. Liu et al., MRM, 2013:**69,**467–76
9. Zhou et al., NMR Biomed, 2014:**27,**312–9

P224.
Estimating the macromolecular proton fraction and the magnetization transfer exchange rate in human brain by inversion recovery with off-resonance saturation

N. Wallstein[1], A. Pampel[1], H. Möller[1]

[1]*Max Planck Institute for Human Cognitive and Brain Sciences, NMR group, Leipzig, Germany*

Introduction: Magnetization transfer (MT) between protons of free water and those bound to macromolecules (semi-solid pool) is used extensively to obtain (indirect) information on tissue composition [1]. A quantitative characterization of this exchange process, which is due to cross-relaxation or chemical exchange, is of particular interest in studies of white matter. However, nonlinear fitting of the typically assumed binary spin bath (BSB) MT model [2] or its extension to include a dipolar reservoir (in investigations of inhomogeneous MT, ihMT [2]) suffers from parameter correlations.

Here, we try to disentangle some of the correlations by using a transient approach, where an inversion-recovery (IR) experiment was combined with different preparation strategies. Compared to similar recent approaches [3, 4], the method was extended by inserting off-resonant pulses before and/or during the inversion time (TI) for improved access to some MT parameters [5].

Methods: Data was acquired at 3 T (MAGNETOM Prisma^{fit}, Siemens). As a model system, ProLipid 161 (PL-161; Ashland) was dissolved in 0.135 mM $MnCl_2$ solution and investigated in a 5 mm NMR tube at ~22 °C using a custom-made Helmholtz coil. An IR sequence (180° and 90° hard pulses; 23 inversion times (TI), logarithmically distributed between 770 ms and 10 s, TR 14 s) without spatial resolution was combined with a flexible sequence building block (sat-SBB) that enables (off-)resonant RF pulse applications (4 ms Gaussian) for MT or ihMT preparation. *In-vivo* experiments were performed with a 32-channel head coil in a healthy male volunteer. The same IR preparation and sat-SBB as in the phantom study were implemented in a single-voxel spectroscopy sequence (PRESS; TE 30 ms, VOI 7 × 7 × 7mm^3) to achieve a high SNR. Four distinct experiments were combined (Fig. 1):

1. *MT-off*: no sat-SBB
2. *MT-prep*: sat-SBB before inversion (60 pulses, 250 µs inter-pulse delay, 300 or 500 Hz, offset 7 or 9 kHz)
3. *MT-evo*: sat-SBB during TI (1.75 ms inter-pulse delay, 125 Hz, offset: 7 kHz)
4. *MT-prep + evo*: sat-SBB before inversion (60 pulses) and during TI (3.25 ms inter-pulse delay, 100 Hz, offset 7 or 8 kHz)

The above frequency offsets refer to either single-sided (positive offset) or dual-sided irradiation (performed with alternating offset sign or cosine modulation of the Gaussian pulses).

Five BSB model parameters were fitted to the data, including the longitudinal relaxation rates (R_1^a,R_1^b), exchange rate (k), pool-size fraction (f) and R_2^b describing off-resonant absorption by the semi-solid pool. Two further parameters accounted for deviations of the amplitude (i.e., reduced inversion efficiency) and partial on-resonance saturation of the semi-solid pool by the inversion pulse. The additional dipolar reservoir was considered by integrating the dipolar relaxation time T_1^D and effective coupling strength ω^D.

Results & Discussion: PL-161 is often used for generating contrast between single- and dual-sided saturation due to dipolar couplings (ihMT). This difference is particularly obvious at short inversion times in the data recorded with saturation before the inversion pulse (Fig. 2). Remarkably, the analysis of the four saturation modes suggests a high quality of all fits for separate analyses of the two preparation strategies (dual- or single-sided), for the standard BSB model and with an additional dipolar reservoir. Excellent fits were also obtained with simultaneous fitting of the combined data of dual- and single-sided saturation when considering a dipolar reservoir but could not be produced with the standard BSB model. This underlines the need to expand the standard BSB model by a dipolar reservoir for extracting a meaningful parameter set in experiments with PL-161.

In the *in-vivo* measurements, dual-sided saturation was limited to alternating offsets (positive/negative) due to SAR constraints. A strong difference compared to single-sided saturation was not evident in this case (Fig. 3). Therefore, BSB-model fitting with and without a dipolar reservoir yielded approximately the same model parameters, suggesting that a simpler model with fewer parameters might suffice in many cases. The results further show that R_1^b substantially exceeds R_1^a ($\approx$3.0 vs. 0.6 s^{-1}), in contrast to often used assumptions of $R_1^b \approx R_1^a$ or $R_1^b \approx$ s^{-1} [6] in analyses of MT experiments (Fig. 4).

Conclusion Despite remaining correlations (Fig. 4) between certain model parameters, our approach yields reasonable estimates for parameters, such as R_1^b, which are routinely set to fixed values that may deviate from their true values. This may have implications for the other BSB model parameters, especially for the estimation of the macromolecular fraction or exchange rate [2].

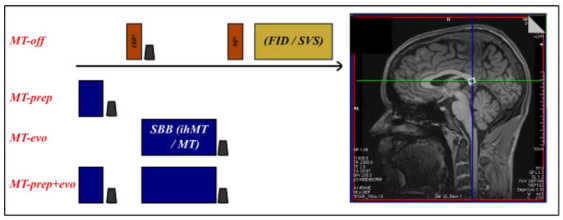

Fig. 1: Diagram (left) illustrating the four sequence types. The readout was an FID for experiments with PL-161. *In-vivo*, the 90° readout pulse was replaced by a PRESS sequence selecting a voxel in the splenium in the corpus callosum (right). Blue boxes indicate the sat-SBB. Gray trapezoids indicate spoiler gradients.

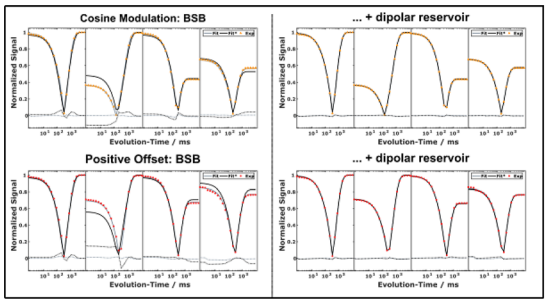

Fig. 2: Experiments in PL-161 (integrated magnitude around peak position (±10 Hz), normalized to max) obtained with (from left to right) *MT-off*, *MT-prep*, *MT-evo*, and *MT-prep+evo*. Top row: dual-sided sat., bottom row: single-sided sat.; left: BSB, right: BSB + dipolar reservoir. Grey and black solid lines show results from separate and simultaneous fits of the dual- and single-sided sat. schemes, respectively.

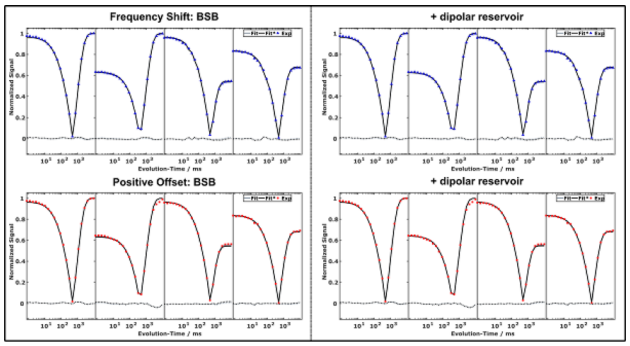

Fig. 3: Similar results as in Fig.2 obtained *in-vivo*.

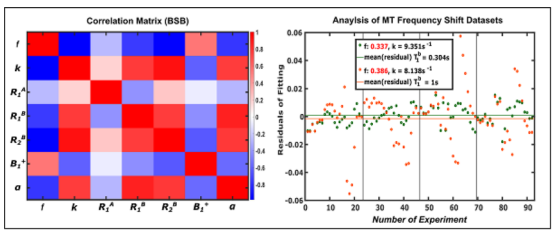

Fig. 4: Left: Correlation matrix for joint fitting of all four measurements modes. Right: Residuals for the same analysis with R_1^b as a free parameter compared to results obtained with fixed R_1^b=1s^{-1}.

References

[1] Morrison et al., JMR B 1995;108(2):103–113.
[2] Manning et al., JMR 2017;274:125–136.
[3] Manning et al., JMR 2021;323:106,909.
[4] Van Gelderen et al., MRM 2017;77(6):2174–2185.
[5] Calucci et al., Prog NMR Spectr 2009;55(4):296–323.

P225.
Quantitative water content mapping by MRI for post-mortem edema characterization

A. M. Oros-Peusquens[1], M. Bauer[2], C. Lenz[2], E. Scheurer[2], N. J. Shah[3,4,1]

[1]*Research Centre Juelich, Institute of Neuroscience and Medicine 11, INM-11, JARA, Jülich, Germany;*
[2]*University of Basel, Institute of Forensic Medicine, Basel, Switzerland;*
[3]*RWTH Aachen University, Department of Neurology, Aachen, Germany;*
[4]*RWTH Aachen University, JARA – BRAIN – Translational Medicine, Aachen, Germany*

Introduction: Brain edema is a pathological change in the living central nervous system that occurs frequently and is important for characterization of the cause of death. Characterizing it post mortem at autopsy is difficult by subsequent changes in brain water content, such as edema accompanying global ischemia at death [1], and post mortem fluid redistribution due to tissue decomposition [2]. The edema assessment using macroscopic pressure signs during autopsies is subjective and observer dependent, but remains the gold standard since correlations with more objective criteria, like wet-dry measurements of tissue samples or histology, were shown to be poor [3]. Imaging modalities are increasingly used preceding and complementing autopsy. Whole-brain water content mapping by MRI offers the advantage of describing local as well as global changes and possibly guiding autopsy. We report first results of an exploratory study of in situ water content mapping by MRI.

Materials and methods: Four cases were included with details given in Table 1.

A fast, single-scan based water content and T2* mapping method [4] was implemented using a multi-echo GRE sequence based on the protocol described in [5]. A combination of long TR (5 s) and low flip angle (25o) are chosen to avoid T1 saturation effects in tissue, complemented by T2* fitting of the signal decay and extrapolation to TE = 0. The combined transmit and receive B1 inhomogeneity, which is a multiplicative factor in this method, is corrected by SPM []. Conversion from signal intensity to water content, expressed as volume % in each voxel, is based on internal calibration using CSF signal (assigned 100% water content).

Results Masks for WM, GM and CSF were produced from SPM tissue class probabilities above 99% and used to determine the normalization value for water content (CSF) and distributions for WM and GM. A brain mask was obtained by summing the 3 tissue class probabilities; a brain tissue mask excluded voxels with probability > 50% of being CSF.

Water content and T2* maps are shown in Figs. 1 and 2 for a representative slice of each case, together with brain and tissue class histograms. The values are summarized in Table 1.

Discussion: Water content is known to be highly regulated in the healthy living brain [4], but was found in this study to be more variable post mortem. Mean GM water content of 88.3% is significantly higher than in vivo (83% [4]) while mean WM water was comparable to that in vivo (70.2% [4]) but slightly higher for two cases (72.7%). The values are consistent with wet-dry measurements [3]. T2* was in all cases shorter than in vivo ($\sim$ 42 ms compared to $\sim$ 52 ms [4]), most likely due to the high concentration of deoxyhemoglobin in blood vessels. The correlation between T2* and water content was low in GM but high in WM (Fig. 3a), the latter being also found for edema in vivo [4]. Only one (#2) of the two cases showing elevated WM water content and T2* was declared edematous by the forensic pathologists; the other (#3) might show advanced signs of decay due to delayed beginning of cooling after death. The

details of the water content distribution are markedly different in the two cases (Fig. 1), and case #2 shows deviations in the correlation between tissue water weight determined by MRI and brain weight at autopsy (Fig. 2b).

T1 saturation effects both in tissue and CSF will depend on temperature [6], but remain negligible for the parameters and the range of temperatures used here, as shown by unchanged signal intensity when TR was increased from 5 to 10 s.

A tacit assumption of the method is that water density as well as its temperature dependence is the same for water in tissue and CSF.

Interestingly, a logarithmic change in the radiodensity (Hounsfield units) of CSF with postmortem interval was reported [7, 8], indicating increasing volume percentage of solutes with increasing PMI, thus possibly the water content of CSF might also measurably change. Use of an external standard with monitored temperature might be better suited for water content calibration in situ than CSF and will be explored in the future. This can also allow monitoring changes in water content of CSF with PMI.

Conclusions: Post mortem in situ water content mapping by MRI with whole brain coverage looks promising, but more cases are needed for reliable conclusions. The simplicity of the method and short measurement time facilitate the inclusion of this measurement whenever post mortem MRI is used.

Parameter	Case 1	Case 2	Case 3	Case 4
	(22_543)	(22_298)	(22_166)	(22_369)
Gender	F	M	F	F
Age [yo]	35	80	82	65
Height [cm]	151	172	156	160
Weight [kg]	70	64	51	55
Brain weight [g]	1030	1530	1150	1290
Cause of death	chronic liver failure	central regulatory failure (hanging)	heart failure	Pneumonia w. heart failure
PMI [h]	36	31.5	42.5-51.5	27.5
Storage time [h]	25.5	25.5	35.25	22.5
Core temperature [°C]	12.5	11.2	6.9	12.1
Brain edema	no	yes	no	no
H_2O WM [vol %]	71.1 (6.5)	72.4 (5.9)	72.9(7.1)	70.2(8.7)
H_2O GM [vol %]	90.0 (8.7)	88.3 (6.8)	88.4(5.8)	86.7(8.4)
H_2O tissue [vol %]	84.0(9.0)	84.5(8.5)	84.1(7.6)	81.7(8.3)
Brain tissue vol [cm^3]	935.4	1460.3	1002.7	1167.7
Water density [g/cm^3]	0.999443	0.999582	0.999909	0.999489
Tissue water weight [g]	785.3	1233.4	843.2	953.5
T_2* WM [ms]	40.7(12.4)	43.0(14.8)	43.8(15.2)	37(17.1)
T_2* GM [ms]	44.0 (24.6)	44.3(19.3)	44.2(20.1)	42.0(21.6)
T_2* tissue [ms]	41.9(12.6)	43.9(12.5)	45.4(13.3)	41.1(13.8)

Table 1: Demographics and qMRI values of the 4 cases investigated.

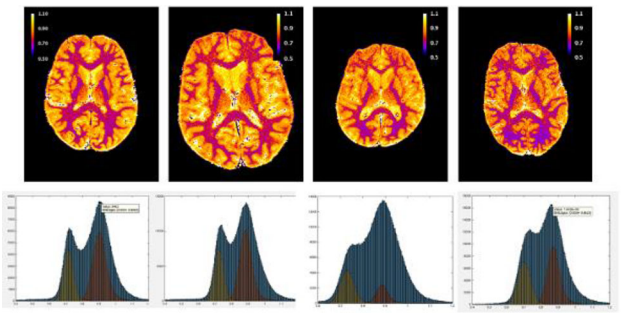

Fig. 1: Exemplary water content maps and whole-brain histograms.

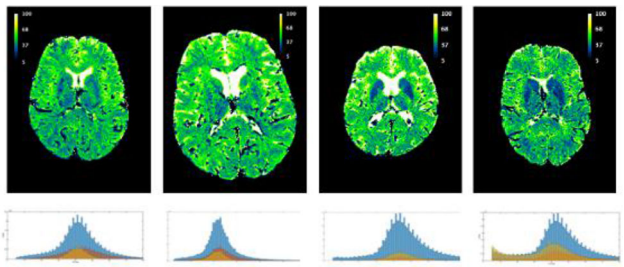

Fig. 2: Exemplary T2* maps and whole-brain histograms.

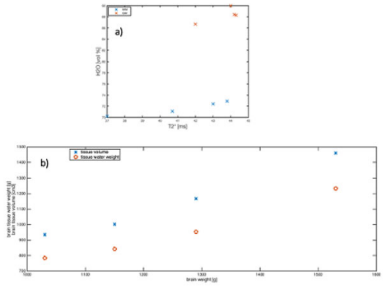

Fig. 3: a) Correlation between water content and T2* for WM and GM. The correlation is more pronounced in WM. b) Correlation between water weight in brain tissue, determined by MRI, and brain weight determined at autopsy.

[1] https://www.ncbi.nlm.nih.gov/pmc/articles/PMC1913020/
[2] https://pubmed.ncbi.nlm.nih.gov/7860007/
[3] https://doi.org/10.1016/j.forsciint.2021.110808.
[4] https://doi.org/10.3389/fneur.2019.01333
[5] https://doi.org/10.1016/j.ymeth.2017.07.025
[6] https://doi.org/10.1515/bmt-2013-4290
[7] https://doi.org/10.1007/s00414-016-1327-2
[8] https://doi.org/10.1007/s00414-021-02698-6

Table 1: Demographics and qMRI values of the 4 cases investigated. MR scanning was performed on a Siemens 3 T PRISMA using body coil transmit and a 20 channel receiver coil array. The scanning parameters included: TR = 5 s, flip = 25o, TE1 = 3.47 ms, dTE = 3.68 ms, 84 slices, 1.5 mm thick, in-plane resolution 1 × 1 mm, TA = 6 min:20 s. For #3 and #4 an additional acquisition with TR = 10 s and flip = 25o was included.

P226.
Evaluation of different approaches to plan radiotherapy with MRI-based proton density quantification

L. Sayaque[1], B. Leporq[1], F. Pilleul[1,2], V. Gregoire[3], O. Beuf.[1]

[1]*Univ Lyon, INSA-Lyon, Universitéʹ Claude Bernard Lyon 1, UJM-Saint Etienne, CNRS, Inserm, CREATIS UMR 5220, U1294, F-69,100, Villeurbanne, France;*
[2]*CLRCC Léon Bérard, Radiologie, Lyon, France;*
[3]*CRLCC Léon Bérard, Radiothérapie, Lyon, France*

Introduction: The treatment adaptation to each patient has led to the consideration of using MR imaging for radiotherapy (RT) planning, due to its capacity to produce high-contrasted images, a better organ at risk (OAR) delineation and quantitative information on the tissues. The main difficulty is the indirect link between MRI and electronic density maps, which are necessary for dose calculation.

To overcome this difficulty, two approaches allow to build a synthetic CT: statistical methods based on bulk density assignment[1], atlas

registration[2], or deep learning[3]; physical methods based on quantitative MRI such as proton density (PD) quantification[4].

Studies[4,5] show that the electronic density can be linked to the hydrogen content of the tissues: its mass stopping power and mass attenuation coefficients are more significant than the other atoms between 0.2 and 8 MeV[4], the knowledge of the hydrogen content of the tissues could be a solution for RT planification. PD is a physical property which can be accessible with specific MRI sequences.

We focuse on head and neck tumors, which require a large field of view in the coronal plane, about 500 mm from the top of the head to the upper part of the humerus. This area has not been clinically validated, unlike brain and pelvis. The numerous OARs (brainstem, optics nerves…) make it a challenging area.

This paper describes a preliminary study on a PD quantification method for head and neck cancers.

Methods: From the magnetization at the origin, PD can be measured with the following equation: $M\_0(x,y,z) = G(x,y,z)°PD(x,y,z)$, with G the coils sensitivity maps.

First, we have constituted a phantom with different concentrations of D2O (ranging from 0 to 80%) in H2O saline solutionmimicking different proton concentrations to measure the relationship between theoretical and experimental PD, see Fig. 1, the other tubes are filled with fat. Second, a 3D Spiral VIBE UTE sequence acquired on a Siemens 3 T Vida (Siemens Healthineers, Germany), with an ultrashort echo time (30 µs) has been used to reach. This sequence has a TR of 3.12 ms and a flip angle of 5°. The echo time is short enough to assume that $S(UTE) \sim M\_0$.

To retrieve the coils sensitivity maps, we evaluated different algorithms: SENSE[6], ESPIRIT[7] and adaptive reconstruction (AR)[8]. Tests on the phantom were performed with different coils setups: Head and neck only, Body only and lower part of Head and neck + Body, which is the configuration we want to use for a protocol on patients with a contention mask. Linear regressions were computed between the tube"s intensities corrected from coils sensitivities and the theoretical value of PD. On-line coil sensitivity correction methods available on our MR system, "Prescan" and "B1-filter", were also evaluated to directly estimate. The phantom was also scanned in the CT scanner for different energies.

Results: The linear determination coefficients of the regressions with the different filters and for the CT images are presented in Fig. 2. Examples of regressions are given Fig. 3.

With a 32 Go RAM, INTEL I7, 2.50 GHz processor personal computer, the computation time for SENSE algorithm was 1 min, 13 min 20 s for ESPIRiT and 2 min for AR.

Discussion: Results show that the spiral VIBE UTE sequence allows to obtain a linear relationship between theoretical PD and MRI signal which is, as expected, better after coil sensitivity correction. The three algorithms used to estimate coils sensitivities provide satisfying results, the MRI filters give even better results. The Head and neck coil only configuration gives the best results, as excepted. The results for the coil configuration of the protocol are a bit worse but sill satisfying. The results of the CT images confirm that there is a relationship between PD content and the Hounsfield Unit values of the CT, which are linked to the electronic density.

Conclusion: Our work demonstrated that MRI could be used for PD quantification in head and neck region, and that PD can be linked to the Hounsfield Unit.

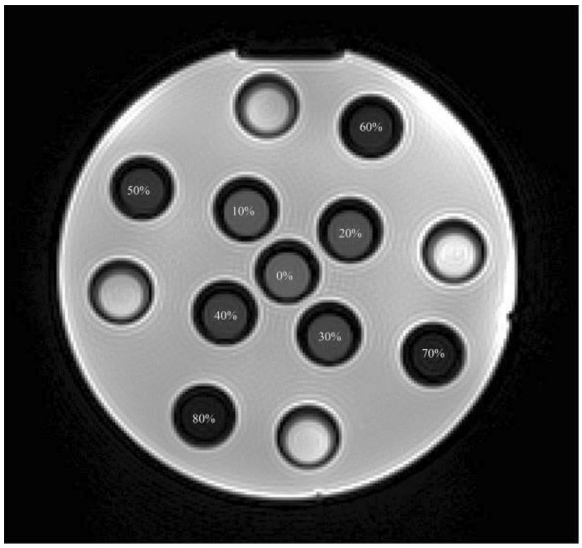

Fig. 1: Phantom concentrations of the percentage is written on the tubes, completed with volumes of in order to measure the relationship between theoretical and experimental proton densities

R^2	Raw image	SENSE	RA	ESPIRIT	B1 faible	B1 moyen	B1 élevé	Prescan modéré	Prescan normal	Prescan large bande
Head	90,9	94,2	93,6	91,9	97,9	97,5	94,5	98,3	98,9	98,9
Body	66,9	66,0	63,9	27,0	97,3	97,0	93,6	93,7	97,2	97,3
Head lower part + body	87,2	90,2	90,6	82,8	98,6	98,4	96,1	96,7	98,8	98,5
R^2	40 keV	45 keV	50 keV	55 keV	70 keV	100 keV	120 keV	140 keV		
CT	83,3	84,6	85,5	86,2	87,0	90,4	94,7	87,7		

Fig. 2: Linear determination coefficients of the linear regressions with the different filters and for the CT images

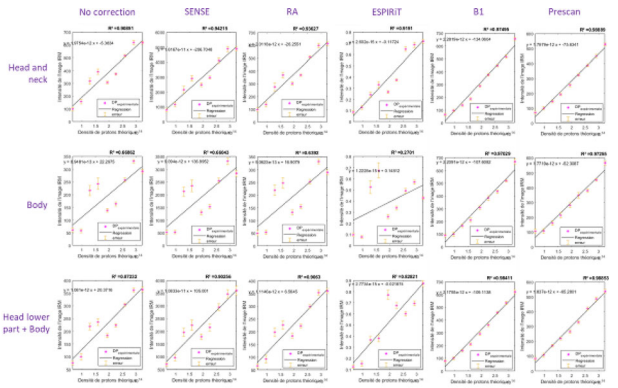

Fig. 3: Example of linear regression for several algorithms

References

1. Largent « Planification à partir d"imagerie par résonance magnétique en radiothérapie» Cancer/Radiothérapie
2. Vanquin « Planification de la radiothérapie du cancer de la prostate par l"imagerie par résonance magnétique» Cancer/Radiothérapie
3. Kazemifar « Dosimetric evaluation of synthetic CT generated with GANs for MRI-only proton therapy treatment planning of brain tumors» Applied Clinical Medical Physics
4. Demol « Monte Carlo calculation based on hydrogen composition of the tissue for MV photon radiotherapy» Applied Clinical Medical Physics

5. Mezer « Evaluating Quantitative Proton-Density-Mapping Methods» Human Brain Mapping
6. https://users.fmrib.ox.ac.uk/∼mchiew/docs/SENSE_tutorial.html
7. Uecker « ESPIRiT — An Eigenvalue Approach to Autocalibrating Parallel MRI: Where SENSE meets GRAPPA» Magnetic resonance in medicine
8. Walsh « Adaptive reconstruction of phased array MR imagery» Magnetic Resonance in Medicine

P227.
Background phase in phase-contrast MRI revisited: Temporal response due to steady-state perturbations

C. Fischer[1,2], P. Speier[1], T. Schaeffter[2,3,4], D. Giese[1,5]

[1]*Siemens Healthcare GmbH, Magnetic Resonance, Erlangen, Germany;*
[2]*Technical University of Berlin, Medical Imaging, Berlin, Germany;*
[3]*King's College London, School of Imaging Sciences and Biomedical Engineering, London, United Kingdom;*
[4]*Physikalisch-Technische Bundesanstalt (PTB), Braunschweig and Berlin, Germany;*
[5]*Friedrich-Alexander-Universität Erlangen-Nürnberg (FAU), Institute of Radiology, Erlangen, Germany*

Introduction: Phase-contrast MRI (PC-MRI) is useful for deriving a wide range of hemodynamic parameters. PC-MRI commonly utilizes gradient and RF spoiled gradient echo steady state sequences (FLASH) and alternates between flow compensated and flow encoded gradients every TR (TR-interleaved).[1] Using only gradient spoiling (FISP) might be useful to increase SNR for vessels with low flow velocities or high-resolution 4D flow. Although both spoiling strategies' effect on signal strength and contrast has been investigated[2], their influence on flow quantification remains to be fully understood. Furthermore, the temporal footprint can be reduced by alternating every ECG cycle (Beat-interleaved), potentially being needed in acquisitions with several flow encoding steps (e.g., in multi-venc imaging[3]).
PC-MRI remains hampered by spatially varying background phase offsets from the alternating gradients mainly due to concomitant fields[4] and eddy currents[5]. The latter are typically corrected by either stationary phantom scans[6] or by extrapolation based on stationary tissue fits[7].
Although achieving a steady state requires constant dephasing before each RF pulse[8], this is violated due to the alternating gradients.
In this abstract, we investigated the steady state responses of background phases and their impact on flow quantification using TR- and Beat-interleaved PC-MRI with FISP and FLASH sequences.
Methods Acquisition: The research sequence is based on a prospectively triggered 2D through-plane PC-MRI sequence. Steady-state triggering is used and one k-space line / ECG cycle acquired. Figure 1a shows a Beat-interleaved acquisition.
Gradient spoiling induces a 2π dephasing in Read + Slice direction and RF spoiling is achieved via a quadratically increasing RF-phase of 50°.[8] All measurements were acquired at 1.5 T (MAGNETOM Sola, Siemens Healthcare GmbH) using an 18-channel knee-coil. Data was reconstructed offline without concomitant field correction.
The phantom has 9 cylinders of different T1-T2 values (Fig. 1b). We focused on 2 regions of interest (ROI) with T1/T2 values of 1489 ms/243 ms (blood-like) and 562 ms/45 ms (tissue-like). By exchanging both tubes, we investigate varying T1/T2 values at fixed locations (i.e., background phase). A simulated RR-Interval of 1115 ms was used.
ECG-triggered in-vivo data was acquired in the left popliteal artery of a healthy volunteer in accordance with institutional regulations. Background phase was estimated using a 2nd-order polynomial surface fit on stationary tissue. Background was fitted to either averages of the first or last 10, or all cardiac phases.
Figure 1c summarizes acquisition details.
Simulation: Bloch simulations including background phase changes, varying spoiling schemes and non-optimal slice profiles were used. Relaxation times, flip angle, repetition times and background phase difference were matched with scanner measurements and tissue properties.
Results: Fig. 2a shows simulated phase evolutions of both ROIs during four ECG cycles of a Beat-interleaved FISP acquisition. The corresponding PC-MRI shows temporally varying background phases throughout the cardiac cycle. This was confirmed in phantom FISP (Fig. 2b) and FLASH (Fig. 2c) acquisitions. We observed stronger effects for longer T1/T2 values and position dependent responses (Fig. 2b-c), in-line with simulation.
The effect is also observed in-vivo, where temporal phase variations affect background phase corrections, mostly for Beat-interleaved FISP imaging (Fig. 3a-d). Comparing the fits of the first to last 10 heart phases, mean (maximum) absolute differences within the tissue masks are 1.4(3.4)cm/s for Beat/FISP, reduced to 0.16(0.22)cm/s for Beat/FLASH and below 0.06(0.15)cm/s for TR-interleaved sequences.
Discussion: Theory predicts time- and tissue-dependent background phase to Beat-interleaved flow acquisitions due to switching of background phase offsets. This behavior was observed in phantom and in vivo scans. Figure 2a-c show that short steady state trigger windows before the next acquisition window do not suffice to recover steady states in Beat-interleaved acquisitions leading to tissue-dependent varying background phase throughout the heart cycle. Measurements confirm that fits are temporally more robust for the Beat-interleaved FLASH and TR-interleaved sequences.
Conclusion: A Beat-interleaved FISP sequence can lead to tissue-dependent temporal steady state responses of background phase offsets. This could restrict the utility of typical phase correction methods. The effect is minimized by using RF spoiling. Longer steady state trigger windows could be used. Phantom based correction methods likely benefit from short relaxation times, while in vivo methods would profit from excluding early cardiac phases.

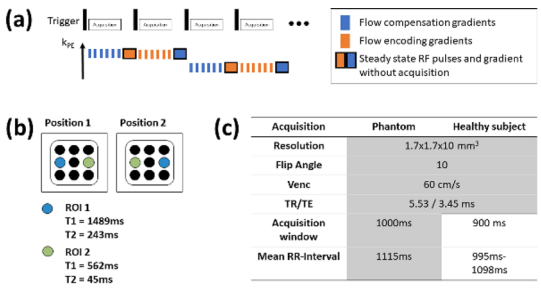

Fig. 1: (a) Beat-interleaved encoding: Gradients alternate with each cardiac cycle. After acquisition is finished, the steady state trigger switches for the next RR-interval. **(b)** Phantom acquisitions setup with marked ROIs; **(c)** Imaging parameters of phantom and in vivo acquisition

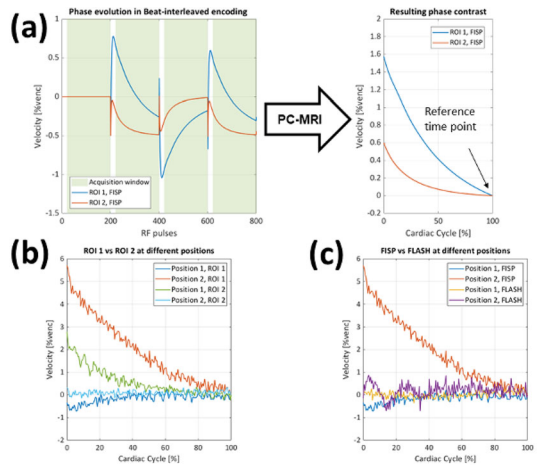

Fig. 2: **(a)** Simulation of Beat-interleaved FISP with acquisition windows, steady state trigger in between and -0.5%venc background offsets. Resulting phase contrast (phase difference of two consecutive acquisition windows with respect to last cardiac phase) is affected by the steady state perturbation. **(b)** Pixel averaged phase response of ROI 1&2 at positions 1&2 with respect to last cardiac phase to FISP. Effect is stronger for ROI 1. **(c)** Analog comparison of FISP&FLASH in ROI 1. Effect is stronger at Position 2.

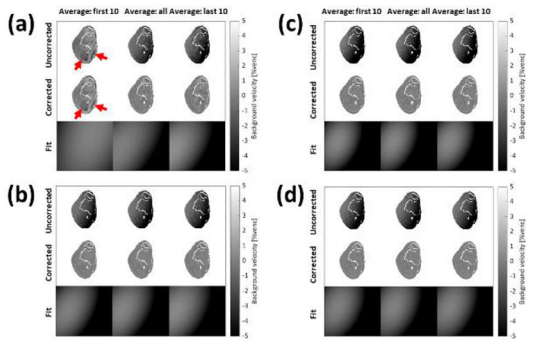

Fig. 3: Background correction based on average of first 10, all or last 10 cardiac phases for different setups; **(a)** Beat/FISP; arrows show tissue-dependence **(b)** Beat/FLASH; **(c)** TR/FISP; **(d)** TR/FLASH

References

[1]Pelc, Magn Res Quart. 1991;
[2]Moersdorf, MRI. 2019;
[3]Bernstein, MRM. 1998;
[4]Gatehouse, JCMR. 2010;
[5]Caprihan, JMR. 1990;
[6]Walker, JMRI. 1993;
[7]Scheffler, Conc Magn Res. 1999

P228.
Shared genetic architecture between tobacco smoking and iron concentration in the brain's striatum

O. Trofimova[1], S. Bergmann[1]

[1]*University of Lausanne, Department of Computational Biology, Lausanne, Switzerland*

Introduction: Tobacco smoking is a major modifiable risk factor for cardiovascular and lung diseases. Better understanding its neurobiological underpinnings will benefit the prevention of smoking-related illnesses and mortality. Recent neuroimaging studies have identified a correlation between smoking and iron concentration in the brain's striatum, a sub-cortical region involved in habit formation and compulsive behaviour, and a central node of dopamine activity [1–3]. Moreover, iron accumulation in the striatum is associated with lower cognitive performance in adults [4].

Methods: Here we investigated phenotypic and genetic correlations and causal relationships, between smoking initiation (ever smoked regularly) and susceptibility-weighted magnetic resonance imaging-derived markers of iron content – T2* and quantitative susceptibility mapping (QSM) – in the bilateral putamen, caudate, and accumbens nuclei. We computed partial correlations between smoking and striatum iron in the UK Biobank, adjusting for age, age^2, and sex. Using larger genome-wide association studies (GWAS) summary statistics [3, 5, 6], we performed linkage disequilibrium score regression (LDSC) [7], cross-GWAS coherence tests at the gene level (PascalX) [8], and causality analysis using Mendelian randomization [9].

Results: Having ever smoked was positively correlated with iron content in the bilateral putamen and caudate, and in the left accumbens (Fig. 1, diamond-shaped markers). LDSC genetic correlation paralleled phenotypic correlation but with larger confidence intervals (Fig. 1, circles). Cross-GWAS signal was coherent in genes involved in glucose transport (SLC45A1), synaptic plasticity and myelination (NCAM1), and dopamine activity (DRD2, PPP1R1B) among others (Fig. 2). There was no evidence of causal relationship in either direction.

Discussion: We replicated the previously reported positive correlation between smoking and striatum iron content, and found a corresponding genetic correlation. Underlying genes code for inter-neuronal communication and dopamine activity modulation, highlighting the role of iron in the nigrostriatal dopaminergic pathway presumably activated during smoking. However, the absence of evidence for causal relationships precludes simple unidirectional interpretation of our results. The left-ward asymmetry found in the nucleus accumbens can be interpreted in the light of disrupted accumbens volume asymmetry reported in alcohol- and nicotine-dependent individuals in a recent multi-cohort study [10].

Conclusion: Our results suggest a common biological mechanism between tobacco smoking and iron concentration in the striatum, that could function as a reinforcing feedback loop rather than a one-way causal sequence of events.

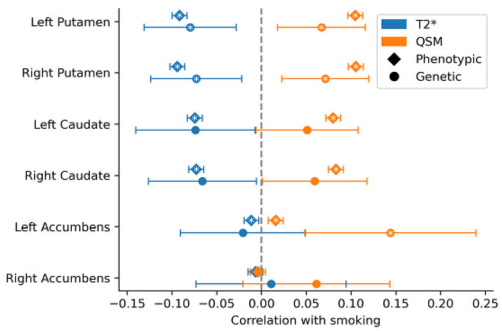

Fig. 1: Correlation coefficients between smoking (ever vs. never) and striatum iron. Diamonds represent phenotypic partial correlation adjusted for age, age^2, and sex, in the UK Biobank (n=37,725). Circles represent genetic correlation estimated with LDSC from separate GWAS summary statistics for smoking (n≈500,000) and striatum iron (n≈30,000). Lower T2* and higher QSM reflect higher iron content. Error bars represent 95% confidence intervals. Asterisks indicate significance at a 0.05 alpha threshold after false discovery rate correction.

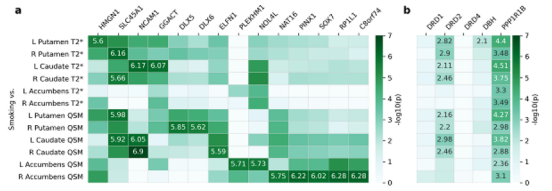

Fig. 2: Cross-GWAS coherence test between smoking and striatum iron performed using PascalX for **(a)** an exhaustive set of 18,344 genes and **(b)** five dopamine-related candidate genes. –Log10(p) values are annotated for Bonferroni-significant pairs, i.e. with p-values below **(a)** 2.73×10^{-6} (0.05/18,344 tested genes) and **(b)** 0.01 (0.05/5 candidate genes). We tested anti-coherence for T2* and coherence for QSM, consistent with correlation coefficient signs.

References

1. Miller, K. L. et al. Multimodal population brain imaging in the UK Biobank prospective epidemiological study. *Nat Neurosci* **19**, 1523–1536 (2016).
2. Trofimova, O. et al. Brain tissue properties link cardio-vascular risk factors, mood and cognitive performance in the CoLaus|PsyCoLaus epidemiological cohort. *Neurobiol Aging* **102**, 50–63 (2021).
3. Wang, C. et al. Phenotypic and genetic associations of quantitative magnetic susceptibility in UK Biobank brain imaging. *Nat Neurosci* **25**, 818–831 (2022).
4. Topiwala, A. et al. Associations between moderate alcohol consumption, brain iron, and cognition in UK Biobank participants: Observational and mendelian randomization analyses. *PLoS Med* **19**, e1004039 (2022).
5. Liu, M. et al. Association studies of up to 1.2 million individuals yield new insights into the genetic etiology of tobacco and alcohol use. *Nat Genet* **51**, 237–244 (2019).
6. Smith, S. M. et al. An expanded set of genome-wide association studies of brain imaging phenotypes in UK Biobank. *Nat Neurosci* **24**, 737–745 (2021).
7. Bulik-Sullivan, B. K. et al. LD Score regression distinguishes confounding from polygenicity in genome-wide association studies. *Nat Genet* **47**, 291–295 (2015).
8. Krefl, D. & Bergmann, S. Cross-GWAS coherence test at the gene and pathway level. *PLoS Comput Biol* **18**, e1010517 (2022).
9. Hemani, G. et al. The MR-Base platform supports systematic causal inference across the human phenome. *eLife* **7**, e34408 (2018).
10. Cao, Z. et al. Mapping cortical and subcortical asymmetries in substance dependence: Findings from the ENIGMA Addiction Working Group. *Addict Biol* **26**, (2021).

P229.
Optimal isochromat frequencies for T2* spin-level simulation

M. Á. Martín-Fernández[1], P. Irarrazaval[1,2], C. Castillo-Passi[2], C. Alberola-López[1]

[1]*University of Valladolid, Signal Theory, Communications and Telematic Engineering, Valladolid, Spain;*
[2]*Pontificia Universidad Católica de Chile, Electrical Engineering, Santiago de Chile, Chile*

Introduction: Simulation plays an important role in MRI development, research, and education [1], especially at the spin level, since this type of simulation captures more faithfully the physical phenomena. Some tissue parameters are well modeled and easy to simulate (i.e., the density and T2 or T1). But simulating T2* is particularly challenging because it depends on local micro variations of the magnetic field. To accurately represent T2* decay many isochromats per location are required, increasing the computational load. This is true for simulations in the "isochromat domain" or Bloch or spin-level simulations and for the "Fourier domain", such as Extended Phase Graphs. Here we only focus on spin-level simulations.

We propose a mechanism for optimally choosing the position, number, and frequency of the isochromats for obtaining a signal which represents well the T2* decay.

Methods: When the frequencies of the isochromats for a given location follow a Lorentzian distribution, the signal has an exponential decay with T2*. First, we propose an optimal sampling of this distribution to reduce the required number of isochromats. Secondly, we propose to jointly consider the sampling in space (typical to spin-level simulations) with the sampling in frequency (needed for T2* decay).

Frequency sampling We find how to sample the Lorentzian distribution to minimize the number of required spins. We choose M frequencies ω that best approximate the expected FID signal, S(t), by minimizing the Mean Square Error (MSE) between S(t) and Sω(t) at N time samples (N = 100 is enough).

We optimized only once for a fixed width of the Lorentzian distribution [2], and the M frequencies are scaled to find them for other widths.

Spatial dependence A typical simulation will use several spins located more densely than the expected resolution of the reconstruction. A direct solution for adding T2* decay would require locating M isochromats (with the frequencies found in the previous section) at each spin location. Here we experiment with the idea of using a different random subset of $L \leq J$ isochromat frequencies at each location. The rationale is that the values associated to the pixels will be obtained by some averaging, and therefore they will include information from many different frequencies.

We assume that the number of spins is J times larger than the expected number of pixels in each dimension. For each spin location we use L frequencies (in 2D, L·J2 spins per pixel). To simulate a generic sequence, for each time instant we average the signal by convolving it with a sinc function adapted to the pixel size. This filtered signal is then sampled at the pixel locations, and ρ and T2* are estimated: ρ as the value of the signal for t = 0, and T2* by fitting an exponential decay to the signal.

We did the simulations in 1D and 2D, employing known objects with different ρ and T2*. We tried different combinations of J (spatial positions) and L (frequencies). We computed the MSE and the relative MSE of the T2* values.

Results and discussion: Fig. 1 shows (left) the optimal 11 frequencies (up), the location of uniformly sampling the cumulative distribution function (Deterministic) with 11 (middle) and 21 frequencies (down). The simulated signal (right) for 11 optimized frequencies has a better fit than the deterministic 11 frequencies (MSE is 35%). For comparison, to obtain a similar fit, 21 deterministic frequencies would be needed.

Figure 2 shows a 1D phantom with the true ρ and T2* and the estimations from the simulation, showing a good match for a total of 44 isochromats per pixel.

Figure 3 shows the error in T2* for different J and L in the 1D phantom. As expected, the more isochromats used in the simulation the better the estimation of T2*. Interestingly, the error is relatively independent of how they are distributed between space and frequency. For this phantom (which has high discontinuities) an average of 33 isochromats per pixel gives errors of only 15%.

Figure 4 shows a 2D phantom, showing a good match for a total of 176 (4 × 4x11) isochromats per pixel. We also show the signal from the simulation (blue dots), the exponential fit (red line) and the theoretical decay (green line) and a profile for ρ and T2* fit.

Conclusions Our method reduces the number of the isochromats needed for obtaining a signal which represents well the T2* decay, better than a deterministic sampling of the Lorentzian distribution. The frequencies need to be computed only once for a given number of isochromats.

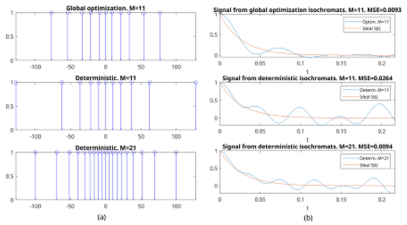

Fig. 1: (a) Isochromat frequencies, (b) Correspondent signal obtained (blue) compared with ideal FID signal (orange) for global optimization with M=11 (upper row), deterministic frequencies with M=11 (middle row) and M=21 (bottom row).

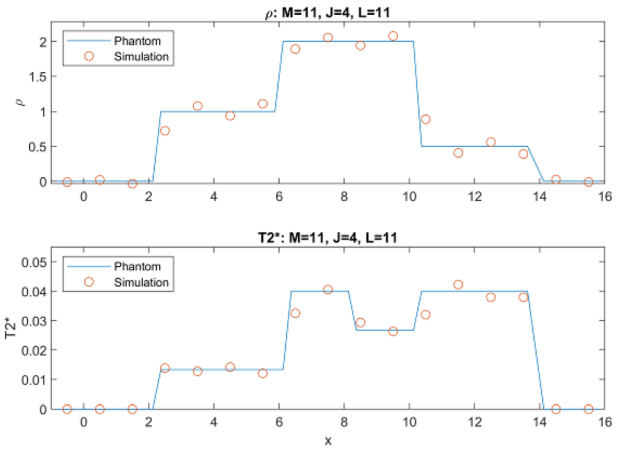

Fig. 2: 1D simulation with M=L=11, J=4. ρ and T2* phantom (blue line) and simulation (orange o).

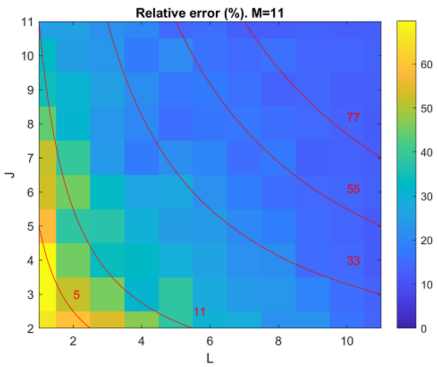

Fig. 3: T2* relative error in percentage between 1D phantom of Fig. 2 and simulation as a function of J and L for M=11. JL=C plotted for reference.

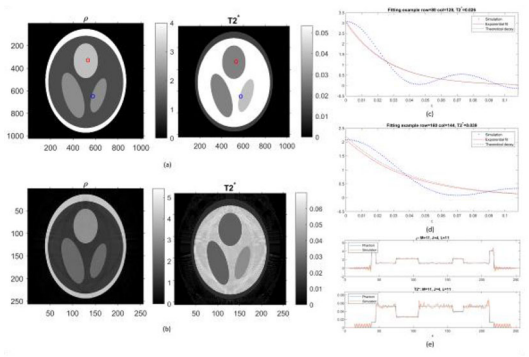

Fig. 4: 2D simulation in 2D. (a) ρ and T2* phantom with two singular points marked in red and blue; (b) Simulation; (c) Signal (blue line), fitting (red), and theoretical decay (black) for red point in (a); (d) Same for blue point in (a); (e) Profiles of ρ and T2* for the central row of the phantom.

References

[1] C. Castillo-Passi, R. Coronado, G. Varela-Mattatall, C. Alberola-López, R. Botnar, P. Irarrazaval. KomaMRI.jl: An Open-source Framework for General MRI Simulations with GPU acceleration. Magnetic Renonance in Medicine, 90(1):329–342, 2023.

[2] Z. Liang and P. Lauterbur. Principles of Magnetic Resonance Imaging: A Signal Processing Perspective. IEEE Press series in biomedical engineering. SPIE Optical Engineering Press, 2000.

P230.
Double flash: accelerated hemo-sensitive clinical measurement using double echo flash and reconstruction of the T_2 decay

A. Mennecke[1], A. L. Mayer[1], M. Zaiss[1,2,3], A. Dörfler[1], M. A. Schmidt[1]

[1]*Friedrich-Alexander-Universität Erlangen-Nürnberg (FAU), Neuroradiologisches Institut, Erlangen, Germany;*
[2]*Max-Planck-Institute for Biological Cybernetics, Magnetic Resonance Center, Tübingen, Germany;*
[3]*Friedrich-Alexander-Universität Erlangen-Nürnberg (FAU), Department Artificial Intelligence in Biomedical Engineering, Erlangen, Germany*

Introduction: The hemo-sensitive flash sequence[1] is a working horse in clinical MRI of intracerebral hemorrhage. Due to the higher susceptibility of blood, the dephasing of spins happens much faster within hemorrhagic lesions than in the surrounding tissue, which results in faster T_2^* relaxation and leads to a strong dark appearance of blood products when using sufficiently long echo times. Due to B_0 field blurring effects, those lesions appear even more prominent. This effect, called blooming, is actually an imaging artifact; however, it leads to a desirable clear distinction of even very small hemorrhages. An overall acceleration of MR imaging is favoured to reduce the patient's burden and to increase the capacity utilization of MR scanners. The shortening of acquisition times of hemo-sensitive flash sequences is not limited by technical restrictions like the minimal echo time but by the time necessary for the spins to de-phase and develop reasonable image contrast.

Here, we present a method to accelerate the hemo-sensitive flash measurement by acquiring a double echo flash ("double flash") with two shorter echo times and creating the hemo-sensitive contrast at longer echo times by calculating the T_2^* relaxation parameters from those two images.

Methods: Images were obtained using a sequence on a Magnetom^{TM} Vida 3 T (Siemens Healthineers, Erlangen, Germany) MR scanner

using a 1Tx/64Rx head and neck coil. The imaging parameters are listed in Table 1. Out of the two double echo images S_1 and S_2 at TE_1 = 5.92 ms and TE_2 = 11.08 ms, a virtual image S_3 at the echo time TE_3 = 19.8 ms of the standard clinical hemo-sensitive measurement was reconstructed using the equation of the T_2^* relaxation decay[2] in every single voxel (see Fig. 1 and 2). Due to noise and very slow T_2^* decay, $S_1 < S_2$ appeared in some single voxels of the cerebrospinal fluid regions, making Eq. (4) incomputable. In these cases ($<< 1\%$), the respective voxels were computed as the average of the surrounding ones. In addition, noise reduction was applied using Gaussian smoothing with filter size 3 and sigma 0.5.

Results: The acquisition of the double flash sequence is possible in 41 instead of 67 s, i.e. 39% reduction of acquisition time compared to the standard clinical measurement. The quality of the reconstructed image at TE_3 is comparable to the standard clinical hemo sequence (see Fig. 3).

Discussion: Using the double flash technique, the acquisition time of the hemo measurement could be reduced to two-thirds of the original measurement time without a significant reduction of image quality and with comparable contrast. The combination of both images leads to error propagation of noise and artifacts from both input images and makes the result slightly more prone to noise and artifacts. This is partly compensated by the higher signal-to-noise ratio of both input images compared to the image of the original hemo-sensitive measurement. Furthermore, using the principle of MR fingerprinting[3], the double flash technique can deliver additional information, like an image at every possible TE or the T_2^* relaxation time within every single voxel.

Conclusion: The acquisition time of the hemo-sensitive measurement in the brain can be reduced by 39% using the double flash method, while the contrast and overall image quality remain similar.

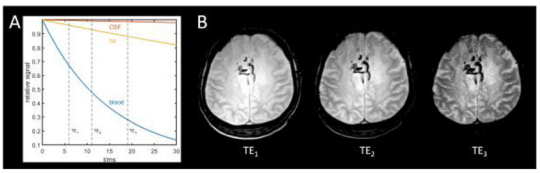

Fig. 1: A) Example of T_2^* decay for blood, fat and CSF. The three echo times TE_1 = 5.92 ms, TE_2 = 11.08 ms and TE_3 = 19.8 ms are marked by dashed lines. ***B)*** Corresponding transversal MR images at the three different echo times (TE_1 and TE_2 measured with double flash and TE_3 acquired with the original hemo-sensitive flash). At TE_3, hemorrhage is most prominent.

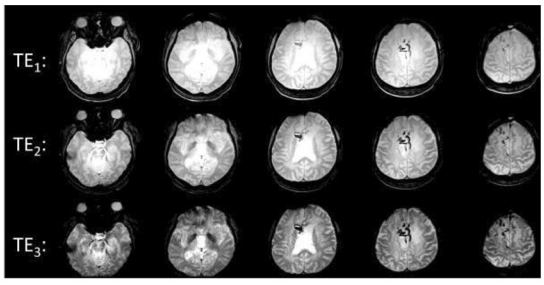

Fig. 2: Results of the double echo flash technique: hemo-sensitive transversal brain images measured at TE_1 = 5.92 ms and at TE_2 = 11.08 ms and calculated at TE_3 = 19.8 ms.

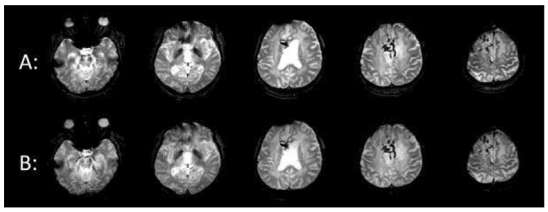

Fig. 3: A) Original standard clinical transversal measurement using TE_3 = 19.8 ms. ***B)*** Double flash reconstructed TE_3 out of double echo measurement at TE_1 = 5.92 ms and TE_2 = 11.08 ms. The quality and contrast of both images are comparable.

	Standard clinical hemo	Double flash
FoV, resolution	220 mm, 0.86 x 0.86 mm²	220 mm, 0.86 x 0.86 mm²
Matrix, slice thickness	256 x 256, 3 mm³	256 x 256, 3 mm³
TR	1070 ms	663 ms
TE_1 / TE_2	19.8 ms / -	5.92 ms / 11.08 ms
Flip angle (FA)	20°	20°
TA	1:07 min	0:41 min

Table 1: Imaging parameters for standard clinical hemo-sensitive measurements (hemo) and the proposed double flash method.

References

[1]Chavhan et al. (2009), RadioGraphics, https://doi.org/10.1148/rg.295095034

[2]Brown, Cheng, Haacke et al. (2014), John Wiley & Sons, Hoboken, New Jersey.

[3]Hsieh et al. (2020), Med Radiat Sci, https://doi.org/10.1002/jmrs.413

Table 1: Imaging parameters for standard clinical hemo-sensitive measurements (hemo) and the proposed double flash method.

P231.
Long-term follow-up of a LPC animal model using optimal control MRI contrast targeting short T2 components

C. Lemoine[1], T. Grenier[1], E. van Reeth[1], S. Gaillard[1], O. Beuf[1], F. Durand Dubief[1], F. Chauveau[2], H. Ratiney[1]

[1]Univ Lyon, INSA--Lyon, Université Claude Bernard Lyon 1, UJM-Saint Etienne, CNRS, Inserm, CREATIS UMR 5220, U1294, Villeurbanne, France;

[2]Centre de Recherche en Neurosciences de Lyon Inserm U1028, CNRS UMR5292,, Lyon, France

Introduction: This work studies, in a Multiple Sclerosis animal model with focal lesion, the behavior over time of a MRI contrast obtained with an optimized magnetization preparation designed with optimal control to obtain a hyperintensity signal from short T2 components which are associated with myelin. An advanced image analysis pipeline was developed to analyze this MRI contrast data and to compare it with histological myelin assessment.

Methods: *Animal Model* A total of 24 animals (adult female Sprague–Dawley rats) were used. Demyelination was induced in the right Corpus Callosum (CC) by stereotactically injecting 4 µl of 1% lysophosphatidylcholine (LPC) dissolved in saline [6]. This model produces controlled, focal demyelinating lesions. The rats were then scanned four times over the course of six months.

MRI acquisition and histological analysis MRI acquisitions were performed on an 11.7 T horizontal MRI system (Bruker Biospin MRI GmbH). In this study, 2 MRI contrasts were obtained according to the following sequences:1) a T2-weighted axial sequence (RARE: TR/

TE = 5500/64 ms, RARE factor = 8) noted T2w in the following. 2) a signal enhancement sequence of short T2 components obtained with optimized magnetization preparation pulses in front of a fast gradient echo sequence (MPRAGE) [5] (noted as OC). The magnetization preparation consisted in (90°)—(8.5 ms) – (180°)—(8.5 ms)—(-90°)—(646 ms) – which resulted in an optimized T2Prep-inversion recovery. (Fig. 1).

These 2 contrast images were acquired with the same field of view, slice thickness and resolution (8 slices of thickness 0.75 mm, resolution in the plane of 117 µm × 117 µm). 23 rats were sacrificed at various time points ranging from 50 to 200 days after injection.

Subsequently, histological analysis was performed using Sudan Black B (SBB) staining to quantify myelin content.

Image Analysis (see Fig. 2)

1. P*reprocessing*

Preprocessing steps applied prior to image analysis consisted of 1) brain mask extraction using a template rat image, [2]. 2) bias artefact supression using the N4 algorithm [3]. 3) co-registration in a longitudinal way on the template rat.

2. *CC Segmentation and tessellation*: CCwere segmented using a UNet model [4]. Data augmentation was used to improve the generalization robustness.

To precisely analyse intensities in the CC, UNet masks were tessellated into 12 regions (see Fig. 2).

3. In order to conduct an analysis of intensities over time longitudinal normalization was performed using healthy contra-lateral regions of the CC as a reference for intensity values and applying an intensity harmonization process to both T2-weighted and optical coherence images.

4. *Histology image processing* we manually selected the 2 slices that best matched the region of interest identified, on T2w, using anterior commissure as landmarks. These 2 slices were then registered on MRI with a rigid registration followed with a deformable one. The CC tessellation of MRI T2w images were then used to obtain the CC tessellation on the histological slices.

Results: For the majority of the rats (13/24) the volume of the ipsilateral corpus callosum measured on OC images was decreasing over time (-1% to – 8%) whereas the volumes of the contralateral either remain within 2% of variation or slightly increasing (from up to 4%) over time.

When considering mean and standard deviation of the signal intensity of each parcel for every acquisition, OC contrast provides a more informative analysis compared to T2 where all acquisitions have same low values. The middle part of Fig. 1 shows two of these representations. For the majority (19/24) the intensity was decreasing between first and last acquisition on the injured CC. The OC contrast appears to be responsive to changes in the myelin content of the corpus callosum over time.

Figure 3 shows profiles and CC thickness measurement on registered in vivo and ex vivo images. The observations indicate that, when it comes to the thickness of the corpus callosum (CC), there is a higher degree of similarity between histology and T2) imaging compared to OC imaging.

Conclusion: Optimal control MRI contrast dedicated to myelin enhancement appear to reveal interesting sensitivity to myelin evolution compared to T2w in a MS model. However, at first sight T2w offer more similarity with ex vivo reality than optimal control images. In this LPC rat model, if remyelination occurred, it happened in the first month, afterwards a slight deterioration of the myelin and loss of volume of the corpus callosum was observed (without the rats showing any disabling clinical signs). Histological images still reveal deteriorated CC on the injured side.

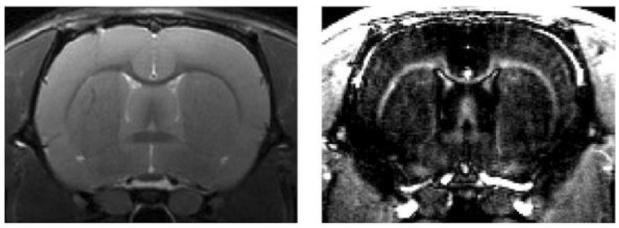

Fig. 1: left T2w RARE image , right OC contrast image enhancing signal of short T2 components.

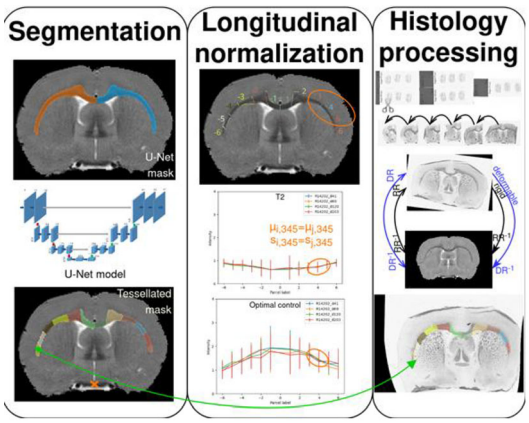

Fig. 2: Illustration of the image analysis pipeline after images were preprocessed to be registered on the same rat template and normalized.

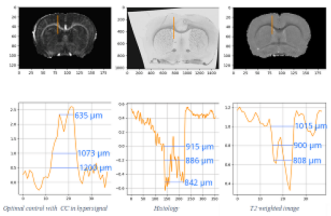

Fig. 3: Comparison of profiles on injured CC for two sequences and histology on a rat LPC model.

References

[1] Khodanovich et al.,Scientific Report, 2017
[2] Klein S.et al.,IEEE TMI, 2010
[3] Tustison N.J., et al. IEEE TMI, 2010
[4] Ronneberger O. et al., MICCAI, 2015
[5] Vernier B., et al. IEEE ISBI, 2021
[6] Zhang M.,et al. Contrast Media Mol Imaging, 2019

P232.
Comparison of Bayesian and non-linear least squares approaches for the quantitative estimation of multi-compartment T2 in fresh breast tumour specimens at 3 T

K. A. Nkonde[1,2,3], N. Senn[2], E. Husain[4], Y. Masannat[5], S. M. Cheung[2], J. He[1,2]

[1]*Newcastle University, Newcastle Magnetic Resource Centre, Translational and Clinical Research Institute, Faculty of Medicine, Newcastle, United Kingdom;*
[2]*University of Aberdeen, Institute of Medical Sciences, School of Medicine, Medical Sciences and Nutrition, Aberdeen, United Kingdom;*
[3]*Mulungushi University, Department of Physics, School of Natural and Applied Sciences, Kabwe, Zambia;*
[4]*Aberdeen Royal Infirmary, Pathology Department, Aberdeen, United Kingdom;*
[5]*Aberdeen Royal Infirmary, Breast Unit, Aberdeen, United Kingdom*

Introduction: Transverse relaxation time (T_2) of breast tumours is affected by the local structural and biochemical micro-environment, and in turn indicative of associated disease processes[1]. Mono-compartment model, although commonly adopted for mathematical simplicity and computational speed, does not capture the complexity of real biological tissue, demanding multi-compartment (MC) approaches[2]. The non-linear least squares (NLLS) and Bayesian parameter estimation (BPE) algorithms have been applied to estimate parameters in MC models in human body outside of the breast[3–5]. NLLS allows the estimation of T_2 based on the minimisation of the sum of squares of errors, suffering from potential overfitting and in turn misinterpretation of the findings owing to increased number of variables. BPE, estimating T_2 using a priori knowledge of the data distribution, has been introduced to mitigate the overfitting using the constraints imposed by neighbouring voxels[5–9]. We set out to examine the NLLS and BPE algorithms for quantitative T_2 maps acquired on a clinical scanner from 20 freshly excised breast tumour specimens.

Methods: Tumour specimens from twenty female patients with breast cancer (invasive ductal carcinoma, 10 grade II and 10 grade III) were placed in 10% buffered solution of formalin immediately after surgery (Fig. 1). The study was approved by the North-West – Greater Manchester East Research Ethics Committee (Identifier: 16/NW/0221), and signed written informed consent was obtained from all participants prior to the study. Five repeated quantitative T2 images were acquired from each specimen on a clinical 3 T MRI scanner (Achieva TX, Philips Healthcare, Netherlands) using a body coil. The multishot gradient and spin echo (GRASE) sequence was used, with 24 echo times (TE) from 13 to 312 ms at an echo spacing of 13 ms, FOV of 141 141 mm2, slice thickness of 2.2 mm and image resolution of 2.2 2.2 mm2.

Voxel-wise mono- and bi-exponential fitting was performed in MATLAB (R2021a, MathWorks, USA), using NLLS based on Levenberg–Marquardt algorithm and BPE based on a flat prior. The fitting was performed over the regions-of-interest (ROIs) encompassing the whole tumour, to compute the T_2 and initial signal intensity (S0) in a mono-compartment model, while short and long T_2 components (T_{2s} and T_{2l}) and volume fractions (f_s and f_l) in a bi-compartment model. The arithmetic mean of each of the outputparameters was calculated within the ROI for each specimen across acquisitions.

Statistical analysis was performed in SPSS statistical software (IBM SPSS Statistics, Version 27.0, USA). The corrected Akaike"s information criterion (AICc)[10] was employed to estimate the quality of fitting in a bi-compartment model against a mono-compartment model. The within-subject coefficients of variations (%wCV) of the BPE and NLLS of the bi-compartment output parameters were calculated[11,12], Wilcoxon tests performed to compare the variations in output parameters between the two methods. The correlations of T_{2s} and T_{2l} between BPE and NLLS were performed using the Spearman"s correlation test[13]. p values < 0.05 considered statistically significant.

Results: The T_{2s} and T_{2l} parametric maps generated from BPE and NLLS (Fig. 2), and the summary statistics of each output parameter for NLLS and BPE (Table 1) are shown. The goodness of fit for the bi-compartment model (AICc = 399.05) was numerically lower than the single compartment model (AICc = 399.94) (Fig. 2). The %wCV in $T_{2s,BPE}$ (4.16), $f_{s,BPE}$ (5.47), $S_{0,BPE}$ (2.11) of BPE were lower than that in NLLS. The %wCV in T_{2l}, NLLS (1.23) of NLLS was lower than that in BPE, although the result was not significant (Table 1). There were significant positive correlations between $T_{2s,BPE}$ and $T_{2s,NLLS}$ (r = 0.385, $p < 0.001$), and $T_{2l,BPE}$ and $T_{2l,NLLS}$ (r = 0.575, $p < 0.001$) (Fig. 3, Table 1).

Discussion: Bi-compartment model may be a more faithful representation of breast tumour cellular structure than the mono-compartment model. The short and long T_2 components from BPE and NLLS showed significant correlations. However, BPE might be valuable in quantifying the long T_2 component since previous NLLS simulation showed more susceptibility to overfitting at low SNR for the long T_2 component.

Conclusion: BPE might be a valuable alternative to NLLS for the analysis of bi-exponential data, generating more faithful estimation of underlying biology in breast cancer.

	Mean ± SD		%wCV		Model stability test: Wilcoxon signed-rank test		Correlation test: NLLS vs BPE	
	NLLS	BPE	NLLS	BPE	(z)	p-value	r	p-value
T_{2l} (ms)	111.11 ± 12.19	107.57 ± 14.82	**1.23**	1.95	-1.12	0.263	0.385	$p < 0.001$
T_{2s} (ms)	49.78 ± 11.24	70.83 ± 14.27	4.86*	**4.16**	-2.32	**0.021**	0.575	
f_s (%)	33.93 ± 9.71	40.77 ± 9.18						
f_l (%)	66.07 ± 9.71	59.23 ± 9.18	7.65**	**5.47**	-2.88	**0.004**		
S_0 (au)	(2.24 ± 1.65) × 10^6	(4.81 ± 0.71) × 10^5	51.27***	**2.11**	-3.920	**p < 0.001**		

*f_s, volume fraction for short component; f_l, volume fraction for long component; S_0, initial signal intensity; *: $p < 0.05$; **: $p < 0.01$; ***: $p < 0.001$.*

Table 1. Model stability and Correlation tests.
The within-subject coefficient of variation (%wCV) was computed to estimate model stability, with lower %wCV in bold. Wilcoxon test performed to test for significance. The Spearman"s correlation between $T_{2l,NLLS}$ vs $T_{2l,BPE}$ and $T_{2s,NLLS}$ vs $T_{2s,BPE}$ was performed. A $p < 0.05$, statistically significant.

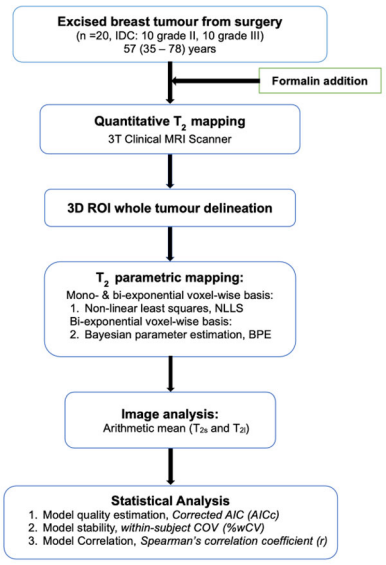

Fig. 1: Study design.
The voxel-wise fitting using the NLLS and BPE. T_{2s} and T_{2l} parametric maps generated, with arithmetic mean computed Model quality estimation of mono- vs bi-exponential fittings performed using AICc. Model stability and the association between T_{2s} and between T_{2l} calculated.

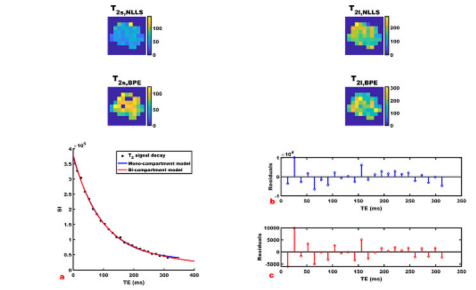

Fig. 2: T_2 Parametric maps, curve fitting and residuals plots.
(a) Mono-exponential vs bi-exponential curve fitting. **(b)** Mono-compartment residuals plot. **(c)** Bi-compartment residuals plots.

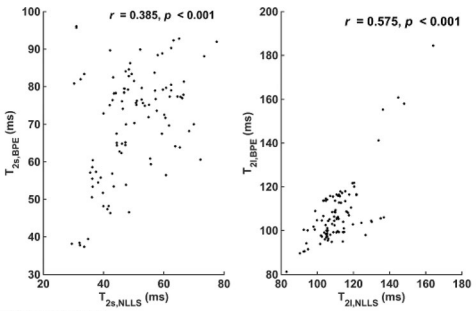

Fig. 3: Correlation plots.
Left: Spearman"s correlation between the T_{2s} components. **Right:** Spearman"s correlation between the T_{2l} components.

References

1. Kiselev et al., *Neuroimage* (2018).
2. Ababneh et al., *Magn Reson Med* (2005).
3. Nikiforaki et al., *Eur Radiol Exp* (2020).
4. Raj et al., *PLoS One* (2014).
5. Kumar et al., *Magn Reson Med* (2012).
6. Gustafsson et al., *Magn Reson Med* (2018).
7. Bouhrara et al., *Magn Reson Med* (2015).
8. Payne., *IEEE Signal Process Lett* (2005).
9. Bretthorst et al., *Magn Reson Med* (2005).
10. Burnham et al., *Sociol Methods Res* (2004).
11. Gurney-Champion et al., *PloS One* (2018).
12. Barnhart et al., *Transl Oncol* (2009).
13. Barnhart et al., *J Biopharma Stats* (2007).

Table 1. Model stability and Correlation tests.
The within-subject coefficient of variation (%wCV) was computed to estimate model stability, with lower %wCV in bold. Wilcoxon test performed to test for significance. The Spearman"s correlation between $T_{2l,NLLS}$ vs $T_{2l,BPE}$ and $T_{2s,NLLS}$ vs $T_{2s,BPE}$ was performed. A $p < 0.05$, statistically significant.

P233.
Accuracy of fast T2 mapping – Comparing whole brain accelerated MRI to a spin echo EPI reference measurement

K. Hirschmüller[1], R. Deichmann[2], U. Nöth[2], C. Preibisch[1]

[1]*TUM, School of Medicine, Neuroradiology, Munich, Germany;* [2]*Goethe University, Brain Imaging Center, Frankfurt am Main, Germany*

Introduction: Over the last years, acceleration techniques rendered quantitative magnetic resonance imaging (qMRI) techniques increasingly feasible. In particular, T2 is frequently applied, e.g., for assessment of cerebral oxygen extraction.[1,2] However, fast MRI techniques and especially 2D-acquistions suffer from systematic bias, mainly T2 overestimation due to stimulated echoes.[3,4,5,6] Thus, 3D gradient-spin echo (GRASE) acquisition[7,8] and a correction procedure for turbo spin echo (TSE) acquisitions[9] have been proposed.
The aim of our study was to investigate the accuracy and repeatability of (accelerated) 3D-GRASE and TSE-based T2 mapping by comparison to a reference experiment consisting of multiple single spin echo (SE) echo planar imaging (EPI) acquisitions in phantoms and in vivo.
Methods: A homogenous phantom (HP) and a phantom containing six flasks (6P) with different T2 relaxation times in the range of typical human brain tissue were scanned up to three times on a 3 T Philips Ingenia (Best, Netherlands) within six months. In addition, one healthy human subject (52y, f) (HS) was scanned twice within two months. The MRI protocol comprised the following:
Multiple single echo SE-EPI TE = 50, 70, 90, 120, 150 ms; TR = 20 s; 24 slices; voxel size $2 \times 2x2.5mm^3$; T_{acq} = 1:20 min/TE; repetitions: 2xHP, 3 × 6P, 2xHS.
Multi-echo 3D-GRASE-I 8 echoes; TE1 = ΔTE = 16 ms; TR = 262 ms; EPI-factor:7; TSE-factor:8; SENSE:no; 50 slices; voxel size $1 \times 1x2.5mm^3$; T_{acq} = 8:32 min; repetitions: 1xHP, 3 × 6P, 2xHS.
Multi-echo 3D-GRASE-II Same as 3D-GRASE-I, but with SENSE:P-2, S-2; T_{acq} = 2:11 min; repetitions: 2xHP, 3 × 6P, 2xHS.
Multiple single echo TSE TE = 17, 51, 86, 103, 120, 187 ms; TR = 18255 ms; CS-SENSE:2; 50 slices; voxel size $1 \times 1x2.5mm^3$; T_{acq} = 2:44 min/TE; repetitions: 3xHP, 3 × 6P, 2xHS.
B1 mapping[10] TE = 2.3 ms; TR = 30/150 ms; α = 60°; CS-SENSE:6; 50 slices; voxel size $4 \times 4x2.5mm^3$; T_{acq} = 3:25 min; repetitions: 2xHP, 1 × 6P, 1xHS.
T2 parameter maps were calculated using monoexponential fits. TSE-based T2 maps were corrected by means of simulation-based B1-dependent correction factors.[9] Quantitative T2 parameter values were evaluated in volumes of interest (VOIs) (Fig. 1) and relative deviations from the SE-EPI-based reference values were calculated.
Results: Axial slices of T2 parameter maps of the phantoms and a healthy subject are shown in Fig. 1. Quantitative T2 values from different VOIs are summarized in Table 1 and demonstrate that the standard deviations across measurements (VOI means across voxels) are consistently lower than averages of standard deviation across voxels in a VOI (averaged across measurements). Uncorrected, TSE-based T2 values exceeded SE-EPI-based reference values by about 18%, which by correction could be reduced to about 5%, except for vessel 1 with T2 = 32 ms. Both 3D-GRASE variants yielded T2 values with deviations of about 4% from the SE-EPI reference values in vitro and in vivo (Fig. 2). Plotting the relative deviation of GRASE- and TSE-based T2 values from the SE-EPI-based reference against these reference T2 values (Fig. 3), shows no indication for a systematic dependency of relative deviations on T2, except for corrected TSE-based values for the lowest T2 of 32 ms.
Discussion: Uncorrected TSE-based T2 mapping clearly overestimates T2 values compared to the SE-EPI reference measurement (Fig. 2 & 3) as expected, which was successfully reduced by applying the correction proposed.[9] The large deviation of corrected TSE-based T2 value from the reference in vessel 1 can be well explained by insufficient sampling in the range of low echo times given the low T2 value of the sample.
Both unaccelerated and accelerated 3D-GRASE sequences yielded T2 values that agree well with the reference SE-EPI-based values across the whole range of T2 values, which is in agreement with results from Kaczmarz and colleagues.[8] Further, the absolute deviation in relative T2 is smallest for the accelerated 3D-GRASE sequence and the small standard deviation across repeated measurements demonstrates excellent repeatability (Table 1), which is encouraging with respect to future applications.

Conclusion We conclude that accelerated multi-echo 3D-GRASE offers fast (2:11 min) and reliable whole brain T2 mapping at high spatial resolution (1 × 1x2.5 mm^3). However, in combination with an appropriate correction[9] TSE-based T2 mapping is also a reliable option when 3D GRASE is not available.

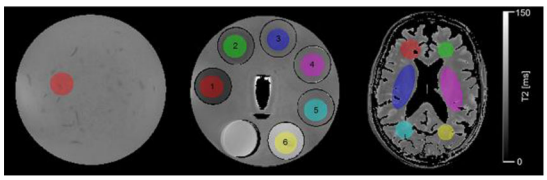

Fig. 1: Axial slice of 3D-GRASE-based T2 maps for both phantoms and in vivo. Evaluated VOIs are superimposed in color.

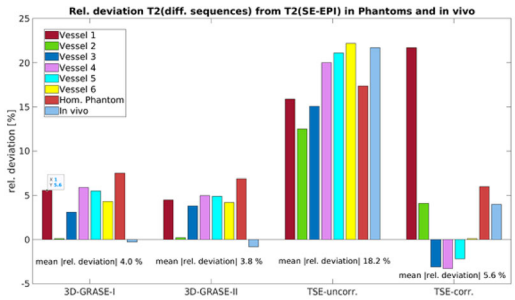

Fig. 2: Relative deviation of T2 values from the SE-EPI-based reference values for 3D-GRASE without (3D-GRASE-I), and with (3D-GRASE-II) SENSE acceleration, as well as TSE without (TSE-uncorr.), and with correction (TSE-corr.).

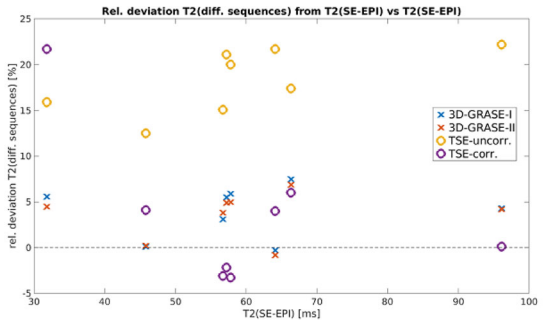

Fig. 3: Relative deviation of T2 values from the SE-EPI-based reference values vs. T2(SE-EPI) for 3D-GRASE without (3D-GRASE-I), and with (3D-GRASE-II) SENSE acceleration, as well as TSE without (TSE-uncorr.), and with correction(TSE-corr.).

T2[ms]	SE-EPI	3D-GRASE-I	3D-GRASE-II	TSE-uncorr.	TSE-corr.
Vessel 1	31.8 ± 1.3 (0.3)	33.6 ± 1.3 (1.1)	33.2 ± 1.2 (0.6)	36.9 ± 2.0 (5.7)	38.7 ± 2.3
Vessel 2	45.8 ± 1.1 (0.5)	45.9 ± 1.3 (0.6)	45.9 ± 1.6 (0.6)	51.6 ± 1.7 (3.8)	47.7 ± 1.5
Vessel 3	56.7 ± 1.6 (1.5)	58.5 ± 2.1 (1.8)	58.9 ± 2.3 (2.1)	65.3 ± 2.4 (2.5)	55.0 ± 1.3
Vessel 4	57.8 ± 1.2 (0.0)	61.2 ± 1.9 (1.4)	60.7 ± 1.8 (0.4)	69.3 ± 2.3 (5.2)	55.9 ± 1.2
Vessel 5	57.2 ± 1.1 (0.8)	60.3 ± 1.8 (0.8)	60.0 ± 1.7 (0.5)	69.2 ± 1.7 (5.0)	55.9 ± 1.4
Vessel 6	96.1 ± 2.6 (0.6)	100.2 ± 3.7 (0.7)	100.2 ± 3.9 (0.6)	117.4 ± 3.5 (5.5)	96.2 ± 1.6
Hom. Phantom	66.3 ± 2.3 (0.6)	71.2 ± 2.2	70.8 ± 2.3 (1.0)	77.8 ± 1.8 (6.9)	70.2 ± 1.6 (6.8)
In vivo	64.1 ± 7.0	63.9 ± 5.4	63.6 ± 5.3	77.9 ± 7.1	66.6 ± 6.7

Table 1: Averages across repeated measurements of VOI mean ± standard deviation (standard deviation of means across repeated measurements) for SE-EPI-based reference values, for 3D-GRASE without (3D-GRASE-I), and with (3D-GRASE-II) SENSE acceleration, as well as TSE without (TSE-uncorr.) and with correction (TSE-corr.). Note: TSE-corr values in 6P and HS represent only one measurement.

References

1: Reiländer,CCCB,2023
2: Kaczmarz,JCBFM,2021
3: Hirsch,NMR Biomed,2014
4: Seiler,Clin.Neuroradiol.,2019
5:, Hennig,JMR,1988
6: Uddin,MRM,2013
7: Oshio&Feinberg,MRM,1991
8: Kaczmarz,Neuroimage,2020
9: Nöth,Neuroimage,2017
10: Yarnykh,MRM,2007

P234.
Assessment of neurodegenerative progression using quantitative T_2 map in the $SOD1^{G93A}$ mouse model

M. Kuramochi[1,2], Y. Komaki[2], H. Kameda[3], K. Kudo[3], J. Hata.[1]

[1]*Tokyo Metropolitan University, Faculty of Health Sciences, Tokyo, Japan;*
[2]*Central Institute for Experimental Animals, Live Animal Imaging Center, Kanagawa, Japan;*
[3]*Hokkaido University, Hokkaido, Japan*

Introduction: Amyotrophic lateral sclerosis (ALS) is a progressive neurological disease that affects motor neurons, leading to the paralysis of muscles, including those required for breathing, and eventually causing death. The underlying cause is still not fully understood, and there is no definitive cure. Early detection of ALS and a more accurate understanding of disease progression are critical to treating patients. This can improve quality of life and prolong survival if the patient receives appropriate treatment. This can also potentially aid in the radical treatments with new drugs. Magnetic resonance imaging (MRI) is a non-invasive imaging technique that can detect early changes in ALS, allowing for early intervention. The aim of this study is to evaluate the early detection and progression of ALS using high field MRI in mice.

Methods: We used mice with a human mutant SOD1 gene, which is responsible for approximately 2% of all ALS cases, and normal mice as controls (wild type: wt). We performed MRI scans on both groups of mice at 7, 11, and 16 weeks of age (7w, 11w, 16w). T_2-weighted images, T_2 maps, voxel-based analysis (VBA), and region of interest (ROI) analysis were used to visually and quantitatively assess changes in the brains of the mice.

T_2-weighted images were acquired using a 7-T MRI scanner (Biospec 70/16, Bruker BioSpin, Germany). T_2 maps were generated by fitting the signal intensity data to an exponential decay function. VBA analysis was performed using SPM12 software. Average images for each age data were created for wt and ALS model, respectively, and voxel values were compared. For ROI analysis, three ROIs were created: trigeminal nerve, corticospinal tract and somatomotor areas.

Results: The T_2-weighted images showed hyperintensities in the area from the trigeminal nerve to the rubrospinal tract and facial nerve in the mutant mice (Fig. 1). T_2 maps demonstrated an increase in T_2 values in the trigeminal nerve and facial nerve with increasing age (Fig. 2). VBA analysis showed that signal intensity differed in the trigeminal nerve and rubrospinal tract with increasing age (Fig. 3). In ROI analysis showed an increase in T_2 values in the trigeminal nerve, somatomotor areas with increasing age. In the trigeminal nerve, T_2 values were significantly higher in the ALS model mice than in the wild-type mice at 11w and 16w.In the corticospinal tract, T_2 values were significantly higher in the wild-type mice than in the ALS model mice at 16w.

Discussion: Signal changes on T_2WI were seen in the trigeminal nerve, the rubrospinal tract, and the facial nerve, which are responsible for transmitting descending information that moves muscles. These areas are known to be impaired by ALS, and T_2WI may have detected neurodegeneration. The high signal on T_2-weighted images is thought to be due to the destruction of the myelin sheath by

demyelination, which allows water molecules inside nerve fiber bundles to move freely. On T_2 map, increased T_2 values of the trigeminal nerve and facial nerves were seen with aging. VBA analysis showed increased T_2 values with age in the trigeminal nerve and rubrospinal tract. ROI analysis showed increased T_2 values with age in the trigeminal nerve. These areas are known to be impaired by ALS as well as T_2WI, and T_2 map, the VBA analysis, the ROI analysis may have detected neurodegeneration. These increases in T_2 values with aging indicate that they are more impaired as the disease progresses.

Conclusion: Our study demonstrated the potential of high field MRI for the early detection and progression of ALS in mice. Our results indicate that T_2-weighted images, T_2 maps, VBA, and ROI analysis can detect early changes in the trigeminal nerve before the onset of symptoms in ALS model mice. These changes may be related to the early stages of ALS and suggest that high field MRI has the potential to aid in the early diagnosis of ALS in humans. Early diagnosis can lead to early treatment. Further studies are needed to confirm our findings and to determine the clinical relevance of early detection and intervention for ALS patients.

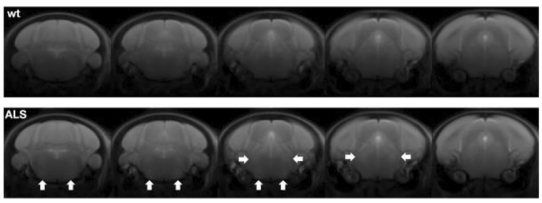

Fig. 1: T_2WI MRI Sections showing areas T_2 value increase in the ALS model mice at 16w. High signal intensity is seen in the trigeminal nerve, rubrospinal tract, and facial nerve on T_2WI of ALS model mice at 16w (White arrows).

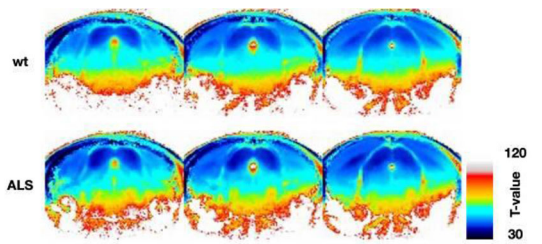

Fig. 2: T_2 map MRI Sections showing areas T_2 value increase in the ALS model mice at 16w. On T_2 map, T_2 value increases significantly in the trigeminal nerve and the facial nerve of ALS model mice at 16w.

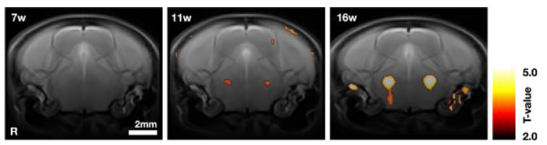

Fig. 3: VBA analysis comparing T_2 map of wt and ALS model with voxel by voxel. T_2 value in the trigeminal nerve and rubrospinal tract of ALS model mice increases significantly with age compared to wt using VBA analysis.

Reference

Zang, D.W., Yang, Q., Wang, H.X., Egan, G., Lopes, E.C. and Cheema, S.S. (2004), Magnetic resonance imaging reveals neuronal degeneration in the brainstem of the superoxide dismutase 1G93A G1H transgenic mouse model of amyotrophic lateral sclerosis. *European Journal of Neuroscience*, 20: 1745–1751.

Weerasekera, A., Sima, D. M., Dresselaers, T., van Huffel, S., van Damme, P., & Himmelreich, U. (2018). Non-invasive assessment of disease progression and neuroprotective effects of dietary coconut oil supplementation in the ALS SOD1G93A mouse model: A 1H-magnetic resonance spectroscopic study. *NeuroImage: Clinical*, *20*, 1092–1105.

Dai, Z., Chen, Y., Yan, G., Gang xiao, Shen, Z., & Wu, R. (2019). Progress of magnetic resonance imaging in amyotrophic lateral sclerosis. *Radiology of Infectious Diseases*, *6*(1), 1–7.

P235.
Repeatability and reproducibility of texture features from of quantitative T1 and T2 of fresh breast tumour specimens in formalin at 3 T

K. A. Nkonde[1,2,3], N. Senn[2], E. Husain[4], Y. Masannat[5], S. M. Cheung[2], J. He[1,2]

[1]*Newcastle University, Newcastle Magnetic Resource Centre, Translational and Clinical Research Institute, Faculty of Medicine, Newcastle, United Kingdom;*
[2]*University of Aberdeen, Institute of Medical Sciences, School of Medicine, Medical Sciences and Nutrition, Aberdeen, United Kingdom;*
[3]*Mulungushi University, Department of Physics, School of Natural and Applied Sciences, Kabwe, Zambia;*
[4]*Aberdeen Royal Infirmary, Pathology Department, Aberdeen, United Kingdom;*
[5]*Aberdeen Royal Infirmary, Breast Unit, Aberdeen, United Kingdom.*

Introduction: Freshly excised breast tumour, although a valuable experimental model[1], requires immediate addition of formalin for tissue preservation, potentially leading to altered image contrast on MRI[2]. Relaxation properties of T_1 and T_2 in the breast are known to alter in the presence of a tumour[3], and the features extracted from texture analysis have shown significant potential in describing tumour pathology and predicting response to therapies[4,5]. Therefore, we hypothesised that tumour texture features extracted from quantitative T_1 and T_2 images are highly repeatable between acquisitions with no significant impact from formalin.

Methods: Twenty breast tumour specimens were removed from female patients undergoing wide local excision, with a mean (range) age of 57 (35 – 78) years, with invasive ductal carcinoma, 10 grade II and 10 grade III (Fig. 1). The specimens were placed in a 10% buffered solution of formalin immediately after surgery. Five repeated acquisitions of T_1 and T_2 quantitative scans were performed overnight. The study was approved by the North-West – Greater Manchester East Research Ethics Committee (Identifier: 16/NW/0221), with signed written informed consent obtained from all participants prior to entry into the study.

Images were acquired on a clinical 3 T MRI scanner (Achieva TX, Best, Philips Healthcare, Netherlands) using a body coil for uniform transmission and a 32-channel receiver head coil. Quantitative T_1 images were acquired using the multi-shot Look-Locker sequence with a trigger delay (TD) = 170 ms, 5 k-*space* lines in a shot, 35 inversion curve sampling points from first inversion time (TI) of 30 ms and an increment of 150 ms, excitation pulse flip angle of 4° and repetition time (TR) of 5132 ms. Quantitative T_2 images were acquired using the multi-shot gradient and spin echo (GRASE) pulse sequence, with 24 echo times (TEs) from 13 to 312 ms. T_1 and T_2 images both had FOV of 141 × 141 mm2, slice thickness of 2.2 mm and an image resolution of 2.2 × 2.2 mm2.

Voxel-wise mono-exponential fitting was performed using non-linear least squares method based on Levenberg–Marquardt algorithm to derive quantitative T_1 and T_2 maps in MATLAB (R2021a, MathWorks, Natick, USA). Whole tumour delineation was conducted on DWI images with a *b*-value of 800 s.mm^{-2}, using MRIcron (University of South Carolina, Columbia, USA) and extracted for

texture analysis on subsequent T_1 and T_2 maps. Five first-order statistics texture features: mean, standard deviation, kurtosis, skewness and entropy were calculated based on histogram analysis of the voxel values within the tumour.

Statistical analysis was performed using the SPSS statistical software (IBM SPSS Statistics, Version 27.0, Armonk, USA). Relative repeatability was conducted using the within-subject coefficient of variation (%*w*CV)[6] of the five repeated acquisitions. The reproducibility was conducted using the two-way intra-class correlation coefficient mixed effect model with absolute agreement ($ICC_{2,1}$), across the 20 tumour specimens with the five repeated acquisitions[7]. An $ICC_{2,1}$ greater than 0.8 indicated a highly reproducible texture feature. A p value < 0.05 was considered statistically significant.

Results: For T_1, the %*w*CV of the mean, standard deviation, kurtosis, skewness and entropy texture features were 2.11, 3.84, 5.02, 7.79 and 3.52, respectively (Table 1, Fig. 2). The $ICC_{2,1}$ (95% CI) of the mean, standard deviation, kurtosis, skewness and entropy texture features were 0.97 (0.91 – 0.99), 0.95 (0.87 – 0.98), 0.98 (0.96 – 0.99), 0.97 (0.94 – 0.99) and 0.62 (0.42 – 0.79), respectively, with a p-value $<$ 0.001 for all texture features (Table 2).

For T_2, the %*w*CV of the mean, standard deviation, kurtosis, skewness and entropy texture features were 1.82, 9.40, 18.61, 103.63 and 4.05, respectively (Table 1, Fig. 2). The $ICC_{2,1}$ of the mean, standard deviation, kurtosis, skewness and entropy of the texture features were 0.98 (0.95 – 0.99), 0.93 (0.88 – 0.97), 0.73 (0.56 – 0.86), 0.70 (0.52 – 0.84) and 0.81 (0.68 – 0.91), respectively, with a p-value < 0.001 for all textures features (Table 2).

Discussion: In T_1, all the metrics were highly repeatable and reproducible, apart from moderate reproducibility in entropy.

In T_2, the mean, standard deviation and entropy were highly repeatable, and moderate repeatability in the kurtosis, but poor repeatability in the skewness. The mean, standard deviation and entropy were highly reproducible, while kurtosis and skewness had good reproducibility.

Conclusion The majority of the first-order texture features from quantitative T_1 and T_2 are highly repeatable and reproducible, apart from T_2 skewness that might have limited repeatability.

			T_1			T_2		
	n	*Trial*	*Global mean* ($\bar{X}$)	σ_r	*%wCV*	*Global mean* ($\bar{X}$)	σ_r	*%wCV*
Mean (ms)			1046.96	22.14	2.11	81.33	1.48	1.82
SD (ms)			210.30	8.07	3.84	10.06	0.95	9.40
Kurtosis (au)	20	5	3.79	0.19	5.02	3.79	0.82	18.61
Skewness (au)			0.95	0.07	7.79	0.26	0.27	103.63
Entropy (au)			6.30	0.22	3.52	3.53	0.14	4.05

Table 1: Repeatability of the five extracted texture features of T_1 and T_2.
The repeatability of the texture features are represented by the relative repeatability, calculated using the within-subject (specimen) coefficient of variation (%wCV, percentage ratio σ_r/X and σ_r is the within-subject SD).

			T_1				T_2			
	n	*Trial*	$ICC_{2,1}$	*95% CI*	*F-test*	*p-value*	$ICC_{2,1}$	*95% CI*	*F-test*	*p-value*
Mean			0.97	0.91 – 0.99	297.32		0.98	0.95 – 0.99	215.22	
SD			0.95	0.87 – 0.98	148.19		0.93	0.88 – 0.97	83.02	
Kurtosis	20	5	0.98	0.96 – 0.99	255.44	$p < 0.001$	0.73	0.56 – 0.86	15.69	$p < 0.001$
Skewness			0.97	0.94 – 0.99	173.51		0.70	0.52 – 0.84	12.00	
Entropy			0.62	0.42 – 0.79	8.61		0.81	0.68 – 0.91	22.60	

Table 2: Reproducibility measurements of the five extracted texture features of T_1 and T_2.

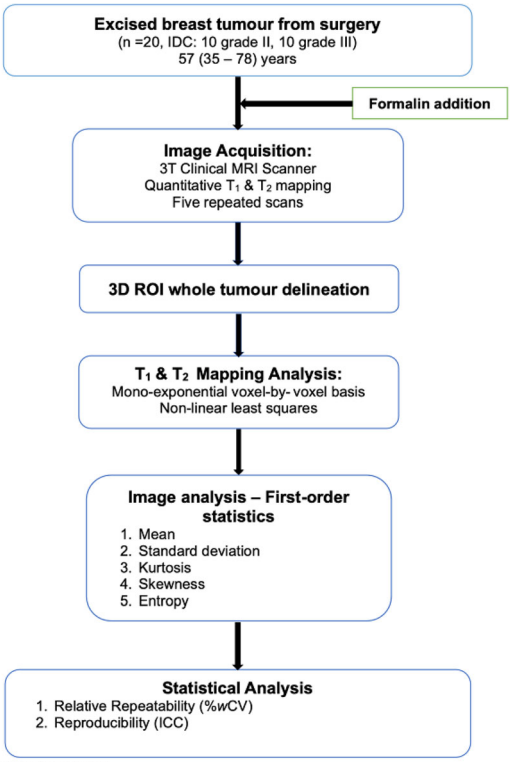

Fig. 1: The study design.
The flow chart shows the study design for the repeatability and reproducibility of texture features extracted from quantitative T_1 and T_2 maps of breast tumours.

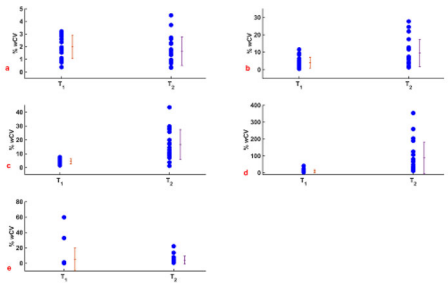

Fig. 2: Repeatability of the T_1 and T_2 texture features.
(a) Mean. **(b)** Standard deviation. **(c)** Kurtosis. **(d)** Skewness. **(e)** Entropy. The error bars indicate the mean and standard deviation.

References

1. Stucht et al., *PLoS One,* (2015).
2. Schmierer et al., *JMRI,* (2010).
3. Shatil et al., *FMED,* (2018).
4. Shur et al., *Eur Radiol Exp,* (2021).
5. Traverso et al., *IJROBP,* (2018).
6. Barnhart et al., *Transl Oncol,* (2009).
7. Barnhart et al., *J Biopharm Stats,* (2007).

P236.

Assessing different registration algorithms for tracking displacement and compression of peritumoral tissue due to mass effect in high-grade gliomas

C. Lopez-Mateu[1], F. J. Gil-Terrón[1], D. Sederevičius[2], K. E. Emblem[2], E. Fuster-García[1], J. M. García-Gómez[1]

[1]*UPV, BDSLab, Valencia, Germany;*
[2]*Oslo University Hospital, Oslo, Norway*

Introduction: The emergence and growth of a high-grade glioma induces a local pressure on the neighboring tissues, which leads to a displacement of tissue referred to as gross mass effect. The ability to accurately understand and quantify this mechanical phenomenon can be decisive in determining the patients" prognosis and treatment [1 2]. One procedure to determine tissue displacement fields and measure tissue compression in the peritumoral region1 is performing non-linear registration on consecutive MRI scans. Although this method is effective, it remains unclear whether different registration algorithms available obtain different quantitative compression. In this study, we compare the displacement fields obtained from the two most commonly used registration algorithms, Greedy[3] and ANTs[4] SyN in synthetic deformation model.

Methods: A total of 200 Brain Tumor Segmentation from the RSNA-ASNR-MICCAI Brain Tumor Segmentation (BraTS) Challenge 2021 images were used as reference images to generate a synthetic tumor growth model. To simulate tumor growth, a scalar field kernel was created by assigning a three-dimensional normal distribution to each voxel within the tumor core. For the generation of the kernel, values of 50 voxels for the width and 600 voxels for the height of the normal distributions were used. The deformation field is then obtained from the gradient of the kernel and applied to a high grade glioma brain MRI. Once we have simulated tumor growth, we use ANTs SyN and Greedy registration algorithms to compute displacement field (see Fig. 1), excluding the tumor core from the registration, and computing divergence of the field to estimate tissue compression. Finally, the similarities between ground truth and estimated compression and magnitude displacement fields in the peritumoral area were assessed using Cross-Correlation metric.

Results: Greedy and ANTs SyN algorithms have shown good performance when estimating magnitude displacement field obtaining a median cross-correlation of 0.97 and 0.98, respectively (see Fig. 2). However, the difference in accuracy of compression was quite noticeable between both algorithms, obtaining a median cross-correlation of 0.90 and 0.85, respectively.

Discussion: The student's t-test has been calculated. The results showed a statistically significant difference in the accuracy of determining the compression map between the two algorithms, with a p-value of 0.005. In contrast, no significant difference was found between the algorithms for the magnitude displacement field, with a p-value of 0.374. Greedy showed better performance in reproducing the compression map in most cases and has shown a shorter execution time (2.74 min) versus ANTs (13.89 min). To sum up, although our study suggests that Greedy and ANTs SyN are both accurate algorithms for determining the magnitude displacement field, Greedy may be a more accurate and efficient algorithm for tracking peritumoral tissue compression caused by mass effect in high grade gliomas.

Conclusion: Future studies can further explore the performance of different registration algorithms in other clinical settings and with larger datasets. On the other hand, the simulation of the mass effect could be improved by assigning privileged growth directions based on diffusion tensor imaging data.

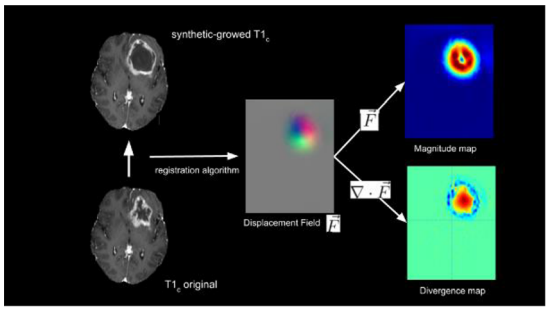

Fig. 1: From two consecutive images (T1c images on the left of the figure) we can obtain the displacement map with a SyN algorithm. The magnitude of the field gives us information on the amount of tissue displacement, while the divergence reflects the compression of the tissue.

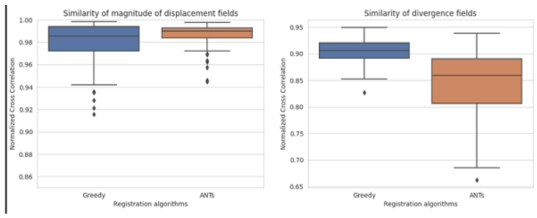

Fig. 2: The images display the median normalized cross-correlation results for the estimated compression (left) and compression fields (right) within the peritumoral area, obtained using the ANTs SyN and Greedy registration algorithms.

[1] Elies Fuster-Garcia et al., Cancers, 2022, 14(7): 1725.
[2] Jain, R. K. et al., Annual review of biomedical engineering, 16: 321–346.
[3] Yushkevich, P. A., Pluta, J., Wang, H., Wisse, L. E., Das, S. and Wolk, D., 2016. Fast Automatic Segmentation of Hippocampal Subfields and Medial Temporal Lobe Subregions in 3 Tesla and 7 Tesla MRI. Alzheimer's & Dementia: The Journal of the Alzheimer's Association, 12(7), pp.P126-P127.
[4] Cullen N, Avants B, Tustison N. ANTsPy: A Python interface to the Advanced Normalization Tools medical image analysis library. Journal of Open Source Software. 2020;5(54):2507.

P237.

The impact of a Siemens scanner upgrade from 3 T trio tim to 3 T prisma fit on the variability of volumetric measurements based on phantom and human data

M. Verleyen[1], P. Clement[2], S. Beun[1], E. Achten[2], S. Bogaert.[2]

[1]*Ghent University, Department of Diagnostic Sciences, Ghent, Belgium;*
[2]*Ghent University, Department of Medical Imaging, Ghent, Belgium*

Introduction: MR volumetry is commonly used to objectively determine significant brain volume changes. Unfortunately, many technical factors can influence image quality and quantitative MR measures, such as a scanner upgrade. Recently, the Ghent Institute for Functional and Metabolic Imaging (GIfMI) implemented a hardware upgrade from a Siemens MAGNETOM 3 T Trio system to a Siemens MAGNETOM 3 T Prisma Fit system, including gradient, radiofrequency and shimming system upgrades. To assess its impact on image quality and volumetric parameters, the impact of this upgrade on quantitative structural imaging was evaluated.

Methods: A visual representation of the study setup is provided in Fig. 1. T1-weighted MPRAGE data from ACR phantom and six human volunteers were acquired twice on the Siemens 3 T Trio Tim,

using a 32-channel head coil (session (ses) 1 and 2), and twice on the Siemens 3 T Prisma Fit using a 64-channel head coil (ses 3 and 4). For the ACR phantom data, seven parameters were assessed according to the Small Phantom Guide(1). For the human data, manual delineation of both hippocampi (HC*man*) was performed according to a ray-tracing protocol(2), and the volumes of the left (L) and right (R) HC were calculated in cm^3. Additionally, the subcortical volumes (SV) of the hippocampus (HC), amygdala (AM), thalamus (Th), nucleus caudatus (NC), putamen (Pu), pallidum (GP), nucleus accumbens (Nacc), and the cortical thickness (CT) of 33 regions for each session were calculated using Freesurfer and the Desikan-Killiany-Tourville (DKT) atlas. Intra- and interscanner consistency was evaluated using a paired T-test between the sessions (ses 1 versus 2, ses 3 versus 4) and between the scanners (mean ses 1 + 2 versus mean ses 3 + 4). All statistics were performed in R and correcting for multiple comparisons was done using the Bonferroni-Holm method.

Results: All ACR phantom parameters passed the acceptance criteria on both MRI scanners, except for the high contrast spatial resolution parameter, failing for both scanners at every time point. Intra- and interscanner mean differences of the SV and CT are summarized in **Tbl 1** and **Tbl 2**, respectively. Intrascanner variabilities for the Trio Tim scanner were found in HC*man* (R), HC (R), AM (R), Pu (R), inferior parietal (L), rostral middle frontal (R), pars orbitalis (R), and transverse temporal (L). Furthermore, intrascanner inconsistencies within the Prisma Fit scanner were only found for these regional CT: posterior cingulate (R), rostral anterior cingulate (L), and superior temporal (R). Interscanner inconsistency was found in bilateral HCman, NC (R), Pu (R), GP (R), Nacc (L), temporal pole (L), bilateral caudal middle frontal, bilateral lateral orbitofrontal, bilateral precentral, bilateral superior frontal, caudal anterior cingulate (R), precuneus (R), rostral middle frontal (R), pars opercularis (R), pars triangularis (R), and pars orbitalis (R). Finally, the mismatch between the regional CT are visualized in Fig. 2, where the green regions indicate significant decreases after the upgrade from **Tbl 2**.

Discussion: The variance of SV and CT due to a scanner upgrade appears to remain within the clinically acceptable boundaries, except for some specific regions. In general, the mean differences between scanners appear to be higher than within scanner mean differences. These findings are consistent with earlier reports(3), but are likely to differ between different scanning facilities. However, the low number of included volunteers limits the generalizability of the study results.

Conclusion: In conclusion, a scanner upgrade appears to slightly impact quantitative structural measurements of the brain. Therefore, it is crucial to evaluate hardware-related variance in quantitative imaging, especially during longitudinal or multi-center studies.

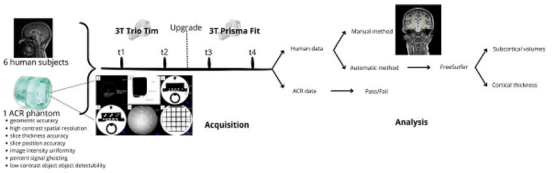

Fig. 1: Visual representation of the study design. T1-weighted MPRAGE images were acquired four times from the ACR phantom and six human volunteers: twice on the Trio Tim and twice on the Prisma Fit. Seven structural parameters were evaluated using the ACR data. The SV and CT were extracted using automatic segmentation and parcellation (respectively) and HC volumes were calculated based on manual delineation.

	3T Trio Tim		3T Prisma Fit		3T Trio Tim vs. 3T Prisma Fit		
	P-val. (corrected)	Mean diff (CI)	P-val. (corrected)	Mean diff. (CI)	P-val. (corrected)	Mean diff. (CI)	Mean volume in cm^3 (SD)
HC*man* R	0.077 (1.0)	0.26 (-0.042;0.56)	0.62 (1.0)	0.046 (-0.18;0.27)	0.029* (0.53)	0.32 (0.047;0.60)	2.59 (0.34)
HC*man* L	0.10 (1.0)	0.26 (-0.077;0.59)	0.776 (1.0)	0.014 (-0.11;0.13)	0.029* (0.53)	0.32 (0.047;0.60)	
HC R	0.056 (0.91)	0.11 (-0.0047;0.23)	0.74 (1.0)	-0.0089 (-0.073;0.056)	0.42 (1.0)	0.035 (-0.069;0.14)	4.50 (0.47)
HC L	0.15 (0.270)	0.042 (-0.022;0.11)	0.57 (1.0)	0.039 (-0.13;0.21)	0.17 (1.0)	-0.094 (-0.24;0.056)	
AM R	0.00089** (0.017*)	-0.10 (-0.14;-0.065)	0.49 (1.0)	-0.033 (-0.15;0.080)	0.40 (1.0)	0.046 (-0.083;0.17)	1.84 (0.15)
AM L	0.16 (1.0)	-0.066 (-0.17;0.037)	0.95 (1.0)	0.0021 (-0.077;0.082)	0.51 (1.0)	0.036 (-0.097;0.17)	
Th R	0.16 (1.0)	-0.091 (-0.23;0.052)	0.15 (1.0)	-0.092 (-0.23;0.046)	0.22 (1.0)	0.24 (-0.20;0.68)	7.86 (0.69)
Th L	0.52 (1.0)	-0.12 (-0.57;0.33)	0.30 (1.0)	0.090 (-0.11;0.29)	0.81 (1.0)	-0.53 (-0.59;0.49)	
NC R	0.49 (1.0)	-0.030 (-0.13;0.075)	0.81 (1.0)	0.0096 (-0.090;0.11)	0.059 (0.89)	0.13 (-0.0075;0.26)	3.55 (0.42)
NC L	0.87 (1.0)	-0.0069 (-0.12;0.10)	0.69 (1.0)	-0.0169 (-0.12;0.087)	0.57 (1.0)	0.026 (-0.085;0.14)	
Pu R	0.042* (0.95)	-0.081 (-0.16;-0.0043)	0.95 (1.0)	-0.0038 (-0.14;0.14)	0.098 (1.0)	0.067 (-0.018;0.15)	4.93 (0.45)
Pu L	0.42 (0.31)	0.048 (-0.19;0.093)	0.31 (1.0)	0.076 (-0.096;0.25)	0.22 (1.0)	-0.055 (-0.16;0.047)	
GP R	0.34 (0.56)	-0.067 (-0.23;0.097)	0.56 (1.0)	0.028 (-0.091;0.15)	0.027* (0.51)	0.072 (0.012;0.13)	2.10 (0.23)
GP L	0.87 (0.20)	0.0078 (-0.11;0.12)	0.20 (1.0)	0.074 (-0.056;0.20)	0.32 (1.0)	0.035 (-0.048;0.12)	
Nacc R	0.24 (0.60)	0.014 (-0.013;0.041)	0.60 (1.0)	-0.021 (-0.12;0.078)	0.32 (1.0)	-0.023 (-0.078;0.031)	0.52 (0.10)
Nacc L	0.58 (0.66)	-0.013 (-0.070;0.044)	0.66 (1.0)	0.022 (-0.096;0.14)	0.029* (0.53)	-0.067 (-0.12;-0.0096)	

Tbl. 1: Intra- and interscanner mean difference, p-values, and 95% CIs of the SV measures, including adjusted p-values. (* = < 0.05, ** = < 0.001, and borderline significant in gray)

Cortical thickness	Trio Tim vs. Trio Tim		Prisma Fit vs. Prisma Fit		Trio Tim vs. Prisma Fit		Mean thickness in mm (SD)
	P-val. (corrected)	Mean diff. (CI)	P-val. (corrected)	Mean diff. (CI)	P-val. (corrected)	Mean diff. (CI)	
caudalanteriorcingulate R	0.86 (1.0)	-0.01 (-0.14;0.13)	0.13 (1.0)	-0.062 (-0.14;0.03)	0.042* (1.0)	0.065 (-0.012;0.14)	2.45 (0.13)
caudalanteriorcingulate L	0.63 (1.0)	0.0082 (-0.03;0.05)	0.58 (1.0)	-0.027 (-0.14;0.09)	0.84 (1.0)	0.008 (-0.09;0.11)	
caudalmiddlefrontal R	0.58 (1.0)	-0.02 (-0.13;0.08)	0.55 (1.0)	-0.021 (-0.11;0.06)	0.009* (0.585)	0.07 (0.03;0.12)	2.59 (0.11)
caudalmiddlefrontal L	0.33 (1.0)	-0.052 (-0.11;0.04)	0.17 (1.0)	-0.051 (-0.13;0.03)	0.09* (1.0)	0.09 (0.01;0.16)	
cuneus R	0.99 (1.0)	0 (-0.07;0.07)	0.81 (1.0)	0.007 (-0.07;0.08)	0.35 (1.0)	0.025 (-0.04;0.09)	1.91 (0.18)
cuneus L	0.71 (1.0)	-0.02 (-0.13;0.09)	0.92 (1.0)	0.005 (-0.07;0.08)	0.26 (1.0)	0.024 (-0.03;0.07)	
entorhinal R	0.13 (1.0)	-0.16 (-0.4;0.07)	0.26 (1.0)	0.04 (-0.04;0.12)	0.59 (1.0)	0.025 (-0.09;0.14)	3.44 (0.28)
entorhinal L	0.23 (1.0)	-0.08 (-0.23;0.07)	0.28 (1.0)	-0.13 (-0.39;0.14)	0.57 (1.0)	-0.029 (-0.15; 0.09)	
fusiform R	0.16 (1.0)	-0.023 (-0.06;0.013)	0.28 (1.0)	-0.018 (-0.06; 0.02)	0.57 (1.0)	-0.012 (-0.06;0.04)	2.74 (0.10)
fusiform L	0.39 (1.0)	-0.02 (-0.07;0.033)	0.82 (1.0)	0.005 (-0.05; 0.06	0.23 (1.0)	-0.017 (-0.07;0.04)	
inferiorparietal R	0.50 (1.0)	-0.016 (-0.07;0.04)	0.71 (1.0)	-0.007 (-0.06;0.04)	0.77 (1.0)	-0.006 (-0.06;0.05)	2.55 (0.09)
inferiorparietal L	0.065 (1.0)	-0.025 (-0.05;0.002)	0.50 (1.0)	-0.011 (-0.05;0.03)	0.27 (1.0)	-0.019 (-0.06;0.02)	
inferiortemporal R	0.38 (1.0)	-0.014 (-0.05;0.05)	0.61 (1.0)	-0.008 (-0.04;0.03)	0.38 (1.0)	0.014 (-0.02;0.05)	2.78 (0.11)
inferiortemporal L	0.72 (1.0)	-0.008 (-0.07;0.05)	0.51 (1.0)	-0.005 (-0.02;0.01)	0.12 (1.0)	-0.02 (-0.04;0.006)	
isthmuscingulate R	0.95 (1.0)	-0.002 (-0.08;0.07)	0.16 (1.0)	0.047 (-0.03;0.12)	0.24 (1.0)	-0.021 (-0.06;0.02)	2.26 (0.19)
isthmuscingulate L	0.56 (1.0)	0.012 (-0.04;0.06)	0.27 (1.0)	-0.027 (-0.08;0.03)	0.56 (1.0)	-0.017 (-0.09;0.06)	
lateraloccipital R	0.58 (1.0)	-0.019 (-0.1;0.06)	0.32 (1.0)	-0.027 (-0.09;0.04)	0.15 (1.0)	0.05 (-0.026;0.13)	2.24 (0.12)
lateraloccipital L	0.84 (1.0)	-0.0068 (-0.09;0.07)	0.26 (1.0)	-0.019 (-0.06;0.02)	0.12 (1.0)	0.045 (-0.02;0.11)	
lateralorbitofrontal R	0.22 (1.0)	-0.1 (-0.29;0.08)	0.90 (1.0)	-0.003 (-0.06;0.06)	0.07 (1.0)	0.05 (-0.005;0.1)	2.58 (0.10)
lateralorbitofrontal L	0.34 (1.0)	-0.022 (-0.07;0.052)	0.63 (1.0)	-0.014 (-0.08;0.06)	0.01* (0.64)	0.08 (0.03;0.14)	
lingual R	0.55 (1.0)	0.018 (-0.05;0.09)	0.75 (1.0)	0.007 (-0.05;0.06)	0.25 (1.0)	0.026 (-0.026;0.08)	1.99 (0.17)
lingual L	0.75 (1.0)	0.013 (-0.09;0.11)	1.0 (1.0)	0 (-0.08;0.08)	0.44 (1.0)	0.025 (-0.05;0.1)	
precentral R	0.58 (1.0)	0.017 (-0.06;0.09)	0.38 (1.0)	-0.017 (-0.06;0.03)	0.017* (1.0)	0.055 (0.009;0.06)	2.58 (0.19)
precentral L	0.59 (1.0)	-0.012 (-0.06;0.04)	0.78 (1.0)	-0.008 (-0.08;0.07)	0.08 (1.0)	0.05 (-0.009;0.12)	
precuneus R	0.49 (1.0)	-0.014 (-0.06;0.035)	0.89 (1.0)	0.005 (-0.05;0.05)	0.008* (0.528)	0.022 (0.009;0.04)	2.41 (0.12)
precuneus L	0.44 (1.0)	0.009 (-0.02;0.055)	0.89 (1.0)	0.005 (-0.05;0.05)	0.10 (1.0)	0.03 (-0.008;0.07)	
temporalpole R	0.92 (1.0)	-0.009 (-0.23;0.22)	0.55 (1.0)	0.04 (-0.12;0.19)	0.10 (1.0)	0.16 (-0.05;0.38)	3.69 (0.31)
temporalpole L	0.36 (1.0)	0.08 (-0.13;0.29)	0.87 (1.0)	0.016 (-0.22;0.25)	0.06 (1.0)	0.13 (-0.01;0.27)	
superiorfrontal R	0.12 (1.0)	-0.03 (-0.07;0.01)	0.25 (1.0)	-0.04 (-0.13;0.04)	0.03* (1.0)	0.087 (0.02;0.15)	2.72 (0.14)
superiorfrontal L	0.68 (1.0)	-0.005 (-0.035;0.03)	0.32 (1.0)	-0.024 (-0.08;0.03)	0.07 (1.0)	0.07 (-0.008;0.15)	
rostralmiddlefrontal R	0.043* (1.0)	-0.05 (-0.1;-0.002)	0.12 (1.0)	-0.031 (-0.09;0.03)	0.06 (1.0)	0.04 (-0.005;0.1)	2.39 (0.11)
rostralmiddlefrontal L	0.10 (1.0)	-0.037 (-0.09;0.01)	0.55 (1.0)	-0.018 (-0.09;0.06)	0.33 (1.0)	0.031 (-0.04;0.11)	
medialorbitofrontal R	0.10 (1.0)	-0.05 (-0.11;0.015)	0.25 (1.0)	-0.048 (-0.14;0.05)	0.20 (1.0)	0.033 (-0.025;0.09)	2.40 (0.11)
medialorbitofrontal L	0.78 (1.0)	0.006 (-0.05;0.06)	0.72 (1.0)	0.008 (-0.047;0.06)	0.40 (1.0)	0.03 (-0.05;0.11)	
middletemporal R	0.61 (1.0)	-0.008 (-0.04;0.03)	0.23 (1.0)	-0.022 (-0.06;0.02)	0.62 (1.0)	-0.01 (-0.06;0.04)	2.90 (0.09)
middletemporal L	0.95 (1.0)	0.001 (-0.04;0.04)	0.39 (1.0)	0.012 (-0.02;0.045)	0.32 (1.0)	-0.011 (-0.04;0.02)	
parahippocampal R	0.49 (1.0)	-0.019 (-0.09;0.05)	0.44 (1.0)	0.021 (-0.04;0.08)	0.79 (1.0)	0.006 (-0.05;0.07)	2.74 (0.33)
parahippocampal L	0.79 (1.0)	0.009 (-0.07;0.09)	0.30 (1.0)	0.028 (-0.03;0.09)	0.92 (1.0)	0.0026 (-0.06;0.07)	
paracentral R	0.94 (1.0)	0.002 (-0.05;0.05)	0.89 (1.0)	-0.0055 (-0.1;0.09)	0.20 (1.0)	0.026 (-0.02;0.07)	2.42 (0.13)
paracentral L	0.94 (1.0)	-0.002 (-0.07;0.06)	0.76 (1.0)	-0.015 (-0.13;0.10)	0.91 (1.0)	-0.003 (-0.06;0.05)	
parsopercularis R	0.26 (1.0)	0.02 (-0.02;0.06)	0.31 (1.0)	-0.03 (-0.1;0.04)	0.019* (1.0)	0.043 (0.011;0.07)	2.59 (0.12)
parsopercularis L	0.11 (1.0)	-0.03 (-0.08;0.011)	0.45 (1.0)	0.021 (-0.04;0.09)	0.18 (1.0)	0.025 (-0.016;0.07)	
parstriangularis R	0.18 (1.0)	-0.04 (-0.1;0.02)	0.44 (1.0)	-0.03 (-0.13;0.07)	0.014* (0.88)	0.029 (0.009;0.05)	2.45 (0.12)
parstriangularis L	0.17 (1.0)	-0.06 (-0.15;0.03)	0.15 (1.0)	-0.05 (-0.12;0.02)	0.69 (1.0)	0.017 (-0.08;0.12)	
pericalcarine R	0.82 (1.0)	-0.01 (-0.14;0.11)	0.96 (1.0)	0.013 (-0.1;0.12)	0.10 (1.0)	0.05 (-0.01;0.11)	1.55 (0.17)
pericalcarine L	0.53 (1.0)	-0.03 (-0.17;0.1)	0.60 (1.0)	-0.05 (-0.16;0.11)	0.17 (1.0)	0.04 (-0.025;0.11)	
postcentral R	0.74 (1.0)	0.006 (-0.04;0.05)	0.87 (1.0)	-0.003 (-0.04;0.04)	0.99 (1.0)	0 (-0.04;0.04)	2.20 (0.14)
postcentral L	0.82 (1.0)	-0.005 (-0.06;0.05)	0.48 (1.0)	-0.017 (-0.07;0.04)	0.75 (1.0)	0.005 (-0.03;0.04)	
posteriorcingulate R	0.50 (1.0)	0.023 (-0.06;0.11)	0.027* (1.0)	-0.06 (-0.10; -0.013)	0.29 (1.0)	0.018 (-0.02;0.06)	2.36 (0.12)
posteriorcingulate L	0.29 (1.0)	0.035 (-0.04;0.11)	0.50 (1.0)	0.029 (-0.07;0.13)	0.51 (1.0)	0.012 (-0.05;0.06)	
parsorbitalis R	0.007* (0.462)	-0.05 (-0.08;-0.021)	0.20 (1.0)	0.049 (-0.04;0.13)	0.04* (1.0)	0.056 (0.004;0.11)	2.63 (0.11)
parsorbitalis L	0.73 (1.0)	-0.014 (-0.11;0.08)	0.44 (1.0)	-0.028 (-0.11;0.05)	0.19 (1.0)	0.0755 (-0.05;0.20)	
rostralanteriorcingulate R	0.36 (1.0)	-0.044 (-0.16;0.07)	0.33 (1.0)	-0.04 (-0.14;0.06)	0.74 (1.0)	0.01 (-0.07;0.09)	2.71 (0.16)
rostralanteriorcingulate L	0.76 (1.0)	0.003 (-0.02;0.03)	0.03* (1.0)	-0.09 (-0.16; -0.02)	0.24 (1.0)	-0.04 (-0.13;0.04)	
superiorparietal R	0.60 (1.0)	-0.019 (-0.1;0.07)	0.72 (1.0)	-0.008 (-0.06;0.04)	0.67 (1.0)	0.007 (-0.03;0.05)	2.28 (0.13)
superiorparietal L	0.47 (1.0)	-0.02 (-0.1;0.05)	0.38 (1.0)	-0.022 (-0.08;0.04)	0.55 (1.0)	0.01 (-0.03;0.05)	
superiortemporal R	0.17 (1.0)	-0.03 (-0.08;0.02)	0.03* (1.0)	-0.02 (-0.04;-0.003)	0.81 (1.0)	-0.005 (-0.05;0.05)	2.93 (0.07)
superiortemporal L	0.37 (1.0)	-0.017 (-0.06;0.03)	0.57 (1.0)	0.012 (-0.04;0.06)	0.74 (1.0)	0.005 (-0.03;0.04)	
supramarginal R	0.45 (1.0)	-0.018 (-0.07;0.04)	0.18 (1.0)	-0.06 (-0.16;0.04)	0.51 (1.0)	-0.02 (-0.08;0.04)	2.66 (0.09)
supramarginal L	0.81 (1.0)	-0.004 (-0.04;0.04)	0.57 (1.0)	0.009 (-0.03;0.05)	0.93 (1.0)	-0.001 (-0.02;0.02)	
frontalpole R	0.35 (1.0)	-0.03 (-0.12;0.05)	0.68 (1.0)	-0.015 (-0.1;0.07)	0.28 (1.0)	0.04 (-0.05;0.13)	2.80 (0.15)
frontalpole L	0.27 (1.0)	0.04 (-0.04;0.12)	0.42 (1.0)	-0.057 (-0.22;0.11)	0.34 (1.0)	0.042 (-0.06;0.14)	
transversetemporal R	0.20 (1.0)	0.04 (-0.03;0.11)	0.61 (1.0)	0.022 (-0.08;0.13)	0.68 (1.0)	0.013 (-0.06;0.09)	2.45 (0.21)
transversetemporal L	0.08 (1.0)	0.08 (-0.01;0.18)	0.63 (1.0)	-0.03 (-0.19;0.13)	0.80 (1.0)	-0.009 (-0.09;0.08)	
insula R	0.62 (1.0)	-0.022 (-0.13;0.08)	0.99 (1.0)	0.0002 (-0.13;0.13)	0.20 (1.0)	-0.03 (-0.09;0.02)	2.98 (0.1)
insula L	0.81 (1.0)	-0.01 (-0.1;0.09)	0.91 (1.0)	0.004 (-0.08;0.09)	0.46 (1.0)	0.016 (-0.04;0.07)	

Tbl. 2: Intra- and interscanner mean difference, p-values, and 95% CIs of the CT measures, including adjusted p-values. (* = < 0.05, and borderline significant in gray)

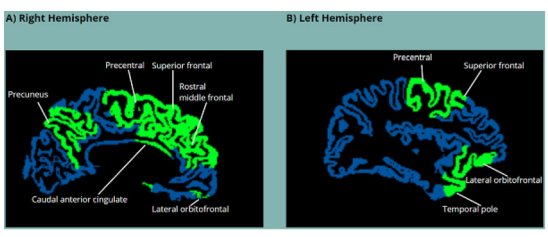

Fig. 2: Medial view of the regional cortical thickness. Regions in green represent a significant difference in thickness between the two MRI scanners. Overall, the measurements nearly always decreased after the upgrade.

References
(1) Radiology, T. A. C. o. Phantom Test Guidance for Use of the Small MRI Phantomfor the MRI Accreditation Program < https://www.acraccreditation.org/-/media/ACRAccreditation/Documents/MRI/SmallPhantomGuidance.pdf > (2018).
(2) Achten, E. et al. Intra- and interobserver variability of MRI-based volume measurements of the hippocampus and amygdala using the manual ray-tracing method. Neuroradiology 40, 558–566 (1998). https://doi.org/10.1007/s002340050644
(3) Plitman, E. et al. The impact of the Siemens Tim Trio to Prisma upgrade and the addition of volumetric navigators on cortical thickness, structure volume, and (1)H-MRS indices: An MRI reliability study with implications for longitudinal study designs. Neuroimage 238, 118,172 (2021). https://doi.org/10.1016/j.neuroimage.2021.118172

P238.
White matter R2* anisotropy is altered during migraine attacks

C. Birkl[1,2], V. Filippi[3], R. Steiger[1,2], S. Mangesius[1,2], E. R. Gizewski[1,2], G. Broessner[1,3]

[1]*Medical University of Innsbruck, Department of Neuroradiology, Innsbruck, Austria;*
[2]*Medical University of Innsbruck, Neuroimaging Research Core Facility, Innsbruck, Austria;*
[3]*Medical University of Innsbruck, Department of Neurology, Headache Outpatient Clin., Innsbruck, Austria*

Introduction: Migraine is a primary headache disorder typically characterized by recurrent attacks of disabling headache and associated with high personal and societal burden. The detailed pathophysiological mechanisms causing migraine are still elusive, however, there is limited evidence that iron might play a role[1]. MRI studies observed altered R2 (= 1/T2) and R2* (= 1/T2*) values in various brain structures of patients with migraine, indicating an iron accumulation compared to healthy controls[2–4]. This increase in iron content was associated with pain processing and the frequency of migraine attacks[2–4]. The aim of this study was to investigate if there are alterations of R2* relaxation rate in white matter during a migraine cycle of 21 days.
Methods: A male patient (age = 26 years) with episodic migraine with aura according to ICHD-3 participated in this study. The participant had a history of 3 to 5 migraine attacks per month prior to the study, each with a duration of around 24 h. During the 21 consecutive scanning days, the participant did not take any preventative or acute medication. MRI was performed at the same time on each day on a 3 T MR system (MAGNETOM Skyra, Siemens Healthineers, Erlangen, Germany) using a 64-channel head coil. The following sequences were acquired: For structural overview and tissue segmentation, a 3D T1 weighted magnetization prepared rapid acquisition gradient echo (MPRAGE). For the estimation of the white matter fiber angle θ, a diffusion weighted single-shot echo-planar imaging DTI sequence and for quantification of R2* relaxation, a multi-echo gradient echo (GRE) sequence. DTI data was analyzed using FSL DTIFIT (FSL version 6.0.5.1) to calculate the diffusion tensor model. To correct for distortions induced by eddy currents and head motion eddy_correct was used. The white matter mask was generated using FSL FAST and eroded with a 3 × 3x3 kernel to avoid partial volume effects of non-white matter tissue. R2* maps were computed voxel by voxel assuming a mono-exponential relaxation. The fiber angle θ was calculated as the angle between the first eigenvector and the direction of the main magnetic field B0 for each voxel, where θ = 0° represents fibers parallel to B0 and θ = 90° represents fibers perpendicular to B0. For plotting fiber orientation dependent R2* voxels from the entire white matter were pooled. Based on fiber orientation dependent R2*, the anisotropy index was calculated according R2* AI = (R2*max – R2*min)/(R2*-max + R2*min). Days without events were further grouped into normal days prior (Normal-pre), between (Normal-between) and after (Normal-post) days with migraine attacks.
Results: On visual inspection of the quantitative maps, no distinct feature to differentiate between days with headache, days with migraine and normal days could be observed (Fig. 1). White matter R2* across all days is shown in Fig. 2 A. R2* increased (p = 0.04) on days with migraine compared to days with headache and days without event (Fig. 2B). On average, R2* increased with increasing fiber angle from 20.1 ± 0.3 Hz at 0° to 22.6 ± 0.2 Hz at 90° (Fig. 3.). Grouping by condition revealed lower orientation dependent R2* on days with migraine as shown in Fig. 3. R2* anisotropy was found to be lower (p = 0.02) on days with migraine compared to days with headache and normal days without event (Fig. 4A and B).
Discussion and Conclusion: Our study revealed that white matter R2* is increased and R2* anisotropy is decreased during migraine attacks. The observed increase in R2* suggests an increase in iron content and might be linked with altered iron content in deep gray matter structures observed in literature[1–4]. The decrease in R2* anisotropy indicates non-iron related tissue changes, such as a decrease in myelin content, during a migraine attack. Our observation, that iron content does not solely affect R2* in migraine is supported by various studies. Granziera et al. reported a decrease in magnetization transfer ratio (MTR) in the thalamus of patients with migraine compared to healthy controls[5]. Thus, migraine related iron changes can be obscured by other disease related tissue changes. Furthermore, it was shown that the cerebral vasculature affects the orientation dependent MRI signal[6]. Therefore alterations in R2* anisotropy could be caused by vascular changes instead or in addition to changes in myelin, which would support the involvement of vascular mechanisms in migraine. We conclude that alterations in R2* during migraine attacks might be caused by changes in iron content accompanied by changes in tissue microstructure.

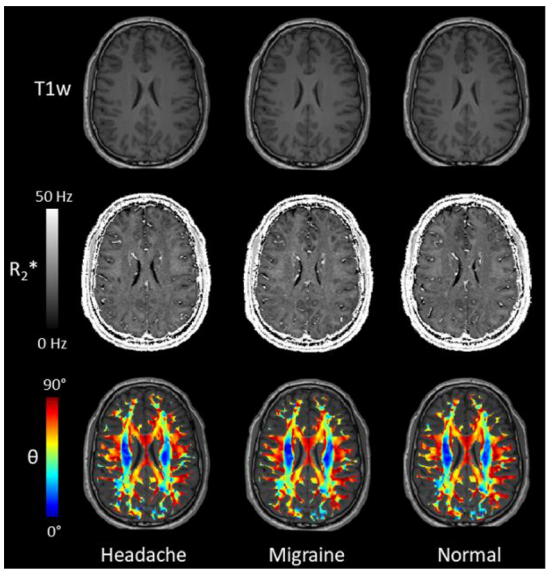

Fig. 1: A representative slice of the T1 weighted image (top row), the R2* map (middle row) and the fiber angle θ overlaid on the T1 weighted image (bottom row) of a day with headache (left column), a day with migraine (middle column) and a normal day (right column).

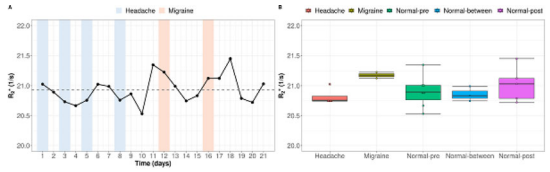

Fig. 2: R2* of white matter at all 21 days (A). R2* averaged across days with headache, migraine, normal days prior (Normal-pre), bteween (Normal-between) and after (Normal-post) days with migraine (B).

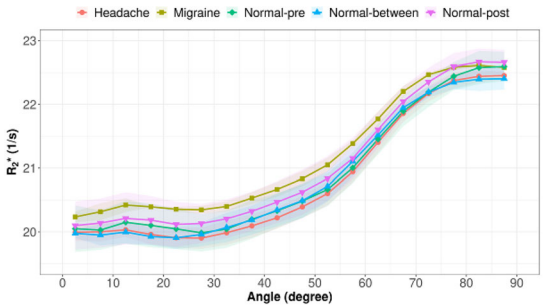

Fig. 3: Fiber orientation dependent R2* averaged across days with headache, migraine, normal days prior (Normal-pre), bteween (Normal-between) and after (Normal-post) days with migraine.

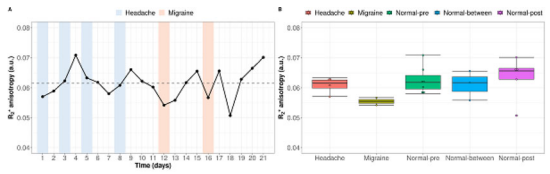

Fig. 4: R2* anisotropy at all 21 days (A) and averaged across days with headache, migraine, normal days prior (Normal-pre), bteween (Normal-between) and after (Normal-post) days with migraine (B).

References

1. Goadsby PJ, et al. Physiol Rev. 2017 Apr 1;97(2):553–622..
2. Domínguez C, et al. Neurology. 2019 Mar 5;92(10):e1076–85.
3. Kruit MCet al. Cephalalgia. 2009;29(3):351–9.
4. Tepper SJet al. Headache. 2012;52(2):236–43.
5. Granziera C, et al. Hum Brain Mapp. 2014;35(4):1461–8.
6. Kaczmarz S, et al. J Cereb Blood Flow Metab. 2020;40(4):760–74.

P239.
White-matter microstructural changes in episodic menstrual migraine patients across the pain cycle

A. R. Fouto[1], R. G. Nunes[1], A. Ruiz-Tagle[1], I. Esteves[1], G. Caetano[1], N. A. Silva[2], P. Vilela[3], R. Gil-Gouveia[4,5], P. Figueiredo.[1]

[1]*Universidade de Lisboa, Institute for Systems and Robotics—Lisboa and Department of Bioengineering, Instituto Superior Técnico, Lisbon, Portugal;*
[2]*Hospital da Luz, Learning Health, Lisbon, Portugal;*
[3]*Hospital da Luz, Imaging Department, Lisbon, Portugal;*
[4]*Hospital da Luz, Neurology Department, Lisbon, Portugal;*
[5]*Universidade Católica Portuguesa, Center for Interdisciplinary Research in Health, Lisbon, Portugal*

Introduction: Migraine is a cyclical neurological disorder that causes mild to severe headache pain followed by periods without attacks[1]. Studies using diffusion tensor imaging(DTI)[2] have shown alterations in the microstructure of multiple white matter(WM) regions in migraine patients[3]. Other studies have also reported variations across the migraine cycle[4,5]. Nonetheless, the description of these cyclic variations has been scarce and mostly using transversal designs. Here, we perform a longitudinal study to investigate microstructural variations along the four phases of the pain cycle in a group of patients with episodic menstrual migraine, including a healthy control group controlled for their menstrual cycle phase. We employ DTI as well as a more complex diffusion model, diffusional kurtosis imaging(DKI)[6], to analyse diffusion-weighted MRI(dMRI) parameters.

Methods: 14 patients with episodic menstrually-related without-aura migraine were scanned during the migraine cycle phases: M-interictal, M-preictal, M-ictal, M-postictal. A control group of 15 healthy females were evaluated during: H-postovulation and H-premenstrual phases of the menstrual cycle, to match the interictal and the peri-ictal phases, respectively. Figure 1 summarises the clinical and demographic data. We acquired 2D-EPI multi-shell dMRI data (3 T Siemens Vida; 64-chan head coil): TR/TE: 6800/89 ms, 66 slices, in-plane GRAPPA = 2, SMS = 3, and 2 mm isotropic resolution, with b-values of 400,1000,and 2000s/mm^2 along 32, 32, and 60 volumes, respectively; 8 b0s. Preprocessing followed the DESIGNER pipeline[7]. Subsequently, we used *dtifit* to perform tensor-fitting and derive fractional anisotropy(FA), mean diffusivity(MD), axial diffusivity(AD), and radial diffusivity(RD) maps. DKI fitting was done with DESIGNER, and the mean kurtosis(MK), axial kurtosis(AK), and radial kurtosis(RK) maps were extracted. All diffusion parameter maps underwent tract-based spatial statistics skeletonization[8]. The ICBM-DTI-81 WM Atlas[9] was used for analysing the data. Right and left WM tracts were combined, and 28 regions-of-interest (ROIs) were defined. A pairwise voxelwise permutation test was applied to compare patients with controls (5000 permutations; cluster-based correction; $p < 0.05$)[10,11] and adjusted for multiple comparisons with Bonferroni. Given the greater sensitivity of DKI compared with DTI (see results), only DKI was considered for further analysis. An ROI analysis was performed to investigate changes across the cycle, by extracting the median of each DKI parameter within each of the 28 ROIs. For each parameter and each ROI, we calculated the difference between each migraine phase (CyclePhase) and the average across subjects of the respective control phase. We evaluated differences along the cycle, with a linear mixed effects model analysis, in R, using CyclePhase as a fixed effect and each subject as a random effect, for each ROI and parameter. Post-hoc analysis was conducted when significant main effects were detected ($p < 0.05$), which were corrected with False Discovery Rate.

Results: Fig. 2 shows the percentage of voxels exhibiting significant differences within each ROI, for significant comparisons, with both DTI and DKI. The reduction of AD estimated with DKI in the interictal phase was the most robust, surviving adjustment for all comparisons. The spatial distribution of these AD changes along the WM skeleton is depicted in Fig. 3. Several WM tracts showed significant differences in FA and AD throughout the migraine cycle which are presented in Fig. 4.

Discussion/Conclusion: This is the first study to perform a longitudinal evaluation of WM changes along the four phases of migraine. We found that DKI has higher sensitivity in identifying microstructural abnormalities than DTI in migraine patients, robustly showing decreased AD across the brain, which is in agreement with the literature[3]. Both AD and FA varied along the cycle, in brain areas involved in pain processing. In particular, decreased AD was found to normalise around the pain period, suggesting that WM may undergo reversible and plastic microstructural changes, possibly concurrently with altered function, in the brain of migraine patients[5].

References: 1P. J. Goadsby et al., *Physiol Rev*, vol. 97, no. 2, pp. 553–622, Apr. 2017; 2R. Rahimi et al., *Brain Imaging and Behavior*. Springer, Oct. 01, 2022; 3 J. H. Jensen, et al., *Magn Reson Med*, vol. 53, no. 6, pp. 1432–1440, 2005; 4 K. K. Marciszewski et al., *The Journal of Neuroscience*, vol. 38, no. 49, pp. 10,479–10,488, 2018; 5B. Ades-Aron et al., *Neuroimage*, vol.

183, no. July, pp. 532–543, 2018; 6S. M. Smith et al., *Neuroimage*, vol. 31, no. 4, pp. 1487–1505, 2006; 7Smith SM, et al., *Neuroimage*. 31(4):1487–1505, 2006; 8S. Wakana et al., *Neuroimage*, vol. 36, no. 3, pp. 630–644, 2007; 9 K. Hua et al., *Neuroimage*, vol. 39, no. 1, pp. 336–347, 2008; 10Winkler AM, et al., *Neuroimage*. 2014;92:381–397; 11Smith SM, et al.,. *Neuroimage*. 44(1); 2009.

P240.
Identification of TERT-p mutations in gliomas using SWI-MRI: A deep learning and radiomics approach

S. Azamat[1,2], A. Ozcan[3], A. Ersen Danyeli[4,5], M. N. Pamir[5,6], A. Dinçer[5,7], K. Ozduman[5,6], E. Ozturk-Isik[1,5]

[1]*Bogazici University, Institute of Biomedical Engineering, Istanbul, Turkey;*
[2]*Basaksehir Cam and Sakura City Hospital, Department of Radiology, Istanbul, Turkey;*
[3]*Bogazici University, Depatment of Electrical and Electronics Engineering, Istanbul, Turkey;*
[4]*Acibadem Mehmet Ali Aydinlar University, Department of Medical Pathology, Istanbul, Turkey;*
[5]*Acibadem Mehmet Ali Aydinlar University, Center for Neuroradiological Applications and Research, Istanbul, Turkey;*
[6]*Acibadem Mehmet Ali Aydinlar University, Department of Neurosurgery, Istanbul, Turkey;*
[7]*Acibadem Mehmet Ali Aydinlar University, Department of Radiology, Istanbul, Turkey*

Introduction: Gliomas are the most common primary central nervous system malignant tumors in adults[1].Despite the advances in treatment strategies, the overall survival rate for aggressive forms of gliomas remains less than 10%[2].A primary contributor to this poor prognosis is the complex molecular heterogeneity exhibited by these tumors[1].A recent study revealed that telomerase reverse transcriptase promoter (TERT-p) mutations were related to poor prognosis[3].Lately, noninvasive advanced magnetic resonance imaging (MRI) techniques have gained attention for their potential to aid in diagnosis and treatment planning of gliomas.Susceptibility weighted MRI (SWI) enables visualization of neovascularization and microcalcification[4].The aim of this study is to preoperatively identify TERT-p mutations in gliomas using features of SWI extracted with radiomics and deep convolutional neural networks (CNN).

Methods: In this retrospective study, 69 patients (37 M/32F) with gliomas, who underwent preoperative MRI on a 3 T clinical MR scanner (Siemens Healthcare, Germany) and had tumor specimens available for DNA extraction, were included.Of these patients, 46 were isocitrate dehydrogenase (IDH)-wild type (IDH-wt), 23 were IDH mutant (IDH-mut), 43 were TERT-p mutant (TERTp-mut), and 26 were TERT-p wild type (TERTp-wt).Among the IDH-wt gliomas, 32 were TERTp-mut, and 14 were TERTp-wt.The MRI protocol included SWI (TR/TE = 28/20 ms, FOV = 220 mm, slice thickness = 1.6 mm) and contrast-enhanced T1W MRI (CE-T1W)(TR/TE = 589/10 ms, FOV = 220 mm, slice thickness = 3 mm).Contrast enhancing lesions were segmented on CE-T1W images in Slicer v4.8.1(http://slicer.org/) and registered onto high-resolution SWI along with the segmentation masks using FSL(http://fsl.fmrib.ox.ac.uk/fsl/fslwiki/).The largest segmentation area in both directions was used to define a rectangular bounding box around the lesion on SWI. Six pretrained deep CNN models (VGG16, VGG19, Xception, ResNet50, InceptionV3, and InceptionResNetV2) and pyradiomics were used to extract SWI image features[5–9].The dataset was then divided into train and test sets with a 0.8:0.2 ratio.The training set was oversampled using synthetic minority oversampling technique[10].Five-fold cross-validation was employed to train the classification algorithms on the training set.The performance of the machine learning algorithms was evaluated on the test set using Pycaret.

Results: The optimal model for identifying TERT-p mutation irrespective of the IDH mutation, with features extracted from InceptionV3, achieved an accuracy of 0.78 (precision = 0.80/recall = 0.88),compared to an accuracy of 0.60 (precision = 0.65/recall = 0.76) for the radiomics model(Table 1).The optimal model for detecting TERT-p mutation among IDH-wt, with features extracted from Xception, achieved an accuracy of 0.80(precision = 0.85/recall = 0.85), compared to an accuracy of 0.70 (precision = 0.75/recall = 0.85) for the radiomics model(Table 2).The feature maps extracted from Xception on SWI images indicated that the vascular regions were crucial for identifying the most relevant features(Fig. 1).

Discussion: Our study demonstrated the potential of SWI, in conjunction with deep CNN to preoperatively identify TERT-p mutations in gliomas.The deep learning-based feature extraction outperformed the radiomics model for identifying the TERT-p mutation. A recent study has found an association between perfusion metrics and TERT-p mutations[11].Similarly, our findings suggest that TERT-p mutations may have an impact on SWI image features.

Acknowledgements This study was supported by TUBITAK 1003 216S432.

Table 1. The performance metrics for the classification algorithms trained on features extracted by radiomics or pre-trained convolutional neural networks for TERT-p mutation detection in all glioma patients

Feature Extraction Method	Best Classification Method	Accuracy	AUC	Precision	Recall	F1
Radiomics	*Ada Boost Classifier*	0.60	0.51	0.65	0.76	0.70
InceptionResNetV2	*Extra Trees Classifier*	0.57	0.17	0.61	0.88	0.72
InceptionV3	*Gradient Boosting Classifier*	0.78	0.86	0.80	0.88	0.84
ResNet50	*Ridge Classifier*	0.78	0.78	0.87	0.77	0.82
VGG16	*Ada Boost Classifier*	0.42	0.37	0.55	0.55	0.55
VGG19	*Extra Trees Classifier*	0.42	0.40	0.54	0.66	0.60
Xception	*Ada Boost Classifier*	0.71	0.84	0.85	0.66	0.75

***AUC stands for area under curve*

Table 2. The performance metrics for the classification algorithms trained on features extracted by radiomics or pre-trained convolutional neural networks for TERT-p mutation detection in IDH-wild type glioma patients

Feature Extraction Method	Best Classification Method	Accuracy	AUC	Precision	Recall	F1
Radiomics	*Ada Boost Classifier*	0.70	0.42	0.75	0.85	0.80
InceptionResNetV2	*Extra Trees Classifier*	0.63	0.42	0.69	0.88	0.77
InceptionV3	*Linear Discriminant Analysis*	0.30	0.38	0.50	0.14	0.22
ResNet50	*Extra Trees Classifier*	0.60	0.33	0.66	0.85	0.75
VGG16	*Extra Trees Classifier*	0.60	0.26	0.66	0.85	0.75
VGG19	*SVN-Linear Kernel*	0.70	0.59	0.75	0.85	0.80
Xception	*SVM-Linear Kernel*	0.80	0.76	0.85	0.85	0.85

***AUC stands for area under curve*

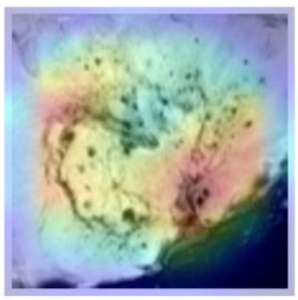

Figure 1. A class activation map extracted from Xception on SWI for TERT-p mutation identification.

References

1. Louis DN et al.The 2021 WHO Classification of Tumors of the Central Nervous System:a summary.*Neuro Oncol* 2021;23:1231–1251.
2. Johanssen T et al.Glioblastoma and the search for non-hypothesis driven combination therapeutics in academia.*Front Oncol* 2022;12:1,075,559.
3. Eckel-Passow JE et al.Glioma Groups Based on 1p/19q, IDH, and TERT Promoter Mutations in Tumors.*N Engl J Med* 2015;372:2499–2508.
4. Haller S et al.Susceptibility-weighted Imaging:Technical Essentials and Clinical Neurologic Applications.*Radiology* 2021;299:3–26.
5. Zisserman KSaA.Very Deep Convolutional Networks for Large-Scale Image Recognition.*arXiv 2021.*
6. Chollet F.Xception:Deep Learning with Depthwise Separable Convolutions.*arXiv 2021.*
7. Kaiming He XZ et al.Deep Residual Learning for Image Recognition *IEEE Conference on Computer Vision and Pattern Recognition.*
8. Christian Szegedy VV et al.Rethinking the Inception Architecture for Computer Vision *IEEE Conference on Computer Vision and Pattern Recognition.*
9. van Griethuysen JJM et al.Computational Radiomics System to Decode the Radiographic Phenotype.*Cancer Res* 2017;77:e104-e107.
10. Nitesh V Chawla KWB et al.Smote:synthetic minority over-sampling technique.*Journal of artificial intelligence research* 2002;16:321–357.
11. Ivanidze J et al.MRI Features Associated with TERT Promoter Mutation Status in Glioblastoma.*J Neuroimaging* 2019;29:357–363.

P241.
Improved automated segmentation of glioblastoma with ensemble learning

C. Passarinho[1], O. Lally[2], P. Figueiredo[1], R. G. Nunes[1]

[1]*Universidade de Lisboa, Institute for Systems and Robotics – Lisboa and Department of Bioengineering, Instituto Superior Técnico, Lisbon, Portugal;*
[2]*King's College London, London, United Kingdom*

Introduction: Glioblastomas (GBM) are the most common and aggressive type of primary brain tumours, and GBM patients undergo intensive MRI protocols before treatment and as follow-up. Image segmentation of the tumour regions, including the necrotic tumour core, the contrast-enhancing tumour, and peritumoural edema or infiltrations, is crucial for precise therapy planning and progression monitoring, as it provides information about tumour volume, location, and shape. The current gold standard is manual segmentation performed by expert neuroradiologists, but this is an arduous and time-consuming task that suffers from inter-observer variability[1]. Reliable automated segmentation methods that can improve the quality and efficiency of diagnosis and patient follow-up would therefore be of great value. The Brain Tumour Segmentation (BraTS) challenge dataset[2] has become the benchmark for the development of multiple automatic segmentation methods, namely based on deep learning. Previous work shows that model performance varies substantially between the different tumour regions, with different models yielding the best performance for distinct regions[3]. We hypothesise that a combination of deep learning models with different strengths may result in the best overall performance and propose an ensemble learning method for brain tumour segmentation, combining the outputs of two distinct architectures based on their segmentation accuracy for each tumour region.

Methods: We tested the performance of two network architectures for brain tumour segmentation implemented in the Medical Open Network for Artificial Intelligence (MONAI[4]), a Pytorch-based open-source framework for deep learning in healthcare imaging: 1) a ResNet-based architecture using autoencoder regularisation[5]; and 2) Swin UNEt TRansfomers (Swin UNETR), a U-shaped network that uses a Swin transformer as the encoder and a CNN-based decoder[6]. The BraTS 2021 challenge dataset includes 1251 GBM patients, each with validated manual annotations of the key tumour substructures and four 3D multi-parametric MRI (mpMRI) volumes of T1-weighted (T1), T2-weighted (T2), T2-weighted FLAIR, and T1-weighted contrast-enhanced (T1ce) scans. This dataset was divided into subsets of 60%, 20%, and 20% for training, validation, and testing, respectively. After normalising the signal intensity of the MRI scans and applying data augmentation transforms, both models were trained using all four MRI modalities. Three nested subregions were considered: Tumour Core (TC), Enhancing Tumour (ET), and the Whole Tumour (WT), including edema.
Considering prior reports on the performance of each network for the different subregions, as well as the Dice Similarity Coefficients (DSC) we obtained with the testing dataset, an ensemble model that combines the WT and TC grading from the ResNet architecture and the ET classification from the Swin UNETR was considered (Fig. 1), due to the higher accuracy of the Swin transformers in classifying smaller regions[7], such as the ET.
Overall model accuracy was assessed using the DSC of each segmented region with the corresponding manual segmentation labels from the BraTS dataset.
Results: The DSC obtained with the two network architectures are presented in Figs. 2 and 3. The results corroborate the selected combination of segmentation outputs from the two networks. The segmentation accuracy of the WT region was consistent across the two models, whereas the TC and ET regions were more accurately delineated using the ResNet architecture and the Swin UNETR, respectively. In Fig. 4, the manual segmentation for a representative subject can be visually compared to the outputs obtained.
Conclusion We investigated the viability of using a fully automated deep learning-based ensemble method for brain tumour segmentation relying on T1, T2, FLAIR, and T1ce images. Our proposed segmentation approach yielded results comparable to the manual segmentation provided in the BraTS dataset. As anticipated, the Swin UNETR architecture was considerably more accurate than the ResNet in the classification of the ET region, with significantly increased DSC due to the self-attention mechanism intrinsic to this network, which improves the definition of smaller structures. We showed that the combination of the two models significantly improved segmentation accuracy, largely due to the better performance of the Swin UNETR model for the ET region. Future work will include training the same models with k-fold cross-validation to ensure results that can be generalised to unknown data.

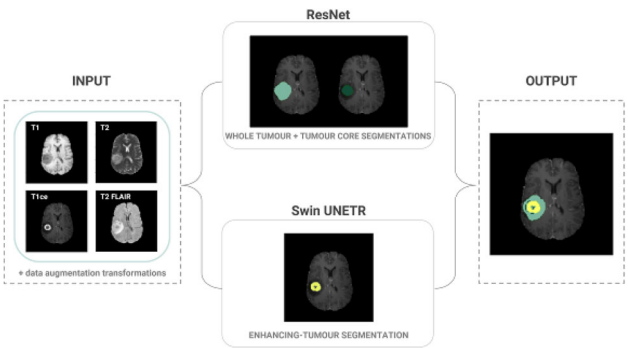

	Whole Tumour	Tumour Core	Enhancing Tumour
ResNet [7]	0.834 [0.828, 0.840]	0.771 [0.748, 0.795]	0.675 [0.665, 0.685]
Swin UNETR [8]	0.838 [0.825, 0.852]	0.726 [0.708, 0.743]	0.753 [0.740, 0.767]
Proposed model	83.4%	77.1%	75.3%

Fig. 2: Median DSC and interquartile range across the testing dataset for the two networks. Circled in red are the models selected for each subregion. The accuracy of the proposed model is summarised in the bottom row.

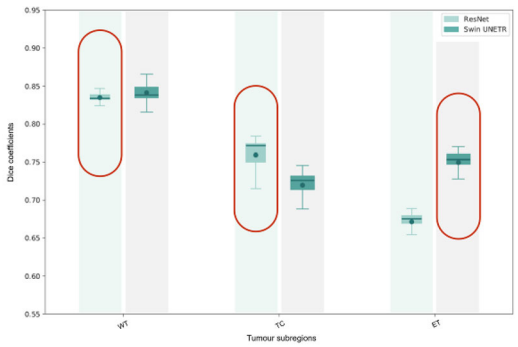

Fig. 3: DSC distributions across the testing dataset for each network and tissue label. The dark green line and dot inside each box denote the median and mean values, respectively. Circled in red are the models selected for each subregion.

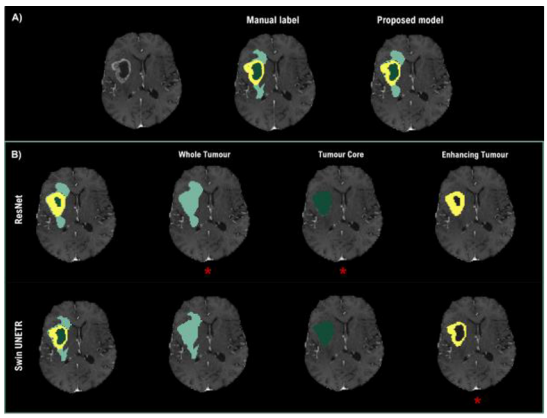

Fig. 4: (A) T1ce image for a representative subject overlayed with the BraTS manual classification and the proposed model output. (B) Segmentation outputs obtained using the two architectures - red asterisks denote the regions selected from each network.

References

[1] Işın A, et al. *Procedia Computer Science.* 2016.
[2] https://www.med.upenn.edu/cbica/brats2021/
[3] Menze et al. *IEEE Trans Med Imaging.* 2015.
[4] https://monai.io/
[5] Myronenko, A. *BrainLes.* Springer, Cham. 2018.
[6] Hatamizadeh A, et al. *BrainLes.* Springer, Cham. 2021.
[7] Liu Z, et al. *IEEE/CVF Intern Conf on Computer Vision.* 2021.

P242.
MRI based radiomics in predicting histologic grade and muscle invasiveness of urinary bladder cancer

C. Das[1], A. S[1], D. Dwivedi[2]

[1]*AIIMS New Delhi, Radiodiagnosis, New Delhi, India;*
[2]*KGMU, Radiology, Lucknow, India*

Histological grade and muscle invasiveness holds a great clinical significance in the management and prognosis of bladder cancer. Our objective was to create a radiomics model based on magnetic resonance imaging that can predict the histological grade and muscle invasiveness of bladder cancer pre-opertaively.

Methods: In a prospective study, we gathered data from 50 bladder cancer patients who had an MRI scan before their surgery. Radiomics features were extracted from T2-weighted, diffusion-weighted, and dynamic contrast-enhanced images obtained from a 1.5 T MRI scanner. The variable clustering algorithm was applied to these features, and all cluster features were univariably assessed using receiver operating characteristic (ROC) curves. Multiple models were created and cross-validated based on multivariable analysis to minimize overfitting and predict the grade of the tumor and muscle invasiveness.

Results Our radiomics model 4 comprising of contrast, age and VIRADS score parameters showed AUC of 0.9(95% CI -1.9, 34.26) and a p value of 0.079, model 5 comprising of contrast and T2 parameters showed AUC of 0.87(95% CI -0.0.13, 0) and a p value of 0.038 and Model 3 comprising of contrast and age parameters showed AUC of 0.86(95% CI -3.65, 37.51) and a p value of 0.017 for differentiating high grade tumors from low grade tumors. Radiomics models 3 for the differentiation of muscle invasion, comprising of T2, DWI and Age had a AUC of 0.91 (95% CI- 0.56, 14.89) and a p value of 0.035.

Discussion: Accurately predicting the histologic grade and muscle invasion of bladder cancer in a noninvasive manner is crucial due to the varying clinical treatments and prognoses. Our study aimed to create multiple models for preoperative assessment of bladder cancer grade and muscle invasiveness. Our radiomics model, which incorporated the optimal radiomics signature along with clinical risk factors such as age and the VIARDS score, exhibited superior diagnostic abilities.

Numerous studies have investigated the potential of radiomics in preoperative assessment of bladder cancer grade. Longchao Li et al. utilized T2 and ADC in their MRI-based radiomics approach, which exhibited strong discrimination between high-grade and low-grade tumors, with an AUC of 0.93 in the validation set. Similarly, Zheng et al. developed a model using T2 and DCE to predict Ki67 expression in bladder cancer, yielding favorable results in both the training (AUC of 0.859) and validation sets (AUC of 0.819).

Wang et al. also reported an MRI-based radiomics approach using T2WI, DWI and ADC maps, that demonstrated effective differentiation between high-grade and low-grade tumors, achieving AUCs of 0.9233 and 0.9276 in the training and validation cohorts, respectively. However, our model did not indicate statistical significance in the DWI features for tumor grade, which may be due to the exclusion of ADC maps and the use of DWIs instead.

When assessing muscle invasion Model 3, which combined T2, DWI, and age parameters, had an AUC of 0.91. The performance of our

radiomics model is in par with other studies showing similar results. Zheng et al. performed a study that included 199 patients of bladder cancer (no prior h/o TURBT). The radiomics model based on T2W images to predict muscle invasion had an AUC of 0.913 in the training set and 0.874 in the validation set.

Conclusion: A multiparametric radiomics approach based on MRI has the potential to serve as a non-invasive imaging tool for preoperative grading of bladder cancer and evaluating muscle invasion.

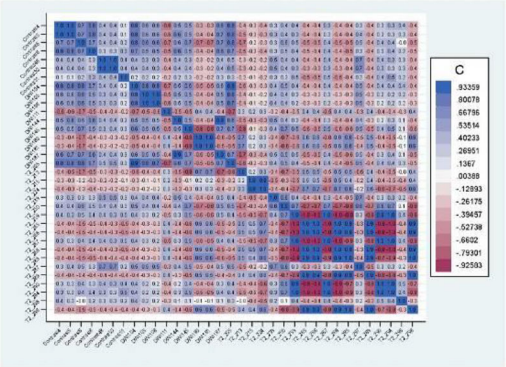

Correlation matrix among MRI parameters that were statistically significant at 2% and AUC>72% either for grade or cases.

Reference

1. Li L, Zhang J, Zhe X, Chang H, Tang M, Lei X, Zhang L, Zhang X. An MRI-based radiomics nomogram in predicting histologic grade of non-muscle-invasive bladder cancer. Frontiers in oncology. 2023 Mar 16;13:1,025,972.

2. Zheng Z, Gu Z, Xu F, Maskey N, He Y, Yan Y, Xu T, Liu S, Yao X. Magnetic resonance imaging-based radiomics signature for preoperative prediction of Ki67 expression in bladder cancer. Cancer Imaging. 2021 Dec;21(1):1–4.

3. Wang H, Hu D, Yao H, Chen M, Li S, Chen H, Luo J, Feng Y, Guo Y. Radiomics analysis of multiparametric MRI for the preoperative evaluation of pathological grade in bladder cancer tumors. European radiology. 2019 Nov;29:6182–90.

4. Wu S, Zheng J, Li Y, Wu Z, Shi S, Huang M, Yu H, Dong W, Huang J, Lin T. Development and validation of an MRI-based radiomics signature for the preoperative prediction of lymph node metastasis in bladder cancer. EBioMedicine. 2018 Aug 1;34:76–84.

Correlation matrix among MRI parameters that were statistically significant at 2% and AUC > 72% either for grade or cases.

P243.
An MRI-based grading system for preoperative risk estimation of positive surgical margin after radical prostatectomy

L. Xu[1], G. Zhang[1], J. Zhang[1], X. Zhang[1], X. Bai[1], L. Chen[1], Q. Peng[1], Z. Jin[1], H. Sun.[1]

[1]*Peking Union Medical College Hospital, Radiology, Beijing, China*

Introduction: Positive surgical margin (PSM) in pathology after radical prostatectomy (RP) indicates unfavorable prognosis (1–3). Preoperative prediction of PSM after RP would benefit the management of prostate cancer. MRI is an important imaging method for prostate cancer diagnosis and staging. Many tumor-related imaging features, such as tumor location determined by MRI, Prostate Imaging-Reporting and Data System (PI-RADS) category, and length of capsular tumor contact, have been reported to correlate with PSM (4–6). However, relevant MRI-based grading systems for preoperative prediction of PSM are lacking in clinical practice.

In this study, we aimed to construct a simplified scoring system using tumor-related MRI features to evaluate the risk of PSM after RP, validate the grading system in an independent cohort, and compare the model with a previously reported one.

Methods: Patients who had undergone prostate MRI followed by RP between January 2017 and January 2021 were retrospectively enrolled as the derivation group, and those between February 2021 and November 2022 were enrolled as the validation group. One radiologist evaluated tumor-related MRI features, including the capsule contact length (CCL) of lesions, capsular irregularity or bulge, neurovascular bundle asymmetry, obliteration of rectoprostatic angle, frank extraprostatic extension (EPE), and apex abutting (Fig. 1). Binary logistic regression and decision tree analysis were used to select risk features for PSM. The area under the curve (AUC), sensitivity, and specificity of different systems were calculated. The interreader agreement of the scoring systems was evaluated using the kappa statistic.

Results: PSM was identified in 29.8% (42/141) of patients in the derivation group and 36.4% (32/88) of patients in the validation group. In combination with binary logistic regression and decision tree analysis, the first grading system was proposed (mrPSM1) using two imaging features, namely, CCL $\geq$ 20 mm and apex abutting.

The second grading system—mrPSM2—in combination with the radiologist"s perspective was also proposed, in which frank EPE was included in Grade 3, as follows:

Grade 1: CCL $<$ 20 mm without apex abutting, low risk of PSM;
Grade 2: CCL $\geq$ 20 mm or apex abutting, intermediate risk of PSM;
Grade 3: CCL $\geq$ 20 mm and apex abutting, or frank EPE, high risk of PSM.

In the derivation group, the AUC was 0.705 (95% CI: 0.614–0.795) for mrPSM1 and 0.713 (95% CI: 0.624–0.802) for mrPSM2. In the validation group, our grading systems showed comparable AUC with Park et al."s model (0.672–0.686 vs. 0.646, $p > 0.05$) and significantly higher specificity (0.732–0.750 vs. 0.411, $p < 0.001$) (Fig. 2). The kappa value was 0.764 for mrPSM1 and 0.776 for mrPSM2. Decision curve analysis showed a higher net benefit for mrPSM2.

Discussion: Our study constructed MRI-based grading systems for preoperative prediction of PSM in patients who underwent RP and validated them in an independent cohort. Both grading systems showed the feasibility of predicting PSM with AUCs of 0.705 and 0.713 in the derivation group and 0.672 and 0.686 in the validation group. The proposed MRI-based grading systems showed significantly higher specificity than Park et al."s system. The mrPSM2 seemed to outperform mrPSM1 and Park et al."s system with higher net benefit.

Conclusion: The proposed mrPSM grading systems for postoperative surgical margin status prediction are simplified and maintain good performance; they show high specificity for identifying patients with the risk of PSM and potentially providing benefit for the management of patients with prostate cancer.

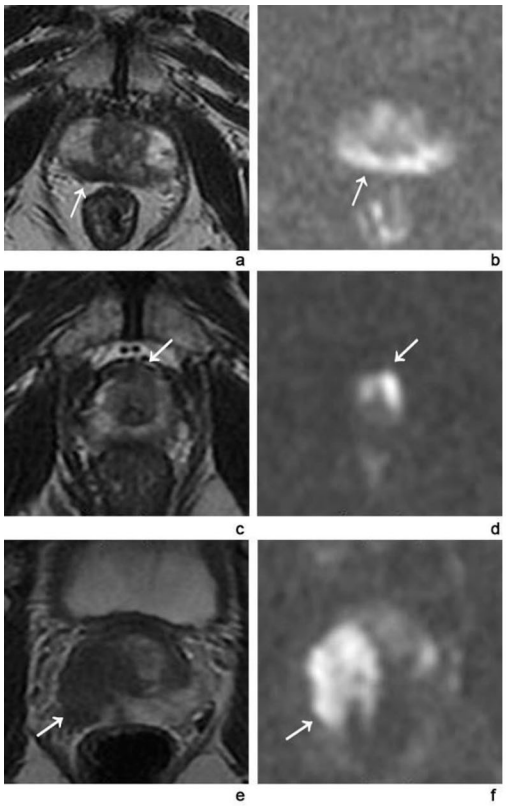

Fig. 1: Examples of MRI features correlate with positive surgical margins after surgery. Images on the left column are axial T2-weighted images and those on the right column are corresponding diffusion-weighted images (b value = 2000). (a–b) A 75-year-old man with prostate cancer. Images show the curvilinear contact length of the lesion in the posterior peripheral zone ≥ 20 mm (arrows). (c–d) A 62-year-old man with prostate cancer. Images show the apex lesion encircling the distal prostatic urethra (arrows) and indicating apex abutting. (e–f) A 73-year-old man with prostate cancer. Images show the frank extraprostatic extension of the right peripheral zone lesion (arrows).

Table 1. Performance of mrPSM grading systems in the derivation and validation groups

	Derivation group		Validation group			*p* values	
Grading systems	mrPSM1	mrPSM2	mrPSM1	mrPSM2	Park et al.'s system	mrPSM1 vs. Park et al.	mrPSM2 vs. Park et al.
Low risk (%) *	17.4 (15/86)	16.7 (14/84)	25.0 (14/56)	24.1 (13/54)	17.9 (5/28)	-	-
Intermediate risk (%) *	37.5 (12/32)	31.8 (7/22)	47.6 (10/21)	40.0 (6/15)	42.6 (20/47)	-	-
High risk (%) *	65.2 (15/23)	60.0 (21/35)	72.7 (8/11)	68.4 (13/19)	53.8 (7/13)	-	-
AUC	0.705 (0.614–0.795)	0.713 (0.624–0.802)	0.672 (0.565–0.780)	0.686 (0.577–0.794)	0.646 (0.542–0.751)	0.566	0.395
Cut-off value	≥ 2	≥ 2	≥ 2	≥ 2	≥ 2	-	-
Accuracy	0.695 (0.692–0.698)	0.695 (0.692–0.698)	0.682 (0.677–0.687)	0.682 (0.677–0.687)	0.568 (0.563–0.574)	0.089	0.078
Sensitivity	0.643 (0.498–0.788)	0.667 (0.524–0.809)	0.562 (0.391–0.734)	0.594 (0.424–0.764)	0.844 (0.718–0.970)	0.008	0.013
Specificity	0.717 (0.628–0.806)	0.707 (0.617–0.797)	0.750 (0.637–0.863)	0.732 (0.616–0.848)	0.411 (0.282–0.540)	< 0.001	< 0.001
PPV	0.491 (0.359–0.623)	0.491 (0.361–0.621)	0.562 (0.391–0.734)	0.559 (0.392–0.726)	0.450 (0.324–0.576)	-	-
NPV	0.826 (0.745–0.906)	0.833 (0.754–0.913)	0.750 (0.637–0.863)	0.759 (0.645–0.873)	0.821 (0.680–0.963)	-	-

Note—AUC = area under the receiver operating characteristic curve, PPV = positive predictive value, NPV = negative predictive value, mrPSM1 = the first MRI-based grading system for positive surgical margin, mrPSM1 = the second MRI-based grading system for positive surgical margin.

* Data are the percentage of PSM.

Fig. 2: Performance of mrPSM grading systems in the derivation and validation groups

References

1. Zhang L, Zhao H, Wu B, Zha Z, Yuan J, Feng Y. Predictive Factors for Positive Surgical Margins in Patients With Prostate Cancer After Radical Prostatectomy: A Systematic Review and Meta-Analysis. Frontiers in oncology 2020;10:539,592.
2. Yossepowitch O, Briganti A, Eastham JA, et al. Positive surgical margins after radical prostatectomy: a systematic review and contemporary update. European urology 2014;65(2):303–13.
3. Matti B, Reeves F, Prouse M, Zargar-Shoshtari K. The impact of the extent and location of positive surgical margins on the risk of biochemical recurrence following radical prostatectomy in men with Gleason 7 prostate cancers. Prostate 2021;81(16):1428–34.
4. Quentin M, Schimmoller L, Ullrich T, et al. Pre-operative magnetic resonance imaging can predict prostate cancer with risk for positive surgical margins. Abdominal radiology (New York) 2022;47(7):2486–93.
McEvoy SH, Raeside MC, Chaim J, Ehdaie B, Akin O. Preoperative Prostate MRI: A 5. Road Map for Surgery. AJR American journal of roentgenology 2018;211(2):383–91.
6. Alessi S, Maggioni R, Luzzago S, et al. Apparent Diffusion Coefficient and Other Preoperative Magnetic Resonance Imaging Features for the Prediction of Positive Surgical Margins in Prostate Cancer Patients Undergoing Radical Prostatectomy. Clin Genitourin Cancer 2021;19(6):e335-e45.

P244.
Delayed MRI scans of living strangulation victims still reveal internal signs

M. Bauer[1], C. Hollenstein[1], J. M. Lieb[2], S. Grassegger[3], T. Haas[2], E. Scheurer[1], C. Lenz[1]

[1]*University of Basel, Department of Biomedical Engineering, Center for Medical Image Analysis & Navigation (CIAN), Basel, Switzerland;*
[2]*University of Basel, Department of Radiology and Nuclear Medicine, University of Basel Hospital, Basel, Switzerland;*
[3]*Österreichische Gesundheitskasse im Gesundheitszentrum für Physikalische Medizin Liezen, Liezen, Austria*

Introduction: Performing neck MRI scans of living strangulation victims is currently not a routine task in forensic medicine [1–4]. Nevertheless, in the standardly performed forensic examination, external signs of the strangulation event may be sparse or may heal rapidly [5]. Therefore, MRI scans of the head and neck can be helpful in revealing the presence and severity of the strangulation event [1, 2]. In existing publications examining strangulation victims, the MRI scans were performed shortly after the incident (on average within 2 days thereafter) [1–4]. In this study, we investigated if delayed MRI scans performed between 5 and 12 days after the event still reveal internal signs of strangulation. Furthermore, the finding locations and the most useful MRI sequence for radiologists were determined.
Methods: 19 living strangulation victims were included in this study and underwent the standard forensic examination as well as a neck examination using a 3 T MRI system (Siemens MAGNETOM Prisma, Siemens Healthineers Erlangen, Germany). The MRI protocol consisted of a coronal T1-weighted TSE, coronal T2-weighted SPACE, transversal T1-weighted Dixon, transversal T2-weighted Dixon, sagittal T1-weighted MPRAGE, transversal RESOLVE diffusion and sagittal FLAIR. Two radiologists, one with experience in clinical and forensic radiology and one with clinical experience in neuroradiology and head and neck radiology but without experience in forensic radiology, evaluated the images blinded to any patient information except age and sex. Statistical analyses and plots were performed using python (version 3.9.13 [6]). This study was approved by the local ethics committee.

Results: The subject overview is given in Table 1. In the 19 MRI data sets, 93 findings were detected by the two radiologists in total, of which 57 were edema and 38 hemorrhages. Two scans did not show any findings. Externally, 46 findings were recorded during the standard forensic examination up to one day after the incident, whereby five subjects showed no external signs. The subjects without internal findings and the subjects without external findings are not the same. Edema were detected most frequently in the thyroid (15% of all findings), subcutis and muscles (each 12%), while hemorrhages are more prominent in the muscles (10%), thyroid (9%) and lymph nodes (8%), as can be seen in Fig. 1. Figure 2 shows that in 65% of the cases with findings, the radiologists declared T2-weighted SPACE as the most useful MRI sequence, followed by T1-weighted TSE (47%) and MPRAGE (41%). The interrater agreement of the two radiologists revealed a low agreement with a Cohen"s kappa of -0.01.

Discussion: More findings were visible in the MR images after 5 to 12 days (n = 93) than externally on the incident day (n = 46), making MRI a valuable documentation tool for strangulation victims. Edema made up 61% of all internal findings, which can be supported by the clearance of hemorrhages leading to edema occurring several days after the incident [7]. In concordance with existing literature, findings in the subcutis, muscles and lymph nodes were observed frequently [1–4]. However, findings in the thyroid were not reported to be frequent until now. Importantly, the MRI protocol acquired in this work was based on sequences adapted for high quality imaging of the neck and ideally needs to be developed as a cooperation between experienced MRI physicists, radiologists and radiographers. Our low interrater agreement can be explained by the different backgrounds of the radiologists in forensic and clinical radiology, leading to differing assessment approaches and results [3, 4].

Conclusion By performing a neck MRI, important internal findings can still be detected 5 to 12 days after a strangulation event. Edema are more frequent findings than hemorrhages. In general, most findings are detectable in the thyroid and muscles, with edema being additionally present in the subcutis and hemorrhages in the lymph nodes. T2-weighted SPACE was assessed to be the most useful MRI sequence.

Characteristic	Distribution
Sex	15 female, 3 male
Age (years)	33 ± 7.5 (mean ± standard deviation); range: 21 - 50
Time between incident and MRI (days)	8 ± 1.7 (mean ± standard deviation); range: 5 - 12

Fig. 1: Subject overview with distribution of sex, age and time between incident and MRI.

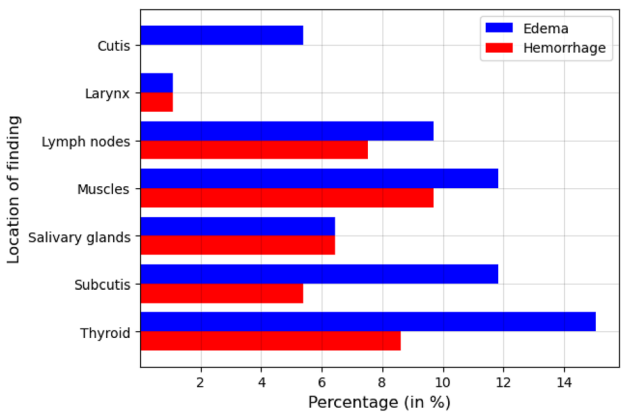

Fig. 2: Locations of MRI findings and corresponding frequencies as percentage of all findings.

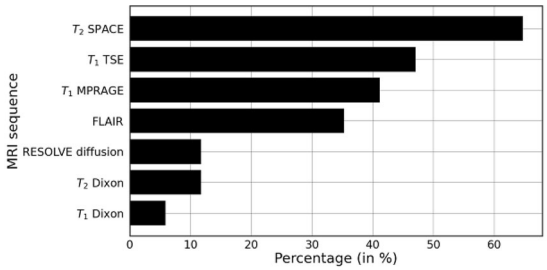

Fig. 3: Preferences of MRI sequences according to the subjective perception of the two radiologists in percent for all scans with internal findings. Multiple nominations of MRI sequences per MRI scan were possible.

References

[1] Yen, K, et al., https://doi.org/10.1007/s00414-006-0121-y
[2] Bruguier, C, et al., https://doi.org/10.1080/20961790.2019.1592314
[3] Heimer, J, et al., https://doi.org/10.1007/s00330-019-06033-x
[4] Pivec, SM, et al., Proc. Intl. Soc. Mag. Reson. Med. 20 (2012).
[5] Sharman, LS., et al., https://doi.org/10.1136/bmjopen-2023-072077
[6] Van Rossum, G, and Drake, FL, 2009. Python 3 Reference Manual. CreateSpace, Scotts Valley, CA.
[7] Pan, P, et al., https://doi.org/10.3389/fnins.2020.00685
[8] Christe, A, et al., https://doi.org/10.1016/j.legalmed.2010.05.004

P245.
Comprehensive multi-pool CEST imaging at 7 T MRI in ischemic stroke patients

T. A. Möhle[1], M. S. Fabian[1], J. R. Rajput[1,2], J. R. Schüre[1], J. A. Sembill[3], J. B. Kuramatsu[3], S. Schwab[3], M. Zaiss[1,4,5], A. Dörfler[1], M. A. Schmidt[1]

[1]*Friedrich-Alexander-Universität Erlangen-Nürnberg (FAU), Department of Neuroradiology, Erlangen, Germany;*
[2]*Friedrich-Alexander-Universität Erlangen-Nürnberg (FAU), Pattern Recognition Lab, Erlangen, Germany;*
[3]*Friedrich-Alexander-Universität Erlangen-Nürnberg (FAU), Department of Neurology, Erlangen, Germany;*
[4]*Max-Plank-Institute for Biological Cybernetics, Magnetic Resonance Center, Tübingen, Germany;*
[5]*Friedrich-Alexander-Universität Erlangen-Nürnberg (FAU), Department Artificial Intelligence in Biomedical Engineering, Erlangen, Germany*

Introduction: Chemical Exchange Saturation Transfer (CEST) imaging has emerged as a promising imaging modality in acute ischemic stroke (AIS). It utilizes the apparent chemical exchange between protons belonging to the proton pool of specific metabolites and protons of the bulk water pool. This allows for pH-dependent image contrasts offering an insight into the metabolic state of affected areas. In this first study at 7 T in AIS using multi-pool CEST, we aim to quantify acidity changes to further reveal pathophysiological processes in the ischemic brain parenchyma and possibly aid individual outcome prediction.

Methods: This prospective cross-sectional study aims to enroll 30 subjects with time from symptomatic onset to MR imaging (TOTI) $\leq$ 96 h. Measurements are acquired by a MAGNETOM Terra X 7 T scanner (Siemens Healthineers AG, Erlangen) with an 8Tx/32Rx head coil (Nova Medical, Wilmington, USA). A clinical stroke protocol was applied, followed directly by a centric 3D snapshot GRE sequence with homogenous MIMOSA pre-saturation (120 Gaussian

pulses 15.36 ms, DC = 60.52%) at three B1 levels of 0.72, 1.0, and 1.5 μT. Saturated images were obtained for 56 frequency offsets distributed non-equidistantly between -100 and + 100 ppm. CEST evaluation was conducted through established methods as in [1], yielding four different CEST contrasts: amide-CEST, dipolar rNOE-CEST, semisolid MT and guanidine CEST. Additionally, a novel approach (PICAE)[2] has been implemented yielding quantitative contrast maps "z1" for the solute pools only dependent on the proton exchange rate and target solute concentration. Manual central 3D ROI segmentation of lesions & references was performed and evaluated using relevant clinical parameters.

Results: Currently, 6 subjects have been recruited. Relevant subject characteristics are shown in Fig. 1. Exemplary CEST maps yielded by the PICAE approach and the corresponding FLAIR image are presented in Fig. 2. In the central AIS area (3D ROI), signal differences compared to the reference presented with a mean (SD) of 16.07% (13.69), 14.18% (12.4), -0.92% (26.02), and 9.01% (14.68) for amide-CEST, dipolar rNOE-CEST, semisolid MT and guanidine CEST, respectively. Subjects with high initial NIHSS (i.e. 16 & 18) showed signal alterations in guanidine of 23.15% and in amide-CEST of 1.78%. For subjects measured less than 60 h post stroke, a gradual amide-CEST signal reduction can be observed; for subjects with later measurements, amide-CEST values seem to increase (Fig. 3). An overall mean amide signal reduction was also evident from comparing the mean values of AIS to the reference tissue (Fig. 4). Figure 4 also demonstrates higher heterogeneity of amide-CEST values than guanidine values. The limitations of employing further statistical analysis due to the small sample sizes are planned to be overcome by the recruitment of more study participants as recruiting is ongoing.

Discussion: The measured amide-CEST values at 7 T, which are solely dependent on amide concentration and their protons' exchange rate, are on average reduced in the ischemic lesion. This signal reduction is consistent with previous studies at 3 T using the MTR asymmetry approach on 2D ROI suggesting higher acidity[3]. However, in our data, this is only true for subjects with lower NIHSS, possibly by varying TOTI. In contrast, in high NIHSS subjects, pronounced signal reductions are observed in the guanidine contrast. Amide-CEST is proven to be pH sensitive. In AIS measured early ($\leq$ 60 h), the observed gradual decrease in amide-CEST is therefore likely due to tissue acidosis following the ischemic event. However, because the amide-CEST value is also influenced by amide concentration, the contribution of solute dilution due to cerebral edema at this stage must also be considered. The subsequently measured AIS (> 60 h) presented with an increase in amide-CEST which may indicate deacidification. Invading microglia and cerebral edema are discussed to be contributing factors to this previously described trend of apparent pH reversal[4]. Consistently reduced rNOE is conformable with reduced lipid contents in AIS, though this might also be due to contributing T1 effects by more facilitated mobility of lipids in AIS. Subject recruitment is ongoing and subjects' outcome is yet to be included. With that, we expect to add validity and statistical power to our results solidifying our preliminary findings.

Conclusion: With this study, we gain insights of employing a 3D multi-pool 7 T CEST protocol and quantitative neural network evaluation in acute stroke patients for the first time. The amide-CEST and guanidine pool showed the most promising signal alterations in AIS compared to reference tissue. With further subject recruitment and more clinical parameters, we plan to confirm our early findings.

Subject	1	2	3	4	5	6	Mean	σ_{SD}
Age	63	73	78	63	67	54	66,33	7,70
Sex	F	M	M	M	M	F	-	-
initial NIHSS	1	2	18	2	16	2	6,83	7,22
TOTI [h]	43,38	67,02	75,07	22,25	76	56	56,62	19,07
AIS Volume [mL]	0,49	4,67	14,28	0,89	3,43	0,82	4,10	4,80

Fig. 1: Relevant subject characteristics (selection). TOTI: Time from stroke onset to MR imaging; NIHSS: National Institutes of Health Stroke Scale.

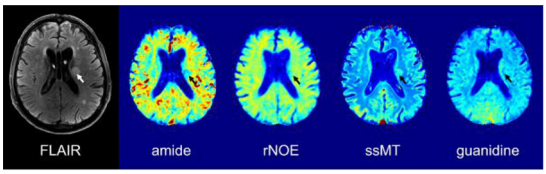

Fig. 2: Exemplary FLAIR image and CEST maps of Subject 2. AIS lesion is marked with an arrow. amide-CEST; rNOE: relayed nuclear Overhauser effect; ssMT: semisolid magnetization transfer.

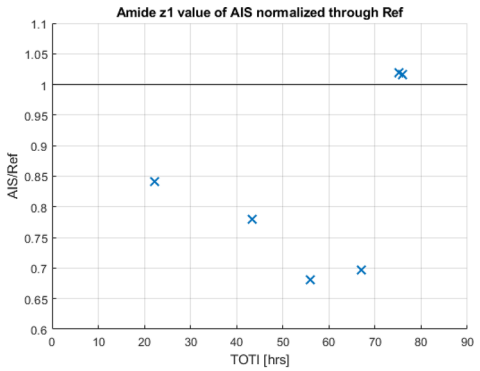

Fig. 3: Mean AIS value of amide contrast normalized by the contralateral reference (Ref). TOTI: time from onset to imaging.

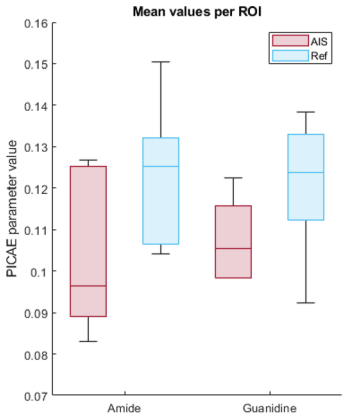

Fig. 4: Mean amide and guanidine values of AIS and contralateral reference. PICAE parameter value = concentration of solute times proton exchange rate of solute.

References

1. Mennecke et al. NMR Biomed 2022,
2. Rajput et al. Manuscript in work 2023,
3. Heo et al. NMR Biomed 2022,
4. Zöllner et al. Stroke 2015.

P246.
Investigating automated acute ischemic stroke lesion delineation based on apparent diffusion coefficient thresholds

V. Gosch[1], K. Villringer[1], I. Galinovic[1], R. Ganeshan[1], S. K. Piper[1], J. B. Fiebach[1], A. Khalil[1]

[1]*Charité Universitätsmedizin Berlin, Center for Stroke Research Berlin, Berlin, Germany*

Introduction: Automated lesion segmentation is increasingly used in acute ischemic stroke imaging. For algorithms based on MRI, most commercially available lesion segmentation algorithms use absolute apparent diffusion coefficient (ADC) thresholds for the determination of the ischemic lesion (1). While the algorithms are already used in clinical practice and were implemented in many multicenter studies, the underlying assumptions behind frequently applied ADC thresholds have not yet been frequently independently replicated (1–3). Therefore, we explored in detail the performance of a widely used ADC threshold for delineating baseline diffusion-weighted imaging (DWI) lesions.

Methods: Retrospective, exploratory analysis of the prospective observational single-center 1000Plus study performed by the Center for Stroke Research Berlin from September 2008 to June 2013 (clinicaltrials.org; NCT00715533) (4). We built a fully automated lesion segmentation algorithm using a fixed ADC threshold ($\leq 620 \times 10 - 6$ mm2/s) to delineate the baseline DWI lesion and analyzed its performance compared to manual assessments. Diagnostic capabilities of best possible ADC thresholds were investigated using receiver operating characteristic curves. Influential patient factors on ADC thresholding techniques' performance were studied by conducting multiple linear regression.

Results: 108 acute ischemic stroke patients were selected for analysis. The median Dice coefficient for the algorithm was 0.43 (IQR 0.20—0.64). Mean ADC values in the DWI lesion ($\beta = -0.68$, $p < 0.001$) and DWI lesion volumes ($\beta = 0.29$, $p < 0.001$) predicted performance. Optimal individual ADC thresholds differed between subjects with a median of $\leq 691 \times 10 - 6$mm2/s (IQR ≤ 660—$750 \times 10 - 6$mm2/s). Mean ADC values in the DWI lesion ($\beta = -0.96$, $p < 0.001$) and mean ADC values in the brain parenchyma ($\beta = 0.24$, $p < 0.001$) were associated with the performance of individual thresholds.

Conclusion: The performance of ADC thresholds for delineating acute stroke lesions varies substantially between patients. It is influenced by factors such as lesion size as well as lesion and parenchymal ADC values.

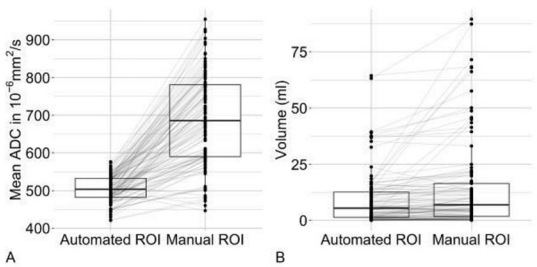

Fig. 1: Mean lesion ADC values (A) and lesion volumes (B) are displayed as boxplots with individual data points (n=108).

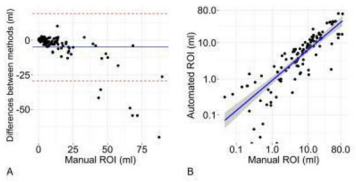

Fig. 2: A: Bland Altman plot of volume differences (n=108). B: Logarithmic scaled scatterplot comparing manual and automated ROI sizes (n=108).

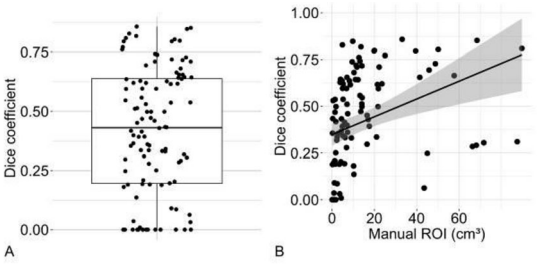

Fig. 3: A: Boxplot with overlain dot plot displaying Dice coefficients of the automated lesion delineations (n=108). B: Manual ROI volume and Dice coefficient for the automated segmentation (n=108).

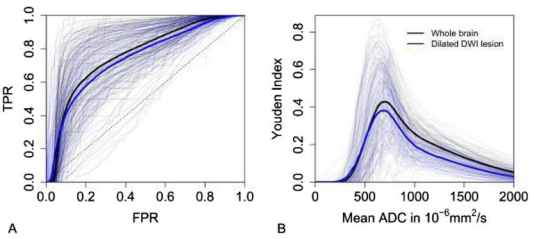

Fig. 4: A: ROC analysis optimal threshold for automated delineation of ischemic lesions (n=108). B: Youden index plotted against individual and pooled ADC thresholds (n=108).

References

1. Kim B, You S–H, Jung SC. A Multicenter Survey of Acute Stroke Imaging Protocols for Endovascular Thrombectomy. Neurointervention. 2021/3;16(1):20–8.

2. Albers GW, Marks MP, Kemp S, Christensen S, Tsai JP, Ortega-Gutierrez S, et al. Thrombectomy for Stroke at 6 to 16 Hours with Selection by Perfusion Imaging. N Engl J Med. 2018 Feb 22;378(8):708–18.

3. Nogueira RG, Jadhav AP, Haussen DC, Bonafe A, Budzik RF, Bhuva P, et al. Thrombectomy 6 to 24 Hours after Stroke with a Mismatch between Deficit and Infarct. N Engl J Med. 2018 Jan 4;378(1):11–21.

4. Hotter B, Pittl S, Ebinger M, Oepen G, Jegzentis K, Kudo K, et al. Prospective study on the mismatch concept in acute stroke patients within the first 24 h after symptom onset—1000Plus study. BMC Neurol. 2009 Dec 8;9:60.

P247.
Detection of cerebral small vessel disease using denoised field-cycling MRI

N. Senn[1], V. Mallikourti[1], P. J. Ross[1], L. Broche[1], G. Waiter[1], M. J. MacLeod[2]

[1]*University of Aberdeen, Aberdeen Biomedical Imaging Centre, Aberdeen, United Kingdom;*
[2]*University of Aberdeen, Institute of Medical Sciences, School of Medicine, Medical Sciences and Nutrition, Aberdeen, United Kingdom*

Introduction: Cerebral small vessel disease (SVD) is associated with increased stroke risk and contributes to cognitive decline [1]. New non-invasive imaging approaches are needed to unravel the pathophysiological processes involved with cerebral SVD progression, inform development of new treatments, and guide individual treatment planning [2]. Field-cycling MRI (FCI) is an emerging technology unique to the University of Aberdeen, that acquires images over multiple magnetic field strengths to provide endogenous contrast R_1 maps at magnetic fields below 0.2 T [3]. The aim of this work was to investigate the effect size obtained from FCI to differentiate tissue regions of SVD and white matter.

Methods: The study was approved by the North of Scotland Research Ethics Committee (21/NS/0128). The initial six patients recruited with clinically determined moderate or severe small vessel disease were included in this preliminary investigation. A total of 9 data sets were included from patients who attended an initial 3 T MRI (Philips 3 T dStream) and FCI scan (N = 6) and repeated scans after 30 days (N = 3). FCI images were acquired across four evolution fields of 0.2, 2, 20 and 200 mT, 5 logarithmically spaced evolution times, TE of 16 ms, matrix size of 90 × 90, in plane resolution of 3.1 mm, and slice thickness of 10 mm. FCI images were denoised using a pre-trained denoising convolutional neural network contained within MATLAB (MathWorks, USA).

R_1 maps were generated for each evolution field using FCI data with and without denoising applied and rescaled to a grey scale dynamic range of 0 – 255. Tissue label maps were generated from 3 T MRI data using an automated approach to produce regions of white matter (WM) and white matter hyperintensity (WMH) associated with SVD. The tissue labels were co-registered to images obtained from FCI and used to interrogate differences and effect size between R_1 values.

Results: Fig. 1 shows the R_1 contrast maps generated from denoised FCI data, alongside co-registered 3 T MRI FLAIR images and tissue label maps. A significant difference was observed between R_1 values (median, IQR) extracted from WM and WMH regions for 0.2 mT (149.9, 147.1 – 159.9 Vs. 124.7, 114.7 – 128.6, p = 0.008) and 2 mT (144.2, 139.1 – 149.9 Vs. 118.2, 110.2 – 124.5, p = 0.008). There was no significant difference (p = 0.314) between the effect size to differentiate WM and WMH regions obtained from 0.2 mT and 2 mT (Fig. 2A). The R_1 map generated at 0.2 mT from denoised FCI data yielded a significantly (p = 0.015) increased effect size (1.52, 0.92 – 1.95) compared to that obtained without denoising (1.38, 0.93 – 1.83), (Fig. 2B, Fig. 3).

Discussion: FCI provides a non-invasive imaging approach to probe the dispersion of R_1 with varied magnetic field to extract unique biomarkers with potential for different medical applications [3]. The preliminary results obtained from this study demonstrate for the first time the feasibility of FCI to detect SVD. Using regions of interest generated from 3 T MRI and co-registered to FCI images, R_1 maps generated at 0.2 and 2 mT yielded sufficient effect size to differentiate SVD and WM tissue. In addition, the denoising approach was shown to further increase the effect size. Future work is required to investigate the primary source of R_1 contrast between SVD and WM and the potential medical applications of biomarkers extracted from R_1 dispersion profiles.

Conclusion: FCI has the potential to provide a feasible non-invasive imaging solution for assessment of small vessel disease severity and progression.

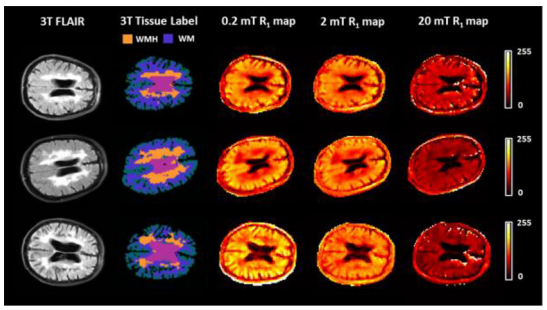

Fig. 1: R1 maps obtained from first 3 participants. Each row corresponds to a single participant data set of co-registered images. The first column shows the 3T MRI FLAIR image. Hyper intense signal corresponds to regions of white matter hyperintensities (WMH) small vessel disease changes. The second column shows the tissue label map generated from 3T MRI data. Subsequent columns of R1 maps were generated at each field and rescaled to a grey scale dynamic range of 0 – 255.

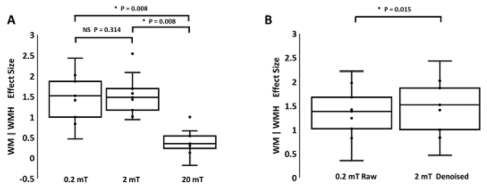

Fig. 2: Effect size comparison. Fig. 2A shows comparison of effect size obtained between white matter (WM) and white matter hyperintensity (WMH) obtained from R_1 maps at each field for denoised FCI data. Fig. 2B shows the comparison of effect size obtained from 0.2 mT for FCI without and with denoising applied.

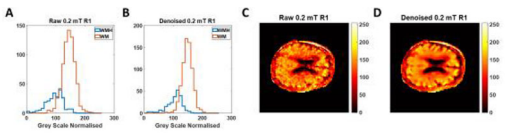

Fig. 3: Example R_1 distribution at 0.2 mT. Fig. 3A–B shows the histogram distributions obtained from WM and WMH for FCI without and with denoising applied. Fig. 3C – D shows corresponding R_1 maps.

References

1. Østergaard L, et al. Cerebral small vessel disease: Capillary pathways to stroke and cognitive decline. J Cereb Blood Flow Metab. 2016;36(2):302–25.
2. Pasi M, Cordonnier C. Clinical relevance of cerebral small vessel disease. Stroke. 2020;51:47–53.
3. Broche L.M., et al. A whole-body Fast Field-Cycling scanner for clinical molecular imaging studies. Sci Rep 2019;9,10402.

P248.
Brain volumetric changes in ALS patients: Post mortem in situ versus *ex-situ* MRI

D. Neuhaus[1,2], M. J. Wendebourg[1,3], E. Scheurer[1,2], T. Haas[4], R. Schläger[1,3], C. Lenz[1,2]

[1]*University of Basel, Translational Imaging in Neurology (ThINk) Basel, Department of Biomedical Engineering, Basel, Switzerland;*
[2]*University of Basel, Institute of Forensic Medicine, Basel, Switzerland;*
[3]*University of Basel, Neurologic Clinic and Policlinic, Departments of Neurology and Clinical Research, Basel, Switzerland;*
[4]*University of Basel, Radiology and Nuclear Medicine, Basel, Switzerland*

Introduction: Amyotrophic lateral sclerosis (ALS) is a fatal neurodegenerative disease. Magnetic resonance imaging (MRI) biomarkers may support diagnosis and prognosis[1]. Nevertheless, to be able to characterise tissue properties and to identify disease-related tissue alterations, a potential biomarker needs to be validated[2].
Validation studies mostly rely on the evaluation of post mortem (PM) ex situ MRI measures acquired in formalin fixed tissue. This approach incorporates several challenges, like a change of tissue volume over time due to formalin fixation[3,4]. For a validation it is hence crucial to differentiate between disease- and methodology-related tissue changes.
The objective of this study was to investigate the influence of tissue extraction and formalin fixation on the brain volumes of patients with ALS.
Methods: Four deceased patients with a clinical diagnosis of definite ALS (according to the revised El Escorial criteria) were investigated in this study. The patients agreed to participate in this study during lifetime (ethical approval: BASEC-Nr. 2020–02179). PM in situ as well as ex situ MRI brain scans have been performed.
In situ: Brain not excised. Scan performed within 24 h after time of death. Prior to the scan, the body was placed in a cooling chamber at 4 °C.
Ex situ: The brains were extracted the day after the in situ MRI scan and immersed in a 4.5% formalin solution. The brains were mounted in patient-specific 3D printed holders and placed in a spherical container, which was then filled with a proton-free and tissue susceptibility matched fluid (Galden®, Solvay SA). The scans were performed after 3 months of fixation on a 3 T Siemens MAGNETOM Prisma device and included anatomical MP2RAGE imaging.
MP2RAGE: 176 slices per slab, FoV = 240 × 256 mm, TR = 5000 ms, TE = 2.98 ms, TI = 700 and 2500 ms, flip angle = 4° and 5°, GRAPPA acceleration factor 3 in 08:20 min, isotropic resolution of (1 × 1x1) mm3.
The data were processed using 3D Slicer for masking and FSL (the FMRIB Software Library) for segmentation and volume analyses:
FSL FAST: Grey matter (GM), white matter (WM), and cerebrospinal fluid (CSF) space.
FSL FIRST: Deep GM structures: Thalamus, Caudate Nucleus, Putamen, Pallidum, Hippocampus, Amygdala, and Nucleus Accumbens.
GM was separated into two regions: cortex and deep GM (the sum of all deep GM structures). The volume of the whole GM and WM was defined as total brain volume (TBV). Intra cranial volume (ICV) was defined as the sum of TBV and CSF space.
In situ vs. ex situ comparison has been performed using a paired sample t-test (SciPy).
Results: The volumes of cortex, deep GM, WM, and CSF space as well as the TBV and ICV are shown in Fig. 1. The deep GM volumes are depicted in Fig. 2.
Figure 3 shows the p-values concerning the cortex, deep GM, WM, CSF space, TBV, and ICV. The p-values regarding the deep GM structures are shown in Fig. 4. There is a significant increase of WM volume ex situ ($p = 0.048$). The CSF space as well as the ICV are significantly reduced in the ex situ measurements ($p = 0.005$ and $p = 0.050$). Furthermore, the volumes of Thalamus, Hippocampus, and Amygdala are significantly reduced (left: $p = 0.016$, $p = 0.010$, $p = 0.027$. right: $p = 0.010$, $p = 0.002$, $p = 0.020$). For the other regions, no significant difference could be found.
Discussion: In this study, we compared brain compartment volumes between PM in situ and ex situ MRI scans in 4 deceased ALS patients to assess the effects of tissue extraction and formalin fixation.
A significant reduction of volume was found for CSF space, ICV, and the deep GM structures Thalamus, Hippocampus, and Amygdala. Conversely, a significant increase was found for the WM volume. Our findings are in line with the results from Ma et al.[4]: as WM contains less water and more lipids than GM, this may lead to different fixation effects on the respective volumes. Furthermore, the ventricles collapse upon fixation, which reduces CSF space. In summary, these ex situ changes might complicate the interpretation of MRI biomarkers. However, limitations are different contrasts used for in situ and ex situ MRI scans, small sample size and an approximation of the ex situ CSF space due to a missing reference skull.
Conclusion: The results of this study suggest that several brain regions are affected by the tissue extraction and formalin fixation. The findings help differentiate between disease-related and methodology-caused tissue alterations, which is important for future MRI biomarker validations. PM in situ MRI measurements may be more appropriate for validation than ex situ measurements, since the former is as close to the in vivo condition as possible. A larger sample size may further be used to derive a correction model for the observed alterations.

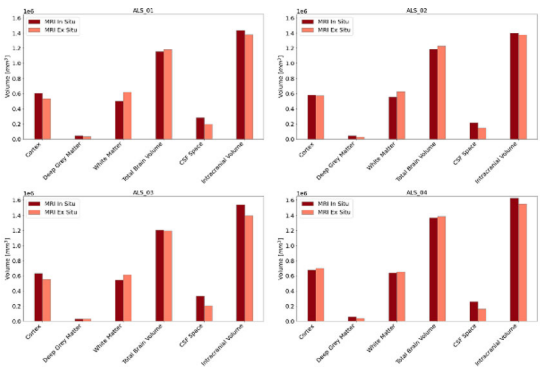

Fig. 1: Comparison in situ vs. ex situ regarding the volumes of cortex, deep grey matter, white matter, total brain volume, cerebrospinal fluid space, and intracranial volume for each of the four brains. Volume: 10^6 mm³

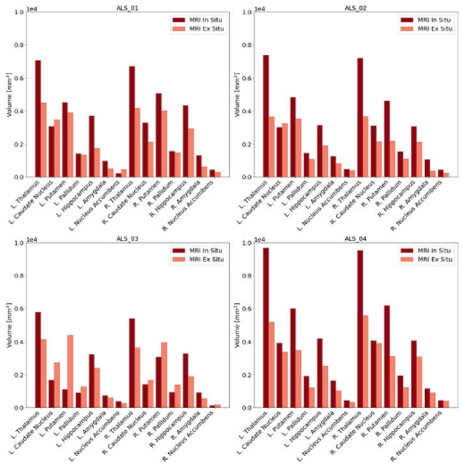

Fig. 2: Comparison in situ vs. ex situ regarding the volumes of the deep grey matter structures (Thalamus, Caudate Nucleus, Putamen, Pallidum, Hippocampus, Amygdala, and Nucleus Accumbens) for each of the four brains. Volume: 10^4 mm^3

Region	Cortex	Deep Grey Matter	White Matter	Total Brain Volume	Cerebro-spinal Fluid Space	Intra Cranial Volume
p-value	0.254	0.071	**0.048**	0.165	**0.005**	**0.050**
t-statistic	1.41	2.76	**-3.23**	-1.83	**7.56**	**3.19**

Fig. 3: p-values retrieved via paired sample t-test. Comparison of cortex, deep GM, WM, TBV, CSF space, and ICV between in situ and ex situ MRI measurements. A positive t-statistic indicates that the mean in situ volume is larger than the mean ex situ volume and vice versa.

Region Left	Thalamus	Caudate Nucleus	Putamen	Pallidum	Hippo-campus	Amygdala	Nucleus Accumbens
p-value	**0.016**	0.461	0.833	0.458	**0.010**	**0.027**	0.951
t-statistic	**4.89**	-0.84	0.23	0.85	**5.95**	**4.08**	0.07
Region Right	Thalamus	Caudate Nucleus	Putamen	Pallidum	Hippo-campus	Amygdala	Nucleus Accumbens
p-value	**0.010**	0.223	0.206	0.479	**0.002**	**0.020**	0.256
t-statistic	**5.94**	1.53	1.61	0.81	**9.61**	**4.57**	1.40

Fig. 4: p-values retrieved via paired sample t-test. Comparison of deep grey matter structure volumes between in situ and ex situ MRI measurements. A positive t-statistic indicates that the mean in situ volume is larger than the mean ex situ volume and vice versa.

References
1. Barritt et al., *Front. Neurol.* **9**, (2018)
2. Alyami et al., *J. Magn. Reson. Imaging* **55**, (2022)
3. Schulz et al., *J. Neurosci. Methods* **202**, (2011)
4. Ma et al., *Front. Neurosci.* **13**, (2019)

P249.
Quantitative MRI visualization of myelination in the brain of patients with schizophrenia using the macromolecular proton fraction method

E. Krupina[1], A. Manzhurtsev[1], M. Ublinskiy[1], T. Akhadov[1], V. Ushakov[2]

[1]*Clinical and Research Institute of Emergency Pediatric Surgery and Trauma, Radiodiagnostics, Moscow, Russian Federation;* [2]*Psychiatric Clinical Hospital No. 1 named after N. A. Alekseev, Moscow, Russian Federation*

Introduction The existing literature provides evidence of changes in myelination in schizophrenia [1]. In this study, we use the method of macromolecular proton fraction (MPF) [2] to quantify violations of myelin content in various brain structures in patients with early stage schizophrenia. Our main goal is to identify potential interregional differences in myelination.

Methods: A total of 45 individuals participated in the present study, comprising 22 healthy controls (10 male and 12 female, with a mean age of 31.6 ± 9.7 years) and 23 patients diagnosed with schizophrenia (11 male and 12 female, with a mean age of 31.5 ± 5.1 years). Imaging data were acquired using a Philips Achieva dStream 3 T MRI scanner equipped with a standard head coil. Specifically, magnetization transfer (MT) (TR = 20 ms, TE = 4.60 ms, FA = 10°), T1-weighted (TR = 20 ms, TE = 4.60 ms, FA = 20°), and PD-weighted (TR = 20 ms, TE = 4.60 ms, FA = 4°) sequences were acquired.

The macromolecular proton fraction (MPF) maps were generated via custom C + + software (accessible at https://www.macromolecularmri.org/) and subsequently underwent non-brain structure removal using the bet2 function in MRIcro. Subsequently, co-regis tration with the standard MNI152 1 mm atlas was performed using FSL software. Quantitative myelin values were determined by com puting the mean values within regions of interest (ROIs), including the left and right cerebral cortex, cerebral white matter, and the entire cerebellum. In addition, myelination across all cerebral cortex and cerebellum regions (as defined by the Harvard Oxford Cortical Atlas) was obtained. Prior to inter-group analyses, the normality of the data distribution was assessed using the Shapiro–Wilk test for each subject group, with the Student's t-test or the Mann–Whitney criterion employed as appropriate to identify between-group differences.

Results: All datasets exhibited normal distribution. A statistically significant decrease in myelination was observed in patients with schizophrenia in both the left and right cerebral cortex (by 3%, p = 0.03 and by 3.2%, p = 0.02, respectively) and in the left and right cerebral white matter (by 3%, p = 0.03 and by 3.3%, p = 0.02, respectively). However, no myelination differences were detected in the entire cerebellum (which was not subdivided into specific regions). Further analysis of the cerebral regions of interest revealed a significant decrease in myelination in patients with schizophrenia in the Superior Temporal Gyrus (anterior division), Heschl's Gyrus, Postcentral Gyrus, Lateral Occipital Cortex (superior division), Pre-cuneous Cortex, Frontal Pole, Paracingulate Gyrus, Cerebellum left crus 2 and Cerebellum Paramedian Lobule. In contrast, myelination in the remaining regions of the cerebellum was not significantly dif-ferent from the control group.

The regions with significantly different myelination between the schizophrenia and normal groups are shown in Fig. 1 and Fig. 2.

Discussion: The study of the connection between different brain areas and schizophrenia is an active research area. Although the mecha-nisms of schizophrenia development are not fully understood, research helps to identify brain areas associated with various symp-toms and behavioral disorders in patients. The study found a decrease in brain myelination consistent with other studies on myelin mea-surement in schizophrenia. Cerebellum myelination was not impaired in early-stage schizophrenia, and certain areas of the cerebrum showed a significant decrease in myelin. Dysfunctions in the frontal, temporal, parietal, and near-lumbar regions have been linked to cognitive impairment, hallucinations, impaired thinking, and social maladaptation in schizophrenia [3–5].

Conclusion: The results obtained confirm the hypothesis of a con-nection between myelination of the brain and the development of mental disorders such as schizophrenia. A decrease in myelin levels can lead to pathological changes in the brain, including cognitive impairment. Our research can help in the development of new methods for the diagnosis and treatment of schizophrenia based on the reduction of myelination of the brain.

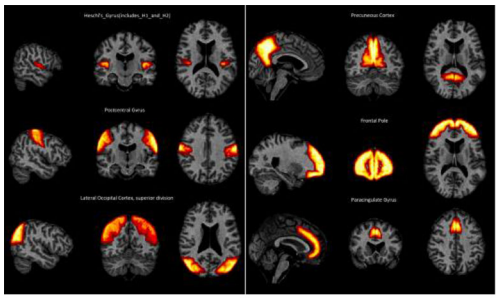

Fig. 1: "Areas of the cerebrum with significantly different myelination between groups of schizophrenia and norm"

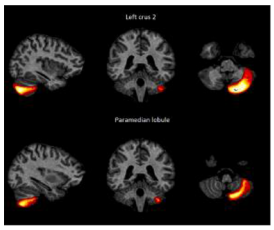

Fig .2 :"Areas of the cerebellum with significantly different myelination between groups of schizophrenia and norm"

References
1. https://doi.org/10.5498/wjp.v12.i2.264
2. https://doi.org/10.3389/fnins.2022.819912
3. https://doi.org/10.1016/j.schres.2006.12.028
4. https://doi.org/10.1016/j.schres.2021.04.014
5. https://doi.org/10.1016/j.schres.2003.12.007

P250.
Studying the role of sex in the creation of machine learning models for diagnosis of Parkinson's disease using features derived from MRI. A pilot study

H. Xicoy[1], J. M. Nunez do Rio[2,3], C. Ventura[2], J. Hernández-Vara[1], D. Pareto[4,1], A. Rovira[4,1], F. X. Aymerich[4,1,5]

[1]*Vall Hebron Research Institute, Neurology and Neurodegenerative Diseases, Barcelona, Spain;*
[2]*Universitat Oberta de Catalunya, Estudis Informàtica, Multimedia i Telecomunicació, Barcelona, Spain;*
[3]*King's College London, Section of Ophthalmology, London, United Kingdom;*
[4]*Institut de Diagnòstic per la Imatge, Section of Neuroradiology. Department of Radiology, Barcelona, Spain;*
[5]*Universitat Politècnica de Catalunya, Automatic Control Department, Barcelona, Spain*

Introduction: Magnetic resonance imaging (MRI) is widely used to study and understand Parkinson's disease (PD), the second most common neurodegenerative disease in elderly adults. Machine learning algorithms can be used to create models that support disease diagnosis. Recent studies[1,2] have demonstrated that there are important sex differences in many clinical features of PD. The aim of this study was to study the role of sex when building machine learning models for automated PD diagnosis using features derived from MRI.
Methods: The study included 112 healthy control individuals (mean age: 59.9 years) and 235 Parkinson's disease patients (mean age: 61.4 years) from the Parkinson's Progression Markers Initiative (PPMI) cohort. MRI images acquired in 3.0 T scanners used to extract structural features with FastSurfer.[3] Ten machine learning algorithms for automated detection of PD individuals (K-nearest neighbor; Logistic regression; Ridge classifier; Lasso classifier; Elastic net; Random forest; Support vector machine; Gaussian Naïve Bayes; AdaBoost; and, XGBoost) were implemented and evaluated using the scikit-learn[4] library as well as an ensemble method of the aforementioned algorithms (soft voting). The diagnostic models were developed and evaluated in different configurations to assess performance in populations with different sex. Performance was evaluated by using the area under receiver operating characteristic curve (AUROC).
Results: Models trained using both female and male individuals showed different performance when evaluated separately in female and male individuals (AUROC for joint female and male evaluation [Lasso classifier], 0.69; AUROC for only male evaluation, 0.66; AUROC for only female evaluation, 0.73). Models trained only with female individuals reached an AUROC of 0.72 when evaluated in female individuals (random forest and Gaussian naïve Bayes) and 0.5 – 0.64 when evaluating in male individuals. Models trained only with male individuals showed an AUROC of 0.77 (logistic regression; lasso; and, soft voting) when evaluated in male individuals and 0.46 – 0.61 when evaluated in female individuals.
Discussion: This study was focused on creating models for PD diagnosis from MRI images demonstrating the existence of sex differences in Parkinson's disease creating these models. This study differs from the previously published research studies that used artificial intelligence techniques on MRI data for the diagnosis of Parkinson's disease in (1) the use of FastSurfer as the method to extract the features to be analyzed, (2) the use of ten algorithms plus one ensemble method (i.e., soft voting) to determine the best model in each case, and (3) the creation of specific models separating the patients by sex.
It is worth noting that there are differences in the selection of the models that offer the best performance when models were created for only female individuals (random forest and Gaussian naïve Bayes) or for only male individuals (logistic regression; lasso; and, soft voting). This agrees with the results that showed that the models built on female individuals do not correctly classify male individuals, and vice versa.
Conclusion: Although this is only a pilot study, ours results suggest that sex is a crucial characteristic in the study of Parkinson's disease and must draw special attention in the design of robust decision support systems across male and female populations.

References
1. Oltra, J. et al. Sex Differences in Brain and Cognition in de novo Parkinson's Disease. *Front. Aging Neurosci.* **13**, 1–9 (2022).
2. Santos-García, D. et al. Sex Differences in Motor and Non-Motor Symptoms among Spanish Patients with Parkinson's Disease. *J. Clin. Med.* **12**, (2023).
3. Henschel, L. et al. FastSurfer—A fast and accurate deep learning based neuroimaging pipeline. *Neuroimage* (2020) https://doi.org/10.1016/j.neuroimage.2020.117012.
4. Pedregosa, F. et al. Scikit-learn: Machine Learning in Python. *J. Mach. Learn. Res.* (2011).

Acknowledgements: Data used in the preparation of this article were obtained from the Parkinson's Progression Markers Initiative (PPMI) database (https://www.ppmi-info.org/access-data-specimens/download-data). For up-to-date information on the study, visit www.ppmi-info.org.
PPMI—a public-private partnership—is funded by the Michael J. Fox Foundation for Parkinson's Research funding partners, including Abbvie, Allergan, Amathus Therapeutics, Avid Radiopharmaceuticals, Biogen, BioLegend, Bristol-Myers Squibb, Celgene, Denali, GE Healthcare, Genentech, GlaxoSmithKline, Handl Therapeutics, Insitro, Janssen Neuroscience, Lilly, Lundbeck, Merck, Meso Scale Discovery, Pfizer, Piramal, Prevail, Roche, Sanofi Genzyme, Servier, Takeda, Teva, UCB, Verily, and Voyager Therapeutics (Golub Capital).No figures

P251.
Distribution of multiple sclerosis lesions within the brain

A. Mennecke[1], S. Hock[1], T. Tsaktanis[2], A. L. Mayer[1], C. Bettray[1], M. A. Schmidt[1], M. Zaiss[1,3,4], V. Rothhammer[2], A. Dörfler.[1]

[1]*Friedrich-Alexander-Universität Erlangen-Nürnberg (FAU), Department of Neuroradiology, Erlangen, Germany;*
[2]*Friedrich-Alexander-Universität Erlangen-Nürnberg (FAU), Neurologische Klinik, Erlangen, Germany;*
[3]*Max-Planck-Institute for Biological Cybernetics, Magnetic Resonance Center, Tübingen, Germany;*
[4]*Friedrich-Alexander-Universität Erlangen-Nürnberg (FAU), Department Artificial Intelligence in Biomedical Engineering, Erlangen, Germany*

Introduction: Multiple Sclerosis (MS) is an inflammatory, demyelinating autoimmune disorder affecting the central nervous system. Radiologically, detectable focal lesions, predominantly found in the myelin-rich white matter, are a common occurrence in the brains of MS patients[1]. These focal lesions are not uniformly distributed throughout the white matter; instead, they exhibit a spatial distribution pattern characterized by periventricular accumulation[2]. To assess the lesion load in individual patients or to determine the presence of new lesions between two time points, automatic lesion detection algorithms are available, offering independence from investigator bias. The aim of this study is to obtain voxel-wise probabilities of lesion occurrence and overall brain lesion distribution by transforming the lesion masks and their corresponding anatomical images into the Montreal Neurological Institute (MNI) space.

Methods: Standard clinical T1- and T2-weighted images of 830 subjects with suspicion of MS were acquired using a Magnetom^{TM} Vida 3 T MR scanner with a 1Tx/64Rx head and neck coil and a Magnetom^{TM} Trio 3 T MR scanner with a 1Tx/32Rx head neck coil (both from Siemens Healthineers, Erlangen, Germany). Standard measurement parameters are provided in Table 1. Extended disability status score (EDSS) was specified by a clinician.

For lesion segmentation, we employed the AI-based segmentation software mdbrain (mediaire GmbH, Berlin, Germany). In accordance with the MAGNIMS guidelines, the software uses a lesion size threshold of 5 µl to minimize false positive T2 hyperintense lesions[3]. All regions identified as lesions were marked in a lesion mask, as demonstrated in Fig. 1 for three example slices. The corresponding MPRAGE sequence was used for normalization to MNI space. The lesion masks were transformed into MNI space using the same warp field.

Results: From 830 subjects, 619 (410 male, 219 female) were ultimately diagnosed with MS or experienced a manifestation of their preliminary diagnosis. At the time of MR measurement, an EDSS of 0, 1, 2 … 5, and "6 or greater" were reported for 91, 148, 154, 94, 37, 28, and 67 patients, respectively. The mean age (SD) of the MS patients was 38.6 (12.4) years. The segmentation software confirmed clusters of lesions in special regions of the white matter. Thereby, the lesions accumulate in regions near the ventricles as shown in Fig. 2.

Discussion: By utilizing standard brain imaging techniques in combination with an automatic lesion detection algorithm, we were able to estimate the spatial distribution of multiple sclerosis (MS) lesions. There might be a distinct spatial pattern of lesions, typical for the pathology of MS. However, this lesion distribution is not yet fully understood, and current research is focused on elucidating these patterns to better understand the pathogenesis of the disease. Some studies have identified distinct subtypes of MS with individual spatial patterns and characteristic clinical parameters using clustering algorithms[4]. MS lesions have been found not to strictly follow typical white matter structures and do not exclusively accumulate in myelin-rich regions.

Conclusion: Our study reveals that MS lesions preferentially accumulate near the ventricles. Understanding the spatial distribution of lesions is crucial for advancing our knowledge of the disease's underlying mechanisms and improving diagnosis and treatment approaches. There is obviously a diverse vulnerability of the white matter cells dependent on their spatial position and the exact reason is unclear up to now. Future research should continue to investigate the relationships between spatial distribution patterns, clinical parameters, and the identification of disease subtypes to optimize patient care and develop personalized therapeutic strategies.

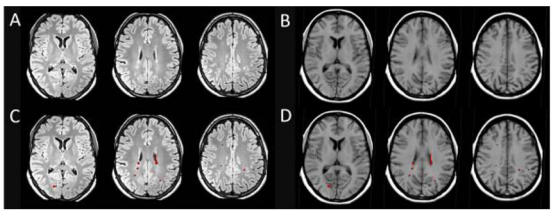

Fig. 1: Three transversal slices of a clinical T2-weighted fluid attenuated (FLAIR, **A**) and T1-weighted magnetization prepared gradient echo (MPRAGE, **B**) after normalization to the standard space. **C, D)** Image of (A) or (B) with the lesion detection by the segmentation algorithm indicated in red (20y f MS patient, EDSS = 1).

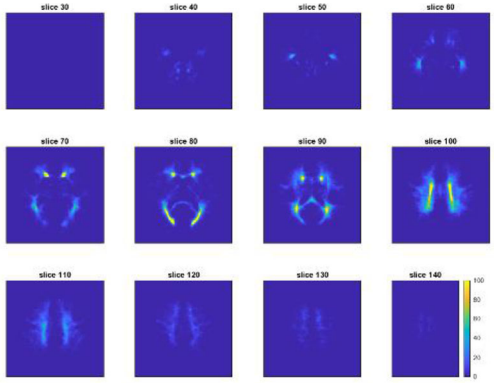

Fig. 2: Lesion distribution. The lesions accumulate periventricular. Only white matter voxels are shown.

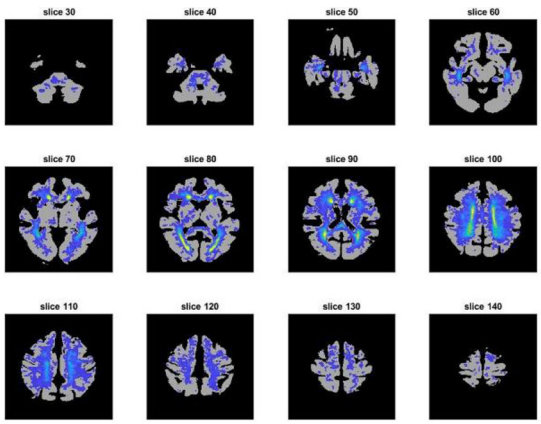

Fig. 3: Lesion distribution overlayed on segmented white matter. Gray voxels are voxels that are segmented as white matter in some cases but don't show any detected lesions.

	T_2 FLAIR	T_1 MPRAGE
Repetition time:	5000 ms	2300 ms
Echo time:	381 ms	3.2 ms
Inversion time:	1800 ms	900 ms
Pixel spacing:	0.6 x 0.6 mm²	1.0 x 1.0 mm²
Slice thickness:	0.6 mm	1.1 mm
Acquisition matrix:	224 x 224	256 x 248
Number of Slices:	288	176

Table 1: Standard measurement parameters of FLAIR and MPRAGE Sequences.

References

[1]Filippi et al. (2016), The Lancet, https://doi.org/10.1016/S1474-4422(15)00393-2

[2]Tur et al. (2022), NeuroImage Clinical, https://doi.org/10.1016/j.nicl.2021.102904

[3]Wattjes et al. (2021), The Lancet, https://doi.org/10.1016/S1474-4422(21)00095-8

[4]Eshaghi et al. (2021), Nature Communications, https://doi.org/10.1038/s41467-021-22265-2

P252.

Is the T1-w/T2-w putative myelin marker affected by iron deposition in globus pallidus, caudate, and normal appearing white matter in patients with secondary progressive multiple sclerosis?

S. Gazdzinski[1], E. Piątkowska-Janko[2], P. Kazulo[2], K. Lipiński[2], A. Karlińska[1], Ł. Smoliński[3], P. Bogorodzki[2], P. Grieb[4], M. Pawlak[5], R. Rola[1], D. Ryglewicz[1], I. Kurkowska-Jastrzębska[3]

[1]*Military Institute of Aviation Medicine, Warsaw, Poland;*
[2]*Warsaw Institute of Technology, Warsaw, Germany;*
[3]*Institute for Psychiatry and Neurology, Warsaw, Poland;*
[4]*Mossakowski Medical Research Institute, Poliah Academy of Sciences, Warsaw, Poland;*
[5]*Poznań University of Medical Sciences, Poznań, Poland*

Introduction: Subcortical nuclei, especially globus pallidus are iron-rich regions in the brain. Additionally, MRI and histological studies have shown altered brain iron levels in the brains of patients with multiple sclerosis, particularly in the deep gray matter. Earlier studies demonstrated altered susceptibility measures among patients with Secondary Progressive Multiple Sclerosis (SPMS), as compared to healthy counterparts, in basal ganglia regions; these changes were related to disability [1].

Quantitative Susceptibility Mapping (QSM) provides quantitative distribution of susceptibility sources in tissue: paramagnetic biometals, especially iron in ferritin or deoxygenated hem, and it was used to evaluate susceptibility in these regions [1].

These regions, especially globus pallidus, are also darker on T2-w images. The ratio of T1-w/T2-w images was shown to correlate with myelination of cortical and subcortical regions [2]. However, tissue contrast is known to be determined by its paramagnetic properties and myelin content, with the differences in contrast attributed mostly to susceptibility differences [3]. Here, we asked if T1-w/T2-w contrast is related to susceptibility within globus pallidus, caudate, and normal appearing white matter (lesions masked out).

Methods: Nine patients with a diagnosis of SMPS (EDSS: 6.38 ± 0.95, 51 ± 6 years, 3 M) without enhancing lesions on MRI were enrolled. All participants underwent imaging in a 3 T GE Discovery 750w with 70 cm wide bore, and a 24-channel receive coil. The T1-w scans were obtained with FSPGR-BRAVO (TR/TE/TI = 8.46/3.25/450 ms, 1 × 1x1mm3), whereas the T2-w scans with CUBE-T2 (TR/TE = 3000/92 ms, 1 × 1x1mm3). T1-w/T2-w ratios were calculated with MRTool. For QSM, a 3D multi-echo gradient-echo sequence (SWAN) was obtained (TR = 60 ms, 1 × 1x2mm3, flip angle = 12 deg, nine TE values ranging from 4.5 to 48 ms). Susceptibility maps were calculated with MEDI [4]. Median T1-w/T2-w and susceptibility values were calculated within manually drawn ROIs of caudate and globus pallidus. For normal appearing white matter, lesion masks obtained with vol2Brain were removed from white matter mask obtained with the same program. Mean values of T1-w/T2-w and susceptibility were calculated.

Results: The measures of T1-w/T2-w were not related to susceptibility values in globus pallidus and caudate over the entire range of susceptibility values (Fig. 1 and Fig. 2). However, in the range of lower susceptibility values a linear relationship is apparent in globus pallidus (Fig. 1). Interestingly, an inverse linear relationship is apparent for normal appearing white matter (Fig. 3), likely reflecting the fact that myelin is diamagnetic and demylinization leads to less negative values of mean susceptibility.

Discussion: The lack of relationship between the measures of demyelination (T1-w/T2-w) and respective susceptibility values over the entire range of QSM values suggest that T1-w/T2-w is not driven by tissue iron content. However, a linear relationship between these measures for lower susceptibility values is apparent. Nonetheless, the small group size and the known effects of age [5], not accounted for in this preliminary study, do not allow us to draw meaningful conclusions. DTI would further validate the T1-w/T2-w myelination marker.

If these results are confirmed in a larger cohort, they may mean that iron deposition present in smoldering lesions (enhanced signal on QSM) may bias their estimation of myelination by the T1-w/T2-w marker.

Conclusion: T1-w/T2-w marker does not appear to be linearly related to iron content within globus pallidus and caudate in patients with Secondary Progressive Multiple Sclerosis.

This study was supported by Medical Research Agency of Poland, grant 2021/ABM/02/00002 – 00.

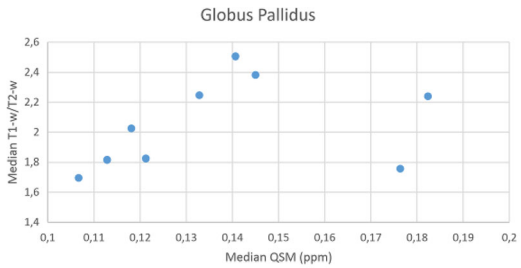

Fig. 1: Relationship between susceptibility (median QSM) and median T1-w/T2-w in Globus Pallidus.

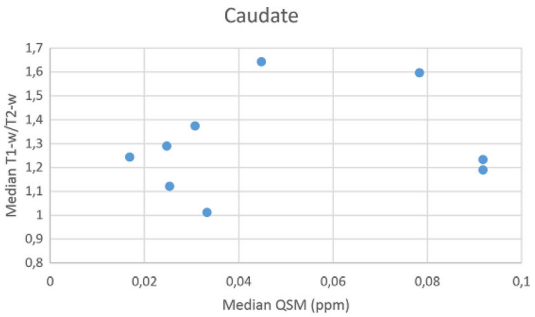

Fig. 2: Relationship between susceptibility (median QSM) and median T1-w/T2-w in Caudate.

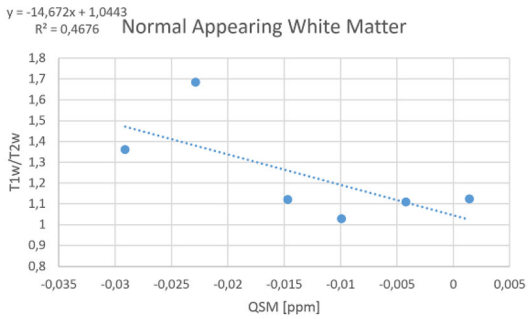

Fig. 3: Relationship between susceptibility (median QSM) and median T1-w/T2-w in normal appearing white matter.

References

1. Zivadinov, R., et al., Radiology, 2018. **289**(2): p. 487–496.
2. Glasser, M.F. and D.C. Van Essen, Journal of Neuroscience, 2011. **31**(32): p. 11,597–11,616.
3. Leuze, C., et al., Neuroimage, 2017. **156**: p. 412–422.
4. Wang, Y. and T. Liu, Magnetic Resonance in Medicine, 2015. **73**(1): p. 82–101.
5. Li, G., et al., NeuroImage, 2023. **269**: p. 119,923.

P253.
AI- based volumetry algorithms to support the MR-imaging in epilepsy diagnostic

A. L. Mayer[1], A. Mennecke[1], M. A. Schmidt[1], A. Dörfler[1], J. Rösch[1]

[1]*Friedrich-Alexander-Universität Erlangen-Nürnberg (FAU), Department of Neuroradiology, Erlangen, Germany*

Introduction: Automatic software programs using AI- algorithms for the calculation of brain volume in MR- examinations could replace time- consuming manual methods and could be a qualitative support in the evaluation by a radiologist. This study analysed the potential of two AI- programs regarding diagnosis of epilepsy caused by hippocampal sclerosis (HS) with volume reduction in clinical radiology. Therefore, two independent software solutions were rated concerning sensitivity and validity for the detection of volume reduced hippocampal sclerosis.

Methods: Preoperative MR- imagings (1,5 T & 3 T, T1w MP- RAGE sag 3D) of 25 patients with histopathological proven hippocampal sclerosis (type 1 n = 20, type 2 n = 4, type 3 n = 1) were retrospective included. The software programs mdbrain Version 3.4.0 (Mediaire, Berlin) and BrainMorphometry VB50B (Syngo.via, Siemens Healthineers, Erlangen) were used for automatic volume measurement and were compared to the volume classification of hippocampi by three independent neuroradiologists using an epilepsy dedicated MRI- protocol.

Results The detection sensitivity of a hippocampal sclerosis (based on volume reduction) was 96,0% for mdbrain and 32,0% for BrainMorphometry. The specifity was each 100% compared to the gold standard. The calculated volume data showed a significant difference between mdbrain and BrainMorphometry (3.2 ml vs. 2.7 ml; $p < 0{,}005$). However, there was a significant positive correlation between the volume data of both software solutions (r = 0,79).

Discussion: AI-based algorithms can be helpful in the detection of volume reduction indicative for hippocampal sclerosis. Thereby, a fast automatic volumetry can support the visual inspection. Both tested AI- based software programs only require a native standard T1w MP-RAGE- sequence for the evaluation that could be easily implied in a standard protocol. But the specific suitability of the chosen software programs must be tested before the routine use because of differences in absolute volume data and volume evaluation considering pathological values. Different sensitivity rates could be caused by different cut off values of the normal reference range of volume. However, hippocampal sclerosis without volume reduction could not be detected with this method.

Conclusion: It depends on the chosen software solution, if a hippocampal sclerosis (with volume reduction) can be discovered by an AI-based brain volumetry. A detection sensitivity of 96.0% and a specificity of 100.0% can be received by a suitable software. Consequently, AI- based algorithms can improve as well as speed up the MR- imaging epilepsy diagnostic and can especially support radiologists that are still unexperienced in volume estimation or if expert knowledge, laborious manual volumetry or special epilepsy MR-protocols are not available.

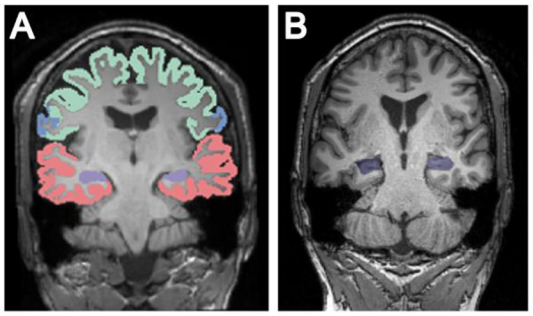

Fig. 1 A: Segmentation mapping of mdbrain software. Hippocampus formation (violet), temporal lobe cortex (red), parietal lobe cortex (blue), frontal lobe cortex (green). **B:** mdbrain segmentation of hippocampus (violet).

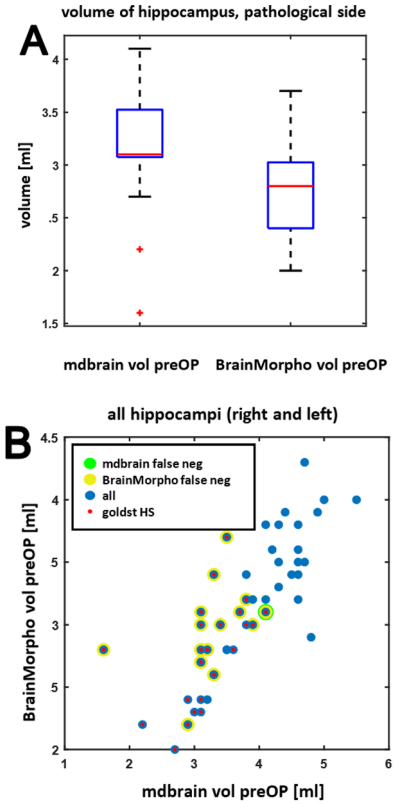

Fig. 2 A: Box plots showing absolute volume data of pathological hipocampus (HC) in milliliter (ml). mdbrain vs. BrainMorphometry (3,2ml vs. 2,7ml; $p < 0{,}005$). **B:** absolute volume data of all hippocampi (HC) in ml (healthy and pathological side) of mdbrain and BrainMorphometry (blue). Representation of volume evaluation: gold standard classificated hippocampal reduction (red), false negative evaluated HC- size by mdbrain (green), false negative evaluated HC- size by BrainMorphometry (yellow).

References
1 Blümcke I, Thom M, Aronica E, Armstrong DD, Bartolomei F, Bernasconi A, Bernasconi N, Bien CG, Cendes F, Coras R, Cross JH, Jacques TS, Kahane P, Mathern GW, Miyata H, Moshé SL, Oz B, Özkara Ç, Perucca E, Sisodiya S, Wiebe S, Spreafico R. International consensus classification of hippocampal sclerosis in temporal lobe epilepsy: a Task Force report from the ILAE Commission on Diagnostic Methods. Epilepsia. 2013 Jul;54(7):1315–29. https://doi.org/10.1111/epi.12220. Epub 2013 May 20. PMID: 23,692,496.
2 Lehéricy S, Dormont D, Semah F, Granat O, Baulac M, Marsault C. L'imagerie par résonance magnétique de l'épilepsie du lobe temporal [Magnetic resonance imaging of temporal lobe epilepsy]. J Radiol. 1996 Nov;77(11):1095–104. French. PMID: 9,033,867.
3. Malmgren K, Thom M. Hippocampal sclerosis–origins and imaging. Epilepsia. 2012 Sep;53 Suppl 4:19–33. https://doi.org/10.1111/j.1528-1167.2012.03610.x. PMID: 22,946,718.
4 Masaki H, Watanabe K, Kakeda S, Ide S, Sugimoto K, Ueda I, Hamamura T, Hisanaga S, Toyota T, Akamatsu N, Shimajiri S, Yamamoto J, Nishizawa S, Adachi H, Korogi Y. Hippocampal sclerosis without visually detectable hippocampal MRI abnormalities: automated subfield volumetric analysis. Jpn J Radiol. 2020 Nov;38(11):1020–1027. https://doi.org/10.1007/s11604-020-01019-y. Epub 2020 Jul 11. PMID: 32,653,988.

P254.
Diagnostic accuracy of magnetic resonance imaging in detection of carotid plaque instability: a systematic review and meta-analysis

D. Pakizer[1], J. Kozel[1], P. Taffé[2], J. Elmers[3], J. Feber[1,4], P. Michel[5], D. Školoudík[1], G. Sirimarco[5,6]

[1]*University of Ostrava, Center for Health Research, Faculty of Medicine, Ostrava, Czech Republic;*
[2]*University of Lausanne, Center for Primary Care and Public Health, Division of Biostatistics, Lausanne, Switzerland;*
[3]*University of Lausanne, Medical Library, Lausanne, Switzerland;*
[4]*Children's Hospital of Eastern Ontario and University of Ottawa, Division of Nephrology, Department of Pediatrics, Ottawa, Canada;*
[5]*University of Lausanne, Stroke Center, Service of Neurology, Department of Clinical Neurosciences, Lausanne, Switzerland;*
[6]*Riviera Chablais Hospital, Neurology Unit, Department of Internal Medicine, Rennaz, Switzerland*

Introduction: There is increasing evidence that unstable plaques in the extracranial carotid artery may lead to an increased stroke risk independently of the degree of stenosis. Over the last few years, MRI has been considered as the imaging method of choice in evaluating high risk plaques. The study aimed to estimate accuracy of diagnostics of vulnerable plaque using MRI when compared to histology with symptomatic and asymptomatic carotid plaques.
Methods: Medline Ovid, Embase, Cochrane Library Wiley, and Web of Science were searched, supplemented by Google Scholar search and citation searching of key studies without any search limitation, for diagnostic accuracy of MRI in the detection of 1) vulnerable plaque, and 2) vulnerable plaque characteristics compared to the gold standard of histology. The quality of included studies was assessed by QUADAS-2 and univariate random-effect meta-analyses were performed.
Results: From final 107 studies, 12 comparisons of vulnerable plaque and 99 comparisons of vulnerable plaque characteristics (intraplaque hemorrhage [IPH], lipid-rich necrotic core [LRNC], ruptured fibrous cap, ulceration, inflammation, and neovascularization) were included in our diagnostic test accuracy meta-analysis. We found that MRI has a high accuracy (90%; 95% confidential interval [CI]: 82–95%) in diagnostics of vulnerable plaque and vulnerable plaque characteristics (86%, 95% CI: 84–88%). MRI can visualize IPH with an accuracy of 86% and moreover can differ the age of IPH (acute/fresh, subacute/recent, old). The accuracy of MRI in the detection of LRNC, ruptured fibrous cap, ulceration, inflammation, and neovascularization is 86%, 85%, 76%, 70%, and 77%, respectively.
Discussion CT and MRI have a similar high performance to detect vulnerable carotid plaques. MRI can identify patients with vulnerable plaques at increased risk of stroke with high accuracy. Therefore, they may be used as the first-choice method to select high-risk patients for clinical trials aiming to reduce the rate of stroke recurrences and the burden of new ischemic lesion on follow-up MRI. All characteristics of a vulnerable plaque were detectable by MRI which can detect vulnerable and stable carotid plaque with high accuracy. MRI could therefore be used to assess the effect of specific treatments targeting the vulnerable plaque characteristics. Examples for such treatment targets could be lipid-lowering and anti-inflammatory strategies.
Conclusion: MRI proved to be good noninvasive method for vulnerable detection with high diagnostic accuracy.
No figures.

P255.
Resting state functional MRI shows post-concussion brain abnormalities persist past symptom resolution: Preliminary findings

E. Danielli[1,2], N. Simard[2,3], D. Kumbhare[1,4], M. D. Noseworthy[2,3,5]

[1]*University Health Network, KITE Research Institute, Toronto, Canada;*
[2]*St. Joseph's Healthcare, Imaging Research Centre, Hamilton, Canada;*
[3]*McMaster University, Electrical and Computer Engineering, Hamilton, Canada;*
[4]*University of Toronto, Faculty of Medicine, Toronto, Canada;*
[5]*McMaster University, Department of Radiology, Hamilton, Canada*

Introduction: Routine clinical magnetic resonance imaging (MRI) scans fail to detect concussion-related brain injuries while symptom self-reporting is highly subjective [1, 2]. However, research has shown that subtle concussion-related brain damage can be detected using advanced MRI analyses [3, 4]. An important return-to-activity safety question remains: Is the brain healed once concussion symptoms are resolved? The objective of this ongoing study is to track recovery post-concussion using personalized MRI methodology in comparison to post-concussion symptoms, and it is hypothesized that objectively measured brain abnormalities identified using resting state functional MRI (rsfMRI) and diffusion tensor imaging (DTI) will align with symptoms acutely but persist beyond symptom resolution.
Methods: Three acutely concussed (< 2 weeks post-injury) adults (2 male 1 female, aged 26.7 ± 0.6) have been enrolled who were all right-handed athletes with no clinical diagnosis of psychiatric or neurological conditions. Participants 1 and 3 had no previous concussion history or diagnosis, and participant 2 had sustained three previous concussions. Participants completed the PCSS and DASS42 questionnaires and an MRI session (3D T1, rsfMRI, and DTI) acutely and 3-months post-concussion. The MRI data was analyzed to measure rsfMRI temporal complexity (Hurst exponent = $\boldsymbol{H}$) and DTI fractional anisotropy (FA) within each brain voxel. Region-of-interest (ROI) masks were applied across 29 cerebral gray matter (GM), 18 cerebral white matter (WM), and 18 cerebellar ROIs to evaluate voxel-wise $\boldsymbol{H}$ values (rsfMRI) and FA values (DTI). These calculations were also made on 243 age and sex-matched healthy controls to

establish a healthy baseline. A personalized ROI-based Z-score analysis was implemented where lower FA and/or reduced ***H*** (i.e., Z-scores < -2.5) was hypothesized to indicate abnormality and compared against clinical tests (Table 1). Recovery was measured using paired t-tests for PCSS score, DASS42 score, and number of cerebral ***H*** abnormalities using RStudio to identify differences between the acute and three-month follow-up values based on confidence intervals; Shapiro-Wilks normality testing was done for each metric prior to performing t-tests.

Results: The mean PCSS and DASS42 scores decreased after 3-months for all three participants (i.e., PCSS went from 24 to 6 and DASS42 went from 15 to 7). The DASS42 scores showed a statistical decrease (95% C.I. 3.7 12.3, p = 0.015). There were numerous brain GM functional abnormalities present acutely (Abnormal ROIs: Participant 1 = 9, Participant 2 = 20, Participant 3 = 24; Figs. 1A, 2A, 3A) and at 3-months post-concussion (Abnormal ROIs: Participant 1 = 10, Participant 2 = 9, Participant 3 = 18; Figs. 1B, 2B, 3B). However, there were only 3 brain WM abnormalities noted (Table 1). Furthermore, the number of GM abnormalities did not statistically decrease by 3-months post-concussion (95% C.I. -9.6 20.3, p = 0.27) as hypothesized. Interestingly, the same ROIs that were abnormal acutely remained abnormal after 3-months. The specific PCSS and DASS42 category scores were not examined at a group level because each participant"s concussion symptoms were unique. From a general observation, self-reported PCSS and DASS42 test scores that were elevated acutely decreased substantially by 3-months.

Discussion: Brain healing and symptom resolution post-concussion remains a challenge for athletes, coaches, parents, and clinicians to monitor recovery and safely manage return-to-activity [5]. The results of these initial findings suggest that many brain abnormalities did not return to within a normal range after 3-months despite symptoms decreasing or resolving. Since two of the three participants had not previously sustained a concussion, the many GM abnormalities detected with our MRI analysis can be more confidently attributed to their recent concussion. It was unexpected to not detect more white matter abnormalities, as white matter injuries have been extensively found in concussion literature [6, 7].

Conclusions: These preliminary results found that symptoms substantially decreased and thus overestimated brain recovery at 3-months post-concussion as numerous brain abnormalities remained present. These results should be corroborated with more participants and additional assessments at 6-months post-concussion when symptoms should be completely resolved.

	Participant 1 (acute / 3-months)	Participant 2 (acute / 3-months)	Participant 3 (acute / 3-months)
PCSS score	Somatic = 1 / 2 Cognitive = 12 / 2 Emotional = 2 / 2 Sleep = 2 / 0 Total = 17 / 6	Somatic = 0 / 0 Cognitive = 2 / 0 Emotional = 0 / 0 Sleep = 5 / 1 Total = 7 /1	Somatic = 26 / 5 Cognitive = 6 / 0 Emotional = 11 / 5 Sleep = 6 / 1 Total = 49 / 11
DASS42 score	Depression = 0 / 4 Anxiety = 4 / 1 Stress = 11 / 1 Total = 15 / 6	Depression = 3 / 0 Anxiety = 2 / 0 Stress = 2 / 1 Total = 7 / 1	Depression = 10 / 3 Anxiety = 1 / 1 Stress = 12 / 10 Total = 23 / 14
MRI abnormalities	FA = 0 / 1 ROIs ***H*** = 9 / 10 ROIs	FA = 2 / 0 ROIs ***H*** = 20 / 9 ROIs	FA = 0 / 0 ROIs ***H*** = 24 / 18 ROIs

Abbreviations: FA: fractional anisotropy, ***H***: Hurst exponent, ROI: region-of-interest

Table 1: A summary of the Post-Concussion Symptom Scale (PCSS) and Depression Anxiety Stress Scale (DASS42) scores and abnormal brain regions-of-interest (ROIs) for the initial three study participants.

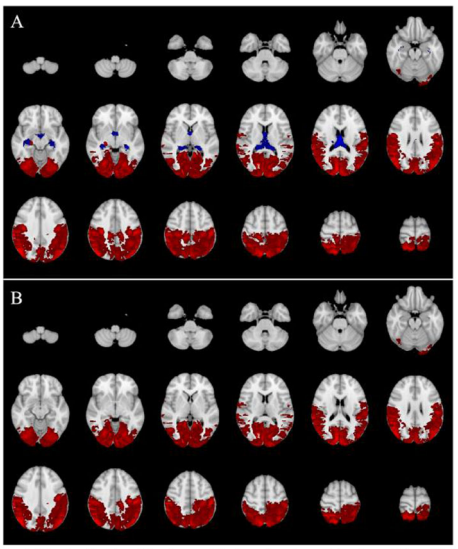

Fig. 1: The visualization of the abnormal brain regions for participant one (A) acutely (9 abnormal ROIs) and (B) after 3-months post-concussion (10 abnormal ROIs). Abnormal gray matter ROIs are coloured red and abnormal white matter ROIs are coloured blue.

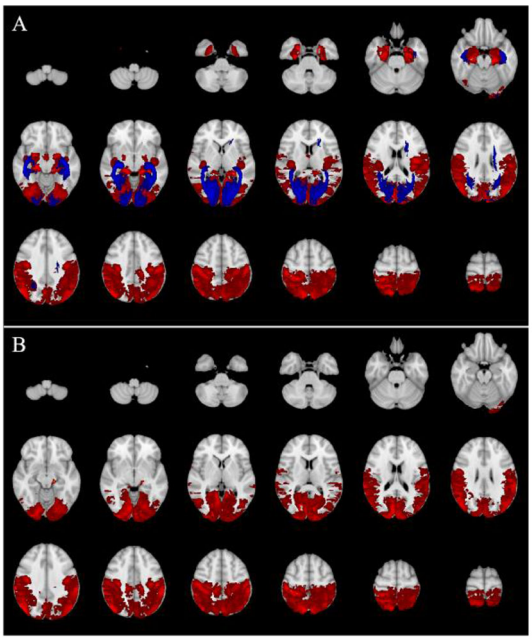

Fig. 2: The visualization of the abnormal brain regions for participant two (A) acutely (20 abnormal ROIs) and (B) after 3-months post-concussion (9 abnormal ROIs). Abnormal gray matter ROIs are coloured red and abnormal white matter ROIs are coloured blue.

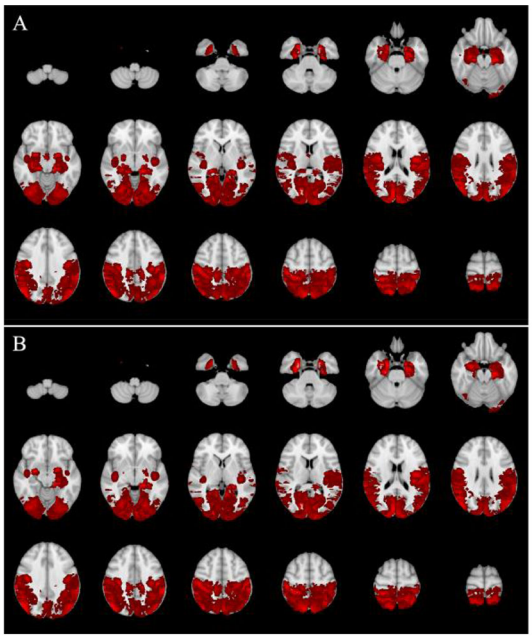

Fig. 3: The visualization of the abnormal brain regions for participant three (A) acutely (24 abnormal ROIs) and (B) after 3-months post-concussion (18 abnormal ROIs). Abnormal gray matter ROIs are coloured red and abnormal white matter ROIs are coloured blue.

References

[1] Chamard E, et al. Brain Injury. 2018;32(7):816–831.
[2] Rose SC, et al. Brain Injury. 2017;31(2):260–266.
[3] Cassoudesalle H, et al. J Neurosci Res. 2021;99(2), 446–454.
[4] Dona O, et al. PLOS ONE 12(1):e0169647.
[5] DeMatteo CA, et al. Clin J Sport Med. 2021;31(6):e406–13.
[6] Asken BM, et al. Brain Imag Behav. 2018;12(2):585–612.
[7] Mustafi SM, et al. J Neurotrauma. 2017;35(22):2653–64.

P256.
The correlation of MRI-PDFF, MRS, and two different histopathologic methods (AI vs. pathologist) for the quantification of hepatic steatosis

C. H. Lee[1], J. W. Kim[1]

[1]*Korea University Guro Hospital, Radiology, Seoul, South Korea*

Introduction: The grade of hepatic steatosis is assessed semi-quantitatively and graded as a discrete value. However, the proton density fat fraction (PDFF) measured by magnetic resonance imaging (MRI) and FF measured by MR spectroscopy (FFMRS) are continuous values. Therefore, a quantitative histopathologic method may be needed. This study aimed to 1) provide a spectrum of values of MRI-PDFF, FFMRS, and FFs measured by two different histopathologic methods [artificial intelligence (AI) and pathologist], 2) to evaluate the correlation among them, and 3) to evaluate the diagnostic performance of MRI-PDFF and MRS for grading hepatic steatosis.
Methods: Forty-seven patients who underwent liver biopsy and MRI for nonalcoholic steatohepatitis evaluation were included. The agreement between MRI-PDFF and MRS was evaluated through Bland–Altman analysis. Correlations among MRI-PDFF, MRS, and two different histopathologic methods were assessed using Pearson correlation coefficient (r). The diagnostic performance of MRI-PDFF and MRS was assessed using receiver operating characteristic curve analyses and the areas under the curve (AUCs) were obtained.
Results: The means ± standard deviation of MRI-PDFF, FFMRS, FF measured by pathologist (FFpathologist), and FF measured by AI (FFAI) were 12.04 ± 6.37, 14.01 ± 6.16, 34.26 ± 19.69, and 6.79 ± 4.37 (%), respectively. Bland–Altman bias [mean of MRS – (MRI-PDFF) differences] was 2.06%. MRI-PDFF and MRS had a very strong correlation ($r = 0.983$, $p < 0.001$). The two different histopathologic methods also showed a very strong correlation ($r = 0.872$, $p < 0.001$). Both MRI-PDFF and MRS demonstrated a strong correlation with FFpathologist ($r = 0.701$, p
Discussion: The values of MRI-PDFF and FFMRS were significantly higher than FFAI and significantly lower than FFpathologist. These results are thought to be due to different histopathological methods; FFpathologist corresponds to the proportion of hepatocytes including macrovesicular fat and FFAI corresponds to the area of macrovesicular fat in the entire area. Except for one case (97,9%, 46/47), FFMRS always showed higher value than MRI-PDFF and the average difference was 2.06%. MRS and MRI-PDFF also showed strong correlation with each other and with each histopathologic method.
Conclusion: Although it is difficult to measure the amount of "real" hepatic fat, the results of our study demonstrated that MRI-PDFF or MRS can be used as an alternative non-invasive reference standard. However, there is a certain difference between two modalities, so care should be taken in their use.

References

1. Kim JW, Lee YS, Park YS, Kim BH, Lee SY, Yeon JE, Lee CH. Multiparametric MR Index for the Diagnosis of Non Alcoholic Steatohepatitis in Patients with Non-Alcoholic Fatty Liver Disease. Sci Rep 2020;10:2671.
2. Park YS, Lee CH, Kim JH, Kim BH, Kim JH, Kim KA, Park CM. Effect of Gd-EOB-DTPA on hepatic fat quantification using high-speed T2-corrected multiecho acquisition in (1)H MR spectroscopy. Magn Reson Imaging 2014;32:886–90.

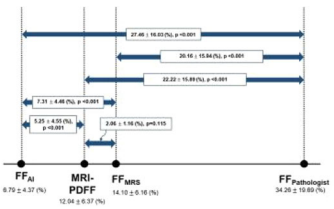

The spectrum of FFMRS, MRI-PDFF, FFAI, and FFpathologist. MRI-PDFF and FFMRS were located between FFAI and FFpathologist. FFMRS and MRI-PDFF were significantly higher than FFAI and significantly lower than FFpathologist (P<0.001). MRI-PDFF and FFMRS did not show a significant difference (P=0.115). FF, fat fraction; FFMRS, FF measured by magnetic resonance spectroscopy, FFAI, FF measured by artificial intelligence, FFpathologist, FF measured by pathologist, MRI-PDFF, magnetic resonance imaging-proton density fat fraction.

P257.
Uncertainty estimations of semi-quantitative dynamic contrast-enhanced MRI parameters

M. Morris[1,2], E. Durie[1,3], N. Tunariu[3], S. Allen[3], K. Downey[3], L. Gothard[1,3], J. Hughes[3], G. Hopkinson[3], E. Scurr[3], M. Tang[2], N. Somaiah[1,3], M. Blackledge[1]

[1]*The Institute of Cancer Research, Division of Radiotherapy and Imaging, London, United Kingdom;*
[2]*Imperial College London, School of Biomedical engineering and imaging science, London, United Kingdom;*
[3]*The Royal Marsden NHS Foundation Trust, London, United Kingdom*

Introduction: To improve standardisation and interpretation of imaging parameters, calculating the uncertainty may prove to be very useful. This has been made use of in diffusion-weighted imaging, where the statistical uncertainty in the Apparent Diffusion Coefficient (ADC) estimation is given alongside the ADC estimation, to

overcome inter- and intra-scanner signal variations and improve reliability[1]. Dynamic contrast-enhanced MRI is another functional imaging modality, which gives information on perfusion and permeability of blood vessels by studying the concentration of a contrast agent in the tissue over time. A semi-quantitative parameter, the area under the concentration curve for the first 90 s (AUC90), captures the initial uptake of the contrast agent[2]. Tumours have a hyperpermeable microvasculature and are densely vascularised, in comparison to healthy tissue. Therefore, there is a steep initial uptake in contrast agent, which the AUC90 captures. The AUC90 may be a powerful biomarker in tumour response to therapy, but to be reliably used in clinic, the uncertainty must also be calculated.

Methods: Patients with locally advanced breast cancer underwent bilateral breast MR-imaging as part of a clinical trial assessing the effectiveness of intra-tumoral H_2O_2 injections as a radiosensitiser (KORTUC Phase 2, ClinicalTrials.gov: NCT03946202). 3D isotropic DCE-MRI were acquired, with pre-contrast variable flip angle acquisitions ($4 \times \mathring{3}$ and $5 \times \mathring{16}$). Contrast injection was performed with a power injector (Dotarem, 0.1 mmol/kg at rate 3 ml/s), with post-contrast dynamic images acquired at $\mathring{16}$ only. A temporal resolution of 12.2 s was achieved using TWIST view-sharing (central region 33%, sampling density 33%), to quantify contrast dynamics while maintaining high spatial resolution to capture intra-tumoral heterogeneity. Tumour volumes of interest were delineated and approved by a consultant radiologist. 4 patients were imaged pre- and post-radiotherapy (RT) treatment.

The mean and corrected sample standard deviation (standard deviation divided by the square root of the number of acquisitions) of the pre-contrast low and high flip angle acquisitions were calculated. To calculate the uncertainty of the AUC90 value, the low flip angle and high flip angle volume was sampled from a normal distribution using the mean and corrected sample standard deviation of the corresponding flip angle. Due to only having one sample of the post-contrast acquisitions, the volume was sampled from a normal distribution with a standard deviation twice the value of the standard deviation of the high flip angle acquisitions. T1 maps were calculated using a variable flip-angle model[3], and then converted into contrast concentration. The AUC90 is calculated from the generated concentration curves for each pixel, and for the whole tumour the median, 25th and 75th percentile, inter-quartile range (IQR), maximum (75th percentile + (1.5 × IQR)), minimum (25th percentile – (1.5 × IQR), mean and standard deviation were calculated. This was repeated 100 times, and the results are given as the mean +—3 × standard deviation (uncertainty) of each statistic.

Results: The mean and uncertainty map of AUC90 at the central slice of the tumour is given in Fig. 1. Examples of the mean and uncertainty of the statistics (given as the error bars) are shown in Fig. 2, for the median and IQR of the AUC90 within the tumours. A post-treatment change greater than the uncertainty is significant. For patient 1, there is no significant change at 2 weeks post-RT in the median AUC90, but there is a significant decrease at 6 months post-RT. Patient 2 has a significant decrease at 6 months post-RT in the median AUC90. Patient 3 has a significant increase at 2 weeks post-RT in the median AUC90, and a significant decrease at 6 months post-RT back to pre-RT values.

Discussion Uncertainty estimations for quantitative parameters to be used in a clinical setting are of utmost importance, to improve the reliability of the parameter when making a clinical decision. Having the uncertainty of the AUC90 statistics will prove useful when determining whether there has been a statistically significant change within the values post-treatment. The gold standard of measuring uncertainty of imaging parameters is to perform a repeat baseline. However a repeat baseline, unlike the method described here, does not provide pixel-wise uncertainty estimates. Repeat baselines will also be acquired, so the two techniques of measuring uncertainty will be compared. This method can be applied to other semi-quantitative measures derived from the DCE data, and possibly even parametric parameters such as Ktrans.

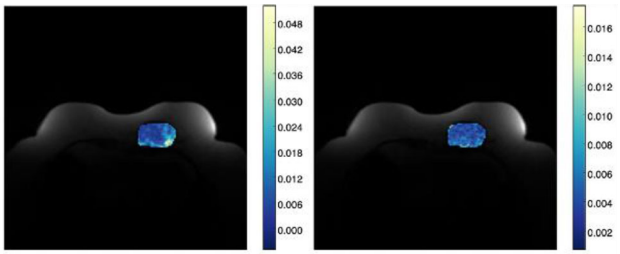

Fig. 1: The mean and uncertainty map of AUC90 at the central slice of the tumour.

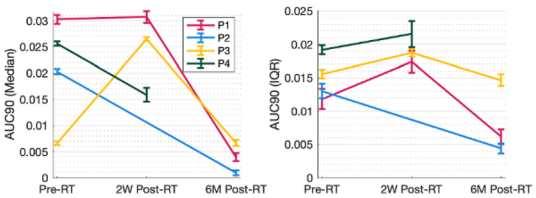

Fig. 2: The mean and uncercainty (given as the error bars) of the median and IQR of the AUC90 within the tumours, pre-radiotherapy (RT) and 2 weeks post-RT and 6 months post-RT.

References

1. Blackledge M, Tunariu N, Zugni F, et al. Front Oncol. 2020;10(704).
2. Medved M, Karczmar G, Yang C, et al. J Magn Reson. 2004;20:122–128.
3. Fram E K, Herfkens R J, Johnson G A, et al. Magn Reson Imaging. 1987;5(3):201–208.

P258.
Harmonization of clinical neuro protocols on multiple systems

P. Pullens[1,2,3], N. van de Velde[1], T. Thienpont[1], P. Devolder[1], G. Villeirs[1]

[1]Ghent University, Department of Radiology and Nuclear Medicine, Ghent, Belgium.

[2]*Ghent University, Ghent Institute of Functional and Metabolic Imaging (GIFMI), Ghent, Belgium;*
[3]*Ghent University, Institute of Biomedical Engineering and Technology (IBiTech), Ghent, Belgium*

Introduction: An MRI protocol tree on a clinical system is a large database containing hundreds of protocols, each containing multiple sequences, and up to 900 parameters per sequence(1). Without proper management, MRI protocol trees can quickly become cluttered.
MRI protocol variation leads to to increased waste in terms of scan time, money, limited patient throughput etc., and less than optimal outcomes for the patient due to variations in diagnostic quality across protocols(2). Structured reporting is also affected by variations in protocols(2).
One of the main causes is protocol creep, where MRI protocols are adapted on a case by case basis, because a standardized protocol catalogue is unavailable or not managed properly. Another common cause is pressure on the MR technologist to make ad hoc changes, or lack of agreement between radiologists(3). Historical errors or copying of protocols from one scanner to the other also contribute largely to protocol creep.
To avoid waste and improve efficiency, all sequences within protocols for one specific goal (i.e. routine brain imaging), should have (see Fig. 1):
(1) the same geometric parameters (coverage, FOV, slice thickness etc.) across all scanners and field strengths;
(2) Identical contrast parameters at the same field strength;
(3) Identical parameters between sequences that have the same purpose (i.e. routine DWI). These can be part of multiple scan protocols.
Here we present real world evidence of protocol creep, and a workflow to resolve protocol differences between scanners, in a university hospital setting.
Methods: A snapshot of Neuro MRI protocols from 3 systems (Siemens PrismaFit 3 T, Aera 1.5 T and AvantoFit 1.5 T, all running VE11C) were exported as xml and exar1 files. The differences between the xml protocol printouts were assessed with a Python script(1), which provides Excel files of differences in naming of Regions, Exams and Programs, as well as detailed differences between sequences that share the same name.
Next, all sequences were renamed following the convention < contrast > _ < sequence_type > _ < orientation > _ < dimension > using a virtual machine of the scanner console. The script was used again to find differences between sequences that share the same name. This process was repeated until all differences were resolved.
In the final step, the cleaned protocols were discussed with the neuroradiology team and lead radiographer to decide which protocols and sequences could be kept.
Results: The snapshot of the original tree and the tree after renaming of all sequences was analysed for differences in naming of Regions, Exams, and Programs. The number of sequences per region was extracted, see Table 1. On PrismaFit, the number of Programs and Sequences was reduced drastically. On Aera the number of sequences increased, because it was harmonized with the AvantoFit tree. The Area contains 23 sequences more than the AvantoFit because of additional capabilities (licenses) of the scanner software.
Next, the number of duplicate sequences was investigated. On PrismaFit, we found 39 unique sequences with 2 to 16 duplicates each. Scout scans were not taken into account. For instance, we found 16 instances of an MP-RAGE sequence, and 15 DWI sequences with the same name. The AvantoFit contained 33 unique sequences with 2 to 15 duplicates each. On Aera, 33 unique sequences were found, with 2 to 16 duplicates each.
Each set of duplicate sequences was inspected for differences, see Fig. 2 for the difference between 2 MP-RAGEs on PrismaFit. Not only the contrast (TR 1550 vs 1570 ms), but the number of slices and slice oversampling (176/27.3% vs 192/16.7%) was different. For the DWI, see Fig. 3, we found small differences in the echo time, bandwidth, number of slices among others.
Sometimes, a more serious error was discovered, i.e. the sequence name did not match the sequence purpose, for example the sequence name contained *fs* for fat suppression, but fat suppression was not turned on, or a *VIBE* sequence name turned out to be a *STARVIBE* sequence. Moreover, some sequence that were optimized on 1.5 T was found to be copied to the 3 T system without adaptation, i.e. some instances of a spin-echo sequence that should have been modified to a TSE sequence.
In the final step, the exar1 tree was copied to the real scanners. This unfortunately causes import errors and slight changes, which again required a comparison of the real scanner"s xml and the virtual machine"s xml files. The whole process took several months.
Conclusion: A workflow is created to manage protocol trees, which saves valuable console time at the scanner. A large number of unwanted or hidden discrepancies between protocols was removed, which results in consistent MRI exams.

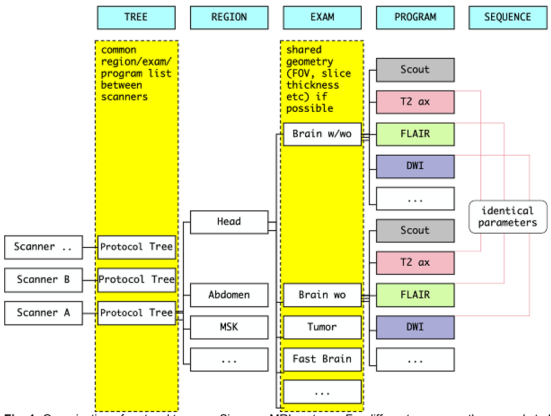

Fig. 1: Organization of protocol trees on Siemens MRI systems. For different scanners, there needs to be a common set of Regions, Exams, and Programs. If technically possible, each sequence within the Exam level needs to have the same geometrical and acquisition parameters.

Before/**After**	Regions	Programs	Exams	Sequences
PrismaFit 3T	1/**1**	32/**9**	2/**1**	238/**147**
Aera 1.5T	1/**1**	2/**6**	1/**1**	54/**112**
AvantoFit 1.5T	1/**1**	4/**4**	1/**1**	91/**89**

Table 1: Number of unique Regions, Programs, Exams, and sequences before renaming according to a standardized scheme.

Comparing	7ca38b1e-38fe-473b-8b00-ad88d6637655	
\\USER\Neuro_Hoofd_Hals\Neuro\Hersenen zonder contrast\mprage_tfl3d_sag_0.9mm-iso *, TA: 3:56 Voxel size: 0.9×0.9×0.9		
with	bef965d8-3b00-4159-a666-72b1d33d0067	
\\USER\Neuro_Hoofd_Hals\Neuro\Spectroscopie\mprage_tfl3d_sag_0.9mm-iso *, TA: 3:59 Voxel size: 0.9×0.9×0.9		
Parameter to change	**From**	**To**
Contrast - Common-TR	1570.0 ms	1550.0 ms
Geometry - AutoAlign-AutoAlign	Head > Basis	---
Geometry - AutoAlign-Initial Rotation	11.28 deg	0.00 deg
Geometry - AutoAlign-L		0.0 mm
Geometry - AutoAlign-Orientation	S > T-10.4 > C-0.9	Sagittal
Geometry - AutoAlign-Position	L0.8 A19.3 F35.2 mm	Isocenter
Geometry - AutoAlign-R	0.0 mm	
Geometry - Common-Orientation	S > T-10.4 > C-0.9	Sagittal
Geometry - Common-Position	L0.8 A19.3 F35.2 mm	Isocenter
Geometry - Common-Slice oversampling	16.7 %	27.3 %
Geometry - Common-Slices per slab	192	176
Geometry - Common-TR	1570.0 ms	1550.0 ms
Inline - MapIt-TR	1570.0 ms	1550.0 ms
Physio - Signal1-TR	1570.0 ms	1550.0 ms
Properties-Load images to graphic segments	Off	On
Routine-AutoAlign	Head > Basis	---
Routine-Coil elements	HEA;HEP	HE1-4
Routine-Orientation	S > T-10.4 > C-0.9	Sagittal
Routine-Position	L0.8 A19.3 F35.2 mm	Isocenter
Routine-Slice oversampling	16.7 %	27.3 %
Routine-Slices per slab	192	176
Routine-TR	1570.0 ms	1550.0 ms
System - Miscellaneous-AutoAlign	Head > Basis	---
System - Miscellaneous-Coil Select Mode	Default	Off - AutoCoilSelect
System - Miscellaneous-Coronal	P >> A	A >> P
System - Miscellaneous-Transversal	H >> F	F >> H

Fig. 2: Differences between MP-RAGEs that are supposed to be identical.

Comparing	b276cc1f-abc3-4b6d-a67d-0e1421e9f626	
\\USER\Neuro_Hoofd_Hals\Neuro\Hersenen zonder contrast\dwi-12d_ep2d_diff_tra_3mm *, TA: 1:14 Voxel size: 0.8×0.8×3.0		
with	31400aaf-8d5a-4699-b019-bf49ed04fd3a	
\\USER\Neuro_Hoofd_Hals\Neuro\Craniale zenuwen\dwi-12d_ep2d_diff_tra_3mm *, TA: 1:10 Voxel size: 0.8×0.8×3.0		
Parameter to change	**From**	**To**
Contrast - Common-TE	80.0 ms	79.0 ms
Contrast - Common-TR	4300 ms	4500 ms
Geometry - AutoAlign-> S	-0.2	
Geometry - AutoAlign-F	1.5 mm	
Geometry - AutoAlign-H		0.0 mm
Geometry - AutoAlign-Initial Orientation	T > C	Transversal
Geometry - AutoAlign-Initial Position	L1.0 P5.0 F1.5	Isocenter
Geometry - AutoAlign-Initial Rotation	-0.29 deg	0.00 deg
Geometry - AutoAlign-L	1.0 mm	0.0 mm
Geometry - AutoAlign-Orientation	T > C-4.5 > S-0.2	Transversal
Geometry - AutoAlign-P	5.0 mm	0.0 mm
Geometry - AutoAlign-Position	L1.0 P5.0 F1.5 mm	Isocenter
Geometry - AutoAlign-T > C	-4.5	
Geometry - Common-Orientation	T > C-4.5 > S-0.2	Transversal
Geometry - Common-Position	L1.0 P5.0 F1.5 mm	Isocenter
Geometry - Common-Slices	35	33
Geometry - Common-TR	4300 ms	4500 ms
Physio - Signal1-TR	4300 ms	4500 ms
Routine-Orientation	T > C-4.5 > S-0.2	Transversal
Routine-Position	L1.0 P5.0 F1.5 mm	Isocenter
Routine-Slices	35	33
Routine-TE	80.0 ms	79.0 ms
Routine-TR	4300 ms	4500 ms
Sequence - Part 1-Bandwidth	1754 Hz/Px	1852 Hz/Px
Sequence - Part 1-Echo spacing	0.65 ms	0.63 ms
Sequence - Part 2-Gradient mode	Performance*	Performance
System - Adjust Volume- F >> H	139 mm	131 mm
System - Adjust Volume- Orientation	T > C-4.5 > S-0.2	Transversal
System - Adjust Volume- Position	L1.0 P5.0 F1.5 mm	Isocenter
System - Adjust Volume- Rotation	-0.29 deg	0.00 deg

Fig. 3: Differences between DWIs that are supposed to be identical.

References

1. Pullens, P et.al.: *Proc ISMRM 2020*;:4160.
2. Boland GW, Duszak R: *J American College of Radiology* 2015; 12:833–835.
3. Ravi KS, Geethanath S: *Magnetic Resonance Imaging* 2020; 73:177–185.

P259.
Machine learning-assisted automated quality control of MR neuroimaging data

A. Kalantari Sarcheshmeh[1], M. Aswendt[1]

[1]*University Hospital Cologne, Neurology, Cologne, Germany*

Introduction: The acquisition of consistent quality magnetic resonance (MR) images, as well as the screening and categorization of large databases, can be challenging. User-dependent manual screening without quantitative criteria is not feasible for large databases. In preclinical, animal imaging, there is no consensus on the standardization of quality control measures or categorization of good vs. bad quality images.

Methods: We developed a tool in Python (Fig. 1) to create a basic overview of MR image datasets including information about the SNR, temporal SNR, Gosting artifacts, spatial resolutions, and movement severity for T2w, DWI, and fMRI sequences (Nifti or Bruker file formats).

1) *Data Parsing:* The user sets the input path and the program will parse through all subfolders. After parsing, only those MR files chosen by the user between the options of T2w, DTI, or fMRI data are selected, and duplicates are eliminated. Finally, csv files are created with the storage path of every selected file. 2) *Feature calculation*: In this step, each sequence's parameters are calculated accordingly. Mutual information was used as a metric to calculate movement severity and hosting artifacts due to its intensity independence. 3) *Outlier detection:* In this step, all of the calculated features will be statistically analyzed with the help of five methods to identify outliers: One class SVM, Isolation Forest, Local Outlier Factor, and Elliptic Envelope. In addition to these, a normal statistical definition of outliers based on the interquartile range is also used.

Results/Discussion: The pipeline now generates a CSV file containing all the results for each defined sequence, including the outlier detectors, which are created in a specified location set by the user at the beginning. Additionally, distribution plots of the SNR, tSNR, and movement severity, along with the outlier detector results, are produced and stored in their corresponding folders. In the final CSV sheet named *voting.csv* are all of the data listed which had at least one vote from the machine-learning outlier detectors ("Judges"). If all five outlier detectors have voted the image as an outlier, there is a high possibility that artifacts exist, maybe directly observable in the image. Based on experience, the images with all five detectors voting for a bad/outlier image are pure noise images or extreme Ghosting artifacts.

AIDAqc was developed to create an easy-to-use command-line tool that categorizes datasets based on image quality and excludes datasets with poor quality from further processing. Furthermore, this tool can be used to create a unified standardization for MR image quality.

Conclusions: AIDAqc is the first automated quality control tool for preclinical MRI that includes machine learning-based outlier detectors. The pipeline can be further improved with the optimization of parallel computing and the implementation of a graphical user interface.

Acknowledgment: This work was supported by the Friebe Foundation (T0498/28960/16) and the Deutsche Forschungsgemeinschaft (DFG, German Research Foundation) – Project-ID 431549029 – SFB 1451.

Disclosure: The authors have no financial interest or relationship to disclose regarding the subject matter of this presentation.

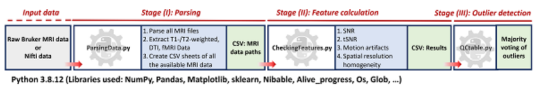

Fig. 1 Pipeline workflow: All of the necessary functions are implemented in this module, SNR is calculated by using the Chang method and also the more popular way with the help of defining regions of interest inside and outside of the brain (I) In this stage, all of the available MR files are parsed and located. (II) In the main block, here all of the parameters are calculated: SNR, tSNR, and Motion artifacts. Spatial Resolution, slice thickness, and the number of repetitions is also extracted. The final output are CSV files located in a folder called "*calculated features*". (III) Five different outlier detectors, each with their own strengths and weaknesses will determine together as a "*major vote*" what image is considered a bad quality image.

P260.
Bringing MRI to low- and middle- income countries: Directions, challenges and potential solutions

S. Adeleke[1], S. Okoli[2], S. Murali[3], M. Umair[4], R. Garg[5], C. Qin[6], J. Obungoloch[7], I. Asllani[8], N. A. B. Ntusi[9,10], R. Mammen[11], N. R. Jagannathan[12,13,14], H. Ninalowo[15], C. Anosike[15,16], K. Eyre[17], K. Menacho[18,19], M. Friedrich[5,20], U. Anazodo[21], T. Niendorf[22]

[1]*King's College London, School of Biomedical engineering and imaging science, London, United Kingdom;*
[2]*University of Bristol, Bristol Medical School, Bristol, United Kingdom;*
[3]*Imperial College London, School of Medicine, London, United Kingdom;*
[4]*Johns Hopkins University, Russell H. Morgan Department of Radiology and Radiological Sciences, Baltimore, MD, United States;*
[5]*Research Institute of the McGill University Health Centre, Departments of Medicine and Diagnostic Radiology, Montreal, Canada;*
[6]*Imperial College Healthcare NHS Trust, Department of Imaging, London, United Kingdom;*
[7]*Mbarara University of Science and Technology, Department of Biomedical Engineering, Mbarara, Uganda;*
[8]*Rochester Institute of Technology, Department of Biomedical Engineering, New York, NY, United States;*
[9]*University of Cape Town and Groote Schuur Hospital, Department of Medicine, Cape Town, South Africa;*
[10]*South African Medical Research Council Extramural Unit on Intersection of Noncommunicable Diseases and Infectious Diseases, Cape Town, South Africa;*
[11]*East Sussex and North East Essex Foundation Trust, The Essex Cardiothoracic Centre, Basildon, United Kingdom;*
[12]*Indian Institute of Technology, Department of Electrical Engineering, Chennai, India;*
[13]*Sri Ramachandra University Medical College, Department of Radiology, Chennai, India;*
[14]*Chettinad Hospital and Research Institute, Department of Radiology, Kelambakkam, India;*
[15]*IRDOC Interventional Radiology Consulting Limited, Euracare Multispecialty Hospital, Interventional Radiology, Lagos, Nigeria;*
[16]*Warrington and Halton Teaching Hospitals National Health Service Foundation Trust, Radiology, Warrington, United Kingdom;*
[17]*Research Institute of the McGill University Health Centre, Montreal, Canada;*
[18]*University College London, Institute of Cardiovascular Science, London, United Kingdom;*
[19]*St Bartholomew's Hospital, Barts Health Center, The Cardiovascular Magnetic Resonance Imaging Unit and The Inherited Cardiovascular Diseases Unit, London, United Kingdom;*
[20]*McGill University, Department of Family Medicine, Montreal, Canada;*
[21]*McGill University, Department of Neurology and Neurosurgery, Montreal Neurological Institute, Montreal, Canada;*
[22]*Max Delbrueck Center for Molecular Medicine in the Helmholtz Association, Berlin Ultrahigh Field Facility (B.U.F.F.), Berlin, Germany*

Introduction: Magnetic resonance imaging (MRI) is a mainstay of diagnostic imaging to evaluate various neurovascular, oncological, musculoskeletal and cardiovascular conditions. Despite its essential clinical role, there is a global disparity as 66% of the world is without access to MRI1. This barrier can be attributed to technological, economic, and social factors. As low- and middle-income countries (LMICs) undergo the pivotal 'epidemiological transition' from communicable to non-communicable disease, broader MRI access is required to improve public health outcomes. With these limitations in mind, we describe a framework of solutions to improve MRI development in low- and middle-income countries.

Methods: We reviewed literature on the development of affordable MRI and its various components, as well as hardware and software challenges and local macro and micro economic policies that could potentially impact the implementation of accessible MRI. Literature searches were performed on Medline, Embase, and the Cochrane Library electronic databases for articles published in English from inception until 1 May 2023.

Results: The scanner density in LMICs is significantly lower than in high-income countries (HICs), with 1.115 MRI units per million population (pmp) in LMICs compared to 26.529 MRI pmp in HICs, as outlined in Fig. 1. HICs have also been found to have a significantly greater proportion of higher magnetic field strength scanners (B0 $\geq$ 1.5 T) compared to LMICs2. Intra-country disparity is prevalent, with a higher density of MRI scanners seen in urbanised regions than in rural communities2. Together, these factors have made MRI inaccessible, despite MRI"s positive impact on quality-adjusted life years (QALYs).

40% of healthcare spending in LMICs is out-of-pocket and expensive (relative to income) (Fig. 2). MRI scanners have specific infrastructure requirements, such as state-of-the-art hardware and software, uninterrupted power supply, supply of cryogenic liquids or industrial gases for magnet cooling, imaging suites and safety zones, which are all challenges in LMICs. The significant proportion of donated medical equipment that becomes non-functional or unutilised could be attributed to the lack of adaptation of new technologies to the local environment2. Social issues such as the scarcity of relevant training, preclude many from understanding and maximising the value of MRI. Finally, on a patient level, healthcare illiteracy and distrust in modern healthcare is also an issue.

Discussion Our solutions to the limited access to MRI technology in LMICs include the development of multipurpose and sustainable, locally produced durable components that can be integrated with the current infrastructure. Given the recent developments in AI based image reconstruction, significant compromise to image quality and spatial resolution can also be spared. Other solutions include use of teleradiology, and educational strategies aimed at changing attitudes towards new imaging technology.

Deep learning-based reconstruction algorithms could benefit from (ultra)low field MRI due to their enhanced immunity to noise and the reduction of reconstruction artefacts. AI could also help to lower the technical specifications for the gradient linearity and magnetic field uniformity, reducing further hardware costs. Highly efficient micro-cooling technology that require just 1 to 7 L of liquid helium for cooling, instead of the 1,500 L that conventional magnets use, should also be explored for LMICs. Finally, the expansion of portable MRI could allow for earlier diagnosis of patients who cannot access conventional MRI facilities or are mistrustful of modern technologies.

To develop this comprehensive solutions framework, we set up a cardiovascular magnetic resonance (CMR) reporting course targeted at LMICs. This initiative will be led by the Society of Cardiovascular Magnetic Resonance (SCMR)-certified radiology and cardiology attendings and fellows. To facilitate this work, we are also testing novel non-contrast CMR and rapid CMR protocols3 and optimising these sequences in healthy volunteers in Lagos, Nigeria.

Conclusion MRI has the potential to become widely available in LMICs. With rapid expansion of the technology, it will not be long before more feasible solutions become widely available at a lower cost. There is a need to emphasise community engagement and co-creation to adapt the technology to local training, hardware and software needs to make it more sustainable.

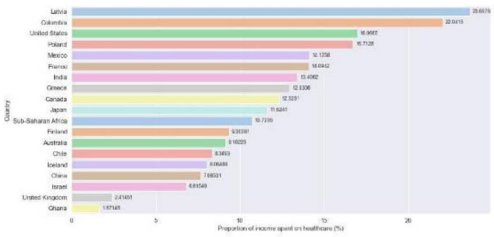

Fig. 1: A bar chart showing the percentage average amount per capita spent on healthcare in each country as a percentage of overall income per capita. The data used to produce this chart was taken from the OECD healthcare spending data and the average income information was taken from the worlddata.info website.

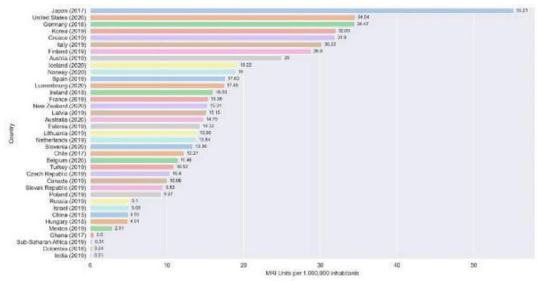

Fig. 2: A bar chart displaying the MRI units per million population, according to the Organization for Economic Co-operation and Development (OECD). This figure shows the average individual healthcare expenditure as a percentage of income in different countries. The data are organised by density. Bar chart is from Qin et al, Eur Heart J Cardiovasc Imaging. 2022;23(6):e246–e260.

References

1. World Health O. Global atlas of medical devices. WHO Medical device technical series. World Health Organization; 2017.
2. Anazodo UC, Ng JJ, Ehiogu B, et al. A Framework for Advancing Sustainable MRI Access in Africa. NMR Biomed. Oct 19 2022:e4846.
3. Friedrich MG, Karamitsos TD. Oxygenation-sensitive cardiovascular magnetic resonance. Journal of Cardiovascular Magnetic Resonance. 2013 Dec;15(1):1–1.

P261.
Neural network informed flip angle optimization for SAR reduced imaging

P. Dawood[1], J. Stebani[1], T. Griesler[1], F. Breuer[2], D. Weber[2], V. Herold[1], S. Malik[3], P. M. Jakob[1], M. Blaimer[2]

[1]*University of Würzburg, Department of Physics, Experimental Physics 5, Würzburg, Germany;*
[2]*Fraunhofer Institute for Integrated Circuits IIS, Division Development Center X-Ray Technology, Magnetic Resonance and X-ray Imaging Department, Würzburg, Germany;*
[3]*King's College London, Department of Biomedical Engineering, London, United Kingdom*

Introduction: A major limitation of Turbo-Spin-Echo (TSE) sequences [1] is the exceeding of specific absorbtion rate (SAR) limits at high field strengths. For mitigation, previous works [2–4] determined variable flip angle (VFA) schemes, but the optimization was limited to only one target tissue and did not take into account the phase-encoding (PE-) ordering. Recently, simulation frameworks for automated VFA determination have been proposed [5, 6], however, long optimization times prevent clinical application. Here we propose a neural network (NN) informed optimization framework for fast VFA determination in SAR-constrained, standard 2D TSE imaging. The framework considers multiple tissues and structural information for optimization as well as PE-ordering. The implementation allows the use of a single NN for a wide range of different echo train lengths.
Methods: Here we employ a fully connected feed-forward NN which predicts a VFA scheme and the contrast-equivalent echo time (TE) simultaneously for a given protocol set. This prediction is used as initialization of the flip angles to yield faster convergence of the constrained optimization problem as prior information about the VFA scheme have been incorporated via the NN. The predicted contrast-equivalent TE determines the adapted sampling pattern (i.e. PE-table). **Database generation** For training, a database has been generated for numerous TSE protocol setttings for various T2 and PD weightings (Tab.1). For all valid imaging settings, the VFA scheme was obtained using the framework depicted in Fig. 1A. It incorporates a projected gradient descent optimization algorithm. The L1 norm between the SAR-reduced simulation and the 100% SAR reference image was used as cost function. The number of iterations was limited to 350. Additionally, the contrast equivalent TE [4] was determined to mitigate for T1 contamination effects. The database contained 1,696 instances in total. To train only one NN for varying echo train lengths, all VFA schemes were interpolated to a uniform length of 70 flip angles. **Neural Network** The employed NN uses a dual-head architecture to predict the VFA scheme and the contrast-equivalent TE simultaneously (Fig. 1B). As input, repetition time (TR), echo train length (ETL), echo spacing (ESP), relative SAR (rSAR) and the effective TE is passed. Head 1 predicts the VFA scheme and consists of 3 hidden layers. Head 2 predicts the contrast-equivalent TE and consists of 3 hidden layers. We used a compound cost function L_{comp},
$L_{comp} = L_{head1} + L_{head2}$,where L_{head1} is the L2-error of the VFA scheme, and L_{head2} is the L2-error of the contrast-equivalent TE. The data was split into training– and test-data (80% and 20%, respectively).
Experiments: Two NN informed VFA schemes were tested experimentally on a healthy volunteer at 3 T (Siemens Magnetom Skyra, Siemens Healthineers) with typical parameters: FOV = 230 × 230 mm^2, slice thickness = 5 mm, ESP = 10 ms. Different effective TE,TR, ETL and rSAR were used. The sequences were implemented using Pulseq [7, 8].
Results: We compared the proposed faster optimization (35 iterations) to the optimization initialized with constant flip angles (350 iterations). Figures 2A and 3A show exemplary VFAs for rSAR = 40% and 30%, respectively. Using only 35 iterations, the NN informed optimization yields as accurate VFA schemes as the fully optimized case. Furthermore, improved error-maps and L1-errors are achieved (Fig. 2B and Fig. 3B) when compared to the rSAR = 100% reference image (i.e. flip angles = 180°). In vivo experiments obtained with the NN informed VFA scheme are shown in Figs. 2C and 3C as well as the reference images with rSAR = 100% for comparison.
Discussion: The proposed NN informed VFA initialization results in a 10 × faster opimization with comparable performance. In 97% of the test cases (350 protocol settings), the error (L1 norm between SAR-reduced and reference image) was at least equivalent to the time extensive optimization. The NN was only used to provide a starting point for a physics-based optimization based on the Extended Phase Graph formalism. Our framework is flexible in terms of TSE protocol setttings. For proof of concept, the optimization was limited to T2- and PD-weighted imaging in this work. However, the framework can be extended to T1 weighted or FLAIR imaging. Future studies will consider extension to 3D imaging with very long ETLs.

Imaging Parameter	Range (Stepsize)
Repetition Time	2,000 ... 4,000ms (500ms)
Effective Echo Time	70 ... 200ms (10ms)
Echo Train Length	9 ... 69 (10)
Echo Spacing	5 ... 250ms (5ms)
Relative SAR	30 ... 50% (10%)

Fig. 1: TSE protocols for database for neural network training.

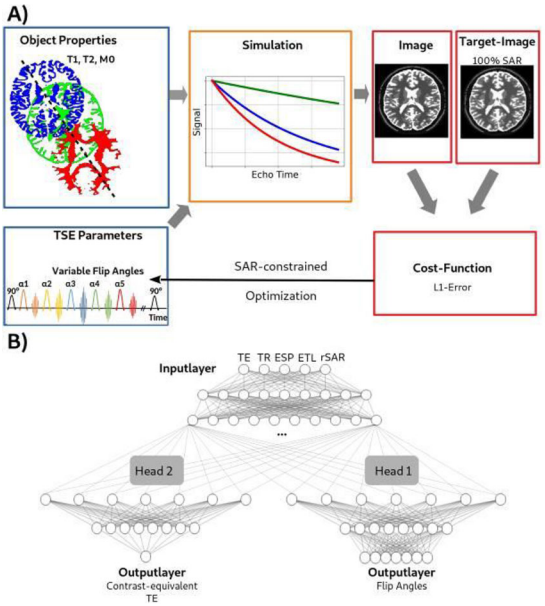

Fig. 2 (A) : Optimization algorithm including a simulation framework via EPG **(B)** Proposed dual-headed neural network to predict VFA and contrast-equivalent TE

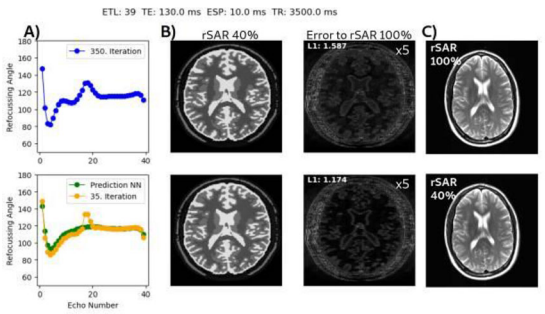

Fig. 3 (A) : VFA scheme via optimization initialized with constant flip angles (350 iterations) (top), and VFA via neural network, and after fast optimization (35 iterations) (bottom) **(B)** Simulations corresponding to VFAs in **(A)** and error maps to rSAR 100% reference **(C)** Experiment for rSAR= 100% reference (top), and for rSAR=40% using the neural network informed VFAs (bottom).

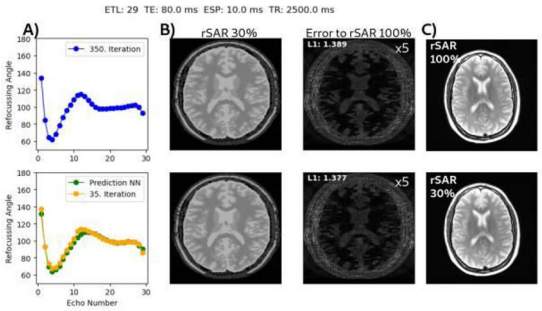

Fig. 4 (A): VFA scheme via optimization initialized with constant flip angles (350 iterations) (top), and VFA via neural network, and after fast optimization (35 iterations) (bottom) **(B)** Simulations corresponding to VFAs in **(A)** and error maps to rSAR 100% reference **(C)** Experiment for rSAR= 100% reference (top), and for rSAR=30% using the neural network informed VFAs (bottom).

References

1. Henning et al. MRM. 1986,3(6):823–33.
2. Henning et al. MRM. 2003,49(3):527–5.
3. Busse et al. MRM. 2006,55(5):1030–7.
4. Weigel et al. MRM.2006,55(4):826–35.
5. Blaimer et al. Magn Reson Matter Phy.2019, 32(Suppl 1) 21.
6. Loktyushin et al. MRM. 2021,86(2):709–24.
7. Layton et al. MRM. 2017,77(4):1544:52.
8. Keerthi et al. JOSS(2019):1725.

Acknowledgements: Bavarian Ministry of Economic Affairs, Infrastructure, Transport and Technology.

P262.
Segmentation of post-operative longitudinal MRIs of high-grade glioma based on transfer learning

F. J. Gil-Terrón[1], K. Skogen[2], C. Lopez-Mateu[1], S. F. Svensson[2], G. Ager-Wick[2], A. Hilde Farstad[2], R. A. B. Bugge[2], J. M. García-Gómez[1], K. E. Emblem[2], E. Fuster-García[1]

[1]*Universitat Politècnica de València, Biomedical Data Science Laboratory—ITACA Institute, Valencia, Spain;*
[2]*Oslo University Hospital, Department of Physics and Computational Radiology, Oslo, Norway*

Introduction: Gliomas are one of the most common types of brain tumors belonging to a highly heterogeneous group of neoplasms. MRI has become the standard for the working diagnosis and follow-up of this kind of tumors. In recent years, deep learning has permeated the research interest in this field, offering fast and high-quality segmentations of pre-surgical cases. However, the same is not true for post-surgery images. Almost all the models have been developed to segment pre-surgical images, so their performance when applied to post-surgical cases drop considerably. This is mainly due to the lack of segmented post-surgical glioma cases for training models capable of learning the differences that might exist in the follow-up of a glioma patient. In this work, we developed automated glioma segmentation models for post-surgical cases, exploiting the combination of large datasets of pre-surgical cases and few post-surgical longitudinal cases.

Methods: The network for this study was the residual-inception U-Net proposed by the ONCOhabitats Software [1] modified to add deep supervision to improve performance. The pre-surgical dataset was the BraTS2021 [2] (1.251 patients), and the post-surgical cases were the image series from 31 patients of the ImPRESS clinical trial (ClinicalTrials.gov Identifier: NCT03951142). The MRI scans from the ImPRESS study are blind to the treatment regimen and only the accuracy of the segmentations is considered regardless of treatment

and the patients' response status. Using both pre-surgical and post-surgical cases, models are developed following two strategies attempting to maximize the DICE score, that is, 1) training with all data together, and 2) training pre-surgical models and fine-tuning them with post-surgical data. The pre-operative model used as baseline to compare the results obtained in this study was the one included in the latest version of ONCOhabitats. For validation, we used 10 patients from the 31 longitudinal ImPRESS studies, independent of training, selected to form a set that was as representative as possible.

Results Our results showed that both approaches achieved competitive segmentation performance for post-surgical glioma cases. Figure 1 shows a complete follow-up case of a patient and its segmentations. Figure 2 summarizes the results achieved in terms of DICE score. In the case of the model trained with pre- and post-surgical data, the DICE score increased (compared to the baseline model) by 3.87% for the enhancing tumor, by 3.12% for the tumor core, and by 6.15% for the whole tumor. For the fine-tuned model, these values increased by 3.74%, 3.18% and 5.34% respectively. The p-values for the paired t-test were 0.037 and 0.023 for both models compared to the pre-op, so we rejected the null hypothesis with a significant difference. The p-value was 0.312 for the test between the post-operative models, indicating no significant difference.

Discussion Our results demonstrate the feasibility of developing automated glioma segmentation models for post-surgical cases by exploiting the combination of large datasets of pre-surgical cases and a few post-surgical longitudinal cases. The proposed strategies achieved competitive segmentation performance, outperforming the pre-operative model used as a baseline. Particularly, the fine-tuning strategy could be useful for developing models that are more adaptable to different clinical scenarios where obtaining annotated post-surgical cases can be challenging.

Conclusion In this work, we proposed and evaluated two strategies for developing automated glioma segmentation models for post-surgical cases, using a combination of pre-surgical and post-surgical datasets. Overall, thework performed is potentially able to streamline the process of segmentation of post-surgical cases by radiologists, in turn enhancing the generation of new segmentations and allowing for the on-going improvement of machine learning models.

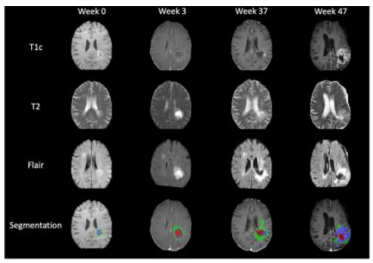

Fig. 1: Follow-up of a patient with glioma showing Contrast-enhanced T1-weighted (T1c), T2-weighted (T2) and Flair MRI and segmentation over time. Enhancing tumor structures visible in blue, surrounding cystic/necrotic core components and post-surgical cavity in red, and edema in green.

Models	Enhancing Tumor	Tumor Core	Whole Tumor
OncoHabitats (pre-operative)	80.89 [61.19-88.27]	77.56 [69.81-85.54]	81.44 [77.34-88.30]
1) Pre + post data together	84.02 [62.56-90.42]	79.98 [76.68-84.23]	86.45 [84.36-92.12]
2) Pre-surgical fine-tuned	83.92 [63.80-88.40]	80.03 [73.22-84.18]	85.79 [83.75-87.16]

Fig. 2: Results are show as the median [Q1-Q3] DICE Score achieved for the subset of follow-up studies belonging to the 10 patients selected for validation, for the three structures to be segmented: enhancing tumor, tumor core and whole tumor. The pre-operative reference model is compared with the two post-surgical models developed in this work, 1) model trained with pre-operative and post-operative data together, and 2) pre-surgical model fine-tuned with post-surgical data.

References

[1] J. Juan-Albarracín, E. Fuster-Garcia, G. A. García-Ferrando, and J. M. García-Gómez, "ONCOhabitats: A system for glioblastoma heterogeneity assessment through MRI," *Int J Med Inform*, vol. 128, pp. 53–61, Aug. 2019, https://doi.org/10.1016/J.IJMEDINF.2019.05.002.

[2] U. Baid et al., "The RSNA-ASNR-MICCAI BraTS 2021 Benchmark on Brain Tumor Segmentation and Radiogenomic Classification," 2021, Accessed: Jun. 13, 2022. [Online]. Available: http://arxiv.org/abs/2107.02314

P263.
Using cosine similarity networks for classifying glioma grades 2 and 3 using preoperative perfusion and diffusion MRI

H. Ayaz[1], D. Tormeey[1], I. McLoughlin[1], S. Unnikrishnan[1]

[1]*Atlantic Technological University Sligo, School of Engineering, Sligo, Ireland*

Introduction: Gliomas account for 80% of all malignant brain tumours, with grade 2 and 3 indicating intermediate levels of malignancy [1]. Classical and advanced machine learning techniques have been evaluated to classify grade 2 and 3 gliomas non-invasively using apparent diffusion coefficient (ADC) [2] and arterial spin labelling (ASL) [3, 4]. This study uses a novel cosine similarity-based neural network instead of conventional CNNs [5] to distinguish grade 2 and 3 gliomas using ADC and ASL-cerebral blood flow (CBF) maps.

Methodology: 63 glioma patients, including 39-grade two and 24-grade three, were examined using the UCSF-PDGM dataset [6]. For pre-processing, six slices of each ADC and CBF map were extracted using the segmentation maps and the principle of co-variance to determine the most tumour information, as shown in Fig. 1. The dataset was first split into train and test sets with an 80/20 ratio. Then training set was split into 80% training and 20% validation set. A novel cosine similarity-based network with 17 layers was trained on 100 epochs using keras-tensorflow library in python. The model was compiled with an Adam optimizer using a learning rate of 0.005. The entire process was separately trained for ADC and ASL maps.

Results The model's training and validation loss plots are given in Fig. 2 and 3 for ASL and ADC. To determine the performance achieved for perfusion and diffusion maps, several statistical measure precision, sensitivity/Recall, and F1-score were measured, as shown in Table 1 and Table 2. The overall accuracy achieved was 0.70% for ASL maps and 0.66% for ADC maps.

Discussion This study investigates a novel cosine similarity technique for classifying grade 2 and 3 gliomas using non-invasive and invasive MRI. The finding suggests that cosine-normalization-based models are able to perform better than classical deep learning models using non-invasive MRI. However, the relatively small dataset cohort leads to underfitting issues. Therefore, the model needs to validate the results using cross-validation and tuning other hyperparameters. Also, deep cosine models are relatively new advancements in deep neural networks, and in the future, these models may be relevant to determine the feature relevance and model explainability of the neural network.

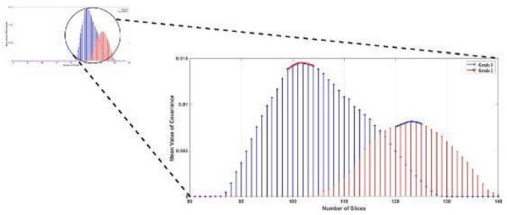

Fig. 1: Co-variance pre-processing plot for grade 2 and 3 patients using segmentation maps. The red line on the grade 3 plot shows the selected images and blue line on grade 2 plot shows the selected images using mean value of covariance.

Fig. 2

Fig. 3

Fig. 4

Table1:Precision, Sensitivity, F1-score of Cosine Similarity model using ASL maps. For each modality network was trained for 100 epochs

ASL	Epochs= 100		
	Precision	Sensitivity	F1-Score
Grade 2	70	80	89
Grade 3	75	82	66
Overall accuracy		69.99	

Table2: Precision, Sensitivity, F1-score of Cosine Similarity model using ADC maps. For each modality network was trained for 100 epochs

ADC	Epochs= 100		
	Precision	Sensitivity	F1-Score
Grade 2	60	77	84
Grade 3	75	82	72
Overall accuracy		66.82	

Reference

[1] Frances, S., Velikova, G., Klein, M., … S. S.-N., & 2022, undefined. (n.d.). Long-term impact of adult WHO grade II or III gliomas on health-related quality of life: a systematic review. *Academic.Oup.Com*. Retrieved April 20, 2023, from https://academic.oup.com/nop/article-abstract/9/1/3/6424719

[2] Xiong, D., Ren, X., Huang, W., Wang, R., Ma, L., Gan, T., Ai, K., Wen, T., Li, Y., Wang, P., Zhang, P., & Zhang, J. (2022). Noninvasive Classification of Glioma Subtypes Using Multiparametric MRI to Improve Deep Learning. *Diagnostics*, *12*(12), 3063. https://doi.org/10.3390/DIAGNOSTICS12123063/S1

[3] Hashido, T., Saito, S., & Ishida, T. (2020). A radiomics-based comparative study on arterial spin labeling and dynamic susceptibility contrast perfusion-weighted imaging in gliomas. *Scientific Reports 2020 10:1*, *10*(1), 1–10. https://doi.org/10.1038/s41598-020-62658-9

[4] Hashido, T., Saito, S., & Ishida, T. (2021). Radiomics-Based Machine Learning Classification for Glioma Grading Using Diffusion- And Perfusion-Weighted Magnetic Resonance Imaging. *Journal of Computer Assisted Tomography*, *45*(4), 606–613. https://doi.org/10.1097/RCT.0000000000001180

[5] Luo, C., Zhan, J., Xue, X., Wang, L., Ren, R., & Yang, Q. (2018). Cosine normalization: Using cosine similarity instead of dot product in neural networks. *Lecture Notes in Computer Science (Including Subseries Lecture Notes in Artificial Intelligence and Lecture Notes in Bioinformatics)*, *11,139 LNCS*, 382–391. https://doi.org/10.1007/978-3-030-01418-6_38/COVER

[6] Calabrese, E., Villanueva-Meyer, J. E., Rudie, J. D., Rauschecker, A. M., Baid, U., Bakas, S., Cha, S., Mongan, J. T., & Hess, C. P. (2022). The University of California San Francisco Preoperative Diffuse Glioma MRI Dataset. https://doi.org/10.1148/Ryai.220058, *4*(6). https://doi.org/10.1148/RYAI.220058

P264.
Multi-parametric optimization of MR-imaging sequences for MR-guided radiotherapy

H. M. Fahad[1,2,3], S. Dorsch[1,3,4], M. Zaiss[5,6], C. P. Karger[1,3]

[1]*German Cancer Research Center (DKFZ), Medical Physics in Radiation Oncology, Heidelberg, Germany;*
[2]*University of Heidelberg, Faculty of Medicine, Heidelberg, Germany;*
[3]*National Center for Radiation Research in Oncology, Heidelberg Institute for Radiation Oncology HIRO, Heidelberg, Germany;*
[4]*University of Heidelberg, Medical Physics in Radiation Oncology, Heidelberg, Germany;*
[5]*Friedrich-Alexander-Universität Erlangen-Nürnberg (FAU), Department of Neuroradiology, Erlangen, Germany;*
[6]*Magnetic Resonance Center, Max- Planck Institute for Biological Cyberrnetics, Tübingen, Germany*

Introduction: Magnetic Resonance Imaging (MRI) is widely used in oncology for staging, tumor response assessment, and radiation therapy (RT) planning due to its ability to provide a wide range of soft tissue

imaging contrast. These contrasts can be optimized by a variety of MR sequence parameter sets (SPS), which directly affect the image quality and efficiency of further image processing. Depending on the sequence and clinical objective, these SPS can include up to 30 individual parameters. Optimization of SPS for a specific clinical scenario is often performed manually, which can be time-consuming. Therefore, an automated sequence optimization process is preferred. In this study, we propose a framework for the automatic optimization of MRI sequences based on SPS that are directly applied on the scanner.

Methods: Measurements were performed on a 1.5 T MR scanner (MAGNETOM Sola, Siemens Healthineers, Erlangen, Germany) with a dedicated phantom consisting of 7 in-house fabricated contrast inserts of different concentrations of agarose, Ni-DTPA, and KCL [1]. The SPS were optimized for a 2D turbo spin echo (TSE) sequence with a constant bandwidth (BW) of 186 Hz/pixel, a resolution of 0.4×0.4 mm^2, a slice thickness of 5 mm, and a turbo factor (TF) of 30. The echo time (TE), repetition time (TR), and flip angle (FA) were allowed to vary within a specific range (TE: 12 ms – 114 ms, TR: 500 ms – 2300 ms, and FA: 140° – 180°). The MR scanner was remotely controlled by Siemens" Access-i-Tool to enable an "on-the-run" optimization process. The proposed framework employed a derivative-free optimization algorithm to repeatedly update and execute a parametrized sequence on the MR scanner to acquire new data. In each iteration, the mean squared error (MSE) was calculated based on one of two clinically relevant optimization goals: achieving the same contrast as in a target image and maximizing the contrast between specified tissue types. The framework was evaluated using two optimization methods: a covariance matrix adaptation evolution strategy (CMA-ES) and a genetic algorithm (GA).

1. Achieving the same contrast as in a target image:

For this study, we used a 0.35 T MR-Linac (MRIdian Linac, Viewray Inc., Oakwood, USA) TSE image as a target image t, with TR = 2000 ms, TE = 35 ms, TF = 15, and resolution = 0.78×0.78 mm^2 parameter values. The SPS on the MAGNETOM Sola MR Scanner resulted in an optimized image m that is optimized during the process. The scanner generates a signal mi for a substitute i, which should match the signal t_i of the same substitute in the target image.

2. Maximize tissue contrast for automated segmentation:

The aim of this study is to enhance the accuracy of automated segmentation of tumors and/or organs at risk by maximizing the contrast between neighbouring tissues. This is achieved by calculating the contrast between pairs of substitute tissues, which is then formulated as a multi-objective optimization problem. To simplify the problem, a weighted sum of individual objective functions is used to arrive at a single objective function. The optimization algorithm is evaluated by conducting experiments with various weighting factors. The resulting objective function is given $F = \Sigma\, \lambda_{ij}\, (m_i — m_j)^2$. Where the λ_{ij} are the weights of the objective functions terms $(m_i — m_j)^2$, and i and j are indices of the substitute tissues.

Results: The results demonstrate that the proposed framework has potential for automatic contrast optimization of MRI sequences. Both CMA-ES and GA methods showed promising results in achieving the optimization goals. However, CMA-ES converged much faster compared to GA. Figure 1 shows how the parameters development during optimization and converged at the same parameter values. Further, Fig. 2 displays the optimization results for two analysed cases. Case 1 (all weights set to 1) showed low contrast between substitutes 3/4 and 4/5, while Case 2 (increasing the weighting factors λ_{34} and λ_{45} to 5) significantly improved contrast between substitutes 3/4 and 4/5 but decreased contrast between the other substitutes.

Discussion: This study presented a fully automatic optimization of contrast in MRI sequences by directly applying the sequence of SPS on the scanner. The optimization was performed for a 2D TSE sequence due to its relatively short acquisition time by changing three parameters (TR, TE, and FA). More parameters could be included in the optimization process. In this proof-of-principle study, the optimization was performed on a phantom. For clinical implementation, the optimized sequences will also be tested in-vivo.

Conclusion: The proposed framework for automatic multi-parametric optimization of SPS directly on the MRI scanner has the potential to enhance the quality of MRI images for dedicated application in MR-guided RT.

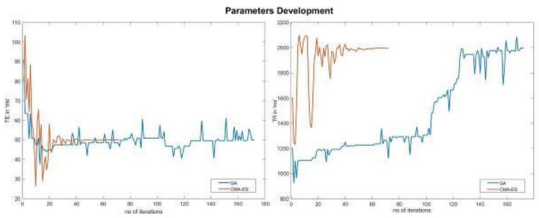

Fig. 1: Parameters development during the optimization process using CMA-ES and GA. CMA-ES converges much faster compared to GA, however, both methods converge at the same parameter and objective function values.

Container	1	2	3	4	5	6	7
Case 1 (λ_{12}=λ_{23}=λ_{34}=λ_{45}=λ_{56}=λ_{67}=1)							
Signal [a.u]	715.43	232.46	826.68	940.52	894.82	1227.79	494.94
Contrast [a.u]		482.97	594.22	113.84	45.70	332.97	732.85
Case 2 (λ_{12}=λ_{23} =λ_{56}=λ_{67}=1, λ_{34}=λ_{45}=5)							
Signal [a.u]	688.79	612.78	1030.27	1627.86	1126.77	1095.36	1213.98
Contrast [a.u]		76.01	417.49	569.59	501.09	31.41	118.59

Fig. 2: Signal and contrast for the measured substitutes for two different sets of weighting factors.

Reference

[1] https://doi.org/10.1088/1361-6560/abd4b9.

P265.
Towards fast estimation of adipose tissue volumes from continuously moving table whole-body MRI

T. Haueise[1,2,3], F. Schick[1,2,3], J. Machann[1,2,3]

[1]*University Hospital Tübingen, Section on Experimental Radiology, Tübingen, Germany;*
[2]*Helmholtz Center Munich, Institute for Diabetes Research and Metabolic Diseases, Tübingen, Germany;*
[3]*German Center for Diabetes Research (DZD), Tübingen, Germany*

Introduction: Abdominal obesity, as manifested by increased VAT, shows a strong correlation to insulin sensitivity and is a key condition of the metabolic syndrome which is associated with the risk of developing type 2 diabetes [1]. Quantification of adipose tissue (AT) from MRI using deep learning-based segmentation methods [2], especially when using Dixon-based imaging techniques, is regarded as a gold-standard enabling a differentiation into various AT compartments, e. g. subcutaneous AT (SAT) and visceral AT (VAT) (see Fig. 1). However, whole-body (WB) MRI using Dixon-based techniques is time-consuming, and requires application of a set of dedicated surface coils and repositioning of the subject.

Contiuously moving table (CMT-)MRI is typically used as localizer for WB examinations providing full 3D information, large field of view, sufficient resolution (5 mm isotropic) and fast acquisition (about 20 s for the trunk) by scanning during continuous movement of the patient table [3]. Due to poor contrast between tissues, AT quantification using a similar approach to [2] yields poor results, especially for VAT.

This work presents the results of a feasibility study to quantify AT volumes using image-based regression from CMT MRI data originally acquired as WB localizers.

Methods: CMT-MRI data-sets from 56 volunteers using free-breathing proton-density weighted 2D axial acquisition with TE = 1.44 ms, TR = 2.56 ms, body coil as transmit/receive coil and 46 mm/s table speed on a 3 T WB imager (Magnetom Vida, Siemens Healthcare, Erlangen) were used to train CNN regression models (2D and 3D, 44 for training, 12 for validation). AT reference values were obtained from segmentation-based quantification in corresponding 3D VIBE Dixon images [2] acquired during the same session. Both baseline regression models consist of 8 convolutional layers (kernel size 3 in every dimension) with instance normalization and leaky ReLU activation. Two fully connected layers were implemented as regression head. VAT and SAT were regressed simultaneously using mean square error (MSE) loss. 2D images were generated from 3D CMT-MRI data using axial, sagittal or coronal projections (see Fig. 2A–C) and their combination (Fig. 2D) similar to the approach presented by Langner [4, 5]. Optimization of regression model architecture has not been considered in this work.

Results: Fig. 3 shows an example of the training and validation loss of the 3D regression model. For the 2D model, the combined input of coronal and sagittal projections (see Fig. 2D) yields best results. Mean absolute difference (MAD) to volumetric reference values is 1.3 l (corresponding to a relative difference of 42%) for VAT and 0.7 l (11%) for SAT. Using 3D input data, MAD is reduced to 1.1 l (35%) for VAT and 0.6 l (8%) for SAT.

Discussion: The findings suggest that using regression on CMT localizer images basically works and provides a very rough estimate of VAT while SAT makes a good compromise. Using 3D data is superior compared to 2D projections. Training times of the 3D models are higher by orders of magnitude. However, nowadays, computing resources are not a limiting factor. Therefore, it is a promising approach for fast assessment of AT volumes requiring less than one-minute of MR scanning time without the extra effort of requiring additional receiver coils.

Conclusion: Future work improving contrast either on imaging side or using postprocessing approaches (e. g. domain adaptation) as well as network optimization should further improve the AT volume estimation.

Fig. 1 Segmentation of VAT and SAT from VIBE Dixon MRI.

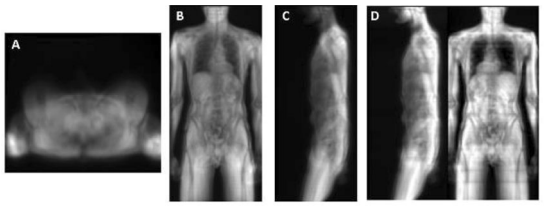

Fig. 2 Mean projections of 3D FastView data used as input data for 2D regression models. A: axial projection, B: coronal projection, C: sagittal projection, D: combination of sagittal and coronal projection.

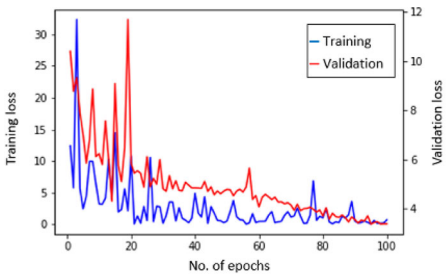

Fig. 3 Example of training and validation loss of 3D regression model.

References

1. Neeland IJ et al. (2019) Visceral and ectopic fat, atherosclerosis, and cardiometabolic disease: a position statement. Lancet Diabetes Endocrinol 7:715–725.
2. Haueise T et al. (2023) Analysis of volume and topography of adipose tissue in the trunk: results of MRI of 11,141 participants in the German National Cohort. Sci Adv, in press.
3. Fenchel M et al. (2008) Automatic labeling of anatomical structures in MR FastView images using a statistical atlas. Med Image Comput Comput-Assist Interv MICCAI Int Conf Med Image Comput Comput-Assist Interv 11:576–584.
4. Langner T et al. (2020) Large-scale biometry with interpretable neural network regression on UK Biobank body MRI. Sci Rep 10:17,752.
5. Langner T et al. (2022) MIMIR: Deep Regression for Automated Analysis of UK Biobank MRI Scans. Radiol Artif Intell 4:e210178.

P266.

A diagnostic model constructed for Alzheimer's disease classification based on MRI images

S. Yu[1,2], W. Feng[1,2], H. Zhang[1,2], L. Tao[1,2], X. Wang[1,2], X. Guo[1,2]

[1]*Capital Medical University, Beijing Municipal Key Laboratory of Clinical Epidemiology, Beijing, China;*
[2]*Capital Medical University, School of Public Health, Beijing, China*

Introduction: With the rapid development of big data analysis methods, image data has become an important data type used in Alzheimer's disease (AD) auxiliary diagnosis models. This study aims to construct Alzheimer's disease risk prediction models using different big data analysis methods by analyzing brain MRI images. Provide more comprehensive data analysis for AD classification and diagnosis, control AD process early, effectively reduced the probability of mild cognitive impairment (MCI) progressing to AD.

Methods: All participants included in this study were from the Alzheimer's Disease Neuroimaging Association. And the data included brain MRI images. This study uses three-dimensional convolutional neural network combined with SVM classifier to construct AD

auxiliary diagnosis model; and, in order to compare with the machine learning method, this study uses the texture extraction of MRI images, thus using machine learning method for the task of AD classification. In this study, the data set was randomly allocated according to the proportion of 80% of the training group and 20% of the test group, the training set was used to build the model, and the test set was used to evaluate the model. This study adopted the evaluation of model performance through the following indicators, including: accuracy, sensitivity, specificity, and area under the curve (AUC).

Results: The results of this study show that the 3D-CNN classification and diagnosis ability is better than the 2D-CNN ($P < 0.05$), and the 3D-CNN-SVM joint model is in the two-class and three-class tasks of AD Both are better than 3D-CNN and 2D-CNN ($P < 0.05$). The accuracy of 3D-CNN-SVM is $92.11 \pm 2.31\%$ in the three-classification task of normal person (NC), MCI and AD in the test set. The accuracy, sensitivity and specificity of 3D-CNN-SVM in three binary classification tasks of AD and NC, AD and MCI, and MCI and NC are (99.10%, 99.80%, 98.40%), (89.40%, 86.70%, respectively), 84.00%) and (98.90%, 98.90%, 98.80%). In this study, the same machine learning method was used to construct the three-classification models based on image texture data, and the best performing machine learning model was the extreme gradient boosting algorithm. But its accuracy in classifying each stage of AD was much lower than that of the convolutional neural network model, and the difference was statistically significant ($p < 0.05$).

Discussion Currently, the diagnostic classification of medical images is mostly performed by experienced and skilled radiologists or imaging technicians, which may cause problems such as reduced clinical diagnostic efficiency, diagnostic inaccuracies, manual errors, and high level of operator skills required [1]. Previous studies have shown the high value and clinical significance of CNN in AD diagnosis [2]. However, there are few studies related to CNNs that consider the construction of 3D MRI image models of the brain for AD triple classification tasks [3]. Therefore, in this study we constructed and developed a new joint model that combines 3D-CNN with SVM for triple classification diagnosis. The results of this study show that 3D-CNN has better diagnostic capability than 2D-CNN, and the joint 3D-CNN-SVM model outperforms both 3D-CNN and 2D-CNN in both binary and triple classification tasks of AD. In addition, the 3D-CNN-SVM constructed by combining deep learning with machine learning in this study outperforms the models proposed in previous studies and has a very high diagnostic power. Finally, this study effectively integrates the preprocessing procedure with 3D-CNN-SVM, thus ensuring that there is no need to manually perform any feature extraction operation and guaranteeing that the image will give valid classification results once it is input to the procedure. This also reveals the importance of this study to apply the present model in clinical hospitals with low clinical care conditions, which can effectively help neurologists in aiding diagnosis and providing suggestions for doctors' treatment decisions.

Conclusion: The 3D-CNN-SVM method is expected to establish a classification model for AD automation, personalization and early screening, in order to increase the full application of MRI data information in the diagnosis of AD and to help prevent the development of AD in the clinical stage.

References

[1] Zhao J, Zhang M, Zhou Z, Chu J, Cao F. Automatic detection and classification of leukocytes using convolutional neural networks. Med Biol Eng Comput, 2017, 55 (8): 1287–1301.

[2] Wang SH, Phillips P, Sui Y, Liu B, Yang M, Cheng H. Classification of Alzheimer's Disease Based on Eight-Layer Convolutional Neural Network with Leaky Rectified Linear Unit and Max Pooling. J Med Syst, 2018, 42 (5): 85.

[3] Suk HI, Lee SW, Shen D. Latent feature representation with stacked auto-encoder for AD/MCI diagnosis. Brain Struct Funct, 2015, 220 (2): 841–859.No figures

P267.
Multiple sclerosis clinical courses classification through morphological connectivity based graph convolutional network

E. Chen[1], A. Clement[1], T. Grenier[2], D. Sappey-Marinier[1]

[1]*Université de Lyon, INSA-Lyon, Université Claude Bernard Lyon 1, UJM-Saint Etienne, CNRS, Inserm, CREATIS UMR 5220, U1206, Lyon, France;*

[2]*Univ Lyon, INSA-Lyon, Université Claude Bernard Lyon 1, UJM-Saint Etienne, CNRS, Inserm, CREATIS UMR 5220, U1294, Lyon, France.*

Multiple sclerosis (MS) is an inflammatory and neurodegenerative disease that affects over 2 million people worldwide. To investigate the brain gray matter (GM) alterations, morphological connectivity methods provide graph metrics based on the measurement of GM features using routinely available T1-weighted MRI. In this study, graph convolutional network (GCN) was used for the classification of MS clinical forms based on morphological features such as GM thickness, a marker of brain atrophy.

MS patient population consisted of 42 relapsing–remitting (RR), 28 secondary-progressing (SP), and 21 primary-progression (PP) subjects for a longitudinal study (7 scans per patient on average) forming a dataset of 660 scans in total. The patients underwent MR scans on a 1.5 T Siemens Sonata system (Lyon CERMEP) including a sagittal millimetric 3D-T1 sequence.

All MRI scans were fed into Freesurfer[1] for brain GM segmentation. GM was then parcellated into q small regions using 3 brain atlases: Desikan-Killiany[2] (q = 68), Destrieux[3] (q = 148), Glasser[4] (q = 360). Then, we extract the distribution of thickness values (mean, std, skewness and kurtosis) of each cortical regions. The graph representation of brain morphology connectivity was defined as the dissimilarity across brain regions using the Mahalanobis distance, and the adjacent matrix was deduced.

Thus, each patient's brain was described as a graph with 4 attributes per node. To counteract the impact of noisy and dense graphs, thresholds were applied to the adjacent matrix and a fixed rejection rate ranging from 60 to 80% based on previous report[5] was evaluated. The classification tasks were performed using a GCN algorithm[6] with the adjacent matrix and the node feature matrix as input (pipeline shown in Fig. 1). We compare our GCN approach with a 3D convolutional image classifier network (3D-CNN). For 3D-CNN, MRI scans were pre-processed using Brain Extraction Tool[7] to isolate brain tissue.

Five classification tasks related to clinical needs were implemented (RR vs SP vs PP; RR vs SP + PP; RR vs SP; RR vs PP; SP vs PP) and evaluated on the F1 score. The results obtained for GCN and 3D-CNN are presented in Fig. 2 and Fig. 3, respectively. The best overall result of GCN classification was obtained when 80% rejection rate was applied on Glasser based graph generation. Compared to the outcome of 3D-CNN, GCN provided a better global result.

GCN based on brain morphological connectivity is an innovative approach for the classification of MS clinical forms. While the 3-classes classification remains a challenging task regarding the imbalanced data distribution, an encouraging result was found when a high rejection rate was applied on Glasser atlas. Tasks 2–4 gave a promising result on separation of inflammatory form (RR) and degenerative forms (SP and PP). We also demonstrated the interest of GCN facing a small dataset where traditional 3D-CNN methods do not perform well. Furthermore, GCN has also gained in computation time as it took one week to train the 3D-CNN network whereas GCN only needed one training day for the most complex scenario.

In this study, we explored the potential of brain morphological connectivity to characterize alterations in MS patients and the benefit of GCN. A transfer learning towards a larger dataset (OFSEP[8]) is in progress to fully exploit the capacity of the proposed pipeline.

This work was supported by the LABEX PRIMES (ANR-11-LABX-0063) of Université de Lyon, within the program "Investissements d'Avenir" (ANR-11-IDEX-0007) operated by the French National Research Agency (ANR).

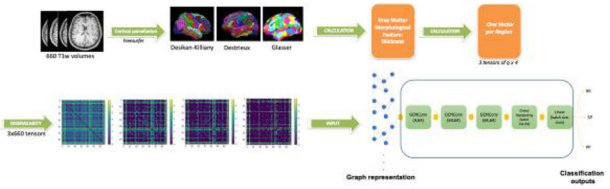

Fig. 1: Pipeline of the proposed image preprocessing and classification network.

Desikan-Killiany	Original	Rejection Rate = 60%	Rejection Rate = 70%	Rejection Rate = 80%
RR vs SP vs PP	0.594(0.047)	0.593(0.059)	0.583(0.049)	0.567(0.043)
RR vs SP + PP	0.658(0.088)	0.648(0.081)	0.647(0.081)	0.638(0.071)
RR vs SP	0.684(0.064)	0.7(0.077)	0.697(0.082)	0.674(0.08)
RR vs PP	0.701(0.076)	0.698(0.068)	0.697(0.069)	0.703(0.052)
SP vs PP	0.438(0.092)	0.475(0.073)	0.46(0.08)	0.466(0.101)

Destrieux	Original	Rejection Rate = 60%	Rejection Rate = 70%	Rejection Rate = 80%
RR vs SP vs PP	0.569(0.037)	0.588(0.059)	0.596(0.063)	0.596(0.066)
RR vs SP + PP	0.649(0.074)	0.657(0.061)	0.656(0.058)	0.642(0.071)
RR vs SP	0.684(0.065)	0.679(0.066)	0.683(0.072)	0.686(0.07)
RR vs PP	0.72(0.103)	0.721(0.089)	0.72(0.092)	**0.725(0.085)**
SP vs PP	0.485(0.05)	0.45(0.054)	0.466(0.071)	0.466(0.073)

Glasser	Original	Rejection Rate = 60%	Rejection Rate = 70%	Rejection Rate = 80%
RR vs SP vs PP	0.609(0.038)	0.634(0.055)	0.638(0.066)	**0.642(0.063)**
RR vs SP + PP	0.627(0.085)	0.681(0.085)	0.687(0.084)	**0.689(0.095)**
RR vs SP	0.711(0.062)	0.71(0.059)	0.712(0.064)	**0.722(0.067)**
RR vs PP	0.702(0.096)	0.722(0.102)	0.713(0.089)	0.714(0.079)
SP vs PP	0.495(0.076)	0.479(0.076)	**0.531(0.115)**	0.471(0.077)

Fig. 2: Mean (standard deviation) of MS clinical forms classification using GCN with graph generation based on Desikan-Killiany, Destrieux and Glasser atlases and four rejection rates (original, 60%, 70%, 80%). Best overall results were highlighted in bold.

	3D-CNN	GCN
RR vs SP vs PP	0.639(0.036)	**0.642(0.063)**
RR vs SP + PP	**0.707(0.066)**	0.689(0.095)
RR vs SP	0.721(0.081)	**0.722(0.067)**
RR vs PP	0.697(0.124)	**0.725(0.085)**
SP vs PP	0.495(0.06)	**0.531(0.115)**

Fig. 3: Mean (standard deviation) of MS clinical forms classification using 3D-CNN and GCN. Best results among the two networks were highlighted in bold.

1: Fischl B. FreeSurfer. Neuroimage. 2012;62(2):774–781.
2: Desikan RS, Ségonne F, Fischl B, et al. An automated labeling system for subdividing the human cerebral cortex on MRI scans into gyral based regions of interest. Neuroimage. 2006;31(3):968–980.
3: Destrieux C, Fischl B, Dale A, et al. Automatic parcellation of human cortical gyri and sulci using standard anatomical nomenclature. Neuroimage. 2010;53(1):1–15.
4: Glasser MF, Coalson TS, Robinson EC, et al. A multi-modal parcellation of human cerebral cortex. Nature. 2016;536(7615):171–178.
5: Barile B, Ashtari P, Stamile C, et al. Classification of multiple sclerosis clinical profiles using machine learning and grey matter connectome. Front Robot AI. 2022;9:926,255.
6: Kipf TN, Welling M. Semi-Supervised Classification with Graph Convolutional Networks. ICLR. 2017.
7: Jenkinson M, Pechaud M, Smith S. BET2: MR-based estimation of brain, skull and scalp surfaces. OHBM. 2005.
8: Vukusic S, Casey R, Rollot F, et al. Observatoire Français de la Sclérose en Plaques (OFSEP): A unique multimodal nationwide MS registry in France. Multiple Sclerosis Journal. 2018;26:118–122.

P268.
Text detection for MRI

J. Bousso[1], S. Boucher[1], E. Grossiord[1], M. M. Serra[1], M. Marteau[1]

[1]*Medexprim, Toulouse, France*

Introduction: Detecting text in medical images is a crucial issue, whether it involves identifying data or important text embedded in the image. Preserving patient privacy is a major concern, particularly in the context of clinical research. Furthermore, in an era where an increasing number of projects are being established and where data is being aggregated retrospectively, the need to verify multicenter data with RGPD conformity is even more important. In the case of medical images such as MRIs, privacy is verified by examining information contained in DICOM (Digital Imaging and Communications in Medicine) tags and the presence of Protected Health Information (PHI) in the image.

Protected health information (PHI) is any information in the medical record or related data that can be used to identify an individual. In the case of medical imaging this kind of information is usually present within DICOM tags, contain a large amount of information such as the patient's name and date of birth, but this kind of information might also be present as burnt-in text pixels within the image. Identifying information may also appear regarding healthcare personnel involved in study indication and acquisition. As it happens with DICOM tags, useful exam-related information may appear as well. However, it is also possible to retrieve text corresponding to important relevant diagnostic information within burnt-in text pixels within the image. In the first case, it is necessary to remove potentially identifying PHI burnt-in text pixels to preserve patient and/or personnel anonymity, while in the second case information contained in the text may hold significant value and therefore should be retained.

Methods: The proposed algorithm can detect and classify different types of text by using a combination of several algorithms. Firstly, a Convolutional Neural Networks (CNN) based on VGG16 is used to determine whether text is present in the image. If text is detected, the algorithm uses Optical Character Recogniton (OCR) to identify the embedded text and its position within the image, then a second CNN is used to classify the text based on its category. If the text is identified as PHI, the corresponding pixels are replaced by background pixels, whereas if the text contains relevant information, the associated pixels and words are extracted and stored in a document.

Our datasets consist of several MRI scans, including brain, lung and liver scans. We used a first train/test dataset, where 76 images were used for training while 24 were for validation. In the 76 images used for the training set, 57 contained text while the others were clean.

Results: Our experiments have yielded zero false negatives, indicating that no images containing text have been missed by the text-detection algorithm.

However, the OCR algorithm might mistake certain structures for text. Coupling it with our detection algorithm based on VGG16 greatly reduced false positives in the text detection. The text classification algorithm also has limitations, one of them being to identify text as PHI, which leads to misclassification.

Discussion: Detected text may not be classified accurately as it can be challenging to differentiate between identifying information and relevant text. One solution could be to rely on the information contained in the DICOM tags, but this approach is only effective if the DICOM tags have not yet been anonymized. Since we cannot guarantee to have access to them, we need to find other methods to improve our algorithm. One strategy could be to improve the training of our algorithm by integrating synthetized images with burnt-in text, in particular in challenging locations within the image, and using data augmentation.

Conclusion: Work is currently under way to reconstruct the image in order to preserve its quality, for both medical diagnosis and training machine learning algorithms. The main purpose is to be able to desidentify and reconstruct the image with high quality.

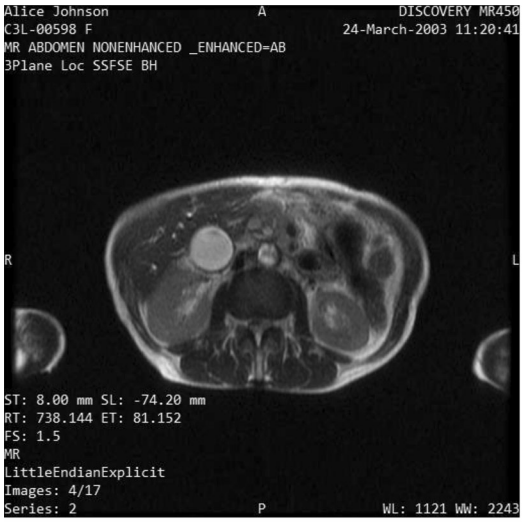

Fig. 1: Axial slice of a abdomino-pelvic MR acquisition with text (PHI and acquisition-related information).

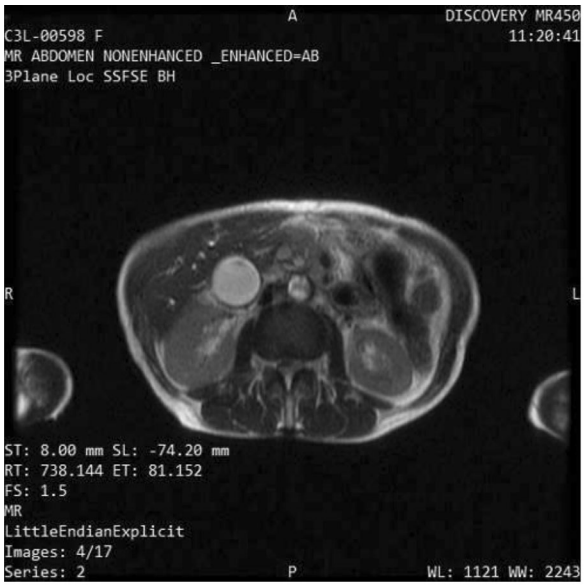

Fig. 2: Axial slice of a abdomino-pelvic MR acquisition after treatment (with PHI removed).

P269.
Effect of acquisition and processing parameters in MRI classification using GCN

A. Clement[1], E. Chen[1], T. Grenier[2], D. Sappey-Marinier[1]

[1]*Universitéde Lyon, INSA-Lyon, Universitéde Claude Bernard Lyon 1, UJM-Saint Etienne, CNRS, Inserm, CREATIS UMR 5220, U1206, Lyon, France;*
[2]*Univ Lyon, INSA-Lyon, Universitéde Claude Bernard Lyon 1, UJM-Saint Etienne, CNRS, Inserm, CREATIS UMR 5220, U1294, Lyon, France*

Machine learning, and more specifically deep learning, allow accurate classifications of MR images in different classes such as healthy/pathological, multiple sclerosis clinical forms, benign/malignant tumors, etc. The major drawback of such approaches is the need of large datasets to train the network, including variability in classes such MR systems and acquisition sequences. Such limitation of network generalization can be overpassed by other techniques such as domain shift but the latter needs more or less paired acquisitions to be trained. In this work, we developed another approach, namely brain morphological connectivity which is based on a graph representation of brain morphological features such as gray matter (GM) thickness following a GM segmentation on T1-weighted (T1w) MRI. In this context, we studied the classification performances of T1w-MR images when B0 fields vary from 1.5 T to 3 T of different T1w types of acquisition sequences.

Methods: OFSEP[1] is the French observatory of multiple sclerosis (MS) including more than 30,000 MRI scans from 36 centers in France. In this study, 2107 T1-w MRI volumes acquired from three different manufacturers (GE, Siemens, Philips) and two different B0 field (1011 patients at 1.5 T and 1096 patients 3 T) were extracted from OFSEP database. Only one scan per patient was included to avoid duplication bias.

Two classification networks were tested: Convolutional Neural Network (CNN) and Graph Convolutional neural Network[2] (GCN). Both architectures were trained with train/test ratio of 0.7/0.3 and performance was assessed by F1-score.

First, we design a CNN architecture Fig. 1a that is small as possible (4843 parameters) using 64 × 64 resized images. The used GCN architecture Fig. 1b is able to classify 3 different MS forms (10,753 parameters) as reported by Chen et al[3].

Concerning the GCN, a graph representation was obtained from each brain"s patient where cortical GM was segmented using Freesurfer[4] and described by 4 attributes of the GM thickness: mean, standard deviation, skewness and kurtosis. After parcellation of the cortical GM in regions, adjacent matrices were obtained using dissimilarity measures between brain regions.

We explored the influence of different parameters: 1) three atlases (Desikan-Killany, Destrieux, Glasser) were used for parcellation of the cortical regions 2) three values of Full-Width-Half-Max (FWHM) smoothness were compared for segmentation, and 3) three rejection rates were applied on adjacent matrices. For statistics, each training (3 × 3x3 for GCN and 1 for CNN) was repeated 10 times.

Results: The classification performances (F1-scores) are summarized in Fig. 2. We observe that CNN is able to efficiently classify 1.5 T vs 3 T images with an F1-score of 0.87 (0.02) despite the resized images (64 × 64) and the small architecture. GCN can also classify 1.5 T vs 3 T graphs with a max F1-score of 0.75 (0.01). When FWHM increases (more smoothing), the F1-score decreases but the difference between FWHM10 and FWHM20 is not significant. As the FWHM increase the loss increases and the accuracy decreases Fig. 3a. Considering a FWHM, there is no evidence of a significant difference in the convergence of the loss and the accuracy between the threshold Fig. 3b.

Discussion: These results showed that B0 field intensity must be considered as a bias in MRI classification even for GCN uses. This study suggested that small changes in segmentation should not be neglected even for GCN classification. Our future work will consist in studying domain shift approaches dedicated to GCN to reduce such hidden bias and thus improve the GCN generalization on multi-center and multi-manufacturer datasets.

This work was performed within the framework of the LABEX PRIMES (**ANR-11-LABX-0063**) of Université de Lyon, within the program "Investissements d'Avenir" (ANR-11-IDEX-0007) operated by the French National Research Agency (ANR).

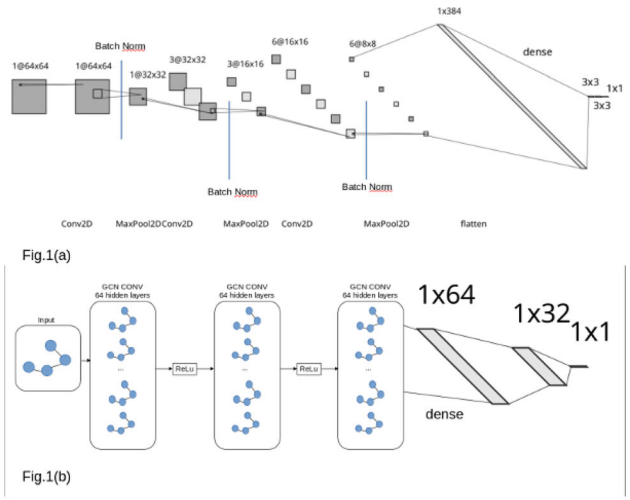

Fig. 1: (a) : Architecture of the CNN used; (b) : Architecture of the GCN used.

		Fwhm0			Fwhm10			Fwhm20		
		60	70	80	60	70	80	60	70	80
GCN	Desikan	0.70 +- 0.02	0.70 +- 0.02	0.71 +- 0.01	0.65 +- 0.01	0.67 +- 0.01	0.67 +- 0.02	0.66 +- 0.02	0.65 +- 0.01	0.65 +- 0.01
	Destrieux	0.73 +- 0.01	0.73 +- 0.01	0.74 +- 0.01	0.67 +- 0.01	0.67 +- 0.01	0.66 +- 0.02	0.64+- 0.02	0.65 +- 0.01	0.64 +- 0.01
	Glasser	0.73+- 0.01	0.74 +- 0.01	0.75 +- 0.01	0.65+- 0.01	0.65 +- 0.02	0.65+- 0.02	0.65 +- 0.01	0.65 +- 0.01	0.65 +- 0.02

Fig. 2: Mean (standard deviation) of classification result evaluated on F1 score with three parcellation atlases (Desikan-Killiany, Destrieux and Glasser), three thresholds (60%, 70%, 80%) and three FWHM values (0, 10 20).

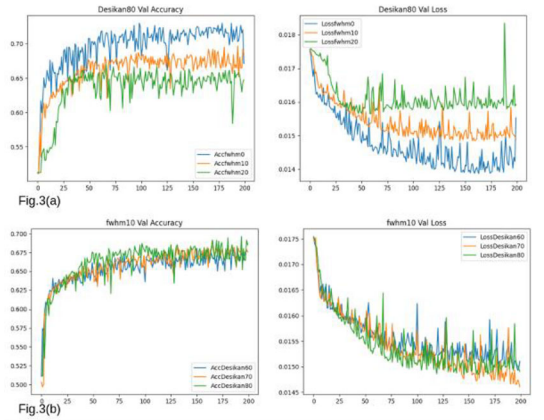

Fig. 3: (a) : Evolution of Accuracy and Loss of the model on Desikan parcellation with an 80% Threshold while increasing the FWHM ; (b) : Evolution of Accuracy and Loss of the model on FWHM10 while increasing the Threshold on Desikan parcellation.

References

1: Vukusic S, et al. Observatoire Français de la Sclérose en Plaques (OFSEP): A unique multimodal nationwide MS registry in France. Multiple Sclerosis Journal. 2018;26:118–122.
2: Kipf TN, Welling M. Semi-Supervised Classification with Graph Convolutional Networks. ICLR. 2017.w
3: Chen E., et al., Multiple Sclerosis Clinical Courses Classification through Morphological Connectivity based Graph Convolutional Network. Submitted to ESMRMB2023.
4: Fischl B. FreeSurfer. Neuroimage. 2012;62(2):774–781.

P270.
Generative pre-training with masked image modelling of k-space for MRI reconstruction

C. Zhu[1,2], T. Doyle[1,3,4], M. D. Noseworthy[1,2,5,3]

[1]*McMaster University, School of Biomedical Engineering, Hamilton, Canada;*
[2]*St. Joseph's Healthcare, Imaging Research Centre, Hamilton, Canada;*
[3]*McMaster University, Electrical and Computer Engineering, Hamilton, Canada.*

[4]Vector Instutute of Artificial Intelligence, Toronto, Canada;
[5]McMaster University, Department of Radiology, Hamilton, Canada

Introduction: Transformers [1] have emerged as a new deep learning architecture pushing the state of the art of language models. Naturally, there is interest applying these advances to image processing, resulting in vision transformer (ViT) [2], which led to masked autoencoders (MAE) for ViT [3]. However, it has been shown that applying deep learning advances from natural images to medical images may not be directly applicable [4]. Currently, there is little work extending advances in vision transformers to medical imaging applications. Nonetheless, masked image modelling has potential for both speeding up MRI acquisition and for self-supervised pre-training of models.

This study proposed generative pre-training of a ViT for MR image reconstruction which may be extended into applications in downstream tasks such as MR fingerprinting. While there are many parameters to be optimized, this initial study focused only on investigating k-space undersampling masks (i.e.the masking ratio) because this approach, although improving speed, will require optimization.

Methods: Data were obtained from the NYU *fastMRI Initiative database* (fastmri.med.nyu.edu) [5, 6] The primary goal of fastMRI is to test whether machine learning can aid in the reconstruction of medical images. As a proof-of-concept, this study was limited to the largest subset of the data, which were 13,704 T2-weighted human brain images acquired from various 3 T MRI vendors using a 16-channel receive-only phase array head coil. The dataset was divided such that each individual coil was a sample for a total of 13,704 × 16 = 219,264 training examples. During pre-processing, k-space from each of the 16 coils were center cropped to be 256 × 256 in size and then further split into both real and imaginary channels. Finally, each matrix was normalized by dividing each element by the real coefficient of the maximum value of the sample.

Model architecture follows as described in the original ViT MAE paper [3], but with differences in inputs. We used an image size of 256 × 256 with 2 input channels (real and imaginary), compared to 224 × 224 RGB images. During training, a range of k-space values (25%, 50%, and 75%) were randomly and identically masked on each channel while training a ViT MAE meant to generate the masked k-space values for 8 epochs with mean squared error (MSE) as the loss. Models were evaluated using both MSE and the self-similarity index measure (SSIM) [7]. SSIM was calculated as a global metric with equal weights for luminance, contrast, and structure. Computation was performed using a Nvidia RTX A6000 GPU.

Results Models were evaluated on the downloaded test set with the same criteria and pre-processing as the training set, for a total of 23,936 samples. The models performed well based on MSE, with all masking ratios achieving < 0.01 average MSE. Opposite to the RGB image implementation in [3], where higher masking ratios were required to learn semantic information, higher masking ratios did not result in better performance as shown by the reconstructions in Fig. 1. However, the reduction in performance was not proportional to the masking ratio. A masking ratio comparison between 25 and 75% resulted in an improvement in SSIM of < 0.15 as shown in Fig. 2.

This difference is an example of difficulties applying deep learning advances in medical imaging contexts.

Discussion The observed MSE performance may be misleading. Due to the sparsity of k-space, where most values approach 0, mathematically, the MSE will tend to 0 regardless of high errors calculated from the center portions of k-space which contain more signal. In this regard, SSIM is a second metric to compare models where a low masking ratio of 25% provided the best results. Although a proof-of-concept, real world undersampling in this manner would not be feasible. Pseudorandom undersampling of phase encoding lines, preserving the centre of k-space, is ideal and will be tested in the next iteration of our work.

Conclusion This study presented a proof-of-concept searching for a masking ratio to train a MAE for reconstruction of MRI images. Our results are in line with the idea that applying deep learning advances from natural images to medical images may not always be directly applicable. It is noted that these results may not generalize across other types of MRI contrast and need further study. There is also room for more optimization and investigation of further training in downstream tasks.

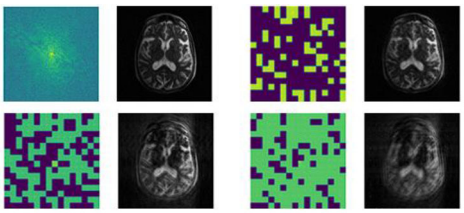

Fig. 1: Top Row: from left to right, the original fully, sampled k-space after preprocessing, a reconstruction of the original, fully sampled coil, the generated k-space values at 25% masking ratio, the reconstructed image using the 25% generated values. Bottom Row: from left to right, the generated k-space values at 50% masking ratio, the reconstructed image using the 50% generated values, the generated k-space values at 75% masking ratio, the reconstructed image using the 75% generated values.

Masking Ratio	Average MSE	Average SSIM
0.75	2.345e-3 Std 0.0115	0.6144 Std 0.1427
0.50	1.363e-3 Std 7.300e-3	0.6622 Std 0.1300
0.25	6.539e-4 Std 0.0448	0.7593 Std 0.1437

Fp212Fig. 2: Table of average SSIM and MSE scores for the three masking ratios. A notable variance in performance across the test set was observed. This was reflected in the large standard deviation values relative to their mean values. This was likely caused by the randomness of the masking pattern as certain portions of k-space are likely more difficult to generate than others.

References

[1] Vaswani et al. Advances in neural information processing systems 30(2017)
[2] Dosovitskiy et al. arXiv preprint arXiv:2010.11929(2020)
[3] He et al. Proceedings of the IEEE/CVF Conference on Computer Vision and Pattern Recognition (2022)
[4] Raghu et al. Advances in neural information processing systems 32(2019)
[5] Knoll et al. Radiology: Artificial Intelligence 2.1(2020): e190007
[6] Zbontar et al. arXiv preprint arXiv:1811.08839 (2018)
[7] Wang et al. IEEE transactions on image processing 13.4(2004): 600-612

Author Index

D

E

F

G

H

I

J

K

L

M

N

O

P

Q

R

S

T

U

V